DECHEMA

BOOK OF FULLPAPER

30 August – 2 September 2026
Salzburg Congress · Austria

13th International Conference on Distillation & Absorption

www.dechema.de/en/da2026

Image source: ©TSG Tourismus Salzburg GmbH / C. Brenegger

EFCE
Event No. 821

COMPANY OVERVIEW

QWP is a leading manufacturer of mass transfer products in the Middle East, with a recently opened branch near Frankfurt, Germany.

CAPABILITIES

Hydraulic and constructive design and manufacturing of standard as well as high-performance trays, random and structured packings, separtion internals, reactor internals, and strainers

PROOF POINTS

- 25+ years of experience
- 100% customer satisfaction
- Worldwide export including supervision and troubleshooting support.

MASS TRANSFER EQUIPMENT

- Structured and random packings
- Support grids and hold-downs
- Sieve trays
- Fixed and floating valve trays
- Bubble cap trays
- Liquid distributors and collectors
- Wire mesh packings

REACTOR INTERNALS

- Catalyst and molecular sieve beds
- Wedge wire screens
- Gratings
- Headers and laterals
- Distributors and collectors
- Moisture probe
- Floating screen

SEPARATION INTERNALS

- High-efficiency demister pads and vane packs
- Heavy-duty vane type inlet devices
- Perforated baffles
- Coalescer plate packs
- Inlet and demisting cyclones
- Sand jetting device
- Dissolvedness
- Candle filters for sulphuric acid plants
- Cartridge filters for special applications

STRAINERS & OTHER PRODUCTS

- Y type strainers
- TEE type strainers
- Basket strainers
- Duplex strainers
- Conical strainers
- Filter elements
- Wire mesh screens
- Perforated metals

TRUSTED SOLUTION PROVIDER FOR VARIOUS INDUSTRIES

OIL & GAS PROCESSING PLANTS

PETROCHEMICAL COMPANIES

WATER PURIFICATION & DESALINATION PLANTS

POWER GENERATION & AIR POLLUTION CONTROL

CONTACT US FOR YOUR NEXT REQUIREMENT
CONSULT OUR SPECIALIZED PROCESS & FILTRATION ENGINEERS.

SEPARATORS & FILTRATION SOLUTIONS

QWP Separations GmbH
Riedstraße 13
67125 Dannstadt-Schauernheim
www.qwp-separations.com

TABLE OF CONTENT

PLENARY 7

LECTURES 14

POSTERS 385

ISBN NUMBER /DOI NUMBER 744

Thank you to our Sponsors and Exhibitors !

GOLD SPONSORS

QWP SEPARATORS & FILTRATION SOLUTIONS

RUHR UNIVERSITÄT BOCHUM RUB Laboratory of Fluid Separations

SILVER SPONSORS

Armour Packing Resistant to all acids, at any temperature.

ENVIMAC Engineering GmbH

HMT HANBAL MASSTECH LIMITED MASS TRANSFER TECHNOLOGY

SPONSORS

IPS Inline Process Solutions

KOCH-GLITSCH™

QWP SEPARATORS & FILTRATION SOLUTIONS

rvt

SULZER

WILEY VCH

EXHIBITORS

benit M MASS TRANSFER PROCESS

RUHR UNIVERSITÄT BOCHUM RUB Laboratory of Fluid Separations

QWP SEPARATORS & FILTRATION SOLUTIONS

Armour Packing

PURE SiC.
PURE PERFORMANCE.

Silicon Carbide Ceramic
Wire Mesh Structured Packing

World's First. Built to Last.

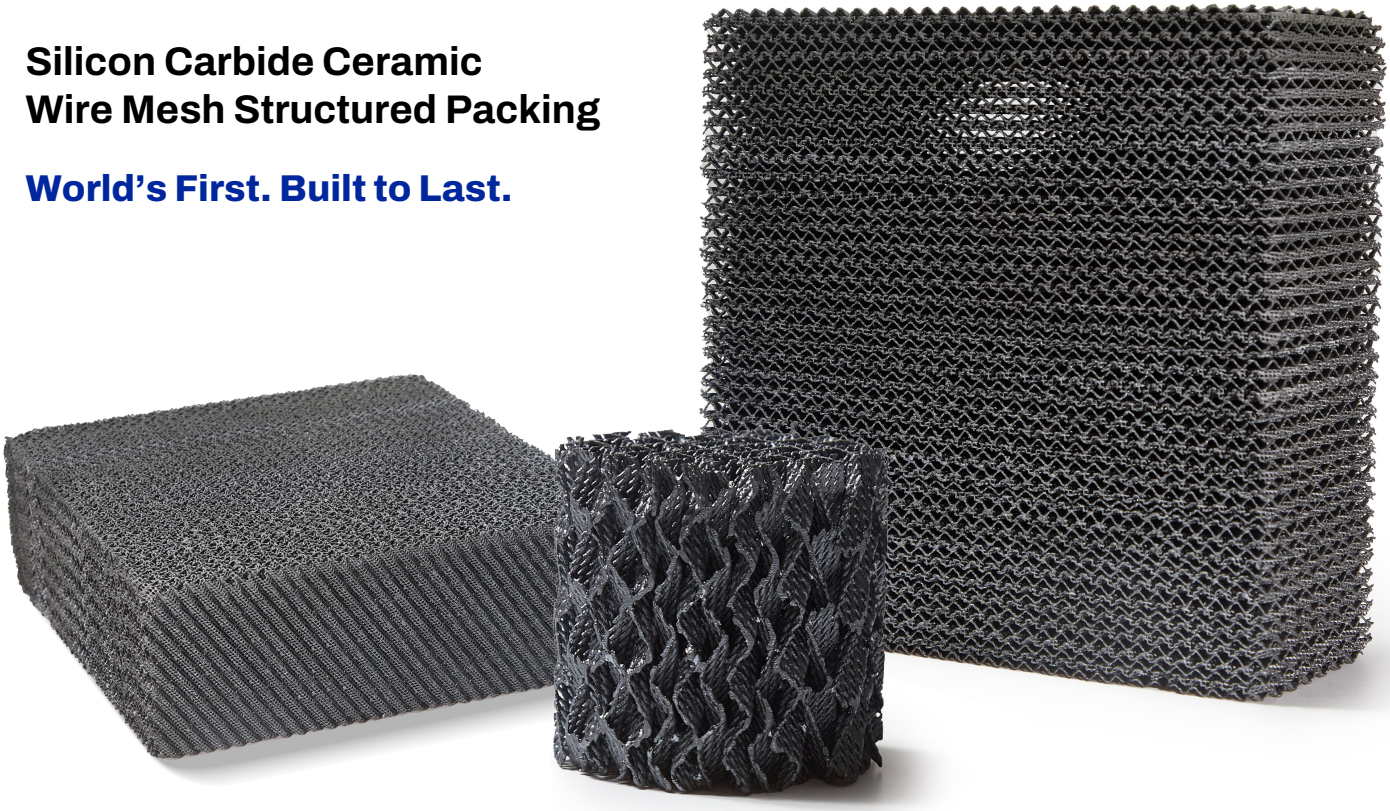

PURE SiC CERAMIC
No metal, no corrosion. Engineered for extreme chemical environments.

ULTIMATE CORROSION RESISTANCE
Outstanding resistance to ALL aggressive acids.

WIRE MESH STRUCTURE
Similar to metal wire mesh packing, maximized efficiency.

Scan for Technical Data & Free Sample

www.armourpacking.com

info@armourpacking.com

RESISTANT TO ALL ACIDS ANY TEMPERATURE

Plenary

Can High Subcooling Cause Premature Flood?

Henry Z. Kister and Michael D. DeBest
Fluor Corporation, Aliso Viejo, CA, USA

SUMMARY

"Subcooling flood" is recognized by premature heavy flooding of the downcomer(s) from the feed tray, propagating downwards but easing off as one descends the tower. A number of trays down the flood completely disappears. Our analysis of data from such case studies revealed that they tend to occur with wide-boiling multicomponent mixtures where there is a path for lights to penetrate downwards past the feed tray. These lights flash in the downcomers below the feed and choke them. The feed tray downcomer is affected most, with the downcomers below progressively less affected. This paper presents key cases, provides mechanistic explanations and diagnostics, and reviews some fixes. The lessons learnt are invaluable for achieving trouble-free design and operation of distillation towers with subcooled multicomponent feeds or refluxes.

KEYWORDS

Subcooling, premature flood, flood, downcomer choke, gamma scans, trays flood

BACKGROUND

"Subcooling floods" are associated with highly subcooled multicomponent feeds or refluxes and occur at much lower hydraulic loads than anticipated flood limits. They cause major capacity bottlenecks.

"Subcooling flood" was first mentioned by Chen et. al.[1] who reported a multicomponent distillation tower with a subcooled feed where replacement of trays by packing gave poor HETP and off-spec bottom product. Preheating the feed to the bubble point solved the problem. Years later, Tru-Tec's Sample Scan Brochure[2] contained a subcooling flood gamma scan (Figure 1) of a refinery deethanizer-absorber column whose feed preheater was bypassed, making the feed 60-80°F colder[3] than the feed tray liquid. Figure 1 shows flooding on trays 12-24 below the feed and no flooding above. The flood was most severe on trays 12-20 and appears to gradually subside between trays 21 and 25. Trays 26 to 29, as well as trays 30-40 (Figure 1 only goes to 29) had froth heights mid-way up the tray spacing, and the vapor peaks approached clear vapor, indicating tray operation a comfortable margin away from flood. Tru-Tec's brochure states, "Conditions when the column comes out of a flooded condition in gradual degrees of entrainment are usually indicative of subcooled stream entering the tower." In that tower, when the feed preheater was operational, the flood disappeared[3].

The explanation provided by Tru-Tec[2] is "A subcooled stream will take heat out of the tower and thus condense a significant portion of the vapor. This condition can easily overload the downcomers with liquid and cause flooding inside the tower. Some vapor/liquid disengagement will begin to occur once enough heat can be obtained from the condensing vapor to bring the liquid back up to its flash point".

Figure 2 challenges the above explanation. The internal reflux below the point where the subcooled reflux reaches its bubble point is given by

$$R_I = R_E \left(1 + \frac{Cp\,\Delta T}{\lambda}\right)$$

Where R_I is the internal reflux, lb/h, R_E the external reflux, lb/h, λ the latent heat, Btu/lb, ΔT temperature, °F, and Cp the specific heat, Btu/ lb °F.

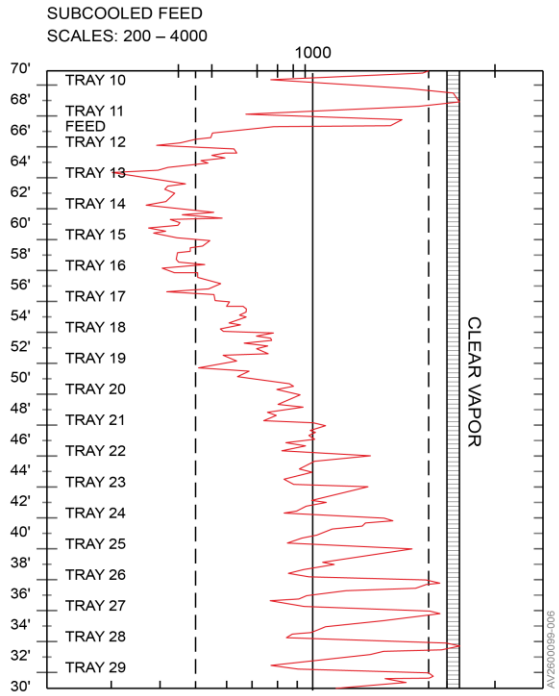

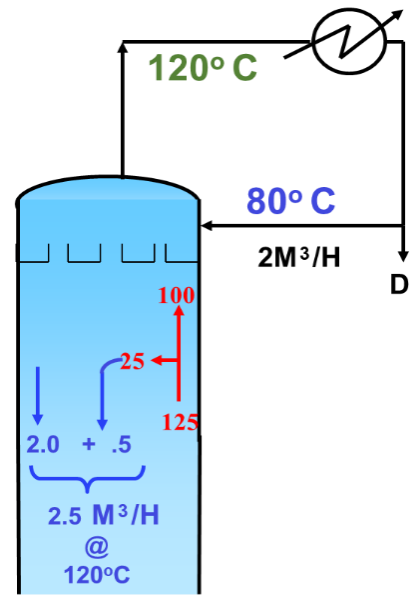

Figure 1: Gamma scan of a deethanizer-absorber with subcooled feed (*from Reference 2. Courtesy of Tracerco*).

Figure 2: The effect of reflux subcooling on vapor and liquid loads *(from Reference 6. Reprinted with permission).*

In Figure 2, the reflux is subcooled by about 40°C. Upon entry the subcool condenses 25 units of vapor, generating 0.5 m^3/h additional liquid traffic. The maximum hydraulic loads are 125 units vapor, 2.5 m^3/h liquid. These will be the maximum hydraulic loads regardless of whether the condensation takes place at the feed point or over many trays. If gradual, the trays immediately below the feed will be less hydraulically loaded than the trays further down. The flooding will take place once the maximum hydraulic loads are reached. Figure 1 shows the flooding to peak at the feed point, subsiding as one descends the column. A similar example and conclusion were presented by Chou[4]. While the explanation remains elusive, Tru-Tec's observations are realistic and concur with ours. A gamma scan showing heavy flooding initiating at a feed or reflux entry point, easing off over several trays and eventually disappearing, is often associated with subcooled feeds or refluxes. As in Figure 1, this subcooling flood is premature and bottlenecks towers. A valid explanation is key to determining when to anticipate and how to debottleneck a subcooling flood.

DOES A SUBCOOLING FLOOD REQUIRE SUBCOOLING?

Subcooling flood with no subcool? Strangely, gamma scans of premature floods with flashing feeds often give the appearance of Figure 1. A common thread is that all these premature floods occurred in wide-boiling multicomponent systems. For one debutanizer with flashing feed[5] we have extensive data on the problem and successful solution, but not on the flood mechanism. Premature flood occurred when charge rate or reflux were excessively raised. Here we revisit the data seeking the premature flood mechanism. Figure 3 shows the gamma scans through the tray active areas. Below the feed the hydraulic liquid and vapor loads for the "increased reflux" (red) scan were 3% and 5%,

respectively, higher than for the “normal reflux” (blue) scan. The red scan shows flood initiating at the feed and propagating into the upper trays. Below the feed, the trays with side downcomers were flooded, with the flooding subsiding from tray 16 to 26. There was no flooding below tray 26. The flooding on the trays with center downcomers was less pronounced, subsided as one descended the tower, and completely disappeared below tray 19.

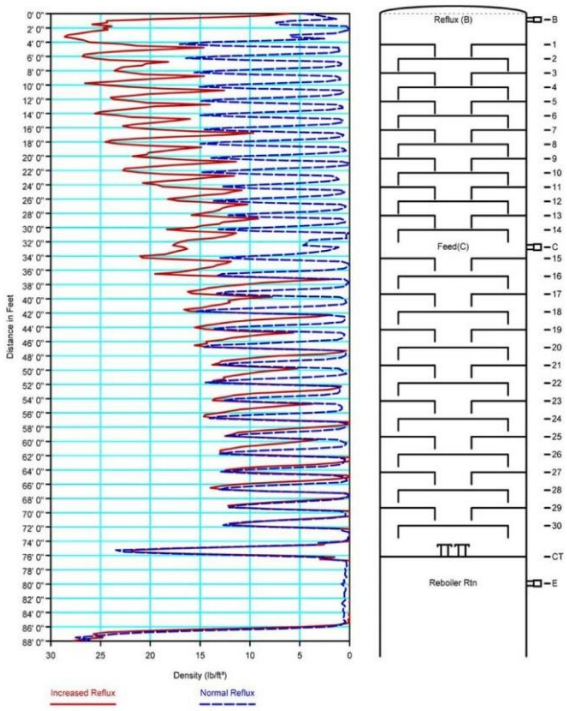

Figure 3: Scan of a debutanizer column that experienced premature flooding *(from Reference 5. Reprinted with permission).*

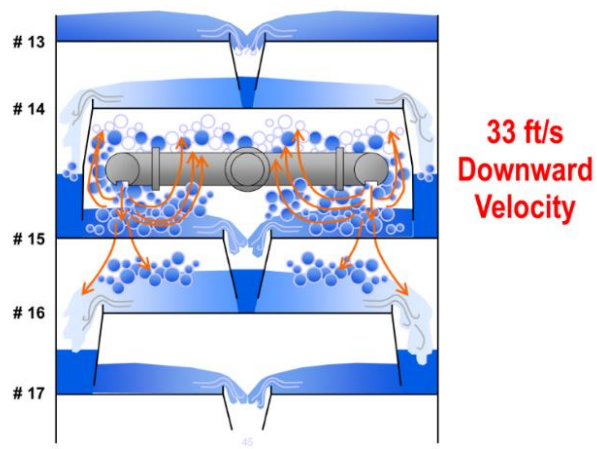

Figure 4: Cause of the premature in the debutanizer *(from Reference 5. Reprinted with permission).*

Table 1: Hydraulic Calculations at the Debutanizer premature flood point (*from Reference 6. Reprinted with permission***).**

	Above Feed	Below Feed	Bottom Trays
C_{NET}, ft/s	0.22	0.13	0.19
Weir load, gpm/in	5.6	11	13
Downcomer entrance velocity, ft/s	0.31	0.44	0.52
% Jet flood	55	39	56
% Froth in Downcomer	56	56	69
% DC choke	71	55	72

Unlike Figure 1, in this case the flood propagated above the feed. Whether the flood propagates to the upper trays depends on the design and geometry of the feed zone and on the design and hydraulic loadings of the upper trays. We have seen subcooling floods with or without propagation to the section above. Common to all is premature

flood initiating at the feed or reflux entry point, easing off as one descends the column, eventually disappearing.
Figure 4 shows the cause of the premature flood. The flashing feed was discharged via downward-oriented slots in the feed pipes at a mixed phase velocity of 33 ft/s, or ρv^2 of 6000 lb/ft sec^2 where ρ is the mixed phase density, lb/ft^3, and v is the mixed phase velocity, ft/s. Besides excessive turbulence and feed re-entrainment, this huge velocity is likely to have caused penetration of the 2-phase feed through the moving valves on the tray floor into the downcomer below. This penetration overloaded trays below the feed and induced lights into their downcomer liquid. Both actions were[5] the root cause for the premature flood. Reducing the velocity and directing the feed away from the tray floor to the outside wall of the downcomers from the tray above eliminated the premature flood.
Table 1 summarizes our hydraulic calculations at the debutanizer flood rate. The C-factor C_{NET} ft/s represents the vapor load, given by

$$C_{NET} = u_{NET} [\rho_V / (\rho_L - \rho_V)]^{0.5}$$

Where u is the vapor velocity, ft/s, ρ is the density, lb/ft^3, subscripts v and L signify vapor and liquid, respectively, and the subscript NET signifies the net area, i.e. the tower area less the area at the top of the downcomer(s).
The vapor and liquid hydraulic loads for the bottom trays (28-29) were 30% and 17%, respectively, higher than just below the feed (trays 16-17), where the flood initiated. The calculated percent flood is also lower on the trays below the feed. The question is then what caused the trays just below the feed to be the first to flood.
Penetration of feed liquid through the valves to the trays below would not overload them, as this liquid would have normally reached these trays. In contrast, vapor penetration below the feed would overload the trays. This vapor would normally separate at the feed zone and flow up, not reaching the trays below.
This penetration would have been similar for the “increased reflux” (red) and “normal reflux” (blue) scans as the feed was unchanged. As the “normal reflux” scan shows the active areas of the trays below the feed nowhere near flood, jet flood (which initiates in active areas) can be ruled out. The flood is therefore a downcomer flood.

POOR MIXING AT THE FEED LEADS TO SUBCOOLING FLOOD

A column using heavy-naphtha (HN) absorption oil to absorb heavies from a gas stream flooded prematurely when either the reflux or the HN flow rates were raised. The flood, indicated by a differential pressure rise, was insensitive to vapor feed or boilup rates. The trays were 4-pass moving valve trays with truncated downcomers.
The dashed green and blue scans on Figure 5 are the unflooded active area and center downcomer (CDC) scans, respectively, of the trays below the HN feed. The solid red scan is the CDC scan at incipient flood. The CDC from the feed tray is heavily flooded. The CDC flooding gradually subsides as one descends the tower. About 10 trays down the CDC’s look the same in the incipient flood and unflooded scans. Figure 5 supports a downcomer flood, as the active areas in the unflooded scan were not highly loaded, while the CDC’s were. Our hydraulic evaluation (similar to Table 1) shows that none of the tray limits were approached. The C-factors were less than 0.25 ft/s, weir loads ranged from 4.0 to 5.7 gpm/in, the trays should have operated at 61% of jet flood, 48% downcomer backup flood, and 53% of downcomer choke. Our calculations also showed absence of vapor or liquid maldistribution on the 4-pass trays.

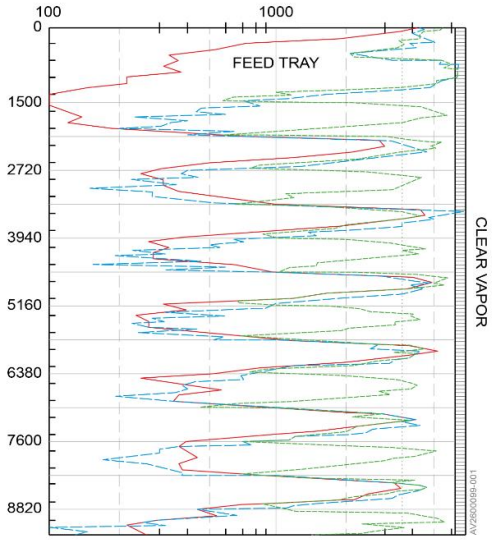

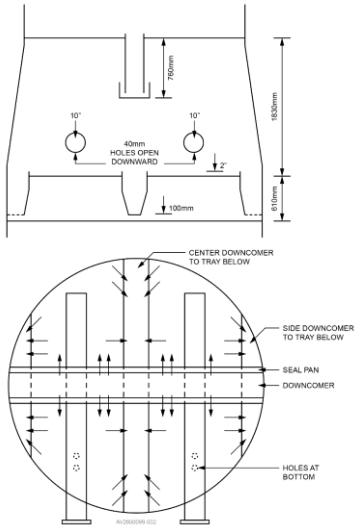

Figure 5: Cold fractionator scans **Figure 6:** Cold fractionator feed zone

Figure 6 (roughly-to-scale) shows 50°F HN issuing downwards at 7.5 ft/s from holes in the 10” feed pipes. The 2-pass tray above the feed zone was rotated 90° to the 4-pass feed tray, terminating in a central seal pan that discharged 5°F reflux via cutouts in its overflow weir. Liquid out of the seal pan free-fell about 3.5 feet, accelerating by gravity to hit the tray floor at 11 ft/s. There would be minimal mixing between the descending reflux and the HN feed. In the downcomer the warm HN would mix with and heat the light reflux, flashing lights that would choke the downcomer and cause a premature subcooling flood. Some of the cold liquid would penetrate into the tray below, causing a lesser choke in the next downcomer. Eventually mixing will be complete and the flooding die down. A well-designed chimney tray at the feed can mitigate the premature flood.

LOW VAPOR PRESSURE LEADS TO SUBCOOLING FLOOD

Another tower that flooded prematurely received a subcooled feed. The degree of subcool is unknown due to measurement issues, but we believe it to be within plus or minus 20°F from the design subcool of 50ºF. The scan (Figure 7) shows flooding at the feed tray (tray 4) propagating upwards, with the subcooling flood pattern 2-3 trays below the feed, down to tray 7. The calculated C-factor for the tray below the feed was 0.18 ft/s based on the bubbling area, the weir load 4.3 ft/s, which put it at 61% of jet flood and 66% of downcomer backup flood. The downcomer inlet velocity was 0.15 ft/s giving 64% of downcomer choke. Again the tray did not near any calculated limit. The feed arrangement (Figure 8) was well within good practice guidelines[7]. The feed issued at 2.3 ft/s from slots in the feed pipe directed 45° towards the downcomer wall (Figure 8).
With a subcool of between 30°F and 70°F, the feed vapor pressure would have been 50-150 psi lower than the tower pressure. Upon entry, the dew point vapor in the tower feed zone would collapse onto the subcooled feed, causing high local velocities and turbulence, which could have induced some of the subcooled lights-rich feed to enter the downcomer and also to penetrate to the tray below via the moving valves on the tray. The lights would flash in the feed tray downcomer, and to a progressively lesser degree in the two downcomers below, giving the familiar subcooling flood pattern.

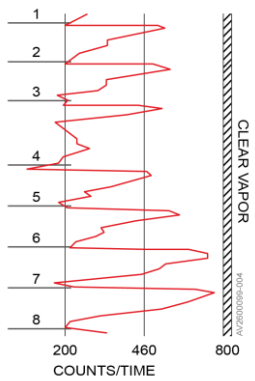

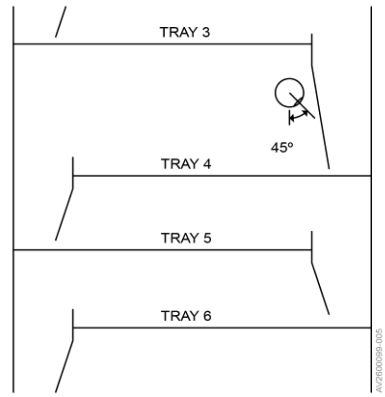

Figure 7: Highly subcooled feed tower scan **Figure 8:** Highly subcooled feed entry

TAKEAWAYS

Subcooling floods are associated with wide-boiling multicomponent mixtures in where a lights-containing feed (often, but not necessarily, subcooled) penetrates downwards past the feed tray. These lights flash and choke downcomers below the feed. The feed tray downcomer is the most prone, with the downcomers below progressively less affected. Subcooling floods occur at operating rates for which the hydraulic calculations indicate operation a comfortable margin below flood. All the subcooling floods we encountered were premature downcomer floods.

A subcooling flood is readily recognizable by tray active area or downcomer gamma scans. It shows up as a flood initiating at the feed point. From the feed point the flood may or may not propagate up the tower. The unique identifying feature of subcooling flood is that it propagates downwards, progressively subsiding as one descends from the feed. It may subside over as few as 2 or 3 trays or as many as 10 or more trays. Sketching the feed entry may reveal a path for lights or feed vapor to descend past the feed tray. Comparing the bubble point pressure of the subcooled feed to the tower pressure gives insights; a large (>20-30 psi) difference signifies possible collapse of column vapor onto the subcooled feed, inducing poor mixing and lights penetration. Reducing subcooling and preheating the feed are obvious cures, but not always economical. Modifying the feed entry piping and avoiding penetration of feed vapor through the tray floor have been effective. Improving mixing of the feed with the tray liquid has alleviated subcooling floods. Finally, replacing the feed tray with a well-designed chimney tray flashes the lights before they bottleneck the downcomers below.

REFERENCES

1. Chen, G. K., T. L. Holmes, and J. H. Shieh, Effects of Subcooled or Flashing Feed on Packed Tower Performance", IChemE Symp. Ser. 94, p. 185, 1985.
2. Tru-Tec Division "Sample Scan Brochure", p.14, 1998 (available from Tracerco, Inc., Pasadena, Texas)
3. Carlson, Ron (Tru-Tec), private communication, 1996.
4. Chou, Y. "Understand the Potential of Subcooled Distillate Condensate", Chem. Eng. Progr., p.59, June 1992.
5. Kister, H. Z., D. E. Grich, and R. Yeley, "Better Feed Entry Ups Debutanizer Capacity", PTQ Revamps and Operation, 2003.
6. Kister, H. Z., "Practical Distillation Technology", course manual, 2025.
7. Kister, H. Z., "Distillation Operation", McGraw-Hill, NY, 1990.

Lectures

Perspectives on Electrification and Flexibility for Distillation and Absorption Processes

Julia Riese[1]
[1]Fluid Process Engineering, Paderborn University, Paderborn, Germany

Abstract
The reduction of CO_2-emissions in the industry is a key factor to meet European climate targets. In particular, the reduction of burning fossil fuels to supply process heat needs to be addressed. Therefore, measures to electrify the process industry are of particular interest. By doing so, low-carbon electricity is used directly or indirectly on equipment, process or utility level. Direct electrification can be facilitated by measures such as Joule heating which leads to a discrete and direct electric heating within the respective equipment. Thus, tailored temperature profiles can be achieved. In contrast to this, electrowetting can be used to achieve tailored fluid dynamics of liquid films on solid surfaces. By applying a sufficient voltage, the wettability of surfaces can be improved which leads to more efficient separation processes. On the other hand, indirect electrification is enabled by the integration of open- or closed-loop heat pumps. Heat pumps enable the upgrading of low-temperature waste heat to a higher temperature level. The integration of heat pumps into separation sequences can be achieved by the development of screening algorithms that allow for informed decision making even for integration problems with very high number of degrees of freedom.

Keywords
Process dynamics, Joule heating, Electrowetting, Heat pumps

1. Introduction

Economic boundary conditions, consumer demands and the overarching challenge of mitigating climate change drive the industry to adapt their way of production by using the todays available assets to cut costs if possible. In this manner, chemical industry relies on distillation and absorption/desorption processes as the work horses in different areas like processing materials from bulk to fine chemicals and cleaning waste streams before being released into the environment. Since many decades, effort is put into the improvement of mass transfer performance, including the development of advanced packings structures or process intensification measures. As an additional result of these efforts, energy savings and thus cost reductions were achieved.

However, in recent years, the perspective broadened and an improvement of energy efficiency together with surrounding utility systems came into focus. [1] This more holistic perspective was caused by recent economic pressure on European (chemical) industry originating from geopolitical developments as well as technological developments like high-temperature heat pumps or direct heating technologies. Therefore, and to reach European climate targets, electrification is one of the key elements for sustainable manufacturing and production [2]. In chemical

industry, electrification can be facilitated in a direct way, e.g. by electrically heated boilers or equipment-integrated Joule heating, or in an indirect way, e.g. by the integration of open- or closed-loop heat pump cycles.
In the following, measures for both direct and indirect electrification are discussed, highlighting the challenges and possibilities those measures enable for absorption/desorption and distillation processes as well as for overall separation sequences.

2. Direct electrification in thermal separation

The three main tools for direct electrification in chemical engineering are Joule heating, microwave heating and induction heating. In reaction engineering, plasma also plays an important role in decarbonizing chemical synthesis. Whereas microwave enhanced separation is an important topic in process intensification, Joule heating enables new possibilities for direct electrification in unit operations.

2.1 Joule heating in thermal separation

Joule heating, or resistive heating, allows for the direct production of heat by applying an electric current though a conductor. This method allows for high energy efficiencies and, compared to the other methods, high scalability as well as retrofit opportunities. In recent years, this method was used together with tools from additive manufacturing to produce and test catalytic [3] and non-catalytic [4] structures that are directly electrified. Apart from the reduction of needed fossil fuels to operate the respective unit operations with steam for the evaporation process streams, the direct electrification allows for more dynamic process operation and overall compact systems.
By combining direct electrification with advanced manufacturing methods such as 3D printing, new degrees of freedoms are introduced with respect to fluid dynamics as well as tailored temperature profiles to increase separation efficiency. Figure 1 shows the idea of direct electrification using distillation as an example. By directly integrating the resistive heating elements into e.g. the structured packings tailored characteristics of power profiles can be realized. By applying sufficient power electronics, which of course is a major challenge, even time-dependent profiles are possible. This enables new possibilities for dynamic operation as rapid changes with low time delays are possible.

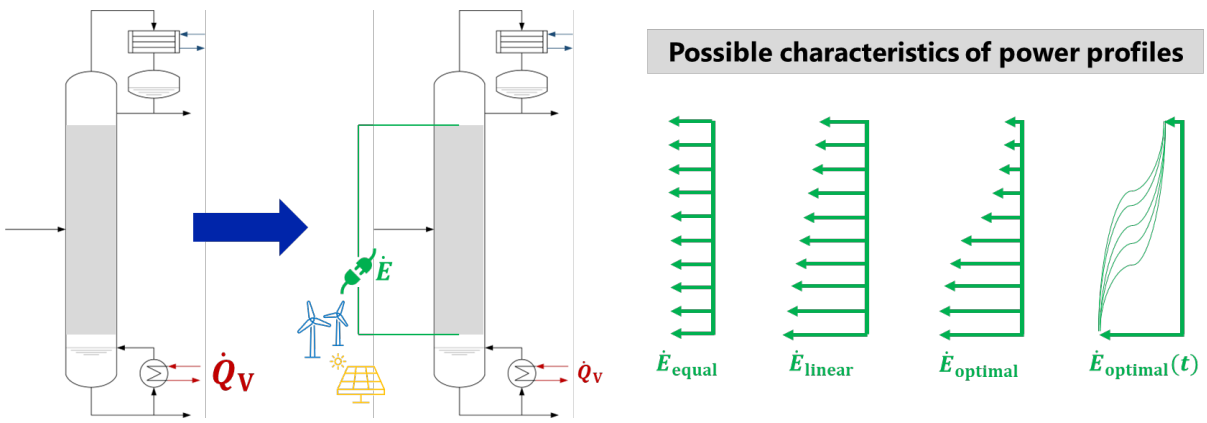

Figure 1: Implementation of direct heating in unit operations exemplified by distillation.

In a recent preliminary theoretical study, we applied the principle of direct heating to the desorption of CO_2 [5]. Results show the potential of tailoring power profiles to process needs. However, major challenges arise in material development and integration of the electric functionality.

2.2 Electrowetting

The phenomenon of electrowetting came back into focus due to the attempts to electrify the chemical industry [6]. Electrowetting describes the phenomenon that by applying a direct current to a conductive material the surface tension between the liquid, the surrounding fluid and the solid material is affected according to Young's relation. Here, the total surface tension is dependent on chemical and electrical characteristics and it follows, according to the principle of electrowetting, that the contact angle is decreased by applying a surface voltage. Looking at conventional absorption and distillation processes using structured packings the contact angle is a crucial parameter strongly influencing the available effective surface area for heat and mass transfer. To evaluate the potential of electrowetting for unit operations like distillation and absorption, initial guiding experiments were conducted: firstly, dynamic contact angle measurements were performed, and secondly, a scale-up approach was followed with water flowing over an inclined steel sheet. In both cases, a specific voltage was applied to the conductive material.

Dynamic contact angle measurements showed a significant reduction of both the advancing and receding contact angle by applying voltages between 1 and 3 V. The advancing contact angle was reduced by appr. 20° whereas the receding contact angle was decreased close to 0° on different sized of circular packing sheets cut-outs.

As the results from the dynamic contact angle measurements showed promising results, a set-up was designed that allows for the testing of different masses and surface sized of the electrodes as well as different liquid loads over a larger inclined steel plate. The experimental set-up is show in the left part of Figure 2.

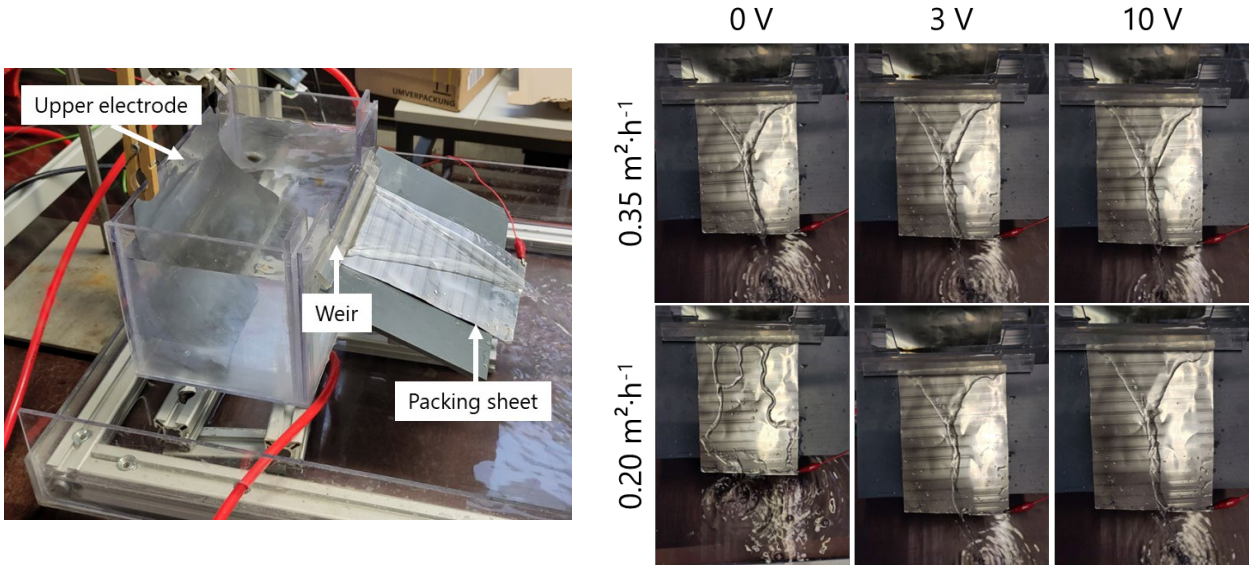

Figure 2: Experimental set-up for the assessment of electrowetting (left) and images of the liquid flow over the flat plate for different voltages applied (right).

As can be seen from the results presented in the right part of Figure 2, the effect of electrowetting seems to be smaller when applied to a moving liquid. Nevertheless, the wetting behavior on the inclined steel plate can clearly be influenced by applying a voltage to the packing sheet. A more precise evaluation of the results showed that the confluence point representing the distance from the inlet to the point where the liquid film breaks up can be enlarged up to four-fold, especially for low liquid loads by applying only a small value for the voltage (e.g. 3 V). Further investigations using aqueous NaOH-solution showed a further increase of the effect of electrowetting. This is due to the increased conductibility of the liquid that flows over the inclined plate which also has an effect on the flow pattern in combination with the voltage applied.
Additionally, the results obtained indicate that the voltage applied can be used as an additional degree of freedom to tune the wetting behavior according to the specific liquid load. This enables more efficient operation under variable process conditions. However, the free flow path for the liquid on the inclined packing sheet is non-representative for real packings structures and was only used to successfully validate the effect of electrowetting for moving liquid flows. Before technical implementation, further systematic investigations on influencing factor above all liquid and surface properties are necessary.

3. Indirect electrification

Indirect electrification can be facilitated by the integration of open- or closed heat pump cycles either close to the equipment or on utility level. Although, the concept of mechanical vapor recompression is known for decades, industrial implementation is still scarce. This is due to the fact that numerous challenges arise when integrating open- or closed-loop heat pump cycles: choice of the correct integration point and the correct placement of the heat pump, respectively, scale of the heat pump integration (e.g. centralized or decentralized), combination with already existing heat integration or available heat integration potentials as well as choosing the best technology and cycle layouts for a given problem. Recently, Adami et al. published a series of work tackling main points of named challenges systematically for single or coupled distillation columns [7-9].
Looking at overall separation sequences, complexity regarding integration increases. As numerous process streams need to be heated or cooled according to set process conditions, the combinatorial problem of the integration task becomes more complex compared to one or two columns. Coping with these challenges is possible by the development of appropriate screening methods in combination with subsequent optimization of resulting, promising integration points.
One of the first question arising when dealing with numerous hot and cold streams is weather to integrate heat pumps centralized or decentralized. The difference between both possibilities is shown in Figure 3 (left) schematically for two columns: a central heat pump collects waste heat streams and cascades the upgraded heat according to the needed temperature levels while decentralized heat pumps are integrated at each unit operation individually. Screening for the one or the other possibility, or a compromise between both is necessary when dealing with numerous hot and cold streams. Therefore, a sufficient screening criterion was defined, e.g. the

temperature difference between the streams as a lower temperature difference allows for higher efficiency. Additionally, an evaluation criterion was defined. This can be CAPEX, OPEX, TAC, CO_2-emissions or a combination of those. [10]

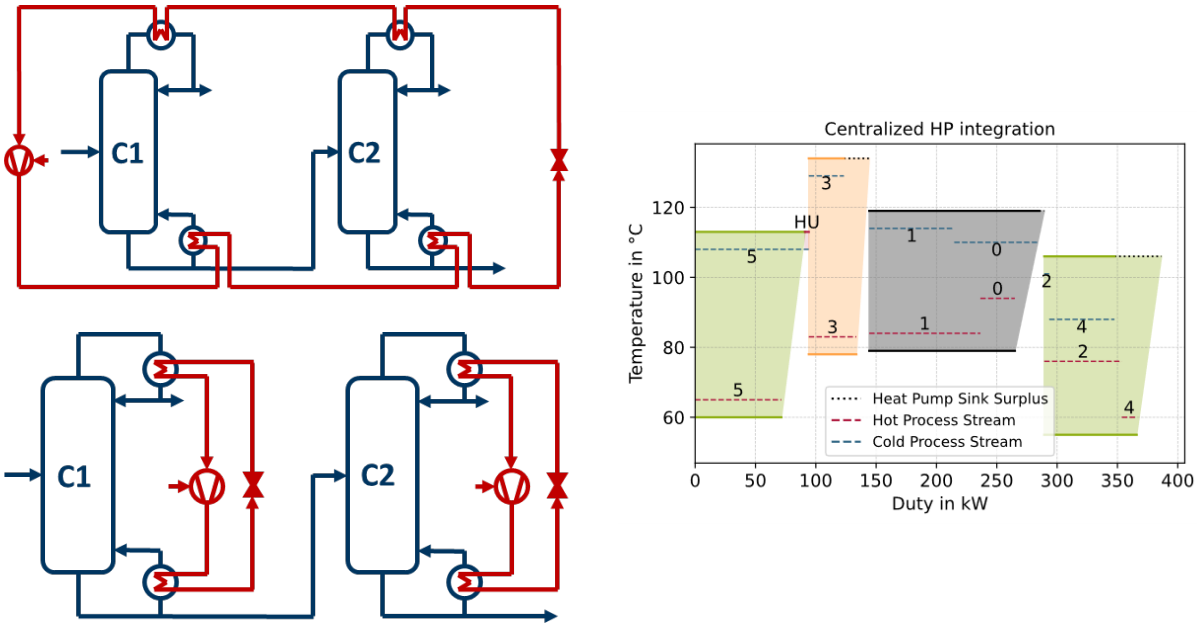

Figure 3: Central and decentral integration of a closed heat pump exemplified with two distillation columns (left), exemplary results of the screening for efficient heat pump integration (right).

Exemplary results of the screening are shown in Figure 3 (right) for the case of six hot and six cold streams. Any utilities were neglected in this example. Each colored area represents a heat pump either integrated in a centralized manner or in a decentralized manner. Centralized heat pumps were chosen to combine the streams “0” and “1” (dark gray area) as well as for the streams “2” and “4” (far right green area). Using the CO_2-emission as evaluation criterion, reduction in CO_2-emissions were achieved by appr. 50% compared to supplying all necessary process heat by burning natural gas.

The advantages of screening algorithms is that efficient calculation for high numbers of streams is possible. Computing time is below one second even for higher numbers of streams. Additionally, fast computing of different evaluation criterion is possible. However, it needs to be stated that fast screening does not guarantee optimal solutions.

4. Conclusions

Electrification of chemical processes is an essential tool to reduce dependencies on fossil fuels in the future and subsequently reach set climate targets. In principle, measures for electrification can be implemented directly e.g. on equipment level by Joule heating or indirectly, e.g. on process level by heat pump integration. However, for both possibilities there are no “one-size-fits-all” solutions, making the future implementation rather challenging.

Direct electrification measures are currently being investigated intensively in the area of reaction engineering and significant progress is also made in the area of

temperature-swing adsorption where direct heating enables for faster cycles and more efficient recovery of the adsorbed molecule. When transferring the idea of direct electrification to other unit operations like distillation and absorption, comprehensive knowledge from those areas can be leveraged. On the other hand, challenges are similar such as material development, equipment design, scalability and power electronics.

Indirect electrification using open- or closed-loop heat pumps seems to be old news. However, more complex integration tasks e.g. in separation sequences or at process scale demand for additional methods to support decision making. Most importantly, fast evaluation of different scenarios applying various evaluation criteria in extensive sensitivity analyses is demanded by industry to cope with a insecure and highly dynamic decision space.

References

[1] R.T. Gooty, J.A.C. Velasco, R. Agrawal, Methods to assess numerous distillation schemes for binary mixtures. *Chemical Engineering Research and Design*, 172 (2021), 1-20, doi: 10.1016/j.cherd.2021.05.022.

[2] P. Sorknæs, R.M. Johannsen, A.D. Korberg, T.B. Nielsen, U.R. Petersen, B.V. Mathiesen, Electrification of the industrial sector in 100% renewable energy scenarios. *Energy*, 254 (2022), 124339, doi: 10.1016/j.energy.2022.124339.

[3] H. Karibe, S. Sair, A. Faik, H.A. Ousaleh, Electrified steam methane reforming: A review of heating technologies, challenges, and prospects. *International Journal of Hydrogen Energy*, 133 (2025), 200-213, doi: 10.1016/j.ijhydene.2025.04.475.

[4] B. Verougstraete, M. Gholami, Y. Gomez-Rueda, E. Pérez-Botella, M. Schoukens, T.R.C. Van Assche, J.F.M. Denayer, Advancements and challenges in electric heating for enhanced temperature swing adsorption processes. *Separation and Purification Technology*, 353 (2025), 128522, doi: 10.1016/j.seppur.2024.128522.

[5] N. Lutters, S. Brüne, J. Riese, Preliminary Numerical Evaluation of Directly Heated Structured Packings to be used for Separation Processes. *Chemie Ingenieur Technik*, under review.

[6] A.A. Papaderakis, R.A.W. Dryfe, The renaissance of electrowetting. *Current Opinion in Electrochemistry*. 38 (2023), 101245, doi: 10.1016/j.coelec.2023.101245.

[7] M. Adami, F. Kayenat, M. Skiborowski, Electrifying distillation − Optimization-based evaluation of internally heat-integrated distillation columns. *Separation and Purification Technology*, 360 (2025), 131061, doi: 10.1016/j.seppur.2024.131061.

[8] M. Adami, J. Schnurr, M. Skiborowski, Electrified distillation – Optimized design of closed cycle heat pumps with refrigerant selection and flash-enhanced mechanical vapor recompression. *Applied Thermal Engineering*, 273 (2025), doi: 10.1016/j.applthermaleng.2025.126559.

[9] M. Adami, D. Espert, M. Skiborowski, Rapid multi-criteria screening of energy-integrated distillation processes for nonideal mixtures. *Separation and Purification Technology*, 377 (2025), 134463, doi: 10.1016/j.seppur.2025.134463.

[10] T. Hochhaus, M. Grünewald, J. Riese, A conceptual approach to heat pump integration in chemical processes. *Annual Meeting Process Engineering and Materials Technology*, 2024.

Interactions of column internals and electrification strategies of separation processes for the optimization of the energy management

Carmen De Santiago[3], Henrik Fasel[2], Lea Wessner[2], Armin Rix[1], Niklas Paul[2], Ralf Höchemer[3]

[1] Evonik Operations GmbH, NextGen Technologies, Marl, Deutschland

[2] Evonik OXENO GmbH & CO KG, Marl, Deutschland

[3] Sulzer Chemtech Ltd, Winterthur, Switzerland

Abstract

In separation processes, heat pumps and vapor recompression can be used effectively to recycle waste heat and condensation heat within the process. Particularly in distillation processes with high throughputs and reflux ratios (e.g., C2- or C3-splitter), the economic attractiveness increases due to reduced compressor costs and increased potential for operating cost savings.

In contrast, wide-boiling mixtures show high temperature differences between top and bottom, resulting in high compression ratios, multi-stage compressors with high duty and low coefficients of performance for these technologies. Consequently, innovative and, above all, economically attractive solutions are needed to achieve the ambitious climate targets of the process industry and society.

This paper presents a real revamp case demonstrating that column internals play a critical role not only in optimizing vapor recompression and heat pump technologies but also in enhancing the energy efficiency of conventional separation processes.

The results show that the modification of column internals saved several thousand tons of CO_2 and several hundred thousand euros, leading to a promising path toward a CO_2-neutral process industry.

Key words

Distillation, vapor recompression, heat pump, column internals, UFM™, energy optimization.

1. Introduction

As climate change progresses and has widespread effects on ecosystems, economies, and societies worldwide, there is an urgent need to pursue decarbonization. This involves reducing carbon dioxide emissions by implementing clean energy, efficiency measures, and innovative technologies. One of the biggest levers to reduce human-made CO_2 emissions is the decarbonization of the energy sector (Papadis and Tsatsaronis, 2020). One of the major energy consumers is the chemical industry (Asprion et al., 2024). This results in emitting approximately 2 billion metric tons of CO_2

($GtCO_2$) annually, including both direct and energy emissions, accounting for roughly 5% of global greenhouse gas (GHG) emissions (P. Gabrielli et al., 2023).
One major lever to reduce the energy consumption of the chemical industry is to optimize the separation processes. Separation systems are typically applied to recycle raw materials that have not been converted and remove unwanted by-products. To reduce the energy demand of separation systems, the first and most promising step is to challenge the conversion and selectivity of these reactions. By reducing the formation of by-products, it is possible to decrease the effort required for by-product removal or even eliminate some separation steps altogether, resulting in simplified separation processes. Next, energy-saving separation sequences and heat integration can offer significant potential for reducing energy demand (Jobson, 2014). There are heuristic approaches for optimal heat integration within chemical industry (Rix et al. 2019). Furthermore, energy consumption is also driven by column internals, as the operation range and the design of the internal itself determine the separation efficiency and capacity. Choosing the right internals for the separation process is therefore crucial for an energy efficient operation.
Distillation accounts for more than 90% of fluid separations. Several thousand distillations columns are in operation (M. Skiborowski, 2023). Its main advantages include its versatility, the ability to produce products of specified purity in a single step, and the availability of design software with appropriate models for vapor-liquid equilibrium (VLE) and hydraulics, as well as support from internals manufacturers with their experience and reliable hydraulic calculations. However, the major disadvantage of distillation is its high energy demand, which often accounts for a significant portion of the operational costs of process plants. The steam used in the reboilers of distillation columns is typically generated from fossil fuels, resulting in a significant carbon footprint.
In most distillation columns, the amount of energy supplied to the reboiler is nearly identical to the amount removed in the condenser at lower temperature. The energy is thus not consumed, but merely degraded. The condensation duty is a low-quality waste heat. To recycle this waste to the column, the overhead vapor stream can be upgraded by compressing it to a sufficiently high condensation temperature to heat the reboiler. Thus, mechanical work counteracts the exergy loss occurring inside the column.

Heat pump and vapor recompression technologies are two methods that can be utilized to upgrade waste heat such as condensation energy, substituting fossil fuels with green electricity.

Heat pump applications need additional equipment compared to direct vapor recompression. While heat pump technology can be applied in a broad field of applications, vapor recompression technology is mainly used with its limitations in distillation or evaporation processes. Vapor recompression technology refers only to gaseous waste heat streams and is widely applied in close boiling systems with high throughputs and reflux ratios (e.g., C2- or C3-splitter) (Kazemi et al., 2018). Economic efficiency increases on the one hand due to the cost degression of the specific investment costs of the compressor and on the other hand due to the increasing savings potential of the operating costs.
To reduce operating costs and make efficient use of scarce green energy, there are many efforts to optimize both technologies. One of the key performance indicators for both technologies is the coefficient of performance (COP) which is defined as the ratio of the thermal energy that is recycled Q_{therm} and the electrical energy Q_{elec} required to drive the compressor.

Most ways to optimize the COP of heat pump or vapor recompression technologies aim to reduce the pressure ratio between the suction and the pressure side of the compressor or the pressure level on the suction side. The pressure ratio p_1/p_0 as well as the volume stream V_0 are therefore the main factors impacting the high energy consumption of the compressor.

Integrating these technologies with optimally designed column internals can unlock a range of operational advantages, such as improved separation efficiency and minimized pressure drop within the column. The lower pressure drop results in a reduced temperature difference or pressure ratio that needs to be managed by vapor-recompression or heat-pump technologies.

2. Results and discussion: Revamp of a narrow boiling distillation column

The revamp presented in this paper is targeted at improving the operation of a distillation column without altering the vessel geometry in two ways. First, the capacity of the distillation column and the output product are limited by the operating range of the bubble cup trays. Since an increase in column throughput is planned for the future, a revamp with more suitable trays will be necessary. Second, given the significant increase in energy costs, reducing the energy consumption of the column is essential to maintain competitive production.
For the revamp, the existing two-diameter shell —Ø 1200 mm (top) and Ø 1400 mm (bottom)— were retained. All trays were converted from 3-inch bubble-cap trays to UFM™ valve trays while maintaining the original tray spacing and downcomer dimensions. To future-proof capacity, the active open area of the tray decks was increased (with unchanged downcomer cross-sections to preserve liquid handling and residence time). This approach limits mechanical intervention to tray decks and hardware, simplifies installation, and keeps hydraulics predictable by preserving weir length and downcomer hydraulics. In fact, for this revamp, the original downcomer panels were reused, minimizing the environmental impact of supplying additional new materials.

2.1. Product background

Bubble-cap trays provide positive liquid sealing and very stable operation at low vapor rates, which historically made them attractive for services with low liquid loads, requiring low leakage, or wide turndowns (FRI Annual Report, 1960). However, they typically exhibit higher pressure drop and lower capacity versus modern valve trays, and their mechanical complexity increases cost and maintenance.

UFM valve trays are Sulzer's proprietary mini floating valve designed to maximize hydraulic capacity and operating range. Compared with conventional sieve or round-valve decks, UFM trays deliver higher capacity, lower pressure drop, equal or better stage efficiency, and high turndown ratios. The performance increases even more when combined with enhanced downcomer designs (e.g., truncated, stepped, or prism downcomers). Functional features include lateral vapor release to minimize weeping, valve orientation parallel to liquid flow and rectangular legs to prevent rotation/wear.

Maintaining the original tray spacing and downcomer dimensions provides a consistent hydraulic framework, enabling a clearer assessment of the performance improvements resulting from the valve upgrade.

2.2. Changes in operation

In the following section, the qualitative impact of the column revamp on the separation efficiency, energy consumption and pressure drop is presented. For the comparison in separation efficiency, test data for both trays has been used, while for the impact on energy consumption and pressure drop plant data has been used. To describe and compare the points of operation, a normalized capacity factor between 0 and 1 is defined, with 1 being the achievable maximum gas load of the column with the given evaporator.

Regarding the data for separation efficiency of the bubble cap tray it becomes clear, why a revamp was necessary. While the separation efficiency for bubble caps seems relatively steady in the lower operation range of the column from a capacity factor of 0.55 to 0.70, beyond 0.70 the separation efficiency falls drastically. This indicates not only a more energy consuming operation at high column loads but also that the capacity limit of the trays is reached.

By utilizing the column with new UFM trays by Sulzer, not only the capacity limitation is increased, but also an overall increase in separation efficiency is achieved, effectively leading to a major reduction in energy consumption. Inside the current operation range, the separation efficiency of the column has increased by 15-20%. Considering the number of totally equipped trays has stayed the same, the overall number of theoretical stages increases, leading to a lower reflux ratio and steam consumption. The total reduction in steam consumption lies between 12-20% depending on the actual operation load.

In addition to the increase in separation efficiency, the capacity of the column is increased significantly by the revamp. The separation efficiency for the bubble cap trays decreases rapidly above capacity factors of 0.7, whereas the separation efficiency for the UFM trays remains relatively constant up to capacity factors of 0,9. Only beyond a capacity factor of 0.9 the separation efficiency also decreases rapidly, indicating the operation limit of the trays. Overall, a capacity increase of up to 20% can be achieved by revamping the column with the new UFM trays.

An additional advantage of the new UFM trays is the significantly lower pressure drop in comparison to the previously equipped bubble cup trays. Plant data has shown, that a pressure drop decrease of up to 50mbar over the entire column is achievable, corresponding to a decrease of 20% in the overall pressure drop. Especially at higher capacity factors, the pressure drop is significantly lower with the UFM trays. Considering a potential further revamp of the column with a vapor recompression, this decrease in pressure drop has a significant impact on the OPEX and CAPEX. By decreasing the pressure difference between the suction and the pressure side of a hypothetical compressor for this specific column, a COP increase is achieved and a total energy savings of up to 3% is possible.

3. Conclusions

This actual revamp of a distillation column where bubble cap trays were replaced by UFM trays, the potential of column revamp in terms of capacity gain and an increase in separation efficiency was demonstrated. Additionally, the theoretical benefit of such a revamp of the column internals for a use of vapor recompression or heat pumps was addressed. It is shown, that not only the coefficient of performance COP needs to be evaluated, but also the compression ratio and the temperature lift must be considered as characteristic parameters for evaluating the concepts and their economic efficiency. Vapor recompression and heat-pump systems should not be treated as pure end-of-pipe designs. Often, changes in process parameters allow substantial energy and/or

cost savings. By adjusting operating parameters such as pressure drop, separation efficiency, driving temperature or liquid entrainment through retrofitting with new column internals, the concepts for vapor recompression or heat pumps can be significantly optimized and the overall process can be optimally electrified.

References

N. Asprion, S. Giesa, J. Mairhofer, N. Poth, M. Reble, J. Rüther, 2024, Energy Management in Chemical Industry, Ullmann's Encyclopedia of Industrial Chemistry.

P. Gabrielli, L. Rosa, M. Gazzani, R. Meys, A. Bardow, M. Mazzotti, G. Sansavini, 2023, Net-zero emissions chemical industry in a world of limited resources, One Earth, 6, 682 -704.

M. Jobson, 2014, Energy considerations in distillation, Chapter. In: Górak, A., Sorensen, E. (Eds.), Distillation: Fundamentals and Principles. Elsevier, Amsterdam.

E. Papadis, G. Tsatsaronis, 2020, Challenges in the decarbonization of the energy sector, Energy, 205, 118025.

A. Rix, C. Hecht, N. Paul, J. Schallenberg, 2019, Design of heat-integrated columns: Industrial practice, Chem. Eng. Res. Des., 147, 83-89.

M. Skiborowski, 2023, Synthesis and design methods for energy-efficient distillation processes, Current Opinion in Chemical Engineering, 42, 100985.

FRI Annual Report, 1960, Box: 2, Folder: 75. Fractionation Research, Inc. Papers, 1998-004. Oklahoma State University Archives.

Single Compressor Heat Pump Cycles for Distillation: A Cost-Efficient Way to Pump Heat Over Large Temperature Differences, and Between Multiple Condensers and Reboilers

*Priyanshu Singh, Akash Nogaja, and Rakesh Agrawal**
Davidson School of Chemical Engineering,
Purdue University, West Lafayette, USA

*Corresponding author: agrawalr@purdue.edu

Abstract
Integrating heat pumps into distillation systems is key to achieving more sustainable and energy-efficient industrial operations. Despite their efficacy, heat pumps are not well suited to scenarios with large temperature differences between the reboiler and condenser or to systems with multiple reboilers and condensers. Current solutions often resort to external cascading, which requires multiple compressors and is capital-intensive. In this work, we propose an 'Internal Cascade Heat Pumps' system that uses a mixture as the heat pump fluid and cascades internally through partial condensation/vaporization to create multiple stages while using a single compressor. We demonstrate its use in two distillation-based case studies, showing reductions in capital cost of up to 49% and in total annualized cost of up to 37%.

Keywords
Heat Pumps, Distillation, Decarbonization, Electrification

1. Introduction

Distillation remains the most prevalent separation technology in the petroleum and chemical industries, traditionally consuming approximately 2.5 Quad of fossil-fuel-derived energy annually in the United States (Chapas and Colwell, 2007). In response to decarbonization mandates and the increasing availability of renewable electricity, there is a significant shift toward replacing combustion-based heating with low-carbon alternatives (Agrawal and Siirola, 2023). A fundamental thermodynamic opportunity arises because distillation columns do not inherently consume heat; instead, they degrade high-grade thermal energy into low-grade "waste heat" at the condenser. Heat pumps are uniquely suited to exploit this by upgrading condenser heat for reuse in the reboiler, often resulting in a work energy that is lower by a factor of 3-10 compared to conventional thermal energy duties (Nogaja et al., 2025b). This synergy between heat pump integration and renewable electrification offers a transformative pathway for reducing the industrial energy footprint (Mallapragada et al., 2023).

Despite their efficiency, implementing heat pumps in distillation faces significant technical hurdles in two primary scenarios. First, challenges occur when the temperature lift, the gap between the heat source (condenser) and heat sink (reboiler), is substantial. This is often observed in binary systems with extreme volatility differences, such as the hexane-hexadecane separation, where reboiler temperatures can reach 260 °C while the condenser drops to 67 °C (Chavez Velasco et al., 2022). Similar constraints apply to fully thermally coupled (FTC) columns, where the temperature disparity is maximized by the association of the reboiler and

condenser with the heaviest and lightest components, respectively (Agrawal, 1999; Halvorsen and Skogestad, 2003).

Second, complexity increases in systems featuring multiple condensers and reboilers. These configurations are determined by the number of components in the feed mixture, the use of intermediate heat exchangers, and the level of process heat integration (Mathew et al., 2021; Mekidiche et al., 2025; Nogaja et al., 2025a,b; Yuan et al., 2022). Integrating heat pumps into these multi-component or highly integrated environments requires managing multiple thermal nodes, which complicates standard heat-upgrading strategies.

In both cases, the existing literature predominantly utilizes a heat pump with multiple stages/loops, also known as external cascading, which involves multiple compressors (Zhu et al. (2021), Bertsch et al. (2014), Huang et al. (2025), Dong et al. (2025)). Though such methods enhance energy efficiency, they also entail higher costs due to the additional compressors required. A higher number of compressors not only increases capital costs but also adds to the system's maintenance and operational complexity. Therefore, while multi-stage heat pumps can offer significant efficiency improvements, economically, they may not always be the most viable option.

We propose a new class of heat pump cycles using only one heat pump compressor, referred to as the *internal cascade heat pump*. It utilizes a mixture as the working fluid, and it cascades internally through partial condensation/vaporization to effectively create multiple stages with a single compressor. This approach aims to combine the benefits of both multi-stage and single-loop heat pumps, achieving a balance between energy efficiency and cost effectiveness. To keep the narrative focused, we will examine the large temperature lift application using the internal cascade architecture and briefly discuss dealing with multiple heat reboilers/condensers.

The proposed internal cascade heat pump employs a multicomponent working fluid to manage high temperature lifts through phase separation. As illustrated in Figure 1, a compressed high-pressure multicomponent vapor (1) undergoes partial condensation in the reboiler, forming a two-phase mixture (2) that is partitioned in separator S1. The resulting vapor fraction (3), rich in lighter components, is further cooled and expanded to provide the required duty at the condenser (10), while the liquid fraction (4), rich in heavier components, is subcooled and throttled (9) for internal vaporization within HEX_2. This configuration is highly flexible: auxiliary exchangers (HEX_1, HEX_3) facilitate specific subcooling or superheating requirements, while a trim exchanger (T1) regulates the thermal balance between the heat source and sink.

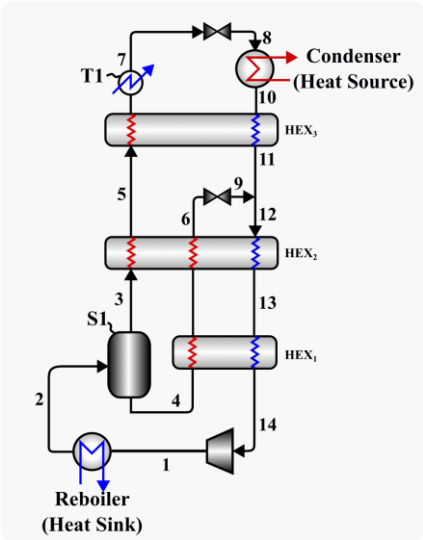

Figure 1: A single-stage internal cascade heat pump flowsheet

In our study, we refer to this process as an *internal cascade heat pump*. In summary, the heat pump cycle capitalizes on the fact that a partially condensed two-phase stream can be separated into a vapor phase enriched in lighter components and a liquid phase enriched in heavier components. Notably, throttling the vapor stream rich in lighter components after its condensation results in a significant temperature drop, even at pressures close to ambient. The process in Figure 1 with a single internal cascading, i.e., with a single vapor-liquid separator, will be referred to as a single-stage internal cascade heat pump.
In Figure 1, the separated vapor from S1 can also be condensed in an intermediate reboiler, thereby extending the use of internal cascade heat pumps in systems with multiple reboilers and condensers. Briefly, the two-phase mixture formed by partial condensation can be separated into vapor and liquid phases. These vapors and liquids have their own bubble and dew points, creating a unique temperature profile if condensed or evaporated against the reboiler or the condenser, respectively. Such vapor and liquids can be created multiple times via partial condensation/vaporization, depending on the required energy and temperature requirements of reboilers and condensers.

2. Results and discussion

We present two distillation-based case studies to demonstrate the application of the internal cascade. We will compare the conventionally used external cascade heat pump configuration with the single-compressor alternative internal cascade configuration based on both energy consumption and cost associated with heat pump compressors. Calculations are performed using Aspen Plus V12.1.

2.1 Hexane(C_6)-Hexadecane(C_{16}) Separation

The implementation of overhead vapor recompression is thermodynamically infeasible due to the critical temperature limit of hexane; hence, Chavez Velasco et al. (2022) utilized a single-stage external cascade heat pump using an intermediate volatility component, undecane (C_{11}), as the heat pump fluid. It resulted in a throttling pressure of 0.01 bar and a pressure ratio across the heat pump compressor of 365. Such impractical low throttling pressure and high compression ratio can be avoided using a heat pump with single-stage internal cascade (Figure 2).

The constituents and mole fractions of the employed mixed-component stream are presented in Table 1. The components are chosen such that the lighter component cascading loop would predominantly have C_5, C_6 and C_7 components. Using this system, the pressure ratio across the compressor reduces to 13.6 compared to 365. The throttling pressure increased from 0.01 bar to 1.1 bar. Consequently, for a feed rate of 250 kmol/s for distillation, the inlet volumetric flow rate to the heat pump compressor reduced from 480 m^3/s to 8.9 m^3/s, which is an approximately 54-fold reduction, signifying a significant reduction in compressor size.

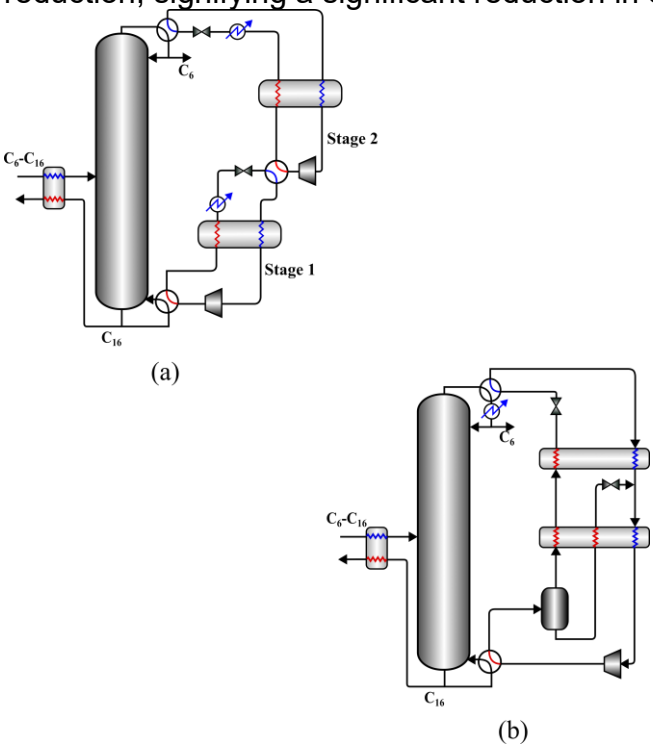

Figure 2: Binary C_6-C_{16} separation distillation column (a) A two-stage external cascade system (b) A single-stage internal cascade system

The power requirement for the benchmark simulation conducted by Chavez Velasco et al. (2022) was 4158 kW. However, with the implementation of internal cascade, the calculated compressor power is reduced to 3675 kW, resulting in an 11.6% energy savings.

Component	C_5	C_6	C_7	C_{15}	C_{16}	C_{17}
Mole Fraction	0.217	0.605	0.108	0.020	0.045	0.005

Table 1: Composition of the heat pump fluid mixture for C_6-C_{16} separation

For cost analysis, we instead compare the internal cascade heat pump with a practically implementable external cascade heat pump comprising multiple stages that possess a viable pressure ratio and volumetric flow rate (Figure 2). It is observed that for the external cascade, the total fixed cost for both compressors is 6.9 million US dollars vs 5.2 million US dollars for the proposed internal cascade process. Considering both operating and fixed costs, the total annualized cost of internal cascade remains 19% lower.

2.2 Heat Pump Associated with Intermediate Reboiler

To further depict the versatility of internal cascade heat pump, we present a case study with two heat sinks (reboiler and an intermediate reboiler) and a single heat

source (condenser). We create a test example using a distillation column with an intermediate reboiler that separates a binary mixture of hexane (C_6) and undecane (C_{11}).

For this, a generally two-stage heat pump system is employed, where the first stage is used to pump heat to the intermediate reboiler and the second stage to pump heat to the reboiler, as shown in Figure 3(a). However, this requires two compressors, which increases the cost of the system. The flowsheet shown in Figure 3(a) is considered as the base case, with hexane (C_6) as the heat pump fluid in Stage I and pentane (C_5) as the heat pump fluid in Stage II. The proposed alternative is to use a single-stage internal cascade heat pump, which can achieve the same result with a single compressor, as shown in Figure 3(b). For the internal cascade, the composition of the heat pump fluid used was 26%, 39%, 7%, 23%, and 5% of propane, butane, pentane, hexane, and heptane, respectively.

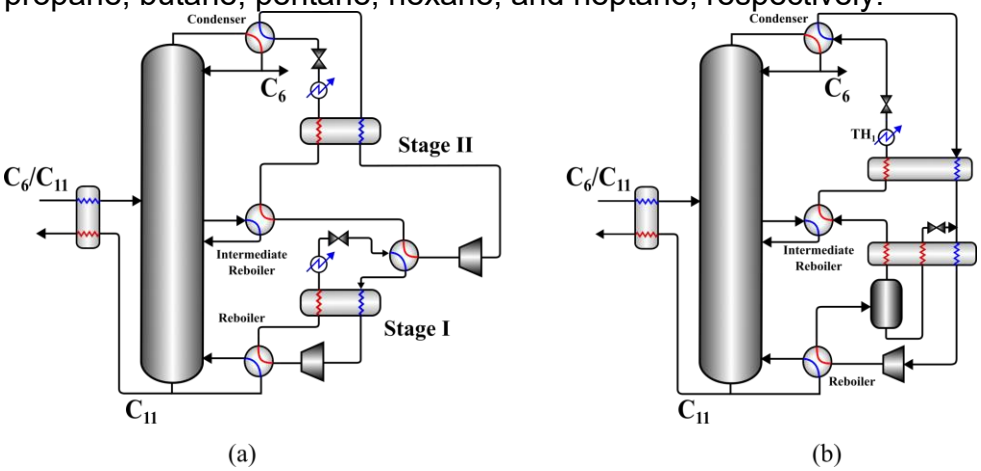

Figure 3: Heat pump assisted distillation with an intermediate reboiler (a) External cascade involving two compressors (b) Internal cascade alternative

First, because a temperature glide is present on all the heat exchangers, an energy savings of 14% is observed. The heat pump compressor CAPEX for the internal cascade is lower by 49% when compared to the external cascade. Similarly, when both capital and operating costs are considered, the total annualized cost of internal cascade remains 37% lower.

3. Conclusions

This paper presents a new class of heat pump, the *internal cascade heat pump*, designed to pump heat from condensers to reboilers with a large temperature difference, and from multiple condensers to multiple reboilers. The current conventional solutions utilize multiple loops or stages of heat pumps, which employ multiple compressors, making the system capital-intensive and creating a significant barrier to practical implementation. The proposed heat pump architecture is designed to overcome these challenges by creating two-phase streams and separating the vapor and liquid phases, which then interact with reboilers and condensers. Partial condensation/vaporization allows the creation of stages/loops internally using a single compressor, thereby reducing overall cost. In our case studies, the calculated CAPEX savings range from 25% to 49%. Furthermore, the total annualized cost savings range from 19% to 37%.

Acknowledgements

The authors thank the Center for Innovative and Strategic Transformation of Alkane Resources (CISTAR), an Energy Research Center (ERC), supported by the National

Science Foundation under the Cooperative Agreement No. EEC-1647722 for funding.

References

1. R. Agrawal. More operable fully thermally coupled distillation column configurations for multicomponent distillation. Chemical Engineering Research and Design, 77(6):543–553, 1999.
2. R. Agrawal and J. Siirola. Decarbonization of chemical process industries via electrification. The Bridge, 53:32–40, 2023.
3. S. Bertsch, M. Uhlmann, and A. Heldstab. Heat pump with two heat sources on different temperature levels. 2014.
4. R. B. Chapas and J. A. Colwell. Industrial technologies program research plan for energy-intensive process industries. Technical report, Pacific Northwest National Laboratory (PNNL), Richland, WA (United States), 2007
5. J. A. Chavez Velasco, M. Tawarmalani, and R. Agrawal. Which separation scenarios are advantageous for membranes or distillations? AIChE Journal, 68(11):e17839, 2022.
6. Y. Dong, H. Madani, X. Kou, and R. Wang. High temperature heat pump with dual uses of cooling and heating for industrial applications. Applied Energy, 379:124962, 2025.
7. I. J. Halvorsen and S. Skogestad. Minimum energy consumption in multicomponent distillation. 3. more than three products and generalized petlyuk arrangements. Industrial & Engineering Chemistry Research, 42(3):616–629, 2003.
8. Y. Huang, G. Li, X. Tang, K. Huang, W. Zhao, and J. Zhang. Thermodynamic analysis of a modified cascade high temperature heat pump with zeotropic mixtures for heating production up to 200° c. Energy Conversion and Management, 324:119307, 2025.
9. D. S. Mallapragada, Y. Dvorkin, M. A. Modestino, D. V. Esposito, W. A. Smith, B.-M. Hodge, M. P. Harold, V. M. Donnelly, A. Nuz, C. Bloomquist, K. Baker, L. C. Grabow, Y. Yan, N. N. Rajput, R. L. Hartman, E. J. Biddinger, E. S. Aydil, and A. D. Taylor. Decarbonization of the chemical industry through electrification: Barriers and opportunities. Joule, 7(1):23–41, jan 2023.
10. T. J. Mathew, R. Tumbalam Gooty, M. Tawarmalani, and R. Agrawal. A simple criterion for feasibility of heat integration between distillation streams based on relative volatilities. Industrial & Engineering Chemistry Research, 60(28):10286–10302, 2021.
11. Z. Mekidiche, J. A. Labarta, and J. A. Caballero. Optimal design of heat pump assisted thermally coupled distillation sequences. Applied Thermal Engineering, page 126753, 2025.
12. A. S. Nogaia, M. Tawarmalani, and R. Agrawal. Comparing exergy and heat pump work in distillation systems. AIChE Journal, page e18895, 2025a.
13. A. S. Nogaia, M. Tawarmalani, and R. Agrawal. A computationally efficient heat pump model for quick and reliable identification of energy-efficient distillation configurations. Chemical Engineering Science, page 122707, 2025b.
14. H. Yuan, Y. Luo, and X. Yuan. Synthesis of heat-integrated distillation sequences with mechanical vapor recompression by stochastic optimization. Computers & Chemical Engineering, 165:107922, 2022.
15. Y.-D. Zhu, Z.-R. Peng, G.-B. Wang, and X.-R. Zhang. Thermodynamic analysis of a novel multitarget-temperature cascade cycle for refrigeration. Energy conversion and management, 243: 114380, 2021.

Comparative flexibility analysis of liquid-only transfer and bidirectionally thermally coupled distillation columns

Jonas Schnurr[1], Mirko Skiborowski[1]
[1]Hamburg University of Technology, Hamburg, Germany

Abstract
Thermally coupled distillation columns, particularly dividing wall columns, are well-established in the chemical industry for enhancing energy efficiency in distillation processes. However, such configurations exhibit increased design complexity and operational limitations due to the inherent vapor transfer. Liquid-only transfer (LOT) can be a viable option to address these challenges, preserving the energy-saving potential while potentially expanding the operating range, at the cost of additional column sections and heat exchangers. In order to investigate the potential for increased flexibility, a shortcut-based screening is applied to compare bidirectionally thermally coupled and LOT side-rectifier configurations. While the same minimum-energy operation is achieved at a distinct combination of operating parameters for both configurations, the LOT side-rectifier exhibits a significantly larger flexibility region for a slightly increased heat duty. Consequently, multiple combinations of operating parameters are possible, highlighting the potential of LOT distillation to enhance operational flexibility while maintaining the energy efficiency of thermally coupled systems.

Keywords
Flexibility analysis, Thermal coupled distillation, Liquid-only transfer, Shortcut framework, Constant molar overflow

1. Introduction

The chemical industry faces an increasing pressure to reduce its energy demand due to rising energy costs, stricter environmental regulations, and global sustainability goals. Distillation remains the dominant fluid separation technique, accounting for approximately 90-95% of all separation tasks [1]. Despite its high energy demand, direct substitution by alternative separation technologies is impractical due to its flexibility in throughput and ability to produce multiple high-purity products [2]. Consequently, energy-integration methods have been widely developed to improve the energy efficiency of distillation processes, particularly for the multicomponent separations that often require column sequences [3].

Thermally coupled distillation is a well-established energy-integration approach that, in combination with the investment savings offered by dividing wall columns, has resulted in several hundred industrial installations [4]. By replacing individual heat exchangers and liquid streams of adjunct columns with a bidirectional vapor and liquid transfer stream, thermally coupled configurations can reduce the energy demand by 30-40% compared to conventional sequences [5], while dividing wall columns may reduce investment costs by up to 30% [6]. For fully thermally coupled configurations, the minimum vapor demand equals that of the most difficult split in an equivalent simple column, which can be systematically analyzed using the V_{min} diagram introduced by Halvorsen and Skogestad [7-9].

Despite their energy-saving potential, thermally coupled columns present design and operational challenges. Vapor transfer requires coupled columns to operate at identical pressure, thereby restricting the applicability and additional heat integration [10]. Additionally, the vapor distribution depends on the column hydraulics and is therefore largely fixed during the design phase. Although active vapor split control has been proposed [11], it has seen limited industrial adoption. By employing the V_{min} diagram, an optimality region [8] in which the configuration operates at minimum vapor demand and a flexibility region [12] where operation is possible up to an allowable excess vapor can be defined. In fully thermally coupled configurations, liquid and vapor splits are correlated within these regions. In contrast, partially thermally coupled side-rectifier arrangements exhibit reduced flexibility, as their operation is governed solely by the vapor flow.

To overcome the limitations imposed by vapor transfer, Agrawal introduced the concept of liquid-only transfer (LOT) distillation [13]. In LOT configurations, the vapor transfer stream is eliminated and replaced by an additional column section with an individual heat exchanger that generates the required vapor, thereby enabling only liquid side streams between columns. Although this requires additional equipment, it introduces additional degrees of freedom, allowing independent adjustment of vapor flows and operating pressures. The thermodynamic equivalence of the minimum energy demand (MED) between bidirectionally thermally coupled and LOT configurations was proven mathematically by Ramapriya et al. [14], who showed that identical liquid-to-vapor ratios in corresponding sections lead to equivalent operation. Halvorsen and Skogestad [15] further extended their V_{min} analysis for fully coupled LOT sequences, demonstrating identical optimality regions and increased flexibility due to operability over a range of side-stream flow rates. While systematic studies of optimality and flexibility regions for dividing wall columns exists [12], corresponding investigation for LOT side-rectifier configurations remains limited, and the flexibility regions of thermally coupled LOT sequences are largely unexplored.

This work addresses this gap by presenting a model-based flexibility analysis framework for LOT configurations, building on the V_{min} methodology of Halvorsen and Skogestad [7-9]. A thermodynamically sound shortcut method is used to determine minimum vapor demand and associated operational flexibility regions. The separation of benzene, toluene and p-xylene (BTX) is studied as a case study to compare the flexibility regions of thermally coupled side-rectifier (TC-SR) and liquid-only transfer side-rectifier (LOT-SR) configurations.

2. Methods

The flexibility analysis framework is comprised of two steps, which are applied to both TC-SR and LOT-SR configurations. Initially, the minimum vapor demand of each configuration is determined. Secondly, the corresponding optimality and flexibility regions are identified. The framework is implemented in MATLAB and builds on the rectification body method (RBM) [16] and the shortcut screening framework of Adami et al. [17]. Thermodynamic properties are computed using external C-based routines provided by AVT.SVT at RWTH Aachen[1].

2.1. Thermally coupled side-rectifier model

Thermal coupling requires bidirectional vapor and liquid transfer between columns. In the present model, this behavior is approximated by subcooling the bottom stream of

[1] https://www.avt.rwth-aachen.de/go/id/iptu

the first column, following Navarro et al. [18]. Accordingly, the TC-SR is modeled as two columns, where the bottom stream of the first column enters the second column after being subcooled by the reboiler duty, as illustrated in Figure 1. The minimum vapor demand of the thermally coupled configuration ($\dot{V}_{min}^{Top}$) is calculated as the sum of the vapor demands of the individual columns,

$$\dot{V}_{min}^{Top} = \dot{V}^{Top,C1} + \dot{V}^{Top,C2} \tag{1}$$

where $\dot{V}^{Top,C1}$ and $\dot{V}^{Top,C2}$ denote the vapor demands at the top of column 1 and column 2, respectively.

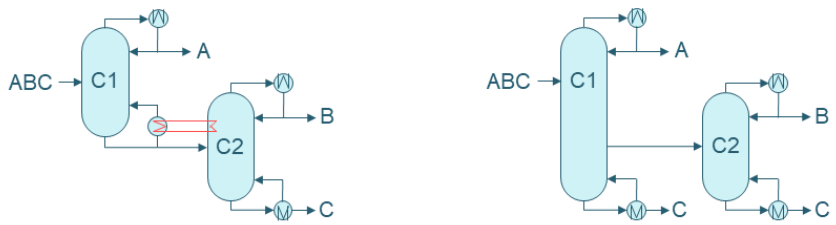

Figure 1: Model of thermally coupled side rectifier (TC-SR) (left) and liquid-only transfer side-rectifier (LOT-SR) (right).

2.2. Liquid-only transfer side-rectifier model

The LOT-SR is likewise modeled as a two-column configuration. In contrast to the TC-SR, the first column provides a liquid side stream from the stripping section, which serves as the feed to the second column, as shown in Figure 1. The minimum vapor demand is calculated using equation (1). The LOT-SR introduces an additional degree of freedom, namely the distribution of the heavy boiler C between the bottom products of both columns. This distribution is described by the split parameter

$$\psi_C = \frac{\dot{n}_C^{Bottom,C1}}{\dot{n}_C^{Feed}}, 0 < \psi_C < 1 \tag{2}$$

where $\dot{n}_C^{Bottom,C1}$ is the molar flow rate of component C in the bottom of column 1 and $\dot{n}_C^{Feed}$ is that in the overall feed. The total vapor demand of LOT-SR depends on ψ_C, which is systematically varied to evaluate the full operating range.

2.3. Determination of the minimal vapor demand

The minimum vapor demand for each configuration and split parameter is determined using the RBM [16], a thermodynamically sound, pinch-based shortcut method assuming infinite equilibrium stages and isobaric operation. The separation is defined as a sharp split or yielding products with the maximum achievable purity [19]. The MED is identified by locating the intersection of the individual rectification bodies of the respective column sections, which approximate feasible, continuous stage-to-stage composition profiles. For zeotropic systems with constant relative volatilities, the results are similar to those obtained with Underwood's method. A detailed overview of pinch-based shortcut methods is provided by Skiborowski et al. [20].

The minimum vapor demand at the column top ($\dot{V}^{Top}$) is calculated from the minimum condenser duty ($\dot{Q}_{Condenser}$) and the mixture's heat of vaporization ($\Delta h_{Vaporization}$).

$$\dot{V}^{Top} = \frac{|\dot{Q}_{Condenser}|}{\Delta h_{Vaporization}} \tag{3}$$

To enable a comparison of liquid-to-vapor ratios across column sections, the current work considers constant molar overflow (CMO), such that all interstage liquid and vapor flow rates remain constant within a given column section.

2.4. Determination of the flexibility regions

The optimality and flexibility regions are defined with respect to the minimum vapor demand of the TC-SR configuration ($\dot{V}_{min}^{Top}$). The optimality region ($\Omega_{optimality}$) comprises all split parameter values (ψ_C) for which the LOT-SR operates at this minimum vapor demand.

$$\Omega_{optimality} = \{\psi_C | \dot{V}_{LOT\text{-}SR}^{Top}(\psi_C) \leq \dot{V}_{min}^{Top}\} \tag{4}$$

The flexibility region ($\Omega_{flexibility}$) extends this definition by allowing operation up to a user-defined excess vapor demand, specified with ϕ_{flex}, which is slightly larger than one.

$$\Omega_{flexibility} = \{\psi_C | \dot{V}_{LOT\text{-}SR}^{Top}(\psi_C) \leq \dot{V}_{min}^{Top} \cdot \phi_{flex}\} \tag{5}$$

These regions provide a basis for systematically evaluating the operational flexibility of variables, such as side-stream flow rates and vapor demand.

3. Results and discussion

Following previous studies on thermally coupled distillation [12], the separation of benzene, toluene and p-xylene is investigated at 1 atm using an equimolar, saturated liquid feed with a total flow rate of 3 kmol/h. The vapor-liquid equilibrium is described using the NRTL activity coefficient model for the liquid phase and ideal gas behavior for the vapor phase, with vapor pressures calculated via the extended Antione equation. Constant molar overflow is enforced by assuming a constant heat of vaporization of 57042 kJ/kmol, corresponding to the heat of vaporization of the feed at 25°C. Sensible heat effects are neglected by setting the ideal-gas heat capacity to zero, while the liquid-phase heat capacity is calculated using DIPPR correlations.

For the flexibility analysis, the split parameter ψ_C is varied from 0.01 to 0.99 in steps of 0.001, resulting in 982 evaluated operating points. Consistent with Ränger et al. [12], ϕ_{flex} is set to 1.08, allowing for an excess vapor demand of up to 8%. The complete evaluation requires approximately 8 seconds on a desktop computer equipped with an Intel i7-14700 CPU, using 20 parallel workers in MATLAB 2023b.

3.1. Vapor-to-feed and liquid-to-vapor ratios at MED

Figure 2 shows the vapor-to-feed (V/F) and liquid-to-vapor (L/V) ratios of the individual columns and the vapor demand of the LOT-SR as a function of ψ_C, together with the corresponding values of the TC-SR as reference. With increasing ψ_C, the V/F ratio of the LOT-SR decreases until an optimal split parameter is reached, at which the minimum value equals that of the TC-SR. At this point, the vapor demands of the A/BC and BC/C splits in the first column are equal, and the stripping sections of both columns operate at the same L/V ratio, consistent with the theoretical results of Ramapriya et al. [14]. The vapor demand of the A/BC split remains constant over the entire range of ψ_C, as it is independent of the distribution of component C. In contrast, the vapor demand of the BC/C split increases with increasing ψ_C, since a larger fraction of component C is separated in the first column, shifting the separation progressively toward the sharp B/C split. At low values of ψ_C, the minimum vapor demand in the first column is governed by the A/BC split, causing the BC/C split to be operated with excess vapor and a lower L/V ratio in the corresponding stripping section. This difference diminishes with increasing ψ_C until both stripping sections perform equivalent separations with similar operating lines defined by identical L/V ratios.

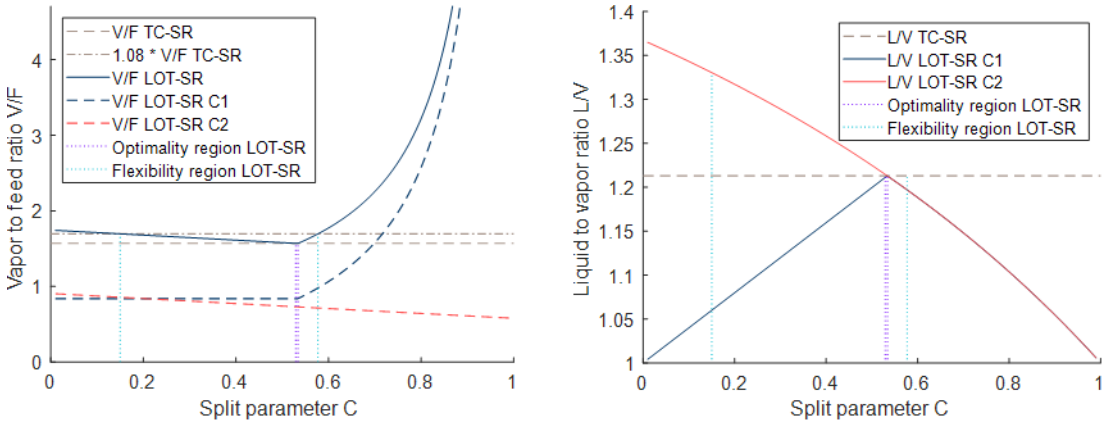

Figure 2: Vapor to feed ratio (left) and liquid to vapor ratio (right) over the split parameter C for SR configurations.

3.2. Flexibility regions and operational implications

The optimality region of both side-rectifier configurations is limited to a single operation point, as neither configuration contains a column section performing the AB/BC split. Consequently, over-purification in one separation will impact the remaining separations and any increase in vapor will affect the entire separation sequence. Allowing excess vapor expands the operability of TC-SR by partially compensating for suboptimal vapor splits, which are otherwise fixed by design. In contrast, the flexibility region of the LOT-SR depends on the selected split parameter ψ_C, which is linearly related to the side-stream flow rate. For a given excess vapor allowance, a finite range of side-stream flow rates exists for which the vapor demand remains below the specified upper limit. This additional degree of freedom enables the LOT-SR to adjust vapor flow and side-stream flow independently, resulting in a substantially larger theoretical flexibility region than that of the TC-SR, as illustrated in Figure 3.

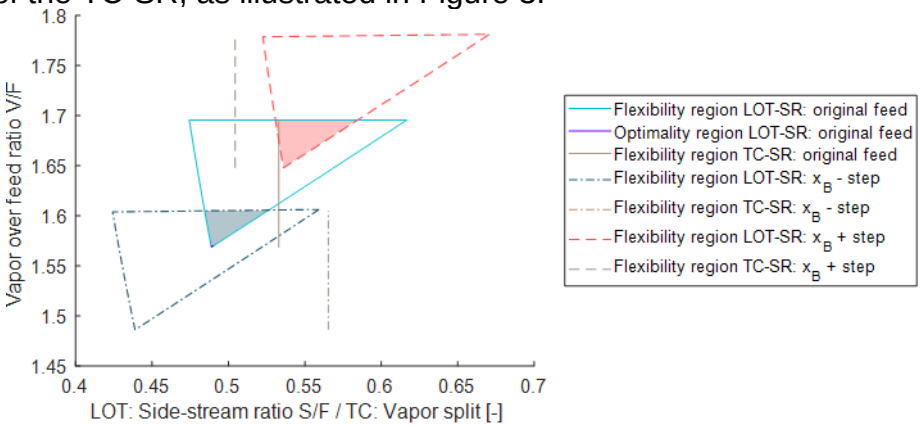

Figure 3: Optimality and flexibility regions for LOT-SR and TC-SR with equimolar feed and, for variations in the feed composition of intermediate-boiling component.

Although it has to be considered that the present analysis assumes an infinite number of stages and equipment sizing and column hydrodynamics are consequently neglected, the results clearly indicate that the LOT-SR has a larger potential to accommodate feed composition disturbances, as illustrated in Figure 3. The variation in the mole fraction of the intermediate-boiling component with a step size of 0.05, can be accommodated within the identified flexibility region. In contrast, the TC-SR configuration can respond solely through changes in vapor flow, due to the fixed vapor split. This distinction underscores the enhanced operational flexibility of LOT configurations in comparison to classical bidirectional thermally coupled systems.

4. Conclusions

Liquid-only transfer distillation eliminates the vapor transfer stream in thermally coupled configurations, thereby introducing additional degrees of freedom that enable more flexible operation. While this potential has been widely suggested in literature [10], the present work provides the first systematic comparison of the optimality and flexibility regions of thermally coupled and LOT distillation sequences. The proposed framework is based on a thermodynamically sound shortcut method and allows the rapid evaluation of a large number of operating points, making it well suited for flexibility analysis.

For single-side-stream configurations, the results confirm earlier theoretical findings that the optimality region is restricted to a single operating point and that thermally coupled and LOT configurations are equivalent at minimum energy demand. However, the LOT side-rectifier exhibits a significantly larger flexibility region, as the additional operational variable can be adjusted independently.

Due to its computational efficiency, the framework enables systematic investigations of flexibility regions under varying feed conditions. Future work will extend the approach to LOT configurations with two side streams and further investigate rigorous equilibrium-stage models to assess stage-wise composition and temperature profiles, thereby enabling a more realistic assessment of operational feasibility.

References

[1]: Oak Ridge National Laboratory. (2005) https://doi.org/10.2172/1218755
[2]: Kiss, Smith. Energy 203:117788 (2020) https://doi.org/10.1016/j.energy.2020.117788
[3]: Blahušiak et al. Sep. Purif. Technol. 194:301-318 (2018) https://doi.org/10.1016/j.seppur.2017.10.026
[4]: Lukač et al. Chem. Eng. Res. Des. 147:367-377 (2019) https://doi.org/10.1016/j.cherd.2019.04.041
[5]: Waltermann et al. Chem. Eng. Process Process Intensif. 146:107688 (2019) https://doi.org/10.1016/j.cep.2019.107688
[6]: Kolbe, Wenzel. Chem. Eng. Process Process Infensif. 43:339-346 (2004) https://doi.org/10.1016/S0255-2701(03)00133-8
[7]: Halvorsen, Skogestad. Ind. Eng. Chem. Res. 42:596-604 (2003) https://doi.org/10.1021/ie010863g
[8]: Halvorsen, Skogestad. Ind. Eng. Chem. Res. 42:605-615 (2003) https://doi.org/10.1021/ie0108649
[9]: Halvorsen, Skogestad. Ind. Eng. Chem. Res. 42:616-629 (2003) https://doi.org/10.1021/ie0108651
[10]: Horsch, Skiborowski. Sep. Purif. Technol. 354:128762 (2025) https://doi.org/10.1016/j.seppur.2024.128762
[11]: Dwivedi et al. Ind. Eng. Chem. Res. 51:15176-15183 (2012) https://doi.org/10.1021/ie3014346
[12]: Ränger et al. Sep. Purif. Technol. 354:129151 (2025) https://doi.org/10.1016/j.seppur.2024.129151
[13]: Agrawal. AIChE Journal 46:2198-2210 (2000) https://doi.org/10.1002/aic.690461112
[14]: Ramapriya et al. AIChE Journal 60:2949-2961 (2014) https://doi.org/10.1002/aic.14468
[15]: Halvorsen, Skogestad. Sep. Purif. Technol. 365:132530 (2025) https://doi.org/10.1016/j.seppur.2025.132530
[16]: Bausa et al. AIChE Journal 44:2181-2198 (1998) https://doi.org/10.1002/aic.690441008
[17]: Adami et al. Sep. Purif. Technol. 377:134463 (2025) https://doi.org/10.1016/j.seppur.2025.134463
[18]: Navarro et al. Comput. Chem. Eng. 36:149-159 (2012) https://doi.org/10.1016/j.compchemeng.2011.06.014
[19]: Sasi, Skiborowski. Ing. Eng. Chem. Res. 59 20816-20835 (2020) https://doi.org/10.1021/acs.iecr.0c04555
[20]: Skiborowski et al. Distillation. Elsevier pp.306-355 https://doi.org/10.1016/B978-0-12-386547-2.00008-9

Uncovering the Role of Sensible Heat: Screening of Integrated Distillation Sequences with Cost-Optimal Heat Exchanger Networks

Monaf Gawish, Momme Adami, Mirko Skiborowski
Hamburg University of Technology, Institute of Process Systems Engineering
Hamburg, Germany

Abstract
Although distillation dominates industrial fluid separation processes, its high energy demand necessitates systematic strategies to improve energy efficiency. However, identifying the optimal combination of distillation sequence and energy integration strategy is challenging due to a vast design space and multiple competing objectives, most notably capital and operating costs. To ensure equal boundary conditions during evaluation, this work proposes a novel framework for the screening of energy-integrated distillation sequences with cost-optimal heat exchanger networks (HENs). The framework combines a thermodynamically sound shortcut screening method with a superstructure-based HEN optimization model. By explicitly considering both latent and sensible heat, the method effectively accounts for variations in operating conditions across intensified distillation sequences. The application of the framework is demonstrated for a large-scale screening of 77 sequences for the separation of a ternary mixture. The results reveal that sensible heat makes a non-negligible contribution to heating and cooling demands, presenting additional opportunities for heat integration, which affect the relative ranking of competing sequences. The introduction of HENs leads to further changes in the ranking, highlighting the importance of a systematic screening for the evaluation of energy-integrated distillation systems.

Keywords
Distillation, Heat Exchanger Networks, Shortcut screening, Process Intensification, Sensible Heat

1. Introduction

Distillation accounts for 90–95% of all fluid separations, with roughly 40,000 columns in the United States alone [1]. However, due to its high energy demand, several strategies have been developed over the past decades to improve its efficiency. These include direct heat integration, heat pumps, and thermal coupling. Amid growing economic and environmental challenges, the chemical industry faces increasing pressure to develop more energy-efficient separation processes.

Distillation is well suited for heat integration, as the condenser typically rejects nearly the same amount of heat as is supplied to the reboiler. Direct integration within a single column is usually infeasible due to the inherent temperature difference, but heat exchange between the reboilers and condensers of different columns is possible and can be highly effective [2]. Beyond latent heat, many streams in distillation systems undergo sensible heat changes, such as the preheating or cooling of feed and intermediate streams, and the cooling of top and bottom products. Sensible energy duties can vary substantially between individual configurations, especially when columns are operated at different pressures, affecting overall heating and cooling demands and presenting additional opportunities for heat integration. Sensible heat

should therefore be explicitly considered for a balanced evaluation of competing distillation sequences.

Process streams are generally classified as hot sources if they require cooling, or cold sinks if they require heating. The transfer of heat from hot sources to cold sinks is commonly formulated as a HEN design problem, traditionally addressed through pinch analysis or mathematical programming [3]. For a given set of streams, multiple alternative HENs can typically be synthesized, differing in the number of heat exchanger units, specific stream matches, and heat exchanger sizes.

Given the wide range of intensified distillation sequences, which exhibit varying sensible heat contributions and offer opportunities for further integration via HENs, several studies have sought to combine sequence screening with heat integration (e.g., [4–8]). However, existing approaches still have notable limitations. For example, screening strategies may exclude advanced configurations such as thermally coupled or dividing-wall columns [4, 7]. Furthermore, screening frameworks often use the Fenske–Underwood–Gilliland shortcut method [4, 6–8], which assumes constant relative volatility (CRV) and constant molar overflow (CMO) and thus limits accuracy for non-ideal mixtures. Additionally, heat integration is sometimes performed using pinch analysis or simplified HEN models, which minimize energy demand but neglect associated capital costs [7, 8]. Finally, heat integration is typically restricted to matches between condensers and reboilers of different columns, which overlooks sensible heat contributions from feed, intermediate, and product streams [4, 5].

To address these gaps, this work proposes a hybrid framework for the automated screening and evaluation of distillation sequences along with their cost-optimal HENs. The approach accounts for both latent and sensible heat and is applicable to a wide range of conventional and intensified distillation configurations, enabling a fair comparison and identification of promising alternatives for early-stage process design.

2. Methodology

The proposed approach consists of a rapid shortcut screening of distillation sequences, followed by rigorous HEN optimization for each configuration evaluated in screening. The entire screening and HEN synthesis process is completely automated, and relies on an implementation of the distillation sequence screening in MATLAB [9] connected to a superstructure-based HEN optimization implemented in GAMS, as illustrated in *Figure 1*.

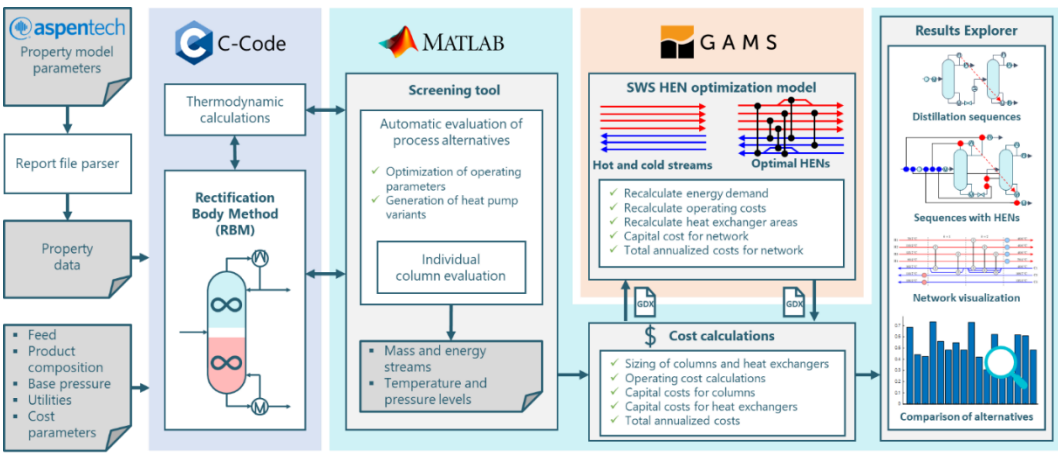

Figure 1: Schematic of the algorithmic framework for automated screening of energy-integrated distillation processes with heat exchanger network optimization.

2.1 Shortcut Screening

The distillation sequence screening builds on a thermodynamically sound pinch-based shortcut method, known as the Rectification Body Method (RBM) [10]. Using the RBM together with a series of individual optimization problems, the screening determines the minimum energy demand for separating a mixture into three product fractions, along with all relevant mass and energy flows, temperatures, and pressures for each sequence. These data are then compiled and passed to the HEN synthesis model.
The screening considers a wide range of sequences, from simple sequences to configurations with direct heat integration, thermal coupling, liquid-only transfer (LOT), multi-effect distillation (MED), as well as combinations with heat pumps. For each sequence, additional equipment sizing and cost correlations are applied to estimate the total annualized cost (TAC). A detailed description of the shortcut screening can be found in Adami et al. (2025) [11].

2.1.1 Quantification of sensible heat contributions

Certain sequences considered in the screening, such as directly heat-integrated and MED sequences, include columns operating at different pressures, which leads to feed and product streams at different temperatures and thus different sensible heat contents, as these streams enter and leave as saturated liquids. This variation results in an imbalanced comparison of competing alternatives. To ensure a consistent evaluation, identical reference conditions for feed and product streams are enforced across all sequences by introducing auxiliary exchangers at the fresh feed and each final product, as illustrated in *Figure 2* for the direct sequence (DS).

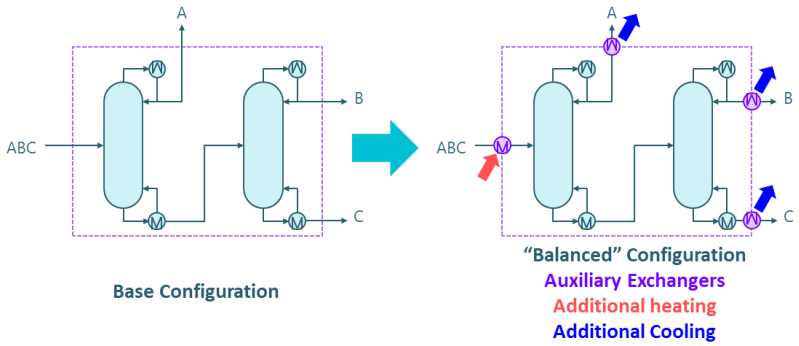

Figure 2: Direct sequence with auxiliary exchangers to adjust feed and product streams to reference conditions.

2.2 Heat exchanger network optimization

To consider further heat integration, the framework performs a HEN optimization based on the stage-wise superstructure (i.e., SWS) model of Yee and Grossmann [12]. The original SWS formulation is further modified in this work to accommodate multiple hot and cold utilities and to properly handle streams undergoing phase change, which are common in distillation processes. Perfectly isothermal streams corresponding to pure-component vaporization or condensation are approximated using a small fictitious temperature difference of 1 K and a heat capacity flow rate equal to the latent heat change. For mixtures undergoing non-isothermal phase change, the associated temperature glide is calculated using rigorous thermodynamics during the screening step, and such streams are treated as non-isothermal within the HEN model.
Following Yee and Grossmann [12], the model is solved in two steps: first, a MINLP problem is solved assuming isothermal mixing at exchanger outlets; then, if stream splitting occurs, the assumption is relaxed and an NLP sub-optimization is performed. Capital costs are estimated using the modular approach of Guthrie (1969) [13], to ensure consistency with the screening and enable more accurate cost estimation that

accounts for differences in operating conditions among individual exchangers. This costing method involves multiple correction factors that depend on exchanger characteristics (e.g., size, materials, temperature, etc.). To accommodate this, a modified solution strategy is implemented in which the MINLP and NLP subproblems are solved iteratively while updating cost parameters.

2. Case study

The separation of 110 mol/s of an equimolar benzene–toluene–ethylbenzene (BTE) mixture into pure components is considered. Reference conditions of 40 °C and 1.013 bar are applied to all fresh feed and final product streams. For sequences requiring pressure modifications (e.g., directly heat-integrated sequences), operating pressures are determined based on individual flash calculations assuming a minimum temperature approach (ΔT_{min}) of 5 K, as described in Adami et al. (2025) [11].

To account for the nonideality of the vapor phase, the fugacity coefficients are calculated using the Redlich–Kwong equation of state. For the nonideality of the liquid phase, the NRTL (Non-Random-Two-Liquid) model is applied to compute the liquid phase activity coefficients. Pure component vapor pressures are estimated via the extended Antoine equation, and DIPPR correlations are used for specific heat capacities and heats of vaporization. All property parameters are extracted from Aspen Plus, as shown in *Figure 1*.

For economic evaluation, an annual operation of 8,000 h is assumed. Three hot utilities, high-pressure (41 barg, 254 ºC), medium-pressure (10 barg, 184 ºC) and low-pressure steam (5 barg, 160 ºC), and two cold utilities, cooling water (30→40 ºC, 1 bar) and refrigerated water (5→15 ºC, 1 bar) are defined following Turton et al. 2012 [14]. A capital charge factor of 0.136 yr^{-1} and an update factor of 6.851, calculated using the June 2024 CEPCI (Chemical Engineering Plant Cost Index) index, are assumed. All heat exchangers are of floating-head type, with carbon steel shells and tubes, and a ΔT_{min} of 5 K. Film heat transfer coefficients are assumed to be 2.00, 2.50, and 1.00 $kW/m^2 \cdot K$ for process streams, hot utilities, and cold utilities, respectively.

Overall, 77 distillation sequences are considered in the screening, covering various thermally-driven concepts, i.e., direct heat integration, thermal coupling, LOT, and MED, limiting the scope to sequences consisting of three or fewer columns. Based on the shortcut screening results, HEN optimization is performed in GAMS 51.1.0 using BARON. To limit solution times, each sequence is limited to three MINLP and two NLP subproblems, with a limit of 600 s per subproblem. BARON's relative optimality gap (optcr) is set to 0.02 (2%), and four superstructure stages are used for all sequences.

The complete screening and HEN optimization of all 77 configurations required approximately 16 hours (wall clock time). For 43 sequences (~60%), all subproblems converged within 600 s to the target optimality criterion. For the remaining sequences, one or more subproblems exceeded the time limit; however, in 24 cases the maximum optimality gap was below 5%, in 8 cases between 5% and 10%, and in only one case as high as 16%. These results indicate that high-quality solutions can be obtained for the majority of sequences within the specified time limit.

Figure 3 illustrates the sensible and latent contributions to heating and cooling for the best 20 configurations from the initial screening, and provides the abbreviations used to denote the different sequences. The screening results indicate that sensible heat represents a substantial fraction in most configurations before HEN integration, with minimum contributions of 11.2% for heating and 14.4% for cooling. Moreover, for several high-pressure, directly heat-integrated sequences (e.g., PF-FC-LOT-HI21-HP in *Figure 3*) sensible heating and cooling dominate the total duty, each exceeding 40%.

Introduction of HENs results in notable energy savings, ranging from 10.5% to 49.0%. These savings primarily reduce sensible heat duties, with reductions between 62.7% and 100% for sensible heating and between 0% to 96.1% for sensible cooling. By contrast, latent heat reductions are smaller, reaching a maximum of 18.7% for heating and 45.8% for cooling.

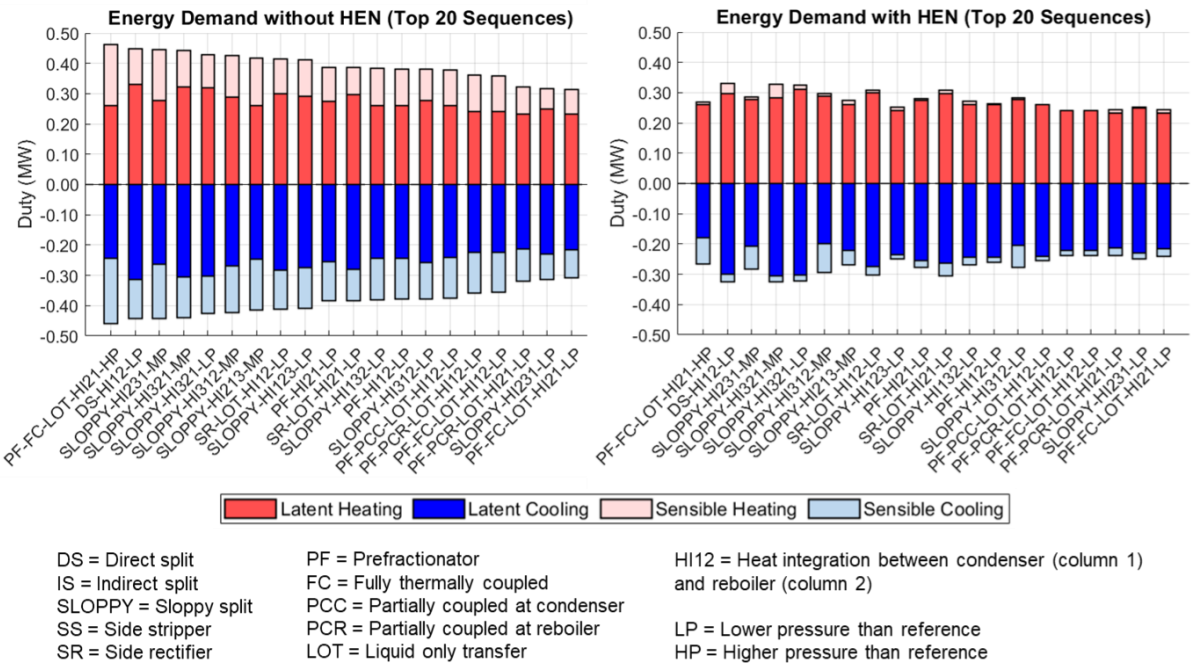

Figure 3: Latent and sensible contributions to heating and cooling duties for different distillation sequences separating BTE, shown before (left) and after (right) the introduction of cost-optimal HENs.

Finally, sensible heat contributions influence the rankings of competing sequences, as shown in *Figure 3*. Notably, the top ten sequences after HEN introduction are within 12% of each other in terms of heating requirements and are within 6% in terms of estimated TAC, indicating that several alternatives can be selected without significantly compromising performance. The proposed approach ensures that promising designs are not overlooked by applying HEN synthesis and optimization to the full solution space generated during screening. This enables informed decision-making based on a set of top-performing sequences rather than relying on a single “best” configuration.

3. Conclusions

This work presents a novel framework for the automated screening and evaluation of intensified distillation sequences with cost-optimal HENs. Reference conditions and auxiliary exchangers were introduced to accurately quantify sensible heating and cooling contributions, enabling a fair and unbiased comparison of competing sequences that accounts for differences in operating conditions. Moreover, the framework relies on rigorous thermodynamics and delivers detailed HEN designs with accurate capital cost estimation using an advanced modular costing approach.

The screening of 77 intensified distillation sequences for the separation of an equimolar benzene, toluene, ethylbenzene mixture reveals that sensible heat introduces additional heating and cooling requirements that are generally non-negligible, especially for high-pressure sequences where they can exceed 40% of the total heat duty. Sensible heat was also found to play a key role in energy integration, with the largest HEN savings predominantly associated with sensible heat recovery.

Both the consideration of sensible heat and the introduction of cost-optimal heat integration alter the relative rankings of competing distillation sequences, which has important implications for process design. The proposed approach provides a robust foundation for advanced decision-making in early-stage process development and grants engineers greater flexibility to account for practical and operational constraints (e.g., safety, control, potential for retrofit, etc.).

4. References

[1] P. Wankat, *Separation process engineering: Includes mass transfer analysis*. Boston: Pearson Education Inc, 2022.

[2] M. Skiborowski, K. F. Kruber, and T. Waltermann, Eds., *Sustainable Distillation Processes*. In *Sustainable Separation Engineering* (eds G. Szekely and D. Zhao). https://doi.org/10.1002/9781119740117.ch12

[3] J. J. Klemeš and Z. Kravanja, "Forty years of Heat Integration: Pinch Analysis (PA) and Mathematical Programming (MP)," *Current Opinion in Chemical Engineering*, vol. 2, no. 4, pp. 461–474, 2013, doi: 10.1016/j.coche.2013.10.003.

[4] K. Wang, Y. Qian, Y. Yuan, and P. Yao, "Synthesis and optimization of heat integrated distillation systems using an improved genetic algorithm," *Computers & Chemical Engineering*, vol. 23, no. 1, pp. 125–136, 1998, doi: 10.1016/S0098-1354(98)00254-3.

[5] A. Harwardt, K. Kraemer, and W. Marquardt, Eds., *Optimization based design of heat integrated distillation processes*. 2009.

[6] S. Farrokhpanah, "Design of Heat Integrated Low Temperature Distillation Systems," Doctoral Thesis, School of Chemical Engineering and Analytical Science, University of Manchester, 2009.

[7] H. Yoo, M. Binns, M.-G. Jang, H. Cho, and J.-K. Kim, "A design procedure for heat-integrated distillation column sequencing of natural gas liquid fractionation processes," *Korean J. Chem. Eng.*, vol. 33, no. 2, pp. 405–415, 2016, doi: 10.1007/s11814-015-0139-2.

[8] Q. Li, A. J. Finn, S. J. Doyle, R. Smith, and A. A. Kiss, "Synthesis and optimization of energy integrated advanced distillation sequences," *Separation and Purification Technology*, vol. 315, p. 123717, 2023, doi: 10.1016/j.seppur.2023.123717.

[9] M. Skiborowski, "Fast Screening of Energy and Cost Efficient Intensified Distillation Processes," *Chemical Engineering Transactions*, vol. 69, pp. 199–204, 2018. [Online]. Available: https://api.semanticscholar.org/CorpusID:53483963

[10] J. Bausa, R. v. Watzdorf, and W. Marquardt, "Shortcut methods for nonideal multicomponent distillation: I. Simple columns," *AIChE J.*, vol. 44, no. 10, pp. 2181–2198, 1998, doi: 10.1002/aic.690441008.

[11] M. Adami, D. Espert, and M. Skiborowski, "Rapid multi-criteria screening of energy-integrated distillation processes for nonideal mixtures," *Separation and Purification Technology*, vol. 377, p. 134463, 2025, doi: 10.1016/j.seppur.2025.134463.

[12] T. F. Yee and I. E. Grossmann, "Simultaneous optimization models for heat integration—II. Heat exchanger network synthesis," *Computers & Chemical Engineering*, vol. 14, no. 10, pp. 1165–1184, 1990, doi: 10.1016/0098-1354(90)85010-8.

[13] K. M. Guthrie, "Capital Cost Estimation," *Chemical Engineering*, vol. 24, pp. 114–142, 1969.

[14] R. Turton, J. A. Shaeiwitz, D. Bhattacharyya, and W. B. Whiting, *Analysis, synthesis, and design of chemical processes*. Boston: Prentice Hall, 2012.

Process Design, Amine Chemistry, and Mass Transfer Equipment for Successful Carbon Capture

Lee Ming Yang[1], Ralf Notz[3], Thomas Winkler[2], Eduard Karslyan[3], Georg Sieder[3], Grace Mierl[4]

[1]Sulzer Singapore Pte Ltd, Singapore; [2]Sulzer Chemtech Ltd, Winterthur, Switzerland; [3]BASF SE, Ludwigshafen, Germany; [4]BASF Corporation, Houston, TX, United States

Abstract

The successful commercialization of carbon capture using amine solvents, especially for flue gases, requires sustainable economics in capital and operational expenditure and proven reliability in plant operation. The paper focuses on three important aspects to achieve these myriad objectives: enhanced amine chemistry, process design optimization, and custom mass transfer equipment. These improvements help to achieve >90% carbon capture, lower the CO_2 absorber column pressure drop, reduce the CO_2 stripper specific reboiler duty, minimize solvent emissions in the treated gas, and mitigate solvent degradation. Operational data from demonstration plants employing BASF's OASE®[1] blue technology and Sulzer's mass transfer equipment validates these improvements. In addition, an overview of onboard carbon capture and storage (OCCS) and the new challenges and development efforts required are presented.

Keywords

Post-Combustion Capture; CO_2 Absorption; Amine; Mass Transfer

1. Introduction

Carbon capture for reducing carbon dioxide (CO_2) emissions has significantly expanded across industries, including natural gas and LNG, refinery, chemicals, syngas (e.g., blue hydrogen, blue ammonia), power, waste-to-energy, cement and steel, with a growing focus on both CO_2 storage and utilization. In several industry sectors, CO_2 removal has been practised for decades in production processes, typically under elevated pressures and in oxygen-free environments. While these applications target for the CO_2 depleted product stream, a highly concentrated CO_2 stream is emitted to atmosphere. Although ideal for sequestration, in the 20th century, only a few plants with CO_2 sequestration or usage were put into operation. However, the number of sequestration projects has increased in the last two decades [1]. Since the beginning of this century, increasingly, attention is shifting towards the removal of CO_2 from oxygen-containing gas streams, including process streams in cement and steel production, and flue gas streams in power generation and waste-to-energy plants, which is typically called post-combustion capture (PCC).

These new applications present unique challenges, including:

- Low CO_2 partial pressures, reducing the driving force and kinetics for CO_2 absorption
- High energy penalty associated with solvent regeneration (stripper reboiler duty)
- Presence of impurities causing amine degradation, foaming, and fouling
- Environmental emissions in the treated gas
- Low gas density resulting in large gas volumetric flowrates and big columns
- Tremendous pressure on capital (CAPEX) and operational (OPEX) expenditure

[1] OASE® is a trademark of BASF, registered in several countries.

2. Development and Optimisations of BASF's OASE blue Technology

Two decades ago, the state-of-the art process for PCC from oxygen-containing flue gas at atmospheric pressure was chemical absorption using monoethanolamine (MEA) in a simple absorber-stripper configuration [2]. Due to several constraints of this process, especially the relatively high specific reboiler duty and significant oxidative degradation of MEA, universities, research institutes, and companies have pursued R&D activities that led to better process configurations, advancements in amine chemistry, and improvements in mass transfer equipment over the past twenty years.

BASF has also devoted substantial resources to the development of optimized solvents for PCC as part of a cooperation between BASF, RWE Power and Linde [3]. Through an extensive evaluation of approximately 400 substances and a subsequent screening of around 70 potential candidates, BASF developed the OASE blue solvent [4]. This proprietary formulation exhibits markedly superior performance relative to MEA, demonstrating enhanced oxidative stability, increased cyclic capacity, and reduced heat of absorption. Notably, the latter two attributes contribute to a decreased regeneration energy requirement.

These efforts, together with the application of optimized process configurations, have resulted in the development of the OASE blue technology that maximizes CO_2 removal and plant reliability, while minimizing waste production, energy consumption, and initial capital expenditure.

An example of the process configuration of the advanced OASE blue process is shown in Figure 1. After the usual flue gas pre-treatment including a direct contact cooler (DCC), the gas stream flows via a blower from the bottom to the top of the absorber column, in counter current flow to the OASE blue solvent. The application of an interstage cooler removes a part of the absorption enthalpy from the system and achieves an increased capture capacity of the solvent, which allows a reduction of the solution flow rate and consequently a reduction in the regeneration energy. Above the absorption zone, the patented emission reduction section OASE aerozone followed by the water backwash section with pump-around loop allows to achieve minimum emissions. For solvent regeneration, the stripper interstage heater (SIH) leads to a further reduction in the regeneration energy requirement.

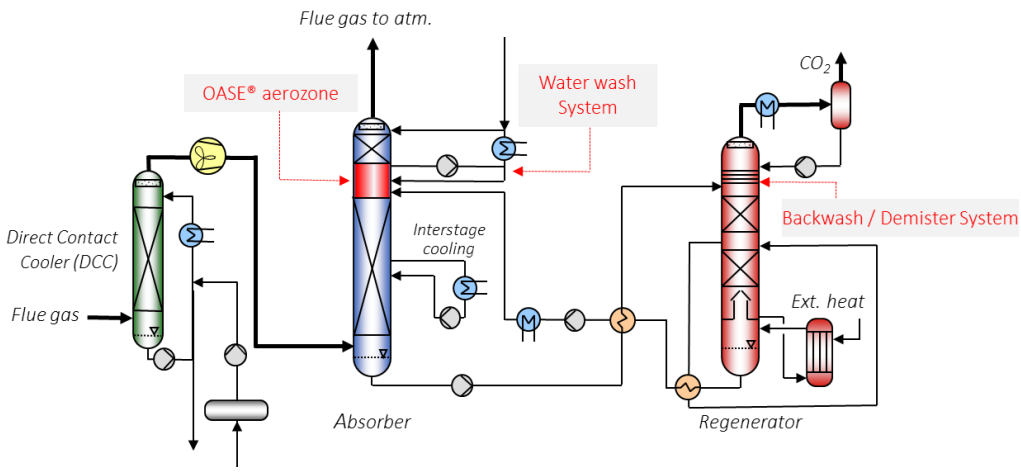

Figure 1: Example of the advanced OASE blue process configuration.

3. Equipment Optimisations in the CO_2 Absorber

The CO_2 absorber is the biggest equipment in a carbon capture unit, especially for PCC. A 500 MW natural gas combined cycle (NGCC) power plant produces ~3 million m^3/hr of flue gas and requires a square absorber of ~18 m in width. The absorber typically comprises two to three packing beds in the CO_2 absorption section, and one to two packing beds in the water wash section (Figure 2). The absorber height can exceed 50 m.

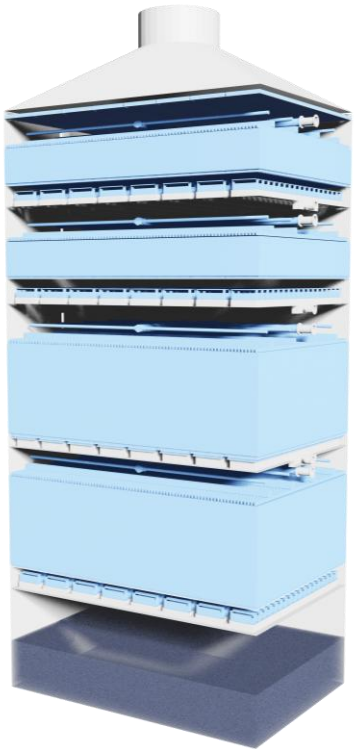

Figure 2: Exemplary drawing of a rectangular CO_2 absorber with two packed beds in the water wash section and two packed beds in the CO_2 absorption section.

3.1 Minimising solvent emissions

There are three mechanisms by which amine molecules leave with the treated flue gas: vaporisation, aerosols, and entrainment of liquid droplets (typically >10 µm). The third mechanism is mitigated by using a phase separation equipment such as a wire-mesh mist eliminator. The first two mechanisms can be mitigated with the OASE aerozone followed by the water wash section.

The OASE aerozone requires the use of mass transfer equipment that can handle low specific liquid loads. Consequently, hydraulic and mechanical designs for initial liquid distribution and liquid leak-tightness become critical. Furthermore, good and consistent liquid spreading on the mass transfer equipment is required to avoid liquid maldistribution and achieve reliable amine removal performance. To overcome this limitation, an upgrade of conventional mass transfer equipment is applied.

3.2 Minimizing the absorber pressure drop

As the flue gas is close to atmospheric pressure, a blower is typically installed upstream or downstream of the DCC column to enable the flue gas to overcome the absorber column pressure drop (Figure 1). The blower electrical duty is the second largest OPEX contributor after the stripper reboiler duty (and excluding CO_2 compression). For the same 500 MW NGCC power plant, a 10 mbar reduction in the absorber pressure drop saves nine million kWh and 450,000 EUR per year [5].

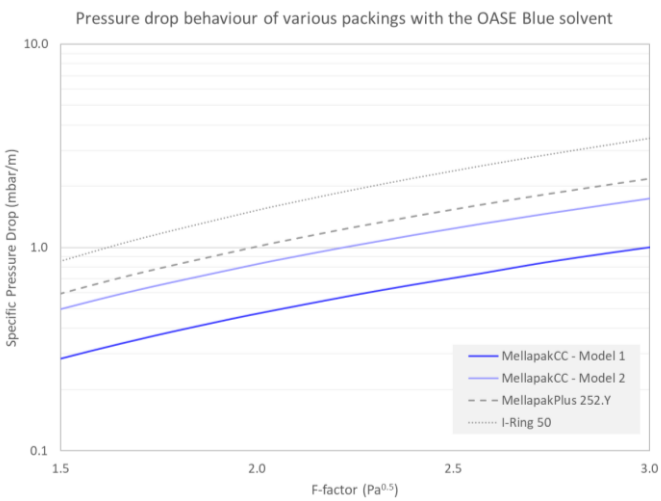

Figure 3: Comparison of pressure drop and hydraulic capacity of four packings for PCC in a NGCC power plant.

Most of the absorber pressure drop stems from the structured packings in the CO_2 absorption section. While the other column internals such as liquid distributors contribute less to the overall

pressure drop, optimized designs for these internals are nonetheless important for both reducing pressure drop and preventing gas maldistribution [5]. With focus on the structured packings, the Sulzer MellapakCC™ structured packing family was developed to minimize the pressure drop without compromising the CO_2 absorption efficiency. Figure 3 compares the pressure drop and hydraulic capacity behaviours of four packings for a representative OASE blue design for a PCC unit in a NGCC power plant: I-Ring™ 50, MellapakPlus™ 252.Y, MellapakCC Model 1, and MellapakCC Model 2. Random packings are no longer used in PCC plants, nonetheless I-Ring 50 is included for instructive purposes.

For a comparison of the mass transfer efficiency and pressure drop of the same four packings, design simulations for 90% CO_2 removal from a defined flue gas stream of a NGCC power plant were carried out with BASF's proprietary rate-based simulation tool OASE connect. To allow a fair comparison for the fixed flue gas flow rate and composition, the absorber F-factor and diameter, lean amine CO_2 loading and specific reboiler duty were fixed. The resulting absorber packing height required for mass transfer and packing pressure drop are compared in Table 1.

Table 1: Comparison of the absorber packing design parameters for a PCC plant in a NGCC power plant, designed with the OASE blue process.

Packing type	Unit	I-Ring 50	MellapakPlus 252.Y	MellapakCC Model 1	MellapakCC Model 2
Packing height	%	174	100	102	81
Packing pressure drop	mbar	62	22	11	15

MellapakCC Model 1 has a slightly lower CO_2 absorption efficiency, better hydraulic capacity and significantly lower pressure drop compared to MellapakPlus 252.Y. MellapakCC Model 2 has a significantly better CO_2 absorption efficiency, better hydraulic capacity and lower pressure drop compared to MellapakPlus 252.Y.

These benefits are also applicable to other carbon capture applications, including coal-fired power generation, cement and steel, to differing extents. The right selection of a structured packing type in the MellapakCC family allows a case-specific optimization of pressure drop, column diameter and absorber height.

4. Insights from Demo Plant Data

During solvent development in the laboratory and mini plant tests for solvent screening, characterisation and modelling, the main emphasis is typically placed on performance determining components like CO_2 and oxygen. In these steps, the impact of flue gas trace components is judged theoretically or with simplified experiments. Mini plants generally do not represent the actual size of full-scale plants and experience certain limitations, such as reduced mass transfer height or discrepancies in heat balance caused by heat losses. To comprehensively validate process performance during both short-term parametric testing and long-term steady-state operation, as well as to validate process simulation models, it is essential to construct demonstration plants at scalable sizes. These facilities should operate under actual flue gas conditions and encompass all aspects of the process, including flue gas pre-treatment and the DCC.

For the OASE blue process, a demonstration plant was built by Linde and operated by RWE at RWE Power's lignite-fired power plant at Niederaussem, Germany [3, 6, 7]. In addition, further OASE blue demonstration plants were built and operated by

Linde, at the National Carbon Capture Center (NCCC) in Wilsonville, Alabama, US [8, 9], and at City Water, Light, and Power (CWLP) in Springfield, Illinois, US [10]. Plant size and flue gas flow rate were increased from Niederaussem (1550 Nm^3/h) to NCCC (approx. 5500 Nm^3/hr) and CWLP (more than 40000 Nm^3/hr). The operation of these demonstration plants at 90% or higher CO_2 removal confirms that the OASE blue technology performs as expected – with lower solvent circulation rates, decreased specific reboiler duty, and less amine degradation compared to MEA.

These demonstration plants also illustrate the operational effectiveness of the mass transfer internals. The Niederaussem plant was originally equipped with a state-of-the-art structured packing and was revamped in a second project phase with a high-performance packing from the MellapakCC family, while at the same time the internal diameter of the column was reduced to allow operation with higher F-factors. Figure 4a) shows the specific pressure drop calculated as average over the absorption beds for both packing types and confirms the improved hydraulic performance of the MellapakCC family. Figure 4b) shows the specific energy consumption versus the solvent circulation rate, while the CO_2 removal rate was kept at 90%. The curves for both packings essentially overlap, indicating comparable mass transfer performance in the absorber.

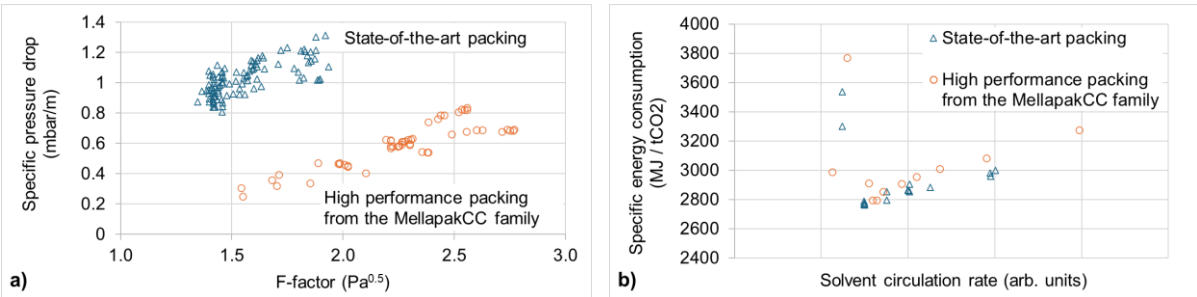

Figure 4: Niederaussem plant: a) specific pressure drop and b) specific energy consumption

The demonstration plants at NCCC and at CWLP are equipped by design with a high-performance packing from the MellapakCC family. Plant operation at 90% CO_2 removal confirms the mass transfer performance of the high-performance packing. The specific pressure drop data, evaluated as average over the absorption beds, are shown in Figures 5a) for NCCC and 5b) for CWLP. The observed values for both plants align with Niederaussem data within acceptable uncertainties, confirming MellapakCC's improved hydraulic performance across varying absorber sizes and flue gas flow rates.

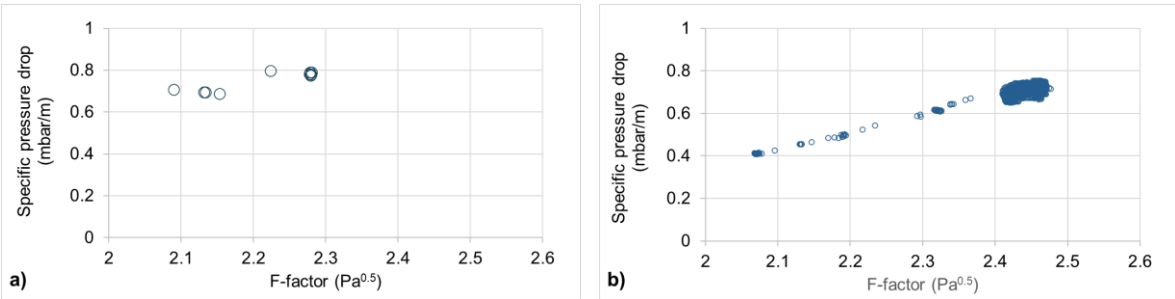

Figure 5: Specific pressure drop at demonstration plants a) NCCC and b) CWLP

5. Onboard Carbon Capture and Storage (OCCS)

The International Maritime Organisation (IMO) aims to achieve net-zero greenhouse gas emissions by around 2050 [11], with onboard carbon capture and storage (OCCS) as a potential solution. OCCS presents different challenges and requirements compared to onshore carbon capture. Primarily, tilt and motion on floating vessels create liquid and gas maldistribution and undermine column performance [12]. Moreover, tremendous space constraints and different energy availabilities demand a different process optimization strategy. For example, the allowed column heights can be severely limiting, requiring highly efficient mass transfer equipment not typically found in onshore carbon capture. These factors necessitate a rigorous "marinisation" study of the columns used in OCCS to assure column performance [12] and promote the development of novel mass-transfer equipment specifically tailored to OCCS applications.

Acknowledgements

The demonstration project at RWE Power's lignite-fired power plant at Niederaussem, Germany, was made possible through funding from the German Ministry of Economics and Technology (BMWi), which is gratefully acknowledged for this joint development programme between BASF, Linde and RWE Power (sponsorship codes: 0327793 A to I for RWE Power, BASF and Linde) as well as the valuable contributions of all project partners is gratefully acknowledged.

The demonstration project at National Carbon Capture Center (NCCC) in Wilsonville, Alabama, US, was made possible through funding from the National Energy Technology Laboratory (NETL) of the U.S. Department of Energy (Contract No. DE-FE0007453), as well as the valuable contributions of all project partners, which all are hereby gratefully acknowledged.

The demonstration project at City Water, Light, and Power (CWLP) in Springfield, Illinois, US, was made possible through funding from the National Energy Technology Laboratory (NETL) of the U.S. Department of Energy (Contract No. DE-FE0031581), as well as the valuable contributions of all project partners, which all are hereby gratefully acknowledged.

References

[1] Global status of CCS 2025 - staying the course, Global CCS Institute

[2] Aaron, D., & Tsouris, C.: Separation of CO_2 from Flue Gas: A Review. Separation Science and Technology (2005) 40(1–3), 321–348.

[3] Moser, P., Schmidt, S., Sieder, G., Garcia, H., Ciattaglia, I., Klein, H.: Enabling Post Combustion Capture Optimization – The Pilot Plant Project at Niederaussem. Energy Procedia 1 (2009) 807 - 814.

[4] Spuhl, O., Garcia, H., Sieder, G., Notz, R.: Comparison and limitation of different evaluation methods for novel PCC solvents. Energy Procedia 4 (2011) 51 - 58.

[5] Lee, M.Y., Ausner, I., Horschitz, B.: Mass transfer technology for next-generation carbon capture. Proceedings of the 16th Greenhouse Gas Control Technologies Conference (2022)

[6] Moser, P., Schmidt, S., Sieder, G., Garcia, H., Stoffregen, T., Stamatovc, V.: The post-combustion capture pilot plant Niederaussem – Results of the first half of the testing programme. Energy Procedia 4 (2011) 1310 - 1316.

[7] Moser, P., Schmidt, S., Wallusa, S., Ginsberg, T., Sieder, G., Clausen, I., Palacios, J. G., Stoffregen, T., Mihailowitsch, D.: Enhancement and long-term testing of optimised post-combustion capture technology – Results of the second phase of the testing programme at the Niederaussem pilot plant. Energy Procedia 37 (2013) 2377 - 2388.

[8] Stoffregen, T., Rigby, S., Jovanovic, S., Krishnamurthy, K. R.: Pilot-scale demonstration of an advanced aqueous amine-based post-combustion capture technology for CO_2 capture from power plant flue gases. Energy Procedia 63 (2014) 1456 - 1469.

[9] Final scientific/Technical report submitted to U.S. Department of Energy under Agreement Number DE-FE0007453: Slipstream pilot-scale demonstration of a novel amine based post-combustion technology for carbon dioxide capture from coal-fired power plant flue gas. (2017)

[10] OBrien, K. C., Krishnamurthy, K. R., Byron, M., Lu, Y., Bostock, D., Patel, V., Brownstein, S., Gioja, L., Dietsch, J., Guth, D., Larson, G., Nichols, J., Becker, P. J.: Large Pilot Testing of Linde-BASF Advanced Post-Combustion Carbon Dioxide Capture Technology at a Coal-Fired Power Plant. GHGT-15. (2021)

[11] International Maritime Organisation (IMO): IMO's work to cut GHG emissions from ships. https://www.imo.org/en/mediacentre/hottopics/pages/cutting-ghg-emissions.aspx (2023)

[12] Notz, R.: The big goal. Hydrocarbon Engineering. (2024)

Pilot-Scale Experimental Study of MDEA-DGA Blends for CO_2 Capture

D. Ricchiari[1], M. Zabatta[1], D. Flagiello[1], S. Marchini[2], A. Erto[1], M. Beckmann[3], F. Di Natale[1], M. Schubert[2]

[1]Department of Chemical, Materials and Production Engineering, University of Naples Federico II, Naples, Italy;
[2]Chair of Chemical Process Engineering, TUD Dresden University of Technology, Dresden, Germany;
[3]Chair of Energy Process Engineering, TUD Dresden University of Technology, Dresden, Germany.

Abstract

Amine-scrubbing is the most mature technology for post-combustion CO_2 capture, but the energy required for solvent regeneration can be substantial (often reported as 15-30% of power-plant output) and limits large-scale application. Blends of primary and tertiary amines have received increased attention as they offer fast reaction kinetics with lower regeneration energy demand. This study assesses the performances of aqueous methyldiethanolamine (MDEA) promoted with diglycolamine (DGA) as a solvent for amine scrubbing. Experiments were performed in a closed-loop pilot absorber/stripper, focusing on the absorption–regeneration trade-off. Three solvents at constant total amine concentration (50 wt%) were tested: 50 wt% MDEA, 45 wt% MDEA + 5 wt% DGA, and 40 wt% MDEA + 10 wt% DGA. Total dissolved CO_2 in lean and rich solvents was quantified using a rapid, modified Hach LCK388 test. Across the investigated loadings, CO_2 removal decreased as solvent loading increased. Relative to neat MDEA, adding DGA consistently enhanced absorption performance, with most of the benefit achieved already at 5 wt% DGA and only marginal further gains at 10 wt%. In contrast, DGA-containing blends showed reduced regeneration efficiency, consistent with stronger chemical binding associated with carbamate formation. Overall, the results support DGA promotion of MDEA as a practical route to increase capture rates while limiting regeneration costs.

Keywords
Carbon capture, absorption, MDEA-DGA blend, amine scrubbing, pilot plant

1. Introduction

Climate change is widely recognized as one of the greatest challenges of the 21st century. Rising greenhouse gas (GHG) emissions pose a serious threat to ecosystems, food security and human well-being. Mitigation strategies (such as improving energy efficiency, expanding the use of renewable energy and deploying sustainable fuels) are essential, but are unlikely to be sufficient on their own to meet international climate targets. Carbon capture, utilization, and storage (CCUS) has therefore emerged as a critical complementary technology to achieve emissions-

reduction goals set by European and international organizations, particularly in hard-to-abate sectors such as cement, steel, and fossil-fuel-based power generation [1].
Post-combustion absorption using liquid solvents is currently the most mature technology for large-scale CO_2 capture. Amine scrubbing has been extensively applied in natural gas processing and synthesis gas purification and is now being adapted for CO_2 capture from power plants and industrial exhaust streams [2]. Nevertheless, major challenges remain in improving the process economics, especially those related to solvent degradation and the high energy demand associated with solvent regeneration.
Among amine solvents, alkanolamines are the most widely applied due to their high reactivity and selectivity. Primary and secondary amines have traditionally been favored because of their high reactivity with CO_2. Among these, diglycolamine (DGA) has recently attracted attention because its reaction characteristics are similar to those of the more established monoethanolamine (MEA), while its lower volatility enables operation at higher aqueous concentrations [3]. This can reduce the required lean solvent flow rate and has shown good performance, particularly for treating low-CO_2 gas streams. However, both DGA and MEA typically exhibit high regeneration energy requirements and are highly susceptible to oxidative and thermal degradation, which limits overall process efficiency and necessitate frequent solvent replacement. To address these limitations, blends incorporating tertiary amines, which are generally more stable and less energy-intensive to regenerate, have received increasing attention (e.g., [4]). Among tertiary amines, methyldiethanolamine (MDEA) is one of the most widely used, valued for its low volatility, chemical stability (including at elevated temperatures) and reduced regeneration energy demand.
To date, only a limited number of studies have investigated the effect of blending DGA with MDEA on absorption kinetics. Pacheco et al. [5] performed a kinetic study, confirming the synergetic effect of these amines and showing an increased absorption rate, compared to MDEA alone, with minimal additions of DGA. Similar trends have been reported in simulation studies by Chang et al. [6] and Zahid et al.[7].
Despite these promising results, experimental work has largely been limited to lab-scale, open-loop setups, with primary emphasis on the absorption step. To close this gap, the presented experimental study investigates the CO_2 capture performance of MDEA–DGA blends in a pilot-scale gas-scrubbing system under various operating conditions and using different MDEA and DGA ratios. This study provides an overall assessment of performance in a closed-loop, pre-industrial-scale configuration, that will support future industrial applications.

2. Experimental setup and methodologies

2.1 Pilot-plant description and operating conditions

CO_2 capture experiments were performed in a pilot-scale unit consisting of an absorption and a desorption section. A picture of the experimental plant is shown in Figure 1-left, while a simplified process scheme is reported in Figure 1-right.
The absorber (C1) consists of a glass column (DN 100 mm) with 3.0 m packing height. The packing is a stainless-steel Novalox-M random packing (15 mm, Vereinigte Füllkörper Fabriken GmbH & Co. KG). The feed gas consisted of CO_2 and N_2 (≥99.9 vol.% purity each) separately regulated, using mass-flow controllers. Before entering the absorption column, the gas was saturated in a humidifier (C3).

The lean solvent was introduced at the top through a pipe-orifice header with multiple drip points, while the gas stream entered from the bottom through a horizontal pipe. The spent solvent was recirculated to the downstream heat exchanger (W2) by a flow-controlled centrifugal pump (P1). Solvent mass flow, viscosity and temperature were measured by a Coriolis mass flow meter Proline Promass 83I from Endress+ Hauser. Two sampling points were also available at the top and bottom of the absorption column to allow the collection of liquid solvent samples.

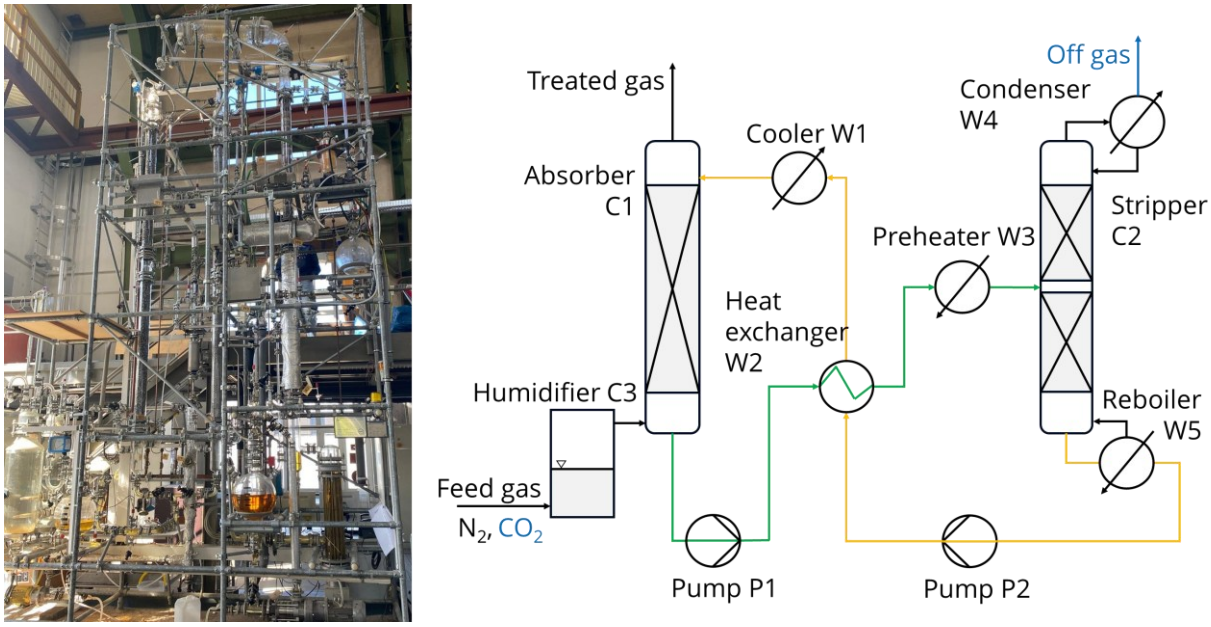

Figure 1: (left) Picture of the pilot-scale absorption/desorption plant and (right) simplified process scheme.

The desorption section was fully insulated with 20 mm mineral wool. The desorption column (C2, DN 100 mm) was packed with two Mellapak 250.Y elements (1.5 m each). The solvent enters the column from the middle section between the two packing beds, flowing downward, while the heat is supplied by a sump reboiler (W5, P_{max} = 9 kW). The gas outlet line of the desorption column is provided with a condenser (W4), which is operated manually (cooling water temperature ~4 °C). In this configuration, only the bottom packed bed is used for the solvent purification, while the upper one serves mainly as a pre-cooling section for the gas, prior to entering the condenser. The CO_2 stream exited the plant through a side outlet. The regenerated solvent is collected in a buffer tank and fed to the absorption column via a level-controlled peristaltic pump (P2). Heat Integration between the absorption and desorption sections is guaranteed via the process heat exchanger. The temperature of the liquid entering the column is controlled via a manual cooler (W1) (cooling water temperature ~4 °C); the cooling water flow rate was adjusted to keep the inlet temperature constant for each operating condition. Temperature measurements at the inlet and outlet of both columns are carried out with PT-100 resistance thermometers. The CO_2 concentration in the gas exiting the absorption column is measured with an infrared gas analyzer Infralyt 40E (measuring range: 0 to 20 vol% CO_2).

The operating condition of the plant covered gas flow rates between 5 and 12 Nm³/h with inlet CO_2 concentrations of 10-20% vol, liquid flow rates of 200, 300 and 400 kg/h, with a L/G ranging between 10 and 50 kg/kg. Pure MDEA (50% wt.) and blends with the addition of 5 and 10% wt of DGA, keeping the total amine concentration

fixed at 50% wt. were tested. Both MDEA (CAS 105-59-9) and DGA (CAS 929-06-6) were of commercial purity (>99%). The mixtures were prepared using tap water (conductivity ca. 350 µS/cm). The absorber inlet temperatures were maintained constant at 40°C (± 1°C). The reboiler duty was set to 28, 23, and 19 kW per ton of liquid flow rate fed.
Absorption and regeneration efficiencies were calculated by measuring the inlet and outlet gas and liquid concentrations in the absorption column at steady state. In addition to the monitoring of the pressure drops, flow rates and temperatures, the achievement of steady state was confirmed via online viscosity measurement of the solvent.

2.2 Liquid samples analysis

Several analytical techniques are reported in the literature to determine CO_2 concentration in rich and lean amine solvents, including volumetric/wet-chemistry methods, gas chromatography (GC), nuclear magnetic resonance (NMR) and titration [8]. These approaches are often applied to investigate CO_2 speciation in amine solutions but may suffer from limited accuracy or require expensive instrumentation. In this work, a simplified and relatively fast liquid-sample method is proposed to facilitate the experimental procedure when the objective is only the total CO_2 content of the solvent, irrespective of whether CO_2 is present as dissolved CO_2, carbonate, bicarbonate or carbamate.
The method is based on a modification of the commercially available LCK388 test kit (Hach), originally designed to quantify inorganic carbon compounds (carbonates and dissolved CO_2) in aqueous solutions (e.g., wastewater, surface water). The sample is acidified to pH < 3 to shift equilibria toward dissolved CO_2. The acidified sample is then digested at 100 °C, promoting CO_2 desorption. The released CO_2 permeates through a membrane and reacts with an indicator solution, producing a visible color change. The color shift is quantified spectrophotometrically, and absorbance is correlated to CO_2 content using a calibration line.
In primary and secondary amine solutions, CO_2 is mainly bound as carbamates and, depending on carbamate stability, also as bicarbonate. In tertiary amines such as MDEA, CO_2 is captured predominantly as bicarbonate. Effective acidification is required to shift equilibria toward dissolved CO_2 [9] and enable its release during digestion. Given the high alkalinity of the amine solutions (pH 10-11), the digestion reagent supplied with the kit did not reduce the sample below the target value. It was therefore replaced with an equal volume of aqueous sulfuric acid. To improve the conversion of carbamates to CO_2, the digestion time at high temperature was increased to 1.5 h. After digestion, samples were analyzed with an Agilent Cary 60 spectrophotometer; representative images of the indicator cuvette color change are reported in Figure 2 (left). The nominal validity range of the Hach test is 50-550 mg/L CO_2, whereas CO_2 concentrations in amine samples can be higher. Consequently, all amine samples were diluted before analysis, with dilution factors ranging from 1:10 to 1:80. Calibration curves were developed using $NaHCO_3$ as a CO_2 source. For each of the three solvents used in the experimental campaign, a six-point calibration set was prepared within the kit validity range: 50, 100, 200, 300, 400 and 500 mg/L CO_2. The reproducibility of the obtained calibration line was satisfactory, with an experimental error <5%. No significant difference was found in the calibration line of the three solvents in the analyzed range, as reported in Figure 2 (right).

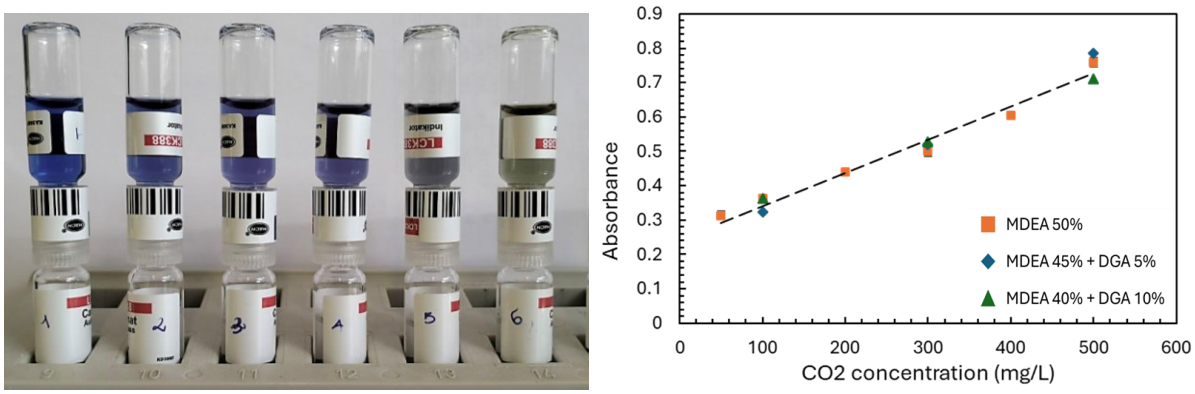

Figure 2: (left) Color change of the indicator increasing CO_2 concentration from left to right, and (right) comparison of calibration curves for different tested solvents.

3. Results and discussion

Figure 3 shows the absorption (η_{abs}) and regeneration efficiencies (η_{reg}) for the different CO_2 loadings investigated and for all tested solvents.

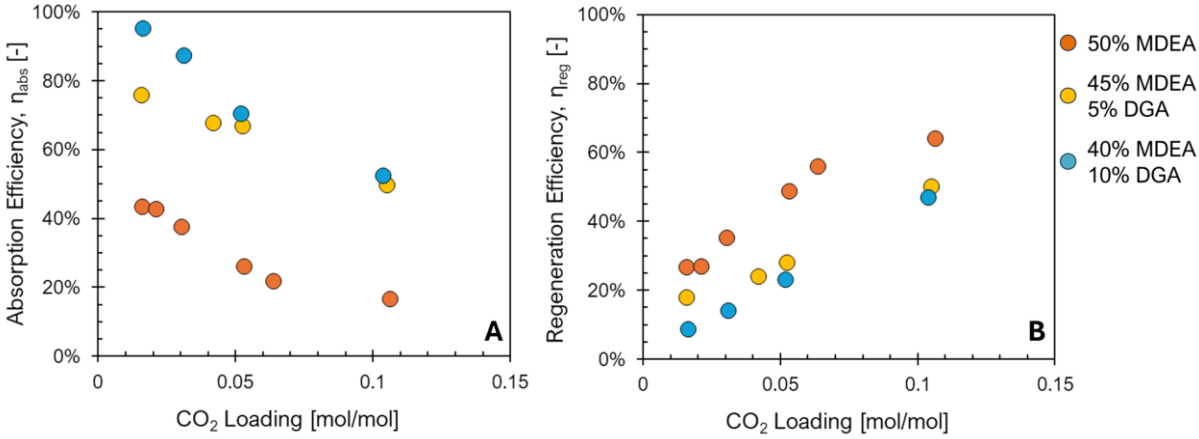

Figure 3: (left) CO_2 removal efficiency, and (right) regeneration efficiency as a function of the CO_2 loading and parametric with the amine blends tested.

As shown in Figure 3-left, the CO_2 removal efficiency decreases with increasing CO_2 loading for all the amine blends investigated. Comparing the performance of the different amine blends, the addition of the primary amine diglycolamine (DGA) to the tertiary amine methyldiethanolamine (MDEA) improves CO_2 absorption. This enhancement is attributed to the introduction of a fast and highly reactive pathway that compensates for the intrinsically slower kinetics of tertiary amines. Specifically, tertiary amines do not form carbamates; they primarily act as bases that promote CO_2 hydration and stabilize dissolved CO_2 as bicarbonate through proton acceptance. In contrast, primary amines react directly with dissolved CO_2 via a zwitterion mechanism followed by rapid deprotonation, leading to carbamate formation and accelerating the overall absorption rate, particularly at low CO_2 partial pressures where interfacial reaction kinetics strongly affect mass transfer. Notably, a small DGA addition (5 wt%) substantially improves the absorption performance of MDEA solutions, whereas increasing the DGA content to 10 wt% yields only a marginal further benefit.

In terms of regeneration (3-right), the highest regeneration efficiency is observed for the 50 wt% MDEA solution, in agreement with the literature [5]. The reduced

regeneration performance of DGA-containing blends is consistent with the stronger chemical binding introduced by primary amines. Carbamate formation is associated with a higher heat of absorption than the bicarbonate-based speciation typical of tertiary amines; consequently, greater reboiler duty is required to reverse the reaction and release CO_2. Moreover, carbamate species lower the equilibrium CO_2 partial pressure at a given temperature, thereby shifting desorption toward higher temperatures and/or higher stripping steam rates to achieve the target lean loading.

4. Conclusions

This work evaluated several MDEA–DGA aqueous blends (total amine 50 wt%) for post-combustion CO_2 capture in a closed-loop, pilot-scale absorber/stripper under a range of gas/liquid flow rates and inlet CO_2 concentrations. A simplified total-CO_2 liquid analysis method was implemented by adapting the Hach LCK388 kit, yielding satisfactory reproducibility and comparable calibration behavior across the tested solvents within the validated range.

From a process-performance perspective, adding DGA to MDEA enhanced absorption efficiency, confirming that introducing a reactive primary-amine pathway compensates for the slower kinetics of tertiary amines. The improvement was already substantial at 5 wt% DGA, while increasing DGA to 10 wt% provided only a marginal additional gain, especially for CO_2 loading higher than 0.05 mol/mol. Conversely, regeneration efficiency decreased for DGA-containing blends relative to neat MDEA, consistent with stronger chemical binding that increases the severity of desorption conditions needed to reach low lean loadings. Overall, the results highlight a clear absorption–regeneration trade-off, suggesting that small DGA additions can be an effective strategy to accelerate capture performance while limiting penalties in solvent regeneration.

References

[1] M.J. Regufe, A. Pereira, A.F. Ferreira, A.M. Ribeiro, A.E. Rodrigues, Current developments of carbon capture storage and/or utilization–looking for net-zero emissions defined in the Paris agreement, Energies 14 (2021) 2406.

[2] F. Meng, Y. Meng, T. Ju, S. Han, L. Lin, J. Jiang, Research progress of aqueous amine solution for CO_2 capture: A review, Renewable and Sustainable Energy Reviews 168 (2022) 112902.

[3] Y.K. Salkuyeh, M. Mofarahi, Comparison of MEA and DGA performance for CO_2 capture under different operational conditions, International Journal of Energy Research 36 (2012) 259–268.

[4] R. Wang, S. Liu, Q. Li, S. Zhang, L. Wang, S. An, CO_2 capture performance and mechanism of blended amine solvents regulated by N-methylcyclohexyamine, Energy 215 (2021) 119209.

[5] M.A. Pacheco, S. Kaganoi, G.T. Rochelle, CO_2 absorption into aqueous mixtures of diglycolamine® and methyldiethanolamine, Chemical Engineering Science 55 (2000) 5125–5140.

[6] H. Chang, C. Shih, Simulation and optimization for power plant flue gas CO_2 absorption-stripping systems, Separation Science and Technology 40 (2005) 877–909.

[7] U. Zahid, Simulation of an acid gas removal unit using a DGA and MDEA blend instead of a single amine, Chemical Product and Process Modeling 15 (2020) 20190044.

[8] N.S. Matin, J.E. Remias, J.K. Neathery, K. Liu, Facile method for determination of amine speciation in CO_2 capture solutions, Industrial & Engineering Chemistry Research 51 (2012) 6613–6618.

[9] Y. Yamamoto, J. Hasegawa, Y. Ito, Kinetic investigation on carbamate formation from the reaction of carbon dioxide with amino acids in homogeneous aqueous solution, Journal of Physical Organic Chemistry 25 (2012) 239–247.

Improving Post-Combustion Carbon Capture Project Economics Utilizing Innovations in Structured Packing

Topham, Taylor; Vennavelli, Anand; Bondley, Zack
Koch-Glitsch LP, Wichita, KS, USA

Abstract
While many novel and innovative technologies have pushed forward the decarbonization efforts on a global scale, post-combustion carbon capture is still a critical technology required to achieve a more carbon neutral future. Many challenges of post-combustion carbon capture exist such as the energy requirements to absorb the carbon dioxide and regenerate the solvents, offsetting the net power output of a power plant, the capital and operation expenses for a post-combustion carbon capture unit, and the size of the equipment required to capture the carbon dioxide at the scale necessary at many facilities. While many of the solvent technology providers have worked to improve the solvent in the critical post-combustion carbon capture technology, Koch-Glitsch saw an opportunity to innovate the structured packing technology.

Many existing technologies utilize and specify conventional structured packings that have been available for over 40 years. Conventional structured packing technology is mature and understood by industry, which leads to confidence in the process design; however, this leads to conservatism when project viability is already tight. Koch-Glitsch took the opportunity to develop a technology that improves project economics and helps increase project viability. Utilizing Koch-Glitsch's in-house 3 tons per day carbon capture unit at its research and development facility in Wichita, KS, FLEXIPAC® CP™ structured packing was developed and validated using both generic solvent technology, with 30% weight MEA (Figure 1), and a proprietary solvent technology (Figure 2). This paper details the innovation of FLEXIPAC CP structured packing specifically optimized for use in the post-combustion carbon capture units. The direct value available from the innovations of FLEXIPAC CP structured packing is explored using multiple case studies to show the economic benefit of this upgrade. The case studies detail not only packing and internal equipment savings, but capital and operational expense savings associated with the improvement in pressure drop and capture efficiency of FLEXIPAC CP structured packing.

Keywords
Carbon capture, structured packing, absorption, energy saving, pressure drop, efficiency

1. Introduction

Global industrial decarbonization is fundamental in achieving a carbon neutral future. While many innovative technologies have emerged, large-scale solutions are needed for effective decarbonization. Post-combustion carbon capture (PCCC) using selective solvent technology to absorb carbon dioxide (CO_2) from flue gases is a key method. Combustion is essential in many industries and managing CO_2 emissions is critical for a carbon neutral future.

Solvent-based absorption of CO_2 is well established in many industries for process reasons. These typically operate under pressure, which minimizes vapor volume in the process to reduce equipment size requirements. In PCCC the flue gases are near atmospheric pressures. This results in very large flue gas volumes at major scale power generation plants, refineries, petrochemical facilities, chemical plants, and other industrial sites. This requires post-combustion carbon capture units with absorber columns greater than 15 meters in diameter and project capital costs reaching billions of dollars.

While the capital cost for the unit is a major hurdle for potential projects, the operating expenses and impact on power generating facilities is another. The net power output is impacted due to the energy required for CO_2 absorption and solvent regeneration. This decrease in power output and the operating expenses of the PCCC unit further impacts the overall project economics.

For PCCC units to become widespread globally, these economic challenges need to be addressed with optimized technologies. Innovations from solvent providers are focused on improving absorption rates, reducing energy required for regeneration, extending solvent life, and addressing issues such as foaming to reducing operational costs significantly.

The other critical component in optimizing the PCCC unit is the absorption media utilized in the columns. Structured packing is used due to its high efficiency and low pressure drop to reduce capital and operating expenses tied to blower size and energy use. It is critical to keep the pressure drop, especially in the absorber, to a minimum for optimal performance. Conventional structured packings, such as FLEXIPAC® structured packing, have been specified in these projects due to their well understood performance in the industry to give confidence in the process design. Koch-Glitsch's expertise in structured packing technology led to the development of FLEXIPAC® CP™ structured packing, an advanced structured packing technology to improve the efficiency, minimize pressure drop, and lower the expenses of these large-scale projects.

Case studies in this paper detail how FLEXIPAC CP structured packing provides savings in internals and packing equipment and reduced capital and operational expenses based on the improved combination of pressure drop and efficiency compared to conventional structured packings.

2. Results and Discussion

The development of FLEXIPAC CP structured packing focused on the specific application of PCCC and the associated physical properties of the liquid and vapor. Conventional structured packings were developed to target a wide range of

applications with varying liquid and vapor properties like density, viscosity, and surface tension. With a narrow range of physical properties in PCCC, Koch-Glitsch used its knowledge and experience with structured packing development to target specific features along with other innovations to provide superior overall performance to existing conventional options.

Koch-Glitsch owns and operates a 3 tons per day carbon capture unit at its research and development facility in Wichita, Kansas. This capability allows for the testing of conventional style structured packings, like FLEXIPAC® structured packing, to baseline against any new packing type for rapid validation of any new structured packing technology. The FLEXIPAC® CP™ structured packing family was developed to be specifically optimized for use in PCCC unit and validated using both generic 30 wt% MEA solvent and a proprietary solvent technology.

The Koch-Glitsch carbon capture unit uses artificially produced flue gas in a closed-loop system to evaluate various performance parameters of structured packings. The system allows for flexibility in testing packing type, packing height in the absorber, CO_2 point source compositions, solvent type, and liquid to vapor ratio. CO_2 concentrations are measured in multiple locations in the absorber while oxygen concentration and moisture content are monitored on the vapor side. Instrumentation on the liquid side includes a total inorganic carbon analyzer and Karl Fischer titration to measure and control water content. Various temperature measurements are taken for a detailed column temperature profile. Packing pressure drop measurements are taken as well to accurately compare overall pressure drop between packings or test cases. This setup allows for validation of critical parameters of PCCC such as pressure drop, capture efficiency, solvent regeneration requirements, and operational limits of the packing.

2.1 Validation Testing and Results

Koch-Glitsch tested multiple packing types to validate the performance of FLEXIPAC CP structured packing. The performance of FLEXIPAC 2X structured packing is well understood in this application and commonly specified in the absorber for PCCC projects. Testing was completed with two different amine-based solvents. Baseline data was collected with 30 wt% MEA, which is a commonly used and well understood solvent for carbon capture. Validated vapor-liquid equilibrium data for 30 wt% MEA is available in various process simulators. With FLEXIPAC 2X structured packing details also included, process models can be accurately tuned and validated to estimate performance under different conditions. A proprietary solvent was tested to further confirm the benefits of FLEXIPAC CP structured packing are maintained in different systems and next-generation solvents.

Testing was completed at various conditions, including liquid-vapor ratios and CO_2 point-source compositions. Figure 1 shows pressure drop comparison between FLEXIPAC CP structured packing and FLEXIPAC 2X structured packing with 30 wt% MEA solvent. FLEXIPAC CP structured packing provides a reduction of 25% when compared to FLEXIPAC 2X structured packing. Since blower operating costs is directly tied to pressure drop in the absorber, reducing this pressure drop results in substantial savings. When considering the performance of two packings, both the relative pressure drop and efficiency need to be considered to confirm higher overall performance.

Figure 2 compares the capture efficiency of FLEXIPAC® CP™ structured packing relative to FLEXIPAC® 2X structured packing on a K_Ga basis. The results show that FLEXIPAC CP structured packing provides a 25% increase in efficiency over FLEXIPAC 2X structured packing. This confirms that the combination of efficiency and pressure drop is improved with FLEXIPAC CP structured packing.

The proprietary solvent testing was also completed at various conditions, including liquid-vapor ratios and CO_2 point-source compositions. Figure 3 compares the pressure drop for FLEXIPAC CP structured packing and FLEXIPAC 2X structured packing with the proprietary solvent. FLEXIPAC CP structured packing provides a similar reduction of 25% when compared to FLEXIPAC 2X structured packing.

Figure 4 compares the capture efficiency of FLEXIPAC CP structured packing to FLEXIPAC 2X structured packing. The results are based on a reduced bed height compared to a typical full-scale absorber to avoid any influence from an equilibrium pinch. In this case, the overall capture efficiency of FLEXIPAC CP structured packing is much improved compared to FLEXIPAC 2X structured packing. This reconfirms that FLEXIPAC CP structured packing offers both higher efficiency and lower pressure drop.

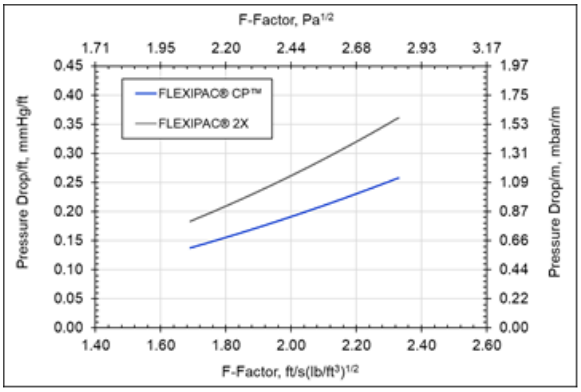

Figure 1 Pressure drop comparison of FLEXIPAC® CP™ structured packing and FLEXIPAC® 2X structured packing in 30 wt% MEA solvent

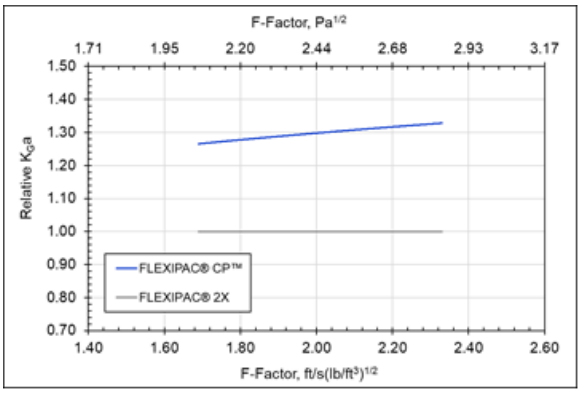

Figure 2 Comparison of relative mass transfer efficiency of FLEXIPAC® CP™ structured packing and FLEXIPAC® 2X structured packing in 30 wt% MEA solvent

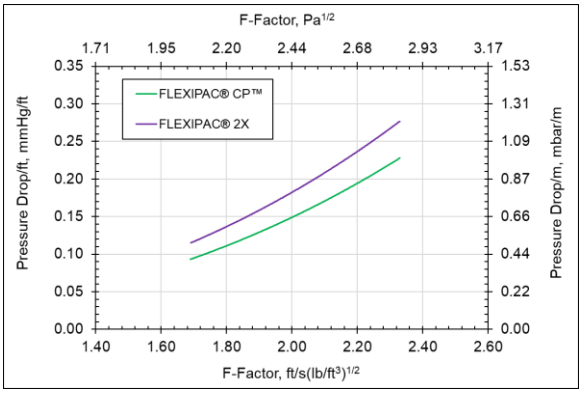

Figure 3 Pressure drop comparison of FLEXIPAC® CP™ structured packing and FLEXIPAC® 2X structured packing with proprietary solvent

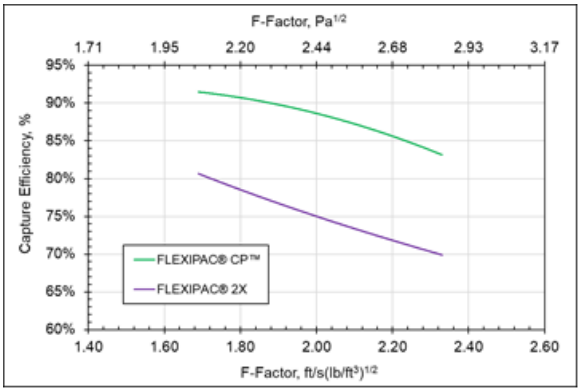

Figure 4 Capture efficiency comparison of FLEXIPAC® CP™ packing and FLEXIPAC® 2X structured packing with reduced packing height with proprietary solvent

2.2 Case Study – Cement Plant

The following two case studies detail the savings from the internal and packing equipment as well as the capital and operational expense savings based on the improved performance of FLEXIPAC® CP™ structured packing.

The first case study considers a cement plant that initially specified FLEXIPAC® 2X structured packing in the absorber. With the advantages seen in the data, there is potential to leverage the superior performance of FLEXIPAC CP structured packing. The flue gas composition in this cement plant is 13 vol% CO_2 with a desired CO_2 capture capacity of 1 million tons/year. FLEXIPAC CP structured packing can provide lower pressure drop for the same height of packing from FLEXIPAC 2X structured packing. FLEXIPAC CP structured packing improves the capture efficiency versus FLEXIPAC 2X structured packing, reducing the required packing height to achieve the target emissions. FLEXIPAC CP structured packing also provides lower pressure drop per height of packing that can lead to a reduction in column diameter.

FLEXIPAC® CP™ structured packing in the absorber reduces the direct pressure drop by 3.0 mbar under the same hydraulic conditions. This saves roughly $100,000 per year in operating expenses. The vessel height and diameter reduction reduces the total packing volume by 25% compared to FLEXIPAC® 2X structured packing, leading to approximately $500,000 in capital expense savings. These direct capital savings do not consider shorter installation time due to less volume, packing brick

quantity, and layer count nor the plot space or foundational savings due to less total vessel weight and operational liquid hold-up with lower volume of packing.

Utilizing FLEXIPAC CP structured packing in place of FLEXIPAC 2X structured packing or other conventional structured packing types provides direct economic benefits for this project. The savings in operational and capital expenses only related to improvements in the packing technology are significant. Other site constraints related to overall absorber height or plot space limitations are eased with the process performance benefits using FLEXIPAC CP structured packing without sacrificing on the desired CO_2 capture efficiency.

2.3 Case Study – Natural Gas Combined Cycle Plant

Replacing a specified conventional FLEXIPAC structured packing with FLEXIPAC CP structured packing provides benefits in this 1200 megawatt in this natural gas combined cycle (NGCC) power plant. The flue gas contains 4 vol% CO_2 and a target capture capacity of 3.5 million tons of CO_2 per year. With the change to FLEXIPAC CP structured packing, similar reductions in pressure drop, vessel height, and vessel diameter can be achieved.

FLEXIPAC CP structured packing lowers pressure drop by 12.5 mbar, which saves approximately $350,000 in annual operating costs. A 6% reduction in tower cross-sectional area and a 15% decrease in the packing height yield $4.5 million in capital savings for the absorber. The savings do not consider the impact on the installation time due to less volume, packing brick quantity, and layer count or the plot space or foundational savings due to less total vessel weight and less operational liquid hold-up due to lower volume of packing.

Utilizing FLEXIPAC CP structured packing in place of conventional structured packing provides direct economic benefits for any PCCC project. The process performance benefits of FLEXIPAC CP structured packing provide significant direct savings without compromising on the desired CO_2 capture efficiency.

3. Conclusions

Due to high costs for large-scale PCCC units, every aspect of the project must be optimized with efficient and innovative technologies to improve economic viability. While solvent providers are improving technology, Koch-Glitsch has driven innovation for greater optimization and efficiency with FLEXIPAC CP structured packing.

FLEXIPAC CP structured packing has been developed, tested, and validated utilizing multiple solvent types to demonstrate its superior performance related to conventional structured packing typically specified in the absorber for these projects. The direct savings in pressure drop with improved capture efficiency can be directly applied to any PCCC project to see immediate savings in operational and capital expenses without compromising the desired carbon capture efficiency.

References

Topham, T., Bondley, Z., Vennavelli, A., Fine, N., Lynch, M., Meuleman, E., Structured Packing Technology for Post-Combustion Carbon Capture, AIChE Spring National Meeting 2024

Topham, T., Bondley, Z., Krela, Mike., Vennavelli, A., Enhancing Post-Combustion Carbon Capture with Advanced Mass Transfer Technology, AIChE Spring National Meeting 2025

Koch-Glitsch. Internals for carbon capture plants. Carbon Capture Journal, Mar-Apr 2013.

Pilot testing of a novel electrochemical carbon capture technology

Sebastian Borgquist[1], Sai Hema Bhavya Vinjarapu[1], Sara Vallejo Castano[2], Tessa Lund Biel-Nielsen[1], Hooman Fatoorehchi[1], Magor Demeter[1], Rasmus K. Engilbertsson[1], Pantelis Bountzis[1], Mads F. Hennings[1], Sebastian F. Balsgaard[1], Nomiki Kottaki[1], Alexandros Gitsoulis[1], Philipp Kuntke[2], Fariborz Shaahmadi[3], Mijndert van der Spek[3], Iasonas Tsilogeorgis[4], Haris Yiannoulakis[4], Elise Michineau[2], Bert V.M. Hamelers[2], Michele Tedesco[2], Grigorios Itskos[5], Valia Chrysovalantou Koutsiantzi[5], Philip Loldrup Fosbøl[1]

[1]Technical university of Denmark, 2800 Kongens Lyngby, Denmark
[2]Wetsus, European Centre of Excellence for Sustainable Water Technology, Oostergoweg 9, 8911 MA, Leeuwarden, the Netherlands
[3]Heriot-Watt University, Edinburgh EH14 4AS, Great Britain
[4]Grecian Magnesite, 63100 Polygyros, Chalkidiki, Greece
[5]Chemical Process and Energy Resources Institute (CPERI), Centre for Research and Technology Hellas (CERTH), Athens, Greece

Abstract

In this study a new carbon capture process is presented. This process used an electrochemically driven pH swing to capture and desorb CO_2. The process consumes no chemicals and does not suffer from solvent degradation issues commonly seen in conventional carbon capture processes.

Instead of conventional amine solvents KOH is used to capture the CO_2. Afterwards the pH of the solvent is reduced in an electrochemical cell. This desorbs the CO_2 in the solvent, which can be collected as a high purity product.

The process was tested on a movable demonstration plant at industrial conditions at a magnesite calcination plant. During this campaign 45 steady state points were identified. It was found that the amount of CO_2 absorbed depended linearly on the amount of current applied to the electrochemical cell. The demonstration plant was capable of removing up to >99% of the inlet CO_2. The maximum CO_2 capture rate was found to be approximately 10 kg/h.

The campaign shows a large capacity for optimizing the process by changing solvent flows in the absorber and electrochemical stack. Generally, the efficiency of the process was highly dependent on the carbon loading in the solvent. Additionally, optimization of the electrochemical stack could significantly lower the energy cost, by lowering the resistance within the stack.

The study is an important step forward in the development and implementation of electrochemically driven carbon capture processes.

Keywords
Carbon Capture; Power-to-X; Pilot scale carbon capture; Electrochemical pH swing; Electrochemical absorption

1. Introduction

Carbon capture, utilization, and storage (CCUS) is a critical technology for mitigating CO_2 emissions from hard-to-abate sectors, such as the cement and mineral industry. Even with a full transition to renewable energy sources, these industries will still emit CO_2, due to the CO_2 emitted from the heating of the mineral itself.

Several CCUS technologies already exist that could be used to mitigate this challenge in the future. Amine-based chemical absorption is currently the most mature method, but it is energy-intensive and suffers from issues with solvent degradation, which can lead to emission of hazardous compounds [1], [2], [3], [4].

Electrochemical carbon capture presents a promising alternative. These processes can be run at ambient temperatures and pressure, are compatible with renewable electricity, and their solvents do not easily degrade [5], [6]. Electrochemical processes also have the potential to be less energy intensive than thermal carbon capture processes. One approach utilizes a pH swing in an electrochemical cell to regenerate solvents such as KOH, which are more stable and environmentally friendly than traditional amines [7], [8].

While lab-scale studies have been performed, few pilot-scale implementations exist [7], [9]. In the ConsenCUS (CarbOn Neutral cluSters by Electricity-based iNnovations in Capture, Utilization, and Storage) project, a first of a kind, 500 Nm^3/h pilot plant was deployed at a magnesite calcination facility in Greece (figure 2). Compared to earlier laboratory experiments this is 100.000 times increase in scale and represents a significant step forward in the readiness of the technology.

Figure 1: *Picture of the ConsenCUS setup on site at Grecian Magnesite in Greece.*

The purpose of the experimental campaign was to test this new process in industrially relevant conditions. Key performance indicators such as energy consumption and electrochemical efficiency were evaluated and will be used for further optimization of the process.

2. Results and discussion

2.1 Method

The carbon capture pilot consists of two processes: an absorber tower, and an electrochemical regeneration unit. The absorber tower works the same as in a

conventional carbon capture process. The flue gas enters the tower from the bottom and encounters a solvent containing KOH. The CO_2 in the flue gas is then absorbed into the solvent while the cleaned flue gas exits the absorber at the top. The solvent exits the absorber at the bottom and is pumped to the electrochemical regeneration unit.

A simplified schematic of the regeneration unit can be seen in figure 2. First the CO_2 rich solvent enters the electrochemical stack. Here H^+ ions are supplied to the solvent from water splitting in the bipolar membranes (BPM) in the cell. This addition of H+ ions causes the pH in the solvent to decrease, which causes CO_2 to desorb. At the same time potassium ions are transported over the cathode exchange membrane (CEM) as shown in figure 2.

After this the solvent is pumped into a desorber where the CO_2 is desorbed and collected. This CO_2 is of a high purity and can be used for the production of chemicals or for long-term carbon storage.

Finally, the solvent is pumped into the other side of the electrochemical stack where OH- ions and potassium ions are supplied by the BPM and CEM as seen in figure 2. This process regenerates the solvent which is now ready to capture additional CO_2 in the absorber tower.

As seen in figure 2 the electrochemical stack also contains an electrolyte loop which pumps a K_2SO_4 electrolyte through the anode and cathode compartments of the electrochemical stack. This electrolyte loop is used purely to facilitate the electrical current running through the stack and does not influence the solvent regeneration process.

The electrochemical regeneration unit in the pilot setup consisted of two electrochemical stacks, each containing 126 cell pairs.

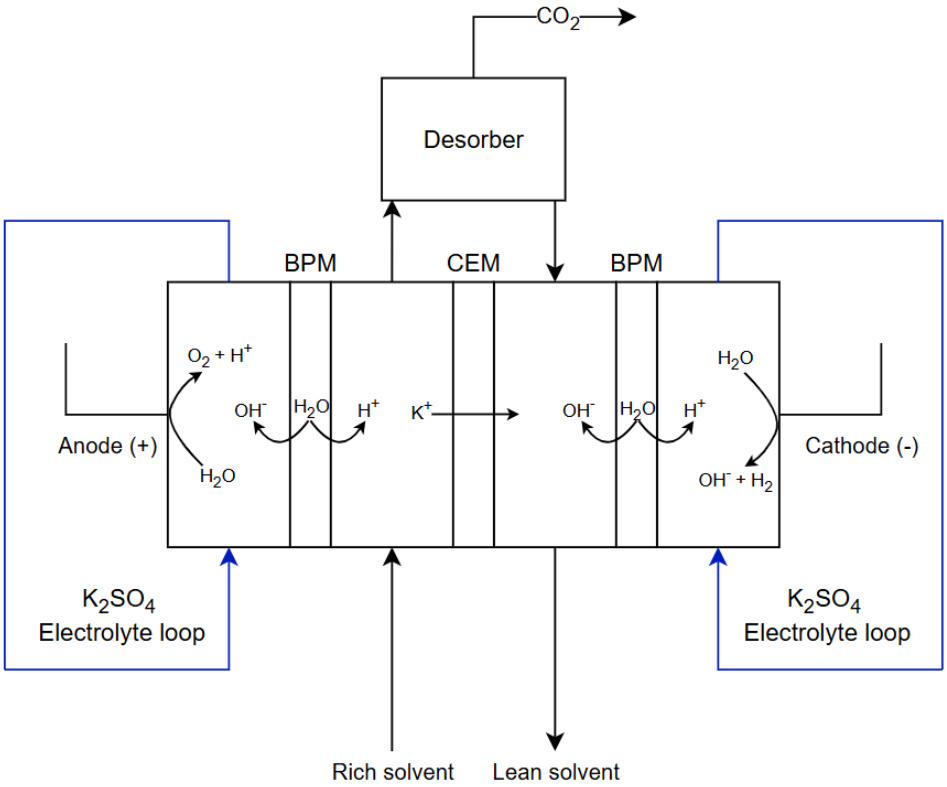

Figure 2: *Simplified schematic of the ConsenCUS electrochemical regeneration module.*

2.1.1 Solvent loading

The solvent loading describes the amount of CO_2 absorbed in the solvent compared to the amount of potassium ions in the solvent. The loading can be calculated in the following way:

$$\alpha = \frac{n_{CO_2}}{n_{K^+}}$$

Where n_{CO_2} is the amount of CO_2 absorbed in the solvent and n_{K^+} is the amount of potassium ions in the solvent. The loading is a number between 0 and 1 where a value of 0 signifies no absorbed CO_2 and a value of 1 signifies a solvent fully loaded with CO_2.

2.1.2 Desorption efficiency

The desorption efficiency is a key performance indicator that describes the performance of the electrochemical stack. It describes the amount of CO_2 desorbed from the solvent compared to the amount of electrons (current) moved through the stack. The desorption efficiency is calculated as:

$$\eta_{des} = \frac{n_{CO_2,des} \cdot F}{I \cdot N}$$

Where $n_{CO2,des}$ is the molar flow of desorbed CO_2, F is Faradays number (96485 C/mol), and N is the amount of cell pairs in the electrochemical stack (126).

2.2 Power consumption

As part of the experimental campaign at Grecian Magnesite the electrochemical stacks were tested at different applied current densities. In figure 3 a) the voltage per cell is plotted against the current density for each of the electrochemical stacks (EC1 and EC2). The two stacks are seen to behave similarly in the tested range. The relationship between applied current density and the voltage per cell is also as expected and is approximately linear within the tested range. This shows that the equipment is still operating far away from the theoretical maximum where an exponential increase in voltage would be expected.

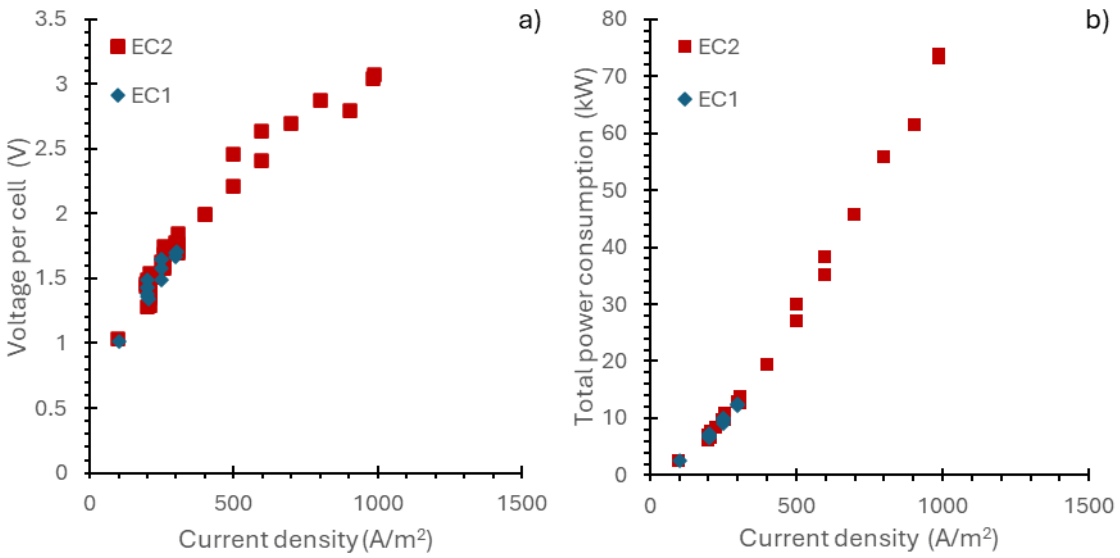

Figure 3: *a) Voltage per cell in the electrochemical stack as a function of current density b) Total power consumption as a function of current density.*

The power consumption of the electrochemical stacks is also plotted as a function of current density (figure 3 b). The maximum power consumption tested during the campaign was approximately 75 kW at a current density of 1000 A/m^2.

2.3 CO_2 desorption in regeneration module

Besides power consumption, several other parameters were also examined during the experimental campaign. On figure 4 a) the desorption of CO_2 is shown as a function of the current density applied to the electrochemical stack. The relationship between CO_2 desorption and current density is seen to be linear, which is expected, since the CO_2 desorption is determined by the production of H^+ ions and the transport of potassium ions as shown in figure 2.

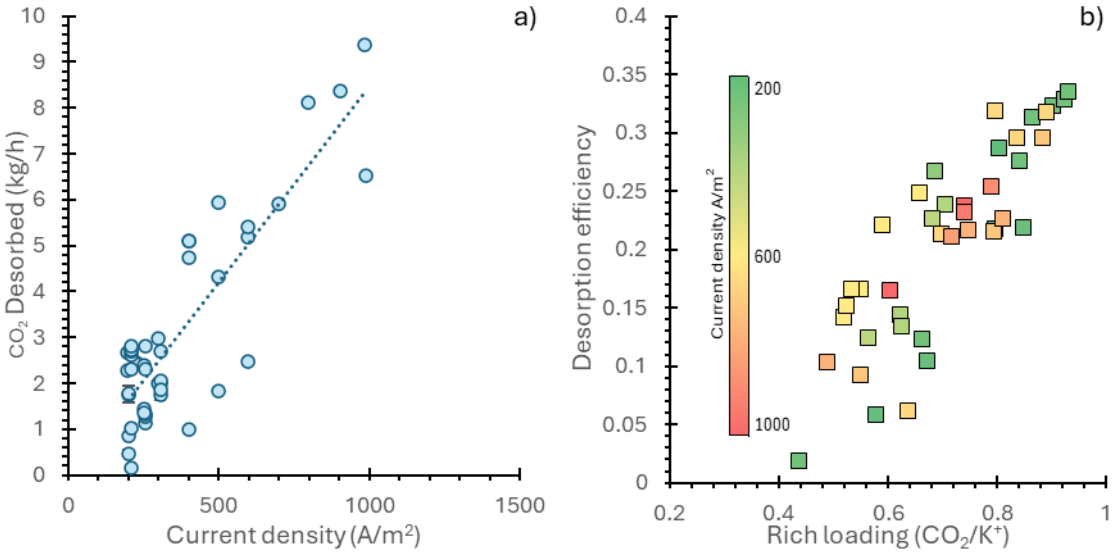

Figure 4: *a) Amount of CO_2 desorbed as a function of current density b) Desorption efficiency as a function of rich CO_2 loading.*

The maximum CO_2 desorption during the pilot tests was found to be 9.5 kg/h. Since this value was achieved at steady state it can be assumed that the CO_2 absorption was also 9.5 kg/h at this steady state.

Depending on process parameters such as inlet gas and absorber solvent flow, the process was capable of removing above 99% of the CO_2 in the inlet flue gas.

On figure 4 b) the desorption efficiency is shown plotted against the rich loading, i.e. the CO_2 loading of the solvent in the bottom of the absorber column.

As seen in figure 4 b) the maximum desorption efficiency achieved during the campaign was approximately 0.35. There is found to be a clear linear correlation between the desorption efficiency and the rich loading of the solvent. This can be explained by the reaction taking place in the electrochemical stack. At a low solvent loading significant power will be used to bring the loading up to 1 by removing potassium ions from the solvent. Only at a loading of 1 will additional current begin to desorb CO_2. This clearly shows the importance of maintaining a high solvent loading for optimal desorption efficiency.

3. Conclusions

In conclusion, the electrochemical CO_2 absorption technology was tested at a pilot scale at real world conditions. During the experimental campaign a maximum of 9.5 kg/h of CO_2 was captured in the pilot setup. The results show that the efficiency of

the process was highly dependent on the solvent loading with higher loading leading to increased desorption efficiency.
Several other parameters were also examined during the experimental campaign. The results of the campaign pave the way for further optimization of this new technology for CO_2 removal.

Acknowledgements
The authors would like to thank the ConsenCUS project for proving financial support. The project has received funding from the European Union's Horizon 2020 Research and Innovation Program under grant agreement No. 101022484.

References

[1] G. T. Rochelle, "Thermal degradation of amines for CO2 capture," *Curr Opin Chem Eng*, vol. 1, no. 2, pp. 183–190, May 2012, doi: 10.1016/J.COCHE.2012.02.004.
[2] S. A. Freeman, J. Davis, and G. T. Rochelle, "Degradation of aqueous piperazine in carbon dioxide capture," *International Journal of Greenhouse Gas Control*, vol. 4, no. 5, pp. 756–761, Sep. 2010, doi: 10.1016/J.IJGGC.2010.03.009.
[3] R. Neerup *et al.*, "Solvent degradation and emissions from a CO2 capture pilot at a waste-to-energy plant," *J Environ Chem Eng*, vol. 11, no. 6, p. 111411, Dec. 2023, doi: 10.1016/J.JECE.2023.111411.
[4] P. Moser *et al.*, "Degradation of the AMP/PZ-based solvent CESAR1 and effects of solvent management in two longtime pilot plant tests," *Chemical Engineering Journal*, vol. 499, p. 155928, Nov. 2024, doi: 10.1016/J.CEJ.2024.155928.
[5] M. Rahimi, G. Catalini, S. Hariharan, M. Wang, M. Puccini, and T. A. Hatton, "Carbon Dioxide Capture Using an Electrochemically Driven Proton Concentration Process," *Cell Rep Phys Sci*, vol. 1, no. 4, p. 100033, Apr. 2020, doi: 10.1016/J.XCRP.2020.100033.
[6] T. L. Biel-Nielsen *et al.*, "Electrochemistry-Based CO2 Removal Technologies," *ChemSusChem*, vol. 16, no. 11, p. e202202345, Jun. 2023, doi: 10.1002/CSSC.202202345.
[7] S. Vallejo Castaño *et al.*, "Optimizing alkaline solvent regeneration through bipolar membrane electrodialysis for carbon capture," *Chemical Engineering Journal*, vol. 488, p. 150870, May 2024, doi: 10.1016/J.CEJ.2024.150870.
[8] M. Shi *et al.*, "Scale-Up of Potassium Hydroxide-Based Co2 Capture: Gas Retention Time and Hydroxide Availability Determine Co2 Capture Performance," 2025, doi: 10.2139/SSRN.5127940.
[9] S. Vallejo Castaño *et al.*, "Optimizing alkaline solvent regeneration through bipolar membrane electrodialysis for carbon capture," *Chemical Engineering Journal*, vol. 488, p. 150870, May 2024, doi: 10.1016/J.CEJ.2024.150870.

CO2-Absorption in Rotating Packed Beds: Exploring the Capacity Limit

Philipp Julian Eichler[1], Georg Brösigke[1], Jens-Uwe Repke[1]
[1]Technische Universität Berlin, Process Dynamics and Operations Group, Berlin, Germany;

Abstract
Climate change is still endangering earth as a whole. The leading contributor to this issue is CO_2 emissions. To lower these emissions, organizations like the International Renewable Energy Agency (IRENA) expect extremely high carbon capture plant demands while simultaneously highlighting, that these plants don't exist today. Conventionally, carbon capture is done in packed columns, but this might be economically infeasible especially for smaller process scales. Here, Rotating Packed Beds (RPBs) are suitable candidates as they promise efficiency increase and cost reduction. Until now, various authors have already shown that RPBs can significantly reduce the required equipment in size. This is achieved by utilization of the rotational force instead of gravitation resulting in increased interfacial area, improved mass transfer and higher flexibility. However, experiments at the very end of the large operating domain of an RPB have been omitted. In this contribution, we aim to close the gap for high gas loads and low L/G ratio by means of an experimental campaign. First results indicate that the RPB is sensitive to gas load and rotational speed alike. While increasing the gas load generally decreases separation efficiency, the overall mass transfer might increase. Furthermore, the capture rate and overall mass transfer coefficient were found to be proportional to the rotational speed with no maximum detected. This is a promising result as previous authors using packings with less specific surface area (A_{spec}) saw a maximum of separation efficiency much earlier. In summary, we will continue to test the RPBs performance at its capacity limit, aiming at further revealing beneficial operating conditions.

Keywords
Carbon Capture, Process Intensification, Rotating Packed Bed

1. Introduction

The effects of climate change on earth are tremendous. They include acidification of the ocean, losses of ice caps and biotopes or extreme weather which in turn cause harm to animals, humans and the nature they live in. The key drivers for this are the greenhouse gases carbon dioxide (CO_2), methane (CH_4) and nitrous oxide (N_2O). Of these, CO_2-emissions are the most extensive and thus impactful type. Alas, the rise of CO_2-emissions has not stopped in recent years [1].

Thus, the issue of tackling their excessive emission into the atmosphere remains of utmost importance and needs to be solved. For existing plants, especially in the chemical or energy industry, retrofits and adaptation to lower emissions at these large point sources of CO_2 will be an important factor. Hence, independent organizations like IRENA calculate demands for carbon capture plants to be as high as 99 Mt. CO_2 per annum until 2050. However, nearly none of these plants exist today [2].

For carbon capture plants, many different solutions exist. The most developed options are ab- and adsorption plants [3]. Absorption is primarily done using (aqueous) amine solutions in packed columns, of which 30 wt-% monoethanolamine (MEA) in water has been a benchmark for the last decades [3, 4]. Even though amine solutions have good absorption capabilities, a lot of energy is lost in the desorption stage to regenerate the solvent, as the present water has to be heated as well to strip the solvent of CO_2. This process step requires 65 % of the total energy for the ab- and desorption needed for an CO_2-absorption application [3]. Consequently, reducing the required solvent amount saves a lot of energy and costs. As a result, research into intensification of the absorption process has been of interest, especially for applications where conventional processes are economically infeasible.

One way to intensify absorption, is by using an RPB. One of the first authors to experimentally prove this were Jassim et al. (2007). They compared an RPB to data from a “conventional absorber” and observed much smaller HTUs and higher mass transfer rates in the RPB [5]. Though, for a fair comparison the liquid to gas ratios (L/G) and amine concentration would have been needed to be more similar and not advantageous for the RPB. Chemcan et. al (2016) showed that when operating an RPB and a packed column with the same flows that much smaller HTUs are achieved in the RPB resulting in an immensely reduced equipment size [6]. Later, experimental studies aimed at enhancing understanding of equipment design and favorable process conditions. For that reason, investigations were conducted into different solvents [8], variation of MEA-concentration [9], intercooling of the rotor [10], or separation performance of different packings [11]. Though necessary at the time to establish a foundation for further research into RPBs, these works largely overlook the operational capabilities of the RPB.

These capabilities shall be explained using Figure 1. Here, the operating principle and design of an RPB is illustrated. An RPB is usually operating in counter-current flow and consist of a rotor disc with a mounted packing. This disc rotates in the casing. Gas travels from casing to the center of the equipment through the packing. This center part is usually referred to as eye of the rotor. Liquid flows from in- to outside, where it gets accelerated continuously through the rotating motion of the packing. Flooding or entrainment like in conventional columns can occur, but both can be overcome by increasing the rotational speed. Liquid will be accelerated more heavily which in turn hinders it from accumulating in the center of the apparatus [7].

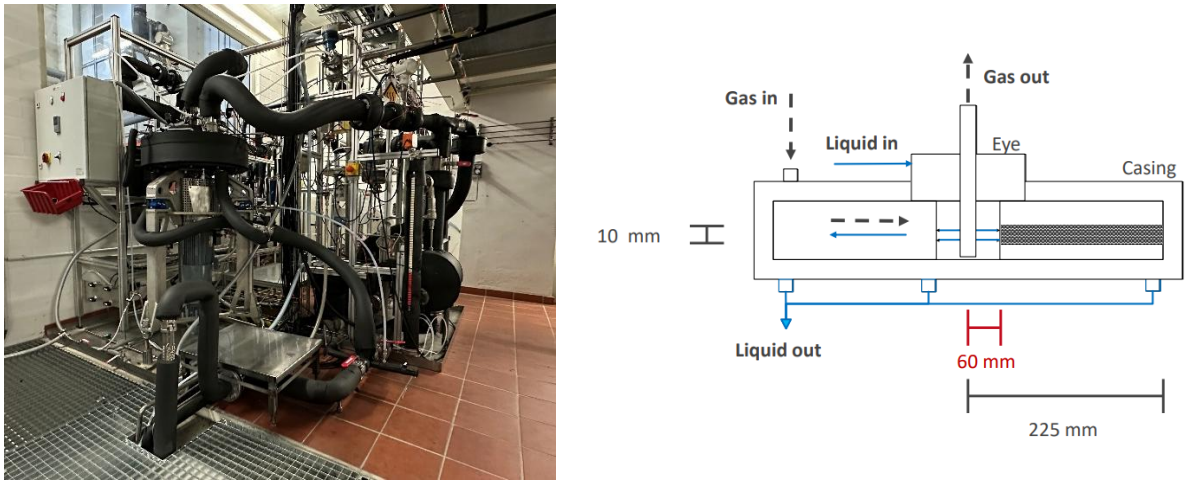

Figure 1: a) Picture of RPB plant for absorption experiments at TU Berlin.b) Flow scheme and dimensions of the RPB used in this contribution.

Hypothetically, for every increment of gas or liquid flow increased an increment of rotational speed exists to again allow for stable operation. Here, stable operation refers to an operating point without entrainment or flooding. This means that theoretically, there is no upper capacity limit regarding fluid dynamics, as long as rotational speed can be increased mechanically.

Reviewing limits of previous works regarding gas load, only [8] extended the experimental matrix and subsequently published data up to an FF of 3.96 $Pa^{0.5}$, but data is not directly comparable as an enzyme additive was used and not solely an amine mixture. [11] showed results for absorption experiments up to an FF of 2.41 $Pa^{0.5}$ using only amine mixtures. Regarding rotational speed, no results above 1200 rpm are reported in [5], [9] or [11]. However, [11] showed promising results for RPBs at high speeds using a metal foam packing. In contrast to the other two investigated packings, mass transfer did not show a maximum in the range of the investigated 1000 rpm. Possibly, further improvements can be discovered by expanding the experiments beyond this investigated range.

Therefore, we expand the experimental matrix to the capacity limit of the RPB at TU Berlin. This means especially missing experimental investigations regarding high gas loads (FF >2.41 $Pa^{0.5}$) and rotational speeds above 1000 rpm. With this, for the first time, we will evaluate the performance of the RPB over its whole operating range, aiming at filling in the gaps in the existing data sets. Furthermore, a new operating range for plants in the field of CO_2-absorption could be discovered altogether.

2. Experiments

2.1 Experiment Matrix

In our experimental study, gas load characterized through the FFs of up until 5.3 $Pa^{0.5}$ are investigated. Simultaneously, the liquid load is varied in relation to the gas load (L/G-ratio) as this defines solvent demand per molecule of gas absorbed. Both, the range usually used for conventional columns (3… 5 kg/kg) and the possibly lower values due to intensified mass transfer for an RPB (1… 3 kg/kg), are investigated. The rotational speed is varied in between 500 and 1500 rpm to explore the interaction between fluid dynamics and mass transfer over the operating domain. For better comparison to existing data, the well-known solvent of 30-wt% MEA in water [3] is used. Ultimately, using higher MEA-concentrations which are only feasible in RPBs due to their higher viscosity shall be investigated as well as [5] and [9] already showed their benefit for the absorption process. Through coupling experiments at the capacity limit with higher MEA-concentrations, a fair assessment of the true RPB capabilities can be done in the future. As packing, a metal foam packing from RECEMAT (NCX1116) is utilized which was found by CT scans to have a A_{spec} of ≈1466 m^2/m^3 [12]. It has an inner (i) and outer (o) radius r_{Pack} of 120 mm and 450 mm. The height h_{Pack} is 10 mm. The gas phase during experiments consists of air with 5$\%_{mol}$ CO_2. Later, concentration will be varied up to 15 $\%_{mol}$ CO_2.

For the absorption experiments, the lean loading of the solvent is kept in between 0.19 and 0.21 mol CO_2/ mol amine. Liquid samples are taken before and after the RPB to analyze the change from lean to rich solvent. Water content is determined using Karl-Fischer-titration, CO_2 and MEA content are determined using direct titration with HCL. Note: Sampling methods need to be adjusted from standard routines to deal with side effects from the alkaline environment of the sample but are not focus of this paper and will not be discussed in detail. Gas samples are taken continuously at the input of the RPB and for every steady state measuring point at the outlet of the RPB. For this, an IR-unit from Leybold GmbH with a measuring range of 0… 20 mol-% CO_2 is used.

2.2 Data Analysis

As a unit of comparison for results, the $K_g\mathrm{a}$ was used. Carbon Capture Rate (CCR) [11], CO_2-penetration [5] or $K_g\mathrm{a}$ [5, 9, 10, 11] have all been used by previous authors. As the definition for $K_g\mathrm{a}$ includes information about the achieved separation efficiency and dimensions of the plant, it is the most useful for comparison of plants of different sizes. The $K_g\mathrm{a}$ is defined as:

$$K_g\mathrm{a} = \frac{F_G}{V_{Pack,tot}} \ \ln\left(\frac{y_{CO_2,out}}{y_{CO_2,in}}\right) \ ,$$

where F_G is the gas flow before the RPB, $V_{Pack,tot}$ is the total volume of the packing and y_{CO_2} is the concentration of CO_2 in the gas stream before (in) and after the RPB (out). $V_{Pack,tot}$ is calculated using the packing dimensions:

$$V_{Pack,tot} = \pi \left(r_{Pack,o}^2 - r_{Pack,i}^2\right) h_{Pack} \ .$$

For very large gas flows, significant losses in capture efficiency can be hidden when comparing these operating points to those with lower gas loads. That is why results of absorption experiments will always be compared with CCR as well. The CCR is defined as follows:

$$\mathrm{CCR} = \frac{y_{CO_2,in} - y_{CO_2,out}}{y_{CO2,in}} \ .$$

3. Results and discussion

In this chapter, the preliminary results of our studies are shown and discussed. Figure 2 shows the CCR a) and $K_g\mathrm{a}$ b) for the same operating points as a function of the rotational speed of the RPB. All operating points were obtained using the NCX1116 metal foam packing. In the figure, values are displayed for two FFs and two liquid loads for one of these FFs. FF values are given in $Pa^{0.5}$ and L/G in kg/kg. In the legend, these units are left out for enhanced clarity of the figure. The results show that for neither investigated FF a maximum over the range of used rotational speeds for CCR and $K_g\mathrm{a}$ could be observed. For an FF of 3.24… 3.29 $Pa^{0.5}$, the CCR and $K_g\mathrm{a}$ both increase with added rotational speed and align onto the same separation efficiency for higher rotational speeds. Thus, the observed higher capture rate for higher L/G ratios compared to lower L/G values at lower speeds diminishes with added rotational speed.

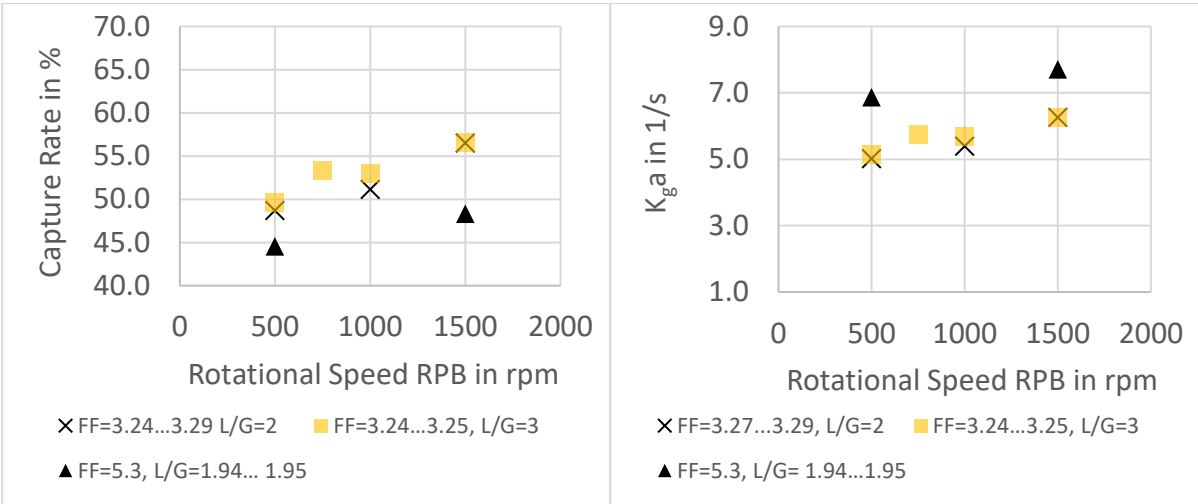

Figure 2: CCR a) and K_ga b) values with varying gas and liquid load obtained with the RPB at TU Berlin as a function of rotational speed at lean loading of 0.2 mol/mol and CO_2 inlet concentration of 5%$_{mol}$.

With higher FF, the capture efficiency drops for a constant L/G. The increased gas flow leads to increased gas flow velocities which in return reduces residence time of the gas in the RPB. Potentially, this could lead to the observed drop in CCR. Regarding the K_ga, it can be seen that the mass transfer in the unit is increased for high FFs even though the CCR drops. Thus, with this process scheme and very high FF, more CO_2 could be separated from the initial gas stream in the same RPB unit. However, the overall quality of the separation declines and outlet concentration of CO_2 in the gas stream increases. In the end, this is a matter of desired process end conditions.

Later in our investigations, we will fill in the gaps with results for FFs from 1.5… 5.3 $Pa^{0.5}$ while including rotational speeds up to 2000 rpm. Effects of liquid load will be researched in more detail by broadening the range of investigates L/G-ratios in between 1…5 kg/kg.

4. Conclusions

First results near the capacity limit of an RPB in CO_2-absorption are presented. These results indicate that increasing the rotational speed until the limit of the RPB's capabilities is beneficial for absorption. This degree of freedom is not available for conventional columns, the current process equipment for CO_2-absorption. Interestingly, this is contrary to previously reported behavior. [9] used a packing with a specific surface area of 663 m^2/m^3 and reported no further benefit to absorption after a rotational speed of 850 rpm. [11] saw similar trends for two packings made of gauze and plastic with comparable $A_{spec.}$ like [9] used. This seems to imply that for absorption there is a clear limit to the achievable separation efficiency with a packing with low $A_{spec.}$ regarding rotational speed.
However, [11] investigated one other packing as well: a metal foam packing with a significantly higher $A_{spec.}$. This packing showed no maximum for separation efficiency for the whole range of rotational speeds (up to 1000 rpm) during the experiments. In [11], it is therefore concluded that overall mass transfer in RPBs is generally 2-5 times greater than in packed columns and additionally highly packing dependent. This supports our findings thus far with the metal foam packing from RECEMAT with relatively high $A_{spec.}$. As our experiments yielded no clear maximum even for

experimental points until 1500 rpms for all gas or liquid loads investigated, we will further increase the rotational speed to find that maximum.

In addition to this, we showed the effect of L/G ratio on separation efficiency decrease with increasing rotational speed. But, to make a full assessment on this phenomena, more operating points are needed. If the observed behavior can be confirmed, RPBs might allow for significantly lower liquid loads to achieve the same desired separation quality. Thus costs, mainly occurring by heating water during desorption, could drop significantly by the reduced solvent demand. To summarize, our work indicates promising operational characteristics for RPBs at their capacity limit which could reveal a new optimal operating range for RPBs. This could be used for both, the design of RPBs in CO_2-absorption and as a data basis for process models. Especially the combined usage of the metal foam packing with higher rotational speeds seems to be beneficial for absorption. Therefore, we will investigate different (high) gas load and corresponding liquid loads, especially paired with high rotational speeds in the continuation of our experiments.

References

[1] IPCC, 2023: Sections. In: Climate Change 2023: Synthesis Report. Contribution of Working Groups I, II and III to the Sixth Assessment Report of the Intergovernmental Panel on Climate Change [Core Writing Team, H. Lee and J. Romero (eds.)]. IPCC, Geneva, Switzerland, pp. 35-115, doi: 10.59327/IPCC/AR6-9789291691647

[2] IRENA, 2025. Regional energy transition outlook: European Union. ISBN: 978-92-9260-658-9

[3] Soo et al., 2024. Advancements in CO2 capture by absorption and adsorption: A comprehensive review. https://doi.org/10.1016/j.jcou.2024.102727

[4] Eimer, D. A., 2014. Gas Treating – Absorption Theory and Practice, p. 43-44 & 55-58. Online ISBN:9781118877746

[5] Jassim et al., 2007. Carbon Dioxide Absorption and Desorption in Aqueous Monoethanolamine Solutions in a Rotating Packed Bed. https://pubs.acs.org/doi/10.1021/ie051104r

[6] Chemcan et al., 2016. Comparison of rotating packed bed and packed bed absorber in pilot plant and model simulation for CO2 capture. http://dx.doi.org/10.1016/j.jtice.2016.08.046

[7] Groß, K.M., 2021. Deaeration in Rotating Packed Beds. URL: https://eldorado.tu-dortmund.de/handle/2003/40163, doi:10.17877/DE290R-22035. accepted: 2021-04-22T06:55:40Z, p. 6-12.

[8] Wojtsaik et al., 2018. Enzyme-enhanced CO2 absorption process in rotating packed bed. Chemical Papers (2019) 73:861–869. https://doi.org/10.1007/s11696-018-0647-8

[9] Kolawole, T.O., 2019. Intensified Post-Combustion Carbon Capture using a Pilot Scale Rotating Packed Bed and Monoethanolamine Solutions. Ph.D. thesis. Newcastle University.

[10] Hendy et al., 2025. Pilot-Scale Carbon Capture in a Heat-Pipe-Intercooled Rotating Packed Bed. Industrial & Engineering Chemistry Research 64, 2872–2879. https://doi.org/10.1007/s11696-018-0647-8

[11] Voice et al., 2024. Performance of Various Packings in a Rotating Packed Bed Absorber for Modular CO2 Capture. Proceedings of the 17th Greenhouse Gas Control Technologies Conference (GHGT-17), 20-24 October 2024. https://dx.doi.org/10.2139/ssrn.5036441

[12] Febrian et al., 2025. Less pressure loss with extra packing – The counterintuitive bahvior of rotating packed beds. Chemical Engineering and Processing – Process Intensification. https://doi.org/10.1016/j.cep.2025.110366

Comparison of heat pump assisted distillation technologies for e-methanol purification

Lucas A.T. Poker,[1*] Anton A. Kiss [1]
1 Department of Chemical Engineering, Delft University of Technology, Van der Maasweg 9, 2629 HZ, Delft, The Netherlands
* Corresponding author: L.A.T.Poker@tudelft.nl (L.A.T. Poker).

Abstract
E-methanol production requires fully electrified purification to minimize carbon emissions. This makes heat pump assisted distillation (HPAD) technologies essential for replacing steam-driven conventional distillation with compressor-based operation. This study rigorously simulates and compares four HPAD configurations, namely two MVR variants (with and without inter-stage pumparound heat recovery) and two D-HIDiC variants (with pumparound and liquid injection inter-stage heat recovery), for binary e-methanol purification from an equimolar methanol-water feed at 200 kton/year scale. The configurations were modeled using the Aspen Plus RadFrac model with NRTL as thermodynamic model. Designs ensure 99.9 wt% methanol purity and full electric operation (at ΔT_{min}=10 °C). Results show comparable modified coefficients of performance (COP_{mod}) of around 5.45 across configurations. MVR requires higher compression ratios (5.13-5.17) due to higher column pressure drop and reboiler duty exceeding condenser duty, necessitating vapor superheating, while D-HIDiC operates at lower ratios (5.03) from higher rectifying vapor flows. The MVR configuration with pumparound loop showed the highest primary energy savings of 56.4%. Dynamic simulations and including impurities are recommended for future optimization.

Keywords
Heat pump assisted distillation, e-methanol purification, mechanical vapor recompression, discretely heat-integrated distillation column, energy efficiency

1 Introduction
E-methanol is as a key carbon-neutral fuel and chemical feedstock. It is produced via CO_2 hydrogenation with green hydrogen, using distillation-based separation and purification. Conventional distillation columns (CDiC) rely on steam, conflicting with electrification goals for renewable integration. Heat pump assisted distillation (HPAD) addresses this by upgrading overhead vapors via compression for reboiler duty, enabling full electric operation with theoretical savings up to 70% [1]. Among HPAD technologies, internally heat-integrated distillation columns (HIDiC) are the most radical approach, having the highest theoretical energy saving potential [1]. By operating the rectifying section at higher pressure, HIDiC enables internal heat integration along the whole rectifying and stripping section, decreasing the required temperature lift. However, due to its complex design and structure, HIDiC has seen very few use in practice [2]. Instead, mechanical vapor recompression (MVR) is the state-of-the-art HPAD technology applied in industry [1]. With the construction of SuperHIDiC in Japan, the discretely heat-integrated distillation column (D-HIDiC) has emerged as a viable HPAD technology for industry. It eliminates the need for complex continuous heat exchange in HIDiC, while being capable of reaching similar energy savings [3]. HPAD is typically used for separation of close boiling point mixtures (ΔT_b < 20 °C), as large temperature lifts require high compression ratios, making HPAD less attractive. Cui et al. have shown that D-HIDiC can reach up to 80% energy savings for methanol-water distillation (ΔT_b = 34.7 °C) [3].

2 Problem statement

To fully electrify the e-methanol production process, electrification of its purification stage is necessary. HPAD is a suitable technology, as it allows full electric operation through compressor shaft work while achieving high energy savings compared to CDiC. Still, when making the choice between the more mature MVR and D-HIDiC, no data is available as D-HIDiC has only been compared to a CDiC [3], [4]. Additionally, methanol-water separations (reboiler duty > condenser duty) challenge MVR superheating needs. Studies comparing HIDiC and MVR are available for multiple cases, but they are not similar in their conclusions, favoring either HIDiC or MVR [5], [6]. Therefore, this study simulates both the D-HIDiC and MVR processes for e-methanol purification at industrial scale to evaluate their energy performance and required heat exchange area.

3 Methodology

3.1 Design approach

The HPAD configurations were rigorously simulated using the RadFrac model in Aspen Plus. To make a fair comparison between the MVR and D-HIDiC, the HPAD configurations were designed using the following design constraints:

- The e-methanol separation is modeled as a binary separation of an equimolar methanol-water feed, saturated at column feed stage pressure.
- Methanol product purity is set to 99.9 %wt, based on AA grade methanol [7]. This corresponds to 99.82 %mol methanol. Bottoms water purity is set at 99.99 %mol.
- Plant capacity is set at 200 kton/year based on the capacities of planned hydrogen electrolyzers in Europe [8], with 8000 operating hours per year.
- The total number of stages is 40, based on the minimum number of stages found using the DSTWU shortcut model in Aspen Plus.
- The HPAD columns need to be capable of full electric operation for e-methanol production, meaning that there is no steam usage at steady state operation.
- The minimum approach temperature for all heat exchangers ΔT_{HX} = 10 °C.
- The compressor system considered uses a 2 stage compressor with equal compression ratios for both stages and an isentropic efficiency of 80%.

Thermodynamic and hydrodynamic models used in the simulations are the following:

- The thermodynamic model used is non-random two-liquid (NRTL), which is suitable and validated for the methanol water system [9].
- Column pressure drop was based on rigorous calculations using Aspen Plus column internals. To ensure high energy efficiency, low pressure drop Mellapak 350Y packing is used for the column internals.
- Packed height per stage was set to 0.5 m, resulting in a packed height of 19 meters for 38 stages. A 20% height oversizing was applied to account for liquid holdup for surge capacity, based on recommendations by Luyben [10].

3.2 Benchmark conventional distillation column

A 40 stage CDiC operating at a condenser pressure of 1 bar with Mellapak 350Y column internals was simulated as reference case. The minimum reboiler duty was found by varying the feed stage and by using design specs to reach the same purity requirements as set for the HPAD configurations. A reboiler duty of 14.43 MW with a condenser duty of -14.18 MW was found for a reflux ratio of 0.855 with stage 33 being the optimal feed stage. This reboiler duty is used to calculate the energy savings for the HPAD designs.

3.3 Mechanical vapor recompression column design

Two MVR columns were modelled: one without interstage cooling for the compressor (MVR 1), and one with interstage cooling where the heat from the interstage cooler is recovered using a pumparound loop and the feed is preheated using a feed effluent heater (MVR 2). They are shown in Figure 1. For the pumparound loop, liquid is drawn from the column, after which it is send through a pump to a liquid-vapor heat exchanger. The pump pressure of 2.5 bar is chosen such that no vaporization occurs. After the heat exchange, the hot liquid is flashed to column pressure and returned. The optimal pumparound stage was determined based on the column grand composite curve (CGCC), selecting the stage with maximum enthalpy difference similar to the approach used by Cui et al [3]. The compression ratio of the compressors is set such that sufficient latent heat is available to cover the entire reboiler duty in the heat exchanger at the minimum approach temperature of 10 °C. The interstage cooling temperature is minimized such that the vapor exiting the compressor remains below the considered maximum allowed temperature (MAT) of 176 °C for a compressor [11] and has 10 °C superheating, to prevent condensation.

3.4 Discretely heat integrated distillation column design

Two D-HIDiC columns were modelled based on the work of Cui et al. [3], [12]: one recovering interstage cooler duty using a pumparound loop (D-HIDiC 1) and one that utilizes liquid injection, which is common in refrigeration cycles (D-HIDiC 2). They are shown in Figure 2. Feed stage was moved from stage 33 to stage 32 for increased energy efficiency. The pumparound loop is executed the same way as the approach described in section 3.3. Interstage cooling temperature is set as to maintain vapor superheating of 10 °C, preventing condensation in the compressor while respecting the MAT of 176 °C. For D-HIDiC 2, both these conditions could not be satisfied at the same time. The compressor MAT of 176 °C was chosen as design criterium. HIDiC typically employs heat integration between stripping and rectifying section. Cui et al. showed that additional internal heat integration on top of the integration of main reboiler with main condenser does not increase energy efficiency for a methanol-water D-HIDiC [3]. Thus, D-HIDiC designs with internal heat integration are not considered in this work.

3.5 Energy usage and heat exchanger comparison approach

Primary energy usage is calculated using a primary fuel to electricity efficiency of 40% [13]. The performance of the HPAD designs is evaluated based on heat pump performance, which is often described using the coefficient of performance (COP). COP is defined as $COP_{std} = (Q_{reb}+Q_{pumparound})/W_{comp}$, which is heat upgraded over heat pump power input. However, if we want to compare which configuration nets the highest energy savings, it makes more sense to compare the benchmark CDiC reboiler duty with the used compression power: $COP_{mod} = Q_{CDiC}/W_{comp}$. Both metrics are shown for all designs in Table 1. To determine the heat exchanger area, the overall heat-transfer coefficient was set to 0.6 kW/(m^{2}K) for tube bundles in vapor space and to 0.85 kW/(m^{2}K) for tube bundles in a liquid pool [14]. Area was then calculated based on log mean temperature difference (LMTD). For the main reboiler/condenser a LMTD value of 10 °C was used based on the set minimum approach temperature. Cooling water was assumed to be 25 °C.

4 Results and discussion

Table 1 shows the results for the energy utilization and required heat transfer area for all designs. It is worth noting that for startup purposes a startup reboiler is needed for MVR and D-HIDiC. Additionally, the auxiliary condenser should be sized such that it can be used for startup, and the D-HIDiC stripper also needs a startup condenser. Assuming a startup duty of 30% of the CDiC design duty, the total heat-exchange areas are 2025 (MVR 1), 1937 (MVR 2), 2054 (D-HIDiC 1), and 2041 m^2 (D-HIDiC 2).

Table 1: Performance metrics for all HPAD designs

	MVR 1	MVR 2	D-HIDIC 1	D-HIDIC 2
Heat exchange duty (kW)	14353	14440	14456	13904
Compression power (kW)	2644	2519	2651	2606
COP_{std}	5.43	5.73	5.45	5.34
COP_{mod}	5.46	5.73	5.44	5.54
Primary energy savings (%)	54.2%	56.4%	54.1%	54.8%
Compression ratio	5.168	5.127	5.052	5.052
# Of heat exchangers	2	4	3	2
Total heat exchange area (m^2)	1824	1796	1674	1660
- Main reboiler/condenser (m^2)	1689	1601	1611	1636
- Auxiliary condenser (m^2)	136	136	26	25
- Intercooler (m^2)		49	37	
- Feed effluent heater (m^2)		10		

4.1 MVR energy savings comparison

The MVR designs utilize higher compression ratio than the D-HIDiC designs. This can be explained by two factors: first, the pressure drop over the 40 stage MVR column is slightly higher than the pressure drop over the 8 stage stripping column, and second; from the benchmark CDiC it can be seen that reboiler duty (14.43 MW) is higher than condenser duty (-14.18 MW). Therefore, not enough latent heat is available to drive the reboiler. To prevent the need for a trim reboiler, the degree of superheating of the vapor has to be increased by increasing the compression ratio to match the available heat from the distillate vapor with the reboiler duty. For MVR 2, the second factor is eliminated by employing a feed effluent heater. Furthermore, compressor efficiency is increased by applying interstage cooling and recovering the heat using a pumparound loop.

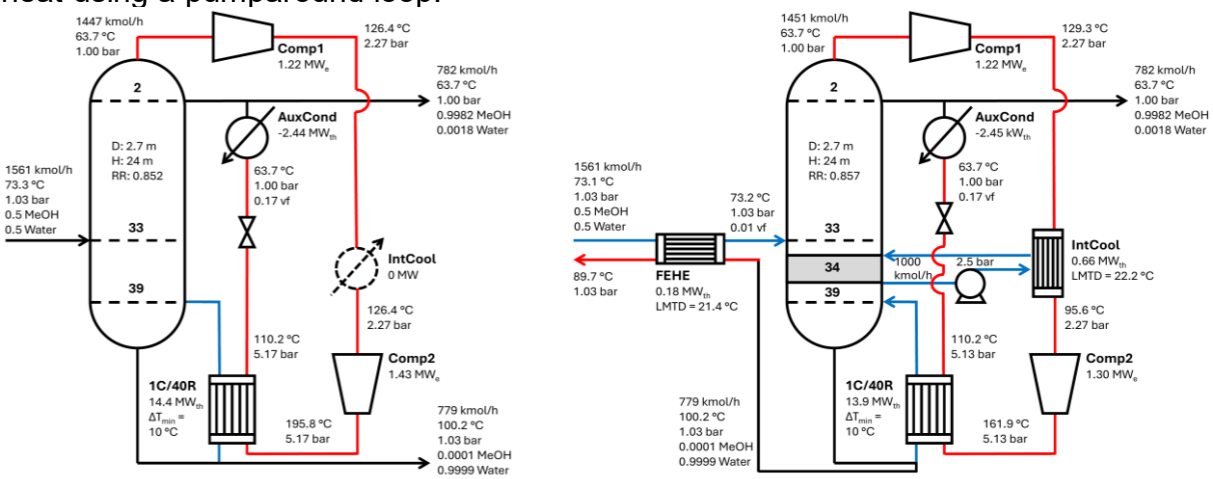

Figure 1: MVR without interstage cooling (left, MVR 1) and MVR with pumparound loop and feed effluent heater (right, MVR 2)

This gives better energy savings for MVR 2 with a COP_{mod} of 5.73 versus 5.46 for MVR 1. Additionally, MVR 1 exceeds the MAT for the compressor, making MVR 2 the preferred configuration.

4.2 D-HIDiC energy savings comparison

D-HIDiC 2 utilizes one less heat exchanger than D-HIDiC 1, but still has higher energy efficiency. For D-HIDiC 2, *Comp 1* has a lowered vapor load, and even though the vapor load for *Comp 2* is slightly higher, this still results in energy savings. Due to the use of liquid injection, the heat from the superheated vapor is used to generate more vapor, ensuring highly effective heat integration. The downside of D-HIDiC 2 is that the interstage temperature was lowered to 103.7 °C to ensure that compressor temperature stayed below the MAT of 176 °C. This is 0.7 °C below the design interstage temperature of 10 °C above the vapor dewpoint to prevent vapor condensation in the compressors. Dynamic simulations are necessary to confirm whether this will be an issue during operation or if the margin of 9.3 °C is sufficient.

4.3 MVR versus D-HIDiC comparison

The D-HIDiC designs operate at lower compression ratio than the MVR configurations. They require a lower temperature lift, since the pressure drop over the stripping section is smaller than the pressure drop over the whole column and they don't need superheated vapor to drive the reboiler (MVR 1). As D-HIDiC uses higher reflux ratio's while having similar boilup ratio's to the MVR configurations, more latent heat is available, eliminating the need for superheated vapor. Nevertheless, MVR 2 outperforms the other designs, having the highest COP_{mod} and primary energy savings of 56.4 %. MVR 2 saves energy by having a lower vapor load for *Comp 2* than D-HIDiC 1 & 2 and *Comp 1* for D-HIDiC 1. Furthermore, due to the use of interstage cooling and the feed effluent heater it negates the drawbacks of MVR 1 of increased compression ratio and higher interstage temperature.

For the heat exchange area, D-HIDiC 2 has the lowest area as this design eliminates the need for an interstage cooler. Nevertheless, if heat exchanging area required for startup is included, MVR 2 has the lowest heat exchanger area of 1937 m^2. This is mainly caused by needing a smaller reboiler/condenser as it recovers heat using the pumparound loop intercooler, while the intercooler has a higher ΔT than the reboiler/condenser resulting in less overall heat exchange area.

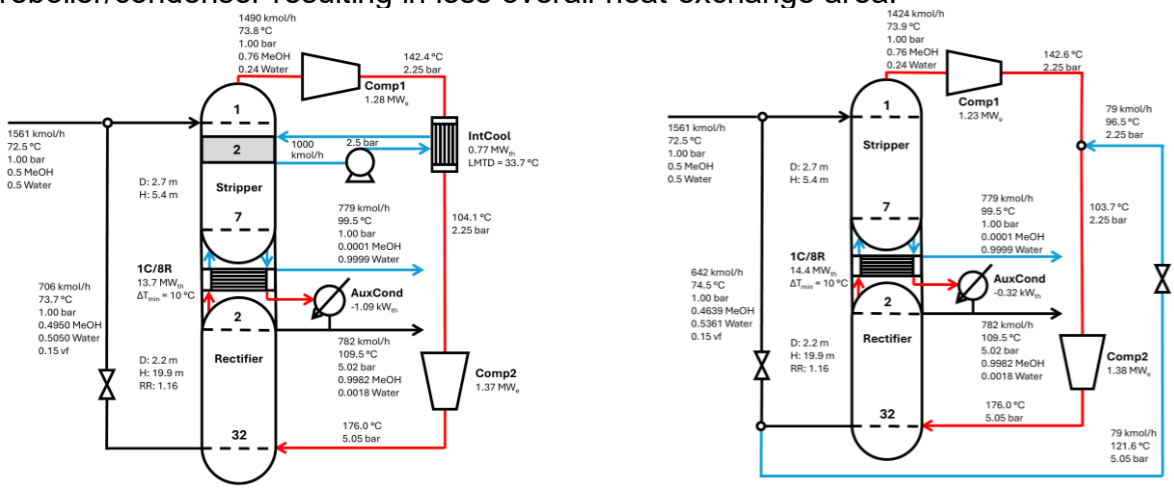

Figure 2: D-HIDiC with pumparound loop (left, D-HIDiC 1) and D-HIDiC with liquid injection (right, D-HIDiC 2)

5 Conclusions

Two MVR configurations and two D-HIDiC configurations were evaluated through process simulation in Aspen Plus to determine the optimal HPAD configuration for full electrification of e-methanol purification. Results showed that HPAD ensures high primary energy savings of more than 54% compared to CDiC. The MVR design using a pumparound loop and feed effluent heater had the highest energy savings of 56.4% for a ΔT_{hx} of 10 °C. It used the smallest heat exchange area of all evaluated HPAD configurations including startup reboiler and condenser, but requires the highest number of heat exchangers. The D-HIDiC configurations had the lowest compression ratios, but required compression power was slightly higher than the MVR configurations due to the higher molar flowrates through the compressors. Based on these results, MVR slightly outperforms D-HIDiC given that the feed can be preheated to prevent the need for vapor superheating by the compressors. Limitations of this work are that no impurities are included, as well as that the dynamic performance of the configurations are not explored.

Further work should build upon these findings by applying rigorous process optimization strategies and by investigating the effect of impurities on the process performance. The economics of the D-HIDiC and MVR should be compared, as well as their dynamic process responses during operation.

6 Acknowledgements

The authors gratefully acknowledge financial support through the EMPHATICaL project. the EMPHATICaL project has received funding from the European union's horizon Europe research and innovation programme under grant agreement no. 101177725.

7 References

[1] A. A. Kiss, 'Distillation technology – still young and full of breakthrough opportunities', *J. Chem. Technol. Biotechnol.*, vol. 89, no. 4, pp. 479–498, Apr. 2014, doi: 10.1002/jctb.4262.

[2] A. K. Jana, 'Advances in heat pump assisted distillation column: A review', *Energy Convers. Manag.*, vol. 77, pp. 287–297, Jan. 2014, doi: 10.1016/j.enconman.2013.09.055.

[3] C. Cui, J. Van Reisen, I. Tyraskis, and A. A. Kiss, 'Efficient heat integration within discretely heat integrated distillation columns using liquid injection', *AIChE J.*, vol. 71, no. 8, Aug. 2025, doi: 10.1002/aic.18861.

[4] T. Wakabayashi, K. Yoshitani, H. Takahashi, and S. Hasebe, 'Verification of energy conservation for discretely heat integrated distillation column through commercial operation', *Chem. Eng. Res. Des.*, vol. 142, pp. 1–12, Feb. 2019, doi: 10.1016/j.cherd.2018.11.031.

[5] J. C. Campbell, K. R. Wigal, V. Van Brunt, and R. S. Kline, 'Comparison of Energy Usage for the Vacuum Separation of Acetic Acid/Acetic Anhydride Using an Internally Heat Integrated Distillation Column (HIDiC)', *Sep. Sci. Technol.*, vol. 43, no. 9–10, pp. 2269–2297, Jul. 2008, doi: 10.1080/01496390802151617.

[6] L. Sun, M. Gadalla, A. de Rijke, and P. J. Jansens, 'Enhancing Thermodynamic Efficiency of Energy Intensive Distillation Columns via Internal Heat Integration', 2009.

[7] Methanol institute, 'Methanol-Technical-Data-Sheet'. 2025. [Online]. Available: https://methanolorg.wpenginepowered.com/wp-content/uploads/2016/06/Methanol-Technical-Data-Sheet.pdf

[8] 'Hydrogen Production and Consumption Projects | European Hydrogen Observatory'. Accessed: Dec. 09, 2025. [Online]. Available: https://observatory.clean-hydrogen.europa.eu/hydrogen-landscape/projects-and-valleys/hydrogen-production-and-consumption-projects

[9] A. A. Kiss, J. J. Pragt, H. J. Vos, G. Bargeman, and M. T. De Groot, 'Novel efficient process for methanol synthesis by CO2 hydrogenation', *Chem. Eng. J.*, vol. 284, pp. 260–269, Jan. 2016, doi: 10.1016/j.cej.2015.08.101.

[10] W. L. Luyben, *Distillation Design and Control Using AspenTM Simulation*, 1st ed. Wiley, 2006. doi: 10.1002/0471785253.

[11] T. Giampaolo, *Compressor Handbook: Principles and Practice*, 2nd ed. New York: River Publishers, 2023. doi: 10.1201/9781003449874.

[12] C. Cui, Q. Li, W. L. Luyben, and A. A. Kiss, 'Dynamics and control of discretely heat integrated distillation columns', *Comput. Chem. Eng.*, vol. 199, p. 109144, Aug. 2025, doi: 10.1016/j.compchemeng.2025.109144.

[13] BP, 'Methodology for converting non-fossil electricity generation to primary energy'. [Online]. Available: https://www.bp.com/content/dam/bp/business-sites/en/global/corporate/pdfs/energy-economics/statistical-review/bp-stats-review-2022-methodology-for-converting-non-fossil-fuel-to-primary-energy.pdf

[14] T. Wakabayashi and S. Hasebe, 'Higher energy saving with new heat integration arrangement in heat-integrated distillation column', *AIChE J.*, vol. 61, no. 10, pp. 3479–3488, Oct. 2015, doi: 10.1002/aic.14865.

Techno-economic assessment of heat pump assisted and cyclic distillation for close-boiling separations

Qing Li, Mattia Vincenti, Anton A. Kiss**
Department of Chemical Engineering, Delft University of Technology, Van der Maasweg 9, 2629 HZ, Delft, The Netherlands

Abstract
Improving the energy and economic performance of close-boiling separations remains a key challenge in industrial distillation. Heat pump assisted distillation (HPAD) and cyclic distillation (CyDist) represent two distinct process intensification strategies focusing on energy integration and mass-transfer enhancement, respectively.
This work presents a systematic techno-economic comparison of three HPAD configurations – vapor compression (VC), mechanical vapor recompression (MVR), and different-pressure thermally coupled distillation (DPTCD) – against CyDist and VC-assisted CyDist under consistent modelling and evaluation.
The results show that HPAD can reduce operating costs by up to 67% for energy-intensive separations, but capital cost increases of ~12% can limit overall economic benefits. HPAD outperforms CyDist in total annualized cost (TAC) only under favorable electricity prices, and long payback periods (>5 years). For high purity close boiling systems, CyDist is a robust alternative, achieving up to 36% capital and 24% operating cost savings; the combined VC-CyDist provides an additional 3% TAC saving. Overall, this study supports the rational selection and design of intensified distillation technologies for close-boiling separations.

Keywords
Cyclic distillation: Heat pump assisted distillation; Techno-economic assessment; Close-boiling separations

1. Introduction

Improving energy efficiency and economic performance of separation processes remains a key challenge in chemical process design, especially for close-boiling (including isomeric) separations where conventional distillation nears thermodynamic limits. Intensified distillation technologies are widely explored to cut energy use and emissions while meeting product specs.
Heat-pump assisted distillation enhances efficiency in close-boiling separations by upgrading low-temperature condenser heat for reboiler use, reducing external heat demand (at added electricity cost). Studies and industrial cases report up to 80% energy savings vs. conventional setups (Kiss, 2020). However, higher CAPEX from compressors and expanded heat exchangers, plus sensitivity to electricity prices, make HPAD's viability case-specific as benefits can fade in poor energy market conditions.
Cyclic distillation (CyDist) takes a distinct approach, improving separation via time-periodic vapor-liquid contacting that avoids liquid remixing, without compression. Patrut et al. (2014) highlight its conceptual edge, with applications showing energy savings over conventional steady-state columns. Yet CyDist lags behind in industry

adoption due to the lack of unified evaluation frameworks and direct, quantitative comparisons with HPAD for close-boiling components separations.
Industry favors intensified technology not just for energy savings but for CAPEX-OPEX balance and utility-price resilience (e.g. electricity-to-steam ratio). Since HPAD targets energy integration and CyDist mass-transfer gains, fair comparisons are difficult. This study fills the gap with a unified techno-economic assessment of CyDist and HPAD for representative close-boiling separations, guiding optimal selection.

2. Methodology

2.1 Overall assessment framework

In order to develop a unified evaluation framework enabling a consistent techno-economic comparison between different configurations for close-boiling separations, all technologies are evaluated under identical separation targets and economic assumption. Three heat-pump configurations are considered as shown in Figure 1: vapor compression heat pumps (VC, Figure 1b), mechanical vapor recompression (MVR, 1c), and different pressure thermally coupled distillation (DPTCD, 1d). These are evaluated alongside CyDist (1e) without external heat pumping, as well as the heat pump assisted cyclic distillation (VC-CyDist, 1f). Conventional distillation is used as a reference for defining energy savings but is not discussed in detail. The assessment focuses on energy usage, CAPEX, and total annualized cost (TAC) as the primary performance indicators.

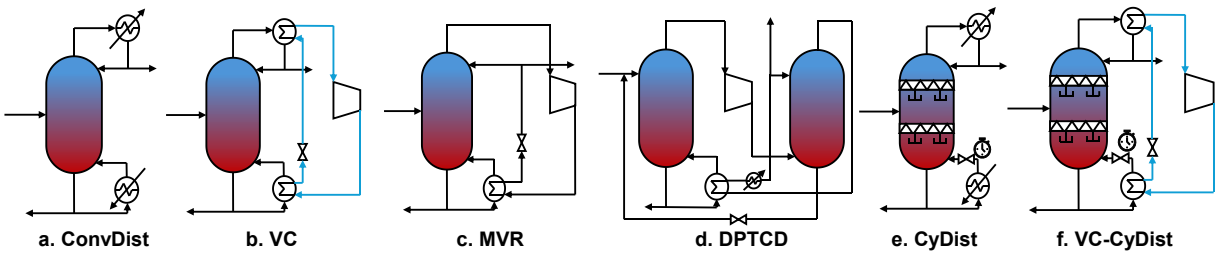

Figure 1. Distillation technologies evaluated in this study

2.2 Modeling of cyclic distillation

Cyclic distillation is modeled using a dynamic, stage-wise approach that captures the periodic vapor–liquid contacting of cyclic operation, which alternates vapor and liquid flow periods within each stage. Due to space limitations here, the reader is directed to the detailed modelling from the work of (Rasmussen et al., 2020). In this study, CyDist is modeled in MATLAB. The solver *ODE45* is used for component balances for the molar liquid holdup on each stage and *fsolve* is used for the non-linear equilibrium equations requiring equality of fugacity coefficients. To compute fugacity coefficients, the analytical Cardano method for third order equations is implemented to solve the equation of state for pure components and mixtures.

2.3 Modeling of heat pump assisted distillation configurations

Heat pump assisted configurations are simulated using Aspen Plus V12. RADFRAC model is used to simulate the conventional distillation columns. Minimum temperature difference ΔT_{min} is set as 10°C, isentropic efficiency of compressor 80%, mechanical efficiency 99%. The working fluid for the external heat pump loop in VC configuration is chosen based on operational safety, environmental sustainability, boiling temperature, high pressure sensitivity and high density from ASHRAE libraries (R-1234Z(E) for C3 splitting and R-1233ZD(E) for B/T separation). Different thermodynamic models are needed for the separation mixture and the working fluid.

For MVR, a trim reboiler and condenser might be required to compensate for the heat duty that could not be fulfilled with the integrated heat.

2.4 Heat pump assisted cyclic distillation

Cyclic distillation has shown promising results for close boiling components (Kiss et al., 2021). Nonetheless, limitations due to low-temperature heat rejection are still present, indicating that coupling the system with a heat pump cycle may provide additional benefits. This combination has never been studied for the following reasons. A key difficulty arises from the periodic nature of cyclic operation: when MVR is considered, the overhead vapor flow to the compressor is inherently intermittent, as vapor withdrawal is only possible during the vapor-flow period, which is incompatible with the required stable compressor performance and complicates both modeling and practical implementation. However, from a column-level perspective, cyclic distillation is operated in a pseudo steady-state mode when cycle-averaged variables are considered. A vapor compression heat pump can be implemented as an external loop without directly interfering with the internal cyclic operation of the column. For this reason, the present work focuses on a VC-CyDist configuration as a representative example of heat pump assisted cyclic distillation, to primarily evaluate its energy and techno-economic performance. The condensation heat generated during cyclic operation is coupled with the VC heat pump that supplies energy to the reboiler. The integration of HPAD and CyDist is modeled as a configuration combining cyclic operation coded in MATLAB as described in Section 2.2 with heat upgrading by VC simulated in Aspen Plus described in Section 2.3.

2.5 Case studies and operating conditions

Benzene/Toluene (B/T) is selected as a reference system to be compared with close boiling separations. Industrially relevant feed conditions and separation specifications were adopted: 400 ktpy saturated feed stream with an equimolar composition. Distillate purity is 99.8 mol% for benzene and bottom purity is 99.5 mol% for toluene. Propane/propylene separation (C3 splitting) is chosen as the close-boiling binary separation case study to evaluate the performance of all proposed technologies. The feed stream is 800 ktpy of saturated liquid containing 70 mol% propylene, product specifications are 99.8 mol% propylene in the distillate and 99.5 mol% in the bottoms. Peng Robinson equation of state is used for simulation. To evaluate the impact of product purity, 99.99 mol% purity products separation requirements are also investigated for both cases. The techno-economic performance of each configuration is evaluated using the following indicators taken from Zhai (2023).

3. Results and discussion

3.1 Economic performance comparison

Figure 2 summarizes CAPEX, OPEX, and TAC for each technology across the investigated case studies, and shows the sensitivity analysis on payback time (PBT) and the electricity costs.

3.1.1 Operating costs comparison

Comparing heat pump options with CyDist and conventional distillation, DPTCD and MVR consistently obtain the lowest operating costs, achieving up to 67% energy savings for C3 splitting and around 40% for B/T separation compared to conventional distillation. VC can still save energy compared to conventional distillation but shows higher operating costs than the other two HP options due to the larger compression duties required. The relative performance of MVR and DPTCD depends strongly on

the operating pressure of the separation. For C3 splitting, conventional columns are typically operated at elevated pressure (~15 bar), which allows a pressure split between the rectifying and stripping sections by operating the latter at a lower pressure. This configuration facilitates effective heat integration and leads to lower OPEX for the DPTCD configuration, as shown in Figure 2a/b. Conversely, B/T separation is usually performed at atmospheric pressure, as vacuum operation is generally not economically viable. Under these conditions, heat integration through DPTCD can only be achieved by increasing the pressure of the rectifying section, which limits the effectiveness of thermally coupled configurations. For this reason, as can be observed from Figure 2c/d, MVR remains more advantageous than DPTCD in terms of operational costs for non-close boiling components.

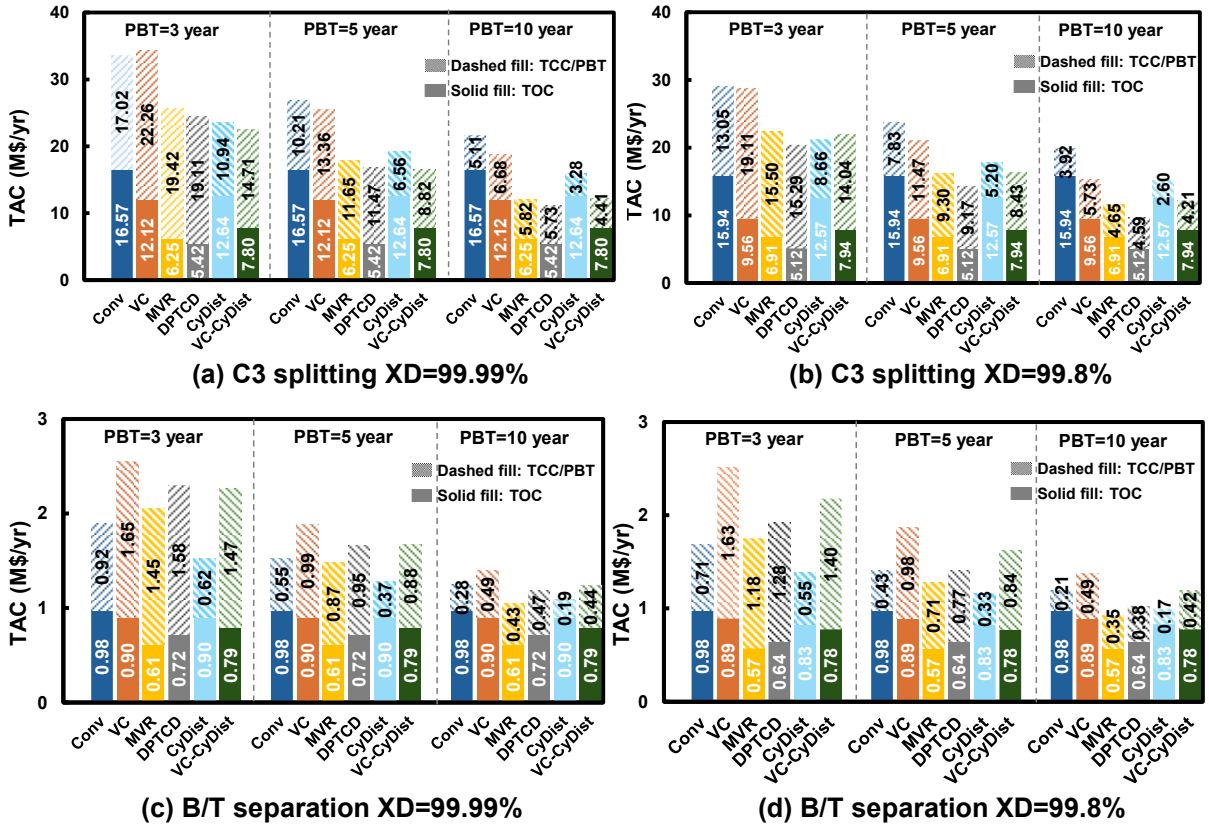

Figure 2. TAC comparison across case studies

3.1.2 Capital costs comparison

At a payback time (PBT) of 3 years, CyDist achieves the lowest capital costs across all cases due to its compact column design stemming from superior mass transfer, yielding savings of 36% for C3 splitting and 33% for B/T separation.

VC demands the highest CAPEX. Its large compression duties require costly compressors and extra heat exchangers in a closed-loop cycle, increasing costs to 128% above conventional distillation for B/T separation.

MVR and DPTCD also raise CAPEX over classic setups via added compression and heat integration equipment. Yet, for close-boiling systems (where base distillation CAPEX is already high and temperature lift needs are modest) the penalty decreases. DPTCD adds just 17% for C3 splitting vs. 66% for MVR in B/T separation.

VC-CyDist offers a balanced option for close-boiling mixtures. Cyclic operation cuts column costs enough to offset much of VC's compression expense, even delivering net CAPEX savings (~15% vs. conventional) for C3 splitting at 99.99% purity.

3.1.3 Total annualized cost comparison (PBT=3)

TAC evaluates whether operational cost savings from advanced configurations justify the added capital investment. Results show the optimal technology hinges on boiling point differences between components.

- For non-close boiling B/T system, compared to conventional column, high compression work in heat pumps fails to offset increased CAPEX despite OPEX gains, driving higher total costs. CyDist outperforms by 19% in TAC.
- In close-boiling separations with high energy demands, heat pumps excel as OPEX savings better justify CAPEX. For C3 splitting at 99.8% purity, CyDist and DPTCD achieve similar TAC savings, but CyDist's simpler design suits plant revamps with smaller equipment.
- HPAD gains clear edge at higher PBTs (10+), which will be discussed in *3.1.4*.
- VC-CyDist delivers the largest TAC savings (up to 33% vs. conventional distillation) for ultra-high purity close-boiling systems (99.99%), yet for other cases it does not outperform CyDist due to the non-preferred heat pump usage.
- CyDist always yields greater savings for close- vs. non-close boiling separations.

3.1.4 Sensitivity analysis

Sensitivity analysis on (1) PBT and (2) electricity price is carried out to investigate the influence of PBT on capital cost correlations and electricity price on OPEX.

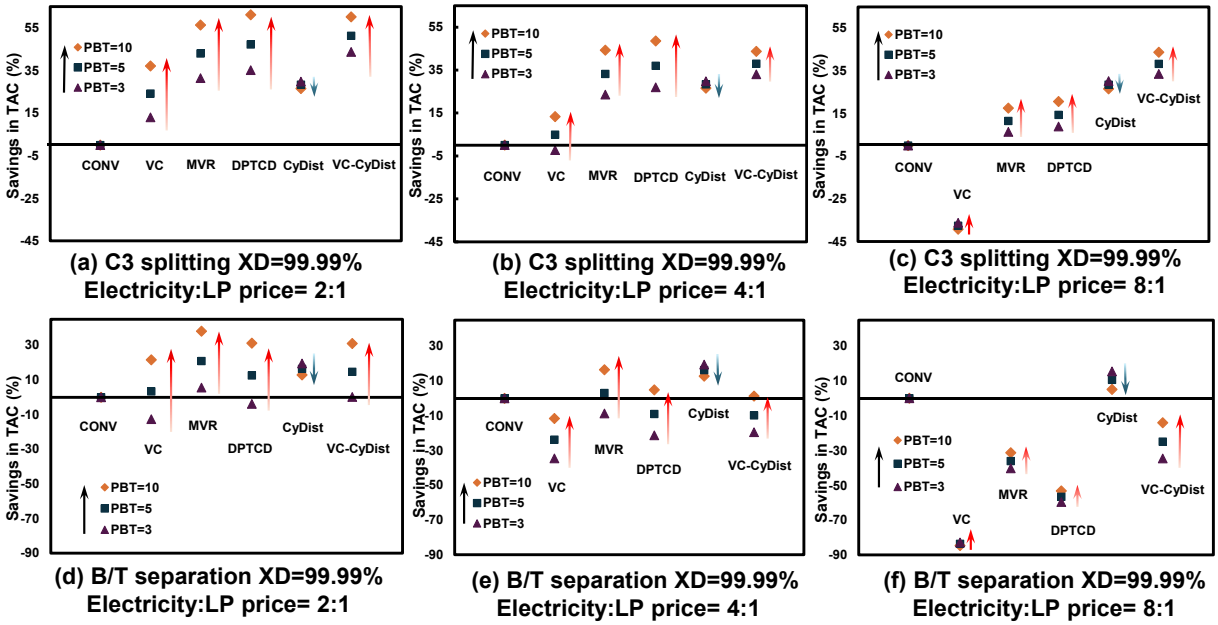

Figure 3. Sensitivity analysis on PBT and electricity price

- Payback time: As shown in Figure 3a/c, with an increase of PBT, the energy-saving configurations are more competitive compared to capital cost saving configurations. For a PBT of 10 years, heat pump technologies (e.g., MVR) become noticeably more advantageous even for non-close boiling B/T systems (Figure 3c). For C3 splitting, heat pump assisted technologies show a clear improvement in performance as the payback time increases, which appears to reduce the annual CAPEX and highlighting more its OPEX savings. CyDist is not overly influenced by PBT. It is dominated more by OPEX, and the influence of the change of PBT and therefore CAPEX is limited. Longer PBT is not beneficial however.
- Electricity price: To assess the impact of electricity cost, simulations were carried out by increasing the price from 9 $/GJ (~2 times the cost of the LP steam) to

18.72 $/GJ and 40 $/GJ (~4 and 8 times the cost of LP steam, respectively). Cyclic and conventional distillation show negligible variation, whereas the advantages of heat pump integration are strongly reduced, confirming their sensitivity to electricity price. Heat pumps remain competitive for close-boiling mixtures (Figure 3b) but become unattractive for benzene/toluene (B/T) separation (Figure 3d).

3.2 Sustainability metric comparison

CO_2 emissions were calculated for all case studies as shown in Figure 4. Heat pump assisted configurations achieve a drastic reduction in CO_2 emissions by upgrading condenser heat to the reboiler temperature level and shifting the energy input from net thermal utility requirements to electrically driven compressors.

CyDist has lower CO_2 emissions than conventional distillation, yet higher than heat pump assisted configurations, as it achieves more reduction on equipment size instead of energy usage, resulting in a modest environmental benefit.

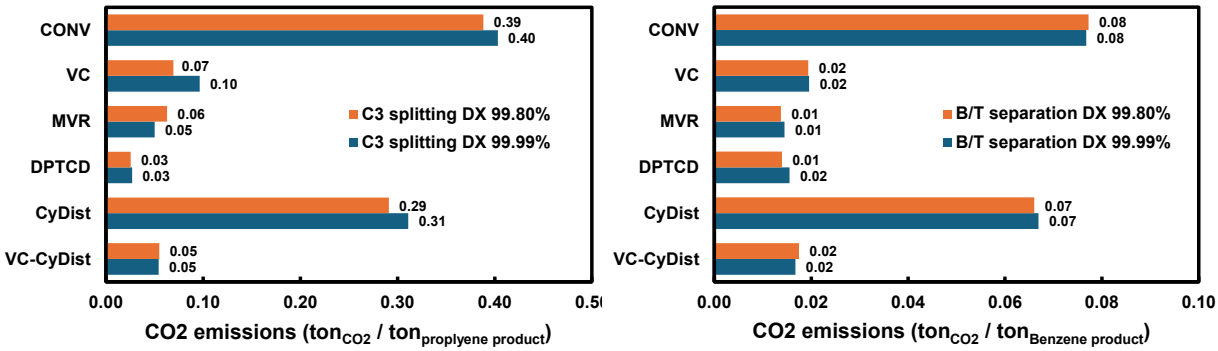

Figure 4. CO_2 emissions comparison across technologies

4. Conclusions

This new techno-economic comparison reveals that heat-pump-assisted distillation (HPAD) achieves substantial OPEX reductions (up to 67%) for close-boiling, high-purity separations. However, CAPEX penalties (related to the boiling point difference) limit TAC benefits, unless electricity prices are low and PBTs exceed 5 years.

Cyclic distillation offers a robust alternative with consistently lower capital costs (36% lower CAPEX) and competitive total annualized costs (up to 30% TAC savings), despite more moderate energy savings, making it ideal for revamps. For high-purity close-boiling separations, vapor-compression-assisted cyclic distillation shows even more cost-saving potential (33% TAC reduction).

Overall, the findings of this work highlight that energy savings alone are insufficient for proper technology selection, and emphasize the importance of balanced techno-economic evaluation in early-stage design.

References

[1] Kiss, A. A., & Smith, R. 2020. Rethinking energy use in distillation processes for a more sustainable chemical industry. Energy, 203, 117788.

[2] Pătruţ, C, Bîldea, CS, Liţă, I & Kiss, AA 2014, 'Cyclic distillation - Design, control and applications', Separation and purification technology, vol. 125, pp. 326-336.

[3] Kiss, A., Maleta, V., Shevchenko, A. and Bedryk, O., 2021. Cyclic distillation—a novel enhanced technology for processing hydrocarbons and their derivatives. Hydrocarbon Process, pp.33-38.

[4] Zhai, J., Chen, X., Sun, X., & Xie, H. 2023. Economically and thermodynamically efficient pressure-swing distillation with heat integration and heat pump techniques. Applied Thermal Engineering, 218, 119389.

[5] Rasmussen, J.B., Mansouri, S.S., Zhang, X., Abildskov, J. and Huusom, J.K., 2020. A mass and energy balance stage model for cyclic distillation. AIChE Journal, 66(8), e16259.

Heat-integrated Liquid-Only Transfer Columns for Energy-efficient Purification of 1-Butanol

Arturo Palacio[1,2], Thomas Grützner[1], Carsten Knösche[2]
[1]Ulm University, Institute of Chemical engineering, Laboratory of Thermal Process Engineering, Ulm, Germany,
[2]BASF SE, Ludwigshafen am Rhein, Germany

Abstract
Distillation remains the predominant separation method in the chemical industry, despite its high energy consumption. Reducing energy demand in distillation processes is therefore essential to meet carbon emission targets and maintain economic viability. Among intensified configurations, the well-established dividing wall column (DWC) offers notable energy and capital savings. While the conventional DWC has been effectively implemented in the industry, addressing its drawbacks could significantly broaden the potential for distillation intensification.
In this regard, the Liquid-Only Transfer (LOT) column presents a promising alternative. LOT columns avoid the uncontrolled vapor split by converting bidirectional thermal couplings into unidirectional liquid transfers, which allow for better controllability and higher flexibility upon varying feedstocks. This is accomplished through additional column sections with a dedicated condenser or reboiler. Additionally, the LOT columns can be operated at different pressures on either side of the wall, which allows for heat integration. Furthermore, LOT columns have gained interest from industry since they are excellent candidates for retrofitting existing direct or indirect sequences to intensified arrangements with relatively low investment.
This study explores the application of LOT in the separation of 1-butanol from a diluted aqueous mixture in the presence of the extractive agent 1-heptanol. The impact of heteroazeotrope is discussed. Various heat-integrated LOT configurations are evaluated by simulation and benchmarked against conventional arrangements, including direct and indirect sequences as well as DWC.

Keywords
Liquid-only transfer, Dividing-wall column, Process Intensification, Azeotropic

1. Introduction

The chemical industry is currently facing significant challenges that necessitate the development of processes that are both energy-efficient and economically viable. Among different separation technologies, distillation remains the most widely applied but also one of the largest consumers of energy in chemical processes. Consequently, substantial efforts have been directed toward improving the energy efficiency of distillation through process intensification (PI) strategies.
The dividing wall column (DWC) is a proven example of intensified distillation for the separation of ternary mixtures. Conceptually, the DWC is equivalent to the fully thermally coupled distillation configuration, commonly known as Petlyuk column (Figure 1a), which integrates a prefractionator with a main column to enable the

withdrawal of three pure product streams [2]. In contrast, the DWC integrates these column sections within a single shell by means of a vertical dividing wall (Figure 1b). As a result, DWC configurations have been reported to achieve capital and operational cost savings of up to 30% compared to conventional distillation sequences [4].

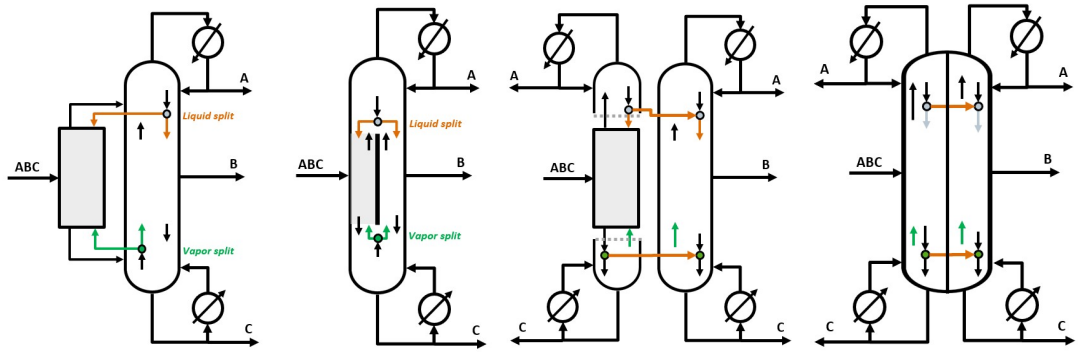

(a) (b) (c) (d)

Figure 1: (a) Petlyuk thermally coupled column, (b) Dividing-wall column, (c) Replacement of thermal coupling with liquid transfer, (d) Liquid-only Transfer column.

Achieving the energetically optimal operation of a dividing wall column (DWC) strongly depends on the appropriate distribution of liquid above the dividing wall and vapor below it. While the liquid split can be effectively manipulated using collecting trays and liquid distributors, the vapor split is typically not directly controlled. Instead, the distribution of vapor between the two sides of the wall is governed by the corresponding pressure drops, which in turn are influenced by the column internals and the liquid flow rates. While Ränger [10] showed that suboptimal vapor distribution can be compensated by accordingly modifying the liquid split, these adjustments are only effective within a certain operation window. An alternative strategy to address this limitation is provided by liquid-only transfer (LOT) configuration, first proposed by Agrawal [1]. In this concept, a rectifying section is added above the prefractionator and a stripping section below it, each equipped with an additional condenser and reboiler, respectively. As a result, the liquid stream that was previously supplied to the prefractionator via the liquid split is instead generated by the newly introduced condenser, while the vapor stream associated with the vapor split is produced by the additional reboiler. Through this modification, the bidirectional vapor-liquid exchange between the prefractionator and the main column is replaced by unidirectional liquid transfer streams (Figure 1c), which can be directly manipulated, thus improving the controllability and flexibility of the column. Similarly to the conventional DWC, the LOT column can be implemented in a single shell, with the dividing wall extending over the entire column height (Figure 1d). A further advantage of LOT columns lies in the decoupling of the two column sides, which allows each to be operated at different pressure levels. This feature allows for heat integration thus increasing the potential for energy savings. Moreover, LOT columns can also be realized as two separate shells, which makes them promising candidates for retrofitting existing direct or indirect distillation sequences into intensified configurations with relatively low investment.

Several studies have investigated the design and control of LOT columns for the separation of ideal mixtures [3, 5, 11]. More recently, interest has also emerged in their application to the separation of non-ideal systems. Wang et.al [12] proposed a liquid-only transfer column coupled with a mid-column decanter for the separation of

the isopropanol-water-dimethyl sulfoxide system. Lyu et. al. [7] presented several LOT arrangements for reducing the energy consumption in the industrial separation of cyclohexane-cyclohexene-benzene mixtures.
Another system that can potentially benefit from intensified distillation is the production of butanol from biomass via fermentation. Biobutanol is an attractive sustainable chemical, as it can serve both as a fuel (given its similar properties to gasoline) and as an important industrial intermediate (for example in the production of butyl acetate and butyl esters). However, the fermentation product consists of a diluted aqueous solution, containing approximately 90% water, making downstream purification by distillation highly energy intensive. To address this challenge, Oh et.al. [8] proposed an initial extraction step using 1-heptanol as a solvent, followed by an indirect distillation sequence for butanol purification. The present simulation study evaluates different configurations for the downstream distillation section, with the aim of identifying more energy-efficient alternatives.

2. Process description and simulation model

The evaluated process is shown in Figure 2. An aqueous process feed of 9.5 t/h containing 5.6 mol% of butanol was adopted from [8]. The feed stream is introduced into an extraction column using 1-heptanol as the solvent, with allowable butanol losses in the raffinate wastewater limited to 100 ppm. The resulting organic extract, comprising butanol, water, and heptanol, is then separated in a distillation sequence. The bottom product consists primarily of the high-boiling component heptanol, containing less than 1 ppm butanol, which is recycled to the extraction column. Due to the formation of a low-boiling heterogeneous azeotrope between water and butanol, the overhead product of the distillation sequence is the aqueous azeotropic phase, which is recycled to the extraction feed to recover residual butanol. High-purity butanol (> 99.99 wt%) is obtained as the main product of the distillation sequence.

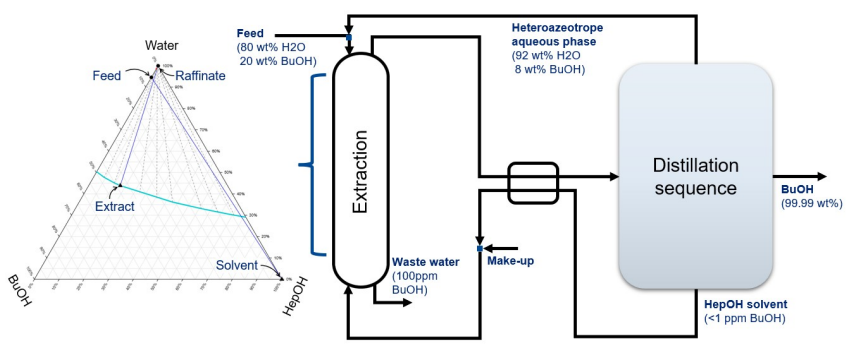

Figure 2: Evaluated process for purification of butanol from an aqueous solution

The process was modeled using BASF's in-house process simulator, CHEMASIM. Thermodynamic non-ideality was described using the Non-Random Two-Liquid (NRTL) activity coefficient model. Two distinct parameter sets were employed: one for the liquid-liquid equilibrium (LLE) relevant to the extraction column, and another for the vapor-liquid equilibrium (VLE) applied in the distillation columns. For the LLE description, binary interaction parameters for the water-butanol and water-heptanol systems were fitted to experimental data obtained from the NIST-TDE database. In the VLE calculations, interaction parameters for the water-butanol system were likewise regressed from NIST-TDE experimental measurements, whereas parameters for the water-heptanol and butanol-heptanol pairs were estimated using the UNIFAC method.

3. Results and discussion

The direct and indirect separation sequences, as well as the DWC and the LOT column, were initially simulated using a large number of theoretical stages to approximate the condition of infinite theoretical stages and minimum energy demand (Qmin). The resulting values are summarized in Table 1.

	Indirect sequence	Direct sequence	DWC	LOT
Minimum energy demand, Qmin (kW)	1348	1086	833	833

Table 1: Comparison of minimum energy demand for the evaluated configurations

The intensified configurations exhibit the lowest minimum energy requirements, approximately 23% lower than that of the conventional direct sequence. Both the DWC and LOT columns show identical values of Qmin, in agreement with previous studies [6,9], which have demonstrated their thermodynamic equivalence in the limit of an infinite number of stages. Figure 3 shows a comparison of the liquid composition profiles at Qmin for the DWC and LOT confirming that both behave identically.

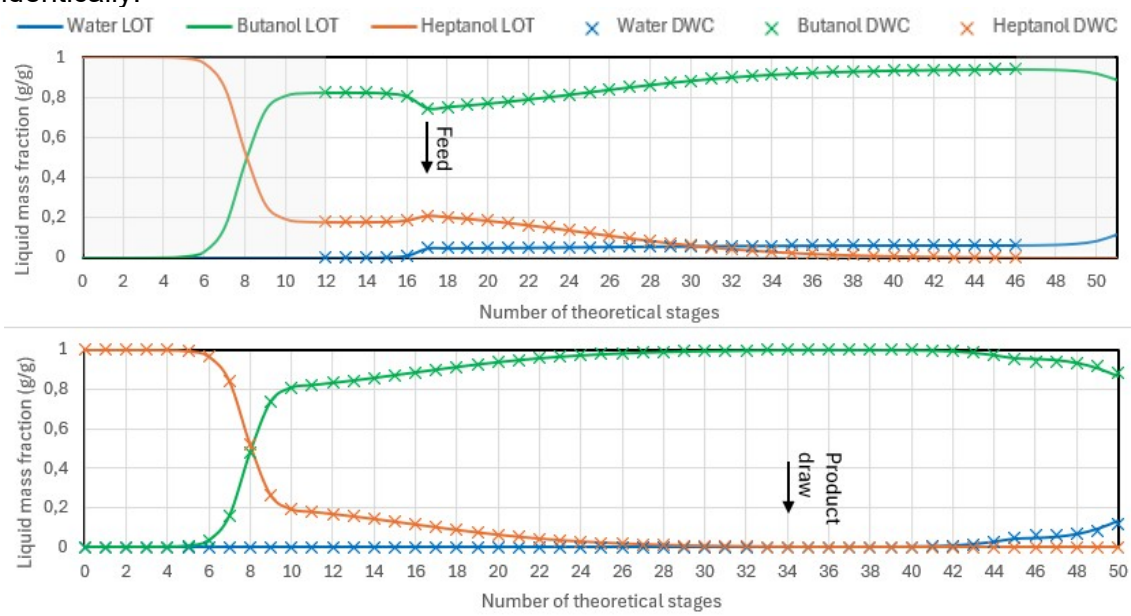

Figure 3: Liquid composition profile for the prefractionator (up) and main column (down) in DWC and LOT at minimum energy demand

To assess the performance of the different distillation arrangements at a finite number of stages, a multicriteria optimization was performed using mixed-integer sequential quadratic programming (MISQP) which yielded Pareto-optimal configurations for the direct and indirect sequences as well as the DWC. For the LOT configuration, the column topology (i.e. the section number of stages as well as the feed and draw locations) was set to match that of the corresponding DWC while the remaining decision variables (the vapor and liquid split ratios, product flowrate, and the reflux and boil-up ratios) were optimized. The resulting Pareto fronts are shown in Figure 4. To ensure a fair comparison with the DWC, the plotted number of theoretical stages for the LOT configuration excludes the prefractionator sections located above the upper liquid transfer and below the lower liquid transfer.

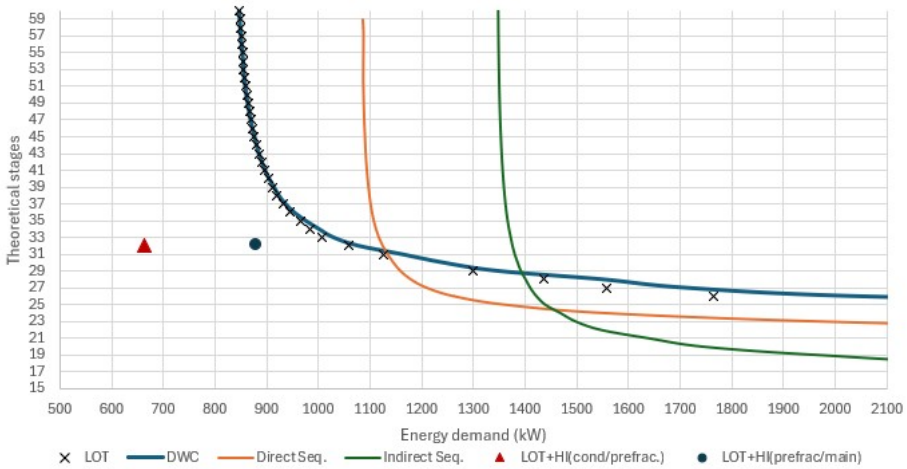

Figure 4: n-Q curves for the evaluated distillation configurations

It is observed that, as the total number of stages decreases, the energy demand of the LOT configuration increasingly deviates from that of the corresponding DWC. Nevertheless, within the stage-range relevant for a practical column design, this deviation remains below 2%. The energy demand of the LOT column can be further reduced through appropriate heat-integration strategies. Previous studies [3] have investigated configurations in which the condenser on one side of the dividing wall is integrated with the reboiler on the opposite side. Although such arrangements can yield substantial energy savings, their practical implementation can be challenging because they require the two sides of the wall to operate at significantly different pressures to achieve the necessary temperature driving force. Alternatively, side reboilers and condensers can be employed to address this limitation. Although this approach yields lower energy savings compared with direct condenser–reboiler integration, these configurations are easier to implement in practice. Two such LOT configurations are illustrated in Figure 5 and their corresponding energy savings are included in Figure 4.

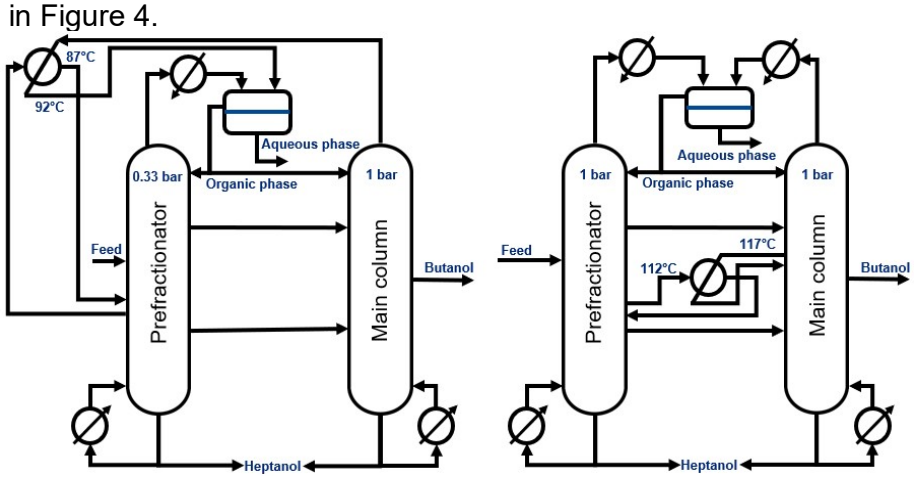

Figure 5: Heat-integrated LOT columns. Condenser/prefractionator integration (left) and Prefractionator/main column integration (right)

For the condenser–prefractionator heat-integration configuration, the prefractionator is operated at 330 mbar and the main column at 1 bar and reaches an energy demand of 664 kW. In contrast, the configuration employing a side reboiler/side condenser integration achieves an energy demand of 880 kW but has the practical

advantage that *no pressure adjustment is required*, i.e. both sides of the column can be operated at 1 bar. This is possible because water forms low-boiling azeotropes with heptanol and butanol, and its presence in the prefractionator sufficiently lowers the temperature profile to enable heat integration with the pure mid-boiler, butanol. The concentration and temperature profile for this integrated side reboiler/side condenser LOT column is presented in Figure 6.

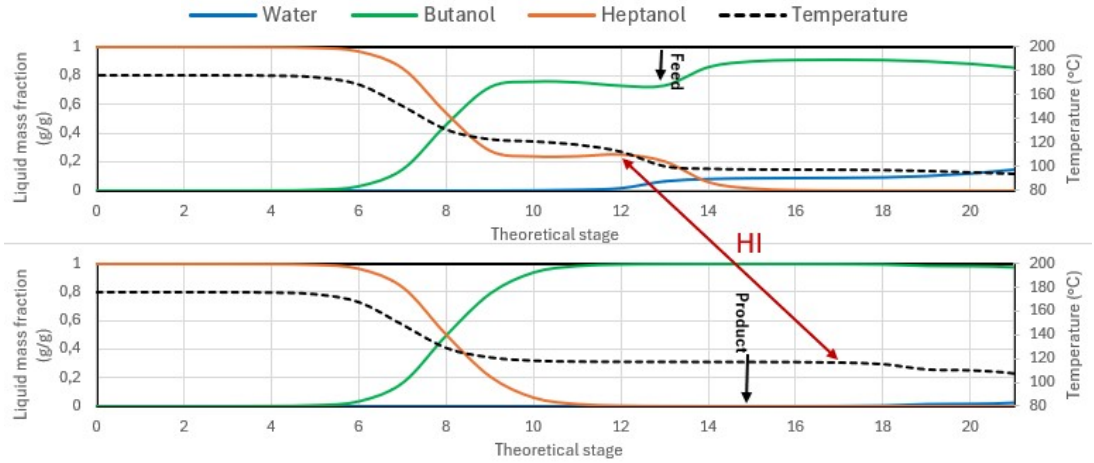

Figure 6: Column profiles for the LOT with side reboiler/side condenser HI

4. Conclusions

The present study successfully demonstrates the application of the liquid-only transfer column (LOT) to a process for purification of biobutanol. The innovative column arrangements proposed can reduce the energy demand of the distillation units while maintaining high product purity (>99.99 wt%).

References

[1] R. Agrawal, Thermally coupled distillation with reduced number of intercolumn vapor transfers. AIChE J., 46 (2000) 2198-2210.

[2] N. Asprion, G. Kaibel, Dividing wall columns: Fundamentals and recent advances. Chem. Eng. Process. Process Intensif. 49 (2010) 139-146.

[3] M. Adami, S. Bertram, D. Espert, M. Skiborowski, Beyond dividing wall columns: Improved process intensification through liquid-only transfer and heat integration, Chem. Eng. Process: Process Intensif. 218 (2025) 110559.

[4] A. Christiansen, S. Skogestad, K. Lien, Complex distillation arrangements: Extending the Petlyuk ideas, Comp. & Chem. Eng. 21 (1997) S237-S242.

[5] C. Cui, Q. Zhang, X. Zhang, J. Sun, Eliminating the vapor split in dividing wall columns through controllable double liquid-only side-stream distillation configuration, Sep. Purif. Tecnol. 242 (2020) 116837.

[6] I. Halvorsen, S. Skogestad, Liquid-only transfer in dividing wall columns – Analytical minimum vapor expressions, Sep. Purif. Technol. 365 (2025) 132530.

[7] H. Lyu, S. Li, C. Cui, X. Yu, J. Sun, Superstructure modeling and stochastic optimization of side-stream extractive distillation processes for the industrial separation of benzene-cyclohexane-cyclohexene, Sep. Purif. Tecnol. 257 (2021) 117907.

[8] H.W. Oh, S.C. Lee, H.C. Woo, Y. Han Kim, Energy-Efficient Biobutanol Recovery Process Using 1-Heptanol Extraction. Chem. Eng. Technol., 44 (2021) 2316-2326.

[9] G. Ramapriya, M. Tawarmalani, R: Agrawal, Thermal coupling links to Liquid-Only Transfer Streams: A Path for New Dividing Wall Columns. AIChE J., 60 (2014) 2949-2961.

[10] L. Ränger, Multi-Objective Optimization of Simple and Multiple Dividing Wall Columns and their Operational Flexibility Close to the Optimum, PhD Thesis, Universität Ulm (2021).

[11] Z. Song, W. Cui, Y. Wu, B. Wu, K. Chen, L. Ji, Energy, exergy, economic, and environmental analysis of a novel liquid-only transfer dividing wall column with vapor recompression, Sep. Purif. Tecnol. 329 (2024) 125122.

[12] Z. Wang, W. Liu, Y. Gao, Z. Huang, Y. Li, G. Li, J. Zhao, C. Xu, Y. Li, H. Pan, H. Ling, Design and control of liquid-only transfer extractive dividing-wall column, Sep. Purif. Tecnol. 354 (2025) 129267.

Dividing wall column control structure for on-line optimisation by extremum seeking

Ivar J. Halvorsen[1,2], Leontine I.M. Aarnoudse[2], Mark A.M. Haring[1], Sigurd Skogestad[2]
[1]SINTEF, Trondheim/Norway, Email: Ivar.j.Halvorsen@sintef.no
[2]Norwegian University of Science and Technology (NTNU), Trondheim, Norway

Abstract
Dividing wall columns (DWC) are attractive for the significant potential savings in energy requirements compared to conventional distillation sequences. Challenges in control have been reported as an obstacle that may hamper the number of industrial applications. In practice, sub-optimal operation normally shows up as inability to obtain the designed product purity and not as increased energy consumption. Herein, we address the practical optimising control of DWC by applying a regulatory layer where the focus is on controlling the top (lights) and bottom (heavies) products to their purity specification. This allows for several approaches for the optimisation layer where the key task is to adjust the prefractionator operation such that high purity can be obtained in all three products including the side product (intermediates). A promising optimisation approach is the model-free Perturb and Observe method which is within the class of extremum seeking algorithms. The proposed structure may also be applied to the so-called liquid transfer only LOT-DWC.

Keywords
Distillation; Dividing Wall Column; Process Control; Optimization; Extremum seeking; Perturb and Observe.

1. Introduction

Distillation columns are usually the main consumers of energy in chemical industries and refineries in form of heating and cooling. Integrated thermally coupled systems like dividing wall columns (DWC) have a potential for reduction of energy for ternary separations in the range of 20-30% and in addition, the capital savings are in the same ballpark due to smaller diameters and reduction of number of shells and heating & cooling units [1].

It is important that the engineering and operating communities are provided with well-prepared procedures and tools necessary for designing and operating dividing wall column just as in available engineering manuals for more conventional distillation technologies. Dividing wall columns are just conventional distillation sections put together such that the overall energy requirements are reduced. In particular, the energy benefit comes from performing the easy separation between lights and heavies in a prefractionator section and reusing energy from the main column in the prefractionator and to avoid any remixing in the fully thermally connections. Sub-optimal operation may e.g. arise from using higher prefractionator vapor rate than the minimum requirement, and in any distillation, this cannot be recovered and will simply lead to non-optimal operation and increased external energy demand. If this demand cannot be fulfilled, e.g. because the column is already operated at its maximum heat supply, the column arrangement will become unable to maintain all product purity

specifications. However, it is possible to monitor the key parameters that characterize close to optimal operation. This information can be used together with knowledge on how to mitigate off-optimal operation to full product recovery and high purity at the capacity that the arrangement has ability to perform [2].
The challenge is to device a control structure that can handle the dual problem of maintaining product purities at specifications and at the same time ensures close to optimal operation. This task should also be demystified such that it is straightforward to realise the control functions for DWCs during normal plant engineering work procedures, just as for conventional sequences.
Extremum seeking, or more precisely, the model-free perturb and observe algorithm is a promising approach to obtain on-line optimizing control for complex processes [3] and is suitable for DWCs. An underlying regulatory layer to for stabilisation and primary dynamic disturbance rejection is a prerequisite of the algorithm. It is key to ensure that this basic layer fits with the optimisation layer where the task is to perturb one or more chosen optimisation variables, observe the impact on a measurable cost function and then iterate towards the optimum. These variables can be available direct manipulative variables, but also setpoints in the regulatory layer.

2. Characterisation of the minimum vapor operation of DWC

We consider a ternary DWC as illustrated in Figure 1 with feed rate (F) liquid fraction (q) and components A,B,C denoting the light, intermediate and heavy keys. In general there are five independent manipulated variables (MV): top reflux (L), reboiler vapor rate (V_b), side-draw rate (S), liquid split above the wall ($R_l=L_1/L$), vapor split below the wall ($R_v=V_{1b}/V_b$). In addition, the feed rate (F) may be manipulated, and even its liquid fraction. Note that the distillate rate (D) and bottoms product rate (B) are also MVs, but these are not independent degrees of freedom due to the overall mass balance.

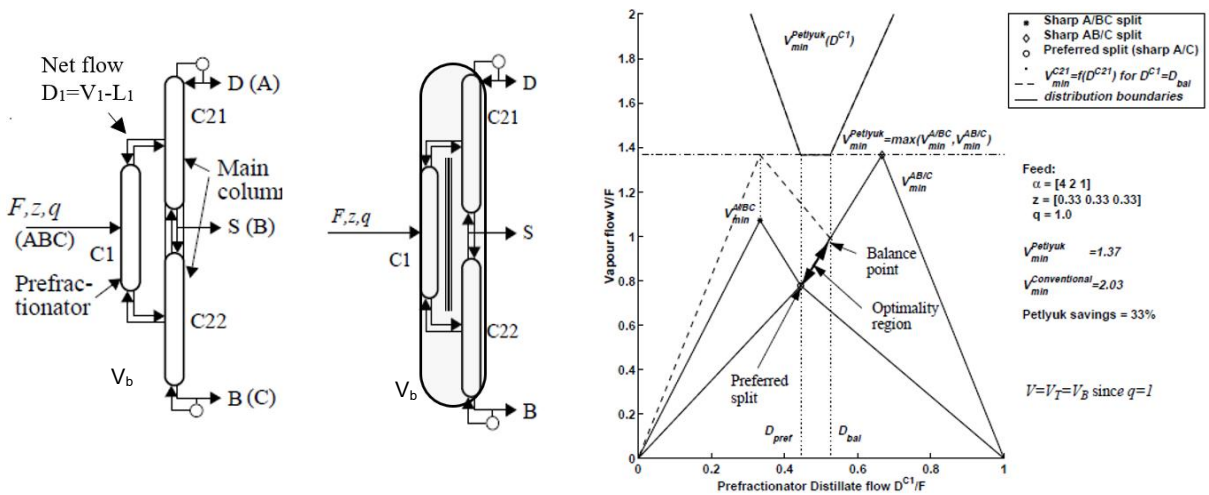

Figure 1. The Dividing Wall Column can be regarded as three fully thermally coupled sub-columns, consisting of the prefractionator (C1, AB/BC split) and the upper- (C21: A/B) and lower (C22: B/C) main column. The Vmin-diagram (right) is based solely on feed properties and illustrates basically components distribution in C1 but also total minimum vapor demand by the maximum peak.

The relationship between the DWC energy consumption, which is usually proportional to the reboiler vapor rate (boilup), and the operating degrees of freedom has been described in detail in previous publications [4]. The overall minimum vapor requirement Vmin (or (V/F)min) is given by the most demanding of the A/BC versus AB/C splits. The key is that the prefractionator (sub-column C1, must be operated

within its optimality region, which is at the particular region in the Vmin-diagram in the vicinity of its preferred split as illustrated in Figure 1 (right).

An example of a sub-optimal operating point in a DWC is illustrated in Figure 2. When operating the prefractionator (C1) at any point away from the so-called preferred split, we must draw new Vmin-diagrams for the succeeding main columns C21 (dashed blue) and C22 (dashed green). Here the C1 operating point (red) is chosen in the region above the preferred split. The impact of-this sub-optimal point is that the demanding rates (illustrated by the new peaks) for sharp A/B separation in C21 and sharp B/C separation in C22 are increased. If the reboiler duty is kept constant, the possible solutions for these columns will be on the horizontal Vb-line; here selected at the minimum for the optimal case given by the original (black) Vmin-diagram. A very interesting solution can be observed, namely, at the intersection between the Vb-line and the new "lifted" Vmin-diagrams peaks giving maximum A- recovery in the top (indicated by "Pure top") and maximum C-recovery in the bottom ("Pure bottom"). The non-recovered A and C must then end up in the side stream S. In this case, if the V could be increased to the maximum level of the new peaks, three pure products could still be obtained, but at higher a energy cost. This is not feasible if the boilup already has been set close to its maximum capacity, as it normally is in many industrial settings. This insight leads to the question that is answered by the proposed basic control structure: *How can we control the DWC to always ensure maximum feasible recovery at specified purity for the top and bottom products, despite possible sub-optimal operation of the prefractionator?* Handling of the sub-optimal prefractionator is dealt with later.

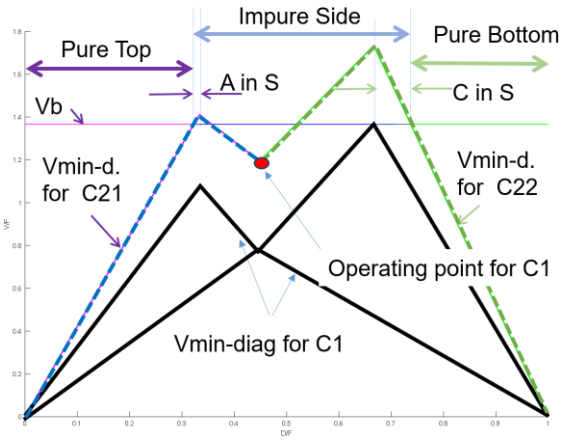

Figure 2. Vmin-diagram for sub-optimal prefractionator operation – indicating a feasible solution for pure top and bottom.

3. The proposed basic DWC control structure

The proposed basic control structure is illustrated in Figure 3. Assume that the boilup (V_b), plus the liquid and vapor splits are set to constant values, and that the feed F is set at a suitable value ensuring $V/F \geq (V/F)_{\min}$. Implement the two basic loops (1&2) as follows:

1. Control the top product purity at its specification manipulate the top reflux L. This is normally done in practice by inferential temperature control (TC) of a point on the temperature profile that is correlated to the composition.
2. Control the bottom purity by a similar TC, but note that this time the MV has to be the side-draw rate S. This is because the boilup rate is fixed, and the side rate is the only available MV to affect the bottom mass balance.

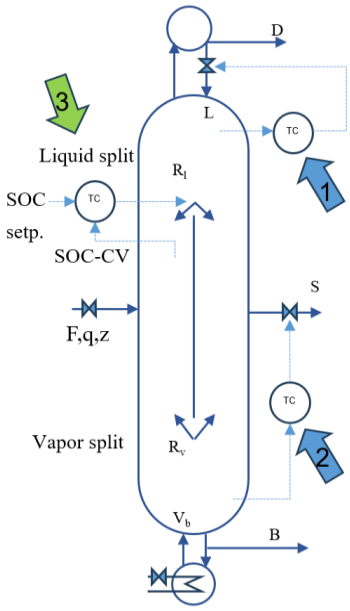

Figure 3. Regulatory control structure for the top and bottom purity control (1&2**).**

The upper loop (1) is quite similar to the top purity control found in many conventional distillation columns. This DWC control structure is not completely new and the transient behaviour has been analysed before and found to be reasonable [5]. For all we know, there may also be industrial implementations of this scheme.
Next, we want to study how this structure can be combined with ensuring that prefractionator operation is within its optimality region. For that, we need a strategy for the remaining available MV, namely the liquid split (R_l).

4. Relationship between liquid split (R_l) and side stream impurity

We illustrate the relationship by a simulation example illustrated in Figure 4. The basic controllers (1&2) in Figure 3 are active. The case used is with constant vapor split, feed and boilup such that V/F is slightly higher than required (the peak). The optimality region in C1, where three pure products become feasible in the DWC, becomes a rectangle [2]. Changing the liquid split makes the C1 operating point being moved along a horizontal line as illustrated in figure (yellow dashed line).

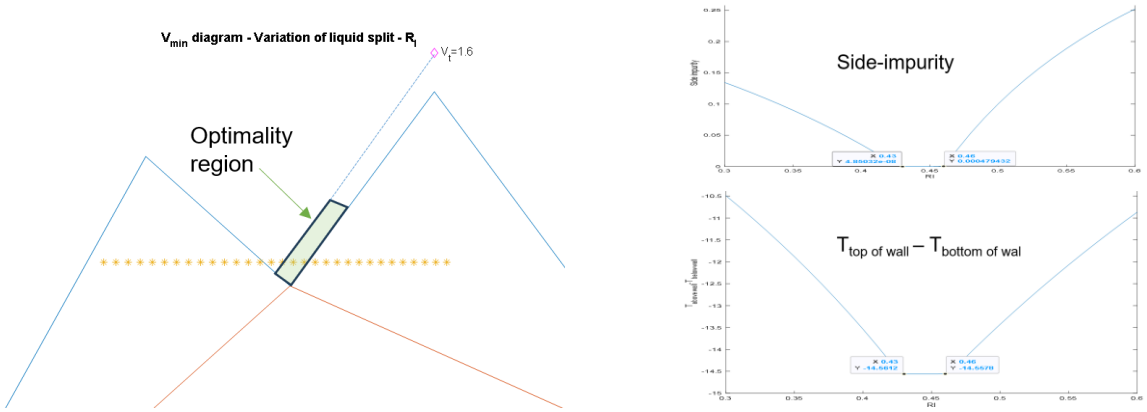

Figure 4. Simulation with proposed control structure and variation of liquid split. The C1 operating point is illustrated in the Vmin-diagram (left) and the impact on side impurity and temperature difference from top to bottom of wall (right). This difference is an alternative cost function.

It is clearly observed that the side impurity can only approach zero when the liquid split adjustment gets the operating point into the optimality region. In practice, we do not know exactly where this region is since it is affected by feed property changes, column performance variation etc. Thus, some kind of adjustment strategy is required.
The interaction between the optimisation layer for adjusting R_l and the basic regulatory layer is such that when the prefractionator operation is iterated towards its optimality region by the optimisation algorithm by direct or indirect manipulation of liquid split, the basic control layer ensures the desired high purity and maximum feasible recovery of the top and bottom products: Then, like magic, the only way out for the intermediate is the side-draw. Finally, assuming that the ratio (V/F) is above its minimum (the highest peak), the feed rate may be increased until the impurity is about to appear in the side-draw again and then (V/F)=(V/F)min.

5. Optimisation layer by perturb and observe (P&O)

The concept of an optimisation layer is illustrated in Figure 5. P&O is basically a model-free optimisation search method based on systematic perturbation of a selected MV and by observing the impact of a measured cost function (here, using the side draw impurity) the algorithm iterates towards the optimum. This is

straightforward to combine with the proposed basic control structure above. A one-dimensional search may be performed by manipulating the liquid split directly. It is recommended to do this via a setpoint to a so-called self-optimising control loop (See controller 3 in Figure 3.) at the regulatory layer to enhance robustness and settling time. It is possible to include manipulation of the "constant" variables (V,F,R_V) on the optimisation level too, possibly combined with optimisation at a plantwide level. In its simplest form, P&O may be an operator.

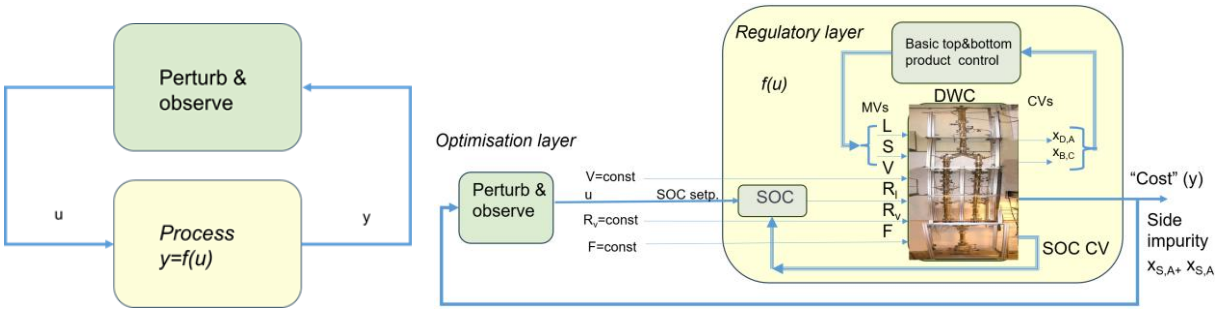

Figure 5. Perturb and observe optimising structure (left) applied to the DWC basic structure (right)

Experiments with this structure are performed at the Kaibel column pilot at NTNU (indicated in the picture) during 2025. The results are promising and selected results from three student internship reports on the issue are submitted for publication [6].

6. Similar Control Structure can be applied to the Liquid Only Transfer - DWC

LOT-DWC [7, 8] has gained recent attention since this structure avoids the practical complication of an on-line adjustment of the vapor split. The same potential savings as in the original DWC can be obtained. A conceptual drawing of LOT-DWC is shown in Figure 6. The proposed control structure fits fine for the main column of the LOT-DWC (Blue arrow 1&2). Just as for the DWC, any sub-optimal operation of the prefractionator rack and insufficient V/F ratio will show up as a side-product impurity. And, as for the standard DWC, the only way to get all three products pure is to ensure a correct prefractionator operation and sufficient V/F ratio. In addition, the basic structure for the prefractionator rack may be configured with a similar structure. Yellow arrow 3: Shows the top purity control by manipulating the top reflux. Arrow 4: Indicates the bottom purity control by manipulating the lower LOT stream (equivalent to the side draw of the main rack). This leaves the prefractionator rack reboiler duty and the upper LOT-stream for control of the inherent prefractionator operation. Note that, for the LOT-DWC, the ratio of the prefractionator side reboiler duty to the total duty is directly equivalent to the vapor split in a classical DWC, and easily accessible as a manipulating variable by adjusting the duty ratio, in contrary to a classical DWC where vapor split is usually given by the pressure drop characteristics on each side of the wall. Green arrow 5 shows an example of control using the upper LOT draw as MV. It is used to fix the temperature profile in LOT-C1. It is just as in the C1 in standard DWC. Like for the ordinary DWC. The result is that when the

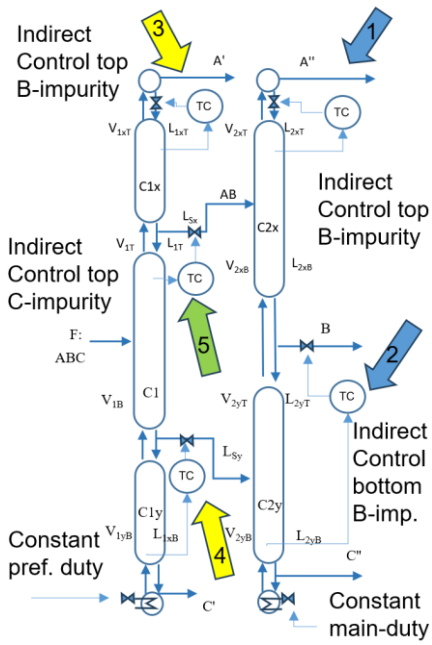

Figure 6. LOT-DWC with proposed basic control structure

prefractionator is operated within its optimality region, as for the standard DWC, the side product automatically becomes pure since the side-stream is the only way out for the intermediate key when all the light key is recovered in the tops and the heavy key in the bottoms.

7. Conclusions

The illustrated control structure at the regulatory layer is a promising solution for DWC and LOT-DWC operation. In summary, this should be a low-threshold control engineering solution for industrial DWCs. This structure can easily be implemented in any conventional control system. It handles the heavy and light key purification with no extra limitations. Then, the focus can be put on the important prefractionator operation. The optimality search may at the simplest level be performed by operators adjusting the liquid split. But we recommend adding a stabilising loop for the prefractionator and add a suitable optimisation strategy on top. For example, the Perturb and Observe method. Further optimisation by pushing feed to the limit is a natural next step. We may add use of the feed liquid fraction and even the column vapor split in the DWC as possible extensions to the set of manipulative variables. Experiments with the P&O method and the proposed regulatory layer have been carried out on a column pilot with promising results.

Acknowledgements

Funded by The Research Council of Norway, Project No.: 345272: Data-driven optimization of industrial pro-cesses in time-varying environments.

References

1. Dejanović I, Matijašević Lj, Olujić Ž (2010) Dividing wall column—A breakthrough towards sustainable distilling. Chem Eng Process Process Intensif 49:559–580. https://doi.org/10.1016/j.cep.2010.04.001

2. Ränger L-M, Halvorsen IJ, Grützner T, Skogestad S (2025) What can go wrong in a dividing wall column and how to detect it. Sep Purif Technol 354:. https://doi.org/10.1016/j.seppur.2024.129151

3. Halvorsen IJ, Aarnoudse LIM, Haring MAM, Skogestad S (2025) Extremum seeking control applied to operation of dividing wall column – DWC. Syst Control Trans 1157–1162

4. Halvorsen IJ, Skogestad S (2003) Minimum Energy Consumption in Multicomponent Distillation. 2. Three-Product Petlyuk Arrangements. Ind Eng Chem Res 42:605–615. https://doi.org/10.1021/ie0108649

5. Qian X, Jia S, Skogestad S, Yuan X (2016) Comparison of stabilizing control structures for dividing wall columns. IFAC-Pap 49:729–734. https://doi.org/10.1016/j.ifacol.2016.07.271

6. Halvorsen IJ, Bergers B, Merlo G, et al (2026) Extremum seeking control by perturb and observe applied to dividing wall column pilot - SUBMITTED to ESCAPE36

7. Ramapriya GM, Tawarmalani M, Agrawal R (2014) Modified basic distillation configurations with intermediate sections for energy savings. AIChE J 60:1091–1097. https://doi.org/10.1002/aic.14324

8. Halvorsen IJ, Skogestad S (2025) Liquid-only transfer in dividing wall columns – Analytical minimum vapor expressions. Sep Purif Technol 365:132530. https://doi.org/10.1016/j.seppur.2025.132530

Identifying the Simpler and Low Heat Duty Dividing Wall Column Configurations for Quaternary Separation

Parikshit S. Kadu[1], Akash Sanjay Nogaja[1], Mohit Tawarmalani[1, 2], and Rakesh Agrawal[†1]
[1]Davidson School of Chemical Engineering; [2]Mitch Daniels School of Business;
Purdue University, West Lafayette, IN, USA

[†] Corresponding author: agrawalr@purdue.edu

Abstract

Dividing wall columns (DWCs) enable the use of thermally coupled multicolumn configurations within a single distillation column shell, thereby reducing implementation costs while retaining energy benefits. For four-component mixtures, the Kaibel, Satellite, and fully thermally coupled (FTC) DWC configurations are of particular interest. While the FTC design offers the minimum vapor duty, its complexity presents operational challenges. This study aims to bridge a critical literature gap by systematically quantifying the heat-duty penalty of the industrially preferred Kaibel configuration, along with three satellite-column arrangements, relative to the FTC configuration. Using a convenient-to-use model based on the Underwood method, we compare the minimum vapor duty for these designs across the 969 feed compositions for each of the eight different relative volatility sets (a total of 7,752 distinct feeds). Our analysis shows that the satellite DWCs are practical alternatives to the more complex FTC configuration, frequently matching its heat duty. In contrast, the simpler Kaibel DWC has the same low heat duty over a much narrower operating window, highlighting its simpler design's limitations.

Keywords

Dividing wall columns, Kaibel, Satellite Columns, Quaternary Separations

1 Introduction

Driven by the industry's focus on process intensification and heat integration, conventional distillation systems are being re-engineered to substantially reduce both energy consumption and capital costs. Besides the traditional sequential multi-column arrangements, process-intensified distillation columns, including the dividing wall columns (DWCs), are economically and energetically rewarding due to their compact single-shell structure. With the successful industrial implementation of DWCs for ternary separations, DWCs for quaternary mixture separation have recently received renewed attention in academic research. The configurations of interest are the Kaibel[1], the Satellite[2], and the FTC[3] DWCs. The various aspects, including the heat duty performance of these configurations, have been explored alongside their hydraulic and control characteristics in the literature[4–8].

The Kaibel dividing-wall column, depicted in the Figure 1(a), is particularly attractive because of its construction and operational simplicities. In this Figure and the rest of this paper, components A, B, C, and D present in the mixture are in descending order of relative volatility. The Kaibel DWC requires only one column shell, one dividing wall, one reboiler, and one condenser. Its popularity is evident from industrial implementations and the large number of papers published on its design and control[9–12]. It is also known that a fully thermally coupled (FTC) column configuration requires the least vapor duty[13,14]. However, a quaternary FTC configuration requires 12 distillation column sections with 5 intercolumn transfer streams, compared with only 7 column sections and 2 transfer

streams in the Kaibel column. As a result, its dividing-wall column analog, also known as the Sargent DWC in the literature[5,10,15], requires two dividing walls within a column shell and many more transfer streams across them, as illustrated in Figure 1(c). This generally makes the FTC DWC less attractive due to higher capital costs and operability issues. As a result, this configuration still awaits industrial implementation. On the other hand, according to Agrawal, for an n-component mixture to be distilled in n product streams, distillation column configurations with one reboiler and one condenser, ranging from a minimum of 4n-6 sections to a maximum of n(n-1) sections, can be drawn[2]. Thus, for quaternary separations, Agrawal proposed three possible satellite configurations, each with 10 distillation sections and 4 intercolumn transfer streams. The DWC version of one of the satellite column arrangements, also known as the Agrawal DWC in the literature[5,15], is shown in Figure 1(b). Christiansen et al.[15] suggested the use of radial walls to draw DWCs of the other two satellite based configurations.

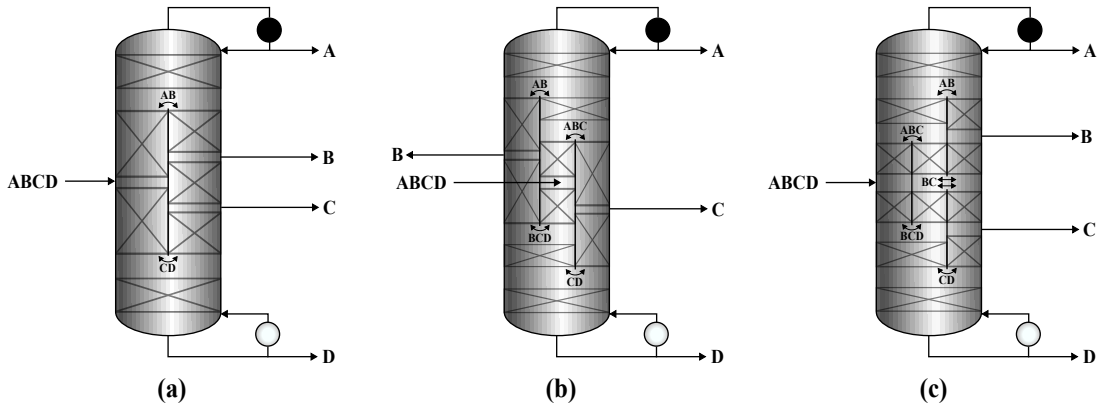

Figure 1: (a) Kaibel configuration, (b) Agrawal (satellite) configuration, (c) Sargent (FTC) configuration

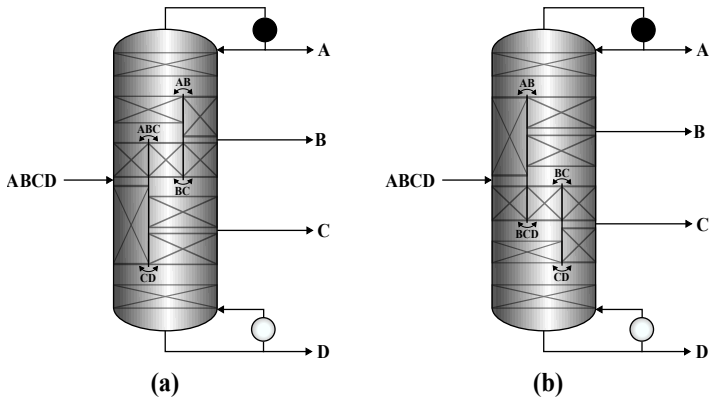

Figure 2: (a) Satellite Derivative I, (b) Satellite Derivative II

A comparison between the Agrawal and Sargent DWCs shown in Figure 1(b) and (c) indicates that the Sargent design utilizes a stream transfer at an intermediate position on the final dividing wall. Since this transfer potentially involves the vapor phase, the practical construction of such a unit is more difficult. As Agrawal points out, two additional satellite column configurations with one reboiler and one condenser, each consisting of 10 distillation sections and 4 intercolumn streams, can be derived from this proposed four-component superstructure[2]. Since each multicomponent distillation configuration consisting of one reboiler and one condenser can be redrawn as a single-column shell with parallel or radial walls relative to the column axis, Figure 2 shows the DWC corresponding to the remaining two satellite-derived configurations[15,16]. It should be noted that the Satellite Derivative 1 DWC shown in Figure 2(a) has been previously drawn and studied by Halvorsen et al.[9], and the

Satellite Derivative II in Figure 2(b) by Ge et al.[17]. Given these four distinct DWC options—all featuring a single reboiler and condenser but employing two dividing walls—it is necessary to evaluate the extent to which their added complexity provides a benefit over the simpler Kaibel DWC.

For the configurations mentioned earlier, is there a specific region defined by the composition and relative volatilities of the feed components where a particular DWC performs better than the others? What should be the trade-off between design simplicity and energy-expenditure? Using the MINLP model proposed by Gooty et al.[18], we compare these configurations for a given feed composition and relative volatilities based on their theoretical minimum vapor duty requirements. The observed trends are expected to be useful to practitioners in making design decisions.

2 Methodology

2.1 Feed Compositions and Relative Volatilities

The performance of a distillation configuration is highly dependent on both the feed composition and the separation difficulty. The separation difficulty is a function of the relative volatilities of the components. As an engineering simplification, we assume that the properly computed constant relative volatilities adequately describe vapor-liquid equilibrium over the temperature and pressure range encountered in the distillation column[19]. Consequently, evaluating a configuration based on a single feed condition provides an incomplete and potentially misleading assessment. A rigorous evaluation requires a thorough examination across the wide range of potential feed compositions and relative volatilities to determine the effectiveness of a configuration.

Giridhar and Agrawal[20] suggested the search space characteristics suitable for such a comprehensive analysis. Following their methodology, we have considered a discrete set of 969 unique feed concentrations from the four-component composition space. The flow rate of the individual components is chosen from the set S = $\{5n \mid n \in \mathbb{Z}, 1 \leq n \leq 17\}$, such that the total flow rate is 100 kmol/hr. A few series points are indicated in Table 1.

The relative volatility of any component A with respect to another component B is denoted as $\alpha_{A,B}$. For a quaternary mixture, $\alpha_{A,D} > \alpha_{B,D} > \alpha_{C,D} > \alpha_{D,D} = 1.0$. To clearly model separation difficulty, we make use of a shorthand notation. Difficult-to-separate mixtures, characteristic of energy-intensive processes, are denoted by the symbol 'd'. This corresponds to a low relative volatility ($\alpha_{i,i+1}$) of 1.1 between the adjoining components. Similarly, easy-to-separate mixtures are represented by the symbol 'e', corresponding to a higher relative volatility ($\alpha_{i,i+1}$ of 2.5). For example, if a given feed is modeled as *eed*, then the $\alpha_{D,D} = 1.0, \alpha_{C,D} = 1.1, \alpha_{B,C} = 2.5, \alpha_{A,B} = 2.5$. All the possible sets based on the above nomenclature are provided in Table 2.

f_A	f_B	f_C	f_D
5	5	5	85
5	5	10	80
5	5	15	75
·	·	·	·
25	25	25	25
·	·	·	·
80	10	5	5
85	5	5	5

Table 1: Feed component flow rates. f_i represents the flow rate of component i.

Difficulty	$\alpha_{A,B}$	$\alpha_{B,C}$	$\alpha_{C,D}$
eee	2.5	2.5	2.5
eed	2.5	2.5	1.1
ede	2.5	1.1	2.5
dee	1.1	2.5	2.5
edd	2.5	1.1	1.1
ded	1.1	2.5	1.1
dde	1.1	1.1	2.5
ddd	1.1	1.1	1.1

Table 2: Different relative volatility sets. 'e' represents easy and 'd' difficult separations.

2.2 Simulation Methodology

We evaluate the vapor flow requirement at minimum reflux operation for each of the DWC versions introduced in the previous section. The analysis includes vapor duty estimation using Underwood's method[21] for 969 compositions at previously defined relative volatility levels for each configuration. To simulate these cases, we use the MINLP model developed by Gooty et al.[18], which provides the vapor duty for each configuration at the minimum reflux condition. As the fully thermally coupled (FTC) configuration has the lowest vapor flow demand for any given composition and separation difficulty, it serves as a benchmark for the other configurations considered. The quaternary feed is assumed to be a saturated liquid. All the products are considered saturated liquids. The model is implemented in Julia and solved using the Gurobi optimizer with 1% optimality gap. The three satellite columns, each with 10 sections and 4 intercolumn transfers, were treated as a single group for comparison.

3 Results and discussion

Based on minimum-vapor-duty calculations across the composition space and for various degrees of separation difficulty, the Kaibel DWC has a very sparse region where its vapor duty is within 5% of that of the FTC DWC. These cases are limited to the feeds with eed and ded relative volatilities. On the other hand, satellite-column arrangements often provide energy savings comparable to those of the FTC DWC. For six of the eight relative volatility sets, i.e., eed, ede, dee, edd, ded, and dde, all the considered composition cases exhibit at least one satellite column configuration with vapor duty within 5% of the FTC DWC vapor duty. As indicated in Figure 3, when feed components have similar relative volatilities, as in cases such as eee and ddd, the satellite configurations have a small number of composition cases in which their vapor duty exceeds 5% of the FTC DWC vapor duty.

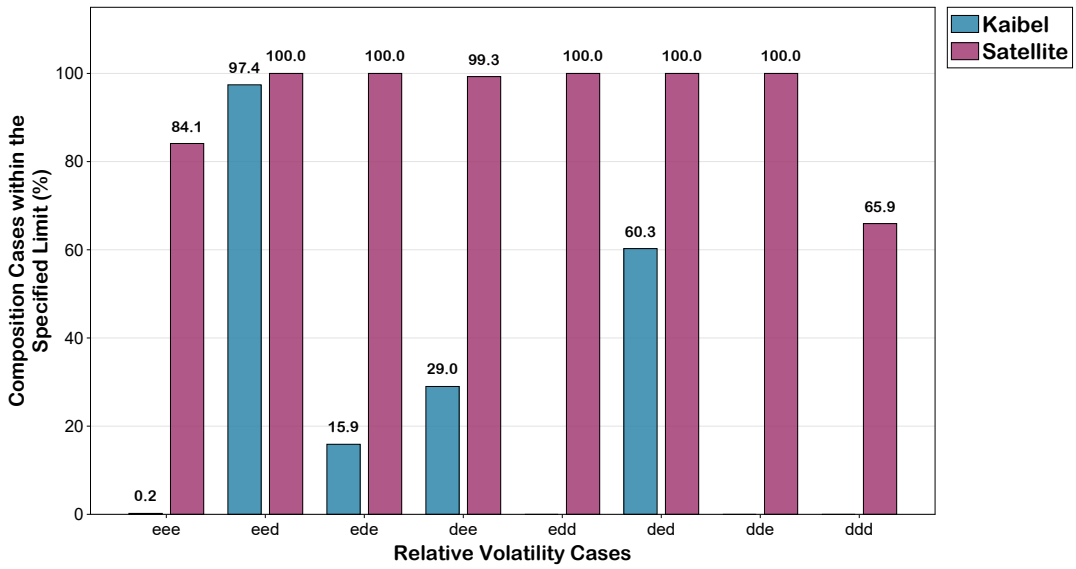

Figure 3: For each relative volatilities set, % of the 969 feed composition cases of Kaibel and Satellite DWCs that have vapor-duty within 5% of the FTC DWC vapor-duty

As shown in Figure 3, for most composition cases under consideration, the structurally simple satellite column arrangements have vapor duties similar to those of the FTC DWC. This means a complex and difficult-to-operate FTC DWC is rarely needed to achieve the minimum vapor duty, and one can always find a simpler satellite DWC alternative for the same task.

Next, in Figure 4, for each set of relative volatilities, from the calculated vapor duties of the 969 compositions, we examine the average vapor duty penalty incurred by the Kaibel and Satellite DWCs

over the FTC DWC. It can be seen that, for feed cases with relative volatility sets such as eee, edd, dde, and ddd, the vapor-duty penalty associated with the Kaibel DWC is substantial, while it is much lower for Satellite DWCs. A large vapor duty penalty will likely lead to larger column diameters and reboiler/condenser heat exchangers, and contribute to increased capital expenditure.

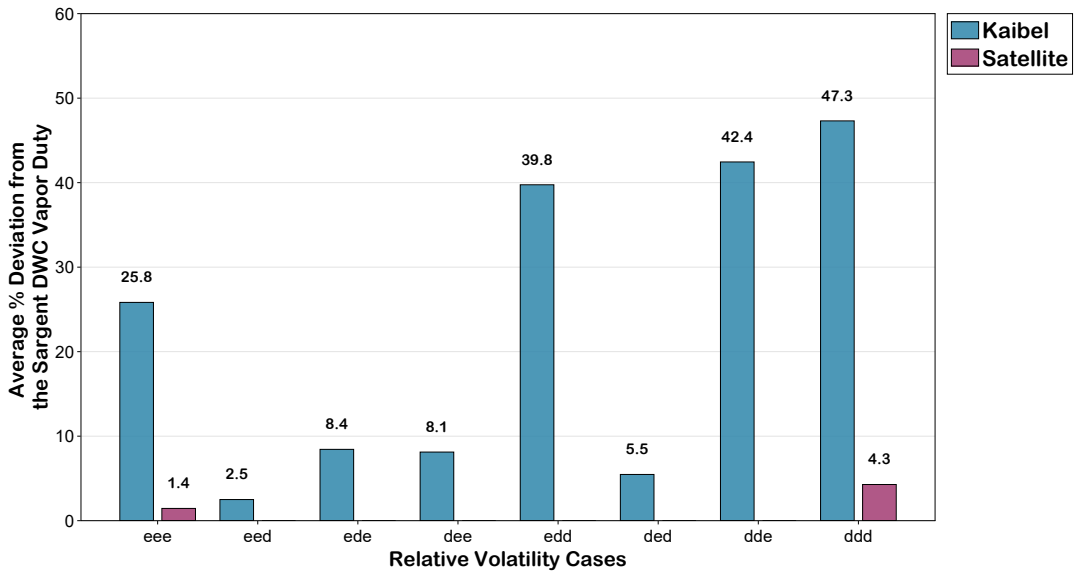

Figure 4: Average % vapor duty penalty associated with Kaibel and Satellite DWCs as against the FTC DWC

4 Conclusions

Among the single-condenser and single-reboiler DWC alternatives for quaternary separations, practitioners still prefer Kaibel DWC because of its simple construction and operation, and consequently, its low capital investment. However, other alternative DWCs remain largely unexplored for practical implementation. We aim to answer a few critical questions about the relative performance of the Kaibel and three distinct satellite-column alternatives, with FTC DWC as the benchmark for the vapor-duty comparison. With a comprehensive analysis of 969 composition cases and 8 relative volatility sets, i.e., a total of 7,752 distinct feed conditions covering a large composition and relative volatility space, we conclude that the satellite DWC alternatives strike a good balance between vapor duty savings and structural complexity, achieving the minimum vapor duty for a given separation in most cases. Furthermore, the Kaibel column is found to be attractive for feeds with eed and ded relative volatility sets, as well as for certain feed compositions with relative volatilities of ede and dee. On the other hand, the Kaibel column incurs a heavy heat-duty penalty for feeds with eee, edd, dde, and ddd relative volatilities.

Acknowledgements

The information, data, or work presented herein was funded by the Center for Innovative and Strategic Transformation of Alkane Resources (CISTAR), an Energy Research Center (ERC), supported by the National Science Foundation under the Cooperative Agreement No. EEC-1647722.

References

[1] Gerd Kaibel. Distillation columns with vertical partitions. Chemical engineering & technology, 10(1): 92–98, 1987.

[2] Rakesh Agrawal. Synthesis of distillation column configurations for a multicomponent separation. Industrial & engineering chemistry research, 35(4):1059–1071, 1996.

[3] R. W. H. Sargent and K. Gaminibandara. Optimum design of plate distillation columns. Optimization in action (L. W. C. Dixon), pages 276–314, 1976.

[4] Thomas Waltermann, Steffen Sibbing, and Mirko Skiborowski. Optimization-based design of dividing wall columns with extended and multiple dividing walls for three-and four-product separations. Chemical Engineering and Processing-Process Intensification, 146:107688, 2019.

[5] Cristopher A Villegas-Uribe, J Rafael Alcántara-Avila, Nancy Medina-Herrera, Ricardo Gómez-González, and Salvador Tututi-Avila. Temperature control of a kaibel, agrawal and sargent dividing-wall distillation columns. Chemical Engineering and Processing-Process Intensification, 159:108248, 2021.

[6] Cristopher A Villegas-Uribe, Nancy Medina-Herrera, Javier A Hernandez-Magallanes, and Salvador Tututi-Avila. Optimal design and control of three simplified sargent four-product dividing-wall columns. Chemical Engineering and Processing-Process Intensification, 174:108860, 2022.

[7] Yannick Waibel, Lea Trescher, Lena-Marie Ränger, and Thomas Grützner. First multiple dividing wall column: Design and operation. Chemical Engineering Research and Design, 193:132–144, 2023.

[8] Yang Yuan, Xinyi Tao, Kejin Huang, Haisheng Chen, Xing Qian, and Liang Zhang. Multi-objective optimization and composition control of sargent dividing-wall distillation columns. Journal of Cleaner Production, 423:138637, 2023.

[9] Ivar J Halvorsen, Igor Dejanović, Sigurd Skogestad, and Žarko Olujić. Internal configurations for a multi-product dividing wall column. Chemical Engineering Research and Design, 91(10):1954–1965, 2013.

[10] Igor Dejanović, Ivar J Halvorsen, Sigurd Skogestad, Helmut Jansen, and Žarko Olujić. Hydraulic design, technical challenges and comparison of alternative configurations of a four-product dividing wall column. Chemical Engineering and Processing: Process Intensification, 84:71–81, 2014.

[11] E Soraya Rawlings, Qi Chen, Ignacio E Grossmann, and Jose A Caballero. Kaibel column: Modeling, optimization, and conceptual design of multi-product dividing wall columns. Computers & Chemical Engineering, 125:31–39, 2019.

[12] Xing Qian, Shengkun Jia, Kejin Huang, Haisheng Chen, Yang Yuan, and Liang Zhang. Optimal design of kaibel dividing wall columns based on improved particle swarm optimization methods. Journal of Cleaner Production, 273:123041, 2020.

[13] Zbigniew T Fidkowski and Rakesh Agrawal. Multicomponent thermally coupled systems of distillation columns at minimum reflux. AIChE journal, 47(12):2713–2724, 2001.

[14] Ivar J Halvorsen and Sigurd Skogestad. Minimum energy consumption in multicomponent distillation. 3. more than three products and generalized petlyuk arrangements. Industrial & Engineering Chemistry Research, 42(3):616–629, 2003.

[15] Atle C Christiansen, Sigurd Skogestad, and Kristian Lien. Complex distillation arrangements: extending the petlyuk ideas. Computers & chemical engineering, 21:S237–S242, 1997.

[16] Gautham Madenoor Ramapriya, Mohit Tawarmalani, and Rakesh Agrawal. Thermal coupling links to liquid-only transfer streams: an enumeration method for new ftc dividing wall columns. AIChE journal, 62(4):1200–1211, 2016.

[17] Xiaolong Ge, Botong Liu, Xigang Yuan, and Botan Liu. Simplifying and synthesizing practical four-product dividing wall column configurations. Chemical Engineering Research and Design, 125:433–448, 2017.

[18] Radhakrishna Tumbalam Gooty, Rakesh Agrawal, and Mohit Tawarmalani. Advances in minlp to identify energy-efficient distillation configurations. Operations Research, 72(2):639–659, 2024.

[19] Tony Joseph Mathew, Radhakrishna Tumbalam Gooty, Mohit Tawarmalani, and Rakesh Agrawal. Quickly assess distillation columns. Chemical Engineering Progress, 116(12):27–34, 2020.

[20] Arun Giridhar and Rakesh Agrawal. Synthesis of distillation configurations: I. characteristics of a good search space. Computers & chemical engineering, 34(1):73–83, 2010.

[21] AJV Underwood et al. Fractional distillation of ternary mixtures. part i. J. Inst. Petroleum, 31(1):1, 1945.

Semi-batch distillation in a dividing-wall column

Bendeguz Kis, Laszlo Hegely
Budapest University of Technology and Economics, Budapest, Hungary

Abstract
A novel semi-batch dividing-wall column (SBDWC) configuration is proposed that aims to combine the advantages of semi-batch operation with those of the DWC.
The proposed column is based on a side-rectifier DWC, with a partition wall extending from the column midsection to the top, equipped with two condensers. The process consists of a batch step where the lightest component is separated from the initial mixture, followed by a semi-batch step where the light and intermediate components are produced as distillates on opposite sides of the wall, while the heaviest component is accumulated in the still pot.
The specific energy demand (SED) of the SBDWC is evaluated for the separation of an equimolar n-hexane/n-heptane/n-octane mixture. Simulations are performed by the professional flow-sheet simulator CHEMCAD. The SED of the process is minimised using the Box-complex method, and the result is compared to those of conventional batch and semi-batch processes from the literature.

Keywords
semi-batch distillation, dividing-wall column, dynamic simulation, process optimisation

1. Introduction

Sustainability is an essential goal of modern engineering. The way towards a more sustainable chemical industry lies in developing more energy-efficient technologies. Batch distillation (BD) is favorable if a high degree of operational flexibility is required and when the processed material varies in terms of its composition. However, it suffers from a high energy demand, which directly leads to a large carbon footprint, as fossil fuels are commonly used to generate the required heating energy.
Dividing-wall columns (DWCs) are special single-shell, thermally coupled distillation configurations that allow for the separation of multicomponent mixtures in a single column, while providing three or more high-purity products, depending on the initial composition and DWC configuration (Dejanović et al. 2010). The dividing-wall structure replicates the operation of multiple distinct columns. The wall splits and recombines the internal liquid and vapor streams on the different sides of the partition. The wall creates a distinct zone on each side of the dividing wall.
In the case of a three-component mixture, the feed side serves to separate the lightest component from the heavier components, while the other one, the product side, is where the intermediate component is withdrawn as a product. Depending on where the wall is located vertically, the following configurations can be distinguished: a) side-rectifier (wall in the upper section), b) side-stripper (wall in the lower section), and c) fully thermally coupled (wall in the middle section) one. DWCs are very attractive, as they can provide on average a 25-30% reduction in the energy demand (Kiss et al., 2012). The literature mostly deals with the fully thermally coupled configuration, DWCs rely on a continuous feed into the tower in order to

achieve the intended effect; without it, the different zones do not appear. This limits their application in BD, where the feed is introduced all at once into the still pot, at the bottom of the column. As a result of this fundamental compatibility issue, the literature contains very few applications of dividing walls in batch columns. Diwekar and Agrawal (2021) created a mathematical model for a batch side-stripper column, optimised its operational parameters and compared it to the conventional and middle-vessel batch processes. The batch DWC was more profitable and yielded a reduced batch time.

In a recent study, Qian et al. (2023) studied the controlability and energy-saving ability of a batch side-stripper DWC, and compared it to traditional batch and middle-vessel configurations. They also reported reduced distillation time and up to 63 % energy savings compared to the conventional batch process.

Semi-batch distillation (SBD) is a special BD process where part of the mixture is introduced into the still pot of the column, as in a traditional batch process, but another part is introduced continuously into the column (Lang and Hegely, 2018). The benefits of such a configuration are a fixed high liquid level in the still pot, the reduction of dead time and reduced energy demand (Ferchichi et al., 2022).

By utilising semi-batch feeding, the compatibility issue of BD and DWCs can be avoided, since a continuous feed is available. The resulting configuration is a semi-batch DWC (SBDWC). In our work, the side-rectifier column configuration (SBDWC-SR) is studied (Figure 1a). The vertical wall is in the upper section of the column, with a condenser on both sides.

The operation of the column is investigated in a case study of the separation of an equimolar mixture of n-hexane, n-heptane and n-octane, taken from Ferchichi et al. (2022). The specific energy demand was minimised using the Box-complex method (Box, 1965) and compared to those of the BD and SBD processes of Ferchichi et al. (2022). The optimisation variables were the reflux ratios and the start time of the continuous feeding. Inequality constraints were given for the three product purities. Simulations were made using the professional flow-sheet simulator CHEMCAD.

2. Separation task and process description

The equimolar ternary feed contains n-hexane (A), n-heptane (B) and n-octane (C). The purity requirement was 95 mol% for each product. The vapor-liquid equilibrium was described by the Soave-Redlich-Kwong (SRK) equation of state.

The scheme of the proposed novel side-rectifier semi-batch dividing-wall column can be seen in Figure 1. The sections of the column (Figure 1b) are: I: feed side above the feed, II: product side, III. feed side below the feed, IV. section below the dividing wall.

Step 1 is heating-up under $R_{I,1} = R_{II,1} = \infty$ (Table 1). This step is finished when A reaches a near-constant value in the reflux stream. The duration of this step is Δt_1. During Step 2, the column is operated like a traditional batch column, with both the feed and the product side producing component A. The reflux ratios are equal on both sides ($R_{I,2} = R_{II,2}$), and the value is an optimisation variable. The aim of Step 2 is to remove most of A from the still pot before the continuous feeding starts; otherwise, it would not be possible to produce B instead of A on the product side in Step 3. Δt_2 is an optimisation variable, as well. The semi-batch Step 3 lasts until the concentration of C in the still pot reaches the purity requirement. The duration of this step is Δt_3.

The SBDWC-SR configuration, apart from the degrees of freedom of a BD column (number of theoretical plates (N), volume of the charge (U_{ch}) in the still pot, (a single) reflux ratio and the heat duty (Q_N)), has several additional ones: length of the wall

(H_w), radial position of wall, vapor split ratio (VSR), the feed tray (f), the feed flow rate (F) and an additional reflux ratio ($R_{II,3}$). As many of these parameters as possible were kept constant in order to make the design process simpler and the results comparable to those of Ferchichi et al. (2022).

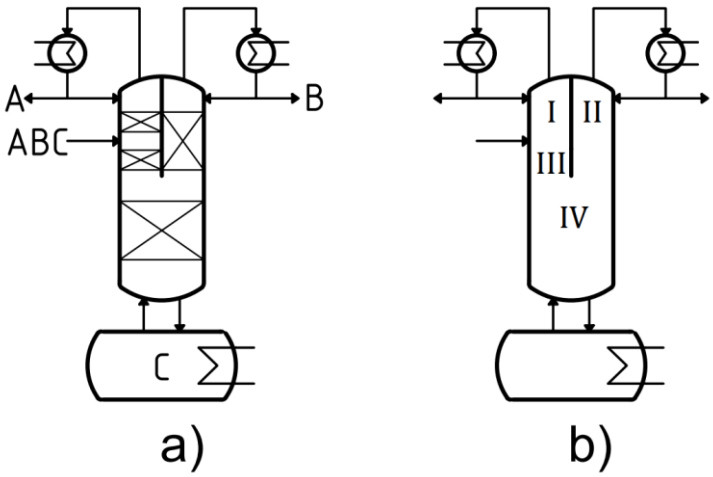

Figure 1: The side-rectifier semi-batch dividing-wall column (SBDWC-SR): a) feed and product distribution: b) sections of the column

Step number	Operation	Continuous feed	Components		
			Distillate I	Distillate II	Still pot
1	Heating-up	No	-	-	A, B, C
2	Batch	No	A	A	B, C
3	Semi-batch	Yes	A	B	C

Table 1: Operational steps

The still pot volume: V_{still} = 9.5 m^3, U_{ch} = 8 m^3. N = 30 (excluding the total condenser and still pot), P = 1.013 bar. The liquid hold-up in the condensers and column were: U_{cond} = U_{col} = 0.08 m^3. The continuous feed is at boiling point with F = 6.862 kmol/h (1 m^3/h) the same composition as the charge. The reboiler heat duty was Q_N = 2872 MJ/h. This was the average heat duty of the direct sequence BD process of Ferchichi et al. (2022), who specified a constant distillate flow rate of 1 m^3/h instead of Q_N. H_w was 22 stages and f = 18 (counted from the top).
Equation (1) was used to approximate the vapor split ratio (VSR), defined as the ratio of the vapor stream that goes to the feed side of the wall when it reaches the lower edge of the partition. R_I, D_I and R_{II}, D_{II} are the feed-side and product-side reflux ratio and distillate flow rate, respectively. VSR was constant (0.6666) throughout the process, but it was calculated for Step 3, when the continuous feed is active.

$$\mathrm{VSR} = \frac{1}{1+\frac{(R_{II}+1)\cdot D_{II}}{(R_I+1)\cdot D_I}} \tag{1}$$

The specific energy demand (SED, MJ/kmol feed) was calculated, excluding the heating-up, using Equation (2). Δt_{total} is the duration of the process ($\Delta t_{total} = \Delta t_1+\Delta t_2+\Delta t_3$), n_{ch} is the charge in the still pot (in kmol). Δt_3 is present in the equation since the duration of the continuous feeding coincides with that of Step 3.

$$\mathrm{SED} = \frac{Q_N \cdot (\Delta t_{total} - \Delta t_1)}{n_{ch} + F \cdot \Delta t_3} \tag{2}$$

The objective function (OF) of the optimisation is given in Equation (3). P = 1000 MJ/kmol and k = 100 MJ/kmol are constants, x_{sp} = 0.95 is the specified molar purity of each product, and x_i is the actual molar purity of a specific component.

$$\mathrm{OF} = \begin{cases} P + k \cdot \sum_i \left(x_{sp} - x_i\right)^2, & \text{if } \exists\, x_i < 0.95 \\ \mathrm{SED}, & \text{if } \forall\, x_i \geq 0.95 \end{cases} \quad ; \text{where } i \in \{A, B, C\} \tag{3}$$

The OF penalises results where the purity requirement is not reached for each component; otherwise, it is equal to SED. The constant term (P) of the penalty function is high enough to ensure that the OF is always considerably higher than SED if the penalty is applied. The concentration-dependent second term ensures that the complex moves toward a direction of satisfying all purity requirements.
The optimisation is performed by using the Box-complex algorithm (Box, 1965) with the following parameters. The number of points in the complex was 8, the reflection coefficient was α = 1.3, and the algorithm stopped when the size of the complex, expressed as the average scaled distance between its points (d_{avg}) decreased below 0.00413. The initial complex includes the results of a base case simulation.

3. Results and discussion

First, the results of a base case are presented, then the optimisation results are discussed, and the minimal SED is compared to that of batch and semi-batch processes of Ferchichi et al. (2022).

3.1. Results of the base case

The reflux ratios and Δt_2 of the base case were determined by sensitivity analyses using the BD and SBD results of Ferchichi et. al (2022) as a starting point. $R_{I,2}$ and $R_{II,2}$ were the same (6.45), as A is produced on both sides of the wall. At the beginning of Step 3, the continuous feeding started, and the column operated in a semi-batch mode. $R_{I,3}$ and $R_{II,3}$ were no longer equal: $R_{I,3}$ was increased to 25.45, while $R_{II,3}$ was decreased to 2.00. At this point, there was very little A left in the still pot; its continued production came mainly from the continuous feed. Moreover, there were fewer theoretical plates for the production of A than in the previous step, explaining the high $R_{I,3}$ value. Compared to the A/B separation, for the B/C one, considerably more theoretical plates were available; thus, a lower $R_{II,3}$ was sufficient.
Δt_{total} was 3.95 h, the duration of the steps were: Δt_1 = 0.37 h, Δt_2 = 1.38 h and Δt_3 = 2.2 h. The product purities were 96.31% (A), 94.89% (B) and 95.00% (C). Component A was too pure, while the purity of B was below the specified value. Reaching the specified purity for all three products at the same time proved be difficult, which can be attributed to the many degrees of freedom of the new SBDWC.
The SED value was 147.04 MJ/kmol feed, which is already significantly lower than the results from the literature for BD and SBD separation (Figure 3).

3.2. Optimal values of the optimisation variables

The optimisation required a total of 336 simulations. $\Delta t_{2,opt}$ decreased very slightly to 1.37 h, and the total process time to 3.90 h. The reflux ratios were reduced. For Step 2, there was a slight reduction to $R_{I,2opt}$ = $R_{II,2opt}$ = 6.28. For Step 3, $R_{I,3opt}$ became 25.16, while $R_{II,3opt}$ remains 2.00.

3.3. Purities of the optimised process

Figure 2 depicts the changes in purities over time for each product, the two distillates and the still residue.

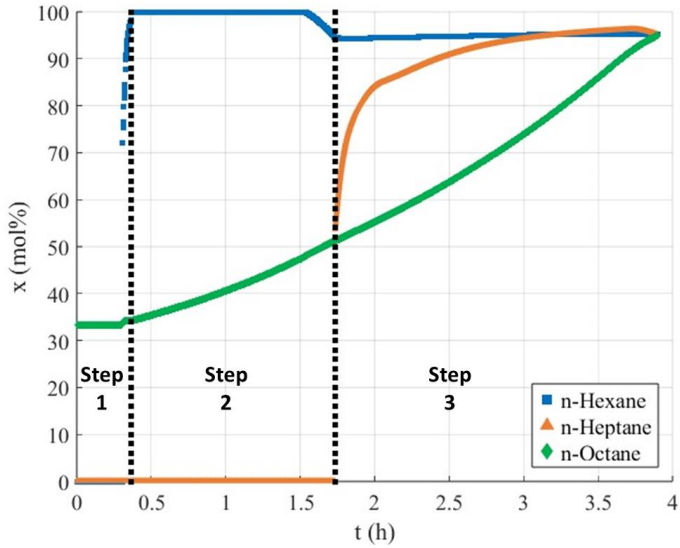

Figure 2: Evolution of product purities

After a steep increase during the heating-up, the concentration of A is virtually constant (and close to 100%) for a long period in Step 2. Shortly before the end of this step, it starts to decrease as $R_{I,2}$ is not sufficient to further maintain the high A concentration. In Step 3, its value becomes almost constant again at the expense of a high $R_{I,3}$. The production of B starts only in Step 3. Its concentration increases quickly due to the low $R_{II,3}$, then shows a maximum shortly before the end of the operation. The concentration of C in the still pot increases monotonously until reaching the specified purity at the end of the process.

After optimisation, the product purities were 95.25% (A), 95.13% (B) and 95.00% (C). Component A is still too pure, although to a lesser extent. Component B reached and exceeded the required purity.

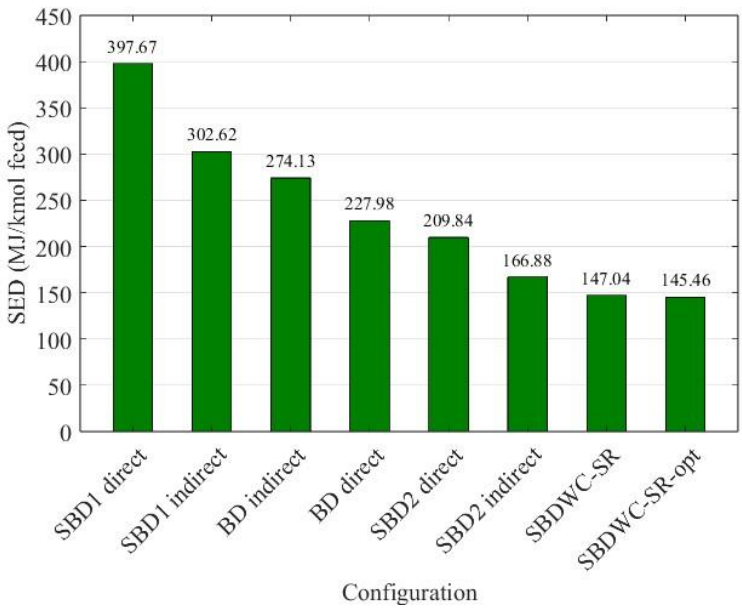

Figure 3: Comparison of energy demands with results from Ferchichi et al. (2022)

3.4. Comparison of specific energy demands

The SED values were compared with those of Ferchichi et al. (2022) obtained for BD and SBD (Figure 3). By SBD1, the continuous feed is introduced into the still pot, while by SBD2, at a constant location into the column. Direct means removing component A first (as distillate), while indirect means producing C first as still residue. SBDWC-SR and SBDWC-SR-opt refer to the base case and the optimised configuration, respectively.

The SED of SBDWC-opt was 145.46 MJ/kmol feed. Compared to the base case result, there is only a slight (1.1%) reduction. However, there is a 36.2% reduction compared to the better batch process, BD direct, and a 12.8% reduction compared to SBD2 indirect, the best of the SBD processes. In the case of SBD2 indirect, there is a higher dead time compared to SBDWC since after separating component C in a semi-batch step, the column needs to be shut down, the still residue has to be removed and the A-B distillate placed into the still pot for a second, batch step.

4. Conclusions

In this work, a novel semi-batch dividing-wall column configuration (SBDWC) was proposed, where the wall is placed in the top of the column. Calculations were performed for the separation of an equimolar mixture of n-hexane/n-heptane/n-octane. The specific energy demand (SED) was optimised using the Box-complex method and compared to previous results for the same separation performed with batch and semi-batch column configurations (Ferchichi et al., 2022). The specification for each purity was 95 mol%, which was reached for all three products, although the higher and intermediate boiling components were slightly too pure. The SED of the new configuration was 36.2% lower than that of the batch process and 12.8% lower compared to indirect semi-batch distillation. A further advantage of SBDWC compared to the latter process is the reduced deadtime.

Acknowledgements

This research was funded by the National Research Development and Innovation Fund of Hungary (OTKA FK-143059) and by the János Bolyai Research Scholarship of the Hungarian Academy of Sciences.

References

Dejanović I., Matijašević Lj., Olujić Ž., 2010. Dividing wall column - A breakthrough towards sustainable distilling. Chemical Engineering and Processing: Process Intensification, 49, 6, 559-580.

Kiss A.A., Flores Landaeta S.J., Infante Ferreira C.A., 2012. Towards energy efficient distillation technologies - Making the right choice. Energy. 47, 531-542.

Diwekar U., Agrawal R., 2021. Novel use of dividing wall columns for intensification multicomponent batch distillations. Chemical Engineering and Processing - Process Intensification, 164, 108400.

Qian X., Xu W., Yuan Y., Li Q., Ding H, Chen H., Huang K., 2023. Controllability and Energy-Saving Ability of the Dividing-Wall Column for Batch distillation. Chemical Engineering & Technology, 46, 2090-2099.

Box M.J., 1965. A new method of constrained optimization and a comparison with other methods. The Computer Journal, 8, 42–52

Ferchichi M., Hegely L., Lang P., 2022. Decrease of energy demand of semi-batch distillation policies. Energy & Environment, 32, 8, 1479-1503.

Lang P., Hegely L., 2018.Different Feeding Policies for Semi-Batch Distillation. Chemical Engineering Transactions, 69, 439-444.

One Separation Task + Seven Engineers = One Column Design? And what about AI?

Friedemann Gaitzsch[1], Michael Haas[1], Laura Fender[1], Lisa Kammer[1], Thomas Heiler[1]
[1]BASF SE, Ludwigshafen am Rhein, Germany

Abstract
Absorption and desorption columns are successfully designed by the BASF gas scrubbing team using rate-based models, which take into account the separation internals and fluid dynamics. The team-wide use of validated mass transfer correlations and largely harmonized design guidelines is intended to ensure that, regardless of which engineer is responsible for the project, a consistent column design is achieved.
To compare working methods within the team and as an onboarding project, seven engineers each designed an absorption column for an identical separation task. Alongside the raw gas to be treated, the purified gas specifications, as well as the solvent and solvent quantity required for physical absorption, were predefined. Using identical physical property data, the requirement for metallic packing, and a specified load range, seven simulations including fluid dynamics were created and the columns were designed individually.
Contrary to expectations, despite the unified requirements, there were significant differences in the choice of column internals and dimensions. The total column volumes varied by more than 200% between the designs.
The reasons for this include so-called “soft factors” such as safety margins for separation performance and fluid dynamics, as well as fundamental design decisions like the selection of packing type or the use of a droplet separator.
It is recommended that recurring similar assignments be used to review and, if necessary, standardize design guidelines and sizing rules. The resulting discussions lead to intensive exchanges within the team and deeper knowledge transfer. In particular, new questions arise for future designs regarding the most economical column design.
To evaluate the performance of current artificial intelligence (AI) models in designing absorption columns and to identify future improvements, we applied the same task previously used for the seven engineers. The AI generated column designs are compared with the human-generated solutions.

Keywords
Gas scrubbing, rate-based modelling, column design, artificial intelligence, AI

1. Introduction

Many processes in the chemical industry involve physical or reactive absorption and desorption steps. At BASF, these unit operations are serviced by the global gas scrubbing team, located in Ludwigshafen (Germany), Houston (USA) and Shanghai

(China). Additional unit operations like gas cooling, direct condensation, quenching and gas saturation are also covered. All these processes are, to a certain extent, heat and mass transfer limited gas-liquid separation processes. Typically, columns, equipped with packing (random or structured), trays, or combinations of thereof, are used.
For column design, as well as retrofitting or debottlenecking of existing equipment, deep knowledge on separation efficiency under mass transfer limited conditions and column fluid dynamics is required. This also plays a crucial role in feasibility studies, optimization projects, trouble shootings and especially Hazard and Operability (HAZOP) assessments.
The global gas scrubbing team is faced with nearly all chemical systems within BASF except BASF OASE® gas technology, which is handled in a separate team. Therefore, a broad understanding of different chemicals and potential reactions is required. Over the decades, a shift from experimental feasibility studies and validation to solely model based column and process design has been experienced.
To ensure the high quality of the deliverables, an intense initial training and a mentoring system for the onboarding phase are applied. Widespread knowledge, covering physical property data, chemical reactions, mass transfer, column fluid dynamics, column internals and the use of appropriate software are required.
The presented work focuses on column design for mass transfer limited absorption columns. The outcome of mass transfer and fluid dynamic column simulation as well as additional design considerations are summarized in form of Process Data Sheets (PDS). Based on the initial training process and experience it is expected that the results of the column design are roughly independent of individuum. To compare working methodologies within the team and support onboarding, seven engineers independently designed an absorption column for an identical separation task.
In addition to the human generated column designs, artificial intelligence (AI) tools were applied. The results of seven human and two AI generated column designs are compared and discussed.

2. Definition of the separation task

For a reasonable comparison and evaluation of different column designs, a consistent separation task and clear boundary conditions must be defined. To put the focus on the design itself, a simple case study is required. For a representative gas scrubbing problem, purely physical absorption is identified as the simplest separation task. The following information is specified for all engineers and used as the main input for the AI prompt.

- off-gas scrubber
- counter-current gas and liquid flow
- once-through operation regarding the solvent
- column top pressure 1 bar abs
- inlet gas flow rate 200 m³/h (standard notation according to German Technical Instructions on Air Quality Control - TA Luft referenced to 293,15 K and 101,3 kPa)
- gas inlet temperature 50°C
- removal of an unsaturated aldehyde (not named here)
- aldehyde inlet concentration 0,0001 mol/mol, rest nitrogen
- aldehyde outlet specification according to TA Luft
- unloaded solvent

- 1000 kg/h water as solvent
- liquid inlet temperature 35°C
- load range gas and liquid 100% without minimum or maximum case
- metal random packing

Identical physical property data for simulation is provided to the engineers. AI uses publicly available information on physical and thermodynamic properties.
For the engineers, the column design is divided into subtasks. The first one comprises mass transfer and fluid dynamic simulation. In subtask 2 the column design is performed, e.g. separation-effective and non-separation-effective internals are specified, and the column dimensions are determined and documented in PDS form. Therefore, the AI prompt includes additionally the demand for the packing (height, diameter, type of internals), dimensioning of the column (spacing, sump level), specification of column internals (distributor, droplet separator, support/hold-down grid) and the determination of total column pressure drop.

3. Approach and results

3.1 Subtask 1 – Column simulation

In the first step, the engineers use the provided physical property data, boundary conditions and specification of the separation task to set up a flow sheet simulation. In an iterative loop the column internal diameter and the metal random packing type and size are selected. Multiple fluid dynamics correlations are available, and fluid dynamic limits must be specified.
By means of rate-based mass transfer correlation for the selected packing the required total packing height is determined. Alternative mass transfer correlations, e.g. Billet & Schultes (B&S), Schultes-Tsai (S-T) or Onda, may be used. Additional iterations may be required to adjust the gas inlet pressure based on the calculated packing or more precisely column pressure drop. The main results of the mass transfer and fluid dynamic simulations include the simulated separation height, the column diameter as well as the packing type and size. Comparing the results offers learnings in the field of how to specify simulation and where to apply hidden safety margins and factors like the distance from TA Luft limit or conservative mass transfer parameters, e.g. correlation, height discretization, film thickness averaging. Seven individual simulations are performed by the team (Table 1). Six engineers selected generation three metal packing, while one and both AI designs use generation two. As AI uses the HTU/NTU model the results are not included in the table. Up to now and to our knowledge, AI does not have access to rate-based simulation.

		A	B	C	D	E	F	G
column internal diameter simulated	m	0,26	0,32	0,26	0,25	0,25	0,26	0,25
packing height simulated	m	2,8	2,2	2,0	2,5	2,0	2,8	2,6
random packing metal		Gen 3	Gen 2	Gen 3	Gen 3	Gen 3	Gen 3	Gen 3
random packing hydraulic diameter	mm	16	11	12	12	12	16	12
mass transfer correlation		S-T	B&S	S-T	S-T	S-T	S-T	B&S
clean gas specification simulated	mg/m³	10	20	12	10	12	10	19
random packing volume simulated	m³	0,15	0,18	0,11	0,12	0,10	0,15	0,13

Table 1: Simulation output overview

3.2 Subtask 2 - Column design Process Data Sheet (PDS)

Based on simulation results and column design considerations the PDS is generated. In most cases the column internal diameter in the simulation and in the PDS are identical. The transfer of the simulated separation height into the number of beds and total packing height is required, e.g. safety factors or inlet and outlet zones may be considered. All non-separation-effective but process relevant internals and distances or volumes must be specified. These include the liquid distribution system and, where applicable, the liquid collection system, as well as packing support and hold-down grids. Together with column internal spacings, sump volume and nozzle dimensioning the total column height, typically defined from tangential line to tangential line (TL-TL), is determined.

All these steps are essential and involve, despite harmonized design guidelines, personal preferences. The engineers of the gas scrubbing team designed seven individual column PDS. Contrary to the standard procedure, the column designs were not reviewed according to the four-eyes principle. Therefore, some of the variances are expected to be corrected or harmonized if the subsequent approval process is applied.

Additionally, two AI generated column designs for the identical separation task are presented. The first AI solution was generated in 2025 while the latter one was performed in 2026 using an alternative AI model. Both AI designs use approx. 13 m packing height compared to a maximum of 2,8 m in engineer design. Even AI use the smallest column diameter, they also design the largest packing size.

Some of the main column key figures are compared in Table 2 for the seven human and two AI generated designs.

		A	B	C	D	E	F	G	AI 2025	AI 2026
column internal diameter simulated	m	0,26	0,32	0,26	0,25	0,25	0,26	0,25	0,21	0,21
column internal diameter design	m	0,26	0,32	0,26	0,26	0,25	0,26	0,26	0,21	0,21
packing height simulated	m	2,8	2,2	2,0	2,5	2,0	2,8	2,6	13,2	13,0
packing height design	m	3,60	3,60	2,50	3,00	2,50	4,80	2,60	13,2	13,00
design / simulated packing height	m/m	1,29	1,62	1,25	1,20	1,25	1,73	1,00	1,00	1,00
column height design (TL-TL)	m	6,5	7,8	4,8	5,9	5,0	9,7	6,0	16,8	16,7
column volume	m³	0,4	0,6	0,3	0,3	0,2	0,5	0,3	0,6	0,6
random packing volume design	m³	0,20	0,29	0,14	0,16	0,12	0,26	0,14	0,46	0,45
random packing hydraulic diameter	mm	16	11	12	12	12	16	12	27	28
column internal / packing hydraulic diameter	m/m	17	31	22	22	21	17	22	8	7
number of packed beds	-	3	2	1	1	1	4	1	1	1
bed height	m	1,2	1,8	2,5	3,0	2,5	1,2	2,6	13,2	13,0
bed height / column internal diameter design	m/m	4,5	5,6	9,5	11,4	10,0	4,5	9,8	62,6	61,9
column height (TL-TL) / packing height design	m/m	1,8	2,2	1,9	2,0	2,0	2,0	2,3	1,3	1,3
normal liquid level	m	0,46	0,50	0,40	0,61	0,50	0,61	0,46	1,50	1,50
droplet separator	y/n	n	y	n	y	y	y	y	y	y

Table 2: Column design parameter overview

4. Discussion

4.1 Which column is the best? How to compare column designs?

Identifying the optimal column design is challenging because well-defined evaluation criteria are missing. While the separation requirements must be met, both overdesign and unacceptably high pressure drops must be avoided.

In general, column design should incorporate investment and operating costs. As process engineers often focus on the separation task and may also include operational cost, like make-up and purge streams, energy consumption for pumps and fans, there may not be full access to investment cost. For example, an energy to investment optimization on the column diameter may be performed, balancing less pressure drop by increasing column cross section or larger random packing size and cost for potentially increased solvent pump around flow rate and shell costs. Even including costs for column shell and internals does not cover piping and instrumentation, transportation or civil engineering costs.

Besides costs, operability and robustness also play important roles in column design. Some additional soft factors can also be included in rating a column design. A reserve for future capacity increase or turndown potential as well as stricter specification on product quality or future off-gas limits (WGC BREF Waste Gas Treatment in the Chemical Sector - Best Available Technique Reference Document) are clear benefits.

For each individual engineer, the column design will also reflect a certain sensitivity for personal experience. Consequently, individual column design may focus more on e.g.

- separation efficiency safety factors
- distance from flooding or dewetting limits
- liquid distributor operating range
- gas distribution
- maximum bed heights
- liquid collector and redistributor
- sump volume respectively residence time
- droplet separation

The bottom line is that probably all column designs can be realized and are expected to fulfill the separation task. So, it needs to be discussed if different designs are a problem.

4.2. Classic absorption column design rules - Are these still valid?

Intense knowledge is present in research and development teams, academia and engineering on column design rules and guidelines. AI has extensive, or more precisely, comprehensive access to publicly available knowledge.

These established and proven guidelines cover specific values or ranges for

- minimum solvent quantity
- fluid dynamic capacities
- column internal to nominal packing size ratio
- maximum bed height to column diameter ratio
- column internal spacing for flow homogenization
- residence time in the sump

Caused by changing energy and material costs these guidelines need to be reevaluated and possibly adopted for future optimal column design.

5. Summary, conclusions and outlook

Even the engineers and AI designs differ more than expected, presumably, all designs may work with respect to the separation task, fluid dynamics and operability. It is expected that for columns with a larger diameter the deviation of the results is reduced as one step in nominal column size does not influence the overall column design by such an extent.

In a first step the time savings and elimination of software tools by AI usage is groundbreaking. While up till now column designers need access to flow sheet and fluid dynamic simulation tools and knowledge on design guidelines, AI just needs a comprehensive prompt. In the future, AI may get access to confidential knowledge and licensed or non-public software tools. Implementing this integration will require resources across several disciplines; however, significant improvements in outcome quality and time savings are anticipated.

Engineers are still required to collect boundary conditions and define scope. The tested AIs fail to define the valid clean gas specification of 20 mg/m³ but use 99% depletion rate or 5 mg/m³. Iterative rework with AI may lead to better results, especially if an experienced engineer is involved and controls the outcome. One optimization would probably be the specification of a certain random packing type and size in a refined prompt.

Challenging the conventional and well proven absorption column design rules to optimally balance ecological and economic considerations is continuously required.

Within a global team, the desire for further harmonization through intensive exchange and repeated parallel test designs continues. Nevertheless, column design, beyond all proven rules, also reflects the current experience of the engineer.

Form follows function - as well as current knowledge and experience by humans and AI!

Remark

AI tools were used to improve grammar and readability. All content was reviewed and verified by the authors.

Droplet Entrainment from Flashing-Feeds with a focus on Viscosity and Surface-Tension Effects

Anna Denecke [1], Stephan Scholl [1], Katharina Jasch[1]
[1] Technische Universität Braunschweig, Institute for Chemical and Thermal Process Engineering, Langer Kamp 7, D-38106 Braunschweig, Germany

Abstract

Flash evaporation can generate fine liquid droplets that are entrained with the vapor, reducing separation efficiency. While entrainment is commonly correlated using the gas load factor (f-factor), most studies are restricted to air-water systems and do not systematically address the influence of liquid properties. This work investigates droplet entrainment in a forced-circulation flash evaporator for three fluids: water, a viscous water-glycerol mixture (0.735 $g_{glycerol}/g_{tot}$), and 1-hexanol with lower surface tension. The atomization at the orifice is classified into regimes using a modified Jakob number and a gas Weber number based on the orifice diameter, showing that the three systems occupy different regimes, with 1-hexanol exhibiting the strongest atomization, while glycerol-water produces larger droplets. Although the atomization is strongly influenced by the liquid's physical properties, the critical droplet size for entrainment is largely governed by the surrounding vapor flow, the density of liquid phase and droplet slip. As a result, differences in droplet size from atomization alone do not fully determine the entrained mass, and similar entrainment levels are observed across all three fluids. Within the experimental scatter, no systematic deviation is detected, indicating that entrainment is predominantly governed by f-factor, whereas differences in viscosity and surface tension play only a minor role under the studied conditions.

Keywords
droplet entrainment, flash evaporation, viscosity, surface tension, superheated atomization, gas load factor

1. Introduction

Thermal separation processes account for 40 % of the total energy demand in the chemical industry [1]. Hence, the optimization of these processes is of great interest. Liquid entrainment with the vapor phase presents a severe cause for inefficient separations [2,3]. Typically, to prevent liquid entrainment droplet separators are employed, which can be for example baffles or wire mesh separators. However, the efficiency of these separators decreases significantly with smaller droplet sizes [4]. Many studies have analyzed liquid entrainment in distillation columns in between of trays [2,3], in packed columns [5] and in evaporators [6,7]. Typically, entrainment in columns is correlated with the gas load factor (f-factor), which relates gas velocity and gas density [2,8]. In most studies, entrainment is investigated using an air-water system, resulting in a limited amount of data for other fluid systems [9]. To the best of the authors' knowledge, there are no studies which systematically vary physical properties to analyze their impact on liquid entrainment with the vapor phase.

In this study the feed section of a forced-circulation flash evaporator is investigated to elucidate the roles of fluid viscosity and surface tension on droplet entrainment in a

gravity-based phase separator. Three fluids, i.e. pure water, a water-glycerol mixture (0.735 $g_{glycerol}/g_{tot}$), and 1-hexanol, were tested.
During flashing, in particular, fine droplets can be formed and subsequently entrained in the vapor flow. This behavior is observed not only at the feed entry of distillation columns, but also at the reboiler return in distillation systems, and it is likewise of importance in desorption columns as well as in vacuum columns [10]. This context combines two research areas: atomization due to flash-evaporation of superheated liquid flows and droplet entrainment. There are numerous studies investigating superheated atomization [11,12]. Although this is not the focus of the present study, the method used to classify sprays into regimes will be applied to examine the atomization of the flashing feed [13].
This study aims to analyze how the fluids, depending on their physical properties (viscosity and surface tension), disintegrate into droplets by classifying them into regimes using dimensionless numbers and whether the resulting spray characteristics influence droplet entrainment. Furthermore, it will be examined whether the f-factor is capable of correlating droplet entrainment capturing the influence of the differing physical properties.

2. Experimental setup and methods

2.1 Experimental setup, fluids and operation

Figure 1 presents the experimental setup:

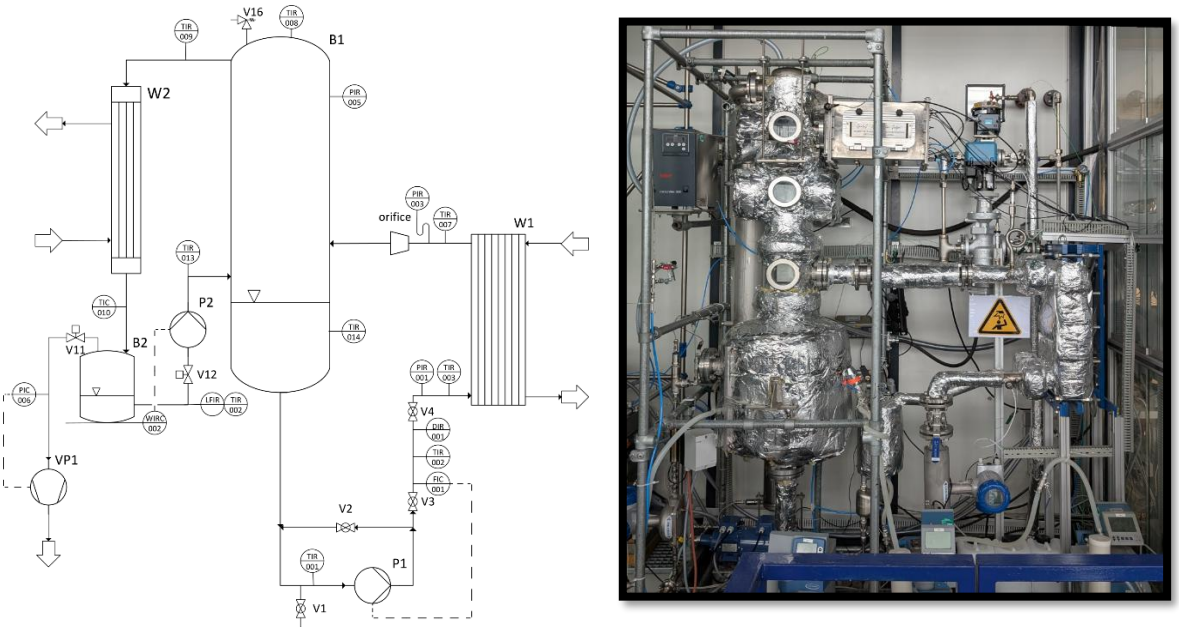

Figure 1: Experimental setup of the forced circulating flash evaporator.

The vessel B1 serves as the phase separator. An orifice is installed in the horizontal feed line at a distance of 60 cm upstream of B1. An well-defined orifice was used to ensure reproducible flash evaporation. For the experiments with water and 1-hexanol, an orifice with a hole diameter of 6 mm and a length of 132 mm was chosen, resulting in a high aspect ratio of L/d = 22. An orifice with a hole diameter of 8 mm and an aspect ratio of 1.33 was used for glycerol-water due to its higher viscosity.
In vessel B1, the vapor phase exits at the top and enters a condenser W2. After condensation, the distillate is collected in vessel B2 and weighed using a scale to

determine the distillate flow. Downstream of B2, the conductivity is measured and the distillate is returned to B1.
The ionic liquid (IL) 1-ethyl-3-methylimidazolium trifluoromethylsulfonate (EMIM OTF) was added to the liquid phase in B1. As this IL does not evaporate under the investigated conditions, its presence in the distillate indicates that liquid has been entrained with the vapor phase exiting the phase separator B1. Using a calibration correlation, the entrained liquid mass can be quantified. For water and glycerol-water 0.0023 g_{IL}/g_{tot} was added and for 1-hexanol 0.01456 g_{IL}/g_{tot}. It was ensured that such a small amount does not change the physical properties. Table 1 lists the relevant physical properties at operating conditions.

Table 1: Physical properties of the liquid phase at operation conditions.

fluid	*p [mbar]*	*T_b [°C]*	*η [mPa·s]*	*σ [mN/m]*
water	100	45	0.6 [14]	68.7 [14]
water-glycerol	100	55	9.5 [15]	64.1 [15]
1-hexanol	70	89.5	0.9 [14]	20.5 [14]

During operation the equilibrium pressure in B1 remained approximately constant for water and glycerol-water at 100 mbar and for 1-hexanol at 70 mbar. The superheating level ΔT, which is the temperature difference of the temperature upstream (TIR007, Figure 1) and downstream (TIR008, Figure 1) of the orifice was varied from (10 – 50) K and the single-phase liquid velocity passing the orifice was varied between (10 – 20) m/s.

2.2. Evaluation concepts and correlation parameters

The ratio of entrained liquid mass to collected distillate mass, hereafter referred to as the entrainment ratio, is defined as follows:

$$E_D = \frac{\dot{m}_{entr}}{\dot{m}_{dist}} \cdot 100\ \% = \frac{\dot{m}_{entr}}{\dot{m}_v + \dot{m}_{entr}} \cdot 100\ \% \tag{1}$$

Entrainment is driven by the vapor flow inside the phase separator B1. The vapor flow velocity inside B1 can be determined using eq.(3). To calculate the evaporated mass $\dot{m}_v$, the measured entrainment is subtracted from the collected condensate in B2 according to (2):

$$\dot{m}_v = \dot{m}_{dist} - \dot{m}_{entr} \tag{2}$$

$$u_v = \frac{\dot{m}_v}{\pi \cdot r_{B1}^2 \cdot \rho_v} \tag{3}$$

In literature, entrainment is usually correlated with the f-factor which is defined as follows:

$$f = u_v \cdot \sqrt{\rho_v} \tag{4}$$

The f-factor is directly connected to the kinetic energy flux of the vapor, which is considered as a physically transparent measure of the gas loading:

$$I = \rho_v \cdot u_v^2 = f^2 \tag{5}$$

To analyze atomization of the liquid flow under flashing feed conditions a classification into regimes was used. In Kitamura et al. [13] the modified Jacob number eq. (6) and the gas Weber number (7) were proposed for the classification:

$$Ja \cdot \varphi = \frac{c_{p,L} \cdot \Delta T}{\Delta h_v} \cdot \frac{\rho_L}{\rho_v} \cdot (1 - e^{-2300 \frac{\rho_v}{\rho_L}}) \tag{6}$$

$$We_v = \frac{\rho_v \cdot d \cdot v_L^2}{\sigma_L} \tag{7}$$

The Jacob number characterizes the intensity of evaporation and is defined by a ratio of sensible heat at the orifice, $c_{p,L}(\Delta T)$, to the heat of vaporization Δh_v inside the vapor separator B1. The parameter φ captures the influence of vapor and liquid density on the atomization. The gas Weber number reflects the mechanical effect of vapor expansion on jet breakup, rather than the classical inertia-to-surface tension ratio of the liquid alone. It is calculated with the vapor density ρ_v, the orifice diameter d, the liquid velocity inside the orifice v_L, and the liquid surface tension σ_L.
In the flow regime map of modified Jacob number and Weber number two boundaries are defined in eqs. (8) and (9). These were identified by Cleary et al. [11]. Pint A marks the boundary between mechanical breakup and the onset of flashing, while boundary B marks the onset of full flashing resulting in a finer spray.

$$\boldsymbol{A}: Ja \cdot \varphi = 55 \cdot We_v^{-\frac{1}{7}} \tag{8}$$

$$\boldsymbol{B}: Ja \cdot \varphi = 150 \cdot We_v^{-\frac{1}{7}} \tag{9}$$

Mechanical breakup is induced by the impulse generated from wall shear stress as the fluid flows through the orifice. During flashing, a second impulse arises, acting on the system due to the collapse of vapor bubble.

4. Results and discussion

In Figure 2 the classification in atomization regimes for all three testing fluids is shown.

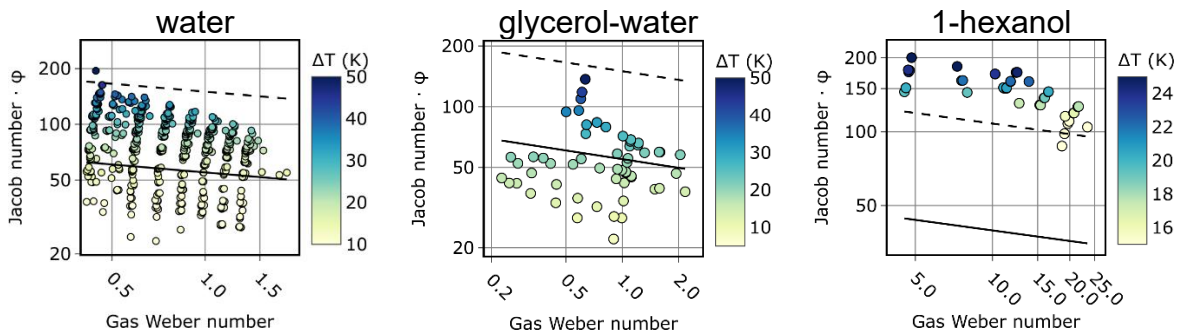

Figure 2: Classification into atomization regimes of water (left), glycerol-water (middle) and 1-hexanol (right) at different superheating levels ΔT.

For water, the transition from mechanically governed atomization to the onset of flashing occurs at a superheat of about 20 K. For the glycerol-water mixture, this transition shifts to a higher superheat, around 25 K. In contrast, 1-hexanol reaches full flashing already at 16 K of superheat, indicating the most pronounced atomization and a higher production of small droplets. By comparison, the glycerol-water mixture is expected to produce the coarsest spray entering the phase separator. As Lefebvre and McDonell [16] show, surface tension resists the formation of new surface area. Consequently, producing more smaller droplets requires more energy with increasing surface tension. In addition, higher viscosity reduces the Reynolds number inside the orifice, stabilizes the jet, delays atomization, and leads to larger droplets.
To analyze entrainment in the vapor stream, Figure 3 shows the entrainment ratio calculated according to eq. (1) as a function of the f-factor. The f-factor was derived from the measured vapor mass (eq. (4)) using the vapor velocity according to eqs. (2) and (3). An exponential trend is observed with a significant increase of entrainment at f-factors above 2.5 $Pa^{0.5}$. Based on the classification into atomization regimes, 1-hexanol, which forms a larger number of smaller droplets, is expected to exhibit the highest entrainment compared to water and the glycerol-water mixture.

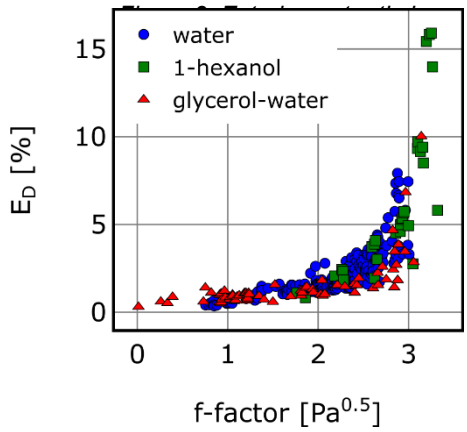

Accordingly, the glycerol-water mixture should show the lowest entrainment due to its coarser spray. Contrary to these expectations, the entrainment is approximately the same for all three fluids. A small difference between water and the glycerol-water mixture suggests slightly higher entrainment for water at higher f-factors. 1-hexanol, which was expected to show higher entrainment than the other two fluids, behaves similarly to water. Overall, only slight differences in entrainment behavior are observed, but less pronounced than expected. When calculating the f-factor using the theoretical vapor fraction assuming an ideal flash, the f-factor for 1-hexanol is lower than the measured value. This discrepancy cannot yet be fully explained. Due to inconsistencies in thermophysical property data reported in the literature, the calculated ideal vapor fraction carries large uncertainties. Furthermore, an analysis of the uncertainties of the measured vapor flow and entrainment needs to be carried out. At present, the experimentally measured data are considered more reliable than the idealized estimates. Therefor the analysis is based on the experimental measurements. However, the behavior observed in the measured data can be rationalized by considering the critical droplet size, i.e. the droplet diameter that separates droplets which are still entrained from those which fall back into the sump section. In this study, the calculations were performed in accordance with Section 7 of the GPSA Handbook [17], assuming that a droplet is in equilibrium when the settling velocity equals the vapor velocity, such that it is neither entrained nor settles. The critical droplet size strongly depends on the droplet drag coefficient, which in turn is a function of the droplet Reynolds number. Due to the higher vapor density of 1-hexanol compared to water, and its lower vapor viscosity, the droplet Reynolds number is increased, resulting in a lower drag coefficient and therefore a smaller critical droplet size. Consequently, although 1-hexanol generally forms smaller droplets, the corresponding critical droplet size for entrainment is also reduced. Table 2 shows the critical droplet sizes of all three working fluids.

Table 2: critical droplet sizes calculated based on [17] of the three working fluids.

	water	glycerol-water	1-hexanol
critical droplet size in µm	861	793	745

As a result, the formation of smaller droplets does not necessarily increase total entrainment. Larger droplets, such as those getting entrained by water, as the critical droplet size is larger, carry more mass each, so less droplets are needed to reach a similar overall entrainment compared to the numerous small 1-hexanol droplets. In the case of the glycerol-water mixture, the higher liquid density leads to a smaller critical droplet size compared to water. Despite this smaller size, the mass of a critical size glycerol-water droplet is approximately equal to that of a water droplet due to its higher density, resulting in a comparable total entrained mass.

5. Conclusions

The atomization behavior at the orifice differs significantly between the investigated fluids. 1-Hexanol exhibits the strongest atomization due to its low surface tension, while the glycerol-water mixture exhibits the weakest due to its high viscosity. However, liquid entrainment in the investigated phase separator is governed primarily by the

vapor dynamic pressure and the corresponding f-factor. All three fluids follow a similar entrainment correlation, with the glycerol-water mixture showing the onset of an exponential increase in entrainment at slightly higher f-factors than water and 1-hexanol. Calculations of the critical droplet size further indicate that vapor flow conditions strongly influence entrainment behavior of droplets. Consequently, to isolate the effect of surface tension on entrainment, identical vapor flow conditions must be maintained for all working fluids; this can, for example, be achieved by adding a surfactant to water to reduce its surface tension while keeping the vapor flow unchanged. Viscosity appears to play only a minor role, as larger droplets, even if fewer in number, carry approximately the same mass as a higher number of smaller droplets. Overall, it remains questionable whether the atomization of the jet, which depends on the fluid's physical properties, has a significant influence on the total entrained mass. The results suggest that entrainment is governed primarily by vapor dynamic pressure and the corresponding f-factor.Acknowledgements

We gratefully acknowledge financial support from the Federal Ministry for Economic Affairs and Climate Action, based on a decision of the German Bundestag. This research was conducted as part of project number 01IF22594N within the framework of the Industrielle Gemeinschaftsforschung (IGF), managed by the German Aerospace Center (DLR).

References

[1] A. A. Kiss, R. Smith, *Energy*. **2020**, *203*, 117788. DOI: 10.1016/j.energy.2020.117788.
[2] H. Z. Kister, W. V. Pinczewski, C. J. D. Fell, *Ind. Eng. Chem. Proc. Des. Dev.* **1981**, *20* (3), 528–532. DOI: 10.1021/i200014a024.
[3] A. Kozioł, J. Maćkowiak, *Chemical Engineering and Processing: Process Intensification*. **1990**, *27* (3), 145–153. DOI: 10.1016/0255-2701(90)87003-2.
[4] H. T. El-Dessouky, I. M. Alatiqi, H. M. Ettouney, N. S. Al-Deffeeri, *Chemical Engineering and Processing: Process Intensification*. **2000**, *39* (2), 129–139. DOI: 10.1016/S0255-2701(99)00033-1.
[5] C. J. Trompiz, J. R. Fair, *Ind. Eng. Chem. Res.* **2000**, *39* (6), 1797–1808. DOI: 10.1021/ie9903902.
[6] V. I. Paradissiadis, F. Widmer, *Chemical Engineering and Processing: Process Intensification*. **1984**, *18* (5), 249–253. DOI: 10.1016/0255-2701(84)80008-2.
[7] V. P. Zhukov, I. A. Kokulin, V. N. Vinogradov, A. E. Barochkin, *Therm. Eng.* **2023**, *70* (11), 957–963. DOI: 10.1134/S0040601523110149.
[8] P. Puppich, R. Goedecke, *Chem Eng & Technol*. **1987**, *10* (1), 224–230. DOI: 10.1002/ceat.270100127.
[9] E. C. Uys, C. E. Schwarz, A. J. Burger, J. H. Knoetze, *Chemical Engineering Research and Design*. **2012**, *90* (12), 2072–2085. DOI: 10.1016/j.cherd.2012.05.008.
[10] M. Wehrli, P. Schaeffer, U. Marti, F. Muggli, in *Distillation and Absorption 2006*, Vol. 152, Rugby, UK **2006**.
[11] H. Witlox, M. Harper, P. Bowen, V. Cleary, *Journal of Hazardous Materials*. **2007**, *142* (3), 797–809. DOI: 10.1016/j.jhazmat.2006.06.126.
[12] V. Cleary, P. Bowen, H. W. M. Witlox, *Journal of Hazardous Materials*. **2007**, *142* (3), 786–796. DOI: 10.1016/j.jhazmat.2006.06.125.
[13] Y. Kitamura, H. Morimitsu, T. Takahashi, *Ind. Eng. Chem. Fund.* **1986**, *25* (2), 206–211. DOI: 10.1021/i100022a005.
[14] P. Stephan, S. Kabelac, M. Kind, D. Mewes, K. Schaber, T. Wetzel, *VDI-Wärmeatlas*, 12th ed., Springer Vieweg, Berlin **n.d.**
[15] K. Takamura, H. Fischer, N. R. Morrow, *Journal of Petroleum Science and Engineering*. **2012**, *98–99*, 50–60. DOI: 10.1016/j.petrol.2012.09.003.
[16] A. H. Lefebvre, V. G. McDonell, *Atomization and Sprays*, 2nd ed., CRC Press, Second Edition. | Boca Raton : Taylor & Francis, CRC Press, 2017. **2017**.
[17] Gas Processors Suppliers Association, Ed. , in *GPSA Engineering Data Book*, 13th ed., Tulsa, Oklahoma **2004**.

Troubleshooting Distillation and Absorption: Practical Examples from a Technology Licensor and Engineering Company

Mariyana Chalakova[1], Ludwig Bauer[1], Felix Flegiel[1], Carolin Schrüfer[1], Maria Magdelena Jarczyk[1]
[1]Linde GmbH, Linde Engineering, Pullach, Germany

Abstract
Linde Engineering is a global T-EPC provider offering engineering, procurement, and construction services combined with proprietary technologies for air separation units, sustainable hydrocarbon solutions, hydrogen and syngas, petrochemicals, and natural gas. We share experiences of troubleshooting and revamp engineering practice around the globe. In the selected cases, the “tooth of time” or overlooked details have led to unexpected operational issues – e.g. column flooding, intermittent entrainment events or performance loss after years of stable operation.
Troubleshooting insights from revamps and lifecycle projects illustrate how seemingly minor details can lead to column malperformance. They demonstrate the value of combining rigorous process and equipment design know-how, hydraulic assessment and targeted field inspection expertise. The case studies emphasize that successful troubleshooting requires questioning assumptions, validating even the obvious, and paying attention to details.
The paper summarizes methodologies, lessons learned, and best practices to help engineers avoid common pitfalls and ensure reliable operation under varying conditions. Through these cases, we aim to inspire readers to challenge assumptions, anticipate the unexpected, and recognize that attention to small details can make the difference between failure and success.

Keywords
troubleshooting; distillation; absorption; column internals; root cause

1. Introduction

Distillation and absorption columns are critical components in industrial gas processing, yet diagnosing operational issues remains challenging due to the limited number of observable indicators. Common parameters such as pressure, temperature, liquid level in the sump or chimney tray, and product composition often serve as primary signals. However, these indicators are inherently ambiguous, as each can be linked to multiple root causes. Consequently, the same observed phenomenon may originate from different underlying mechanisms [1].
Despite this complexity, the initial assumption in case of a column’s malfunction is often flooding. This paper presents a variety of actual root causes from selected industrial case studies from various plant types and column configurations. The objective is to demonstrate that operational problems may arise from less obvious factors and to emphasize the importance of comprehensive data analysis
Practitioners should be encouraged to maintain an unbiased approach, even under stressful conditions, by questioning assumptions and avoiding premature exclusion of potential scenarios.

2. Case A: Reported flooding at the top” in a distillate stripper

Linde Engineering performed a lifecycle study of a naphtha cracker originally licensed by Linde in 1970. The scope included an extensive modernization program to ensure safe and stable operation until 2035.

Operational issue “flooding at the top” was reported for the distillate stripper, where lighter hydrocarbons are removed from the gasoline entering the top of the column, before it is fed to the hydrogenation section. The stripped hydrocarbons exit overhead and are recycled to the raw gas upstream.

Originally designed in 1969, the column was equipped with 18 single-pass trays and revamped in 2000 with cage valve trays featuring increased downcomer width.

The reported phenomenon contradicts the general hydraulic characteristics of this application. Based on available plant data, a rigorous process simulation and hydraulic evaluation of the internals were performed. Here selected data are shown.

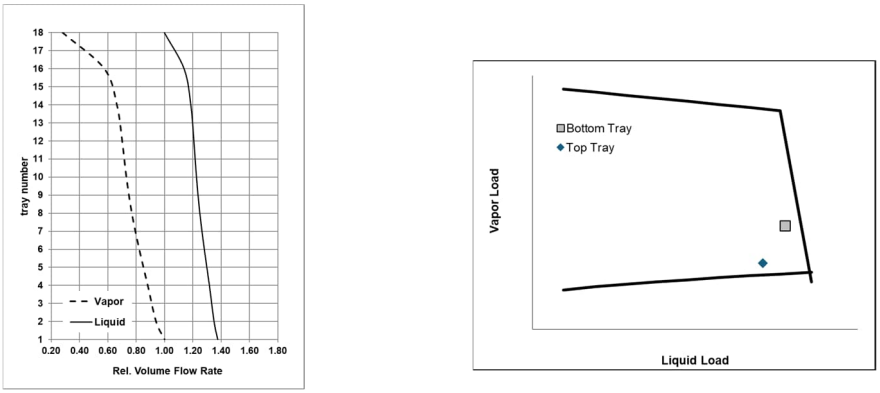

Figure 1. a) Vapor and liquid profiles and b) tray operating window of the distillate stripper

Figure 1a illustrates the vapor and liquid profiles along the column height. The Y-axis represents tray numbers with 1 for bottom tray. The X-axis shows the ratio of the volumetric flow rate at the tray to the inlet flow rate. The vapor flow rate decreases significantly toward the top. As is only 28% of the bottom load the reported “flooding at the top” cannot be attributed to jet flooding at top only. Similarly, liquid load increases toward the bottom, ruling out downcomer flooding as a cause. Hydraulic flooding typically would start at the bottom, where both vapor and liquid loads are highest. Summarized the evaluation of the reference plant data and as-built conditions confirmed that the trays were not hydraulically overloaded.

The operating diagram [3] for the top and bottom tray (Figure 1b) also indicates that the top of the column operates close to the weeping line.

The root cause was verified during a scheduled plant turnaround, when a Linde Engineering expert was able to inspect the column.

Figure 2. Inspection results feed inlet conditions

Figure 2 shows the top tray and feed inlet device, which explains the problem:

- Incorrect tray orientation: Liquid entering the column was partially directed straight into the active area.
- Improper inlet device: Instead of an impingement baffle (covered at the top, open at the sides and bottom) a kind of splash baffle was installed.

Under low vapor load and near-weeping conditions at the top tray, these inappropriate inlet conditions caused separation of liquid and vapor flows. The inspection of the trays below revealed that maldistribution persisted for at least three trays, reducing the performance by more than 15%. Furthermore, the splash baffle accelerated the issue by generated liquid droplets splashed upwards, which could be entrained with the overhead vapor.

As an immediate corrective measure Linde Engineering designed a false downcomer to guide liquid within the inlet zone and prevent splashing. After the installation within the same turnaround no operational issues have been reported since

2. Case B: Off-spec product purity in a CO_2 distillation column

Linde has extensive experience in the design and supply of CO_2 purification and liquefaction plants based on standardized, modular concepts. These plants comprise prefabricated skids integrating piping, instrumentation, and key equipment. A central component is the elevated-pressure CO_2 distillation column. The successful operation with structured packing in this high-pressure application, achieving on-spec liquid CO_2 product has been demonstrated [1].

A recently commissioned CO_2 purification and liquefaction plant licensed by Linde exhibited product purity deviations shortly after start-up. Operators observed off-spec bottom product purity, with too high O_2 and CH_4 concentrations.

The CO_2 distillation column shell had been manufactured in China, and column internals were installed at the shell manufacturer's workshop. No Linde inspector was present during internals installation; acceptance was documented by a local inspector. All available specifications, drawings, QA/QC reports, and photographs were requested and examined as part of the troubleshooting.

Given the symptoms, multiple root cause branches were evaluated in parallel. A summary of selected branches, outcomes, and next steps is provided in Table 1.

Table 1: Summary of selected root cause branches

Root cause	Major outcome	Status	Next step
Feed composition deviation	Composition favorable; impurities significantly lower than specified.	closed	
Hump condition	Multiple successful references for hydraulic loads and bed heights	closed	
Transportation damage	Documentation reviewed; no indication of damage	open	inspection on site
Incorrect fabrication of internals	Drawings and QA reports in line with specifications	closed	
Incorrect installation of internals	Internals arrangement as per drawings reported, no conclusive evidence	open	inspection on site
Wrong packing type	Documentation reviewed; packing type/manufacturer not documented	open	To be explicitly requested
Incorrect packing installation	Documentation reviewed; packing not explicitly mentioned	open	inspection on side

Following targeted requests to the column manufacturer for explicit confirmation of the structured packing type, delivery and installation status, the vendor issued a written statement confirming that the CO_2 column had been delivered without packing. After installation of the packing, the plant achieved design capacity and met the required product purity.

2. Case C: Reduced performance of an air separation distillation column

One of the distillation columns in an air separation process showed reduced efficiency years after commissioning. As no hydraulic issues could be identified during the troubleshooting, the inspection remained as final open step. During the next scheduled shutdown, the column was opened, and damage was discovered. The column, built in the late 1990's, was equipped with structured packing beds each with a liquid collector, pre- and final distributor. The liquid enters from the top through a central pipe and is guided into the pre-distributor. A filter basket is placed beyond the pipe to remove any particles which may clog the final liquid distributor outlet holes. Inside, the filter basket is filled with structured packing (Figure 5a). The packing acts as an energy dissipator and calms the liquid. Over decades of

Figure 5 Filter basket types: a) without and b) with additional energy breaker

continuous direct liquid flow from above, this structured packing eroded and disintegrated into small fragments, which accumulated inside the filter basket. Once the structured packing was destroyed down to the bottom, the wire mesh of which the filter basket is made was attacked and developed localized perforations. As a result, the aluminum fragments could pass through these holes and enter the liquid distributor, where they lodged in the distributor openings and partially blocked them (Figure 6). This not only led to a liquid maldistribution across the packed bed, but

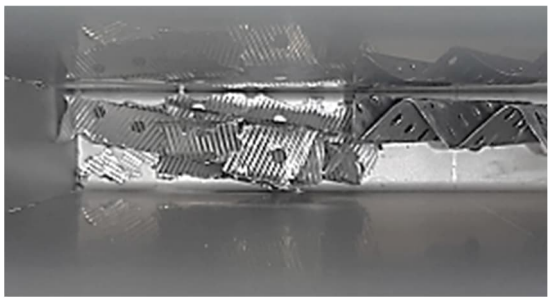

Figure 6. Plugged distributor

probably to liquid distributor overflow, thus significantly reduced efficiency of the affected sections.

However, some filter baskets had an additional separate energy breaker above the structured packing, consisting of horizontal metal rods (Figure 5b). These rods prevented the liquid jet from directly hitting the structured packing with full force. These filter baskets remained undamaged.

As a corrective measure all fragments were removed. The affected filter baskets were replaced with new ones equipped with additional metal rods to improve mechanical stability and prevent future erosion.

2. Case D: Reduced capacity of an absorber after revamp.

A methanol wash column with an interstage cooler was revamped for significantly higher loads. The liquid is withdrawn from a chimney tray, routed through the heat exchanger and then returned to the column directly below the chimney tray (Figure 7). The pressure drop across the heat exchanger loop is provided by the driving liquid head on the chimney tray.

To enable a higher plant capacity the trays in the sections above and below the chimney tray were replaced by new trays with a new liquid distribution device below the chimney tray. In parallel the existing piping and heat exchanger were investigated by an independent team. It turned out that the piping arrangement to and from the heat exchanger also needed modification and replacement.

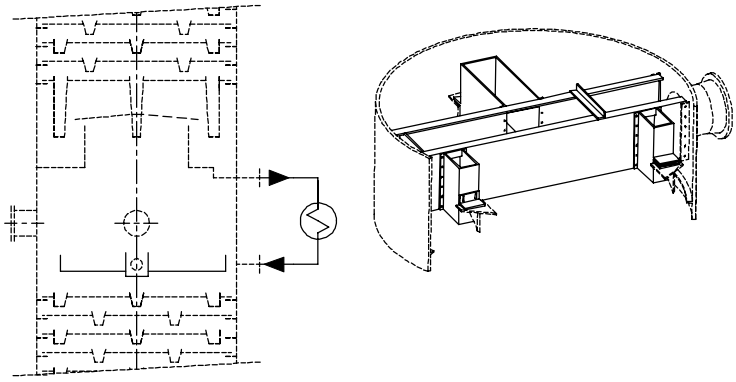

Figure 7. Chimney tray and sketch of the tailor-made inlet trough

After restarting the plant, the liquid level on the chimney tray was already significantly higher even at low load, and before reaching the design load, the chimney tray began to overflow. The analysis revealed that despite the modifications, the new piping rooting, heat exchanger and liquid distribution device exhibited a significantly higher pressure drop than before. Consequently, this resulted in a substantially higher liquid level on the chimney tray. An immediate plant shut down could be avoided, as the process evaluation showed that a temporary operation with overflowing chimney tray was feasible. From different discussed options the team selected a tailor–made, pressure–drop-minimized trough (Figure 7) as the fastest corrective measure. During a short subsequent shutdown, the new distribution trough was installed, and the column could be operated at full load without overflowing chimney tray.

2. Case E: Intermittent entrainment events in a N2 stripper

A N_2-stripper column located in a coldbox was part of a project for eliminating bottlenecks and known operational issues of an LNG plant. Approximately ten years after commissioning, repeated liquid carry-over and elevated pressure drop were observed under varying production loads and conditions. Nevertheless, the column generally operated with acceptable performance under normal conditions, so that immediate actions were not required.

A comprehensive root cause analysis was performed with the objectives to determine the entrainment drivers, to plan inspection and repairs under coldbox constraints within a narrow outage window, and to validate the efficiency of corrective actions. The flashing 2-phase LNG is fed at the top of the column, where a vertical vane-type demister is installed to ensure liquid-free overhead gas. While the analysis did not

reveal a single root cause, it enabled a systematic evaluation of plausible mechanisms. Rigorous simulations and hydraulic assessments of demister loading, vapor traffic, and packing hydraulic and separation margins showed that vapor from the flashed LNG feed was the critical component for the malfunction.
The inspection confirmed seven of the ten identified root causes. Several failures around the vane type demister (Figure 9) such as broken drainpipe, damaged welding seam at the bottom dividing baffle next to the gas outlet were identified.

Figure 3. Inspection findings: a) missing drainpipe; b) vane demister damage.

Corrective actions included welding to restore integrity of the dividing baffle, installation of a new drainpipe and two-phase inlet device with enhanced mechanical stability, targeted welding and cleaning of affected internals by trained personnel. All measures were completed within the five-day outage. No subsequent entrainment events were observed post-restart, confirming the effectiveness of the mitigations.

3. Conclusions

The troubleshooting examples illustrate how thinking beyond conventional assumptions can reveal non-obvious root causes and enable straightforward corrective actions. Across five case studies, we showed that similar symptoms - such as perceived top flooding, off-spec purity, or intermittent entrainment – can come from distinct and sometimes non-obvious root causes. Effective troubleshooting benefits from an iterative, evidence-based workflow that couples rigorous simulation and hydraulic checks with targeted field inspection. Small mechanical details matter: inlet device orientation, distributor pressure drop, inspection expertise, demister tightness, and robust supports can determine whether a column operates as designed or suffers inefficiencies.
Our key recommendations to all engineers are: (i) avoid defaulting to flooding as the first diagnosis and think beyond conventional assumptions; (ii) verify internals against as - built and QA/QC documentation - including the obvious; (iii) assess ageing mechanisms and design for durability (e.g., energy breakers, hold-downs); (iv) look beyond individual components to understand the entire system and ensure integrated design reviews; (v) plan intrusive inspections with contingency repairs. Implementing these practices improves reliability, accelerates startups, safeguards product quality, and enables sustained operation at full load.

References

[1] Kister, H.Z., Distillation Troubleshooting, Wiley-VCH, 2006.

[2] Lockett, M.J., Distillation Design, McGraw-Hill, 1986.

[3] A. Perschmann, M. Chalakova, and A. Kutzschbach, “High Pressure CO2 Column With Structured Packing – From Concept To Successful Column Operation,” in *Proc. of the 12th International Conference on Distillation & Absorption*, Toulouse, France, 2022.

Slicing and Dicing: On the Thickness of Packing Slices to Use in a Rate-Based Model

Emma Russell[1], Callan Abel[1], Dale L. Embry[2], Hendrik A. Kooijman[1], Ross Taylor[1]
[1]Clarkson University, Potsdam, NY, USA;
[2] LNG Technology & Licensing, ConocoPhillips, Houston, TX, USA

Abstract

At the 2024 AIChE Spring meeting, we posed this question: "How do you slice a column filled with packing?" Our goal was to recommend the minimum stage height for packing depth in non-equilibrium packed column models. Prior to that investigation, our standard suggestion was three rate-based stages for each equilibrium stage, with a packing depth in each equal to one-third of the expected HETP. However, the dependence of this on HETP was unsatisfactory, as this required a priori knowledge of the HETP.

To answer this question, we initiated an in-depth and lengthy study to provide an initial recommendation for the minimum stage height in non-equilibrium (rate-based) column simulations of packed columns, a quantity we named the Height Equivalence of a Rate-Based Stage (HERBS). After more than half a million column simulations we propose here some simple correlations that will permit the a-priori estimation of an appropriate depth of packing to use for each rate-based stage.

Our recommendations are based upon the use of a correct plug flow model for packed columns. The plug flow model allows the largest HERBS value or fewest model stages to be used to meet the HERBS precision criteria.

Keywords

Nonequilibrium (NEQ); Rate-based; HERBS; HETP; Packed column

1. Introduction

Separations processes, most notably distillation, comprise a significant portion of many chemical processes, and use a large fraction of the total energy consumption in the industrial sector[1,2]. Because distillation alone accounts for a substantial fraction of industrial energy use, realistic modelling is essential for achieving desired product quality, process efficiency, and safe operation.

Historically, the equilibrium stage (EQ) model has been the standard in distillation design and simulation[2–4]. This approach assumes that the vapor and liquid streams leaving each stage are in equilibrium, and relies on the simultaneous solution of material balances, equilibrium relations, summation constraints, and heat balances[2,4]. The simplicity and computational efficiency of the EQ model contributed to its widespread use[5]. However, the assumption of equilibrium rarely reflects the actual behavior of real-world columns. Finite mass-transfer resistances, temperature

differences between phases, and non-ideal flow dynamics introduce complexities that the EQ model cannot fully and accurately describe.[5]

To address these limitations, nonequilibrium (NEQ), or rate-based, models were developed. Rate-based models incorporate explicit descriptions of mass- and heat-transfer rates and do not assume streams surrounding a stage are at equilibrium with one another. Their governing equations, Material and Energy balances, mass/heat transfer Rate equations, mole fraction Summation equations, Hydraulic equations (pressure drop), and eQuilibrium equations (MERSHQ equations) form the basis for rate-based models and are solved simultaneously to provide a more physically realistic representation of column behavior[5]. Work by Krishnamurthy and Taylor established a general NEQ framework for both tray and packed columns, later extended to include stage pressure as a variable and to support automated design calculations[6,7].

An additional modeling choice that strongly influences rate-based simulations of packed columns is the assumed flow behavior within each stage. Two commonly implemented flow models are mixed-flow and plug-flow[2,8]. In mixed-flow, both phases are considered to be “well mixed”, whereas plug-flow is based on the premise of phases flowing up and down over one another in plugs. However, actual flow, within a column falls into neither absolute category, but would actually be somewhere in between. For the purposes of design and modelling, plug-flow is considered to more closely resemble realistic phase flow behavior compared to completely mixed-flow models. As a general rule of thumb, mixed-flow models generally require a much larger number of stages to achieve the same degree of separation as a properly implemented plug-flow model.

When implementing a plug-flow model in a process simulation tool, it is critical that the mixed-flow model and plug-flow model converge to the same result as the number of stages becomes very large (as the stage height approaches zero). Failure of the plug-flow model to adhere to this behavior indicates that the model is incorrectly implemented and could result in inaccurate column design. As such, it is important to verify correct model behavior within design software before application to process design.

For tray columns, there is a clear one-to-one correspondence between the number of trays and the rate-based model stages. For packed columns, however, this correspondence is less clear. Instead, a packed column must be divided into a series of rate-based stages, each representing a vertical slice of packing. The issue then, is to determine what the height of one of these “slices” should be.

Two of the authors of this paper (R. Taylor and H.A. Kooijman) are the creators of the column simulation software, ChemSep[9], which is capable of correctly implementing rate-based models. One of the most frequently asked questions they are posed is: “What depth of packing should we assign to a single rate-based stage?”

The standard suggestion (prior to this investigation) was to use three rate-based stages for each equilibrium stage, with a packing depth in each equal to one-third of the expected HETP. However, the dependence of this answer on HETP was unsatisfactory, as this required a priori knowledge of the HETP, which is a value predicted using rate-based model simulations.

To address this, we conducted an extensive study across a wide range of chemical systems, operating conditions, and packing types, using the column simulation software ChemSep[9]. The outcome of this effort is a set of correlations and guidelines for determining HERBS without relying on HETP, along with an examination of how HERBS varies with relative volatility, pressure, packing characteristics, and other thermophysical properties. These results provide a sound basis for determining stage height in rate-based modeling of packed columns and offer the potential for improved accuracy and more reliable designs.

2. Results and discussion

To date, this study has involved eleven different chemical systems: Isobutane-n-Butane, Cyclohexane-n-Heptane, p-Xylene-o-Xylene, Isopentane-n-Pentane, 1-Butene-n-Butane, 1-Pentene-n-Pentane, Argon-Oxygen, Ethylbenzene-Styrene, Methanol-Water, Acetone-Ethanol, and Ethanol-1-Propanol. For each system, two to three different pressures (ranging from 0.02 to 20.68 bar depending on the system), and various types of packing identified in Table 1 (both random and structured) were included in this study.

Random Packing Types	*Nominal Sizes*
Cascade Mini-Rings	1, 2, 3
IMTP	25, 50, 70
Raschig Super Rings	0.7, 1, 2
Sulzer Pall Rings	1, 2
Structured Packing Types	*Nominal Sizes*
Koch-Glitsch Flexipak	250Y
Norton Intalox	1T
Sulzer BX	-
Sulzer Mellapak	125Y, 250Y, 350Y, 500Y

Table 1: Packing types and nominal sizes investigated

Three different mass-transfer coefficient (MTC) models and two flow models (mixed and plug-flow) were explored. Bravo-Fair 1982, Onda et al. 1968, and Billet Schultes were the selected MTC models for the random packing types, and Bravo-Rocha-Fair 1985, Bravo-Rocha-Fair 1992, and Billet Schultes 1992 were the selected MTC models for structured packings (see Kister for more details)[2].

A total of over half a million column simulations were performed. For each chemical system and type of packing we systematically varied the packing slice thickness (stage height), the column section height, the operating pressure, the mass transfer coefficient model, and the flow model. The results of these simulations gave us a set of parameter values as a function of slice thickness. From this, extrapolation of the top or bottom product composition to a slice thickness approaching zero was used to define a converged reference solution, from which the minimum HERBS value corresponding to 99% of the limiting performance was determined. A representative example for one particular system is shown in Figure 1. The left panel in Figure 1 is an expanded view of the top left corner of the right-hand panel. Note that the data for mixed flow and for plug flow extrapolate to the same mole fraction (as they should).

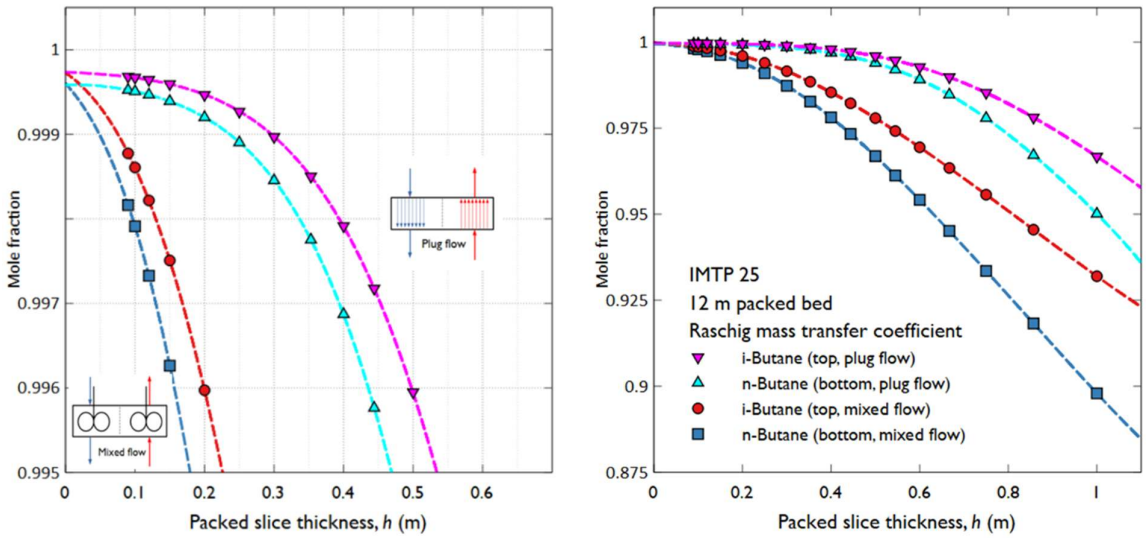

Figure 1: Example of product composition as a function of packing slice thickness

One important conclusion from Figure 1 is that the use of a correctly implemented theoretical plug-flow model allows the use of a larger HERBS value than is needed for mixed-flow models. What this means in practice is that mixed-flow models require substantially more stages (packing slices) to achieve comparable accuracy.

Further inspection of the simulation data revealed that relative volatility is the dominant physical property parameter influencing HERBS. Figures 2 and 3 show HERBS as a function of relative volatility for random and structured packings. Figure 2 shows HERBS for three different random packings (left panel) and three different Raschig packings (right panel).

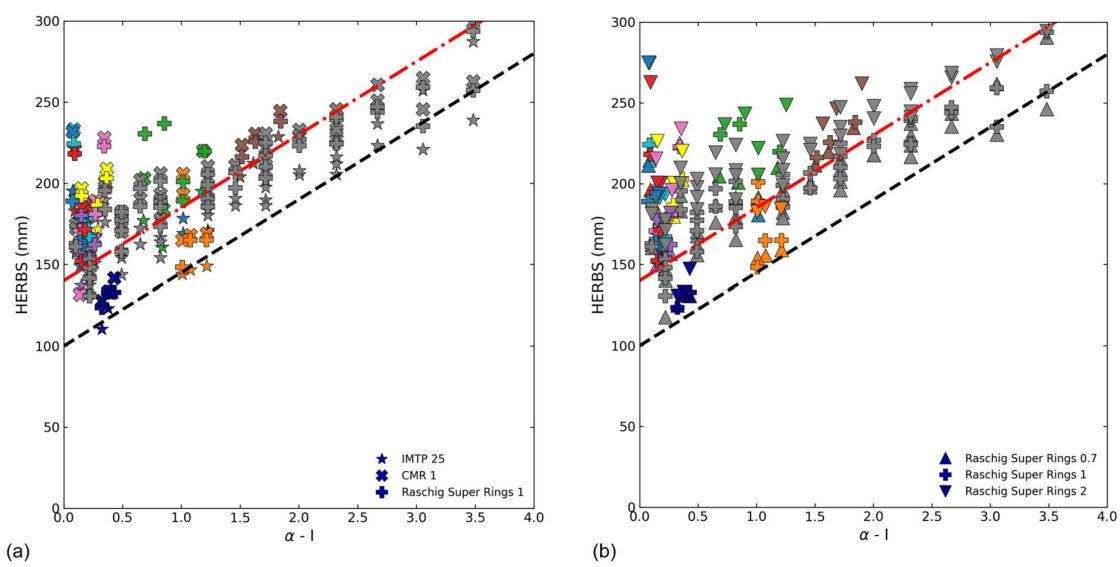

Figure 2: HERBS correlations with respect to relative volatility, α, for random packings

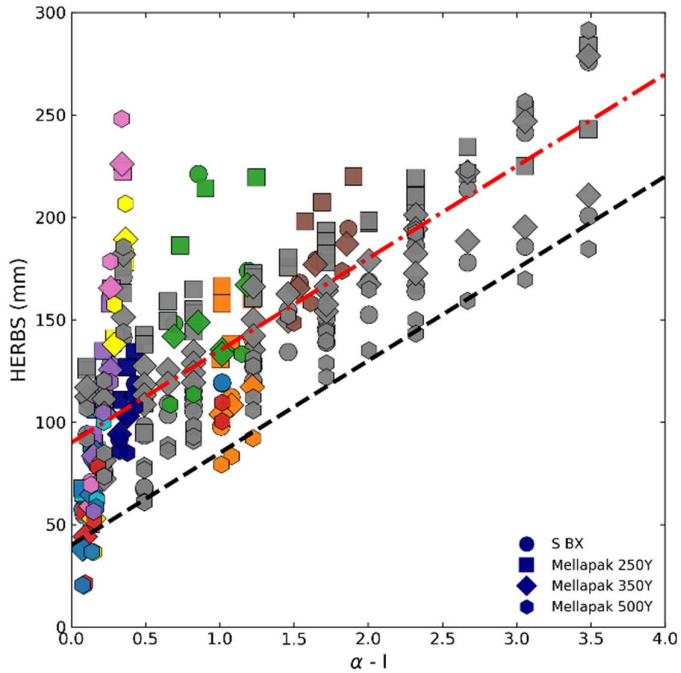

Figure 3: HERBS correlations with respect to relative volatility, α, for structured packings

The points in Figures 2 and 3 are color-coded as follows: Isobutane-n-Butane in yellow, Cyclohexane-n-Heptane in pink, Isopentane-n-Pentane in cyan, 1-Butene-n-Butane in red, 1-Pentene-n-Pentane in blue, Argon-Oxygen in purple, Ethylbenzene-Styrene in navy blue, Methanol-Water in brown, Acetone-Ethanol in green, and Ethanol-1-Propanol in orange. The gray colored points represent hypothetical mixtures based on Isopropanol in which only the vapor pressures were adjusted to expand the range of relative volatilities investigated (from 1.1 to 4.5).

Based on the results in Figures 2 and 3, simple correlations were developed:

$$HERBS = A + 45(\alpha - 1) \qquad [1]$$

where α is the relative volatility. The parameter A is defined in Table 2.

Correlation	A	*Line in Figure*
Random Packings (Conservative)	100	Black; Dashed; Fig. 2
Random Packings (Average)	140	Red; Dash-Dot; Fig. 2
Structured Packings (Conservative)	40	Black; Dashed; Fig. 3
Structured Packings (Average)	90	Red; Dash-Dot; Fig. 3

Table 2: Values of Parameter A by Packing Type for Use with Plug-Flow Model

These correlations provide a conservative estimate of the minimum HERBS value (in *mm*) required for packed column design when used with a correctly implemented plug-flow model.

These correlations provide a practical method for selecting a rate-based stage height prior to simulation, without requiring advance knowledge of concepts such as HETP. When applied across the full set of systems examined, the correlations reproduced converged reference solutions from industrial case studies with reasonable accuracy while significantly reducing the number of stages required.

3. Conclusions

Based on the results of an extensive investigation covering a wide range of chemical systems, operating conditions, and packing types, correlations relating HERBS to relative volatility are recommended for practical use in rate-based column simulations of packed columns. Separate parameters are provided for random and structured packings. These correlations provide a conservative estimate of the minimum HERBS value required to for use in packed column design.

We also emphasize that the use of a *correctly* implemented plug-flow model is essential for the proper application of these correlations. Predictions obtained using the recommended HERBS values represent a slight underestimation of the number of stages required for a true plug-flow model (which would require an infinite number of stages), and the mixed-flow model requires a significantly greater number of stages to achieve the same degree of separation compared to the plug-flow model.

Current extensions to this study are underway to include more data points and a wider range of relative volatilities. The concept of a “graduated” or non-constant HERBS value is also being explored, where the recommended stage height may be varied along the column, providing better optimized column designs.

References

(1) Oak Ridge National Laboratory; BCS Inc., Laurel, MD (United States). *Materials for Separation Technologies. Energy and Emission Reduction Opportunities*; 1218755, 4571; 2005; p None, 1218755, 4571. https://doi.org/10.2172/1218755.

(2) Kister, H. Z. *Distillation Design*; McGraw-Hill: New York, 1992.

(3) Halvorsen, I.; Skogestad, S. Distillation Theory. *Encycl. Sep. Sci.* **2000**. https://doi.org/10.1016/B0-12-226770-2/00631-1.

(4) Seader, J. D.; Henley, E. J.; Roper, D. K. *Separation Process Principles : Chemical and Biochemical Operations*, 3rd ed.; Wiley: Hoboken, NJ, 2011.

(5) Taylor, R.; Krishna, R.; Kooijman, H. Real World Modeling of Distillation. *Chem. Eng. Prog.* **2003**, *99* (7), 28–39.

(6) Krishnamurthy, R.; Taylor, R. A Nonequilibrium Stage Model of Multicomponent Separation Processes. Part I: Model Description and Method of Solution. *AIChE J.* **1985**, *31* (3), 449–456. https://doi.org/10.1002/aic.690310312.

(7) Krishnamurthy, R.; Taylor, R. A Nonequilibrium Stage Model of Multicomponent Separation Processes. Part II: Comparison with Experiment. *AIChE J.* **1985**, *31* (3), 456–465. https://doi.org/10.1002/aic.690310313.

(8) Kooijman, H. A. *Dynamic Nonequilibrium Column Simulation: A Dissertation*; Ph.D. Thesis, Clarkson University, Potsdam, NY, 1995 http://www.chemsep.org/downloads/documentation.html.

(9) Kooijman, H. A.; Taylor, R. ChemSep, 2022.

Investigations of Crystallization Fouling on Pall-Rings

Korbinian Inderwies[1], Patrick Rock[1], Manuel Mörtl[1], Harald Klein[1], Sebastian Rehfeldt[1]
[1]Technical University of Munich, TUM School of Engineering and Design, Department of Energy and Process Engineering, Institute of Plant and Process Technology, Garching/Germany
korbinian.inderwies@tum.de; harald.klein@tum.de; sebastian.rehfeldt@tum.de

Abstract
Fouling on column internals, such as trays and packings, is a major challenge in chemical processes, leading to increased pressure drop, reduced throughput, and costly shutdowns. To address the lack of standardized evaluation methods, the new VDI Standard 2774 introduces a unified procedure for assessing fouling tolerance. As part of its development, a standard test rig was set up at the Technical University of Munich to investigate crystallization fouling under accelerated conditions using a saturated NaCl-water solution and air. Fouling growth is quantified by the increase in pressure drop and correlated with the evaporated water mass, accounting for mass transfer. Experiments with metallic Pall-Rings examined the influence of the water loading of the inlet gas and scalability. Results show that higher water loading significantly increases fouling tolerance by reducing the fouling growth rate, while removal remains constant. Furthermore, the packing element size has no noticeable effect on fouling tolerance as long as the ratio of random packing element diameter to column diameter remains constant. This work contributes to creating reference values for fouling tolerance of column internals.

Keywords
fouling, column, random packing, crystallization, standard test rig

1. Introduction

Fouling, the undesired formation of deposits on heat or mass transfer surfaces, is a major challenge in chemical processes. Depending on the fluid system, these deposits can strongly impair performance. According to a study by Kister [1], fouling on column internals, in particular trays, random packings and structured packings, is the leading cause of operational malfunctions.

The deposits reduce the free cross-sectional area for gas flow and increase pressure drop, which can lower throughput and, in severe cases, lead to shutdowns. Fouling also promotes liquid maldistribution in packed columns and entrainment in tray columns, which ultimately can impair separation efficiency [2]. To mitigate these risks, the equipment is often oversized, which leads to higher investment and operating costs and higher energy consumption. In addition, fouling necessitates regular cleaning of the equipment. Reducing fouling is therefore of substantial economic and ecological relevance.

Despite its importance, there are only a few systematic studies on fouling of column internals, and standardized evaluation methods have been lacking so far. The new VDI Standard 2774 [3] addresses this gap by providing a unified procedure for measuring and comparing fouling tolerance of different column internals.

As part of the development of this standard, a first standard test rig for investigating crystallization fouling on column internals was put into operation at the Technical University of Munich. This paper presents insights and results regarding the influence of the water loading of the inlet gas and the scalability of fouling behavior of metallic Pall-Rings.

2. Experimental

The aim of the investigations using the standard test rig is to quantitatively and reproducibly determine the fouling tolerance of the column internals regarding to crystallization fouling. Since fouling is typically a very slow process, often requiring months or even years to observe significant effects, crystallization fouling is artificially accelerated in the standard test rig by using a saturated sodium chloride-water solution (NaCl-water solution) and air, allowing results within a single day. Further details on the reasoning behind the choice of this fluid system are provided by Inderwies et al. [4]. In the following sections the setup of the test rig and the evaluation of the experimental results are described.

2.1 Standard test rig

The setup of the standard test rig is shown simplified in the piping and instrumentation diagram (PI&D) in Figure 1. The cycle of the saturated NaCl-water solution is shown in red. The solution is stored in tank T1. The heating hood H1 is used to regulate and maintain the temperature of the solution throughout the experiment.

The progressive cavity pump P1 (pump capacity $0.08 - 7.5\,\mathrm{m^3/h}$) draws in the solution and pumps it to the top of the columns. In filter F1 (felt filter bag, perforation $100\ \mu\mathrm{m}$), undissolved salt particles are removed before the solution enters the column. The Flowmeter FIRCAL 5.02 measures the liquid volumetric flow rate $\dot{V}_{L,in}$ at the column inlet. Temperature sensor TRC 5.03 measures the liquid inlet temperature $T_{L,in}$. A setpoint of $T_{L,in} = 25°\mathrm{C}$ is specified for this temperature.

Using the three-way valves V204 and V303, the liquid flow can be directed either to column C1 or C2. At the bottom of the columns, the three-way valves V401 and V402 are adjusted accordingly so that the NaCl solution flows back into tank T1. At the outlet of the columns, temperature sensor TR 6.01 measures the liquid outlet temperature $T_{L,out}$.

For the investigation of fouling tolerance on column internals, the two packed columns C1 and C2 are used. Column C1 has a diameter of $D_C = 300\,\mathrm{mm}$ and a packing height of $H_P = 1.6\,\mathrm{m}$. The diameter of Column C2 is $D_C = 150\,\mathrm{mm}$ and the packing height is also $H_P = 1.6\,\mathrm{m}$. The gas stream for columns C1 and C2 is supplied by the Roots-type blower B1 (air flow rate up to $700\,\mathrm{m^3/h}$), which draws in ambient air. Usually, the gas stream is humidified in column C3 with demineralized water so that the difference between the water loading Y_{in} of the inlet gas and the water loading Y_{out} of the outlet gas according to Equation (2) is approximately $\Delta Y = 6\,\mathrm{g(H_2O)/kg(Air)} \pm 2\,\mathrm{g(H_2O)/kg(Air)}$ to ensure comparable test conditions. Afterwards, the volumetric flow rate $\dot{V}_{G,in}$ of the gas is measured by FR 2.02, and the relative pressure $p_{in,rel}$ at the inlet is measured by PR 2.03. The combined temperature/humidity sensor TR 2.04 and MR 2.04 measure the inlet gas temperature $T_{G,in}$ and the relative humidity φ_{in}. By opening valve V101 or V102, the gas stream is directed into either column C1 or column C2.

At the top of the columns, entrained droplets are separated using a demister mesh. Afterwards, the outlet gas temperature $T_{G,out}$ and the outlet relative humidity $\varphi_{G,out}$ are measured by the combined temperature/humidity sensor TR 3.01 and MR 3.01. The

gas stream is then released back into the environment. The absolute ambient pressure p_{amb} is monitored by pressure sensor PR 3.02.
The increase in pressure drop caused by fouling on the column internals in column C1 or C2 is measured by the differential pressure transmitter PDIRAH 1.01. The pressure drop is measured in both columns over the entire packing height, including the support grid. Using the two three-way valves V501 and V502, either column C1 or C2 can be selected for pressure drop measurement.
After the experiment, the respective column is rinsed two times with demineralized water from tank T2 to remove all deposits from the internals. The column is rinsed using the pump P2 and adjusted settings of the three-way valves V204, V303, V401, and V402. This rinsing loop is shown in the P&ID in Figure 1 in blue.
With the equipment and instrumentation, the maximum possible liquid load in column C1 is $B = 100\ \mathrm{m^3/(m^2h)}$, and the minimum possible liquid load in column C2 is $B = 5\ \mathrm{m^3/(m^2h)}$. The maximum gas load in column C1 is $F = 3.0\ \mathrm{Pa^{0.5}}$ and the minimum gas load in column C2 is $F = 0.5\ \mathrm{Pa^{0.5}}$.

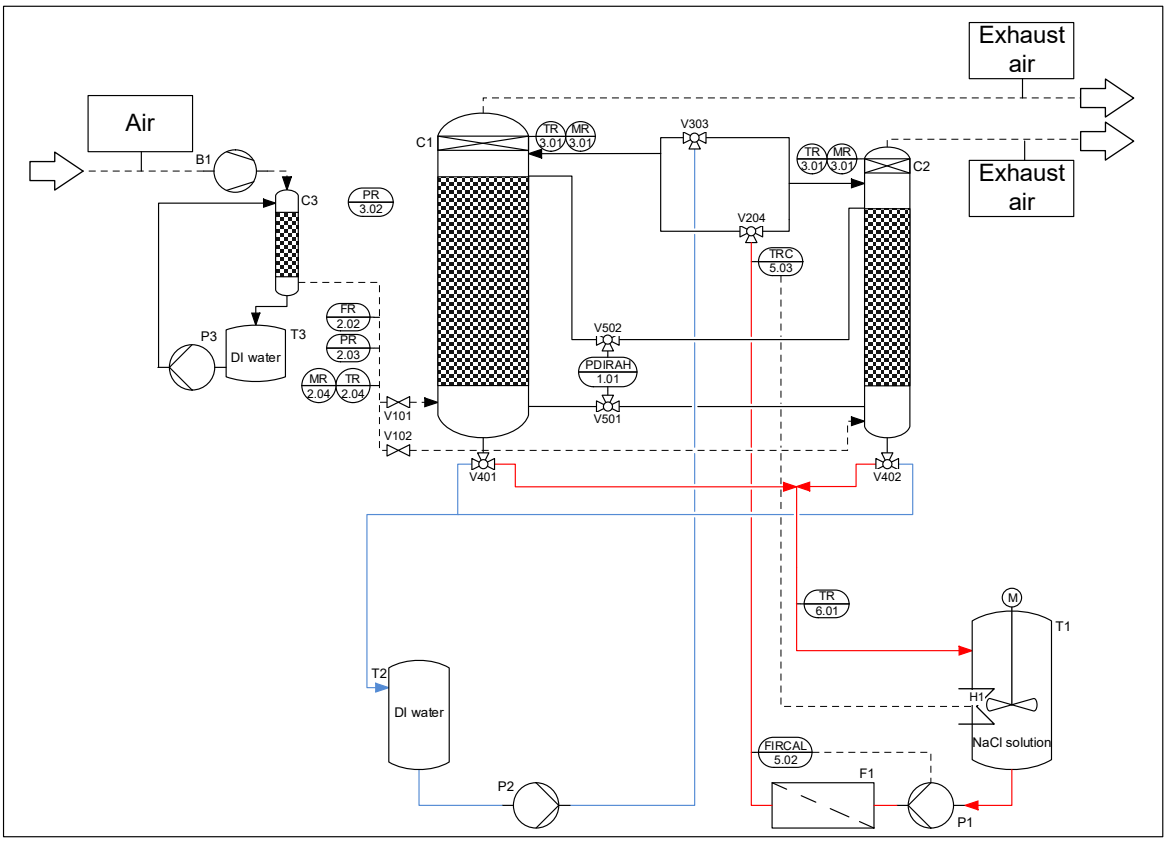

Figure 1: Simplified piping and instrumentation diagram of the standard test rig.

2.2 Evaluation of the experiments

Similar to the fouling resistance in heat exchangers, the fouling index R_F is used as a measure of fouling progress and is defined by:

$$R_F = \frac{\Delta p}{\Delta p_0}\ . \qquad (1)$$

Here, the current pressure drop Δp over the internals is referred to the initial pressure drop Δp_0 over the internals.
To compare the fouling tolerance independently of separation efficiency, the mass transfer in the column must be considered. Therefore, the mass M_W of evaporated

water during the experiment is used as a measure of mass transfer. The evaporated water mass can be determined from the measured relative humidity $\varphi_{in/out}$ of the gas stream at the inlet and outlet of the column. For this purpose, the water loading of the gas stream Y_{in} at the inlet and Y_{out} at the outlet of the column is calculated using the following equation:

$$Y_{in/out} = \frac{\bar{M}_W}{\bar{M}_d} \cdot \frac{\varphi_{in/out}\, p_{sat,in/out}}{p_{in/out} - \varphi_{in/out}\, p_{sat,in/out}} \,. \quad (2)$$

The saturation vapor pressure $p_{sat,in/out}$ of water at the inlet or outlet of the column is determined using the Wagner equation [5]. Additionally, the molar masses $\bar{M}_W$ of water and $\bar{M}_d$ of dry air are required. The pressure p_{in} of the gas at the inlet of the column is calculated from the absolute ambient pressure p_{amb} and the relative pressure $p_{in,rel}$:

$$p_{in} = p_{amb} + p_{in,rel} \,. \quad (3)$$

The outlet pressure p_{out} of the gas stream is equal to the absolute ambient pressure p_{amb}.

In addition, the gas mass flow rate $\dot{M}_G$ is required for determining the evaporated water mass. It is calculated from the density $\varrho_{G,in}$ and the volumetric flow rate $\dot{V}_{G,in}$ of the gas at the inlet of the column:

$$\dot{M}_G = \varrho_{G,in} \cdot \dot{V}_{G,in} \,. \quad (4)$$

For this, the density $\varrho_{G,in}$ of the gas at the inlet of the column is calculated via the ideal gas law using the specific gas constant R_m of humid air, the pressure p_{in} and temperature $T_{G,in}$ of the gas at the inlet:

$$\varrho_{G,in} = \frac{p_{in}}{R_m \cdot T_{G,in}} \,. \quad (5)$$

The specific gas constant R_m of humid air is calculated by the specific gas constant R_d for dry air, the specific gas constant R_v of water vapor, the relative humidity φ_{in}, the saturation vapor pressure $p_{sat,in}$ and the inlet pressure p_{in} (Inderwies et al. [6]):

$$R_m = \frac{R_d}{1 - \varphi_{in} \cdot \frac{p_{sat,in}}{p_{in}} \cdot \left(1 - \frac{R_d}{R_v}\right)} \,. \quad (6)$$

Finally, the evaporated water mass M_W is determined from the gas mass flow rate $\dot{M}_G$ and the water loading Y_{in} at the inlet and Y_{out} at the outlet of the column according to the following equation:

$$M_W = \sum_{i=0}^{n} (\dot{M}_{G,i} \cdot (Y_{out,i} - Y_{in,i}) \cdot \Delta t) \,. \quad (7)$$

For this purpose, the evaporated water mass is calculated for each time interval $\Delta t = 1\ \mathrm{s}$ and summed up to a particular point in time t. To compare the fouling tolerance of different internals and at various operating points, the evaporated water mass $M_{W,1.5}$ is calculated until the fouling index of $R_F = 1.5$ is reached using the following equation:

$$M_{W,1.5} = M_W[\, t(R_F = 1.5)\,] \,. \quad (8)$$

The greater the mass of evaporated water before reaching this criterion, the higher the fouling tolerance of the column internals.

3. Results and discussion

The investigations of this paper focus on the influence of the inlet water loading of the gas flow on the fouling tolerance and the scalability of fouling. For this purpose, the relative humidity of the gas stream at the inlet was systematically varied between $25\ \%\mathrm{rH}$ and $75\ \%\mathrm{rH}$, which corresponds to a water loading of the gas stream at the inlet of $3.5 - 8.8\ \mathrm{g(H_2O)/kg(Air)}$. Figure 2 shows the evaporated mass of water $M_{W,1.5}$ required to reach $R_F = 1.5$ as a function of the average inlet water loading $Y_{in,avg}$ of the gas stream. The inlet water loading is averaged over the duration of each experiment.

The investigations were carried out in column C2 using metallic Pall-Rings 15 (diameter $15\ \mathrm{mm}$) at a gas load of $F = 1.0\ \mathrm{Pa}^{0.5}$ and a liquid load of $B = 12\ \mathrm{m}^3/(\mathrm{m}^2\mathrm{h})$. With increasing average water loading of the gas stream, the fouling tolerance increases with superlinear growth. The higher water loading of the gas stream at the column inlet reduces the driving force for the evaporation of water from the saturated NaCl-water solution. As a result, mass transfer within the packing decreases, leading to a slower fouling growth rate.
Besides the formation of deposits on the column internals, part of the fouling is continuously removed. This removal rate of the fouling is assumed to be largely independent of the mass transfer in the column and may be primarily determined by the liquid load B. As the fouling formation rate decreases with increasing water loading of the inlet gas while the removal rate remains constant, the fouling tolerance consequently increases.

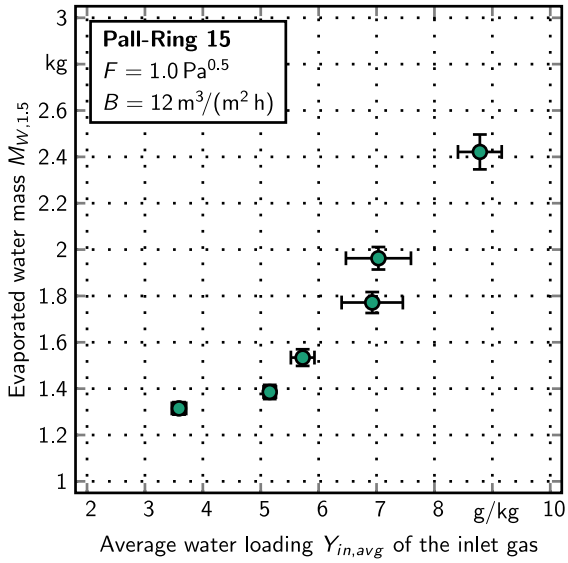

Figure 2: Evaporated water mass as a function of the average water loading of the inlet gas stream for a packing of metallic Pall-Rings 15 in column C2 at a gas load of $F = 1.0\ \mathrm{Pa}^{0.5}$ and liquid load $B = 12\ \mathrm{m}^3/(\mathrm{m}^2\mathrm{h})$.

In addition to the influence of the water loading of the inlet gas on the fouling tolerance of the column internals, the scalability of the fouling was also investigated. For this purpose, the fouling tolerance of metallic Pall-Rings 15 in column C2 and metallic Pall-Rings 25 (diameter $25\ \mathrm{mm}$) in column C1 is determined at the same packing height and under same operating conditions. The use of different column diameters ensures a similar ratio of packing diameter to column diameter.
Figure 3 shows the evaporated water mass $M_{W,1.5}$ required to reach $R_F = 1.5$ normalized by the column cross-sectional area A_C over the gas load F at a liquid load of $B = 12\ \mathrm{m}^3/(\mathrm{m}^2\mathrm{h})$ for both measurement series. The evaporated water mass is normalized by the cross-sectional areas of C1 and C2 in order to account for the different gas volumetric flow rates, and thus mass transfer rates, at the same gas load. The results show a similar fouling tolerance for the Pall-Rings 15 and Pall-Rings 25, indicating that the size of the packing, provided that the ratio of packing diameter to column diameter is maintained, has no significant influence on the fouling tolerance. This may be due to the fact that the two packings are geometrically similar in their design and therefore show comparable fluid dynamic properties, which essentially influence fouling growth.

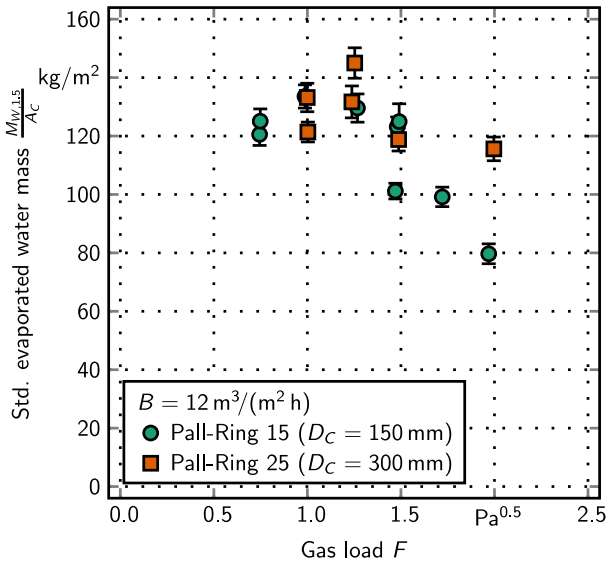

Figure 3: Standardized evaporated water mass, normalized to the column cross-sectional area A_C, as a function over the gas load F for metallic Pall-Rings 15 and Pall-Rings 25 at a liquid load of $B = 12\ \mathrm{m}^3/(\mathrm{m}^2\mathrm{h})$.

4. Conclusion

Using the standard test rig, the tolerance of column internals to crystallization fouling can be quantified and reproduced, enabling direct comparison of different internals and operating conditions. In this contribution, the influence of the water loading at the inlet on fouling tolerance and the scalability of fouling behavior was investigated using the standard test rig. Increasing inlet humidity was found to increase fouling tolerance, as the fouling growth rate decreases while the removal rate remains constant. The scalability study further showed that the packing diameter has no noticeable effect on fouling tolerance as long as the ratio of packing diameter to column diameter is maintained. Therefore, it is essential to ensure comparable test conditions when assessing and comparing fouling tolerance of different column internals.

Acknowledgements

The authors gratefully acknowledge the financial support of the joint project SAMARA by the Federal Ministry for Economic Affairs and Climate Action (BMWK, FKZ 03EN2007K) and the project supervision by the project management organization Projektträger Jülich (PtJ).

References

[1] Kister, H. Z. What Caused Tower Malfunctions in the Last 50 Years? *Chem. Eng. Res. Des.* 2003, *81*, 5−26.

[2] Großerichter, D. *Fouling in Boden- und Packungskolonnen für Gas-Flüssig-Systeme*; Shaker: Aachen, 2004; PhD dissertation.

[3] Association of German Engineers (VDI Verein Deutscher Ingenieure e.V.). *Operation of Process Plants − Energy Efficiency of Process Plants − Fouling in Heat Exchangers and Columns. VDI 2774 Part 1, ICS 27.060.30: Düsseldorf, Germany, 2025.*

[4] Inderwies, K.; Kappes, J.; Klein, H.; Rehfeldt, S. Investigation of Crystallization Fouling on Column Internals using a Screening Test Rig. *Chem. Ing. Technol.* 2024, *96*, 1419−1428.

[5] Wagner, W. New vapour pressure measurements for argon and nitrogen and a new method for establishing rational vapour pressure equations. *Cryogenics* 1973, *13*, 470−482.

[6] Inderwies, K.; Boden, S.; de Assis Dias, F.; Kryk, H.; Schubert, M.; Hampel, U.; Klein, H.; Rehfeldt, S.: *Investigation of Fouling on Random Packing Using Microfocus X-ray Computed Tomography*. Industrial & Engineering Chemistry Research 64.43 (2025), p. 20744–20756.

Feedforward versus feedback thinking for distillation column control

Sigurd Skogestad[1] and Ivar J. Halvorsen[1,2]
[1]Norwegian University of Science and Technology (NTNU), Trondheim, Norway
[2]SINTEF, Trondheim, Norway

Abstract. Feedforward and feedback present two fundamentally different approaches to automatic control, and in this paper, we discuss how this applies to distillation column control. The focus in this paper is on adjusting the product split using temperature control. Applications include conventional distillation, complex dividing-wall (Petlyuk) arrangements and batch distillation.

Keywords. Process control, control architecture, PID control

1. Introduction

Chemical engineers are trained to be steady-state feedforward thinkers, and dynamics and feedback control are counterintuitive for most people. Without control, distillation dynamics are often very slow, and this has created the myth that "distillation columns are inherently slow and hard to control". However, feedback control can change the dynamics. As shown in Section 2, for a conventional distillation column (Figure 1), a seemingly very small difference in the manipulated flows L and V (Figure 2) can speed up the response time by a factor 10. However, a more important fact is that only by feedback, the flows can be set with sufficient accuracy. In particular, it is important to set the product split D/F accurately.

The paper extends previous work of the first author on understanding the dynamics and control of distillation columns (e.g., Skogestad, 1997).

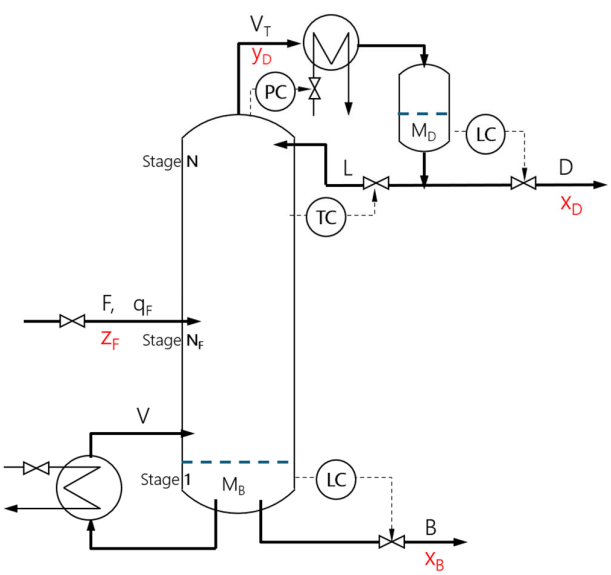

Nominal steady-state data («column A»)

z_F = 0.5 (fraction light component in feed)
q_F = 1 (liquid feed)
$x_D = y_D$ = 0.99 (light component)
x_B = 0.01 (ligh component)
D/F = 0.5, B/F = 0.5
$V/F = V_T/F$ = 3.206, L/F = 2.706
F = 1 kmol/min
N = 40, N_F=21 (equlibrium stages)
M_D = 10 kmol , M_B = 10 kmol
M_l/F = 0.5 kmol (stage holdup)

Model assumptions
- Constant molar flows
  - Steady state: $V+B = L + q_F F$
- Constant relative volatility, α = 1.5
- Constant pressure (using cooling V_T)
- Total condenser
- Variable stage holdup: Francis' weir formula

Figure 1. Conventional distillation column using LV-configuration (L and V are left for control x_D and x_B, with F given and V_T, D and B used for pressure and level control).

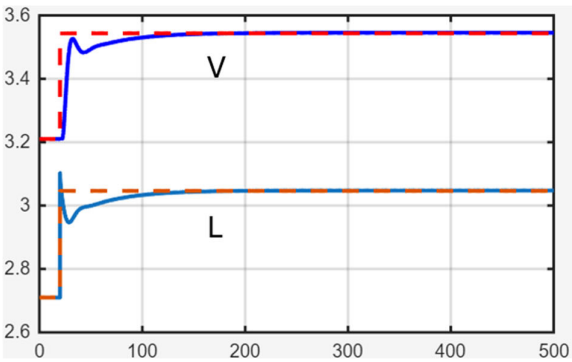

Red dashed lines: ΔL=0.3364 kmol/min, ΔV=0.3337 kmol/min.

Blue solid lines: The PI-controller for L uses y_D (and not x_D) as the measurement. The controller was tuned based on the initial integrating response (upper left in Figure 5) using the SIMC rule with tauc=5 min, giving K_C=80 and KI=5. The PI-controller for V using x_B as the measurement. It was tuned based on the initial integrating response (lower right in Figure 5) using the SIMC rule with tauc=5 min, plus a delay of 1.5 min, giving K_C=50 and KI=3. The level controllers are PI-controllers with K_c=0.5 and KI=0.025.

Figure 2. Changes in reflux (L) and boilup (V) made by perfect feedforward operator (red dashed lines) and two feedback PI controllers (blue solid lines). The resulting changes in product compositions are shown in Figure 3.

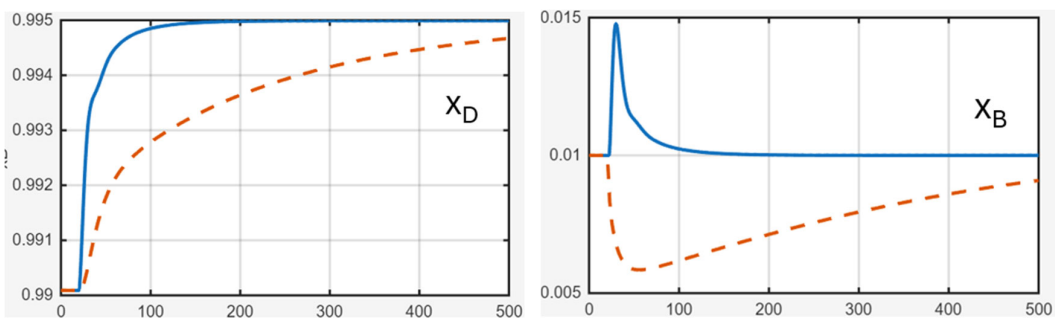

Figure 3. Comparison of composition responses with feedforward control (red dashed line) and feedback PI control (blue solid line).

2. Feedforward versus feedback control - Motivating example

Assume that we want to use the reflux L and boilup V to make a setpoint change in the top composition (x_D) for a conventional binary distillation column (data in Figure 1). More precisely, the task is to increase x_D from 0.99 to 0.995 at time t=20 min, while keeping the bottom purity constant (x_B=0.01). Here, x_D and x_B denote the mole fraction of light component, so this is a high-purity separation.

Figures 2 and 3 compares how this is accomplished by a “perfect feedforward operator” versus using two PI feedback controllers. The “perfect feedforward operator” (who may be a chemical engineer) knows that at steady state, the desired increase in x_D is accomplished by increasing reflux L by 0.3364 kmol/min and increasing boilup V by 0.3337 kmol/min. The “perfect operator” does this in a feedforward fashion by making a step change in L and V at t=20 min (Figure 2). The two PI controllers make a very similar change in L and V, although seemingly a little delayed (Figure 2). The surprising fact is that the composition response is much faster with feedback control (Figure 3). The time constant for x_D (defined as the time where 63% of the change is accomplished) is reduced from 123 minutes (feedforward control) to 11 minutes (feedback control). Also note that the feedforward operator needs to increase both reflux L and boilup V by almost the same amount, such that the difference D=V-L is reduced only slightly from 0.5000 to 0.4973 (this is because a little more of the heavy component needs to go to the bottom). Such an accurate change is impossible to

accomplish in practice by flow control, so not only is the feedforward solution inferior dynamically, it is also unrealistic.

3. Dynamic response without control – understanding distillation

The two manipulated variables for composition control for the column in Figure 1 are the reflux L and the boilup V. Figure 4 shows the open-loop response in product compositions (x_D and x_B) to individual step changes by $\pm$0.1 kmol/min (about $\pm$3%) in L and V. Figure 5 is a blow-up of the initial response (first 10 minutes), which is more relevant for controller design.

The most striking thing about Figure 4 is how similar the responses are for changes in L and V when we change them in opposite directions ($\Delta L = - \Delta V$). The reason is that at steady state D=V-L, so both changes have the same effect on the distillate flow D. In general, for high-purity separations, the product split D/F (i.e., the external flows) has a very large effect on compositions. One may view the distillation column as a tank with light component in the top and heavy component in the bottom. An increase in D/F (external flows) moves the "level" (interface between light and heavy component) up the column, and increases both x_D and x_B at the same time (so top product gets purer and bottom product less pure). In Figure 4 the change in external flows (ΔD) completely overshadows the much smaller effect of changes in internal flows ($\Delta L=\Delta V$ with D constant), which stretches the profile and makes both products purer. Actually, the much smaller effect on composition of internal flow changes is seen in Figure 3. This differences in sensitivity (process gains) for external and internal flow changes means that the process is "ill-conditioned" with large values of the steady-state relative gain array (RGA) for high-purity separations. This is an important reason why in distillation it is difficult to control both compositions ("two-point control"). However, as we will see shortly, there is some hope because of the liquid flow dynamics.

We also note from Figure 4 that the process is strongly nonlinear as the effect (gain) of positive and negative changes in L (and V) are very different. At steady-state it is almost a factor 20 in this case. This makes feedforward control difficult, but it is usually not a big problem for feedback control. The reason is that feedback reacts on a fast time scale where the nonlinearity is much smaller. This is illustrated in Figure 5, which shows that the initial response may be approximated as an integrating process plus a delay. We note that the slopes are fairly similar in all four cases, which means that nonlinearity is not significant for the initial response. The most important thing about Figure 5 is the apparent delay of about 3 min in the response from reflux L to bottom composition x_B (bottom left). This is because it takes some time (about 3 min in this case) for a change in reflux L to reach the bottom of the column. This means a change in reflux L initially only affects the top composition x_B, so the initial response is one-way decoupled and therefore not ill-conditioned in terms of the "initial" RGA, and this is the reason why we were able in Figure 3 to achieve good control of both product compositions (x_D and x_B) independently. In Figure 3, the closed-loop time constant was selected to be about 5 min, which is a bit large compared to the 3 min decoupling, and the resulting interactions between the top and the bottom loops is the reason why x_D moves a bit slowly towards the steady state of 0.995 in Figure 3. The spike in x_B is unavoidable with two PI controllers, but could be reduced using decoupling or multivariable control (e.g., MPC).

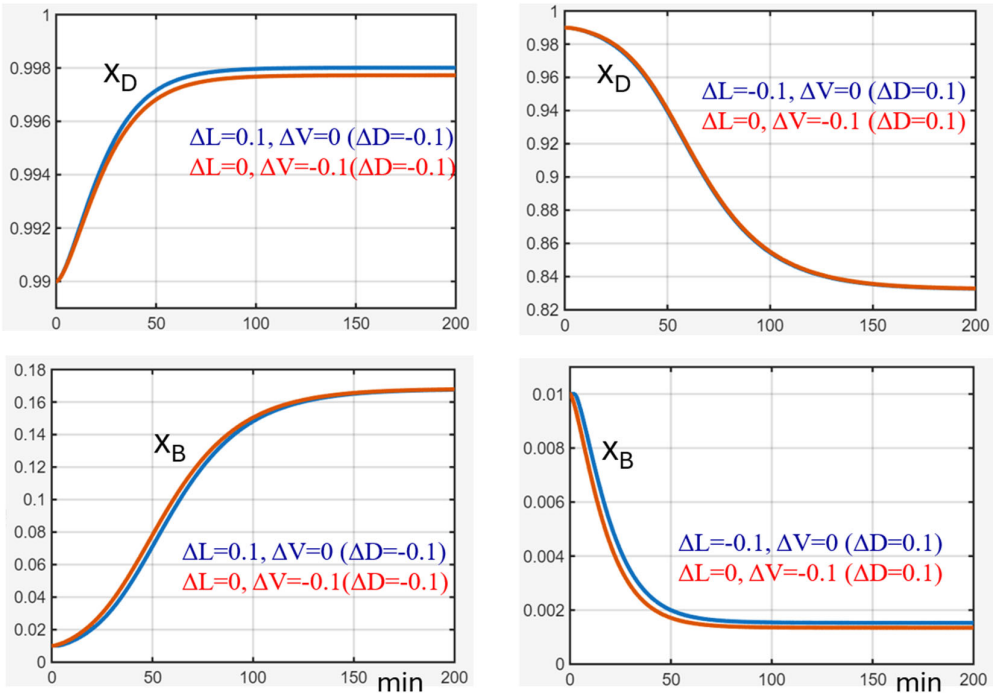

Figure 4. Effect of individual changes in L and V (which change the flow split D/F).

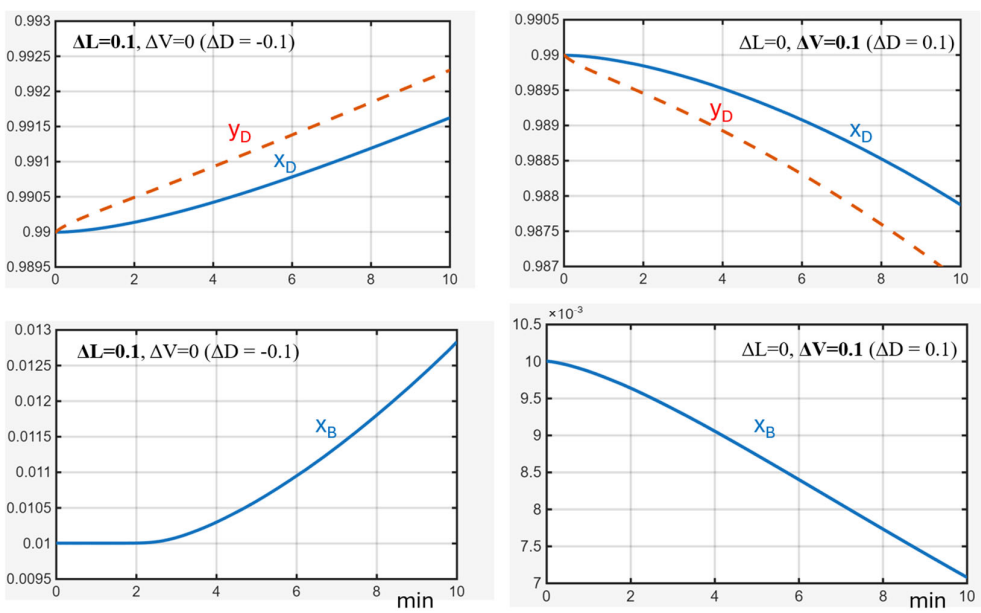

Figure 5. Initial response for some of the step changes in L and V in Figure 4.

Another thing to note about Figure 5 is that there is an effective delay for the top composition x_D, as it does not start changing immediately following a step in L. The reason is twofold. First, for a total condenser there is no immediate effect of a change in L because the inflow and outflow have the same composition at stead state (y_D=x_D). Second, this effect is made more significant because the condenser holdup (M_D/F =10 min) is large compared to the holdup on each stage (M_i/F=0.5 min). Thus, from a control point of view, it is better to measure and control the overhead composition y_D (red line) (or a temperature inside the column) as we did in the simulations in Figures 2 and 3.

4. Setting the product split – temperature control

A conventional continuous distillation column (Figure 1) with 2 products (and given throughput F and pressure), has 2 steady-state degrees of freedom, which be chosen as the product split and the energy input or internal reflux. Of these two, the product split is by far the most important to set correctly. A main difference between feedforward and feedback thinking comes in how to set the product split during operation. Feedforward thinkers aim at setting flows accurately, while feedback thinkers aim at adjusting the flows to keep compositions or temperatures (which are measured dependent variables) constant. In general, we have the following rules:

Rule 1: For each "column" that separates between two products (one light and one heavy), we need to set one product split
Rule 2. From an operation point of view, the product split is usually most easily set by fixing (controlling) one sensitive temperature in each "column".

For example, a conventional continuous column (Figure 1) with feed F and products D and B, has one product split that needs to be set (say D/F; which sets B/F=1-D/F). In Figure 1, a temperature in the top section is controlled using the reflux L, but if there is no sensitive temperature in the top section of if the bottom purity is more important to control tightly, then one may instead control a temperature in the bottom section using the boilup V. Of course, if we have fast composition measurements then this is even better than temperatures, but fast composition measurements are not available for most applications. In any case, composition measurements may be used in a cascade manner to update the setpoints of temperature controllers (TC). It is usually important that the temperature control loop is fast to provide fast adjustment of the split in response to flowrate disturbances (e.g. in feedrate or boilup). To have high sensitivity (gain) for control, the temperature measurements need to be located a little away from the products, especially for high-purity products.

A complex Petlyuk arrangement with three products (Figure 6), contains 3 two-product separation "columns" (prefractionator and upper and lower part of main column) and one needs to set 3 splits, which is most easily done by controlling 3 temperatures as shown in Figure 6.

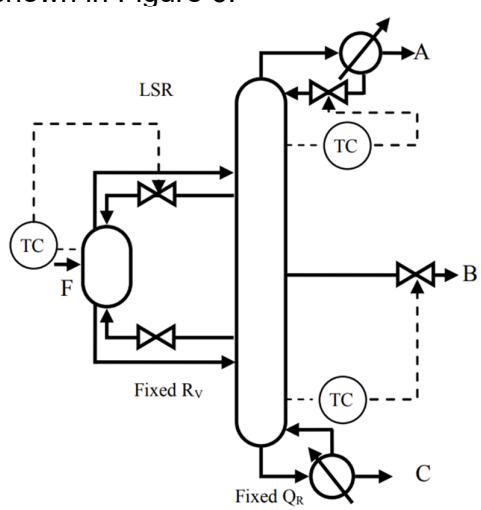

A Petlyuk column is thermodynamically equivalent to a dividing-wall column. The vapor split R_V is assumed fixed. The heat input Q_R (which sets the boilup V) may be set in ratio to the feed F and the ratio may be changed on a slow time scale to satisfy specifications on product composition. The temperature setpoint in the prefractionator should be set to minimize the required heat input.

Figure 6. Temperature control of Petlyuk arrangement with 3 sub-columns (Qian et al, 2016).

Closed operation of batch columns (Figure 7) offers a compelling case for the effectiveness of setting the correct product split using temperature control. In particular, it demonstrates that *temperature control provides indirect level control,* because the holdups in the vessels move towards a steady state determined by the feed charge composition, in spite of having no level controllers (Wittgens and Skogestad, 2000). With the temperature sensor located in the middle of each column section, the setpoints for the temperature may as a starting point be set as the average between the boiling points for the component being separated in this section. In conclusion, the main reason for using temperature feedback is that it is very difficult to set flows very accurately. In addition, temperatures are better (although not perfect) in terms of handling unmeasured feed composition disturbances.

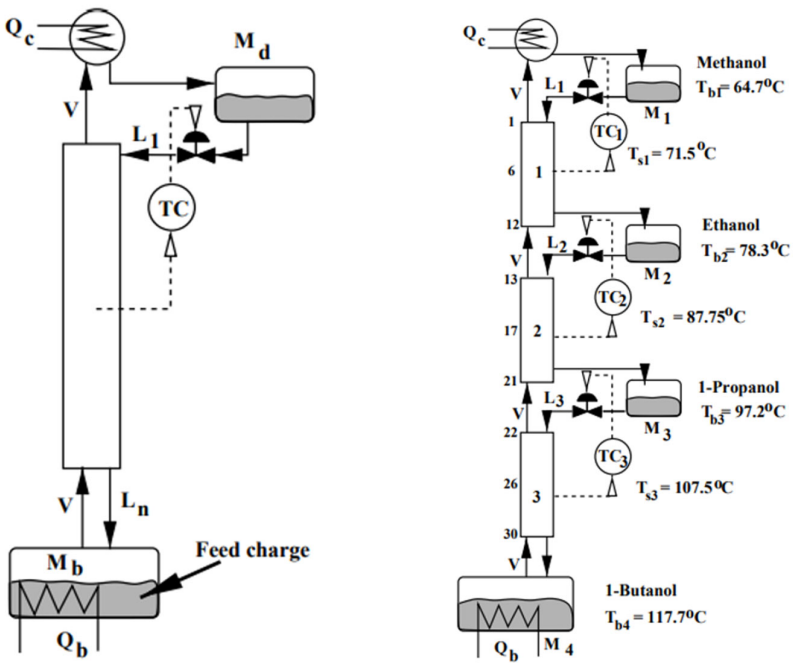

Figure 7. Temperature control of closed batch distillation columns with two (left) and four (right) products (Wittgens and Skogestad, 2000). The heat input Q_b (which sets the boilup V) is usually set at the maximum allowed value to minimize the batch time.

References

1. Qian, Xing; Jia, Shengkun; Skogestad, Sigurd; Yuan, Xigang. “Comparison of stabilizing control structures for dividing wall columns”. IFAC-PapersOnLine Volum3 49.(7) s. 729-734 (2016)
2. S. Skogestad, “Dynamics and control of distillation columns – a critical survey”. MIC Journal, **18,** 3, 177-217.(1997). DOI: 10.4173/mic.1997.3.1
3. B. Wittgens and S. Skogestad, «Closed operation of multivessel batch distillation: Experimental verification”, *AIChE J.*, **46**, 1209-1217 (2000).

Thermally Coupled Distillation: Why We Have Hit a Wall and How to Move Past It?

Anton A. Kiss[1], Harry Kooijman[2], Rakesh Agrawal[3], Thomas Grützner[4], Ross Taylor[2], Žarko Olujić[5], Igor Dejanović[6]
[1]Delft University of Technology, Delft, Netherlands;
[2]Clarkson University, Potsdam, NY, USA;
[3]Davidson School of Chemical Engineering, Purdue University, West Lafayette, USA
[4]Ulm University, Ulm, Germany;
[5]Retired, Makarska, Croatia;
[6]University of Zagreb, Faculty of Chemical Engineering and Technology, Zagreb, Croatia;

Abstract

Thermally coupled distillation (TCD) configurations for four or more products remain rarely implemented industrially, despite their clear and significant benefits. They can reduce energy use, capital expenditure, and emissions in multi-product separations. Though single-wall, three-product dividing wall columns (DWC) are now well established, growth in the number of multi-wall, four-product systems has stalled due to perceived operability risks, control concerns, and organizational barriers.

This perspective paper combines industrial and academic insights to bridge this gap, offering three contributions:

1. A structured overview of adoption barriers, distinguishing solved issues (e.g. thermodynamics) from persistent industrial challenges like vapor split sensitivity and commissioning risks.
2. A classification of lower-risk TCD pathways, linking energy benefits to complexity: a) liquid-only transfer (LOT) revamps of direct column sequences operating at independent pressures yielding up to 20% savings with no risk, b) transformer DWCs (with up to 30% energy savings) enabling fallback to conventional mode, c) Kaibel four-product DWCs with minimal additional complexity offering up to 40% savings.
3. A pragmatic roadmap prioritizing revamps, fallback designs, standardized screening workflows, and education to align the risk perception with thermodynamic gains.

With this perspective, the process industry can retrofit existing column line-ups and accelerate the sustainability of its distillation operations.

Keywords

TCD, DWC, LOT revamp, transformer column, process intensification

1. Introduction

Thermally coupled distillation, including dividing wall columns, can cut energy use by 20-30% in three-product separations and offers even greater potential for multi-product systems. Single-wall three-product DWCs are now the industrial standard, yet advanced configurations (such as multi-wall four-product DWCs) see limited use despite thermodynamic advantages approaching 40% savings (Kaibel, 1987). This discrepancy between potential and very limited industrial implementation suggests that the remaining barriers are no longer purely technical in nature.

This mismatch stems from non-technical barriers: operability risks (e.g. vapor split sensitivity), control uncertainty, commissioning challenges, and organizational misalignments where engineers bear the risks, but management reaps the benefits. To explore this issue, a round-table discussion was held during the Expert Symposium on Thermally Coupled Distillation in Ulm in October 2025, bringing together academic researchers, technology vendors, and industrial practitioners.
This perspective paper combines symposium insights with industrial and academic experience to explain why adoption of advanced TCD configurations has “hit a wall” and how this situation can be resolved. Key contributions include:

- Structured barriers distinguishing research from practice – see **Table 1**.
- Low-risk pathways trading energy gains for simplicity, e.g. LOT revamps, transformer columns (fallback flexibility), Kaibel DWCs (high efficiency, medium risk) – see **Table 2**.
- A roadmap emphasizing revamps, screening workflows, and education.

By prioritizing configurations that preserve conventional fallbacks and limit vapor complexities, we bridge thermodynamic promise to routine practice.

2. Low-risk pathways for industrial TCD implementation

The limited industrial uptake of advanced thermally coupled distillation (TCD) configurations does not indicate a lack of viable technical solutions. It instead reflects a persistent perception of industrial risk. In this context, configurations that preserve familiar equipment, limit operational uncertainty, and provide fallback options are generally favored over designs that pursue maximum theoretical efficiency (at the expense of robustness or flexibility).
Based on the barriers identified at the expert symposium, the key technical, organizational, and operational obstacles to wider industrial adoption of advanced TCD configurations are summarized in **Table 1**. These barriers help explain why many advanced concepts, although well understood, are often ruled out early in a project (as implementation of such is considered to carry too much risk).
Building on this barrier analysis, **Table 2** provides a comparison of achievable energy benefits and process complexity for selected lower-risk TCD pathways. The comparison is intended as a qualitative guide and reflects typical industrial perceptions rather than idealized performance.
The following sections briefly discuss three representative approaches: revamps based on liquid-only transfer (LOT) between existing columns (Figure 1), transformer columns (that allow switching between conventional and thermally coupled operation), and simplified four-product DWC concepts (that avoid the most complicated multi-wall arrangements). The discussion focuses on practical considerations relevant to early-stage screening and technology selection.

2.1 Liquid-Only Transfer

LOT sequences move only liquids between columns via pumps or gravity, avoiding vapor transfer internals that complicate control and commissioning. This yields stable pressure dynamics and easy retrofits on existing equipment, delivering up to 20% energy savings compared with conventional setups. Operational advantages include simplified startup, reduced maintenance, and compatibility with heat pumps. Rerouting of liquid draws adds controlled flows between shells. LOT is the pragmatic first step towards TCD for legacy sites: control systems in place can be maintained and there is little to no project risk. It can also be commissioned with minimal disruption.

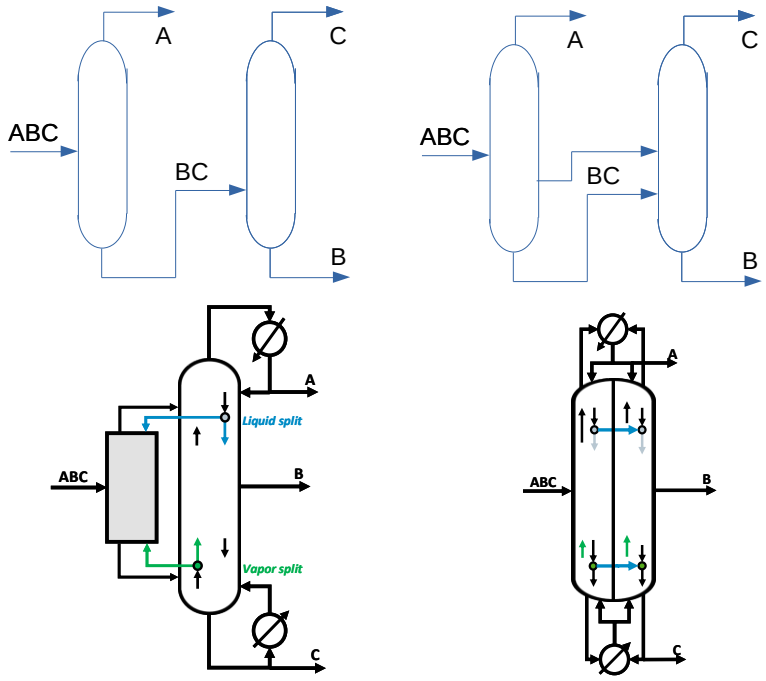

Figure 1. Left: direct (top) and Petlyuk configuration (bottom); Right: LOT implementations

2.2 Transformer Columns

Transformer columns feature multiple feed and draw points, enabling operation of a column with a wall to function both in a conventional, as well as in a thermally coupled mode. This dual-mode flexibility provides a low-risk entry to the energy gains available from TCD. Preserving a fallback to normal column operation can be key for first-of-a-kind projects. Benefits include adaptability to feed variations, market shifts via flow reconfiguration, and multi-product manufacturing. For distillation tollers, transformer columns can provide flexibility between high volume production and performing two separations simultaneously, using a single column shell (eliminating time required for cleaning or product losses from multiple inventories).

2.3 Single wall four-products DWCs

Multi-wall DWCs complicate design, control, and commissioning. Kaibel columns (Kaibel, 1987) offer a simpler alternative to obtain a four-cut split by using a single, off-center wall. Up to 40% energy savings can be obtained (Olujić et al., 2009). By employing tuned free area in the collectors/chimney trays (Dejanović et al., 2014, Kang et al., 2017), along with packings with different pressure drops, Kaibel columns have proven suitable for large-scale applications.

2.4 Revamping three column sequences into fully thermally coupled equivalent of a multi-wall DWC configuration

Retrofitting existing three-column sequences into thermally coupled arrangements mimicking two-partition-wall DWCs by connecting single-wall DWC shells in series (Jansen et al., 2014, 2016) avoids three parallel vapor sections and related vapor split uncertainties. This eliminates dual vapor distribution challenges, yielding full thermal coupling benefits (Christiansen et al., 1997).

Execution during maintenance shutdowns: convert columns to single-wall DWCs, add vapor/liquid transfer lines and nozzles; use pumps for liquids, pressure differentials for vapors. Upgrade controls accordingly. Welding is minimal with non-welded walls; perform shell integrity checks pre-commissioning.

Table 1: Core barriers and mitigation pathways for advanced TCD/DWC adoption

Barrier	Why it blocks adoption (industrial view)	Status	Potential solutions / mitigation pathways
Risk–reward mismatch	Engineers and operations teams bear most start-up and reliability risks, while management captures most of the benefits. This leads to conservative choices.	Persistent	Link savings to CO_2/KPI targets and compliance; Stage adoption via low-risk revamps; Define fallback capability (LOT and Transformer columns).
Stakeholder misalignment	Process/ops/control priorities diverge; unfamiliar options get dropped early.	Persistent	Early cross-discipline reviews; Define roles and clear “go/no-go” decision gates; Involve ops/control at concept stage.
Lack of fast, standardized screening workflows	Without simple screening, TCD/DWC is not shortlisted.	Persistent	Provide a transparent screening workflow and a decision tree; Simple KPI-based ranking before detailed simulation.
Not a standard design	Not part of standard design packages or handbooks; persistent misconceptions amplify perceived risk.	Persistent	White paper and standard checklists; Clarify what is proven vs emerging; Make “consider DWC/LOT/Kaibel” routine.
Control complexity / unclear control structure (LOT and transformer modes)	The control structure is often not defined clearly (manipulated variable assignment, inventory control, disturbance handling), increasing the risk of loop interactions	Persistent in industry	Add concise control and operability guidance: loop pairing, inventory strategy, key constraints, and measurements.
Sensitivity to feed variability	Concerns about robustness under disturbances/variable feeds.	Partly solved; persistent	Prefer low-risk configurations (LOT, single-wall/Kaibel); Avoid 3-parallel-channel sections using multi-shell revamps; Define operating envelope.
Constructability and commissioning risk	Nonstandard internals increase schedule uncertainty and troubleshooting burden.	Persistent	Prefer simplified designs; constructability checklist; early vendor engagement; standardized commissioning procedures and diagnostics.
Capability & knowledge-transfer gap	Limited internal experience; lessons learned not shared widely	Persistent	Education modules and short courses; Publish benchmark examples; Maintain periodic community meetings and shared guidance documents.

Table 2: Indicative trade-off between energy benefit and implementation complexity for “low-risk” TCD pathways

Configuration category	Typical application	Indicative energy benefit vs conventional sequence*	Mechanical complexity	Control/ operation complexity	Revamp suitability	Key “industrial hesitation” points	Risk-reduction / mitigation strategies
Baseline: conventional sequence (no coupling)	Any	Reference case	Low	Low	Existing	High energy use; larger footprint	N/A
Single-wall 3-product DWC (well-established)	New build and some revamps	Commonly reported significant savings; often cited around 20–30%	Medium	Medium	Medium	Split sensitivity; commissioning learning curve	Proven internals; vendor experience; clear control structure; operator training
LOT revamp (liquid-only transfer between shells)	Revamp of existing sequences	Moderate to high savings; generally below full vapor-coupled TCD, but often “good enough” for revamps*	Low / Medium	Medium	High	Pump-around/inventory issues; “where do I control what?”	Explicit inventory control scheme; minimum instrumentation list; staged commissioning plan
Distributed coupling avoiding 3 parallel channels (revamp rearrangement of shells / piping)	Revamps where multi-wall DWC is desired but parallel channels are avoided	Moderate to high, case-dependent*	Medium	Medium / High	Medium / High	Integration complexity; interconnecting piping; pressure balance	Site-specific pressure management; robust operability review; clear fallback procedure
Transformer column (mode-switchable: conventional ↔ coupled)	New build (and some revamps) where fallback is valued	Moderate to high in coupled mode; lower in conventional mode; value is flexibility/risk reduction*	Medium	Medium / High	Medium	“Mode switching” concerns; instrumentation + procedures	Define mode-switch logic, permissives, transition steps; operator training; start in conventional mode
Kaibel (single-wall 4-product DWC)	4-product separations seeking simplicity	High (close to advanced coupling); sacrifices some optimum vs multi-wall*	Medium / High	High	Low / Medium	Split robustness; product interaction; tuning effort	Conservative design margins; defined operating envelope; vendor know-how
Multi-wall 4-product DWC (2 or 3 walls, parallel sections)	4-product separations targeting near-maximum thermodynamic efficiency	Potentially highest, but highly case-specific*	High	High	Low	Vapor split robustness, commissioning risk, uncertain troubleshooting burden	

3. The Path Forward: Education and Design Workflow

To unlock the full potential of advanced TCD configurations, coordinated action is needed across both technical and organizational domains. The key challenge remains risk aversion, rather than tool availability. While academic literature and industrial applications have demonstrated large benefits, practical expertise in management is lagging. To accelerate advanced TCD adoption, focus should be placed on:

- *Education and training*. Update curricula with hands-on TCD modeling, pilot modules, and control design for LOT, three-cut DWC and four-cut Kaibel columns, and consider transformer designs. Industry-academia programs should embed revamp cases and troubleshooting exercises. Professional societies (AIChE, IChemE) to offer TCD workshops and webinars, emphasizing benefits and operability.
- *Design workflows*. Standardized early screening: transparent decision trees to rank TCD options by KPIs (energy savings vs. risk) before detailed simulation. Integrate rigorous tools like ChemSep (CAPE-OPEN compatible) into familiar environments.
- *Control and operability*. Allow early control engineer involvement with operability reviews on loop pairings, inventory strategies, disturbance envelopes, response times, and contingencies. Specify fallback modes (e.g., transformer start-up).
- *Organizational incentives*. Link cost savings to CO2 KPIs and compliance for management buy-in. Share pilot results (e.g. BASF Kaibel columns, Benit M splitters) via white papers and checklists. Appoint TCD champions and conduct cross-discipline reviews with clear go/no-go gates.

4. Conclusion

Although TCD technologies offer compelling advantages in energy, capital, and sustainability metrics, industrial implementation of advanced multi-wall and flexible designs remains limited. Progress requires a focus on low-risk revamp opportunities, workflow standardization, and sustained investment in education and control strategies. By disseminating practical case studies, developing accessible design tools, and promoting collaborative learning, engineers and managers alike can gain confidence in new configurations, moving Thermally Coupled Distillation from specialized pilot projects toward robust, widespread adoption.

References

Kaibel,G.,Chem.Eng.Technol. 10(1), (1987), 92–98.
Olujić,Ž., Jödecke,M., Shilkin,A., Schuch,G., Kaibel,B., Chem.Eng.Process. 48,(2009), 1089–1104.
Dejanović,I., Halvorsen,I.J., Skogestad,S., Jansen,H., Olujić,Ž., Chem.Eng.Process. 84,(2014), 71–81.
Kang, K. J., Harvianto, G. R., Lee, M., Ind. Eng. Chem. Res. 56, (2017), 6493–6498.
Christiansen, A. C., Skogestad, S., Lien, K., Comput. Chem. Eng. 21(Suppl.), (1997), S237–S242.
Jansen, H., Dejanović, I., Kaibel, B., Olujić, Ž., Chem. Eng. 121(8), (2014), 40–48.
Jansen, H., Dejanović, I., Rietfort, T., Olujić, Ž., Chem. Ing. Tech. 88(1–2), (2016), 200–207.

Experimental Assessment of Orifice Plates and Gravity Splitters for Internal Liquid Splitting in a DWC

Anand Vennavelli[1], Izak Nieuwoudt[2]
[1]Koch-Glitsch, Wichita, USA;
[2]Fractionation Research, Inc., Stillwater, USA;

Abstract
Internal liquid splitting is required when introducing feed streams into columns that cannot accommodate external splitting hardware[1]. In Dividing Wall Columns (DWC), achieving the correct liquid split is essential because deviations shift liquid-to-vapor (L/V) ratios on either side of the wall, altering pressure drop, hydraulics, and separation performance. This work evaluates internal liquid splitters for a trayed DWC feed system designed for a 2:1 split. Water testing was performed under realistic piping constraints, including sharp elbows and tight directional changes.

Restriction orifices were first assessed. Initial designs did not deliver the target ratio. Reducing orifice sizes increased pressure drop but still did not achieve the split. Visual checks and in-line pressure gauges both confirmed a strong swirl in the larger branch. Several flow-straightening and orifice size adjustments were implemented; however, maldistribution persisted. Testing indicated that momentum effects generated by upstream piping primarily influenced orifice performance, thereby limiting the effectiveness of pressure-drop-based splitting control.

To address these limitations, a compact gravity splitter was designed and fabricated. Its two-stage arrangement dissipates incoming momentum in the first stage, and the second stage uses multistage orifices to set the split ratio. Experimental results showed that the gravity splitter consistently delivered the intended 2:1 split across the tested flow range, even under the same piping constraints. Videos and measurements documented stable hydraulic behavior and confirmed that the device removed swirl-driven bias present in the orifice tests.

The study demonstrates that restriction orifices can perform sub-optimally under realistic industrial layouts, whereas gravity-based devices provide a robust and accurate internal liquid-splitting solution.

Keywords
Dividing Wall Column (DWC), Restriction Orifices, Gravity Splitter, Flow Maldistribution, Hydraulic Performance

1. Introduction

Liquid streams entering a distillation column often must be divided between two internal flow paths, and the effectiveness of this division depends strongly on the hydraulic conditions created by the surrounding piping and internal geometry. In systems that incorporate parting boxes or a dividing wall, the feed location and the manner in which the liquid is introduced can influence how the column operates. These installations may limit the available space for external hardware, requiring the liquid to be split inside the tower rather than upstream in the piping system. Such constraints define the practical boundaries for designing equipment intended to deliver a specific internal distribution.

Distillation towers that employ a dividing wall place additional demands on the feed arrangement. The wall divides the column into parallel sections, and the incoming liquid must be sent to each side in a predetermined proportion. Although external splitters are capable of metering and controlling such flows, many column layouts cannot accommodate them. When this occurs, internal devices must be relied upon to divide the flow while operating under the hydraulic disturbances created by elbows, short inlet runs, and downpipes.

Internal splitters typically function either by forcing a pressure drop across restriction orifices or by using gravity to neutralize the influence of incoming momentum before directing the liquid to the required branches. Each approach responds differently to asymmetry in the piping and to localized variations in flow structure. These sensitivities make it necessary to examine how real-world layouts influence performance rather than assuming ideal feed conditions.

The present study focuses on an internal liquid division required for the feed to a trayed system with a dividing wall, where a 2:1 split is specified. The device needed to accommodate a broad operating range for the DWC research test carried out jointly by Koch-Glitsch and Fractionation Research, Inc. (FRI). The arrangement includes tight elbows and limited straight-run lengths, which introduce swirl and momentum effects that can influence how the flow divides. Water testing was used to evaluate how restriction orifices behave under these constraints and to determine whether an alternative gravity-based design can provide consistent performance when installed in the same geometry.

Restriction orifices are simpler and less expensive to fabricate, and they can often be installed within the available space without major modifications to the column feed arrangement. Given the broad operating envelope and the practical considerations of cost and installation complexity, a restriction-orifice approach was chosen as the first method to evaluate. The intent was to confirm that an orifice-based device could achieve the required split before pursuing alternative configurations. To verify this, the orifices were tested in the Koch-Glitsch test facility in Wichita, Kansas, using the same geometric constraints as the planned tower installation

2. Results and discussion

2.1 Measurement Method

For each water flow test, the system was first allowed to stabilize at the desired operating rate. Once steady conditions were reached, the liquid from each branch was collected in a container of known volume, and the time required to fill the container was measured using a stopwatch. Depending on the flow rate, the collection time varied from approximately 30 seconds to more than 2 minutes. The total system flow was verified independently using a mag flow meter. The split ratio was then calculated as the ratio of the measured filling times for the container, allowing direct comparison of the relative branch flows under each test condition.

2.2 Restriction Orifice Performance

The first set of restriction orifices was selected to generate adequate pressure drop while remaining within the available pump head. The initial diameters—43.18 mm on the large branch and 30.48 mm on the small branch—provided an area ratio of 2.0. Despite this sizing, the measured split remained below 1.7 at the lower flow rates and only reached 1.9 at the higher rates far from the intended value of 2.0, as shown in Figure 1. In these tests simplified downpipes were employed downstream of the orifices.

Due to concerns regarding insufficient pressure drop, the orifice sizes were adjusted to 26.75 mm and 19.2 mm. The larger branch orifice remained marginally oversized to enhance flow on that side. Although this modification resulted in improved flow distribution, the split did not conform to the specified target, as shown once more in Figure 1.

The assembly was then modified to reflect the tower installation by adding the corresponding downpipes and elbows. This modification additionally influenced the split ratio and resulted in varying levels of flow instability at intermediate rates. Visual observations identified significant swirl on the large-side branch as flow rates increased. A flow straightener was installed upstream of the orifice to reduce momentum effects from the elbow. Swirl remained visible even with the straightener, as depicted in Figure 2, and the performance did not improve, as shown in Figure 1.

Additional trials increased the large-branch orifice diameter to 27.1 mm, then 27.4 mm, and finally 27.9 mm. These increases did not improve the split ratio. In some cases, the ratio declined slightly. Flow instability persisted, demonstrating that restriction orifices could not achieve the desired distribution under the given piping arrangement. These results are summarized in Figure 3.

2.3 Gravity Splitter Performance

A compact multilevel gravity splitter was then designed and installed, as shown in Figure 4. The splitter delivered a stable split near the target value of 2.0 across the full operating range. Flow behavior was steady, swirl was eliminated, and the distribution matched the design intent. The results in Figure 5 confirm that the gravity splitter achieved the required flow split under the same piping constraints

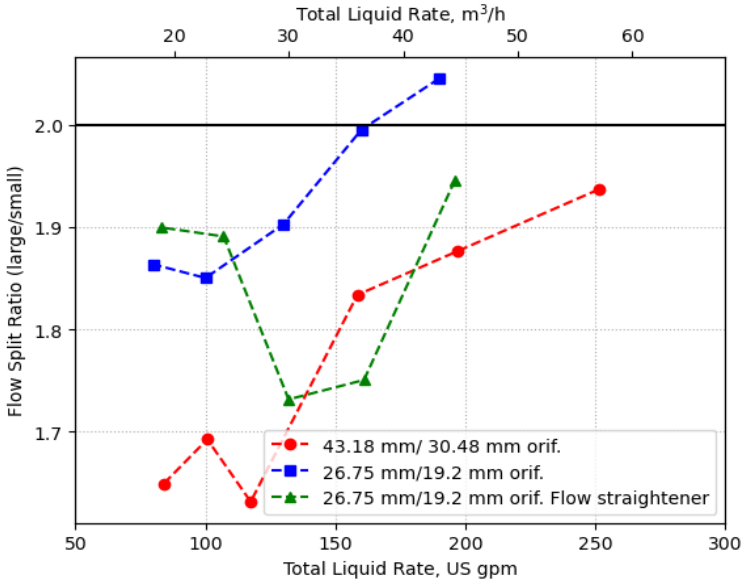

Figure 1: Effect of orifice size reduction and flow straightener on the flow split ratio. The desired split ratio was not achieved

Figure 2: Orifice plate setup with flow straightener. Swirl in the large-side flow is visible, and the required split ratio was not obtained.

.

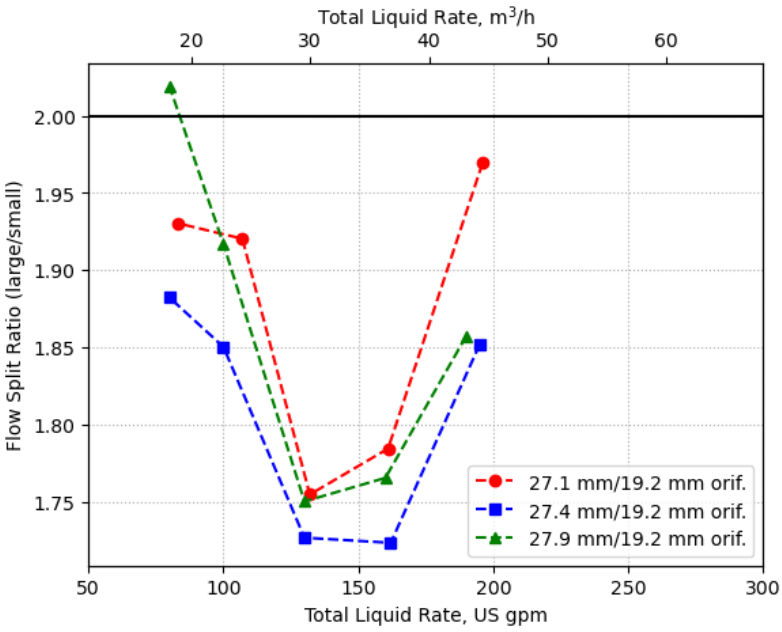

Figure 3: Further changes to the orifice sizes did not resolve the flow swirl or achieve the desired flow split ratio.

Figure 4: A compact multilevel gravity splitter with a simplified elbow. Flow was steady, and the desired split ratio was achieved with this design.

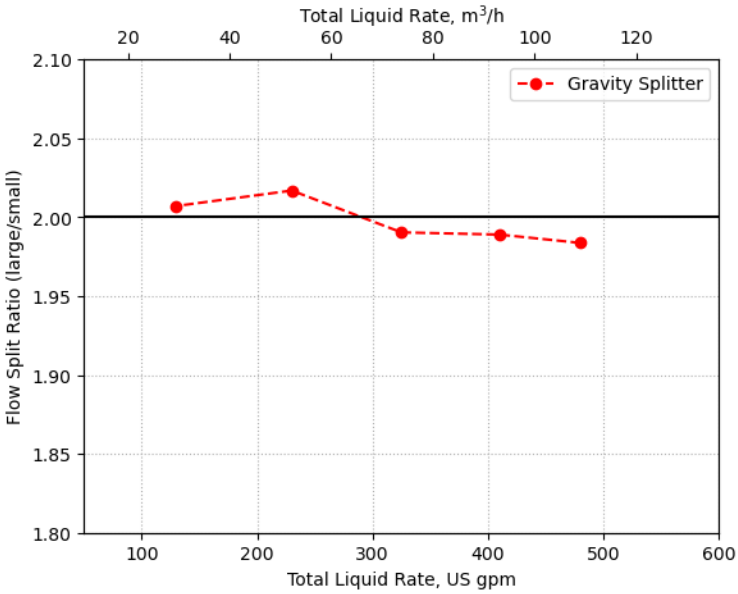

Figure 5: Achieved flow split ratio across the operating range with the gravity splitter, showing performance near the target value of 2.0.

3. Conclusions

The testing demonstrated that restriction orifices did not produce the required 2:1 liquid split when installed under the piping constraints of the system. Adjustments to orifice size, the addition of a flow straightener, and multiple configuration changes did not overcome the swirl and momentum effects introduced by the elbows and limited straight run. The resulting split ratios remained inconsistent, and flow instability persisted across the operating range. In contrast, the compact multilevel gravity splitter achieved stable and accurate distribution under the same geometric conditions and delivered the intended split throughout testing. These results show that, for this configuration, the gravity-based design provided the reliable liquid split that the restriction-orifice approach could not achieve.

The broader implications of this work extend to any internal liquid-splitting arrangement installed under constrained piping geometry. The testing, under actual flow conditions and geometric layout, showed that swirl and momentum effects created by elbows and limited straight runs can dominate the behavior of pressure-drop-based devices, even when the orifices are sized to the intended split ratio. The success of the compact gravity-based splitter in the same configuration demonstrates that designs which neutralize inlet momentum can provide more reliable performance when space and layout impose restrictions that pressure-driven devices cannot overcome.

Acknowledgements

The authors thank Koch-Glitsch for providing access to the Wichita test facility and supporting the experimental work. Koch-Glitsch's experience with commercial column internals and test facilities was important in defining realistic test conditions for this study. The collaboration and technical contributions from FRI, who has a long history of evaluating distillation equipment, are also appreciated.

References

Montz GmbH. Reflux Splitters – Functional Elements for Rectifying Columns. Hilden, Germany. Available at: https://www.montz.de/en-gb/newpage2 (accessed 2026).

Challenging the Norm: Dividing Wall Columns without Substantial Middle-Boilers in the Feed

Yang, Quan1, Lee, Ming Yang1, Agrawal, Gaura2, Kek, WanSeang3, Wang, Zongliang3,
[1]Sulzer Chemtech, Singapore, Singapore
[2]Sulzer Chemtech, Houston, America
[3]Sulzer Chemtech, Shanghai, China

Abstract
Dividing Wall Columns (DWCs) represent a powerful process intensification technology for distillation, delivering significant reductions in capital and operating costs. Despite these proven benefits, DWC adoption is often constrained by an empirical screening criterion published two decades ago (Schultz et al., 2002). This simple but restrictive rule suggests that DWCs with a middle dividing wall are only suitable when the middle-boilers constitute a substantial portion, preferably 60–70 mol%, of the feed.
This paper presents four industrial case studies that invalidate this longstanding requirement for a high concentration of middle-boilers. The consistent and substantial energy savings (ranging from 20 to 35 %) across diverse industrial applications, even when middle-boiler concentrations are as low as 8.3 mol%, demonstrates that the potential for DWC implementation is broader than previously assumed.

Keywords
DWCs, screening criteria, middle-boiler, energy saving

1. Introduction

Distillation remains a cornerstone of the chemical, petrochemical, and refining industries. However, it is an energy-intensive separation process, often consuming more than 40% of a process plant's total energy budget. Consequently, the pursuit of enhanced energy efficiency in distillation has become critical, driven by economic pressures and the global necessity to reduce CO_2 emissions.
DWCs are an important process intensification technique to address this challenge. The DWC, a single column shell that consists of a pre-fractionator section and a main fractionator section across a physical wall, potentially offers substantial thermodynamic advantages by reducing remixing of middle-boilers.
Over the past two decades, research into DWC technology has matured significantly, shifting focus from foundational concepts to advanced topics such as rigorous process simulation, sophisticated control strategies, and optimization of mass transfer equipment and column internals. This maturity has fueled the rapid industrial adoption of DWCs.
Despite the proven advantages and rising adoption, DWCs are not a one-size-fits-all solution. For instance, technical constraints, such as the DWC column head pressure and the resulting temperature profiles and heat transfer medium requirements, can limit its applicability. Furthermore, the significant effort involved in a formal feasibility study is typically only justified if the potential energy savings exceed a 10% threshold.

Crucially, the process design of a DWC remains more trial-and-error than a systematic design process, and the DWC model is not readily available in commercial flowsheet software (e.g., Aspen and Pro/II). In addition, the lack of readily implementable, reliable screening criteria is another major impediment to wider adoption. The only complete set of empirical screening criteria was published two decades ago by Schultz et al. (2002). The most easily implemented criterion in the review paper is the composition rule, which states that the middle-boilers must exist in a substantial amount (60-70 mol%) in the feed, with light and heavy boilers equally distributed. Due to the lack of alternative screening criteria, this composition rule has been widely cited as the de facto standard (Lorenza, et al., 2018; Patidar and Gupta, 2018).

As a result of the above limitations, DWCs are often only applied in experienced applications, such as the separation of benzene, toluene and xylenes (BTX), the separation of a naphtha stream into multiple products, and various separation tasks of paraffins, olefins and aromatics.

This work challenges this two-decade-old composition rule. Four distinct industrial case studies are presented where the feed composition falls significantly outside this established range. The results demonstrate that the concentration of the middle-boilers in the feed is not associated with DWC energy savings, proving the composition rule unduly stringent and partially responsible for overlooking substantial energy-saving opportunities across industries.

2. DWC Design Methodology

To establish a basis for comparison, the conventional two-column separation sequence (Figure 1a) was first evaluated. It serves as the benchmark against which the performance of a DWC with a middle dividing wall is measured. It should be noted that the direct separation sequence is appropriate for all case studies discussed in this paper. The usual rigorous sensitivity studies were conducted, encompassing the optimization of the Number of Theoretical Stages (NTS) against the required column duties, as well as determining the optimal feed location separately for each column.

The DWC configuration was simulated utilizing the Sulzer in-house process simulation method (Sulzer E10935 en 8.2025, 2025), which was established upon the concept of Modular Fusion.

This methodology stands in contrast to the widely adopted V_{min} method (Halvorsen and Skogestad, 2003; Dejanović et al., 2011; Schulz, 2024). The V_{min} approach is fundamentally a shortcut technique requiring extensive trial-and-error optimization during the rigorous simulation stage. This iterative process is particularly challenging when simultaneous optimization is required for the typically tripled number of design variables in a DWC (e.g., NTS for six sections, vapor/liquid splitting ratios, and condenser and reboiler duties). Under the Modular Fusion Approach, the separation task for each DWC section (Figure 1b) is rigorously simulated in advance, where fewer variables need to be simultaneously optimized. These six pre-optimized sections are then fused into the final DWC model. This method eliminates the necessity for complex, large-scale trial-and-error optimization. This significantly reduces computational time and, critically, prevents the potential omission of the true optimal design.

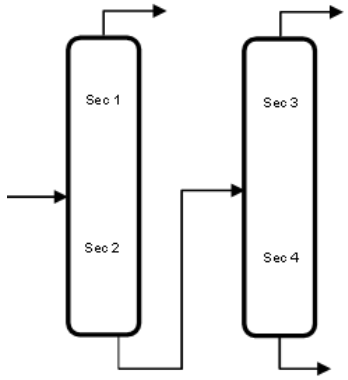

Figure 1a: Two columns in series (direct sequence).

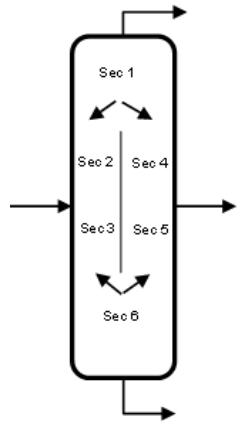

Figure 1b: DWC with a physical middle dividing wall.

It is also recognized that an alternative DWC design method widely exists in industry where the vapor splitting ratio (shown in Figure 1b, vapor to Sec. 3 / vapor from Sec. 6) is often fixed at 0.5. This approach slightly reduces optimization complexity at the cost of no longer treating the vapor splitting ratio as an optimization variable.

3. Case Studies

3.1 Case A: Naphtha Splitter

The first case study highlights performance improvements achieved by converting a conventional naphtha splitter into a middle-wall DWC in a refinery. The naphtha splitter columns split the straight-run naphtha cut into an iC_5 - rich top product, a normal paraffin-rich C_5 - C_6 middle product, and a C_{7+} bottom product. The conventional process utilizes a two-column sequence, with 70 and 46 NTS respectively, operating at a pressure of 3.0 bar(a). The normal paraffin-rich C_5 - C_6 middle boilers, which constitute 27.9 mol% of the naphtha feed (Table 1), are subsequently routed to an isomerization unit to enhance the octane number.

The DWC designed with 100 NTS at the same column head pressure delivers energy savings while improving the quality of the products.

3.2 Case B: C_9 Aromatic Splitter

The second case study deals with the separation of a heavy aromatic liquid stream, the bottom product from an aromatic complex plant's xylene tower within the xylene fractionation unit. This stream is a highly valuable feedstock for production of fine chemicals due to its rich C_9 compounds.

The standard industrial practice employs a four-column distillation train in series to achieve the necessary separations, which include:

- Cumene, Propyl-benzene (PRBENZEN) and lights
- ethyl-3-methylbenzene (M3EZ) and 1-ethyl-4-methylbenzene (M4EZ)
- 1,3,5-trimethylbenzene (135MBENZ) and 1-ethyl-2-methylbenzene
- 1,2,4-trimethylbenzene and heavies

The close boiling points of these isomers impose an extremely difficult separation task. Consequently, conventional columns are required to up to 182 NTS per column and are typically operated under a vacuum of 250 mbar (a).

DWCs offers multiple possibilities for process intensification in the complex separations. This paper focuses on one specific DWC option with NTS of 251 where the cut composed of M3EZ and M4EZ is withdrawn as the side product. The detailed feed composition for this case is provided in Table 1.

Table 1 The feed composition percentage in the four cases studied

	Rate	Light	Middle	Heavy	Representative components in the 3 respective boilers
	Kmol/h	mol %			
Case A	586.0	7.7	*27.9*	64.4	iPentane-，*normal* C_5 - C_6, C_7+
Case B	167.2	10.4	*27.2*	62.4	PRBENZEN-，*M3EZ & M4EZ*，135MBENZ+
Case C	18.0	1.2	*48.2*	50.6	IPM & Myristic acid-, *IPP*, Palmitic acid+
Case D	60.6	73.9	*8.3*	17.9	C_{12}–C_{14}-, C_{16}, C_{18}+

3.3 Case C: Isopropyl Palmitate Purification

This case study examines the purification of isopropyl palmitate (IPP), a high-value product for the cosmetic and pharmaceutical industries manufactured via Sulzer's reactive distillation process.

Traditionally, the stringent product specifications for IPP are achieved using a two-column distillation sequence: one column removes the lights including isopropyl myristate (IPM) and myristic acid, and the other column removes the heavies including palmitic acid and isopropyl stearate. The representative feed composition is given in Table 1.

With a DWC, myristic acid and other light components are removed via the distillate stream and a purge stream at the top of the column. Conversely, the heavies, including palmitic acid, are removed in the bottom stream, which contains up to 30% IPP and is recycled to the upstream reaction process. The main IPP product is withdrawn as a side stream, with the critical specification requiring the combined impurity level of isopropyl myristate and palmitic acid to be below 0.02 mol%.

The column is operated under 10 mbar (a), thus the temperature of process gas at the condenser is able to generate a low-pressure steam. Meanwhile the overall pressure drop across the DWC is set as 10 mbar to avoid thermal decomposition at the bottom. The NTS for the DWC is 89, while the two conventional columns feature 52 and 80 NTS respectively.

3.4 Case D: Palm Kernel Fatty Acid Purification

The final case study examines the purification of Palm Kernel Fatty Acid. Traditionally, crude mixtures are separated into high-purity fractions (>99%), such as C_8 - C_{10}, C_{12} - C_{14}, C_{16} and C_{18}, using a sequence of at least four columns. Various DWC configurations were previously published by Yang et al. (2020), and this study isolates two columns out of the four to demonstrate our findings. The representative components in the feed are given in Table 1.

A conventional two-column series requires approximately 45 NTS per column. In contrast, a DWC configuration achieves the same objectives with 60 NTS. Both setups operate under vacuum to prevent thermal decomposition. Unlike previous cases, the feed is primarily composed of light boilers (73.8%), while middle-boilers represent less than 9% of the total composition.

4 Results and Discussions

The comparative performances between the conventional two-column sequence and the optimized DWC configuration are summarized in Table 2. The reboiler duties are proportional to the feed flow rates, which can be found in Table 1.

Table 2: The reboiler duty (MWatt) for both options in the four cases.

		Case A	Case B	Case C	Case D
Conventional route	Column 1	5.0	11.7	0.7	1.3
	Column 2	5.2	9.7	1.1	1.1
	Total, combined	10.2	21.4	1.8	2.4
DWC route		6.6	16.4	1.4	1.9
Energy saving %		35.3	23.3	22.2	20.3

4.1 Energy Performance and the Composition Rule

The energy saving percentage is defined as the duty difference between the two options, expressed relative to the duty of the conventional configuration. Across all four industrial cases, the DWCs achieved substantial energy reductions ranging from 20.3 to 35.3%, despite that the concentration of middle-boilers in the feed were all below the 60% threshold.

Notably, Case A achieved the maximum energy savings of 35.3% with a concentration of middle-boilers of 27.9 mol%. In contrast, Case C, despite having the highest concentration of middle-boilers at 48.2 mol%, yielded only 22.2% in savings. Even with the lowest concentration (8.3 mol%), Case D maintained significant savings of 20.3%. it is also found that Case B showed 34% lower savings than Case A (23.3%), despite having a similar concentration of middle boilers in the feed. These results clearly demonstrate that feed composition alone is an unreliable criterion for determining DWC feasibility.

4.2 Optimization of Splitting Ratios

During the rigorous simulation phase, the liquid and vapor split ratios, defined as the fraction directed to the feed side of the wall relative to the total available flow, were identified as critical optimization variables. The optimized values extracted from the Modular Fusion Approach are presented in Table 3.

Table 3 liquid and vapor splitting ratios

	Case A	Case B	Case C	Case D
Liquid splitting ratio	0.27	0.73	0.51	0.48
Vapor splitting ratio	0.59	0.76	0.55	0.70

As shown in Table 3, the optimal vapor splitting ratios deviate significantly from the common industrial assumption of 0.5. These findings confirm that fixing the vapor splitting ratio at 0.5 during the design prevents the system from reaching its true, most energy-efficient design.

5. Conclusions

Through four diverse industrial case studies, this research demonstrates that the composition rule is overly restrictive and has likely caused many viable energy-saving opportunities to be overlooked. The investigations into the purification of fatty acids and isopropyl palmitate also demonstrate that the industrial applicability of DWC is significantly broader than established precedents such as BTX and naphtha splitting. Ultimately, the findings also highlight that traditional design methods, characterized by shortcut calculations followed by trial-and-error, provide no guarantee of reaching the optimal energy savings.

References

- Schultz M. A. et al., Reduce costs with dividing-wall columns, CEP, May 2002
- Patidar P. and Gupta A., Savings using divided wall columns, PTQ Q4 2018
- Lorenza H. et al., Divided Wall Columns: Usefulness and Challenges, Chemical Engineering Transactions 69, 2018
- Sulzer Brochure DWC 2025
- Halvorsen I. J. and Skogestad S., Minimum Energy Consumption in Multicomponent Distillation. 1. V_{min} Diagram for a Two-Product Column, Ind. Eng. Chem. Res., 42, 2003
- Dejanoviæ I. et al., An effective method for establishing the stage and reflux requirement of three-product dividing-wall columns, Chem. Bio chem. Eng. Q. 25 (2), 2011
- Schulz, R., Design and construction of dividing wall column distillation processes, EFCE, 2024
- Yang Q. et al., Dividing wall columns for fatty acids fractionation, Hydrocarbon Processing, 2020

Enhanced Process Monitoring of Pilot-scale and Industrial Distillation using Data-Driven Soft Sensors

Søren Villumsen[1], Jakob K. Huusom[1], Xiaodong Liang[1], Jens Abildskov[1]

[1]Department of Chemical Engineering, Technical University of Denmark, 228a Søltofts Plads, 2800 Kgs. Lyngby, Denmark

Abstract

Data-driven soft sensors enable reliable inference of critical quality parameters during distillation processes with uncertain process dynamics. This work introduces a methodology for developing simple yet effective data-driven soft sensors from sparse, noisy data. The methodology is demonstrated on a pilot-scale batch rectifier separating ethanol and water, as well as an industrial tar distillation plant, to estimate pitch softening temperature. The resulting soft sensors achieve test performances of $R^2 = 0.95$ in both cases, enabling real-time product quality estimation.

Keywords

Soft sensor, PLS, SVR, distillation, pilot scale, industrial scale

1. Introduction

Distillation processes rely on hardware instrumentation to create product of sufficiently high quality. However, many critical quality parameters, such as product purity or physical properties, cannot be measured using inline hardware sensors and require laboratory analysis. Between samples, product quality may drift, resulting in delayed corrective action and motivating the use of virtual sensing technologies—soft sensors—that estimate unmeasured variables from process data[1].

Many distillation systems exhibit complex behavior, stemming from equipment-specific behavior, drifting feed compositions, and changing operating conditions. As such, soft sensors based on ideal mechanistic models may not accurately describe the system. To better explain the system, historical process data can be correlated to sampled product quality, yielding data-driven soft sensors. Industrial deployment of these sensors remains challenging as real-world process data is often characterized by multi-rate sampling, outliers, and drift[1].

Given these constraints, pilot-scale systems serve as an ideal environment for developing robust soft sensors. They exhibit complex behavior and instrumentation and data limitations like those of full-scale plants, while still allowing controlled experimentation. This work uses a pilot-scale batch rectifier to demonstrate a generalizable methodology for selecting model inputs and validating soft sensor models by estimating distillate purity. The methodology is also applied to an industrial tar distillation column to estimate the pitch softening temperature, demonstrating its broader applicability. Special attention is drawn to the selection of model inputs, the incorporation of process knowledge, and the choice of model complexity appropriate for the available data.

2. Methodology for Pilot-scale Batch Rectifier

2.1 Pilot-Scale Batch Rectifier

At the Technical University of Denmark, a pilot-scale batch rectifier is used routinely to separate water-ethanol solutions for educational purposes. A process and instrumentation diagram of this unit is shown in Figure 1. The column, reboiler, and

reflux lines are equipped with online temperature sensors, and rotameters show the reflux and product flow rates. Near each temperature sensor is a valve for sampling the product. A comprehensive description of the equipment and operating procedure is presented by Stevnsborg et al.[2]

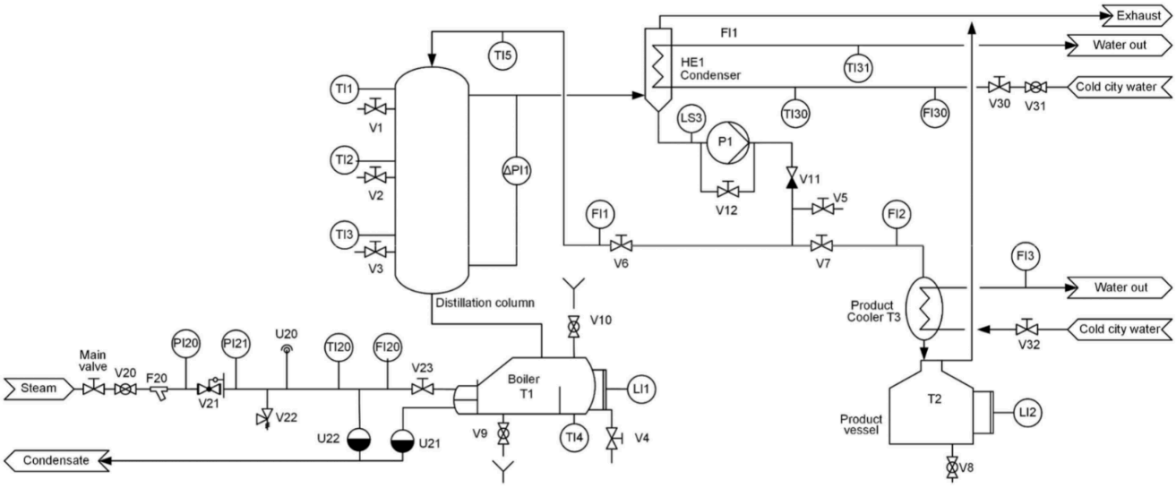

Figure 1: Piping and instrumentation diagram for the pilot-scale batch rectifier.

Water-ethanol distillation is performed at a reflux ratio of 1.0-2.0 until the reboiler temperature reaches 100°C, taking approximately 1 hour. During operation, at-line samples are taken at the V5 valve, and their density is measured using a handheld Anton Paar DMA35 densitometer. The densitometer is calibrated to the ethanol-water density at 20°C, and measurements are reported as ethanol volume fraction. Concurrently with sampling, the operator records the observed reflux ratio and adjusts it as needed.

Data from nine batches of water-ethanol distillation were collected, each manned by different operators and with varying nominal reflux ratios between 1.0 and 2.0. Each batch collected composition samples every 20 mins, yielding 2-3 at-line samples per batch; one batch collected samples every 10 mins, yielding five samples. In total, 26 samples were collected. The sampled ethanol volume fractions are converted to molar ethanol fraction using internal calibration curves. Most measurements of molar ethanol fraction from the distillate stream were between 0.6-0.8, with some between 0.4-0.6.

2.2 Model and Input Selection Strategy

Evaluation of the historical data for the pilot-scale batch rectifier showed that a model-based soft sensor would not be feasible: an energy balance could be established with the cooling water loop, but heat loss varied widely from batch to batch and could not be explained using the available data. Thus, two regression techniques were investigated to develop data-driven soft sensors based on only measurements from the column itself. The two models are partial least squares (PLS) regression, a linear latent-variable method well-suited for correlated inputs, and support vector regression (SVR), representing a nonlinear alternative. This comparison allows assessing the extent to which nonlinear regressors outperform linear methods.

The temperatures in the column (TI1-3), the distillate stream (TI5), and the reboiler (TI4) are examined for correlation with distillate composition. Of these, the TI5 is essentially constant throughout operation due to distillate overcooling, TI2 is unstable due to liquid channeling, and TI4 was discarded because it showed a strong correlation with TI3. As such, TI1 and TI3 were evaluated as model inputs, and they correlate well

with the distillate ethanol composition, as shown in Figure 2. The reflux and product flow rates were used to calculate a third potential input: the reflux ratio (RR).

For TI1 and TI3, vapor–liquid equilibrium (VLE) was calculated using Modified Raoult's Law with Non-Random Two-Liquid (NRTL) activity coefficients, yielding ethanol liquid- and vapor-phase mole fractions (x, y) at the two sensor locations: $\{x, y\}_{\text{TI1}}, \{x, y\}_{\text{TI3}}$. NRTL parameters were taken from Kurihara et al.[3]

To estimate performance on unseen batches, a nested batchwise leave-one-out cross-validation and hyperparameter optimization strategy was used. A visual representation of this technique for five total batches is shown in Figure 3. For PLS, the number of latent variables was tuned. For SVR, the regularization parameter, epsilon-insensitive width, and kernel parameters were tuned.

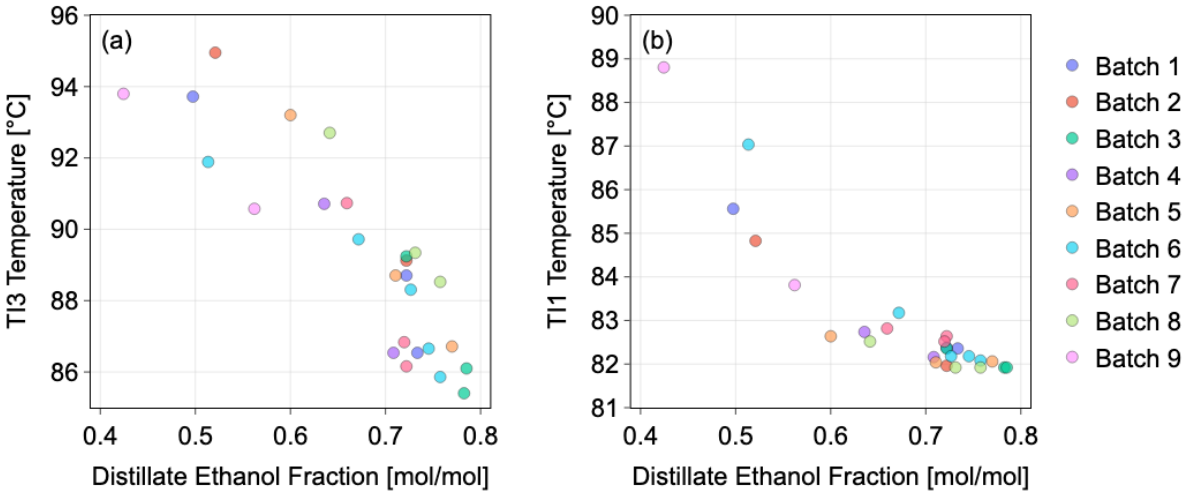

Figure 2: Correlations of (a) TI3 and (b) TI1 against the distillate composition at the time of measurement.

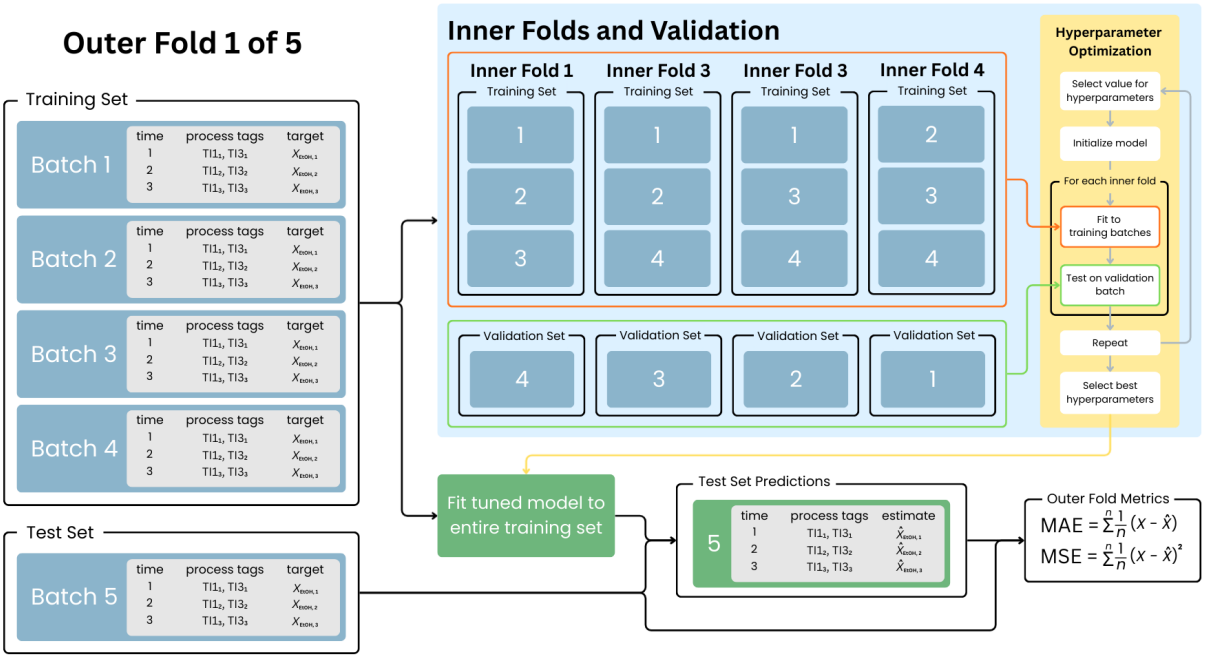

Figure 3: Schematic of the nested batchwise leave-one-out cross-validation strategy.

3. Results

The results for a subset of the developed PLS soft sensors are shown in Table 2. The out-of-fold R^2 (Q^2), mean absolute error (MAE), and root-mean-squared error (RMSE) are shown. The IDs for models presented in this table will be referenced going forward.

Table 1: Cross-validation metrics of select PLS-based soft sensors.

ID	Features	Q^2	MAE	RMSE
PLS1	TI1, TI3	0.936	0.0198	0.0241
PLS2	TI1, TI3, y_{TI1}, x_{TI3}	0.952	0.0165	0.0210
PLS3	TI1, TI3, $\{x,y\}_{\text{TI1}}$, $\{x,y\}_{\text{TI3}}$	0.938	0.0198	0.0238
PLS4	TI1, TI3, RR	0.893	0.0249	0.0296
PLS5	TI1, TI3, RR, y_{TI1}, x_{TI3}	0.941	0.0170	0.0221
PLS6	TI1, TI3, RR, $\{x,y\}_{\text{TI1}}$, $\{x,y\}_{\text{TI3}}$	0.904	0.0240	0.0281

PLS1 represents the simplest data-driven soft sensor that achieves good performance. Limiting PLS to either TI1 or TI3 was inferior to using both. PLS3 incorporates mechanistic knowledge from VLE calculations. Including all six variables yields similar performance compared to PLS1. PLS2 uses a subset of the engineered features used in PLS3 and notably improves performance. The various possible combinations of features were evaluated, including models using only VLE compositions as input features, yet TI1, TI3, y_{TI1} and x_{TI3} were found to be best. The selection of specifically y_{TI1} and x_{TI3} is physically motivated. y_{TI1} represents the expected composition of the vapor entering the condenser, a direct precursor to the product. x_{TI3} estimates the liquid composition entering the reboiler from the column, indicating ethanol depletion. Together, these features characterize the thermodynamic state of the column and the driving force available for separation. Adding features beyond this introduces overlapping and potentially misleading information, encouraging the model to learn spurious correlations that do not generalize well. In Figure 4, the PLS2 soft sensor estimates for a batch are shown, with the soft sensor tracking the measured ethanol concentration and continuously providing estimates. Because the temperature signals are not filtered, the soft sensor is very responsive, yet also sensitive to noise.

PLS4-6 are counterparts to PLS1-3, respectively, in which the RR is also used as model input. In all cases, these models performed worse than those not given the RR. Although RR is commonly manipulated to control distillate purity, its inclusion counterintuitively degrades predictive performance. A plausible explanation is that RR influences purity only indirectly by altering internal column flows and energy balances, which, in turn, are captured implicitly in column temperatures. This represents another instance of the issue described above: explicitly providing RR adds redundant, potentially misleading information, thereby encouraging the model to learn spurious correlations that do not generalize well. Worse results were observed for models that were explicitly provided with the distillate and reflux flow rates. This highlights the importance of carefully selecting and limiting input features for effective generalization.

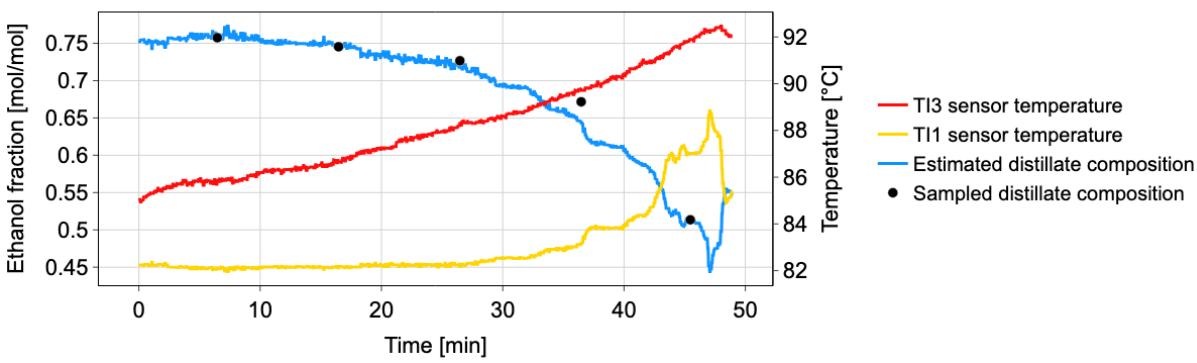

Figure 4: Estimates of the PLS2 soft sensor on one of the batches.

SVR models were subsequently assessed, and the best-performing feature set was also TI1, TI3, y_{TI1} and x_{TI3}. Table 2 shows the performance of three of the tested SVRs.

Table 2: Cross-validation metrics of select SVR-based soft sensors

ID	Kernel	Features Used	Q^2	MAE	RMSE
SVR-LIN	linear	TI1, TI3, y_{TI1}, x_{TI3}	0.953	0.016	0.021
SVR-POLY	polynomial	TI1, TI3, y_{TI1}, x_{TI3}	0.952	0.016	0.021
SVR-RBF	RBF	TI1, TI3, y_{TI1}, x_{TI3}	0.938	0.019	0.024

The SVR-LIN and SVR-POLY models achieve comparable performance because SVR-POLY identified a degree-1 polynomial as the best-performing kernel basis, reducing the model to a linear kernel. The performance of these models closely matches that of PLS2, but they are structurally different: they use margin-based regression rather than PLS's latent-structure-based approach. The SVR-RBF sees a performance reduction, which can be attributed to overfitting by the more flexible RBF kernel. Here, there is no benefit to increasing performance beyond a linear model, as it provides, at best, no performance gains.

4. Industrial Investigation

To investigate the industrial application of this framework, it was applied to an industrial tar distillation process producing pitch, described in detail in Villumsen et al. (2026)[4]. In this system, production is governed by the pitch softening point, which operators sample up to four times daily to inform operational decisions. A real-time soft sensor estimating the pitch softening point would allow proactive intervention to maintain product quality. Unknown, time-varying feed composition and unmeasurable mass and energy balances prevent the use of VLE-based features or mechanistic models, warranting data-driven soft sensing.

Because the plant runs continuously, a five-fold cross-validation strategy was used to fit the soft sensor regressor. Historical hourly data, including temperatures, pressures, densities, and flows, were aligned with the corresponding laboratory softening-point measurements. After filtering out startup and shutdown periods, 950 records remained. A subsequent test campaign of 170 records served as the independent evaluation set.

Both PLS and SVR models were evaluated across different feature sets. Features were grouped according to the infrastructure required for real-time deployment. The simplest models used only contemporaneous measurements, making them directly implementable within the Supervisory Control and Data Acquisition (SCADA) environment. More advanced variants incorporated lagged features, the previously measured softening point, or expanding-window retraining, each of which requires dedicated digital infrastructure to deploy. The soft sensors' performance was evaluated using operationally relevant and statistical metrics: the percentage of predictions within ±2°C of the laboratory value and the test set R^2.

Multiple models were identified. The simplest, a PLS-based soft sensor, could be deployed in the SCADA environment and predicted the pitch softening point within tolerance for 58.3% of the test samples. Incorporating historical data increased this performance to 77.6%. An SVR-based soft sensor achieved an initial performance of 66.9%; incorporating historical data and expanding-window retraining increased performance to 91.9% and achieved a value R^2 of 0.951.

5. Discussion and Perspectives

The pilot-scale batch rectifier demonstrates that effective soft sensor deployment does not require large datasets. Even with sparse data, parsimonious linear models such as PLS can deliver strong performance when input features are physically meaningful.

In the pilot-scale system, constructing thermodynamically motivated features yielded an approximately linear input–output mapping, despite underlying nonlinear process physics. In such cases, linear models are preferable, as they provide more reliable generalization. In contrast, more flexible nonlinear estimators tend to overfit in low-data regimes, where noise can induce spurious correlations. In the industrial case study, the larger dataset provided sufficient information to reliably identify nonlinear input-output relationships, enabling the SVR to outperform linear alternatives.

Together, these results highlight the relationship between feature quality, data volume, and model complexity. When effective linearity can be achieved through effective feature design, linear models offer greater generalization. This manifests in the following soft sensor development strategy: begin with linear models and physically meaningful features, and introduce additional model complexity only when effective linearity cannot be achieved and sufficient data are available.

Overall, soft sensors are valuable in production environments where product quality is measured via infrequent at-line sampling. By reducing reliance on delayed laboratory measurements, they provide real-time visibility into hard-to-measure quality variables and enable proactive process interventions. Beyond monitoring, soft sensors can support control strategies based on estimated product quality, thereby further improving economic and environmental sustainability.

Accuracy and operational value can be further enhanced by incorporating at-line measurements during inference and by using uncertainty-aware estimators to guide selective sampling. Reliable deployment, however, depends on appropriate safeguards. Faulty hardware sensors can propagate errors into soft sensor predictions, making continuous validation, sensor reconciliation, and post-inference checks essential. When integrated with automated process actions, these guardrails help ensure safe operation and clearly indicate when human oversight is required.

Soft sensors are therefore best viewed as decision-support tools whose performance and applicability are inherently tied to data quality and process stability. Beyond initial deployment, the long-term value of soft sensors depends on effective lifecycle management under changing operating conditions, which requires continuous monitoring and periodic updates to remain reliable.

5. Conclusion

This work demonstrates that data-driven soft sensors can estimate hidden quality variables otherwise accessible only through at-line sampling at both pilot and industrial scales. Two soft sensors were implemented: one for distillate purity in a pilot-scale batch rectifier and another for pitch softening point in an industrial tar distillation column. The case studies underscore the importance of constructing physically meaningful features and using cross-validation to select appropriate models for robust soft sensor performance.

Acknowledgements

The authors thank the students and staff in the DTU-KT Pilot Plant for collecting the data, and the Novo Nordisk Foundation for the grant NNF19SA0035474.

References

(1) Kadlec, P. et al. 2009. *Comput. Chem. Eng.* 2009, *33* (4), 795–814.
(2) Stevnsborg, M et al. 2025. *European Symposium on Computer Aided Process Engineering*.
(3) Kurihara, K et al. 1993. *J. Chem. Eng. Data*, *38* (3), 446–449.
(4) Villumsen, S. et al. 2026. Constraint-Aware Design of Data-Driven Soft Sensors for Industrial Processes. *Manuscript submitted to Computers & Chemical Engineering.*

Optimization of distillation columns using gray-box models

Syed E. Haider, Ville Alopaeus
Department of Chemical and Metallurgical Engineering, School of Chemical Engineering, Aalto University, P.O. Box 11000, FI-00076, Espoo, Finland

Abstract
The chemical industry relies heavily on distillation columns for the effective separation of multicomponent mixtures. Identifying the optimal distillation sequence and operational parameters is therefore essential for reducing the capital and operating costs. Traditionally, heuristic methods have been employed to guide the design and sequencing decisions. However, these methods may not explore all possible configurations, which may lead to suboptimal solutions. Conversely, superstructure-based optimization is a smart process systems engineering methodology that simultaneously evaluates all possible configurations using an equation-oriented approach. However, this technique can be computationally expensive and prone to convergence issues when complex unit operation models are involved. To address this, we proposed a simplified gray-box surrogate model, capable of predicting column outputs as a function of feed, number of stages, and reflux ratio, while keeping the predictions physically consistent and limited to feasible ranges. Subsequently, this model was employed to optimize a distillation system in a test case, resulting in an optimal design and configuration at reduced computational cost.

Keywords
Distillation, gray-box model, optimization, optimal configuration

1. Introduction

Distillation is the most commonly used unit operation in the chemical and petrochemical industries. For mixtures comprising more than two components, a sequence of distillation columns is generally required to achieve effective separation of each constituent. Prior research has demonstrated that optimization of column design and sequencing can significantly reduce the capital and operating costs of the overall process [1].

The number of possible distillation column arrangements increases rapidly, following the Catalan number sequence, with the number of components in a mixture, making the selection of an optimal sequence a highly combinatorial and complex problem. The conventional method for identifying the optimal sequence typically depends on heuristics rules and experience [2], which may fail to explore the entire design space and potentially overlook the optimal solution. In contrast, optimization-based approaches provide a systematic framework that embeds all of the plausible process units and potential structural alternatives within a single flowsheet, known as a superstructure. This superstructure is formulated as a mathematical programming problem incorporating all relevant process models and is solved to guide design and selection decisions [3].

Process models are mathematical representations that predict the behavior of chemical systems. They can be categorized into three types: 1) mechanistic (white-box) models, which rely on fundamental physical and chemical principles to describe

underlying mechanisms; 2) data-driven (black-box) models, which use statistical or machine learning methods to establish input–output empirical relationships between process variables, and do not respect the underlying physical laws; and 3) hybrid (gray-box) models, which integrate mechanistic knowledge with data-driven techniques to combine the strengths of both approaches.

Mechanistic models provide detailed and accurate insights, however, they often lead to large-scale mixed-integer nonconvex optimization problems that are hard to solve. To address this, simplified surrogate models, such as black-box or gray-box models, are frequently used to replace rigorous, complex unit models. While purely data-driven surrogates (e.g., polynomials, kriging, artificial neural networks) offer a computationally efficient alternative to first-principle models [4, 5], they often exhibit poor extrapolation capabilities that can lead to unreliable or physically implausible predictions. Conversely, a grey-box model strikes a balance between white-box and black-box approaches by first deriving a simplified model structure from the state-of-the-art white-box models and then using data-driven methods to estimate the resulting model parameters.

We therefore proposed a gray-box modelling framework for distillation optimization. The first-principles model of the isothermal flash tank was modified to capture multistage behavior, while data-driven methods were applied for parameter estimation. The resulting simplified model was subsequently employed within an optimization framework to design and sequence simple distillation columns for the non-sharp separation of a near-ideal ternary mixture in a test case.

2. Surrogate model formulation

A gray-box surrogate model should be solver-friendly, physically consistent, and capable of accurate extrapolation. However, formulating such a model for distillation is challenging, as it must be able to reflect changes in relative volatilities, number of stages, reflux ratio, and distillate-to-feed ratio while maintaining consistency in the mass and energy balances.

The simplest physics-based model for distillation is the isothermal flash, which determines phase splits and compositions using first-principles thermodynamics and mass conservation laws. In this unit model, a feed stream is separated into a vapor stream (V) and a liquid stream (L) that are in phase equilibrium at a specified constant temperature and pressure.

The equilibrium constant K_i (also called K-value) is a commonly used method in flash calculations to quantify the distribution of a single component i between the vapor or liquid phases at vapor-liquid equilibrium:

$$K_i = \frac{y_i}{x_i} \tag{1}$$

Where y_i and x_i represent the vapor-phase and liquid-phase mole fractions of component i, respectively. The equilibrium constant is typically obtained from thermodynamic models, such as equations of state or activity coefficient models, depending on the nature of the system at hand. In most systems, it can be expressed using the extended Raoult's law:

$$K_i = \frac{p_i^v(T)\gamma_{iL}(T,P)}{P} \tag{2}$$

where p_i^v is the vapor pressure of the pure component i, γ_{iL} is the activity coefficient of the component i in the liquid phase, and P is the pressure of the system. However, for ideal mixtures, activity of a component equals its mole fraction ($\gamma_{iL} = 1$), and Raoult's law holds exactly:

$$K_i = \frac{p_i^v(T)}{P} \tag{3}$$

The Rachford-Rice equation further relates this K-value to the vapor fraction, which is iteratively solved to determine the vapor and liquid flows and compositions. However, this mechanistic model is limited to single-stage flash calculations. To approximate the multistage behavior, we therefore modified the K-value expression by introducing an exponential function $g(N, R)$, where N denotes the number of stages and R denotes the reflux ratio. After modification and rearrangement, Equation 1 takes the form shown in Equation 4:

$$y_i = K_i^{g(N,R)} x_i \tag{4}$$

Here, g is expected to be higher than one for multi-stage operations. This formulation shares structural similarities with some algebraic analytical methods for stage-wise separations (e.g. Kremser method), where equilibrium coefficients are raised to a power proportional to the number of stages. The present method, however, allows us to retain structural simplicity and physical consistency of a simple single-stage flash.

In isothermal flashes, temperature must be iteratively adjusted during the flash calculations to ensure that the distillate mole fractions satisfy the condition: $\sum y_i = 1$. However, incorporating temperature iterations directly into the surrogate model increased its nonconvexity, leading to potential convergence issues. To address this, we introduced a scaling parameter 'a', which is iterated instead of temperature to enforce the condition: $\sum y_i = 1$.

$$y_i = aK_i^{g(N,R)} x_i \tag{5}$$

$g(N, R)$ is a hypothetical function that incorporates the number of stages and reflux ratio, thereby extending the capabilities of a single-stage flash model to approximate multistage column behavior. The remaining challenge is to accurately determine the function g so that the simplified model accurately reflects the real column operations.

Firstly, an artificial neural network (ANN) was trained on simulation data to approximate the function g. The training data were obtained using a rigorous Aspen Plus RadFrac distillation column model, varying the key operating parameters such as feed composition, feed vapor fraction, total number of stages, feed stage location, reflux ratio, and distillate-to-feed ratio. The quality of the fit can be observed from the parity plots in Figure 1.

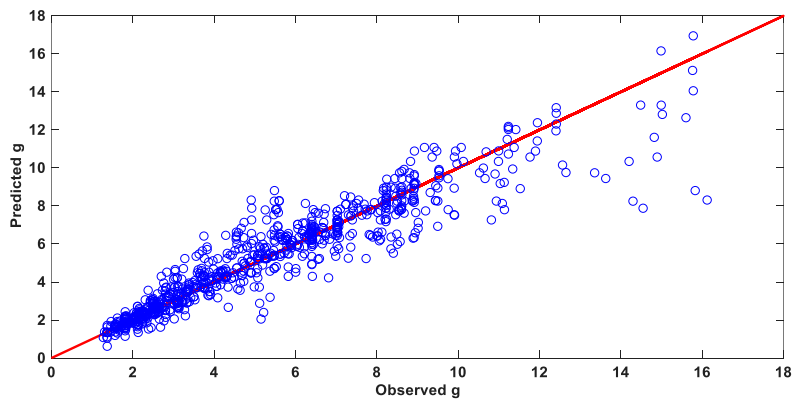

Figure 1: Parity plot for ANN predicted g

However, the ANN-based models failed to converge with global solvers within a practical computational time. Research is progressing on exploring alternative solution strategies and implementing linearization or simplification techniques to improve computational efficiency. Subsequently, an empirical function for g was proposed, represented by Equation 6:

$$g = R^p N^q \tag{6}$$

where p and q are model parameters, determined by fitting to the simulation data. The resulting empirical function, with optimized parameters, is expressed in Equation 7:

$$g = R^{0.36} N^{0.62} \tag{7}$$

This empirical function is used in the next section to optimize distillation systems.

3. Problem Statement

The primary objective of this study is to identify the optimal design and sequencing of normal distillation columns that minimize the total annualized cost for a non-sharp separation of a multicomponent feed stream of known composition and flow rate into multiple product streams. For illustration, we investigated the separation of a near-ideal ternary mixture consisting of pentane, hexane, and octane into its individual components. The optimization process could be structured into three main steps: 1) Development of a superstructure 2) Formulation of a mathematical optimization model, and 3) Solution of the resulting mathematical optimization model.

4. Development of Superstructure

Distillation column optimization begins by defining a superstructure with a maximum of (n-1) columns for the separation of an n-component feed. Superstructures in process synthesis are generally categorized into two main types: 1) the state-task network (STN), and 2) the state-equipment network (SEN). The STN is used in this study because the task of each equipment is fixed. Figure 2 illustrates the overall superstructure considered in this study.

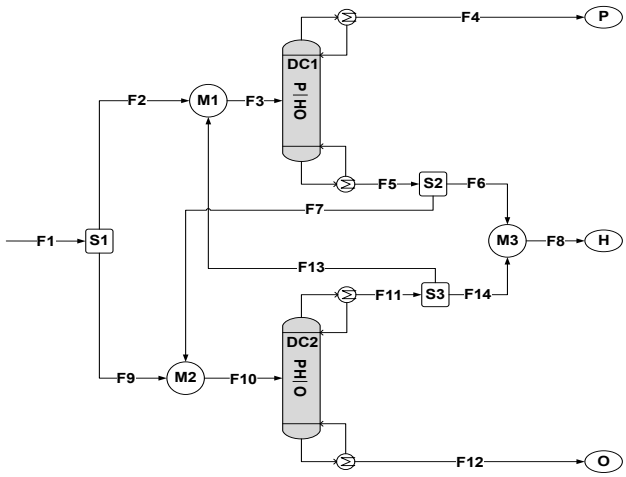

Figure 2: Superstructure for three-component separation.

Because the columns are simple and non-sharp, a single feed stream is split into two product streams containing both light and heavy key components. The key components are pentane (P) and hexane (H) in column 1 and hexane (H) and octane (O) in column 2. The feed can flow to both columns. The top of column 1 and the bottom of column 2 can yield the final desired products. A stream from the bottom of column 1 or the top of column 2 can be recycled to the inlet of the other column if it contains their key components; otherwise, it flows to the final desired product. Splitters and mixers serve as the structural elements that enable the representation of all

possible flow configurations and sequencing alternatives within a single optimization framework.

5. Formulation of Mathematical Model

This step involves translating the superstructure into a mathematical programming problem. The objective function is to maximize the total profit, calculated as revenue from product sales minus total annualized costs. This total cost includes the capital and operating costs, as well as the cost of the feedstock. Mathematically, the objective function can be expressed in Equation 8:

$$Max\ profit = \sum_{(i,s)\in PROD} price_i\, x_{i,s} F_s - cost_{feed} F_{feed} - \sum_{col\in DC} \left(C_{col}^{capex} + C_{col}^{opex}\right) \quad (8)$$

The functions for capital and operating costs of the column were developed based on the key design and operating variables (number of stages, reflux ratio, feed flowrate, and distillate-to-feed ratio). These functions were regressed using the economic data obtained from Aspen Plus. The following functions best represent the column costs:

$$C_{col}^{capex} = 2.25 + (1.15 * 10^{-4}) F_s^{0.5} + \left(2.3 * 10^{-5}\right)\left(\frac{F_{s'}}{F_s}\right) R_{col} F_s^{0.5} + (2.25 * 10^{-7}) N_{col}^2 F_s^{0.5} \quad (9)$$

$$C_{col}^{opex} = (1.84 * 10^{-3}) F_s^{0.5} + (5.45 * 10^{-5}) F_{s'} R_{col} + (5.45 * 10^{-5}) F_{s'} \quad (10)$$

$\forall col \in DC, \forall s \in DCI, \forall s' \in DCT$

If the index sets $\mathrm{DC} = \{\mathrm{col}\}$, $\mathrm{DCI} = \{\mathrm{s}\}$, $\mathrm{DCT} = \{\mathrm{s'}\}$ represent all distillation columns, input streams to columns, and top streams of columns, respectively, then F_s, $F_{s'}$, R_{col}, N_{col} denote the molar flowrates of inlet streams to columns, molar flowrates of top streams of columns, reflux ratios of columns, and the number of stages of columns, respectively.

The next step is to formulate the optimization model by defining variables, index sets, and constraints. The main variables include flow rates (F), compositions of all streams (x), scaling factor (a), reflux ratio (R), and number of stages (N) for each column. The following index sets were defined to characterize the topology of the superstructure. First, the set of all components and streams was denoted by the index sets: $\mathrm{I} = \{\mathrm{i}\}$, and $\mathrm{S} = \{\mathrm{s}\}$, respectively. The sets of mixers and splitters inlets and outlets by the index sets: $\mathrm{MI} = \{\mathrm{s'}\}$, $\mathrm{MO} = \{\mathrm{s}\}$, $\mathrm{SI} = \{\mathrm{s}\}$, and $\mathrm{SO} = \{\mathrm{s'}\}$, respectively. The index set $\mathrm{DC} = \{\mathrm{C}\}$ represents the set of all columns, while the index sets $\mathrm{DCI} = \{\mathrm{s}\}$, DCT ={s'}, DCB ={s''} indicate the sets of inlet, top, and bottom streams of each column, respectively. The corresponding constraints for the superstructure can then be written as follows:

$$x_{i,s} F_s = \sum_{s'\in MI} x_{i,s'} F_{s'} \quad (11)$$

$\forall s \in MO, \forall i \in I$

$$F_s = \sum_{s'\in SO} F_{s'} \quad (12)$$

$\forall s \in SI$

$$x_{i,s} = x_{i,s'} \quad (13)$$

$\forall s \in SI, \forall s' \in SO, \forall i \in I$

$$x_{i,s} F_s = x_{i,s'} F_{s'} + x_{i,s''} F_{s''} \quad (14)$$

$\forall s \in DCI, \forall s' \in DCT, \forall s'' \in DCB, \forall i \in I$

$$x_{i,s} = a_C K_i^{g_C} x_{i,s'} \quad (15)$$

$\forall s \in DCT, \forall s' \in DCB, \forall C \in DC, \forall i \in I$

$$g_C = R_C^{0.36} N_C^{0.62} \quad (16)$$

$\forall C \in DC$

$$\sum_{i} x_{i,s} = 1 \tag{17}$$

$\forall s \in S, \forall i \in I$

6. Solution of Optimization Model

All potential candidates were embedded in a superstructure, which was translated into a nonlinear programming problem (NLP) in the previous section. The NLP model was implemented in GAMS and solved using the KNITRO local solver to generate initial values for the decision variables. These values were subsequently used as the starting point for the BARON global solver. The resulting solution produced the optimal distillation sequence, along with the optimal reflux ratios and the number of stages for each column. Figure 3 presents the optimal solution.

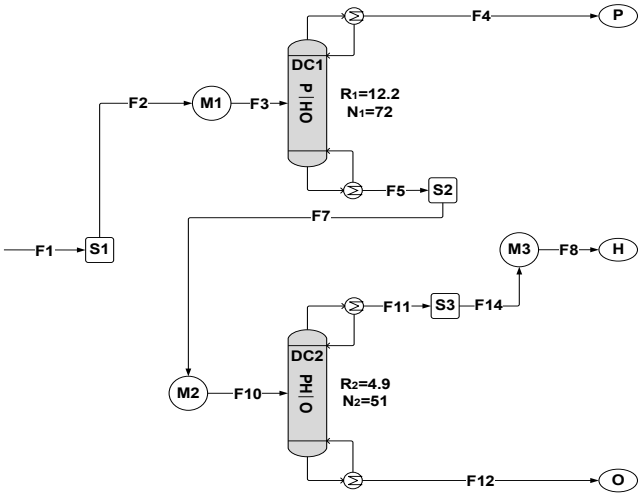

Figure 3: Optimal solution

7. Conclusion

In principle, mathematical optimization can be more powerful than the traditional heuristics-based approach for designing distillation systems. However, the complex process models often lead to hard-to-solve optimization problems. We therefore derived a simplified physics-based surrogate model for distillation columns based on the mass balances of a single-stage flash tank and extended it to approximate multistage behavior. This model is capable of predicting column outputs as a function of feed, number of stages, and reflux ratio while keeping the predictions physically consistent. This surrogate model was subsequently applied to optimize the distillation column system for the non-sharp separation of a near-ideal ternary mixture, and it worked properly with reduced computational cost.

Acknowledgements

Business Finland is gratefully acknowledged for their financial support for the UrbanFactory project (project number 4162/31/2024).

References

1. Smith, R., Chemical process: design and integration. 2005: John Wiley & Sons.
2. Westerberg, A.W., The synthesis of distillation-based separation systems. Computers & chemical engineering, 1985. 9(5): p. 421–429.
3. Grossmann, I.E., Mixed-integer optimization techniques for algorithmic process synthesis, in Advances in Chemical Engineering. 1996, Elsevier. p. 171–246.
4. McBride, K. and K. Sundmacher, Overview of surrogate modeling in chemical process engineering. Chemie Ingenieur Technik, 2019. 91(3): p. 228–239.
5. Henao, C.A. and C.T. Maravelias, Surrogate-based superstructure optimization framework. AIChE Journal, 2011. 57(5): p. 1216–1232.

A data-informed mechanistic framework for predicting gas maldistribution in structured packed beds

Vassilis Charitatos, Marc Fernandez, Alice Miranda, Thomas Linder, Mathias Hack

Sulzer Chemtech AG, Winterthur, Switzerland

Abstract

A data-informed mechanistic framework for fast prediction of gas maldistribution in structured packed beds is presented. The model is rooted in momentum conservation at the unit-cell level, where characteristic resistances are used to describe flow along and between corrugated channels. Model parameters are calibrated using high-fidelity single-sheet gas CFD simulations. The calibrated formulation is upscaled to full columns by stacking packing elements rotated by 90° and enforcing inter-element continuity. Validation with experiments under controlled maldistribution (MellapakPlus™ 252.Y) is performed; when driven by the experimentally measured velocity field after two elements, the model prediction after a third element shows strong agreement with experiments, with most of the cross-section remaining within ±20% relative error and larger deviations localized near walls and low-velocity regions. By combining experimental validation with high computational efficiency, the framework establishes a solid basis for an effective design tool capable of delivering actionable insights into gas maldistribution for column design and the development of new packing concepts.

Keywords

Gas maldistribution, Mechanistic model, Structured packing, Flow visualization, Scale-up

1. Introduction

Gas maldistribution in structured packed columns disrupts uniform flow, leading to reduced separation performance and increased pressure drop; accurate prediction of gas flow is therefore critical for reliable design and operation. In industrial practice, parallel-column models such as the two-column approach of Billingham & Lockett [1] are often employed to predict column performance under maldistribution. In recent works, such models have been extended to multi-stream frameworks and are available in tools like the ChemSep Parallel Column Model [2]. Although these methods are valuable for sensitivity studies, they do not resolve how momentum redistributes within the packing geometry. At the other end, computational fluid dynamics (CFD) studies provide high-fidelity insights into local gas hydrodynamics but remain too computationally expensive for routine full-column simulations. [3],[4]

Here, a computationally efficient, data-informed mechanistic model is introduced that enables rapid prediction of gas flow across entire packed columns. The formulation is developed at the scale of a fundamental unit cell, allowing the essential flow physics of structured packing to be captured without resolving the full geometry. Model parameters are then calibrated using high-fidelity CFD simulations of single packing

sheets, ensuring that small-scale hydraulic behavior is reflected in the model. To assess the model at column scale, dedicated gas-flow experiments under controlled maldistribution were performed to generate a validation dataset. The following sections describe the development and calibration of the unit-cell model (Section 2.1), the experimental procedure used to obtain validation measurements (Section 2.2), followed by a comparison of model predictions with the large-scale flow-visualization data (Section 2.3). These components establish a physically motivated framework capable of delivering column-scale predictions within minutes, offering practical insights for packing development and column performance analysis.

2. Results and discussion

2.1 Model development

2.1.1 Unit cell concept and model formulation

The model is built as a mechanistic framework grounded in first principles, with its foundation being the unit cell, the smallest repeating geometry forming the corrugated channels of a structured packing sheet. By focusing on this elementary component, the essential hydraulic behavior is captured without resolving the full packing structure, enabling scalability while preserving physical meaning. For illustration, a typical low–surface-area corrugated sheet of ~1 m length and ~0.22 m height contains roughly 200 unit cells. That count applies to one sheet only; a 1 m-diameter packing element of the same height, composed of many sheets arranged in parallel, contains ~10 000 unit cells. At larger scale, a 5 m-diameter element of the same height contains ~200 000 unit cells. These examples show why a unit-cell formulation is essential, capturing key flow physics while keeping large-scale computations feasible.

The model assumes that gas flows along channels and can switch to an adjacent channel at defined junctions, with no lateral movement beyond these discrete transitions. Momentum conservation is applied through a network of lumped resistances representing pressure losses due to channel friction, wall interactions, and directional flow switching. For a given inlet velocity profile, the model iteratively solves pressure and velocity distributions by minimizing the overall pressure drop under these resistance constraints. Once the velocity field is established, a simplified mixing model [5] computes concentration redistribution independently, using the solved flow pattern. This approach combines physical rigor with computational efficiency, forming a mechanistic model that can be scaled from the unit cell to full-column predictions.

2.1.2 Data-driven model calibration

A data-driven calibration approach was adopted for the tuning of the resistance parameters, while retaining a fully mechanistic model structure. High-fidelity CFD data of gas flow in single packing sheets which were previously validated against experimental pressure drop and concentration mixing measurements, were used to guide model calibration [6]. The CFD dataset provided detailed pressure and velocity profiles along the sheet length at multiple elevations, which served as targets for optimization. The tuning process was formulated as a constrained nonlinear problem solved with the Sequential Least Squares Programming (SLSQP) algorithm in Python. The algorithm adjusts the characteristic resistances until discrepancies in axial pressure drop and channel-wise velocity profiles are minimized across all conditions,

yielding packing-specific parameter sets that generalize well within the calibrated range.

Figure 1 compares velocity and pressure profiles predicted by the tuned mechanistic model (solid lines) with those obtained from the high-fidelity CFD simulations (dashed lines) at three relative heights along the packing sheet (*z/L* = 0.15, 0.29, and 0.73, where the sheet length *L*~0.22m). The agreement is strong across all positions: the model reproduces both the velocity decay along the sheet as well as the corresponding pressure drop trends, confirming that the resistance-based formulation captures the dominant physics of channel flow and pressure equalization. At lower heights (*z/L* = 0.15, 0.29), both CFD and model show a steep velocity gradient near the sheet entrance followed by a gradual decline, while the pressure profile decreases almost linearly, reflecting momentum losses along the corrugated channel. At higher elevation (*z/L* = 0.73), velocities flatten and pressure losses become minimal, consistent with reduced acceleration near the sheet exit. Minor discrepancies appear in regions of sharp velocity transitions, where CFD predicts localized variations (likely due to small-scale vortices and secondary flows) which the simplified resistance network is not intended to capture. Nevertheless, the model replicates the overall behavior without requiring full geometric resolution. This demonstrates that the model retains the essential physics of momentum conservation and channel switching while remaining computationally efficient.

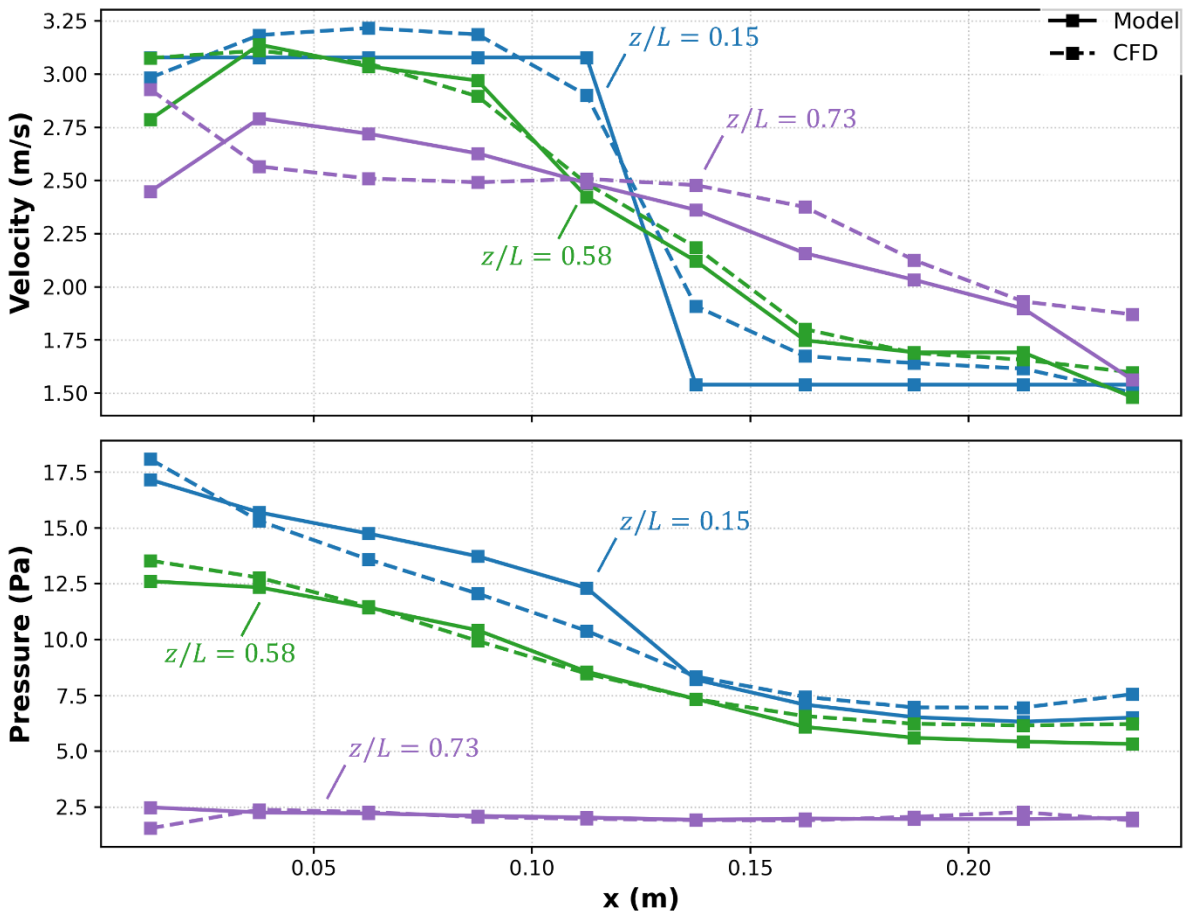

Figure 1: Comparison of mechanistic model (solid lines) and CFD (dashed lines) predictions for a single packing sheet. Velocity (top) and pressure (bottom) profiles along the sheet at three relative heights (z/L = 0.15 (blue), 0.29 (green), 0.73 (purple), where the sheet length L~0.22m).

2.1.3 Scale-up

To scale the unit-cell model to a full column, the packed bed is represented as a stack of packing elements, each consisting of multiple sheets arranged in parallel to form a circular cross-section when viewed from above. Successive elements are rotated by 90° to mimic the alternating orientation of structured packing layers. The solution begins by prescribing the inlet velocity profile at the bottom of the first element and the outlet pressure at the top of the last element of the packed bed. During the iterative procedure, the top velocity of each element becomes the inlet for the next, while pressures are adjusted so that the interface between elements satisfies continuity. Initially, pressures are guessed using a simple profile, then refined together with velocities until both fields converge and the pressure at the top of element *i–1* matches the bottom of element *i*. Since each element solve involves only momentum balances and resistance-based pressure drop calculations, the global iteration is computationally lightweight. For a typical case with a 1 m-diameter and 2 m-tall packed bed (about 10 packing elements), the full-column simulation converges *in under five minutes* on a standard workstation using 12 parallel nodes.

2.2 Experimental setup

For mutual validation, experimental studies were carried out to characterize the gas flow field above structured packings under conditions of controlled, simulated maldistribution. The experiments took place in a column with an inner diameter of 1 m. Air was introduced from the bottom at various F-factors between 1 and 5 $Pa^{0.5}$., covering typical industrial gas-flow conditions. Local gas velocities inside the column were measured using a Procap five-hole pressure probe, whose position was continuously monitored by a camera system (Streamwise GmbH, Männedorf, Switzerland).

Once a uniform flow was achieved, a controlled maldistribution was introduced by blocking half of the column cross-section using a metal plate installed at the packing support grid level. Above this, the test section comprised of one, two, or three MellapakPlus™ 252.Y elements, each rotated by 90° relative to the adjacent element. During each experiment, a stable operating point was first established at the selected F-factor. Subsequently, the probe was moved across the entire column diameter at heights ranging from 10 to 100 mm above the top packing element. By simultaneously recording the three-dimensional velocity vectors and the probe position with millimeter accuracy, a detailed 3D flow field was obtained. This experimental dataset formed the basis for independent validation of the modeling approach, with no model parameters fitted to the large-scale experimental data.

2.3 Model validation

Figure 2 illustrates the validation workflow at F-factor = 2 $Pa^{0.5}$. The left panel shows the inlet velocity field used as input to the model, obtained experimentally after two MellapakPlus™ 252.Y elements under controlled maldistribution. The center panel compares the experimentally measured velocity field after three elements (top) with the model prediction for the same plane (bottom), demonstrating how the model propagates the inlet profile through one additional MellapakPlus™ 252.Y element. The right panel presents the relative error between model and experiment.

The comparison shows strong agreement: both model and experiment exhibit a high-velocity band in the upper region and a gradual decay toward the lower region, indicating that the mechanistic framework captures the dominant redistribution trend. Most of the cross-section relative errors in gas velocity falls within ±20%, confirming that the model realistically predicts maldistribution evolution over an additional layer. Deviations are concentrated near the column wall and in low-flow zones, where errors can exceed ±30%. These discrepancies can arise from several factors. On the modeling side, the framework assumes idealized channel switching without continuous lateral flow and does not account for edge effects or small-scale recirculations near the wall. On the experimental side, gas velocities are measured slightly above the packing exit, where mixing may have already smoothed gradients. Additionally, in low-flow zones, the inherently low signal levels obtained by the pressure probe can lead to larger relative errors, even when using a multi-hole probe with high accuracy across a wide velocity range. Despite these limitations on both sides, the overall agreement validates the model's ability to predict maldistribution evolution across additional packing layers with high fidelity and minimal computational cost, offering a practical alternative to full CFD simulations.

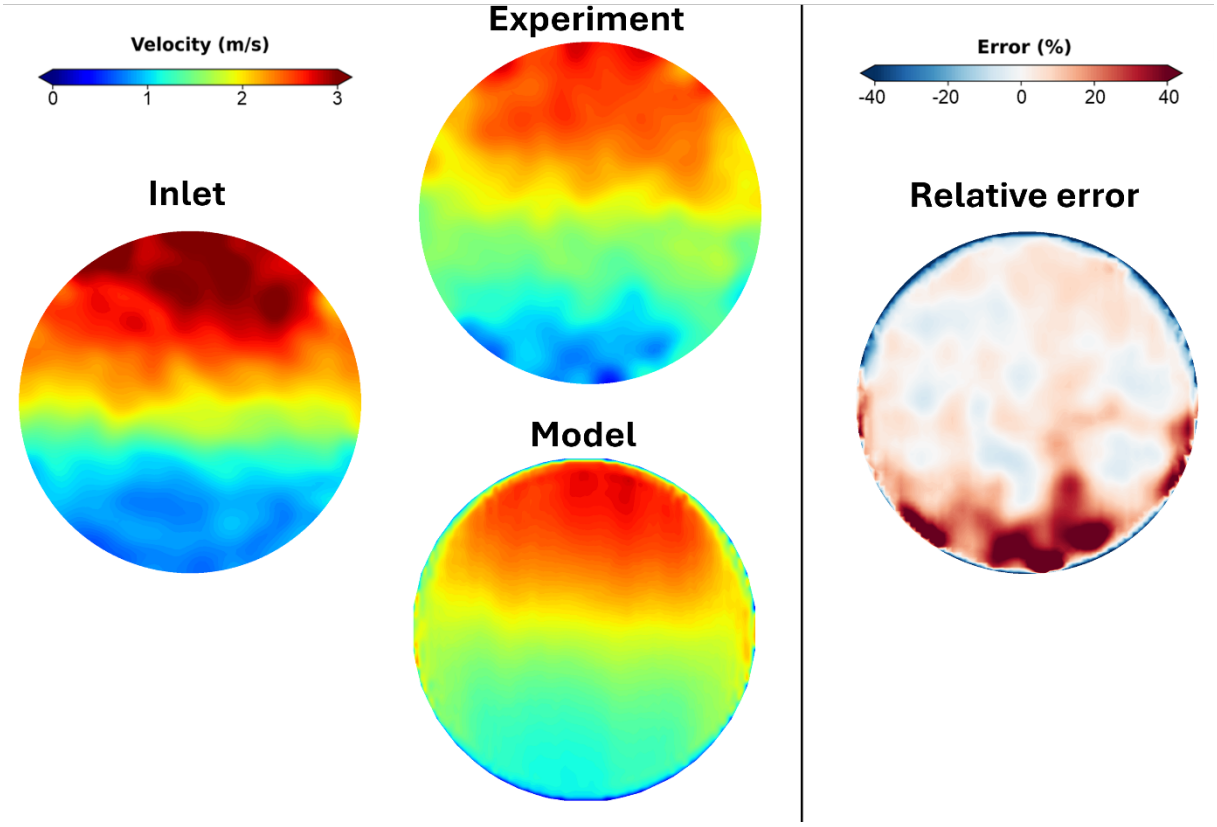

Figure 2: Validation of maldistribution prediction. The inlet to the model (left) is the experimental gas velocity field at F-factor of 2 $Pa^{0.5}$ after two MellapakPlus™ 252.Y elements. The center panel shows the experimental velocity field after three MellapakPlus™ 252.Y elements (top) and the model prediction for the same plane (bottom). The right panel presents the relative error between model and experiment.

3. Conclusions

A data-informed mechanistic model was developed to predict gas maldistribution in structured packed columns by combining first-principles momentum conservation with

resistance-based formulation and CFD-driven parameter calibration. The model accurately reproduces velocity and pressure trends at the single-sheet level and scales efficiently to full-column simulations, requiring only minutes of computation. Validation against flow visualization experiments under controlled maldistribution shows strong agreement, with most regions within ±20% error and discrepancies primarily near walls and low-velocity zones due to model simplifications and experimental limitations. These results confirm that the framework captures the key physics governing gas redistribution while offering orders-of-magnitude lower computational cost than full-geometry CFD. The approach therefore provides a practical and predictive tool for column design, performance assessment, and faster packing development. Future work will extend the methodology to liquid maldistribution and two-phase flow to enable comprehensive hydrodynamic predictions for industrial packed columns.

References

[1] J. F. Billingham and M. J. Lockett, "A simple method to assess the sensitivity of packed distillation columns to maldistribution," *Chemical Engineering Research and Design,* vol. 80, no. 4, pp. 373-382, 2002.

[2] H. A. Kooijman, J. Zhou and R. Taylor, "Application of a new parallel column model to simulating maldistribution in packed columns," *Chemical Engineering and Processing - Process Intensification,* vol. 171, p. 108436, 2022.

[3] M. Isoz, "CFD study of gas flow through structured separation columns packings Mellapak 250. X and Mellapak 250. Y," in *Proceedings of the conference TPFM*, 2017.

[4] Y. Amini and M. Nasr Esfahany, "CFD simulation of the structured packings: A review," *Separation Science and Technology,* vol. 54, pp. 2536-2554, 2019.

[5] N. Tavare, "Mixing, reaction, and precipitation: Interaction by exchange with mean micromixing models," *AIChE Journal,* vol. 41, no. 12, pp. 2537-2548, 1995.

[6] A. Miranda and M. Hack, "The Onset of Turbulence: Computational Fluid Dynamics Insights into the Hydrodynamics of Structured Packings," in *DECHEMA 13th International Conference on Distillation & Absorption*, Salzburg, 2026.

How to reduce the effort for the prediction of basic performance data of a structured packing without experiment

Halina Murasiewicz[1], Jerzy Maćkowiak[2], Jan Maćkowiak[2], Reiner Chromik[2]
[1]West Pomeranian University of Technology, Szczecin, Poland
[2]ENVIMAC Engineering GmbH, Oberhausen, Germany

Abstract
Traditionally, formulating design principles for structured packings in distillation and absorption has relied on resource-intensive, multi-year experimental campaigns. These investigations are essential for determining Basic Performance Data (BPD), such as hydraulic capacity and pressure drop profiles, representing a significant bottleneck in the development cycle due to high capital and temporal requirements.
This study proposes a simulation-driven methodology to bypass traditional experimentation by integrating a physical "Suspended Bed of Droplets" (SBD) model with high-fidelity Computational Fluid Dynamics (CFD). This synergetic framework enables the autonomous generation of comprehensive BPD—specifically flooding load characteristics and irrigated pressure drops—without the prerequisite for experimental input. To demonstrate the model's efficacy, results are validated against empirical datasets for the industrial-standard R500Y structured packing. This approach marks a transition toward an agile, predictive design paradigm in separation technology, significantly accelerating the optimization of packing geometries.

Keywords
structured packing, distillation, absorption, hydraulics, CFD modelling, low experimental effort

1. Introduction

Structured packings have revolutionised separation technology by offering high mass transfer efficiency and exceptionally low pressure drop compared to trays or random packings. Despite their technical superiority, the development and optimisation of these internals have traditionally been constrained by the intricate coupling between complex geometry and multi-phase hydrodynamics. Historically, the acquisition of Basic Performance Data (BPD)—essential for industrial scale-up—demanded exhaustive experimental campaigns. While established test systems (Zuiderweg, 1969) and contemporary air-water benchmarks (Maćkowiak, 2010, 2022) provide necessary empirical correlations, they are increasingly viewed as time-intensive and cost-prohibitive.
In this context, Computational Fluid Dynamics (CFD) has emerged as a transformative methodology to supplement or circumvent traditional BPD acquisition. Over the last two decades, CFD has matured from an optimisation tool for non-active internals into a high-fidelity predictive framework for packing performance. Foundational studies on Mellapak 250Y by Szulczewska et al. (Szulczewska et al., 2003) demonstrated the capacity of CFD to resolve the influence of wetting rates on interfacial area. The predictive accuracy of CFD has been further validated across diverse geometries, including Mellapak 250X/Y, 350Y, and 500Y, to quantify dry

pressure loss (Isoz & Haidl, 2018). High-resolution validation techniques, such as the Volume-of-Fluid (VoF) method coupled with tomography (Bertling et al., 2023) have confirmed the ability of simulations to reproduce complex holdup profiles and residence time distributions.
However, a significant gap remains in the literature: the transition from computationally expensive, small-scale high-fidelity models to the rapid prediction of BPD for industrial-scale columns. This work addresses this challenge by proposing a streamlined CFD methodology using simplified turbulence models, such as (k-ε). By prioritising computational efficiency without sacrificing physical relevance, this approach provides a novel pathway to predict fundamental performance parameters, significantly reducing the reliance on long-term experimental investigations.

2. Results and discussion

2.1 CFD modelling

2.1.1 Mathematical framework and governing principles

Simulations were based on mass and momentum conservation for an incompressible Newtonian fluid (Byron Bird et al., 2006). Turbulence was modelled using the Reynolds-Averaged Navier-Stokes (RANS) equations with a standard k-ε model. Scalable wall functions were employed to maintain numerical accuracy at solid boundaries while optimising computational efficiency.

2.1.2 Geometry and mesh development

The study utilised a 50 mm column with R500Y structured packing, comparing configurations with and without wall wipers (Figure 1a). Geometries designed in AutoCAD were discretized using unstructured tetrahedral meshes (Figure 1b). Following a grid independence study, the final meshes comprised 4.51 million elements for the wiper configuration and 1.62 million for the standard setup. Mesh quality was confirmed through high orthogonality and low skewness metrics.

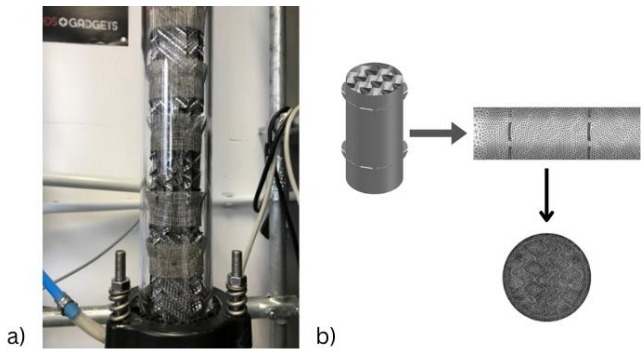

Figure 1: a) view of the investigated metallic structured packing R500Y in the test plant d_S = 50 mm and H = 1.0–1.5 m and b) view of the digital geometry and mesh of the structured packing with wipers used for CFD simulation.

2.1.3 Boundary conditions and numerical strategy

The steady-state, isothermal model was solved using ANSYS Fluent 2023 R2. Boundary conditions were defined as a velocity inlet ranging from 0.5 to 4.0 m/s, a pressure outlet set at 0 Pa, and walls characterised by a no-slip condition with a specifically defined roughness. Pressure-velocity coupling was handled by the SIMPLE algorithm. A second-order upwind differencing scheme was used for all

variables to ensure higher-order accuracy. Convergence was achieved when normalised residuals dropped below 10^{-5}, typically within 3,000 iterations.

2.2 CFD results: pressure analysis

The CFD results analyse pressure drop, static pressure contours, and velocity patterns at u_V = 0.5 m/s and 4.0 m/s. This approach evaluates the influence of geometric features, such as wall wipers, on local flow dynamics and energy consumption. Due to space constraints, Figure 2 and Figure 3 present only the static pressure results for both configurations (with and without wipers) at the velocity extremes.

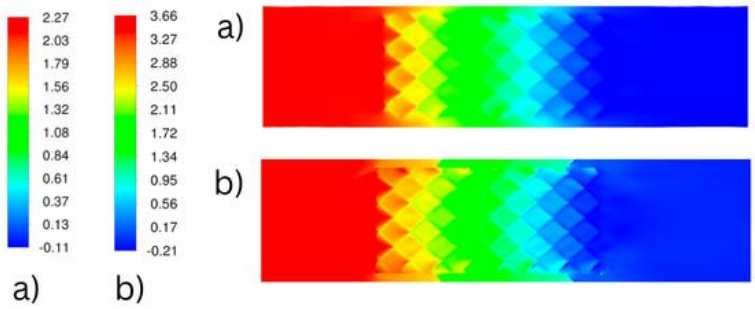

Figure 2: Static pressure profile in standard metallic structured packing R500Y a) without wipers, and b) with wipers (d_S = 50 mm, u_V = 0.5 m/s).

The hydraulic performance of the R500Y structured packing is characterised by a complex interplay between gas velocity and mechanical configuration. The current simulation results, presented in Figure 2 and Figure 3, establish a "without wipers" baseline that reveals how the system behaves under varying loads. At a low gas velocity of u_V = 0.5 m/s, the system exhibits minimal resistance, with static pressure decreasing vertically from an inlet to an outlet.

CFD modelling confirms that while corrugations redirect flow, reduced resistance at the column wall leads to significant gas bypassing. At higher velocities (u_V = 4.0 m/s), this creates a steep pressure gradient as gas preferentially follows the smooth wall boundary, bypassing the high-resistance packing core and reducing mass transfer efficiency.

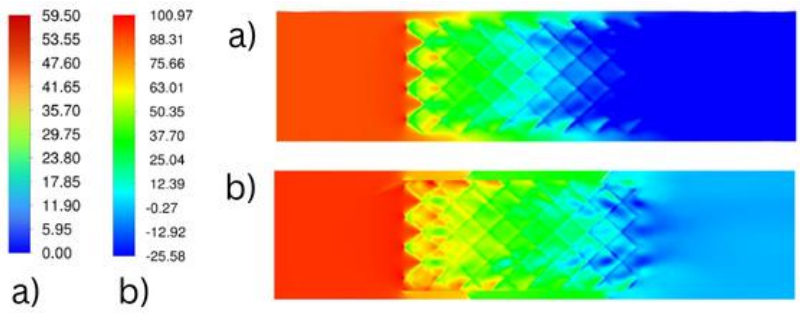

Figure 3: Static pressure profile in standard metallic structured packing R500Y a) without wipers, and b) with wipers (d_S = 50 mm, u_V = 4.0 m/s)

Wipers mitigate wall bypassing by redirecting gas into the active packing core. While this ensures uniform contact, it creates a technical trade-off: eliminating the low-resistance wall "shortcut" increases overall hydraulic resistance and inlet static pressure.

Additionally, wipers disturb the wall boundary layers, inducing localised pressure drops and turbulence that contrast with the smoother gradients of the baseline profile. This comparative analysis successfully defines the dry pressure drop for R500Y packing, establishing the necessary reference points for subsequent SBD calculations and process optimisation.

2.3 Comparison of experimental tests with CFD simulation data?

To validate this new method for predicting BPD data using CFD, experimental hydraulic investigations were conducted. These were performed using a laboratory distillation plant, which is shown in Figure 1a. Experiments were carried out under low and atmospheric pressures ranging from 0.3 bar to 1 bar, as detailed in Table 1 and shown in Figure 4.

packing R500Y (RVT) a = 500 m^2/m^3, ε = 0,970 m^3/m^3 φ_P = 0.80	d_S [mm]	H [m]	p_T [mbar]	T [K]	ρ_V [kg/m^3]	$F_{V,fl,exp}$ [$Pa^{1/2}$]	$F_{V,fl,CFD}$ [$Pa^{1/2}$]	$\delta(F_{V,fl})$ [%]
air	50 52 54	1.0 1.5	1013	293	1.20	—	—	—
cyclohexane/*n*-heptane $\dot{L}/\dot{V} = 1$	50	0.5 1.0 1.5	950	360	2.80	2.20	2.23	-1.4
			300	327	1.00	2.33	2.43	-4.3
ethanol/*n*-butanol $\dot{L}/\dot{V} = 1$	50	0.5	950	364	1.62	2.40	2.54	-5.8
			300	345	0.60	2.71	2.63	+3.0
ethanol/water $\dot{L}/\dot{V} = 1$	50	0.5	300	345	0.45	2.60	2.80	-7.7

Table 1: Comparison of measured gas load factor $F_{V,fl}$ at flooding point and estimated acc. to CFD simulation data in combination with SBD model for different test systems by Maćkowiak (Maćkowiak, 2010), valid for investigated structured packing R500Y by RVT.

A comprehensive description of the experimental procedure is provided in the collaborative study between academia and industry (Neumann et al., 2025) .
In addition to the primary hydraulic parameters, this investigation elucidates the critical role of peripheral elements—specifically wipers—on the global hydrodynamic behaviour of the structured packing. The observed influence of these boundary features aligns with established literature, confirming their necessity in achieving uniform fluid distribution and minimizing wall effects (Figure 4 & Figure 5).
The knowledge of the resistance factor $\psi = f(Re_V, \varphi_P)$ is the most important factor for the prediction of BPD data for all types of random and structured packing (Maćkowiak, 2010, 2022).
According to this model, the flooding gas load factor $F_{V,fl}$ was calculated from CFD data and compared with the experimental values (Table 1). Quantitative analysis reveals a superior level of agreement between the experimental observations and the simulated datasets, with a maximum relative error of ± < 8%, as detailed in Table 1.

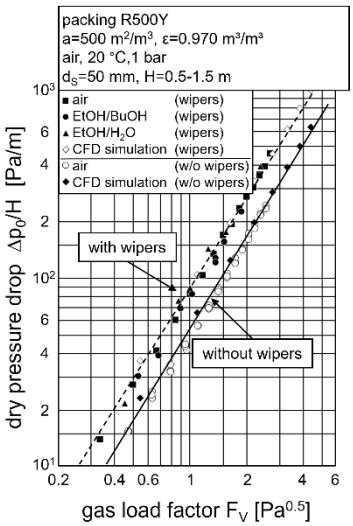

Figure 4: Comparison of experimental and CFD results for single-phase flow in a packed column filled with metallic structure packing R500Y with and without wall wipers.

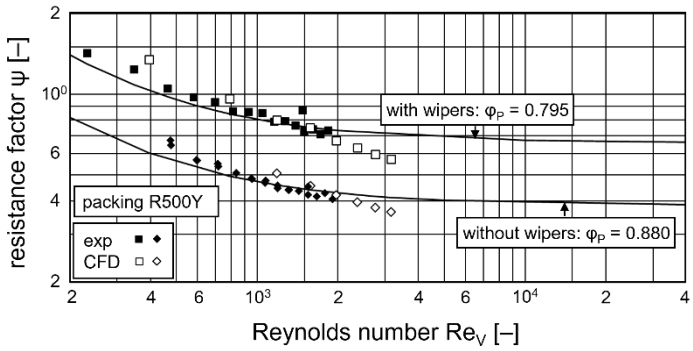

Figure 5: Resistance factor ψ as function of Reynolds number of gas $\psi = f(Re_V, \varphi_P)$ for investigated structured packing R500Y with and without wipers.

Ultimately, this research substantiates that the synergistic integration of CFD simulations and the SBD model provides a robust, rapid, and highly reliable methodology. By leveraging these high-accuracy CFD results as a primary predictive tool, the necessity for resource-intensive experimental campaigns is significantly mitigated, facilitating the streamlined modelling, optimisation, and scaling of structured packing performance data without the traditional reliance on extensive empirical testing.

3. Conclusions

The estimated flooding gas load factor and dry pressure drop characteristics were benchmarked against high-fidelity CFD simulations conducted for the commercial structured packing R500Y (RVT), as illustrated in Table 1 and Figure 5.
The determination of the BPD was executed via the SBD model, utilising the theoretical frameworks established by Maćkowiak (Maćkowiak, 2010, 2022).
The correlation between the CFD-derived values and the analytical model is very good; the simulation successfully captured the intricate gas-phase interactions and momentum transfer within the packing geometry with exceptional resolution.

Symbols

d_S	[m]	column diameter
Fl		at flooding point
F_V	[$Pa^{0.5}$]	gas load factor in relation to full column cross section
L | V		liquid phase | gas/vapour phase
$\dot{L}$ | $\dot{V}$	[kmol/h]	liquid molar flow | gas molar flow
p	[Pa]	pressure
$\Delta p_0/H$ | $\Delta p/H$	[Pa/m]	dry | irrigated pressure drop per 1 m packing height
u	[m/s]	velocity in relation to full column cross section
Greek symbols		
ε	[m^3/m^3]	void fraction of packing
φ_P	[-]	packing form factor (Maćkowiak, 2010)
ν_v	[m^2/s]	kinematic viscosity of gas or vapour
ρ	[kg/m^3]	density
ψ	[-]	resistance coefficient for single gas flow
dimensionless numbers		
$d_P = \frac{6 \cdot (1-\varepsilon)}{a}$		particle diameter
$\mathrm{Re_V} = \frac{u_v d_p}{(1-\varepsilon)\nu_V}$		Reynolds number for gas or vapour

References

Bertling, R., Hack, M., Ausner, I., Horschitz, B., Wehrli, M., & Kenig, E. Y. (2023). Simulation of liquid flow in structured packings using CFD-methods. *Chemical Engineering Science*, *269*. https://doi.org/10.1016/j.ces.2022.118405

Isoz, M., & Haidl, J. (2018). Computational-Fluid-Dynamics Analysis of Gas Flow through Corrugated-Sheet-Structured Packing: Effects of Packing Geometry. *Industrial and Engineering Chemistry Research*, *57*(34). https://doi.org/10.1021/acs.iecr.8b00676

Maćkowiak, J. (2010). Fluid Dynamics of Packed Columns. In *Fluid Dynamics of Packed Columns*. https://doi.org/10.1007/b98397

Maćkowiak, J. (2022). Rapid method for prediction of random packing performance based on minimized experimental effort. *12th International Conference on Distillation and Absorption, 18-21 September 2022, Toulouse - France*, 1–6.

Neumann, M., Xia, M., Pöschmann, R., Merkel, A., Staud, R., Schneider, H., Ehlert, T., Paschold, J., Müller, S., Harding, L. S., Neukäufer, J., Hiller, C., Ausner, I., Gäbler, A., Chromik, R., Maćkowiak, Jan, Maćkowiak, Jerzy, Sola Cervera, J. L., Geipel, C., Rehfeldt, S. (2025). Towards reliable HETP values: Lessons learned from standardized separation efficiency measurements. *Separation and Purification Technology*, *361*, 131436. https://doi.org/10.1016/J.SEPPUR.2025.131436

R. Byron Bird, Warren E. Stewart, & Edwin N. Lightfoot. (2006). *Transport Phenomena* (2nd ed.). Wiley.

Szulczewska, B., Zbicinski, I., & Górak, A. (2003). Liquid flow on structured packing: CFD simulation and experimental study. *Chemical Engineering and Technology*, *26*(5). https://doi.org/10.1002/ceat.200390089

Zuiderweg, F. J. (1969). *Recommended Test Mixtures for Distillation Columns*. Tbc Institution of Chemical Engineers.

Investigation of the Influence of Dynamic Operating Conditions on HETP Values Using a Miniaturized Distillation Measuring Cell

Julia Gramann [a], Amlie Merkel [a], Maria Polyakova [a], Marcus Grünewald [a]
[a] Ruhr University Bochum, Laboratory of Fluid Separations, Universitätsstraße 150, 44801 Bochum, Germany

ABSTRACT Reliable prediction of separation performance in distillation columns with structured packings requires a detailed understanding of hydrodynamics and mass transfer behaviour under changing operating conditions. Conventional design methods combine empirical correlations with experimental data obtained from laboratory- and pilot-scale studies. While these approaches are well established, their extrapolation to structured packings and real technical mixtures is often associated with increased effort and uncertainty, particularly with respect to HETP estimation and column sizing. In response to these challenges, the operating window of a miniaturized distillation column was investigated to assess the transferability of HETP data to industrial-scale packed columns and to support further process optimization. The results show that separation efficiency strongly depends on packing height, with increasing HETP values observed for larger packing heights due to rising mass-transfer resistances. While variations in the F-factor influence column performance within each configuration, elevated F-factors may lead to performance limitations caused by delayed boiling and local backflows. Overall, the findings provide new quantitative insight into packing-height-related scale effects under otherwise comparable hydrodynamic conditions. Furthermore, the stable and reproducible trends observed across the operating range confirm the suitability of miniaturized measuring cells for generating HETP data transferable to industrial-scale packed columns. The results support reliable model parameterization and provide a sound basis for improved scale-up strategies in the design of energy- and resource-efficient distillation columns.

KEYWORDS Miniaturized measuring cell, Scale-up, Distillation, Structured packings, Separation performance, HETP

1. Introduction

Distillation is one of the most widely applied separation techniques in the chemical and petrochemical industries. Owing to its high energy demand, improving the efficiency and reliability of distillation processes remains a central objective in process development [1,2]. In particular, the growing industrial use of structured packed columns, which are commonly applied in modern distillation columns due to their high separation efficiency and low pressure drop [2,3], requires a high level of design accuracy to ensure both efficient separation and energy-optimal operation. Consequently, reliable prediction of mass transfer performance and column efficiency is of central importance during process design.

Conventional design methodologies for structured packed distillation columns, however, are inherently associated with significant uncertainties. These methods are largely based on empirical correction factors, simplified models, and experimental data obtained from standard test systems that may not be representative of the actual industrial system. A key parameter in this context is the height equivalent to a theoretical plate (HETP), which is commonly determined using empirical correlations. While such correlations provide a practical basis for preliminary design, their applicability to real technical mixtures, modern structured packings, or non-standard operating conditions such as vacuum operation is often limited [4,5] This limitation arises because the empirical correlations and semi-empirical models used in column design require specific model parameters, which are predominantly supplied by packing manufacturers and are generally restricted to standard test systems, such as water/air, even for modern packings. As a result, key mixture- and packing-specific effects are often not explicitly captured during early design stages and are instead accounted for using empirical correction factors. These simplifications represent a major source of uncertainty in conventional scale-up procedures and may lead to conservative design margins and iterative redesign steps [6–8].

A further source of uncertainty arises from the late availability of mixture- and packing-specific data in the design process. Typically, laboratory-scale experiments are conducted using small column diameters, from which scale-up factors are applied to estimate industrial column performance. In parallel, pilot-scale studies are often employed to improve design reliability. However, the transfer of results between laboratory, pilot, and industrial scales involves multiple correction steps and assumptions. In practice, this introduces several transfer factors accounting for scale effects, hydrodynamics, and mass transfer behavior, which are often unreliable for non-ideal or complex systems. The inherent uncertainty associated with these scale-up procedures highlights the need for experimental validation, which is, however, often costly and time-consuming. Laboratory- and pilot-scale column experiments require substantial material, time, and energy, and technical mixtures are therefore frequently replaced by standardized test systems. As a result, the extrapolation of experimental results to industrial conditions relies on scaling factors that may further

increase uncertainty. Consequently, early design decisions are commonly based on rough measurements and incomplete system knowledge. [6,9] As a result, the conventional design workflow becomes highly time- and material-intensive, requiring extensive experimental effort at different scales. Despite this effort, the cumulative uncertainties associated with scale-up procedures and empirical correlations may still result in significant deviations between predicted and actual industrial performance. This highlights the need for alternative approaches that enable a more direct, accurate, and efficient determination of mass transfer characteristics for structured packed columns under industrially relevant conditions.

To address these limitations, miniaturized measuring cells have emerged as a promising laboratory-scale approach for investigating the performance of structured packed columns. These systems enable early mixture- and packing-specific characterization of hydrodynamics and mass transfer under well-defined conditions while significantly reducing experimental effort and material consumption [4,5,10]. By providing high-resolution data and realistic HETP values at an early stage of process development, miniaturized measuring cells support informed decision-making and enable a more efficient, knowledge-based scale-up of packed distillation columns.

2. Materials and Methods

2.1. Experimental setup

At Ruhr University Bochum, *Hapke (2022)* [4] established a concept of a miniaturized measuring cell for absorption studies in which a rectangular cross-section is used to enable controlled investigations of hydrodynamics. Building on this concept, a miniaturized distillation measuring cell was developed for characterizing modern structured packings under well-defined operating conditions. Its compact design reduces material and energy use while allowing precise control of flow rates, temperature, and liquid distribution. Short test cycles, high reproducibility, and low measurement uncertainty enable small-scale reproduction of industrial effects and generation of data suitable for direct scale-up [5].

Figure 1 shows the miniaturized distillation cell with six individually labeled modular sections, which are connected by flanged joints to enable rapid reconfiguration while maintaining precise alignment. [5]. The bottom section serves as a double-walled reboiler heated with thermal oil to provide stable vapor generation. In earlier experimental studies, the formation of a bubble layer in the column bottom was observed with liquid entering the sample section. To prevent this effect, an empty intermediate section was integrated directly above the column bottom, which suppresses boiling in the subsequent sampling and separation sections.

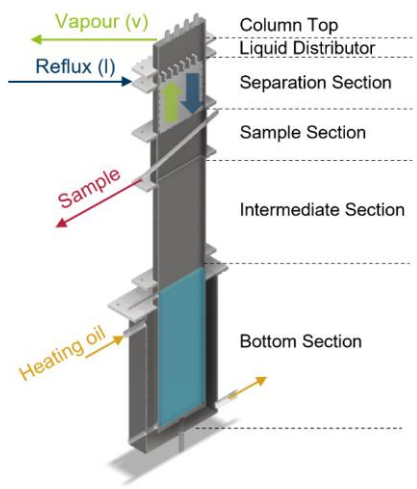

Figure 1: Schematic illustration of the miniaturized distillation measuring cell, showing the six modular sections and inlet and outlet streams

The sampling section, located immediately below the packing, is equipped with a cross lance that collects an integral liquid sample across the entire column width, ensuring reproducible and load-independent sampling. The separation section contains structured packings of the type Mellapak™ 500.Y supplied by Sulzer Chemtech©, all equipped with wall wipers to prevent liquid flow along the column walls. The modular design allows the installation of packings with dimensions of 100x100 mm and 200x100 mm (see Figure 2), as well as a packing interface comprising two of the 100x100 mm packings (2x100x100 mm). In conventional columns the packing sheets are rotated by 90° to promote uniform liquid redistribution, but this is not feasible in the rectangular geometry of the measuring cell. The packing plates are therefore rotated by 180°, creating a zigzag arrangement that improves fluid distribution and maintains a sufficient interface for mass transfer [11]. The liquid distributor, located above the packing section, delivers a controlled liquid feed and ensures uniform wetting of the packing surface, which is essential for reproducible mass

transfer. It distributes the reflux from the reflux drum over the packing through fourteen angled capillary tubes, resulting in one drip point per channel and an effective drip-point density of 19,000 m^{-2}.

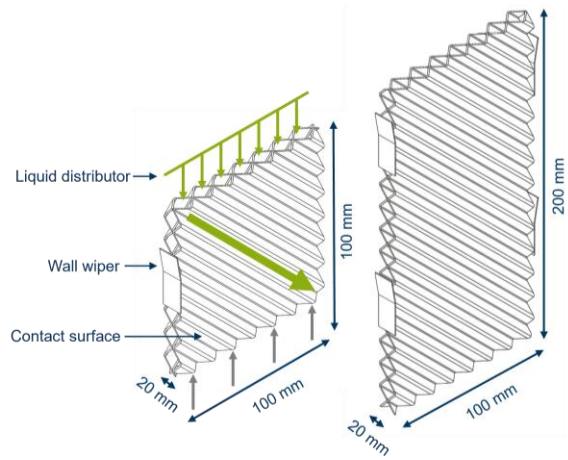

Figure 2: Schematic illustration of the packing configurations with wall wipers and the separation section, left: 100x100 mm packing, right: 200x100 mm packing

2.2. Experimental procedure and evaluation

All measurements are conducted at 300 mbar under total reflux using a cyclohexane/n-heptane (C_6/C_7) mixture. Vapor generated in the reboiler is condensed, collected in a reflux drum and then reheated to near-boiling conditions before being redistributed over the packing. Under these conditions, steady state is typically reached within 20 minutes. The experimental operating window is defined by thermal-oil temperatures of T_B = 65, 73, 75, 87°C, corresponding to gas loads (F-Factors) of F_G = 0.4 - 1.5 $Pa^{0.5}$. Previous studies identified F_G = 0.4 $Pa^{0.5}$ as the lower limit due to increasing maldistribution [5]. Liquid loads between u_L = 0 - 0.7 $m^3 \cdot m^{-2} \cdot h^{-1}$ allow the systematic characterization of both dry and irrigated operation.

The height equivalent to a theoretical plate (HETP) is determined by evaluating the separation efficiency of the column using a stage model analogous to the McCabe-Thiele approach [12], in which the MESH equations are solved iteratively. A detailed description of the methodology is given by *Pöschmann et al. (2023)* [10]. For the nearly ideal cyclohexane/n-heptane system under total reflux and short packed beds, the number of theoretical stages is estimated using the Fenske equation [13], assuming constant relative volatility. The HETP is then calculated as the ratio of the packed-section height (H_P) to the number of theoretical stages (n_{th}) providing a reproducible measure of the packing performance under the applied operating conditions:

$$HETP = \frac{H_P}{n_{th}} \tag{1}$$

This approach ensures a consistent and comparable evaluation of separation efficiency across all investigated packing configurations.

3. Results and Discussion

3.1 Effect of Packing Height on HETP

The influence of packing height on separation efficiency was investigated using three structured packing configurations: 100×100 mm, 2×100×100 mm, and 200×100 mm. Mean HETP values were evaluated as a function of the F-factor to assess the column performance. The F-factors were measured three times to validate reproducibility, thus obtaining three series of measurements. For the evaluation, the arithmetic mean value of the measuring points over the last 10 min was calculated from the sum of the individual measured values divided by the number of measured values for both the HETP value and the F-factor, and the respective error was determined using the standard deviation. The comparison of the HETP values as a function of the F-factor for all three setups are shown in Figure 3.

For the 100×100 mm packing (setup 1), the measured HETP values range from 0.17 m to 0.20 m, with a mean HETP value of $HETP_{mean,1}$ = 0.19 m. At the lowest investigated F-factor (F_G = 0.41 $Pa^{0.5}$), an HETP value of 0.19 m was obtained. With increasing F-factor, the HETP initially decreases, reaching values of 0.18 m and 0.17 m at the intermediate F-factors. A further increase of the F-factor results in a renewed increase in HETP, yielding a value of 0.20 m at F_G = 1.50 $Pa^{0.5}$. The elevated HETP observed at the lowest F-factor can be attributed to operation close to the minimum F-factor (F_{min} = 0.4 $Pa^{0.5}$, see chapter 2.2). Under these conditions, insufficient hydrodynamic interaction

is known to impair liquid distribution, promoting maldistribution effects and reducing effective mass transfer efficiency [14,15]. At the intermediate F-factors, more stable hydrodynamic conditions lead to improved separation performance and reduced HETP values. At higher F-factors, the increase in HETP indicates the onset of unfavorable hydrodynamic effects, such as increased flow resistance or local backflows, which have been reported to negatively affect mass transfer efficiency in structured packings [15,16].

The 2×100×100 mm packing (setup 2) exhibited significantly higher HETP values compared to the single-layer 100×100 mm packing. The HETP values ranged from 0.29 m to 0.34 m, with $HETP_{mean,2}$ = 0.32 m, which represents an increase of approximately 68 % compared to setup 1. This clearly demonstrates that separation efficiency decreases with increasing packing height, which is reflected by the corresponding increase in HETP [17,18]. The observed deterioration is most likely caused by maldistribution of vapor and liquid flows within the column [18]. At F_G = 0.46 $Pa^{0.5}$, an HETP value of 0.34 m is obtained. With increasing F-factor, the HETP continuously decreases, reaching 0.31 m at F_G = 1.53 $Pa^{0.5}$. This reduction in HETP reflects an improvement in mass transfer performance within the operating window investigated [15,16]. The observed trend can be attributed to enhanced evaporation of the C_6 component and a gradual suppression of the boiling layer, resulting in more favorable hydrodynamic conditions [14]. At low F-factors, the presence of a boiling layer limits separation efficiency, resulting in elevated HETP values [14,15]. With increasing F-factor, the boiling layer becomes less dominant, and evaporation of C_6 increasingly contributes to the separation process, leading to a more homogeneous hydrodynamic regime and improved column performance [15,16]. Within the investigated range, no adverse hydrodynamic effects were observed at higher F-factors, indicating operation below critical loading conditions [15].

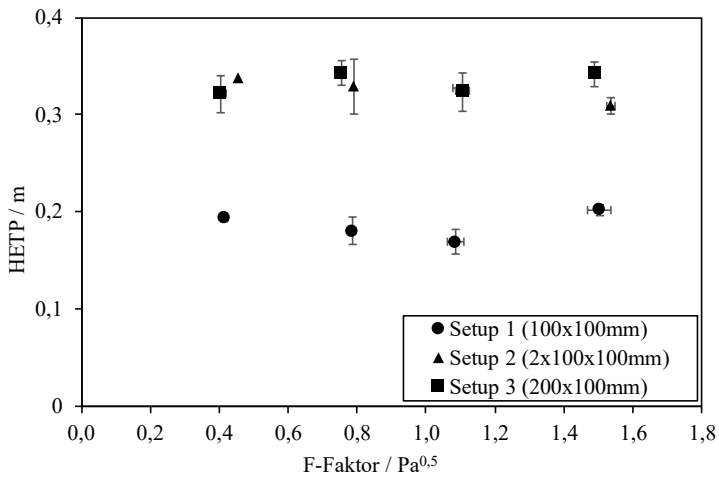

Figure 3: Comparison of the men HETP values as a function of the mean F-factors for the standard test mixture C6/C7 for the setups 1, 2 and 3 at 300 mbar.

For the 200×100 mm packing (setup 3), HETP values were found to be in the range of 0.32 m to 0.34 m, with $HETP_{mean,3}$ = 0.33 m, which corresponds to an increase of approximately 74% compared to setup 1. For this setup, the HETP values exhibit a trend like that observed for setup 1. At F_G = 0.40 $Pa^{0.5}$, an HETP of 0.32 m is obtained. Increasing to F_G = 0.75 $Pa^{0.5}$ results in a slight increase in HETP to 0.34 m. With a further increase to F_G = 1.10 $Pa^{0.5}$, the HETP decreases again to 0.32 m, followed by a renewed increase to 0.34 m at F_G = 1.49 $Pa^{0.5}$. Overall, the results indicate only minor variations in HETP over the investigated F-factor range, suggesting a comparable hydrodynamic behavior to setup 1.

It was further observed that the influence of the packing interface on separation efficiency is not very pronounced, as comparable HETP values were obtained for setup 2 and setup 3. As discussed previously, the reduction in separation efficiency with increasing packing height is mainly attributed to enhanced maldistribution of the liquid flow within the column. Overall, the results show that separation efficiency strongly depends on packing height, with significantly higher HETP values observed for increased packing heights irrespective of the packing configuration. Although changes in the F-factor influence HETP, the results indicate that increased packing height remains the primary factor limiting separation efficiency due to enhanced maldistribution.

3.2 Proof of Concept: Comparison with Cylindrical Test Rigs

To validate the experimental results, a proof of concept was established by comparing the HETP values obtained from the miniaturized measurement cell with data provided by the industrial partners Evonik Operations GmbH and BASF SE. The test rigs, DN80 (Evonik) and DN50 (BASF), are conventional cylindrical columns operated at a pressure of 300 mbar using C_6/C_7 as standard test system as well. Despite differences in column diameter and geometry,

the comparable operating conditions allow for a meaningful evaluation of HETP trends and F-factor dependencies (see Figure 4) [15].

The HETP values measured in the BASF DN50 column range from 0.18 m to 0.23 m ($HETP_{mean,B}$ = 0,21m) over F-factors of F_G = 0.21 - 1.79 $Pa^{0.5}$. This range is in good agreement with the HETP values obtained for the 100 × 100 mm packing in the miniaturized setup (0.17 – 0.22 m), indicating that the measurement cell can reproduce the separation efficiency observed in the cylindric test rig. The mean HETP value of the DN50 column is approximately 11% higher than that of setup 1 ($HETP_{mean,B}$ = 0,21m compared to $HETP_{mean,1}$ = 0,19m), which represents a reasonable deviation considering the differences in column diameter, geometry and larger range of gas loads. The slight increase in HETP at medium F-factors in the DN50 column reflects the trend observed in setup 1, where higher F-factors lead to a minor deterioration in performance, which has also been reported in the literature for structured packings operated under comparable conditions [15,16].

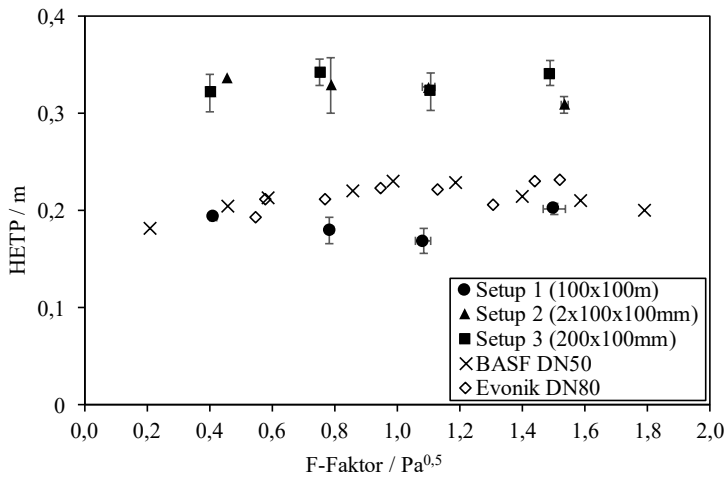

Figure 4: Comparison of the mean HETP values as a function of the mean F-factors for the standard test mixture C6/C7 for the setups 1, 2 and 3 at 300 mbar with HETP values of cylindrical test rigs provided by the industrial partners partners

Similarly, the Evonik DN80 column exhibits HETP values between 0.19 m and 0.23 m ($HETP_{mean,E}$ = 0,22m) for F-factors of F_G = 0.55 – 1.52 $Pa^{0.5}$. Although this column is operated at a larger scale, the HETP values remain comparable to those obtained in setup 1, with the mean HETP value being approximately 16% higher than that of the miniaturized setup ($HETP_{mean,E}$ = 0,22m compared to $HETP_{mean,1}$ = 0,19m). The observed trends, characterized by a slight increase in HETP at medium F-factors and a decrease at the highest F-factor, are consistent with the behavior observed in setups 1 and 3 and align well with previously reported hydrodynamic and mass transfer trends for structured packings [14,15].

Overall, the comparison demonstrates that experiments using small-scale structured packings can capture both the magnitude and the F-factor dependence of HETP observed in the conventional cylindrical test rigs. The results further indicate that increasing packing height leads to higher HETP values across both experimental platforms, highlighting the importance of packing height and flow distribution for separation efficiency. [15]

4. Conclusion and Outlook

4.1 Conclusion

In this study, the effect of packing height on the separation efficiency of structured packed columns was systematically investigated using a miniaturized measurement cell. The results clearly demonstrate that packing height is the dominant parameter influencing HETP, with significantly higher HETP values observed for increased packing heights, independent of the specific packing configuration. While variations in the F-factor affect separation performance within each setup, these effects are secondary compared to the pronounced deterioration caused by enhanced maldistribution at larger packing heights.

The comparison with data from DN50 and DN80 columns further confirms the validity of the experimental approach. The miniaturized measurement cell successfully reproduces both the magnitude of HETP values and their dependence on the F-factor observed in the conventional cylindrical test rigs, demonstrating its suitability as a tool for early-stage performance evaluation of structured packings.

4.2 Outlook

Based on the results of this work, future experiments should initially focus on F-factors in the range of F_G = 0.75 – 1.50 $Pa^{0.5}$ to more precisely identify the onset of unfavorable hydrodynamic phenomena observed at

elevated operating loads. Investigating this targeted operating window will allow a clearer distinction between beneficial mass transfer effects and the beginning of performance deterioration.

Future work should further extend the experimental scope to include additional operating parameters, such as liquid and vapor loading, as well as alternative structured packing geometries, to deepen the understanding of the scale-up effects identified in this study. In particular, the pronounced influence of packing height on HETP and the deviations observed at higher F-factors underline the need for targeted investigations of hydrodynamic phenomena in the column bottom.

To address the effects of delayed boiling, future studies should investigate the formation and development of bubble layers in the column bottom in more detail. The integration of an endoscopic camera into the column bottom would enable direct visualization of bubble formation and boiling behavior under varying operating conditions and support the identification of suitable F-factor ranges for reliable measurements. This may be complemented by a potential enlargement of the empty lance section to further suppress liquid entrainment and mitigate undesired boiling effects.

In addition, a detailed quantification of liquid maldistribution within the packing should be conducted. Systematic measurements of the extent and evolution of liquid maldistribution would provide valuable insight into its contribution to the observed HETP trends and support the development of more reliable, packing-specific experimental correlations for structured packed columns.

References

[1] A.A. Kiss, Ž. Olujić, A review on process intensification in internally heat-integrated distillation columns, Chemical Engineering and Processing: Process Intensification 86 (2014) 125–144. https://doi.org/10.1016/j.cep.2014.10.017.

[2] A.A. Kiss, R. Smith, Rethinking energy use in distillation processes for a more sustainable chemical industry, Energy 203 (2020) 117788. https://doi.org/10.1016/j.energy.2020.117788.

[3] H. Leuner, M. Hapke, J. Sacher, M. Grünewald, J.-U. Repke, Miniaturisierte Messzellenversuche als potenzielles Auslegungswerkzeug für Kolonnen mit strukturierten Packungen, Chemie Ingenieur Technik 91 (2019) 110–117. https://doi.org/10.1002/cite.201800057.

[4] M. Hapke, Entwicklung einer Miniaturmesszelle zur zeit- und kosteneffizienten Charakterisierung der Fluiddynamik in strukturierten Packungen. Dissertation, Bochum Deutschland, 2022.

[5] A. Merkel, M. Polyakova, M. Grünewald, A miniaturized measuring cell to assist in the design of packed columns for distillation, Separation and Purification Technology 380 (2026) 135282. https://doi.org/10.1016/j.seppur.2025.135282.

[6] U. Eiden, Scale-up von Destillationskolonnen, Chem.-Ing.-Tech 67 (1995) 269–279.

[7] L. Deible et al., Investigations into the Scale-Up of Laboratory Distillation Columns, Inst. Chem. Eng. Symp. Series (1997) 1021–1030.

[8] L. Deible et al. (Ed.), Miniplant-Technik: In der Prozessindustrie, 1st ed., Wiley-VCH Verlag GmbH & Co. KGaA, Weinheim, 2006.

[9] M. Schultes, Research on Mass Transfer Columns: passé?, Chem Eng & Technol 36 (2013) 1539–1549. https://doi.org/10.1002/ceat.201300192.

[10] R. Pöschmann, J. Paschold, S. Mueller, L.-S. Harding, N. Lachmann, C. Hiller, I. Ausner, A. Gäbler, M. Illner, G. Brösigke, J.-U. Repke, Will laboratory and pilot plant columns soon become superfluous? – A concept for the determination of structured packing characteristics in a measuring cell under distillation conditions, Separation and Purification Technology 325 (2023) 124617. https://doi.org/10.1016/j.seppur.2023.124617.

[11] A. Gorak, Z. Olujic (Eds.), Distillation: Equipment and Processes, Elsevier, 2014.

[12] W. L. McCabe (Ed.), Unit Operations of Chemical Engineering, McGraw-Hill, New York, 1993.

[13] M.R. Fenske, Fractionation of Straight-Run Pennsylvania Gasoline, Industrial and Engineering Chemistry (1932).

[14] J. Stichlmair et al., Distillation: Principles and practice, Second edition, Wiley-AIChE, Hoboken, New Jersey, 2021.

[15] M.S. R. Billet, Prediction of Mass Transfer Columns with Dumped and Arranged Packings, Chemical Engineering Research and Design 77 (1999) 498–504.

[16] J. Rocha et al., Distillation Columns Containing Structured Packings, Ind. Eng. Chem. Res. (1996) 1660–1667.

[17] L. Valenz, J. Haidl, V. Linek, The Effect of Column Diameter and Packing Height on the Pressure Drop and on the HETP of Structured Packings, Ind. Eng. Chem. Res. 52 (2013) 5967–5974. https://doi.org/10.1021/ie302397q.

[18] N.I. Pecherkin, A.N. Pavlenko, V.E. Zhukov, A.D. Nazarov, G. Meski, P. Houghton, Mixture separation in distillation column with semicylindrical structured packing, J. Phys.: Conf. Ser. 1105 (2018) 12064. https://doi.org/10.1088/1742-6596/1105/1/012064.

Additively-Manufactured Lab-Scale Distillation Packings for Process Development and Scale-up

Mohamed Adel Ashour[1], *Dennis Stucke*[1], *Thomas Grützner*[1]
[1]*Ulm University, Institute of Chemical Engineering, Laboratory of Thermal Process Engineering, Albert-Einstein-Allee 47, 89081 Ulm, Germany*

Abstract
Additive manufacturing enables rapid development of structured packings for miniaturized laboratory distillation columns used in process development and scale-up. This paper introduces the novel HP-Pak design and compares it to a reference structure, the XW-Pak introduced in the D&A 2022 conference. A CFD-based screening workflow guides the design and interpretations. It starts with a dry pressure drop constraint, then a gas-side mass transfer proxy, and finally liquid-interface-related corrections based on irrigation simulations. The HP-Pak showed 29.4 % to 45.4 % improved $HETP$ values compared to the XW-Pak across the measurement range coming with a penalty of up to 2.7 folds increase in pressure drop.

1. Introduction

Distillation continues to be the backbone of industrial separation processes and remains indispensable in the chemical and petrochemical sectors. It represents one of the largest consumers of energy in chemical production. Consequently, even incremental improvements in column design and scale-up can translate into substantial economic and energetic benefits. This places emphasis on robust and reliable approaches during the stages of process development.

Lab-scale packed columns are often used to generate data for new or uncommon mixtures during scale-up. Industrial practice relies on calibrated laboratory columns combined with transferability correlations to larger diameters [1,2]. Conventional calibrated columns are recommended to have a minimum diameter of 50 mm [1]. Further miniaturization to 20 mm (DN20) diameter reduces chemical inventory and operational effort but amplifies wall effects and exposes limitations of conventional packing manufacturing methods, limiting reliable adaptation of DN20 columns.

Recent efforts have addressed these limitations using additive manufacturing (AM) from different perspectives and presented AM packings tailored for DN20, including the XW-Pak design that is used as a reference in this paper [3–5]. Building on these learnings, the present study introduces the novel HexaPy-Pak (HP-Pak) and evaluates it against XW-Pak using pragmatic CFD screening and experimental validation.

2. Materials and methods

The present contribution focuses on the development and comparative assessment of structured packings. Accordingly, both the CFD and experimental approaches are only outlined concisely and further details can be found in previous work [3–5].

2.1 CFD screening approach

In this study, simulations are a comparative screening tool for packing development rather than as a predictive description of coupled gas-liquid mass transfer. Single-phase gas flow simulations and two-phase liquid irrigation simulations were carried out independently in OpenFOAM utilizing CAD models of the reference XW-Pak and the new HP-Pak structures with the setup shown in Figure 1.

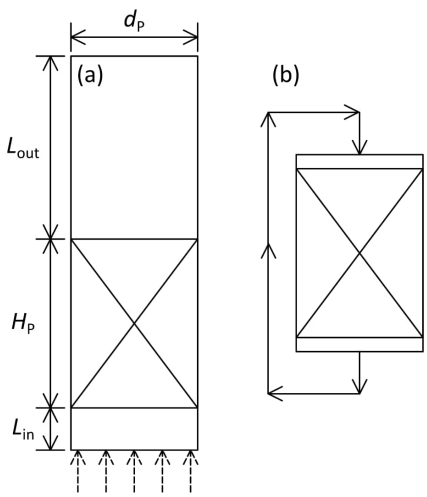

Figure 1: CFD simulations simplified geometric setup: (a) gas phase and (b) irrigation.

The hierarchical CFD screening strategy starts with a representative packing layer in a DN20 cylinder. In a first step, gas-phase stationary simulations are performed at an F-factor of 1 Pa$^{0.5}$ using the $k-\omega$ SST model with the setup shown in Figure 1a. They yield two integral quantities, the first is the dry specific pressure drop $\Delta p_{\mathrm{dry}}/H_{\mathrm{P}}$, applied as a strict exclusion criterion with a threshold of 3 mbar m^{-1}. The second integral quantity is an *idealized* volumetric mass transfer coefficient $(\beta a)_{\mathrm{geo}}$ obtained from the transport of a hypothetical passive scalar c. The value of the passive scalar was set as constant values of c_{in} at the inlet and c_{PW} at all solid surfaces of the packing and its surrounding walls. This configuration enforces a scalar flux from the gas toward the geometric surface area $A_{\mathrm{geo,PW}}$ ideally available for the creation of interfacial contact area. $(\beta a)_{\mathrm{geo}}$ can be calculated via mass balance and a logarithmic mean driving force as in equation (1). Despite $(\beta a)_{\mathrm{geo}}$ not representing a validated transfer coefficient, it still provides a comparative proxy for gas-side mass transfer *potential* under the ideal assumptions of infinitely thin liquid film and full wetting, which was previously proven to satisfactorily predict experimental trends. [4]

$$(\beta a)_{\mathrm{geo}} = \beta a_{\mathrm{geo,PW}} = \frac{\dot{V}}{A_{\mathrm{geo,PW}}} \cdot \ln \frac{c_{\mathrm{PW}} - c_{\mathrm{in}}}{c_{\mathrm{PW}} - c_{\mathrm{out}}} \cdot a_{\mathrm{geo,PW}} \tag{1}$$

In the second CFD screening step, two-phase transient irrigation simulations are performed, at a liquid load equivalent to an F-factor of 1 Pa$^{0.5}$ assuming total reflux conditions, using a modified volume-of-fluid *interFoam* solver with the setup shown in Figure 1b and described in more detail in [5]. Cyclic boundary conditions of the top and bottom patches enable the achievement of a developed irrigation state in few seconds of simulation time at a reduced computational cost. After this irrigation state is reached, the liquid interface is reconstructed as an iso-surface, assuming it lies at a volume fraction α_{L} of 0.5, and integral parameters are obtained as time-averaged quantities over a quasi-steady period. The total interfacial area A_{int}, specific interfacial area a_{int}, and relative specific interfacial area $a_{\mathrm{rel}} = a_{\mathrm{int}}/a_{\mathrm{geo,PW}}$ can all be calculated from the iso-surface. a_{rel} can then be used to correct $(\beta a)_{\mathrm{geo}}$ from the gas-phase simulations for partial wetting as shown in equation (3).

Moreover, due to the decoupled nature of the two simulation types, an *interfacial mobility distribution* is constructed as shown in Figure 3 to consider that not all portions of the interfacial area contribute equally to mass transfer. The distribution is obtained by ascendingly sampling the velocity magnitude $u_{\mathrm{L,int,i}}$ directly on the liquid interface

in uniform discrete steps and calculating their corresponding interfacial area fractions $A_{\mathrm{int,i}}/A_{\mathrm{int}}$. Then, an *interfacial mobility factor* ϕ is derived from the distribution as defined in equation (2). This factor represents an integral correction factor where each interfacial area fraction is weighted by how fast it moves relative to a maximum reference velocity, taken to be the 99.9th interface velocity percentile. After the partial wetting adjustment, $(\beta a)_{\mathrm{geo}}$ is further corrected by ϕ as in equation (3) thus yielding a single ranking index I_{IMC} that serves as the primary CFD-based ranking metric within the present screening framework. I_{IMC} should not be interpreted as a quantitative prediction of experimental mass transfer but as an empirical comparative index that integrates gas-phase transport potential with interface availability and mobility.

$$\phi = \sum_{\mathrm{i}} \left(\frac{A_{\mathrm{int,i}}}{A_{\mathrm{int}}} \cdot \frac{u_{\mathrm{L,int,i}}}{u_{\mathrm{L,int,99.9\%}}} \right) \tag{2}$$

$$I_{\mathrm{IMC}} = (\beta a)_{\mathrm{geo}} \cdot a_{\mathrm{rel}} \cdot \phi \tag{3}$$

Additionally, valuable insights into the bulk flow of the gas and liquid phases can be obtained through constructing *gas transverse mobility* and *liquid mobility distributions*. Both plots are derived with the same logic as the interfacial mobility distribution but using bulk volume fractions instead of area fractions. The gas volume fractions $V_{\mathrm{G,i}}/V_{\mathrm{G}}$ over the transverse velocity magnitude, defined as $u_{\mathrm{G,trans}} = \left(\mathrm{u}_{\mathrm{G},x}^2 + \mathrm{u}_{\mathrm{G},z}^2\right)^{0.5}$, are calculated from the gas-phase simulations. While the liquid volume fractions $V_{\mathrm{L,i}}/V_{\mathrm{L}}$ over the liquid velocity magnitude are computed from the irrigation runs. Also, a wall-to-packing wetting ratio ψ is defined in equation (4) to further quantify the extent of preferential liquid coverage of the column wall. Both the bulk mobility distributions and ratio ψ are not used for ranking purposes but rather to deepen the understanding.

$$\psi = \frac{A_{\mathrm{wet,W}}/A_{\mathrm{geo,W}}}{A_{\mathrm{wet,P}}/A_{\mathrm{geo,P}}} \tag{4}$$

Finally, absolute agreement of CFD-driven data with experimental values is not to be expected, given the decoupled nature of the screening strategy and known mechanistic limitations such as turbulence modelling inaccuracies and interface smearing due to finite and coarse mesh. Nonetheless, the simulations provide robust metrics that allow comparing different geometries via physically-motivated criteria.

2.2 Experimental setup overview

Experiments were carried out in a flexible lab-scale distillation setup [3]. The test rig combines standard equipment with polyamide 12 column components produced by selective laser sintering. The measurements are performed with the cyclohexane *n*-heptane mixture under total reflux at 900 mbar in an AM DN20 column of 1 m packed height. Above and below the packing, a differential pressure sensor is connected, and samples can be withdrawn for composition analysis. Thus, irrigated specific pressure drop $\Delta p_{\mathrm{irr}}/H_{\mathrm{P}}$ and separation efficiency can be quantified. The column temperatures and reflux flow are measured, allowing the determination of the F-factor. Therefore, the experiments produce classic plots of $HETP$ and $\Delta p_{\mathrm{irr}}/H_{\mathrm{P}}$ over the F-factor.

3. Results and discussion

3.1 Geometric and CFD characterization

Figure 2 shows the design of the new HP-Pak compared to the reference XW-Pak. The HP-Pak unit cell (UC) starts from a hollow hexagonal bipyramid, consisting of two

mirrored pyramids sharing a regular hexagonal base, thus the full name HexaPy-Pak. Then, three alternating faces are cut from the top pyramid followed by the same cut to the bottom pyramid rotated by 60° around the vertical axis. This results in the repetitive UC in Figure 2b. The UC is multiplied horizontally in a way that allows the exact matting of the top and bottom triangular-like faces forming a web or grid of interconnected rhombic-shaped bars referred to as crosspieces. This layer is cylindrically cut to the DN20 diameter and stacked vertically reaching the desired packing height H_{P}.

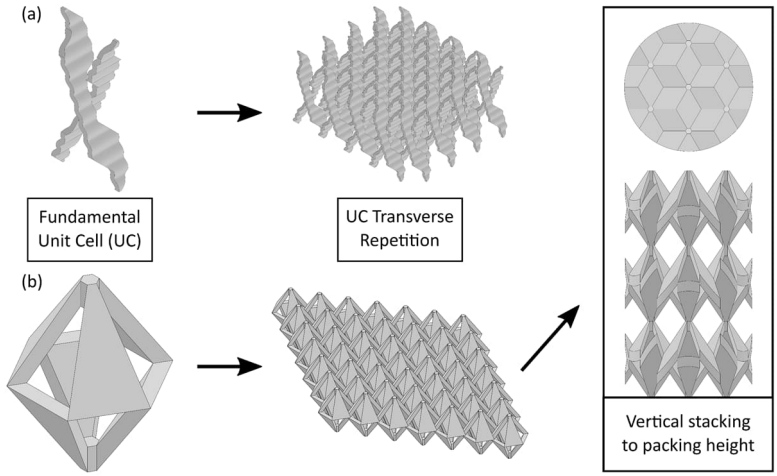

Figure 2: Geometric characteristics comparison: (a) XW-Pak vs (b) HP-Pak.

The vertical layers are joined at the top and bottom tips of each UC, forming hypothesized liquid remixing points, facilitating liquid combination and redistribution in three directions. Moreover, the six vertices of the pyramid base act as remixing points as the interconnected crosspieces meet. The XW-Pak vertical stacking is similar with the distinction that X-shaped UC would: (1) allow the descending liquid redistribution in only two directions, and (2) provide only one remixing points at the UC center.

As for the hierarchical CFD framework, it is implemented for only one HP-Pak variant with close specific geometric surface and void fraction to the XW-Pak with Table 1 summarizing the results. The HP-Pak exhibits a 59.7 % higher dry specific pressure drop than the XW-Pak despite the comparable void fraction. Moreover, HP-Pak shows 23.8 % higher idealized volumetric mass transfer coefficient $(\beta a)_{\mathrm{geo}}$ indicating a better gas-side transport potential under the fully wetted surface assumption.

Table 1: Summary of geometric parameters and CFD simulations results

Packing		XW-Pak	HP-Pak
Geometric characteristics	Void fraction ε / 1	88.6 %	88 %
	Specific geometric surface area $a_{\mathrm{geo,PW}}$ / m^{2}m^{-3}	529	583
Gas-phase simulations	Dry specific pressure drop $\Delta p_{\mathrm{dry}}/H_{\mathrm{P}}$ / mbar m^{-1}	1.24	1.98
	Idealized volumetric mass transfer coefficient $(\beta a)_{\mathrm{geo}}$ / s^{-1}	10.20	12.63
Irrigation simulations	Time-averaged specific interfacial area a_{int} / m^{2}m^{-3}	286.51	229.30
	Relative wall-to-packing liquid coverage ratio ψ / 1	1.197	1.595
	Relative specific interfacial area a_{rel} / 1	0.541	0.393
	Interfacial mobility factor ϕ / 1	0.150	0.204
Combination	Interfacial-mobility-corrected ranking index I_{IMC}	0.830	1.013

In contrast to $(\beta a)_{\mathrm{geo}}$ trend, irrigation runs show that the XW-Pak creates 25 % more specific interfacial area despite the higher geometric one of the HP-Pak. In addition, the ratio ψ values indicate a stronger preferential wall wetting for HP-Pak. Despite these unfavorable trends, HP-Pak exhibits a higher interfacial mobility factor. After

correcting $(\beta a)_{\mathrm{geo}}$ by both a_{rel} and ϕ, the higher value of the ranking index I_{IMC} favors HP-Pak. To further explore this, the interfacial mobility distribution is plotted in Figure 3.

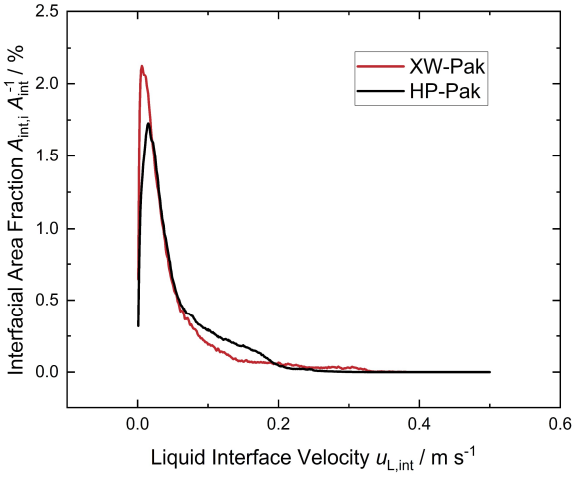

Figure 3: Comparison of interfacial mobility distributions from irrigation simulations.

As illustrated in Figure 3, XW-Pak shows a larger fraction of interfacial area concentrated at lower interface velocities. In contrast, HP-Pak shifts a good portion of the interfacial area toward moderate velocities, while exhibiting a more pronounced distribution tail. Moreover, the HP-Pak shows better statistical interface velocity descriptors such as 8.9 % higher volume-averaged mean and 25.9 % increased median velocities, all while maintaining a lower coefficient of variation of the interface velocity spectrum. Combining all these observations hints towards a statistically more homogenous but mobile liquid interface for the HP-Pak over the XW-Pak.

3.3 Experimental performance

Figure 4 compares the measured separation efficiency and pressure drop. HP-Pak exhibits 29.4 % to 45.4 % lower $HETP$ values than the XW-Pak across the investigated range. The superior HP-Pak's $HETP$ comes with a remarkably higher pressure drop culminating to almost three folds at the highest F-factor. The experimental results therefore confirm the trend and trade-off indicated by the earlier CFD screening.

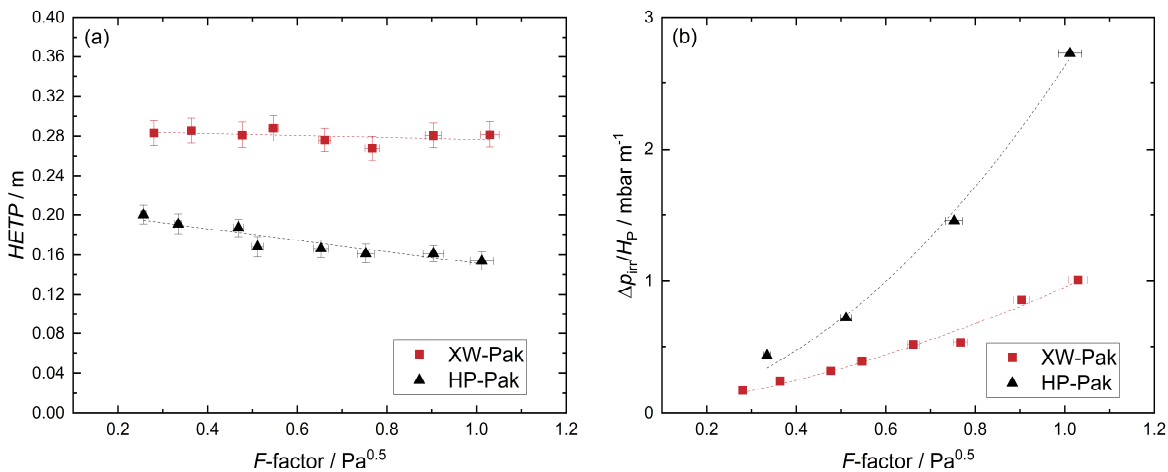

Figure 4: Experimental comparison plots: (a) separation efficiency, (b) irrigated pressure drop.

Deeper insights can be obtained from the CFD simulations by analyzing the bulk mobility distributions in Figure 5 that when interpreted within the defined screening logic, they offer plausible explanations for the observed experimental trends.

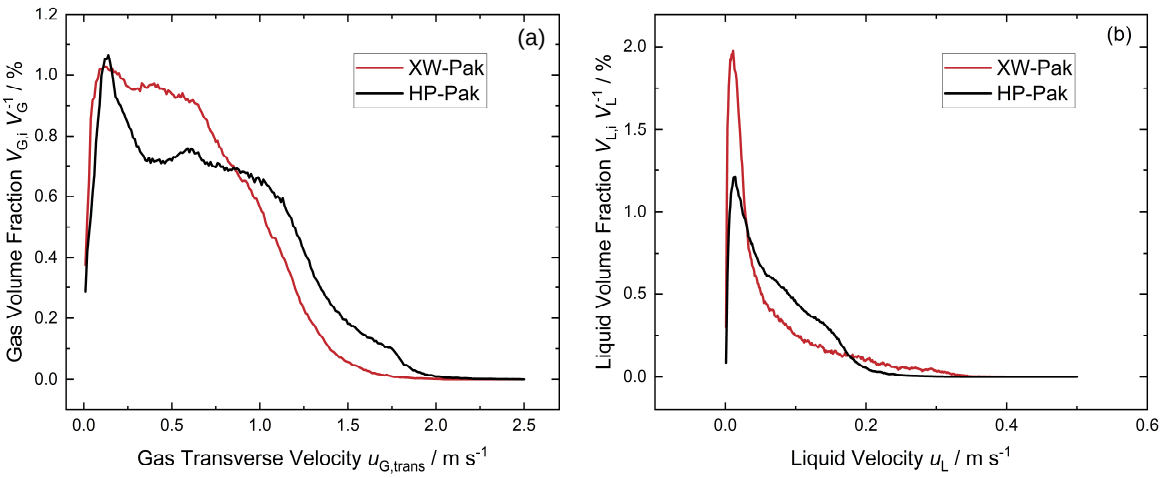

Figure 5: Bulk mobility distributions: (a) gas transverse mobility and (b) liquid mobility.

On the gas side, HP-Pak shifts a larger fraction of the gas volume toward higher transverse velocities. This is reflected by a higher median transverse velocity as well as the substantially larger tail fraction. This indicates stronger lateral mixing and flow redirection, consistent with a geometry that forces stronger non-axial motion and interaction between the gas and mass transfer surface. Such behavior explains the higher pressure drop and the enhanced gas-phase transport. On the liquid side, the HP-Pak distribution shows more liquid volume remaining closer to the mean velocity, as indicated by a lower coefficient of variation in Table 2. Despite the higher median velocity of the HP-Pak, the upper quantile is lower than XW-Pak. These combinations suggest a comparatively more uniform liquid flow for the HP-Pak with reduced occurrence of relatively fast fractions that can possibly form undesired rivulets.

Table 2: Summary of statistical descriptors of the bulk volume mobility distributions

Packing		XW-Pak	HP-Pak
Gas-phase simulations	Gas velocity coefficient of variation / 1	0.635	0.643
	Transverse gas velocity quantiles $u_{\mathrm{G,trans},50\%}$ / m s^{-1}	0.525	0.639
	$u_{\mathrm{G,trans},95\%}$ / m s^{-1}	1.201	1.466
Irrigation simulations	Liquid velocity coefficient of variation / 1	1.093	0.773
	Liquid velocity quantiles $u_{\mathrm{L},50\%}$ / m s^{-1}	0.0359	0.0576
	$u_{\mathrm{L},99\%}$ / m s^{-1}	0.3005	0.2166

4. Conclusion

To sum up the entirety of the presented data, the CFD results and diagnostics show the new HP-Pak imposing stronger gas flow redirection and transverse mixing, while also generating a more mobile interfacial area with higher median velocity, even though the total interfacial area is lower and wall wetting is more pronounced than the XW-Pak. Therefore, the superior experimental $HETP$ can be attributed primarily to enhanced gas-phase transport and liquid interface mobility.

References

[1] H. Schoenmakers, L. Spiegel, in: A. Górak, Ž. Olujić (Eds.), Distill. Equip. Process., Elsevier, 2014, pp. 319–339.
[2] U. Eiden, R. Kaiser, G. Schuch, D. Wolf, Chem. Ing. Tech. 67 (1995) 269–279.
[3] J. Neukäufer, N. Sarajlic, H. Klein, S. Rehfeldt, H. Hallmann, C. Knösche, T. Grützner, AIChE J. 67 (2021).
[4] J. Neukäufer, M.A. Ashour, N. Sarajlic, H. Klein, S. Rehfeldt, H. Hallmann, S. Meinicke, J. Paschold, C. Knösche, T. Grützner, AIChE J. 69 (2023).
[5] N. Rausch, J. Neukäufer, M.A. Ashour, T. Grützner, S. Meinicke, C. Knösche, J. Paschold, H. Klein, S. Rehfeldt, Chem. Eng. Res. Des. 196 (2023) 28–39.

Model-based sensitivity analysis of vapor–liquid equilibrium estimation from batch distillation

Henning Gröschl[1], Snehaa Ganesh[1], Till Königs[1], Andreas Jupke[1,2]
[1]Fluid Process Engineering (AVT.FVT), RWTH Aachen University, Aachen/Germany
[2]Forschungszentrum Jülich GmbH, Institute for Bio- and Geosciences (IBG-2), 52428 Jülich/Germany

Abstract
This contribution presents a model-based sensitivity analysis investigating how the quality of estimated vapor–liquid equilibrium (VLE) data from batch distillation experiments is influenced by operational and design parameters. A semi-rigorous batch distillation model incorporating stationary liquid holdup and pressure drop is developed and validated against both rigorous process simulations (AVEVA) and experimental data from a laboratory column. Using synthetic (simulated) experimental data for an acetone–methanol–butanone system, the influence of reflux ratio on binary interaction parameter estimation was analyzed. Results indicate that while the reflux ratio has minimal impact on estimation quality, column design parameters - specifically the number of theoretical stages - are critical for accurate VLE estimation. The developed event-driven framework enables the simulation of dynamic operating strategies, providing a foundation for optimized experimental protocols to efficiently characterize complex mixtures.

Keywords
batch distillation, NRTL parameter estimation, non-linear regression, sensitivity analysis, modelling

1. Introduction

The transition towards sustainable chemical value chains increasingly requires the processing of complex multi-component mixtures from recycling streams, such as pyrolysis oils from plastic waste [1]. Distillation remains a suitable separation technology for such feedstocks due to its technical maturity, scalability and robustness. However, these mixtures often contain components for which the boiling behavior and molecular interactions have not been characterized. This lack of data poses a significant challenge for designing and operating efficient distillation sequences, which rely on accurate thermodynamic parameters at process conditions.A promising approach to address this challenge is the estimation of thermodynamic parameters directly from batch distillation experiments. This method offers several advantages: it covers the full concentration range relevant to the actual process, inherently accounts for multi-component interactions, and reduces experimental effort compared to classical VLE measurements [2]. Although the feasibility of this method has already been demonstrated by Egly et al. [2], Bausa et al. [3] and Bortz et al. [4], a systematic analysis of the influence of operational and design parameters of batch distillation columns, experimental protocols and modeling assumptions on the quality of the estimated VLEs has not yet been conducted. The authors address these questions through a comprehensive in-silico sensitivity analysis. The developed event-driven semi-rigorous batch distillation model extends previous approaches by incorporating stationary liquid holdup and a linear pressure drop across the column height. Vapor–liquid equilibrium (VLE) behavior is described using the Antoine equation for vapor

pressures and the NRTL model for activity coefficients. The following sections discuss the model development, validation, and initial results from parameter fitting trials.

2. Modeling approach

The batch distillation process is modeled using an equilibrium stage approach. The column is discretized into N+1 theoretical stages, the reboiler being stage N+1. Necessary inputs for the column model are the number of theoretical stages, the reflux ratio and the initial sump charge and composition. Furthermore, the model requires the top pressure and the total pressure drop, which is assumed to be distributed linearly across the column. To replicate experimental protocols, the simulation utilizes an event-driven architecture, enabling dynamic changes to operating conditions (e.g. reflux ratio) triggered by state variables such as distillate mass or top temperature. Simplified assumptions include negligible vapor holdup, constant stage holdup, and total condensation. Following the modeling approach of Bortz et al. [4] the time variable is eliminated from the differential equations and the sump holdup used as the independent variable. This yields the following differential equation system:

$$dB = -dD \tag{1}$$

$$\frac{dx_{B,i}}{dB} = \frac{1}{H_B}\left[(1+R)\cdot y_{B,i} - R\cdot x_{N,i} - x_{B,i}\right] \tag{2}$$

$$\frac{dx_{j,i}}{dB} = \frac{1}{H_j}\left[(1+R)\cdot\left(y_{j,i} - y_{j+1,i}\right) - R\cdot\left(x_{j-1,i} - x_{j,i}\right)\right] \quad j = 2 \dots N-1 \tag{3}$$

$$\frac{dx_{1,i}}{dB} = \frac{1}{H_1}\left[(1+R)\cdot\left(y_{1,i} - y_{2,i}\right) - R\cdot\left(y_{1,i} - x_{1,i}\right)\right] \tag{4}$$

$$y_i \cdot P = \gamma_i \cdot x_i \cdot P_i^* \tag{5}$$

where B denotes the sump holdup, D the cumulative distillate, x and y the liquid and vapor composition, H the stage holdup, R the reflux ratio, P the total pressure and $P*$ the pure component vapor pressure. Subscript i indicates the component, whereas subscript j indicates the stage indices. The VLE is calculated using the modified Raoult's law (Eq. (5)) with activity coefficients calculated using the NRTL model [5]. Pure component vapor pressures are computed via the Antoine equation. The model implementation is realized in Python using the library SciPy [6] for numerical integration of the differential equation system. The model supports fitting of NRTL parameters, Antoine coefficients, molar masses, as well as the number of theoretical stages and stage holdup. The objective function is formulated as the weighted sum of the mean absolute relative error (MARE) for k sets of n_k experimental datapoints as shown in equation (6)

$$\min_{\theta} OF = \sum_k w_k \cdot \frac{1}{n_k} \cdot \sum_i \frac{\left|y_{k,i} - \hat{y}_{k,i}(\theta)\right|}{\left|y_{k,i}\right|} \tag{6}$$

Datasets can contain temperature data and/or concentration data, whereas all measured datapoints, or just a certain subset (e.g. only datapoints with a high concentration of a certain component) can be selected. The non-negative weights w_k

can be used to tune the influence of certain dataset on the objective function. This enables the model to fit parameters to specific operating points, which will be discussed in future work.

3. Model validation

The semi-rigorous batch distillation model was validated against rigorous simulations performed in AVEVA Process Simulation [7] and against experimental data from a laboratory batch distillation column (Pilodist Quickdist 500 CC [8]) equipped with Sulzer EX structured packing (inner diameter 24 mm, packing height 0.594 m).

3.1 Comparison with rigorous simulation

The proposed semi-rigorous model was first validated against a rigorous batch rectification model implemented in AVEVA to verify the numerical implementation and the event-driven architecture. While both models utilize an equilibrium-stage approach, the AVEVA model calculates liquid holdup and pressure drop dynamically for each stage and time step, whereas the semi-rigorous model assumes constant values. The calculated stage holdup and the pressure drop from the Aveva model were averaged over all simulated time steps and used as input for the custom model. Both simulations used the same number of stages, top pressure and initial feed mixture. For calculating the activity coefficients both models employed the NRTL model with parameters from the Aveva database. The pure component vapor pressures in the Aveva model were calculated using an internal function, whereas the semi-rigorous model used the Antoine equation with parameters from the NIST database [9]. As shown in Figure 1, the temperature profiles of both models are in good agreement with a mean absolute error (MAE) of 1.06 °C for the sump and 1.29 °C for the top stage over the entire distillation run.

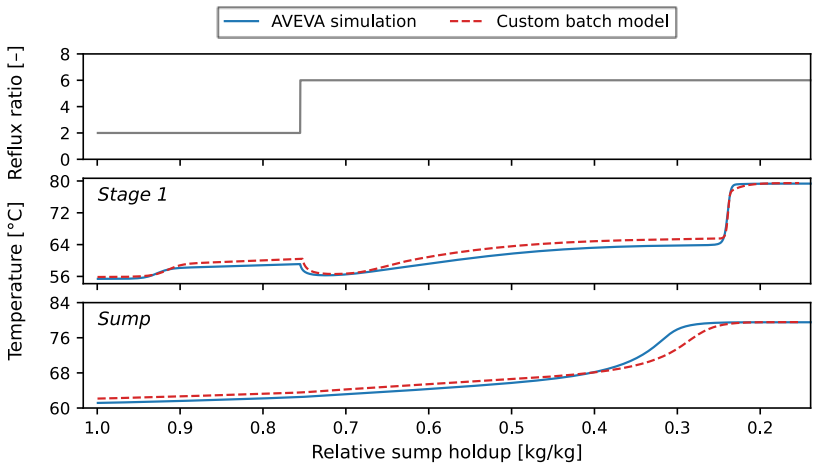

Figure 1: Comparison of temperature profiles between AVEVA rigorous simulation and the semi-rigorous Python model for the acetone–methanol–butanone system, using 24 stages at 1.01325 bar

3.2 Comparison with experimental data

To assess the model's ability to describe real experimental processes, an experiment was conducted using an acetone–methanol–butanone mixture (initial charge ~226 g; mass fractions 0.3, 0.3, 0.4). The column was operated with a dynamic reflux policy, collecting the first 5 fractions at reflux ratio 2 and the subsequent 10 fractions at reflux ratio 6, while maintaining a pressure drop between 2–3 mbar. All samples were analyzed via gas chromatography. Determining the effective number of theoretical stages and liquid holdup for high-efficiency structured packings in laboratory columns is not trivial, as these parameters are heavily dependent on operating conditions and cannot be measured directly. Since initial estimates based on previous experiments

and the Stichlmair correlation [10] proved unreliable, a grid search optimization was performed. As illustrated in Figure 2, the deviation between measured and simulated receiver concentrations was minimized at 24 theoretical stages with a total stage holdup of 0.03 kg. It should be noted that these values are specific to the operating conditions and substance system used. Notably, within the investigated range, the model sensitivity to the holdup parameter was significantly higher than to the number of theoretical stages.

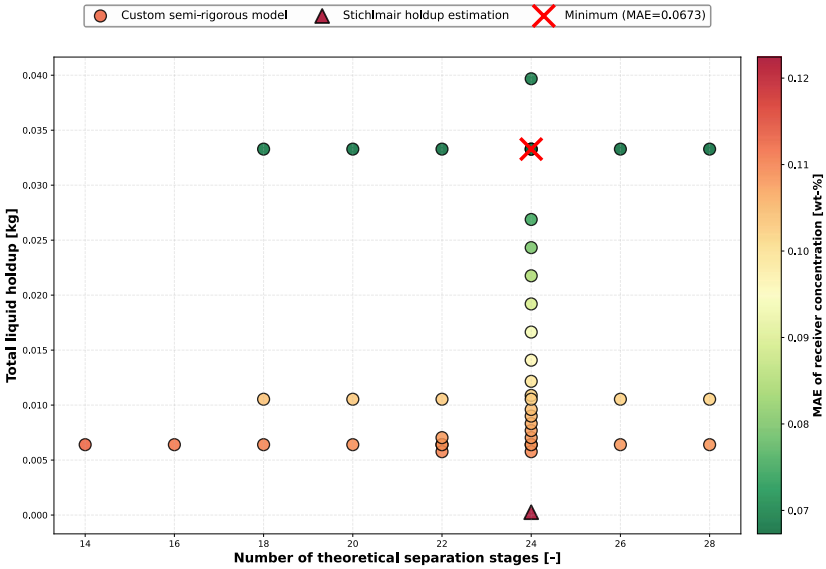

Figure 2: Dependence of mean absolute error for receiver compositions between experimental and simulated data (Python model) of total stage holdup and number of theoretical stages

Using these optimized parameters, the experimental column profiles could be reasonably reproduced by the model, as shown in Figure 3. The event-driven formulation successfully captures the temperature response to the reflux ratio change, demonstrating the model's capability to simulate dynamic operating strategies. This enables the investigation of more sophisticated experimental procedures designed to increase information content within a single experiment.

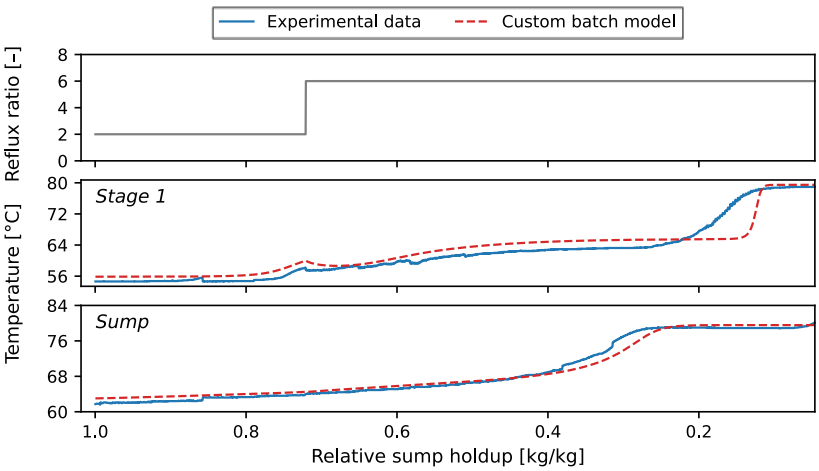

Figure 3: Comparison of temperature profiles of the sump and top stage of the experimental and simulated batch distillation data (Python model)

4. Results and discussion

A first in-silico sensitivity analysis was conducted to evaluate the influence of the reflux ratio on the VLE parameter estimation. To allow for direct validation against a "ground truth" synthetic experimental data was generated using the rigorous AVEVA

simulation. Following the experiment done by Bortz et al. [4], the separation of the acetone–methanol–butanone system into 40 fractions was simulated using 5 theoretical stages and 3 different reflux ratios (2, 5, 8). For each synthetic experiment, the stage holdup was averaged and used as input for the semi-rigorous model. The binary interaction parameters B_{12} and B_{21} describing the acetone–methanol interaction were fitted, while the other binary interaction parameters were fixed. Parameter estimation was performed using the differential evolution algorithm [6], minimizing the objective function (Eq. (6)) using the sump temperature, top temperature, and receiver composition. The minimal residual is obtained at reflux ratio of 8 with the parameters $B_{12} = -134.95$ and $B_{21} = 409.17$. However, despite variations in operating conditions, the estimated NRTL parameters across different reflux ratios converge to similar values, yielding nearly identical residuals. This indicates that the reflux ratio has no significant influence on the quality of the parameter fit. Figure 5 (a) presents the original and fitted binary VLE diagrams. The fitted VLE captures the overall phase-equilibrium behavior and reproduces the main trends of the experimental data, although deviations remain in the detailed description. The temperature and concentration errors exhibit opposing tendencies. While the temperature error peaks at an acetone mol-fraction of 0.15 (relative deviation -0.75%) and 0.75 (relative deviation +0.85%), the vapor mol-fraction error is highest at an acetone mol-fraction of 0.4 with a relative deviation of -4%. This is further illustrated in panels (b) and (c) of Figure 5, which show the relative error of the activity coefficients for acetone and methanol. An opposing deviation in activity coefficients correlates with a deviation in vapor concentration, whereas a concurrent deviation leads to a deviation in boiling temperature.

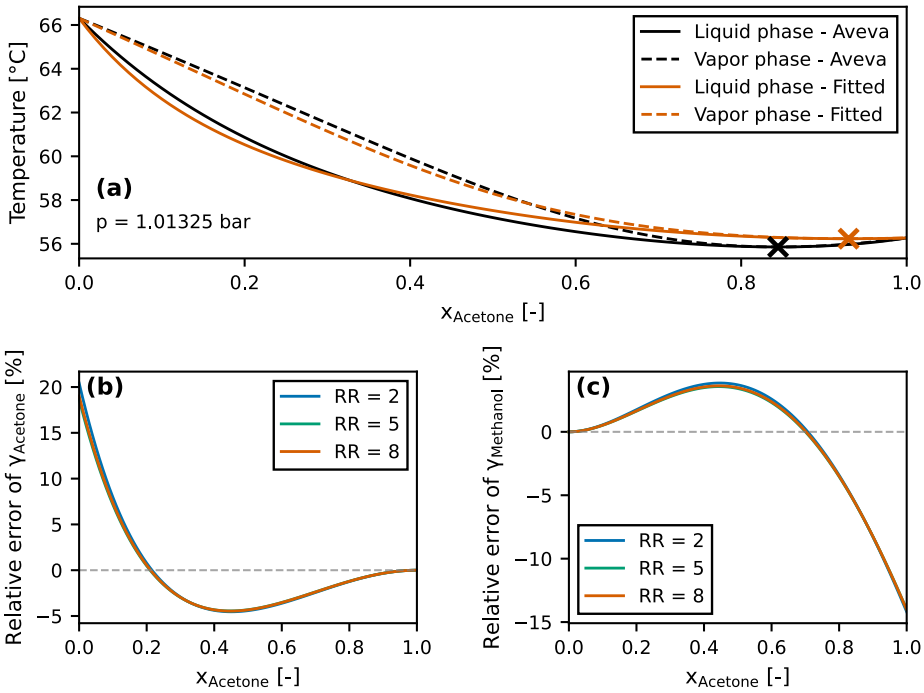

Figure 4: (a) Comparison between original and fitted binary VLE between Aceton and Methanol using a reflux ratio of 8. (b) Relative error of the activity coefficient of acetone. (c) Relative error of the activity coefficient of methanol.

The azeotropic point deviates significantly from the reference data. The distillation profiles in Figure 6 show that five stages are insufficient to reach higher acetone mole fractions and the azeotrope, even under total reflux conditions at a relative sump holdup of 100 %. Consequently, the available data are inadequate to accurately fit the azeotropic properties. The influence of the number of stages on the quality of the fitted VLE will be investigated in future work.

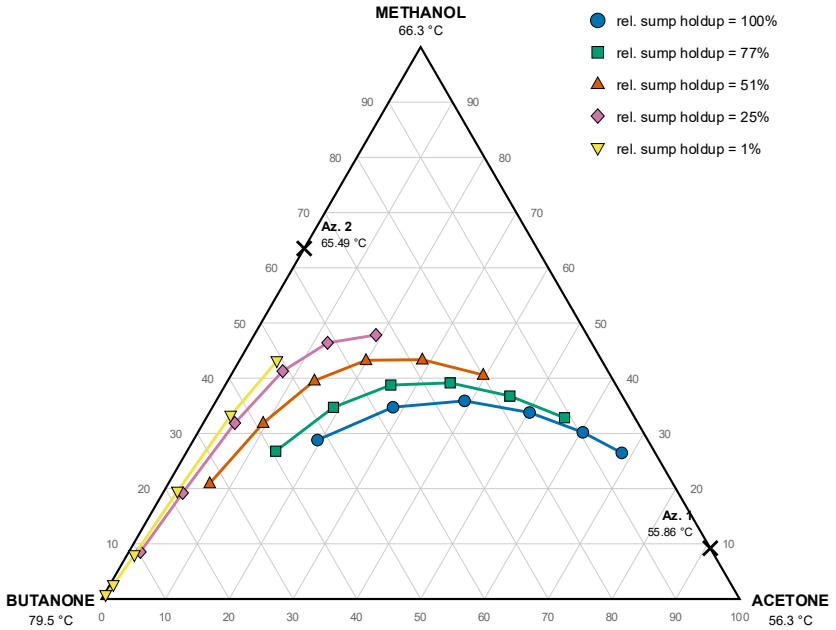

Figure 5: Distillation profiles for different relative holdups for 5 theoretical stages and reflux ratio 8 in wt-%

3. Conclusions

This contribution presents a semi-rigorous batch distillation model for VLE parameter estimation that accounts for stationary liquid holdup and pressure drop, extending previous approaches for NRTL parameter fitting. The model was validated against rigorous AVEVA simulations and experimental data from a laboratory batch distillation column. Sensitivity analysis showed that the (static) reflux ratio has little effect on the fitted VLE parameters. Accurate VLE fitting requires a wide accessible composition range, which in terms of column design translates to a higher number of stages. Future work will extend the sensitivity analysis to additional factors, including the stage holdup and number of theoretical stages.

References

[1] M. Pillich, J. Schilling, L. Bosetti, und A. Bardow, „What to do with polyurethane waste? The environmental potential of chemically recycling polyurethane rigid foam“, *Green Chem.*, Bd. 26, Nr. 21, S. 10893–10906, 2024, doi: 10.1039/D4GC02594F.

[2] H. Egly und W. Ruppel, „Bestimmung der Stoffwerte nichtspezifizierter Gemische“, *Chemie Ingenieur Technik*, Bd. 56, Nr. 9, S. 716–717, 1984, doi: 10.1002/cite.330560917.

[3] J. Bausa und C. Michalik, „Bestimmung eines groben thermodynamischen Modells auf Basis von Destillationsversuchen“, gehalten auf der PROCESSNET: Jahrestreffen der Fachgruppen Fluidverfahrenstechnik und Wärme- und Stoffübergang, Baden-Baden, 20. März 2013.

[4] M. Bortz, R. Heese, A. Scherrer, T. Gerlach, und T. Runowski, „Estimating mixture properties from batch distillation using semi-rigorous and rigorous models“, in *Computer Aided Chemical Engineering*, Bd. 46, Elsevier, 2019, S. 643–648. doi: 10.1016/B978-0-12-818634-3.50108-9.

[5] H. Renon und J. M. Prausnitz, „Local compositions in thermodynamic excess functions for liquid mixtures“, *AIChE Journal*, Bd. 14, Nr. 1, S. 135–144, Jan. 1968, doi: 10.1002/aic.690140124.

[6] P. Virtanen *u. a.*, „SciPy 1.0: fundamental algorithms for scientific computing in Python“, *Nat Methods*, Bd. 17, Nr. 3, S. 261–272, März 2020, doi: 10.1038/s41592-019-0686-2.

[7] „AVEVA - Weltweit führend in Industriesoftware“. Zugegriffen: 31. Januar 2026. [Online]. Verfügbar unter: https://www.aveva.com/de-de/

[8] „Pilodist GmbH - distillation systems“. Zugegriffen: 31. Januar 2026. [Online]. Verfügbar unter: https://pilodist.de/?lang=de

[9] P. Linstrom, „NIST Chemistry WebBook, NIST Standard Reference Database 69“. National Institute of Standards and Technology, 1997. doi: 10.18434/T4D303.

[10] J. Stichlmair, J. L. Bravo, und J. R. Fair, „General model for prediction of pressure drop and capacity of countercurrent gas/liquid packed columns“, *Gas Separation & Purification*, Bd. 3, Nr. 1, S. 19–28, März 1989, doi: 10.1016/0950-4214(89)80016-7.

Distillation System Off-line Data Assimilation Based on Rate-based Model

Peilin Yang, Shengkun Jia, Yiqing Luo*, Xigang Yuan, Xinlei Liu, School of Chemical Engineering and Technology, Tianjin University, Tianjin, China*

Distillation is the most widely employed unit operation, its operational performance directly determines product purity and yield as well as the stability of the overall processes. Therefore, critical issues in distillation systems—such as optimization design, process control, and fault diagnosis—still require resolution, while addressing these challenges relies on mechanistic modeling and simulation. Rate-based model[1] currently represents the most rigorous solvable mechanistic model. Nevertheless, it still incorporates several assumptions: 1) perfectly mixed; 2) two-film theory; 3) neglection of axial back-mixing; 4) adiabatic system; In addition, the calculation of rate-based model relies on mass transfer coefficients, which are difficult for theoretically solving. Therefore, these coefficients are often empirical or semi-empirical correlations based on dimensionless numbers. Due to these facts, discrepancies between simulation results and actual processes are inevitable. In recent years, advances in computational technology have enabled the emergence of data assimilation techniques, which integrate process data with traditional mechanistic models to estimate model parameters and reduce systematic errors between simulations and actual processes. In distillation systems, data that collected through instruments can be used to calibrate model parameters, thereby improving simulation accuracy.

Due to the high cost of monitoring points in distillation systems, data are typically limited with few or no monitoring points available along the column internals. This data sparsity can compromise the accuracy of model assimilation. However, fluctuations in feed conditions and variations in operating parameters during actual operation can generate multiple datasets, helping to mitigate the lack of monitoring points. In this work, gradient-based optimization algorithm is adopted to get the mass transfer coefficients of each operating condition, while each mass transfer coefficients serve as the initial values of next operating condition. After optimization, mass transfer coefficients constitute a set of mappings to the operating conditions, which is represented as a neural network. In addition, systematic error items are added to mass balance equations to improve simulation accuracy.

Two temperature monitoring instruments were installed at each section. Experimental data were replaced using the BRF92 model[2]. Multiple datasets were generated from fluctuations in feed conditions and variations in operating parameters during operation. The HC model[3] served as the original model, which provide the initial values of mass transfer coefficients. All cases were converged by PT rate-based method[4]. Results indicated that the data assimilation process exhibits good convergence and optimization efficiency. The assimilation model can effectively improve accuracy of product streams compared to the original model. With the assimilation model, the composition and status of streams within the column can also be accurately predicted.

2. Data Assimilation Method

The objective of data assimilation is to mitigate the inevitable discrepancy between simulation results and actual process by adjusting changeable parameters of rate-based model using real processes data, thereby obtaining more accurate simulation outcomes. This section will introduce the data assimilation method, the assimilation strategy for a single operating condition, and the parameter handling method for multi-condition assimilation.

2.1 Assimilation Model

Given the complexity of factors influencing mass and heat transfer rates, rigorous theoretical calculation remains challenging. Therefore, mass transfer coefficients are commonly expressed using empirical or semi-empirical correlations composed of dimensionless numbers. These correlations are often incorporated into empirical formulas for mass transfer coefficients expressed using dimensionless numbers such as Sh, Re, and Sc:

$$Sh_L = \alpha Re_L^a Sc_L^b \tag{1}$$

$$Sh_V = \beta Re_V^c Sc_V^d \tag{2}$$

Thus, the constant coefficients and exponents of the dimensionless numbers can be adjusted based on actual conditions and are therefore the parameters to be estimated in this work.

Besides the mass transfer coefficients, the effective area participating in mass and heat transfer, influenced by fluid dynamics, needs to be calculated for both packing and trays. This is also generally represented by empirical or semi-empirical correlations:

$$\frac{a_e}{a_d} = \gamma Re_V^e Re_L^f We_L^g Fr_L^h (\rho_V/\rho_L)^i (\mu_V/\mu_L)^j (\cos(\theta)/\cos\left(\frac{\pi}{4}\right))^k \quad (3)$$

The constant coefficients and exponents of the dimensionless numbers in this model are also estimable parameters.

2.2 Assimilation Strategy

Typically, only the compositions of the top and bottom product streams are directly measurable, while internal column measurements are scarce, often limited to a few temperature points. Furthermore, estimating these exponent terms could easily cause simulation failure. Therefore, this work only considers the three linear terms α, β, γ and the vapor and liquid Reynolds number exponent as the parameters for assimilation.

Additionally, the distribution characteristics within a distillation column are that flow conditions typically differ significantly between column sections, while conditions within a single section are relatively uniform. each set of assimilated parameters represents one column section. If more than one measurement point exists within a section, the assimilation parameter groups are divided according to these points, meaning each parameter group represents the stages near that measurement point.

The parameter assimilation problem can be formulated as the following optimization problem:

$$\min \sum_i^n [\mathbf{x}^* - \mathbf{x}_0]^T W_i [\mathbf{x}^* - \mathbf{x}_0]$$

s.t.:

$$NEQ(Feed, RR, P, V_f) = 0$$

where $\mathbf{x}_0$ represents the measured variables, $\mathbf{x}^*$ represents the simulated variables.

For different conditions, the essence lies in variations in feed conditions and operating parameters. Therefore, after optimizing for multiple single conditions, a mapping relationship $\alpha(opera, feed)$, $\beta(opera, feed)$, $\gamma(opera, feed)$, $w(opera, feed)$ betwe en the operating/feed conditions and the assimilated parameters is obtained.

Thus, when feed conditions and operating parameters change, parameters for that condition can be generated via this mapping. To achieve this, this work employs a data-driven neural network to generate condition-mapped parameters. The multi-condition processing strategy is illustrated in Figure 1.

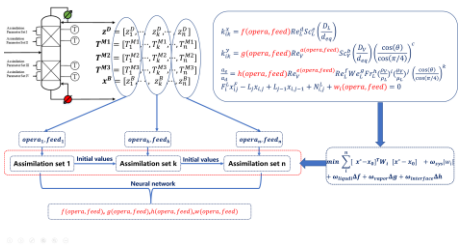

Figure 1: The framework of data assimilation for distillation system based on rate-based model

3. Case Study

To validate the methods described in Section 2, this study selects the common non-ideal methanol-water system for parameter assimilation. The NRTL method is chosen for thermodynamics. A distillation column with a diameter of 0.5 m is packed with 4 m of BX-type packing, with the feed introduced at the 2 m point. The feed fluctuates with methanol mole fraction between 0.2 and 0.3, and the reflux ratio operates between 0.9 and 1.1. The top pressure is 1 bar, and pressure drop is neglected.

3.1 Impact of the Number of Measurement Points

More measurement points can improve the quality of assimilated parameters, but installing them incurs additional costs, making it impractical to have them on every stage. This section therefore investigates assimilation results for scenarios with: no internal measurement points, two measurement points per column section, and measurement points on every stage.

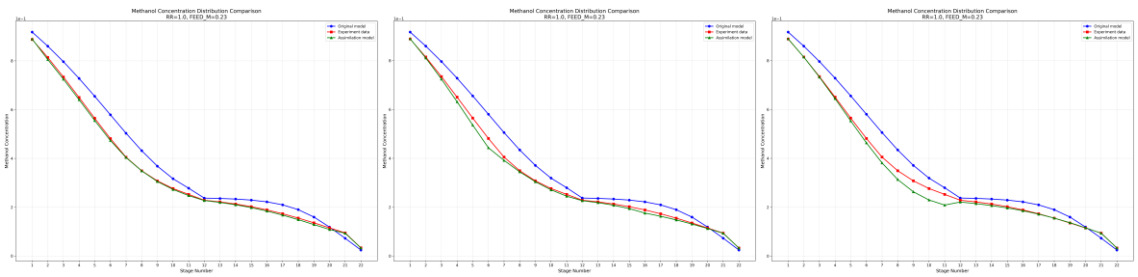

Figure 2: assimilation results of (a) measurement points in every stage, (b) 2 measurement points in each section, (c) no measurement point.

From Figure 2, it can be observed that the placement of measurement points can significantly improve the quality of the assimilated data. This is because the significant difference in surface tension between water and methanol, which causes the distribution within column obtained by the SRP method to be notably influenced by surface tension. However, considering the high cost associated with installing

measurement ports on the column, the approach illustrated in Figure 3(b) represents a relatively reasonable strategy for setting measurement points.

3.2 Impact of Sampling Frequency

To explore the effect of sampling frequency on assimilation results, this study performs assimilations for: methanol mole fraction fluctuations between 0.2-0.3 sampled every 0.1 and every 0.2; and reflux ratio operations between 0.9-1.1 sampled every 0.1 and every 0.2.

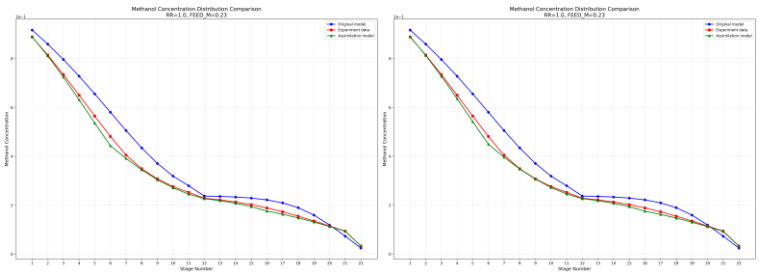

Figure 3: assimilation results of (a) sampled every 0.1, (b) sampled every 0.2

Based on the results from Figure 3, the method proposed in this study does not require extensive operational data; instead, it achieves satisfactory assimilation outcomes with only sparse measurement data.

3.3 Extrapolation Capability

To investigate the extrapolation capability of the assimilation model when the column operates outside the sampled range, this study simulates results for reflux ratios of 1.2 and 0.8, and methanol mole fractions of 0.35 and 0.15.

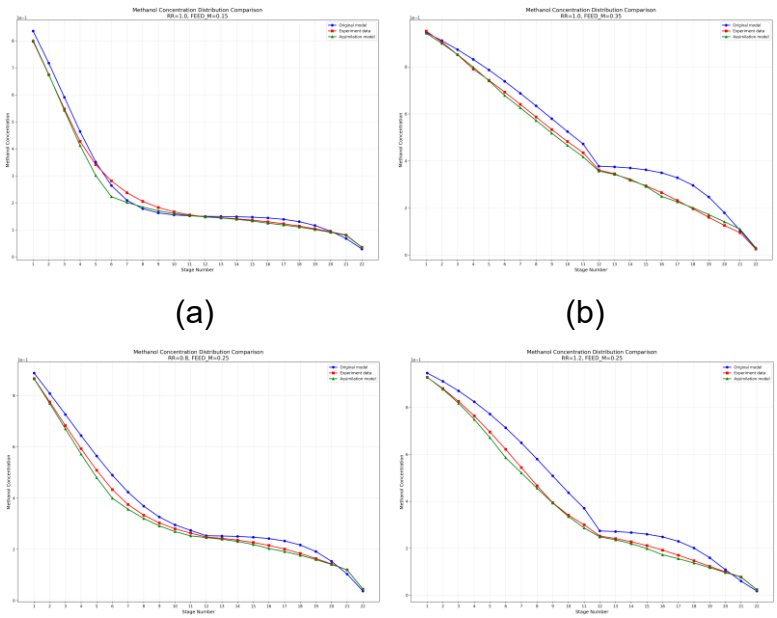

(a) (b)

(c) (d)

Figure 4: Extrapolation results of (a) RR=1,z_{metha}=0.15 (b) RR=1,z_{metha}=0.35 (c) RR=0.8,z_{metha}=0.25 (d) RR=1.2,z_{metha}=0.25

According to the results in Figure 4, when predicting operating conditions outside the range of the measurement data, the simulation results based on the neural network's predicted values still exhibit certain deviations. However, the simulation performance remains significantly superior to that of the original model. Therefore, the method proposed in this study demonstrates a notable extrapolation capability.

Conclusion

The method proposed in this study can effectively calibrate the simulation results of different mass-transfer models. This method does not require extensive measurement data to achieve accrete outcomes. The assimilation model demonstrates certain robustness against measurement noise and possesses good extrapolation capability. In summary, the method presented in this study provides a viable approach for constructing more accurate steady-state simulation models.

References

1. Krishnamurthy R, Taylor R. A nonequilibrium stage model of multicomponent separation processes. Part I: Model description and method of solution. *AIChE Journal*. 1985;31(3):449-456. doi:10.1002/aic.690310312
2. Rocha JA, Bravo JL, Fair JR. Distillation columns containing structured packings: a comprehensive model for their performance. 1. Hydraulic models. *Ind Eng Chem Res*. 1993;32(4):641-651. doi:10.1021/ie00016a010
3. Hanley B, Chen C. New mass-transfer correlations for packed towers. *AIChE Journal*. 2012;58(1):132-152. doi:10.1002/aic.12574
4. Wu J, Luo Y, Yuan X. A pseudo transient nonequilibrium method for rigorous simulation of multicomponent separation columns. *Chinese Journal of Chemical Engineering*. 2023;62:57-64. doi:10.1016/j.cjche.2023.04.011

Thermophysical and transport properties in choline-based ionic liquids: hydration and structural insights

Magdalena Bendová,[1,3] Jan Heyda,[1] Mahasoa-Salina Souvenir-Zafindrajaona,[1,2,3] Zdeněk Wagner,[3] Jean-Pierre Mbakidi,[2] Sandrine Bouquillon[2]
[1]Department of Physical Chemistry, University of Chemistry and Technology, Prague/Czech Republic
[2]Institute of Molecular Chemistry, University Reims Champagne-Ardenne, Reims/France
[3]Institute of Chemical Process Fundamentals of the CAS, v.v.i., Prague/Czech Republic

Lignocellulosic biomass is an excellent sustainable source of valuable materials; however, the current industrial processes often use toxic solvents and operate under harsh conditions. Novel, sustainable solvents that will allow for the dissolution of lignocellulosic biomass under mild conditions are therefore extensively studied. Choline-based ionic liquids proposed in our previous work [1] found to show good dissolution efficiency for Kraft lignin, may be considered promising candidates for such applications.

In the present study, we investigate thermophysical and transport properties in choline-based ionic liquids in the presence of water. The acoustic properties and conductivity as a function of temperature and water content are examined in light of our previous study on the apparent thermophysical properties (volume and heat capacity) [2]. Molecular dynamics simulations complement these experiments by elucidating the solution structure, namely ion pairing, ion hydration, and water-water interactions. Furthermore, MD simulation confirmed the dissolution of lignin-proxy in the studied aqueous IL systems.

Indeed, this combined approach provides a fundamental understanding of aqueous IL solutions at both molecular and macroscopic level leading to a predictive framework for designing novel sustainable solvents for chemical processes.

Keywords
Bio-based ionic liquids; Kraft lignin; dissolution; hydration; electric conductivity; speed of sound; MD simulation; liquid structure

1. Introduction

Even though most of the conventional ionic liquids have been regarded as a potentially sustainable substitutes for conventional solvents for a considerable number of years, their toxicity has frequently been identified as a significant disadvantage when considering their utilization on an industrial scale. Consequently, ionic liquids derived from natural compounds are designed and considered more promising and environmentally friendly. For instance, choline-derived ionic liquids have been demonstrated to possess potential application as solvents in catalysis, tribology, gas

sorption, CO_2 capture, or drug delivery, to name but a few [3-7]. Choline acetate has been identified as an efficient and cost-effective organocatalyst for the hydroboration of several carbonyl compounds [8]. Poly-ionic liquids derived from choline have been demonstrated to enhance the performance of lithium-sulfur (LiS) battery systems, thereby facilitating enhanced confinement of polysulfide species within the cathodic compartment [9].

In our previous work [1], we proposed a novel approach towards synthesizing choline-based ionic liquids (CHILs) with lactate and levulinate anions. Subsequently, the mixtures with water were characterized in terms of their volumetric and thermal properties, with a view to facilitating their utilization in environmentally sustainable processes, such as the treatment of lignocellulosic biomass [2].

As demonstrated in the previous study, the interaction between the studied CHIL ions and water molecules is reflected in the measured bulk properties, namely density and heat capacity. To further elucidate the molecular level interaction, the present research combines an experimental study of transport properties in aqueous mixtures of choline lactate and choline levulinate with molecular dynamics (MD) simulations. Progressive hydration of the studied ionic liquids is studied, ranging from near-dry states to compositions dominated by water but comprising the ionic liquids. The speed of sound and specific conductance are measured for this purpose. Indeed, it has been demonstrated that bulk transport properties can be used as indicators of solution structure and solvation. For instance, isentropic compressibility can be derived from speed of sound and density measurements using the Laplace-Newton equation; its deviation from ideality may be related to the proximal solvent structure [10]. In addition, the molar conductivity of an ionic liquid solution can provide insight into the aggregation or dissociation of ions [11].

Furthermore, to complete a preliminary assessment of the application potential of the studied CHILs in lignin dissolution, the solubility of a lignin-proxy in the studied aqueous CHIL systems was modelled by MD simulation, to establish the link between the presence of water and lignin solubility enhancement.

2. Materials and methods

3.1 Chemicals used

Two choline-based ionic liquids synthesized in our previous work [1] are listed in Table 1. Both were purified after synthesis by liquid-liquid extraction and drying under vacuum. To prepare samples with different water contents, the studied ionic liquids were dried under vacuum (approx. 2 mbar) to reach the water concentration range from <1 to 15 % by mass. After each drying, the water content was determined using the Karl Fischer titration. To obtain samples with water content higher than 15% by mass, a defined mass of water was added to the ionic liquids with the previously determined water content. Such mixtures were then homogenized by stirring, and the water content was checked again by KF titration.

3.2 Measurement of speed of sound and conductivity

The speed of sound as a function of temperature at 0.1 MPa was measured by means of an Anton Paar DSA5000 Density and Sound Velocity Analyzer within the temperature range from 288.15 to 343.15 K. The speed of sound analyzer working frequence is of 3MHz. Calibration for speed of sound measurements was carried out

using degassed redistilled water (ρ = (0.997043±0.00001) g·cm^{-3}) and dry air at T = 298.15 K. The apparatus is kept at the experimental temperature within 0.001 K by means of a built-in solid-state thermostat.
Conductivity was measured in the temperature range from 298.15 to 323.15 K by means of an inoLab 7310 conductometer with a WTW TetraCon 325 cell calibrated using a 1413 μS/cm KCl solution conductivity standard prepared in-house. Demineralized water with a conductivity of 0.0001 S/m was prepared in-house using Millipore Synergy Purification System.

Table 1: Ionic liquids studied in this work

Ionic liquid	M / g·mol^{-1}	Final purity
Choline Lactate	193.24	> 95 %
Choline Levulinate	219.28	> 95 %

3.3 MD simulations

Simulations of lignin proxy (pentamer of *p*-coumaryl alcohol, abbreviated as PCA5) in water and aqueous mixtures of the studied CHILs (Chol Lac, Chol Lev) were performed in GROMACS simulation package [12]. Technical parameters of simulations and force-field for novel molecules followed the recommended protocols and were the same as in our recent investigation of lignin with green solvents [13]. More specifically, SPC/E water model was used together with GAFF parameterizations (with RESP partial charges) of CHILs and PCA5. MD simulations were performed in isothermal-isobaric (*NpT*) ensemble at standard temperature (298 K) and pressure (1 bar), which were controlled by V-rescale thermostat (τ_T = 0.5 ps) and C-rescale barostat (τ_p = 2.0 ps). LINCS algorithm was used to constrain all bonds involving hydrogen atoms. 1 nm cut-off was used for short range Lennard-Jones and electrostatics. The Particle mesh Ewald (PME) method on a 0.16 nm grid accounted for long-range electrostatics. Studied systems consisted of 8 PCA5 molecules and 3750 water molecules or in 300 IL molecules randomly distributed in the simulation box of ~125nm^3 by PACKMOL software [14]. For water/IL mixtures of molar fraction of water (x_w=0.1, 0.5, 0.8, 0.95) an appropriate number of water and IL molecules was used. After minimization and short equilibration (5 ns), the system reached a size of ca 4.8x4.8x4.8 nm^3. The system was propagated with 2 fs time-step (leap-frog integrator) and 1 ps sampling frequency for 100 ns, resulting in 100 000 configurations for data analysis. Equilibrium distribution of RLP5 in simulation box was determined and solution structure (IL, water) in bulk was characterized by radial distribution function (RDF).

4. Results and discussion

4.1 Transport properties as a function of water content

Speed of sound was measured in the temperature range from 287.15 to 313.15 K as a function of water content. Within the range of measured water mole fractions from 0.1 to 0.8, the speed of sound was found to exhibit an increasing trend in relation to the water content.
The speed of sound appears to be an increasing function of the water content for the studied CHILs, however, the difference between the measured values for both ionic liquids appears to be very weak. To capture the difference in anion structure in terms

of hydration, isentropic compressibility was therefore obtained using the Newton-Laplace equation

$$\kappa_S = \frac{1}{u^2 \rho} \quad (1)$$

where u is the speed of sound in m/s and ρ is the density in kg/m^3. Density data were taken from our previous work [2].

Specific conductance was subsequently measured within the temperature range of 298.15 to 323.15 K and the water mole fraction range of 0.4 to 0.8. Within this range of concentrations, the specific conductance appears to show a non-monotonous trend for both CHILs, in accordance with the assumption of possibly non-trivial hydration effects observed in the study of volumetric and thermal properties in [2].

To provide a more illustrative discussion of the hydration regimes of the studied CHILs, the isentropic compressibility (Figure 1a) and the specific conductance (Figure 1b) are discussed herein at 298.15 K as a function of the water-to-CHIL molar ratio:

$$R = \frac{n_{H2O}}{n_{IL}} = \frac{x_{H2O}}{x_{IL}} \quad (2)$$

The studied CHILs present a 1:1 stoichiometry, the amount of substance n_{IL} thus corresponds to the number of ion pairs. This facilitates direct interpretation of the R ratio directly as the number of water molecules per ion pair.

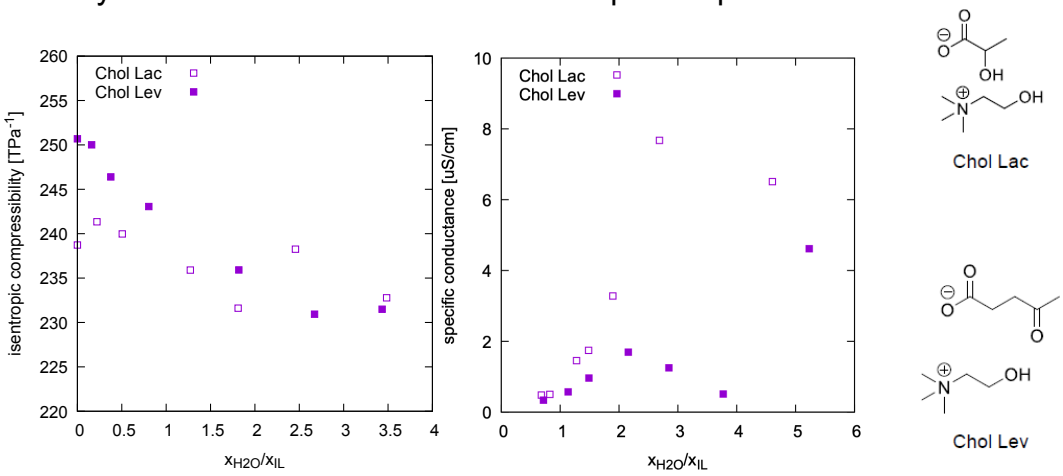

a) b) c)

Figure1: a) Isentropic compressibility of aqueous Chol Lac and Chol Lev as a function of R; b) Specific conductance of aqueous Chol Lac and Chol Lev as a function of R; c) Structures of the studied CHILs.

As shown in Figure 1a, the isentropic compressibility is observed to decrease in proportion to the water content for both CHILs studied, reaching a plateau at approximately R=2. The relatively rapid decrease in isentropic compressibility at the low hydration regime suggests a rapid rearrangement of the IL structure as the ion aggregation decreases, with the plateau indicating the formation of a more rigid structure as the hydration shells fill with water molecules.

This appears to be mirrored by the concentration trend in the measured specific conductance which increases for both CHILs until what appears to be a local maximum at R≈2 for Chol Lac and at R≈3 for Chol Lev is reached (see Figure 1b).

These trends may indicate the shifts between the individual hydration regimes. At R≤1, i.e. at a low hydration regime, water is strongly bound to the CHIL ions and the specific conductivity is a weak function of water content. At intermediate hydration, i.e. at 1≤R≤3, partial hydration shells are expected to form, leading to the restructuring of the ionic networks leading to substantial increase of conductivity, as water-ion interactions

compete with ion-ion interactions. Above R=3, the ions are expected to be fully hydrated.
Although the concentration ranges studied in this work are limited, the data seem to corroborate observations from analogous systems studied by other research groups (see e.g. [11] and references therein).

4.2 MD simulations
We performed MD simulations of lignin proxy in water/IL mixtures under experimental conditions (T,p). Figure 2 shows that while lignin precipitates in neat water (first two panels), already 5 mol% of IL leads to visible stabilization of lignin in solution (i.e., lignin dissolution), and 20 mol% performs even better. This confirms the potential of Chol Lac for lignin solubilization. It should be noted that above 50 mol% of IL, the viscosity of solution significantly increases, and consequently the direct conformational sampling of lignin within simulation timescale becomes challenging.

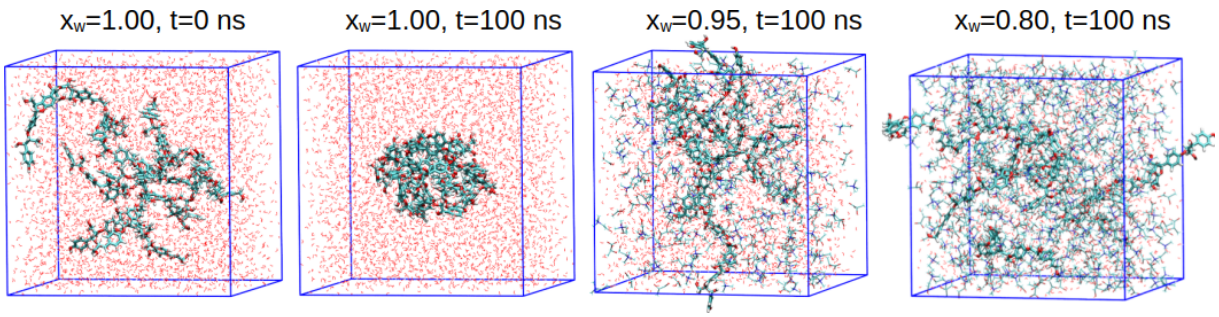

Figure 2: Final distribution of lignin molecules (after 100 ns of simulation) in aqueous solutions of Chol Lac of decreasing water concentration (x_w=1.00, 0.95, 0.8). The most left panel presents initial distribution (same in water and in mixtures). Water is shown in red lines, IL in thin and lignin molecules in thick licorice representations.

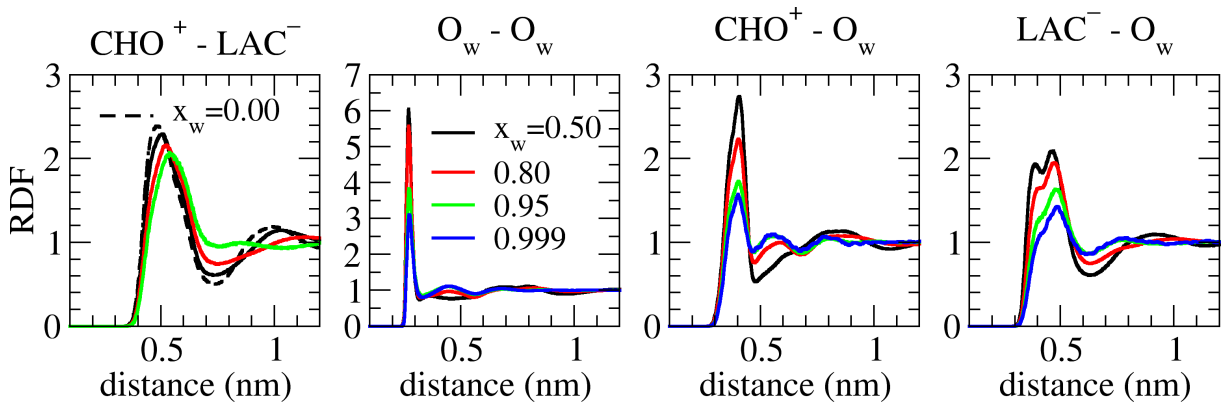

Figure 3: The most prominent radial distribution functions (RDF), which describe the IL/wat solutions; cation-anion, water-water, and cation and anion hydration. RDFs in pure solvents and their changes with composition are indicated by color.

Figure 3 presents a basic view into the solution structure of the bulk CHIL/water mixture. The cation-anion pairing is the most structured in neat CHIL and decreases only weakly with added water. In contrast, the CHIL hydration relatively increases with decreasing water content (probably due to selective hydration of carboxyl, carbonyl, and hydroxyl group). The most characteristic is the significant increase of the first peak in water-water, which indicates strengthening water-water interaction at increased IL concentrations.

5. Conclusions

In a preliminary study of lignin dissolution in the investigated CHILs an optimum solubility in mixtures containing 15 to 30 wt. %, i.e. 65 to 82 mol. % water was found. These observations were corroborated herein by the speed of sound and specific conductance measurements of aqueous IL mixtures which enabled us to distinguish IL hydration regimes. At a low hydration regime, water appears to be strongly bound to the CHIL ions whereas at intermediate hydration, partial hydration shells are expected to form, leading to the restructuring of the ionic networks as water-ion interactions compete with ion-ion interactions. These results are consistent with ionic liquid hydration as captured in radial distribution functions obtained in MD simulations. The improved hydration of the CHIL ions may be a potential reason for an enhanced lignin dissolution which we observed in our MD simulations.

The experimental and simulation protocol developed in this study may be extended to cover other IL/CHIL structures for a fundamental understanding of the relation between IL hydration and biomass dissolution, contributing to process optimization.

The authors gratefully ack

Acknowledgements

nowledge funding from LUABA24070 joint project of the Ministry of Education, Youth and Sports of the Czech Republic and The Bavarian-Czech Academic Agency (JH) and the 8J21FR0027 Czech-French Mobility project of the Ministry of Education, Youth and Sports of the Czech Republic (MB+SB). Computational resources were provided by the Ministry of Education, Youth and Sports of the Czech Republic through the e-INFRA CZ (ID:90254).

References

1. Souvenir-Zafindrajaona, M.-S.; Nadir, S.; Mbakidi, J.-P.; Jandová, V.; Ndong, M.-A.; Lequart, V.; Martin, P.; Bendová, M.; Bouquillon, S. J. Mol. Liq. 2025, 429, 127642.
2. Souvenir-Zafindrajaona, M.-S.; Mbakidi, J.-P.; Wagner, Z.; Bouquillon, S.; Bendová, M. RSC Adv. 2026, 16, 4129.
3. Chan, K. K.; Yong, K. J.; Ho, Y. K.; Wu, T. Y.; Ooi, C. W. Int. J. Biol. Macromol. 2025, 307, 141697.
4. Shaikh, A. R.; Grillo, A.; D'Alterio, M. C.; Pajski, J. J.; Amran, S. I.; Karim, H.; Chawla, M.; Talarico, G.; Poater, A.; Cavallo, L. J. Mol. Liq. 2025, 424, 127084.
5. Gadilohar, B. L.; Shankarling, G. S. J. Mol. Liq. 2017, 227, 234.
6. Dong, Z.; Zhang, L.; Li, G.; Li, Y.; He, H.; Lu, Y.; Wu, W.; Qi, J. J. Controlled Release 2024, 375, 812.
7. Li, X.; Ma, N.; Zhang, L.; Ling, G.; Zhang, P. Int. J. Pharm. 2022, 612, 121366.
8. Krupa, B.; Nowicki, M.; Huninik, P.; Szyling, J.; Walkowiak, J. Organocatalytic Hydroboration of Carbonyl Compounds Promoted by Choline-Based Ionic Liquids. ChemRxiv 2024. https://doi.org/10.26434/chemrxiv-2024-z8lqq
9. Hernández-Sánchez, A.; Jarib Alcaraz-Espinoza, J.; St Thomas, C.; Jiménez-Regalado, E.; Mayrén, A.; González, I.; Ramos Sánchez, G. J. Energy Storage 2025, 106, 114746.
10. Douhéret, G.; Davis, M. I.; Reis, J. C. R.; Blandamer, M. J. ChemPhysChem 2001, 2 (3), 148–161.
11. MacFarlane, D. R.; Chong, A. L.; Forsyth, M.; Kar, M.; Vijayaraghavan, R.; Somers, A.; Pringle, J. M. Faraday Discuss. 2018, 206, 9.
12. Abraham, M. J.; Murtola, T.; Schulz, R.; Páll, S.; Smith, J. C.; Hess, B.; Lindahl, E. GROMACS: High Performance Molecular Simulations through Multi-Level Parallelism from Laptops to Supercomputers. SoftwareX 2015, 1–2, 19.
13. Schweiger, M.; Lang, T.; Müller, E.; Jeřábek, V.; Heyda, J.; Klajmon, M.; Touraud, D.; Bendová, M.; Řehák, K.; Kunz. W. RSC Sust. 2025, 3, 4533.
14. Martinez, L.; Andrade, R.; Birgin, E.G.; Martinez, J.M. J Comput Chem. 2009, 30(13), 2157.

Good Intentions Meet Reality: A Liquid Distributor Story

Armin Rix[1], Henrik Fasel[2], Andreas Lange[1], Marc Xia[1], Christoph Hiller[1]
[1] Evonik Operations GmbH, NextGen Technologies, Marl, Germany;
[2] Evonik Oxeno GmbH & Co. KG, Marl, Germany

Abstract
Adequate liquid distribution is critical for packed column performance, impacting separation efficiency, energy demand, and column uptime, especially in fouling service. In a wastewater stripper, severe fouling led to distributor failure and packing blockage. A makeshift solution involved removing the distributor and feeding liquid directly via a feed pipe, stabilizing operations but reducing distribution quality. Especially in fouling service, achieving good wetting can be crucial. Using the cell model in TrayHeart, a ladder type distributor with seven drip points was identified as a compromise between fouling resistance and distribution quality. The number of drip points must stay low to keep the orifices sufficiently sized to prevent blockage by fouling. This design enhanced separation efficiency, reduced fouling, extended column uptime, and increased operational reliability. The results show the possibility of achieving sufficient liquid distribution even with a significantly lower drip point density than industry standard. In this case, the arrangement of the few drip points in an optimal way is more important than a high drip point density.

Keywords
Distillation, liquid distributor, maldistribution, fouling, random packing

1. Introduction

An optimal packed column operates in plug flow with gas and liquid in countercurrent (Stichlmair et al., 2021). In other words, the optimal performance of a packed column requires a homogeneous distribution of liquid and gas over its cross-section (Towler and Sinnott, 2022). According to Stichlmair et al. (2021), this ideal flow regime is characterized by uniform flow profiles and the absence of axial back mixing. Deviations from this ideal are unavoidable and called maldistribution. Maldistribution is a frequent reason for failure and troubleshooting in columns with packings according to Kister (2006). In contrast to trayed columns, packings rely on the quality of the initial liquid distribution for their performance. Otherwise, the L/V ratio in the radial direction of the column may not be uniform, which affects the separation efficiency negatively (Gorak and Olujic, 2014). Maldistribution can also occur in the gas phase. The effect is usually not as severe as with liquid maldistribution since the pressure drop in the internals is often sufficient to enforce an even gas distribution across the column diameter (Stichlmair et al., 2021).

While small-scale maldistribution can be corrected by the packing itself due to its self-distributing structure, a large-scale initial maldistribution will persist and have a notable effect on the separation efficiency of the bed below, as investigated by Kunesh et al. (1987) at Fractionation Research Inc. (FRI), Stillwater, Oklahoma. To achieve a good initial liquid distribution, liquid distributors are employed. There exists a variety of designs, e.g., feed pipe, spray nozzle, deck type, pan type, ladder type, and trough type, fitted to the type of service and the respective loadings. An important design parameter is the number of drip points per square meter of column cross-section. The

requirement for this so-called drip or pour point density is dependent on the packing underneath. A typical range for industrial scale distributors is 100 to 150 drip points per square meter to achieve an adequate distribution (Gorak and Schoenmakers, 2014), while Moore and Rukovena (1987) recommend a minimum of 65.

A simple but powerful tool based on geometric reasoning was presented by Moore and Rukovena (1987). With their method, the cross-section of the column is covered by several drip points which each irrigate a circular area, so-called point circles, so that the total area covered by the drip point circles equals the cross-sectional area of the column. With this method under- or overirrigated areas can be easily spotted qualitatively. A quantification of the distributor quality Q_D can be achieved by using following equation:

$$Q_{\mathrm{D}} = 0.40 \cdot (100 - A) + 0.60 \cdot B - 0.33 \cdot (C - 7.5) \qquad (1)$$

Wherein A is the non-irrigated area of the column cross-section in %, B the coverage of the worst covered 1/12th section of the column in %, and C the overlap area of the point circles in %. At the time of publication, Moore and Rukovena (1987) found common distributors to have a distributor quality Q_D between 10 – 70%; they qualified everything above as intermediate- or even high-quality distributors. These methods for evaluating distributor quality allow engineers to quickly identify poorly irrigated areas visually.

Besides suboptimal initial liquid distribution, other factors can play a role in creating maldistribution. Some prominent examples are fouling, mechanical damage, corrosion, or installation errors. These factors can impact the packing as well as the liquid distributor and, therefore, the initial liquid distribution (Gorak and Olujic, 2014).

The description of liquid maldistribution using a model that does not require experimental data for parameter fitting was proposed by Wild and Engel (2007) and implemented as part of the WelChem Cell Model in the proprietary software TrayHeart. The model employs spread factors, which are determined from CAD data and irrigation simulations of individual random packing elements with varying orientations.

This model was extended and validated experimentally by Hanusch et al. (2019a) resulting in the TUM-WelChem Cell Model. The column cross-section is represented as layers of hexagonal cells, each representing a single randomly oriented packing element, with the cell size correlating to the bulk density of the packing. The random orientation of packing elements, wall flow, increased lateral distribution at high liquid loads, and the influence of the gas load are considered. Inputs for the model are a dry pressure drop correlation, a CAD model of the random packing, the bulk density, the porosity, and the specific surface area (Hanusch et al., 2019a, Hanusch et al. 2019b, Stichlmair et al., 2021).

In a new wastewater stripper with a diameter D_P of 600 mm, two beds with random packings were installed, see Figure 1. Above each bed, wastewater from different sources is fed into the column. The top product is off gas containing stripped low boiler while the bottom product is mostly water. The most severe fouling was expected in the lower section of the column. To exclude reboiler fouling, direct steam injection was chosen. Process data for steam supply, temperatures, and pressure drop are tracked using a process information management system.

Above each packed bed, liquid is introduced and must be distributed in some way. The lower bed with a depth H_P of 6.5 m and distributor 2 are the subjects of the following studies. Due to the heavy fouling service, the initial liquid distribution must be evaluated.

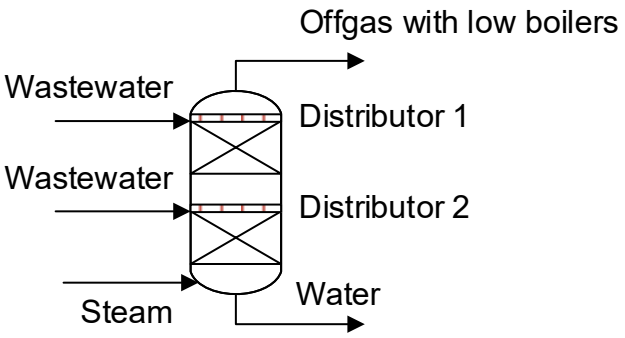

Figure 1: Wastewater stripper with two beds of random packings for fouling service.

2. Results and discussion

Since insufficiently irrigated areas can accelerate fouling (Xia et al., 2024) and decrease efficiency and uptime, a high-quality distributor was installed. Nevertheless, fouling was severe and led to unacceptably short uptimes. Two distributor designs intended to alleviate the problem are described in the following. Therefore, three different operational setups are discussed in the following, which are labled as initial, makeshift, and engineered setup. The differences in distributor quality Q_D and distribution quality D_Q are shown using TrayHeart. From process data, the fouling progress can be tracked via the pressure drop while the steam supply required is an indicator for the separation efficiency, with a higher steam demand correlating with a lower efficiency.

2.1 Initial Setup

The initial distributor for the lower bed was a pan distributor with small orifices, resulting in 40 drip points and 141 drip points per square meter. The distributor quality Q_D was 67%, according to Equation (1).

In Figure 2, the distribution quality D_Q computed from the TUM-WelChem model is shown for all three distributors as a function of bed depth H_P. In this paper, the deviation in liquid irrigation is used to estimate the degree of maldistribution.

The highest distribution quality is obtained with the original pan distributor with D_Q reaching its peak at 82% after 0.5 m and slowly deteriorating due to evolving wall flow. In the top slice, the red hexagons do not accurately represent the locations of the drip points. The seemingly irregular distribution is caused by a mismatch of the hexagonal grid, which directly results from packing element size, and the grid of drip points.

After the column's first startup, reality challenged both theory and design. Despite expectations of excellent liquid distribution, severe fouling caused significant maldistribution, and pressure drop as well as steam demand in the stripper increased. Later inspection confirmed the fouling.

Fouling likely began with plugged orifices, leading to distributor overflow and heavy wall flow. Despite some operational changes, runtime remained insufficient, forcing a temporary solution: operation without a distributor.

2.2 Makeshift Setup

Following the pan distributor's failure, it was removed, and liquid was introduced at the center of the packed bed's top using a 50 mm feed pipe with an elbow.

This radical change stabilized operations, extended the uptime of the column, and enabled tolerable separation performance. The distributor quality Q_D of such a feed pipe exceeds 97%, as calculated using Equation (1) from Moore and Rukovena (1987), implying a superb distributor quality. This single drip point scenario shows the limits of

the equation and the method in general, as they do not consider drip point density. As shown by the dashed line in Figure 2, the distribution quality is unsatisfactory. Only after 4 m, or more than half the bed, the “natural” distribution quality of the installed packing is reached. The slices on the right of Figure 2 show the slow lateral spread from the center drip point. Even after 4 m, a homogeneous distribution is not reached.

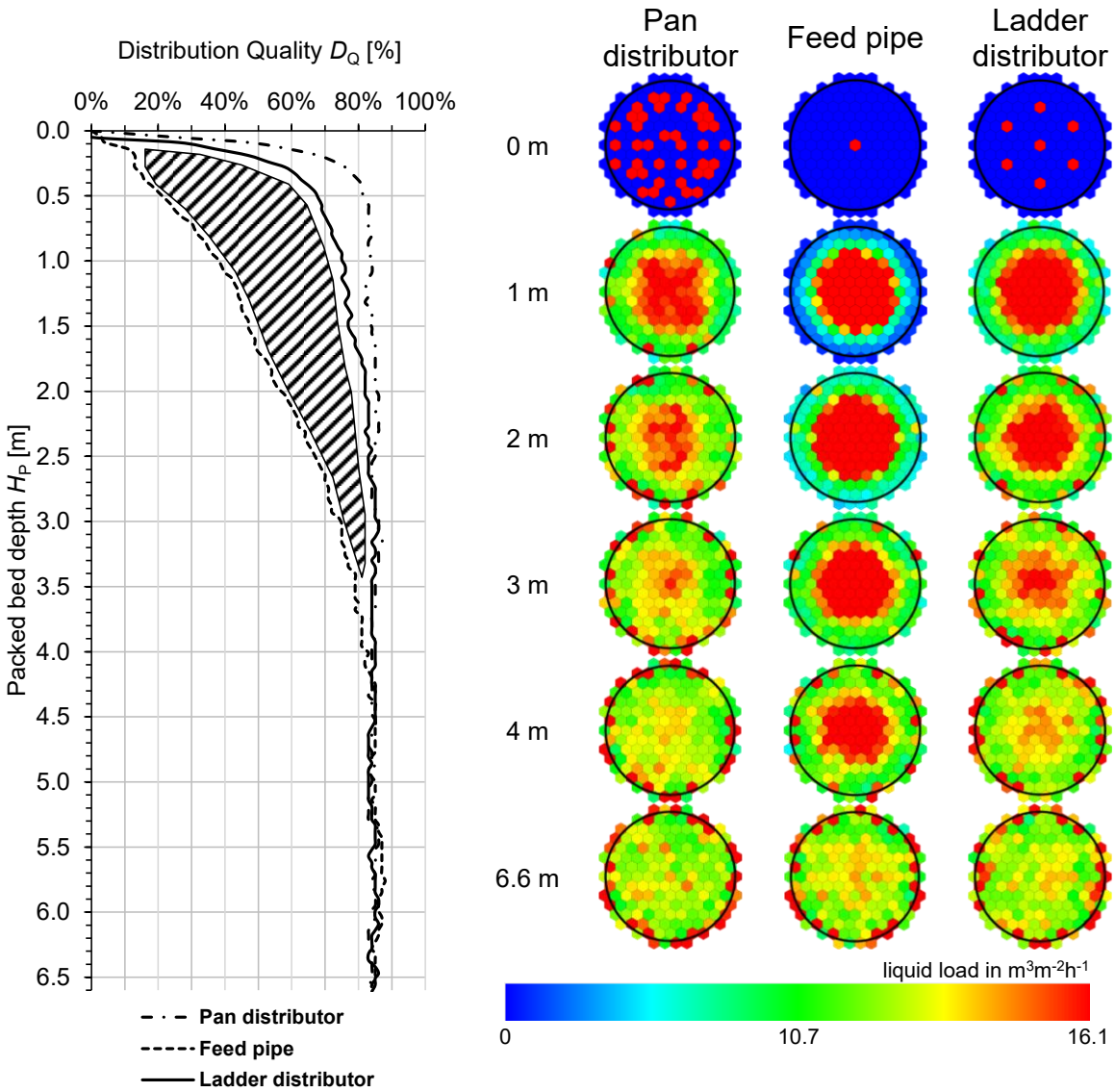

Figure 2: Liquid distribution quality D_Q and cell model from TrayHeart (Wild and Engel, 2007) plotted over the packed bed depth H_P for a pan distributor, a feed pipe, and a ladder distributor. The hatched area between two curves qualitatively indicates lost efficiency due to bad irrigation.

Nevertheless, wastewater quality was still maintained, although separation efficiency was likely lost. Plant data of the steam supply in Figure 3 (a) shows higher steam consumption from the middle of the production campaign onwards. The purple line shows that the maximum steam supply m_S of 1500 kg/h was frequently reached throughout the campaign, confirming reduced separation efficiency. In Figure 3 (b), the column pressure drop Δp is plotted for the production campaign. After 40% of the campaign, the pressure drop reached almost five times the initial value. The feed pipe as a distributor did not plug, but fouling was still a problem, originating in the packing

due to non-irrigated zones. The fouling rate is reduced compared to the pan distributor, where distributor fouling introduced severe maldistribution right from the initial distribution.

2.3 Engineered Setup

Based on the operational experience with an excellent distributor prone to fouling and an operable, but subpar liquid distributor with a single drip point, an improved, robust distributor design was desired to save stripping steam and further extend the runtime. As a compromise, a new ladder distributor with 7 larger orifices, i.e., drip points was designed and implemented in the column. The distributor quality Q_D of 60%, according to Equation (1), is high for a standard distributor. A drip point density of 25 points per square meter is achieved, still far below the recommended minimum value of 65. According to Figure 2, the distribution quality D_Q of the ladder distributor is, as expected, also between the previous extremes. After 0.5 m in the packed bed, a distribution quality of about 67% is reached. As shown in Figure 3, pressure drop decreases and steam demand is reduced compared to operation with the feed pipe. The improved distribution quality in the upper part of the lower bed appears to enhance separation efficiency and may postpone fouling onset. Fouling progress was probably slowed down due to better wetting. Unexpected shutdowns due to fouling were eliminated.

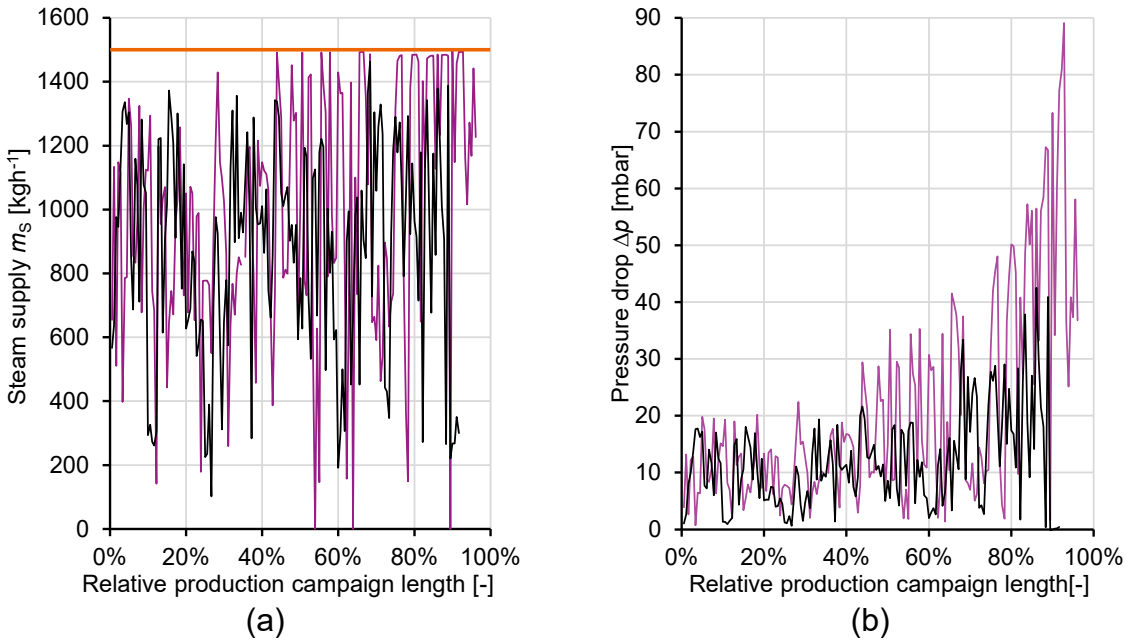

Figure 3: Process data for (a) steam supply and (b) pressure drop over relative production campaign length (black: ladder, purple: pipe). Reference time frame is a standard campaign duration.

2.4 One step further

Figure 2 indicates that the gap in distribution quality between the ladder and pan distributors is smaller than that between the feed pipe and ladder. Although the drip point density of the ladder distributor is far lower than the recommended minimum of 65 points per square meter, an acceptable distribution quality is predicted and ultimately observed during operation. Would an increase in drip points to industry standard improve the distribution quality enough to consider a new distributor? According to geometrical considerations using the Moore and Rukovena method, the next best distributor with a triangular drip point pattern has 19 drip points, which results

in a density of 67 drip points per square meter. According to TrayHeart, a slight improvement of distribution quality can be observed in the beginning, with the values lying below the pan distributor but above the ladder with seven drip points. The distributor quality is even slightly worse with Q_D being 57%, caused by the strict triangular positioning without optimizing individual drip point positions to close the wall gap. All in all, the small benefit in distribution quality is not worth the risk of more narrow orifices, which come with an increase in the number of drip points.
The results show that it is possible to achieve sufficient liquid distribution even with a significantly lower drip point density than recommended if the overall arrangement is correct and the distribution in the packed bed below is investigated.

3. Conclusions

Optimal performance of packed columns requires homogeneous liquid and gas distribution, which is a challenge in fouling applications. Liquid maldistribution, caused by fouling and non-ideal distributor design, reduces separation efficiency and favors fouling formation. In an industrial wastewater stripper with a 600 mm diameter, three liquid distributor setups were implemented and evaluated: a pan distributor, a feed pipe, and a ladder distributor. The pan distributor, despite its theoretical supremacy, failed due to fouling, causing severe maldistribution and frequent shutdowns. A makeshift feed pipe with only a single drip point improved uptime but resulted in poor distribution, packing fouling, and higher steam demand. A systematic analysis of different distributor designs based on Wild and Engel (2007) and the findings of Moore and Rukovena (1987) led to an engineered ladder distributor. The improved design successfully proved a balance between distribution quality and robustness in operation, reducing fouling and energy consumption.

References

Gorak, A.; Olujic, Z., 2014. Distillation: Equipment and Processes. Elsevier.

Gorak, A.; Schoenmakers, H., 2014. Distillation: Operation and Applications. Elsevier.

Hanusch, F.; Kender, R.; Engel, V.; Rehfeldt, S.; Klein, H., 2019a. TUM–WelChem cell model for the prediction of liquid distribution in random packed columns. AIChE Journal, 65 (8), e16598. DOI: 10.1002/aic.16598.

Hanusch, F.; Künzler, M.; Renner, M.; Rehfeldt, S.; Klein, H., 2019b. Liquid distributor design for random packed columns. Chemical Engineering Research and Design, 147, 689 - 698. DOI: 10.1016/j.cherd.2019.05.035.

Kister, H.Z., 2006. Distillation Troubleshooting. John Wiley & Sons, New Jersey.

Kunesh, J.G.; Lahm, L.L.; Yanagi, T., 1987. Controlled maldistribution studies on random packing at a commercial scale. EFCE Publication Series (European Federation of Chemical Engineering). 62, A233-A244.

Moore, F.; Rukovena, F., 1987. Liquid and Gas Distribution in Commercial Packed Towers. CPP Ed. Eur., 11.

Stichlmair, J.; Klein, H.; Rehfeldt, S., 2021. Distillation - Principles and Practice (2nd Edition), John Wiley & Sons, New Jersey.

Towler, G.; Sinnott, R., 2022. Chemical Engineering Design - Principles, Practice and Economics of Plant and Process Design (3rd Edition), Elsevier.

Wild, A.; Engel, V., 2007. Ein neuartiges Zellenmodell zur Maldistribution und Verteilgütebestimmung. ProcessNet-Conference, Karlsruhe.

Xia, M.; Inderwies, K.; Klein, H.; Rehfeldt, S. 2024. Where Does Fouling Occur in Individual Random Packing Elements? A Simulative Investigation. Chemie Ingenieur Technik, 96, 1433-1440. DOI: 10.1002/cite.202300220.

Characterization of liquid distribution in structured packings by a novel film thickness sensor in a miniaturized measuring cell

Pascal Pötter [a], Maria Polyakova [a], Marcus Grünewald [a]

[a] Ruhr University Bochum, Laboratory of Fluid Separations, Universitätsstrasse 150, 44801 Bochum, Germany
poetter@fluidvt.rub.de; polyakova@fluidvt.rub.de; gruenewald@fluidvt.rub.de

Abstract. The reliable design of packed columns requires accurate knowledge of local hydrodynamics to consider maldistribution effects. Yet most established methods provide only integral values such as pressure drop, hold-up or HTU/NTU values. To address this gap, a new liquid film thickness sensor was designed that combines high spatial resolution, eliminating sensitivity to conductivity variations, and the ability to measure local film velocities. The sensor was implemented in a miniaturized measuring cell to investigate film flow at the surface of structured packings. The results show a strong dependency on film distribution, temporal fluctuation intensity and wetted area on the gas load. At low gas loads, film flow inside the packing is dominated by rivulets and large un-wetted regions, while the beginning of the loading range results in a pronounced homogenization of the flow and a significant increase in the wetted area and the average film thickness. In the wall gap, a clear increase in liquid carryover was observed, consistent with known trends in literature [1,2]. The study demonstrates that the sensor provides locally resolved hydrodynamic data and offers a basis for improved model parameterization.

All rights reserved by the authors as per DA2026 copyright notice.

Keywords miniaturized measuring cell, structured packing, local measurement, liquid distribution, film thickness sensor

1. Introduction

Key design decisions for packed columns must be made at very early stages of a development process, even though only limited information on the mixture properties, operating conditions, or expected hydrodynamic behaviour is available at that point [3]. As the project progresses, both model complexity and the effort required for design modifications increase substantially, meaning that insufficiently validated assumptions can lead to significant costs in later phases [4,5]. At this stage, design decisions are necessarily based on predictive models that must later be transferred from laboratory or pilot scale to industrial column dimensions.

For this scale-up, different models are employed, which are all limited in their application. Established design methods predominantly rely on global quantities such as pressure drop, liquid hold-up, and HTU/NTU values [6], but they do not resolve local effects such as maldistribution or wall flow. Because of this, the accuracy is limited. The equilibrium stage model, for instance, neglects radial inhomogeneities [7], whereas rate-based models require hydrodynamic input such as HTU values, mass-transfer coefficients, and the effective interfacial area; quantities that often can only be estimated with limited accuracy [7]. Even modern modelling approaches, including rigorous, dynamic, or AI-based models [8], rely on both reliable global and local data. Robust model parameterization therefore necessitates experimental methods capable of capturing local flow phenomena. Due to these uncertainties, experiments remain essential to secure the scale-up and the models [5].

However, many established experimental techniques still primarily provide global or integral quantities and do not resolve local liquid distribution on packing surfaces. This limitation is critical, as liquid maldistribution has a decisive influence on separation efficiency and must therefore be considered. One option for measuring liquid distribution is the use of segmented liquid collectors, which provide cross-sectionally resolved data but are highly invasive. Consequently, several new local measurement techniques have been developed, including chromatographic methods, wire-mesh sensors, and optical systems [9]. However, these approaches still face limitations, such as restricted optical access or complex evaluation procedures, and in the case of chromatographic techniques, the restriction to quasi-steady conditions. Conductivity- and capacitance-based film-thickness sensors represent a promising alternative. Their foundations go back to Van Rossum (1959) [10] and Coney (1973) [11]. With the introduction of printed circuit board technology after 2009, high-resolution sensors became feasible [12], followed by conductivity-compensated layouts [13], velocity measurements for thin films [14], and first applications on structured packing sheets [15,16]. Existing approaches, however, typically offer either high spatial resolution without temperature compensation or robust signals

at coarse resolution (>70.5 mm²). To date, no sensor-based approach provides spatially and temporally resolved film-thickness data inside structured packings with sufficient resolution for direct hydrodynamic model validation. The objective of this work is therefore the development and experimental investigation of a new liquid film thickness sensor featuring high spatial resolution, reduced sensitivity to temperature effects, flexible applicability, and the ability to measure local film velocities. The sensor is first calibrated and subsequently integrated into a miniaturized measuring cell to analyse film-thickness distribution, wall-flow phenomena, and wetting behaviour within the channels of structured packings.

2. Film Thickness Sensor Concept and Measurement Principle

This chapter presents the newly developed sensor concept which, compared to existing approaches, offers both a better spatial resolution and a substantially reduced sensitivity to variations in liquid conductivity, while additionally enabling the determination of local film velocities. As outlined before, established liquid film thickness sensors typically face two fundamental limitations: either their spatial resolution is insufficient, or their signals respond strongly to global conductivity changes in the medium. The sensor introduced here addresses both constraints by combining a conductivity-compensated signal evaluation with a finely resolved matrix architecture. The characterization begins with an introduction to the measurement principle and electrode geometry, followed by calibration procedures and capacitive proof of concept. Experimental verification is carried out on a planar plate which, due to its optical accessibility, stable film flow, and widespread use in literature, represents a suitable benchmark system and prepares the transition toward application in the miniaturized measuring cell.

2.1 Measurement Principle and Sensor Design

The measurement principle is based on a conductivity-based film thickness measurement in which an electric field is generated between a transmitting and one or more receiving electrodes. When a conductive liquid film covers the flush-mounted electrodes, a three-dimensional potential field forms and closes the current path. The measured current depends on the local film thickness, the lateral extent of the film, the medium's conductivity, and the electrode geometry. For small film heights, the effective cross-section of the current path increases, reducing electrical resistance and increasing the signal. Beyond a characteristic saturation thickness, further increases in film height only marginally affect the current. This saturation behaviour is determined primarily by electrode geometry and spacing. The resulting asymptotic relationship yields a nonlinear calibration curve, well described by a Gompertz function. Conventional sensor designs face several limitations, including temperature and conductivity sensitivities, restricted spatial resolution, and crosstalk between neighbouring measurement fields, while lacking the capability for simultaneous velocity measurements. The present design overcomes these issues through a tailored electrode matrix, conductivity-compensated signal evaluation, and a two-row layout enabling cross-correlation-based velocity determination.

The electrode layout is printed onto a flexible circuit board with a minimum bending radius of 1.9 mm. It comprises 128 measurement points with a pixel size of 4.4 × 2.6 mm² (Figure 1a), allowing the detection of liquid distribution both within and between channels of structured packing sheets. Each transmitter is paired with two receivers (according to the concept of Lee [17]), providing two current signals per measurement point. Their ratio forms a conductivity-compensated signal that suppresses temperature- and concentration-driven variations. Ground electrodes are placed between adjacent pixels to limit lateral field expansion and reduce crosstalk. All electrodes are gold-plated to prevent corrosion and ensure long-term stability. The transmitters can sequentially be activated up to 10 kHz, enabling the detection of unsteady wavy film flows and velocity fields. The circuit board has a thickness of 0.16 mm.

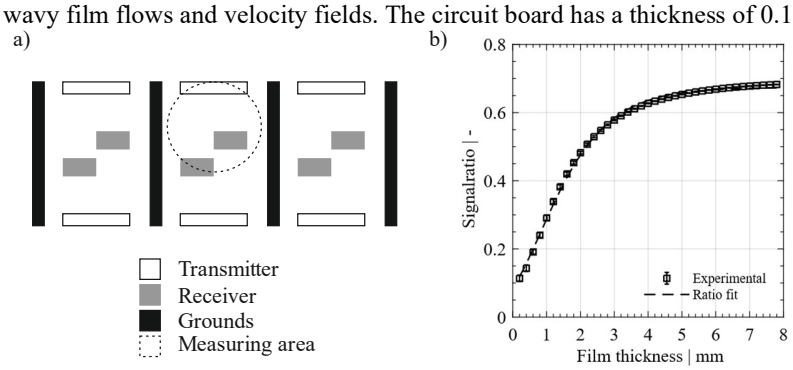

Figure 1: a) Design of the liquid film thickness and b) calibration curve.

2.2 Calibration Concept

To quantify the sensor characteristics, the relationship between signal and film thickness is determined experimentally. Calibration is performed by lowering a planar plate onto the sensor, which is submerged in a container filled with deionized water adjusted to a target conductivity of 300 µS/cm using sodium chloride (NaCl). The plate can be moved vertically with a resolution of 2.5 µm. From the movement speed and time, a defined film thickness above the sensor is obtained. The sensor is connected identically to later flow experiments, and a dry measurement is used for offset correction. Signals are recorded across the full relevant film-thickness range—from direct plate contact to well beyond saturation. The measured currents are plotted against the corresponding film thicknesses, and a Gompertz function is fitted to the data. Due to local fabrication variations, an individual inverse Gompertz function is determined for each measurement point.

The calibration shows excellent agreement between data and fit ($R^2 \approx 0.998$). Below approximately 0.5 mm, the relative signal noise increases; above roughly 4 mm, the calibration curve flattens (Figure 1b). The optimal measurement range therefore lies between 0.5 and 4 mm but can be shifted for other liquid systems by adjusting electrode spacing. The influence of global conductivity variations amounts to only ±3.2 %, confirming the effectiveness of the signal-ratio compensation approach.

3. Miniaturized Measuring Cell Concept

As shown, experimental investigations employing high-resolution measurement systems are indispensable. However, such experiments are time- and resource-intensive. Over the past years, miniaturized experimental setups have therefore emerged as a promising alternative to conventional laboratory and pilot-scale equipment [18]. Miniaturized measuring cells address this gap by combining a representative flow field with the flexibility and low material demand of laboratory-scale experiments. At the same time, they retain the small internal volume of laboratory columns while significantly reducing scale-dependent deviations such as pronounced wall effect. This enables the essential flow phenomena of industrial columns to be represented under controlled and scalable conditions. For structured packings, this typically involves rectangular column segments that reproduce the hydrodynamic behaviour of the packing as realistically as possible, including film flow, liquid distribution, channel-to-channel interactions, and wall effects. Previous studies demonstrated that miniaturized measuring cells can accurately reproduce pressure drop, hold-up, and separation performance of pilot-scale columns while requiring only a fraction of the typical liquid inventory [18–20]. A major advantage of miniaturized measuring cells is their significantly improved accessibility for advanced measurement techniques. Their compact geometry facilitates the integration of high-resolution measurement techniques, and the reproducible flow conditions allow targeted variation of operating points and systematic assessment of the system response to changes in liquid and gas load. They enable detailed investigations of channel-resolved liquid distribution, wall flow, the effectiveness of wall wipers, and maldistribution. These phenomena strongly influence separation performance but remain inaccessible in many conventional laboratory setups.

In this work, the miniaturized measuring cell serves as the platform for implementing and testing a newly developed liquid film thickness sensor. Its geometry, the excellent accessibility of the packing surfaces, and the well-defined boundary conditions allow the integration of electrodes directly onto the packing sheets, enabling spatially resolved measurement of local film thickness under realistic operating conditions. The miniaturized measuring cell thus forms the intermediate step between sensor calibration and future applications in more complex column sections.

4. Application in the Miniaturized Measuring Cell

4.1 Experimental Setup and Procedure

The sensor concept is subsequently transferred to more technical and hydrodynamically complex geometries. Measurements were conducted in a miniaturized measuring cell based on Hapke (2022), consisting of a rectangular packing cross-section. Three structured sheets of Montz Pak B1-250 are used as packing elements with a width of 300 mm and a height of 196 mm. The lateral wall gap is 6 mm wide and equipped with a wall wiper designed to redirect liquid back into the packing core.

An air–water system is used; for conductivity-based measurements, deionized water is adjusted to a conductivity of 300 µS/cm. Liquid is introduced via an idealized distributor providing one drip point per channel. Measurements are carried out at several gas loads (0–2.27 $Pa^{0.5}$) at a liquid load of 40 m^3/m^2h. To determine the local flow patterns, four sensors are installed in the measuring cell: one in the wall gap and two within the packing, with one of these positioned near the distributor to record the initial liquid distribution. The fourth sensor is positioned at the lower end of the packing, representing the lateral liquid distribution (Figure 2). The evaluation of two of these will be presented

below as examples. The measurement duration per operating point was 20 s, and the sampling rate of 2.5 kHz enabled both time-averaged and transient evaluations.

Data processing is based on the individual calibration functions for each measurement point. First, the local time-averaged film thickness is obtained using the inverse Gompertz function. The resulting two-dimensional film-thickness fields allow differentiation between flow regimes such as dry regions, rivulet paths, and fully wetted areas. The wetting fraction is determined from the ratio of wetted to total measurement points. The temporal standard deviation at each pixel is used to identify unsteady phenomena such as waves or local transition points.

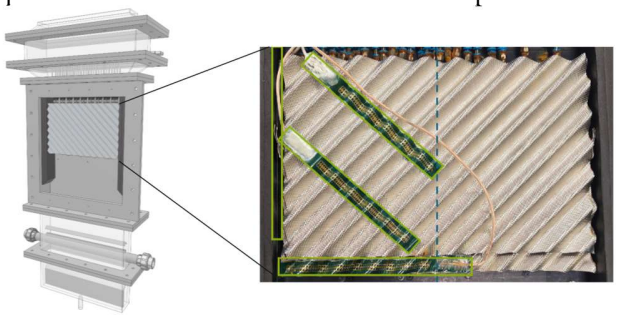

Figure 2: Sensor positions inside the packing: wall gap, lower end, two inside of the packing.

4.2 Results

The time-averaged film-thickness fields of the sensor inside the packing show a dependence of the flow structure on gas load (Figure 3). At low gas loads, the liquid distribution is strongly inhomogeneous. The surface is dominated by rivulets and unwetted regions, reflected in low wetting fractions of 29.6 % (1.41 $Pa^{0.5}$) and 26.8 % (2.04 $Pa^{0.5}$). The mean film thicknesses are comparable at 0.69 mm and 0.65 mm. At specific sensor locations (e.g., row 2, column 21), pronounced local film accumulation occurs for both conditions, characteristic of rivulet formation in channel-guided film flows. The temporal standard deviation increases from 0.103 mm (1.41 $Pa^{0.5}$) to 0.171 mm (2.04 $Pa^{0.5}$), indicating stronger gas–liquid interactions.

Once the loading point (2.24 $Pa^{0.5}$) is reached, the flow visibly homogenizes. The liquid spreads more broadly, and although some unwetted areas remain, they are significantly reduced. The wetting fraction increases to 59.9 %, and the mean film thickness rises to 0.748 mm. Simultaneously, temporal fluctuations intensify (0.255 mm), reflecting enhanced interfacial interactions and increased local hold-up. The spatial standard deviation decreases from roughly 0.45 mm to 0.347 mm, corroborating the observed homogenization of the liquid distribution.

At the flooding point (2.27 $Pa^{0.5}$), this trend continues. The liquid distributes almost completely across the sensor area, and the wetting fraction increases further to 68.7 %. The mean film thickness remains almost constant at 0.745 mm, whereas temporal fluctuations reach its maximum at 0.290 mm, characteristic of the onset of vigorous wavy-film motion directly prior to full flooding. The transition from local rivulets to a dynamic, spatially extensive film flow is clearly visible. The measured quantities correlate well with the increasing hold-up and expected hydraulic regime transitions.

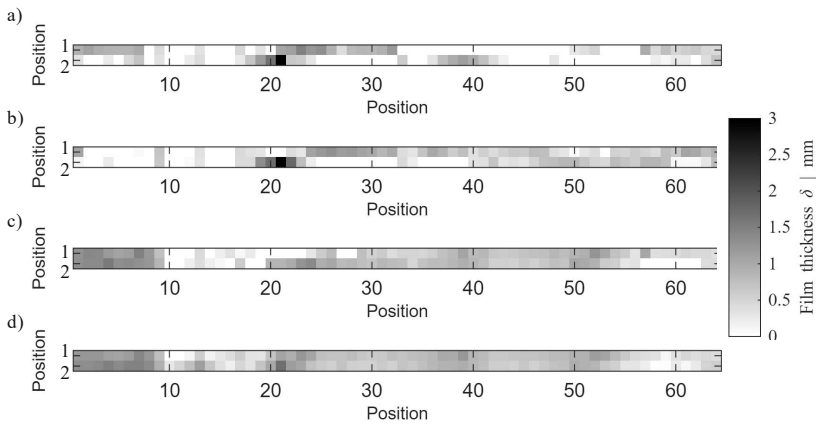

Figure 3: Mean liquid distribution inside the packing for gas loads at a) 1.41 $Pa^{0,5}$, b) 2.04 $Pa^{0,5}$, c) 2.24 $Pa^{0,5}$ and d) 2.27 $Pa^{0,5}$.

The sensor in the wall gap provides additional insight into wall flow behaviour and the effectiveness of the wall wiper (Figure 4). At low gas loads, a small liquid hold-up forms above the wall wiper (row 2, column 21). Below the wiper, the wall region remains largely dry until, at position 17, a packing channel reaches the wall and induces localized wetting. The liquid spreads across the width of the gap and drains laterally. It should be noted that due to the slight elevation of the sensor relative to the wall surface, a portion of the liquid likely bypasses the sensor laterally; this does not affect the qualitative interpretation of the hydrodynamics. The mean film thickness is 0.651 mm, and the wetting fraction is 13 %, confirming the low degree of wall channelling at low loads. The temporal standard deviation is 0.138 mm.

At the flooding point, the flow pattern changes fundamentally. Liquid accumulates in the wall gap: the wetting fraction increases to 44.3 %, and the mean film thickness rises to 0.693 mm. This demonstrates a clear intensification of wall flow, qualitatively consistent with the observations in the literature [1,2], who also reported increased wall channelling in the loading regime. The temporal standard deviation increases to 0.290 mm, indicating that the flooding process in the wall gap is governed by a continuous rise in liquid hold up and pronounced dynamic fluctuations.

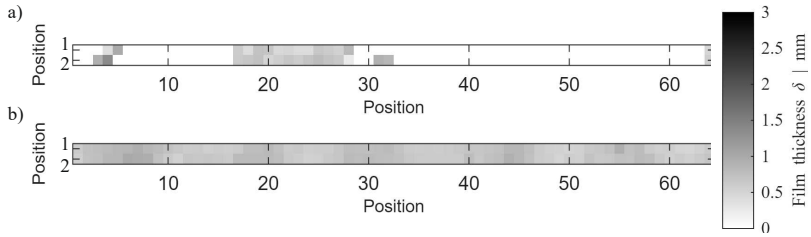

Figure 4: Mean liquid distribution inside the wall gap at a) 2.04 $Pa^{0,5}$, b) 2.27 $Pa^{0,5}$.

5. Conclusions and Outlook

The results demonstrate that the presented liquid film thickness sensor enables reliable and spatially high-resolution measurement of local flow phenomena in structured packings. Within the miniaturized measuring cell, the measurement principle was successfully transferred to more complex, channel-guided film flows. The measurements revealed a pronounced dependence of film-thickness distribution, wetting behaviour, and temporal unsteadiness on operating conditions. At low gas loads, the flow was dominated by distinct rivulet systems and low wetting; the transition into the loading regime led to a marked homogenization of the flow and an increase in local hold-up. In the wall gap, a progressive increase in wall channelling was observed, qualitatively consistent with trends reported in the literature. Combining high spatial resolution, conductivity-compensated signal processing, and the capability for velocity determination, the sensor provides a powerful tool for the local characterization of packing hydrodynamics.
There are several prospects for future work. First, the sensor design should be extended to non-conductive systems and smaller film thicknesses. This will require adapting the evaluation unit and further reducing the distance between the electrodes. Second, transferring the measurement methodology to different packaging geometries, surface modifications, and liquid systems will enable a systematic investigation of the influence of channel structure and physicochemical properties. In the long term, the combination of a miniaturized measuring cell with high-resolution film thickness measurement has the potential to provide a valuable database for the development of improved hydraulic models and data-driven scale-up methods.

REFERENCES

[1] M. Grünewald, G. Zheng, M. Kopatschek, Auslegung von Absorptionskolonnen - Neue Problemstellung für eine altbekannte Aufgabe, Chemie Ingenieur Technik 83 (2011) 1026–1035. https://doi.org/10.1002/cite.201100041.
[2] R.J. Kouri, J. Sohlo, Liquid and gas flow patterns in random packings, Chemical Engineering Journal 61 (1995) 95–105.
[3] W. Frey, F. Heimann, S. Maier, Wirtschaftliche und technologische Bewertung von Verfahren, Chemie Ingenieur Technik 62 (1990) 1–8. https://doi.org/10.1002/cite.330620103.
[4] J. Strube, F. Grote, J.P. Josch, R. Ditz, Process Development and Design of Downstream Processes, Chemie Ingenieur Technik 83 (2011) 1044–1065. https://doi.org/10.1002/cite.201100017.
[5] S. Ripperger, K. Nikolaus, Entwicklung und Planung verfahrenstechnischer Anlagen, Springer Berlin Heidelberg, Berlin, Heidelberg, 2020.

[6] M. Schultes, Research on Mass Transfer Columns: passé?, Chemical Engineering & Technology 36 (2013) 1539–1549. https://doi.org/10.1002/ceat.201300192.
[7] E. Kenig, State-of-the-Art Modeling of Separation Columns: A Review, Chemical Engineering Transactions 94 (2022) 325–330.
[8] J.-U. Repke, Distillation and Absorption in the light of current challenges and new technical chances – Special Issue concerning the 12th International Conference on Distillation and Absorption Toulouse, France, Chemical Engineering Research and Design 197 (2023) 581–582. https://doi.org/10.1016/j.cherd.2023.08.015.
[9] U. Hampel, M. Schubert, A. Döß, J. Sohr, V. Vishwakarma, J.U. Repke, S.J. Gerke, H. Leuner, M. Rädle, V. Kapoustina, L. Schmitt, M. Grünewald, J.H. Brinkmann, D. Plate, E.Y. Kenig, N. Lutters, L. Bolenz, F. Buckmann, D. Toye, W. Arlt, T. Linder, R. Hoffmann, H. Klein, S. Rehfeldt, T. Winkler, H.-J. Bart, D. Wirz, J. Schulz, S. Scholl, W. Augustin, K. Jasch, F. Schlüter, N. Schwerdtfeger, S. Jahnke, A. Jupke, C. Kabatnik, A.S. Braeuer, M. D'Auria, T. Runowski, M.F. Casal, K. Becker, A.-L. David, A. Górak, M. Skiborowski, K. Groß, H. Qammar, Recent Advances in Experimental Techniques for Flow and Mass Transfer Analyses in Thermal Separation Systems, Chemie Ingenieur Technik 92 (2020) 926–948. https://doi.org/10.1002/cite.202000076.
[10] J.J. van Rossum, Experimental investigation of horizontal liquid films, Chemical Engineering Science 11 (1959) 35–52.
[11] M.W.E. Coney, The theory and application of conductance probes for the measuremnt of liquid film thickness in two-phase flow, Journal of Physics E: Scientific Instruments 6 (1973).
[12] M. Damsohn, H.M. Prasser, High-speed liquid film sensor with high spatial resolution, Meas. Sci. Technol. 20 (2009) 114001. https://doi.org/10.1088/0957-0233/20/11/114001.
[13] M.S. Ko, B.A. Lee, W.Y. Won, Y.G. Lee, D.W. Jerng, S. Kim, An improved electrical-conductance sensor for void-fraction measurement in a horizontal pipe, Nuclear Engineering and Technology 47 (2015) 804–813. https://doi.org/10.1016/j.net.2015.06.015.
[14] H. Ding, Z. Chen, H. Sun, Y. Yang, Z. Liang, Y. Zhang, Measurment of the thin liquid film at the wet-gas outlet of the supersonic separator by FPC conductance sensor, Open Research Exeter (2023).
[15] P. Pötter, K. Mielke, M. Grünewald, M. Polyakova, Application of Film Thickness Sensors in Miniaturized Experimental Setups, Bochum, 2025.
[16] P. Pötter, M. Polyakova, M. Grünewald, Entwicklung eines flexiblen Filmdickensensors zur Bestimmung der Flüssigkeitsverteilung in einer Packungskolonne, Bochum, 2024.
[17] K.B. Lee, J.R. Kim, G.C. Park, H.K. Cho, Feasibility Test of a Liquid Film Thickness Sensor on a Flexible Printed Circuit Board Using a Three-Electrode Conductance Method, Sensors 17 (2016). https://doi.org/10.3390/s17010042.
[18] A. Merkel, M. Polyakova, M. Grünewald, A miniaturized measuring cell to assist in the design of packed columns for distillation, Separation and Purification Technology 380 (2026) 135282. https://doi.org/10.1016/j.seppur.2025.135282.
[19] M. Hapke, Entwicklung einer Miniaturmesszelle zur zeit- und kosteneffizienten Charakterisierung der Fluiddynamik in strukturierten Packungen. Dissertation, Bochum, 2022.
[20] R. Pöschmann, J. Paschold, S. Mueller, L.-S. Harding, N. Lachmann, C. Hiller, I. Ausner, A. Gäbler, M. Illner, G. Brösigke, J.-U. Repke, Will laboratory and pilot plant columns soon become superfluous? – A concept for the determination of structured packing characteristics in a measuring cell under distillation conditions, Separation and Purification Technology 325 (2023). https://doi.org/10.1016/j.seppur.2023.124617.

Design and experimental analysis of liquid distributors for laboratory columns

A. Dobschall[1], H. S. Rennebaum[1], J. Bindseil[1], A. Penn[1], M. Skiborowski[1]
[1]Hamburg University of Technology, Hamburg, Germany

Abstract
The liquid distribution is a key parameter for the mass transfer efficiency of separation columns. Particularly for laboratory-scale columns, which are characterized by a large wall area relative to the column volume, a uniform initial distribution is crucial. Therefore, different distributor designs are developed and tested with water. In integral experiments, the initial distribution is measured with a liquid collector directly below the distributor. Furthermore, the liquid distribution below different structured packing elements made from metal and additive manufacturing is measured and compared for the distributor and a single drip point. Additional insights on the development of the liquid distribution inside the packing are gained via magnetic resonance imaging. The maldistribution factor is used to quantify the uniformity of the liquid distribution. A pressure-driven liquid distributor is identified as the most efficient providing an excellent initial liquid distribution with a maldistribution factor of 0.08. The good initial distribution is however not preserved for the additively manufactured packings due to a large amount of wall flow.

Keywords
Additive manufacturing, Integral experiments, Laboratory-scale column, Liquid distributor, Magnetic resonance imaging, Structured packing

1. Introduction

Due to the wide application and high energy demand of gas-liquid separation processes, improved column internals are of high interest. To save resources, experimental investigations are often conducted in laboratory scale columns, assuming a sufficient transferability of the results, which becomes challenging as the ratio of wall area to column volume decreases with column diameter. The liquid distribution is an important performance parameter which is essential for an efficient mass transfer [1]. In order to operate laboratory columns in an effective manner, it is necessary to ensure a uniform initial liquid distribution with the presence of adequate liquid distributors. The common industrial designs of liquid distributors encompass nozzles, weirs, perforated plates or troughs [2,3]. The specific designs cannot directly be transferred to laboratory scale since the liquid distribution is significantly influenced by the scale down due to an increased occurrence of wall flow [4]. Consequently, the optimum drip point density increases for decreasing diameters due to higher tendency towards wall flow [5]. Da Cunha et al. [6] proposed a nature-inspired tree structure, which was designed and tested for a DN150 column. However, liquid distributor designs and design methods intended for laboratory or pilot plant scale are scarce. Only some general guidelines for the design of liquid distributors including density and uniformity of the drip points are available [5]. Hanusch et al. [5,7] presented a design approach based on the TUM WelChem Cell Model including the interaction between the liquid distributor and the usually neglected packing. In contrast to the design of liquid distributors, the liquid

distribution itself has been more extensively researched, especially using a collector to conduct integral experiments for different distributor designs, packings and operating conditions [5,6,8]. The maldistribution factor (M_f) or coefficient of variation are used to determine the uniformity of the liquid distribution. Few tomographic or optical methods have been applied yet to evaluate the liquid distribution along the packed bed. Hill et al. [9] used tomographic measurements to qualitatively compare them to the phase distribution from computational fluid dynamics (CFD) simulations. Guo et al. [10] simulated multiphase flow on plates with different corrugation patterns, which they validated qualitatively via Particle Image Velocimetry. They used small particles of 10 µm to be able to trace the flow without affecting it. Mahr and Mewes [11] used X-ray computer tomography to determine the liquid holdup in a cut-out of a corrugated sheet packing and measured the liquid film thickness by X-ray projection. So far, magnetic resonance imaging (MRI) has not been used in this context, which is, however considered a promising approach [12].
In this contribution, different designs of liquid distributors for a laboratory DN54 column are presented and evaluated through rigorous testing. Integral experiments are carried out using a collector tailored to the design of the liquid distributors. Furthermore, MRI measurements are conducted for locally resolved information on the liquid distribution. Due to its high design freedom and MRI-compatibility, additive manufacturing (AM) is employed to produce the column internals.

2. Methodology

Four different distributor types based on two different working principles are designed and investigated as depicted in Figure 1. A pressure-driven distributor is consisting of a channel structure with flat and tapered ends, referred to as 1a and 1b in the following. Furthermore, two gravity-driven distributors are designed. Distributor 2 features a small reservoir to accumulate the liquid until the outlet level is reached. The outlet flow is guided towards the drip points by capillary structures. Distributor 3 consists of a tree structure and is based on the design described by da Cunha et al. [6].

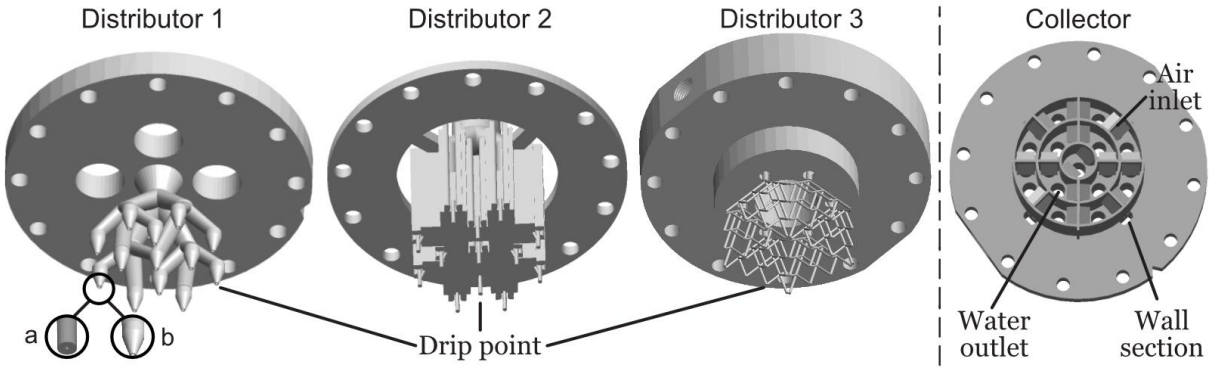

Figure 1: Side views of pressure-driven distributor with flat ends (1a) and tapered ends (1b), gravity-driven distributors including capillary structure (2) and tree structure (3) as well as top view of the corresponding liquid collector (from left to right).

Distributors 1a, 1b and 2 have 13 drip points each, which are uniformly distributed across the cross-section. This corresponds to a drip point density of 5676 m^{-2}, compared with 26197 m^{-2} for Distributor 3. Both values are 1-2 orders of magnitude above the rule-of-thumb recommendation of 65 to 100 drip points per square meter for industrial applications [3]. This aligns with the trend of increasing optimum drip point density for decreasing column diameters [5]. For reference, experiments are also conducted with a single drip point corresponding to a drip point density of 437 m^{-2}. The collector for the integral experiments, shown on the right in Figure 1, is engineered to

be compatible with the distributors 1a, 1b and 2. It offers one section for each drip point and two additional sections at the outer edge to quantify the wall flow. All 15 sections are identical in size. The liquid distributors and collector are printed from Clear Resin by means of stereolithography with a Formlabs Form 3+ printer. For the integral and MRI experiments, a test stand with a DN54 column and water at a liquid load of 20 $m^3m^{-2}h^{-1}$ is used. Modular sections of varying length can be used to adjust the height of the column to the desired conditions. Different configurations are investigated measuring the initial liquid distribution directly below the liquid distributor and with 260 mm distance between the liquid distributor and collector to allow for the incorporation of different structured packing elements of 100 mm height. As depicted in Figure 2, a metal corrugated sheet Montz B1-500 with and without wipers and an additively manufactured replica are used. For the MRI experiments, a spatial resolution of (1 x 1 x 1) mm^3 is used. The measurements encompass 105 horizontal slides with a scan duration of 34 s. For both methods, the experiments are performed in triplicate and M_f is used to quantify the uniformity of the liquid distribution, calculated as:

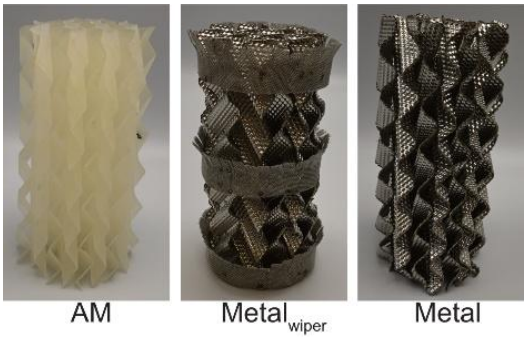

Figure 2: Structured packing element made from AM and a metal packing of type Montz B1-500 with and without wipers (from left to right).

$$M_f = \sum_{i=1}^{n} \left| \frac{u_{L,i} - u_L}{u_L} \right| \cdot \frac{A_i}{A} \qquad (1)$$

with n sections, the local and mean liquid velocity $u_{L,i}$ and u_L, the local area A_i and total cross-sectional area A [8]. For the utilized collector with 15 sections, M_f ranges from 0 (liquid is uniformly distributed across all sections) to 1.9 (liquid accumulates in a single section). The liquid velocity is determined gravimetrically in the integral experiments and based on the spin density in the MRI experiments. Given that no wall flow occurs for the measurements of the initial distribution, only the 13 inner sections of the liquid collector are taken into account for the determination of the M_f, whereas for the measurements below the packing, the wall sections are also considered. They are referred to as $M_{f,13}$ and $M_{f,15}$ respectively.

3. Results and discussion

The integral experiments cover all distributors and operating conditions, whereas the locally resolved MRI results are examined for the best distributor and the AM packing.

3.1 Integral experiments

A comparison of the initial liquid distribution for the different distributor types is shown in Figure 3. The pressure-driven distributor with tapered ends (1b) exhibits the lowest maldistribution factor of 0.08, indicating a nearly ideal initial distribution. For the same distributor with flat ends (1a), droplet retention was observed at several drip points due to increased surface tension at the outlet. As a result, this distributor exhibits a substantially higher $M_{f,13}$ of 0.42. A comparable distribution quality is achieved with the gravity-driven distributor based on a capillary structure (2), whereas the gravity-driven distributor featuring a tree structure (3) yields the least uniform distribution, with an $M_{f,13}$ of 1.0.

Figure 4 enables a more detailed comparison of the distributors based on the liquid distribution across the collector sections. The pressure-driven distributor with tapered ends (1b) generates an excellent distribution with a maximum deviation from the mean

flow of 17 %. The pressure-driven distributor with flat ends (1a) and the gravity-driven capillary structure (2) show much larger variations of up to 80 %. For the tree structure (3), the liquid load in individual sections deviates more than 300 % from the mean value. In addition, low reproducibility was observed for this distributor, as repeated measurements yielded markedly different distributions. The most efficient pressure-driven distributor with tapered ends (1b) is further applied in a study of structured packings, for which also a hose as a single drip point was tested for comparison to evaluate the efficiency of the liquid distributor.

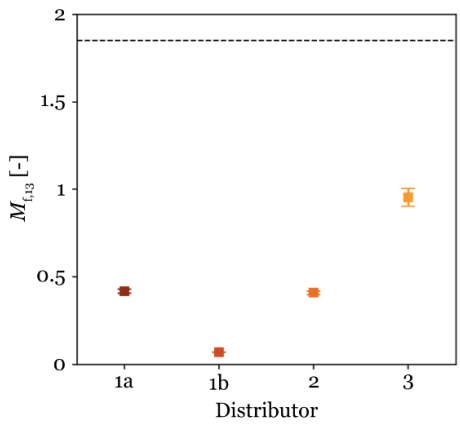

Figure 3: Maldistribution factor $M_{f,13}$ for different distributors; dashed line marks worst possible M_f.

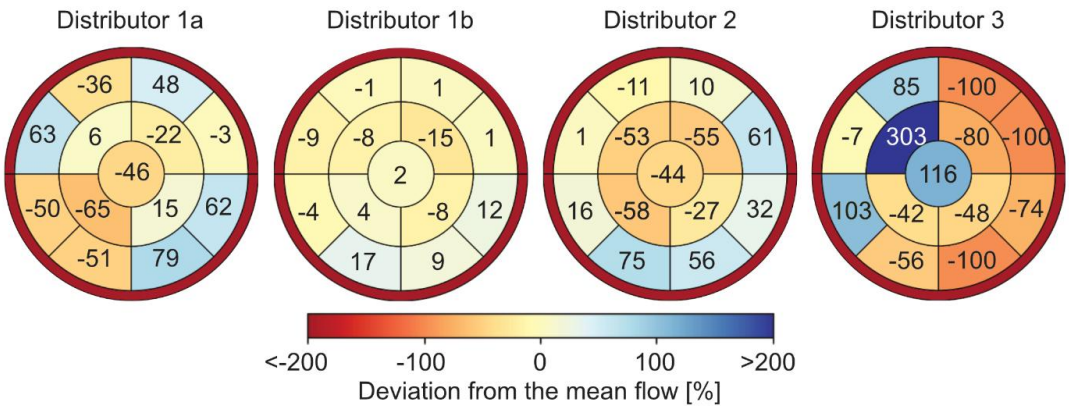

Figure 4: Visualization of the deviation of the flow inside the sections from the mean flow directly below the distributors averaged over triplicate measurements.

Figure 5 illustrates the resulting maldistribution factor and the wall flow below the structured packing elements. The wall flow quantifies the proportion of liquid collected in the two outer wall sections of the collector. It can be observed that $M_{f,13}$ increases from 0.08 to 0.3 for the empty column due to the increased distance between distributor and collector from 0 to 260 mm. The use of the distributor generally improves the liquid distribution in comparison with the single drip point, reducing $M_{f,13}$ by 40 % for the metal packing with wall wipers and by 21 % for the AM packing. For the latter, the single drip point, however, generates lower wall flow than the distributor due to its greater distance from the wall and the absence of wipers, which results in a decrease in $M_{f,15}$. While M_f increases significantly for all packings compared with the empty column, the metal packings tend to exhibit lower M_f values than the AM packing, while both $M_{f,15}$ and $M_{f,13}$ are interestingly lower without wipers than with wipers. Obviously, the AM packing produces an extreme and undesired wall flow of more than 50 %. A visual observation revealed a markedly faster lateral acceleration of the liquid toward the wall in the AM packing compared with the metal packing. This is likely a result of a poor wetting behavior of the AM resin and the absence of surface structuring, both of which promote channeling and result in the significant deviation in spite of the same macrostructure.
Figure 6 provides a more detailed insight into the distribution along the cross-section. While more than 50 % of the liquid in the AM packing is collected from the wall, the remaining liquid is distributed fairly equal among the cross-section. For the industrial metal packings, the wipers effectively reduce wall flow but cause a marked increase in liquid accumulation in the second outer ring. In addition, a less uniform distribution is

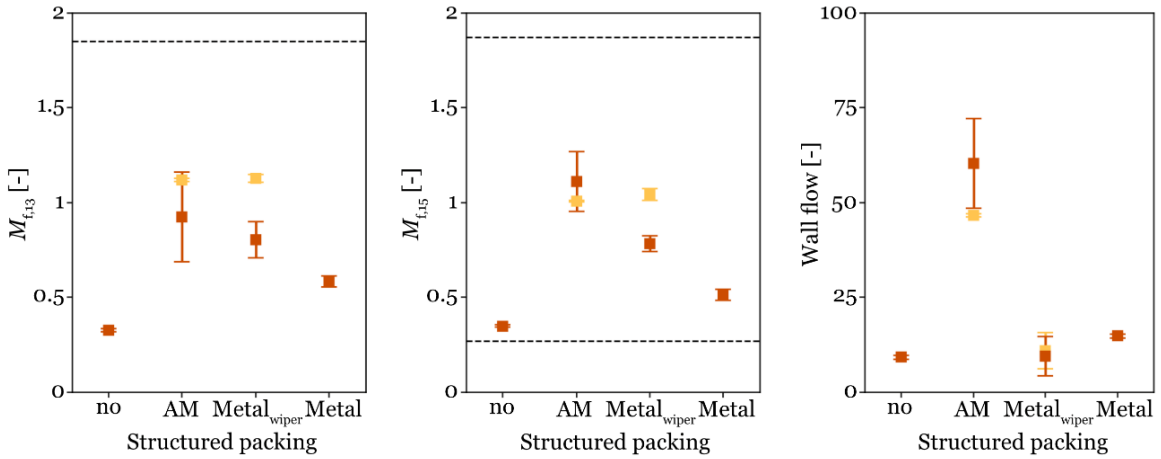

Figure 5: Maldistribution factors $M_{f,13}$ (left) and $M_{f,15}$ (middle) and wall flow (right) for different structured packings using distributor 1b (red) and a single drip point (yellow) from integral experiments; dashed lines mark best and worst possible M_f.

observed in the two inner rings. Both effects contribute to an increased M_f, which explains the differences in Figure 5. The resulting M_f values are consistent with the work of Ashour et al. [8], who reported M_f values ranging from 0.8 to 1 and wall flow between 80 and 95 % in a DN20 column equipped with an AM replica of a Rombopak 9M packing. However, it needs to be noted that the collector in the current study has a higher resolution that is adjusted to the distributor. In ongoing work, additional operating points that include counter-current air flow are being investigated. A publication presenting the results, along with a detailed description of the methodology, is currently in preparation [13].

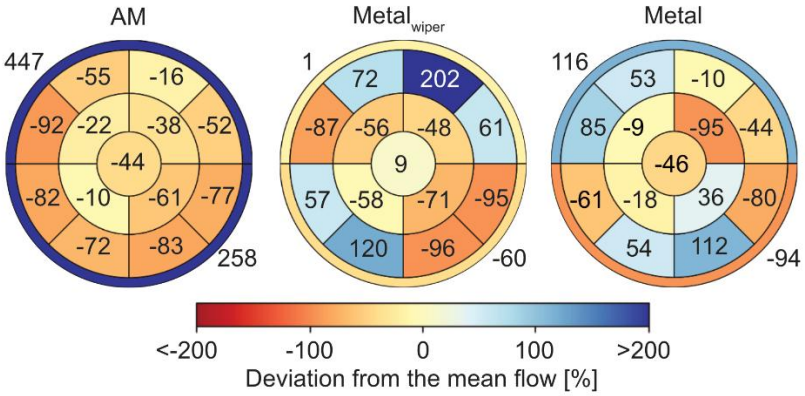

Figure 6: Visualization of the deviation of the flow inside the sections from the mean flow below the different structured packing elements.

Overall, it can be concluded that the current AM packing does not show a sufficent transferability towards the industrial metal packing and requires further refinement and investigations to allow for transferable results. Yet the AM packing enables a more resolved analysis of the development of the M_f and wall flow by means of MRI measurements.

3.2 MRI experiments

The respective MRI measurements are depicted in Figure 7 and elucidate the evolution of M_f and the wall flow as a function of height of the packing element. Due to insufficient signal intensities, reliable MRI evaluation is limited to the region between 16 – 88 mm from the top of the packing. The MRI data are complemented with results from the integral experiments, rising from 0.22 above the packing to 1.11 below the packing. The MRI-derived values elucidate the almost linear increase of $M_{f,15}$ and the wall flow along the flow direction and align very well with the integral measurements, confirming the validity of the MRI-based approach.

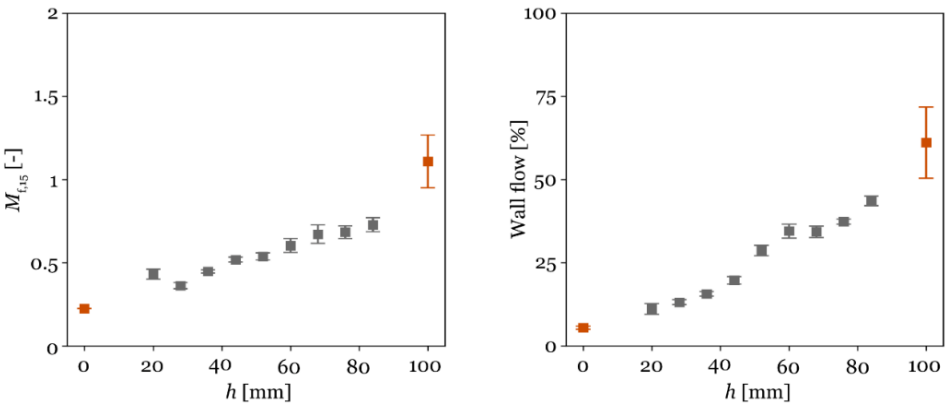

Figure 7: Maldistribution factor $M_{f,15}$ (left) and wall flow (right) depending on the height for the AM packing and distributor 1b from MRI (grey) and integral experiments (red).

4. Conclusion

Four liquid distributors based on pressure- and gravity-driven principles were designed for a DN54 column. In integral experiments with a matching collector, the pressure-driven distributor with tapered ends was identified as the most efficient, exhibiting an excellent initial $M_{f,13}$ of just 0.08. This distributor was subsequently examined in combination with different corrugated sheet structured packings, printed with AM or commercially manufactured. M_f significantly increased, particularly for the AM packing. Nevertheless, the distributor achieved a reduction in $M_{f,13}$ of up to 40 % compared with a single drip point. MRI measurements further showed that M_f increases along the flow direction. Future work will pursue modifications of the AM packing to achieve a comparable wettability to the industrial metal packing.

Acknowledgements

Funded by the Deutsche Forschungsgemeinschaft (DFG, German Research Foundation) – 544956881.

References

[1] M. Fourati et al., “Experimental study of liquid spreading in structured packings”, *Chem. Eng. Sci.,* vol. 80, pp. 1-15, 2012.
[2] J. R. Fair et al., “Gas absorption and gas-liquid system design”, In *Perry’s chemical engineers’ handbook*, R. H. Perry and D. W. Green, Eds. New York: McGraw-Hill, 1999.
[3] J. Stichlmair et al., “*Distillation: Principles and practice*”, 2nd ed. Hoboken: Wiley-AIChE, 2021.
[4] A. Reitze et al., „Characterization of liquid-phase distribution in 3D printed structured packings with an enclosed column wall“, *Ind. Eng. Chem. Res.*, vol. 61, pp. 740–746, 2022.
[5] F. Hanusch et al., “Liquid distributor design for random packed columns”, *Chem. Eng. Res. Des.*, vol. 147, pp. 689-698, 2019.
[6] S. da Cunha et al., „Design, conception, and assessment of an innovative liquid distributor for separation column“, *Chem. Eng. Res. Des.*, vol. 196, pp. 377-389, 2023.
[7] F. Hanusch et al., „Development and application of the tum-welchem cell model for prediction of liquid distribution in random packed columns“, *Chem. Eng. Trans.*, vol. 69, pp. 739-744, 2018.
[8] M. A. Ashour et al., “Flexible 3D-printed test rig for liquid distribution characterization of laboratory-scale packings”, *Chem. Ing. Tech.,* vol. 94, no. 7, pp. 1010-1016, 2022.
[9] S. Hill et al., “Quantifizierung der Trenneffizienz einer strukturierten Packung mittels numerischer Simulation”, *Chem. Ing. Tech.,* vol. 91, no. 12, pp. 1833-1841, 2019.
[10] Y. Guo et al., “Hydrodynamics of new structured packings: an experimental and micro-scale CFD Study”, *Microgravity Sci. Technol.*, vol. 30, pp. 911-924, 2018.
[11] B. Mahr and D. Mewes, “Two-phase flow in structured packings: modeling and calculation on a macroscopic scale”, *AIChE Journal*, vol. 54, no. 3, pp. 614–626, 2008.
[12] M. Schubert et al., “Advanced tomographic techniques for flow imaging in columns with flow distribution packings”, *Chem. Ing. Tech.,* vol. 83, no. 7, pp. 979-991, 2011.
[13] H. S. Rennebaum et al., “Integral experiments and magnetic resonance imaging of lab-scale liquid distributors” (in preparation).

Energy consumption in mass transfer processes

Izak Nieuwoudt
Fractionation Research, Inc., Stillwater, USA;

Abstract
Mass transfer processes, including distillation, are vital in producing compounds that are important for our quality of life and standard of living. These processes are, however, generally quite energy intensive. With most of the current energy mix still coming from fossil fuels, the contribution of these processes to CO_2 emissions is significant. The use of electricity from renewable energy is considered as a way to substantially decarbonize this sector. However, the techno-economic impact of decarbonization decisions need to be carefully analyzed. Rather than just focusing on decarbonization and electrification, the first order of business should be to understand whether a process is truly needed, or whether it could be replaced by a process consuming less energy. If a process is currently irreplaceable, the second order of business should be to look for technologies to reduce the energy consumption. A case study is used to illustrate these points. This case study includes considering different processes, using more efficient equipment, and using technologies that significantly reduce the energy consumption. It is demonstrated that very significant reduction in energy consumption is possible, which leads to significant CO_2 emission avoidance. This will reduce the cost of renewable energy infrastructure and the need for other costly decarbonization strategies.

Keywords
Energy, Distillation, Electrification, Decarbonization, Extractive Distillation, Heat pump, Heat integration

1. Introduction

The decarbonization of the world's energy is moving forward, but there is still a lot of discussion about what this transition should look like. Rather than having a purely idealistic view, techno-economic analyses and rigorous fact-based debate are needed. Some sectors contribute only a small amount to the overall CO_2 emissions, and are difficult to decarbonize. Aviation, at a 2% contribution, is such an example and would benefit from some form of sustainable aviation fuel, rather than transitioning away high energy density fuels. Other sectors, such as ground transportation, are already benefitting from a switch to electricity or hybrid technologies. There is no one-size-fits-all solution and each industry must go through its own techno-economic analyses.

The chemical, gas processing and refining sectors are energy intensive, and fossil fuels are predominantly used to satisfy the energy needs. Replacing these energy sources has led to studies into electrification and the use of alternative energy carriers, including hydrogen. Distillation is the separation workhorse in these industries, and decarbonization of the energy requirements of distillation is thus on the front burner for engineers in this field. Several options are discussed in this paper.

2. Relevance of distillation

Distillation is undeniably the separation workhorse of the chemical, refining and gas processing industries with more than 100 000 columns all over the world. It is an energy intensive unit operation, but no technology has been able to displace it. Significant resources have been ploughed into membrane research over several decades, for example, but it is nowhere near the point where it can replace distillation in large-scale separations in these industries. These industries supply energy, which could potentially be replaced by renewable sources, but they also supply energy to areas that are hard or very expensive to decarbonize. These industries also supply the feedstocks to a myriad of products upon which our quality of life and standard of living rest. We will have to keep producing these feedstocks, and distillation will remain the primary separation technology.

Even as we transition to sustainable liquid fuels or the use of feedstocks not derived from crude oil for the synthesis of complex molecules, separations will still need to be performed, and distillation will still be the primary separation technology.

With distillation being a critical and indispensable part of our quality of life, but being energy intensive, it is incumbent upon engineers to figure out ways to reduce the energy consumption of distillation processes. One such approach is to electrify these processes using renewable energy. Simply electrifying distillation presents no real technical challenge anymore. The open questions are more related to infrastructure, logistics, economics and optimization.

3. Electrification of a distillation column

3.1 Photovoltaic energy

Since the commercial introduction of solar panels 70 years ago, the cost has come down tremendously and the quality and conversion efficiency has improved significantly. However, there is a plateau that is a function of many factors, including the costs of the trichlorosilane process for making high-efficiency monocrystalline solar cells.

The current installed cost for solar panels in a solar farm is approximately \$ 180/ m^2 and the nameplate energy production is in the order of 260 W/m^2. It needs to be recognized that the costs will be different in different parts of the world and that this cost excludes switchgear, substations, distribution and storage. There are insurmountable challenges that have to be factored in: (1) The sun only shines for part of the day, (2) The amount of sunlight is influenced by weather conditions, the seasons and the distance from the equator. A power factor is used to account for these issues. In the USA a power factor of 0.24 is typically used.

Assuming a distillation column with a 10 MW reboiler will be configured to run on solar electricity. A reboiler of this size is typical for distillation columns with a diameter of 2.5 to 4.0 meter and operating at a moderate reflux ratio. At 260 W/m2 with modern solar panels, and a power factor of 0.24, 160 256 m^2 of solar panel area would be required. At \$180/m^2 of installed cost the price tag would be \$ 29 million. If the solar panels cover 45% of the solar farm area, a 600 x 600 meter plot area will be needed for the panels alone. This cost and area excludes substations, switchgear

and transmission lines. It also does not include any provisions for storing energy to level out the supply over days and weeks. The total cost will thus be significantly higher than $ 29 million. This is a very high cost, and is most likely significantly higher than the installed cost of the distillation column. If ways could be found to reduce the energy consumption of this distillation column the cost of the electrification cost will be reduced proportionally to the reduction in energy consumption.

3.2 Wind energy

The first wind turbines were built shortly after the development of the generator, which means that this technology has been around for almost 150 years. Improvements in material technology and fabrication methods have increased the size of these units and have driven the cost down. The largest offshore unit in operation has a nameplate generation capacity of 26 MW and a rotor diameter of 310 meter. The largest onshore unit has a nameplate generation capacity of 15 MW and a rotor diameter of 270 meter. The initial cost, installation and maintenance cost of offshore units are significantly higher than that of onshore units. Typical onshore units have nameplate generation capacities of 5-6 MW with rotors of 165 meter diameter. The installed cost of a 6 MW onshore unit is approximately $ 8 million, but this can vary from country to country. This excludes substations, switchgear and transmission lines. The amount of wind power that can be harvested inevitably depends strongly on the location, weather patterns and geography. A power factor is used to account for these issues. In the USA an average power factor of 0.36 is typically used, but this is obviously a strong function of how windy the area is.

Assuming a distillation column with a 10 MW reboiler will be configured to run on wind electricity. A reboiler of this size is typical for distillation columns with a diameter of 2.5 to 4.0 meter and operating at a moderate reflux ratio. At a power factor of 0.36 it means that the equivalent of 4.6 units of 6 MW will be needed. The installed cost will be $ 36 million. This excludes substations, switchgear and transmission lines. It also does not include any provisions for storing energy to level out the supply over days and weeks. The total cost will thus be significantly higher than $ 36 million. This is a very high cost, and is most likely significantly higher than the installed cost of the distillation column, as is the case with solar power. If ways could be found to reduce the energy consumption of this distillation column the cost of the electrification cost will be reduced proportionally to the reduction in energy consumption.

4. Reducing the energy consumption of a distillation system

4.1 Optimize tower internals

The choice of internals can have a significant effect on the performance of a distillation column, including the energy consumption. Figure 1 presents an example based on FRI data. In this case a tray at 457 mm tray spacing has the same efficiency and capacity as a tray at 609 mm tray spacing. This could allow more trays to be installed in the same tower shell, which could allow operation at a lower reflux ratio and thus reducing the energy consumption. Operating at a lower reflux ratio could also reduce the pressure drop, but this also depends on the open area % of the

trays. It is very important to also understand the impact of the selection of mass transfer internals on the energy consumption of the tower.

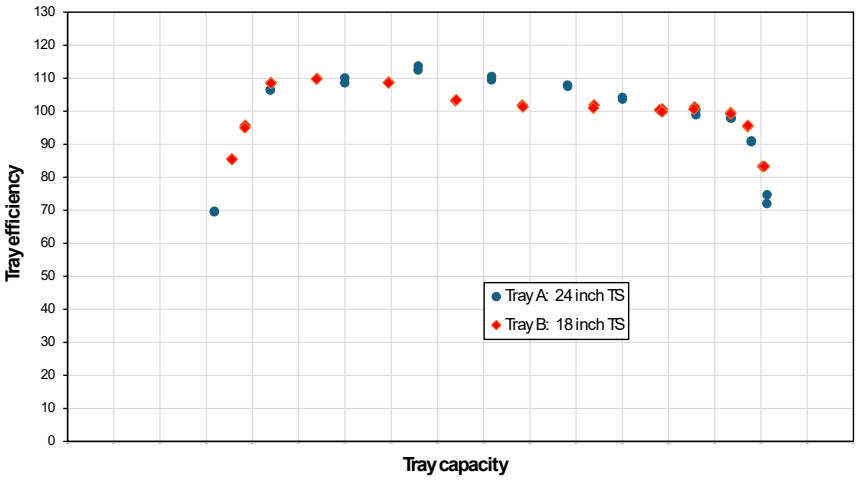

Figure 1: Effect equipment selection on distillation tower performance

4.2 Heat integration (Pinch analysis)

Exchanging energy between hot and cold streams is the simplest way to reduce energy consumption. A systematic methodology for heat integration (pinch analysis) was introduced by Linnhoff more than 40 years ago. This provides a systematic way op pairing streams to optimize energy recovery. It is advised that this methodology is definitely employed, and that it is also used in conjunction with other methods to arrive at the optimum arrangement.

4.3 Advanced contacting arrangements

One such advanced contacting technology is Dividing Wall Columns (DWC) which is applied in multi-component separations. This can be seen as a direct contact internal heat integration scheme that allows multiple columns to be housed in a single column. There are more than 300 DWC's in the world and energy and capital saving of as high as 30% have been reported. The simulation and operation of DWC's are less daunting than is sometimes claimed. HIDIC columns where column segments at different pressures are combined with heat exchangers is a way of doing internal heat integration without contacting the process fluids. Even though there are relatively few of these columns in operation, large energy savings are claimed. Not all separations will benefit from these technologies, but a review is generally warranted.

Other separation schemes, such as extractive or azeotropic distillation, adsorption or liquid extraction, or a combination of these technologies should also be explored.

4.4 Heat pumps and related technologies

These technologies essentially take energy at low temperature and transform it to energy at higher temperature by using mechanical work. The benefit is that the coefficient of performance (CoP), which is the ratio of useful energy (heat) delivered to the mechanical work (energy) that had to be used, can be significantly higher than 1 and can reach values in the range of 4 - 7. The technologies that fall in this category are heat pumps and vapor recompression systems. In vapor recompression systems, a compressor is used to compress the overhead vapor from the column to a pressure where its bubble point is higher than the reboiler outlet

temperature. This allows this compressed vapor stream to be used at the heating medium in the reboiler. In heat pump systems a similar approach is employed, but the process vapor is not being used as the energy carrier. An external loop with a working fluid, a compressor and heat exchangers transfer the energy from the overhead vapor stream to the reboiler. All of these technologies mean more capital expenditure, but the long-term energy savings could be very significant.

4. Case Study

The system acetone + methanol forms a low boiling azeotrope at atmospheric pressure and can thus not be separated by conventional distillation. Alternative separation schemes will have to be employed.
The composition of this azeotrope is pressure dependent. ***Pressure swing distillation*** can thus be used to separate these components in a 2-column system. Two columns at different pressures offer *heat integration* opportunities. A *heat pump* system between the condenser of the low-pressure column and the reboiler of the high-pressure column offers significant energy savings. (See Figure 2a)
Alternatively, ***Extractive distillation*** with water as a solvent can be used to separate acetone and methanol. In a 2-column extractive distillation scheme there are opportunities for a reduction in energy consumption via *heat integration*. The extractive distillation can also be performed in a *dividing wall column (DWC)* where the wall goes all the way to the top of the column. Additionally, a *heat pump* system can be used between the condensers and the reboiler to further reduce the energy consumption. (See Figure 2b)
The additional equipment to affect the reduction is energy consumption will increase the capital expenditure, but it has to be weighed against the energy savings, and the savings in the energy generation infrastructure, by means of a rigorous economic analysis.

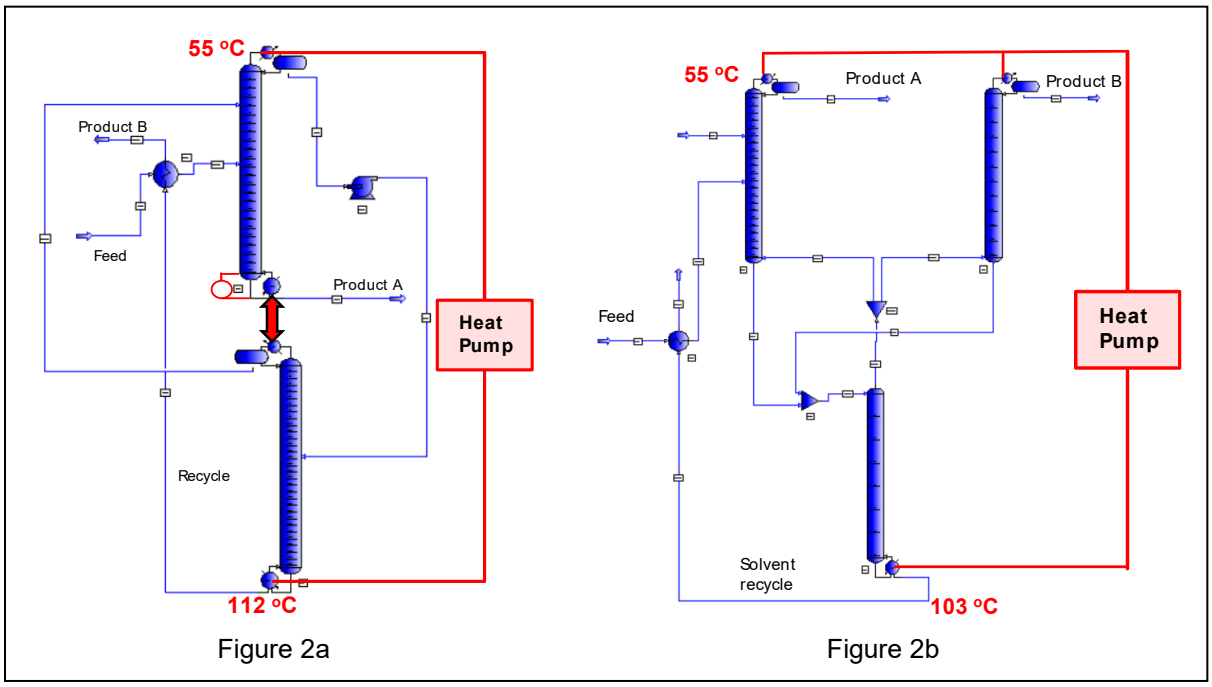

Figure 2: Pressure swing distillation (2a) and Extractive distillation (2b) flowsheets for the separation of acetone and methanol using energy reduction technologies

A qualitative assessment of the equipment sizes and energy usage for this case study is shown in Table 1. This analysis is based on a 10 000 kg/h feed stream with a 50/50 wt% composition and both products having a 99.6 wt% composition. It is assumed that the heat pump has a CoP = 4 and that in heat integration equipment 90% of the theoretical maximum energy transfer is obtained.

Table 1: Comparison of the equipment sizes and energy consumption for the separation of a 10 000 kg/h 50/50 wt% mixture of acetone and methanol to produce 99.6 wt% products

	Heating duty MW	Cooling duty MW	Heat pump duty MW	Col 1 diam m	Col 2 diam m	Col 1 height m	Col 2 height m	Relative energy input
Conventional distillation	**Not technically feasible**							
Extractive distillation with heat integration	9.89	8.67	0	1.45	1.55	31	17	100
Extractive distillation in a DWC	9.26	8.06	0	2.0		37		93.6
Extractive distillation with DWC and Heat pump	1.2	0.8	1.8	2.0		37		30
Pressure swing distillation	14	13.7	0	2.0	1.8	18	22	142
Pressure swing distillation with heat integration	8.3	8.0	0	2.0	1.8	18	22	84
Pressure swing distillation with heat integration and a heat pump system	2.0	1.7	1.6	2.0	1.8	18	22	37

From Table 1 it is evident that the choice of technology could have a very significant impact on the energy consumption of the separation system. If renewable energy is used, the size and cost of this energy infrastructure will be proportionally impacted. This can have large impact on the economics of the project.

5. Conclusions

Distillation will remain the separation workhorse in the chemical, refining and gas processing industries for the foreseeable future. These industries will change, but the need for separation technology will remain. Renewable energy is abundant, but it is not cheap and costs are starting to plateau. Indiscriminately using renewable energy to decarbonize distillation systems will simply not make economic sense. A more prudent approach will be to reduce the energy consumption of separation processes as a precursor for using renewable energy. In general, energy should be used as close to the source as possible. Any additional conversion steps, such as converting electricity to other carriers, have inevitable thermodynamic inefficiencies, which will drive up costs. Electricity can be seen as energy at "infinite" temperature. Engineers already have enough tools to make a huge difference on the energy and CO_2 footprint of distillation. Heat pumps systems can be further improved by developing systems that can work at high temperature and high temperature differentials, multi-stage heat pump systems, exchangers with low dT, and combining all of this with heat integration and HIDIC type arrangements.

A systematic framework for automated screening and selection of energy-efficient distillation technologies

Qing Li, Ruby Roberg, Willem Engel, Mattia Vincenti, Teo Yordanov, Ana Somoza Tornos, Anton A. Kiss**
Delft University of Technology, Delft, The Netherlands

Abstract
Advanced distillation technologies under process intensification (PI) principles, are designed to enhance the thermodynamic efficiency of distillation columns while maintaining their industrial advantages. However, the effectiveness of each technology depends strongly on mixture characteristics, process bottlenecks and specific design objectives, making consistent evaluation and selection challenging.
This work introduces a systematic and automated PI matrix for distillation processes, quantitatively screening 21 intensified distillation technologies at the pre-design stage, based on multi-criteria evaluation within a single Excel-based workflow that requires no specialized software and minimal expertise. Each criterion is pre-scored using consolidated data derived from literature sources, regressions from rigorous simulations performed in this work, and expert inputs from academia and industry. Once a separation task is defined, the matrix automatically assigns scores and weightings to generate a ranked list of technologies with a detailed report.
A live demo will be shown at the presentation. Validation across 3 industrially relevant case studies demonstrated complete agreement between PI Matrix rankings and rigorous simulations, accurately identifying the top-ranked technologies in terms of energy usage and total annualized costs, substantially reducing the search space for further process synthesis or optimization. The PI Matrix represents the first validated and fully automated framework for ranking intensified distillation technologies, bridging the gap between academic innovation and user-friendly industrial application.

Keywords
Process intensification, process design, energy savings, techno-economic analysis, distillation, (non-)azeotropic separation

1. Introduction

The rapid development of intensified distillation technologies has greatly expanded the design space for energy-efficient separations. The diversity of intensified technologies, such as heat-pump-assisted distillation (HPAD), dividing-wall columns (DWC), internally heat-integrated distillation columns (HIDiC), cyclic distillation (CyDist), high-gravity distillation (HiGee), membrane assisted distillation (MAD), creates new opportunities for process improvement, but also complicates early design decisions. In industrial practice, conservative and well-established configurations are generally preferred, while less familiar alternatives that require extensive modeling effort and offer uncertain payoff are often viewed with caution. As a result, this tendency reinforces the dominance of conventional or well-established systems and limits the adoption of novel intensified technologies whose potential advantages cannot be assessed reliably without detailed simulations. The

performance of intensified distillation technologies depends on many aspects, e.g. mixture thermodynamics, process constraints, operating objectives. Consequently, technology evaluation is typically carried out on a case-by-case basis through detailed simulations or experimental studies and is difficult to generalize or apply systematically across separation tasks. To address these challenges, this study develops a quantitative and automated pre-screening framework of distillation technologies, providing a fast and transparent tool that helps users identify which options are promising or can be safely excluded, avoiding unnecessary modeling effort, and accelerating the adoption of energy-efficient distillation technologies.

2. Methodology

2.1 Development of the PI matrix

The complete PI matrix tool structure is briefly shown in Figure 1. Five high-level pre-screening questions (Li et al., 2024) are checked to preliminarily evaluate if distillation is applicable to the user's separation task. If distillation is favorable, one of the three sub-matrices are implemented: a binary-zeotropic matrix, a ternary-zeotropic matrix, and a binary-azeotropic matrix. The multicomponent azeotropic systems are highly case-dependent and must be designed individually, while the multicomponent zeotropic framework is treated separately through a superstructure-based optimization study due to the large number of possible sequences (Li et al., 2023). Each matrix contains a specific set of technologies relevant to its mixture class.

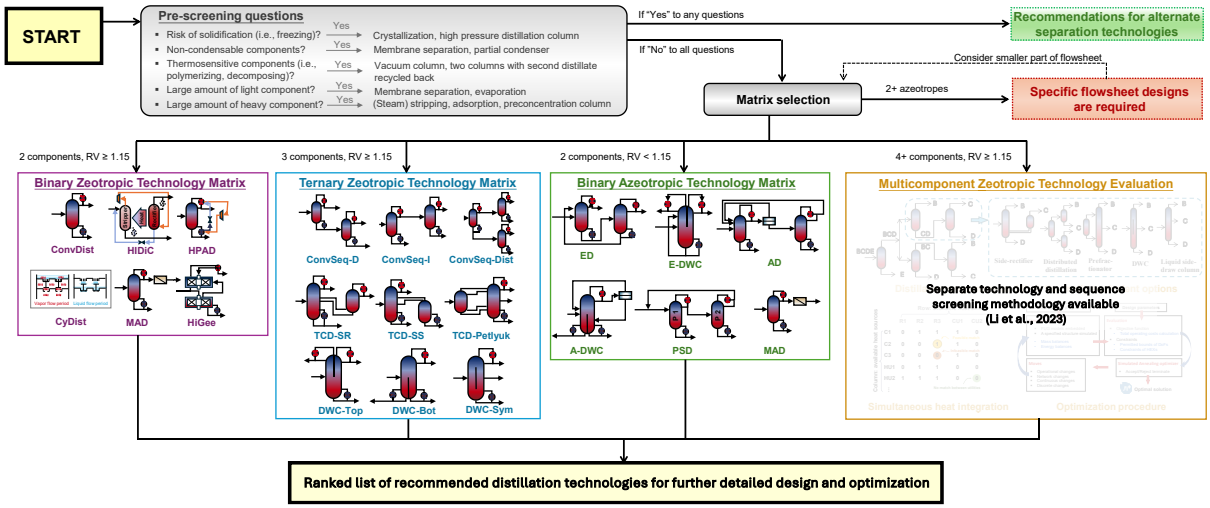

Figure 1: Complete PI matrix tool overview workflow

The structure of each submatrix is demonstrated in Figure 2 which includes columns representing technologies and rows representing evaluation criteria. All technologies are evaluated by elimination criteria, identifying limiting characteristics of the user's separation task which make some of the technologies unfeasible based on the user inputs (e.g., feed capacity, boiling points, feed composition, viscosity, utility limits) and limitations (i.e., thermosensitive components, corrosivity, solvent toxicity). Then, the feasible technologies are scored by performance criteria to identify unique characteristics which make some technologies more suited to achieve CAPEX/OPEX savings. Note that although the present framework applies binary elimination rules for efficiency, this may oversimplify practical feasibility in borderline cases or hybrid configurations (e.g., staged compression for HIDiC under vacuum operation). Such limitations are acknowledged, and future work may adopt fuzzy or probabilistic feasibility scores and introduce sub-criteria (e.g., maximum temperature tolerance) to better capture mitigated or thermo-sensitive systems. The value assignment for

performance criteria is based on the relative performance of each technology compared to the other evaluated technologies, dependent on user input parameters. They are scored from 1 to 5 using a rule-based, fitted discretization scheme, where literature and simulation data are first regressed to define performance ranges, which are then mapped to discrete score levels. The total score of the technologies is calculated as the sum of the individual score times the corresponding criterion weight. Then each criterion is assigned a weight between 0 and 1 to represent its relative importance in the overall score based on the influence on operating and capital cost of the technologies. These weights have default values in the matrix which can be customized using the "custom weighting" function (see section 2.2).

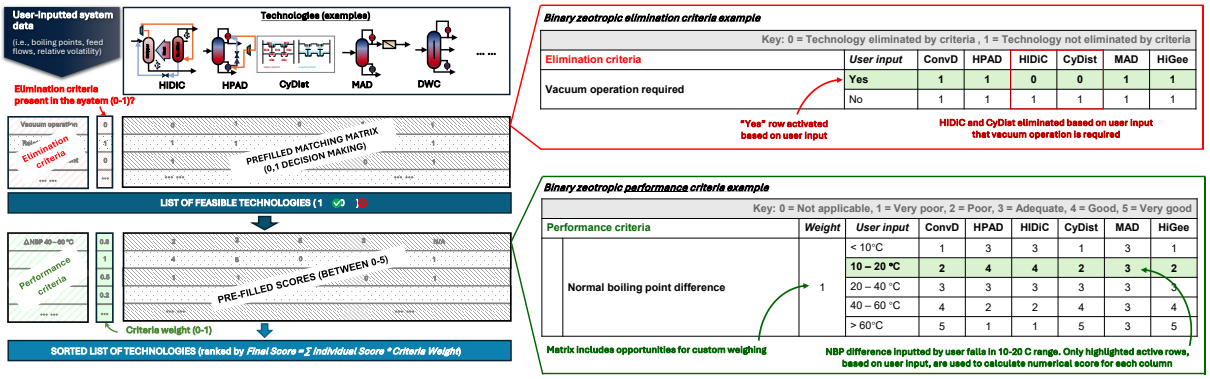

Figure 2: Matrix structure including examples of elimination and performance criteria

2.2 Automation of the matrix

After getting the individual score of each technology, a rank can be generated. A step-by-step guidance interface is provided, and a report with rankings and suggestions are produced automatically after getting the scores from the matrix.

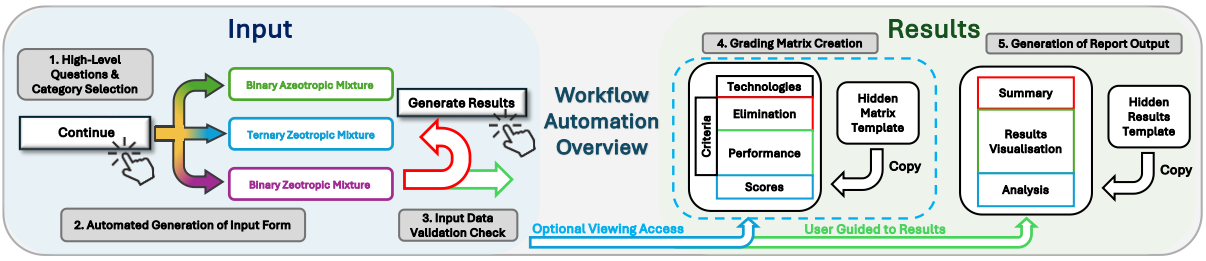

Figure 3. Workflow overview for the PI matrix automation

Three functions can be chosen from the automated matrix:

- Basic PI matrix: An Excel VBA script generates the corresponding input form. After the user has completed all required fields and the inputs are validated for consistency, the results can be generated with a single click, as shown in Figure 3. This action triggers the creation of a customized results worksheet, produced by copying and adapting a blank matrix and results worksheet to the user's input. It contains a graph that positions the evaluated technologies across zones of attractiveness, a graph showing the breakdown score for each criterion. Then it automatically generated analysis and suggestions based on these scores. The user can also access the PI matrix for detailed scoring if needed.
- Sensitivity analysis on key thermodynamic criteria: since the matrix is designed as a screening tool excluding detailed property models, the results of the sensitivity analysis highlight the uncertainties/errors coming from the simplified thermo-dynamic inputs. This helps engineers to assess whether the current suggestions are conservative or optimistic. Key thermodynamic related criteria include normal

boiling point difference, relative volatility, thermal energy demand, and inverse of Carnot efficiency (related to the potential of using heat pumps).

- Custom weighting: The default weight suggested in the matrix for criteria can be customized based on the needs of the user, i.e., if the user would like to input a different thermal energy to electricity ratio, or OPEX reduction is preferable in some cases (e.g., revamping of the columns), etc., the custom weighting function can be activated and the new results can be checked next to the original rankings without changing the master matrix.

3. Validations of the matrix

The PI Matrix was validated using three industrially relevant case studies covering the main three mixture categories: (1) binary non-azeotropic mixture separation of methanol (MeOH)/water; (2) ternary non-azeotropic mixture separation of pentane/hexane/heptane (C5/C6/C7), (3) binary azeotropic mixture separation of dimethyl carbonate (DMC)/MeOH. The aim of the matrix is to support early-stage decision making by reducing a large set of candidate technologies to a limited number of competitive options for a user's separation task. The matrix is considered validated if the technology rankings predicted by the PI matrix are consistent with the relative performance (total annualized cost (TAC)) obtained from rigorous simulations. Each technology is rigorously simulated under identical feed compositions, product specifications, and operating conditions. TAC is calculated using the cost correlations reported by (2012) and Turton (2018). It should be emphasized that these simulations are conducted solely for the purpose of validating the PI Matrix during its development. Once validated, the matrix is intended to be applied as a standalone screening tool, enabling users to identify promising intensified separation technologies without needing detailed process simulations at the early design stage.

4. Results and discussion

4.1 Binary zeotropic mixture separation: MeOH/H_2O separation

A capacity of 21.94 ktpy is considered. HiGee and MAD are excluded as these technologies typically do not achieve savings at this scale, and sufficient design information is difficult to obtain. The rest are modeled rigorously.

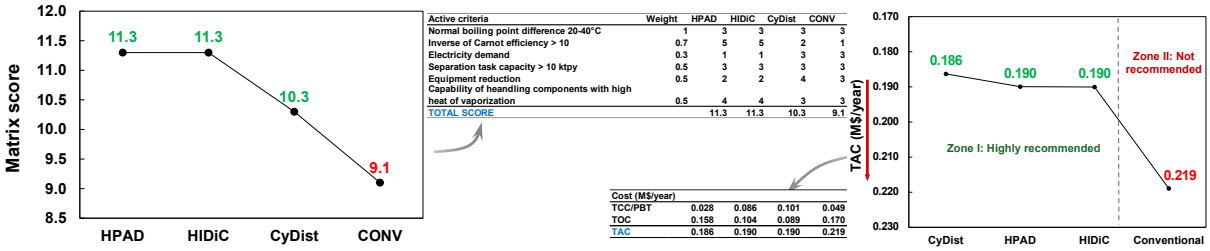

Active criteria	Weight	HPAD	HIDiC	CyDist	CONV
Normal boiling point difference 20-40°C	1	3	3	3	3
Inverse of Carnot efficiency > 10	0.7	5	5	2	1
Electricity demand	0.3	1	1	3	3
Separation task capacity > 10 ktpy	0.5	3	3	3	3
Equipment reduction	0.5	2	2	4	3
Capability of heandling components with high heat of vaporization	0.5	4	4	3	3
TOTAL SCORE		11.3	11.3	10.3	9.1

Cost (M$/year)				
TCC/PBT	0.028	0.086	0.101	0.049
TOC	0.158	0.104	0.089	0.170
TAC	0.186	0.190	0.190	0.219

Figure 4: Methanol/Water matrix results (left) and validation from simulation (right)

The matrix results (Figure 4) correctly classify HPAD, HIDiC and CyDist as "highly recommended", indicating their potential to outperform conventional distillation. However, the relative ranking within this zone could differ from that obtained through rigorous simulations. HPAD and HIDiC get 2.6-point advantage over CyDist because (1) this case falls into "inverse Carnot efficiency above 10" providing energy-saving potential; (2) the high latent heat of vaporization of water benefits HP configurations by eliminating the net hot utility requirement. Cyclic distillation, in contrast, scores more favorably in electricity demand and CAPEX reduction potential, outperforming heat-pump options by 1.6 points and resulting in only a one-point difference in total score. However, rigorous simulations show that although HPAD and HIDiC achieve

operational cost savings of up to 48%, the high capital investment required offsets these benefits, leading to TAC reductions of 13.2% relative to conventional distillation. Cyclic distillation enables reductions in both capital and operating costs, resulting in a slightly higher TAC reduction of 14.9%.

4.2 Ternary zeotropic mixture separation: C5/C6/C7 separation

For a 37.7 ktpy equimolar saturated liquid feed of C5/C6/C7, 9 technologies are modeled using RADFRAC model in Aspen Plus V12 at 2 bar column pressures. This case study represents a ternary zeotropic system with an ESI close to 1 with an equimolar feed. Figure 5 (left) shows the scoring results from the matrix, indicating that DWC-Sym and TCD-Petlyuk configurations could be the most cost-effective options. Compared to the detailed TAC calculation based on the rigorous simulation (Figure 5, right), the matrix can reliably indicate the highest scoring technologies (with lowest TAC). Further analyzing the results for this case study, the mixture is not wide boiling nor are there other restrictions against single pressure operation. Symmetric DWC and Petlyuk configurations outperform due to their ability to reduce both the OPEX and CAPEX by thermal coupling and column combination. The other thermally coupled sequences are still more attractive than conventional sequences. Of the conventional sequences, the direct sequence is most attractive.

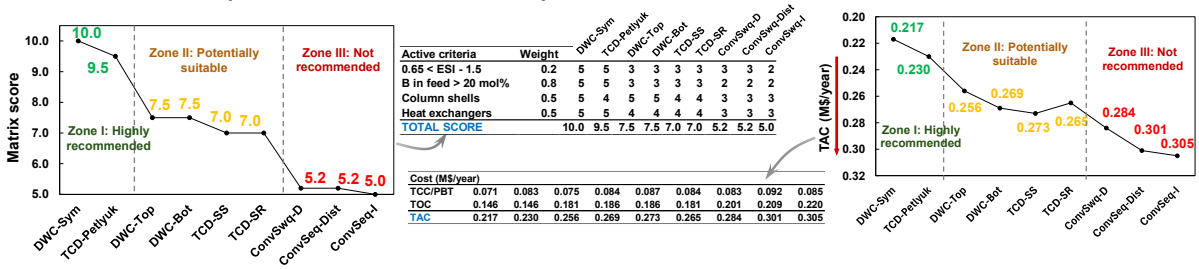

Active criteria	Weight	DWC-Sym	TCD-Petlyuk	DWC-Top	DWC-Bot	TCD-SS	TCD-SR	ConvSwq-D	ConvSeq-Dist	ConvSeq-I
0.65 < ESI - 1.5	0.2	5	5	3	3	3	3	3	3	2
B in feed > 20 mol%	0.8	5	5	3	3	3	3	2	2	2
Column shells	0.5	5	4	5	5	4	4	3	3	3
Heat exchangers	0.5	5	5	4	4	4	4	3	3	3
TOTAL SCORE		10.0	9.5	7.5	7.5	7.0	7.0	5.2	5.2	5.0

Cost (M$/year)									
TCC/PBT	0.071	0.083	0.075	0.084	0.087	0.084	0.083	0.092	0.085
TOC	0.146	0.146	0.181	0.186	0.186	0.181	0.201	0.209	0.220
TAC	0.217	0.230	0.256	0.269	0.273	0.265	0.284	0.301	0.305

Figure 5: C5/C6/C7 matrix results (left) and validation from simulation (right)

4.3 Binary azeotropic mixture separation: DMC/MeOH separation

Three typical approaches, ED, AD and PSD, to separate azeotropic mixtures are rigorously simulated. Aniline is used as the solvent for ED process, water is used as the entrainer for AD to form a low-boiling azeotrope with DMC. The PSD configuration consists of a high-pressure column (13 bar) followed by a low-pressure column (1 bar), giving an azeotrope compositional shift of ΔX = 8.2 mol%. All three configurations are evaluated for the separation of a feed stream of 54.7 kt/py with 86 mol% MeOH. As shown in Figure 6, the technology rankings obtained from rigorous simulations (right) are in good agreement with those predicted by the PI matrix screening (left), confirming the ability of the matrix to correctly capture the relative potential for azeotropic mixture separations. Note that although ED with aniline as solvent has the lowest TAC for this separation, it is accompanied by the frequent use of toxic solvents, which sometimes makes the solution unfeasible for products with stringent tolerances for purity.

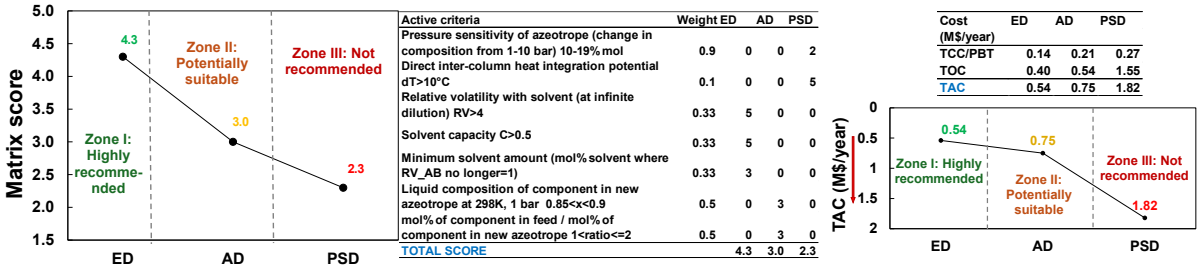

Active criteria	Weight	ED	AD	PSD
Pressure sensitivity of azeotrope (change in composition from 1-10 bar) 10-19% mol	0.9	0	0	2
Direct inter-column heat integration potential dT>10°C	0.1	0	0	5
Relative volatility with solvent (at infinite dilution) RV>4	0.33	5	0	0
Solvent capacity C>0.5	0.33	5	0	0
Minimum solvent amount (mol% solvent where RV_AB no longer=1)	0.33	3	0	0
Liquid composition of component in new azeotrope at 298K, 1 bar 0.85<x<0.9	0.5	0	3	0
mol% of component in feed / mol% of component in new azeotrope 1<ratio<=2	0.5	0	3	0
TOTAL SCORE		4.3	3.0	2.3

Cost (M$/year)	ED	AD	PSD
TCC/PBT	0.14	0.21	0.27
TOC	0.40	0.54	1.55
TAC	0.54	0.75	1.82

Figure 6: DMC/MeOH separation matrix results (left) and simulation results (right)

4.4 Sensitivity analysis and custom weighting

Figure 7 presents a comparison of the automated results (a,d), sensitivity analysis (b,e), and custom weighting outcomes (c,f) on zeotropic binary and ternary case studies. The automated results are consistent with Figure 4&5, confirming that the underlying decision logic of the matrix remain unchanged. The sensitivity analysis indicates that the technologies assigned to different zones do not overlap, validating the robustness of the matrix. The custom weighting results show how user-defined priorities influence the ranking. For the MeOH separation case, when increasing the price of electricity, heat pump related technologies become less favorable than cyclic distillation for this specific case. For C5/6/7 separation, CAPEX-related criteria are weighed twice as strongly as OPEX-related criteria. This shifts the evaluation more towards technologies that reduce the capital costs, such as DWC-technologies. The addition of sensitivity analysis and custom weighting show that the matrix provides the user with a way to assess how sensitive the outcome is to uncertainty and a method to explore how rankings change under different priorities.

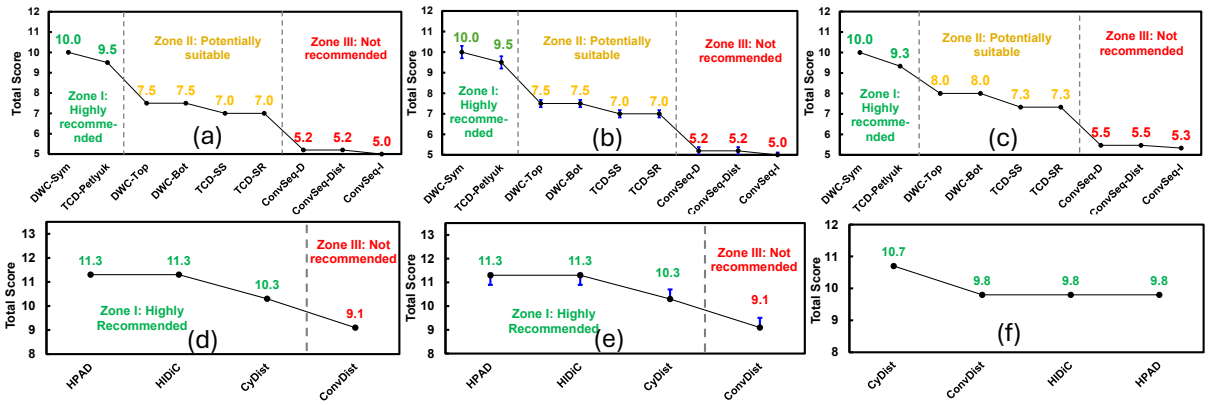

Figure 7. Matrix results (M/W, a; C5/6/7,d); sensitivity analysis (M/W, b; C5/6/7,e); custom weighting (M/W electricity:thermalenergy=2:1, c; C5/6/7 CAPEX:OPEX=2:1, f)

5. Conclusions

The developed PI matrix provides the first simple, practical, computationally efficient and fully automated framework enabling rapid and reproducible evaluations on screening and ranking energy-efficient distillation technologies. By integrating quantitative evaluation criteria in a single, transparent tool, the methodology bridges the gap between conceptual screening and rigorous design. Validation using industrial relevant case study confirms its ability to reproduce realistic performance trends while substantially reducing the effort required for early-stage assessment. Sensitivity analysis shows the reliability of the ranking, and custom weighting allows users to customize the tool based on different needs in practice. Embedding this framework into process-design workflows can accelerate technology evaluation and support digital and sustainable process intensification.

References

1. Kiss, A. A., & Ignat, R. M. (2012). Enhanced methanol recovery and glycerol separation in biodiesel production – DWC makes it happen. Applied Energy, 99, 146–153.
2. Turton, R. (Ed.). (2018). Analysis, synthesis, and design of chemical processes (5th edition). Prentice Hall.
3. Li, Q., Somoza-Tornos, A. and Kiss, A.A., 2025. A systematic selection and decision matrix for energy-efficient intensified distillation technologies. Chemical Product and Process Modeling, 20(2), 293-307.
4. Li, Q., Finn, A.J., Doyle, S.J., Smith, R. and Kiss, A.A., 2023. Synthesis and optimization of energy integrated advanced distillation sequences. Separation and Purification Technology, 315, 123717.

Operational Robustness on Energy Saving Performance in Discretely Heat Integrated Distillation Column

Toshihiro Wakabayashi[1], Haruka Shimomura[2], Shinji Hasebe[3]
[1]Toyo Engineering Corporation, Chiba, Japan;
[2]Maruzen Petrochemicals Co. Ltd., Tokyo, Japan;
[3]Kyoto University, Kyoto, Japan

Abstract

Heat Integrated Distillation Columns (HIDiCs) have drawn attention as a promising technology for significant energy savings in distillation. They are designed with the aim of approximating the composition-enthalpy profile in the column to that of a reversible distillation operation, which is recognized as ideal from energy efficiency perspective. However, conventional HIDiCs, which place the rectifying and stripping sections in parallel and perform internal heat exchange at the same height, have the problem of being unable to supply the necessary heat to the required locations. To overcome this problem, author(s) developed an advanced HIDiC in using a novel thermodynamics analysis method to perform internal heat exchange discretely at a limited number of stages such as two to four. This discrete HIDiC(D-HIDiC) has been in operation at a commercial petrochemical plant in Japan since 2016, demonstrating excellent energy saving of 50% and over. Through nine years of operation, operating data has demonstrated the robustness of the energy-saving performance of the D-HIDiC against the variation in allocating heat duties among internal heat exchangers, etc. In this paper, such operating data are disclosed and evaluated how the energy saving performance is well maintained.

Keywords

HIDiC, Discrete HIDiC, Energy Saving, Operational Robustness

1. Introduction

Since the concept of the heat integrated distillation column (HIDiC) was proposed by Mah et al. (1977), many researchers have attempted to verify its energy-saving performance (Horiuchi et al. (2008), Bruinsma et al. (2010)). The structures of HIDiC proposed so far assume that the rectifying and the stripping sections are installed in parallel, and the internal heat exchange is executed through the wall between the rectifying and stripping sections. Such HIDiC is hereafter called the conventional HIDiC. Although many types of research have been made on the conventional HIDiC, there has been no commercial application. This is because it has inherent drawbacks for realizing its concept. One of the serious drawbacks is that the internal heat exchanges cannot be optimized since the heat is simply transferred between the stages in the rectifying and stripping sections at the physically same elevation. Authors showed that better energy conservation effect could be achieved by simply performing the heat exchange at several pairs of stages in the rectifying and stripping sections discretely (Wakabayashi and Hasebe, 2011). Moreover, authors developed a new design methodology to derive the optimal heat exchanger arrangement. In the proposed methodology, a plausible heat exchange manner is interactively derived by the graphical approach using the extended Ponchon-Savarit *H-xy* diagram

(Wakabayashi and Hasebe, 2013). Furthermore, authors extended the proposed methodology to multi-component system and proposed a new HIDiC structure to realize outcomes through the design methodology (Wakabayashi and Hasebe, 2015). At a commercially operating petrochemical plant at Maruzen Petrochemical Co. Ltd., Japan, a conventional distillation column was replaced with the discrete HIDiC (D-HIDiC) having the proposed structure. The D-HIDiC is being operated stably since August in 2016 in keeping commercial production without major trouble. Over nine years of commercial operation, the D-HIDiC has successfully accommodated fluctuations in process conditions, such as heat allocation among internal heat exchanges, cooling medium temperature, etc. In this paper, the operational robustness of the system to these fluctuation from the perspective of energy conservation performance is discussed on the basis of actual operating data.

2. Design Methodology

The process flow scheme of the D-HIDiC is shown in Figure 1. By compressing the vapor from the stripping section to the rectifying section, the heat in the rectifying section can be used as heat source to the stripping section. The heat exchanger used for this purpose is hereafter called the side heat exchanger (SHX). In this section, the outline of the design procedure of D-HIDiC is explained. The unique feature of the proposed design method is that two dominant design variables related to the performance of the energy conservation, reboiler duty, Q_R, and compressor power, Ws, are first assumed in referring to the reboiler duty of the conventional distillation column, $Q_{R\text{-conv}}$. The operating pressure in the stripping section, P_s, and the number of SHXs are also determined in advance. Then, the arrangement of SHXs is decided by using the extended *H-xy* diagram. The number of theoretical stages, NTS, at each section, the operating pressure in the rectifying section, P_r , and the heat transfer area for each SHX are derived as a result of the design procedure. The design steps are explained by referring to Figure 2.

Step 1: For the given feed and product conditions, $Q_{R\text{-conv}}$ and the NTS for a conventional column, $N_{T\text{-conv}}$, are calculated. The operating pressure is assumed to be the same as that in the stripping section of D-HIDiC, P_s.

Step 2: Determine the target values of Q_R and Ws in D-HIDiC in referring to $Q_{R\text{-conv}}$. Then, assume NTS in the stripping and rectifying sections of D-HIDiC in referring to $N_{T\text{-conv}}$.

Step 3: *H-xy* diagram is used to derive the design variables of D-HIDiC. First, provide the enthalpy curves at saturated conditions and the equilibrium lines, EqLs, of the stripping section ((1)EqL in Figure 2), and draw the reversible distillation curve, RDC, in the stripping section ((2)RDC in Figure 2).

Step 4: The curve obtained by shifting the RDC downward is hereafter called the shifted reversible distillation curve, S-RDC ((3)S-RDC in Figure 2). Derive the NTS in the stripping section by using the EqLs and the S-RDC. Adjust the distance between RDC and S-RDC so that the NTS takes the pre-specified value.

Step 5: Depict the operating locus, OpL, so as to overlap S-RDC ((4)OpL in Figure 2). Figure 2 shows a case where four SHXs are installed. q_i in Figure 2 corresponds to the amount of heat transferred at the *i*-th SHX. B in the figure is the bottom molar flow rate.

Step 6: Derive the NTS in the stripping section by similar procedure of Ponchon-Savarit method in using the EqLs and the OpL. Adjust the OpL by changing the composition where the heat is supplied and/or by changing each heat duty if the derived number is not adequate,

Step 7: Calculate the operating pressure in the rectifying section, P_r, by Eq. (1).

$$Ws = \frac{V_{in}}{\eta}\frac{\gamma}{\gamma-1}RT_{in}\left[\left(\frac{P_r}{P_s}\right)^{\gamma-1/\gamma} - 1\right] \quad (1)$$

Here, V_{in}, T_{in} and γ are the vapor molar flow rate, temperature and specific heat ratio respectively at the inlet of the compressor, which can be regarded as the vapor ascending from the top of the stripping section (See Figure 1).

Step 8: Show the enthalpy curves at saturated conditions and the EqLs in the rectifying section ((5)EqL in Figure 2), then draw the RDC in the rectifying section ((6)RDC in Figure 2).

Step 9: From the overall heat balance ((7)OHBL in Figure 2), the position of the S-RDC in the rectifying section can be derived ((8) S-RDC in Figure 2). Then, confirm the NTS when the composition-enthalpy changes in accordance with the S-RDC. If the derived number is not adequate, return to Step 4 and re-allocate the overall NTS to the stripping and rectifying sections.

Step 10: Depict the OpL so as to overlap the S-RDC ((9)OpL in Figure 2). As the amount of heat transferred at each SHX has been decided at Step 5-6, the size of step change of the OpL in the rectifying section must be q_i/D in the figure.

Step 11: Derive the NTS in the rectifying section by similar procedure of Ponchon-Savarit method using the EqLs and the OpL. Adjust the composition where the OpL is broken if the derived number is not adequate. If it is difficult to derive the desired NTS, return to Step 5 and readjust the OpL of the stripping section.

Step 12: By utilizing second ordinate, draw the bubble point temperature to the liquid

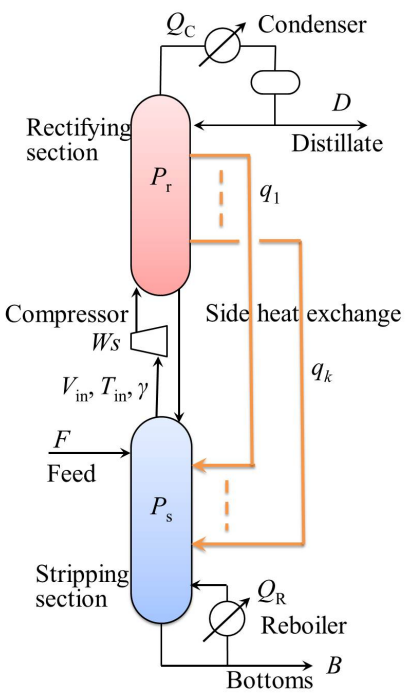

Figure 1: Brief process flow scheme

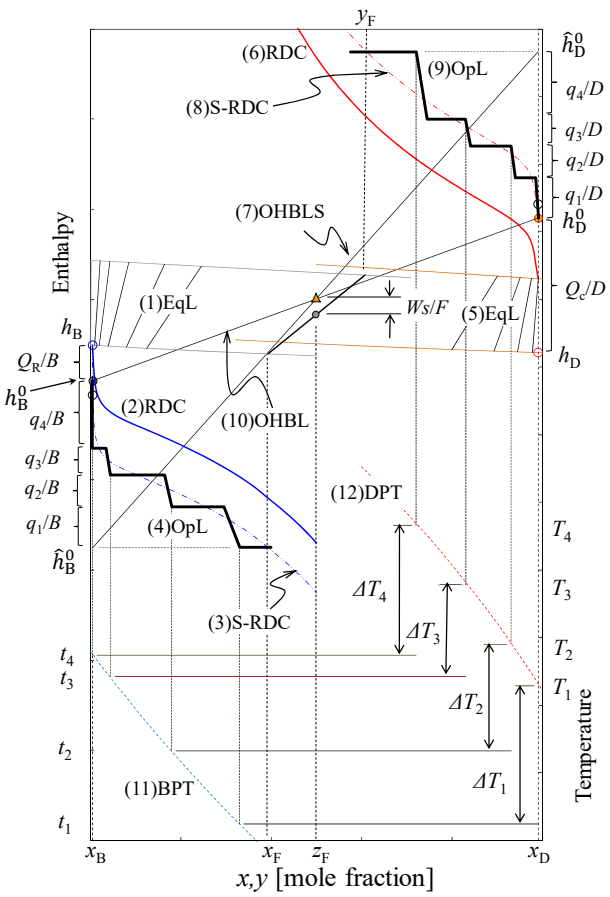

Figure 2: *H-xy* and *T-xy* diagrams that largely modified Ponchon-Savarit *H-xy* diagram

composition in the stripping section on *T-xy* diagram ((11)BPT in Figure 2). Similarly, draw the dew point temperature to the vapor composition in the rectifying section ((12)DPT in Figure 2).

Step 13: ΔT_1 through ΔT_4 in the figure are the temperature differences between the hot and cold streams. From these values, calculate the heat transfer areas of SHXs. In the case where the sufficient temperature difference cannot be obtained, re-examine the profiles of the operating loci. If such approach cannot remedy it, return to Step 2 and reconsider the target of energy saving.

3. Process Disturbance to Energy Saving Performance

The D-HIDiC was implemented in methyl ethyl ketone fractionator at Maruzen Petrochemical Co. Ltd., Japan, with the objective of reducing energy consumption. It replaced the existing conventional distillation column while maintaining identical separation specifications. Since its initial start-up in 2016, this D-HIDiC has been operated in commercial production for more than nine years without any major issue.

The stages for integrating the SHXs are determined during the design phase, and the plant is constructed accordingly. Consequently, once the plant is in operation, there is no possibility of changing the stages where heat is removed or supplied. Instead, operators can adjust individual heat duties of SHXs. However, such adjustments require a thorough understanding of the background described in Section 2. If variations in operating conditions or external disturbances require continuous tuning of the heat duty distribution among SHXs to achieve sufficient energy saving performance, this would impose a significant burden on the operators. In this section, the operational robustness is discussed with respect to the distribution of the heat duty allocation to SHXs and the disturbances of cooling medium temperature.

3.1 Heat Duty Allocation among Side Heat Exchanges

Process flow diagram of the commercially operating plant in Maruzen Petrochemicals is provided in Figure 3. As shown, four SHXs are installed for implementing heat integration between appropriate stages. Three SHXs, SHx#1 to SHx#3, are installed in the stripping section and one SHX, SHx#4, is installed outside the column. R*i*-S*j* means the heat exchange between theoretical stage *i* in the rectifying section and theoretical stage *j* in the stripping section. In Table 1, three sets of operating data are presented to discuss the effect of heat duty allocation among four SHXs from energy saving perspective. As an example, operating parameters in operating mode 1 are presented in Figure 3.

Because it is complicated to manipulate the heat duties of multiple SHXs to meet given product specification, in actual operation only the heat duty of one SHX is used as the manipulated variable, and as a result, the heat duties of the other SHXs also change as shown in Table 1. It is remarkable that the energy saving is almost the same in any operating mode. Here, the energy saving is evaluated based on how much overall energy consumed in D-HIDIC can be reduced to that in conventional distillation. In this evaluation, power is converted to heat by utilizing power generation efficiency of 36.6%. To understand why the D-HIDiC is robust to variations of heat duty allocation among side heat exchangers, the operating loci for three operating modes are depicted on *H-xy* diagram (Figure 4). Here, temperature information are omitted for clarity. As can be seen in Figure 4, the operating loci are different, but not very deviated from S-RDC. This helps the D-HIDiC maintain a high level of energy saving performance despite some variation in heat duty allocation among the side heat exchangers. The evaluation suggests that the D-HIDiC is robust to the variation

of heat duty allocation among side heat exchangers. This robustness is crucial in commercial operation to maintain a high energy saving performance without introducing complicated process controls, such as advanced process control systems.

Table 1: Operating conditions of commercially operating D-HIDiC

Operating Mode		1	2	3
Flowrate	[kg/h]	15994	14874	11761
	[kmol/h]	219.9	204.6	161.7
Temperature	[K]	366.0	366.4	365.7
Composition	[weight frac]			
light non-keys		0.000158	0.000184	0.000160
methyl ethyl ketone		0.720506	0.731325	0.726280
intermediate		0.001723	0.000887	0.000674
sec-butanol		0.270165	0.261809	0.265556
heavy non-keys		0.007448	0.005795	0.007330
Separation Specifications				
methyl ethyl ketone in distillate	[weight frac]	0.99918	0.99942	0.99958
methyl ethyl ketone in bottoms	[weight frac]	0.00020	0.00020	0.00037
Heat Duty				
Side heat exchanger #1 (SHx#1)	[MW]	0.307	0.798	0.803
Side heat exchanger #2 (SHx#2)	[MW]	1.103	0.904	0.787
Side heat exchanger #3 (SHx#3)	[MW]	0.791	0.564	0.144
Side heat exchanger #4 (SHx#4)	[MW]	3.894	3.415	3.244
Energy Saving Performance				
Reboiler duty in conv. distillation	[kW]	6055	5720	4739
Pump power in conv. distillation	[kW]	64	61	51
Reboiler duty in D-HIDiC	[kW]	0	0	0
Compressor power in D-HIDiC(*)	[kW]	917	847	716
Pump power in D-HIDiC	[kW]	90	85	76
Energy saving	[%]	55.9	56.7	55.6

* : Mechanical loss of 7% and motor efficiency of 93.4% are taken into account

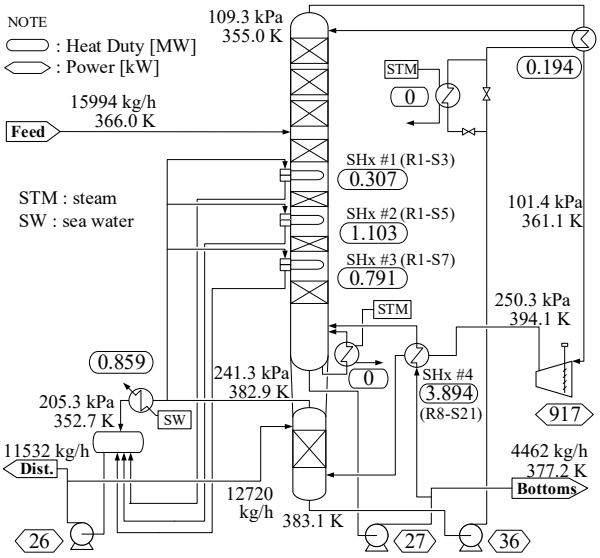

Figure 3: Brief process flow scheme for operating mode 1

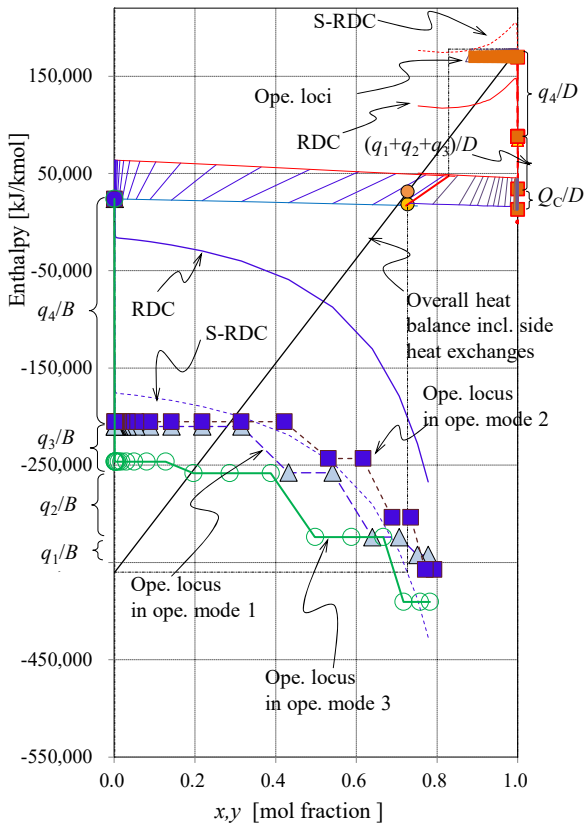

Figure 4: Comparison of operating loci for operating mode 1, 2 & 3 on *H-xy* diagram

3.2 Cooling Medium Temperature

In this plant, variations in the feed flowrate have little effect on the product qualities as long as compressor discharge pressure is controlled to remain constant. This is because controlling the discharge pressure keeps the ratio of compressor inlet flowrate to the feed flowrate essentially constant, as shown in Figure 5(a). Seawater is used as the cooling medium at the condenser, which is the only component to reject heat of the D-HIDiC system to the surroundings. The temperature variation of the seawater at condenser then becomes the primary disturbance to the plant. As an example, the seawater temperature fluctuated by more than 7 deg C over 36 hours. Figure 5(b) shows the concentrations of impurity analyzed by online analyzer at both distillate and bottoms during such fluctuation. Even such rapid disturbance in the cooling medium, the D-HIDiC demonstrated stable separation only controlling the heat duty of one SHX. This shows the excellent robustness of the D-HIDiC.

4. Conclusions

The D-HIDiC has demonstrated through commercial operation that its performance is not sensitive to the heat duty allocation among the side heat exchangers, even when adjustments are made manually during actual operation. Furthermore, the D-HIDiC has shown strong robustness against fluctuation of cooling medium temperature. These operational records indicate that the D-HIDiC is easy to operate and does not require special attention when introducing this system into chemical complexes.

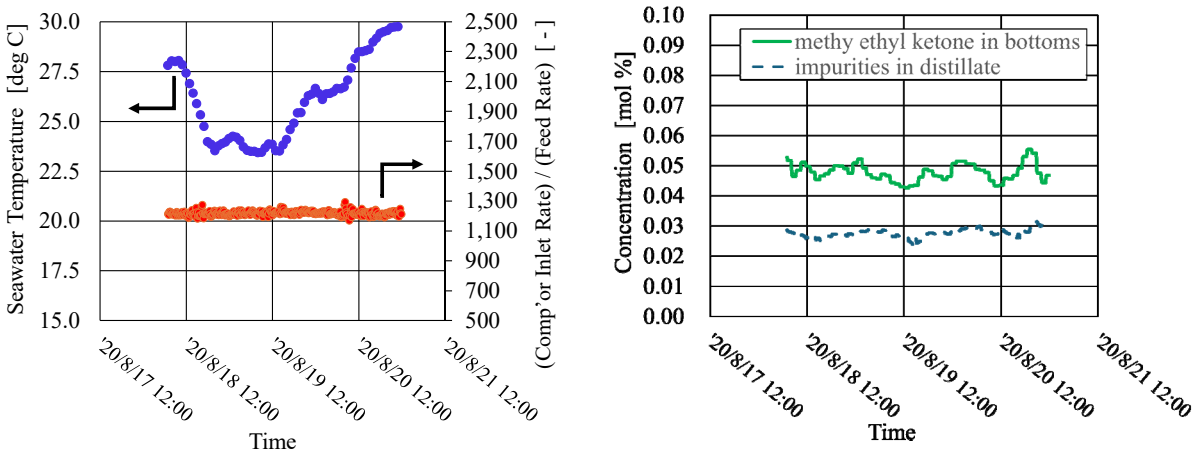

(a) Trend data on seawater and flowrate (b) Trend data on product purities

Figure 5: Separation stability against the fluctuation of seawater temperature

References

Bruinsma O.S.L., Tromp S.A., Strijker M., Malhotra A., Saric M., Cot J., Olujic Z., 2010, Heat Integrated Distillation using a Plate-fin Heat Exchanger, CHISA, Prague.

Horiuchi K., Nakaiwa M., Iwakabe K., Matsuda K., Toda M., 2008, Intensification of the Process Flow in the Pilot Plant of Internally Heat-Integrated Distillation Column(HIDiC), Kagaku Kogaku Ronbunshu, 34, 70–75.

Mah R.S.H., Nicholas Jr. J.J., Wodnik R.B., 1977, Distillation with Secondary Reflux and Vaporization: A Comparative Evaluation, AIChE Journal, 23, 651–658.

Wakabayashi T., Hasebe S., 2011, Effect of Internal Heat Exchange Rate Distribution on Energy Saving in Heat Integrated Distillation Column (HIDiC), Kagaku Kogaku Ronbunshu, 37, 499–505.

Wakabayashi T., Hasebe S., 2013, Design of Heat Integrated Distillation Column by using *H-xy* and *T-xy* diagrams, Computers and Chemical Engineering, 56, 174–183.

Wakabayashi T., Hasebe S., 2015, Higher Energy Saving with New Heat Integration Arrangement in Heat-Integrated Distillation Column, AIChE Journal, 61, 3479–3488.

Optimization of an Ethylbenzene/Styrene Splitter with RMP SP-type Structured Packings – A Case Study

Jose L. Solà Cervera*, Benjamin Pechtold, Tim Eller, Christian Geipel

RVT Process Equipment GmbH
jl.sola@rvtpe.de

Abstract

RVT Process Equipment´s newest generation structured packing, the RMP SP, is an in-house development that has demonstrated its excellent performance at pilot and industrial scale columns with standard test systems but also in many different chemical and petrochemical applications in which it has successfully been introduced in the last decade [1-3]. Main performance advantage of the RMP SP-packing is its significantly lower pressure drop and higher capacity compared to 2nd generation high-capacity structured packings while delivering the same efficiency level which makes the RMP SP the best performing packing in the market. These outstanding performance features make the RMP SP packing very attractive for revamping existing 2nd generation structured packings in every pressure drop depending process column as for example in the Ethylbenzene/Styrene Monomer production.

Styrene monomer (SM) is among the most extensively manufactured chemicals in the global chemical industry and represents the feedstock for the production of key petrochemicals as polystyrene and other synthetic resins. Styrene monomer is produced by the catalytic dehydrogenation reaction of ethylbenzene (EB). The dehydrogenated mixture is vacuum fractionated in a series of four or five columns to recover high purity styrene monomer product and recycle ethylbenzene. The ethylbenzene/styrene (EB/SM) splitter is the key distillation column within that fractionation chain. EB/SM splitters are operated under vacuum due to the polymerization potential of styrene at elevated temperature.

During the early days of SM production in the 50´s, the EB/SM splitters were equipped with mass transfer trays. Nevertheless, the high pressure drop and long residence time of trays led to many problems due to polymerization in this service. After the 1st generation structured packing was launched in the 1980s, the 250.Y type packing was used to revamp the EB/SM splitters with great success due to the major process improvements derived from its significantly lower pressure drop and liquid hold-up. With the introduction of high capacity structured packings in the late 1990s, the 1st generation packings were progressively replaced by 2nd generation 250 m^2/m^3 and 350 m^2/m^3 high-capacity structured packings [4].

This paper presents the substantial improvements that can be achieved by revamping a state-of-the-art EB/SM splitter equipped with 2nd generation high-capacity RMP S 250-type structured packing by the new generation RMP SP 350 structured packing in form of a case study. Revamping the EB/SM splitter with RMP SP 350 significantly enhances column performance by increasing the achievable number of theoretical stages by approximately 30 % allowing for a substantial decrease in the reflux ratio, while simultaneously reducing total pressure drop by up to 29 %. Furthermore, the sump temperature is lowered by 3,2 K, thereby reducing reboiler heat duty and annual steam consumption as well as reducing styrene polymerization risk and inhibitor consumption, resulting in significant operating cost savings. Moreover, column hydraulic capacity could be increased by 16 % without increasing the total pressure drop.

1. Introduction

Styrene monomer (SM) is a major petrochemical intermediate extensively used in the production of polystyrene and other styrenic polymers, including acrylonitrile–butadiene–styrene (ABS) and styrene–acrylonitrile (SAN) resins. Commercial SM production is predominantly based on ethylbenzene (EB), which is synthesized via the alkylation of benzene with ethylene and subsequently converted to styrene through catalytic dehydrogenation.

The reactor effluent, consisting of styrene, unreacted ethylbenzene, steam, and by-products, is subsequently processed in downstream distillation units consisting of a 3- or 4-column configuration. Among the downstream separation units, the ethylbenzene/styrene splitter column, responsible for separating unreacted ethylbenzene and styrene monomer from the dehydrogenation product mixture, represents one of the most critical and energy-intensive operations in the styrene monomer production process. With commercial designs of 100+ theoretical stages in 5 to 7 packed beds and tower diameters of up to 12 m (39 ft), the splitter is furthermore one of the largest commercial applications of distillation worldwide. The overhead ethylbenzene stream is recycled to the dehydrogenation reactors, while the styrene-rich bottoms product is forwarded to the styrene finishing column for removal of heavier impurities. To meet downstream processing and product quality requirements, the ethylbenzene content in the styrene product is typically maintained within the range of approximately 50–500 ppm.

EB/SM splitter columns are operated under vacuum conditions to limit styrene polymerization, which becomes increasingly problematic at elevated temperatures. Polymer formation within the monomer distillation system is highly undesirable, as it can result in fouling, plugging of distributors or packing elements, and unplanned unit shutdowns. The rate of styrene polymerization increases exponentially with temperature and is directly proportional to residence time; therefore, both liquid hold-up and bottom temperature must be carefully controlled. In industrial practice, suitable stabilizers/inhibitors are employed to limit the column bottom temperature to approximately 110 °C (corresponding to 350 mbar) in order to mitigate styrene polymerization [5].

Given these constraints, the hydraulic and mass-transfer design of the EB/SM splitter is critical. Due to the close boiling points of ethylbenzene and styrene and the large column sizes required, the internal mass-transfer efficiency of this column has a direct impact on product purity, energy consumption, and overall plant performance. Column internals are selected to minimize overall pressure drop, reduce liquid residence time and limit hold-up. Thereby risk of polymer formation is minimized. Depending on product purity specifications, EB/SM splitters typically require on the order of 80-100 theoretical stages. These are commonly arranged in multiple packed beds (often 5 to 7) requirying high-performance liquid distributors and collectors to ensure uniform flow distribution. In many designs, the overhead condenser and reboiler are also specifically engineered to further reduce total column pressure drop.

Early styrene production facilities commonly utilized sieve trays for EB/SM separation; however, the inherently high pressure drop of trays led to elevated column bottom temperatures and an increased susceptibility to fouling and polymer formation. Beginning in the 1980s, first generation, corrugated sheet structured packings with a constant corrugation angle of 45° (Y-type) and 60° (X-type) to the horizontal, were introduced and gradually replaced trays in EB/SM splitter service, primarily due to their significantly lower pressure drop and lower liquid holdup. Further advances in packing design around the year 2000 led to the development of a second generation high-capacity structured packings, characterized by a corrugation angle change from 45° in the layer central section to approx. 90° at the packing layer top/bottom ends, driving to a pressure drop reduction and hydraulic capacity increase while delivering a similar efficiency level. Under vacuum styrene conditions, these enhancements result in significant process improvements: higher throughput, lower bottom temperatures and liquid holdup, reduction of polymer formation, fouling and inhibitor consumption. Consequently, first generation structured packing has been gradually replaced by second-generation high-capacity structured packing, which has established as the standard internal configuration for present EB/SM splitter columns.

In this context, the application of new-generation structured packings offers significant potential for improving separation efficiency, reducing pressure drop, and enhancing the operational reliability of styrene monomer fractionation systems.

The RVT Process Equipment RMP SP Packing

RVT Process Equipment's newest generation of structured packings, the RMP SP, is an in-house development launched in 2015, marking the culmination of years of R&D. The SP-packing consists of similar enhanced/textured and perforated microstructure metal sheet as typically used in metal structured packings but optimized corrugation/crimp size macrostructure. The middle sheet section consists of different varying inclination angle sub-sections with different crimp size dimensions driving to different density of contact points between consecutive criss-crossed corrugated sheets, therefore reducing the pressure drop and increasing packing capacity on the one side and enhancing mass transfer at the same time. At the top and bottom layer ends, a high inclination angle for optimum liquid drainage and related capacity increase as commonly used in high-capacity metal packings is implemented in the SP geometry as well (see Figure 1).

Figure 1: RVT´s first generation conventional RMP N 250Y (left), standard high capacity RMP S 250 (center) and new-generation high-capacity development RMP SP 250 (right)

Development was supported by distillation test campaigns in the 428 mm-ID pilot-sized column with the standard Cyclohexane/n-Heptane (C6/C7) system at the Separation Research Program (SRP) of the University of Texas at Austin, USA. The four standard measurement series run at the absolute pressures of 0.165, 0.33, 1.65 and 4.14 bara at total reflux showed excellent distillation performance data. While maintaining the same efficiency level (HETP-baseline level) as standard high-capacity S-shaped 250 m^2/m^3 area structured packings (RMP S 250-type),

the RMP SP 250 packing achieved a remarkable 25 % reduction in specific pressure drop accompanied by a related increase in capacity up to +10 %.

The FRI (Fractionation Research Inc.) membership selected the RMP SP 250 as the 2020 Category 1 packing device to be tested at FRI´s 1,22 m-ID industrial sized distillation column. The packing was tested not only with the same system and two pressures: C6/C7; 0.31 & 1.62 bara as in the SRP facility but also with another commonly used and well established standard binary organic system: o/p-Xylene at a deeper vacuum level of 0.1 bara and at atmospheric pressure: 1.0 bara. Tower internals: a multi-stage high-capacity and high drip point density trough type liquid distributor and packing support grid for the test campaign were designed and manufactured by RVT. The performance data delivered by the RMP SP 250 packing confirmed the data obtained at the SRP pilot scale unit. Compared to standard high-capacity structured packings with the same surface area tested at the FRI-unit under the same operating conditions: system and pressure, RMP SP 250 performed with a similar mass transfer efficiency level while significantly reducing specific pressure drop by around 25 % translated into a +10 % hydraulic capacity increase. These performance figures can be seen in Figure 2 for the o/p-Xylene System test campaign at 0.1 bara.

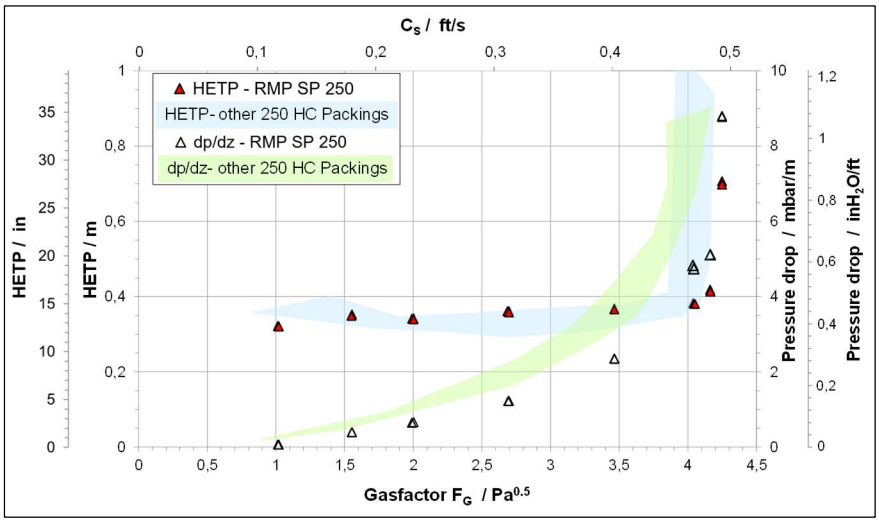

Figure 2: RMP SP 250 distillation test data: HETP and pressure drop/hydraulic capacity, measured with o/p-Xylene System at 0,1 bara at the 1,22 m-ID FRI column including comparison with data obtained for other 250 m^2/m^3 high-capacity packings

The higher surface area RMP SP 350 structured packing was selected and tested at the FRI unit in 2024 with exactly the same test systems and pressures and identical tower configuration including reutilization of RVT´s liquid distributor and support grid. The performance data obtained with the RMP SP 350 packing showed an even larger pressure drop reduction and higher extend in hydraulic capacity compared to other high capacity 350 m^2/m^3 structured packings tested in the same unit with the same systems and operating pressure. Specific pressure drop is reduced by approx. 50 % translating into a throughput increase up to +15 % whereas HETP reaches the level of other 350 m^2/m^3 high-capacity structured packings. These performance figures are presented in Figure 3 for the o/p-Xylene System test campaign at 0.1 bara.

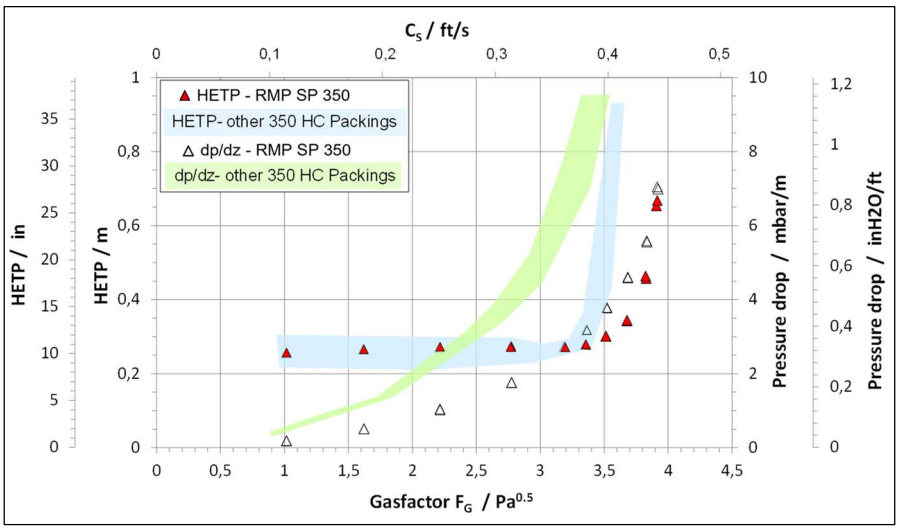

Figure 3: RMP SP 350 distillation test data: HETP and pressure drop/hydraulic capacity, measured with o/p-Xylene System at 0,1 bara at the 1,22 m-ID FRI column including comparison with data obtained for other 350 m^2/m^3 high-capacity packings

These outstanding performance features make the RMP SP-type structured packings very attractive for revamping existing 2nd generation structured packings in every pressure drop depending process column and especially EB/SM splitters because of its direct potential of significantly improving the overall process performance.

This paper will present the potential improvements that can be achieved in a EB/SM splitter by using RMP SP 350 replacing 2nd generation high capacity RMP S 250-type structured packings in form of a case study.

2. Case Study – Ethylbenzene/Styrene Monomer (EB/SM) - Splitter

Figure 4 shows the operational parameters of the EB/SM-Splitter column selected for the case study. A feed stream of 32,4 t/h containing 62-w% SM, 33-w% EB and 5-w% Heavies is separated into a distillate of 98,3-w% EB and a bottoms product of 92,7-w% SM and less than 120 ppm EB. The tower has a diameter of 4,6 m and consists of 6 packed beds equipped with high-capacity structured packing RMP S 250 each, representing the typical packing configuration in EB/SM-splitters. As highlighted in the introductory part, the column is operated under top vacuum pressures between 0,1 and 0,4 bara in order to keep the column sump temperature below a temperature level of approx. 120°C and reduce the risk of SM polymerization.

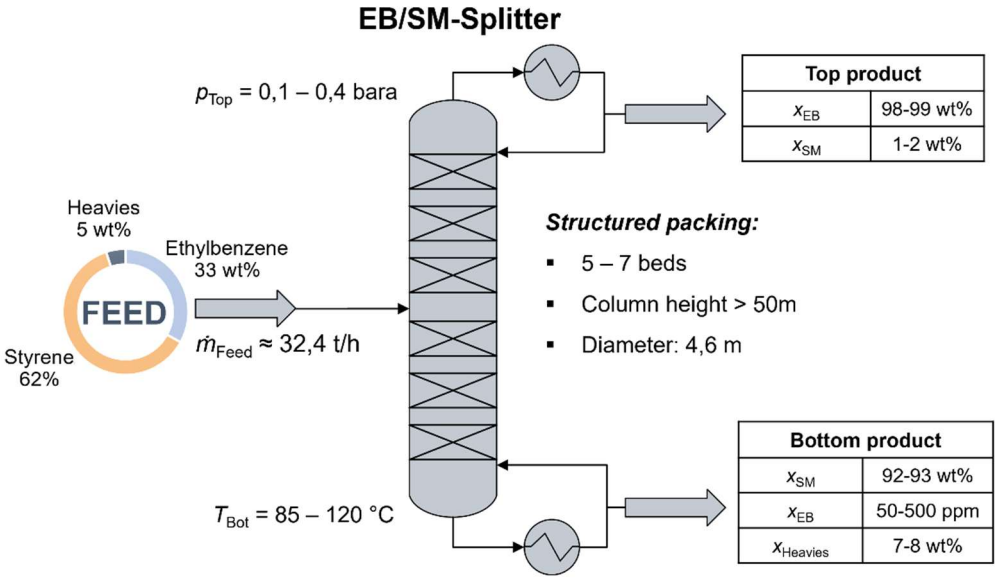

Figure 4: EB/SM-Splitter case study

The EB/SM-splitter is simulated using ASPEN Plus V15, which is the latest commercially available version and includes RVT Process Equipment random and structured packings. The selected thermodynamic model is NRTL-RK which is validated against available experimental data for EB/SM-System at the absolute pressure of 200 mbara. The relative root mean squared error over all data points is lower than 1% meaning that the model can very well represent the vapor-liquid equilibria of the system.

The column is first simulated with the state of art high-capacity structured packing type RMP S 250. Scenario analysis will show the effects of the replacement of RMP S 250 by the RMP SP 350 structured packing. Boundary condition for the simulation with RMP SP 350 are the product qualities at top and bottom and the column top pressure. A top column operating pressure of 100 mbar has been chosen for presenting the results in the next chapter. The results and derived main conclusions can nevertheless be extrapolated to the whole typical operating range of 0,1 to 0,4 bara top pressure in EB/SM-splitters.

3. Results

The left-hand diagram in Figure 5 presents the sensitivity of the number of stages to variations in the reflux ratio in the EB/SM splitter.

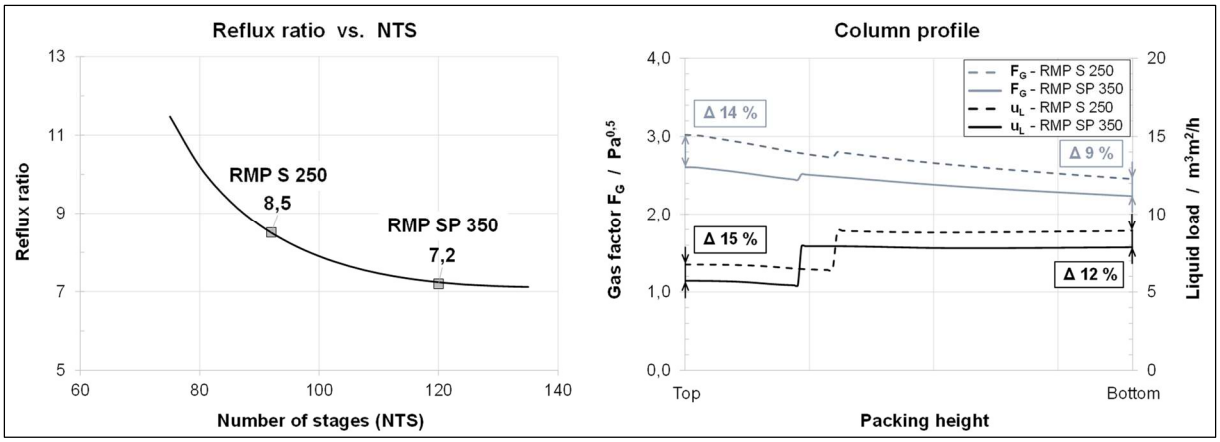

Figure 5: Sensitivity analysis of the number of stages with respect to the reflux ratio in the EB/SM-Splitter (left). Gas factor and liquid load along the EB/SM-Splitter equipped with RMP S 250 and RMP SP 350 (right).

Two points have been highlighted on the dashed line corresponding to the two simulated packings. For the RMP S 250 the reflux ratio is 8,5 whereas for the RMP SP 350 structured packing required reflux ratio reduces to 7,2. Replacement of the RMP S 250 packing with RMP SP 350 packing, which provides a higher specific surface area, resulted in enhanced mass transfer efficiency and a corresponding increase in the calculated number of theoretical stages. For the evaluation of the efficiency of both packings, their HETP values measured under vacuum conditions (0.1 bara) with the o/p-Xylene system were considered.

Figure 6 shows that the HETP-baseline for the standard high capacity 250 m^2/m^3 structured packing comparable to RMP S 250 is approximately 340 mm. As expected, the RMP SP 350 packing shows a significantly lower baseline HETP-value of approximately 260 mm. These HETP-baseline levels, applied to the EB/SM-splitter presented above, translate into 92 number of stages for the configuration with the RMP S 250 and 120 number of stages with the configuration with the RMP SP 350. This represents an efficiency increase of approx. +30 % by revamping the EB/SM-splitter from RMP S 250 to RMP SP 350 structured packing.

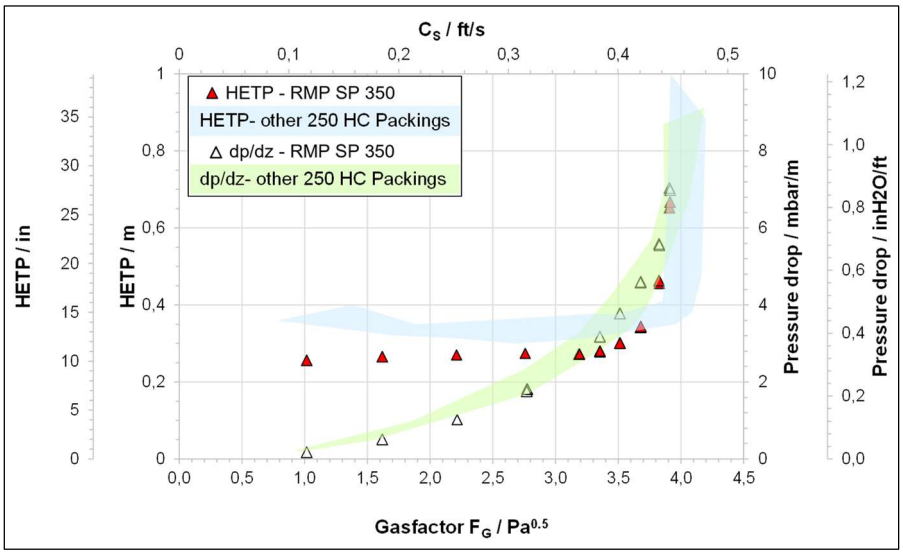

Figure 6: RMP SP 350 distillation test data: HETP and pressure drop/hydraulic capacity, measured with o/p-Xylene System at 0,1 bara at the 1,22 m-ID FRI column including comparison with data obtained for other 250 m^2/m^3 high-capacity packings

Another relevant packing performance figure directly impacting the process performance is the packing pressure drop and its related hydraulic capacity. As it can be identified from the diagram above, RMP SP 350´s specific pressure drop is even slightly lower (up to -15 %) compared to standard high capacity 250 m^2/m^3 structured packings analogue to RMP S 250 despite being a much more dense/high surface area structured packing. Beyond the loading point, at elevated loads (F_G > 3,2 $Pa^{0,5}$), both packings exhibit similar pressure drop behaviour and comparable hydraulic capacity. This has an additional positive impact on the overall process performance since total packing pressure drop can even be significantly reduced in respect to the RMP S 250 packing, not only if the packing is operated below its loading point but also because of the reduction of the column internal vapor and liquid streams that takes place as a consequence of the reduction of the reflux ratio from 8,5 to 7,2. As depicted in Figure 5, the gas factor F_G exhibits its greatest reduction at the top of the column, with a decrease of approximately 14 %

from 3,0 to 2,6 $Pa^{0,5}$, while this difference gradually diminishes along the column, reaching about 9 % at the bottom (from 2,5 to 2,2 $Pa^{0,5}$). The liquid load follows the same general pattern, with a reduction of roughly 15%, from approx. 6,8 to 5,7 m^3/m^2h in the upper section of the column, gradually declining to approximately 12 % toward the bottom (from approx. 8,9 to 7,9 m^3/m^2h).

As illustrated in the central diagram of Figure 7, the resulting total packing pressure drop is substantially reduced by approximately 29%, decreasing from 58 to 41 mbar. This has a direct impact on the column bottom pressure and the related bottom temperature which reduces by 3,2 K from 85,3 to 82,1 °C. Sump temperature reduction translates into a steam rate and reboiler duty reduction in an order of magnitude of 14 %. For a typical plant operating time of 8,000 h per year, the projected steam demand reduction amounts to approximately 20,000 t annually. Based on regional steam pricing and the location of the EB/SM splitter unit, the corresponding annual economic benefit is estimated to lie between 0,5 and 4,0 million USD. A further relevant advantage associated with a lower sump temperature is the diminished risk of SM polymerisation and the potential to reduce inhibitor costs through a decrease in required dosage.

The 29 % reduction in pressure drop at the specified feed mass flow rate of 32400 $kg \cdot h^{-1}$, together with the comparable or slightly improved hydraulic performance of the RMP SP 350, indicates the potential for a further increase in column capacity. By progressively increasing the feed mass flow rate until the internal gas and liquid traffic returns to the original hydraulic loading level (total packing pressure drop approx. 58 mbar), the feed rate can be raised to approximately 37720 $kg \cdot h^{-1}$, corresponding to a capacity increase of about 16 % as the right-hand diagram in Figure 7 shows.

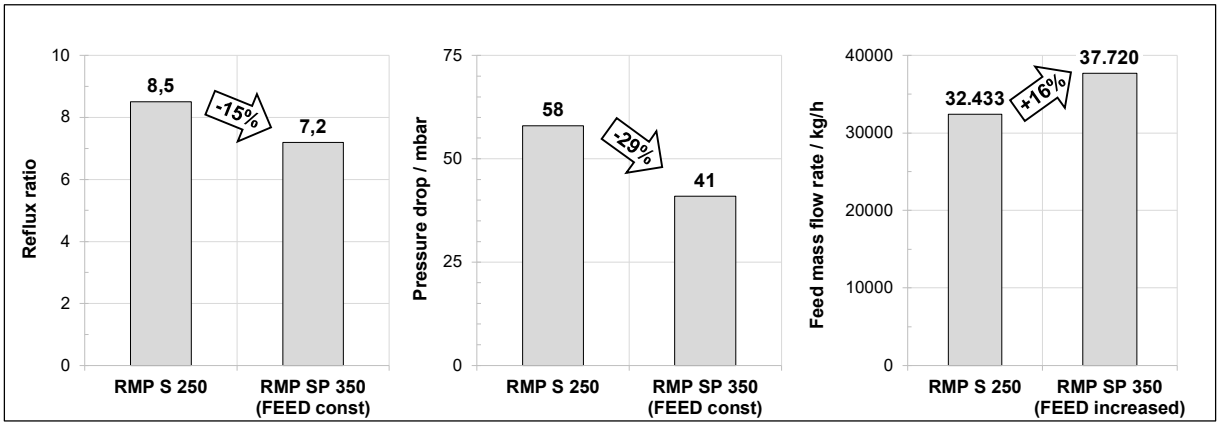

Figure 7: Reflux ratio and total packing pressure drop levels incl. %-differences between RMP S 250 and RMP SP 350 as packing regarded in the EB/SM-Splitter case study (left and center diagrams). Feed mass flow rate increase feasible by revamping RMP S 250 with RMP SP 350 in the EB/SM-Splitter (right).

4. Conclusions

The revamp of a state-of-the-art EB/SM splitter equipped with high-capacity RMP S 250 structured packing to RMP SP 350 demonstrates a substantial improvement in overall process performance and operating economics. The performance characteristics of the RMP SP 350, namely its enhanced mass transfer efficiency combined with a reduced pressure drop, result in an approximately 30% increase in the achievable number of theoretical stages. Notably, this improvement is achieved without the pressure drop penalty typically associated with higher specific surface area structured packings. On the contrary, the total packing pressure drop decreases by up to 29 %, primarily due to the optimized geometrical design of the RMP SP 350 and the associated reduction in vapor and liquid traffic resulting from the lower reflux requirement.

In addition, the reduced reflux ratio leads to a decrease in sump temperature by 3,2 K, directly lowering the reboiler heat duty and the annual steam consumption. This translates into significant operating cost savings in the million-USD range per year. The lower sump temperature further mitigates the risk of styrene polymerization and enables a reduction in inhibitor dosage, while also allowing extended column operability and longer maintenance intervals.

Overall, the demonstrated advantages of the RMP SP 350 packing are not limited to the investigated system but can be extended to comparable vacuum distillation columns across the industry.

References

[1] Sola Cervera, J. L., Geipel, C., Seibert, F., 2016. *Distillation performance characteristics of RMP-type standard and high capacity structured packings*, 2016 AIChE Spring Meeting, Houston (TX, USA)

[2] Sola Cervera, J., Pechtold, B., Geipel, C., 2022. *Distillation performance of RMP SP 250 high capacity structured packing at the FRI test facility*, 2022 AIChE Spring Meeting, San Antonio (TX, USA)

[3] Sola Cervera, J., Pechtold, B., Geipel, C., 2025. *Distillation performance of RMP SP 350 high capacity structured packing at the FRI test facility*, 2025 AIChE Spring Meeting, Dallas (TX, USA)

[4] Faessler, P. W., Kolmetz, K., Kiong Ng, W., Senthil, K., Yee Lim, T., Sloley, A. W., Zygula, T.M., 2005. Design *Guidelines for distillation columns in ethyl-benzene and styrene monomer service*, 2005 AIChE Spring Meeting, Atlanta (GA, USA)

[5] Rix, A., Schröder, M., Paul, N., 2023. *Vapor recompression: An interesting option for vacuum columns?*, Chemical Engineering Research and Design, 191, 226-235.

Low-Pressure, High Performance: A New Benchmark in C2 Splitter

Senthil Krishnamoorthy, Sulzer Chemtech USA Inc, USA
Peter Wilkinson, Sulzer Chemtech Netherlands B.V.,
Harry Kooijman, Shell Global Solutions International B.V, Netherlands.
Matthew Lunsford, Shell Global Solutions (US) Inc, USA.

Abstract:
This paper presents the performance evaluation of the Ethane-Ethylene (C2) splitter at a Shell US Ethylene plant which operates at 8 barg pressure using Shell HiFi Plus# trays. The column pressure is lower than other documented C2 splitter operations to increase both the relative volatility and the liquid viscosity. This enhances mass transfer and influences the separation efficiency of the tray. To further contextualize the C2 Splitter column's performance, operational data were compared with those from FRI Plant Test 18 (1963) which involved a C2 splitter equipped with one-pass bubble cap trays operating at approximately 11 barg on a U.S. Gulf Coast Ethylene plant. Compared to the historical FRI test, this Ethylene plant C2 Splitter achieved comparable tray efficiency, validating the effectiveness of the high-capacity Shell HiFi Plus tray design for the low-pressure Ethane-Ethylene separation. These findings establish a practical benchmark for future low-pressure C2 splitter designs.

Keywords : C2 Splitter, HiFi Plus trays, MMVG Valves

1. Introduction

This C2 splitter separates ethylene from ethane at a low top pressure of 7.7 barg, well below the typical 15–22 barg. Operating data, compared with published C2 splitter performance, show that HiFi Plus trays maintain strong efficiency under low-pressure conditions. The results confirm the design's robustness and highlight potential for future capacity increases in similar low-pressure systems.

2. C2 splitter tray design

Figure 1. HiFi Plus tray for the Shell US C2 splitter

The C2 splitter uses 116 Shell HiFi Plus trays (Figure 1) with 400 mm spacing above the feed and 360 mm below. The column diameter is 6400 mm with ~ 550 mm flow path length. MMV™ fixed valves and push valves are installed. The feed tray is 40 trays from the bottom, and the column has no pasteurization section. Overhead vapor is condensed in the heat-pump system and returned as superheated reflux (~3% vapor), with a portion withdrawn as polymer-grade ethylene

3. Tray performance evaluations

The Shell C2 splitter has been in operation since 2022, achieving the design throughput and quality specifications as per guarantee, and the column operates without any sign of hydraulic constraints. As this was the first 'low' pressure C2 splitter with HiFi Plus trays, there is a clear wish to get a more detailed analysis of the tray performance and especially focus on tray efficiency. This evaluation is based on operating data collected during 2024. The top and bottom product flow rates and compositions are used to reconcile the feed flow rate and composition. The overall mass balance is presented in Table 1: Operating Data. Note: All flow rates in the tables have been normalized to a design feed flow rate of 1000 kg/hr. The column is simulated using equation of state VLE with Sulzer's proprietary interaction parameters to generate internal vapor and liquid loads. The number of theoretical stages is adjusted until the simulation matches the measured reflux and top/bottom impurities. Figure 2 illustrates the impact of the number of theoretical stages (NTS) on reflux flow rate. A small reflux flow measurement error will have a significant impact on the estimated tray efficiency. To get as much confidence as possible in the test-run evaluation, the site places considerable emphasis on checking flow meters (±2%), heat-balances etc. The resulting tray efficiency is in the range of 83 ± 5% which is consistent with other C2-splitters[4,5] using high capacity HiFi Plus and CS Plus# trays across a wide range of operating pressures (Figure 3). The hydraulics ratings at these operating conditions are presented in Table 2.

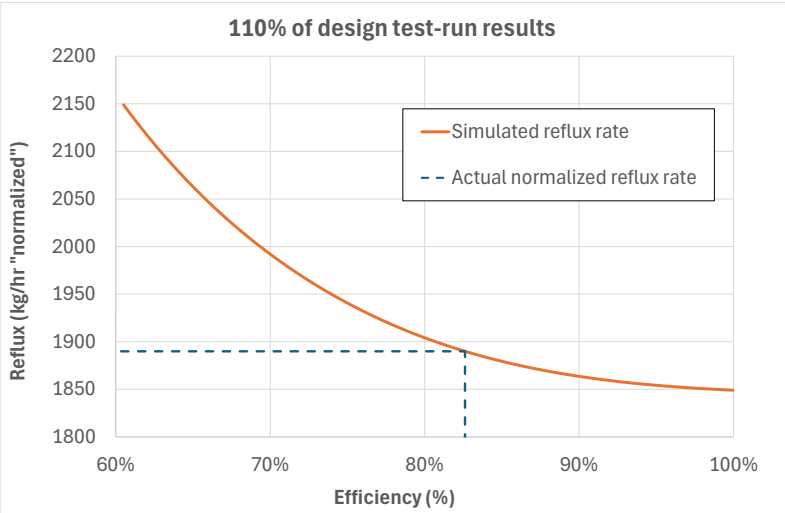

Figure 2. Predicted normalized Reflux rates versus efficiency at 110% of design

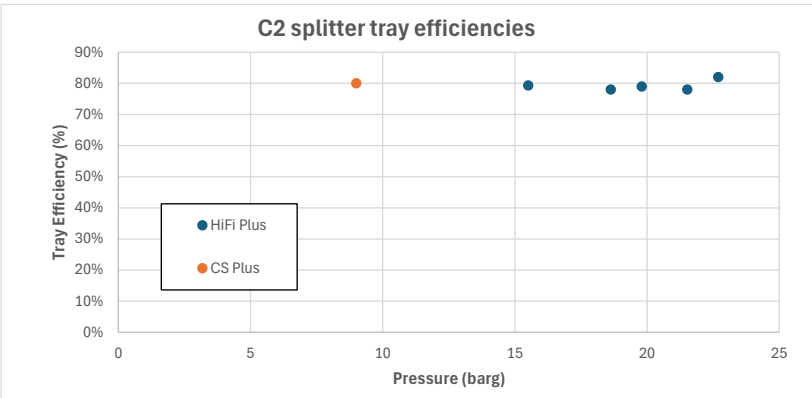

Figure 3. Tray Efficiency from test-runs for C2 splitters with Shell HiFi Plus & CS Plus trays

Table 1: Operating Data C_2 Splitter

Composition, mol%	Feed	Ethylene Product	Ethane Product
Methane	0.02	0.026	0
Ethane	39.72	0.013	98.891
Ethylene	60.16	99.961	0.850
C3/ Propylene	0.1	0	0.259
Total	100	100	100
Phase	Mixed	Liquid	Liquid
Flow rate, kg/hr	1,114[(a)]	648	466.3
Temperature, °C	-45.6	-55.9 (column top)	-34.4
Pressure, bar(g)	8.68	7.69 (column top)	8.36
Reflux Rate, kg/hr	1890		
Reflux temperature , °C	-51.6		
Reflux pressure, bar(g)	19.4		
ΔP -Upper section, bar	0.44		
ΔP -Lower section, bar	0.23		

Table 2: Tray Hydraulics of Shell HiFi Plus Trays with 6400mm column diameter

Trays	Tray Count	Section	Useful Capacity %	Weir Load, m3/m-hr	DC Velocity, m/sec	ΔP[(b)], mbar/Tray
41-116	76	Above Feed	82	25.56	0.096	5.53
1-40	40	Below Feed	76	34.56	0.094	4.93

[(a)] 1000 kg/hr represent design feed rate. The column operates ~ 110% of design.,
[(b)] including vapor head

To further check the accuracy of the model a comparison between the predicted and measured tray temperature profile was also made including a sensitivity check on reflux flow (measured reflux rate and +/- 2% reflux flow conditions). Figure 4 shows that the temperature point at Tray #16 matches best for an assumed reflux flow corrected by -2% (corresponding to 97% tray efficiency), while the Tray #50 temperature fits more closely to predictions using the exact measured reflux flow. These observations support the conclusion that tray efficiency is probably close to 83% and may be even higher.

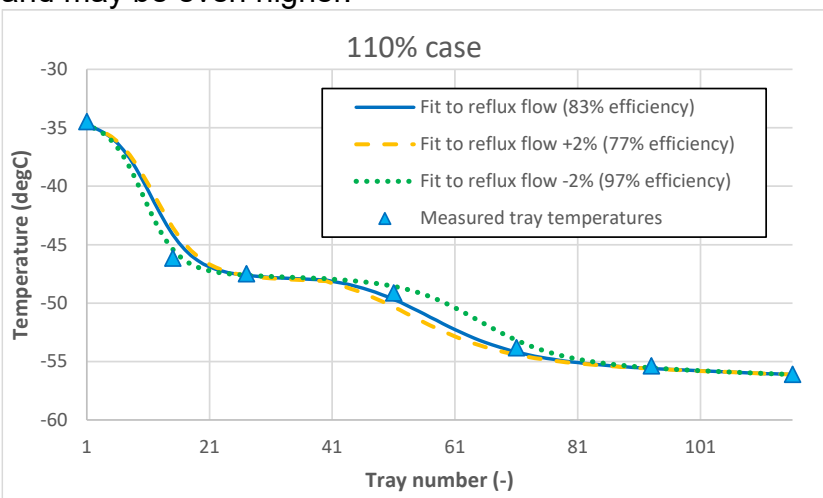

Figure 4. Predicted and measured temperature profile Shell US C2 splitter

4. Impact of flow path length and operating pressure

For C2 splitters, tray efficiency remains relatively constant across different operating pressures when HiFi Plus trays are employed. Most likely the 'simple' explanation for this is that for HiFi Plus trays the flow path length is typically longer when operating at low pressures as compared to high pressures due to differences in liquid load and downcomer area requirement. For high pressure systems the tray typically requires a larger downcomer area and longer weir-lengths which ultimately 'translate' into shorter flow path lengths. In other words, the 'point efficiency' is likely to be higher at high pressure conditions while at low pressure the reduced point efficiency is largely compensated by a longer flow path length. Additionally, an increased weir height, often incorporated in HiFi/CS Plus tray designs at low pressures, further contributes to maintaining overall efficiency.

5. The C2 Splitter performance reported in the literature

Fractionation Research Inc (FRI) has published[1] very detailed performance data for a 6-foot (1.829 m) diameter C2 splitter with 18 inch (457mm) tray spacing operating at 11 barg pressure operated by a Dow Chemical's plant located on the US Gulf Coast. This column was equipped with single-pass bubble-cap trays having a flow path length of 1.2 m which is more than twice as long as the flow path length applied for the Shell C2 splitter and therefore it is of interest to compare the performance of these two columns. The tray composition was measured on 10 different trays in addition to the column top and bottom composition allowing for a close comparison between measured and predicted compositions as shown in Figure 5 below. The match between predicted and measured compositions is fairly good and attempts to get a better fit by using different tray efficiencies for the rectification and stripping section does not show a clear improvement.

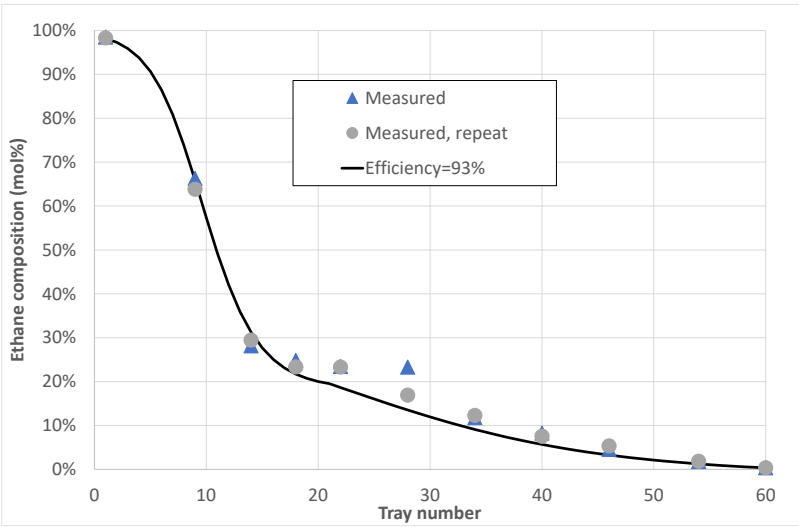

Figure 5. Comparison between predicted and measured ethane content in a C2 splitter.

Based on this evaluation, the tray efficiency appears to be about 93%, which is higher than the tray efficiencies for the Shell C2 splitter. Clearly, the fact that this is a single-pass tray with a flow path length of 1.2 m has contributed to the high tray efficiency. Furthermore, the operating pressure for the Dow C2 splitter is 4.3 bar higher than the Shell US C2 splitter and therefore the 'point-efficiency' will also be higher for the Dow C2 splitter.

Another industrial C2 Splitter operating at 19 barg with Multiple Downcomer trays was reported in Distillation[2] (section 5.2.1). The column was equipped with 165 trays with a tray spacing of 381 mm top /338 mm bottom. The column was operating with a reflux ratio of 4.96 and tray efficiency of 73%. Even though this column operated at higher pressure, which should strongly favor a better point efficiency, the Multiple Downcomer Tray still didn't achieve a better overall tray efficiency. The irregular flow path length of these trays was cited[2] as a possible reason for the reduced efficiency. A rate-based prediction of the impact of the flow path length for a C2 splitter equipped with HiFi Plus trays operating at 8-9 bar is shown in Figure ***6***. A flow path length of ~350 mm or higher is normally preferred in view of efficiency considerations.

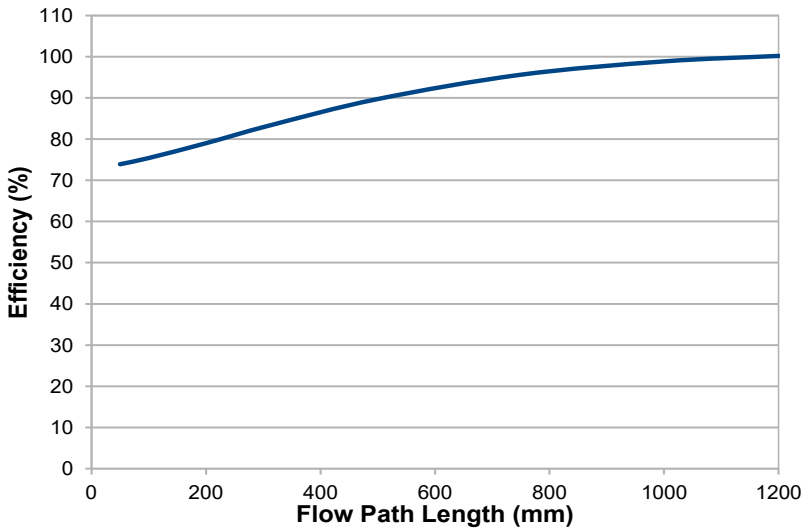

Figure 6. Tray Efficiency as a function of flow path length using rate-based model[2]

6. Revamp options for the Shell US C2 splitter

Based on the current evaluation the trays will have enough spare capacity to increase the capacity to 130% of design capacity (at 100% maximum useful capacity). Given this large capacity margin, there is clearly no need to consider any tray revamps at the moment. Nevertheless, an assessment has been made to showcase that despite using high-capacity trays for this new column there are still significant options to further increase the capacity in future if needed. This evaluation is based on the assumption of same conversion in the cracker (equal feed composition). As mentioned earlier, the column has been designed to be close to minimum reflux conditions and consequently the capacity of the column may be increased by selecting trays with a larger tray spacing. This will lead to a reduction in the stage-count (and a slight reduction in energy efficiency) but will allow for a capacity increase. A rough estimate of the attainable capacity gain of this column is shown in Table 3.

Table 3. Impact of increasing tray spacing (assuming same tray efficiency post revamp).

Tray replacement	Resulting Tray spacing (mm)	Increase over design feed rate (%)
5 for 6	480 / 432	143
4 for 5	500 / 450	144
3 for 4	533 / 480	147
2 for 3	600 / 540	152

To take this thought even further, using Shell ConSep# Plus trays would also be an option. In the past one C2 splitter has been revamped with Shell ConSep trays having

a tray spacing of 450 mm. With the more recently developed improved Shell ConSep Plus trays the capacity and efficiency are further improved and will be very close to the efficiency of a Shell HiFi Plus tray but with a much higher capacity as illustrated in Figure 7 which shows some data[3]. Obviously, both these options would most likely require an investment in heat exchangers and compressors to enable the higher reflux rate requirements to fully load the column. Nevertheless, these examples clearly show that the C2 splitters designed with high-capacity trays can often be revamped further to achieve significant capacity gains.

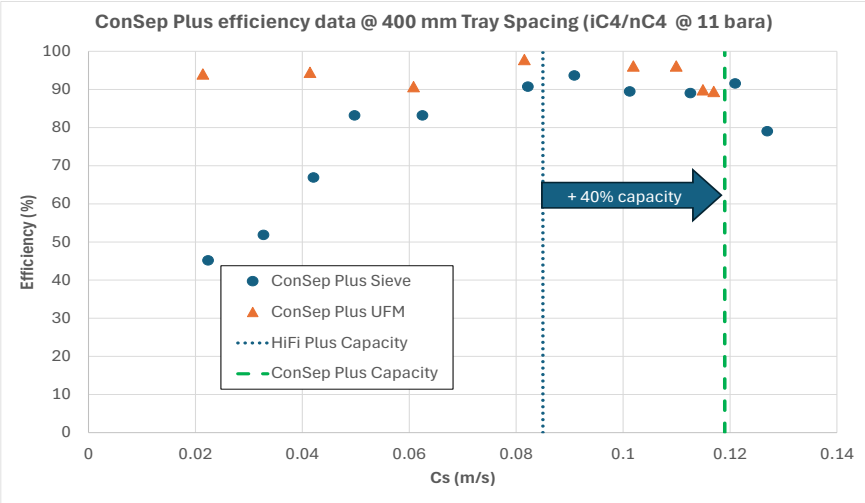

Figure 7. Tray Efficiency pilot plant test results for ConSep plus trays at low tray spacing[3].

7. Conclusions

Designing a C2 splitter at relatively low pressures has the advantage that the relative volatility increases will reduce the required tray-count (that can also help to reduce the column diameter). The Shell US C2 splitter performance review in combination with the experience of other C2 splitters designed with Shell HiFi Plus and CS Plus trays clearly shows that the tray efficiency appears to be approximately constant across a wide range of operating pressures. Furthermore, the data presented shows that there remains considerable scope to increase the capacity of C2 splitters designed with high-capacity trays by changing tray spacing and/or applying ultra-high capacity trays such as ConSep Plus trays.

References

[1] Fractionation Research, Inc. Plant test report no. 18, Efficiency test of a 6-foot diameter Ethane-Ethylene splitter, T. Yanagi, and T.R. Barben II, July 15th, 1963.

[2] Hendrik A. Kooijman, Ross Taylor, Ch 5 - Distillation of Bulk Chemicals, Editor(s): Andrzej Górak, Hartmut Schoenmakers, Distillation, Academic Press, 2014

[3] Ultra-High Capacity ConSep Trays. Prakash Katre, Rajeev Narayan. Distillation Conclave meeting 2022.

[4] C2 Splitter revamp takes interesting path, D.R.Summers, S.Krishnamoorthy, T.M. Zygula, 2023 AIChE Spring Meeting, Houston, TX

[5] C2 Splitter revamp with Shell HiFi Plus Trays, S Krishnamoorthy, A Bernard, 2024 AIChE Spring meeting, New Orleans, LA

Note

HiFi Plus, CS Plus, ConSep - Trademark owned and used by the companies of the Shell Group.

Hydraulic Investigations of Fixed Valve Trays Using Conductivity Sensor Arrays

Felicitas S. Engel[1], Philipp Wiedemann[2], Eckhard Schleicher[2], Cornelia Maier[1], Markus Schubert[3], Uwe Hampel[2,4], Harald Klein[1], Sebastian Rehfeldt[1]

[1]Institute of Plant and Process Technology, Department of Energy and Process Engineering, TUM School of Engineering and Design, Technical University of Munich, Garching/Germany;

[2]Institute of Fluid Dynamics, Helmholtz-Zentrum Dresden-Rossendorf, Dresden/Germany;

[3]Chair of Chemical Process Engineering, Dresden University of Technology, Dresden/Germany;

[4]Chair of Imaging Techniques in Energy and Process Engineering, Dresden University of Technology, Dresden/Germany

Abstract

The optimal hydraulic design of column trays relies on a detailed understanding of the spatial distribution of the gas and liquid phase and global flow patterns on the tray. For this purpose, two high-resolution conductivity sensor arrays with 360 sensor probes and a sampling rate of 5000 Hz were developed and applied in a 1.2 m diameter tray column test rig operated with air and water. The investigations cover sieve trays and fixed valve trays, different weir configurations and a wide range of gas and liquid flow rates. The experimental results provide detailed insights into phase distribution and flow patterns within the two-phase layer. The type of tray openings has a significant impact on the behavior of the entering gas jets. A particularly strong influence is exerted by variations in gas and liquid load, as they significantly affect the gas inlet behavior and, consequently, the phase distribution throughout the entire two-phase layer. Under certain gas and liquid loads and especially at increased weir height, a tendency for the formation of dead zones was observed.

Keywords

Tray Column, Hydraulics, Fixed Valves, Conductivity Sensor Arrays, Phase Distribution, Flow Characterization

1. Introduction

The increasing use of renewable energy leads to fluctuating electricity availability, requiring flexible operation of tray columns in thermal separation processes with regard to future electrified column processes. A promising type of internals for these columns are fixed valve trays, as they offer high capacity and good separation efficiency across a wide operating range.

Nevertheless, trays and tray openings need to be properly designed to align with the defined range of operating conditions to deliver optimal phase distribution and flow patterns for attaining high separation efficiencies. Although two-phase layers on column trays have already been analyzed in several experimental studies, the measurement principles used in these studies cannot resolve the two-phase layer in detail. Examples are gamma-ray scans (e.g. [1]) that can only return an integral value along the penetration path, post-processed video recordings (e.g. [2]) providing only 2D projections from the column outside, or single-point measurements (e.g. [3]) that are assumed being representative for the whole tray. Hence, the detailed spatial distribution of phases and global flow patterns are unattainable with these approaches.

In the present work, these characteristics are investigated experimentally using two novel conductivity sensor arrays in a 1.2 m diameter tray column.

2. Experimental setup

Two high-resolution conductivity sensor arrays were developed and allow spatially resolved measurements of gas-liquid flow characteristics based on 360 probes with equidistant spacing of 45 mm. All probes are sampled at 5000 Hz. The first sensor array enables measurements of phase distributions within the two-phase froth layer, whereas the second array is designed to suppress the influence of the gas to the signals and to track injected liquid tracer pulses passing the tray in order to study global liquid flow and dispersion across the tray. The basic measuring principles of the two sensors are described in [4] and [5].

Both sensor arrays were installed in a 1.2 m diameter tray column test rig operated with air and water, with the sensor positioned concentrically regarding the column axis. A detailed description of the column test rig can be found in [6]. The vertical position of the sensor arrays was adjusted to cover measuring heights of $z = (20 \ldots 260)\ \mathrm{mm}$ above the upper tray. The geometrical details of the applied trays are specified in Table 1. A standard weir height of $h_\mathrm{w} = 50\ \mathrm{mm}$ was installed initially.

Table 1: Geometrical data of the trays: relative open area $\boldsymbol{\varphi}$, hole diameter $\boldsymbol{d_\mathrm{h}}$, valve lift height $\boldsymbol{h_\mathrm{lift}}$ and number of elements $\boldsymbol{N}$

Tray type	φ in %	d_h in mm	h_lift in mm	N
Sieve	10	10	-	1093
R-FV fixed valve	10	-	7	189

3. Results and discussion

The two sensor arrays were used to investigate two-phase flow characteristics while operating the test rig with different tray types, weir configurations and a wide range of gas and liquid flow rates (indicated by F-factor F_ac and liquid flow rate $\dot{V}_\mathrm{L}$). Selected results from the numerous findings are presented in the following with a focus on the R-FV fixed valve tray.

3.1 Gas-liquid phase distributions

Figure 1 shows the measured gas-liquid phase distributions for the two tray types (topview, liquid flow direction from bottom to top) at a height of $z = 40\ \mathrm{mm}$ above the tray. For each of the 360 probe positions, the value of the gas fraction is averaged over a measuring time of $\Delta t = 3\ \mathrm{min}$.

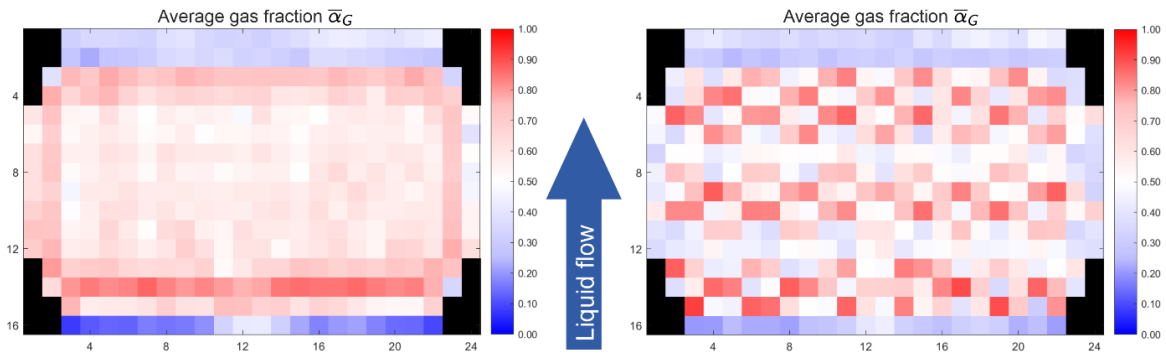

Figure 1: Time-average gas fraction at $\dot{V}_\mathrm{L} = 10\,\frac{\mathrm{m}^3}{\mathrm{h}}$ and $F_\mathrm{ac} = 2.2\,\sqrt{\mathrm{Pa}}$ at a height of $z = 40\ \mathrm{mm}$ for the sieve tray (left) and the R-FV tray (right).

The calming zones without gas inlet elements near the liquid inlet and outlet are clearly visible in both cases, characterized by a low gas fraction (shown in blue). However, there are clear differences in terms of the active area: The sieve tray (left) shows a

homogeneous froth with medium to high gas fractions, whereas the valve tray (right) features lower and higher local gas fractions with a distinct pattern. This is caused by the valves having significantly larger openings along with coarser spacing, resulting in larger gas jets with liquid-dominated regions in between, which are detected depending on the positions of gas openings and sensor probes.

By combining the height profiles of the 360 sensor probes, an overall spatial phase distribution map can be developed. Figure 2 shows the profiles for the previously presented tray configurations. The phase fraction is represented by the liquid holdup at the abscissa. Each line corresponds to one of the 360 sensor probes, colored according to their radial position on the tray, i.e. red lines represent positions near the column wall, whereas blue lines refer to the tray center. The black line represents the cross-sectionally averaged profile of all 360 probes.

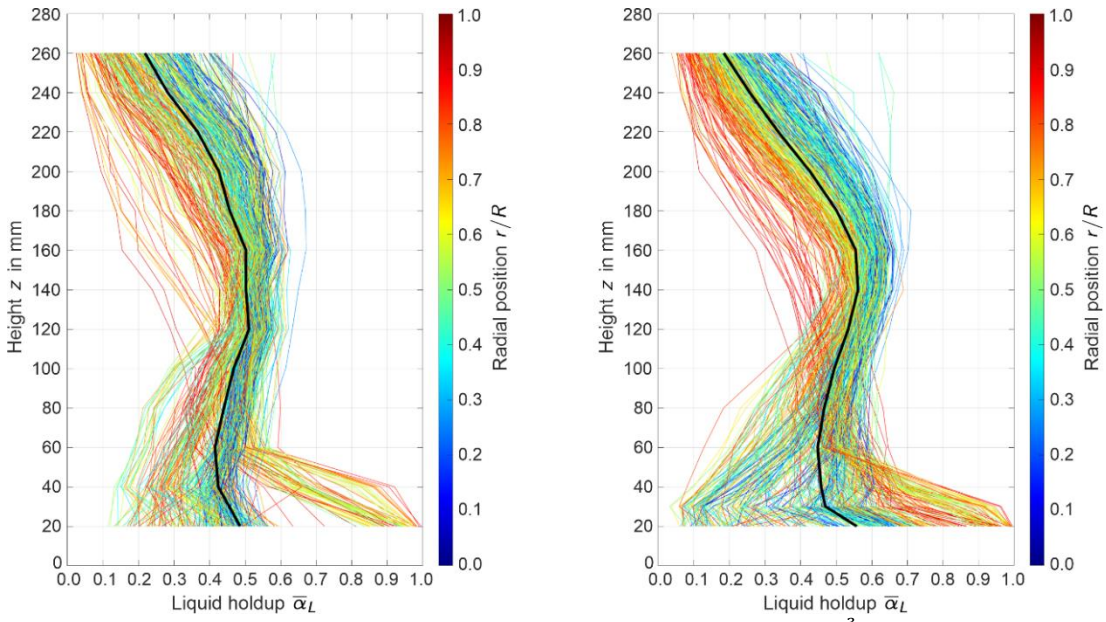

Figure 2: Spatial distribution maps of liquid holdup over height at $\dot{V}_\mathrm{L} = 10\,\frac{\mathrm{m}^3}{\mathrm{h}}$ and $F_\mathrm{ac} = 2.2\,\sqrt{\mathrm{Pa}}$ for the sieve tray (left) and the R-FV tray (right).

The differences in the phase distributions observed in Figure 1 are also visible in the lower parts of Figure 2. For the fixed valve tray (right), a wide scattering of holdup values is obtained caused by the local gas jets and liquid-dominated zones. The sieve tray (left) can be divided into two distinct sections here, representing the homogeneous froth area with moderate liquid holdup and the calming zones with very high liquid holdup. At elevations $z > 60\ \mathrm{mm}$, however, the two-phase layer is rather homogeneous and shows no major differences between the two tray types.

Figure 3 shows the same map for a variation of the liquid load for the fixed valve tray. Although the figure on the right shows a fourfold increase in liquid flow rate, the averaged profile exhibits only minor changes, mainly in the form of slight vertical stretching. Considering the spatial resolution, the column wall region (red lines) also shows rather small variation. However, notable differences can be observed at the tray center (blue), where at $z = 20\ \mathrm{mm}$ significantly lower liquid holdups are seen, indicating stronger or more frequent gas jets. These dominant jets transport more liquid upwards, as can be seen by nearly constant holdup values of $\overline{\alpha}_\mathrm{L} = 0.5 \ldots 0.7$ at elevations $z = (60 \ldots 160)\ \mathrm{mm}$.

Another important factor for the operation of fixed valve trays is the gas load. Figure 4 shows that at high gas load (right), significantly more dominant gas jets are observed

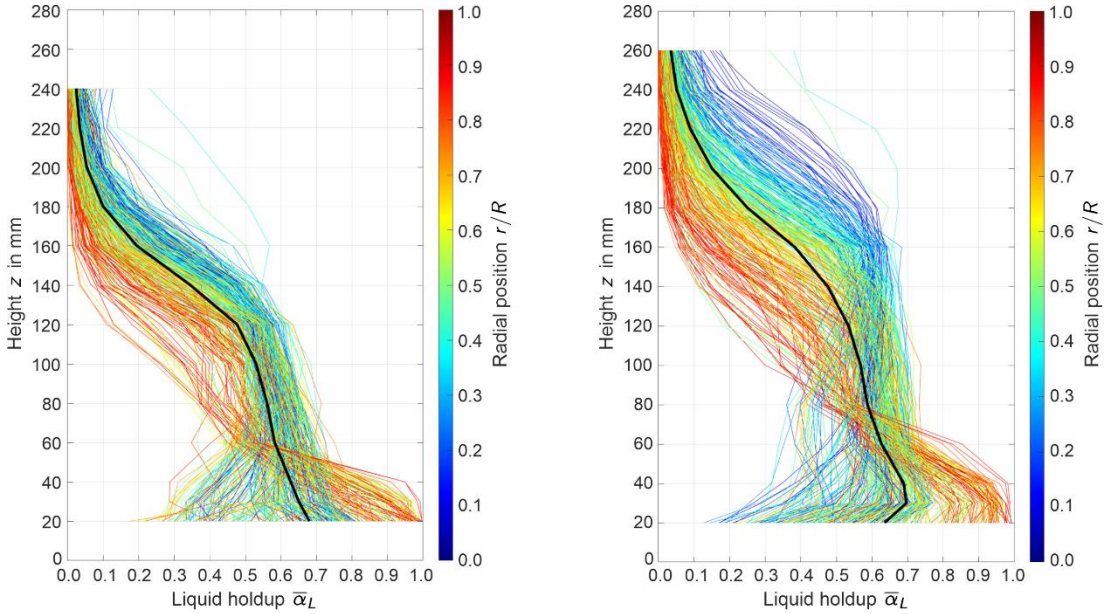

Figure 3: Spatial distribution maps of liquid holdup over height for the R-FV tray at $F_{\mathrm{ac}} = 1.0\,\sqrt{\mathrm{Pa}}$ and $\dot{V}_{\mathrm{L}} = 10\,\frac{\mathrm{m}^3}{\mathrm{h}}$ (left) and $\dot{V}_{\mathrm{L}} = 40\,\frac{\mathrm{m}^3}{\mathrm{h}}$ (right).

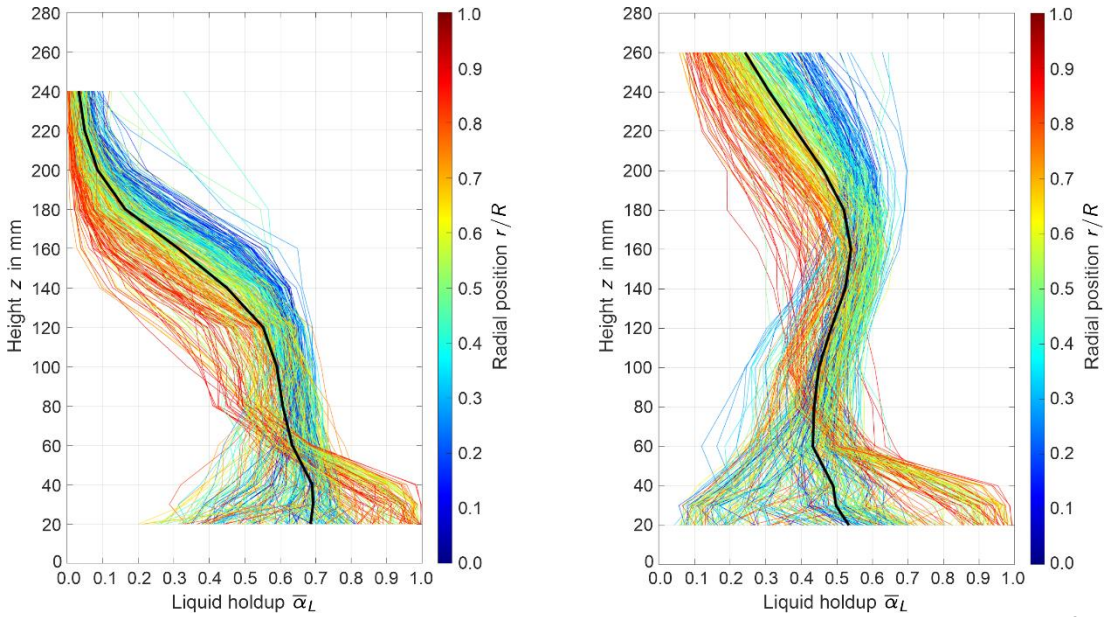

Figure 4: Spatial distribution maps of liquid holdup over height for the R-FV tray at $\dot{V}_{\mathrm{L}} = 20\,\frac{\mathrm{m}^3}{\mathrm{h}}$ and $F_{\mathrm{ac}} = 1.0\,\sqrt{\mathrm{Pa}}$ (left) and $F_{\mathrm{ac}} = 2.2\,\sqrt{\mathrm{Pa}}$ (right).

at $z = 20\ \mathrm{mm}$, indicating a higher inlet momentum of the gas jets, which results in a lower average holdup value at low elevations. As can be seen in the height profiles, the gas jets transport a larger amount of liquid upwards both in the tray center (blue) and in the wall area (red), resulting in a significant increase of liquid holdup at $z > 120\ \mathrm{mm}$. This leads to a qualitative change in the cross-sectionally averaged profile (black) with an additional local maximum at $z = 160\ \mathrm{mm}$. However, changes in the gas load contribute less to horizontal holdup variance compared with variation of the liquid load, as can be seen from a more uniform phase distribution across the tray.

3.2 Liquid flow characterization

The liquid flow behavior on the tray is measured via the tracer sensor array. It detects the passage of conductivity tracer pulses fed into the liquid inlet for a period of

$\Delta t = 3\ \mathrm{s}$. The measurement data are analyzed in terms of mean appearance time and mean unidirectional liquid velocity. For each of the following results, the data from five repetitive measurements are averaged.

Figure 5 shows the results obtained for a height of $z = 40\ \mathrm{mm}$ above the tray for different liquid loads (same configuration as shown in Figure 3). Regardless of the liquid load, similar qualitative behavior was observed for the mean appearance time, where the injected tracer pulses spread laterally toward the column walls and disperse in the main flow direction, which broadens the pulses and increases mean appearance times. At higher liquid load (right), the low mean appearance times (shown in blue) across the whole tray indicate a plug flow behavior with a low tendency to form dead zones on the tray. This is supported by larger unidirectional liquid velocities on the active area at higher liquid load. Additionally, recirculation effects at the liquid inlet are observed at the given measurement height.

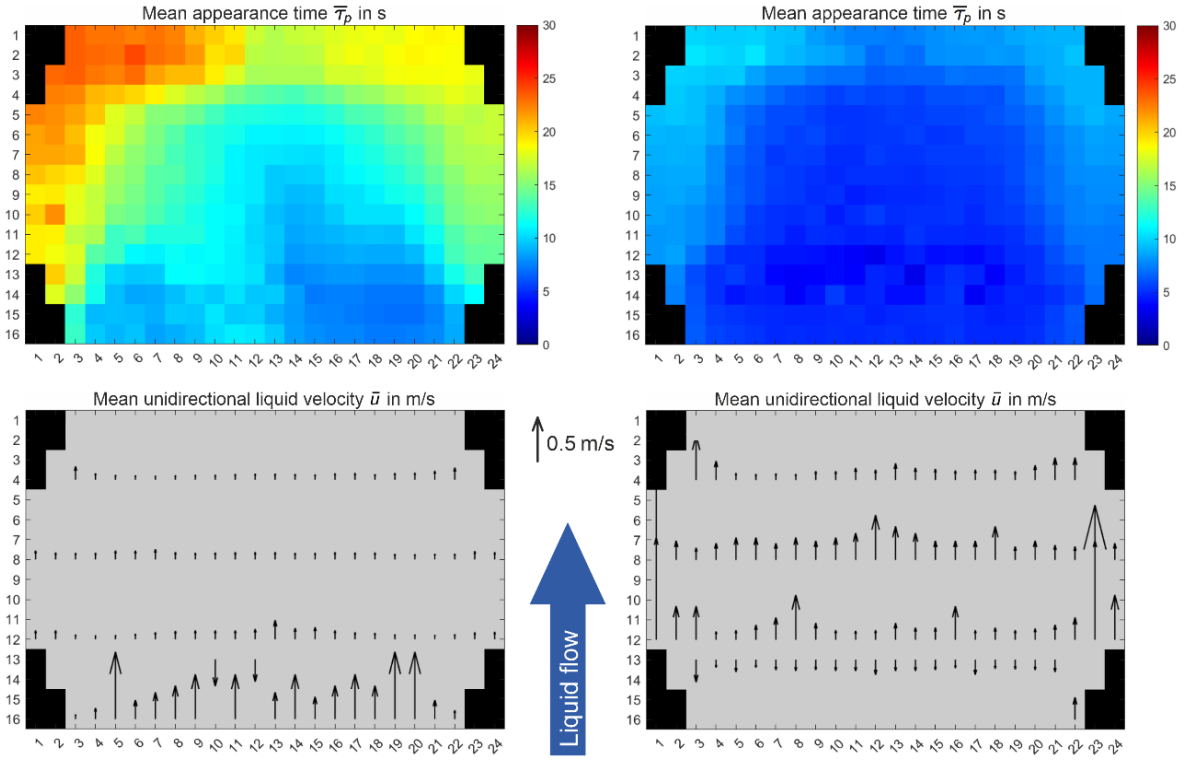

Figure 5: Liquid flow parameters for the R-FV tray at a height of $z = 40\ \mathrm{mm}$ at $F_{\mathrm{ac}} = 1.0\ \sqrt{\mathrm{Pa}}$ and $\dot{V}_{\mathrm{L}} = 10\,\frac{\mathrm{m}^3}{\mathrm{h}}$ (left) and $\dot{V}_{\mathrm{L}} = 40\,\frac{\mathrm{m}^3}{\mathrm{h}}$ (right).

For a variation of the gas load, Figure 5 (left) and Figure 6 (left) can be compared. For a higher gas load (Figure 6, left), the mean appearance time is slightly lower, resulting in a lower tendency to form dead zones. The velocity profiles show only minor differences suggesting a slightly higher liquid velocity near the outlet at high gas loads. As a last comparison in Figure 6, the weir height is increased to $h_{\mathrm{w}} = 100\ \mathrm{mm}$ (right). It can be seen that the higher weir has a clear effect on both flow profile parameters. The mean appearance time increases at the outlet weir, with a greater tendency to backmixing as revealed by the liquid velocities. This stagnation influences the overall flow pattern on the tray, as can be seen from the higher mean appearance times and lower velocities in the center of the tray.

4. Conclusions

In this work, the experimental results of two high-resolution conductivity sensor arrays for spatially resolved measurements of two-phase characteristics were presented.

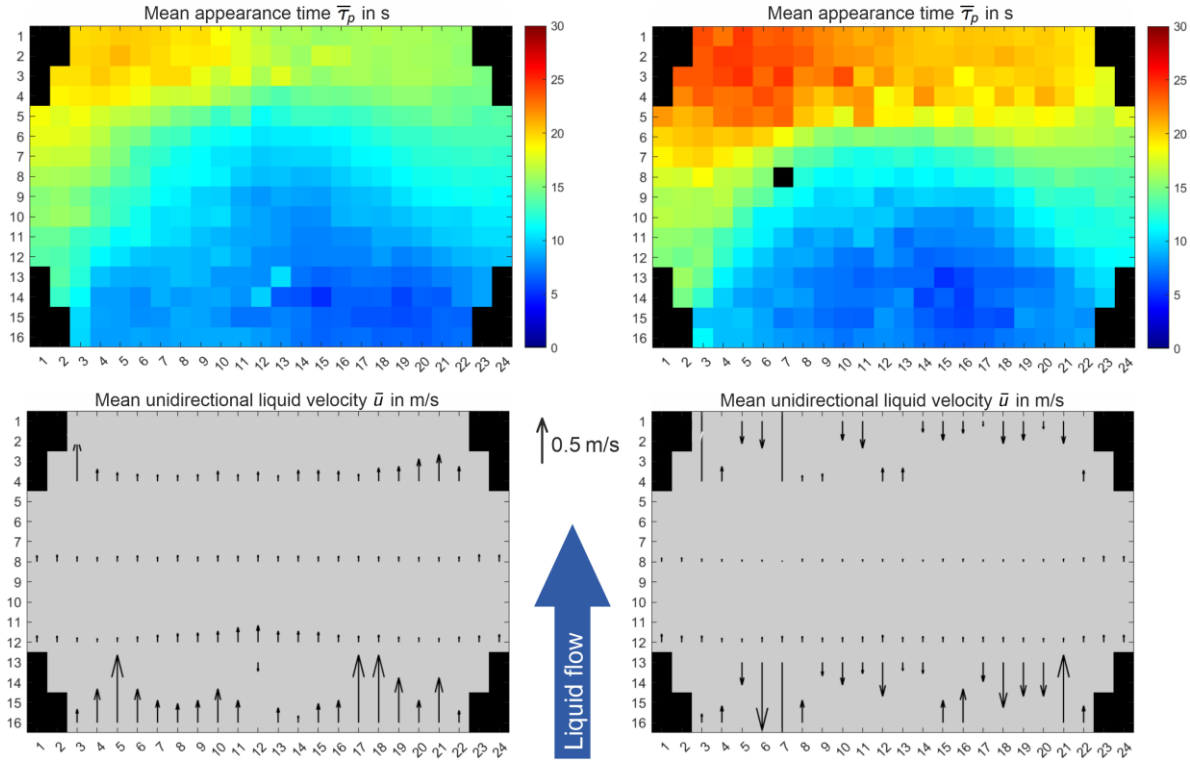

Figure 6: Flow profile parameters for the R-FV tray at $\dot{V}_\mathrm{L} = 10\,\frac{\mathrm{m}^3}{\mathrm{h}}$ and $F_\mathrm{ac} = 1.8\,\sqrt{\mathrm{Pa}}$ with $h_\mathrm{w} = 50\ \mathrm{mm}$ at a height of $z = 40\ \mathrm{mm}$ (left) and $h_\mathrm{w} = 100\ \mathrm{mm}$ at a height of $z = 30\ \mathrm{mm}$ (right).

They provide exceptional insights into the local gas-liquid phase distributions and liquid flow behavior on column trays. The measurements of the local phase distribution reveal that the type of gas openings as well as the operating conditions have significant impact on the behavior of gas entering the tray and on the phase distribution pattern along the froth height. The liquid tracer measurements visualize the tendency to the formation of dead zones at different gas and liquid loads as well as with higher weir. Overall, these measurements provide new insights into hydraulic tray characteristics, supporting future design and operation of tray columns with fixed valves.

Acknowledgements

The authors gratefully acknowledge the financial support of the IGF project 20835 BG by the Federal Ministry for Economic Affairs and Climate Action and the supply of column equipment and trays by RVT Process Equipment GmbH and Raschig GmbH.

References

[1] P. A. M. Hofhuis, "Flow Regimes on Sieve-Trays for Gas/Liquid Contacting", PhD thesis TU Delft, 1980.

[2] R. Brahem, A. Royon-Lebeaud, D. Legendre, M. Moreaud, L. Duval, "Experimental hydrodynamic study of valve trays" *Chem. Eng. Sci.* 100, pp. 23-32, 2013.

[3] W. V. Pinczewski and C. J. D. Fell, "The transition from froth-to-spray regime on commercially loaded sieve trays" *Trans. Inst. Chem. Engrs.* 50, pp. 102-108, 1972.

[4] V. Vishwakarma, S. A. Haq, E. Schleicher, M. Schubert and U. Hampel, "Experimental analysis of the hydrodynamic performance of an industrial-scale cross-flow sieve tray" *Chem. Eng. Res. Des.* 174, pp. 294-306, 2021.

[5] V. Vishwakarma, E. Schleicher, A. Bieberle, M. Schubert and U. Hampel, "Advanced flow profiler for two-phase flow imaging on distillation trays" *Chem. Eng. Sci.* 231, p. 116280, 2021.

[6] F. S. Engel, H. Klein and S. Rehfeldt, "Hydraulic investigations of standard and high performance trays in a DN1200 column" *Chem. Eng. Res. Des.* 194, pp. 478-486, 2023.

Weeping Behavior and Pressure Drop of Moving Valve Trays at Low to Disappearing Vapor Loads

Patricia Polgár[1], Christian Hoffmann[1], Markus Illner[1], Jens-Uwe Repke[1]
[1]Technische Universität Berlin, Process Dynamics and Operations Group, Berlin, Germany

Abstract
Moving valve trays are high-performance distillation trays designed to prevent weeping even at low vapor loads by self-adjusting their free area according to the vapor load. This results in flow regimes, pressure drop, and weeping characteristic differing from the well-studied sieve trays: At medium gas loads, separate bubbling and non-bubbling areas form on the tray. At low gas loads, the regime switches to a state where all valves periodically oscillate between bubbling and weeping (surging) and the hydraulic behavior changes fundamentally. Both hydraulic states were reported before, but a systematic fluid-dynamic study for a broad range of liquid and gas loads is currently missing. To this end, the contribution presents experimental data for pressure drop, weeping ratio, fractional bubbling area and hydraulic state from a DN650 column with three trays. It was shown that weeping ratios above 10% only occur in the surging state. The transition point from bubbling to surging, the fractional bubbling area and the weeping rate were all found to correlate with the Froude number, and simplified correlations for their prediction were proposed, allowing an accuracy improvement of rigorous process models when describing valve tray column behavior.

Keywords
Weeping; Moving valve; Distillation; Tray column; Fluid dynamics

1. Introduction

Distillation columns – and especially tray columns – rank among the most widely used separation units in the chemical industry (Kiss, 2014). The most simple and common tray types are sieve trays, which were extensively studied from normal operation down to an empty column state both under steady-state and dynamic operating conditions (cf. Raddant et al. (2025)). Moving valve trays were developed to prevent weeping and increase the turndown ratio of the column by dynamically closing the tray orifices at low vapor loads to reduce their free area. This variable geometry fundamentally changes the hydraulic behavior, resulting in a different pressure drop characteristic and other flow regimes on the tray.

In a dry state at low gas loads, all valves are closed up until the closed balance point (CBP), where they transition to an inclined state. This is followed by a region in which pressure drop remains nearly constant while the valves gradually open. At the open balance point (OBP), all valves are fully open, and the pressure drop increases quadratically. When liquid is introduced, different hydraulic states form, which are directly connected to the operating region (closed/inclined/open) of the valves. When the vapor load is insufficient to keep all the valves inclined or open (fully bubbling state), a separate bubbling area with open and inclined valves and a non-bubbling area with closed valves develop on the tray (random bubbling state). Wang et al. (2019) studied the fractional bubbling area θ and weeping behavior in this state for a wide range of

gas velocities at different weir heights and liquid loads, but the investigation did not include weir loads below 10 m³/(m h) or low to near-zero gas loads, and consequently any operation points with high weeping rates. They proposed a model for describing the clear liquid height h_{cl} in the bubbling and non-bubbling zone separately, as well as a correlation for the fractional bubbling area θ and weeping flow rate. The model can describe the experimentally measured operating range with an accuracy of $\pm$ 25%, but has no solution when the gas load converges towards zero. Ma et al. (2021) showed that at very low gas loads, the tray transitions to a different state where all valves oscillate between an open ("bubbling") and closed ("weeping") state, causing high amplitude vibrations and mechanical damage (ordered surging state). They presented experimental data of h_{cl} and weeping ratio Ω at very low vapor loads combined with different liquid loads and weir heights and proposed a correlation for the Froude number at the transition point from random bubbling to ordered surging $\mathrm{Fr_t}$. A model describing the amplitude and frequency of the valve oscillations was proposed in this work as well. However, a detailed analysis of pressure drop and weeping covering both states is still missing. An experimental study of the hydrodynamic behavior of valve trays from standard operation to zero gas flow is therefore presented in this contribution.

2. Results and discussion

A transparent and modular acrylic glass column (DN 650) with three trays was used to conduct fluid dynamic experiments with an air-water system (Figure 1). The column, automated via the process control system Siemens PCS 7, can be operated at F-Factors F_{act} between 0 and 2.5 Pa$^{0.5}$ (based on active area) and weir loads $F_{\mathrm{w}}^{\mathrm{L}}$ between 1 and 23 m³/(m h). The simplified piping and instrumentation (P & I) diagram of the plant, including the measuring range of all relevant sensors, is given in Figure 2.

Dry tray pressure drop was measured over the middle tray with the external differential pressure sensor PDI01 by blocking the downcomers as well as all outlets except for the column head to prevent gas bypass. Subsequently, steady-state experiments measuring pressure drop and weeping flow were conducted with a 0.02 m inlet and 0.025 m outlet weir following a full factorial design covering the entire operating range. Total pressure drop was measured with the same external differential pressure sensor (PDI01), while weeping liquid was collected on the gas distributor and weeping collector (D/C) tray and quantified with the magnetic-inductive flow sensors FI06 and FI07. After both liquid and gas loads reached the chosen setpoint, we waited 90 s to achieve steady state. It was previously verified that this time is sufficient for both pressure drop and weeping flow to reach their respective steady-state value. Each measurement was recorded for 180 s and repeated three times to account for both process fluctuation and reproducibility. The measurement error is given as the double standard deviation over the recorded time period of 3 x 180 s. The hydraulic state of the tray (fully bubbling, random bubbling or ordered surging) was obtained via visual observations. To characterize θ, images were recorded of all three trays, which were evaluated by laying a grid on each image and analyzing which grid tiles cover the bubbling area.

The measurement results for dry tray pressure drop, hydraulic state, fractional bubbling area, hydrostatic pressure drop and weeping are discussed in the following sections.

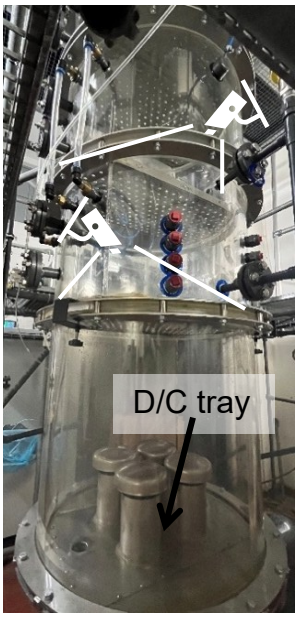

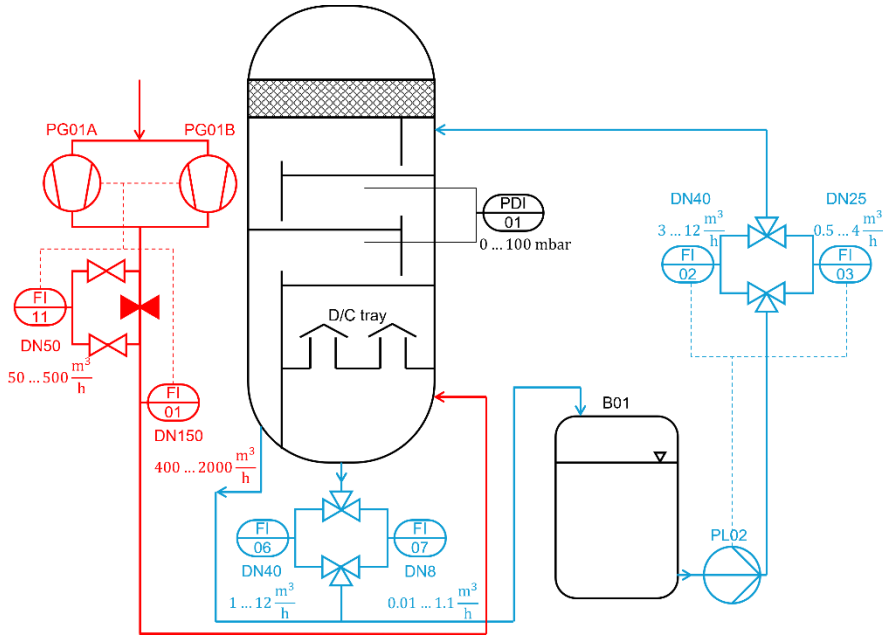

Figure 1: Bottom view of the tray column test rig.

Figure 2: Simplified P & I Diagram of the tray column test rig at Technische Universität Berlin.

2.1 Dry tray pressure drop

The measured dry pressure drop for a tray ΔP_d is presented in Figure 3 as a function of the F-Factor F_act. The pressure drop ΔP_d is commonly described with an orifice-dependent equation (Equation (1)) that represents the F-Factor in the orifice as a function of F_act and the relative free area φ. The latter represents the ratio of total orifice A_hole and active area A_act:

$$\Delta P_\mathrm{d} = \frac{\zeta_\mathrm{c/i/o}}{2} \cdot \left(\frac{F_\mathrm{act}}{\varphi}\right)^2 \tag{1}$$

The three operating regions (closed, inclined, and open) of the valves are described with different friction coefficients ζ (Lockett, 1986; Wang, et al., 2019).

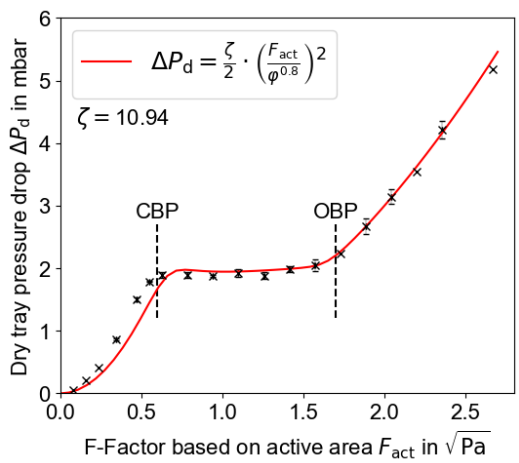

Figure 3: Measured dry tray pressure drop ΔP_d and developed correlation.

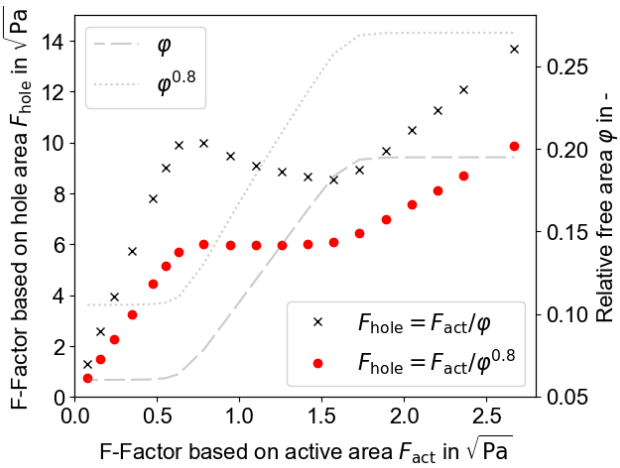

Figure 4: Comparison of different hole area calculation methods.

The valve opening characteristic assumed in Equation (1) results in a decreasing hole velocity between the CBP and OBP, as shown by the black crosses in Figure 4. This is contrary to the constant pressure drop behavior shown in Figure 3. To overcome this inconsistency, a different definition of F_{hole} is proposed in this work, where an exponent is added to φ, resulting in a steeper increase of the free area in the inclined state. This new approach is given by red dots in Figure 4, illustrating that the new relationship results in a constant hole velocity in the inclined valve state, which aligns with the observed characteristic of ΔP_{d} between the CBP and OBP. Equation (1) with this modified F_{hole} is also shown in Figure 3 to demonstrate that the new approach requires only one (tray-specific) value for ζ to describe the dry pressure drop for all three operating regions.

2.2 Valve behavior and pressure drop under wet conditions

To also capture hydraulic behavior, liquid is introduced to the column tray. The previously introduced three hydraulic states (fully bubbling, random bubbling and ordered surging) are shown in Figure 5. The share of the bubbling area on the tray decreases with decreasing gas load or increasing liquid load (cf. Figure 5 (b) and (c)). The results of the image analysis for characterizing θ in the bubbling states are shown in Figure 6, where the model of Wang et al. (2019) is given by dotted lines as well. While the predicted values are in a similar order of magnitude, the dependence of θ on $F_{\mathrm{w}}^{\mathrm{L}}$ is much stronger in the model than in our experimental data. Our findings show that θ is rather related to the Froude number Fr, which describes the ratio of the uplifting forces to the hydrostatic pressure working on the tray. In our experiments, $\theta = 1$ is reached at $\mathrm{Fr} \approx 0.1$ for all studied liquid loads, while the model of Wang et al. (2019) predicts that the transition to full bubbling shifts to higher Fr with increasing liquid load.

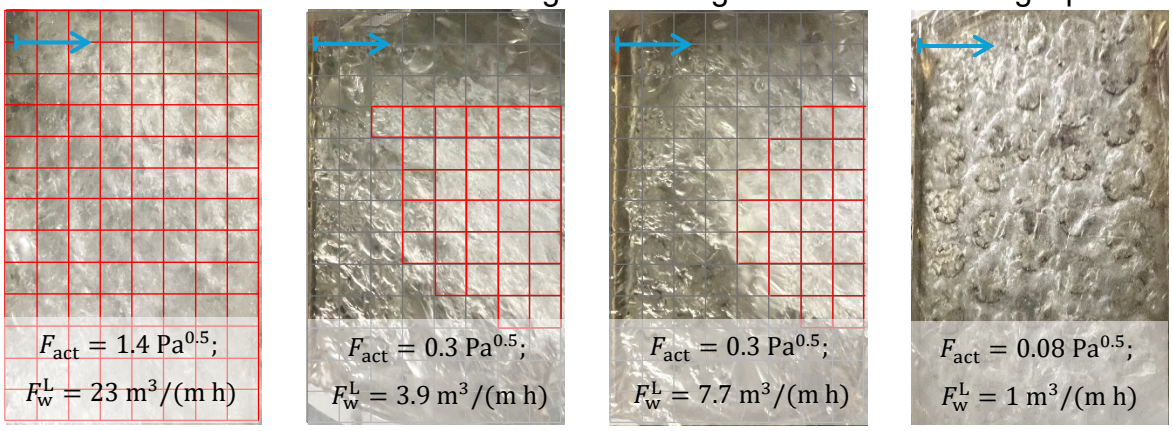

(a) *Fully bubbling state.* (b) *Random bubbling state.* (c) *Random bubbling state.* (d) *Ordered surging state.*

Figure 5: Valve operation in different states. Top view of the top tray is shown, with inlet weir being on the left and outlet weir on the right side of each image. Liquid flow direction is given by the blue arrow, while the bubbling area is marked with red rectangles where applicable.

Figure 7 shows the hydrostatic pressure drop ΔP_{h}, which was obtained by subtracting the previously determined ΔP_{d} correlation (see Figure 3) from the experimentally measured total pressure drop of the tray. The hydraulic states are marked as well, showing that with increasing liquid load, ordered surging shifts to lower and full bubbling to higher F_{act} so that the random bubbling state covers a wider range of F-Factors. At each studied liquid load, full bubbling is reached below the OBP,

demonstrating that open and inclined valves both contribute to the bubbling area. Between OBP and CBP, ΔP_h remains almost constant, similarly to ΔP_d. In this region, θ is always above 0.6. Below the CBP, ΔP_d decreases rapidly (see Figure 3) while the total pressure drop is almost constant, which suggests a strong increase of ΔP_h in this region. Simultaneously, θ drops below 0.5, indicating that a large non-bubbling area might strongly increase the hydrostatic pressure of the tray. For the lowest measured liquid load, stable operation for both an ordered surging and a random bubbling state was possible between $F_\mathrm{act} = 0.3$ Pa$^{0.5}$ and the CBP, resulting in different pressure drop and weeping characteristics depending on the hydraulic state. The correlation of Ma et al. (2021) for the transition point $\mathrm{Fr_t}$ with parameters fitted to our experimental data is shown in Figure 7 as well, giving a good accuracy. Once the gas load is sufficiently reduced, ΔP_h rapidly decreases for all studied liquid loads.

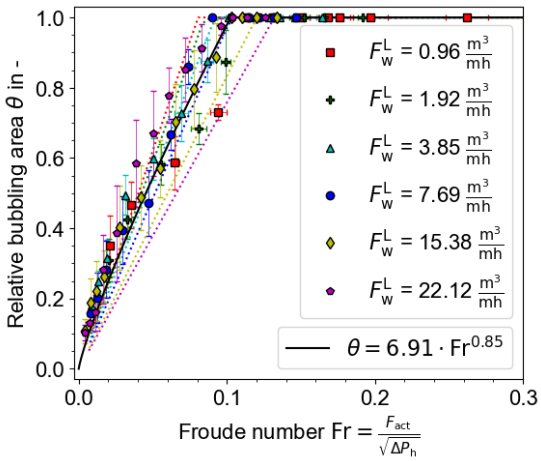

Figure 6: Relative bubbling area θ over the Froude number Fr for different weir loads F_w^L. The experimental data is given with markers, while the correlation of Wang et al. (2019) with dotted lines.

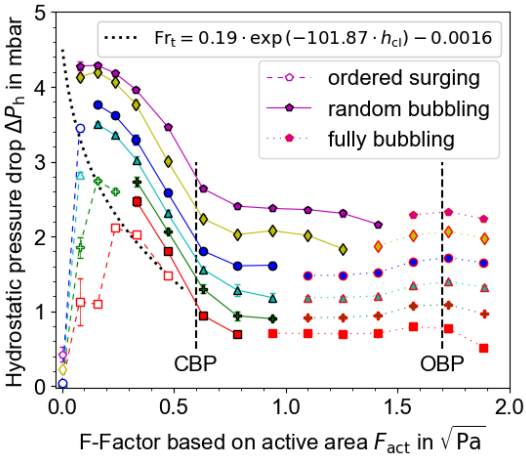

Figure 7: Hydrostatic pressure drop ΔP_h over the F-Factor F_act. For the markers denoting different weir loads F_w^L, refer to the legend entries in Figure 6.

2.4 Weeping

The experimantally measured weeping ratio $\Omega = F^\mathrm{L,W}/F^\mathrm{L}$ is presented in Figure 8. No weeping occurs at any liquid load in the fully bubbling state. During random bubbling, the weeping ratio remains below 10% for all F_act while high weeping rates only occur in the ordered surging state, indicating fundamentally different weeping mechanisms. This is further supported by the aforementioned operating points at $F_\mathrm{w}^\mathrm{L} = 0.96$ m³/(m h) for F_act between 0.3 and 0.6 Pa$^{0.5}$ that could be operated in both states, resulting in different ΔP_h and Ω.

The weeping ratio in the random bubbling state is further examined in Figure 9, where Ω is plotted over Fr. The weeping ratio Ω decreases with increasing Fr and reaches zero at $\mathrm{Fr} = 0.1$, i. e., the transition point from random bubbling to full bubbling. The figure also captures this trend in a correlation.

During the ordered surging state, the amplitude of the oscillations and the lift height of the valves decrease with decreasing gas load, resulting in prolonged weeping and a shorter bubbling state. The consequent increase of Ω coincides with the decrease of ΔP_h (see Figure 7). This relationship between weeping and hydrostatic pressure at low gas loads can also be observed on sieve trays as shown by Raddant et al. (2025). At zero gas load, the entire tray area dumps.

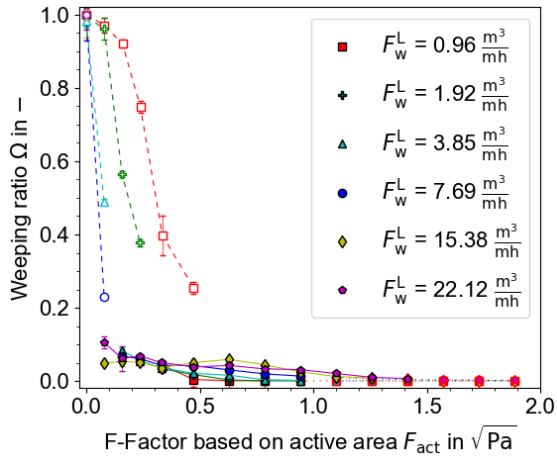

Figure 8: Weeping ratio Ω over the F-Factor F_{act} for different weir loads F_w^L. For the markers denoting different hydraulic states, refer to the legend entries in Figure 7.

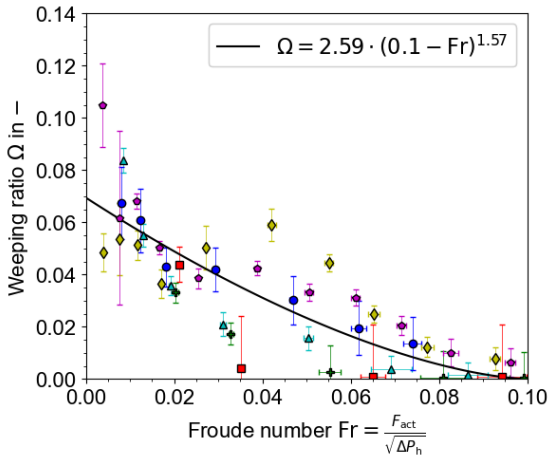

Figure 9: Weeping ratio Ω over the Froude number Fr in the random bubbling state. For the markers denoting different weir loads F_w^L, refer to the legend entries in Figure 8.

3. Conclusions

Recent studies of moving valve trays have shown that a bubbling and a non-bubbling zone develop on the tray under medium vapor loads (random bubbling state), while a transition to an ordered surging state occurs at very low vapor loads. Here, all valves oscillate periodically between weeping and bubbling. These hydraulic states were confirmed in the present contribution as well. Moreover, the ratio of the bubbling area θ in the bubbling state and the weeping ratio Ω were further characterized for a broad range of liquid loads. It was found that both properties strongly correlate with the Froude number Fr, and a significantly simpler approach for their prediction was proposed compared to available literature models. It was shown that the weeping mechanism fundamentally differs in the bubbling and surging state, and high weeping rates together with a decline in pressure drop only occur during surging. Further research is needed to describe pressure drop and weeping rate in all hydraulic states with first-principles models, including the transition from one state to another. Such models are crucial for the simulation of highly dynamic safety scenarios, such as start-up and shutdown procedures, load changes or equipment failures.

Acknowledgements

The authors gratefully acknowledge that the valve trays used in this work were provided by Sulzer AG.

References

Lockett. (1986). *Distillation tray fundamentals.* Cambridge University Press.

Ma, Y., Liu, Y., Cao, R., Shang, W., & Li, G. (2021). Mechanism and fundamental models of gas–liquid surging. *AIChE Journal, 67*, e17369. doi:10.1002/aic.17369

Raddant, H., Polgár, P., Hoffmann, C., Illner, M., Fath, V., Kirschbaum, J., & Repke, J.-U. (2025). Experimental and Model-Based Investigation of Weeping in Tray Columns for Distillation and Absorption: Steady-State and Dynamic Shutdown Scenarios. *Industrial & Engineering Chemistry Research, 64*(46), 22428-22444. doi:10.1021/acs.iecr.5c03242

Wang, J., Leng, Y., Shao, H., Li, W., Xue, B., Huang, C., & Tan, Q. (2014). A Fundamental Model for Valve Tray Vapor Cross-Flow. *AIChE Journal, 61*, 1032-1042. doi:10.1002/aic.14691

Wang, J., Zhou, X., Gao, B., Huang, C., Sun, J., & Sun, X. (2019). Experimental study and modeling of weeping rate. *AIChE Journal, 65*, e16722. doi:10.1002/aic.16722

Analysis of local flooding phenomena and froth formation in columns with sandwich packings via ultrafast X-ray tomography

Pietro Giustacori[1], Sara Marchini[2], Alexander Döß[3], Frank Barthel[3], Elisabetta Brunazzi[1], Markus Schubert[2], Holger Kryk[3]

[1]Department of Civil and Industrial Engineering (DICI), University of Pisa, 56122, Pisa, Italy;
[2]Chair of Chemical Process Engineering, Technische Universität Dresden, 01062 Dresden, Germany;
[3]Institute of Fluid Dynamics, Helmholtz-Zentrum Dresden-Rossendorf, 01328 Dresden, Germany

Abstract

A sandwich packing configuration, composed of alternating layers with distinct geometric surface areas, enhances gas-liquid mass transfer by generating two characteristic flooding points within a column. The larger-surface-area holdup (or flooded) layer and the smaller-surface-area de-entrainment layer create a controllable froth zone once the holdup layer begins to flood, while the column as whole remains below its global flooding limit. This partially flooded regime intensifies turbulence and interfacial area, creating an operating window that is particularly advantageous for reactive-absorption and reactive-distillation where increased contact efficiency and tunable hydrodynamics directly support reaction–mass-transfer coupling.

In this study, ultrafast electron-beam X-ray computed tomography (UFXCT) was employed to investigate fluid dynamics within sandwich packings. The UFXCT system provides noninvasive, high-speed visualization of multiphase flow structures with 1 mm spatial and 1 kHz temporal resolution. Experiments were performed in a 100 mm Perspex column using titanium structured packings (Montz-Pak B1 series) across a wide range of liquid and gas loads. Tomographic cross-section scans revealed spatial and temporal distributions of liquid holdup, enabling quantification of local flooding and froth formation. The image analysis provides a novel characterization of hydrodynamics in sandwich packings, supporting the understanding of their froth behavior in sandwich packings.

Keywords

Sandwich packing, ultrafast X-ray computed tomography (UFXCT), pressure drop, liquid holdup, signal fluctuations analysis

1. Introduction

Structured packings are widely applied in gas-liquid contactors for absorption and distillation due to their high interfacial area and low pressure drop. They are conventionally operated below the flooding limit, where liquid flows as thin films over the packing surface and gas flows countercurrently through open channels. Under these conditions, mass transfer is governed by wetted area, film thickness, and turbulence intensity, while pressure drop remains moderate [1, 2].

Sandwich packing configurations have been proposed to intensify gas-liquid mass transfer by stacking alternating layers with different geometric surface areas and hydraulic characteristics. Typically, a high surface area holdup layer is followed by a

lower surface area de-entrainment layer, resulting in two distinct flooding points instead of a single global limit [3, 4]. With increasing gas and liquid loads, the holdup layer reaches flooding while the de-entrainment layer remains below its threshold, leading to the formation of a localized froth or partially flooded zone.
This controlled froth regime alters the hydrodynamics relative to conventional structured packings. Liquid accumulation and gas dispersion dominate in the flooded holdup layer, while the de-entrainment layer promotes phase disengagement and froth stabilization. The resulting flow regime is characterized by enhanced turbulence, increased interfacial area, and frequent gas-liquid renewal, which can significantly intensify mass transfer. However, these advantages are accompanied by increased pressure drop and a higher sensitivity to hydrodynamic instabilities, making a detailed understanding of froth structure and dynamics essential. Yet, experimental data on froth behavior remain limited due to the fast temporal scales involved [5].
In this work, froth evolution in structured sandwich packings is investigated using UFXCT [6, 7]. This noninvasive technique provides time-resolved visualization of gas-liquid flow structures, from which dynamic parameters such as local liquid holdup fluctuations and spatial correlations are extracted. The study examines the influence of liquid flow rate on froth formation and dynamics under gas flow conditions promoting partial flooding of the holdup layer.

2. Experimental setup

The experimental study was conducted in a pilot-scale gas-liquid test rig designed to investigate hydrodynamics and froth dynamics in structured sandwich packings. A schematic of the setup is shown in Figure 1.

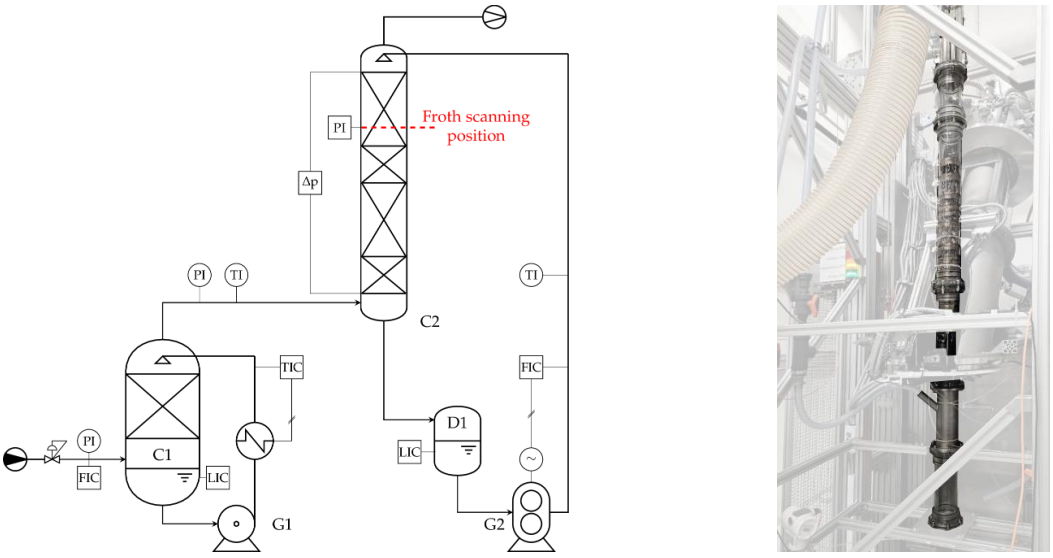

(a) (b)

Figure 1: (a) Schematic diagram of the experimental test rig, red dashed line indicates plane for tomographic analysis (G: pumps, C: columns, D1: liquid tank, PI: pressure indicator, FIC: flow controller, LIC: level controller, TIC: temperature controller, TI: temperature indicator, Δp: differential pressure sensor). (b) photo of the experimental setup installed inside the tomograph.

Compressed dry air at a constant pressure of 4 bar was used as the gas phase and first passed through a pre-saturation column to minimize evaporation effects. This column, with an inner diameter of 300 mm packed with plastic Pall rings, was irrigated with water to ensure full gas saturation. Gas flow rate was controlled by a flow controller and monitored together with temperature and pressure upstream of the pre-saturator.

The humidified gas entered the bottom of a vertical Perspex test column with an inner diameter of 100 mm. The transparent material ensured visual access and compatibility with X-ray measurements. The column operated in countercurrent mode, with water introduced at the top through a distributor designed for uniform liquid distribution.
The column was equipped with structured packings from Julius Montz GmbH. Two Montz B1-250 elements were installed upstream of the sandwich section to promote gas redistribution. The sandwich packing section consisted of three identical segments; each composed of a 50 mm high holdup layer Montz B1-500 packing followed by a 220 mm high de-entrainment layer Montz B1-250.60 packing. Including the redistribution elements, the total packed height was approximately 1200 mm. All packing elements were made of titanium to minimize X-ray attenuation and beam hardening effects during tomography measurements [8, 9].
Water at ambient conditions was circulated in a closed loop as the liquid phase, with flow rates controlled by a frequency-regulated pump. Three liquid loads were investigated, L = 12.5, 25, and 50 $m^3m^{-2}h^{-1}$. For each liquid load, the gas flow rate was varied from zero up to the global flooding limit of the column. Pressure drops across the entire packed bed and pressure fluctuations within the froth zone of a single sandwich element were recorded to support correlation with tomographic data.
Local phase distribution and froth dynamics were analyzed using UFXCT. The UFXCT system generates a rotating X-rays source by rapid deflection of an electron beam along a semicircular tungsten target, while a stationary ring detector records the transmitted radiation. Measurements were performed with temporal resolutions up to 1000 cross-sectional images per second and a spatial resolution of about 1 mm, enabling capture of rapid froth fluctuations. Scans were conducted at selected axial positions within both the holdup and de-entrainment layers and along axial lines covering entire sandwich segments. In the present work, only the scans acquired at the froth location are reported, as indicated in Figure 1. Reference scans of dry and fully flooded packings were used to quantitatively reconstruct pixel-wise liquid holdup from normalized attenuation differences.

2. Results and discussion

Figure 2 presents the measured pressure drop across the entire packed bed as a function of the gas-phase F-factor for the three investigated liquid loads and in dry condition. The pressure drop curves were primarily used to characterize the global hydraulic behavior of the system and to identify suitable operating points for the subsequent tomographic analysis of froth dynamics.
At the lowest liquid load, L = 12.5 $m^3m^{-2}h^{-1}$, the pressure drop profile clearly exhibits two distinct changes in slope, which can be associated with two characteristic flooding points. The first change corresponds to the flooding of the holdup layers, while the second marks the onset of flooding of the de-entrainment layers and, consequently, the global flooding of the sandwich packing. Between these two points the transition zone is observed. This zone is characterized by a lower but continuous increase in pressure drop compared to the previous trend. This operating region corresponds to partial flooding conditions, where the holdup layers are fully flooded and a froth zone progressively develops within the de-entrainment layers. This transition zone represents the regime of greatest interest in the present work, as it is associated with the formation, growth, and dynamic evolution of froth, which governs the intensified gas-liquid interaction in sandwich packings. With increasing liquid load, the pressure drop curves become steeper and the distinction between the two flooding points becomes less pronounced.

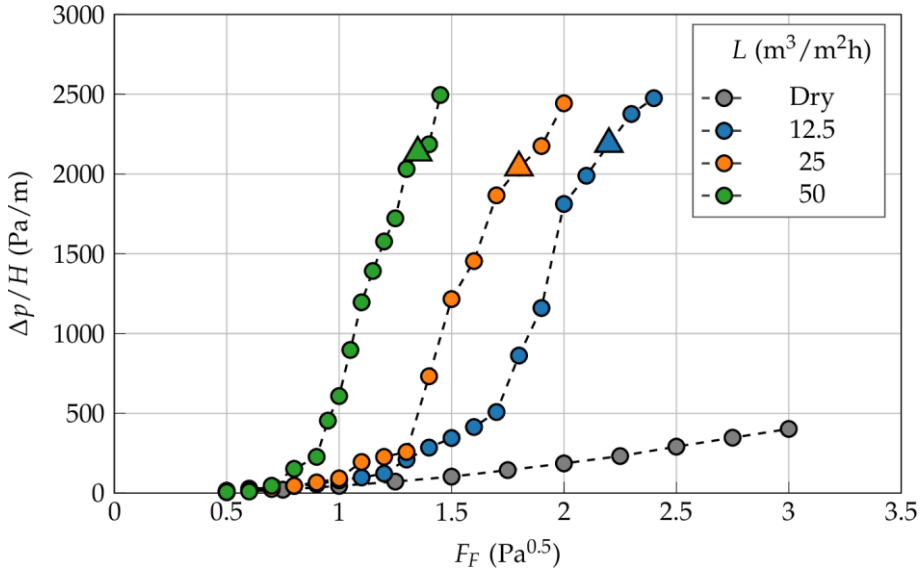

Figure 2: Pressure drop curves of the sandwich packing column under different operating conditions, triangle makers show tomography test points.

Based on the pressure drop characteristics, specific operating points were selected for detailed analysis of the froth dynamics. These points were chosen to represent typical and practically relevant operating conditions of a sandwich packing. For each liquid flow rate investigated, a reference operating point was defined at 90% of the total column flooding gas load, as determined from the pressure drop curves, and marked with a triangle in Figure 2.

At these conditions the holdup layers are fully flooded and a well-developed froth is present within the de-entrainment layers, while complete column flooding is avoided. Focusing the analysis on these reference points allows a consistent comparison of froth structure and dynamics across different liquid loads. Moreover, it enables isolation of the effects of liquid flow rate on froth behavior under comparable relative proximity to flooding. The analysis therefore concentrates on tomographic and dynamic investigation performed at these reference operating points, providing insight into the hydrodynamic mechanisms governing froth evolution in sandwich packings.

To quantitatively assess the hydrodynamic behavior observed in the sandwich packing, two parameters were derived from the reconstructed tomographic data. First, the local cross sectional liquid holdup was calculated for each reconstructed slice. Second, the temporal variation coefficient of the holdup was determined, defined as the ratio between the standard deviation of the holdup data and the mean holdup over time. These parameters provide complementary information, as the average holdup describes the spatial distribution of the liquid, while the variation coefficient highlights the intensity of temporal fluctuations associated with unsteady flow phenomena. Both metrics were subsequently time-averaged over the acquisition window [10].

The resulting time-averaged holdup and variation coefficient maps are presented in Figure 3. Figures 3a and 3b correspond to the lowest and highest liquid flow rates investigated, 12.5 and 50 $m^3m^{-2}h^{-1}$ respectively. Time-averaging of the holdup enables the identification of regions within the column cross-section that are persistently wetted and those where liquid accumulation is more pronounced. At operating conditions approaching the flooding regime, these regions are associated with the formation of froth, characterized by a highly aerated liquid phase and intermittent gas entrainment. While the averaged holdup maps indicate that, for both liquid loads, the liquid phase appears to cover the column cross-section in a broadly similar manner, they also reveal

zones of persistent maldistribution. These zones are likely linked to non-uniform liquid spreading and preferential flow paths, which reduce effective gas-liquid interfacial contact and can negatively impact mass transfer efficiency.

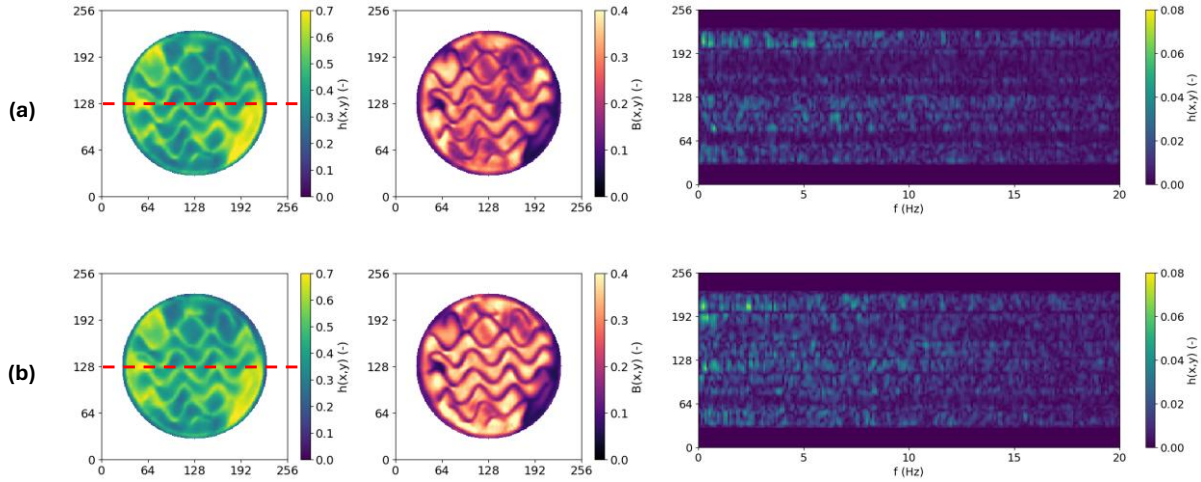

Figure 3: from left to right holdup (h), variation coefficient (B) section averaged, and FFT of eulerian slice of the central plane (indicated with dashed line). (a) L = 12.5 m³m⁻²h⁻¹/F_F = 2.2 Pa$^{0.5}$, (b) L = 50 m³m⁻²h⁻¹/F_F = 1.35 Pa$^{0.5}$.

The variation coefficient maps provide additional insight into the dynamic nature of the flow. At the lower liquid flow rate, elevated fluctuations are confined to limited regions of the cross-section, suggesting localized froth activity and relatively stable flow elsewhere. In contrast, at the higher liquid flow rate, the variation coefficient increases over a much larger fraction of the cross section, indicating that the entire section becomes intrinsically more dynamic.

Further insight into the temporal characteristics of the flow was obtained through Fast Fourier Transform (FFT) of Eulerian slices along the column centerline, shown in the third image in Figure 3. The FFT spectra allows the identification of dominant frequencies associated with liquid motion in different regions of the cross-section. At higher liquid loads, the spectra exhibit a broader range of significant frequencies with increased intensity, indicating more frequent oscillations of the liquid phase. This enhanced temporal activity reflects faster liquid renewal and more vigorous interfacial dynamics within the froth zone. Such behavior is generally associated with improved mass transfer performance, as increased surface renewal reduces.

Overall, the combined analysis of averaged holdup, variation coefficients, and FFT-derived frequencies demonstrates that increasing the liquid flow rate in sandwich packings leads to a more active and spatially extended froth regime. While maldistribution effects remain visible in the mean holdup fields, the increased temporal dynamics at higher liquid loads suggest enhanced interfacial renewal, which may partially compensate for non-uniform liquid distribution and contribute to improved mass transfer efficiency.

3. Conclusions

The results indicate that UFXCT is a powerful tool for resolving the complex hydrodynamics of sandwich packings operating close to flooding. The analysis highlights the strong sensitivity of local liquid holdup and froth structure to variations in liquid loads, particularly within the transition region between the two characteristic flooding points of the sandwich configuration.

Beyond the identification of mean holdup levels, the developed methodology enables a detailed characterization of froth evolution dynamics. Time-resolved tomographic data allows the detection of spatial and temporal changes in the froth structure, making it possible to identify zones affected by liquid maldistribution as well as regions where the froth evolves in response to variations in gas flow rate.

Due to the limited length of the abstract, only a few representative results are presented here. However, the experimental campaign covered three different liquid flow rates, and for each liquid load the system was first operated at a reference condition corresponding to the selected normal operating point of the sandwich packing. Starting from this reference state, the gas flow rate was systematically varied within a range of ±10% in order to investigate the evolution of the froth regime as a function of both gas and liquid loads. This approach allowed the characterization of transitions from localized froth formation to more spatially extended and dynamic froth structures. In addition, both steady-state experiments and dynamic tests involving controlled variations of operating conditions were performed, enabling the assessment of transient hydrodynamic responses and the sensitivity of the froth behavior to flow perturbations. Spatially averaged, time-dependent holdup signals were further correlated with simultaneously recorded pressure drop fluctuations, providing insight into the coupling between local phase distribution dynamics and global hydrodynamic instabilities.

Overall, the proposed approach provides a quantitative framework for linking local, transient flow phenomena to macroscopic hydraulic behavior, offering valuable guidance for the design, operation, and control of intensified structured packing systems operating near their hydraulic limits.

Acknowledgements

This work is supported by the EXAIMS Project funded within the Lab2Lab framework of the Graduate Academy of TU Dresden, supported by Federal and State Funds.

References

[1] Brunazzi E., Paglianti A. (1994) A mechanistic pressure drop model for columns containing structured packings. AIChE Journal, 43, 317-327,10.1002/aic.690430205

[2] Aferka S., Viva A., Brunazzi, E.,Marchot P., Crine M., Toye D. (2011). Tomographic measurement of liquid hold up and effective interfacial area distributions in a column packed with high performance structured packings. Chemical Engineering Science, 66, 3413-3422, 10.1016/j.ces.2011.01.022

[3] Brunazzi E., Paglianti A., Pintus S., A., (2001) A capacitance probe and a new model to identify and predict the capacity of columns equipped with structured packings. Industrial & Engineering Chemistry Research, 40, 1205-1212,10.1021/ie000546u

[4] Flechsig, S., Yildirim, Ö. and Kenig, E.Y., 2016. Sandwich packings: State of the art. ChemBioEng Reviews, 3(4), pp.174-185.

[5] Olujić Ž., Jansen, H., Kaibel, B., 2021. Advances in structured packing design for process intensification. Chemical Engineering and Processing, 163, 108361.

[6] Fischer F,, Hoppe D,, Bieberle M,, Schleicher E,, Hampel U,, Mattausch G,, Flaske H,, Bartel R, (2007) Development of an ultra-fast scanned electron beam X-ray CT, 5th World Congress on Industrial Process Tomography, 03.-06.09.07, Bergen, Norway

[7] Windisch D.,Kelling J., Juckeland G., Bieberle A., (2023), Real-time data processing for ultrafast X-ray computed tomography using modular CUDA based pipelines, Comp. Phys. Communications, 237

[8] Bieberle M., Papapetrou T.N., Lecrivain G., Windisch D., Bieberle A., Wagner M., Hampel U., Simplified Beam Hardening Correction for Ultrafast X-ray CT Imaging of Binary Granular Mixtures. Sensors 2024, 24, 2964. 10.3390/s24102964

[9] Bieberle M., Papapetrou T.N., Lecrivain G., Windisch D., Bieberle A., Wagner M., Hampel U., Simplified Beam Hardening Correction for Ultrafast X-ray CT Imaging of Binary Granular Mixtures. Sensors 2024, 24, 2964. 10.3390/s24102964

[10] Flechsig S., Sohr J., Schubert M., Hampel U., Kenig E., 2022, A new tomography-based approach for the fluid dynamic description of conventional structured packings and sandwich packings,

Multiple Short Path Distillation versus High Vacuum Rectification

Ralf Proplesch[1], Lukas Bolenz[2], Robin Schulz[2]
[1] DSM-Firmenich/Asset Technology, Sisseln, Switzerland;
[2]Koch Engineered Solutions GmbH, Hilden, Germany;

Abstract
Short path distillation and high vacuum rectification are two alternatives to purify highly heat-sensitive components. In this contribution, the benefits and drawbacks of both concepts are explained and the development of a new high vacuum rectification process in an industrial plant is reported. In this context, measures to reduce thermal stress in the rectification column as well as the appropriate choice of the column internals are discussed. As the liquid distributor played a key role in achieving the required separation efficiency, two different types of distributors are compared by a literature model.

Keywords
Short path distillation, Molecular Distillation, Vacuum rectification, Structured packings, Liquid distribution, Heat-sensitive components

1. Introduction

Many fine chemicals or active pharmaceuticals ingredients are highly sensitive to elevated temperatures. When processing mixtures containing such components, distillation or rectification is often applied to purify the value components. As distillation and rectification are inherently connected to operating temperatures around the mixture's boiling point, special attention must be paid to the design of the column internals and selection of the equipment. Only if all parts are well-matched, it can be ensured that the products are not damaged.
Short path distillation and high vacuum rectification are two alternatives suitable for the purification of heat-sensitive components. Both come with different benefits and drawbacks and the choice between one method or the other heavily depends on the specific requirements of the separation task. In this contribution, both methods are introduced. A case study from the fine chemicals industry about the construction and commissioning of a high vacuum rectification column, which had the purpose of replacing multiple short path distillation units, is presented. Finally, different types of liquid distributors that have been installed in the rectification column are evaluated by means of a literature model.

2. Purification of heat-sensitive components

2.1 Short path distillation

Short Path Distillation (SPD), also referred to as Molecular Distillation, is presented as a gentle, low-pressure purification technique particularly suited for thermally sensitive compounds. The method operates under high vacuum conditions in the range of 0.001–1 mbar, which significantly reduces boiling temperatures and thereby minimizes thermal degradation of processed materials. In addition, SPD systems typically offer residence times of less than one minute, resulting from the small liquid hold-up. This is crucial for preserving sensitive molecules, as shorter thermal exposure enhances product quality and reduces by-product formation. The separation efficiency corresponds to approximately one theoretical stage.

In industrial molecular distillation processes, a single short path distillation stage often fails to achieve the required product purity due to its low separation efficiency. To overcome this limitation, multiple SPD units can be arranged in counter-current configurations or operated as sequential molecular distillation stages, thereby enhancing the overall separation performance. Published optimisation studies also show that the configuration and recycling structure of multi-stage SPD systems play a vital role in efficiently separating thermally sensitive, high-boiling substances on an industrial scale [1]. However, in cases where separation is particularly challenging due to small boiling point differences, multiple short-path distillation can become cost-prohibitive and ineffective, necessitating the exploration of alternative solutions.

2.2 High vacuum rectification

A high vacuum rectification is, in principle, an ordinary rectification with a very low top pressure (values below 2 mbar can be reached), and a very low pressure drop along the column height. To achieve a very low pressure drop, vacuum rectification columns are designed with a relatively large diameter ensuring a low gas load with F-Factors < 1 $Pa^{½}$ and in addition, the packing beds are kept short to minimize the temperature increase by adding pressure drop. These characteristics often result in unusually low ratios of packing height to diameter smaller than 1.5. To minimize the pressure drop, mass transfer equipment, column internals and auxiliary equipment such as condenser, reboiler and vacuum pump have to be selected and designed carefully. Among these, the mass transfer equipment and liquid distributors are of particular importance and will be discussed in more detail.

2.2.1 Mass transfer equipment

Structured packings provide a high separation efficiency combined with a relatively small pressure drop [2] and thus, are the preferred choice over random packings or trays. In particular, wire gauze structured packing is selected due to its extraordinarily high separation efficiency at low F-Factors [3].

2.2.2 Liquid distributor

Because of the short packing beds, the liquid distributor plays a crucial role in the high vacuum rectification process. By optimizing the initial distribution of the liquid phase, i.e. maximizing the number of drip points, the highest separation efficiency in the structured packing can be achieved. This becomes even more challenging for the very low liquid loads that are usually seen in high vacuum rectification columns.

An overview of different types of liquid distributors, such as baffle plate distributors and drip tube distributors, can be found elsewhere [4]. For low liquid loads, a special design is used to enhance the distribution of drip tube distributors. A drip point multiplier (Figure 1) is attached to the bottom end of the drip tube, and the liquid is spread over drip fingers. In this way, a high number of secondary drip points is created.

When increasing the number of drip fingers, the cross-section of the drip point multiplier changes from circular to rectangular at some point. Liquid distributors with such a design can operate at extremely low liquid loads and are usually referred to as capillary box liquid distributors.

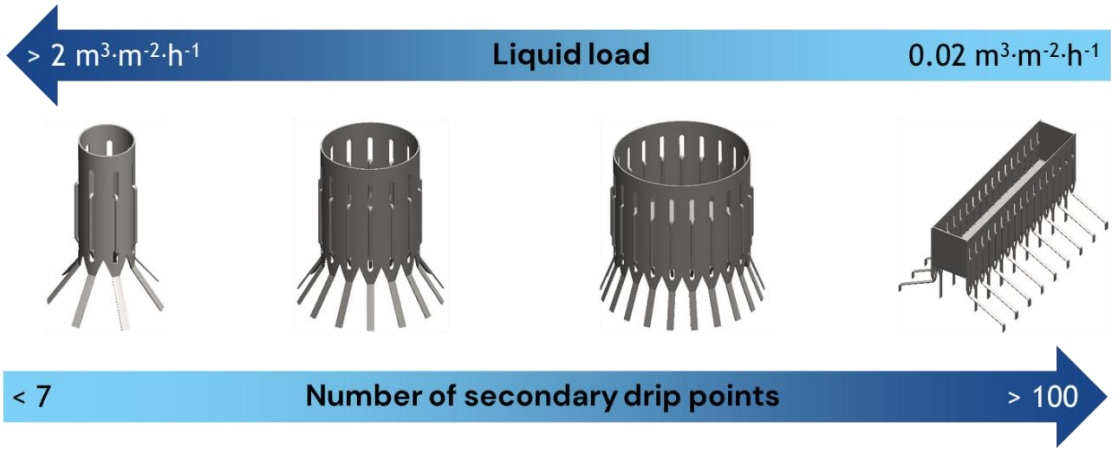

Figure 1: Different types of drip point multipliers with increasing number of drip points

The liquid distributors in high vacuum rectification columns can carry an additional feature to protect heat-sensitive components. By reducing the residence time in the column, the exposure of the components to heat is minimized. Liquid distributors account for the major share of the liquid hold-up in a rectification column and thus mainly contribute to the residence time of the liquid. By bringing displacement bodies into the distributor channels, the liquid hold-up and the residence time can be significantly reduced.

3. Industrial case study

Due to rising demand, it was necessary to increase the production capacity of a thermally sensitive product. In this production process, multi-stage short-path distillation was a key purification process.

In order to develop a more efficient and cost-effective purification process, high-temperature rectification tests were carried out on mini-plant scale within the technology center of dsm-firmenich in Sisseln, Switzerland. These tests showed that the required product purity and quality could be achieved under certain conditions. A cost comparison between multi-stage short-path distillation and two-stage high-temperature rectification also demonstrated that rectification had significant advantages.

In addition to the mini-plant tests, pilot tests were carried out at a mass transfer equipment manufacturer who subsequently developed the plant design and implemented the industrial plant. A picture of shell of one of the rectification columns is shown in Figure 2. Unfortunately, shortly after the plant was commissioned, it became apparent that the required product purity could not be achieved due to insufficient separation performance of the columns. Another problem arose with the baffle plate liquid distributors. Due to the extremely small hole diameters, the distributors tended to clog, which promoted severe maldistribution of the liquid, and this naturally had fatal consequences with very short packing bed heights.

Further troubleshooting quickly revealed that the liquid distributors used were the main problem and had to be replaced with more suitable ones. The advantages of Montz capillary box liquid distributors (very high drip point density with much larger hole diameters) were quickly recognised and implemented.

Fortunately, after installing the capillary box liquid distributors, the desired product purity was finally achieved and the problem of clogging of the liquid distributors no longer occurred.

Figure 2: Column shell of a high vacuum rectification column.

4. Evaluation of the distributor quality

The operation of the rectification column showed that the choice of liquid distributor had a significant impact on the column performance. To investigate the reasons for this considerable difference, both liquid distributors have been evaluated and compared through a theoretical model.

4.1 Literature models

There are two well-established models in the literature to assess the quality of a liquid distributor. While the model of Moore and Rukovena [5] can only be applied to tube distributors with distinct dripping points, the model of Spiegel [4] was especially developed to compare tube distributors with baffle plate distributors in columns equipped with structured packing. For this reason, the latter one was chosen in this work.

According to the model of Spiegel, the quality of a liquid distributor can be represented by the Wetting Index (WI), which is defined by

$$WI = \frac{wetted\ area\ in\ reference\ plane}{cross\ sectional\ area\ in\ reference\ plane} \tag{1}$$

As the reference plane, the cross section of the packed bed after the first layer of structured packing below the liquid distributor is suggested.

To determine WI, the reference plane is divided into square cells with an edge length equal to the hydraulic diameter d_H of the structured packing:

$$d_H = \frac{4}{a_g} \tag{2}$$

where a_g is the geometrical surface area of the structured packing. An exemplary image can be seen in Figure 3. Subsequently, the position where the liquid enters the packing bed is marked in the reference plane. For tube distributors, this is equivalent to the position of the drip points of the liquid distributor. For baffle plate distributors, drip lines are formed due to the liquid spreading on the baffle plate.

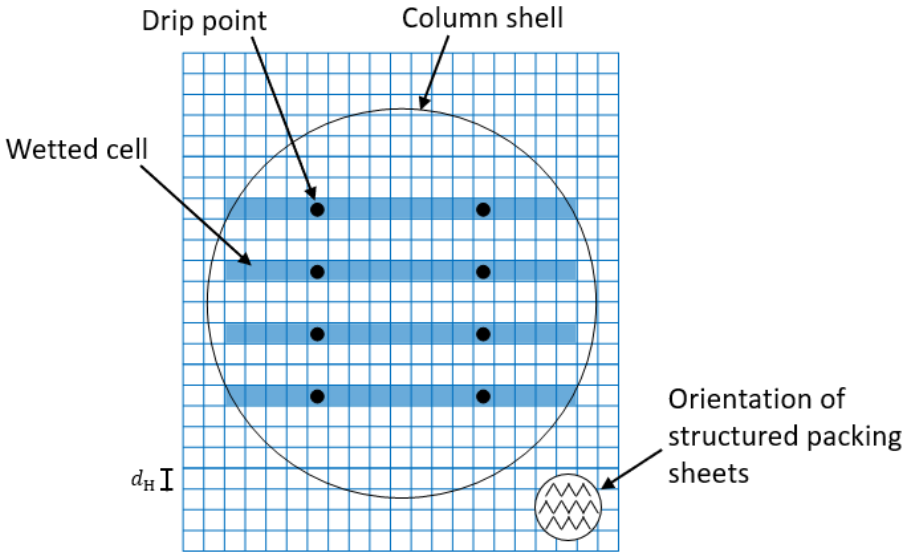

Figure 3: Exemplary image of the determination of the Wetting Index in a structured packing below a tube distributor.

It is assumed that the liquid distributes ideally in lateral direction across the packing sheets when flowing through the packing layer. To which extent the spreading occurs can be derived from geometrical considerations combined with empirical observations and is described in detail in the literature [4]. Each cell that is reached by the liquid within the reference plane is marked as wetted cell. With this, Eq. 1 can also be written as

$$WI = \frac{number\ of\ wetted\ cells\ in\ reference\ plane}{number\ of\ cells\ in\ reference\ plane} \tag{3}$$

The Wetting Index was determined for the baffle plate distributor and the capillary box liquid distributor that have been installed in the high vacuum rectification column. For both distributors an underlying packing of Montz-Pak A3-500M wire gauze packing with a corrugation angle of 60° and a layer height of 169 mm was considered. Measurements of the spreading of a water-surfactant mixture on a metal sheet showed that for the present orifice diameters and liquid levels in the channels of the baffle plate distributor, a lateral liquid spread of 50 mm on the baffle plate can be assumed.

4.2 Results and discussion

Figure 4 shows the graphical determination of the Wetting Index for the baffle plate distributor and the capillary box liquid distributor illustrated for an excerpt of the reference plane. Applying Eq. 3 results in a Wetting Index of 30 % for the baffle plate distributor and 54% for the capillary box liquid distributor. The lower value for the baffle plate distributor mainly results from the fact that the drip lines are not connected in their direction of propagation, but instead significant gaps can be observed between adjacent drip lines. This shows an inherent drawback of baffle plate distributors compared to capillary box liquid distributors for operations at low liquid loads: the lateral spreading of the liquid on the baffle plate is limited. This disadvantage is even amplified for liquids that are prone to fouling and thus require relatively large orifices to avoid the risk of plugging. In such cases, the distance between the orifices in the distributor channel becomes large since the overall number of orifices must be kept small to reach the required low liquid volume flows.

In contrast, the volume flow through an orifice of a drip tube can be arbitrarily multiplied by the design of the drip point multiplier. In this way, the number of drip points is uncoupled from the orifice diameter in the drip tube. This clearly shows that a drip tube distributor with a drip point multiplier is the preferred type of distributor for rectification columns operating at low liquid loads.

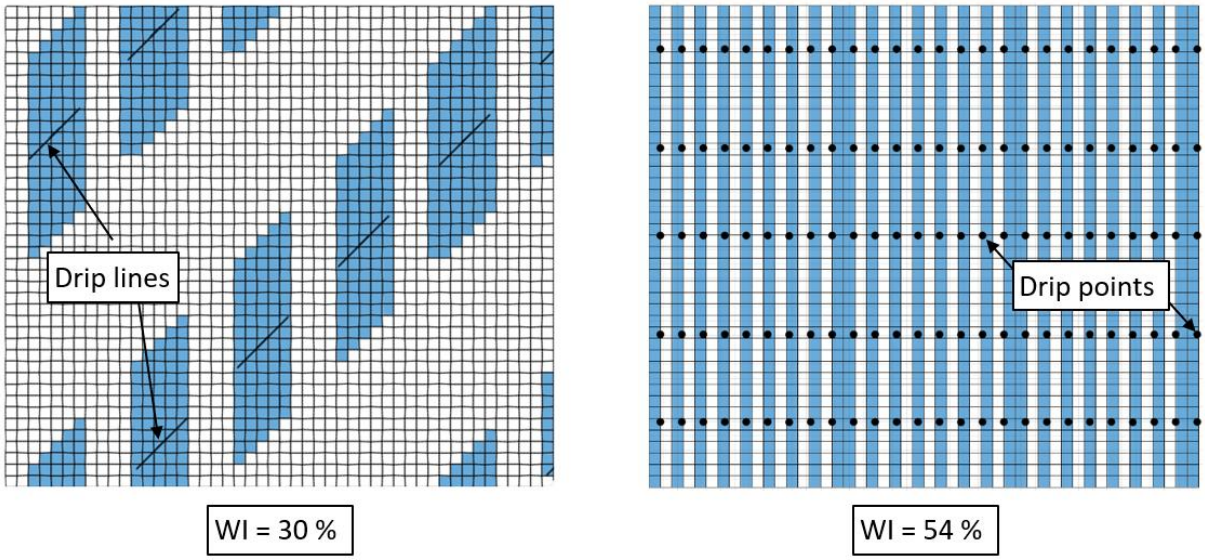

Figure 4: Illustration of the determination of the Wetting Index for a baffle plate distributor (left) and a capillary box liquid distributor (right). Wetted cells in the reference plane are shown in blue.

5. Conclusions

Short path distillation and high-vacuum rectification are both relevant for thermally sensitive separations. The choice of technology depends on the characteristics of the mixture, the required throughput and the target specifications. Multiple SPD is straightforward and effective for extreme thermal sensitivity but is limited for close-boiling systems. High-vacuum rectification offers higher separation efficiency and energy/equipment advantages when thermal stability is manageable. Success critically depends on liquid distribution technology; capillary-box distributors outperform baffle-plate designs at low liquid loads. Theoretical evaluation of the Wetting Index for baffle plate distributors and capillary box liquid distributors confirmed this observation.

References

[1] Laoretani, D.S.; Iribarren, O.A. (2018). *Optimization of the recycle structure of multiplestages molecular distillation*, Chemical Engineering Research and Design 130, https://doi.org/10.1016/j.cherd.2017.12.002.

[2] Olujic, Z.; Jansen, H.; Kaibel, B.; Rietfort, T.; Zich, E. (2001). *Stretching the Capacity of Structured Packings*, Industrial & Engineering Chemistry Research 40, https://doi.org/10.1021/ie010323j

[3] Schulz, R.; Rietfort, T.; Jansen, H.; Olujic, Z. (2019): *Hydraulics and mass transfer performance of anadvanced wire gauze structured packing underdeep vacuum distillation conditions,* Chemical Engineering Research and Design 145, https://doi.org/10.1016/j.cherd.2019.03.029.

[4] Spiegel (2006): *A new method to assess liquid distributor quality*, Chemical Engineering and Processing: Process Intensification 45 (11), doi.org/10.1016/j.cep.2006.05.003

[5] Moore, F.; Rukovena, F. (1987): *Liquid and gas distribution in commercial packed towers*, Chem. Plants Process.

Greener solvents for more sustainable extractive distillation

Dhoni Hartanto[1,3], Samar Vonk[1], Boelo Schuur[2], Anton A. Kiss[1], André B. de Haan[1]
[1]Department of Chemical Engineering, Delft University of Technology, Van der Maasweg 9, 2629 HZ Delft, The Netherlands;
[2]Sustainable Process Technology, Faculty of Science and Technology, University of Twente, Enschede, 7500 AE, The Netherlands;
[3]Department of Chemical Engineering, Faculty of Engineering, Universitas Negeri Semarang, Semarang, 50229, Indonesia

Abstract

A multi-stage solvent selection methodology was employed, combining predictive and experimental approaches to define effective greener entrainers to replace N-methyl-2-pyrrolidone (NMP) in the n-hexane–ethanol (azeotrope) and methylcyclohexane–toluene (close-boiling) separations. Initial screening via quantum chemical (COSMO-RS) and group contribution (UNIFAC, UNIFAC Dortmund) methods predicted key performance metric such as a selectivity (relative volatility). Best candidates were then experimentally validated through miscibility tests, relative volatility measurements, and vapor-liquid equilibrium (VLE) analysis. Process simulations in Aspen Plus compared predictive thermodynamic models (COSMO-RS/SAC, UNIFAC) against an experimental NRTL model for extractive distillation design. The processes were evaluated based on total annual cost (TAC).

Predictive and experimental results show that greener entrainers showed better or comparable selectivity (relative volatility) to that of NMP. According to the miscibility and the relative volatility measurements, some of the greener entrainers were selected as effective solvents, such as gamma-valerolactone (GVL), n-butyl-2-pyrrolidone (NBP), and dimethyl isosorbide (DMI) for the methylcyclohexane–toluene mixture, and NBP, DMI, and guaiacol for the n-hexane–ethanol mixture. VLE data confirm that these greener entrainers can effectively increase the relative volatility and remove azeotropic and close-boiling behavior in the mixtures.

Process simulations demonstrated that predictive models can be effectively utilized in the early-stage entrainer selection and process design of extractive distillation (ED). This is supported by the TAC deviations within the ±50% range compared to the results obtained with the NRTL data correlations. For a more detailed process design, the NRTL model was adopted. NBP, guaiacol, and DMI-based processes had comparable TAC to that of NMP-based processes for n-hexane-ethanol separation. In the methylcyclohexane-toluene separation, GVL-based processes exhibit better TAC, while DMI- and NBP-based processes demonstrate similar TAC to NMP-based processes. The selected greener entrainers are promising alternatives to substitute NMP for the separation of azeotropic and close-boiling mixtures to facilitate the transition to more eco-efficient extractive distillation processes for sustainable separations.

Keywords

Green entrainers, extractive distillation, azeotropic mixture, close-boiling mixture, process simulation

1. Introduction

Accelerating the search for greener entrainers in ED that are sustainable and non-toxic to replace NMP, is currently of great interest. Various green entrainers, such as ionic liquids (Rao et al., 2025), biobased solvents (Li et al., 2025), and a biological buffer (Hartanto et al., 2016), have been studied. However, their applicability is hindered by high cost, immiscibility issues, and potential toxicity. Emerging green entrainers, particularly biobased and greener organic solvents and natural deep eutectic solvents (NADESs), possess advantageous properties, such as high boiling points, strong solvency, and low environmental impact, yet their potential in ED has not been thoroughly assessed. In addition, existing studies lack combining molecular screening, experimental validation, and process-level assessment within a single entrainer selection framework. To fill this gap, this study proposes a comprehensive, multi-step methodology that integrates predictive thermodynamic models, experimental phase equilibrium, and process simulation to evaluate the key performance metric, such as TAC in the separation of the azeotropic mixture of n-hexane-ethanol and the close-boiling mixture of methylcyclohexane-toluene. An initial screening of entrainer candidates was performed using COSMO-RS for the quantum chemical calculation and UNIFAC and modified UNIFAC Dortmund for the group contribution approach to predict separation-performance parameters, including selectivity (relative volatility). Entrainers candidates showing favorable predictions were further assessed through experimental studies on miscibility, relative volatility, and vapor-liquid equilibrium data. Process-level performance was investigated using Aspen Plus software. Subsequently, the accuracy of the prediction-based models in ED was compared to the experimental-based model through the TAC evaluation.

2. Methods

COSMO-RS calculation was employed to predict selectivity and activity coefficients at infinite dilution. To predict relative volatility, COSMO-RS, UNIFAC, and Modified UNIFAC Dortmund models were utilized. Miscibility tests were conducted at 293.15 K for both mixtures and at 343.15 K and 373.15 K for the n-hexane-ethanol and methylcyclohexane-toluene mixtures, respectively, using entrainer-to-feed ratios (E/Fs) of 1–5. Relative volatility and VLE were measured using a Fischer Labodest VLE602 ebulliometer. Additionally, ED was simulated using Aspen Plus V.12, employing RadFrac for the modelling of the distillation columns.

3. Results and discussion

3.1 Selectivity and activity coefficients at infinite dilution

Two different temperatures were evaluated, as shown in Figures 1 and 2. For both mixtures, increasing the temperature leads to reduced selectivity due to weakened intermolecular interactions, which in turns decreases nonideality of the mixtures. Figure 1 illustrates that activity coefficients for entrainer-n-hexane are higher than for entrainer-ethanol, indicating that the entrainer exhibits a stronger interaction with ethanol than with n-hexane. In Figure 2, activity coefficients at infinite dilution for entrainer-methylcyclohexane are higher than for entrainer-toluene. This indicates that the entrainer possesses stronger interactions with toluene than with methylcyclohexane. Furthermore, in both mixtures, all NADESs and biobased and green organic solvents exhibit better or comparable selectivity with NMP.

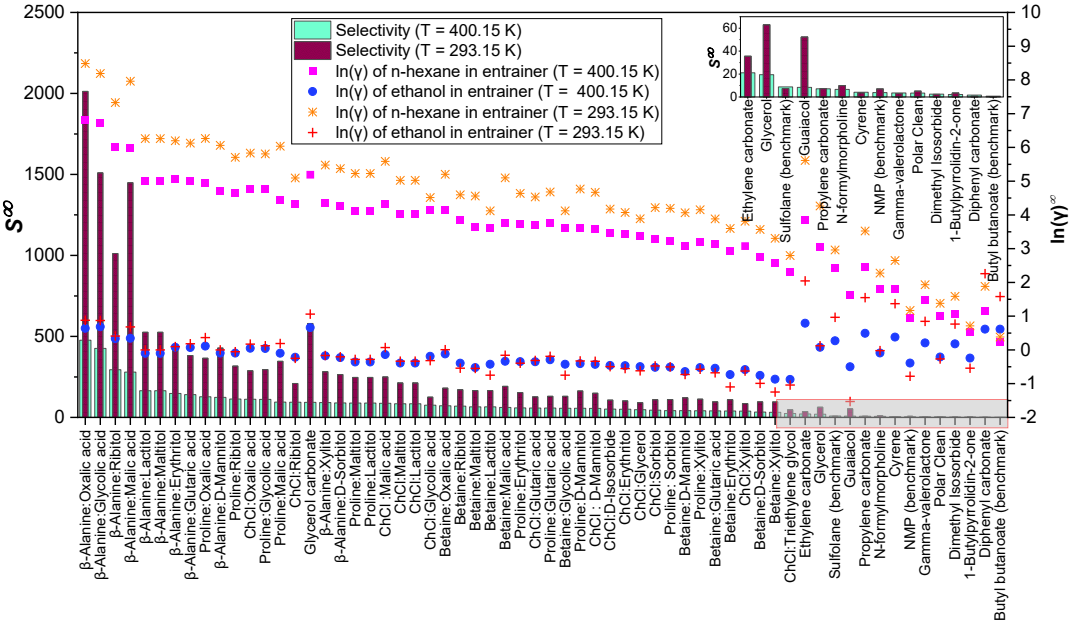

Figure 1. Predicted (COSMO-RS) selectivity at infinite dilution for the n-hexane-ethanol mixture and activity coefficient at infinite dilution for n-hexane and ethanol in the entrainer, respectively.

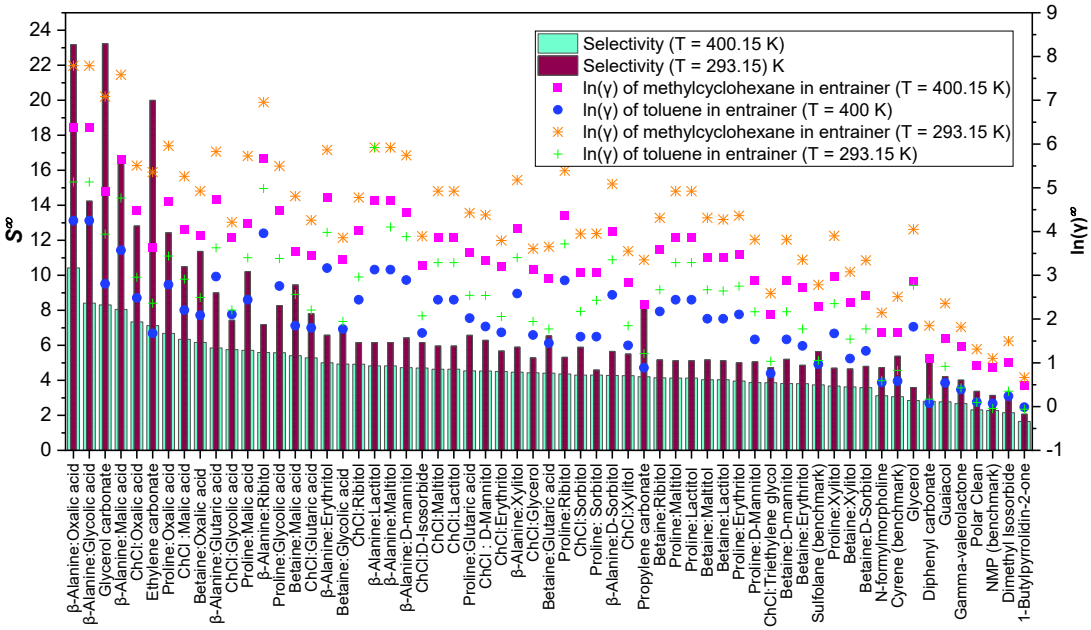

Figure 2. Predicted (COSMO-RS) selectivity at infinite dilution for the n-hexane-ethanol mixture and activity coefficient at infinite dilution for n-hexane and ethanol in the entrainer, respectively (Hartanto et al., 2024).

3.2 Miscibility, relative volatility, and vapor-liquid equilibrium data

The miscibility experiment of entrainer candidates was conducted prior to the relative volatility measurement. All studied NADESs and several green entrainers were immiscible in both mixtures at the investigated E/Fs and temperatures, due to their high polarity and therefore restricted favorable interactions with hydrocarbons. By incorporating miscibility, the proposed framework effectively distinguishes viable

entrainers from those rejected due to polarity incompatibility. Several entrainers are found to be perfectly miscible in the investigated composition, such as GVL, NBP, DMI, guaiacol, and NMP in the n-hexane-ethanol mixture and NBP, GVL, DMI, guaiacol, propylene carbonate, NMP, ethylene carbonate, and N-formylmorpholine (NFM) in the methylcyclohexane-toluene mixture. For these selected entrainers, the relative volatility was measured, and the results were benchmarked against predicted values from COSMO-RS, UNIFAC, and Modified UNIFAC Dortmund, as depicted in Figure 3. The relative volatility measurements were conducted in duplicate with a deviation of 0.05, indicating good reproducibility of the data. The relative volatility values for Cyrene and Sulfolane were taken from literature (Brouwer & Schuur, 2020). While immiscibility limits are observed for numerous green entrainers, predictive models provide valuable insight into the theoretical separation performance of the investigated entrainers. Favorable consistency with experimental results was observed for miscible entrainers, validating the use of UNIFAC-based models and COSMO-RS as reliable tools in early-stage entrainer selection. Furthermore, the VLE data of the n-hexane-ethanol mixture with the selected entrainers of NMP, DMI, guaiacol, and NBP, and the methylcyclohexane-toluene mixture with entrainers NMP, NBP, GVL, and DMI were measured, as these entrainers exhibit complete miscibility with n-hexane and methylcyclohexane over the entire composition range. The detailed VLE data were provided in our earlier works (Hartanto, Schuur, Ammerlaan, et al., 2025) (Hartanto, Schuur, A. Kiss, et al., 2025) (Hartanto, Schuur, Schuttevaer, et al., 2025).

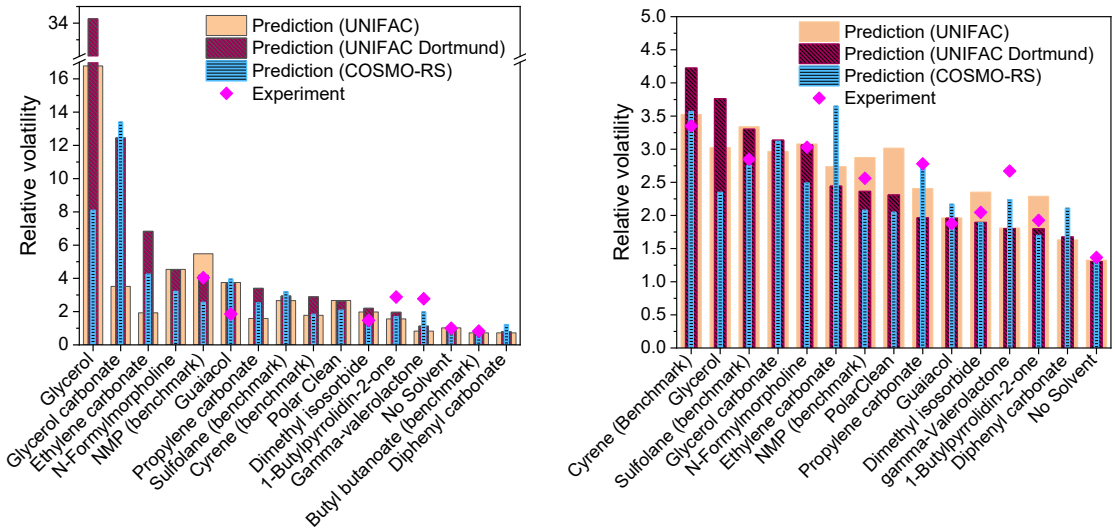

a) b)

Figure 3. Relative volatility of the mixtures in the presence of entrainer: a) n-hexane (1) and ethanol (2) mixture at azeotropic composition (x_1 = 0.66); and b) methylcyclohexane (1) and toluene (2) mixture at x_1 = 0.5. Entrainer-to-feed ratio of entrainer = 1, pressure of 100 kPa. For Cyrene and Sulfolane, the data were obtained from literature (Brouwer & Schuur, 2020).

3.3 Process simulation results

3.3.1 Total annual cost evaluation

The economic feasibility of ED using alternative entrainers was assessed by comparing the TAC for green entrainers with that of conventional solvent NMP. For the TAC evaluation, feed rates of 100 kmol/hr and a payback period of 3 years were

used, Column, plate, and heat exchanger costs were included for equipment expenses. Steam and cooling water were considered for utilities costs. As illustrated in Figure 4, all three green entrainers exhibit TAC values comparable to NMP for the n-hexane-ethanol mixture. In the methylcyclohexane-toluene mixture, GVL achieves a lower TAC than NMP, while DMI and NBP show comparable TAC, indicating that they are economically viable substitutes.

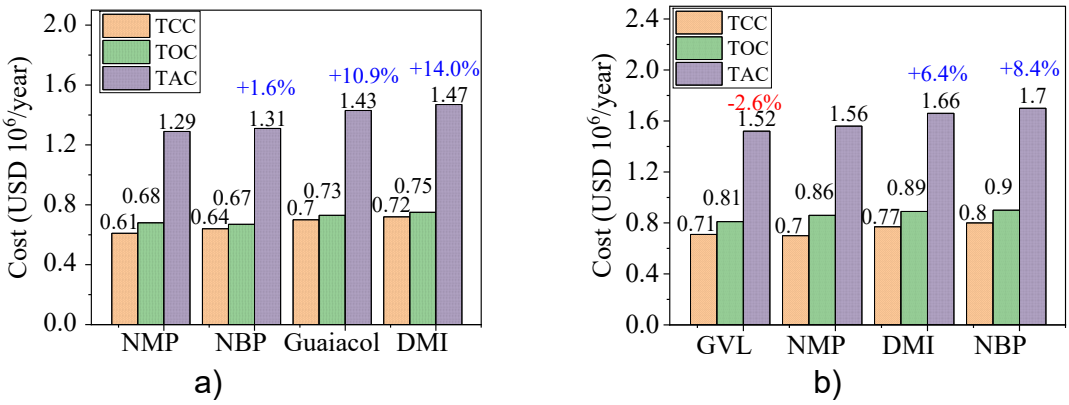

Figure 4. Economic results for: a) n-hexane and ethanol mixture, b) methylcyclohexane and toluene mixture.

3.3.2 Prediction-based model evaluation on process simulation

The accuracy of the prediction-based model in both mixtures was assessed relative to the experimental-based model. Model reliability was examined by comparing TAC from process simulations using COSMO-based models (COSMO-RS and COSMO-SAC) and UNIFAC with those obtained from the NRTL model. As shown in Figure 5, TAC values predicted by COSMO-based and UNIFAC models generally agree well with NRTL results, despite some cases of over- or underestimation. The largest deviation is 31.5%, which remains within the generally acceptable 20-50% uncertainty range for preliminary chemical process design (Harmsen et al., 2024). However, the limitation of the COSMO-based model was found in the n-hexane-ethanol-DMI mixture due to the prediction of non-existing azeotropic behavior between ethanol and DMI at the liquid phase mole fraction of n-hexane (x_1) of 0.190. This prevents the simulation from converging. Therefore, predictive models are valuable for initial entrainer screening and process design of ED, yet their prediction should be verified using experimental data.

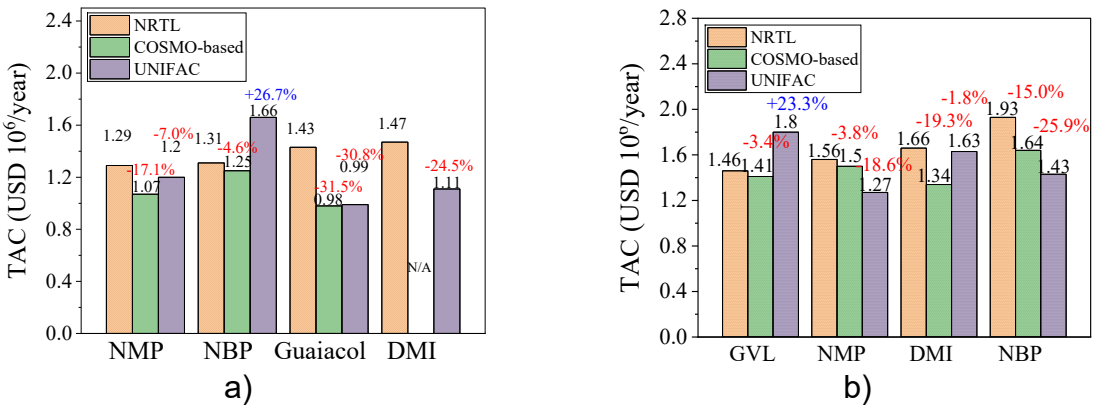

Figure 5. TAC comparison obtained from NRTL, COSMO-based, and UNIFAC models: a) n-hexane and ethanol mixture, b) methylcyclohexane and toluene mixture.

4. Conclusions

According to selectivity prediction and experimental results for miscibility, relative volatility, and VLE, candidate entrainers were selected. Based on TAC, predictive and experimental results demonstrate that the investigated green entrainers in the n-hexane-ethanol mixture are comparable to the conventional entrainer NMP. In the methylcyclohexane-toluene mixture, GVL outperforms NMP, while DMI and NBP are comparable to NMP. Predictive models (COSMO-based and UNIFAC) showed acceptable TAC with maximum deviations of 31.5% relative to the NRTL model. This confirms their applicability for early-stage entrainer screening and process design of ED. Yet, limitations were identified for the COSMO-based model, which predicted a non-existing azeotrope between ethanol and DMI, making it fail to converge the simulation. Therefore, while predictive models are valuable, their use must be validated against experimental data. In addition, the validated framework confirms its reliability as an effective tool for selecting sustainable entrainers.

Acknowledgements

The authors thank to the Indonesia Endowment Fund for Education (LPDP), Ministry of Finance of the Republic of Indonesia, for the PhD scholarship awarded to Dhoni Hartanto (grant number SKPB-1597/LPDP/LPDP.3/2024).

References

Brouwer, T., & Schuur, B. (2020). Bio-based solvents as entrainers for extractive distillation in aromatic/aliphatic and olefin/paraffin separation. *Green Chemistry*, *22*(16), 5369–5375. https://doi.org/10.1039/D0GC01769H

Harmsen, J., de Haan, A. B., & Swinkels, P. L. J. (2024). *Product and Process Design: Driving Sustainable Innovation*. De Gruyter. https://doi.org/doi:10.1515/9783110782127

Hartanto, D., Gupta, B. S., Taha, M., & Lee, M.-J. (2016). Isobaric vapour–liquid equilibrium of (tert-butanol+water) system with biological buffer TRIS at 101.3kPa. *The Journal of Chemical Thermodynamics*, *98*, 159–164. https://doi.org/10.1016/j.jct.2016.03.013

Hartanto, D., Schuur, B., A. Kiss, A., & de Haan, A. B. (2025). Isobaric vapor-liquid equilibrium of the azeotropic mixture n-hexane + ethanol with 1-butylpyrrolidin-2-one as a greener entrainer and 1-methylpyrrolidin-2-one as a benchmark entrainer. *Journal of Chemical & Engineering Data*, *70*(10), 4091−4104. https://doi.org/10.1021/acs.jced.5c00445

Hartanto, D., Schuur, B., Ammerlaan, M., Kiss, A. A., & de Haan, A. B. (2025). Vapor–Liquid Equilibrium for the Separation of the Close-Boiling Mixture Methylcyclohexane–Toluene with Dimethyl Isosorbide as a Biobased Entrainer and 1-Butylpyrrolidin-2-one as a Greener Entrainer. *Industrial & Engineering Chemistry Research*, *64*(38), 18927–18937. https://doi.org/10.1021/acs.iecr.5c01616

Hartanto, D., Schuur, B., Kiss, A. A., & de Haan, A. B. (2024). Effective selection of green organics and natural deep eutectic solvents as advanced entrainers by COSMO-RS and group contributions methods for enhanced design of extractive distillation. In F. Manenti & G. V. B. T.-C. A. C. E. Reklaitis (Eds.), *Computer Aided Chemical Engineering* (Vol. 53, pp. 1387–1392). Elsevier. https://doi.org/10.1016/B978-0-443-28824-1.50232-5

Hartanto, D., Schuur, B., Schuttevaer, T., Kiss, A. A., & de Haan, A. B. (2025). Isobaric Vapor–Liquid Equilibrium of Methylcyclohexane + Toluene with Gamma-Valerolactone as a Biobased Entrainer and 1-Methylpyrrolidin-2-one as a Conventional Entrainer. *Journal of Chemical & Engineering Data*, *70*(3), 1339−1351. https://doi.org/10.1021/acs.jced.4c00509

Li, J., Li, R., Yang, J., Li, S., Zhang, Z., Liu, H., Ma, Z., & Sun, L. (2025). Biobased Solvents as Entrainers for Extractive Distillation in Isobutyl Acetate–Isobutanol Separation: Experimental Investigation, Toxicity Evaluation, and Mechanism Analysis. *Journal of Chemical & Engineering Data*, *70*(11), 4648–4663. https://doi.org/10.1021/acs.jced.5c00514

Rao, J., Tian, X., Wang, H., Liu, J., & Li, C. (2025). Ionic liquids as extractants in extractive distillation: A review of advances in screening methods and their mechanisms of action. *Separation and Purification Technology*, *364*, 132372. https://doi.org/10.1016/j.seppur.2025.132372

Irreproducible Magic: Why are so many process-simulation-based papers not worth the bits (and bytes) used in their creation?

Ross Taylor[1] and Hendrik A. Koojiman[1]
[1] Clarkson University, Potsdam, New York 13699-5705, USA

Abstract
The majority of published papers that rely on process simulation tools should never have appeared in print as, regrettably, many of the reported results are impossible to reproduce; sometimes not even by those that claim to have been involved in their creation in the first place. (Is this because a worm ate their process simulation?)

Issues in published process simulation papers include violations of the laws of conservation of mass and energy. The most common reason for irreproducibility is the failure to properly document the thermodynamic (and other physical property) models and their model parameters employed. Similarly, not (properly) disclosing the reaction kinetics or leaving out key condenser or reboiler column specifications. An additional concern is that sometimes the specifications imposed are not realistic.

As authors of a process simulation tool that has been around for more than three decades, we understand that adequately documenting a process simulation can be challenging; it is however, necessary. It is not sufficient to say only that we used [insert here the name of your process simulator] since not all of us have access to that package, but also because simulation software providers continue to revise their libraries of pure component data and interaction parameters.

Our view is that irreproducibility and/or "magical" engineering should disqualify any such paper from further consideration. We propose criteria that should be adopted by all appropriate journals and applied to any submitted manuscript that relies wholly or in-part on results from a process simulator, before it goes out for review.

Keywords
Process Simulation, Documentation, Flowsheet, Reproducible.

1. Introduction

Why do we need to recreate a simulation already carried out by someone else and described in print? We have many reasons:

- Just for fun (something we happily acknowledge that we do).
- To verify claims in manuscripts submitted for publication (we do this too)
- To use as the basis for further investigations of our own.
- To use as the basis for examples and/or exercises for our students.

We regret to report that, all too often, published simulations are difficult, sometimes completely impossible, to recreate. This lack of reproducibility is, if anything, most serious in the extensive and very rapidly growing literature on life-cycle and techno-

economic analyses, reliant, as are many of these studies, on irreproducible simulations.

There are multiple reasons behind this lack of reproducibility.

- Not all of us have access to the process simulator used in the original work.
- Complete and accurate information about the thermodynamic models used in the simulation is lacking
- The same might be true for any kinetic models in use in the simulation
- Inert and/or minor compounds are omitted from the published version.
- Some (or all) of the specifications used in the simulation are not mentioned. While this is generally an issue, it is particularly problematic for distillation columns as well as for reactors in the simulation.
- Many published flowsheets violate the laws of mass and energy conservation!
- Not all stream data (flows, temperatures, pressures, compositions) is provided and it is impossible to back-calculate missing information.
- Inconsistent rounding of composition and reactor conversions.
- The process simulator version used no longer runs (as Microsoft Windows moved on) or newer versions no longer can read the original file (because vendors broke backwards compatibility).
- Even if the software still runs and loads the old files, new libraries are used which contain different parameters. (Such may well be more accurate but lead to different results. Simulator tools often do not always inform users when differences occur; this then becomes an exercise in forensic thermodynamics.)

Our goal with this paper is to encourage our friends and colleagues to reach for a higher standard of work and publish simulations that *everyone* can recreate!

2. Cases in Point

Frequently, authors fail to adequately report the necessary specifications to fully recreate the presented simulations. In one example case, we attempted to recreate the flowsheet for producing Acetone, 1-Butanol, and Acetone (ABE) as in Figure 8.12 of the book by Dimian et al. (2019). We used the freely available process simulator COFE (www.cocosimulator.org); the columns were modeled with ChemSep LITE (www.chemsep.com). The flowsheet will be posted on www.chemsep.com/downloads (after 15/5/2026).

Our version of this flowsheet is qualitatively similar to that of Dimian et al., but it is ***not*** quantitatively equivalent. Our column designs differ in their numbers of stages, feed stage locations, and, probably, in the operational specification. While they identify the underlying thermodynamic model, they did not provide a complete set of binary interaction parameters in their book, nor did they specify exactly what operational specifications were employed. As such, the authors made it impossible to fully reproduce their simulation. Unfortunately, such is the case for many if not most modern published descriptions of process simulations.

Panjapakku & El-Halwagi (2018) studied multiple routes to the manufacture of isopropanol. Sadly, their first process simulation in their paper description breaks the law of conservation of mass. An inevitable consequence is the violation of the first law of thermodynamics (conservation of energy.) We do not suggest that these authors

broke the law on purpose; we are sure that the actual simulation was carried out correctly, it is the paper that contains errors and omissions. We suspect that two components were inadvertently interchanged, but that cannot be the whole story because, try as we might, we cannot reconstruct the material balance using the information in the paper. When asked for a correct material balance the authors were unable to provide one, no longer having the simulator files used as the basis for writing their paper! Their paper also fails to provide any information about the thermodynamic model used, thereby reducing the value of their contribution even if it had not already broken the laws.

Agarwal et al (2018) describe – sort of – a simulation of an Oleflex process for dehydrogenation of propane as a vehicle to explore concepts in sustainable process design. Specifically, they include economic and environmental metrics to look at the impact of process integration and intensification techniques. The basis for their analysis is a process flowsheet simulation in Aspen HYSYS. Some of our concerns are identified in what follows (space limitations mean that others are omitted).

- The thermodynamic model used in the simulation is never identified. This matters not just because the results of any process simulation are critically dependent on the choice of thermodynamic model; the design of the C3 splitter – likely the single most expensive piece of equipment in their process flowsheet – is quite sensitive not just to the thermodynamic model selected, but particularly also to the model parameters employed.
- The stream tables do not conserve mass. These discrepancies are small for the most part and likely have no impact on their conclusions; nevertheless, they should not exist. In part these discrepancies arise from the lack of precision used to report mole fractions (always 4 digits, but not 4 significant figures). That, however, cannot explain all of the discrepancies (compare the total molar flows around their de-ethanizer, for example). In addition, some of the streams are incorrectly numbered in the tables. This makes tracking the flows through the flow diagram more difficult than should be the case.
- The pressure of the propane feed (their stream 101) magically changes from the pressure shown for that stream in the stream table (6894.8 kPa) to the pressure of the feed to the column (stream 102 at 1514.8 kPa)? (No pressure changing device is shown.)
- The pressure in the depropanizer is higher than the pressure of the feed to that column (stream 102). This is impossible in practice (although, we acknowledge that many steady state simulators will permit this sort of thing).
- The drop in pressure from stream 117 (the feed to the de-ethanizer column) to that inside the column itself seems extreme, albeit not impossible. However, no pressure changing device is indicated on the flowsheet. How does this pressure change influence the design of the de-ethanizer?
- The column designs are incomplete. What specifications were used in the simulation? How many stages were needed as a result? How does the number of stages translate to actual height and, hence, cost?
- No reaction chemistry or reaction kinetics are provided for any of the reactors.
- No details concerning the cold-box, stated to be based on a patent from Chart Energy, are provided. Our own simulation of a Chart Energy cold box can be

found on www.chemsep.com/downloads where it becomes clear that a cold box is a small chemical plant all by itself!

- The bottom product from a distillation column would be expected to be in the liquid state. There is no heat exchanger between the bottom of the de-ethanizer and the C3 splitter shown in their Figure 2. How, then, does stream 119 (the bottom product from the de-ethanizer column) get to be nearly 60% vapor?
- The pressure drops over the columns appears to be arbitrary and not consistent with proper column design. Consider the C3 splitter, for example; the pressure of the propane recycle (the bottom product from the C3 splitter appears to have been arbitrarily set to the pressure of the feed to the depropanizer? How did this impact the column design? If the columns were not simulated with an arbitrary bottom pressure, how do they then attain the pressure indicated in the stream table?

It is completely plausible that none of the issues identified above would in any way change the conclusions of their work as they pertain to sustainability. It is, however, impossible to ascertain this, since their work cannot be reproduced using only the information in their paper, the thesis of Agarwal (2018), and their cited references.

Yang et al. (2024) discuss the separation of isopropanol and iso-octane by extractive distillation. They mention the use of the NRTL activity coefficient model but no parameters are given. In connection with fitting that model they cite a paper that does not appear in their list of references.

Kim et al. (2024) present a flowsheet for the synthesis of dimethyl carbonate from CO_2. They show phase diagrams apparently created with a model based on UNIQUAC, but no parameters are provided. The tables of specifications for their columns are reasonably complete, but their extensive stream tables lack sufficient significant digits; thus, compounds appear absent from streams when, in fact, they are not.

The number improperly documented simulations that actually exists is vastly greater than the number discussed here!

3. The Remedy

We now propose criteria to ensure that process simulations can be reproduced.

Whenever possible (i.e. the simulations are not proprietary) the process simulator files should be included as supplementary material with any paper submitted to a journal, preferably in a format that is readable by a human. **(**If the simulations are considered proprietary one might wonder why the paper was submitted in the first place!)

Submission of actual simulator files is, at best, only a partial remedy because, at some point, most simulator files will become unreadable, even to later versions of the same software tool used in their creation. Thus, the only real solution is to properly document the simulation (probably in a supplement to the main paper). The short version here is that all simulation-based papers must include:

- Identification of the simulator employed. This includes the version number and, if available, the actual build number (these things are not the same).
- An exact copy of the visual depiction of the process simulation.

- Complete documentation of the thermodynamic & physical property models (see last section of Table 1).
- Complete documentation of all chemical reaction model(s).
- Accurate material and energy balances.
- Details of *all* of the specifications used to create the entire simulation. Table 1 provides a detailed list of what is required for column simulations.

Configuration Parameters/Variables Number of stages (including condensers and reboilers) Number (and stage numbers) of condensers Number (and stage numbers) of reboilers Stage numbers of all feeds Stage numbers for all sidestreams For DWCs: Stage numbers for the top of each wall For DWCs: Stage numbers for the bottom of each wall Stage numbers identifying the top and bottom of each reactive section *Important: stage numbering needs to be complete and unambiguous (i.e. are any condensers included in the stage numbering? What about any reboilers?*
Feed Specifications Flowrate, Temperature, pressure, compositions, and flashed vapor fraction of all feeds.
Product Specifications Condenser specification (e.g., reflux ratio, product flow rate, mole fraction, or other) Reboiler specification (e.g., boilup ratio, product flow rate, mole fraction, or other) Sidedraw specification(s) (e.g., sidestream ratio, flow rate, mole fraction, or other)
Other Column Specifications Pressure on all stages (or a way to calculate the pressure profile) Heat duties for all stages, including condensers and reboilers Holdup on each reactive stage
Dividing Wall Operational Specifications (when needed) Split ratio for each vapor stream at the bottom of each wall (unless wall ends at the bottom) Split ratio for each liquid stream at the top of each wall (unless wall extends to top) Heat transfer coefficients and area of the wall (if accounting for wall heat transfer)
Thermodynamic Model(s) Complete Vapor-Liquid Equilibrium (VLE and/or VLLE) model. This includes: - Identification of all of the pieces of the VL(L)E model (Any activity coefficient model, any EOS, the Poynting factor, if present, etc.) - Critical properties and acentric factors and α-function for a cubic EOS - Any vapor pressure model (with parameters) - All interaction parameters *with units where appropriate.* Complete enthalpy model including the ideal gas heat capacity correlations Compete reaction kinetic and reaction equilibrium models (including holdup)

Table 1: Summary of Specifications Required for a Column Simulation

4. Conclusions

We contend that a large fraction of the papers that are based wholly or in part on results obtained with a process simulator should not have been published (in the form in which they appeared in print) because it is not possible for anyone not the author to reproduce those simulations. What we do from hereon is up to us.

Authors: Properly document your simulations. Please! When you think you have done so, ask yourself this question: *Can somebody else, somebody using a software package that differs from the one I used, recreate my simulation?* Pause and think. Do not reflexively answer "yes" to this question. If you answer "No," then document some more (guidelines appear above).

Editors: Revise the instructions for prospective authors that appear on the web pages of your journal so that authors know what is expected of them ahead of time. On receiving a submission, quickly check if the authors have included the appropriate level of documentation. If not, return the paper for revision. If it passes your preliminary review, find a reviewer willing to check that the documentation is complete.

Reviewers: Ask yourself this question: Can I recreate the simulation described in this paper? If not, reject the paper. Ignore the real story the paper was written to tell. Remember that (paraphrasing Richard Hamming here), *the purpose of a simulation is insight* and know that i*rreproducible simulations cause ineffectual results and perverse conclusions.* *

* Our concluding phrase is a deliberate, misquote from *Get Off the Unicorn* (Del Rey Ballantine, 1977) by the writer Anne McCaffrey. The first two words in her original are "improper equations." The late Ms. McCaffrey wrote science fiction and fantasy!

References

Agarwal, A., 2018. A Design Approach for On-Purpose Propylene Production With Safety and Sustainability Considerations (Masters). Texas A&M University.

Agarwal, A., Sengupta, D., El-Halwagi, M., 2018. Sustainable Process Design Approach for On-Purpose Propylene Production and Intensification. ACS Sustainable Chem. Eng. 6, 2407–2421. https://doi.org/10.1021/acssuschemeng.7b03854

Dimian, A.C., Bildea, C.S., Kiss, A.A., 2019. Applications in Design and Simulation of Sustainable Chemical Processes. Elsevier. https://doi.org/10.1016/C2015-0-06856-3

Kim, S., Lee, S.G., Jeong, D.H., 2024. Direct synthesis of dimethyl carbonate from CO2: From the perspective of dimethyl-carbonate, a promising material for the future. Chemical Engineering Research and Design 203, 630–639. https://doi.org/10.1016/j.cherd.2024.02.010

Panjapakkul, W.; El-Halwagi, M. M. Technoeconomic Analysis of Alternative Pathways of Isopropanol Production. *ACS Sustainable Chem. Eng.* **2018**, *6* (8), 10260–10272. https://doi.org/10.1021/acssuschemeng.8b01606.

Yang, Q., Xu, W., Li, J., Wang, Z., Xu, H., Zhou, M., Wang, Y., Li, X., Zhong, L., Cui, P., 2024. Molecular mechanism of efficient separation of isopropyl alcohol and isooctane by extractive distillation. Chemical Engineering Research and Design 204, 269–281. https://doi.org/10.1016/j.cherd.2024.02.043

How to Build Feasible Separation Regions for Ternary Homogeneous Mixtures?

Lechoslaw J. Krolikowski
Wroclaw University of Science and Technology, Wroclaw, Poland

Abstract
Synthesizing distillation processes requires the identification of feasible separations. For this purpose, this paper describes the structure of feasible separation regions for ternary systems. An analysis of these regions revealed that they are the union of two product composition sets. These two sets either overlap or one set includes the other. One of these sets is bounded by a generalized distillation limit and a product composition multitude. Conversely, the border of the second set is determined by the feed distillation line and a product composition multitude. The boundaries of both sets consist of several curves that are related to specific types of operating modes of the column. The shape and extent of the product composition sets depend significantly on the univolatility lines that intersect these sets and the distillation boundaries. A simple algorithm was developed and implemented to construct feasible separation regions. This software is available on the Mendeley Data website.

Keywords
distillation line, residue curve, azeotrope, distillation boundary, distillation limit, product composition multitude, univolatility line

1. Introduction

Continuous distillation is a process commonly used to separate multicomponent azeotropic mixtures in the modern chemical industry. Such mixtures are difficult to separate into desired products: they typically require multiple distillation steps, the addition of separating agents, changes in pressure between columns, recycling, and crossing distillation boundaries. Skiborowski et al.[1] have reviewed the current state of knowledge of the conceptual design of azeotropic distillation processes. During the synthesis of distillation processes, it is essential to be able to quickly identify the feasible separations. For a given feed, the feasible separations can be described as a set of possible distillate and bottoms compositions. If this set includes all the possible product compositions, then it is called the *feasible separation region* (FSR).
FSRs comprise distinct overlapping sets[2]—one defined by only the total reflux conditions; the other, by all the column's extreme operating modes—bounded by two curves, one of which is common to both sets. This common curve, representing a set of possible distillate and bottoms compositions for a column possessing infinitely many theoretical stages and operating at the total reflux, is called the *product composition multitude* (PCM).[3,4] The second curve through the feed composition point is defined by assuming the total reflux for a number of equilibrium stages ranging from one to infinity[4] and is called the feed distillation line (FDL). The PCM and FDL neither depend on the condenser and reboiler types (partial or total) nor the feed quality. Alternatively, the second curve is determined at a variable finite reflux or reboil ratio when the column operates at the minimum reflux, and in the zone just below or above the feed entry point, the liquid and vapor compositions do not change

between stages.[5,6] In this zone, the liquid (vapor) composition represents the limit of the column section's composition profile and is called the *pinch point*. For a fixed distillate (bottoms) composition, the pinch points calculated with changing reflux (reboil) ratio form a *pinch point curve* (PPC), and each column section possesses one PPC each for liquid and vapor phases. The PPC defined for the feed composition connects stable and unstable nodes and passes through the feed composition point. The part of the liquid's PPC between the stable node and feed composition point restricts the bottoms compositions. In contrast, the part of the vapor's PPC connecting the feed composition point with the unstable node limits the distillate compositions. Although this approach is appropriate in some cases, it does not include the influences of the feed quality and condenser and reboiler types on the FSR border. However, the approach can be modified by assuming that the second curve of the FSR border is determined by the column's extreme operating modes, such as those corresponding to a column operating without boil-up or reflux or without the distillate or bottoms product being drawn off.[7] The resulting curve is called the *generalized distillation limit* (GDL). An example of curves that limit the FSR is shown in Figure 1. Clearly, only the FDL limits the set of bottoms compositions. However, because the GDL limits the set of distillate compositions, the FSR can be determined from the union of two sets: $FSR = FSR_{GDL} \cup FSR_{FDL}$, where the sets FSR_{GDL} and FSR_{FDL} are bounded by the GDL and FDL, respectively, and the PCM.

This study investigated the influence of *univolatillity lines* (UVLs), $\alpha_{ij} = 1$, on the FSR structures. Consequently, an algorithm, including all the possible zeotropic and homogeneous azeotropic ternary mixtures, was developed for constructing FSRs[8] and is available at the Mendeley Data website.[9] Continuous distillation in trayed single-feed columns, saturated liquid or vapor products, and constant pressure along the columns were all considered. For the VLE calculations, the vapor phase's ideality and nonrandom two-liquid (NRTL) or Wilson equations for the liquid phase were assumed.

2. Influences of distillation boundaries on the FSR

Distillation boundaries influence the shape and extent of the FSR. The total reflux boundary (TRB) for trayed columns divides the composition space into regions such that distillation lines from different regions begin or end at different nodes, which represent pure components or azeotropes. The PCM can only cross this boundary if the feed composition point is between the boundary (on its concave side) and the segment connecting its ends.[4] For example, the distillate composition points can be on the convex side of the stable TRB, i.e., the TRB connecting the saddle azeotrope with the stable node (Figure 2). Otherwise, the TRB modifies the PCM so that it partially runs along the distillation boundary. Similarly, bottoms composition points can be on the convex side of the unstable boundary.

Additionally, the extent of the FSR is influenced by overlapped distillation regions, which areas extend between the TRB and a pitchfork distillation boundary (PDB).[10] The PDB divides the composition space such that PPCs determined for distillate (bottoms) composition points on different sides of the PDB begin or end at different nodes. Similar to the TRB, the PDB begins at a saddle azeotrope but can end at the edge of the composition space or at an intersection point with the TRB originating from a different azeotrope and is always on the convex side of its associated TRB. For the feed composition point on the concave side of the stable TRB, the additional bottoms composition points can be between the PDB and its associated TRB and are delimited by a segment of the PCM starting at the feed composition point and ending

at the intersection point with the PDB (Figure 2). Similarly, the unstable TRB restricts distillate but not bottoms composition points.

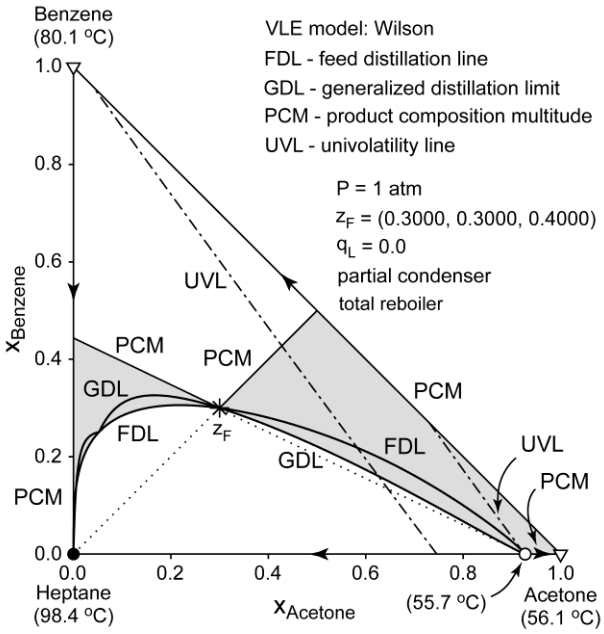

Figure 1. Curves defining the FSR for trayed column.[8]

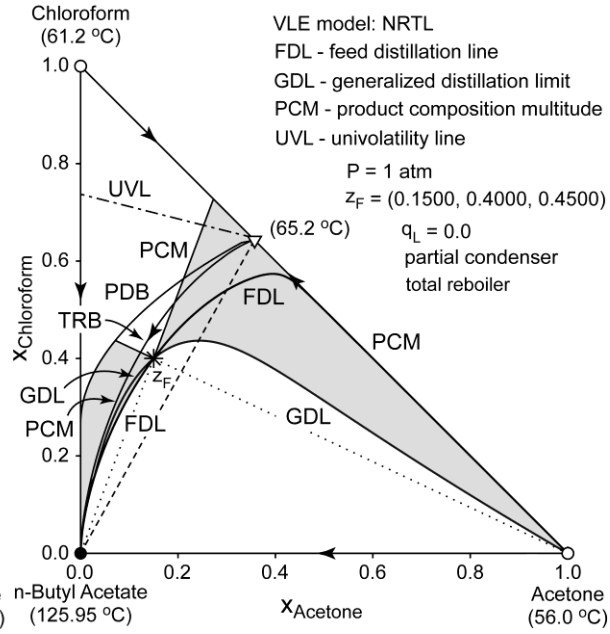

Figure 2. FSR for trayed column and feed composition point between the TRB and the segment connecting its ends.[8]

The properties of the case in which the feed composition point is between the PDB and TRB distinguish it from all others. Unlike usual, the GDL and FDL only share one common end point. For the stable (unstable) TRB, these curves join the same stable (unstable) node with different unstable (stable) nodes. There are also two different PCMs possessing ends identical to those of the corresponding curves. Consequently, different FSRs should be considered separately.[2]

3. Influences of UVLs on the FSR

Because the influences of UVLs on FSR_{FDL} are similar to those of UVLs on FSR_{GDL}, only the latter must be investigated. The only difference is the curve that UVL crosses. FDL intersections can change FSR_{FDL}. However, the influences of UVLs on FSR_{GDL} are more complex. GDLs are determined based on liquids' and vapors' PPCs passing through the feed composition point ($\boldsymbol{z}_F$) and possessing the same end nodes as those of the GDLs. Because only intersections of vapors' or liquids' PPCs between the point $\boldsymbol{z}_F$ and the unstable or stable node through UVLs can change FSR_{GDL}, GDLs are determined for the partial reboiler, total condenser, and boiling liquid's feed in this section to avoid misinterpretation of both the text and figures. This means that GDLs coincide with bottom liquids' and distillate vapors' PPCs. Herein, these relationships are explained for the mixtures.

For a binary unstable azeotrope (i.e., azeotrope being an unstable node) that generates a single UVL and is one end of the GDL, FSR_{GDL} is not modified without the UVL intersecting with the GDL (Figure 3a). When the UVL and a straight line through $\boldsymbol{z}_F$ and either GDL end node simultaneously intersect the GDL between the azeotrope and $\boldsymbol{z}_F$, an extra set of product composition points appears near the azeotropic point on the convex side of the GDL (Figure 3b) and is limited by a segment on the straight line through $\boldsymbol{z}_F$ and tangent to the GDL. The intersection of

the GDL by a straight line through the stable node and $\boldsymbol{z}_F$ can generate additional areas for both the distillate and bottoms composition sets and change the lines and characteristic points of these sets' borders, as shown in Figure 4a. However, when an unstable azeotrope generates a UVL that intersects the GDL between the stable node and $\boldsymbol{z}_F$, no extra distillate or bottoms areas are generated (Figure 4b). The binary stable azeotrope (i.e., azeotrope being a stable node) is analogous to the unstable node's azeotrope.

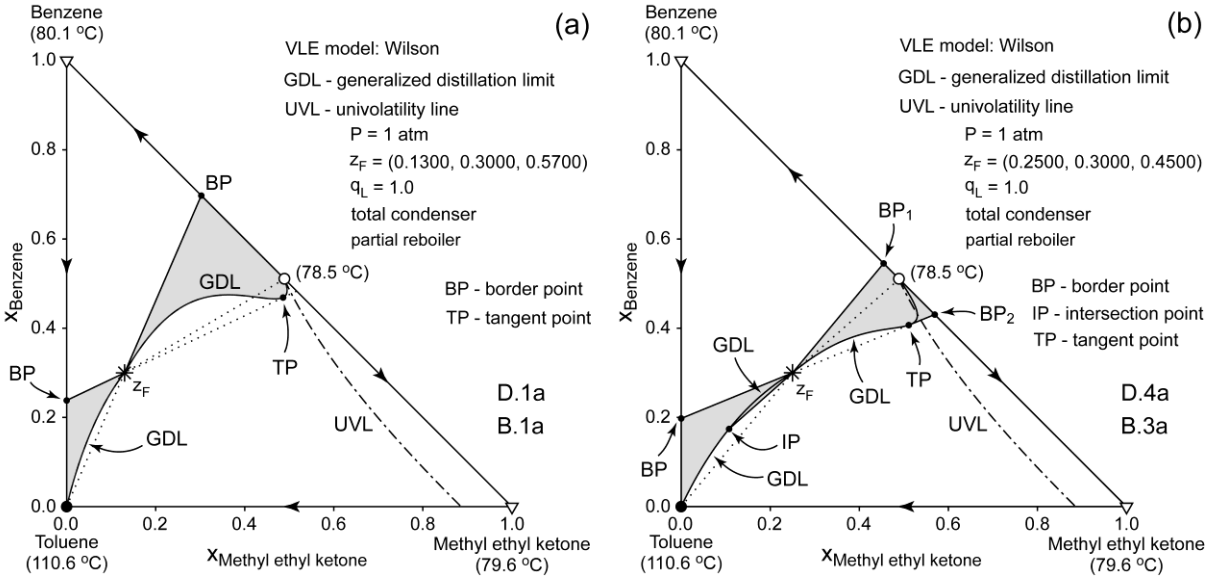

Figure 3. FSR_{GDL} for the trayed column and (a) 1a and 1a and (b) 4a and 1a distillate and bottoms sets' border types, respectively.[8]

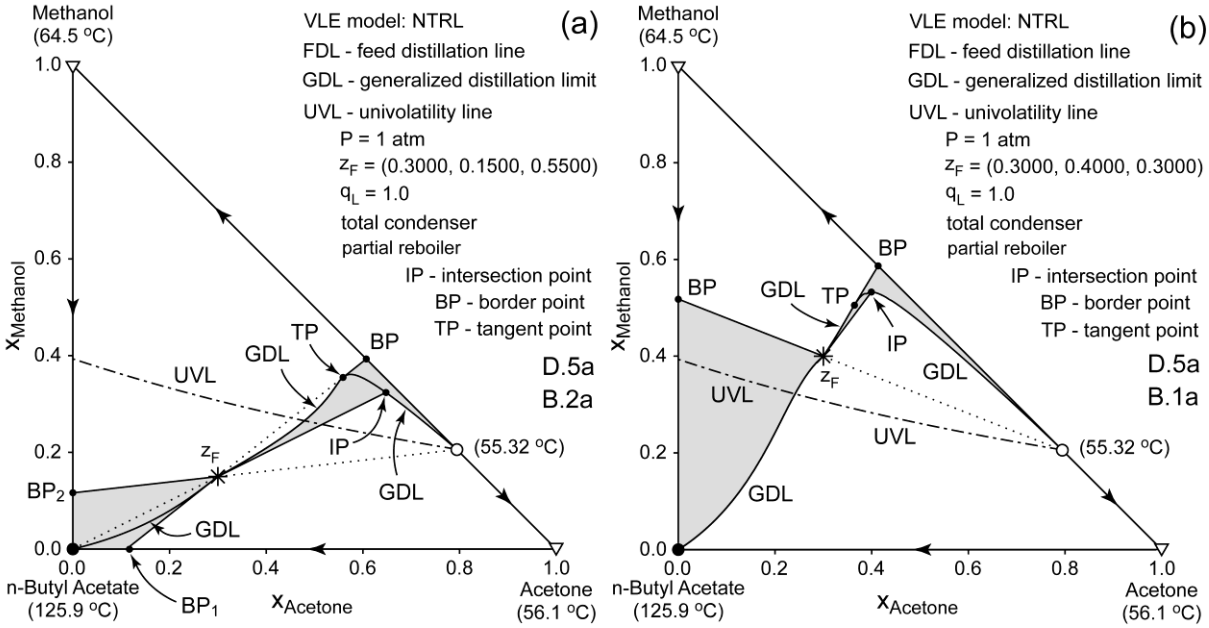

Figure 4. FSR_{GDL} for the trayed column and (a) 5a and 2a and (b) 5a and 1a distillate and bottoms sets' border types, respectively.[8]

For a ternary node azeotrope possessing three UVLs, one or two of them may intersect a given GDL. If the GDL is intersected by both an azeotrope-generated UVL and a straight line through $\boldsymbol{z}_F$ and one GDL end node, the effect is the same as that of a binary node azeotrope.

Similar to ULVs generated by binary unstable and stable azeotropes, binary saddle-point azeotrope-generated UVLs act on FSR_{GDL}. However, this effect is related to the stability of the TRB generated by the same binary-saddle-point azeotrope as the UVL. For a stable boundary, extra FSR_{GDL} areas appear for both the distillate and bottoms compositions when the GDL, between $\boldsymbol{z}_F$ and the unstable node at the end of the GDL, is intersected by the UVL and the straight line through the stable node of the GDL and $\boldsymbol{z}_F$ (Figure 5a). In other words, the end node of this part of the GDL intersected by the UVL cannot be an end node of the TRB. When the UVL intersects with the GDL between $\boldsymbol{z}_F$ and the stable node, FSR_{GDL} does not change (Figure 5b). The case with an unstable boundary is analogous.

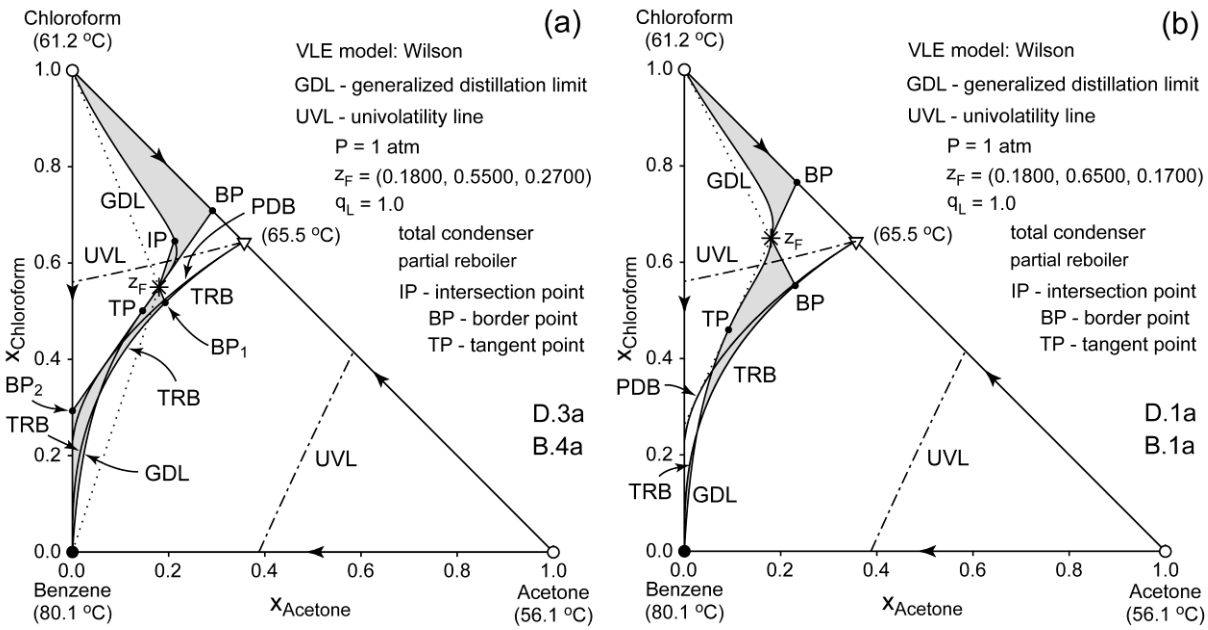

Figure 5. FSR_{GDL} for the trayed column and (a) 3a and 3a and (b) 1a and 1a distillate and bottoms sets' border types, respectively.[8]

The case with ternary saddle point azeotropes is somewhat more complex. The effect of a UVL, originating from the azeotrope and intersecting with the GDL, on the FSR_{GDL} depends on whether it terminates at a binary node azeotrope or at the edge of the composition space. UVLs intersecting the edge of the composition space do not generate any extra sets of the distillate or bottoms composition points on the convex side of the GDL. However, if the GDL is intersected by exactly one UVL ending at a binary node azeotrope and by a straight line defined by $\boldsymbol{z}_F$ and one GDL end node, FSR_{GDL} changes in a similar manner to that for an appropriate binary node azeotrope.

4. Border structure of the distillate and bottoms composition sets

Knowledge of the border types of the distillate and bottoms composition sets limiting the FSR_{GDL} (FSR_{FDL}) is necessary to formulate an algorithm for obtaining FSRs. A distillate or bottoms composition set may be in one or two adjacent distillation regions and attached to common parts of other external distillation regions. The areas where the distillate and bottoms composition sets can be found are designated as C_D and C_B, respectively. In Figure 2, the distillate and bottoms composition sets appear in two distillation regions and one distillation region enlarged by a part shared with the adjacent region, respectively.

The border of the distillate or bottoms composition set can comprise GDL parts, segments, and a part of the border of C_D or C_B. The "segment" is part of a straight line passing through $\boldsymbol{z}_F$. If the line goes through a stable or unstable node, the segment is a part of the PCM defined for the total reflux condition and an infinite number of column stages. When the line is tangential to the GDL, the segment demarcates the sloppy splits from regions not accessible by distillation in the same way as the GDL. The "border" is a part of the distillation boundary (i.e., PDB or TRB) or the composition space border. According to the observations, eight border types exist, alternately comprising characteristic points (BP, EN, IP, TP) and various line types (see Figures 3−5). BP is an intersection point of a straight line through $\boldsymbol{z}_F$ and one of the end nodes of the GDL or tangent to the GDL with the border. IP is an intersection point of a straight line through $\boldsymbol{z}_F$ and one of the end nodes of the GDL with considered part of the GDL. TP is the tangent point of the straight line through $\boldsymbol{z}_F$ with the GDL. EN is the end node of the considered part of the GDL. For product composition sets, characteristic points unambiguously determine their border types and facilitate the development of an algorithm for determining FSRs.[8] The software is available at the Mendeley Data website.[9]

5. Conclusions

Azeotrope-generated UVLs affect the borders of distillate and bottoms composition sets that form FSRs, enabling the generation of eight border types containing characteristic points that uniquely define products' border types for the GDL and FDL, regardless of which curves are included in the border structure, and facilitate the development of a simple algorithm for determining FSRs. The algorithm is a tool needed for conceptual design methods for azeotropic distillation processes. It allows not only for testing the feasibility of the currently considered separation but also, which was not possible so far, provides an overall view of possible separations.

References

(1) Skiborowski, M.; Harwardt, A.; Marquardt, W. Conceptual design of azeotropic distillation processes. In Distillation: Fundamentals and Principles; Górak, A., Sorensen, E., Eds.; Academic Press: London, **2014**; pp 305−355.

(2) Krolikowski, L. J. Feasible separation regions for distillation with ternary systems: An algorithm. *Ind. Eng. Chem. Res*. **2020**, 59, 18579−18594.

(3) Serafimov, L. A.; Zharov, V. T.; Timofeev, V. S. Rectification of multicomponent mixtures I. Topological analysis of liquid−vapor phase equilibrium diagrams. *Acta Chim. Acad. Sci. Hungaricae* **1971**, 69 (4), 383−396.

(4) Petlyuk, F. B.; Avetyan, V. S. Investigation of three-component distillation at infinite reflux. *Theor. Found.Chem. Eng*. **1971**, 5, 457−463.

(5) Wahnschafft, O. M.; Koehler, J. W.; Blass, E.; Westerberg, A. W. The product composition regions of single-feed azeotropic distillation columns. *Ind. Eng. Chem. Res*. **1992**, 31, 2345−2362.

(6) Fidkowski, Z. T.; Doherty, M. F.; Malone, M. F. Feasibility of separation for distillation of nonideal ternary mixtures. *AIChE J*. **1993**, 39, 1303−1321.

(7) Krolikowski, L. J. Feasible separation regions for distillation II: A generalized distillation limit. *AIChE J*. **2017**, 63, 4862−4869.

(8) Krolikowski, L. J. Feasible separation regions for the conventional distillation of ternary systems: An implemented algorithm. *Ind. Eng. Chem. Res*. **2025**, 59, 12755−12769.

(9) Krolikowski, L. J. *Software FeaSepReg for Calculating the Feasible Separation Region for Ternary Mixtures*; Mendeley Data, V2, **2025**.

(10) Davydyan, A. G.; Malone, M. F.; Doherty, M. F. Boundary modes in a single feed distillation column for the separation of azeotropic mixtures. *Theor. Found. Chem. Eng*. **1997**, 31, 327−338.

Influence of Feed Composition on the Optimum of Batch Distillation Determined by Surrogate Model-Based Optimisation

Laszlo Hegely, Peter Lang
Budapest University of Technology and Economics, Budapest, Hungary

Abstract
A surrogate model-based optimisation (SMBO) method is proposed to determine how the feed composition (x_F) influences the optimum of batch distillation (BD) processes. Profit of a single batch of a BD process (OF), where methanol is recovered from a five-component mixture, is maximised. Optimisation variables are the reflux ratios of the steps and the stopping criteria of the fore-cuts. OF is estimated by surrogate models (SMs) fitted to simulation results (mass of product, mass of first fore-cut, process duration) by ALAMO, which uses a machine-learning approach to generate algebraic models. The influence of x_F is taken into account by including the mass fraction of three components as input variables of the surrogate models along with optimisation variables. Using Latin hypercube sampling, a large number of simulations are performed in the space of x_F and optimisation variables by using a professional flow-sheet simulator. OF calculated by the SMs is optimised for 31 different charge compositions by sequential quadratic programming (SQP), and variation of the value of optimisation variables over the composition space is evaluated. The method enables the estimation of the optimal value of operational parameters for a wide range of x_F without any further simulation.

Keywords
batch distillation, optimisation, surrogate model, variable composition, machine learning

1. Introduction

The optimisation of batch distillation (BD), applied for variable feed composition (x_F), is usually performed using evolutionary algorithms (e.g., genetic algorithm (GA)) (Hegely, 2023), requiring a large number of simulations to evaluate the objective function (OF). Since BD is a dynamic process, its simulation and, consequently, its optimisation is very time-consuming. In the case of variable x_F, the optimum determined for a given (e.g., average) composition is clearly not optimal for other compositions. The distance from the true, concentration-dependent optimum is a function of the deviation of the composition, the separation task, the properties of the column, and the OF selected. Moreover, the previously determined optimal parameters might even result in infeasibility if optimisation constraints (such as product purity specifications) are violated.

Generally, determining the concentration dependence of the optimum with evolutionary algorithms is practically infeasible, as the computationally intensive optimisation would have to be repeated for a large number of compositions. An exception is when the dependency of OF on the optimisation variables is simple, that is, it can be described with a low number of parameters. In such a case, which is more likely to occur if the concentration ranges are narrow, a suitable approximation of the optimal OF can be achieved by performing the optimisation only for a few x_F

values. For example, Nemeth et al. (2020) fitted response surfaces to the optimal values of the optimisation variables and the specific energy demand of a two-column BD process, obtained by GA.
Local methods, such as the Nelder-Mead simplex and Box-complex, were successfully applied by Hegely (2023). The profit of a single batch of a BD process, recovering methanol (B) from a five-component waste solvent mixture, was maximised. The mixture contained three organic pollutants (acetone (A), tetrahydrofuran (C) and toluene (E)) and water (D). However, while local methods require a lower number of simulations, the problem of the computational intensity of determining the concentration-dependent optimum persists.
The optimisation problem of Hegely (2023) was also solved by SMBO by Hegely et al. (2023). OF was estimated by SMs fitted to a large number of simulation results. Model fitting was performed by using ALAMO (Cozad et al., 2014), which applies a machine-learning approach to generate algebraic models. The OF value obtained by SMBO approached the best one found previously by Hegely (2023) within 1 %.
SMBO can not only reduce computational intensity but, since the optimisation of OF itself is almost instantaneous, makes it possible to determine the optimum for many different parameter values, such as x_F or prices. This can be achieved by including these parameters as input variables of the SMs along with optimisation variables.
The goal of the present work is to determine how the feed composition influences the optimum of the BD process previously studied by Hegely (2023) and Hegely et al. (2023). The concentration of three components (B, C and E) are included in the SMs, which were fitted by ALAMO to the results of the professional flow-sheet simulator CHEMCAD. The profit calculated by the SMs is optimised for 31 different charge compositions by sequential quadratic programming, and the variation of the optimisation variables over the composition space is evaluated.
To the best of our knowledge, the method proposed here is the first one enabling the estimation of the optimal operational parameters for a wide range of charge compositions without requiring any further simulation.

2. Separation process

The mixture to be separated contains, in the order of increasing boiling point, acetone (A), methanol (B), tetrahydrofuran (C), water (D) and toluene (E). B must be recovered with a purity of 99.5 mass%. Based on industrial data, the potential variation of the x_F was determined. A is present in only a very low concentration. Therefore, its variation is neglected, and its value is fixed at 0.07 mass%. The concentration ranges in mass%: 27 %<$x_{F,B}$<50 %, 3 %<$x_{F,C}$<7 % and 0.5 %<$x_{F,E}$<3 %; that of D can be obtained from the summation equation.
The components form five minimum boiling-point azeotropes: AB, BC, BE, CD and DE (by increasing boiling point). Taking into account the low A concentration, the production of B is hindered by the azeotropes BC and BE, meaning that C and E must be removed in fore-cuts. The vapour-liquid equilibrium is described by the UNIQUAC model (Hegely and Lang, 2016).
The process consists of the following steps:

- Step 0: heating-up under total reflux for 360 min. At the end of the step, the composition of the condensate is close to the BC azeotrope.
- Step 1: Fore-cut 1 containing considerable amounts of B, C and E. It is incinerated to remove the organic pollutants C and E and finished when the concentration of C in the distillate falls below a stopping criterion: $x_{D,C}$<Cr_1.
- Step 2: Fore-cut 2, which is recycled to a next batch to limit the loss of B. It is finished when $x_{D,C}$<Cr_2.

- Step 3: main cut (high purity B), finished when the B concentration in the cut decreases below 99.52 mass% ($x_{MC,B}$>99.52 %).
- Step 4: after-cut to remove the remaining B from the residue, sent to biological purification. It contains B and D, and is recycled. The step is finished when the B content of the residue falls below 0.25 mass%: $x_{SR,B}$<0.25 %.

The column has 25 theoretical stages (excluding the condenser and the reboiler). Its top pressure is atmospheric, while the pressure drop is 0.25 bar. The volume of the charge is 25 m^3, the liquid hold-ups are 0.45 m^3 for the condenser and 0.05 m^3/stage for the column. The reboiler heat duty is Q_{st}=1800 MJ/h.

3. Calculation method

Dynamic simulations were performed with the CHEMCAD professional flow-sheet simulator. The column was modelled with the SCDS module, the still pot and the receivers for the cuts by Dynamic Vessels.

The objective function (OF) to be maximised is the profit of a single batch:

$$OF=p_B \cdot m_{MC}-p_{inc} \cdot m_{FC1}-p_{st} \cdot Q_{st}/r_{st} \cdot t \quad (1)$$

where p_B is the price of methanol (0.46 \$/kg), p_{inc} is that of incineration (0.21 \$/kg), and p_{st} is that of the heating steam (57.6 \$/t), whose heat of condensation is r_{st}=2263.5 MJ/t. m_{MC} and m_{FC1} are the mass of the main cut and the first fore-cut, while t is the duration of the process. The optimisation variables are the reflux ratios of the steps (R_1, R_2, R_3, R_4) and the stopping criteria of the fore-cuts (Cr_1, Cr_2).

Inequality constraints are $x_{MC,B,max}$≥99.5 mass%, $x_{FC2,C}/x_{FC2,B}$≤0.107 and $x_{FC2,E}/x_{FC2,B}$≤0.120. Violations of the constraints are penalised by setting OF to -10000 \$. In Eq. (2), the maximal and not the final concentration of B is considered. This makes it possible to judge how close the constraint is to being violated.

The amount of feed placed into the still pot is specified as a mass in the simulation. In order to ensure that the feed volume is always 25 m^3, this mass is calculated from the volume and the density of the mixture. The density is described as a function of the x_F in the following way. By Latin hypercube sampling (LHS), 500 compositions are generated in the concentration ranges by a code written in Excel VBA. For each composition, Excel calls a simulation to calculate the density. By using ALAMO, an algebraic SM is fitted to simulation results by minimising the Bayesian information criterion (BIC). ALAMO constructs the model by choosing from preselected basis functions, such as linear, polynomial and exponential functions.

Subsequently, 1000 points are generated by LHS in the 9-dimensional space of the feed concentrations and optimisation variables. The lower and upper bounds of the latter ones are: 3<R_1<10, 1<R_2<9, 1.5<R_1<4 ,1<R_1<10, 13 %<Cr_1<30, 2 %<Cr_2<5 %.

In each point, a simulation is performed; the results necessary to calculate OF (m_{MC}, m_{FC1}, t) and the constraints ($x_{MC,B,max}$, $x_{FC2,B}$, $x_{FC2,C}$, $x_{FC2,E}$) are returned to Excel, and SMs are fitted using ALAMO. In addition to the terms used by the model of density, different powers of the variables, of their binary and ternary products and of their ratios are allowed, as well as logarithmic and exponential terms. The coefficients of determination (R^2) of the models vary between 0.989 and 1.0.

The optimisation problem formulated by using the SMs is solved in Maple by SQP for 30 different feed compositions (Table 1) generated by LHS. The bounds of the variables are included as inequality constraints, as well. Additionally, the composition studied by Hegely (2023) and Hegely et al. (2023) is also included (point no. 14). Starting from this composition, the optimisaton is initialised for each composition by the solution obtained for the closest one. If the optimal value of one or more optimisation variables is at its lower or upper bound, a visual inspection of OF is performed. If OF plotted as the function of two variables shows a steep decrease at a

bound, it is likely that erroneous extrapolation is happening. Outside the convex hull of all the points generated by LHS, but within the allowed ranges of the variables, the models are always extrapolating.

4. Results and discussion

Table 1 shows optimal values of the variables and the objective function calculated with the SMs (OF*) and by performing a simulation with the given values (OF).

No.	$x_{F,B}$	$x_{F,C}$	$x_{F,E}$	R_1	R_2	R_3	R_4	Cr_1, mass%	Cr_2, mass%	OF*, $	OF, $
1	0.2705	0.0503	0.0091	3	2.97	3.66	1.22	18.2	2.63	-372.0	-188.0
2	0.2801	0.0593	0.0246	infeasible							
3	0.2866	0.0402	0.0113	5.39	2.46	3.84	1.34	22.5	2.33	-86.9	-81.1
4	0.3003	0.0694	0.0161	3	2.77	3.67	1.22	19.7	2.69	-348.1	-362.9
5	0.3018	0.0552	0.0271	3	2.87	3.88	1.32	13.7	2.15	-482.7	-480.0
6	0.3113	0.0653	0.0217	10	1	2.66	1	13	2.03	653.0	494.7
7	0.3184	0.0353	0.0092	8.75	2.10	3.28	1.05	22.2	2.13	498.9	515.8
8	0.3252	0.0312	0.0150	3	3.66	3.62	1.20	16.9	3.30	409.8	414.9
9	0.3332	0.0384	0.0070	10	1.50	3.07	1	21.6	2.12	644.9	625.5
10	0.3409	0.0329	0.0251	4.18	2.62	2.26	1	17.6	3.18	1149.9	1128.4
11	0.3533	0.0673	0.0204	4.26	2.91	3.11	1	18.9	1.19*	-56.45	-154.1
12	0.3573	0.0521	0.0280	3	3.04	3.31	1.07	14.9	3.12	-32.2	-63.2
13	0.3640	0.0539	0.0190	4.43	2.96	3.04	1	18.3	3.13	255.4	244.9
14	0.3714	0.0489	0.0156	5.00	2.71	3.77	1.28	21.4	2.35	104.6	125.3
15	0.3761	0.0628	0.0208	4.54	2.92	2.93	1	18.4	3.13	159.9	156.5
16	0.3828	0.0371	0.0227	3	2.90	3.04	1	15.9	3.26	556.1	541.8
17	0.3892	0.0617	0.0130	10	1	2.58	1	13	2.30	772.0	562.1
18	0.3991	0.0684	0.0107	10	1	2.24	1	13	2.46	1496.1	1444.1
19	0.4075	0.0639	0.0195	5.57	3.08	2.68	1	18.5	3.33	413.9	417.1
20	0.4142	0.0607	0.0286	3.76	2.74	2.74	1	17.6	3.19	240.3	235.8
21	0.4195	0.0475	0.0055	10	1	2.50	1	13	2.58	1312.9	1160.6
22	0.4253	0.0434	0.0079	infeasible							
23	0.4355	0.0490	0.0118	10	2.02	2.49	1	19.1	2.66*	1179.9	905.7
24	0.4401	0.0361	0.0167	5.89	3.33	2.51	1	17.4	3.66	1206.0	1225.2
25	0.4471	0.0458	0.0182	6.30	3.21	2.46	1	17.8	3.60	1039.0	1057.0
26	0.4590	0.0322	0.0064	10	1	2.35	1	13	3.00	1809.9	1722.4
27	0.4618	0.0568	0.0140	10	1	2.33	1	13	2.74	1260.7	1147.9
28	0.4722	0.0433	0.0266	4.46	2.60	2.38	1	17.7	3.29	1032.5	1011.0
29	0.4774	0.0563	0.0241	5.80	3.24	2.30	1	17.6	3.58	899.3	919.8
30	0.4860	0.0467	0.0155	10	1	2.48	1	13	2.59	1371.7	1232.0
31	0.4930	0.0417	0.0293	4.18	2.62	2.26	1	17.6	3.18	1149.9	1128.4

Table 1: Optimisation results.

Four types of results can be distinguished. For ca. half of the points (denoted as “Regular” in Figure 1), the values of all optimisation variables are within the ranges on which the SMs were fitted, with the exception of R_4, which is often at its lower bound. While the optimal R_4 might be below 1.0, previous calculations indicate that its effect on OF is slight. For points no. 4-6, 8-9, 12, 16 and 23 (“Out of bounds” in Figure 1), the value of R_1 is either at its lower or upper bound, as well. This indicates that the optimum lies outside of the range used for R_1, and SMs should be fitted over a wider range. In the case of points no. 17-18, 21-22, 26-27 and 30 (“Extrapolation” in Figure 1), four variables are at one of their bounds: R_1 at its upper, R_2, R_4 and Cr_1 at their lower ones. These points have a high B and low E concentration. It was not possible to determine whether the optimum is truly outside the ranges of these variables, or, more likely, that OF* had a maximum here because the SMs were used for extrapolation, thereby overestimating it. Finally, by points no. 2 and 22, it was not

possible to reach the specified B purity, and the separation was infeasible. These two points have low B and high E concentration, under which conditions the production of B is the most difficult. It must be noted that in two cases (points no. 11 and 23), the specification could only be reached by making the second fore-cut longer by decreasing the original value (2.92 and 3.09 %, respectively) of Cr_2.

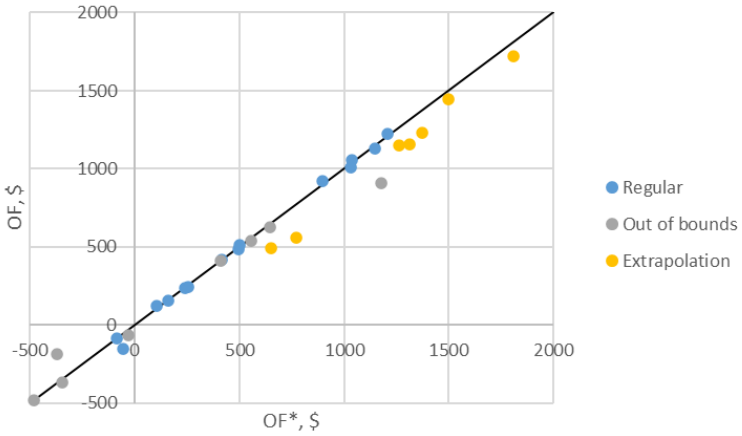

Figure 1: Profit by simulation (OF) as a function of values estimated by SMs (OF*).

By comparing the OF values obtained by simulations with those obtained by the SMs (Figure 1), it can be seen that the models are accurate in the case of the "regular" points (with a maximum error of 22 $), with the exception of point no. 11 (where Cr_2 was modified). By the majority of "out of bounds" points, the prediction error is similarly small; however, OF is considerably overestimated for point no. 23 (where Cr_2 was modified) and underestimated for point no. 6. On the other hand, OF is overestimated (by at least 50 $) for all the "extrapolation" points, confirming the suspicion that the models incorrectly extrapolate in these points.

By plotting OF in the composition space (Figure 2), its strong concentration dependence can be observed. (Triangles show "extrapolation" points, asterisks infeasible points). OF increases with increasing B, decreasing C, and, to a lesser degree, with decreasing E content of the feed. For six compositions, the regeneration of B is not profitable (OF is negative), but is economical, since incinerating the whole feed would be more expensive.

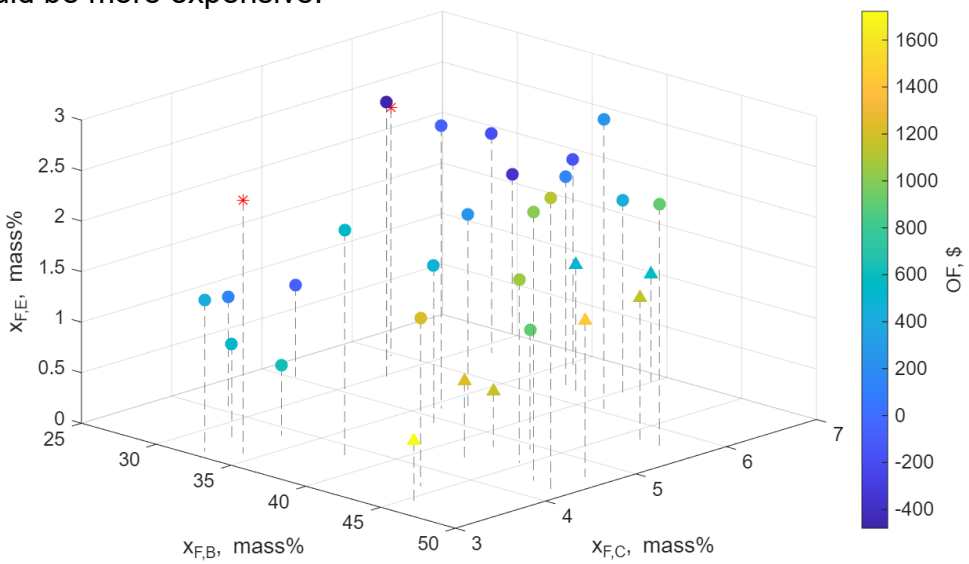

Figure 2: Profits obtained by simulation (OF).

x_F has the following influence on the optimal values of the optimisation variables. R_1 increases on the decrease of $x_{F,E}$. Generally, a higher R_2 is needed if $x_{F,E}$>1.5 %. R_3 depends very strongly on $x_{F,B}$: the higher $x_{F,B}$, the lower R_3 (Figure 3). R_4 starts to increase only as $x_{F,B}$ decreases below ca. 35 %, leading to a $x_{SR,D}$ at the start of after-cut. Cr_1 tends to increase, which corresponds to a decreasing amount of Fore-cut 1 on the decrease of $x_{F,E}$. The highest values are obtained at low $x_{F,B}$ and $x_{F,E}$ values. Cr_2 is mostly influenced by $x_{F,B}$: it increases on the increase of the B content, that is, the amount of Fore-cut 2 decreases.

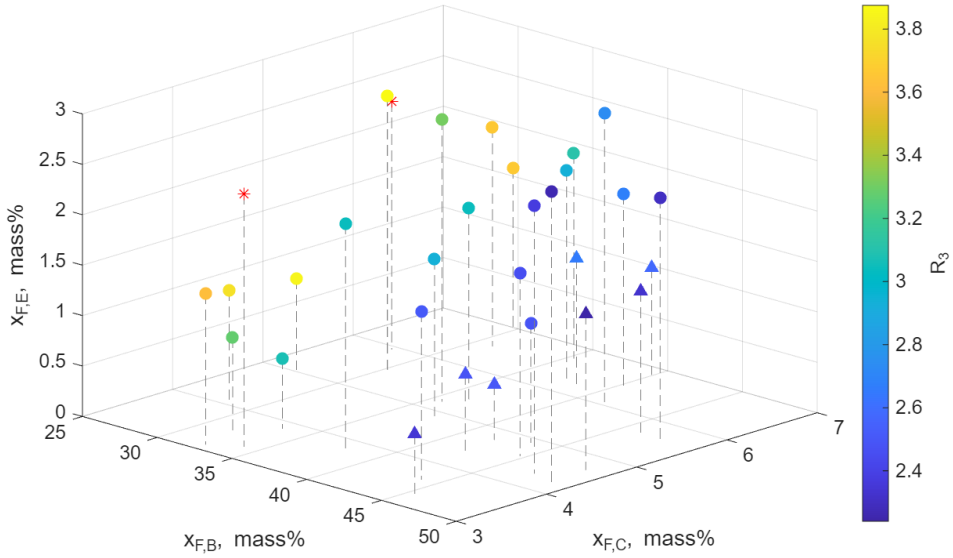

Figure 3: Optimal values of R_3 by SMBO.

5. Conclusions

The recovery of methanol from a five-component mixture was optimised with SMBO. Profit (OF) of a 4-step BD process was maximised for one batch. The influence of the feed composition (x_F) was estimated for the optimal reflux ratios of the steps and stopping criteria of two fore-cuts. Compared to commonly used, computationally intensive methods, much fewer simulations were needed to fit the SMs for calculating OF. For ca. half of x_F values, the optimum was found with good accuracy. For a quarter, the error of the SMs was also low, but the optimum lay outside the bounds of R_1, requiring later widening its range. In some cases, the SMs extrapolated with high errors, or it was not possible to reach the specified product purity.

The method enables estimation of the optimal value of operational parameters of BD processes for a wide range of x_F without any further simulation.

Acknowledgements

This research was funded by the National Research Development and Innovation Fund of Hungary (OTKA FK-143059) and by the János Bolyai Research Scholarship of the Hungarian Academy of Sciences.

References

Cozad, A., Sahinidis, N.V., Miller, D.C., 2014. Learning surrogate models for simulation-based optimization. AIChE J. 60, 2211-2227.

Hegely, L., 2023. Direct search methods for the fast optimisation of batch distillation processes. Sep. Purif. Technol. 306, 122448.

Hegely, L., Lang, P., 2016. Optimization of a batch extractive distillation process with recycling off-cuts. J. Clean. Prod. 136, 99-110.

Hegely, L., Karaman, Ö.F., Szucs, M.T., Lang, P, 2023. Surrogate model-based optimisation of a batch distillation process. Chem. Eng. Res. Des. 192, 456-467.

Nemeth, B., Lang, P., Hegely, L., 2020. Optimisation of solvent recovery in two batch distillation columns of different size. J. Clean. Prod. 275, 122746.

Validating Visual Analysis and CFD of Tray Valves to Improve Column Performance

Emily Ruhl, Koch-Glitsch, Wichita, KS

Abstract

Distillation tray valve features play a key role in tray performance, with energy efficiency and high capacity as the target outcomes for operating columns. Traditional methods for comparing valve types often relied on complex test data and disparate charts, making direct comparisons challenging. Visual methods are a much more intuitive method to evaluate valve features. This paper discusses using Computational Fluid Dynamics (CFD) simulations to create visualizations that allow engineers to directly observe how specific valve features affect tray efficiency, capacity, and turndown. The study also includes pilot column observations to validate CFD findings under real operating conditions.

By visually comparing trays equipped with different valve types, this paper demonstrates how advanced features, such as the downward-turned cap and extruded orifice of the FLEXIPRO® valve, result in more uniform froth profiles, improved vapor distribution, and greater operational flexibility. These features can be taken advantage of in an operating column and various applications will be discussed on how valve features can be used to reduce column size by approximately 30% for new applications and increase throughput up to 30% in existing assets and improve energy efficiency.

Keywords

Valve Trays, CFD

Introduction

With energy efficiency and optimizing column throughput is becoming more critical, more scrutiny is given to the column internals and their performance since they directly influence these goals. For distillation columns with trays, the valve type plays a key role in determining the overall capacity and efficiency of the column. Valve features affect vapor distribution, froth uniformity, and operating range which have a direct influence on the overall capacity and efficiency of the column.

Distillation trays have been used for centuries. The earliest trays, sieve trays, had simple holes in the deck. Around the same time, Cellier-Blumenthal patented the “bubble cap” in 1815[1], a large, formed cap that covers a riser from the deck. Both devices served the industry for over a century, with the bubble cap tray preferred in services where a wide operating range was required.

In the 1950's, movable valve trays were developed. These were smaller, movable devices, that had higher capacity than bubble caps and improved on the performance at lower rates (turndown) compared to sieve trays by providing a cover over the hole. In the early 1990's, valves that are punched directly from the deck material were developed. These improved further on capacity over the movable valves and provided additional reliability. In recent years, valve performance has been further optimized, and several new valve devices with additional features have been developed to increase capacity and efficiency compared to earlier generations.

Because of the wide variety of valve devices introduced over the years, the task of choosing the correct valve for a specific application is not an easy one. Previously, engineers would have to only rely on reported test results from tray vendors and potentially interpret difficult charts to figure out the capacity and turndown capability of the valve type and then extrapolate that data into a practical consideration. In many cases, the charts available would not be on the same basis, making comparison even more difficult.

In an effort to make evaluating valve types much easier, Koch-Glitsch has focused on visual analysis of valve performance, allowing engineers to make a faster, more intuitive evaluation of how valves would perform in the column. Computational Fluid Dynamics (CFD) simulations model fluid behavior by using numerical methods to solve equations governing fluid flow. CFD techniques have been specifically developed to help analyze valve efficiency and capacity by providing a visual representation of how valve features impact the performance of the valve. Vapor velocity vectors leaving the valve correspond to how well the vapor and liquid mix and are also related to the capacity of the device.

Valve Features and Performance

The features of an active device will have a direct influence on its performance. By examining the specific features of a device, and verifying them with CFD, we can directly correlate this to the performance in the column.

The most basic deck device is the sieve hole. This is simply a hole in the deck without any added features to direct vapor flow or prevent liquid from weeping through the opening. Looking at the CFD of a basic sieve hole (Figure 1), the first portion of the CFD analysis shows the vapor path leaving the hole. We can see that the vapor exiting the hole has an upward trajectory with minimal horizontal spreading. Without any protection over the hole, vapor will carry the liquid upward meaning that the capacity limit is reached relatively quickly. The second part of the CFD is of the deck level, showing the vapor velocity close to the deck. This shows areas of blue, indicating large zones of liquid on the deck that does not interact with the vapor. This lack of vapor and liquid mixing will impact the efficiency on the deck.

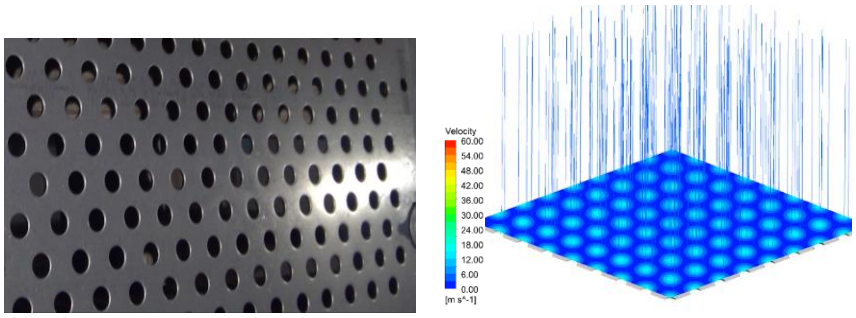

Figure 1: Sieve Tray and CFD of a Sieve Tray

If we look at Koch-Glitsch air/water test apparatus at a tray with sieve holes (Figure), we see this upward trajectory in the froth profile. The vapor is carrying the liquid up in jets off the deck, there is little separation between the “jets” on the deck and the tray above which indicates that the capacity is limited.

Figure 2: Sieve Tray in Operation

Bubble caps consist of a riser, often welded to the deck, and a cap that goes over the top. They are still used for low liquid rate applications since the riser in the deck prevents the liquid from falling through as the vapor rate decreases. In the CFD image (Figure), we see the vapor exit the bubble cap in the downward direction. Although the area taken up by the cap itself means that the vapor and liquid have a limited amount of space to contact, which will limit the capacity.

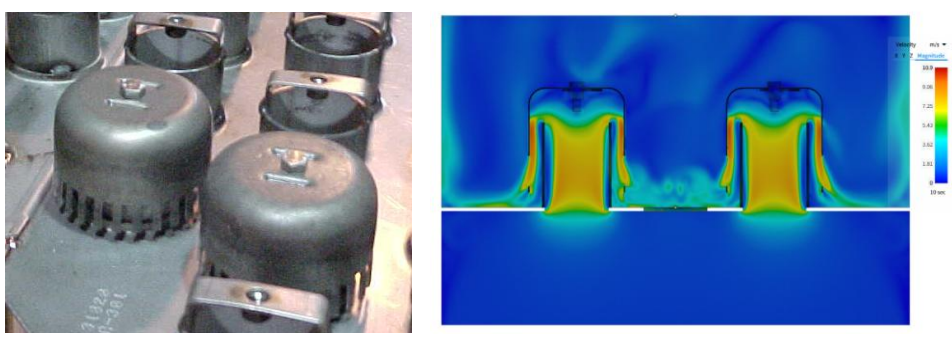

Figure 3: Bubble Cap and CFD of Bubble Cap

Movable valves, such as type T valves, have a cage and moving valve cap over the deck hole. This gives the hole some protection from liquid weep at low vapor rates and blocks the hole as the valve closes. Looking at the CFD of a T valve (Figure), the trajectory of the vapor is still generally in the upward direction, carrying the liquid with the vapor directly upward. We also see a good number of blue zones on the CFD, indicating little mixing between the vapor and liquid at the deck level, impacting the efficiency of the tray.

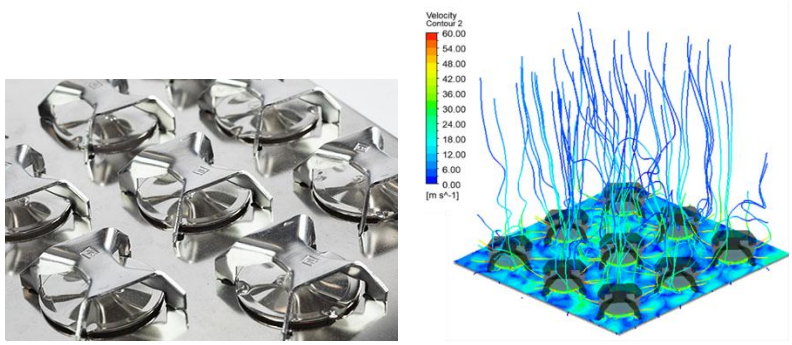

Figure 4: T Valve Tray and CFD of a T Valve Tray

The latest generation of valves have a variety of features specially designed to enhance efficiency, capacity and turndown performance. FLEXIPRO® floating valve trays have a contoured cap that directs the vapor flow leaving the valve downwards. The valve shape, with a narrower downstream leg, helps create a forward pushing action which helps minimize gradients in the froth. The deck hole is extruded upward, creating a barrier to help prevent liquid from weeping through the hole. The FLEXIPRO® floating valve also includes a moving cap that is able to close at reduced vapor rates to improve vapor distribution and further prevent the liquid from weeping through the cap.

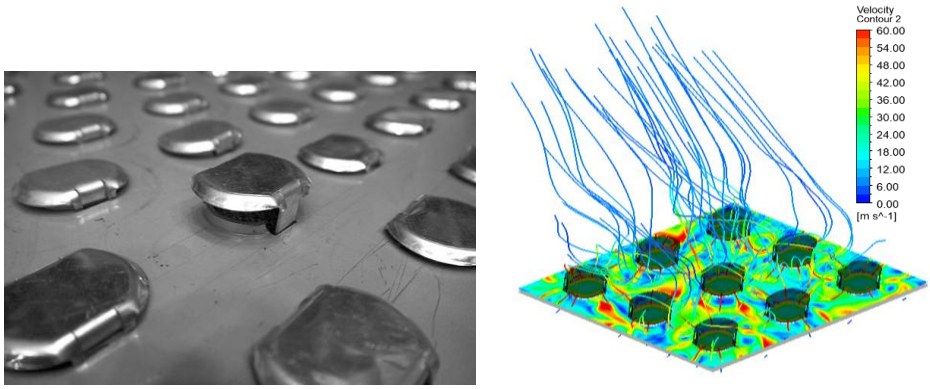

Figure 5: FLEXIPRO® Floating Valve

If we look at the CFD of a FLEXIPRO® floating valve tray (Figure 5), the downturned cap on the valve directs the vapor leaving the valve downward which reduces the entrainment of liquid to the deck above, directly translating to more capacity. The CFD image shows that the downward turn also results in more intense mixing at the deck level that enhances the efficiency as shown by the high vapor velocity zones (in red and yellow). In addition, we can see the forward motion to the vapor as it leaves the valve,

resulting in a pushing action, as shown by the vapor profile lines pointing in the direction of the liquid flow on the deck. This reduces the amount of entrainment and reduces gradients in the froth profile.

In Koch-Glitsch's air/water test apparatus, we can see the performance of FLEXIPRO® valve trays at the same time as T valve trays at the same conditions (Figure 6). Each tray has the same tray design, with only the valve type differing between the two trays. The first image shows conditions at both high liquid and vapor rate (Figure 6, left), where the T valve tray on the bottom level is entraining 10% of the liquid to the tray above and the FLEXIPRO® floating valve tray on top is in normal operating conditions. The downward turn of the FLEXIPRO® floating valve cap and the push effect of the valve can be seen in the froth profile with a flat froth profile across the flow path. The upward trajectory on the T valve creates a mountain-like, non-uniform profile of froth that peaks around the middle of the flow path, indicating vapor maldistribution. We also see less clear disengagement area above the froth on the T valve deck, which translates to less capacity, while the FLEXIPRO® floating valve tray has additional capacity to spare as indicated by the space between the froth and the tray above.

Figure 6: FLEXIPRO® floating valve trays (top) and T valve trays (bottom) operating at high liquid loads (left) and low liquid loads (right)

At a relatively low weir loading, we see some of the turndown enhancement features creating a noticeable difference in the froth profile on the tray (Figure 6, right). The T valve tray has nothing protecting it from liquid coming out of the downcomer and the liquid is scooped into the valve opening, particularly at the first row of valves next to the downcomer exit. This inlet weep is detrimental to the efficiency of the tray as the liquid bypasses two trays worth of contact. The upward trajectory of the vapor creates a clear layer of liquid at the deck level on the T valve tray deck where there is no vapor liquid contact at all. At these conditions, additional energy would be required to maintain the efficiency of the column. The wider upstream leg and extruded orifice protect the FLEXIPRO® floating valve tray from weeping. The contoured cap and pushing action of the valve create a well-mixed, uniform froth across the tray deck and also at the deck level. This means that for applications with low liquid load, less vapor is required to maintain the efficiency of the column, resulting in less energy use.

This data has also been supported by the operational data. Sieve trays have measured less capacity and start to weep first. On the upper end, FLEXIPRO® valve trays have approximately 35% higher capacity than the T valve tray. On the lower end, FLEXIPRO® valve trays have more turndown than T valve trays, doubling the operating range.

Case Studies

As shown in the visual analysis, the various features of the latest generation of tray valves translate into better performance. Looking at a Deisobutanizer as an example, sizing the column with sieve trays results in a 14'-6" ID vessel size. Keeping the performance the same, the vessel diameter can be reduced to 12'- 0" ID by taking advantage of the features of FLEXIPRO® valve trays, which will result in about a 30% reduction in the capital cost of the column. In addition, the turndown performance can be improved. For sieve trays efficient operation declines below 60% of the loads while efficiency declines below 15% of the loads by using FLEXIPRO® valve trays, eliminating the energy inefficiencies that the sieve trays would experience at lower inlet gas rates.

Conclusions

Visual methods, such as operating videos, and CFD to evaluate tray valve design and performance have evolved as the valve features have also evolved. As the industry continues to prioritize operational excellence, the adoption of advanced valve features that have been visually validated will be essential for optimizing column performance and meeting the evolving demands of the industry.

References

[1] Best of Both, Nieuwoudt, Penciak, Spencer, Hydrocarbon Engineering,July 2007

Smoothed Particle Hydrodynamics (SPH) Modeling of Interfacial Heat and Momentum Transfer in Distillation Trays

Carlos E. Alvarado-Rodriguez[1,3], Diego Ian Agabo-Aguilar[1], Christian Ricardo Lino-Andrade[1], Jazmín Cortez-González[2], Rodolfo Murrieta-Dueñas[2], Juan Gabriel Segovia-Hernández[1]

[1]Universidad de Guanajuato, Campus Guanajuato, Departamento de Ingeniería Química, Noria Alta s/n, 36050, Guanajuato, Gto., México
[2]Tecnológico Nacional de México/ Campus Irapuato, Departamento Ingeniería Química, Silao-Irapuato km 12.5 El Copal, 36821 Irapuato, Gto., México.
[3]Secretaria de Ciencias, Humanidades, Tecnología e innovación, CDMX, México

Abstract

Distillation is a fundamental separation process in chemical engineering. Its efficiency is related to mass and heat transfer between phases, so improving the interaction between the liquid and vapor phases would increase separation efficiency. Traditional distillation column design focuses on macroscopic analysis of the column's behavior, neglecting the microscopic processes occurring within it. To perform this analysis, it is necessary to implement modeling tools capable to capture the complex hydrodynamics and interfacial heat transfer occurring on trays. This analisys realize througth Computational Fluid Dynamics (CFD). In this paper, the main objetive is to simulate liquid-vapor interaction on a sieve tray within distillation column using Smoothed Particle Hydrodynamics (SPH). SPH is a mesh-free Computational Fluid Dynamics technique, has been used in chemical engineering for the analysis of multiphase fluids. For this analysis, a binary column previously optimized using stochastic methods for Benzene-Toluene separation was selected. The simulation was performed in AspenONE. NTRL was chosen to model the liquid-vapor equilibrium. Both products achieved purities and recoveries of 98%. The data obtained from this simulation were used as input parameters for the numerical simulation in CFD using SPH. Three-dimensional tray geometries and coulumns were developed in SolidWorks and imported into DualSPHysics for particle-based simulations. The analysis centers on stage eight, using inlet vapor and liquid conditions obtained from adjacent stages. Two enhanced SPH formulations—a variable smoothing-length approach and a two-pair force model—were incorporated to improve interface resolution and capture bubble deformation. Postprocessing yielded detailed velocity and temperature fields. According to the results, High-velocity regions formed near the downcomer and weir, while stagnant zones appeared at tray corners. Vapor flow generated vortices that enhanced mixing and heat transfer. The results confirm that SPH effectively captures interfacial momentum and heat

transfer, offering valuable insights for optimizing tray geometry and improving distillation performance.

Keywords

Distillation, CFD, SPH, Sieve tray, multiphase, heat transfer.

1. Introduction

Distillation is one of the most important and widely applied unit operations in the chemical, petrochemical, and energy industries, playing a central role in the purification and separation of valuable products. Despite its technological maturity, distillation remains highly energy-intensive, accounting for approximately 3% of total global energy consumption and nearly 50% of the energy demand within the chemical and petrochemical sectors. Consequently, even marginal improvements in distillation efficiency can lead to substantial reductions in operating costs and environmental impact. However, achieving high thermodynamic and operational efficiency in distillation columns has historically been a major challenge due to the complex interplay between hydrodynamics, heat transfer, and mass transfer phenomena occurring at the tray level.

Over the past decades, extensive research efforts have focused on improving distillation column performance through optimization of both column configuration and operating parameters. While macroscopic design methodologies based on MESH equations and sequential simulators have proven effective for column-level synthesis and steady-state analysis, they inherently rely on simplifying assumptions regarding phase equilibrium and mixing. As a result, these approaches are unable to explicitly resolve the local hydrodynamic behavior, interfacial interactions, and transport mechanisms that govern tray efficiency and ultimately limit column performance. In practice, optimal separation efficiency is strongly influenced by tray design and operating conditions, which determine the prevailing flow regime, bubble dynamics, liquid distribution, and interfacial renewal within each stage.

In this context, Computational Fluid Dynamics (CFD) has emerged as a powerful complementary tool for the detailed analysis of distillation trays. CFD enables the direct simulation of momentum, heat, and mass transfer processes, providing spatially and temporally resolved information that is inaccessible through traditional design methods. Numerous studies have applied CFD to investigate industrial-scale trays with specific geometries and configurations [1]. Reported efforts include modifications to tray deck area, orthogonal and non-uniform hole patterns [2], inclined perforations [3], and the influence of hole size and bubble diameter on hydrodynamic performance [2]. Different tray types—such as sieve trays [4], valve trays [5], and conical valve trays—have also been analyzed, with performance evaluated in terms of velocity distribution, clear liquid height, pressure drop, and liquid holdup.

Nevertheless, the widespread industrial adoption of CFD for tray design has been limited by its high computational cost. The solution of millions of coupled partial differential equations governing multiphase flow, heat transfer, and turbulence often requires simplifying strategies, including transient flow approximations, axisymmetric or quasi-two-dimensional models, and localized analysis of selected tray regions.

While these approaches reduce computational demand, they may fail to fully capture complex flow structures, particularly in regions such as downcomers, weirs, and liquid–vapor interfaces, thereby restricting their predictive capability and general applicability.

As a result, CFD is increasingly recognized as an indispensable tool for chemical engineers, extending beyond traditional design methodologies and enabling more physically realistic analysis of distillation processes. Conventional Eulerian CFD approaches, which rely on fixed meshes, face inherent challenges in accurately tracking moving interfaces, resolving bubble dynamics, and modeling turbulence in highly transient multiphase systems. In contrast, Lagrangian particle-based methods represent fluids as discrete particles, naturally accommodating large deformations, free surfaces, and complex interfacial behavior.

Among these methods, Smoothed Particle Hydrodynamics (SPH) has gained increasing attention as a robust, mesh-free Lagrangian technique for simulating multiphase flows in complex geometries. SPH is particularly well suited for modeling liquid–vapor interactions in distillation trays, as it accurately captures bubble formation, coalescence, interface deformation, and turbulent structures without requiring explicit turbulence models. This capability enables a refined analysis of flow regimes, temperature fields, and geometric effects at the tray scale, providing insights that are directly relevant for tray design optimization and performance enhancement.

From an industrial perspective, the relevance of this study is significant, as distillation remains a cornerstone separation technology in chemical and petrochemical production. The efficiency and reliability of distillation columns directly influence energy consumption, operating costs, and product quality. By providing a detailed and physically consistent simulation of liquid–vapor interactions at an equilibrium stage, this work contributes to a deeper understanding of tray-scale transport phenomena. Such knowledge can support the development of improved tray designs and operating strategies, leading to reduced energy requirements, lower operational costs, and enhanced process sustainability—key factors for maintaining industrial competitiveness in an increasingly energy-constrained environment.

2. Methodology

For this work a benzene–toluene mixture was selected for this analysis due to its industrial relevance and the essential role both compounds play in manufacturing processes. Their separation is relatively simple because of the significant difference in boiling points and their slight positive deviation from ideal behavior. An equimolar mixture was chosen to simplify the analysis and enable a balanced evaluation of distillation performance. A sieve tray distillation column was selected due to its widespread industrial use and its effectiveness in handling mixtures with variable properties. Sieve trays offer advantages such as efficient liquid-vapor contact, operational versatility, easy maintenance, and scalability.

The column design was carried out in AspenONE using the RadFrac model, which applies rigorous MESH equations. The NRTL thermodynamic model was selected to represent liquid–vapor equilibrium in this non-ideal mixture. A 14-stage column with a total kettle condenser and feed at stage 6 was defined. AspenONE v14 provided

stage wise thermophysical properties including enthalpy, thermal diffusivity, and surface tension used as input for the CFD simulations of the benzene–toluene system. The CFD simulations were performance with the SPH free code DualSPHysics where implemented equations to model the heat transfer, the surface tension and a variable smoothing length. According to the model setting in DualSPHysics the calculation of momentum and heat transfer was performed using the corresponding CFD equations momentum (Eq. 1), continuity (Eq. 2), and energy (Eq. 3). The surface tension between the liquid and vapor phases was modeled using the formulation and the variable smoothing length model, was implemented within the SPH framework to more accurately capture the interaction between liquid and vapor particles.

$$\frac{d\mathbf{v}}{dt} = -\frac{1}{\rho}\nabla P + \Gamma + g, \qquad \text{(Eq. 1)}$$

$$\frac{d\rho}{dt} = -\rho\nabla\cdot\mathbf{v}. \qquad \text{(Eq. 2)}$$

$$\frac{dT}{dt} = \frac{1}{\rho C_p}\nabla\cdot(k\nabla T), \qquad \text{(Eq. 3)}$$

Where ***v*** is velocity, *ρ* is density, *P* is pressure, *Γ* is the dissipative (viscous) term, *g* is gravity, *t* is time, *T* is temperature, *Cp* is the heat capacity, and *k* is the thermal conductivity constant.

Table 1 reports the parameters defined for the initial conditions of the SPH simulations, where *v* is the kinematic viscosity and T_0 is the temperature at the initial simulation time. This work focuses exclusively on heat transfer between the liquid and vapor phases; therefore, the mixture properties at stage 8 are used rather than component wise properties. Since stage 8 is the stage of interest, the initial temperature of each phase is assigned according to the adjacent stages: the liquid temperature corresponds to stage 7, while the vapor temperature corresponds to stage 9. Due to the expensive computational demand in the SPH simulation, only a 3D simulation of the central section of the tray, show in figure 1, was performed. The boundary conditions are shown in Figure 1, at the inlet the volumetric flow is 4.53×10^{-5} m^3/s for vapor and 6.35×10^{-5} m^3/s for liquid, for outlet are consider nonreflecting outlet boundary conditions. Initial conditions consider that the liquid is quiet on the sieve tray as is shown in Figure 1 with the temperature reported in Table 1.

Table 1. Parameter setting in the SPH simulations.

Parameter	Phase	
	Liquid	Vapor
ρ (kg/m^3)	789.21	3.99
C_0 (m/s)	20	150
v (m^2/s)	2.44x10-6	3.22x10-7
T_0 (K)	374.34	388.76

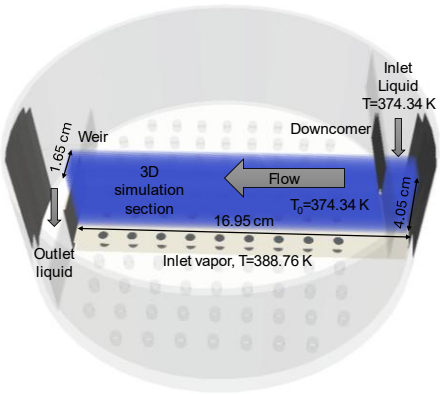

Figure 1. 3D simulation section, initial and boundary conditions for the SPH simulation.

3. Results and discussion

This section presents the results of the numerical simulations. The numerical analysis is divided into two stages: hydrodynamics and heat transfer. The hydrodynamic analysis addresses the flow behavior of both phases, including bubble generation. Heat transfer consists of the heat exchange between liquid and vapor.

3.1Hydrodynamics Results

The numerical simulation depicts the expected phenomenon in distillation columns. The liquid flows from the downcomer to the landfill. Meanwhile, the vapor rises through the liquid via the holes in the sieve tray, promoting intimate contact between the two phases and favors mass and heat transfer. Focusing in the hydrodynamics analysis is shows that the highest fluid velocities are observed near the downcomer and weir, while low-velocity zones form in the tray and column walls intersection. The Figure 2a, clearly shows the streamlines, velocity field, and vortices resulting from the interaction between the rising vapor bubbles and the liquid flow in the sieve tray at 2 seconds of simulation. The mean vortex is formed by the free fall of fluid in the downcomer and the bubbles make ways indicated that the flow is ascend near to the tray surface and then continue in the liquid direction from the downcomer to the weir. Vapor motion induced multiple vortices, promoting interfacial mixing and enhanced heat transfer. According to the numerical results of the SPH simulation, the non-dimensional numbers that characterize the bubble flow are Re_{bub}=876.108, We=18.5657 and Eo=46.63, all these numbers indicate that is a intertia-dominaded flow and viscous forces are negligible. In other words, the fluid's motion is primarily governed by its mass and velocity. The bubble motion are unsteady and are cap shaped bubbles meaning that gravity dominates surface tension. This phenomenon is known to enhance heat transfer through convective transport in the surrounding medium, a process that is particularly advantageous in the context of distillation columns.

3.2 Heat Transfer Results

Respect to the heat transfer, and considering a turbulent flow according to the hydrodinamics results, the heat transfer coefficient in the bubbly turbulent regime was estimated using a generalized semi-empirical scaling of the form (Eq. 4):

$$Nu = C\, Re_{bub}{}^{a}\, Pr^{b} We^{c} Eo^{d} \qquad \text{(Eq. 4)}$$

Where, for turbulent bubbling C=0.02, a=0.8, b=0.33, c=0.2 y d=0.1. So, using the correlation Nu=10.5. The effective Nusselt number of 10.5 indicates that heat transfer in the bubbling bed is substantially lower than that predicted for an isolated rising bubble under comparable hydrodynamic conditions. This reduction reflects the complex multiphase interactions in the bed—such as bubble coalescence, wake interference, and limited interfacial renewal—which collectively diminish convective transport relative to idealized single-bubble behavior. Equations 5, 6, and 7 allow the convective coefficient, flux, and heat flow to be determined, respectively.

$$h = \frac{Nu\, k_l}{d_b} \qquad \text{(Eq. 5)}$$

$$q = \left(\frac{Nu\, k_l}{d_b}\right)(T_b - T_l) \qquad \text{(Eq. 6)}$$

$$Q = q * A_T \qquad \text{(Eq. 7)}$$

Where, A_T is the average total area of bubbles formed during simulation The obtained results are h = 5x10^3 W/(m^{2}K), q= 7.258x10^4 W/m^2 and Q=1.82x10^{-2} W, respectively. For this case Q=1.82x10^{-2} W, this low value is according to the theory that consider an equilibrium stage where there Q=0, however the difference of temperature between the phases L-V and the interaction between them generates a heat interchange from the vapor to the liquid that is possible calculate with this methodology. This information is relevant because makes possible to compare different tray designs and operation conditions.

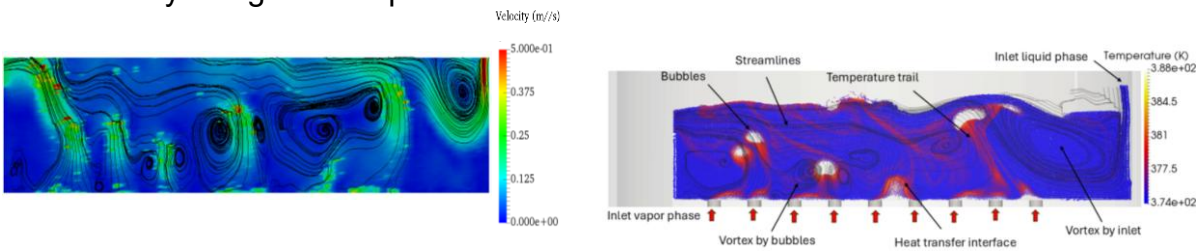

a) Hydrodynamics on sieve tray *b) Heat transfer on sieve tray*

Figure 2. The streamlines, the velocity field and vortices formed by bubbles ascension on sieve tray.

3. Conclusions

In this work, Smoothed Particle Hydrodynamics was successfully applied to investigate hydrodynamics and heat transfer on a sieve tray within a distillation column. By coupling rigorous process simulation in AspenONE with high-resolution SPH simulations in DualSPHysics, a multiscale framework was established that links column-level design with tray-scale transport phenomena. The results demonstrate that SPH effectively captures key features of tray hydrodynamics, including bubble formation, vortex generation, stagnant zones, and high-velocity regions near critical geometric elements such as the downcomer and weir. These flow structures play a decisive role in enhancing interfacial mixing and convective heat transfer. The heat transfer analysis confirms that, even under near-equilibrium conditions, localized thermal gradients and multiphase interactions lead to measurable heat exchange between liquid and vapor phases. From an engineering perspective, the findings highlight the potential of SPH as a powerful complementary tool for distillation tray design and optimization. The detailed insight provided by particle-based simulations can support the development of improved tray geometries, reduced energy consumption, and enhanced separation efficiency. Future work will extend this approach to include mass transfer modeling, alternative tray configurations, and parametric studies under different operating conditions.

References

1. Yu, K. T.; Yuan, X. G.; You, X. Y.; Liu, C. J. Computational fluid dynamics and experimental verification of two-phase two-dimensional flow on a sieve column tray. Chem. Eng. Res. Des. 1999, 77 (6), 554− 560.
2. Rahimi, R.; Sotoodeh, M. M.; Bahramifar, E. The effect of tray geometry on the sieve tray efficiency. Chem. Eng. Sci. 2012, 76, 90−98.
3. Kállai, V.; Mizsey, P.; Szepesi, G. L. CFD Investigation of Dry Tray Pressure Drop of Perforated Trays without Downcomer. Period. Polytech., Chem. Eng. 2023, 67 (2), 310−315.
4. Zarei, A.; Hosseini, S. H.; Rahimi, R. CFD and experimental studies of liquid weeping in the circular sieve tray columns. Chem. Eng. Res. Des. 2013, 91 (12), 2333−2345.
5. Cortez-González, J., Murrieta-Dueñas, R., Alvarado-Rodríguez, C. E., Segovia-Hernández, J. G., Hernández, S., & Gutiérrez-Guerra, R. (2024). New Approach Lagrangian for Numerical Analysis Within LV One Equilibrium Stage of a Distillation Column Using the SPH Method. Industrial & Engineering Chemistry Research, 63(50), 21974-21990.

Understanding Student Perceptions of Calculation Tasks in Distillation and Absorption

Verena Wolf-Zoellner[1], Leonore Peer[1]
[1]Technical University Leoben, Leoben, Austria;

Calculation-based problem solving is a central competence in chemical engineering education, particularly in courses focused on distillation and absorption. Despite their importance, calculation tasks are often perceived by students as demanding or tedious. This study investigates students' perceptions of calculation-related burden and explores potential sources of these difficulties in a course on thermal separation processes.
Using a mixed-methods design, data were collected through a pre- and post-course survey and student-generated artifacts collected throughout the semester. The results indicate that students generally recognize the value of calculation tasks for understanding theoretical concepts and future professional practice. However, difficulties arise primarily from the challenge of structuring complex multi-step solution processes rather than from negative attitudes or lack of prior knowledge.

Chemical Engineering Education; Calculation-Based Problem Solving; Reflective Learning; Flipped Classroom

1. Introduction

Calculation-based problem solving is a core competence in distillation and absorption. Designing and analyzing such operations requires the structured application of mass and energy balances, equilibrium relations, and transport models. Mastery in this domain depends not only on conceptual understanding but also on the ability to navigate multi-step solution procedures, make methodical decisions (e.g. selecting appropriate balances or equilibrium representations), and interpret intermediate results critically.
The present study examines how calculation tasks in a course on separation processes are perceived by students and how structured learning activities can support engagement with these tasks. The course covers distillation, absorption, extraction, drying, and general mass transfer principles and is organized as a lecture with integrated exercise sessions. Following a flipped classroom model, foundational theoretical content is provided through preparatory videos and materials prior to class, while in-class time is dedicated to guided application and discussion. Such approaches shift lower-order cognitive activities to the individual preparation phase and reserve contact time for higher-order cognitive engagement (Howell, 2021; Thai et al., 2017). To support preparation, a low-stakes "ticket to class" system was introduced, rewarding completion rather than correctness.
Within this course framework, calculation practice follows a structured sequence. Prior to class, students engage with instructional videos presenting fully worked examples and additional problems designed for independent solution. These self-calculation tasks are accompanied by Moodle-based quizzes for formative self-assessment. After completing the quizzes, detailed solution videos are released, allowing students to access targeted support according to individual needs. During in-class sessions, more complex problems are solved collaboratively in groups or stepwise in plenary discussions, with emphasis on reasoning processes and

methodological choices rather than on final results alone. Together, these elements provide instructional scaffolding, i.e., structured guidance that helps students navigate complex multi-step calculation tasks. In addition, structured opportunities for reflection were integrated, inviting students to share questions, difficulties, and conceptual insights that emerged while working on calculation tasks during their individual preparation in the in-class problem-solving sessions.

Against this background, the study examines students' perceived calculation-related burden and explores how students explain and reflect on sources of difficulty, including mathematical complexity and challenges related to structuring multi-step engineering reasoning.

2. Methodology

The study follows a mixed-methods design combining survey data with student-generated artifacts analyzed qualitatively. The aim was to capture students' perceived burden related to calculation tasks and to identify patterns in their reflections on the learning process, thereby gaining deeper insight into their learning experiences.Data were collected through two main sources:

- pre-and post-course surveys and
- anonymous Padlet reflections during the semester, where students shared reflections related to their work with calculation tasks.

The reflective calculation portfolio itself was implemented as a pedagogical intervention intended to support structured reasoning and metacognitive reflection. Students were encouraged to document their solution processes and reflect on difficulties and insights; however, these portfolio entries were not systematically collected or analyzed as research data.

The course was attended by 19 students. Of these, 18 completed the pre-course survey at the beginning of the semester and 18 the post-course survey at the end of the course. Participation was voluntary.

The initial survey first collected basic demographic information, including gender, study program, and study level. This was followed by Likert-scale items (1 = strongly disagree to 5 = strongly agree) assessing students' general attitudes toward calculation tasks. These items addressed affective responses, perceived usefulness of calculations for conceptual understanding, perceived relevance for professional practice, motivation, and self-efficacy in solving engineering calculations.

To further explore the reasons why calculation tasks may be experienced as demanding, students were asked a filter question regarding whether they generally perceive solving calculation tasks as tedious in engineering courses. Depending on their response, participants answered additional items investigating possible sources of difficulty. These items were grouped into several categories: complexity and cognitive load, prior knowledge and knowledge transfer, time investment and workload, affective and emotional responses, perceived relevance and meaning of calculation tasks, and instructional design and feedback.

In addition, the initial survey included a short diagnostic mini-test assessing transferable prior knowledge through basic tasks involving unit conversions, Dalton's law, elementary integration, and solving simple algebraic equations.

The final survey repeated the filter question and the items addressing perceived difficulty, enabling descriptive pre–post comparisons of students' perceptions. Additional Likert-scale items assessed students' experiences with the instructional intervention, as for example the reflection activities for supporting regular engagement with calculation tasks, improving understanding of solution procedures, and structuring individual learning efforts. The questionnaire also included several

open-ended questions asking students which elements of the course helped them most, what benefits they perceived from the portfolio and reflection activities, and which improvements they would suggest.
Likert-scale responses were analyzed descriptively, while qualitative responses were used to identify recurring themes in students' experiences and get deeper insight into their learning experiences
In addition to the questionnaires, students´ written reflections were collected during the semester through short reflection activities. For most course topics, students were invited to submit anonymous reflections via Padlet during the in-class sessions. These reflections prompted students to share questions, describe perceived difficulties, or note conceptual "AHA moments" related to the calculation tasks. The contributions were visible to the class and served as a basis for brief plenary discussions.
In addition, one structured written reflection activity was conducted at the end of the topic on drying, where students documented their reasoning processes and typical difficulties while solving a calculation task.
The Padlet contributions and written reflections were analyzed qualitatively as student-generated artifacts. Entries were reviewed and grouped thematically in order to identify recurring patterns in students' reported difficulties, conceptual insights, and problem-solving strategies and get deeper insight into students´ learning processes and approaches to calculation tasks.
Due to space limitations, the present contribution focuses on the pre-course survey and qualitative reflections collected during the semester. Selected insights from the post-course survey are referenced where relevant, particularly students' responses to open questions on which course elements supported their learning and how the reflection activities and the calculation portfolio were perceived.

3. Results

3.1 Initial perceptions of calculation tasks and prior knowledge

The initial survey explored students' general attitudes toward calculation tasks in engineering courses. Overall, the results indicate that students recognize the educational value of calculation-based problem solving. In particular, students agreed that calculation tasks support the understanding of theoretical concepts and are relevant for their future professional practice, while reporting moderate confidence in their ability to solve such problems.
At the same time, responses related to motivation and effort showed a more neutral pattern. Statements describing calculation tasks as intellectually stimulating challenges (e.g., "calculation tasks are like puzzles") or as motivating when solutions are not immediately found did not show a clear tendency toward agreement or disagreement. Similarly, the perceived balance between effort and benefit of calculation tasks was rated rather neutrally.
Figure 1 illustrates the overall pattern of these responses. It shows that students generally acknowledge the usefulness of calculation tasks while simultaneously expressing moderate levels of perceived effort. It should be noted that for the dimensions *attitude* and *perceived utility*, both positively and negatively phrased items were included as control items. In the figure, items are grouped thematically for clarity, although they appeared in mixed order in the questionnaire.
In addition to the perception-related items, the initial survey included a short diagnostic mini-test assessing transferable knowledge and basic mathematical skills relevant for calculation tasks. The results indicate that most students possessed solid

prior knowledge in fundamental engineering calculations. High percentages of correct responses were observed for the unit conversion task (89%) and the application of Dalton's law (94%).

For the mathematical tasks, performance varied more strongly. While most students correctly solved basic integrals such as $\int 1/x \, dx$ (94%), lower success rates were observed for more complex expressions such as $\int e^{3x} \, dx$ (22%) and algebraic equation transformations (22–50%). Overall, the mini-test suggests that while basic transferable knowledge is largely present, certain mathematical operations required for multi-step engineering calculations may pose challenges for some students.

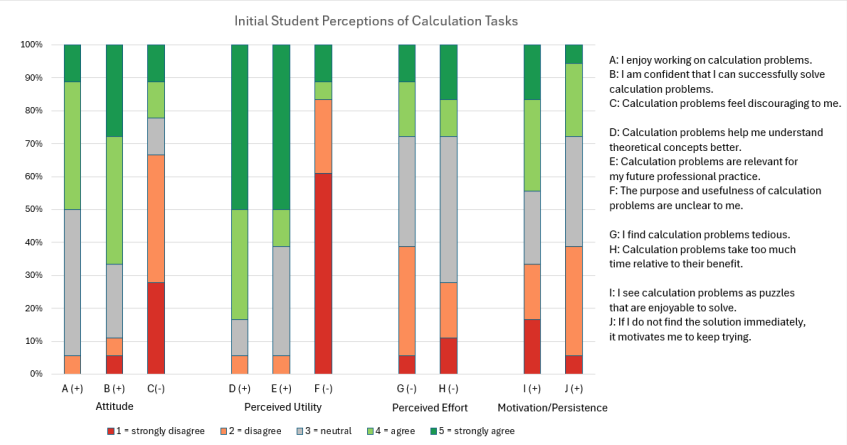

Figure 1: Initial student perceptions of calculation tasks measured on a five-point Likert scale (1 = strongly disagree, 5 = strongly agree). Items are grouped into four dimensions: attitude toward calculation tasks, perceived utility and relevance, perceived effort, and motivation/persistence (N=18).

3.2 Sources of perceived difficulty

To better understand why calculation tasks are experienced as demanding, the questionnaire included a filter question asking whether students generally perceive such tasks as tedious. Sixteen students responded "yes" or "sometimes" and two selected "no". Depending on their response, students completed different follow-up items addressing possible sources of difficulty. Figure 2 summarizes the responses of the "yes/sometimes" group, which represents the large majority of participants.

The results indicate that the perceived difficulty of calculation tasks is primarily associated with challenges in structuring complex solution processes. Higher levels of agreement were observed for statements describing difficulties in identifying appropriate formulas or solution strategies and in keeping track of multiple intermediate steps. Students also reported challenges when several conceptual elements needed to be combined within a single problem.

Emotional factors such as stress, fear of making mistakes, or loss of motivation showed comparatively low levels of agreement. Similarly, students generally did not report that the purpose or practical relevance of calculation tasks was unclear. These patterns suggest that the perceived burden of calculation tasks is l related to negative attitudes or lack of perceived usefulness and more closely associated with the cognitive demands of organizing multi-step reasoning processes.

Overall, the results suggest that the perceived burden of calculation tasks is primarily linked to the challenge of structuring complex solution processes rather than to isolated conceptual or motivational barriers.

3.3 Student-generated artifacts and learning processes

Student-generated artifacts collected during the semester provide further insight into how students engaged with calculation tasks. Padlet reflections and written reflections revealed several recurring themes.

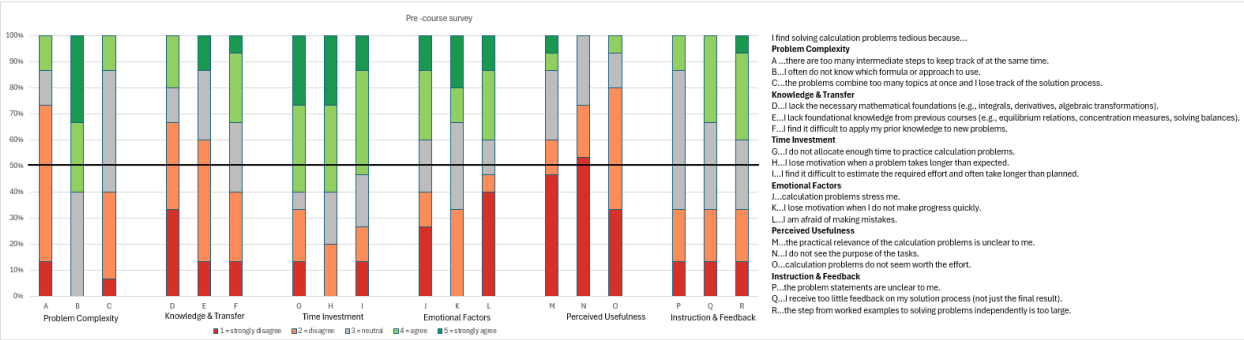

Figure 2: Reported sources of perceived difficulty when solving calculation tasks on a five-point Likert scale (1 = strongly disagree, 5 = strongly agree).

First, many contributions documented conceptual “AHA moments” in which students connected calculation procedures with underlying physical principles of separation processes. Examples included recognizing relationships between concentration and pressure, understanding the interpretation of equilibrium lines in absorption processes, and identifying analogies between heat and mass transfer correlations.
Second, reflections frequently highlighted difficulties related to structuring solution strategies. Students described uncertainty about selecting appropriate balances, formulas, or intermediate steps, confirming the patterns observed in the survey.
Third, several reflections emphasized the importance of graphical representations, such as McCabe–Thiele diagrams or triangular phase diagrams, which helped students relate numerical calculations to physical interpretation of processes.
Finally, many reflections illustrated iterative learning processes in which students refined their understanding through repeated attempts and error correction.

3.4 Perceived support for learning calculation tasks

Open-ended responses in the final questionnaire provide additional insights into which elements of the course students perceived as most helpful. A large proportion of students explicitly highlighted the instructional videos as the most important support for understanding calculation tasks. Many responses emphasized that step-by-step explanations in the videos helped clarify intermediate solution steps and allowed students to revisit complex calculations at their own pace.
Students also frequently mentioned the structured progression of examples and the opportunity to practice similar problems as helpful for developing routine and confidence when solving calculation tasks.
In contrast, the reflection activities and the calculation portfolio were perceived as moderately helpful. While several students reported that these elements encouraged them to engage more regularly with calculation tasks during the semester, they were less frequently described as direct support for understanding solution strategies.

3.5 Summary of key findings

Taken together, the results reveal four central findings.
First, students generally recognize the importance and usefulness of calculation tasks for understanding theoretical concepts in engineering courses.
Second, calculation tasks are frequently experienced as cognitively demanding.
Third, the perceived difficulty appears to be primarily related to structuring complex solution strategies rather than performing mathematical operations.
Finally, student-generated artifacts reveal that engaging with calculation tasks can trigger conceptual insights and iterative reasoning processes, particularly when supported by structured explanations and worked examples such as instructional videos.

4. Discussion

The results reveal an interesting discrepancy between students' perceptions of the learning activities and the learning processes observable in the student-generated artifacts. In the survey responses, students reported only moderate perceived benefits of the reflection activities and the calculation portfolio. Many students primarily valued the portfolio for encouraging continuous engagement with the material throughout the semester rather than explicitly recognizing its role as a learning tool for developing problem-solving strategies. Similarly, reflective tasks were sometimes perceived as additional effort rather than as a direct support for learning. However, the student-generated artifacts collected during the course provide a different perspective. The Padlet reflections and written reflections frequently documented conceptual "AHA moments", connections between theoretical concepts, and iterative reasoning processes while solving calculation tasks. These observations suggest that the reflection activities successfully activated metacognitive processes even when students did not strongly perceive their benefits.

An important finding of this study is that students clearly recognize the value and relevance of calculation tasks for understanding theoretical concepts and for their future professional practice. The perceived burden of calculation tasks therefore does not appear to stem from a lack of perceived usefulness. Instead, the results suggest that the challenge lies primarily in structuring multi-step reasoning processes required for solving complex engineering problems. In other words, students do not reject calculation tasks nor question their relevance; rather, they struggle with structuring the complex reasoning processes required to solve them.

Another important aspect highlighted by the qualitative responses concerns the role of instructional videos. Many students identified the worked-example videos as the most helpful element for understanding calculation tasks. The videos appear to provide essential scaffolding for structuring solution strategies, allowing students to follow complex reasoning processes step by step and revisit explanations when needed. Taken together, the findings suggest that students do not reject calculation tasks nor question their relevance; rather, they struggle with structuring the complex reasoning processes required to solve them. The combination of worked examples, structured practice through the calculation portfolio, and reflective activities appears to support students in engaging with these reasoning processes. While students did not always explicitly perceive the reflective activities as beneficial, the artifacts suggest that these activities nevertheless activated metacognitive processes.

However, the findings should be interpreted with caution, as the study is based on a small cohort (N = 19) from a single course at one institution. Further research across different courses and larger cohorts is required to better understand how reflective practices influence students' experiences with calculation-based learning.

Future work could further investigate how different forms of instructional scaffolding influence students' ability to structure multi-step solution strategies. In particular, it would be interesting to examine whether more explicit guidance in identifying solution strategies and intermediate steps reduces the perceived burden of calculation tasks while maintaining their conceptual learning benefits.

References

Howell, R.A. (2021): Engaging students in education for sustainable development: The benefits of active learning, reflective practices and flipped classroom pedagogies. Journal of Cleaner Production, 325. doi.org/10.1016/j.jclepro.2021.129318

Thai, N.T. T.; Wever, B.; Valcke, M. (2017): The impact of a flipped classroom design on learning performance in higher education: Looking for the best "blend" of lectures and guiding questions with feedback. Computers & Education, 107, 113-126. doi.org/10.1016/j.compedu.2017.01.003

A Multinational Blended-Course on Energy-Efficient Distillation with Mechanical Vapor Recompression

V. López López[1], C. Heine[1], R. Mato[2], L. Vaquerizo[2], J. García-Serna[2], E. Barbera[3], H. Hänninen[4], A. Àgueda[5], V. A. Sangiorgio[6]
[1]Hochschule Kaiserslautern, Kaiserslautern, Germany
[2]Universidad de Valladolid, Valladolid, Spain
[3]Università degli Studi di Padova, Padova, Italy
[4]Turku University of Applied Sciences, Turku, Finland
[5]Universitat Politècnica de Catalunya, Barcelona, Spain
[6]Sulzer Chemtech, Allschwil, Switzerland

Abstract

Training future process engineers requires developing both technical capabilities and essential transversal skills including teamwork, digital proficiency, sustainability consciousness, and cross-cultural understanding. To cultivate these competencies, the collaborative initiative "Decarbonisation Strategies in Process Engineering" was established within the Erasmus Blended Intensive Programmes (BIP) framework, engaging students and faculty from five European institutions.

This BIP centers on mechanical vapor recompression (MVR) for energy efficient distillation processes. Students work in multinational teams of 5 to 6 members to analyze an industrial case study provided by Sulzer Chemtech, comparing conventional distillation energy requirements with MVR enabled configurations using process simulation software. The initiative is structured in two phases: a 7 to 8 week virtual mobility period involving online lectures, simulation training, and remote collaborative project work, followed by a one week in person mobility at Kaiserslautern University of Applied Sciences. The physical phase includes project presentations, industry expert lectures, technical visits to chemical companies, and laboratory activities.

Three editions (2023 to 2025) have engaged 87 students total, with international participation growing from 20 to 24 students per edition. Student feedback has been overwhelmingly positive, with over 95% recommending this BIP. Most valued aspects include engaging with international peers, gaining insight into different educational systems, establishing industry connections, and working on realistic energy integration case studies. This initiative has proven effective in developing both technical and transversal competencies while fostering multi-level collaboration among students and faculty. A fourth edition is planned for summer term 2026.

Keywords

Erasmus, Blended Intensive Programme, mechanical vapor recompression, distillation, process engineering education, international collaboration.

1. Introduction

Successfully addressing the complexities of today's world requires professionals to acquire essential competencies, frequently referred to as future skills [1]. These encompass self-management, teamwork, communication abilities, digital proficiency, sustainability consciousness, analytical thinking, and cross-cultural understanding. Additionally, the training of future process engineers must incorporate environmental and sustainability considerations as fundamental technical capabilities to ensure their capacity to design efficient and responsible processes.

To cultivate these competencies among process engineering students within an international and interdisciplinary learning environment, Erasmus Blended Intensive Programmes (BIPs) offer a promising framework [2]. An Erasmus+ BIP is an innovative short term learning format that combines virtual coursework with a short period of physical mobility, jointly designed and delivered by several European higher education institutions.

The main formal requirements for a BIP include:

- Hybrid structure: Virtual component plus a short physical mobility phase lasting 5 to 30 days
- Consortium-based delivery: At least three universities from three different Erasmus+ Programme Countries
- Academic credit: A minimum of 3 ECTS credits for students
- Group size: Minimum 15 travelling students
- Formal requirements: Inter-institutional Erasmus agreements and a Learning Agreement are required
- Funding model: Sending institutions fund student and staff travel through Erasmus+ mobility grants; the coordinating institution receives organizational support funds up to 8000€

This framework enables institutions to collaborate on specialized topics while providing students with international exposure and hands-on learning opportunities that would be difficult to achieve within traditional single-institution courses.

2. Results and discussion

2.1 Programme Description and Evolution

The collaborative initiative "Decarbonisation Strategies in Process Engineering" was established in 2023 within the Erasmus BIP framework. The programme brings together students and faculty from five European institutions:

- Kaiserslautern University of Applied Sciences (Germany) – coordinating institution
- University of Valladolid (Spain)
- Turku University of Applied Sciences (Finland)
- University of Padua (Italy)
- Polytechnic University of Catalonia (Spain) – incorporated in 2024

The BIP is structured in two complementary phases that combine technical competence development with transversal skills training, aligning with the competencies required to address decarbonisation challenges in the process industry [3].

2.1.1 Phase 1: Virtual Mobility (7-8 weeks)

This phase establishes the technical and organizational foundations for collaborative work. Students are organized into multinational teams of 5 to 6 members, with

deliberate mixing of nationalities to ensure team heterogeneity. The composition of each team also integrates students with different academic backgrounds: some from master programs with prior simulation knowledge, others from bachelor programs, deliberately fostering peer learning.

The technical support structure has evolved significantly across editions. The first edition (2023, using Aveva Process Simulation) included virtual Q&A sessions with designated instructors. With the transition to Aspen Process Simulation in 2024 (provided by Universidad de Valladolid), introductory courses on simulation software were incorporated, with active involvement of teaching staff from Valladolid and Padua. In 2025, refresher lectures (coordinating institution) linking distillation fundamentals with heat pump technology through MVR were added. This collaborative teaching approach strengthens not only the student learning experience but also professional collaboration among faculty from different institutions.

The industrial case study, provided by Sulzer Chemtech, consists of a distillation column separating water and ethanol to concentrations near the azeotrope, including minor components typically found in industrial fermentations. Teams work autonomously to compare the energy requirements of the column operating conventionally versus with mechanical vapor recompression (MVR). This analysis allows students to investigate how MVR technology can significantly reduce energy consumption, contributing to process electrification and thus decarbonisation.

Figure 1: Programme logo schematically illustrating the MVR concept applied to distillation, which forms the technical core of the student case study.

Shared academic IT infrastructure facilitates collaborative work across institutions. Each team is responsible for planning and executing the project autonomously, with instructor support available when needed, thereby strengthening their coordination and organizational capabilities. This phase establishes the technical and organizational foundations for collaborative work.

2.1.2 Phase 2: Physical Mobility (one week in Kaiserslautern)

This phase, funded by the European Union under the BIP framework, includes:

- Project presentations with technical discussions
- Workshop on industrial MVR applications (Sulzer Chemtech)
- Technical visits to leading chemical companies (BASF, Evonik)
- Social and cultural activities

Since 2025, taking advantage of new laboratory facilities at Kaiserslautern University of Applied Sciences, a full day of process engineering laboratory activities has been incorporated, with active participation of teaching staff from collaborating universities. The activities include:

- Combined extraction and distillation processes
- Pump testing station
- Plant design exercises using VR technology

This addition enriches the hands-on learning experience while facilitating direct faculty exchange and collaborative teaching among partner institutions.

2.2 Participation and Growth

The three editions conducted show growth in both participation and scope:

Year	Universities	Countries	Total Students	International Students	International Teaching Staff
2023	4	4	27	20	3
2024	5	4	30	22	5
2025	5	4	30	24	5

Table 1: Participation across three BIP editions

This increase in international diversity reflects the growing interest in this BIP. The minimum participation requirements for BIP status have been consistently exceeded across all editions. Currently, the coordinating institution limits participation to approximately 30 students to ensure effective group dynamics during industry visits, where smaller groups enable more meaningful interaction with company personnel and technical facilities. Since 2025, participants also receive virtual badges as formal recognition of their participation and achievement.

2.3 Student Engagement and Feedback

Student assessment is based on a presentation of project results. An ongoing challenge is identifying the individual work of each participant within the collaborative team environment. However, a notable characteristic of this BIP is that for most students, this course is additional to their regular curriculum and does not count toward their degree grades. Despite this voluntary nature, the engagement level is consistently high, reflecting the genuine interest and motivation of participants.

Student feedback has been overwhelmingly positive, with over 95% of respondents indicating they would recommend this BIP to others. Analysis of feedback reveals that the most valued aspects were:

- Opportunity to engage with peers from diverse countries
- Gaining insight into how process engineering is taught across different educational systems
- Industry connections established during mobility week
- Working on a realistic industrial case study involving energy integration concepts

Students particularly appreciated the combination of technical challenge (realistic MVR case with energy integration) with professional networking and cross-cultural exchange.

2.4 Faculty Engagement Multi-Level Collaboration

Significantly, this BIP fosters collaboration not only at the student level but also among teaching staff from partner institutions. The involvement of faculty from Valladolid and Padua in simulation training courses, and the active participation of teaching staff from all partner universities in the mobility week, creates opportunities for staff mobility and professional exchange. This multi-level collaborative model strengthens inter institutional relationships and enriches the learning environment for all participants.

This initiative has fostered strong personal networks among both students and faculty that support long term professional and cross cultural connections. Three successful editions have established the BIP as an ongoing collaboration among partner universities.

3. Conclusions

The Erasmus BIP *Decarbonisation Strategies in Process Engineering* has proven an effective model for developing both technical and transversal competencies among process engineering students. The combination of remote collaborative work on industrial case studies with in person mobility for industry engagement and cultural exchange creates a learning environment that prepares future engineers for the complex demands of a rapidly changing world.

A notable strength of this initiative is its multi level collaborative nature. Beyond student teamwork, the BIP actively promotes faculty mobility and collaboration among partner institutions. The involvement of teaching staff from multiple universities in simulation training and laboratory sessions enriches the learning experience while simultaneously strengthening professional networks among faculty.

This programme has evolved incrementally since its first edition, incorporating introductory simulation courses (2024) and laboratory sessions with collaborative teaching staff (2025). The sustained high engagement level, despite the voluntary nature of participation for many students, demonstrates the genuine value that participants find in this BIP.

Building on three successful editions, a fourth edition is planned for summer term 2026. The BIP continues to provide engineering students with competencies necessary for addressing sustainability challenges in the process industry, preparing professionals equipped with both technical expertise and essential transversal skills.

Acknowledgements

The authors gratefully acknowledge the support of the European Union through the Erasmus+ programme. Special gratitude to Thomas Raiser in memoriam (Sulzer Chemtech) for initiating this programme initiative.

References

[1] U.F. Ehlers, Future skills: The future of learning and higher education, BoD – Books on Demand, 2020.

[2] European Commission, Blended Intensive Programmes in KA131 Higher Education projects, https://wikis.ec.europa.eu/display/NAITDOC/Blended+Intensive+Programmes+in+KA131+Higher+Education+projects (accessed January 2025).

[3] Cefic – European Chemical Industry Council, European Green Deal, https://cefic.org/ (accessed August 2025).

Rate-Based Modeling and Experimental Validation of a Rotating Packed Bed for CO_2 Chemisorption in Aqueous MEA Solutions

J. Orthey[1], J. Mach[1], F. Gaßdorf[1], G. Brösigke[1], M. Illner[1], J.-U. Repke[1]

[1]Technische Universität Berlin, Process Dynamics and Operations Group, Berlin, Germany

Abstract

A rate-based model for CO_2 chemisorption in aqueous MEA solutions is developed in Aspen Custom Modeler ® (ACM) to investigate the intensified separation performance of Rotating Packed Beds (RPBs) and explore the potential of hybrid configurations with packed columns. Based on the two-film theory, the steady-state model accounts for multicomponent mass transfer and liquid-phase reactions, incorporating Electrolyte-NRTL (eNRTL), and the Maxwell-Stefan approach to describe diffusive fluxes. Doing so relevant phenomena resulting from the superimposed complex force fields, such as centrifugal field and electromagnetic potential and resulting nonlinear transport mechanisms and fast system dynamics due the reaction kinetics are accounted for. Preliminary studies indicate accurate prediction of carbon capture rates under varying liquid-to-gas ratios and lean loadings for two different RPB geometries. Future studies will focus on extensive model validation using pilot-plant data and the coupling of RPBs with conventional packed columns in Aspen Plus®. This allows for the analysis of hybrid RPB–column and identifying energy-efficient and cost-effective operation conditions, as well as experimental validation, using a more rigorous rate-based model formulation than typically applied in the literature.

Keywords

Carbon Capture, Rotating Packed Bed, Process Intensification, Rate-Based Modeling, Aspen Custom Modeler (ACM), Validation

1. Introduction

Despite the rapid expansion of renewable energy capacities, the continued reliance on fossil fuels in the global energy system necessitates effective CO_2 mitigation strategies such as carbon capture, utilization, and storage (CCUS), with solvent-based from flue gas being the most mature and industrially viable option.

Conventional packed-bed (PB) absorption columns are commonly employed in PCC processes. However, they are often characterized by large equipment size and high capital costs. These drawbacks become particularly critical for small and medium scale applications, where economic feasibility is challenged. Process intensification has therefore emerged as a promising strategy to overcome these limitations by enhancing mass transfer performance, reducing equipment size, and enabling more compact and cost-effective CO_2 capture systems, such as offshore installations. [1,3].

RPBs represent a promising process intensification approach for thermal separation and reactive systems and thus particularly for carbon capture by chemical absorption. In contrast to conventional PB columns, where gravity dictates the maximum liquid phase flow, RPBs generate centrifugal acceleration fields up to 1000 times higher than standard gravitational forces. In an RPB, gas–liquid contact occurs within a rotating packing mounted on a circular rotor disk, where centrifugal forces replace gravity as the dominant driving force. Liquid is transported radially outwards through annular packings under centrifugal force, while the gas phase flows counter currently driven by pressure gradients. The centrifugal acceleration results in an intensified environment regarding fluid dynamics with improved liquid distribution and enlarged gas–liquid interfacial area. This results in enhanced gas–liquid mass transfer rates by up to one to three orders of magnitude compared to conventional PBs, yielding a significantly improved CO_2 capture performance [2]. Consequently, RPBs enable substantial reductions in equipment size while allowing for flexible operation by adjustment of the rotational speed and operation at higher flooding limits. Together with the ability to process high-viscosity fluids RPBs are particularly attractive for industrial gas purification processes aiming at reducing greenhouse gas emissions.

For the development and advancement of RPB technology, experimental investigations and mathematical modeling are both mandatory. Experimental investigations under high-gravity conditions are inherently complex and time-consuming and, when considered alone, are often insufficient to fully resolve the detailed interactions between complex fluid-dynamic phenomena, mass transfer, and chemical reaction kinetics occurring within RPBs. Therefore, rigorously developed and experimentally validated process models and simulation frameworks are required to enable systematic process analysis, optimization, design, and scale-up by providing insight into the influence of operating conditions, solvent properties, and RPB design parameters.

Table 1: Overview of selected literature studies regarding the modeling and simulation of the chemical absorption processes in RPBs in Aspen.

Reference	Description	Solvent
Joel et al. [2014] [4]	Aspen Plus® simulation of chemical absorption with embedded mass transfer subroutines; validated using experimental data (Jassim, 2002; Jassim et al., 2007).	MEA at 55 to 75% weight.
Thiels et al. [2016] [5]	Chemical CO_2 absorption in conventional and rotating packed bed columns modeled in Aspen Custom Modeler® and validated using experimental data and literature results from Jassim et al. (2007).	MEA at 30 w.%
Otitoju, Wang [2023] [6]	Rate-based RPB absorber model developed in Aspen Custom Modeler® and integrated into Aspen Plus® for MEA-based post-combustion CO_2 capture and process optimization.	MEA at 30 wt% to 80 wt%.

Several studies on modeling chemical absorption in RPBs have been reported in literature [4–6] (Table 1). However, most existing studies rely on simplified or semi-empirical frameworks and therefore lack a detailed, physics-based description of the

coupled fluid dynamics, mass transfer, and reaction phenomena within the rotating packing. In contrast to approaches based on constant enhancement factors or correlation adjustments via Aspen Fortran scripts, the present work employs a fully rate-based modeling framework based on the Maxwell–Stefan formulation, implemented in Aspen Custom Modeler. The model framework is the cornerstone for further assessment of hybrid process configurations also deploying packed bed columns with the goal to minimize specific costs of CO_2 capture. With identifying suitable operation regions for RPB and columns for absorption and desorption, respectively, optimal hybrid configurations are designed and further on validated experimentally.

2. Results and discussion

2.1 Model Development

A rate-based model for the chemisorption of CO_2 in aqueous MEA solutions is developed, with particular emphasis on mass transfer enhancement through chemical reaction. The two-film theory is employed to account for non-equilibrium effects and to describe the coupled transport and reaction processes. Designed for steady-state operations, the model considers all relevant species, including gas components/Henry components (N_2, CO_2, O_2), solvents (MEA, H_2O) and ionic species stemming from liquid-phase reactions. Selected reactions are treated kinetically to explicitly capture rate-limiting effects governing reactive mass transfer.

Table 2: Liquid-phase reaction network considered in the rate-based CO_2–MEA model [7].

Equilibrium Reactions	Kinetic Reactions
q_1:$MEAH^+ + H_2O \rightleftharpoons MEA + H_3O^+$	k_1:$CO_2 + OH^- \rightarrow HCO_3^-$
q_2:$2H_2O \rightleftharpoons H_3O^+ + OH^-$	k_2:$HCO_3^- \rightarrow CO_2 + OH^-$
q_3:$HCO_3^- + H_2O \rightleftharpoons CO_3^{2-} + H_3O^+$	k_3:$MEA + CO_2 + H_2O \rightarrow MEACOO^- + H_3O^+$
	k_4:$MEACOO^- + H_3O^+ \rightarrow MEA + CO_2 + H_2O$

The model incorporates multicomponent mass transfer [8], equilibrium and kinetic reactions in the liquid phase (Table 2), and mass transfer resistances in both phases. The gas phase assumes non ideal gas behavior (Redlich–Kwong), while the liquid phase accounts for non-idealities using activity coefficients calculated via the eNRTL model. Conventional models for mass transfer, often based on Fick's law, lack validity in scenarios involving non-linear and coupled force fields like those in centrifugal fields and electromagnetic force fields. To overcome this hurdle, the Maxwell-Stefan approach [9] is applied to describe multicomponent diffusion and mass transfer, allowing for a rigorous representation of coupled transport phenomena in non-ideal mixtures. Specifically, the molar flux of a component is expressed in the k-formulation as:

$$N_i = -c_t[k](\Delta x) + x_i N_t = -c_t([R]^{-1}[\Gamma])(\Delta x) + x_i N_t$$

where N_i is the molar flux of component i, c_t is the total molar concentration, x_i is the mole fraction, N_t is the total molar flux, k is the Maxwell–Stefan diffusivity matrix, R is the resistance matrix, and Γ is the thermodynamic factor matrix. While phase equilibria are described using the eNRTL model, the Maxwell–Stefan equations currently assume an ideal liquid phase, with the thermodynamic factor matrix simplified to the identity matrix. The liquid holdup is calculated using the correlation of Yang [10], while the effective interfacial area is determined from the correlation of

Onda [11]. Gas- and liquid-phase mass transfer coefficients are determined using the correlations of Onda [11] and Tung [12], respectively. The RPB packing is discretized into 20 equidistant radial stages, which was found to be a suitable number based on a grid convergence study. The liquid film is modeled as a planar layer with one film element to capture the dominant interfacial gradients relevant for mass transfer and component-specific liquid-phase reactions.

The model is implemented in Aspen ACM and solved using the integrated Newton Solver for Non-Linear Equation (NLE) systems. ACM is explicitly used to facilitate the commercial deployment of RPBs for absorption processes by making the model available in commercial simulation frameworks. It provides an integrated database of physical and thermodynamic property parameters and supports straightforward implementation of the eNRTL model. In addition, a homotopy-based approach was implemented via a Visual Basic script, enabling efficient initialization of simulations across a wide range of parameter settings, while solution performance exhibits robust convergence behavior for a broad range of initial conditions.

2.2 Experimental Data

The present model is validated against experimental data for the reactive absorption of CO_2 from flue gas using aqueous monoethanolamine (MEA), comprising data from a lab-scale RPB reported by Thiels et al. [5] as well as measurements obtained from a larger scale inhouse pilot-plant:

Thiels et al. [5] deployed a relatively small RPB unit equipped with a wire mesh packing and an inner and outer packing diameter of 25 and 125 mm, respectively, with a packing height of 23 mm. The packing is characterized by a porosity of 0.96 and a specific surface area of 887.6 $m^2\ m^{-3}$. All experiments were performed at a rotational speed of 1600 rpm with gas and liquid inlet temperatures of 50 °C, covering a wide range of liquid-to-gas (L/G) ratios and lean solvent loadings. The inlet gas composition was fixed at 10 mol% CO_2 in N_2. Experiments were conducted using a 30 wt% MEA solution at a constant liquid flow rate of 0.1 L min^{-1}, while gas flow rates ranged from 0 to 60 L min^{-1}. Lean solvent loadings of X_{CO_2} = 0, 0.157, 0.249, 0.380, and 0.442 mol CO_2 mol^{-1} MEA were investigated, corresponding to a liquid load of 3.3 $m^3\ (m^2\ h)^{-1}$, F-factors between 0.05 and 0.58 $Pa^{0,5}$, and mass-based L/G ratios from 18 to 1.5.

The inhouse pilot-plant comprises two RPBs, operated as absorber and stripper units, respectively, with thermal solvent regeneration provided by a kettle reboiler. Both RPBs are equipped with NC 1116 metal foam packing, characterized by an average specific surface area of 1000 $m^2\ m^{-3}$ and a porosity of 92.2%. The rotor has an inner diameter of 160 mm, an outer diameter of 540 mm, and a height of 30 mm. Liquid distribution in each RPB is achieved using two flat-spray nozzles. The pilot plant is designed for continuous operation with full solvent regeneration and integrated heat recovery, enabling absorption and desorption experiments in a closed loop. The mini-plant is installed at an industrial site, processing flue gas from a cement production facility. For modeling purposes, the real flue gas is abstracted to the main modeled gas components (N_2, O_2, H_2O, CO_2. During the first experimental campaign, the absorber RPB was operated at an absolute pressure of 1 bar, while the stripper was operated at 2 bar. All experiments were conducted at a rotational speed of 800 rpm for both RPBs. The solvent inlet temperature was maintained at approximately 40 °C. Experiments were conducted using a 30 wt.% MEA solution at a constant liquid flow rate of 117 kg h^{-1}, while gas flow rates was 25, 40, 55 kg h^{-1}. A

liquid loading of 8.3 m³ m⁻² h⁻¹ was investigated, while the gas flow rate was adjusted to obtain F-factors of 0.42, 0.68, and 0.93 $Pa^{0.5}$. The lean solvent entering the absorber had a CO_2 loading of X_{CO_2}= 0.3 mol CO_2 mol⁻¹ MEA. The stripper regeneration temperature was set to 120 °C. Due to the on-site installation, gas inlet temperatures varied with 28.9, 20.9 and 30.3 °C.

2.2 Simulation Results

The results of the model validation study are presented in Figure 1. The experimental measurements reported by Thiels et al. [5], shown in Figure 1(a), reveal two trends: CO_2 removal decreases with increasing gas throughput as well as with increasing lean solvent loading. These trends are consistently captured by the model. The quantitative agreement between model predictions and experimental data, assessed using the root mean square error (RMSE) over the range of investigated lean loadings, yields values between 5.47% at X_{CO_2}= 0.380 and 16.41% at X_{CO_2}= 0.442.

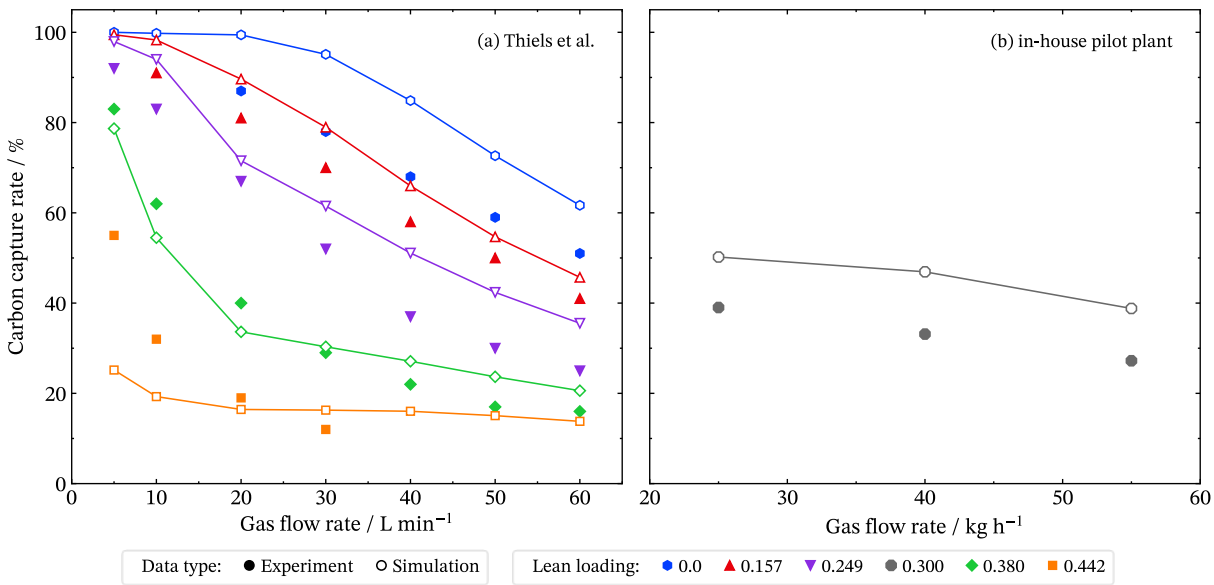

Figure 1 Comparison experimental data with ACM Simulation. Left data of M. Thiels et al. [5], right inhouse data. Carbon capture rate (CCR) is calculated: CCR = 1 - $y_{CO_2,out}/y_{CO_2,in}$.

As shown in Figure 1(b), the simulation results for the inhouse pilot-plant capture the trends observed in the experimental campaign. For the inhouse experiments, a quantitative comparison between model predictions and experimental data yields a RMSE of 12.25% based on three data points. This level of deviation indicates a moderate discrepancy, with the model exhibiting a systematic overprediction of the experimental values.

These discrepancies are mainly attributed to the currently neglected thermodynamic factor matrix Γ, as this results in not representing non-ideal liquid-phase interactions. Given the observed sensitivity to liquid-phase resistance, the inclusion of non-ideality effects is expected to further improve model accuracy and constitutes a key motivation for further model development. In addition, the experiments by Thiels et al. [5] were conducted in a very small lab-scale RPB, for which the so-called inner end effect zone with a maximum in gas-liquid interaction and thus local mass transfer performance exerts a disproportionately large influence due to the limited radial extent of the packing. This also highlights the importance of suitable correlations for mass transfer, interfacial area, and hold-up to be available for the given RPB rotor

type and dimensions. These correlations are currently under development and will be presented at the conference.

3. Conclusions

RPBs represent a promising process intensification technology for CO_2 absorption due to their high mass transfer efficiency and compact design: Their effective application however requires rigorously developed and experimentally validated process models. In this work, a detailed rate-based model for CO_2 absorption in an RPB was developed, incorporating two-film mass transfer, reaction kinetics, and non-ideal thermodynamics for phase equilibria. The model was validated against experimental data from Thiels et al. [5] and an inhouse pilot-plant with real complex flue gas, demonstrating its ability to capture the trends in RPB systems. Further validation and refinement of the model will be performed using pilot-plant experimental data from an inhouse RPB pilot plant operated under well-defined and application-relevant conditions. Beyond standalone RPB operation, the validated model will be extended to hybrid process concepts combining RPBs with conventional packed columns. These hybrid configurations will be investigated using Aspen Plus® simulations and validated against experimental results to assess their potential for intensified and energy-efficient CO_2 absorption processes.

Acknowledgements

This research was supported by funding from the Federal Ministry for Economic Affairs and Climate Action of Germany under project code 03EE5103C. The author gratefully acknowledges the financial support provided.

References

[1] Oko, Eni, Meihong Wang, und Atuman S. Joel. „Current Status and Future Development of Solvent-Based Carbon Capture." (2017) https://doi.org/10.1007/s40789-017-0159-0

[2] Zhang W., Li X., Fu C., Huang B., Li Y., Xie P. "CFD Modeling of Reactive Absorption of CO2 by Aqueous MEA Solution in a Rotating Packed Bed". (2024) https://doi.org/10.1021/acs.energyfuels.4c01409

[3] C. Shukla, P. Mishra, and S. K. Dash, "A review of process intensified CO2 capture in RPB for sustainability and contribution to industrial net zero." (2023) https://doi.org/10.3389/fenrg.2023.1135188

[4] Joel, Atuman S., Meihong Wang, Colin Ramshaw, und Eni Oko. „Process Analysis of Intensified Absorber for Post-Combustion CO2 Capture through Modelling and Simulation ". (2014) https://doi.org/10.1016/j.ijggc.2013.12.005

[5] M. Thiels, D. S. H. Wong, C.-H. Yu, J.-L. Kang, S. S. Jang, and C.-S. Tan, "Modelling and design of carbon dioxide absorption in rotating packed bed and packed column." (2016) https://doi.org/10.1016/j.ifacol.2016.07.303

[6] Otitoju, Olajide, Eni Oko, und Meihong Wang. „Modelling, Scale-up and Techno-Economic Assessment of Rotating Packed Bed Absorber for CO2 Capture from a 250 MWe Combined Cycle Gas Turbine Power Plant." (2023) https://doi.org/10.1016/j.apenergy.2023.120747

[7] Aspen Technology, Inc. (2014): "Rate-Based Model of the CO2 Capture Process by MEA using Aspen Plus". Version V10

[8] R. Krishnamurthy and R. Taylor, "A nonequilibrium stage model of multicomponent separation processes. Part I: Model description and method of solution." (1985) https://doi.org/10.1002/aic.690310312

[9] R. Krishna and J. A. Wesselingh, "The Maxwell-Stefan approach to mass transfer," (1997), https://doi.org/10.1016/S0009-2509(96)00458-7

[10] Y. Yang et al., "A noninvasive X-ray technique for determination of liquid holdup in a rotating packed bed," (2015) https://doi.org/10.1016/j.ces.2015.07.044

[11] K. Onda, H. Takeuchi, and Y. Okumoto, "MASS TRANSFER COEFFICIENTS BETWEEN GAS AND LIQUID PHASES IN PACKED COLUMNS." (1968) https://doi.org/10.1252/jcej.1.56

[12] H.-H. Tung and R. S. H. Mah, "MODELING LIQUID MASS TRANSFER IN HIGEE SEPARATION PROCESS." (1985) https://doi.org/10.1080/00986448508911667

Experimental and Modeling-based Scale-Up of Rotating Packed Beds for Industrial CO_2 Capture

Je Young Kim[1], Nguyen Van Duc Long[2,3], Nhu Nga Nguyen[4], Choongyong Kwag[1], Hong Kyu Park[1], Dongyoung Lee[1], Youngmok Lee[1], Sungwon Lee[1]
[1]Hanbal Masstech, Ltd., Gimhae 50969, Republic of Korea;
[2]School of Chemical Engineering, Adelaide University, Australia;
[3]School of Engineering, University of Warwick, United Kingdom;
[4]School of Chemical Engineering, Yeungnam University, Gyeongsan 38541, Republic of Korea

Abstract
Carbon capture is a leading solution for reducing greenhouse gas emissions, with absorption being the most widely used method due to its maturity, flexibility, and compatibility with pre-combustion, post-combustion, and oxy-fuel processes. However, traditional absorption systems face challenges such as limited vapor capacity, corrosion, solvent degradation, high regeneration energy demand, and large equipment size. To address these issues, industries are adopting advanced process modifications, integration techniques, and intensification methods, including rotating packed beds (RPBs) that use centrifugal force to improve mass transfer and handle higher-viscosity solvents. RPB technology, in particular, enables thinner liquid films, smaller droplets, and higher solvent concentrations, offering a path to more compact, energy-efficient CO_2 capture systems. There is a strong need to develop industrial-scale RPBs design for large-scale CO_2 capture applications. In this work, two approaches are proposed: (1) conducting lab-scale RPB experiments followed by scale-up using similarity theory, and (2) developing a process model in Aspen Custom Modeler (ACM). Experimental results show that 90% CO_2 removal can be achieved at a liquid-to-gas ratio (Q_L/Q_G) of 10 L/m^3 using a 50% MEA solvent. Scale-up studies indicate that the RPB volume can be reduced by a factor of 6.4–11.2 compared to a conventional absorber with identical Q_L/Q_G ratios, CO_2 removal efficiency (HETP: 0.2–0.35 m). Moreover, our ACM model provides higher accuracy than that reported by Otitoju, with CO_2 removal efficiencies of 89.9% (experiment), 91.6% (our model), and 93.6% (Otitoju's model).

Keywords
CO_2 capture; Experiment; Rotating packed beds; RPBs; Scale-up; Process modeling.

1. Introduction

The rapid growth of industry together with the continuous increase in the world's population is placing unprecedented pressure on the environment, primarily through rising greenhouse gas (GHG) emissions that drive climate change. Hence, to address these alarming trends, embracing and advancing a sustainable environment becomes imperative. Carbon capture stands out as one of the most effective means to mitigate GHG emissions. Among the available CO_2 mitigation technologies, gas-liquid absorption remains the most widely applied and technologically mature option, owing to its flexibility and proven performance in pre-combustion, post-combustion,

and oxy-fuel capture processes. Its robustness and ability to operate under a broad range of conditions make absorption the current benchmark for large-scale CO_2 separation [1]. Despite these advantages, conventional absorption systems suffer from several inherent limitations, including restricted mass-transfer capacity, high corrosion rates, solvent degradation, large energy demand for solvent regeneration, and large equipment requirements [2]. Consequently, process industries have been actively exploring advanced and intensified configurations to overcome these challenges.

A wide range of solutions has been proposed to overcome the inherent limitations of conventional carbon capture processes, including process modification technologies, such as utilizing alternative solvents like phase change-solvent, optimizing operating temperature and pressure conditions, employing high-performance internals in columns, incorporating intercoolers, interheaters, and flue gas pre-coolers, as well as adopting flue gas compression and expansion, multiple feeds, semi-lean solvent configurations, rich solvent recycling schemes, and square columns [3]. In parallel, process integration concepts, including heat pumps and self-heat recuperation systems [4], have been explored to reduce overall energy consumption. Beyond these incremental improvements, process intensification, such as swirling gas flow [5], and rotating packed beds (RPBs) [6], offers a transformative pathway toward more compact, safer, and energy-efficient capture technologies.

Recently, RPBs have attracted increasing attention as a promising technology for process intensification. By generating a strong centrifugal field, RPBs significantly enhance phase contact, leading to markedly improved mass-transfer performance. In particular, the centrifugal force reduces liquid film thickness and breaks the liquid into finer droplets within the packing, thereby enlarging the effective gas-liquid and liquid-solid interfacial areas [13]. Figure 1a illustrates the basic configuration of a single-block RPB. The liquid is introduced at the centre of the rotor through a distributor and is driven radially outward across the packing by centrifugal acceleration. For counter-current operation, the gas is introduced at the outer casing and flows radially inward through the rotating packing under an imposed pressure gradient. The axial width of the rotor (h) primarily governs the throughput capacity, while the radial distance between the inner and outer radius (r_i and r_o) determines the available contact area and thus the mass-transfer capacity of the RPB [14].

(a) (b)

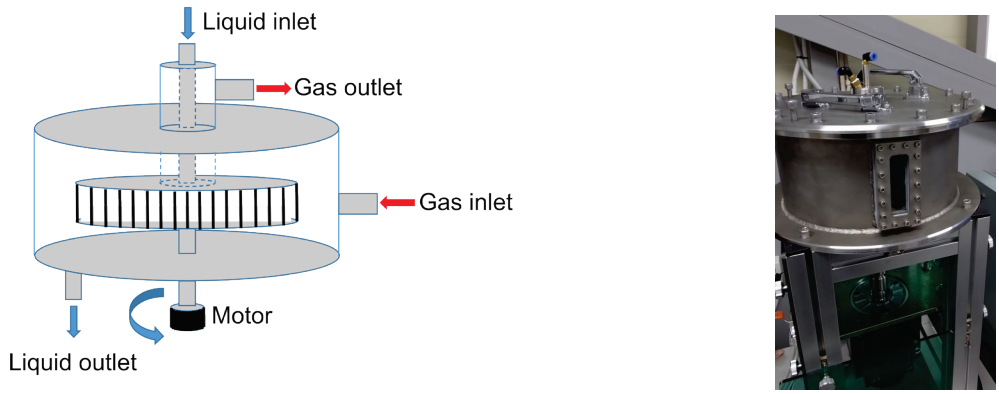

Figure 1. (a) Conceptual diagram of a RPB absorber; (b) RPB unit.

The key advantages of RPBs arise from the intense centrifugal field generated by rotation, which markedly enhances mass-transfer rates by increasing the gas–liquid interfacial area and thinning the liquid film within the packing [7, 8]. As a result, the required packed volume can be substantially reduced compared with conventional

columns [8]. Rotation also enables the efficient handling of more viscous solvents, such as highly concentrated MEA, allowing lower solvent circulation rates and consequently reduced regeneration and pumping (and, in some cases, rotational) energy demands [9]. Nevertheless, the overall energy consumption of an RPB system can exceed that of a conventional packed column due to the additional power required to drive the rotor [8]. Despite this, RPBs show strong potential for post-combustion CO_2 capture from flue gas, where their intensified mass-transfer performance can significantly decrease the size of both absorbers and strippers.
To enable their practical deployment, robust design and scale-up methodologies for industrial-scale RPBs are urgently needed. In this work, two complementary approaches are proposed: (1) performing laboratory-scale RPB experiments followed by scale-up based on similarity theory, and (2) developing a rigorous process model using Aspen Custom Modeler (ACM) to support design, simulation, and performance prediction for large-scale CO_2 capture applications.

2. Methodologies

2.1. Lab-scale experiment

The experimental system employed an aqueous monoethanolamine (MEA) solution and a CO_2-N_2 gas mixture. A 50 wt.% MEA solution was prepared using distilled water, while gas mixtures with controlled compositions of CO_2 and N_2 were supplied to simulate flue gas conditions. As illustrated in Figure 1b, the RPB unit operates with lean MEA entering the rotor for CO_2 absorption, and rich MEA leaving the unit after capturing CO_2. In the absorption experiments, the flue gas from a coal-fired power plant was represented by a mixture containing 10% CO_2 and 90% N_2. The CO_2 concentration at the inlet and outlet of the RPB was measured using a portable gas analyser GASTiger 2000, allowing direct evaluation of the capture performance.

2.2. Scale-up using similarity theory

The scale-up of the RPB was carried out based on similarity theory and dimensional analysis. According to Zlokarnik [10], reliable scale-up requires maintaining geometric similarity and matching the key governing dimensionless groups between the laboratory-scale and industrial-scale systems. However, for complex multiphase processes, strict similarity is often impractical, and scale-up is therefore typically based on partial similarity. In this study, the main similarity criteria considered were the gas residence time in the contactor, the gas-to-liquid flow rate ratio, the ratio of column diameter to column height, and the specific surface area of the packing. Preserving these parameters during scale-up ensures that the hydrodynamic and mass-transfer characteristics of the RPB are reasonably maintained from the lab scale to the larger scale design.

2.3. Model assumptions

To develop a reliable model for the RPB absorber, the following assumptions were adopted based on Ref. [11]:

- Steady-state operation is assumed.
- The gas phase behaves as an ideal gas.
- The vapor phase consists of CO_2, H_2O, N_2 and MEA.
- One-dimensional differential mass and energy balances are applied to both the gas and liquid phases.
- Fluid flow is considered only in the radial direction.
- All chemical reactions occur within the liquid film and are incorporated through an enhancement factor.

- The liquid phase comprises CO_2, H_2O, N_2, MEA, OH^-, H_3O^+, HCO_3^-, CO_3^{2-}, $MEAH^+$, and $MEACOO^-$
- Only CO_2, H_2O, N_2 and MEA participate in interphase mass transfer.
- Heat losses to the surroundings are neglected.

In the RPB, the gas and liquid phases operate in a counter-current radial flow arrangement [11]. The gas enters at the outer radius r_o and moves radially inward toward the inner radius r_i, while the liquid is introduced at the inner radius and flows outward toward the outer radius. Accordingly, the absorber is described by a one-dimensional radial domain extending from r_i to r_o, which defines the spatial variation of all model variables.

The mathematical model consists of a set of coupled algebraic and partial differential equations. These equations are solved numerically by discretising the radial domain into 20 finite elements (21 nodes) using a first-order backward finite difference method (BFDM). Node 0 corresponds to the inner radius r_i, and node 20 represents the outer radius r_o. The complete set of governing equations is reported in Ref. [11]. ACM was employed to implement and solve the RPB model.

3. Results and discussion

3.1. Experiment results

The effects of solvent flow rate and rotational speed on CO_2 recovery from flue gas were investigated by varying both parameters over a wide operating range. In addition, two RPB units with different geometries and packing configurations were tested. RPB1 had an outer radius r_o of 0.06 m, an inner radius r_i of 0.02 m, and an axial height h of 0.03 m, whereas RPB2 had a larger outer radius of 0.08 m, the same inner radius of 0.02 m, and a greater axial height of 0.06 m. To achieve an identical CO_2 removal efficiency of 90%, RPB1 required a rotational speed of 2400 rpm, while RPB2 achieved the same performance at a lower speed of 1200 rpm, reflecting the increased contact area and residence time provided by the larger rotor.

Several types of packing, including random packing, wire mesh, two-strand wire mesh, and nickel foam, were evaluated. Among them, the two-strand wire mesh demonstrated the highest CO_2 removal efficiency at a rotational speed of 1200 rpm using 50 wt.% MEA. Nickel foam also exhibited good mass-transfer performance; however, its high cost (approximately five times that of wire mesh) and the difficulty associated with its fabrication limit its practical application.

Compared with conventional wire mesh, the two-strand wire mesh offers higher packing density and a larger specific surface area, while remaining significantly cheaper and easier to manufacture than nickel foam. For these reasons, the two-strand wire mesh was selected as the optimal packing material for the RPB and was used for comparison with a conventional absorber. The specific surface area and porosity of the two-strand wire mesh are 2787.5 m^2/m^3 and 91.6%, respectively.

3.2. Calculation results

Mass transfer in an RPB is significantly intensified by the strong centrifugal field, which enhances phase mixing and increases the effective interfacial area. At the same time, rotation has a subtantial influence on the hydrodynamics of the system. Consequently, a key objective of both the experimental study and the modelling work is to quantify the effect of rotational speed on flooding behaviour and the corresponding flooding gas velocity. As shown in Figure 2, increasing the rotor speed results in a higher superficial gas velocity at flooding. This highlights one of the major operational advantages of RPBs: they can be operated at much higher gas and/or liquid throughputs than conventional packed columns, since the intensified centrifugal

field suppresses liquid holdup and delays the onset of flooding at higher rotational speeds.

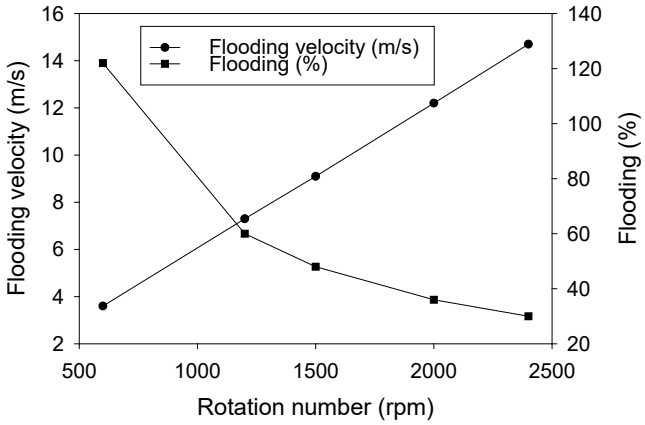

Figure 2. Effect of the rotation speed on the flooding velocity and flooding.

For a scale-up factor of 10, the liquid (L) and gas (G) flow rates were adjusted to maintain the same L/G ratio and a flooding level of 80% at a rotational speed of 1200 rpm for the large-scale RPB. Once the corresponding L and G values satisfying these conditions were obtained, they were used as input to simulate a conventional packed absorber in Aspen HYSYS. Both the RPB and the conventional column were operated with the same solvent composition (50 wt.% MEA in water), identical L/G ratios, and the same target CO2 removal efficiency. Under these equivalent operating conditions, the results indicate that the required reactor volume of the RPB can be reduced by a factor of 6.4-11.2 compared with that of a conventional packed absorber, assuming a height equivalent to a theoretical plate (HETP) in the range of 0.2–0.35 m.

3.3. Modeling results

The developed model was validated by comparing the results from the numerical model reported by Otitoju [11] and the experimental data of Jassim et al. [12], obtained using an RPB with an inner diameter of 0.156 m, an outer diameter of 0.396 m, and an axial height of 0.025 m. The CO_2 absorption simulation was conducted with a lean MEA solution at an average concentration of 55 wt.% and a liquid mass flow rate of 0.35 kg/s. The flue gas was supplied at a flow rate of 2.87 kmol/h and a temperature of 283.15 K, while the rotor was operated at a rotational speed of 1000 rpm.

Under these conditions, the experimental CO_2 removal efficiency was 89.9% [12]. The present model predicted a capture efficiency of 91.6%, which is in closer agreement with the experimental data than the value of 93.6% reported by Otitoju [11]. This improved predictive accuracy demonstrates the reliability of the proposed model. Moreover, such model-based investigations can significantly reduce both time and cost compared with extensive laboratory-scale experimentation, making them highly attractive for design, optimisation, and scale-up of RPB-based CO_2 capture systems.

4. Conclusions

The two-strand wire mesh, which offers higher packing density and larger specific surface area than conventional wire mesh, demonstrated superior performance while remaining significantly cheaper and easier to fabricate than nickel foam. Experimental results showed that a CO_2 removal efficiency of 90% could be achieved at a liquid-to-gas ratio (Q_L/Q_G) of 10 L/m^3 using a 50 wt.% MEA solution. Scale-up

analysis further indicated that, for the same L/G ratio and CO_2 removal efficiency, the required volume of an RPB can be reduced by a factor of 6.4-11.2 compared with a conventional packed absorber, corresponding to a height equivalent to a theoretical plate (HETP) in the range of 0.2–0.35 m. In addition, the developed ACM model was shown to predict CO_2 capture performance with high accuracy. Specifically, while the experimental removal efficiency was 89.9%, the present model predicted 91.6%, which is in closer agreement with the experimental data than the value of 93.6% reported by Otitoju's model.

Acknowledgements

The authors acknowledge the support from the Korea Institute of Energy Technology Evaluation and Planning (KETEP) funded by the Ministry of Trade, Industry and Energy (MOTIE) (No. 20224C10300050).

References

[1] U. Khan, C.C. Ogbaga, O.-A.O. Abiodun, A.A. Adeleke, P.P. Ikubanni, P.U. Okoye, J.A. Okolie, Assessing absorption-based CO2 capture: Research progress and techno-economic assessment overview, Carbon Capture Science & Technology 8 (2023) 100125. https://doi.org/https://doi.org/10.1016/j.ccst.2023.100125.

[2] N.V.D. Long, D.Y. Lee, C. Kwag, Y.M. Lee, S.W. Lee, V. Hessel, M. Lee, Improvement of marine carbon capture onboard diesel fueled ships, Chemical Engineering and Processing - Process Intensification 168 (2021) 108535. https://doi.org/https://doi.org/10.1016/j.cep.2021.108535.

[3] N.V.D. Long, D.Y. Lee, C. Kwag, Y.M. Lee, S.W. Lee, D. Lewis, E. Rebrov, V. Hessel, M. Lee, Removal of marine NOx, SOx, and CO2 from flue gas: Simulation and experiment on a pilot plant, Separation and Purification Technology 359 (2025) 130558. https://doi.org/https://doi.org/10.1016/j.seppur.2024.130558.

[4] N. Van Duc Long, M. Lee, Novel acid gas removal process based on self-heat recuperation technology, International Journal of Greenhouse Gas Control 64 (2017) 34-42. https://doi.org/https://doi.org/10.1016/j.ijggc.2017.07.003.

[5] K.H. Javed, T. Mahmud, E. Purba, Enhancement of Mass Transfer in a Spray Tower Using Swirling Gas Flow, Chemical Engineering Research and Design 84(6) (2006) 465-477. https://doi.org/https://doi.org/10.1205/cherd.05119.

[6] C.-C. Lin, W.-T. Liu, C.-S. Tan, Removal of Carbon Dioxide by Absorption in a Rotating Packed Bed, Industrial & Engineering Chemistry Research 42(11) (2003) 2381-2386. https://doi.org/10.1021/ie020669+.

[7] C. Ramshaw, HIGEE Distillation-An Example of Process Intensification, Chem. Engr. 389 (1983) 13-14.

[8] D. Im, H. Jung, J.H. Lee, Modeling, simulation and optimization of the rotating packed bed (RPB) absorber and stripper for MEA-based carbon capture, Computers & Chemical Engineering 143 (2020) 107102. https://doi.org/https://doi.org/10.1016/j.compchemeng.2020.107102.

[9] M.S. Jassim, Process intensification: absorption and desorption of carbon dioxide from monoethanolamine solutions using Higee technology, Newcastle University, 2002.

[10] M. Zlokarnik, Similarity and scale-up, in: M. Zlokarnik (Ed.), Dimensional Analysis and Scale-up in Chemical Engineering, Springer Berlin Heidelberg, Berlin, Heidelberg, 1991, pp. 39-50. https://doi.org/10.1007/978-3-642-76673-2_4.

[11] O. Otitoju, E. Oko, M. Wang, Modelling, scale-up and techno-economic assessment of rotating packed bed absorber for CO2 capture from a 250 MWe combined cycle gas turbine power plant, Applied Energy 335 (2023) 120747. https://doi.org/https://doi.org/10.1016/j.apenergy.2023.120747.

[12] M.S. Jassim, G. Rochelle, D. Eimer, C. Ramshaw, Carbon Dioxide Absorption and Desorption in Aqueous Monoethanolamine Solutions in a Rotating Packed Bed, Industrial & Engineering Chemistry Research 46(9) (2007) 2823-2833. https://doi.org/10.1021/ie051104r.

Novel anisotropic T-S structured packing for improved hydrodynamic performance in Rotating Packed Bed.

Viraj Santosh Pawar[1], Thibaut Triquet[1], David Rouzineau[1], Michel Meyer[1]

[1]Chemical Engineering Laboratory, University of Toulouse, CNRS, INPT, UPS, Toulouse, France.

Process Intensification (PI) aims to overcome the limitations of conventional gravity-driven processes to developed new technologies with higher mass and heart transfer rate, smaller size equipment or lower energy consumption. The High-Gravity (HiGee) technologies have been proved as a prominent approach. Rotating Packed Beds (RPBs) use centrifugal forces to enhance gas–liquid contact, resulting in higher mass transfer rates, compact equipment, and improved efficiency. RPBs are widely applied in CO_2 capture, distillation, and absorption. Hydrodynamic understanding is essential for determining operating limits and energy requirements in RPBs. Conventional isotropic packings, such as wire mesh, are unsuitable due to the radially varying flow area in RPBs. To address this, we have developed an anisotropic 3D-printed packing with four concentric rings of varying void fraction. Comparative studies showed that this packing reduced pressure drop ~3-10 folds across all conditions, with no flooding even at high flow rates. Improved liquid distribution in the inner rings also increased the effective interfacial area, leading to enhanced mass transfer performance.

1. Introduction

Rotating packed beds (RPBs) are centrifugal process intensification devices capable of achieving high gravitational fields, significantly enhancing gas–liquid mass transfer compared to conventional packed columns. Originally proposed by Podbielniak [1] and later developed by Ramshaw and Mallinson [2], RPBs use a porous packing to generate thin liquid films, droplets, and rivulets, resulting in increased interfacial area and compact equipment size. Owing to these advantages, RPBs have been applied in carbon capture, distillation, extraction or nanoparticle synthesis. Despite their superior mass transfer performance, RPBs suffer from high pressure drop and a limited operating window [3]. Pressure drop from the casing, packing, and inner cavity can contribute significantly to overall energy consumption, particularly in gas-handling applications such as CO_2 capture [4]. At elevated gas flow rates or rotational speeds, flooding, characterized by liquid accumulation near the rotor center, leads to a sharp increase in pressure drop and deteriorated performance [5]. These limitations are strongly influenced by packing morphology, which governs liquid distribution, gas–liquid contact, and hydrodynamic resistance. Conventional wire mesh and metal foam packings offer high effective interfacial area but typically exhibit high pressure drop and narrow operating ranges [6]. Recent studies have shown that anisotropic packings with radially varying porosity can reduce pressure drop while maintaining or enhancing mass transfer [7]. The emergence of additive manufacturing enables the realization of such complex packing designs with precise control over geometry and porosity [8]. In this work, a novel anisotropic packing based on a 3D-printed tetra-spline (T-S) open cellular structure is proposed for RPB applications. The packing was designed to improve the hydrodynamic behaviour of RPB (lower pressure drop and reducing flooding phenomenon) while preserving high effective interfacial area. Wet pressure drop and effective interfacial area were experimentally evaluated using air–water and CO_2–NaOH systems over a range of operating conditions and compared against conventional wire mesh packing.

1.1 Experimental set up & methods

1.1.1 RPB set-up

A Rotating Packed Bed (RPB500) unit was purchased from ProCeller (Poland). The rotor has an inner diameter of 160 mm, an outer diameter of 500 mm, and an axial height of 40 mm. The RPB can be operated at rotational speeds of up to 1500 rpm, with maximum liquid and gas flow rates of 1 m^3/h and 600 Nm^3/h respectively. The setup includes two tanks, each with a volume of 0.6 m^3 filled with water of solution of 0.1 M of NaOH depeding on experiments. Compressed air is supplied by a compressor (BUTSCH SAMOS, SB 0430 DO) and introduced into the casing through two gas inlets (2 × DN120). The pressure drop across the RPB was measured using a Rosemount 3051 differential pressure transmitter, installed between the air inlet and outlet. P&ID is shown in figure 1

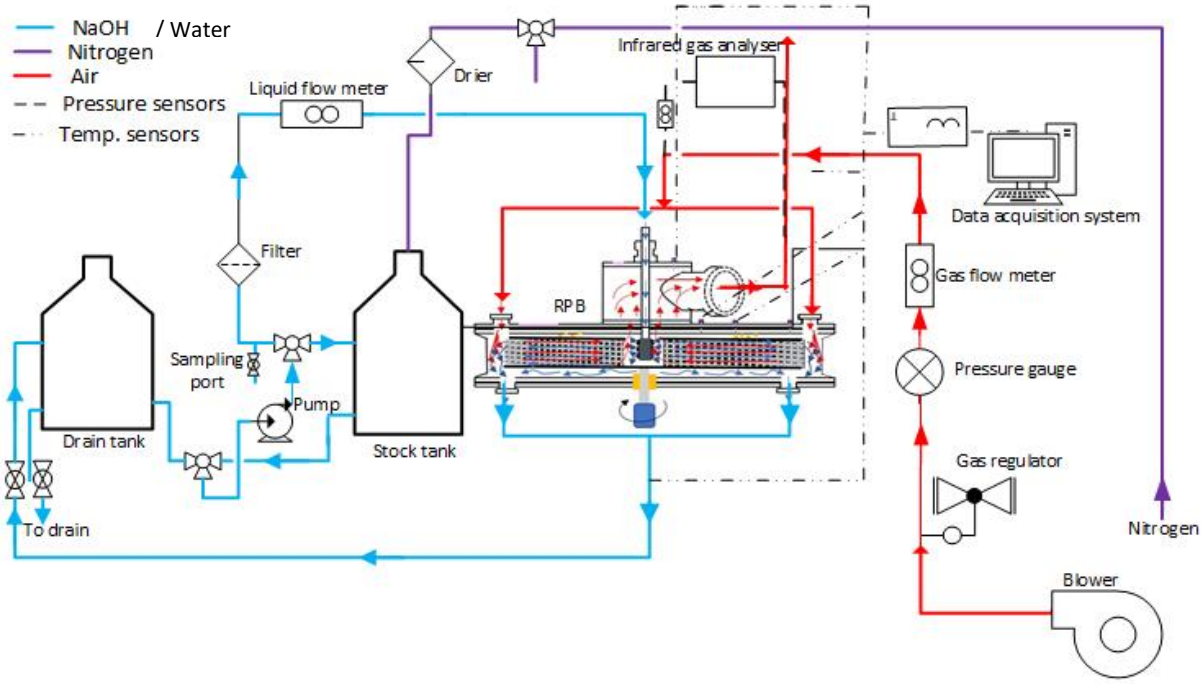

Figure 1 - Experimental setup for measuring interfacial area [10]

1.1.2 Hydrodynamic experiments

In each experiment, two parameters were fixed while the third was varied. After setting the conditions, data were collected for 10 minutes under steady operation. The averaging method is reported [6]. Tests began at the highest rotational speed and were then reduced stepwise, with gas and liquid flow rates kept constant. To measure, flooding/entrainment, a hydroclone was attached to the gas outlet to remove the rejected liquid.

1.1.3 Mass transfer experiments

To calculate effective interfacial area, CO2 (in air) – 0.1 M NaOH system was utilised. N_2 gas was continuously supplied to tank maintain an inert atmosphere and prevent contamination or moisture in the air. Inlet and outlet gas concentrations were measured using a GRUTER ET MARCHAND MG300 gas analyzer. The concentrations of carbonates (CO_3^{2-}) and hydroxides (OH^-) were measured using an

automatic titrator (Metrohm AG, Switzerland, model 2.1008.0010). Effective interfacial area was calculated by equation 1 [3].

$$a_e = \frac{G\,H_e(T)}{RTEk_L z\pi(r_{out}^2 - r_{in}^2)}\left(lny_{CO2(in)} - lny_{CO2(out)}\right) \quad (1)$$

All the Kinetics of the reaction are calculated as per Pohorecki et al [9]

1.1.3 T-S structured anisotropic RPB tailored packing

The new RPB packing is a wire-based design inspired by periodic open cellular structures (POCS) with repeating unit cells. Modeled in Autodesk Inventor, each T-S unit is defined by five parameters: regular tetrahedron length (l_1), irregular tetrahedron length (l_2), regular edge angle (θ_1), irregular edge angle (θ_2), and wire diameter (d_w). The schematic of the design and extrusion is shown in Figure. 2. The anisotropic packing was made using four rings from the inside to the outside. The lengths of the regular and irregular tetrahedron sectors were changed, while the wire diameter and angles stayed the same. This varied the surface area and porosity of each ring, giving the packing its anisotropic structure (table 1). After designing the packing in Inventor, the pieces were 3D printed using the SLA method. After printing, all pieces were assembled using Knapp joints. Some pieces were designed with holes for screws to attach them to the central packing support ring.

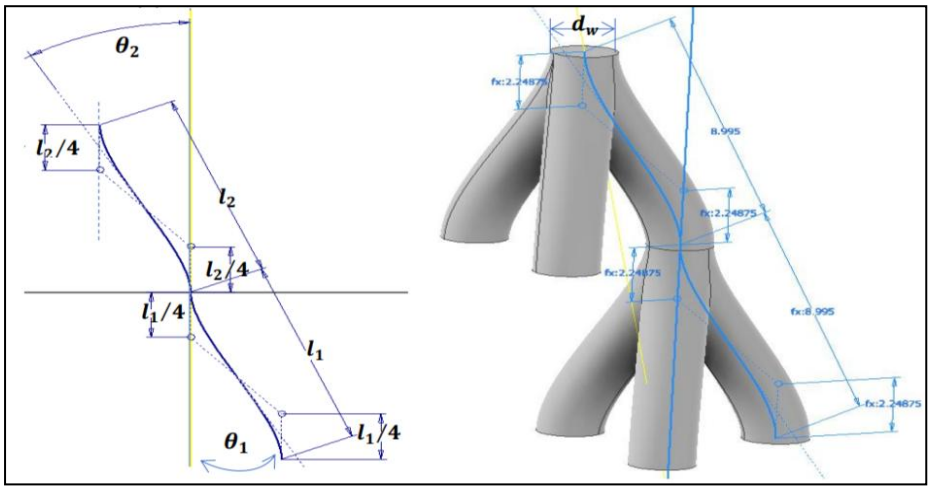

Figure 2 - Schematic diagram of single T-S structure; (a) Sketch of the model (b) Extrusion of the sketch [10].

Table 1- dimensions & Specifications of T-S structured packing

RING NO	Di (mm)	Do(mm)	$l_1 = l_2$ (mm)	$\Theta_1 = \Theta_2$ (°)	d_w (mm)	Local Specific Surface Area (Ap) (m^2/m^3)	Porosity (e%)	Total Specific surface area (SSA) (m^2/m^3)
1	160	285.5	8.995	30	1.1	193.92	95	591.468
2	285.6	371.1	3.608	30	1.1	455.72	72	
3	371.2	440.2	3.546	30	1.1	785.78	61	
4	440.3	498.9	3.345	30	1.1	1870.81	54	

2. Results & Discussion

2.1 Pressure drop

Figure 3 shows pressure drop versus rotational speed for both packings at a constant liquid flow and varying gas flow rates. The results show that pressure drop increases with rotational speed. For wire mesh packing, high pressure drop occurs at low speeds across all gas flows, mainly due to small centrifugal force at the inner edge, which blocks pores and reduces flow area. As the rotational speed increases beyond 300 rpm, centrifugal force is increased & removes the accumulated liquid, improving permeability and lowering pressure drop. At speeds above 600 rpm, the pressure drop increases again due to higher dynamic pressure, stronger swirling flows, and increased interaction between the fluid and packing. Contrarily, the T-S structured packing shows much lower pressure drop under all conditions. At 200 m^3/h and 100 rpm, the wire mesh packing gives a pressure drop of about 1.4 kPa, while the T-S packing shows only about 0.1 kPa, nearly seven times lower. This improvement is due to the high porosity and anisotropic design of the T-S packing, especially near the inner region, which reduces liquid buildup and flow resistance thus avoiding entrainment/flooding.

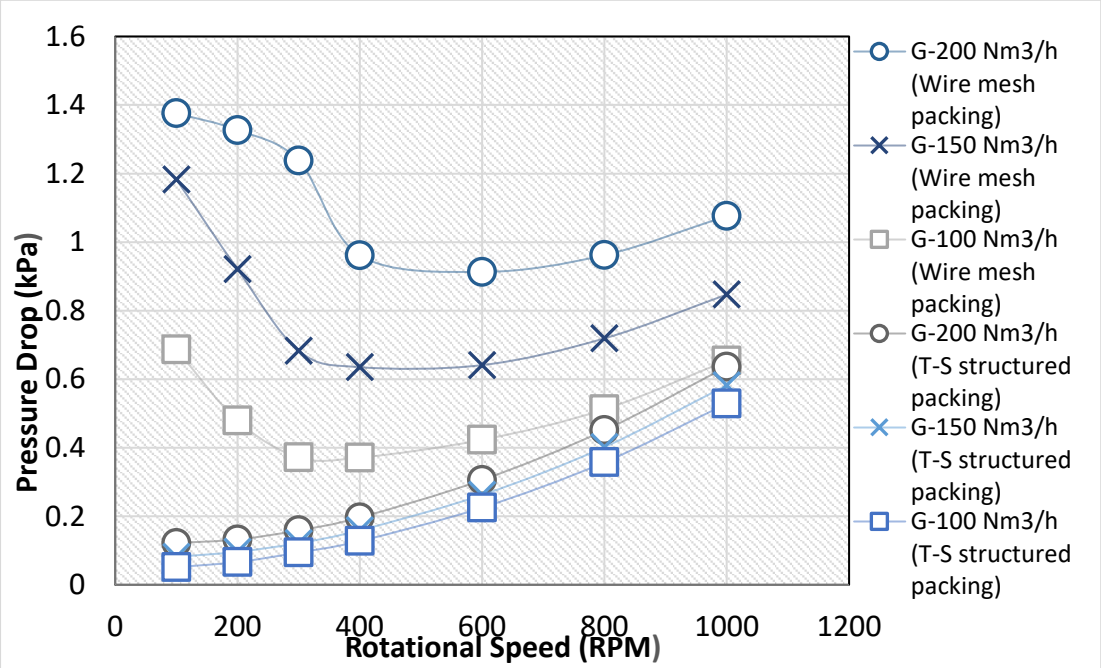

Figure 3- Effect of rotational speed on pressure drop for Wire mesh packing and T-S structured packing for constant liquid flow rate of 0.39 m^3/h.

3.2 Effective Interfacial area

Figure 3 shows that regardless the packing used, the effective interfacial area increases with rotational speed. Higher rotational speeds enhance the production of thinner liquid films, ligament or smaller droplets, thus, improving the gas–liquid contact. Increasing gas flow rate also enhances turbulence, further raising the interfacial area. Wire mesh packing exhibits a higher effective interfacial area, reaching about 1908 m^2/m^3 at a gas flow rate of 200 m^3/h, mainly due to its inherently high surface area (2400 m^2/m^3). For easier comparison, the ratio of effective interfacial area to specific surface area (Ae/Ap) was used, which indicates the wetted area of the packing [30,53]. The T-S structured packing shows higher Ae/Ap values under all conditions. At 600 rpm and a gas flow rate of 200 m^3/h, it reaches 830 m^2/m^3, corresponding to an Ae/Ap of 1.40, much higher than the wire

mesh value of 0.63. The method used to determine the interfacial area is a global approach that accounts for the phenomena occurring within the packing as well as those at the outlet, where the majority of droplets can be observed due to the higher liquid velocity. Consequently, interfacial area ratios Ae/Ap greater than unity are not unexpected, as the gas–liquid interfacial area within the casing is also taken into consideration. Furthermore, higher ratios may be explained by the fact that the entire packing is wetted in the form of a liquid film, while rotation simultaneously induces film break-up into ligaments and fine droplets as mention above. These additional liquid structures drastically increase the gas–liquid interfacial area, thereby further demonstrating the relevance and effectiveness of this intensified process. Between 700 and 900 rpm, rotational speed has little effect, suggesting that the anisotropic design promotes uniform wetting of the packing. At 1000 rpm, the interfacial area increases to 1001 m^2/m^3 (Ae/Ap-1.69), nearly twice the packing surface area. This is attributed to the high porosity of the inner rings, which improves liquid distribution, enhances hydrodynamics, and increases gas–liquid contact.

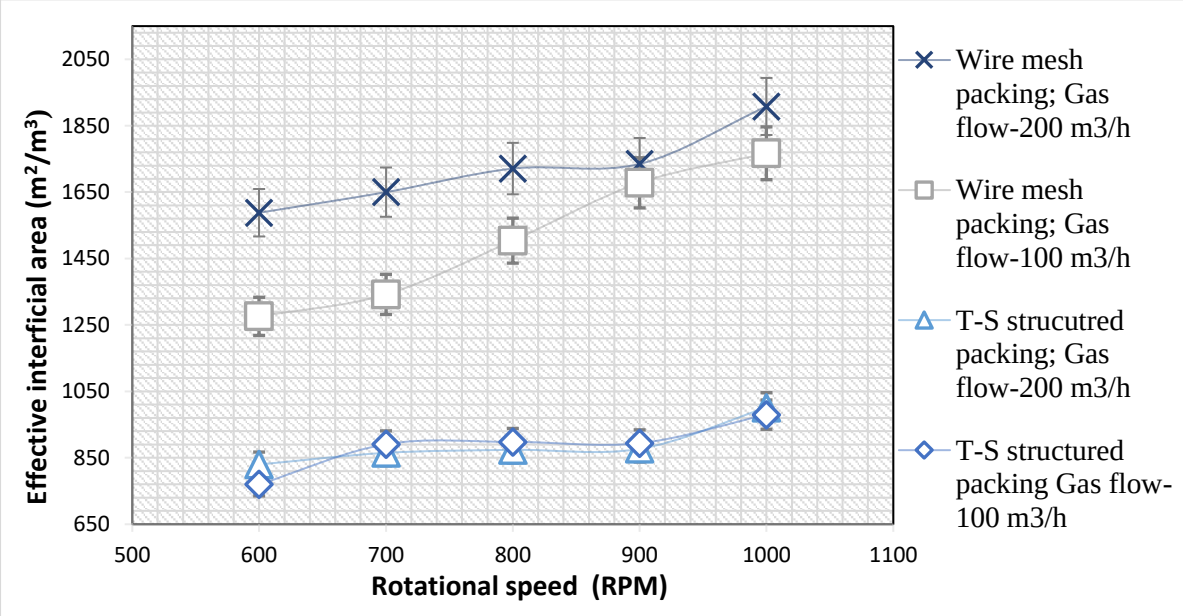

Figure 3- Effect of rotational speed on effective interfacial area for Wire mesh packing and T-S structured packing for constant liquid flow rate of 0.39 m^3/h.

3. Conclusion

Based on hydrodynamic investigations conducted on both T–S structured packing and wire mesh across different rotational speeds, it was observed that the pressure drop decreased by nearly ten-folds under low operating conditions and by approximately three-fold under high operating conditions. In experiments, where the gas flow rate was varied while maintaining constant liquid flow and rotational speed, the wire mesh exhibited a substantial increase in pressure drop, whereas only a minor increase was observed for the T–S structured packing. The mass transfer results show that the wire mesh achieves a maximum (Ae/Ap) ratio of approximately 0.71, whereas the T–S packing attains a significantly higher value of about 1.79. This disparity arises from the anisotropic nature of the T–S packing. The uniform porosity of the wire mesh limits effective solvent distribution and surface wetting. In contrast, the initial two rings of the T–S packing promote dispersion, leading to more uniform liquid distribution and enhanced wetting of the subsequent rings, thereby improving mass transfer performance.

Nomenclature

G – Gas flowrate, Nm^3/h

y_{Co_2} – mole fraction of Co_2

R – gas constant, $Pa.m^3/mol.k$

T- Temperature, K

r_{out} – Outer radius, m

E – Enhancement Factor

k_L – Liquid phase mass transfer coefficient, m/s

$H_e(T)$ – Henry constant, $Pa.m^3/mol$

Acknowledgements

Authors would like to acknowledge IMOSYCCA grants (Grant Number: 22-PESP-0008) under the PEPR 2030 project for the financial support.

References

[1] Water J. Podbielniak, CENTRFUGAL COUNTER CURRENT CONTACT APPARATUS , 2,004,011, 1935.

[2] Colin Ramshaw, Roger H. Mallinson, MASS TRANSFER PROCESS, 4,283,255, 1981.

[3] V.S. PAWAR, U. GARBA, T. TRIQUET, D. ROUZINEAU, M. MEYER, Novel anisotropic T-S structured packing for improved hydrodynamic and mass transfer performance in rotating packed bed: A pathway for new generation packings, Chemical Engineering and Processing - Process Intensification 217 (2025) 110476. https://doi.org/https://doi.org/10.1016/j.cep.2025.110476.

[4] D. Im, H. Jung, J.H. Lee, Modeling, simulation and optimization of the rotating packed bed (RPB) absorber and stripper for MEA-based carbon capture, Comput. Chem. Eng. 143 (2020) 107102. https://doi.org/https://doi.org/10.1016/j.compchemeng.2020.107102.

[5] Y. Yang, Y. Xiang, G. Chu, H. Zou, Y. Luo, M. Arowo, J.-F. Chen, A noninvasive X-ray technique for determination of liquid holdup in a rotating packed bed, Chem. Eng. Sci. 138 (2015) 244–255. https://doi.org/https://doi.org/10.1016/j.ces.2015.07.044.

[6] U. Garba, A. Adamu, T. Triquet, D. Rouzineau, M. Meyer, Experimental study of the effect of viscous media on the hydrodynamic characteristics of a rotating packed bed, Chemical Engineering and Processing - Process Intensification 191 (2023) 109482. https://doi.org/https://doi.org/10.1016/j.cep.2023.109482.

[7] K. Gładyszewski, K. Groβ, A. Bieberle, M. Schubert, M. Hild, A. Górak, M. Skiborowski, Evaluation of performance improvements through application of anisotropic foam packings in rotating packed beds, Chem. Eng. Sci. 230 (2021) 116176. https://doi.org/https://doi.org/10.1016/j.ces.2020.116176.

[8] K. Gładyszewski, M. Skiborowski, Additive manufacturing of packings for rotating packed beds, Chemical Engineering and Processing - Process Intensification 127 (2018) 1–9. https://doi.org/https://doi.org/10.1016/j.cep.2018.02.024.

[9] R. Pohorecki, W. Moniuk, Kinetics of reaction between carbon dioxide and hydroxyl ions in aqueous electrolyte solutions, Chem. Eng. Sci. 43 (1988) 1677–1684. https://api.semanticscholar.org/CorpusID:96943078.

[10] U. Garba, M.R. Meyer David, Etude de l'incidence de la morphologie d'un contacteur G/L sur l'hydrodynamique et le transfert de matière dans un RPB : application au traitement de gaz dans un procédé embarqué, 2023. http://www.theses.fr/2023INPT0055/document.

CarDiBi - Fundamental analysis of carbon dioxide absorption from biogas in rotating packed beds

Michał Blatkiewicz[1], Ondřej Hájek[2], Jonathan Mach[3], Małgorzata Majdzik[1], Patrik Rapta[2], Georg Brösigke[3], Maciej Jaskulski[1], Mariia Sobulska[1], Milan Malý[2], Anastasiia Wróbel[1], Maciej Wróbel[1], Ewa Zoń[1], Jens-Uwe Repke[3], Andrzej Górak[1], Miroslav Jícha[2]

[1] Lodz University of Technology, Faculty of Process and Environmental Engineering, 93-005 Łódź, Poland

[2] Brno University of Technology, Faculty of Mechanical Engineering, Technická 2896/2, 616 69 Brno-Královo Pole, Czech Republic

[3] Technische Universität Berlin, Process Dynamics and Operations Group, Berlin, Germany

Abstract

Rapid climate change demands a transition from fossil-based energy, highlighting the need for economically viable renewable alternatives. Methane-rich biogas is a promising option, offering near carbon-neutral energy while reducing methane emissions. However, raw biogas contains impurities such as CO_2, water vapor, and hydrogen sulfide, limiting its direct use and necessitating enrichment to biomethane (~95% CH_4) for injection into conventional gas grids. Rotating Packed Beds (RPBs) offer intensified mass transfer via high centrifugal forces, enabling finer liquid structures, enhanced micro-mixing, and higher throughput, leading to smaller footprint due to smaller equipment size and higher flexibility, compared to conventional absorption columns.

The trilateral CarDiBi project investigates RPB behavior for biogas enrichment, including solvent screening, novel packing design from triply periodic minimal surfaces, as well as kinetic and hydrodynamic modeling. Furthermore, a rigorous rate-based RPB model considering gas- and liquid-side transport resistances using the generalized Maxwell-Stefan approach, incorporating all these phenomena, is being developed. The model will be subsequently validated with CO_2 absorption experiments from biogas in an in-house pilot-scale RPB unit. In this contribution, we present first results from the holistic investigations from all project participants.

Keywords

Carbon capture, reactive absorption, biogas enrichment, process intensification, Rotating Packed Bed, triply periodic minimal surface

1. Introduction

Biogas is a highly promising energy source and a viable renewable alternative to natural gas, a fossil fuel that contributes to global warming through CO_2 emissions. Since biogas is made from biological materials via anaerobic digestion, its production has significantly lower net CO_2 balance. However, besides methane (typically 50-70 vol-%), raw biogas also contains other components such as CO_2, water vapor, and hydrogen sulfide, making it unsuitable as a direct natural gas substitute [1]. While it's often incinerated on-site for heat or small-scale electricity production, large-scale use requires biogas enrichment through selective removal of impurities to methane concentrations of about 95 vol-%. The resulting biomethane has a significantly higher caloric value and is less corrosive, allowing it to be directly introduced into conventional

gas grids [1]. Although the market for biogas is constantly growing, the large-scale implementation of biomethane in the global industry is hindered by economical and process bottlenecks. CO_2 removal from biogas streams is achieved via various technologies, including reactive and non-reactive absorption, membrane separation, pressure swing adsorption, and cryogenic separation [1]. In general, reactive CO_2 absorption in stationary columns, with the use of mainly primary or secondary amines, results in high reaction rates and is relatively well-studied [2]. However, the process is often limited by gravity-driven phase throughput and mass transfer [3]. Additionaly, the high toxicity and corrosivity of amines raises environmental and equipment issues.

Rotating Packed Beds (RPBs) are apparatuses for intensified mass and heat transfer, which belong to the high gravity (HiGee) class of process equipment. An RPB comprises a rotor equipped with an annular packing, encased in a stationary outer shell. It can operate in co-current, cross-current, and, most often, in counter-current mode, as shown in Figure 1. The liquid is introduced in the eye of the rotor, where it is sprayed onto the packing and subsequently accelerated outwards by the rotor's centrifugal field. The gas is introduced in the outer cavity and flows inwards due to pressure difference. A comprehensive review of existing RPB variations and other HiGee equipment is given in [3]. The centrifugal force in the RPB, which can be several orders of magnitude greater than gravity, enables the formation of very fine liquid structures and intense micro-mixing of the phases, leading to significantly higher mass transfer rates and allowing the processing of higher-viscosity systems compared to traditional stationary packed beds [3]. All in all, the use of RPBs enables a reduction in equipment size by about ten-fold, reduces energy consumption due to higher solvent loading, and offers better flexibility and safety control [3].

Despite growing interest over the past decade, RPBs remain a relatively young technology that is not yet fully understood, resulting in a lack of reliable design methodologies. Existing mass transfer models for RPBs largely rely on empirical correlations with often tight validity bounds, which severely limits their general applicability. Moreover, although novel packing designs have been proposed, RPBs continue to suffer from non-uniform phase distribution and unfavorable trade-offs between mass transfer performance and pressure drop [3]. Thus, key RPB phenomena, such as phase distribution, effective interfacial area, and mass transfer, require further fundamental investigation. In addition, while several solvents are suitable for CO_2 capture in conventional columns, the short residence times in RPBs can significantly limit process efficiency when reaction kinetics are slow [4].

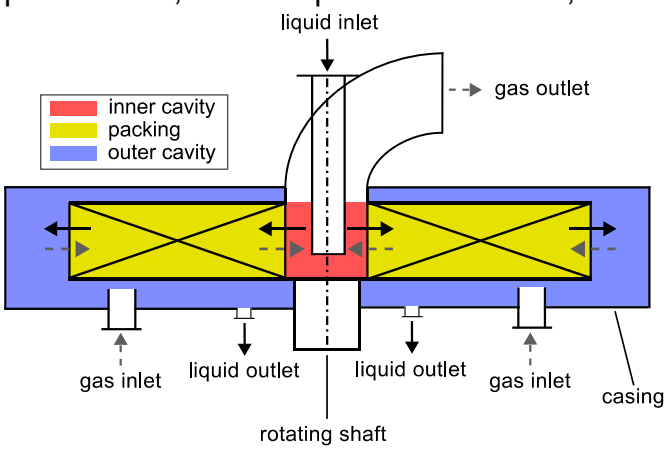

Figure 1: Schematic representation of a single-block counter-current Rotating Packed Bed.

This project transfers the biogas enrichment process from stationary packed beds to RPBs to enable fundamental investigation of RPB behavior. The study focuses on solvent screening and kinetic modeling to determine viable alternative solvents, packing design and hydrodynamic modeling to mitigate liquid maldistribution and pressure drop while maintaining high mass transfer performance, and the development of a rigorous rate-based RPB model validated by biogas enrichment experiments. Together, these efforts seek to facilitate the practical

application of RPB technology and to deepen the understanding of mass transfer phenomena in RPBs.

2. Methodology

The project is carried out in three-sided cooperation between Lodz University of Technology (TUL), Brno University of Technology (BUT), and Technische Universität Berlin (TUB), which allows for a holistic view on the process to deeply understand heat and mass transfer, fluid dynamics, and chemistry involved, by each partner focusing on a topic best fitting their respective expertise.

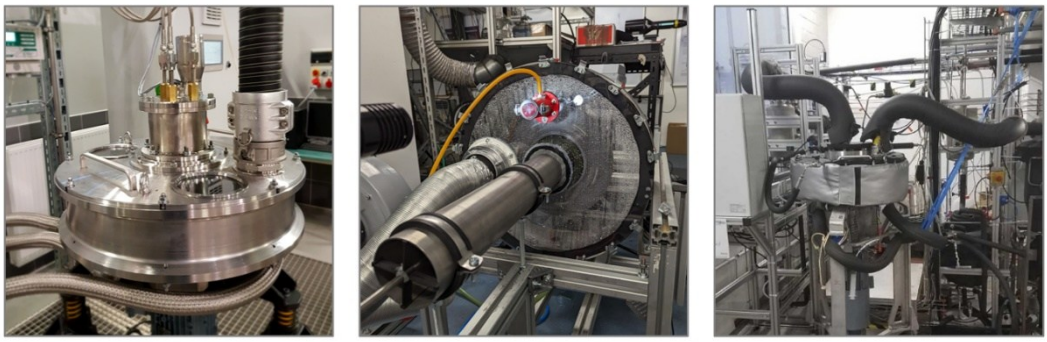

Figure 2: RPB units from TUL (left), BUT (center), and TUB (right).

2.1 Investigation of solvent properties

Choosing a solvent is a complex issue. Reactive solvents differ in kinetics, CO_2 loading capacity, reversibility of the reaction, and physicochemical properties, all of which can be a deciding factor. Many solvents have additional drawbacks of high toxicity and market prices. Literature data, especially regarding reaction kinetics, show many inconsistencies due to the system's sensitivity to differences in measurement methods. That is why it is recommended to compare the solvents using one common methodology. The first step in TUL's work was to perform preliminary screening and comparative analysis of chosen solvents. A funnel strategy with defined knockoff criteria (toxicity, corrosivity, regenerability, bulk availability and price, reaction kinetics, CO_2 loading, physicochemical properties) was used to filter out less suitable chemicals. Out of 46 solvents proposed in literature, the group was narrowed down to eight most promising solvents, plus two industrial standards – monoethanolamine (MEA) and methyldiethanolamine (MDEA) – as benchmarks. The comparative analysis included the measurements of reaction kinetics, max CO_2 load capacity, viscosity, surface tension, heat of reaction, and regeneration stability. The group of ten chemicals was further narrowed down to six, using preliminary reaction kinetics screening. The solvents which ended up in the final experimental campaign were: potassium L-argininate (ArgK, 0.5 M), tetraethylenepentamine (TEPA 1 M), potassium L-glycinate (GlyK 0.6 M), hexamethylenediamine (HMDA, 0.4 M), potassium L-lysinate (LysK,0.3 M), and MEA (5 M) as the benchmark. The concentrations were chosen according to the available literature, as they reportedly relate to the reported k_{OV} value of 3000 s^{-1}. The second order reaction kinetic coefficients k_{II} [m^3/(mol s)] were determined using the methodology analogous to [5]. Viscosity μ [Pa s] was determined with the use of a standard Höppler viscosimeter. CO_2 load capacity α_{max} [mol/mol] was measured using the same equipment as the kinetics experiments, until equilibrium between the gas and the liquid was achieved.

2.2 Development of novel RPB packings and hydrodynamic modeling

Recent advances in additive manufacturing enable the design and production of complex structures, such as triply periodic minimal surfaces (TPMS). These surfaces

distribute liquid uniformly [6], maximizing interfacial area without special atomizers. The team in the Laboratory of Multiphase Flow at BUT specializes in hydrodynamics for various industrial applications, including combustion in jet engines, absorption in static columns [7], and rotating packed beds [8]. In this project, we plan to conduct a parametric study of various TPMS structures, investigating their hydrodynamics via experimental and numerical methods. The base TPMS elements, shown in Figure 3, are connected to form an annular packing shape. Key variables include the TPMS type, wall thickness, number of elements, and their sizes in the radial and axial directions. This study focuses on one such packing (inner/outer diameter is 150/300mm), with an overall porosity of 79% and a specific surface area of 1053 m²/m³. It features gyroid elements with a wall thickness of 200 µm arranged around the perimeter; the base element size is 6.25 mm in the radial direction and 5 mm in the axial direction.

Figure 3: Base gyroid element.

The primary experimental technique is phase Doppler anemometry (PDA), which measures droplet size and velocity and correlates these parameters [8]. This yields unique data on droplets formed at the packing's outer surface and traversing the cavity zone. Although indirect for quantifying liquid holdup, PDA effectively assesses liquid distribution in all directions, particularly axially.

The full PDA setup depicted in Figure 2 (centre) is described in [8]. In the present study, however, the measurement line is oriented parallel to the axial direction (Figure 4). Thirteen positions, spaced 2.5 mm apart, are located 35 mm above the packing. This configuration enables analysis of droplet number, size, and velocities in the tangential and radial directions.

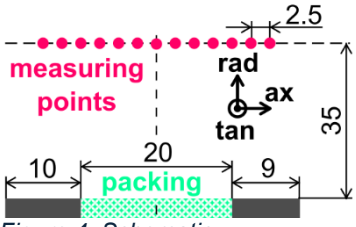

Figure 4: Schematic representation of PDA setup.

2.3 Development of a rigorous rate-based RPB model

The Process Dynamics and Operations group at TUB is focusing on the development of a rigorous, rate-based, steady-state model for CO_2 absorption in RPBs. The model follows the rate-based framework by Krishna and Taylor [9], which is based on the two-film theory. Multi-component mass transfer in electrolyte solutions subject to chemical reactions is described using the generalized Maxwell-Stefan (MS) approach [10], accounting for transport resistances on gas and liquid sides. The gas phase is assumed to behave ideally. The RPB packing is discretized on an equidistant grid. Within each discretized stage, the gas and liquid phases are each assumed to be ideally mixed. The model has reached a first level of implementation complexity. Next development steps include the incorporation of non-idealities in the liquid phase using the electrolyte NRTL model and a logarithmic discretization of the liquid film. These enhancements are expected to improve model accuracy, as non-idealities in electrolyte systems can be significant, and liquid-phase reactions can give rise to strongly non-linear concentration and temperature profiles.

Since no literature data on biogas enrichment in RPBs are currently available, the model is initially applied to the CO_2 absorption from flue gas using aqueous MEA solutions. Following packing development, screening of solvents, and the development of kinetic, physicochemical, and fluid dynamic sub-models, these elements will be integrated into the process model, which will subsequently be applied to biogas enrichment. To the best of our knowledge, rigorous RPB modeling at this level of detail has not yet been reported in the literature, particularly for biogas enrichment and RPB models employing the generalized MS-approach. An overview of existing modeling approaches is given in [11]. Artificial biogas enrichment experiments with a mixture of

CO_2/CH_4 will then be conducted at an in-house, pilot-scale, RPB unit (Figure 2 right) and used for further validation of the process model.

3. Results and discussion

3.1 Solvent system screening

Figure 5 shows values of key parameters of the chosen solvents: overall second order reaction kinetic coefficient k_{II}, maximum CO_2 loading capacity α_{max} and the reciprocal of liquid dynamic viscosity. Since high viscosities have an overall negative impact on the process, μ^{-1} is used instead of μ for clarity. All values were calculated regarding concentrations presented in Section 2.1. It can be seen that most investigated chemicals show better load capacity than MEA, however MEA shows second highest value of k_{II} in the group. Amino acid solutions show similar viscosities, lower than those of amines. Overall, the two most promising solvents are ArgK and TEPA.

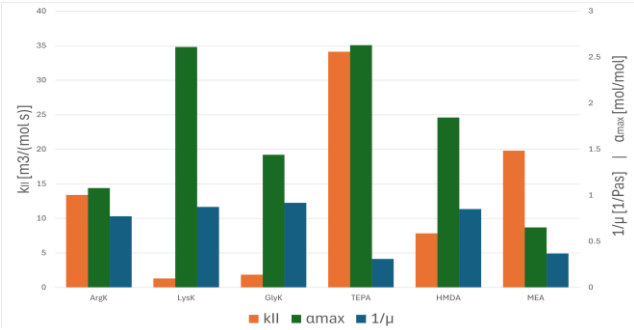

Figure 5: Kinetic coefficient k_{ov} [m3/(mol s)], load capacity α_{max} [mol/mol], and viscosity reciprocal μ^{-1} [1/Pas] for chosen solvents at 20°C.

3.2 Gyroid packing and its hydrodynamic performance

In the context of packing development, hydrodynamic measurements (liquid distribution, pressure drop) of gyroid TPMS packings were conducted, which is shown in Figure 6. Figure 6 a) illustrates the influence of packing rotational speed *N* on droplet distribution and constant liquid and gas flow rates, *L* and *G*, respectively, presented in relative terms. In absolute terms, higher rotational speed increases the number of droplets while decreasing their size. In relative terms, the number of droplets at each position is normalized by the total number detected in that regime. Figure 6 a) also reveals that rotational speed does not affect the overall droplet distribution, as all regimes keep identical profiles. However, this gyroid packing does not support the hypothesis of even axial liquid distribution: the droplet distribution is skewed toward the left side of the graph, possibly due to the orientation of gyroid structures at the packing's outer surface. This would explain detected droplets at position -12.5 mm. Figure 6 b) shows the effect of *G* on wet pressure drop over various *N*. Higher gas flow rates increase the pressure drop, with the flooding point occurring at 400 rpm across all *G*.

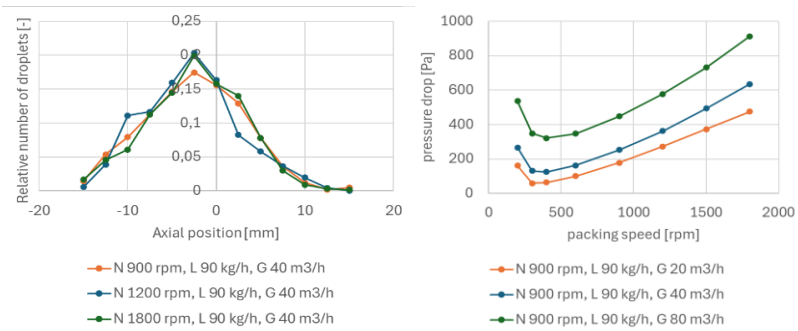

Figure 6: Results of a) relative number of droplets (LDA); b) pressure drop in gyroid TPMS packing for constant liquid flow rate L.

4. Conclusions

In this contribution, the CarDiBi project is presented, which is a joint research initiative between BUT, TUL, and TUB, the goal of which is transferring the biogas enrichment process from stationary packed beds to RPBs, thereby enabling fundamental research on RPB behavior in reactive absorption of CO_2. The scope of the project includes physicochemical measurement, kinetic and hydrodynamic modeling, TPMS packing development, and rate-based modeling.

Preliminary screening of solvents indicates five promising candidates based on measurements of CO_2 load capacity, viscosity, surface tension, heat of reaction, and reaction kinetics. Among those, TEPA is the most promising candidate, as it shows the highest kinetic coefficient and load capacity toward CO_2. However, due to its toxicity, ArgK emerges as a strong alternative, offering comparable performance values while avoiding negative environmental impact.

Regarding the packing development, initial measurements on hydrodynamics, i.e. liquid distribution and pressure drop, of gyroid TPMS packings were conducted. The rotational speed was found to have no influence on the liquid distribution. Furthermore, the flooding point for the packing was identified to be at 400 rpm, across all gas flow rates. Further experiments with different type of TPMS packings will be conducted.

Towards the development of a rigorous, rate-based model for reactive CO_2 absorption in RPBs, an initial level of complexity is reached by accounting for transport resistances in both the gas and liquid phases. Following the full implementation and integration of all submodels developed within this project, the model will be applied to biogas enrichment and further validated using in-house biogas enrichment experiments.

Acknowledgements

This work was supported partially by the German Research Foundation (DFG) under project number 544949629, partially by the Czech Science Foundation under project number GA 25-14506L, and partially by the National Science Center Poland (NCN) under project number 2023/51/I/ST8/01852 within the LAP/Weave program between TU Berlin, UT Brno, and UT Lodz.

References

[1] O. W. Awe, Y. Zhao, A. Nzihou, D. P. Minh, and N. Lyczko, “A Review of Biogas Utilisation, Purification and Upgrading Technologies,” *Waste Biomass Valor*, vol. 8, no. 2, pp. 267–283, Mar. 2017, doi: 10.1007/s12649-016-9826-4.

[2] N. Muntaha, M. I. Rain, L. K. M. O. Goni, Md. A. A. Shaikh, M. S. Jamal, and M. Hossain, “A Review on Carbon Dioxide Minimization in Biogas Upgradation Technology by Chemical Absorption Processes,” *ACS Omega*, vol. 7, no. 38, pp. 33680–33698, Sep. 2022, doi: 10.1021/acsomega.2c03514.

[3] G. E. Cortes Garcia, J. Van Der Schaaf, and A. A. Kiss, “A review on process intensification in HiGee distillation,” *J of Chemical Tech & Biotech*, vol. 92, no. 6, pp. 1136–1156, Jun. 2017, doi: 10.1002/jctb.5206.

[4] M. Blatkiewicz *et al.*, “Modeling and simulation of an enzymatic reactive absorption process in the internal zone of a rotating packed bed apparatus,” *Chemical Engineering and Processing - Process Intensification*, vol. 189, p. 109409, Jul. 2023, doi: 10.1016/j.cep.2023.109409.

[5] J. G. M.-S. Monteiro, H. Knuutila, N. J. M. C. Penders-van Elk, G. Versteeg, and H. F. Svendsen, “Kinetics of CO2 absorption by aqueous N,N-diethylethanolamine solutions: Literature review, experimental results and modelling,” *Chemical Engineering Science*, vol. 127, pp. 1–12, May 2015, doi: 10.1016/j.ces.2014.12.061.

[6] N. C. Ellebracht *et al.*, “3D printed triply periodic minimal surfaces as advanced structured packings for solvent-based CO_2 capture,” *Energy Environ. Sci.*, vol. 16, no. 4, pp. 1752–1762, 2023, doi: 10.1039/D2EE03658D.

[7] M. Maly *et al.*, “Importance of atomizer choice for CO2 capture in spray columns,” *Fuel*, vol. 385, p. 134078, Apr. 2025, doi: 10.1016/j.fuel.2024.134078.

[8] M. Blatkiewicz, O. Hájek, M. Majdzik, M. Malý, and M. Jaskulski, “Advanced absorption model of rotating packed beds: Mass transfer in packing and cavity zone,” *Chemical Engineering Journal*, vol. 524, p. 169734, Nov. 2025, doi: 10.1016/j.cej.2025.169734.

[9] R. Krishnamurthy and R. Taylor, “A nonequilibrium stage model of multicomponent separation processes. Part I: Model description and method of solution,” AIChE Journal, vol. 31, no. 3, pp. 449–456, Mar. 1985, doi: 10.1002/aic.690310312.

[10] R. Krishna and J. A. Wesselingh, “The Maxwell-Stefan approach to mass transfer,” Chemical Engineering Science, vol. 52, no. 6, pp. 861–911, Mar. 1997, doi: 10.1016/S0009-2509(96)00458-7.

[11] M. Illner, M. Hilpert, and J.-U. Repke, “Rotating packed beds in distillation: rate-based modeling for multicomponent systems,” in *Process Intensification: by Rotating Packed Beds*, M. Skiborowski and A. Górak, 2nd Edition. De Gruyter, 2022, pp. 209–266, doi: 10.1515/9783110724998-202.

Important aspects within absorption mass transfer measurements

Valenz L.[1], *Rychlá V.*[1], *Siuda A.* [1], *Čmelíková T.* [1], *Rejl F. J.* [1]

[1]*University of Chemistry and Technology, Prague, Czech Republic*

Abstract

It is currently impossible to measure the necessary properties of all combinations of packings and systems under distillation and absorption conditions. Therefore, there is an effort to develop a general model that will predict transport and hydraulic characteristics under conditions other than those under which it was developed and verified. Current models differ by up to several times in the prediction of transport characteristics. In addition, most models have not been verified on new packings. In order to develop a reliable model for the ever-evolving random and structured packings, it needs to be verified on as large a database as possible. However, to create such a database would be an enormous undertaking for a single workplace. The published mass transfer characteristics obtained at different workplaces using the same method could differ by up to several times. The aim of this paper is to highlight important aspects of experimental techniques and surprising properties of standard absorption systems. The dependence of the transport characteristics on the input SO_2 concentrations for $k_G a$ is discussed in detail. The location and method of gas and liquid sampling are also discussed. The repeatability of the measurements, the effect of washing the packing during the experimentation and the comparison of the characteristics determined in two absorption columns of different diameters are shown.

Key words

mass-transfer characteristics, random and structured packing

1. Introduction

Gas-liquid mass transfer plays a central role in the design and scaling of absorption and distillation equipment employing random and structured packings. Reliable prediction of transport and hydraulic characteristics is therefore essential for both the development of new internals and the optimization of existing separation processes. Despite decades of research, the accurate determination and generalization of mass transfer parameters remain challenging, primarily due to the wide range of operating conditions, system properties, and packing geometries encountered in industrial practice.

It is well recognized that direct experimental determination of mass transfer characteristics for all possible combinations of gas-liquid systems, packings, and operating conditions is impractical. Consequently, significant effort has been devoted to the development of generalized models capable of predicting mass transfer and hydraulic behavior beyond the conditions under which they were originally established. However, existing models often exhibit substantial discrepancies, with reported deviations of transport parameters reaching several-fold differences. Moreover, many correlations have been validated only on a limited set of packings and have not been systematically tested on newly developed random or structured packings.

The reliability of any generalized model strongly depends on the quality and consistency of the experimental data upon which it is based. Ideally, model development should rely on extensive and diverse databases composed of data generated using comparable experimental methodologies. In practice, however, the creation of such comprehensive datasets is hindered by the considerable experimental effort required and by methodological differences among laboratories. Even when identical experimental techniques are applied, published mass transfer characteristics for nominally identical systems and packings can differ significantly. These discrepancies raise fundamental questions regarding experimental procedures, data evaluation methods, and the intrinsic properties of commonly used absorption systems.

This contribution aims to draw attention to several important and sometimes overlooked aspects of absorption mass transfer measurements. Particular emphasis is placed on the influence of inlet SO_2 on the determination of the overall gas-side mass transfer coefficient, k_Ga. The paper further discusses the impact of gas and liquid sampling location and methodology on the measured transport characteristics. Additionally, issues related to measurement repeatability, the effect of packing washing during experiments, and the comparison of mass transfer characteristics obtained in absorption columns of different diameters are systematically investigated.

By highlighting these experimental sensitivities and unexpected behaviors of standard absorption systems, this work seeks to contribute to a more critical interpretation of mass transfer data and to support the development of more reliable and broadly applicable predictive models for packed columns.

2. Results and discussion

2.1. Repeatibility of the k_Ga values

Ensuring repeatability in the measurement of mass-transfer characteristics of packed beds is essential for obtaining reliable and scientifically meaningful data. Packed columns are highly sensitive to variations in liquid distribution, ga-liquid hydrodynamics, and temporary changes in packing wetting, all of which can introduce systematic errors if measurements are not reproducible. By performing repeated experiments under identical conditions, researchers can verify that observed trends truly reflect the behavior of the system rather than random fluctuations or transient fouling effects. High repeatability therefore strengthens the validity of experimental conclusions and enables confident comparison between different packings, operating conditions, or modelling approaches.

Repeatability of the measurements was tested on an atmospheric absorption column with an internal diameter of 300 mm during the determination of the gas-phase volumetric mass-transfer coefficient, k_Ga, using the NeXRing #0.7 random packing. In contrast to structured packings, random packings are sensitive to repeated column refilling, even when the packing density is kept constant. The obtained k_Ga values may also be affected by the positioning of the liquid distributor - its distance from the packing or its orientation relative to the packing. Atmospheric pressure and the calibration of the analytical instruments can likewise play a role. All of these aspects were slightly varied during measurements performed over several weeks, as illustrated in Figures 1 and 2. The resulting net k_Ga values obtained by the subtraction method for liquid loads B = 20 and 40 m/h show no significant differences within the experimental uncertainty, as can be seen in Figures 1 and 2. It can therefore be concluded that the repeatability of measurements on our experimental apparatus is sufficient.

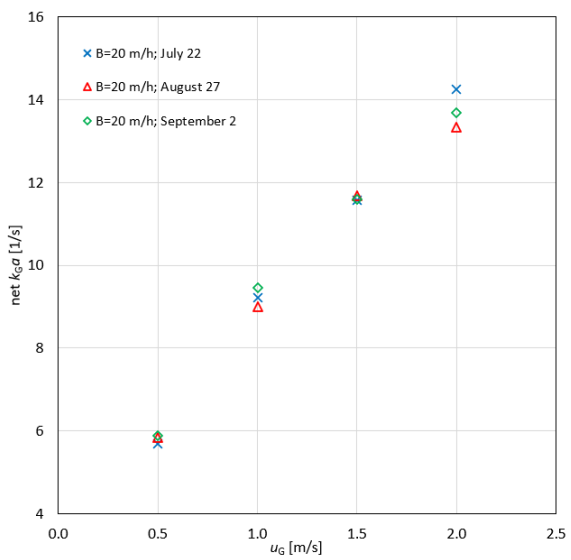

Figure 1: Dependence of net k_Ga values on gas velocity; NeXRing #0.7; liquid load B = 20 m/h; DN 300

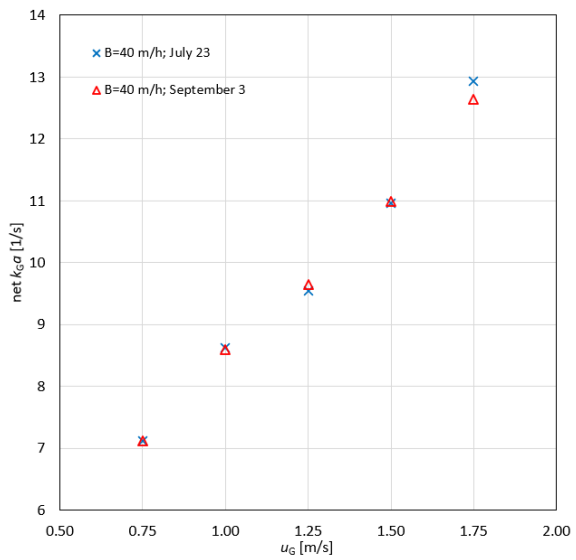

Figure 2: Dependence of net k_Ga values on gas velocity; NeXRing #0.7; liquid load B = 40 m/h; DN 300

2.2. Influence of the packing purity on the k_Ga values

The purity of random packing affects the gas-side volumetric mass-transfer coefficient k_Ga primarily through its impact on hydrodynamics, surface characteristics, and the effective interfacial area. Impurities on packing elements - such as residual manufacturing residues, surface oxides, deposits, or incomplete cleaning - can modify surface wettability and roughness, which in turn alters the liquid distribution, local film thickness, and the realized interfacial effective area. Comprehensive reviews of gas - liquid mass transfer in packed-bed columns emphasize that even small deviations from nominal surface properties may introduce non-ideal wetting patterns and maldistribution, leading to measurable changes in k_Ga. According to physically based correlations for random packings (e.g., the Billet and Schultes model (1999)), the gas-side coefficient depends strongly on local hydrodynamics and effective interfacial area, both of which are sensitive to surface cleanliness, roughness, and the presence of contaminants that alter liquid spreading behavior. Reduced packing purity thus tends to lower or destabilize k_Ga, especially under conditions where gas-side resistance dominates and precise wetting behavior is required to maintain the expected interfacial area. Proper cleaning, handling, and quality control of packing materials are therefore essential to ensure reproducible k_Ga values and reliable scale-up.

During the determination of k_Ga values for the air-SO_2/water-NaOH system, sodium sulfate deposits form on the packing. Figure 3 shows the packing freshly washed with a sulfuric acid solution (left) and the packing with deposits after three days of measurements (right). Figure 4 plots the net k_Ga values obtained by the subtraction method for packing that is freshly washed (blue), after one day (red), and after two days (green) of measurements. The data shown correspond to a low liquid load of B = 5 m/h, where the influence of packing fouling is expected to be the highest. As can be seen, the data measured with clean packing are on average 7% lower (except at the highest gas-phase velocity) than the data obtained with fouled packing. For higher liquid loads, this effect becomes entirely negligible.

Figure 3: Freshly washed NeXRing #0.7 packing (left) and packing with surface deposits (right) after three days of measurement, most likely sodium sulfate

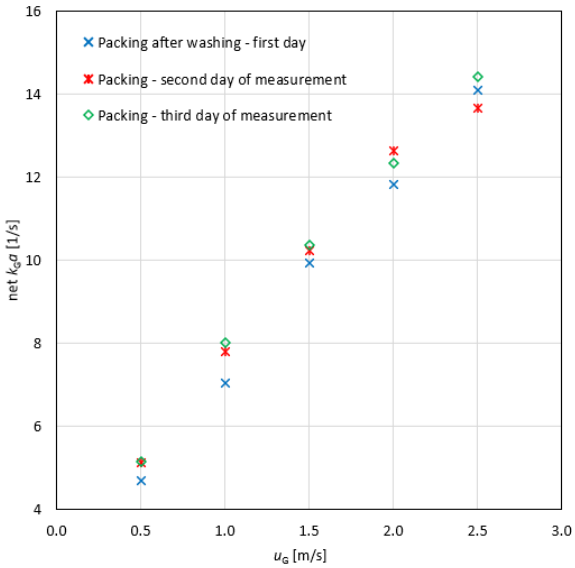

Figure 4: Dependence of net k_Ga values on gas velocity; NeXRing #0.7; liquid load B = 5 m/h; DN 300

2.3. Influence of the inlet tracer concentration on the k_Ga values

In order to obtain the volumetric mass transfer coefficient in the gas phase (k_Ga) with the air-SO_2/water-NaOH system, it is necessary to take gaseous samples. One option is to take them directly just before and just after the inlet and outlet of the packed bed, or directly within the packing. However, it is problematic to take a representative sample of the gaseous phase. Furthermore, the sampling point must be designed to prevent the liquid phase from being drawn in. The second option is to sample the gaseous phase at locations where the liquid phase is not yet or no longer present and the bulk of the gaseous phase is well mixed. However, this experimental design requires measurements at a minimum of two different packed bed heights in order to subtract end effects. A further challenge in the practical implementation of the experiment lies in the instantaneous reaction at the phase interface, which results in a substantial change in tracer concentration on a relatively low bed. This is particularly important for new packings with high k_Ga values, where the use of a single analyzer typically involves measuring at packed bed not exceeding 0.5 m. This may not be entirely feasible for design of industrial columns. In our laboratory, we utilize two SO_2 analyzers: a SICK analyzer with a range of 30 to 2000 ppm and a Horiba analyzer with a range of 50 to 2000 ppb. This enables to conduct two identical measurements with 1000 times different inlet SO_2 concentrations, inlet and outlet concentrations being measured by a single analyzer (SICK-SICK configuration or Horiba-Horiba configuration). Measurements were conducted at packed bed heights of 0.21 m and 0.42 m in both configurations. Additionally, it is possible to measure at significantly higher bed heights of 0.63 m and 0.84 m, where the input concentration is measured using the SICK analyzer and the output concentration is measured on the Horiba analyzer (SICK-Horiba configuration). The raw k_Ga values at the MellapakPlus 252.Y packing for liquid phase flow rate B = 10 m/h are shown in Figure 5.

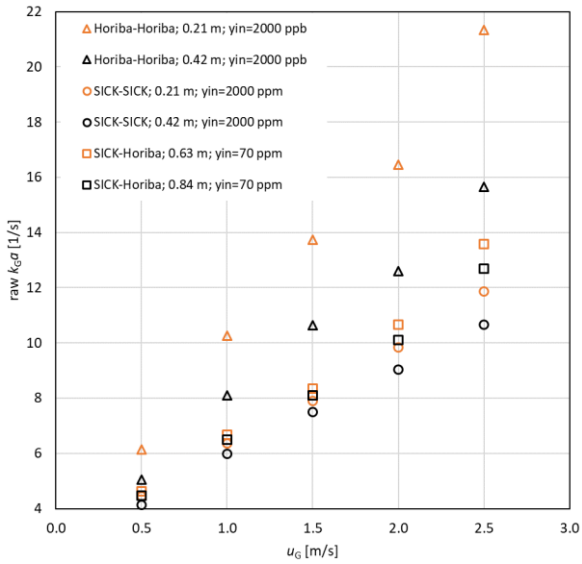

Figure 5: Dependence of raw k_Ga values on gas velocity; MellapakPlus 252.Y; liquid load B = 10 m/h; DN 300

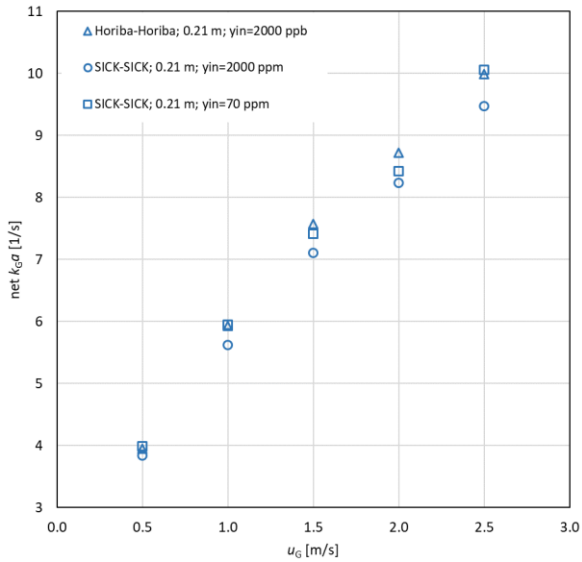

Figure 6: Dependence of net k_Ga values on gas velocity; MellapakPlus 252.Y; liquid load B = 10 m/h; DN 300

Figure 5 shows that the raw k_Ga values can vary by up to a factor of two depending on the input concentration. However, after subtracting the end effects, all values are comparable (Figure 6) and do not differ by more than 6 %. This indicates that the concentration dependence of k_Ga is due to the end effects. Those can be minimized / subtracted if the experiment is performed correctly.

2.4. Influence of the column diameter on the k_Ga values

For random packings, the literature generally states that a direct influence of column diameter on Δp, k_La and k_Ga is not explicitly included in standard design correlations; in practice, however, wall effects and maldistribution become more pronounced in smaller diameters. Regarding mass transfer, comprehensive reviews and models for random packings (Onda et al. (1968); Billet and Schultes (1999); Rocha et al. (1996)) describe k_La and k_Ga in terms of local hydrodynamics and effective interfacial area, not directly through column diameter, so the diameter influence appears secondarily - a smaller diameter implies stronger wall channeling and greater sensitivity to distributor performance, which may lead to lower and more variable k_Ga (and less consistent effective interfacial area), whereas k_La is generally less sensitive to column diameter provided proper wetting and redistribution are maintained. This is consistent with practical rules for random packings, such as the requirement that column diameter should be ten times the packing size to limit wall effects and channeling.

This rule was examined using the modern random packing NeXRing #0.7, which has a nominal size of 25 mm. Experiments were carried out in two absorption columns with inner diameters of 150 mm and 300 mm, corresponding to diameter-to-packing-size ratios of 6 and 12, respectively. The k_Ga values were determined using the air-NH_3 / water-H_2SO_4 absorption system. Measurements were conducted at two packed-bed heights, 42 cm and 21 cm, and the net k_Ga values were evaluated by the subtraction method for two liquid loads, B = 5 m/h (Figure 7) and B = 20 m/h (Figure 8). The results show that, within experimental accuracy, the k_Ga values are practically identical, and no influence of column diameter on k_Ga can be observed. This can be attributed mainly to the fact that the modern high-capacity packing NeXRing #0.7 no longer resembles a classical ring in the strict sense: due to its geometry, more elements fit into the column cross-section than would be expected from the simple diameter-to-size ratio.

It can therefore be concluded that modern random packings effectively minimize wall effects and channeling, even in columns of relatively small diameter.

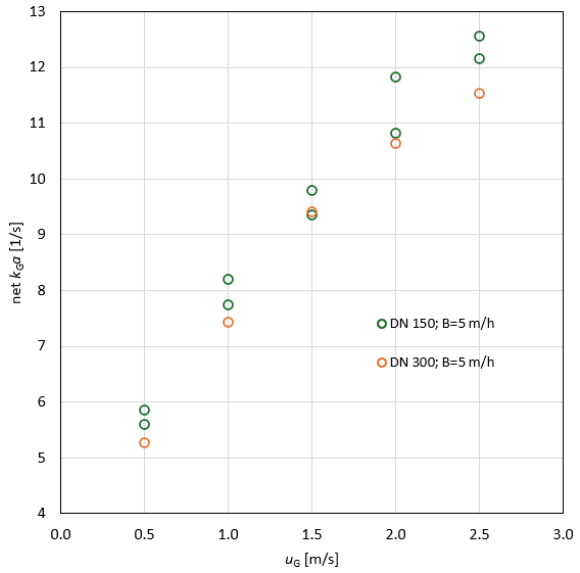

Figure 7: Dependence of net k_Ga values on gas velocity; NeXRing #0.7; liquid load B = 5 m/h

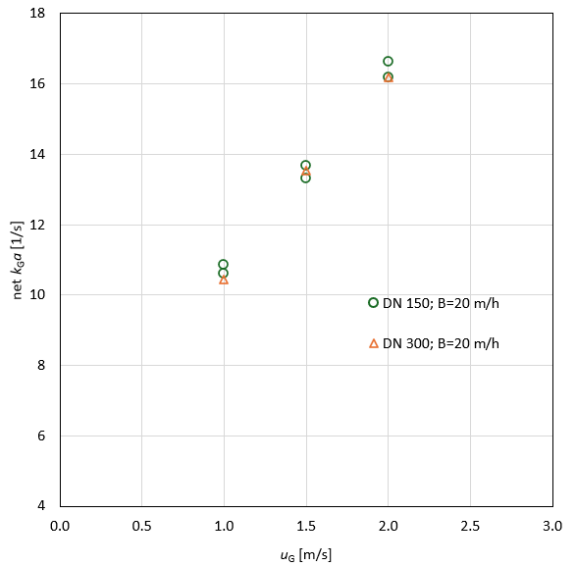

Figure 8: Dependence of net k_Ga values on gas velocity; NeXRing #0.7; liquid load B = 20 m/h

3. Conclusions

This study highlights several critical aspects that substantially influence the determination and interpretation of gas-liquid mass-transfer characteristics in packed absorption columns. The results demonstrate that, despite the inherent sensitivity of random packings to hydrodynamic variations, the repeatability of k_Ga measurements can be maintained at a high level when appropriate experimental procedures are applied. The influence of packing cleanliness was shown to be relevant only at very low liquid loads, where partial fouling may increase the effective interfacial area; at typical operating conditions, this effect becomes negligible. A detailed analysis of the inlet SO_2 concentration revealed that the pronounced dependence of raw k_Ga values originates from end effects rather than intrinsic mass-transfer behavior. When these effects are properly accounted for, the resulting net k_Ga values converge within a narrow uncertainty range. Finally, a comparison of two column diameters showed no measurable influence on k_Ga for the modern random packing NeXRing #0.7, confirming that contemporary high-capacity packings effectively suppress wall effects even in relatively small laboratory columns. These findings underline the importance of rigorous experimental methodology and provide guidance for generating consistent datasets suitable for the development and validation of generalized mass-transfer models.

Acknowledgements

Workplace is deeply grateful to Sulzer Ltd. for providing of packing samples.

References

Billet, R.; Schultes, M., Prediction of mass transfer columns with dumped and arranged packings: Updated summary of the calculation method of Billet and Schultes. *Chemical Engineering Research & Design* 1999, 77 (6), 498-504

Rocha, J. A.; Bravo, J. L.; Fair, J. R., Distillation Columns Containing Structured Packings: A Comprehensive Model for Their Performance. 2. Mass-Transfer Model. *Industrial & Engineering Chemistry Research* 1996, 35 (5), 1660-1667

Onda, K.; Takeuchi, H.; Okumoto, Y., Mass transfer coefficients between gas and liquid phases in packed columns. *Journal of Chemical Engineering of Japan* 1968, 1 (1), 56–62.

Modeling and Validation of Tar Absorption from Biomass-Derived Syngas

Simon Brinkmann[1,2], Thomas Grützner[1], Bernhard C. Seyfang[2]
[1] Ulm University, Institute of Chemical Engineering, Laboratory of Thermal Process Engineering, Ulm, Germany;
[2] Bingen Technical University of Applied Sciences, Life Sciences and Engineering, Bingen am Rhein, Germany

Abstract
Within biomass-derived syngas plants, tar removal remains a key challenge for the reliable operation of downstream processes. Recent studies and reviews indicate that absorption using bio-based solvents, such as fatty acid methyl esters and vegetable oils, represents a promising and sustainable alternative to conventional washing liquids. However, the design and scale-up of such scrubbers are hindered by limited vapor–liquid equilibrium data and a lack of experimental validation for novel absorber concepts. In this contribution, a newly developed modular absorption column with fully 3D-printed internals is presented to investigate tar scrubbing under laboratory conditions. The DN50 column design enables flexible adaptation of packing geometry and provides a well-defined basis for systematic studies of hydrodynamics and mass transfer. Rate-based absorber models are implemented in Aspen Plus using AI-predicted thermodynamic properties from the literature to support sensitivity analyses of solvent composition and choice of an appropriate model. Preliminary simulations demonstrate the strong impact of thermodynamic assumptions and mass transfer parameters on predicted toluene removal as a model compound for light tars. The constructed test rig and GC-based analytics provide the basis for forthcoming absorber campaigns, linking 3D-printed hardware with model-guided experimentation toward efficient bio-based tar scrubbing.

Keywords
Tar scrubbing; AI thermodynamics; Absorption; Rate-based modeling; 3D-printed column

1. Introduction

Biomass gasification is a mature thermochemical route to convert renewable feedstocks into raw product gas for heat and power generation or for upgrading to syngas. A persistent challenge is the presence of condensable organic contaminants, referred to as tars, including light aromatics and polycyclic aromatic hydrocarbons, which can condense during cooling and cause fouling, blockages, and catalyst deactivation. Effective tar removal is therefore a requirement for stable and reliable operation of downstream equipment [1].

Wet scrubbing is widely used as a secondary gas cleaning step due to its robustness and scalability. While water scrubbers primarily remove heavy tars by cooling-induced condensation, they exhibit limited absorption capacity for light aromatics such as benzene and toluene [2]. In contrast, hydrophobic solvents such as diesel, biodiesel, and vegetable oils show higher affinity toward aromatic tar compounds and have been reported to achieve markedly higher removals of BTX species than water under

comparable conditions [3–5]. Laboratory-scale packed-bed studies with vegetable oils further confirm effective absorption of light aromatics from tar-laden gases [3].
Despite these promising results, the design and optimization of oil-based tar scrubbers remain uncertain. A key limitation is the lack of reliable thermodynamic parameters for representative tar–solvent systems. Consequently, models often rely on UNIFAC estimates with limited validation for these mixtures [5–7]. AI-based property predictions [8, 9] are promising, but are not yet widely established for tar scrubbing.
Additive manufacturing offers a pathway to advance absorber design by enabling packed columns with precisely defined tailor-made internals. Fully 3D-printed structured packings have demonstrated high separation efficiency and reproducible hydrodynamics in laboratory-scale distillation and offer scalable, precisely defined geometries [10]. However, their application to gas absorption for bio-based tar scrubbing has not yet been explored. In this work, tar absorption is investigated in a modular DN50 3D-printed packed column using rapeseed methyl ester (RME) and rapeseed oil as readily available, bio-based solvents. A complementary modeling framework quantifies sensitivities to thermodynamic assumptions and mass transfer, building on our previously published code-based approach for syngas composition [11] to support systematic experiments, improved scrubber design, and scale-up.

2. Methodology

The methodological approach follows an integrated workflow combining thermodynamic property prediction, absorber modeling, and subsequent validation using the 3D-printed absorption column.
RME and rapeseed oil are complex bio-based solvents composed of multiple fatty acid methyl esters and triglycerides, respectively. To quantify the effect of solvent description and property prediction route on toluene solubility, thermodynamic modeling systematically varies three independent factors, namely the solvent, the solvent composition, and the thermodynamic data source, as summarized in Table 1.

Table 1: Methodological Factors Considered for Thermodynamic VLE Modeling.

Factor	Cases	Purpose
Solvent	RME; rapeseed oil	Comparison of different bio-based solvents
Solvent composition	Single-component surrogate; multi-component mixture with five representative species	Assessment of solvent complexity on predicted VLE
Thermodynamic data source	Classical (UNIFAC); AI-based (HANNA & GRAPPA) [8, 9]	Evaluation of different property prediction approaches

For each solvent, two composition models are considered: (i) a single-component surrogate representing the dominant molecular functionality and (ii) a five-component mixture of representative fatty acid methyl esters or triglycerides reflecting the main compositional fractions, following typical rapeseed-based profiles [3]. This enables quantifying how compositional detail affects predicted VLE and absorber performance.
Thermodynamic property prediction is carried out using two complementary approaches. Activity coefficients are estimated either by UNIFAC or by the machine-learning models HANNA and GRAPPA [8, 9] as data-driven alternatives. UNIFAC group assignments are available for all components considered. Both routes are used to generate consistent equilibrium datasets, which are subsequently regressed to NRTL binary interaction parameters. The resulting NRTL parameter sets provide a

unified thermodynamic basis for implementation in Aspen Plus V14 and allow a direct comparison between group-contribution and AI-supported predictions.
Absorber performance is simulated in Aspen Plus using a rate-based packed column model. Table 2 shows the input parameters. The 3D-printed packing is parameterized by literature-based geometric properties [10], while model predictions are evaluated in terms of toluene removal efficiency and sensitivity to mass transfer parameters.

Table 2: Aspen Plus Input Parameters.

Parameter	Value
Column diameter	DN50
Packing height	0.80 m
Operating conditions	T = 25 °C, P = 1.013 bar
Gas feed	N_2 + toluene, $y_{tol,in}$ = 0.01 (mole-based)
Liquid feed	RME / rapeseed oil, L/G = 0.002
Thermodynamics	NRTL (fit to UNIFAC- or AI-generated VLE data) + Henry (N_2)
Mass transfer correlation	Bravo–Rocha–Fair
Packing representation in Aspen	Structured packing; specific surface area a_p and void fraction ε set to literature values for the XW packing (Table 3) [10]

Experimental measurements in the modular 3D-printed column will subsequently be used to validate the model trends and to determine effective transport characteristics for the novel packing under relevant operating conditions.

3. Experimental Setup

Experimental investigations are conducted in a modular laboratory-scale absorption setup designed for systematic studies of tar scrubbing under well-defined conditions. A schematic overview is given in Figure 1, while Figure 2 shows the assembled column system (Figure 2a) and the 3D-printed packing structure (Figure 2b).

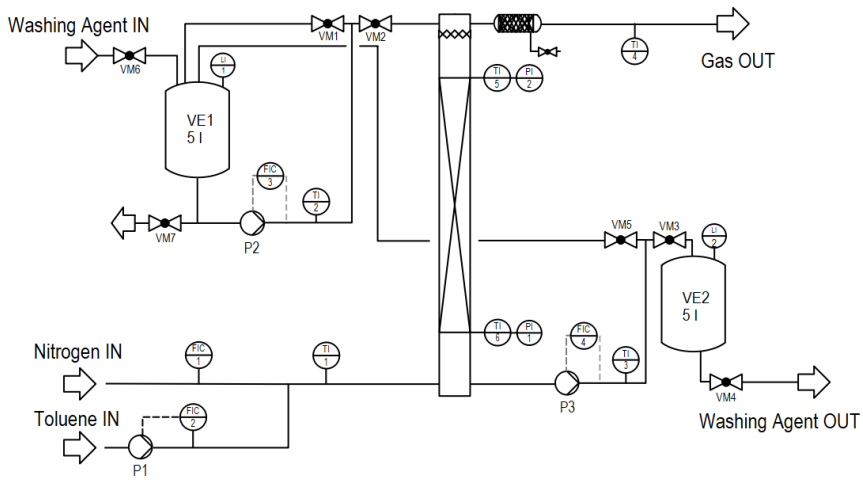

Figure 1: Flow Diagram of the 3D Printed Absorption Column.

The core unit is a vertical DN50 absorption column with a total height of 1.0 m, additively manufactured from polyamide PA12 with integrated internals. The packed section, 0.80 m high, is operated countercurrently, with gas entering at the bottom and washing liquid introduced at the top. Operation is currently single-pass, while liquid recirculation can be implemented in future campaigns. The solvent is supplied from a 5 L buffer vessel upstream of the column. A second 5 L vessel collects the spent solvent at the outlet. Both vessels are jacketed, enabling future temperature control between 20 and 60 °C, whereas the investigations reported here are conducted at

ambient temperature. Nitrogen is used as carrier gas and can be enriched with defined toluene amounts via a pump dosing unit. The N_2 and toluene streams are mixed upstream to ensure a reproducible inlet composition, which is verified by GC. Gas flow rates are controlled by mass flow controllers, and temperatures and pressures are monitored at the column inlet and outlet.

(a) (b)

Figure 2: 3D Printed Absorption Column (a) and 3D Printed Packings (b).

The packed section is equipped with additively manufactured XW-type structured packings. Originally developed for laboratory-scale distillation, these packings feature high void fraction, homogeneous channel geometry, and enhanced radial mixing. Their geometric characteristics are summarized in Table 3 based on literature data [10]. While favorable separation efficiency and scalability have been reported for distillation, the present work investigates the XW packing in gas absorption for the first time.

Table 3: Geometric Properties of the Applied XW Structured Packing for DN50 Columns [10].

Property	Symbol	Value	Unit
Void fraction	ε	0.89	-
Specific surface area (packing)	$a_{geo,\,P}$	349	m^2m^{-3}
Specific surface area (column wall)	$a_{gep,\,PW}$	420	m^2m^{-3}

Gas-phase compositions at the absorber inlet and outlet are quantified using a Nexis GC-2030 gas chromatograph from Shimadzu equipped with one TCD for permanent gases and two FIDs for hydrocarbons. Light hydrocarbons up to C6 are analyzed via FID1, whereas heavier hydrocarbons, including toluene, are quantified by FID2. The detector channels are connected by a valve-based switching system for automated sample routing. Hydrocarbons larger than C6 are separated using a polar capillary column (SH-PolarWax, 30 m × 0.32 mm × 1.0 µm), with helium as carrier gas. Gas-tight sampling is performed under steady-state conditions. Calibration is based on certified gas mixtures; for toluene, a six-point external calibration is used to derive linear response functions. For higher toluene levels expected in future experiments, dedicated N_2–toluene mixtures will be prepared for calibration. The detection limit for toluene is approximately 10 ppm, which is sufficient for the planned absorber studies.

4. Preliminary Results & Outlook

Figure 3 compares predicted infinite-dilution activity coefficients of toluene in RME and rapeseed oil across thermodynamic data sources, namely UNIFAC and AI-based predictions, and across solvent composition models, namely a single-component surrogate and a five-component mixture. Rapeseed oil consistently exhibits higher

activity coefficients than RME, indicating a lower affinity and reduced predicted solubility of toluene in the triglyceride-based solvent. This trend is plausible given the molecular nature of the solvents: compared to rapeseed oil, RME is composed of smaller fatty acid methyl ester molecules with higher polarity and less pronounced steric constraints, which can promote stronger interactions with aromatic solutes and facilitate toluene uptake. Across both solvents and both representations, AI-based predictions yield higher activity coefficients than UNIFAC, implying systematically lower predicted solubilities. In contrast, the effect of solvent representation is moderate and becomes most visible for the AI-based case, where the multi-component description tends to increase predicted non-ideality.

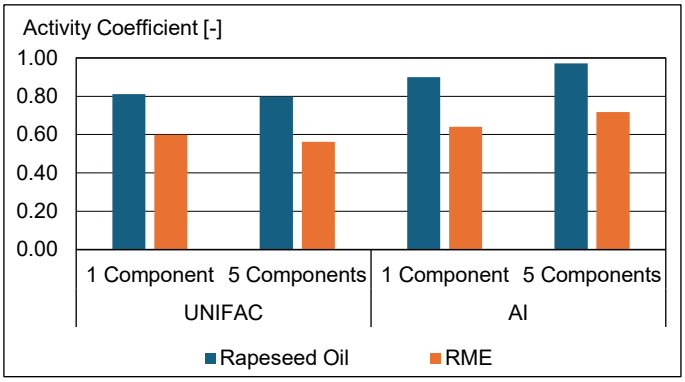

Figure 3: Predicted Activity Coefficients of Toluene at Infinite Dilution in Bio-based Solvents.

The impact of these thermodynamic differences on absorber performance is shown in Figure 4 for selected representative rate-based simulations. Removal efficiency is reported on a molar basis as $\eta = 1 - \dot{n}_{out}/\dot{n}_{in}$. A dimensionless mass transfer multiplier f_{MT} is introduced for sensitivity screening of the currently uncertain packing-specific mass transfer. The multiplier is varied from 0.1 to 2.0 and applied to the baseline gas- and liquid-side coefficients k_G^0 and k_L^0 obtained from the Aspen Plus Bravo–Rocha–Fair correlations, such that $k_G = f_{MT} k_G^0$ and $k_L = f_{MT} k_L^0$. For all cases, removal is low at small f_{MT}, indicating transport limitation, and rises steeply with f_{MT} before approaching an equilibrium-limited plateau. The plateau is governed mainly by solvent choice and thermodynamic description: RME enables higher removal than rapeseed oil, and UNIFAC predicts higher plateaus than the AI-based parameterization, consistent with Figure 3. Thus, thermodynamics set the upper bound, while mass transfer determines how closely it is reached within the available packing height.

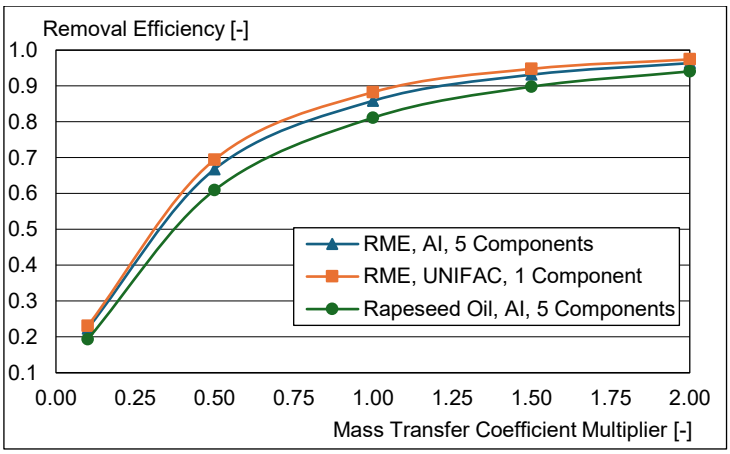

Figure 4: Sensitivity of Predicted Toluene Removal Efficiency to Mass Transfer Coefficients.

Overall, the pronounced sensitivity of predicted removal to f_{MT} highlights that uncertainties in effective interfacial area, wetting, and transport correlations for novel 3D-printed packings can translate into substantial deviations in predicted absorber performance. This directly motivates targeted experiments in the 3D-printed column to determine effective mass transfer parameters and associated hydrodynamics under relevant operating conditions and to enable quantitative validation of the rate-based modeling framework.

5. Conclusions

This work presents an integrated experimental–modeling framework for bio-based tar scrubbing using a modular DN50 absorber with fully 3D-printed internals. Thermodynamic screening predicts lower toluene affinity in rapeseed oil than in RME, and AI-based property models, namely HANNA and GRAPPA, yield higher activity coefficients than UNIFAC, implying reduced solubility and lower attainable removal. Rate-based simulations further show strong sensitivity of removal efficiency to mass transfer, with performance approaching a thermodynamically limited plateau as transport resistances decrease. These results motivate dedicated column experiments to determine effective mass transfer and hydrodynamic parameters and to validate the modeling framework for reliable design and scale-up.

References

[1] N. Abdoulmoumine, S. Adhikari, A. Kulkarni, and S. Chattanathan, "A review on biomass gasification syngas cleanup," *Applied Energy*, vol. 155, pp. 294–307, 2015, doi: 10.1016/j.apenergy.2015.05.095.

[2] B. Ozturk and D. Yilmaz, "Absorptive Removal of Volatile Organic Compounds from Flue Gas Streams," *Process Safety and Environmental Protection*, vol. 84, no. 5, pp. 391–398, 2006, doi: 10.1205/psep05003.

[3] P. R. Bhoi, R. L. Huhnke, J. R. Whiteley, S. Gebreyohannes, and A. Kumar, "Equilibrium stage based model of a vegetable oil based wet packed bed scrubbing system for removing producer gas tar compounds," *Separation and Purification Technology*, vol. 142, pp. 196–202, 2015, doi: 10.1016/j.seppur.2014.12.044.

[4] T. Phuphuakrat, T. Namioka, and K. Yoshikawa, "Absorptive removal of biomass tar using water and oily materials," *Bioresource Technology*, vol. 102, no. 2, pp. 543–549, 2011, doi: 10.1016/ j.biortech.2010.07.073.

[5] X. Zhang *et al.,* "COSMO-based solvent selection and Aspen Plus process simulation for tar absorptive removal," *Applied Energy*, vol. 251, p. 113314, 2019, doi: 10.1016/j.apenergy.2019. 113314.

[6] A. Almoslh, F. Alobaid, C. Heinze, and B. Epple, "Comparison of Equilibrium-Stage and Rate-Based Models of a Packed Column for Tar Absorption Using Vegetable Oil," *Applied Sciences*, vol. 10, no. 7, p. 2362, 2020, doi: 10.3390/app10072362.

[7] R. Harb, R. Rivera-Tinocco, M. Nemer, B. Zeghondy, and C. Bouallou, "Process Simulation of Tar Removal from Gasification Producer Gas," *Chemical Engineering Transactions*, vol. 81, pp. 931–936, 2020, doi: 10.3303/CET2081156.

[8] M. Hoffmann *et al.,* "A machine-learned expression for the excess Gibbs energy," *arXiv preprint arXiv:2509.06484*, 2025.

[9] T. Specht, M. Nagda, S. Fellenz, S. Mandt, H. Hasse, and F. Jirasek, "HANNA: hard-constraint neural network for consistent activity coefficient prediction," *Chemical Science*, vol. 15, no. 47, pp. 19777–19786, 2024, doi: 10.1039/D4SC05115G.

[10] J. Neukäufer *et al.,* "Development of enhanced three-dimensional printed packings for scale-up of distillation columns: A successful case study," *AIChE Journal*, vol. 69, no. 3, 2023, doi: 10.1002/aic.17902.

[11] S. Brinkmann and B. C. Seyfang, "Building a Code-Based Model to Describe Syngas Production from Biomass," *ChemEngineering*, vol. 8, no. 5, p. 94, 2024, doi: 10.3390/chemengineering 8050094.

Designing Bubbles for Better Batteries: CO_2-Driven Lithium Recovery in Bubble Columns

Florian Klapal[1], Stefanie Flatscher[1], Manuel C. J. Schachinger[2], Mark W. Hlawitschka[1]

[1]Institute of Process Engineering, Johannes Kepler University Linz, 4040 Linz, Austria;
[2]University of Applied Science Upper Austria, Campus Wels, 4600 Wels, Austria;

Abstract

Lithium carbonate (Li_2CO_3) precipitation is a central unit operation in lithium processing, where lithium recovery, product purity and process robustness must be balanced. Compared to conventional precipitation, gas-liquid precipitation using carbon dioxide (CO_2) introduces additional process degrees of freedom through mass transfer and hydrodynamics enabling in addition direct CO_2 utilization. The influence of reactor design and gas dispersion on process performance is insufficiently understood. In this work, conventional precipitation pathways were benchmarked against gas-liquid Li_2CO_3 precipitation in bubble columns of laboratory and technical scale. The effect of alkalinity, gas flow rate and bubble size on mass transfer, reaction kinetics, lithium recovery, product purity and CO_2 capture efficiency were analyzed. The results show that bubble size directly governs absorption efficiency, supersaturation and crystallization behavior. Small bubbles enhance CO_2 capture but promote rapid precipitation and impurity inclusion, whereas larger bubbles improve mixing and product purity, by reducing supersaturation and slowing down reaction kinetics. Disperser design is a scalable process-engineering level to balance lithium recovery, purity and CO_2 utilization in bubble column reactors.

Keywords

Lithium carbonate precipitation; Bubble column reactor; Gas-liquid mass transfer; Disperser design; CO_2 utilization

1. Introduction

Lithium carbonate (Li_2CO_3) is the most important lithium compound for the production of lithium-ion batteries and currently accounts for approximately 60% of global lithium consumption (Kim et al. 2024). Driven by the rapid growth of electric mobility and stationary energy storage, global Li_2CO_3 demand is projected to exceed 2 million ton per year by 2030, with further increases expected toward midcentury (Kim et al. 2024; Aprilianto et al. 2024). At the same time, lithium supply chains face increasing pressure due to limited geographical availability, rising extraction costs and environmental constraints, highlighting the need for more efficient and sustainable lithium recovery processes.

Industrially, Li_2CO_3 is predominantly produced by chemical precipitation using sodium carbonate (Na_2CO_3) from lithium-containing brines leachates or recycled battery streams (Han et al. 2020; Aprilianto et al. 2024). While this route enables high lithium recovery, it is frequently associated with sodium contamination, occlusion and limited purity control, particularly under highly supersaturated conditions. Several studies report that rapid precipitation kinetics promote impurity inclusion and require additional washing or recarbonation steps to meet battery-grade purity specifications (Han et al. 2020; Kim et al. 2024).

An alternative approach is the use of CO_2 as carbonate source, which enables lithium precipitation through gas-liquid reactive crystallization. Beyond avoiding direct sodium introduction, CO_2-based precipitation offers the potential for simultaneous CO_2 utilization, linking lithium production to carbon management strategies (Kim et al. 2024). Previous studies have demonstrated that CO_2 precipitation can produce Li_2CO_3 with high purity, but often at the expense of lithium recovery due to carbonate speciation, pH limitations and gas-liquid mass transfer constraints (Han et al. 2020; Shin et al. 2022). As a result, CO_2-based routes are commonly regarded as kinetically and hydrodynamically limited rather than chemically constrained.

From a process-engineering perspective, gas-liquid mass transfer and hydrodynamics play a decisive role in CO_2-driven Li_2CO_3 precipitation by controlling carbonate availability and local supersaturation. In this work, classical solid-liquid and liquid-liquid precipitation routes are benchmarked against CO_2-driven gas-liquid precipitation in laboratory- and technical scale bubble columns. In a first step, laboratory-scale experiments were conducted to compare how different reaction pathways control carbonate availability and supersaturation during Li_2CO_3 precipitation. The objective was to identify fundamental differences in precipitation kinetics between solid-liquid, liquid-liquid and gas-liquid systems, which later serve as benchmarks for understanding purity, yield and scale-up behavior.

By focusing on disperser design in the bubble column experiments as a process control lever, the trade-offs between lithium recovery, product purity and CO_2 utilization are systematically investigated.

2. Results and discussion

2.1 Experimental setup and methodology

Solid-liquid and liquid-liquid experiments were all performed in a 1L glass beaker, equipped with a stirrer and pH sensor. Li_2SO_4 (Thermo Scientific.; 99.7%) was dissolved with deionized water, depending on the reaction type Na_2CO_3 (VWR Chemicals; 99.8%) was either also dissolved or added in solid form. Reaction progress was tracked with the pH sensor and the precipitate was after finishing the reaction filtrated and then dried at 110°C.

Gas–liquid precipitation experiments were conducted in bubble column reactors at laboratory and technical scale, specific setup values are listed in Table 1. At laboratory scale, experiments were primarily used to assess feasibility, reaction behavior, and the influence of gas flow rate and alkalinity. The bubble columns were also equipped with a pH sensor to determine the endpoint of the reaction. A pH of 10 was selected as the reaction endpoint, as it maintains favorable carbonate formation prior to the predominance of bicarbonate species. Similar to the benchmark experiments, the precipitate was filtered and dried after finishing the reaction. The CO_2 (purity 4.5, Linde) introduction was regulated with a mass flow controller (Brooks Instruments; SLA5850SGAB1C2A1). Technical scale experiments focused on hydrodynamic control and reactor design effects, with particular emphasis on gas disperser geometry. By influencing the bubble size, the hydrodynamics of the reactor can be regulated. This was investigated by varying the pore size of the 3D-printed Plug-In disperser (PP). The exact specification of the used dispersers can be taken from Table 2 and the schematic buildup from Figure 1a. The amount of unabsorbed CO_2 was tracked with a mass flow meter at the end of the bubble column, the complete reactor setup is depicted in Figure 1b. Scale-up was achieved by increasing reactor diameter and liquid volume while maintaining comparable superficial gas velocities.

Across all gas–liquid experiments, alkalinity and gas dispersion were identified as key control parameters. Sodium hydroxide concentration was varied to influence carbonate availability through CO_2 speciation, while disperser pore size was systematically changed to modify bubble size, gas–liquid contact, and mass transfer. Lithium recovery, product purity with respect to sodium contamination, and CO_2 uptake were used as performance indicators. Solid products were separated after reaction completion and analyzed (ICP-OES; XRD; IC and SEM) following drying.

Table 1: Operating conditions and geometric parameters of the laboratory and technical scale.

	DN [mm]	H_{column} [mm]	$V_{reaction}$ [L]	$H_{filling}$ [mm]	c(NaOH) [mol L^{-1}]	β(Li^+) [g L^{-1}]
Laboratory	30	1000	0.4	600	5; 20	20
Technical	100	2000	7	900	20	20

Table 2: Gas disperser design parameters and operating gas flow rates for the laboratory and technical scale.

	Disperser	Pore size [mm]	Number	Free Area %	Gas flowrate [NL min^{-1}]
Laboratory	Plate	0.5	177	5	0.3; 0.6; 1
Technical		1; 1.5; 2.5	74	2.5; 5.7; 15.7	10

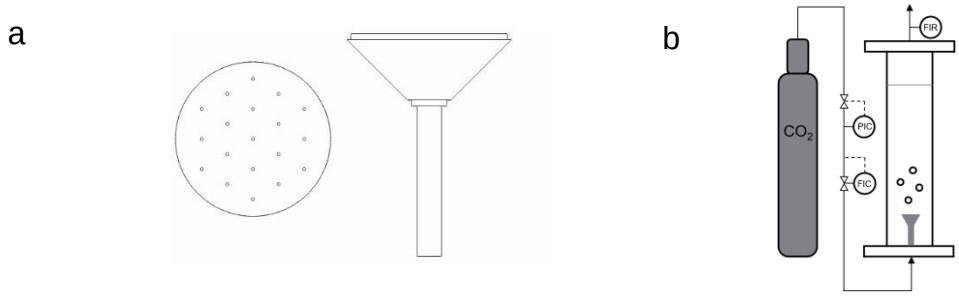

Figure 1: Disperser design and technical-scale bubble column setup.

2.2 Reaction pathway comparison and carbonate availability at laboratory scale

Solid-liquid precipitation was investigated as a reference case with direct carbonate dosing. In this pathway, carbonate availability is governed not only by stoichiometry but also by the dissolution rate of solid Na_2CO_3. To avoid extreme local supersaturation. Na_2CO_3 was added stepwise. Despite this controlled addition, an immediate increase in pH and temperature was observed after each dosing step, followed by a gradual pH decrease. This behavior indicates rapid dissolution and near-instantaneous carbonate consumption through Li_2CO_3 formation, demonstrating that carbonate availability is high and precipitation kinetics are fast. The need for stepwise addition highlights the intrinsic limitation of solid-liquid systems, where carbonate release cannot be decoupled from local supersaturation effects.

Liquid-liquid precipitation was studied to assess whether homogeneous carbonate distribution mitigates the limitations observed in solid-liquid systems. Here, lithium sulfate was added to a pre-dissolved sodium carbonate solution, ensuring uniform carbonate availability throughout the reactor. This resulted in a high initial pH (11.5) and temperature, followed by rapid stabilization of both parameters. The abrupt pH decrease observed after mixing confirms immediate carbonate consumption and fast precipitation consistent with high initial supersaturation under homogeneous conditions. While improved mixing eliminates dissolution limitations, carbonate availability remains instantaneous and precipitation kinetics are still dominated by rapid supersaturation.

Gas-liquid precipitation was investigated to introduce a kinetic limitation on carbonate formation via CO_2 absorption and subsequent speciation under alkaline conditions. In contrast to direct carbonate addition, pH decreases gradually from 11.5 to the targeted pH of 10 over time, reflecting absorption-controlled carbonate availability. The absence of abrupt pH jumps and the delayed temperature increase demonstrate moderated supersaturation and slower precipitation kinetics. Carbonate availability is therefore governed by gas-liquid mass transfer and hydroxide concentration rather than instantaneous dosing.

Overall, direct carbonate addition leads to immediate availability and fast supersaturation, while gas-liquid operation enables kinetic control over carbonate formation. These differences form the mechanistic basis for the observed variations in precipitation behavior and motivate the subsequent analysis of yield, purity and hydrodynamic control.

2.3 Lab scale: Comparison between classical precipitation and lab scale bubble column experiments

A central objective of Li_2CO_3 precipitation is the recovery of lithium at high yield while maintaining strict control over product purity. Building on the differences in carbonate availability identified at laboratory scale, comparing different reaction pathways enables the identification of inherent trade-offs between lithium utilization and impurity incorporation. In this study, yield and purity were evaluated for solid–liquid, liquid–liquid, and gas–liquid precipitation routes using lithium recovery and sodium contamination as key performance indicators.

Liquid–liquid precipitation achieved a lithium recovery of approximately 82% under the investigated conditions. Rapid mixing and immediate carbonate availability promoted fast precipitation, enabling high conversion. However, the resulting product contained around 85% Li_2CO_3 with a sodium contamination of 3.2%, indicating that rapid crystallization under highly supersaturated conditions favors occlusion and liquid entrapment. Solid–liquid precipitation resulted in an even higher lithium recovery of 88%, but with substantially reduced product purity. Sodium contamination increased to 8.9%, and the Li_2CO_3 content dropped to approximately 72%. This behavior is attributed to incomplete dissolution of solid sodium carbonate, leading to localized supersaturation and precipitation near undissolved solids increase mother liquor entrainment and Na carry over.

Gas–liquid precipitation introduces carbonate gradually via CO_2 absorption, which fundamentally alters precipitation kinetics. At low hydroxide concentrations, lithium recovery was limited to 26–28% due to carbonate speciation, with a significant fraction of absorbed CO_2 converted into bicarbonate rather than carbonate ions. Bicarbonate formation reduces carbonate availability, causing a fraction of lithium to remain in solution. Despite this limitation, the gas–liquid route yielded products with high purity, containing 88–92% Li_2CO_3 and sodium contamination as low as 0.2%. The high product purity obtained via gas-liquid precipitation is further supported by the observed particle morphology, which shows aggregated plate-like Li_2CO_3 crystallites (Figure 2). Increasing the hydroxide concentration removed the carbonate limitation and significantly improved lithium recovery to approximately 87%. However, this improvement came at the expense of purity, with sodium contamination increasing to 6.8% and Li_2CO_3 content decreasing to 92 %. The rapid and efficient CO_2 absorption at high alkalinity led to elevated carbonate concentrations and fast precipitation under supersaturated conditions, increasing the likelihood of liquid entrapment and impurity inclusion. Overall, these results demonstrate a clear trade-off between lithium recovery

and product purity. While direct carbonate addition favors high recovery with limited purity control, gas–liquid precipitation enables superior purity through kinetic moderation, provided that alkalinity and absorption rates are carefully balanced.

2.4 Technical-scale investigation: Disperser design as a process control lever

2.4.1 Influence of disperser design on lithium recovery and product purity

The disperser with the smallest pore size achieved a lithium recovery of 65% with a product purity of 95% Li_2CO_3 and a sodium contamination of 1.7%. While purity increased compared to laboratory-scale results, lithium recovery remained limited. This behavior is attributed to rapid precipitation under conditions of high local supersaturation. Small bubble diameters enhanced gas-liquid mass transfer, leading to fast CO_2 absorption and rapid carbonate formation. As a result, the system quickly transitioned into an absorption-limited regime governed by hydroxide depletion, causing an early CO_2 breakthrough. This limited the effective carbonate availability and reduced the achievable lithium recovery. In addition, the smaller bubbles provided only limited mixing intensity, promoting early particle settling below the disperser. The increased residence time in low-flow regions favored continued crystal growth and impurity incorporation contributing to the observed sodium contamination.

The intermediate pore-size disperser resulted in the highest lithium recovery of 68% while maintaining a product purity of 96% Li_2CO_3 and a sodium contamination of 1.2%. Improved mixing and moderated precipitation kinetics reduced impurity inclusion while preserving sufficient absorption capacity, leading to the most balanced performance among the investigated designs.

The largest pore-size disperser exhibited the lowest lithium recovery due to early CO_2 breakthrough, which limited the overall extent of precipitation. However, this configuration produced the highest product purity, reaching 99% Li_2CO_3 with minimal sodium contamination. Early reaction termination at high pH restricted supersaturation and favored selective Li_2CO_3 formation. Overall, these results demonstrate that disperser design governs the balance between lithium recovery and purity through its combined influence on mass transfer and mixing.

2.4.2 Influence of disperser design on CO_2 capture behavior

The precipitation of Li_2CO_3 via CO_2 absorption enables the simultaneous capture and utilization of CO_2. Since unabsorbed CO_2 was not recycled in the investigated system, direct absorption efficiency was a key performance metric. Figure 3, shows the reaction behavior of the smallest-pore disperser. Very low outlet CO_2 flow rates were observed during the early phase of the experiment. This behavior is attributed to residual nitrogen from the initial mixing phase and increasing gas holdup. During the intermediate phase, outlet CO_2 flow rates approached zero, indicating near-complete absorption. After approximately 750 s, a sharp increase in outlet flow marked the onset of CO_2 breakthrough and the transition to an absorption-limited regime. Overall, 200 L of CO_2 were absorbed, corresponding to an absorption efficiency of 91%.

The intermediate pore-size disperser exhibited a higher baseline outlet flow and did not reach near-zero values. A gradual increase in outlet flow indicated that the absorption limit was approached more slowly. This design absorbed 173.3 L of CO_2 with an efficiency of 88.9%.

In contrast, the largest pore-size disperser showed a relatively constant outlet flow and experienced early CO_2 breakthrough, limiting total uptake to 96.9 L with an absorption efficiency of 74.0%. Increasing pore size resulted in larger bubbles with shorter residence times and reduced interfacial area, significantly lowering mass-transfer efficiency. Although the initially high pH provided a strong driving force for absorption,

this could not compensate for the reduced gas–liquid contact once hydroxide was depleted, leading to early absorption limitation.

Overall, the results show that disperser design effectively tunes CO_2 capture behavior. Smaller bubbles enhance CO_2 absorption efficiency but promote rapid precipitation that can impair product quality, while larger bubbles cause earlier breakthrough and reduced lithium recovery but enable higher product purity. These findings highlight that CO_2 capture efficiency and CO_2 utilization efficiency must be considered separately when optimizing gas–liquid precipitation systems.

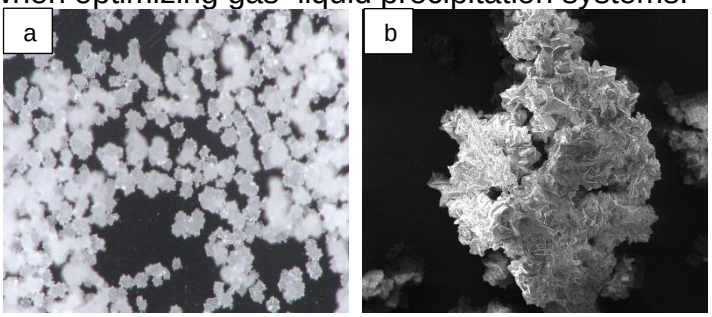

Figure 2: Morphology of Li2CO3 precipitated via gas-liquid reaction. (a) optical microscopy and (b) SEM.

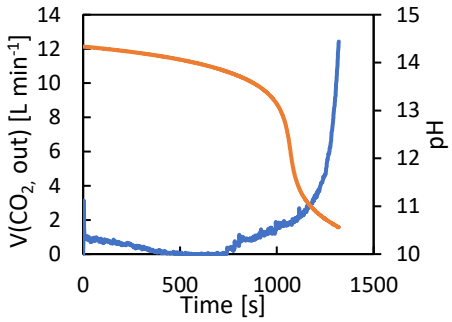

Figure 3: pH and outlet gas flow during technical CO_2 precipitation.

3. Conclusions

This work shows that lithium carbonate precipitation is governed by the interplay between carbonate availability, supersaturation, and crystallization kinetics, which together determine lithium recovery and product purity. Conventional solid–liquid and liquid–liquid routes provide rapid carbonate availability but promote strong supersaturation, leading to fast crystallization and impurity incorporation. In contrast, CO_2-driven gas–liquid precipitation imposes mass-transfer-controlled carbonate formation, moderating supersaturation, improving product purity, and enabling CO_2 utilization. Technical-scale experiments further demonstrate that reactor hydrodynamics critically influence process performance. Disperser design was identified as a key control parameter governing bubble size, gas–liquid contact, and absorption efficiency. Small bubbles enhance CO_2 uptake but accelerate precipitation and limit lithium recovery, whereas larger bubbles reduce mass-transfer efficiency, promote earlier CO_2 breakthrough, and enable higher product purity at the expense of recovery. Overall, the results reveal a clear trade-off between lithium recovery, product purity, and CO_2 utilization. Rather than maximizing a single metric, gas–liquid Li_2CO_3 precipitation can be flexibly operated within a defined process window through appropriate selection of alkalinity and disperser design, establishing bubble-scale hydrodynamic control as a central design principle for scalable lithium recovery processes.

References

Aprilianto, Doni Riski; Perdana, Indra; Rochmadi; Petrus, Himawan Tri Bayu Murti (2024): Effect of Sulfate and Carbonate Ions on Lithium Carbonate Precipitation from a Low Concentration Lithium Containing Solution. In: *Ind. Eng. Chem. Res.* 63 (11), S. 4918–4933. DOI: 10.1021/acs.iecr.3c04294.

Han, Bing; Anwar Ul Haq, Rana; Louhi-Kultanen, Marjatta (2020): Lithium carbonate precipitation by homogeneous and heterogeneous reactive crystallization. In: *Hydrometallurgy* 195, S. 105386. DOI: 10.1016/j.hydromet.2020.105386.

Kim, Sung-hwan; Yoon, Hongsik; Min, Taijin; Han, Bangwoo; Lim, Sungil; Park, Joonwoo (2024): Carbon dioxide utilization in lithium carbonate precipitation: A short review. In: *Environmental Engineering Research* 29 (3), 230553-0. DOI: 10.4491/eer.2023.553.

Shin, Junho; Jeong, Jae-Min; Lee, Jin Bae; Cho, Hey-Jin; Kim, Young Ho; Ryu, Taegong (2022): Preparation of lithium carbonate from waste lithium solution through precipitation and wet conversion methods. In: *Hydrome*

Advancing Reverse Jet Scrubber design through experiments integrated modeling approaches

Pietro Giustacori[1], *Elisabetta Brunazzi*[1]
[1]*Department of Civil and Industrial Engineering (DICI), University of Pisa, 56122, Pisa, Italy*

Abstract
Conventional wet scrubbers are often unsuitable for space-limited applications, where compact and efficient gas treatment systems are required. In this field Reverse jet scrubbers (RJS) have emerged as promising multifunctional units capable of simultaneously performing gas quenching, particulate removal, and chemical absorption within a compact design. The RJS employs a countercurrent liquid jet injected into a descending gas stream within a vertical channel, forming an intense turbulent froth zone that enhances gas-liquid interactions. Owing to their simple geometry and lack of moving parts, RJS systems offer operational robustness for high-temperature and fouling-prone gas streams. Despite their growing industrial relevance, limited data exists on their hydrodynamic and mass transfer characteristics.
This study presents a detailed experimental investigation of a pilot-scale RJS operated over a broad range of gas and liquid flow conditions. Phase-specific mass transfer resistances were examined using volatile organic compounds (VOCs) of varying solubility. Semi-empirical and mechanistic correlations were developed to predict mass transfer coefficients. The proposed model, validated against experimental data for isopropanol and butyl acetate absorption, showed excellent predictive capability, with most predictions within ±30% of measured values.

Keywords
Gas–liquid contactor, compact scrubber, semi-empirical correlation, jet height model, mass transfer model

1. Introduction

Combustion based energy generation in stationery and mobile applications remains a major contributor to anthropogenic air pollution. Emissions of sulfur dioxide, nitrogen oxides, volatile organic compounds, and incomplete combustion products adversely affect air quality and pose significant risks to human health [1]. In response, environmental regulations have become increasingly stringent. Progressive tightening of air quality standards by agencies such as the U.S. Environmental Protection Agency, together with international measures including the sulfur limits imposed under MARPOL Annex VI, have intensified the demand for efficient and reliable gas cleaning technologies [2].
Conventional emission control systems including flue gas desulfurization units, electrostatic precipitators, and selective catalytic reduction reactors achieve high removal efficiencies in large, centralized facilities. However, their application in decentralized, mobile, or space constrained environments is limited by high energy demand, large footprint, and operational complexity. Sectors such as maritime transport, offshore installations, and distributed industrial processes require compact

treatment solutions that maintain performance under constraints on space, weight, and maintenance access

Wet scrubbing remains a robust and widely used approach for the removal of acid gases, VOCs, and particulate matter. Traditional packed columns and spray towers rely on counter current operation, which restricts allowable gas velocities and leads to large equipment dimensions in order to avoid flooding and excessive pressure drop. These limitations have motivated growing interest in intensified gas liquid contactors capable of delivering high interfacial area and mass transfer rates within compact geometries [3].

Among emerging compact scrubber designs, the Reverse Jet Scrubber has attracted attention as a space efficient and mechanically simple technology. By injecting liquid jets directly against the incoming gas flow, the RJS generates a highly turbulent contact zone with fine droplet dispersion and rapid interfacial renewal. This hydrodynamic regime supports effective gas cooling, particulate capture, and absorption of soluble or reactive pollutants, while maintaining tolerance to solids and reducing fouling risks [4]. Despite these advantages, broader industrial implementation has been limited by the lack of detailed understanding of its hydrodynamics and mass transfer behavior, as well as the absence of reliable design and scale up correlations.

This study addresses these limitations by developing an integrated experimental and modeling framework for Reverse Jet Scrubber performance assessment, with the objective of supporting rational design, optimization, and scale up for compact gas treatment applications.

2. Experimental setup

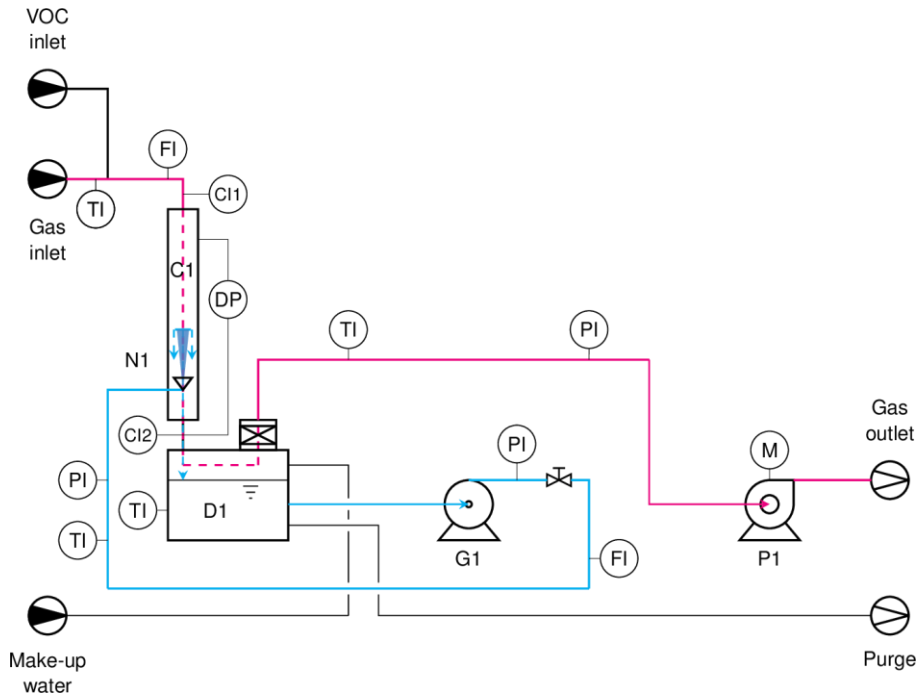

Figure 1: Schematic diagram of the experimental test rig, cyan and magenta lines represent the liquid and gas flow paths, respectively (C1: vertical contact section, D1: liquid tank, G1: centrifugal liquid pump, P1: centrifugal fan, CI: concentration indicator, FI: flow indicator, PI: pressure indicator, TI: temperature indicator, DP: differential pressure sensor, M: motor).

A series of experiments were conducted using a pilot-scale setup designed to investigate gas-liquid interactions and mass transfer performance. Figure 1 shows a

schematic of the experimental setup, where the liquid and gas flow paths are indicated by cyan and magenta lines, respectively. The test rig is composed of a contact section (C1) wherein the gas and liquid phases interact and auxiliary equipment such as a pump (G1), fan (P1), and sensors that are necessary for the circulation of fluids and monitoring. The contact section, with an internal diameter of 300 millimeters, is equipped with a 30-degree solid cone nozzle (N1) that directs the liquid flow upward.
The current configuration enables the investigation of liquid flow rates (L_v) up to 40 m^3/h and gas flow rates (G_v) up to 3,500 m^3/h. For the mass transfer experiments, the gas phase was doped with volatile organic compound (VOC) at tracer levels to evaluate the performance of the compact scrubber. Two VOCs with differing solubilities in water were selected to assess absorption behavior. The concentration of VOCs was measured using two inline multi-gas analyzers, positioned upstream and downstream of the liquid jet. The range of VOC concentrations recorded varied from 600 to 50 ppm_v. Further details on the design, instrumentation, and operation of the experimental setup are provided in [5].

3. Results and discussion

The molar flux of VOC from gas to liquid, N_{VOC}, is described by Whitman's two-film theory, which attributes all mass transfer resistance to stagnant films on both sides of the interface.

$$N_{VOC} = K_G a \cdot V \cdot \Delta \mathrm{C_{LM}} \tag{1}$$

Experimentally, the molar flux was determined from the measured decrease in VOC concentration in the gas stream after contact with the liquid jet. For dilute systems, N_{VOC} is expressed as $G_V(C_{\mathrm{IN}} - C_{\mathrm{OUT}})$. By equating the theoretical expression for the molar flux with the experimentally determined gas-phase removal rate, the overall gas-side volumetric mass transfer coefficient, $K_G a$, was calculated. This procedure was applied to both isopropanol (IPA) and butyl acetate (BA) absorption systems.
To better understand the mass transfer processes occurring in the reverse jet scrubber, the overall volumetric mass transfer coefficient was separated into its gas-side and liquid-side contributions, $k_G a$ and $k_L a$, respectively. This was performed using an iterative procedure derived from the two-film theory, in which the inverse of the overall gas-side mass-transfer coefficient (i.e., the overall resistance) is expressed as the sum of the gas-phase and liquid-phase resistances.
The iterative procedure was applied at identical liquid and gas flow rate conditions for both systems. Calculations were initiated with the IPA system due to its high solubility in water, which implies that mass transfer resistance is predominantly located in the gas phase. This assumption was used to generate an initial estimate of the resistance distribution and to calculate $k_G a$ for IPA from the measured $K_G a$. The gas-side coefficient for BA was then obtained by scaling the IPA value with the square root of the ratio of their gas-phase diffusivities, in accordance with Higbie's penetration theory. Using the scaled gas-side coefficient, the gas-phase resistance for BA was determined and subtracted from the experimental overall resistance to obtain the liquid-side resistance, from which $k_L a$ for BA was calculated. The liquid-side coefficient for IPA was subsequently estimated by scaling the BA value with the square root of the ratio of the liquid-phase diffusivities of IPA and BA, again following penetration theory. With both $k_G a$ and $k_L a$ estimated for IPA, the overall resistance was recalculated and compared to the experimental value. The procedure was repeated until convergence was reached, by agreement between calculated and measured overall resistances. At

convergence, single-side volumetric mass transfer coefficients were obtained for both compounds at each tested combination of gas and liquid flow rates, yielding a complete dataset for the investigated operating conditions.
To establish a framework for describing mass transfer performance in reverse jet scrubbers, inspiration was drawn from the theoretical model for gas-side mass transfer coefficients proposed by Calvert et al. [6] for Venturi scrubbers. Calvert's method, based on Higbie's penetration theory, relates the mass transfer coefficient to the square root of the molecular diffusivity and a characteristic contact time. For the RJS, this contact time was taken as the ratio between the characteristic size of dispersion elements (d_d) and the relative velocity between gas and liquid phases (u_r).

$$k_G = 2\sqrt{\frac{D_G u_r}{\pi d_d}} \tag{2}$$

The size of the drop was set at 5 millimeters, according to the values provided by the nozzle manufacturer. The gas-side mass transfer coefficient can be calculated independently by applying this theoretical model to the known physical properties and flow conditions. This methodology enables the extraction of the specific interfacial area, a, from experimental volumetric mass transfer coefficients. The results showed that the interfacial area depends significantly on the gas power consumption per unit volume. Accordingly, the values of a were correlated with $G_V \cdot \Delta p/V$, where Δp is gas pressure drop across the liquid jet, yielding the following equation:

$$a = 23.71\left(\frac{G_V \Delta p}{V}\right)^{0.35} \tag{3}$$

The specific interfacial area values were subsequently employed to determine the liquid-side mass transfer coefficient from butyl acetate absorption data, by dividing the experimental $k_L a$ values by the model derived area.
The reverse jet contactor may be viewed as a conceptual inversion of a distillation tray, in which the gas phase is introduced into a continuous liquid medium, generating a froth-like dispersion comparable to that observed on conventional trays. This analogy provides a useful framework for interpreting the hydrodynamic behavior and mass transfer mechanisms in the RJS, since interphase mass transfer is primarily controlled by the dynamics of the dispersed phase within the froth region. To model the liquid side mass transfer coefficients of the RJS, established theoretical frameworks for froth systems have been employed. These frameworks often describe the liquid Sherwood number (Sh_L) as a function of dimensionless groups representing flow (Reynolds number, Re) and diffusion characteristics (Schmidt number, Sc)
In this study, the exponent of the Schmidt number was fixed at 1/2, consistent with the correlation for gas-liquid mass transfer in large bubble froth. This value is also consistent with the iterative procedure, where the liquid side mass transfer coefficients were assumed to scale with the square root of the liquid diffusivity. The remaining parameters, pre-exponential and Reynolds exponent were fitted through linear regression analysis using experimental data, yielding the following empirical correlation:

$$Sh_L = 1.21 \times 10^6 Re_r^{1.74} Sc_L^{0.5} \tag{4}$$

In this correlation, the characteristic dimension employed for calculating the Sherwood and Reynolds numbers was the representative diameter of large bubbles within the froth phase, which was assumed constant at 10 mm. For additional information on the model derivation the reader can refer to [7].
The proposed framework integrates a penetration theory based estimation of the gas-side mass transfer coefficient with an empirically determined specific interfacial area and a Sherwood number correlation for the liquid side, allowing the prediction of overall volumetric mass transfer coefficients across different solute systems and operating conditions. The resulting model was validated against experimental absorption data for both IPA and BA.

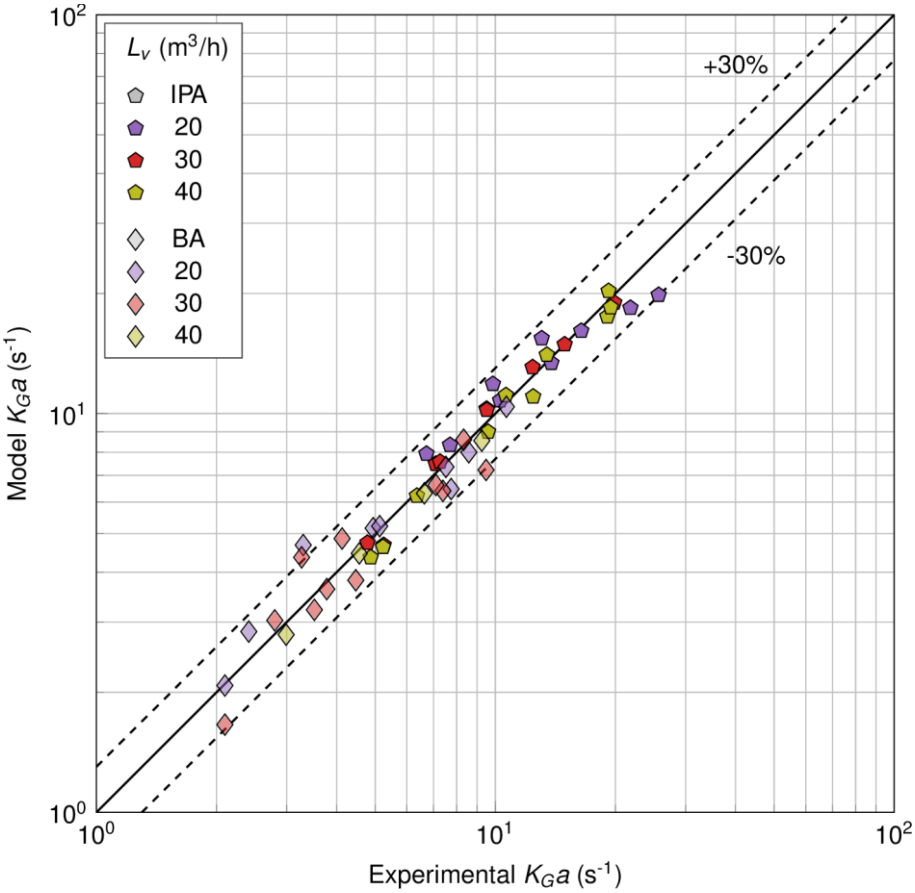

Figure 2: log-log parity plot of the overall mass transfer coefficients for IPA and BA.

Figure 2 presents a parity plot comparison between experimentally measured and model-predicted overall mass transfer coefficients for IPA and BA. The model exhibits good predictive performance, with most data points lying within ±30% of the experimental values. Larger discrepancies observed for BA can be ascribed to its lower aqueous solubility, which increases sensitivity to local mass transfer resistances that are not fully resolved in the present formulation. Despite these deviations, the level of agreement is adequate for engineering purposes, such as the design and optimization of RJS units. Future developments may focus on incorporating more detailed hydrodynamic descriptions or explicitly accounting for froth dynamics, with the aim of improving the representation of transient interfacial phenomena. As an additional validation and robustness assessment of the proposed model under realistic industrial conditions, it was applied within the framework of the TRAFUCER project to estimate the removal and abatement efficiencies of selected pollutants in gaseous effluents from

the ceramics industry. Field-scale experimental campaigns are currently underway to validate model predictions.

4. Conclusions

This work reports the development and semi-empirical modeling of a compact reverse jet scrubber intended for high-efficiency gas purification in industrial applications where space limitations are a critical constraint. An extensive experimental campaign was performed over a broad range of gas and liquid flow rates to systematically characterize the mass transfer behavior of the reverse jet scrubber. Based on the experimental dataset, mechanistic correlations were formulated to describe the single-side mass transfer coefficients as functions of the governing operating parameters.

The resulting correlations exhibit strong predictive performance and provide a practical, design-oriented tool for the analysis, sizing, and optimization of compact gas–liquid contactors. The experimental results confirm the effectiveness of the reverse jet scrubber configuration for pollutant removal and highlight its operational flexibility across a variety of industrial sectors, including maritime applications, offshore facilities, and densely populated urban industrial environments.

The model developed in this study addresses a notable gap in the existing literature by offering an experimentally validated framework specifically tailored to compact scrubbing devices, thereby enabling more reliable and accurate engineering design. Current activities within the TRAFUCER project are directed toward further validation of the model using representative pollutants typically encountered in ceramic industry exhaust streams, as well as toward evaluating long-term operational stability under realistic industrial operating conditions.

Overall, the outcomes of this work constitute a significant contribution to the advancement of compact gas purification technologies and support the development of more sustainable and regulation-compliant industrial emission control solutions.

Acknowledgements

The authors acknowledge the financial support of the Regione Toscana for the TRAFUCER project (Innovative process for treating gaseous effluents from ceramics production) through the fund PR FESR TOSCANA 2021-27, AZ 1.1.4 (Bando 2) (CUP: 27717.29122023.043000343). We are also grateful to AWS Corporation Srl for generously providing the experimental equipment.

References

[1] World Health Organization, WHO Global Air Quality Guidelines: Particulate Matter, Ozone, Nitrogen Dioxide and Sulfur Dioxide, WHO, 2021.

[2] International Maritime Organization (IMO), Marpol annex vi: Prevention of air pollution from ships, IMO Publications, 2020.

[3] F. Khan, S. Rathnayaka, S. Ahmed, Offshore process safety: Technical and operational challenges, Process Safety and Environmental Protection 116 (2018) 439–452. doi:10.1016/j.psep. 2016.11.016.

[4] R. M. James, Application of dynawave scrubber for particulate and sulfur dioxide control in a chemical recovery boiler, in: IPPTA Convention Issue 1996, 1996, pp. 135–138.

[5] P. Giustacori, E. Brunazzi, Characterization of a reverse jet scrubber for gas/liquid absorption, Chemical Engineering Science 308 (2025) 121391. doi:10.1016/j.ces.2025.121391.

[6] S. Calvert, J. Goldshmid, D. Leith, D. Mehta, United States Environmental Protection Agency Office of Air Programs Control Systems Division, Scrubber Handbook, Wet Scrubber system study, APT, 1972.

[7] P. Giustacori, E. Brunazzi, Hydrodynamic and mass transfer in a reverse jet scrubber: Models development and experimental validation, Chemical Engineering Journal 526 (2025) 171327. doi:10.1016/j.cej.2025.171327.

Posters

New Cubic Equation of State Mixing Rules with COSMOSPACE

Emma Russell[1], Hendrik A. Kooijman[1], Ross Taylor[1]
[1]Clarkson University, Potsdam, NY, USA

Abstract
Accurate prediction of phase equilibria is essential for the design and safe operation of separation processes, which account for a significant portion of industrial energy consumption. Recent work has demonstrated that the Wilson model performs well as a gamma-model in Gibbs excess energy mixing rules. Building on the largely ignored study by Bosse and Bart (2005), in which COSMOSPACE (a surface-pair interaction-based model derived from COSMO-RS) achieved comparable accuracy to the Wilson model and outperformed UNIQUAC for the selected cases, we propose the implementation of COSMOSPACE in a Gibbs excess energy mixing rule model: COSMOSPACE-G^E for cubic equations of state.

COSMOSPACE-G^E is shown to provide accurate predictions for vapor-liquid equilibrium (VLE. To accomplish this, the performance of COSMOSPACE-G^E is benchmarked against the Wilson model (and variations with G^E mixing rules) and UNIQUAC using a database of 200 nonelectrolyte binary systems. We also highlight the importance of the choice of combinatorial terms, emphasizing the use of the Flory-Huggins term over the commonly used Staverman-Guggenheim term. Comparisons between variants of UNIQUAC, and COSMOSPACE-G^E using different combinatorial terms are made to determine the most accurate model combinations for phase equilibrium prediction.

Keywords
Phase equilibria, COSMOSPACE, Mixing rules, EOS/G^E models

1. Introduction

The reliable and accurate prediction of thermodynamic properties is an important aspect of process design. Phase equilibrium calculations are especially important, as they are involved at virtually every turn in design and simulation. This is particularly true in the cases of separations processes, where realistic modelling is essential for achieving desired product quality, process efficiency, and safe operation.

Separations processes, most notably distillation, comprise a significant portion of many chemical processes, accounting for approximately 40% of energy consumption in the industrial sector[1]. In the majority of chemical processes, there will, at some point, be a need for the separation and/or purification of components. Many such processes involve contact of phases during operation and therefore depend on accurate and reliable phase equilibria predictions. Mixture behavior greatly influences process design and decision making. Inadequate model predictions risk non-optimal design decisions, with the potential to result in costly, or unsafe operation conditions. As a result, the accurate

representation of vapor-liquid equilibria (VLE) and liquid-liquid equilibria (LLE) is considered essential to the design and simulation of chemical processes.

The most widely used thermodynamic models in process simulations are equations of state (EOS) and activity coefficient models[2,3]. Cubic equations of state (CEOS) (i.e. Peng-Robinson and Soave-Redlich-Kwong), are widely applied due to their simplicity and reasonable accuracy for VLE, particularly at elevated pressures[2,3]. However, conventional EOS models often struggle with strongly non-ideal or complex systems. Activity coefficient models, such as Wilson and UNIQUAC, on the other hand, describe non-ideal behavior based on predictions of the excess Gibbs energy, and are most successful at lower pressure VLE calculations and in LLE predictions. Activity models tend to rely on empirical/semi-empirical parameter fitting, requiring regression to datasets to improve accuracy.

To combine the strengths of both EOS and activity coefficient models, excess Gibbs energy (G^E) mixing rules were developed[2,3]. By implementing a term for the excess Gibbs energy in an EOS mixing rule, the strengths of both approaches can be combined. Mixing rules involve using a “matching equation” in which the residual terms of the EOS and activity coefficient model are made equal at a given reference pressure[2]. The excess Gibbs energy is described by three terms: the combinatorial term (describing molecular size/shape effects), the residual term (accounting for molecular interactions), and a pressure and excess volume term[2].

Group contribution methods were developed to address some of the previously listed model limitations by implementing predictions based on molecular sub-groups in addition to semi-empirical data fitting. In particular, UNIFAC uses functional groups, which use the interactions of these sub-groups to represent the interactions between whole molecules in a mixture[2,3]. As an alternative to these group contribution methods, approaches such as COSMO-RS (Conductor-like Screening Model for Real Solvents) emerged in the early 2000’s, using molecular surface interactions to predict thermodynamic properties[4]. A significant advantage of this model is its generality and applicability to a wide range of compounds without the need for parametrization based on experimental data.

An extension of the COSMO basis, the ‘COSMO Surface-Pair Activity Coefficient Equation’ (COSMOSPACE) model was developed by Klamt et al. and presented as “an analytical solution to the statistical thermodynamics of a model of pairwise interacting surfaces”[5]. Based on the COSMO-RS model as a flexible G^E model, COSMOSPACE goes further and introduces interacting surface-pair segments, which allow for the more straightforward calculation of activity coefficients[5]. Later work by Bosse and Bart compared the COSMOSPACE model to the well-established activity coefficient models Wilson and UNIQUAC, and also to the full COSMO-RS method[6]. After rigorous evaluation against experimental data, they concluded that the COSMOSPACE model achieved results similar to that of the Wilson model, while both significantly outperformed UNIQUAC and COSMO-RS. Wilson was found to perform with a slightly higher degree of accuracy, however, the model’s inability to predict liquid-liquid phase splitting limited its applicability. The COSMOSPACE model on the other hand, does not exhibit this restriction and is only limited by the availability of model parameters[6]. Despite this

promising start, COSMOSPACE has been largely ignored and has not, for example, become one of the mainstream activity coefficient models.

In recent years, efforts have been made to refine models using mixing rules and EOS/G^E frameworks to extend the range of conditions for the prediction of thermodynamic properties and phase equilibria calculations. Privat et al. demonstrated that residual activity coefficient models (in their case the Wilson model in residual form, meaning the combinatorial term is dropped) can provide improved accuracy when paired with EOS frameworks[7]. More recent work by Privat et al. revisited the theoretical basis for mixing rules and their frameworks, emphasizing the importance of developing physically and thermodynamically consistent mixing rules[8].

Several comparative studies regarding the use of the Wilson model in an EOS/G^E framework have been published in recent years, where good predictive results have been obtained[7,9,10]. Piña-Martinez et al. combined EOS with various residual terms of Wilson, NRTL, and UNIQUAC, and found that the Wilson's residual form with an EOS gave the best results[9]. Similarly, Matsuda et al. in comparing the residual Wilson form to UNIQUAC with an EOS in a mixing rule, found that Wilson's residual form in an EOS/G^E framework performed slightly better than UNIQUAC for the cases examined[10]. Similar conclusions were drawn by Lasala et al. for CO2-containing mixtures, where Peng-Robinson EOS coupled with residual Wilson in a mixing rule provided superior agreement with experimental data terms[11].

The developments noted above suggest that there exists a unique opportunity to present a novel model implementing the strengths of COSMOSPACE model in a G^E mixing rule as a new EOS/G^E framework.

2. Results and discussion

The central focus of this research is the implementation and evaluation of COSMOSPACE as the residual term in an EOS/G^E mixing rule. Limitations of space mean that only the general overall expressions and excess Gibbs energy terms for CEOS and activity coefficient models will be presented in this short paper. The approach below (detailed in numerous textbooks and sources, but selected from Privat et al. for their simplified, easy-to-digest form) describes the combinatorial and residual excess Gibbs energy terms for a general CEOS model[12].

$$\begin{cases} \frac{g^{E,EOS}}{RT} = \frac{a_{comb}^{E,EOS}}{RT} + \frac{a_{res}^{E,EOS}}{RT} + \frac{P\nu^{E,EOS}}{RT} \\ \frac{a_{comb}^{E,EOS}}{RT} = \sum_{i=1}^{2} x_i \ln\left(\frac{\nu_i - b_i}{\nu - b}\right) \\ \frac{a_{res}^{E,EOS}}{RT} = \sum_{i=1}^{2} x_i \frac{a_i}{b_i RT(r_1 - r_2)} \ln\left(\frac{\nu_i - r_2 b_i}{\nu - r_1 b}\right) - \frac{a}{bRT(r_1 - r_2)} \ln\left(\frac{\nu - r_2 b}{\nu - r_1 b}\right) \\ \nu^{E,EOS} = \nu - \sum_i x_i \nu_i \end{cases} \quad [1]$$

where x is the component composition, ν the volume parameter, r is the relative surface fraction (as in UNIQUAC), and a and b are the classical attractive coefficient and covolume of the CEOS respectively. In general practice, a mixing rule is assumed for b and a is therefore determined from the a/bRT expression.

Also keeping in mind, the conclusions drawn by Privat et al. for the development of a consistent mixing rule, the matching equation described in the following Eqn. 2 will be implemented by equating the residual contributions of the CEOS and the activity model[8].

$$a_{res}^{E,EOS}\left(T, P_{ref}, \boldsymbol{x}, \boldsymbol{\alpha}\right) = a_{res}^{E,\gamma}(T, \boldsymbol{x}, \boldsymbol{\alpha}) \qquad [2]$$

COSMOSPACE models mixtures using pairwise interacting surface segments. The number of segments used to describe each component increases the model complexity as the segment number increases, giving COSMOSPACE greater inherent flexibility compared to existing activity coefficient models. The general form for the segment activity coefficients, $\gamma^{\boldsymbol{\nu}}$, is

$$\frac{1}{\gamma^{\boldsymbol{\nu}}} = \sum_{\mu} \tau_{\mu\nu} \Theta^{\mu} \gamma^{\mu} \qquad [3]$$

where $\tau_{\mu\nu}$ is the interaction parameter, Θ^{μ} is the segment fraction (based on the segment number and component composition), and μ and ν are the segment and species indices, respectively. The most basic form of this model is the homogeneous double-binary case, which describes a mixture of two different components, each represented by just one type of segment[5].

Some promising early preliminary results have been obtained using COSMOSPACE in an EOS/G^E framework. Figure 1 shows the VLE of Nitrogen-Methane at four different temperatures.

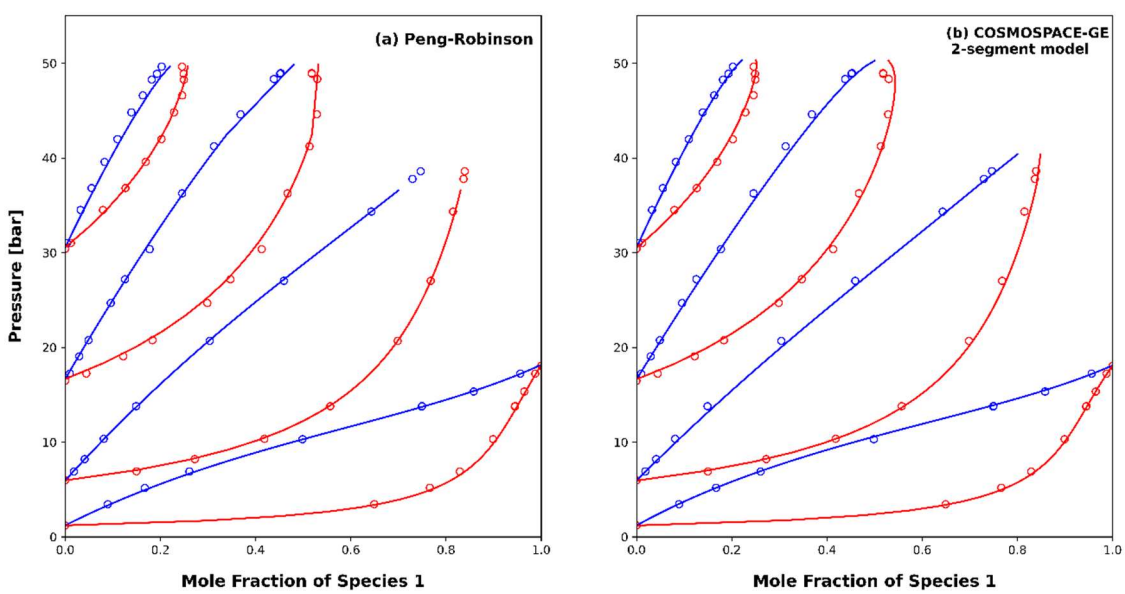

Figure 1: (a) Standard Peng-Robinson and (b) COSMOSPACE-G^E using Peng-Robinson as EOS and UMR as the mixing rule for the system Nitrogen-Methane at 114, 139, 161, and 178 K[13].

Results in Figure 1-b are achieved using Peng-Robinson as the underlying CEOS, with the Universal Mixing Rule (UMR), and the residual COSMOSPACE contribution (simple homogeneous double-binary case for ease of initial model integration). The segment sizes were fit to the 114K dataset along with $\tau_{\mu\nu}$. The $\tau_{\mu\nu}$ at other temperatures were fit to their

respective datasets. The segment sizes for this case are very close to the values suggested by Klamt et al. $(2q)$[5]. Compared to the phase diagrams in Figure 1-a, using the standard Peng-Robinson model, this rudimentary version of COSMOSPACE-G^E performs similarly with marginal improvements.

A second example is shown in Figure 2; the system Ethanol-Water at a pressure of 100 kPa. For this second case, the segment sizes and $\tau_{\mu\nu}$ were fit to the single dataset. Although not shown, it is well known that the original Peng-Robinson does not model this system well at all.

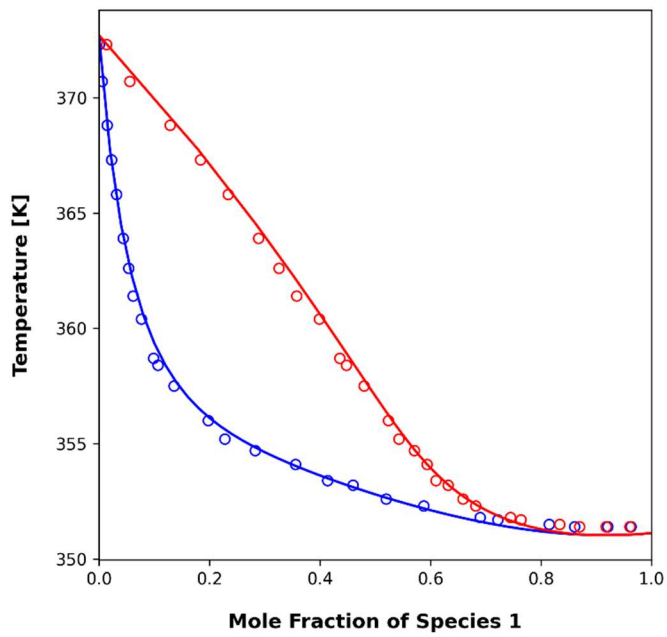

Figure 2: COSMOSPACE in an EOS/G^E framework using Peng-Robinson as EOS and UMR as the mixing rule for the system Ethanol-Water at 100 kPa[14].

COSMOSPACE-G^E fits the data for the very different systems shown in Figures 1 and 2 reasonably well. This is particularly encouraging given that this preliminary implementation of COSMOSPACE only allows for one segment type for each component. While this is a reasonable approach for the nitrogen – methane mixture, it should be less successful for the ethanol – water mixture where we would anticipate that a successful model would need at least two, and possibly three, segments. Adding further model complexity in the form of increasing the number of segments should yield even better results, providing a promising outlook for the future development of COSMOSPACE-G^E.

3. Conclusions

This work introduces COSMOSPACE-G^E, a new EOS/G^E model framework that incorporates COSMOSPACE as the residual excess Gibbs energy contribution within a CEOS model. Limited benchmarking against established activity coefficient and EOS/G^E models shows that even the simplest version of COSMOSPACE-G^E is capable of excellent fits to binary VLE data.

The next phase of our work will be to conduct a large-scale evaluation of the proposed COSMOSPACE-G^E model. Jaubert et al. recently compiled a high quality database

consisting of 200 nonelectrolyte binary systems for the purpose of benchmarking and comparing the accuracy of thermodynamic models[15]. This large, high-quality dataset will be the foundation for the validation of COSMOSPACE-G^E. To quantify the performance of each model, the grading system proposed by Jaubert et al. (based on model prediction deviations and calculated properties) will be employed as an initial measure[15].

References

(1) Oak Ridge National Laboratory; BCS Inc., Laurel, MD (United States). *Materials for Separation Technologies. Energy and Emission Reduction Opportunities*; 1218755, 4571; 2005; p None, 1218755, 4571. https://doi.org/10.2172/1218755.

(2) Kontogeorgis, G. M.; Folas, G. K. *Thermodynamic Models for Industrial Applications: From Classical and Advanced Mixing Rules to Association Theories*, 1st ed.; Wiley, 2010. https://doi.org/10.1002/9780470747537.

(3) Gmehling, J.; Kleiber, M.; Kolbe, B.; Rarey, J. Chemical Thermodynamics for Process Simulation (2nd Completely Revised and Enlarged Edition).

(4) Klamt, A.; Eckert, F. COSMO-RS: A Novel and Efficient Method for the a Priori Prediction of Thermophysical Data of Liquids. *Fluid Phase Equilibria* **2000**, *172* (1), 43–72. https://doi.org/10.1016/S0378-3812(00)00357-5.

(5) Klamt, A.; Krooshof, G. J. P.; Taylor, R. COSMOSPACE: Alternative to Conventional Activity-coefficient Models. *AIChE J.* **2002**, *48* (10), 2332–2349. https://doi.org/10.1002/aic.690481023.

(6) Bosse, D.; Bart, H.-J. Binary Vapor−Liquid Equilibrium Predictions with COSMOSPACE. *Ind. Eng. Chem. Res.* **2005**, *44* (23), 8873–8882. https://doi.org/10.1021/ie0487991.

(7) Privat, R.; Jaubert, J.-N.; Kontogeorgis, G. M. The Secret of the Wilson Equation. *Fluid Phase Equilibria* **2024**, *579*, 114018. https://doi.org/10.1016/j.fluid.2023.114018.

(8) Privat, R.; Jaubert, J.-N.; Kontogeorgis, G. M. Let Us Rethink Advanced Mixing Rules for Cubic Equations of State. *Fluid Phase Equilibria* **2025**, *596*, 114455. https://doi.org/10.1016/j.fluid.2025.114455.

(9) Piña-Martinez, A.; Privat, R.; Nikolaidis, I. K.; Economou, I. G.; Jaubert, J.-N. What Is the Optimal Activity Coefficient Model To Be Combined with the *Translated – Consistent* Peng–Robinson Equation of State through Advanced Mixing Rules? Cross-Comparison and Grading of the Wilson, UNIQUAC, and NRTL a^E Models against a Benchmark Database Involving 200 Binary Systems. *Ind. Eng. Chem. Res.* **2021**, *60* (47), 17228–17247. https://doi.org/10.1021/acs.iecr.1c03003.

(10) Matsuda, H.; Kurihara, K.; Ochi, K.; Kojima, K. Prediction of Liquid–Liquid Equilibria at High Pressure for Binary Systems Using EOS-*G*E Models: Methanol+hydrocarbon Systems. *Fluid Phase Equilibria* **2002**, *203* (1), 269–284. https://doi.org/10.1016/S0378-3812(02)00188-7.

(11) Lasala, S.; Chiesa, P.; Privat, R.; Jaubert, J.-N. VLE Properties of CO2 – Based Binary Systems Containing N2, O2 and Ar: Experimental Measurements and Modelling Results with Advanced Cubic Equations of State. *Fluid Phase Equilibria* **2016**, *428*, 18–31. https://doi.org/10.1016/j.fluid.2016.05.015.

(12) Privat, R.; Jaubert, J.-N.; Kontogeorgis, G. M. Can Liquid-Liquid Equilibria Be Predicted by the Combination of a Cubic Equation of State and a g E Model Not Suitable for Liquid-Liquid Equilibria? *Fluid Phase Equilibria* **2025**, *589*, 114249. https://doi.org/10.1016/j.fluid.2024.114249.

(13) Stryjek, R.; Chappelear, P. S.; Kobayashi, R. Low-Temperature Vapor-Liquid Equilibriums of Nitrogen-Methane System. *J. Chem. Eng. Data* **1974**, *19* (4), 334–339. https://doi.org/10.1021/je60063a023.

(14) Badajoz, P. S.; García-Vera, D.; Herrera-Vega, P.; Marrero-Pérez, A. High-Pressure Phase Equilibria in an Ethanol/Water Binary System: Experimental Data and Modeling. *J. Chem. Eng. Data* **2021**, *66* (2), 928–946. https://doi.org/10.1021/acs.jced.0c00686.

(15) Jaubert, J.-N.; Le Guennec, Y.; Piña-Martinez, A.; Ramirez-Velez, N.; Lasala, S.; Schmid, B.; Nikolaidis, I. K.; Economou, I. G.; Privat, R. Benchmark Database Containing Binary-System-High-Quality-Certified Data for Cross-Comparing Thermodynamic Models and Assessing Their Accuracy. *Ind. Eng. Chem. Res.* **2020**, *59* (33), 14981–15027. https://doi.org/10.1021/acs.iecr.0c01734.

Absorption Hydraulic and Mass-Transfer Characteristics of NeXRing #0.7

Rychlá V.[1], Valenz L.[1], Čmelíková T.[1], Rejl F. J.[1], Hojgrová A.[1], Svoboda V.[1]

[1]University of Chemistry and Technology, Prague, Czech Republic

Abstract

Mass transfer research is crucial for optimizing separation processes in industries such as chemical manufacturing, environmental engineering and energy production. Absorption column apparatuses are essential for studying mass transfer efficiency and fluid–phase interaction characteristics, offering valuable insights into distillation processes and supporting the design of effective gas treatment and separation systems. This paper refers on the hydraulic and mass-transfer characteristics of NeXRing #0.7 random packing under absorption conditions. Pressure drop measurements were performed using an air – water system. The mass-transfer characteristics were measured using standard absorption systems of oxygen desorption from water ($k_L a$ measurement), chemisorption of SO_2 into an aqueous solution of NaOH ($k_G a$ measurement) and chemisorption of CO_2 into an aqueous solution of NaOH (effective area, *a*, measurement). All mass-transfer characteristics were evaluated using a subtraction method. Measurements were performed in a column with inner diameter of 0.3 m with different packed bed heights ranging from 0.21 m to 1.3 m. The hydraulic (C_S, C_{Fl} and $C_{P,0}$) and mass-transfer (C_L and C_V) parameters of the Billet & Schultes model (1999), obtained using experimental data, are presented.

Keywords

absorption, random packing, mass-transfer coefficients

1. Introduction

The design and optimization of industrial absorption columns and strippers rely heavily on a precise understanding of a packing's rate-based mass-transfer characteristics - specifically the liquid and gas-phase mass-transfer coefficients (k_L, k_G) and the effective interfacial area (*a*). These parameters, combined with hydraulic properties such as pressure drop and capacity, are fundamental for evaluating packing performance and ensuring operational efficiency. However, as current literature models lack the fidelity to fully predict how specific geometric nuances - such as the large, open-ring structure of modern high-performance packings - influence these properties, empirical measurement remains a necessity for each new design. This contribution presents the determined mass-transfer and hydraulic data for NeXRing #0.7 (NXR 0.7), a 4th generation random packing engineered to enhance surface exposure while minimizing dry zones and lowering pressure drop.

The measurements were carried out in an atmospheric column with an inner diameter of 0.3 m and adjustable height. The column consisted of several interchangeable sections of varying lengths, allowing both the packed-bed height and the overall column height to be modified as required. The column was packed with NXR 0.7 random packing supplied by Sulzer Ltd. The experiments were performed with packed-bed heights ranging from 0.21 m to 1.30 m. Liquid distribution over the column cross-section was achieved using a pipe-type distributor with a drip-point density of 1 405 dp/m^2. The

gas entered the column through a large calming drum, which ensured flow stabilization before the gas passed into the column through a chimney tray. This configuration provided uniform gas distribution across the entire column cross-section.
All transport characteristics were evaluated using the subtraction method, which eliminates end effects present in the raw transport characteristics. Equation (1) illustrates this procedure for the volumetric mass-transfer coefficient in the gas phase. The determination of the raw characteristics is described in detail in the corresponding sections.

$$net\ k_G a = \frac{1}{H_2 - H_1} \cdot (raw\ k_G a_2 \cdot H_2 - raw\ k_G a_1 \cdot H_1) \tag{1}$$

2. Results and discussion

2.1 Specific pressure drop measurement

The pressure drop of the packing was measured using an air-water system. The pressure drop normalized to 1 m of packing height was evaluated using the relationship given in Equation 2.

$$\Delta p = \frac{p^{in} - p^{out}}{H} \tag{2}$$

The experimental data for the specific pressure drop are presented in Figure 1. These data were subsequently fitted using the Billet & Schultes model (1999), and the resulting model constants - both those evaluated for each individual liquid flow rate and their corresponding average values - are summarized in Table 1. The largest deviations were observed for the pressure-drop values of the dry packing and for the pressure drops at high liquid flow rates, particularly in the case of the average substituted constants. When constants specific to each liquid flow rate are employed, substantially improved agreement with the experimental data is obtained. Specifically, using average constants results in deviations of approximately 12% on average and up to 15% at maximum, with the model exhibiting a consistent positive bias. When flow-rate-specific constants are used, the deviation decreases markedly to an average of 1.9% and a maximum of 3.4%. For gas-phase velocities below 2.3 m/s, the model underpredicts the values of specific pressure drop, while above this threshold it systematically overpredicts it.
At low liquid loads (B = 5, 10, and 20 m/h), the prediction of the model employing flow-rate-specific constants is highly reliable. The average deviations amount to 1.1% for B = 5 and 10 m/h and 1.9% for B = 20 m/h. In contrast, the model based on average constants exhibits higher deviations - 2.7% for B = 5 m/h, 2.3% for B = 10 m/h, and 4.9% for B = 20 m/h. The modelled values generally underestimate the experimental pressure drop, except at high gas-phase velocities for B = 20 m/h, where the measured values fall below the predictions. At these liquid loads, the modelled values are lower than the experimental ones up to high gas-phase velocities, beyond which they become higher.
At higher liquid loads (B = 40 and 60 m/h), the deviation between the calculated and measured values is greater than at lower flow rates. The average deviation is identical for both loads, amounting to 2.8%. The maximum deviation reaches 5.3% for B = 40 m/h and 4.0% for B = 60 m/h. In several regions of the graph, the modelled data intersect the diagonal of the measured values; however, they predominantly yield lower pressure-drop values than those obtained experimentally, except at high gas-phase velocities, where the model predictions become higher.

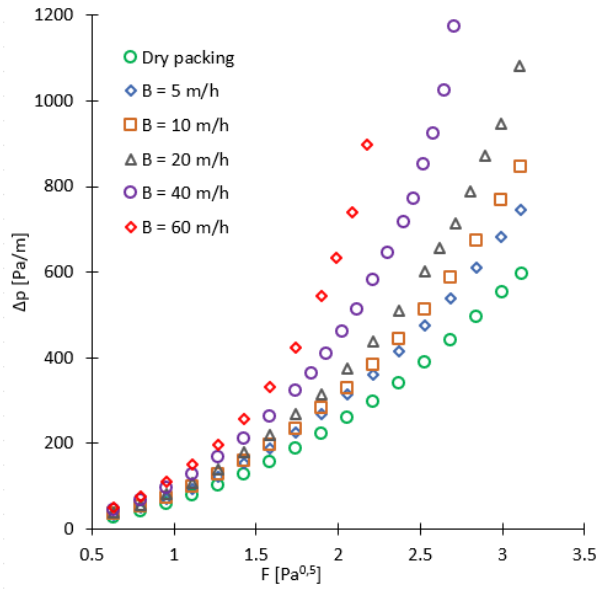

Figure 1: Specific pressure-drop values for several liquid loads as a function of the F-factor

B [m/h]	C_{P0}	C_S	C_{Fl}
Dry packing	0.635	-	-
5	0.682	2.53	1.56
10	0.683	3.04	1.79
20	0.693	3.36	1.93
40	0.690	3.58	1.99
60	0.687	3.22	1.75
Average	0.678	3.14	1.80

Table 1: Specific and average constant values for the Billet & Schultes model (1999)for NeXRing #0.7

2.2 Mass-transfer measurement in the gas phase

The absorption of sulfur dioxide from air into an aqueous sodium hydroxide solution was used to determine the volumetric mass-transfer coefficient in the gas phase, k_Ga. Owing to the instantaneous reaction at the gas-liquid interface, the system exhibits mass-transfer resistance solely in the gas phase. The raw k_Ga values were evaluated from the measured sulfur dioxide concentrations in the gas phase, assuming plug-flow behavior of the gas, using the relationship given in Equation (3) Rejl et al. (2009). The sulfur dioxide concentration was measured using an infrared analyzer (ppm range) and a UV fluorescence analyzer (ppb range).

$$raw\ k_G a = \frac{u_G}{H} ln \frac{c_{SO_2,G}^{in}}{c_{SO_2,G}^{out}} \tag{3}$$

To determine the volumetric mass-transfer coefficients in the gas phase, the concentrations of the tracer (SO_2) in gas phase samples must be measured downstream and upstream of the packed bed. The apparatus used for the measurement was designed to collect samples just before the gas comes into contact with absorption liquid in the absorption column, and after the gas flow meter (orifice) on the gas outlet where SO_2 concentration in the bulk is homogeneous. To obtain k_Ga of the packed bed itself, net k_Ga, it is necessary to implement a subtraction method, which requires measurements to be performed on two different packed bed heights. Packed bed heights of 0.55 and 0.84 m were utilized during the experiment. Dependence of k_Ga values determined on two packed bed heights on gas velocity is shown on Figure 2 for liquid load B = 20 m/h. As expected, end effects are more apparent on k_Ga values obtained with 0.55 m packed bed than on the ones obtained with 0.84 m. Values representing net k_Ga of the packing are the lowest ones.

Values of k_Ga for 5 different liquid loads ranging from 5 to 60 m/h obtained using the subtraction method are shown on Figure 3. The data were fitted using power functions with exponents ranging from 0.6 to 0.7, which is consistent with most published models. The resulting net k_Ga values (for B = 5, 10, and 20 m/h) were fitted using the Billet & Schultes model (1999), from which the corresponding multiplicative model

constant C_V was obtained. This constant is not known for modern types of packings. The optimal value of C_V was found to be 1.02, yielding an average relative deviation of 26% between the modelled and experimental data. It is worth noting that the k_Ga values representing liquid loads of 20, 40 and 60 m/h are almost identical. This unusual phenomenon was confirmed by several repeated measurements. Since most mass transfer theories and models assume that k_G does not depend on the liquid phase flow rate, the increase in k_Ga values with the liquid flow rate must be caused by the dependence of effective interfacial area on the liquid load.

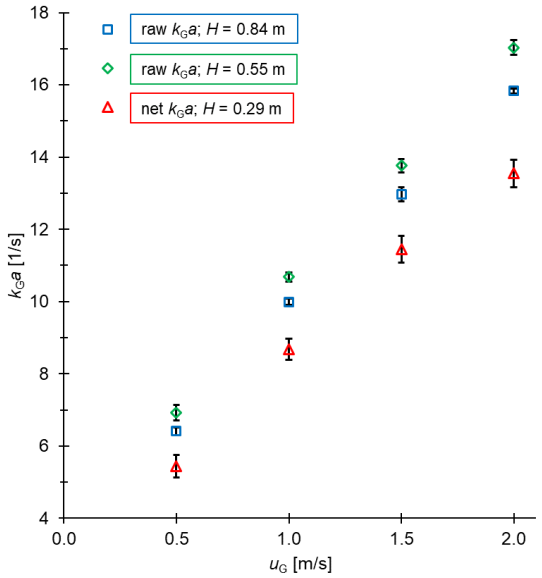

Figure 2: Dependence of k_Ga values on gas velocity, B = 20 m/h, error bars represent 95% confidence interval

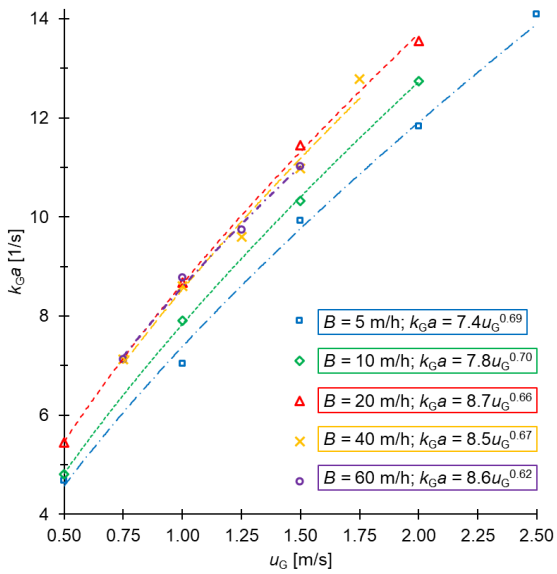

Figure 3: Dependence of k_Ga values on gas velocity for five different liquid loads

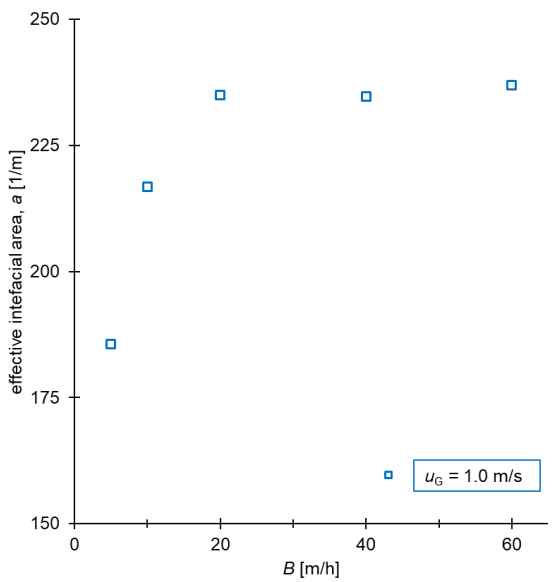

Figure 4: Dependence of "*a*" values on liquid load

If the above assumptions were correct, this behavior would have to be seen in the values of the effective interfacial area. This was again determined by the subtraction method at two packed bed heights of 0.4 m and 1.3 m. The resulting values as a function of the liquid load can be seen in Figure 4 for a gas velocity of u_G = 1 m/s. It is obvious that the effective interfacial area of the packing increases negligibly for liquid loads 20, 40 and 60 m/h. This confirms that the effective interfacial area in our absorption column has reached its maximum and is no longer increasing with the liquid phase flow rate, which is why k_Ga is independent of the liquid phase flow rate.

Effective interfacial area has been measured by absorption of the diluted CO_2 from the air into the aqueous sodium hydroxide solution, which is the system, where the gas-phase relative mass-transfer resistance is low and the rapid reaction of CO_2 with OH^- consumes quantitatively CO_2 within the liquid film. In such case, the mass-transfer rate is determined by the reaction-

transport phenomena in the liquid film and is determined solely by the physical quantities of the system. Effective interfacial area can be calculated by combination of the relation for the CO_2 local mass-transfer rate and its balance along the height of the packing Equation 4 Rejl et al. (2009).

$$a = \frac{(K_{OG}a)_{CO_2}}{He\sqrt{D_{L,CO_2}k_{OH}c_{OH,ave}}} = \frac{1}{He\sqrt{D_{L,CO_2}k_{OH}c_{OH,ave}}}\frac{u_G}{H}ln\frac{c^{in}_{CO_2,G}}{c^{out}_{CO_2,G}} \quad (4)$$

Value of the reaction term $He\sqrt{D_{L,CO_2}k_{OH}} = 2.24 \cdot 10^{-3}\ m/s$ (20 °C and 1 M NaOH solution) was determined by still level experiments (Linek et al. (1995)).

2.3 Mass-transfer measurement in the liquid phase

The volumetric mass-transfer coefficient in the liquid phase, k_La, was determined by stripping dissolved oxygen from the water into a nitrogen stream. Under these conditions, the system exhibits mass-transfer resistance exclusively in the liquid phase. The raw k_La values were evaluated from the measured oxygen concentrations in the liquid phase, assuming plug-flow behavior of the liquid, using the Equation (5) Rejl et al. (2009). The oxygen concentration was measured with optical oxygen probes.

$$raw\ k_La = \frac{u_L}{H}ln\frac{c^{in}_{O_2,L}}{c^{out}_{O_2,L}} \quad (5)$$

Measurements were conducted at four packing heights: 63, 42, 21, and 20 cm. The latter two heights were measured at different packing densities to determine the influence of packing density on the resulting liquid-phase volumetric mass transfer coefficient. The determined raw k_La values for these two heights were nearly identical; consequently, the k_La values were evaluated based on three packing heights (63, 42, and 21 cm). These values, along with the average values corrected for end effects by subtraction method, are plotted in Figure 5. The individual raw k_La values including end effects are represented by colored squares, diamonds, and circles. It is evident from the graph that the raw k_La values increase as the packing height decreases. This phenomenon is attributed to end effects - since these effects are consistent across all measurements, they are more significant at lower heights (corresponding to lower concentration ratios) than at higher packing heights. This observation is clearly visible in the aforementioned graph. As the packing height increases, the raw k_La values approach the net values (red triangles) which are free of end effects.

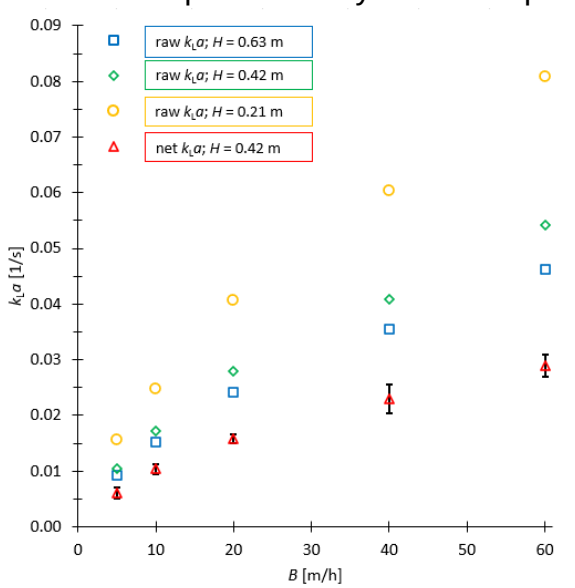

Figure 5: Dependence of k_La values on liquid load, error bars represent 90% confidence interval

The resulting net k_La values were fitted using the Billet & Schultes model (1999), from which the corresponding multiplicative model constant C_L was obtained. This constant is not known for modern types of packings. The optimal value of C_L was found to be 1.35, yielding an average relative deviation of 10% between the modelled and experimental data. At lower liquid flow rates, the Billet & Schultes model (1999) provides a reasonably good representation of the experimental results, whereas at higher flow rates the deviations become more pronounced. The

obtained value of C_L is very similar to the constants published by Billet & Schultes (1999) for earlier generations of packings. Billet & Schultes (1999) also published a dependence of k_La on the irrigation density raised to the power of 0.733, which is approximately 19% higher than the exponent determined for the NXR 0.7 packing in this study. Conversely, the agreement with the model proposed by Song et al. (2018) is very good.

3. Conclusion

This study presents a consistent hydraulic and mass-transfer characterization of the NeXRing #0.7 random packing under absorption conditions. The specific pressure-drop data are well captured by the Billet & Schultes (1999) framework when flow-rate-specific constants are used, with average deviations near 2% and maxima below 4% - 5% in the investigated range; models based on averaged constants exhibit higher bias, particularly at dry and highly irrigated conditions. Net gas-phase mass-transfer data show the expected insensitivity of k_G to liquid load once the effective area saturates, as confirmed by the weak increase of a beyond B = 20 - 60 m/h. For the liquid phase, fitting the Billet & Schultes model (1999) yields a multiplicative constant C_L=1.35 with an average relative deviation of ~10%, consistent with values reported for earlier packing generations and in good agreement with the correlation by Song et al (2018). Overall, NeXRing #0.7 combines low pressure drop with competitive mass-transfer performance, and the reported parameters enable predictive, rate-based design in the studied range.

Acknowledgements

Workplace is deeply grateful to Sulzer Ltd. for providing of packing samples.

References

Billet, R.; Schultes, M., Prediction of mass transfer columns with dumped and arranged packings: Updated summary of the calculation method of Billet and Schultes. *Chemical Engineering Research & Design* 1999**,** *77* (6), 498-504

Linek V., Sinkule J., Brekke K., A critical evaluation of the use of absorption mass transfer data for the design of packed distillation columns, *Chemical Engineering Research and Design*, 73 (Part A) 1995, 398–405

Rejl, J. F.; Linek, V.; Moucha, T.; Valenz, L., Methods standardization in the measurement of mass-transfer characteristics in packed absorption columns. *Chemical Engineering Research & Design* 2009, 87 (5), 695-704

Song, D.; Seibert, A. F.; Rochelle, G. T., Mass Transfer Parameters for Packings: Effect of Viscosity. *Industrial & Engineering Chemistry Research* 2018, 57 (2), 718-729

Effect of the surface tension character of the distilled system on the separation efficiency with modern structured and random packings

F. J. Rejl, T. Čmelíková, L. Valenz,
University of Chemistry and Technology, Prague.

Abstract
The separation efficiency of packed distillation columns is influenced not only by hydrodynamic and geometric characteristics of the packing but also by system-specific surface tension connected liquid-phase properties. Surface-tension-related effects are commonly associated with the classification of distillation systems as positive, neutral, or negative, yet their interpretation for modern packings remains ambiguous.
In this work, experimental *HETP* data obtained with modern structured and lattice-type packings are combined with a conceptual analysis of system classification under distillation conditions. Measurements were carried out in a pilot-scale column using two structured packings (MellapakPlus™ 252.Y and 452.Y) and a lattice-type random packing (NeXRing™ 0.7) for three binary hydrocarbon systems representing positive, nominally neutral, and negative behavior. The results reveal a systematic dependence of separation efficiency on system positivity, with negative systems exhibiting *HETP* values approximately 15–25 % higher than positive systems across all investigated packings.
A revised stabilization index based on surface-tension differences between equilibrium-related liquid states is introduced, explicitly accounting for the coupled influence of composition and temperature. The analysis shows that nominally neutral systems may exhibit ambivalent behavior when thermal effects are included. Finally, a hypothesis for a reformulated solutal Marangoni number is proposed to provide a more consistent scaling of surface-tension-related effects for modern packed columns.

Keywords
Distillation, Marangoni effects, *HETP*, Mellapak, NeXRing

1. Introduction

The separation efficiency of packed distillation columns is governed not only by hydrodynamic, geometric and common physicochemical properties of the phases and characteristics of the packing but also by system-specific liquid-phase properties. Among these, surface-tension-related effects have long been recognized [6] as a potential source of systematic deviations in separation efficiency, particularly when comparing so-called positive and negative distillation systems.
While classical studies associated such effects primarily with Marangoni-driven interfacial flows, the relevance and interpretation of these phenomena for modern structured and lattice-type packings remain subject to debate. Contemporary mass-transfer models [1], [2], [5] if dealing with them at all, incorporate surface-tension effects through gradient-based corrections, yet their predictive capability with respect to system positivity or negativity is inconsistent.

Recent experimental evidence indicates that differences in separation efficiency between positive and negative systems persist even for advanced packings, but the magnitude of the effect is significantly smaller than would be expected from earlier experiments with wetted wall columns and first-generation packings.

The present contribution addresses the problem by presenting the experimental *HETP* data obtained with modern industrial packings and a conceptual analysis of system classification. Particular emphasis is placed on distinguishing between system-level descriptors and local driving forces, and on identifying a physically consistent framework for interpreting surface-tension-related effects under distillation conditions.

Surface-tension-driven phenomena in liquid films are fundamentally governed by gradients of surface tension along the interface. For a binary system under distillation conditions, the local surface-tension gradient can be expressed as

$$\frac{d\sigma}{dz} = \frac{\partial \sigma}{\partial x_A}\frac{dx_A}{dz} + \frac{\partial \sigma}{\partial T}\frac{dT}{dz} \tag{1}$$

where *z* denotes a spatial coordinate along the liquid film. Equation (1) describes a local mechanical driving force and depends explicitly on spatial gradients of composition and temperature.

While Eq. (1) is essential for the physical description of Marangoni-driven flows, it is not suitable for classifying distillation systems as positive, neutral, or negative. Such a classification requires a system-level descriptor that does not rely on an assumed spatial scale and yields a single characteristic value for a given mixture.

In our earlier work [4], system positivity or negativity was characterized by a stabilization index based on the difference in surface tensions of the pure components evaluated at their respective boiling points. In its original form, this index can be written as

$$M_{\mathrm{nom}} = \left({\sigma_A}^{\mathrm{bp}} - \sigma_B^{\mathrm{bp}}\right)(x_A - x_A^*) \tag{2}$$

where and denote the liquid compositions of equilibrium-related states. Equation (2) provides a single scalar value characteristic of the system and intentionally avoids any explicit spatial or transport-related assumptions.

The formulation in (2) implicitly assumes that surface tension differences between equilibrium-related liquid states arise solely from differences in composition. Under distillation conditions, however, surface tension depends on both composition and temperature, and the temperature itself varies systematically with composition along the equilibrium curve. As a result, compositional and thermal contributions to surface tension may partially compensate or reinforce each other over the composition range.

To account for this coupling, a revised stabilization index (3) is introduced based on the surface-tension difference between equilibrium-related liquid states evaluated under distillation conditions,

$$\Delta\sigma_{\mathrm{dist}} = |\sigma(x_A, T(x_A)) - \sigma(x_A^*, T(x_A^*))| \tag{3}$$

while the corresponding nominal system descriptor is then defined as

$$M_{\mathrm{dist,nom}} = \max_{x_A \epsilon [0,1]} \Delta\sigma_{\mathrm{dist}} \tag{4}$$

Equation (4) provides a system-level classification parameter that incorporates both compositional and thermal effects without introducing a spatial scale. Importantly, this

index does not represent a driving force for interfacial flow but rather quantifies the potential imbalance in surface tension characteristic of the system.

2. Experimental part

The experimental data analyzed in this work were obtained in a pilot-scale distillation facility operated at the University of Chemistry and Technology Prague. Experiments were carried out in a cylindrical column with an inner diameter of 0.30 m, operated under total reflux and atmospheric pressure at the column head. The height of the packed bed was approximately 2.5 m.

Three industrial packings were investigated: two structured packings, MellapakPlus™ 252.Y and MellapakPlus™ 452.Y, and a lattice-type random packing, NeXRing™ 0.7, all manufactured from stainless steel.

Three binary hydrocarbon systems were studied: n-hexane/cyclohexane (positive system), cyclohexane/toluene (nominally neutral system), and cyclohexane/n-heptane (negative system). Liquid and vapour compositions were determined from samples taken above and below the packed bed, and *HETP* values were calculated from the number of theoretical stages obtained by a stage-to-stage equilibrium calculation.

3. Results and Discussion

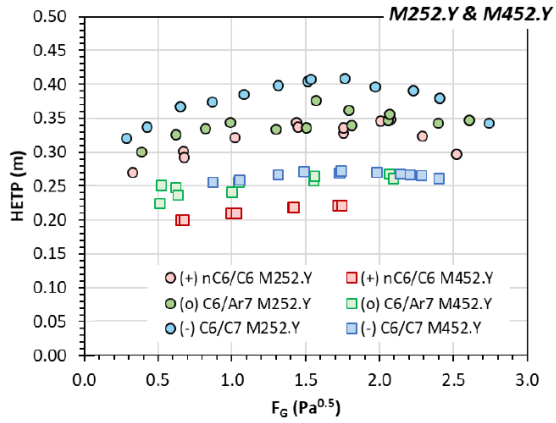

Figure 1a: *HETP* of structured packings [3]

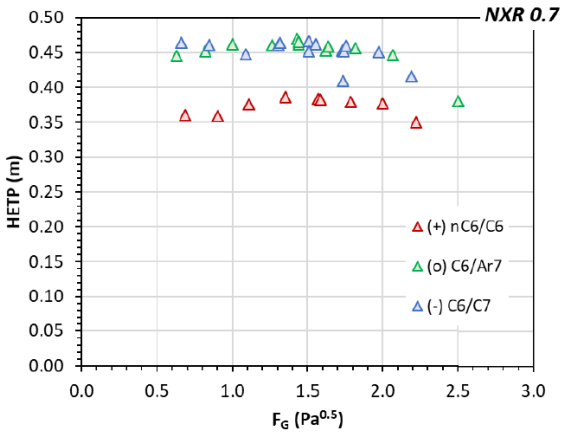

Figure 1b: *HETP* of the random packing [3]

Figures 1a and 1b show the experimentally determined *HETP* values as a function of the F-factor for all investigated packings and systems. For all packings, negative system exhibits consistently higher *HETP* values than positive system, while the nominally neutral system shows intermediate behaviour. The observed differences amount to approximately 15–25 % and significantly exceed experimental uncertainty.

Although absolute *HETP* values differ between packings due to geometric effects, the relative influence of system positivity or negativity remains comparable. This indicates that the observed effect is system-related rather than packing-specific.

Model predictions incorporating Marangoni-based correction factors capture the general dependence on system positivity/negativity but fail to reproduce the magnitude of the effect. Moreover, the models predict different effect of system positivity; while BS model predicts no effect, the Xu model assumes separation efficiency enhancement. The assessment of the model success is depicted in Figure 2.

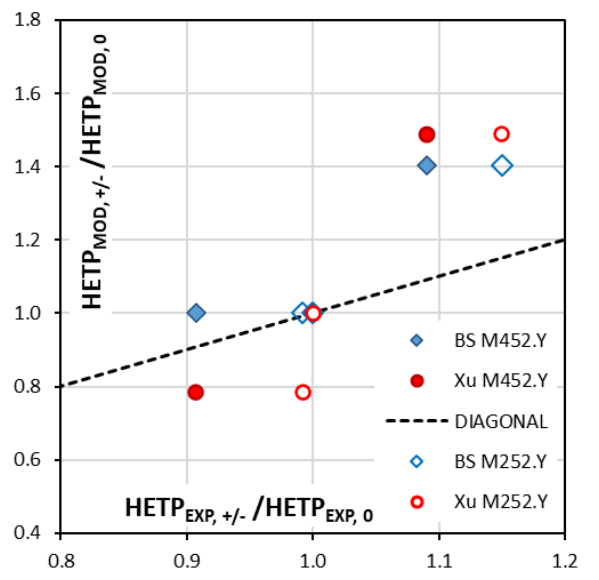

Figure 2: *Model success in prediction of the surface tension gradient effect on HETP.*

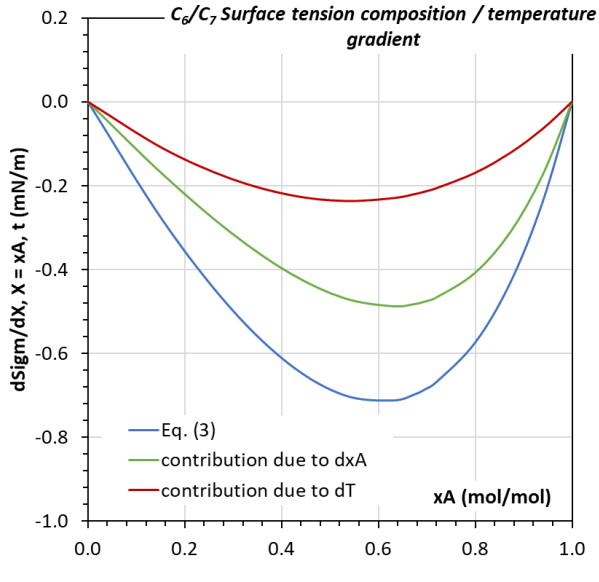

Figure 3: *Surface tension gradient of the C_6/C_7 system on composition and temperature.*

When revised nominal stabilization index (4) is introduced, only slightly different values are obtained for utilized systems (Table 1) in comparison to that defined by (1). However, the nominally neutral system is found to exhibit negative as well as positive behavior over the composition range (Figure 4), providing ambiguous nominal values according to (4) and suspicious behavior with respect to its assumed ideal neutral performance.

	M **(Eq. 1) (mN/m)**	***M*$_{nom}$ **(Eq. 4) (mN/m)**
C_6/C_7 33 kPa	-0.85	-0.94
C_6/C_7 100 kPa	-0.66	-0.71
C_6/C_7 180 kPa	-0.56	-0.60
$_nC_6/C_6$ 100 kPa	+0.43	+0.44
$C_6/Ar_7$100 kPa	+0.02	+0.21 / -0.22

Table 1: Comparison of the values of the former definition of the stabilization index (Eq. 1) and values according to Eq. 4.

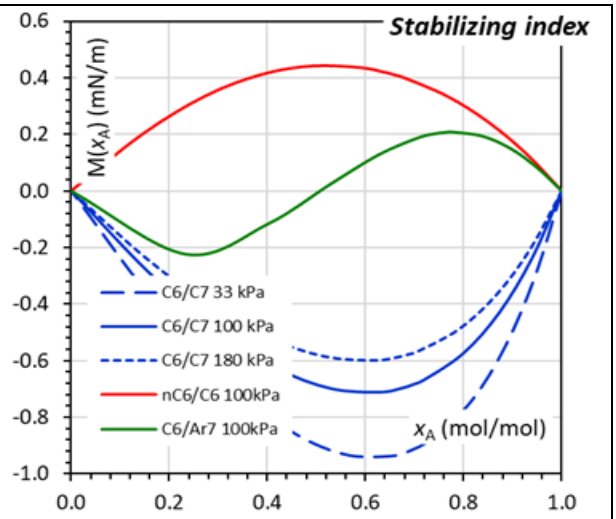

Figure 4: Stabilizing index according to Eq. 3.

4. Conclusions

The present study demonstrates that the separation efficiency of modern industrial packings is systematically influenced by the positivity or negativity of the distillation

system. Negative systems exhibit consistently higher *HETP* values than positive systems, with differences of 15–25 %.
Existing mass-transfer models incorporate surface-tension-related effects and predict a non-zero influence of system positivity, yet the magnitude of this influence differs systematically from experimental observations. The magnitude of the effects is predicted on the basis of various surface tension gradient related quantities with dimensionless Marangoni number being the one with the most corroborated physical imagination behind its definition. However, its extreme values put the choice of the affecting phenomena in question.
Systems classified as neutral based solely on pure-component surface tensions may exhibit ambivalent behavior when surface-tension variations with both composition and temperature are considered. A truly neutral system must therefore display only small differences in both composition and temperature between equilibrium-related liquid states, which is practically attainable perhaps only for systems with relative volatility close to unity.

5. Outlook

A plausible direction for future work is to reformulate the solutal Marangoni number such that concentration equalization within the liquid film is not implicitly assumed to be diffusion controlled. For liquid films on modern packings, lateral concentration smoothing is primarily governed by hydrodynamic mixing. The intensity of this mixing is suggested to be represented by the liquid-side mass transfer coefficient $k_{L,\mathrm{abs}}$determined under neutral absorption conditions.

In this spirit, an effective solutal Marangoni number may be hypothesized as

$$\mathrm{Ma}_L^{\mathrm{eff}} = \frac{\Delta\sigma_{dist}}{\mu_L}\,\frac{h_L}{a_w}\,\frac{D_{\mathrm{dist}}}{L_s^2 k_{L,\mathrm{abs}}^2} \tag{5}$$

where $\Delta\sigma_{\mathrm{dist}}$is the local surface-tension difference under distillation conditions as defined in Eq. (4). The diffusivity D_{dist}enters Eq. (5) solely as a conversion factor linking absorption-based values of $k_L$to distillation conditions and does not represent a competing physical mechanism. The scale factor Ls is interconnected with the packing geometry. When surface texture pitch is taken as a scale factor, the values of the reformulated Marangoni number are in the order of unity.

5. References

[1] Billet R., Schultes M., 1993. Predicting Mass Transfer in Packed Columns, Chem. Eng. Technol. 16, 1–9.

[2] Billet R., Schultes M., 1999. Prediction of mass transfer columns with dumped and arranged packings. Updated Summary of the Calculation Method of Billet and Schultes, Chem. Eng. Res. Des. 77, 498–504.

[3] Čmelíková, T., Valenz, L., Rejl, F. J., 2026. Comparison of the mass transfer efficiency of random and structured packings under distillation of positive, neutral, and negative systems in the i.d. 0.3 m column.
International Journal of Heat and Mass Transfer 260 (2026) 128476.

[4] Čmelíková T., Valenz L., Mařík, K., Rejl F. J., 2023. Mass-Transfer under distillation of positive, neutral and negative system in the I.D. 0.3m column packed with structured packing. Chem. Eng. Res. Des. 196, 52–60. doi.org/10.1016/j.cherd.2023.06.007

[5] Xu Z., P., Afacan A., Chuang K., T., 2000. Predicting Mass-Transfer in Packed Columns Containing Structured Packings. Trans IChemE, 78 Part A.

[6] Zuiderweg F. J., Harmens A., 1958. The influence of surface phenomena on the performance of distillation columns. Chem. Eng. Sci. 9, 89 – 103.

Distillation composition profiles – measurement and interpretation

Čmelíková T., Rejl F.J., Valenz L.
University of chemistry and technology, Prague, Czech Republic

Abstract
This contribution focuses on an advanced experimental technique designed to obtain composition profiles along a packed bed during distillation and their interpretation with respect both to interphase mass transfer and to the hydrodynamics of the phases. The composition profiles of cyclohexane/n-heptane mixture were measured under atmospheric distillation conditions for two types of structured packings - MellapakPlus™ 452.Y and MellapakPlus™ 252.Y – as well as for the random packing NeXRing™ 0.7. The work presents a practical set of recommendations for obtaining accurate composition profiles addressing sampling strategy and enhancement of the phase hydrodynamics in the packed bed.

Keywords
Distillation, composition profiles, mass-transfer coefficients, Mellapak, NexRing

1. Introduction

From the shape of the composition profiles along the column (Figure 1), the volumetric mass-transfer coefficients $k_G a$ and $k_L a$ can be evaluated by the *profile method* [1]. When constructing a mass-transfer model for packed distillation columns, the modeling can therefore start directly from the experimentally determined $k_G a$ and $k_L a$ values and use them to refine the model equations and its parameters.
The observed separation between the liquid- and vapor-phase composition profiles (Figure 1) is attributed to axial mixing of the phases and is modelled as plug flow with axial dispersion. However, from the divergence of the two profiles, the axial dispersion coefficient can be inferred for only one of the phases. Based on independent hydrodynamic measurements, axial mixing during distillation - and thus a nonzero axial dispersion coefficient - is considered only for the liquid phase.

2. Results and discussion

The composition profiles along the column are constructed from the compositions of liquid, x_A, and vapor, y_A, samples taken directly from the packed bed. The packed bed was formed either by structured packings MellapakPlus™ 452.Y (M452.Y) or MellapakPlus™ 252.Y (M252.Y) or by random packing NeXRing™ 0.7 (NXR 0.7).

2.1 Packed bed

The individual elements of the structured packing forming the packed bed were modified to accommodate the sampling devices (SDs) by spark-eroding 30 mm diameter holes through the metal sheets in the middle of each element. In this article, the packed bed was 2.5 m high, formed by twelve elements (two intact elements in the top and ten sparked ones under them). The influence of spark eroding was detected as a decrease in HETP by 2 % (Figure 2, intact vs. spark-eroded) and the pressure drop did not change significantly up to the loading point (Figure 3).

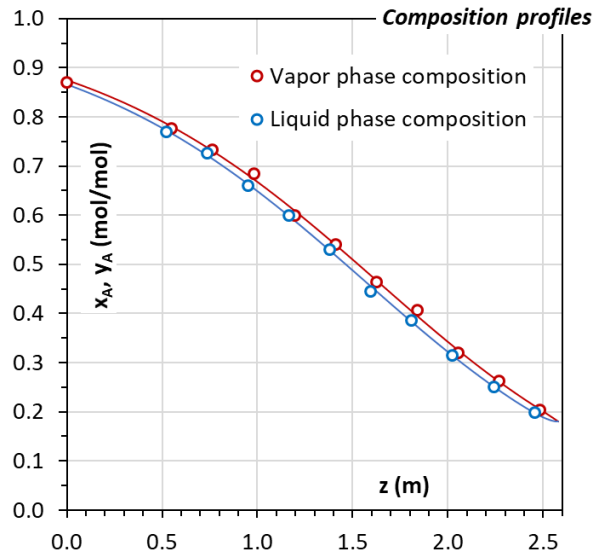

Figure 1: Liquid and vapor composition profiles.

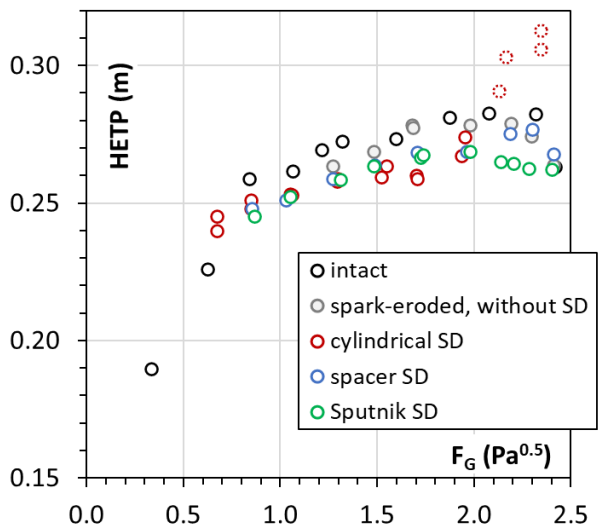

Figure 2: HETP of MellapakPlus™ 452.Y packed bed – intact, without SDs and outfitted with different types of SDs. Cyclohexane/n-Heptane distillation system.

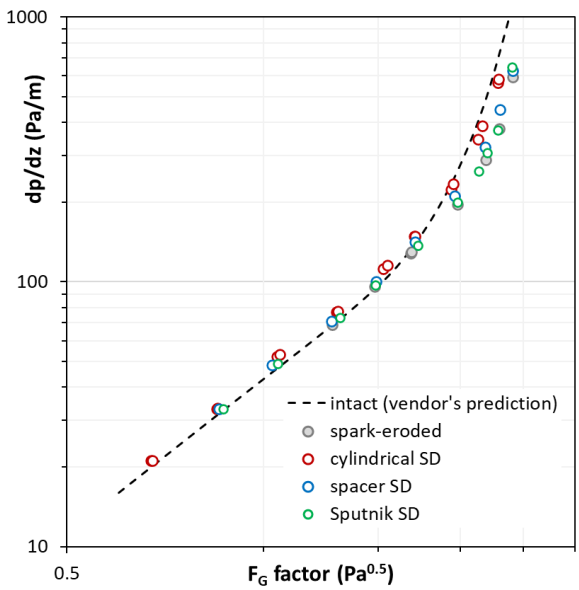

Figure 3: Pressure drop of MellapakPlus™ 452.Y - intact, without SDs and outfitted with different types of SDs. Cyclohexane/n-Heptane distillation system.

In the case of random packing, the SDs were inserted stepwise and backfilled with the packing until the bed height reached 2.5 m. For a random packing bed, there is a potential risk of low reproducibility of the packing procedure. However, the bulk density differed by less than 5% for packing without the sampling devices (1 repetition) and by less than 1.5% for packing with the sampling devices (2 repetitions). The HETP differed up to 14% (bed without SDs) and up to 8% (bed with SDs) upon repetition (Figure 4).

2.2 Sampling device

Typically, ten SDs were installed at various heights within the packed bed. Several SD designs were gradually developed for this purpose (Figure 5). The first design was a *cylindrical* SD, which enabled collection of three liquid samples and three vapor samples at a single column cross-section. The *cylindrical* SD occupied approximately 11% of the column cross-section (which is expected to increase the pressure drop, Figure 3). The separation efficiency, expressed as HETP, of the M452.Y packing equipped with SDs differed by up to 5% from that of the unmodified packing. This small difference in HETP is offset by the ability to obtain more informative composition profiles along the bed and, if desired, to evaluate the HETP of the packing without end effects. However, it was found that with *cylindrical* SDs the HETP increased abruptly by about 15% relative to the prior trend at column loadings above approximately 80% of capacity (Figure 2).

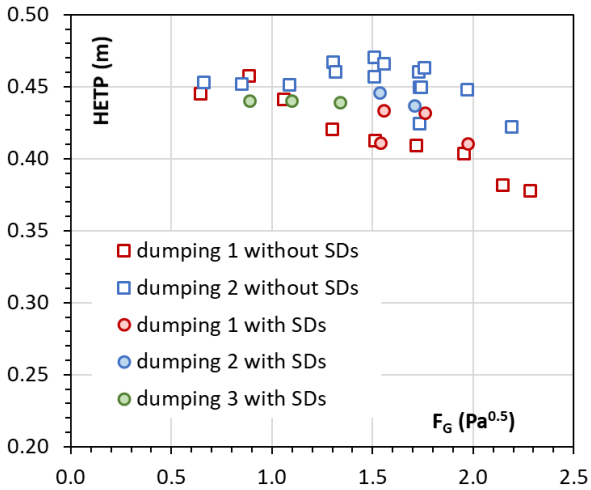

Figure 4: HETP of NeXRing™ 0.7 upon repetition. Cyclohexane/n-Heptane distillation system.

Figure 5: Different sampling devices (SD) designs. Cylindrical SD, spacer SD, Sputnik SD, Sputnik 3Plus SD.

Using Fenske's equation with constant relative volatility the molar fraction profile along the packed bed is given by

$$\ln \frac{x_A}{1 - x_A} = -\frac{\ln \alpha_{AB}}{HETP} z + \ln \frac{x_{A0}}{1 - x_{A0}} \tag{1}$$

which, assuming constant HETP value, is a straight line relationship. According to Zuiderweg [2], maldistribution manifests itself as nonlinearity of composition profiles plotted as $\ln(x_A/(1-x_A))$ versus the axial coordinate z.

When the profiles obtained with the *cylindrical* SDs were examined according to Zuiderweg's procedure, the profiles at lower reboiler duties were smooth curves, whereas a distinct break was identified in the profiles at higher duties. Based on these analyses, it was considered that the undesirable effects were caused by the "robustness" of the *cylindrical* SDs. The measurements were therefore repeated with the *spacer* SDs, created by removing selected parts from the *cylindrical* SDs; the *spacer* SD occupied approximately 6 % of the column cross-section. During distillation with the *spacer SD*, the HETP of M452.Y was 4 % lower than that of the intact bed. No abrupt increase in HETP occurred. However, at the highest reboiler duty a break was again identified in the composition profile.

Based on these results, a structurally different SD *Sputnik* was manufactured. This device consisted of only two sampling cups and occupied < 1 % of the column cross-section. During distillation with the *Sputnik* SDs, the HETP of M452.Y was evaluated to be about 5 % lower than that of the intact bed.
The *cylindrical* and *spacer* SDs enabled sampling of both liquid and vapor at the center of the cross-section and at two additional positions on a circle at approximately 0.5R. The vertical composition profile for evaluating mass-transfer coefficients could be assembled either from cross-sectional averages or from the centerline compositions. The coefficients evaluated by the profile method from these two variants differed by at most 10 %. Therefore, it was deemed sufficient to manufacture the new *Sputnik* SD for M452.Y testing with only one liquid and one vapor sampling position.
For M252.Y testing, however, the Sputnik SD had to be equipped with additional cups to obtain two further liquid and vapor samples. This configuration was called *Sputnik 3Plus*. The *Sputnik 3Plus* SD was also used for testing NXR 0.7.
From the SDs located directly in the packed bed, individual samples were led out of the column by tubing. The tubes were connected in series to a metal condenser, a shut-off device (tube clamp), a small-ID capillary to limit the sampling rate, and an evacuated vial.

2.3 Process conditions
Composition profiles were obtained in a distillation column with an inner diameter of 300 mm at various reboiler duties, under total reflux, and at atmospheric pressure. A cyclohexane/n-heptane mixture was used as the batch charge. The batch composition of cyclohexane was adjusted such that the resulting composition profile was symmetric (e.g., x_A: 0.95–0.05 from top to bottom) and the equimolar composition occurred in the middle of the packed bed.

2.3 Composition profiles
Ideally, without considering flow maldistribution, (i) the phase composition should be homogeneous in the radial direction, and (ii) the molar fractions of the vapor and liquid samples at a given column cross-section should coincide.
If (i) holds, the conditions are met for evaluating $k_L a$ and $k_G a$ from the composition profile using the applied 1D model. If (ii) holds, the hydrodynamics can be represented by a plug-flow model. A divergence of the profiles such $y_A - x_A$ can be described by a plug-flow model with axial dispersion, as noted above.
However, in the first composition profiles obtained during distillation on M252.Y, more than half of the liquid samples exhibited a higher mole fraction than the corresponding vapor samples (which is physically inconsistent in the ideal case). In addition, the radial standard deviation of composition was high. This manifested as approximately a twofold increase in the terminal value of the objective function of the optimization problem, whose outputs are the optimal $k_L a$ and $k_G a$ taken as the experimental values. Moreover, the optimal $k_L a$ appeared improbable low compared with $k_L a$ for M452.Y, and the degree of axial dispersion was likewise low. It thus appeared that the *profile method* was attributing hydrodynamic maldistribution to an apparent resistance in the liquid phase.
Several attempts were undertaken to improve the phase-flow hydrodynamics and thus enable the focus to be placed on mass-transfer study. An enhancement was achieved by installing two additional solid-sheet wall wipers on each packing element (in addition to the original wire-mesh wall wipers). These improved radial

homogeneity (the standard deviation decreased three times) and eliminated the physically inconsistent negative difference ($y_A - x_A$).
In the case of NXR 0.7, the negative difference ($y_A - x_A$) was not significant, but the radial inhomogeneity was strong, about twice that of the structured packing before modification.
With the idea that liquid wall flow outside the packing might be responsible for the radial inhomogeneity, the inner wall of the column was equipped, at approximately 0.5 m intervals, with thin metal annular baffles designed to drain liquid from the wall back into the packed bed. After this modification, the standard deviations of the three liquid and three vapor sample compositions were reduced twice. The objective function of the optimization problem (seeking optimized $k_L a$ and $k_G a$) was likewise reduced twice.
The task of measuring composition profiles in a random-packing bed is not yet fully resolved, however, the installation of annular baffles appears promising.

3. Conclusions

Measurement of distillation composition profiles for structured packings requires modifications to insert the sampling devices, our approach utilizes spark eroding of the 30 mm hole perpendicular to the sheets. The changes in pressure drop and overall separation efficiency are insignificant over entire range of loads when the sampling devices are of an open structure design (like *Sputnik 3Plus*)
Measuring the composition profiles for packings with a lower geometric area (M252.Y and NXR 0.7) needs certain adjustments to improve the phase hydrodynamics. Extra solid-sheet wall wipers were installed on the M252.Y packing elements, and thin annular baffles were installed on the column wall when the column was loaded with the random packing NXR 0.7.
For measuring the composition profiles, the following proved effective:
i) using a slender sampling device rather than a robust one (in this study, *Sputnik 3Plus*)
ii) collecting more samples from different positions across the column cross-section, for both liquid and vapor
iii) examining the profiles according to Zuiderweg and monitoring both radial homogeneity and the liquid–vapor composition difference helps assess a character of the phase hydrodynamics and possible deviation from its ideality.

References

[1] Rejl F.J., Čmelíková T., Valenz L., Haidl J., Moucha T., Kracík T., 2019. Liquid phase axial mixing in distillation column packed with structured packing: Effect on column performance. Chem. Eng. Res. Des. 148, 129-141.
[2] Zuiderweg, F.J., 1999. Distillation composition profiles - what do they tell us? Chem. Eng. Res. Des. 77, 475-481.

Numerical and Experimental Investigation of Liquid Distribution and Wetting Behavior of Innovative Structured Packings on a Laboratory Scale with a Modular Test Rig

Samuel Wurmannstätter[1], Nadin Rausch[1], Harald Klein[1], Sebastian Rehfeldt[1]
[1]Technical University of Munich, TUM School of Engineering and Design, Department of Energy and Process Engineering, Institute of Plant and Process Technology, Garching/Germany
samuel.wurmannstaetter@tum.de; nadin.rausch@tum.de; harald.klein@tum.de; sebastian.rehfeldt@tum.de

Abstract
In Computational Fluid Dynamics (CFD), the wetting behavior of liquids on solid surfaces is typically modeled using a contact angle. However, finding reliable data on contact angles in the literature can be challenging. Therefore, this contribution presents a method to determine contact angles for application in CFD simulations of additively manufactured structured packings on a laboratory scale. This is achieved by combining time-efficient measurements and CFD simulations, while the discrepancies between the experimental and numerical results are attempted to be reduced by varying the contact angle. Four new structured packings with a diameter of DN20 are introduced and investigated. In the CFD simulations with the initially selected contact angle of 10°, the numerical results showed a significant deviation of the relative wetted cross-sectional area by approximately 8 % to 42 % compared to the experiments. The contact angle variation of one packing indicates that a contact angle between 1° and 5° results in a more accurate liquid distribution. However, the reliability of the presented method for quantitatively evaluating the contact angle must be further investigated using other packings and materials.

Keywords
CFD, distillation, structured packing, contact angle, additive manufacturing

1. Introduction

Distillation is one of the most essential and well-established thermal separation processes in the chemical industry. For the design of distillation columns with structured packings, experiments on a laboratory scale are still necessary. Data are obtained in columns with diameters typically ranging from 30 to 80 mm and used for scale-up to larger columns. A reduction of the column diameter to 20 mm was studied by Neukäufer et al. 2022, resulting in decreased manufacturing and operating costs of the test rig required for the experiments.

Columns on a laboratory scale present a particular challenge due to the increased wall-to-packing ratio and the associated high wall flows of the liquid phase. Consequently, new innovative packings are required which lead to a more uniform liquid distribution over the cross-sectional area of the column. This strongly depends on the wetting behavior of the liquid on the solid surface. In Computational Fluid Dynamics (CFD), the interaction between the liquid and the solid surface is typically described using a contact angle θ, which is formed by the liquid surface on the solid surface at the contact point of the gas, liquid, and solid (Rausch et al. 2023). However, finding reliable data

on the experimentally evaluated contact angle in the literature can be challenging due to the difficulty and frequent unreliability of the contact angle measurements. In fact, data on contact angle measurements of additively manufactured surfaces are scarce and depend on the orientation of the sample during printing (Neukäufer et al. 2020).
This contribution presents the evaluation of the liquid distribution in four additively manufactured structured packings on a laboratory scale with a diameter of 20 mm. Additionally, CFD simulations of the experimental setup are performed in OpenFOAM to numerically reproduce the measurements. The simulated liquid distribution of the packings is compared to the experimental results. By variation of the contact angle, deviations between the experiment and the simulation are reduced.

2. Setup

This chapter describes the experimental and CFD simulation setup.

2.1 Experimental setup

The experimental evaluation of the liquid distribution in additively manufactured structured packings through optical analysis is determined as described in Sarajlic et al. 2022. The packings are irrigated with dyed *n*-heptane (Bayer dark blue) at a single central drip point with a volume flow rate of 10 ml/min. After the experiments, the *n*-heptane evaporates in a drying oven, leaving behind colored flow paths of the liquid on the packing. These are then optically evaluated using an automated process controlled by a Python script running on a Raspberry Pi. Photographs of the bottom of the packing are acquired and used as experimental results. The four investigated additively manufactured structured packings with a diameter of 20 mm are illustrated in Figure 1. The detailed procedure of the experiments and the evaluation of the results are documented in Ertl 2023.

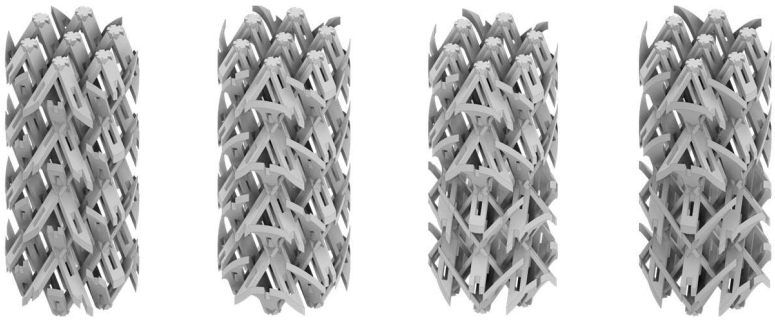

Figure 1: Structured packings under investigation: Artist (left), Artist Paddle (ArtistP, middle left), Artist Paddle Twist (ArtistPT, middle right), Artist Paddle Twist No Rivulets (ArtistPTNR, right) (Rausch 2025).

In total, four structured packings are investigated, which can all be derived from the initial Artist packing (see Figure 1, left). The Artist packing consists of perforated bars that are connected to tetrahedral structures and is therefore similar to the packing *ARTIST-550* investigated by Neukäufer et al. 2019 and the packing *APTwist-XL* analyzed by Sarajlic et al. 2022. In this study, the Artist and Artist Paddle (ArtistP) packing are analyzed using two representative units stacked vertically, whereas the Artist Paddle Twist (ArtistPT) and the Artist Paddle Twist No Rivulets (ArtistPTNR) are examined using a single representative unit. The geometry of the four structured packings and their differences are described in detail in Rausch 2025.

2.2 Numerical setup

The CFD simulations of the two-phase flow in the packings are conducted using the *incompressibleVoF* transient solver provided by OpenFOAM Version 13. It is a solver

module based on the volume of fluid (VoF) method using the phase-fraction interface capturing approach for fluid flows involving two incompressible, isothermal, immiscible fluids (Greenshields 2025). Since the experiments are used to validate the CFD simulations, the computational domain is adapted to match the experimental setup. Consequently, the packing, including the column wall and the needle for the liquid inflow, is simulated. To account for the needle, the computational domain extends 6 mm beyond the top end of the packing. Furthermore, the domain is extended by 5 mm below the packing. This allows droplets to form at the lower end of the packing, which detach during the simulation.

The inlet of the needle is specified with a *fixedValue* boundary condition (BC) for the fields of velocity u and liquid volume fraction α, and with a *zeroGradient* BC for the pressure field p. The vertical component of the velocity field is set to a value equivalent to a volume flow of approximately 10 ml/min, and the liquid volume fraction is specified as $\alpha = 1$ to ensure liquid inflow. At solid surfaces, i.e., the packing, the column wall, and the needle, typical no-slip boundary conditions are chosen for the pressure and velocity, i.e., *fixedFluxPressure* for the pressure field and *noSlip* for the velocity field. Additionally, the *contactAngle* BC, in accordance with the type *dynamic*, defines the shape of the gas-liquid interface near the wall with a dynamic calculation of the contact angle. The dynamic contact angle θ_{Dyn} is calculated employing the equation

$$\theta_{\mathrm{Dyn}} = \theta_{\mathrm{S}} + (\theta_{\mathrm{A}} - \theta_{\mathrm{R}}) \tanh\left(\frac{u_{\mathrm{s}}}{u_{\theta}}\right), \tag{1}$$

where θ_{S} denotes the static contact angle, θ_{A} the advancing contact angle, θ_{R} the receding contact angle, u_{s} the velocity at the three-phase contact line on the wall, and u_{θ} a scaling velocity (Rausch et al. 2023). The boundary patches at the sides, top, and bottom of the computational domain are initialized so that both liquid and gas flow out of the domain, but only gas flows in. This is achieved by using the *pressureInletOutletVelocity* BC for the velocity field with a tangential inlet velocity of zero, the *prghTotalPressure* BC for the pressure field, and the *inletOutlet* BC for the liquid volume fraction with an inlet value of zero.

The simulations were carried out for the system of air and *n*-heptane. In this work, changes in fluid properties due to the dye are not considered. The fluid properties of the liquid phase are those of *n*-heptane, and the fluid properties of the gas phase are those of air. The initially selected contact angles are $\theta_{\mathrm{S}} = 10°$, $\theta_{\mathrm{A}} = 11.8°$, and $\theta_{\mathrm{R}} = 1°$. The employed contact angles correspond to isohexane on stainless steel, since isohexane has fluid properties comparable to *n*-heptane. Direct contact angle measurements of *n*-heptane on additively manufactured surfaces were precluded by strong wetting. Detailed specifications of the fluid properties are provided in Rausch et al. 2023.

The simulation results are visualized using ParaView. To compare the simulation results with the experimental data, the simulated relative wetted cross-sectional area ψ of each packing is determined. This is achieved by solely visualizing the liquid adhering to the packing surface while viewing the bottom of the packing, similar to the photographs of the packing experiments. The relative wetted cross-sectional area is calculated from the ratio of the number of colored pixels due to the adhering liquid to the total number of pixels in the image generated in ParaView. Additionally, the relative wetted area ϕ of the packing is evaluated during the runtime of the simulation using the *areaAverage* function object in OpenFOAM. The relative wetted area is specified as the ratio between the wetted area and the geometrical surface area of the packing.

3. Results and discussion

This section presents and discusses the results of the mesh studies, as well as the experimental and numerical investigations of the four packings.

3.1 Mesh study

The meshes of the packings are generated using *blockMesh*, resulting in a hexahedral background mesh, and subsequently refined to match the solid surfaces with *snappyHexMesh*. A level one surface refinement, combined with a level one explicit feature edge refinement, is specified for the mesh generation. A mesh study is performed by varying the size of the hexahedral cells in the background mesh with a cell count ranging from approximately 4 to 16 million cells. Figure 2 illustrates the relative wetted area ϕ of the packing for different cell numbers after 3 seconds of simulation time.

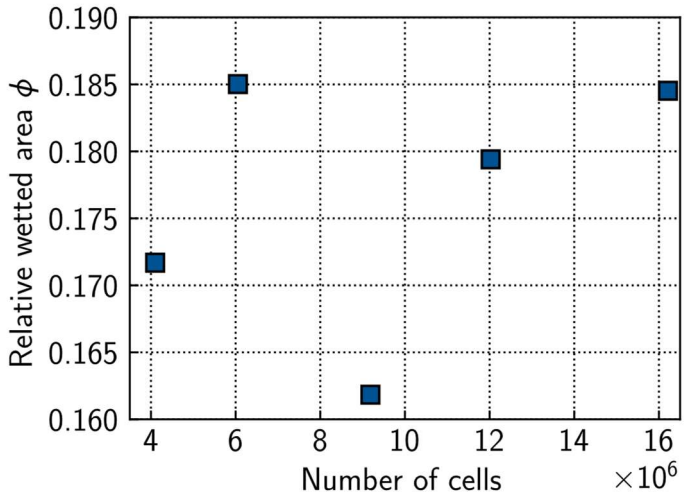

Figure 2: Results of the mesh study for five different meshes

Figure 2 shows that no convergence is obtained between the relative wetted area and the number of cells in the mesh. However, all results are in a similar value range with a maximum relative deviation of approximately 14 %. Compared to the mesh with 4 million cells, all meshes, except that with approximately 9 million cells, exhibit a higher relative wetted area. Notably, simulations with meshes containing 6, 12, and 16 million cells yield similar relative wetted areas. However, the computational cost of meshes with 9 million cells or more is enormous, so simulating high count meshes is not feasible for this study. Consequently, since

- no convergence is achieved,
- the relative wetted area of the mesh with 6 million cells falls within the same range as that of the two highest cell count meshes,
- and, considering the factors of time and computational costs,

the mesh with six million cells is employed for further simulations.

3.2 Experimental and numerical results of the liquid distribution

The results of the liquid distribution from the simulations with the initial contact angles are analyzed after a simulation duration of 4 to 7.5 seconds, as the relative wetted area ϕ and the relative wetted cross-sectional area ψ show only minor variations within a reasonable computation time. The experimental (Exp) and simulation (Sim) results of the liquid distribution for the investigated packings are illustrated in Figure 3.

Figure 3 shows that, for all packings except the ArtistPTNR packing, the simulations exhibit a relative wetted cross-sectional area ψ that is approximately 8% to 42% lower than the experimental values. In contrast, the simulation of the ArtistPTNR packing

yields a value that is 35 % higher than the experimental result. The visualization of the relative wetted cross-sectional area (circles), with liquid colored black and gas colored white, indicates that the liquid distribution within the packing is more uniform in the experiments than in the simulations. Specifically, the simulations show a pronounced one-sided liquid distribution for all packings except the ArtistP packing. One possible reason for this discrepancy between simulation and experiment is the fluid inflow through the needle, as the geometry of the needle is not accurately reproduced in the simulation. Furthermore, the wetting behavior of the liquid may be inaccurately represented due to inappropriate contact angle specifications. This aspect is investigated in the following section.

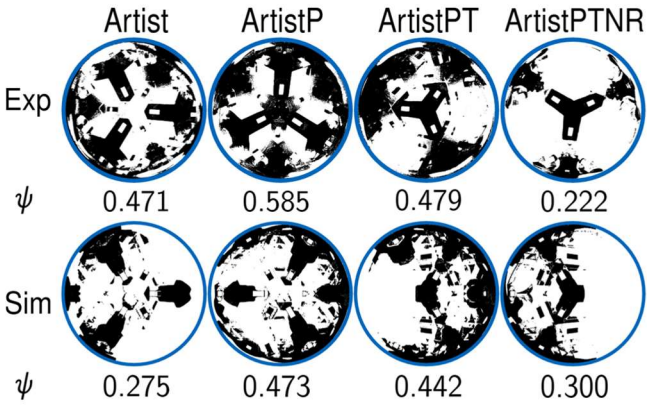

Figure 3: Experimental (Exp) and simulative (Sim) results of the relative wetted cross-sectional area ψ in the four packings Artist, ArtistP, ArtistPT, and ArtistPTNR.

3.3 Numerical results of the contact angle variations

By modifying the contact angle, the discrepancies between experiments and simulations are attempted to be reduced. A contact angle that yields good agreement between numerical and experimental results is likely more appropriate for CFD simulations of *n*-heptane on this additively manufactured surface. The static contact angles in the simulation range from 1° to 20°. The new advancing and receding contact angles are equivalent to the new static contact angle multiplied by the ratios θ_A/θ_S, and θ_R/θ_S of the initially employed contact angles. The results of the contact angle variations are shown in Figure 4.

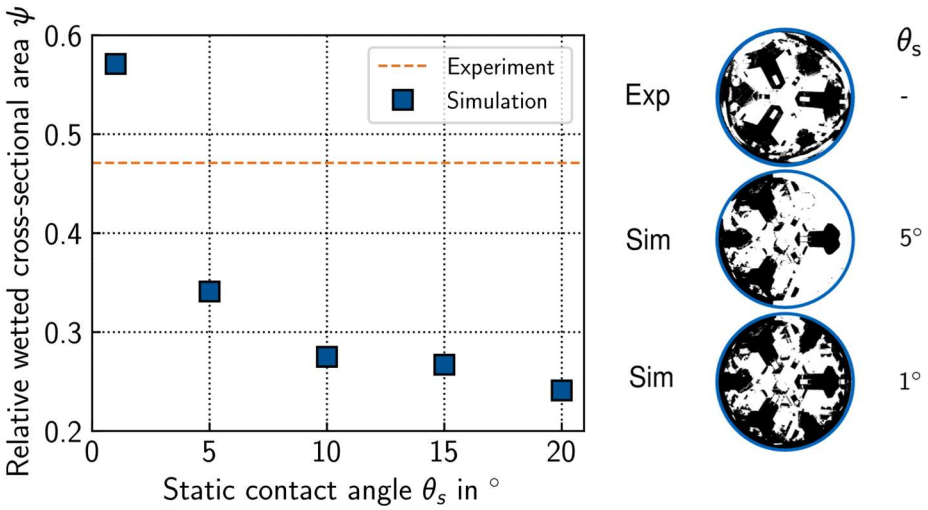

Figure 4: Changes of the relative wetted cross-sectional area ψ for different contact angles (left); visualization of the wetted cross-sectional area at the bottom of the Artist packing with liquid (black), packing and gas (white) of a representative experiment (top) and simulations with a static contact angle of 5° (middle) and 1° (bottom) (right).

Figure 4 (left) depicts the simulated relative wetted cross-sectional area ψ of the Artist packing for varying static contact angles. The horizontal line represents the measured experimental value. It illustrates that ψ decreases with increasing contact angle. At high wettability, characterized by a static contact angle of 1°, the simulated values exceed the experimental results by 21 %, whereas the simulation with a contact angle of 5° underestimates the experimental values by 28 %. In Figure 4 (right), the visualization of the relative wetted cross-sectional area is shown for the experiment (Exp) and two simulations (Sim) with a static contact angle of 5° and 1°, respectively. While the experiments show a uniform liquid distribution throughout the cross-sectional area, the simulation with a static contact angle of 5° still exhibits mainly left-sided wetting of the packing. With a static contact angle of 1°, the right side of the packing internal is also wetted, leading to a qualitative liquid distribution similar to that obtained in the experiments. However, a contact angle of 1° results in an overestimation of wettability compared to the experiment. Consequently, a static contact angle between 1° and 5° is more accurate than the initially employed static contact angle of 10°. Further simulations are in progress to accurately determine the contact angle.

4. Conclusions

This contribution investigates the liquid distribution of four additively manufactured structured packings on a laboratory scale. By combining time-efficient measurements with contact angle variation simulations, a method is introduced for evaluating contact angles for use in CFD simulations. With the initial contact angle defined in the CFD simulations, significant discrepancies of 8 % to 42 % were observed between the experimental and numerical results. The variation of the contact angle results in an overestimation at $\theta_S = 1°$ and an underestimation at $\theta_S = 5°$, indicating that a contact angle between 1° and 5° provides higher accuracy in the CFD simulations. This study serves as a basis for further investigations of contact angle variations for the remaining structured packings.

Acknowledgements

The authors gratefully acknowledge the Gauß Centre for Supercomputing e.V. (www.gauss-centre.eu) for funding this project by providing computing time on the GCS Supercomputer SuperMUC-NG at the Leibniz-Supercomputing-Centre (www.lrz.de).

References

Ertl, Thomas (2023): Experimentelle Validierung von CFD Simulationen der Flüssigkeitsverteilung in 3D gedruckten strukturierten Laborpackungen. Semester thesis. Technical University of Munich, Munich.

Greenshields, Christopher (2025): OpenFOAM v13 User Guide. London, UK: The OpenFOAM Foundation.

Neukäufer, Johannes; Adel Ashour, Mohamed; Sarajlic, Nadin; Klein, Harald; Rehfeldt, Sebastian; Hallmann, Heiko et al. (2022): Development of enhanced three-dimensional printed packings for scale-up of distillation columns: A successful case study. In: *AIChe Journal*.

Neukäufer, Johannes; Hanusch, Florian; Kutscherauer, Martin; Rehfeldt, Sebastian; Klein, Harald; Grützner, Thomas (2019): Methodology for the Development of Additively Manufactured Packings in Thermal Separation Technology. In: *Chemical Engineering Technology* 42, p. 190–1977.

Neukäufer, Johannes; Seyfang, Bernhard; Grützner, Thomas (2020): Investigation of Contact Angles and Surface Morphology of 3D-Printed Materials. In: *Industrial and Engineering Chemistry Research* 59, p. 6761–6766.

Rausch, Nadin (2025): Entwicklung innovativer strukturierter Packungen im Labormaßstab durch CFD-Simulation und additive Fertigung. Ph.D. thesis. Technical University of Munich, Munich.

Rausch, Nadin; Neukäufer, Johannes; Ashour, Mohamed Adel; Grützner, Thomas; Meinicke, Sebastian; Knösche, Carsten; Paschold, Jürgen; Klein, Harald; Rehfeldt, Sebastian (2023): Simulation of the liquid flow distribution in laboratory-scale additively manufactured structured packings. In: *Chemical Engineering Research and Design* 196, p. 28–39.

Sarajlic, Nadin; Stadler, Michael; Ashour, Mohamed Adel; Neukäufer, Johannes; Grützner, Thomas; Paschold, Jürgen; Knösche, Carsten; Klein, Harald; Rehfeldt, Sebastian (2022): Untersuchung der Flüssigkeitsverteilung in additiv gefertigten strukturierten Packungen. In: *Chemie Ingenieur Technik* 94, p. 1002–1009.

A fast data and mechanism fusion modeling method for dynamic absorption/distillation processes

Xing Qian[1], Haotong Wu[1], Yuhui Yin[2], Shengkun Jia[2], Yiqing Luo[2], Xigang Yuan[2]
[1]College of Information Science and Technology, Beijing University of Chemical Technology, Beijing, China;
[2]School of Chemical Engineering and Technology, State Key Laboratory of Chemical Engineering, Tianjin University, Tianjin, China

Abstract
Due to the maturity and widespread use of absorption and distillation in large process industries, accurate modeling is essential for the prediction, optimization, and control of the process. However, traditional mechanistic models inherently have nonlinearity, strong coupling, and high dimensionality, which lead to high hardware requirements, slow solution speed, and poor convergence stability. This paper proposes a data and mechanism fusion modeling method, Physics-constrained Dynamic Mode Decomposition (PCDMD), that enhances the dynamic modeling of absorption processes through systematic integration of mechanistic equations with DMD method. The proposed method demonstrates strong performance in both state reconstruction and prediction through absorption cases. Furthermore, we conduct sensitivity analyses to quantify the impact of key hyperparameters. The results show that the PCDMD method not only preserves computational efficiency inherent to data-driven model, but also enhances generalization and robustness through mechanistic equations. Its successful application in absorption shows its potential in process system engineering.

Keywords
Dynamic modeling; Distillation and absorption; Fusion modeling; Dynamic Mode Decomposition; Kalman filter

1. Introduction

In large process industries such as petroleum and chemical engineering industries, multistage separation processes, including distillation, absorption, and extraction, are the most mature and widely used separation unit operations. Their separation effects directly affect product quality, and their operating stability affects the stability of the entire process (Kiss and Smith, 2020; Sangal et al., 2012). Therefore, optimization, control, and state monitoring of multistage separation processes, represented by distillation and absorption units, have become key technologies to improve their efficiency, energy consumption, and overall economic benefits of chemical production. Although mechanism models based on MESH equations possess advantages in accuracy and interpretability, their inherent strong nonlinearity and high-dimensional structure led to high computational costs, difficult solution, and poor convergence, limiting their application in real-time optimization and control. On the other hand, data-driven models exhibit high computational efficiency and can obtain low-order surrogate models in complex systems; however, their predictive performance heavily depends on data quality, often losing accuracy in the presence of noise, bias, or distribution shift beyond the training range, while simultaneously lacking physical

consistency, making it difficult to employ them independently in industrial scenarios. Therefore, establishing a data and mechanism fusion method has become a recent research hotspot.

The authors proposed the Physics-constrained Dynamic Mode Decomposition (PCDMD) method (Yin et al., 2024) in previous work, which combines DMD-based rapid linear approximation with real-time Kalman filter correction, where residuals derived from mechanistic equations serve as measurement errors. The generalization and robustness of DMD have been enhanced in diverse partial differential equation and fluid mechanics problems. As a general algorithm framework for integrating mechanistic and data-driven models, PCDMD can also be applied to dynamic systems beyond partial differential equations. The authors enhanced the PCDMD method to incorporate external inputs and apply it to the modeling of complex absorption chemical processes which is governed primarily by differential-algebraic equations. The improved method could overcome the original limitation that restricted the method to partial-differential-equation systems without input consideration.

This paper proposes a fusion modeling method based on the Kalman filter, which integrates mechanistic and data-driven models. As shown in Figure 1, it integrates the dynamic mechanistic model with the data-driven model in the absorption system effectively. The framework comprises two parts. Part I involves collecting training and validation data from the rigorous equilibrium-stage model of the chemical process and training the DMDc data-driven model required by the PCDMD model. Part II concerns the implementation of the deep integration between the data driven model and the mechanistic model via the Kalman filter. It is noteworthy that the Kalman filter algorithm employed in PCDMD differs from the traditional Kalman filter. In PCDMD, apart from the already trained A and B matrices and the known input variables, the computation in the second part of the Kalman filter introduces no collected data in Part I or other measurement data.

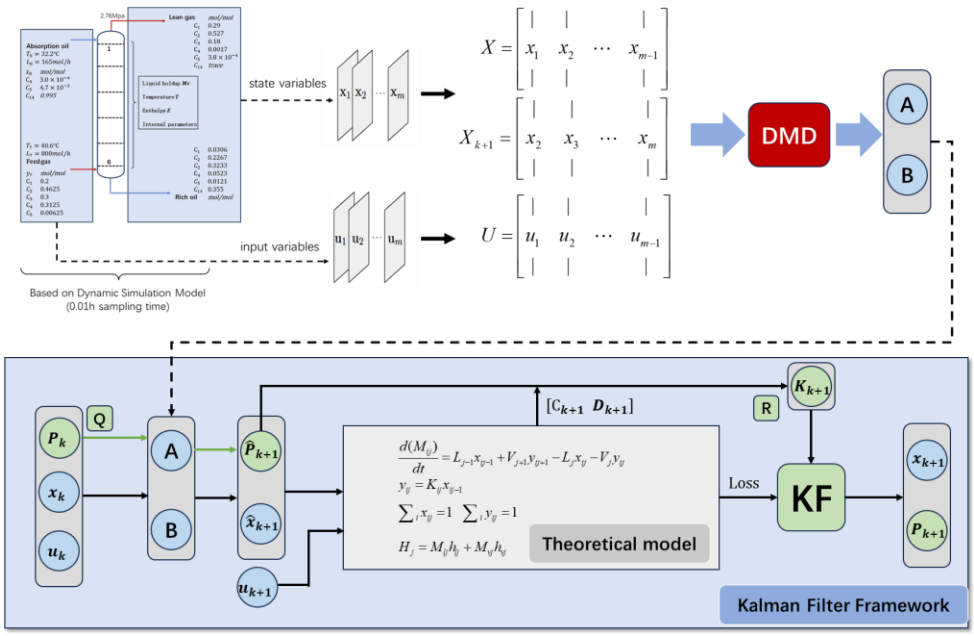

Figure 1: The PCDMD algorithm framework combining DMDc with MESH mechanistic equations

2. Results and discussion

2.1 Absorption Column Model

The absorption column model employed in this section is depicted in Figure 2. It consists of six trays (equilibrium stages) with an operating pressure of 2.76MPa and features a countercurrent contact design for gas-liquid mass transfer. The feed added at the top is absorption oil with tetradecane as the main component (99.5 mol%).

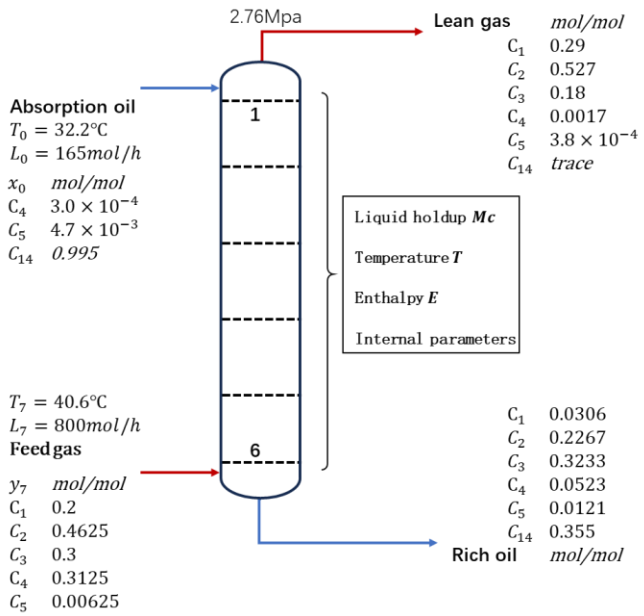

Figure 2: Absorption column model

2.2 Reconstruction and Prediction

In this case, data collection is conducted within the rigorous equilibrium-stage mechanistic model of the absorption column. When there are random disturbances in the feed flowrate and concentration of the absorption oil, data collection is carried out at intervals of 0.01 hours, and the total sampling duration is 5 hours. Therefore, in this paper, the first 5 hours with sampling data are referred to as reconstruction, and the subsequent 25 hours without data are referred to as prediction. The results of some state variables reconstructed and predicted by the PCDMD method are shown in Figure 3.

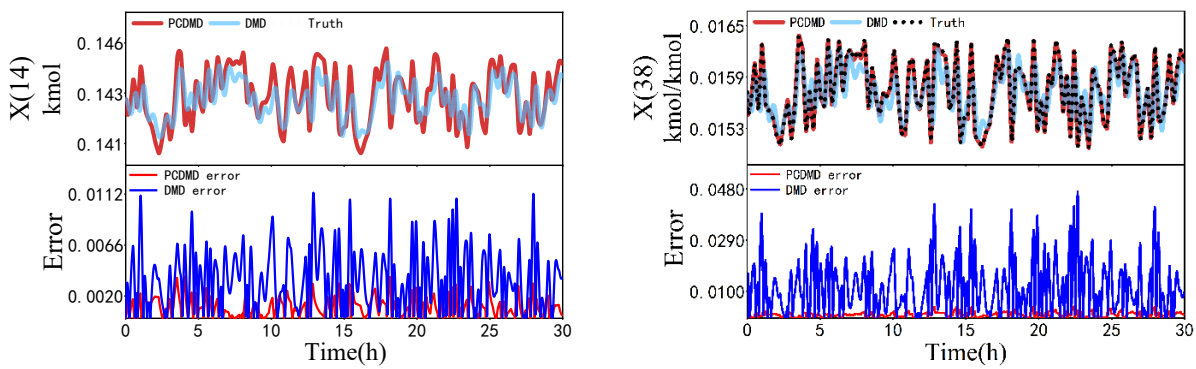

(a) (b)

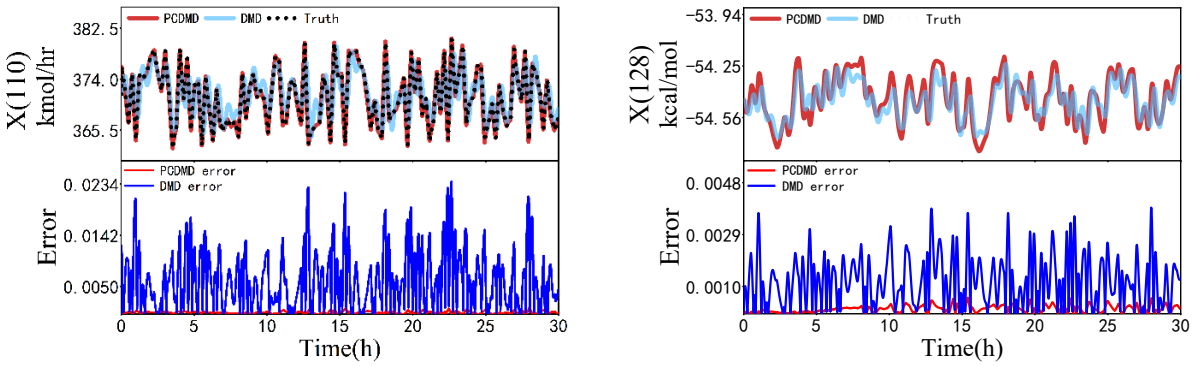

(c) (d)

Figure 3: Reconstructed/prediction results and relative errors of the third tray of the absorption column. (a) tray liquid holdup of component; (b) liquid molar fraction of component; (c) liquid flow rate; (d) liquid molar enthalpy

These PCDMD prediction results are compared with the results of the initial DMD model and the high-fidelity mechanistic simulation, and calculate the relative errors compared with the mechanistic simulation results.

As can be seen from Figure 3, when there are random disturbances in the input, the reconstruction and prediction results of the PCDMD method are highly consistent with the mechanistic simulation results. In contrast, the DMD method performs poorly in the peak and valley regions where the state variables fluctuate complexly, with the prediction trajectory significantly deviating from the mechanistic benchmark. As shown in the error curves of Figure 3, the total average relative errors of the PCDMD method are all below 1×10^{-3}, which is significantly lower than 1×10^{-2} of the DMD method. This is because PCDMD method introduces the MESH equation residuals and the Jacobian gradient matrix, conducts multi-variable coupling compensation and local gradient correction for the linear model generated by DMD. Therefore, PCDMD can effectively compensate for the inherent defects of the linear model, thus ensuring better prediction performance under the conditions of intense input fluctuations and state coupling.

Table 1 counts the computational time for each method. The mechanistic method has the longest computational time. The mechanistic model employed in this paper is a rigorous equilibrium-stage model whose governing equations form a DAE system. During solution, integration of the differential equations must be coupled with iterative solution of the algebraic equations, so the computation time is relatively long. The DMD method has the shortest computational time, with an average single-step execution time of only 1.41×10^{-4} seconds. Since PCDMD adds the steps of mechanistic residual calculation and Kalman filter correction based on DMD, the computational time is increased by two orders of magnitude compared with DMD. However, it is still much less than that of the mechanism simulation. The PCDMD significantly reduces the computational complexity of mechanistic fusion, and can achieve the real-time and rapid integrated modeling of mechanism and data-driven fusion.

Table 1: Computational time of each method

	Mechanistic Method	DMD	PCDMD
Total Computational Time (s)	207.562	0.424	9.156

2.3 Influence of Hyperparameters

The DMD method reduces the order of models by extracting the main dynamic modes. When constructing approximate linear model, the PCDMD method proposed in this paper also needs to preset the truncation order p of the state matrix. As a hyperparameter of the PCDMD method, the value of the order has an effect on the prediction accuracy. When truncation order p is relatively small, although the computational efficiency can be improved, many dynamic details will be lost. In Section 2.2, both the PCDMD and DMD methods set the truncation order to 7 for reconstruction and prediction. In this section, four truncation orders of 7, 30, 80, and 130 are selected to systematically analyze the influence of the truncation order. This paper shows the prediction results of the liquid molar fraction of component on the second tray in Figure 4.

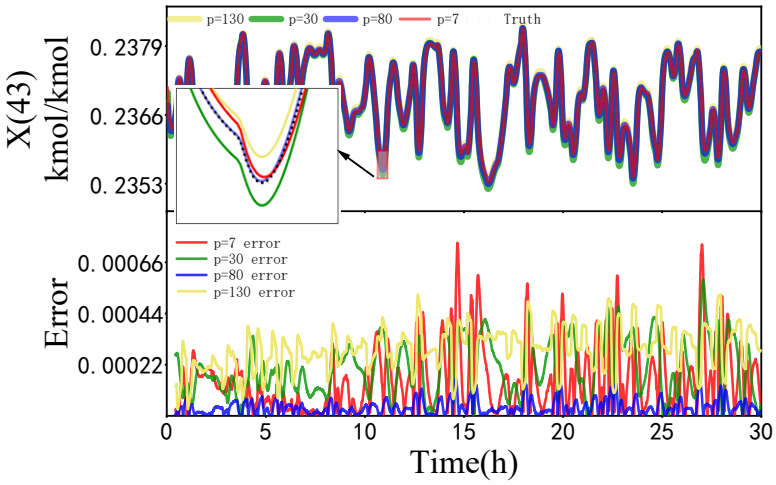

Figure 4: Effect diagrams of various order reduction truncation values of PCDMD method

As shown in Figure 4, when the truncation order $p = 80$, the predicted statistical average relative error is on the order of 1×10^{-5}, which is better than the other three orders. When the truncation order is set relatively low ($p = 7\ or\ 30$), the constructed model cannot fully capture the dynamic modes of the system, resulting in the loss of kinetic characteristics, and leading to deviations in prediction accuracy. Conversely, at higher truncation order ($p = 130$), the model includes redundant modes unrelated to the essential dynamics of the system, as well as introduces computational errors and noise disturbance, ultimately leading to deviations in prediction results. This phenomenon indicates the non-monotonic of prediction accuracy with respect to truncation order , and the selection of truncation order needs to balance the retention of dynamic features and noise suppression. In this paper, benefiting from the correcting effect of the mechanistic equations in the PCDMD and the support of the high-quality dataset, the prediction errors of different truncation orders are all maintained within the range acceptable in engineering.

3. Conclusions

For absorption multi-stage separation processes in chemical engineering, this paper proposes an improved Physical Constrained Dynamic Mode Decomposition (PCDMD) method, aiming to achieve in-depth fusion modeling of data-driven and mechanism quickly. This paper improves the PCDMD framework through the DMD method with

control, generates the data-driven model rapidly, substitutes the prediction results into MESH mechanistic equations to calculate the residuals, and finally achieves real-time correction of all state variables through the Kalman filter. This paper investigates the reconstruction and prediction of state variables in absorption cases and analyzes the influence of key hyperparameters (truncation order) on prediction accuracy.
The reconstruction and prediction results show that the error of the PCDMD method in long-term prediction is lower than 1%, which is significantly lower than that of the pure data-driven DMD method. The successful application of the PCDMD method in the absorption/distillation multi-stage separation processes further proves its versatility in interdisciplinary fields.

Acknowledgements
Financial support from the National Natural Science Foundation of China (22308251 and 22378304) are gratefully acknowledged.

References
Kiss, A.A., Smith, R., 2020. Rethinking energy use in distillation processes for a more sustainable chemical industry. Energy 203, 117788.
Sangal, V.K., Kumar, V., Mishra, I.M., 2012. Optimization of structural and operational variables for the energy efficiency of a divided wall distillation column. Computers & Chemical Engineering 40, 33-40.
Yin, Y., Kou, C., Jia, S., Lu, L., Yuan, X., Luo, Y., 2024. PCDMD: Physics-constrained dynamic mode decomposition for accurate and robust forecasting of dynamical systems with imperfect data and physics. Computer Physics Communications 304, 109303.

High-Gravity Biogas Enrichment: Rigorous Rate-Based Modeling of Reactive CO_2 Absorption in Rotating Packed Beds

Jonathan Mach[1], Joshua Orthey[1], John Paul Gerakis[1], Georg Brösigke[1], Markus Illner[1], Jens-Uwe Repke[1]
[1]Affiliation: Technische Universität Berlin, Process Dynamics and Operations Group, Berlin, Germany

Abstract
High-Gravity (HiGee) units such as Rotating Packed Beds (RPBs) are a process intensification technology that offers significant advantages over conventional columns for separation operations such as absorption by inducing high centrifugal force fields.
For this reason, research interest in RPBs has grown over the past few decades in the western world. However, their industrial implementation remains limited, which is partially due to the lack of reliable rate-based models for the design of RPB-based CO_2 absorption processes. Therefore, this contribution presents the first stage of a rigorous, steady-state, rate-based model for reactive CO_2 absorption from biogas in RPBs. The model incorporates gas- and liquid-phase transport resistances using the generalized Maxwell-Stefan approach, which, to our knowledge, has not yet been reported in the literature for RPB models.
The model is validated against experimental data from the literature for the reactive absorption of CO_2 from flue gas in aqueous MEA solutions. The model reproduces the qualitative trends observed in the experiments, indicating that the model captures operational characteristics of RPBs. Moreover, future enhancements including incorporation of non-idealities in the liquid phase using the electrolyte NRTL model and logarithmic discretization of the liquid film, are expected to improve model accuracy quantitatively. Following validation, the model can serve process and plant design for CO_2 absorption to facilitate application of this technology, and enhance fundamental understanding of mass transfer phenomena within RPBs.

Keywords
Carbon capture, reactive absorption, Rotating Packed Bed, rate-based modeling, Maxwell-Stefan equations

1. Introduction

High-Gravity (HiGee) technologies, such as Rotating Packed Beds (RPBs), have emerged as promising equipment for process intensification in separation operations, including absorption, distillation, or deaereation [1]. As a subgroup of HiGee units, RPBs operate by rotating a dedicated section of the equipment, thereby generating centrifugal forces that are several orders of magnitude greater than gravity. As a result, RPBs enable intensified mixing and mass transfer, expanded operating windows, higher flexibility through adjustable rotational speeds, and the ability to handle highly viscous solvents compared with conventional columns. These characteristics make RPBs particularly attractive for CO_2 absorption, where efficient gas-liquid contacting for high removal rates is essential. As CO_2 is among the most significant anthropogenic greenhouse gases (GHGs), effective capture technologies are crucial for climate change mitigation. CO_2 absorption plays a key role in this context, with biogas

enrichment being a relevant example. This process yields purified CO_2 and methane, from which the latter is a potential carbon-neutral alternative energy source to fossil fuels. As biogas production is relatively decentralized, small-scale equipment such as RPBs is particularly advantageous. At the same time, capturing and processing biogas produced from biomass waste prevents methane emissions, which is considered a significantly more potent GHG than CO_2.

Due to their potential for process intensification and promising advantages they offer over conventional columns, research interest on RPBs has increased in recent years in the Western world, particularly regarding carbon capture technologies, such as reactive CO_2 absorption [2,3]. Nevertheless, industrial applications of this technology remain limited. This is partly due to the fact that reliable, rate-based model approaches are not yet well-established, and often lack rigorous formulations despite being essential for process design and for advancing the mechanistic understanding of transport and reaction phenomena under high-gravity conditions. Developing rigorous rate-based models for RPBs poses a greater challenge than for conventional packed columns, given the need to accurately capture the interplay between the rotating apparatus and the resulting transport phenomena, including heat and mass transfer as well as complex fluid flow.

Therefore, in this contribution, we present the first stage of a rigorous, steady-state, rate-based model for reactive CO_2 absorption in RPBs for biogas enrichment, accounting for gas- and liquid-side transport resistances.

2. Model development

The model is based on the two-film theory, as it is a well-established and proven theoretical concept which forms the basis of the non-equilibrium modeling framework proposed by Krishna and Taylor [4]. The model considers multi-component mass transfer in electrolyte systems subject to chemical reactions. Ideal gas behavior is assumed for the gas phase due to the low operating pressures typically encountered in CO_2 absorption. Although non-idealities in the liquid phase are currently neglected, they will be incorporated in the next stage of model development using the electrolyte NRTL model [5]. As shown in Figure 1, the RPB packing is radially discretized on an equidistant grid. On each stage *j*, the gas (V) and liquid (L) bulk phases are assumed to be ideally mixed each.

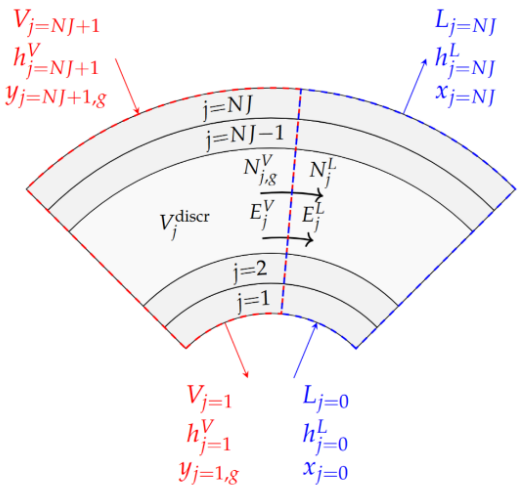

Figure 1: Schematic representation of radial packing discretization and model approach.

2.1 Heat and mass transfer

Following the rate-based framework of Krishna and Taylor [4], the model incorporates energy and mass transfer rates comprising conductive/diffusive and convective transport mechanisms. Diffusive fluxes of species are described by the generalized Maxwell–Stefan approach [6], considering the chemical and electrostatic potential in the driving forces. To the best of our knowledge, this has not yet been reported in the literature for RPB modeling. For a given radial stage *j* and component *c*, the resulting Maxwell-Stefan equation for the driving force d_c, neglecting non-idealities, reads

$$d_c \equiv -\frac{x_c}{RT}(\nabla_{\mathrm{T}}\mu_c + z_c F \nabla\Phi) \approx -\left(\nabla x_c + \frac{z_c F}{RT}\nabla\Phi\right) = \sum_{\substack{k=1\\k\neq c}}^{Nc} \frac{x_k J_c - x_c J_k}{c_t Đ_{ck}}, \quad (1)$$

where $x_c, \mu_c, z_c,$ and J_c denote the mole fraction, chemical potential, ionic charge, and diffusive flux of species *c*, respectively. The universal gas and Faraday constants are given by R and F, respectively. Furthermore, $\boldsymbol{c_t}$ represents the total concentration, T the temperature, and $Đ_{ck}$ the binary Maxwell-Stefan diffusivity of species *c* in *k,* and $\nabla\Phi$ is the electrostatic potential gradient. The overall mass transfer rate N_c of component c is defined as

$$N_c = \underbrace{J_c A}_{\text{diffusive}} + \underbrace{x_c \sum N_c}_{\text{convective}}, \quad (2)$$

where A is the interfacial area. The electrostatic potential gradient is taken into account solely for ionic species, for which the electroneutrality and zero net current constraints are imposed [6], i.e.

$$0 = \sum x_c z_c\,, \quad (3)$$

$$0 = \sum z_c N_c. \quad (4)$$

Heat conduction is modeled according to Fourier's law, yielding the overall heat transfer rate

$$E = \underbrace{\lambda \frac{dT}{dz} A}_{\text{conductive}} + \underbrace{\sum N_c h_c}_{\text{convective}}, \quad (5)$$

where $\lambda, z,$ and h_c are the thermal conductivity, spatial film coordinate, and specific enthalpy of species c, respectively. The interfacial area is determined assuming a planar liquid film with liquid holdup and interfacial area being calculated using the correlations proposed by Yang [7] and Onda [8], respectively. The film thickness, i.e., the boundary layer thickness, for the calculation of the gradients of both phases is estimated using the film theory, yielding

$$l_c^{film} = \frac{D_c}{k_c}, \quad (6)$$

where gas- and liquid phase mass transfer coefficients k_c are calculated using correlations by Onda [8] and Tung [9], respectively. The diffusion coefficients D_c for the gas and liquid phases are calculated using the model by Chapman-Enskog-Wilke-Lee and Wilke-Chang together with Nernst-Hartley, respectively, as given in [10].

2.1 Reactive absorption

The reactive absorption process is modeled by a reaction network comprising both equilibrium and kinetic reactions [11], which is shown in Table 1. The equilibrium reactions q_1-q_3 mainly cover proton transfer in dissociation, whereas k_1-k_4 are the rate equations for the CO_2-amine interaction. The system includes H_2O, MEA, CO_2, N_2, O_2, and the ionic products of the liquid-phase reactions. Equilibrium reactions are modeled using the standard chemical equilibrium approach based on the law of mass action, while kinetic reactions are modeled using a formal kinetic approach [11].

Equilibrium Reactions	Kinetic Reactions
$q_1: MEAH^+ + H_2O \rightleftharpoons MEA + H_3O^+$	$k_1: CO_2 + OH^- \rightarrow HCO_3^-$
$q_2: 2H_2O \rightleftharpoons H_3O^+ + OH^-$	$k_2: HCO_3^- \rightarrow CO_2 + OH^-$
$q_3: HCO_3^- + H_2O \rightleftharpoons CO_3^{2-} + H_3O^+$	$k_3: MEA + CO_2 + H_2O \rightarrow MEACOO^- + H_3O^+$
	$k_4: MEACOO^- + H_3O^+ \rightarrow MEA + CO_2 + H_2O$

Table 1: Overview of the reaction network [11] used for the model.

The model is implemented in MOSAICmodeling [12], an equation-oriented modeling environment that enables export to various simulation platforms. The model is solved in AMPL using the CONOPT solver.

2. Results and discussion

Since no data on biogas enrichment in RPBs are currently available in literature, the model is applied to describe reactive absorption of CO_2 from flue gas in aqueous MEA solutions and will be extended to biogas enrichment in the future, following full implementation of the methodology and subsequent validation using own experiments. Consequently, model validation is conducted in Figure 2 by comparing the simulated CO_2 removal with experimental data from Thiels et al. [13] for a lab-scale RPB, with an inner and outer packing diameter of 25 and 125 mm, respectively, and a packing height of 23 mm. The experiments were conducted for a 30-wt% aqueous MEA solution, a liquid flow rate of 0.1 L/min, gas flow rates V from 0 to 60 L/min, and lean loadings X_{CO2} of 0, 0.157, 0.249, 0.380, and 0.442 mol CO_2/mol MEA. The liquid and gas flow rates correspond to a liquid load of 3.3 $m^3/(m^2h)$ and F-Factors from 0.05 to 0.58 $Pa^{0.5}$, respectively. The mass-based L/G-ratios reach from 18 to 1.5. The rotational speed is 1600 rpm, and the liquid and gas inlet temperatures are 50°C. The composition of the gas inlet is 10 mol% CO_2 and 90 mol% N_2. The corresponding RPB parameters are summarized in Table 2, whereas the operating conditions are provided in Table 3.

RPB Parameter	Value
Inner rotor diameter / mm	25
Outer rotor diameter / mm	125
Packing height / mm	23
Porosity / 1	0.96
Specific surface area of packing/ m^2/m^3	887.6

Table 2: RPB parameter from Thiels et al. [13].

Operating Condition	Value
Rotational Speed / rpm	1600
Liquid load and flow rate / L/min	3.3 / 0.1
Liquid load / $m^3/(m^2h)$	3.3
Gas and liquid inlet temperature / °C	50
Gas CO_2/N_2 concentration / mol%	10/90
Liquid MEA concentration / wt%	30
Gas flow rate V / L/min	0, 5, 10, 20, 30, 40, 50, 60
Lean loading X_{CO2} / molCO_2/molMEA	0, 0.157, 0.249, 0.380, 0.442
F-Factors / $Pa^{0.5}$	0.05, 0.10, 0.19, 0.29, 0.39, 0.48, 0.58
L/G ratio (mass)	18, 9.0, 4.5, 3.0, 2.2, 1.8, 1.5

Table 3: Operating conditions for experiments by Thiels et al. [13] and simulations from the RPB model in this work.

The experimental data in Figure 2a) show two distinct trends: a decrease in CO_2 removal with increasing gas flow rate, and a decrease with higher lean loading. Both trends are qualitatively reproduced by the simulated CO_2 removal.

However, a relatively large deviation between both data sets remains, as shown in Figure 2b), where only a few data points fall within the ±20% parity band. At the same time, the deviation decreases with increasing lean loading. This is expected, as higher lean loadings correspond to inlet concentrations closer to the equilibrium, limiting the extent of CO_2 absorption. Overall, the model still shows good agreement with the experimental data. Since film discretization has not yet been applied and non-idealities are neglected, accuracy is expected to improve once both aspects are incorporated into the model.

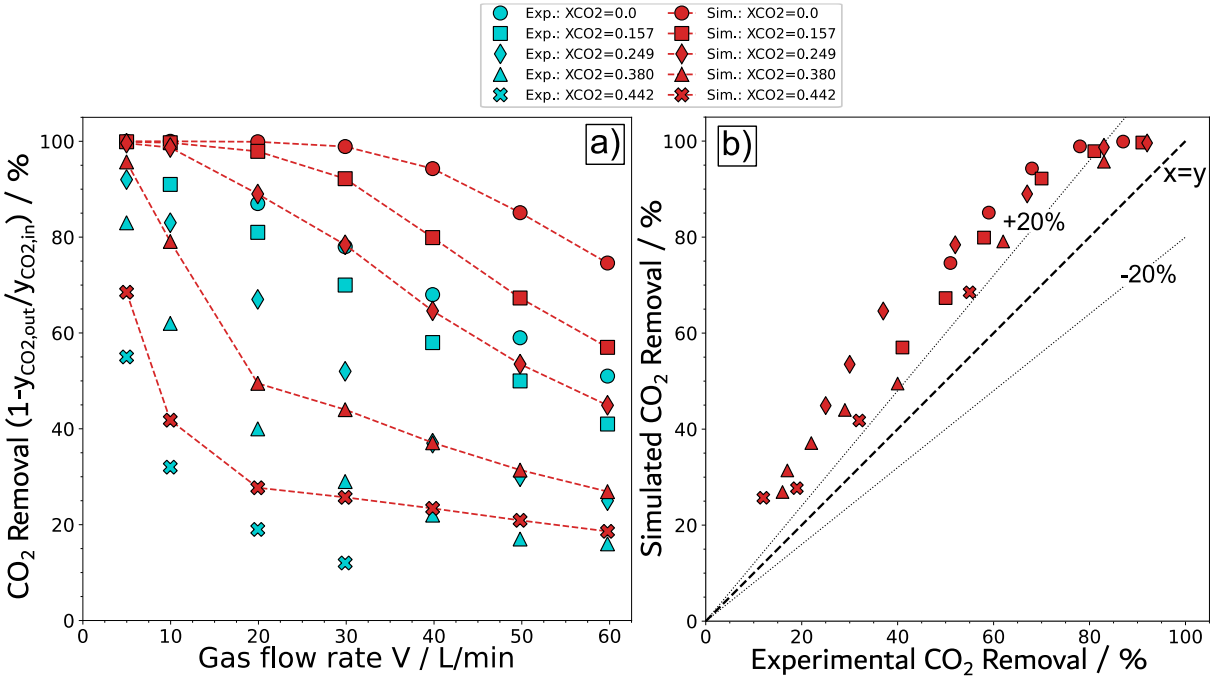

Figure 2: a) Comparison of simulated and experimental Carbon capture rate CO2 removal and b) parity plot for simulated and experimental CO2 removal with experimental data by Thiels et al. [13] for varying gas flow rates (0-60 L/min) V and lean loadings XCO2 (0, 0.157, 0.249, 0.380, and 0.442) with a constant liquid flow rate of 0.1 L/min and rotational speed of 1600 rpm.

The present simulation results are calculated with 20 radial stages *j*. To better reflect reality, the composition of the liquid feed for lean loadings greater than zero is calculated using a mixer model in Aspen Plus, considering the reactions shown in Table 1. For the liquid feed, a modified reaction network is used, comprising only equilibrium reactions rather than both equilibrium and kinetic reactions. This means k_1-k_4 are modeled as equilibrium reactions, and the liquid feed contains not only CO_2 but also ionic species. The overall lean loading remains unchanged, as it is now defined by all CO_2- and MEA-related species rather than only molecular CO_2 and MEA alone, as given by

$$X_{CO2} = \frac{x_{CO2} + x_{HCO_3^-} + x_{CO_3^{2-}} + x_{MEACOO^-}}{x_{MEA} + x_{MEAH^+} + x_{MEACOO^-}}. \quad (7)$$

3. Conclusions

This work presents preliminary results from the first stage of a rigorous, rate-based, steady-state RPB model for reactive CO_2 absorption considering gas- and liquid side transport resistances. The model is validated against literature data for CO_2 absorption experiments from flue gas. The predicted values reproduce the qualitative trends observed experimentally, indicating that the model captures the operational characteristics of RPBs. Nonetheless, a quantitative mismatch between the data sets remains. A subsequent step in model development involves accounting for non-

idealities in the liquid phase using the electrolyte NRTL model, which is expected to enhance accuracy. Additionally, the high reaction rates of primary amines such as MEA with CO_2 give rise to strongly non-linear concentration and temperature profiles within the liquid film. Logarithmic discretization of the film using a finite-difference scheme is therefore expected to further enhance model accuracy.

At present, the model is applied to describe reactive absorption of CO_2 from flue gas in aqueous MEA systems. In the future, the model will be extended to the biogas enrichment process by varying the gas mixture, solvent system, and packing geometry. Moreover, hydrodynamic correlations for liquid holdup, interfacial area, and pressure drop, as well as reaction kinetics for a suitable solvent, will be developed by our project partners and incorporated into the model. Further model validation is then planned through biogas enrichment experiments on our in-house RPB plant. The validated model can subsequently support process and plant design for CO_2 absorption in RPBs, deepen the understanding of mass transfer phenomena, and potentially serve as foundation to other applications.

Acknowledgements

This work is partially supported by the German Research Foundation (DFG) under project number 544949629 within the LAP/Weave program together with UT Lodz and UT Brno. This work is partially supported by funding from the Federal Ministry of Economic Affairs and Climate Action of Germany under project code 03EE5103C.

References

[1] A. Ressemann, M. Illner, and J.-U. Repke, “Local Separation Performance for Distillation Processes in Rotating Packed Beds: Transferability and Applicability,” Ind. Eng. Chem. Res., vol. 63, no. 30, pp. 13291–13307, Jul. 2024, doi: 10.1021/acs.iecr.4c01422.

[2] G. E. Cortes Garcia, J. Van Der Schaaf, and A. A. Kiss, “A review on process intensification in HiGee distillation,” *J of Chemical Tech & Biotech*, vol. 92, no. 6, pp. 1136–1156, Jun. 2017, doi: 10.1002/jctb.5206.

[3] C. Shukla, P. Mishra, and S. K. Dash, “A review of process intensified CO2 capture in RPB for sustainability and contribution to industrial net zero,” *Front. Energy Res.*, vol. 11, p. 1135188, Apr. 2023, doi: 10.3389/fenrg.2023.1135188.

[4] R. Krishnamurthy and R. Taylor, “A nonequilibrium stage model of multicomponent separation processes. Part I: Model description and method of solution,” AIChE Journal, vol. 31, no. 3, pp. 449–456, Mar. 1985, doi: 10.1002/aic.690310312.

[5] C. Chen and L. B. Evans, “A local composition model for the excess Gibbs energy of aqueous electrolyte systems,” AIChE Journal, vol. 32, no. 3, pp. 444–454, Mar. 1986, doi: 10.1002/aic.690320311.

[6] R. Krishna and J. A. Wesselingh, “The Maxwell-Stefan approach to mass transfer,” Chemical Engineering Science, vol. 52, no. 6, pp. 861–911, Mar. 1997, doi: 10.1016/S0009-2509(96)00458-7.

[7] Y. Yang *et al.*, “A noninvasive X-ray technique for determination of liquid holdup in a rotating packed bed,” *Chemical Engineering Science*, vol. 138, pp. 244–255, Dec. 2015, doi: 10.1016/j.ces.2015.07.044.

[8] K. Onda, H. Takeuchi, and Y. Okumoto, “MASS TRANSFER COEFFICIENTS BETWEEN GAS AND LIQUID PHASES IN PACKED COLUMNS,” *J. Chem. Eng. Japan / JCEJ*, vol. 1, no. 1, pp. 56–62, 1968, doi: 10.1252/jcej.1.56.

[9] H.-H. Tung and R. S. H. Mah, “MODELING LIQUID MASS TRANSFER IN HIGEE SEPARATION PROCESS,” *Chemical Engineering Communications*, vol. 39, no. 1–6, pp. 147–153, Dec. 1985, doi: 10.1080/00986448508911667.

[10] Aspen Technology, Inc., *Aspen Physical Property System: Physical Property Models*, Version 12.1, Bedford, MA, USA, May 2021. [Online]. Available: http://www.aspentech.com

[11] Aspen Technology, Inc. (2014): “Rate-Based Model of the CO2 Capture Process by MEA using Aspen Plus”. Version V10

[12] Process Dynamics and Operations Group, Technical University of Berlin, MOSAICmodeling, https://mosaic-modeling.de/ (2025, June 20) 10.1002/aic.690320311.

[13] M. Thiels, D. S. H. Wong, C.-H. Yu, J.-L. Kang, S. S. Jang, and C.-S. Tan, “Modelling and design of carbon dioxide absorption in rotating packed bed and packed column,” IFAC-PapersOnLine, vol. 49, no. 7, pp. 895–900, 2016, doi: 10.1016/j.ifacol.2016.07.303.

Opening the Black Box of Rotating Packed Beds – Revealing the Flow Morphologies through Fluid Simulations

Felix Febrian[1], Georg Brösigke[1], Jens-Uwe Repke[1]
[1]Technische Universität Berlin, Process Dynamics and Operations Group, Berlin, Germany

Abstract
Rotating packed beds have been applied in a limited number of industrial processes as process intensified alternatives to conventional columns for absorption and (reactive) distillation. Despite their considerable potential for enhanced mass transfer, broader industrial implementation in Europe remains challenging due to persistent knowledge gaps, particularly regarding gas/liquid flow morphology and the local specific interfacial area within the packing, introducing uncertainty into design process. In this work, these gaps are addressed through a numerical investigation of multiphase flow to evaluate the interfacial area between the two phases within the complex packing geometry. The results provide qualitative insights into the morphology of the gas/liquid interface under the variation of the rotational speed and gas flowrate, as well as detailed local distributions of liquid holdup and effective surface area that are difficult to access experimentally. These profiles of local effective interfacial area in particular could not yet be determined experimentally and may lay a foundation for the development of more precise correlations for process modeling.

Keywords
Rotating packed bed, HiGee, Gas/Liquid/Solid flow, VOF, CFD, Open-cell foams

1. Introduction

The chemical industry is constantly evolving to address numerous challenges such as improving economics while maintaining environmental and safety metrics. Process intensification is a vital concept essential to this transformation to achieve significant reductions in equipment dimension, energy consumption, or waste generation while accomplishing a given production goal. One example for process intensification is the development of the Rotating Packed Bed (RPB) as part of the high-gravity (HiGee) technology. Devices under the category of HiGee exploit centrifugal fields up to 1000 times earth gravity in order to enhance heat and mass transfer, allowing for a reduction in size [1].

Use cases of HiGee devices are in particular absorption, stripping, distillation, deaeration and reactive distillation. There are several documented industrial applications of RPBs [1]. Prominent examples of these applications lie in the ab- and desorption of gases, such as the stripping of oxygen in oil, SO_2 absorption from tail gas, selective H_2S absorption, and reactive absorption of HOCl. On the distillation side, the commercialization of Rotating Zigzag Beds (RZBs), a device in the HiGee family with alternating stationary and rotating baffles, was also reported for methanol rectification. In each of these applications, equipment size reduction by factors of 4 to 40 compared to “conventional” columns has been reported. Other promising potentials of

RPBs include quick startup and shutdown as well as offshore usage of the device, as its performance is unaffected by surrounding motions.
Apart from these few industrial applications, carbon capture projects have also driven research on RPB applications for CO_2 absorption [2]. Direct comparison of RPBs with packed columns for post-combustion CO_2 absorption has also been reported in more recent studies [3,4]. Concurrently, more authors have also explored further applications of RPBs as intensified distillation unit [5–7]. These developments show an uptrend in the importance of both RPBs in particular and HiGee devices in general for thermal separation processes.
Despite the stated relevance of the RPB, the pathway toward a more extensive industrial implementation of the technology remains challenging. Several critical aspects, for example, reliable process models as tool in systematic process synthesis and design and scale up rules for HiGee devices, remain insufficient and require further investigation [8]. Recent experimental studies on RPBs have contributed useful data, such as the overall volumetric mass transfer coefficient [6,9] or the liquid holdup in the packing [10,11]. However, several knowledge gaps, in particular the morphology of the gas/liquid flow and local specific surface area in the packing, remain inadequately studied. One reason for these gaps is the difficulty of direct measurements of these quantities inside the packing.
Over the past decades, substantial progress has been achieved in numerical methods for multiphase flow simulations. The interface-capturing Volume of Fluid (VOF) framework has been successfully applied in the multiphase flow simulation of the RPB with wire mesh packing [12]. In these studies, the wire mesh packing is modeled as uniform formation of cylinders. While assuming idealized cylindrical geometry is reasonable for wire mesh packing, an analogous assumption does not hold for the similarly commonly applied metal foam packings (Figure 1 left). Accordingly, this work addresses the existing research gap through numerical investigation of flow morphology and interfacial area within the 3D complex geometry with counter current gas flow and VOF framework. Based on the simulation results, we report the qualitative gas/liquid flow morphologies under different operating conditions as well as detailed local distributions of liquid holdup and effective surface area, thus opening the black-box that is the metal foam packing.

2. Simulation setup

The metal foam NCX 1116 by Recemat BV, which is extensively employed in RPB research [6,9], is reconstructed to finely resolve the phase distribution of the two-phase flow in the simulations. We implement a reconstruction procedure for the metal foam and utilize the produced foam surface in the grid generation process. The reconstruction workflow is described and validated in [13] and the reconstructed foam is illustrated in Figure 1.

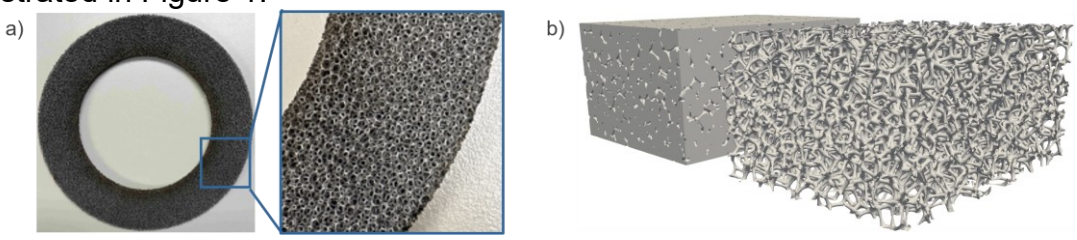

Figure 1: One segment of the NCX1116 metal foam used as RPB's packing (a) as well as the reconstructed foam and the resulting mesh for the CFD simulations (b).

The interface-capturing method VOF within the CFD toolbox OpenFOAM for the multiphase flow framework is chosen due to its simplicity, its minimal need of closure models, and its ability to resolve the interface. The fluids consist of a water/air system and assumed to be incompressible, isothermal and immiscible. To minimize the computational cost, the domain is reduced into a periodical slice, imposing cyclical boundary conditions on the two sides of the domain (Figure 2). The kω-SST model is applied in the simulation based on previous experience [13]. The metal foam spans from the inner radius $r_i = 0.073$ m to the outer radius $r_o = 0.1$ m. The rotation is achieved through the multiple reference frame method. In the simulations, the rotational speed of the packing bed is varied ($n = 5 – 20\ s^{-1}$). The liquid flow rate amounts to $F_L = 0.378\ m^3\ h^{-1}$ and gas flows counter-currently ($F_G = 0 – 60\ m^3\ h^{-1}$). The integral liquid holdup is monitored during the simulation and the simulation is terminated after a quasi-steady state of the holdup is achieved.
Special treatments are applied to the inlet outlet boundaries specified in Figure 2. Firstly, the rotating liquid jet at liquid inlet is programmed to mimic the experimental condition reported in [11] and is dependent on the rotational speed. Secondly, as the liquid should flow outwards and gas flow inwards simultaneously through the green surface in Figure 2, the simulation is set to be pressure-driven, that is the Neumann condition is applied for the velocity field at both gas inlet boundary (green surface) and gas outlet boundary (red surface) and the Dirichlet condition is applied to the pressure field on the corresponding boundaries. Lastly, a PID-feedback control loop is programmed for the value of the pressure at the gas inlet boundary to achieve a specified gas flowrate.

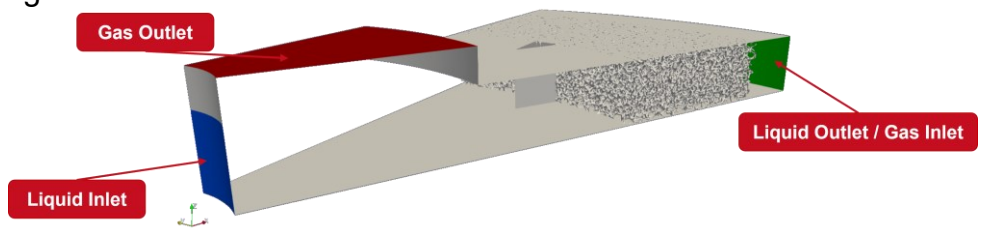

Figure 2: Computational domain for the multiphase simulation as an axisymmetric slice of the RPB – grey surfaces are wall boundary conditions, the periodical boundary surfaces are omitted and the rest of the boundaries are specified.

3. Results and discussion

Based on the simulation setup described above, this section presents the simulation results for insights on the multiphase flow morphologies and the process variables liquid holdup and interfacial area, which are relevant for mass transfer quantification. Qualitatively, various morphologies of the liquid such as rivulets and droplets inside the pores of the metal foam can be observed. Figure 3 shows the distribution of the interface for gas counter-current flowrate $F_G = 60\ m^3\ h^{-1}$ and four different rotational speeds ($n = 5$, 10, 15, and 20 s^{-1}). At low rotational speed, the liquid tends to fill the pores in the metal foam and flows as rivulets. By contrast, the liquid becomes more dispersed as the rotational speed increases. The liquid fills the pores in the form of smaller droplets and the size of the droplets is apparently smaller than the pores of the foam packing. These observations of droplet and rivulet flows are consistent with the visual study conducted in [10] and are far from the ideal film model assumed by many mass transfer correlations [14].
The visualization of the gas/liquid interface in Figure 3 also reveals the effect of the gas counter-current flow, particularly in the deflection of the liquid jet upstream from

the metal foam. At low rotational speed of n = 5 s^{-1}, the deflection of the liquid jet appears to inflict liquid maldistribution, where the upper part of the metal foam appears to be less wetted than its lower counterpart.

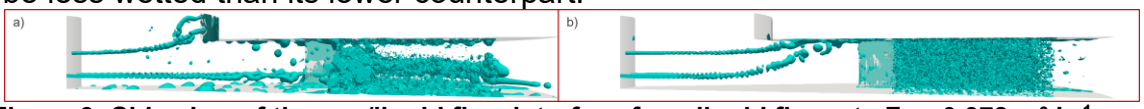

Figure 3: Side view of the gas/liquid flow interface for a liquid flowrate F_L = 0.378 m^3 h^{-1}, gas flowrate F_G = 60 m^3 h^{-1}, and rotational speeds 5 s^{-1} (a) and 20 s^{-1} (b).

The flow morphologies of rivulets and droplets are also visible from another perspective illustrated in Figure 4. Furthermore, Figure 4 reveals liquid maldistribution in the tangential direction, which is consistent with [10]. At n = 5 s^{-1}, the pores directly behind the packing support ring (triangular structure at the center of the domain) are visibly less wetted than the rest as highlighted with the red ellipses. Increasing the rotational speed reduces this liquid maldistribution, albeit imperfectly.

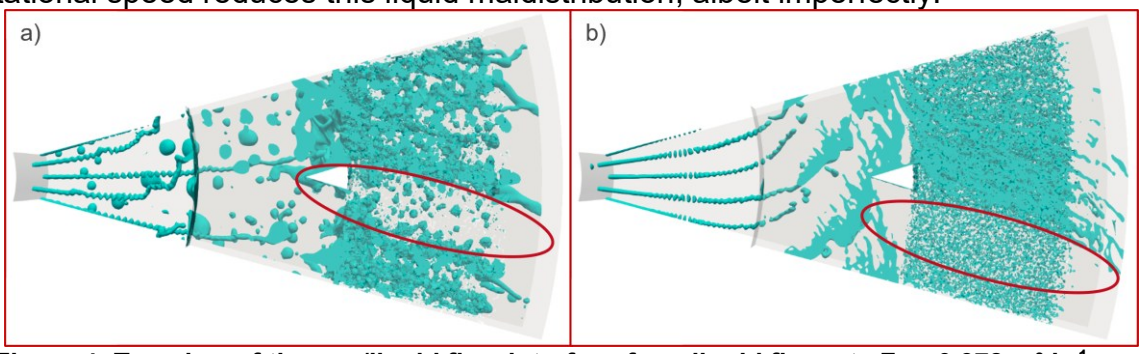

Figure 4: Top view of the gas/liquid flow interface for a liquid flowrate F_L = 0.378 m^3 h^{-1}, gas flowrate F_G = 60 m^3 h^{-1}, and rotational speeds 5 s^{-1} (a) and 20 s^{-1} (b).

Quantitatively, time-averaged radial profiles of the specific holdup $\varepsilon = V_{liq}/(V_{liq} + V_{gas})$ of the liquid and the specific interfacial area $a_{eff} = A_{int}/(V_{liq} + V_{gas})$ between the two phases can be derived from the simulation results. As depicted in Figure 5, these radial profiles are shown with markers for F_G = 60 m^3 h^{-1} and as dashed line for F_G = 0 m^3 h^{-1} with the corresponding colors. In general, the data show that the liquid holdup decreases with increasing rotational speed (Figure 5 left). Consistent with [11,15,16], the counter-current gas flow has little effect on the liquid holdup ε for rotational speeds above 10 s^{-1}. Only for n = 5 s^{-1} is a significant reduction of the liquid holdup visible with gas counter-current flow. However, the presence of gas counter-current flow has more significant effect on the effective interfacial area a_{eff} (Figure 5 right). For rotational speeds below 15 s^{-1}, the gas counter-current flow appears to reduce the local effective interfacial area, whereas the effect is less significant for n = 20 s^{-1}.

The radial profiles of both liquid holdup ε and effective surface a_{eff} also reveal higher values at the inner radius of the packing, in particular for operations with lower rotational speed. These peaks near the inner radius are more pronounced with gas counter-current flow and are generally followed with diminishing trend with increasing radius. At higher rotational speeds, these peaks are less distinct and the profiles of liquid holdup and effective surface are more uniform along the radius. As the mass transfer rate depends on the available interfacial area, peaks of the effective surface near the inner radius are consistent with the documented end-effect zones in numerous mass transfer studies [14].

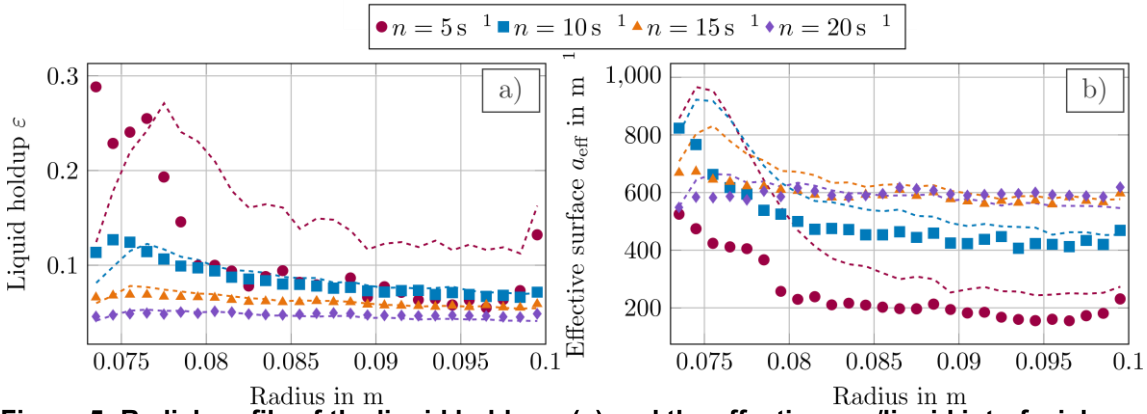

Figure 5: Radial profile of the liquid holdup ε (a) and the effective gas/liquid interfacial area a_{eff} (b) for F_G = 0 m³ h⁻¹ (dashed lines) and F_G = 60 m³ h⁻¹ (markers) for a constant liquid flowrate F_L = 0.378 m³ h⁻¹.

The influence of both the rotational speed n and the gas flowrate F_G are more visible when the averaged values within the packing are considered. Higher rotational speed decreases the overall liquid holdup ε as shown in Figure 6 left. Nevertheless, the gas flowrate has only significant effect on the holdup for n = 5 s^{-1} as noted above. Figure 6 right shows an increase in effective surface area a_{eff} up to a maximum at n = 15 s^{-1} with increasing rotational speed. For F_G = 40 m^3 h^{-1} and below, the gas counter-current flow has little effect on the effective surface, whereas for F_G = 60 m^3 h^{-1} the gas flow negatively affects the effective surface.

The observed maximum in surface area may indicate a possible limitation of the mass transfer rate at higher rotational speeds. On the one hand, the mass transfer rate is directly proportional to the available surface area. Moreover, the decrease in effective surface area, together with a reduction in liquid holdup, may also suggest a shortened liquid residence time, which could in turn limit the mass transfer coefficient. On the other hand, a relatively high surface area combined with lower liquid holdup is only achievable in the presence of smaller liquid droplets, implying a reduced mass transfer resistance and consequently an increased mass transfer coefficient. These considerations suggest that the effect of rotational speed on surface area, mass transfer coefficient, and eventually the mass transfer rate is highly nonlinear. A detailed quantification of the relative contributions of both surface area and mass transfer coefficient is therefore required and should be addressed in future work.

Figure 6 right also shows that the absolute values of the effective surface at maximum is roughly 600 m^{-1}, substantially less than the specific surface of the packing of 1000 m^{-1} based on the product specification for NCX 1116. This indicates that the assumption of packings specific area as the mass transfer area frequently adopted in mass transfer studies [14] appears to be inaccurate.

4. Conclusions

In our contribution, we report on the flow morphologies and local liquid holdup as well as effective gas/liquid area inside the metal foam packing NCX 1116 inside the RPB. To the best of our knowledge, this is the first study to employ CFD simulations resolving the metal foam geometry under gas/liquid counter-current flow conditions. Qualitatively, flow morphologies in forms of rivulets and droplets can be observed, consistent with previous studies. Quantitatively, time-averaged radial profiles of the specific holdup ε and the specific interfacial area a_{eff} can be derived from the simulation results. The results hint toward an optimal surface area as a function of the rotational

speed, whereas higher gas counter-current flowrate appears to reduce the available transfer area. These profiles of local effective interfacial area in particular could not yet be determined experimentally and may lay a foundation for the development of more precise correlations for process modeling. However, the ultimate influence of the surface area and liquid holdup on overall mass transfer is still unclear and should be addressed in future work.

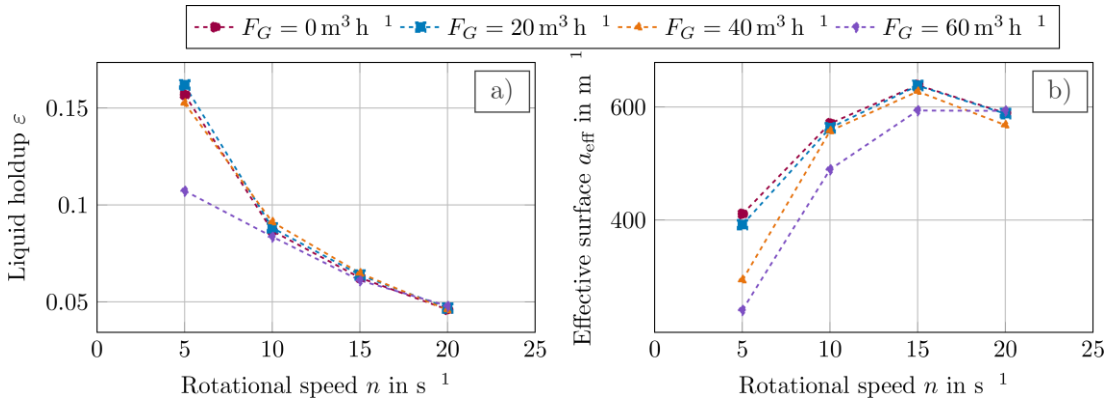

Figure 6: Average liquid holdup ε (a) and effective gas/liquid interfacial area a_{eff} (b) inside the metal foam packing for different gas flowrates and a constant liquid flowrate F_L = 0.378 m^3 h^{-1}.

Acknowledgements

The authors gratefully acknowledge the computing time granted by the Resource Allocation Board and provided on the supercomputer Lise and Emmy at NHR@ZIB and NHR@Göttingen as part of the NHR infrastructure. The calculations for this research were conducted with computing resources under the project bec00282.

References

[1] G. E. Cortes Garcia, J. Van Der Schaaf, A. A. Kiss, *J. Chem. Technol. Biotechnol.* **2017**, *92* (6), 1136–1156. DOI: 10.1002/jctb.5206.

[2] M. Wang, A. S. Joel, C. Ramshaw, D. Eimer, N. M. Musa, *Appl. Energy*. **2015**, *158*, 275–291. DOI: 10.1016/j.apenergy.2015.08.083.

[3] M. Thiels, D. S. H. Wong, C.-H. Yu, J.-L. Kang, S. S. Jang, C.-S. Tan, *IFAC-Pap.* **2016**, *49* (7), 895–900. DOI: 10.1016/j.ifacol.2016.07.303.

[4] M. Akram, A. Gheit, K. Milkowski, W. Gale, M. Pourkashanian, *Fuel*. **2025**, *388*, 134484. DOI: 10.1016/j.fuel.2025.134484.

[5] T. Pyka, A. Ressemann, C. Held, G. Schembecker, J.-U. Repke, *Ind. Eng. Chem. Res.* **2023**, *62* (33), 13274–13279. DOI: 10.1021/acs.iecr.3c01947.

[6] A. Ressemann, M. Illner, J.-U. Repke, *Ind. Eng. Chem. Res.* **2024**, *63* (30), 13291–13307. DOI: 10.1021/acs.iecr.4c01422.

[7] T. Pyka, V. Backhaus, C. Held, G. Schembecker, *Ind. Eng. Chem. Res.* **2023**, *62* (46), 19855–19861. DOI: 10.1021/acs.iecr.3c03173.

[8] I. Pazmiño-Mayorga, Q. Li, A. A. Kiss, *Curr. Opin. Chem. Eng.* **2025**, *47*, 101071. DOI: 10.1016/j.coche.2024.101071.

[9] M. Hilpert, J.-U. Repke, *Ind. Eng. Chem. Res.* **2021**, *60* (14), 5251–5263. DOI: 10.1021/acs.iecr.1c00440.

[10] J. R. Burns, C. Ramshaw, *Chem. Eng. Sci.* **1996**, *51* (8), 1347–1352. DOI: 10.1016/0009-2509(95)00367-3.

[11] K. Groß, A. Bieberle, K. Gladyszewski, M. Schubert, U. Hampel, M. Skiborowski, A. Górak, *Chem. Ing. Tech.* **2019**, *91* (7), 1032–1040. DOI: 10.1002/cite.201800085.

[12] W. Zhang, P. Xie, Y. Li, L. Teng, J. Zhu, *Chem. Eng. J.* **2022**, *427*, 130874. DOI: 10.1016/j.cej.2021.130874.

[13] F. Febrian, G. Brösigke, P. H. Kamm, J.-U. Repke, *Chem. Eng. Process. - Process Intensif.* **2025**, *216*, 110366. DOI: 10.1016/j.cep.2025.110366.

[14] F. Ghadyanlou, A. Azari, A. Vatani, *Sustainability*. **2021**, *13* (14), 8046. DOI: 10.3390/su13148046.

[15] J. R. Burns, J. N. Jamil, C. Ramshaw, *Chem. Eng. Sci.* **2000**, *55* (13), 2401–2415. DOI: 10.1016/S0009-2509(99)00520-5.

[16] Y. Yang, Y. Xiang, G. Chu, H. Zou, Y. Luo, M. Arowo, J.-F. Chen, *Chem. Eng. Sci.* **2015**, *138*, 244–255. DOI: 10.1016/j.ces.2015.07.044.

Enhancing Crude Vacuum Distillation Unit Performance and Availability Using AI Predictive Solution

Ahmad Bunaiyan
Saudi Aramco
R-1265, Floor 12, Al-Midra Tower
Dhahran 31311, Saudi Arabia
E-mail: Ahmad.bunaiyan@aramco.com

Anas H. Safar
Saudi Aramco
RW-1203, Floor 12, Al-Midra Tower
Dhahran 31311, Saudi Arabia
E-mail: Anas.safar@aramco.com

Jesus Montilla Rodriguez
Saudi Aramco
WC-1209, Floor 12, Al-Midra Tower
Dhahran 31311, Saudi Arabia
E-mail: Jesus.montillarodriguez@aramco.com

Omar Naeem
Saudi Aramco
R-4IRC, Floor 13, Al-Midra Tower
Dhahran 31311, Saudi Arabia
E-mail: Omar.naeem@aramco.com

Vasileios Tsachouridis
Saudi Aramco
WC-1206, Floor 12, Al-Midra Tower
Dhahran 31311, Saudi Arabia
E-mail: Vasileios.tsachouridis@aramco.com

Hissah M. Alkhaldi
Saudi Aramco
R-4IRC, Floor 13, Al-Midra Tower
Dhahran 31311, Saudi Arabia
E-mail: Hissah.alkhaldi@aramco.com

Fatima M. Alomair
Saudi Aramco
R-4IRC, Floor 13, Al-Midra Tower
Dhahran 31311, Saudi Arabia
E-mail: Fatimah.omair@aramco.com

Shahd O. Aljabarti
Saudi Aramco
R-1120, Floor 1, West-Adm. Building
RasTanura 31311, Saudi Arabia
E-mail: shahd.aljabarti@aramco.com

Abdulaziz M. Warthan
Saudi Aramco
WC-1203, Floor 12, Al-Midra Tower
Dhahran 31311, Saudi Arabia
E-mail: Abdulaziz.warthan@aramco.com

ABSTRACT

This paper presents the development and deployment of the AI and ML tools used in the Vacuum Distillation Unit (VDU) solution model, outlines the methodology behind anomaly detection and root cause analysis, and showcases real-world applications that highlight the transformative potential of predictive diagnostics in the refining industry. This model is designed to optimize VDU performance and availability, addressing real-world issues of premature fouling and monitoring rooms for improvement that can lead to partial or total shutdowns, resulting in significant economic losses. The initiative integrates troubleshooting, lessons-learned capture, and data correlation into a comprehensive diagnostic and forecasting framework, utilizing real-time process data and advanced machine learning (ML) tools. By incorporating an analytical model with a fault tree structure and interdependent parameters, the solution enables early anomaly detection and generates actionable insights, supporting data-driven decision-making and enabling proactive maintenance strategies. This approach helps to minimize downtime, reduce maintenance costs, and improve overall VDU efficiency. The solution was validated through actual case studies across multiple refineries. In one case, the system identified early signs of fouling in a condenser 24 hours before a significant vacuum pressure fluctuation occurred. This early warning allowed for timely maintenance intervention, preventing a potential 30% loss in distillate product over a seven-day period. In another case, the model successfully predicted the remaining useful life of wash oil packing by analyzing key performance indicators, enabling operators to schedule replacement within a six-month window and avoid unplanned downtime.

Keywords: CDU/VDU, Ejector, Vacuum column, Regression analysis, Artificial Intelligence, Wash oil packing.

• INTRODUCTION

Figure 1 shows a simplified diagram for a common refinery scheme. A Crude Distillation Unit (CDU) is a critical processing unit in petroleum refineries, responsible for separating crude oil into its various components or fractions based on their distinct boiling points. Through controlled distillation process, the crude oil is transformed into a range of valuable products, including:

- Naphtha, used as feedstocks for further refining to obtain Gasoline.
- Kerosene as a basic to produce jet fuel and also for industrial applications.
- Diesel and fuel oil, employed as fuels for transportation, heating, and power generation.
- Residual fuels, such as vacuum gas oil and residue, which can be further processed into lubricants, asphalt, and other petroleum products.

The atmospheric residue from CDU is subsequently processed in the Vacuum Distillation Unit (VDU), which further refines the heavy residuum. Operating under vacuum conditions, the VDU enables the separation of heavier fractions into lighter, more valuable products, such as Vacuum Gas Oil (VGO). The VGO is then further processed downstream allowing for an increase in valuable final products such as ultra-low sulfur diesel, as shown in **figure 1**.

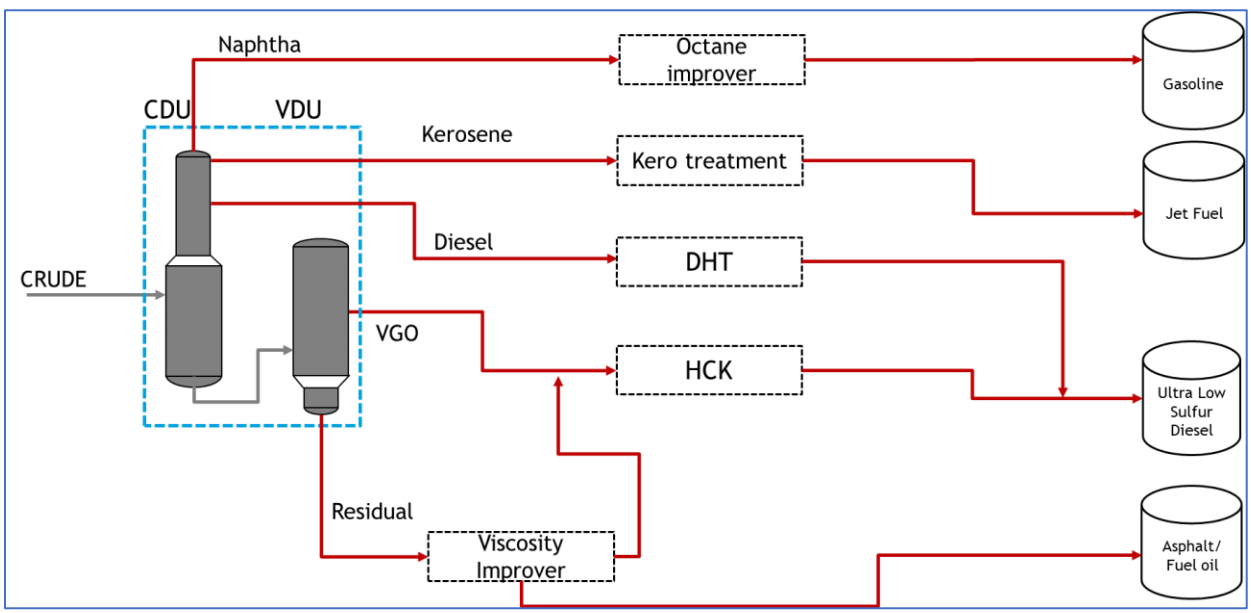

Figure 1. Typical Refinery scheme

VDU is an integral part of the refining process. However, the VDU is also prone to fouling buildup and coke formation, which can lead to reduced efficiency, increased energy consumption, and decreased product quality. One of the critical sections in the VDU is the wash bed which is a packed section, often located above the flash zone, designed to remove entrained liquid droplets from vapor to prevent coking. As such, effective control of the VDU is essential to ensure optimal performance, successfully plan for maintenance activities without minimize profitability. wash bed in VDU is a packed section, often located above the flash zone, designed to remove entrained liquid droplets from vapor to prevent coking

This requires careful monitoring of process conditions, regular maintenance scheduling, and proactive measures to prevent fouling and other issues that can impact unit reliability and efficiency. Figure 2 shows a typical configuration for VDU.

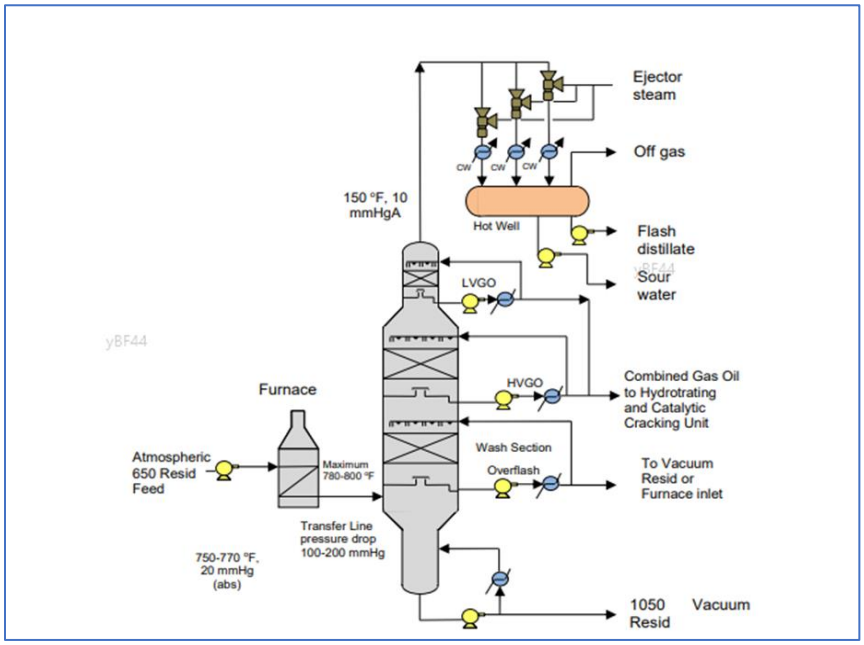

Figure 2. Typical Vacuum Distillation Column (VDU)

- **SOLUTION DESCRIPTION**

To address these challenges, a VDU Performance Predictive Solution has been developed, leveraging real-time process data and advanced machine learning (ML) tools. The solution integrates an analytical model that includes a fault tree structure with interdependent parameters, enabling early detection of anomalies and the generation of actionable insights

The enablers are Machine Learning, Data regression, Thermodynamic calculations and troubleshooting fault tree analysis. The regression capabilities provide the model with Statistical Control Process Features that enable the model to detect the cause of a variation.

Figure 3 shows a simplified troubleshooting fault tree analysis. It considers six events of malfunction, leading to accurate guidance for operational facilities.

Figure 4 shows how the fault tree works from the first event, the relevant message and how the model detect the deviation. It also shows how the model compute the variables storing the relevant difference in real time. For example, if VDU pressure condition is YES, model check if recycle control valve position is less than certain value, calculated based on regression. If TRUE, model print “proceed to check the discharge pressure condition”, ELSE: “Align as per P&ID/Enhance procedure”

The model was built based on real events that happened in refineries. It utilizes Process data such as VDU operating parameters, digital data access such as laboratory results, in addition to the Machine learning tool, 4 main pillars are envisaged:

- Ejector performance
- Yield optimization
- Ejectors Condensers Fouling buildup
- Wash oil bed coke performance.

This model allows operators to implement proactive maintenance strategies by detecting early signs of equipment degradation—such as fouling or packing wear—enabling timely interventions that prevent unplanned downtime. Beyond maintenance, the model also forecasts performance trends, including product yield shifts due to changing process conditions.

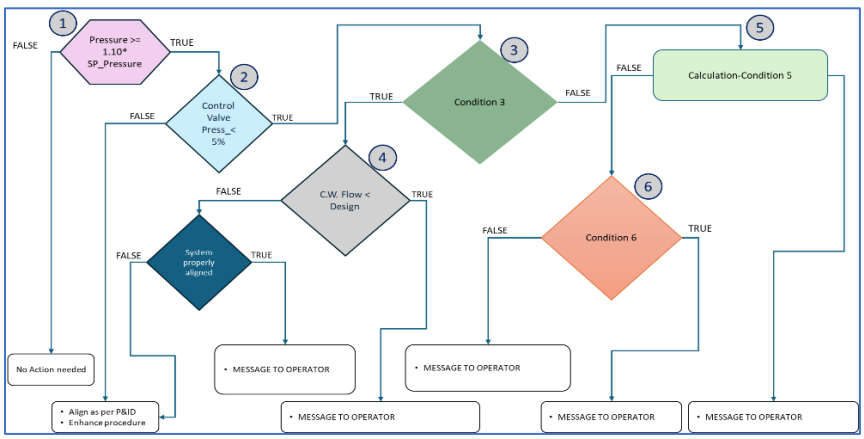

Figure 3. Troubleshooting fault tree analysis

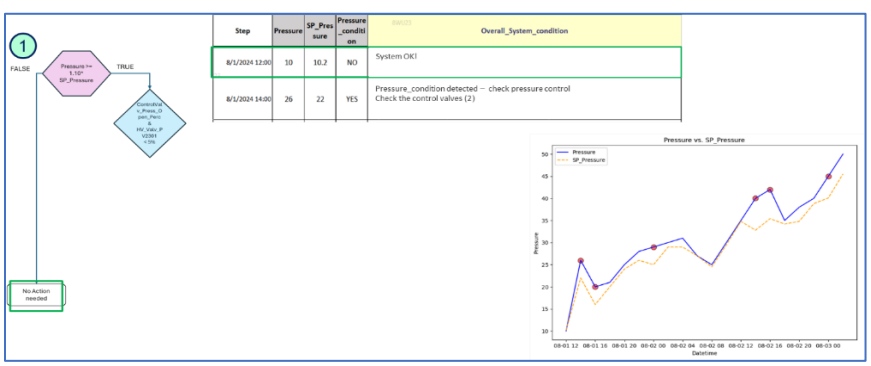

Figure 4. Model performance

The solution went through below development process:

- Development of logic diagram to find out the inter-dependency of vacuum pressure with other process variables (Medium-Pressure (MPS) Temperature, MPS Pressure, Discharge Pressure etc.)

- Generating interactive logic functions to capture all possible connections and interactions, as per process operations
- Programming the logic in AI/ML platform representing the logic functions (iteratively) including data wrangling
- Testing the logic with demo data (iteratively)
- Executing the logic program with real process data
- Developing the predictive model to predict Remaining Useful Life (RUL) of Wash Oil Bed.
- Creating end-user visualization for the messages

- **MODEL VALIDATION IN REAL CASES**

- **Ejector malfunction early detection**

  In one case, as shown in Figure 5, the system identified early signs of fouling in a condenser 24 hours before a significant vacuum pressure fluctuation occurred.

  Off-line data was introduced into the model to evaluate the response. Due to the predictive feature, it detected the fouling in the relevant exchanger 24 hours before the vacuum fluctuation, which represents a window to proactively proceed with the equipment backwash and potentially would have avoid the fluctuation in the Vacuum Column.

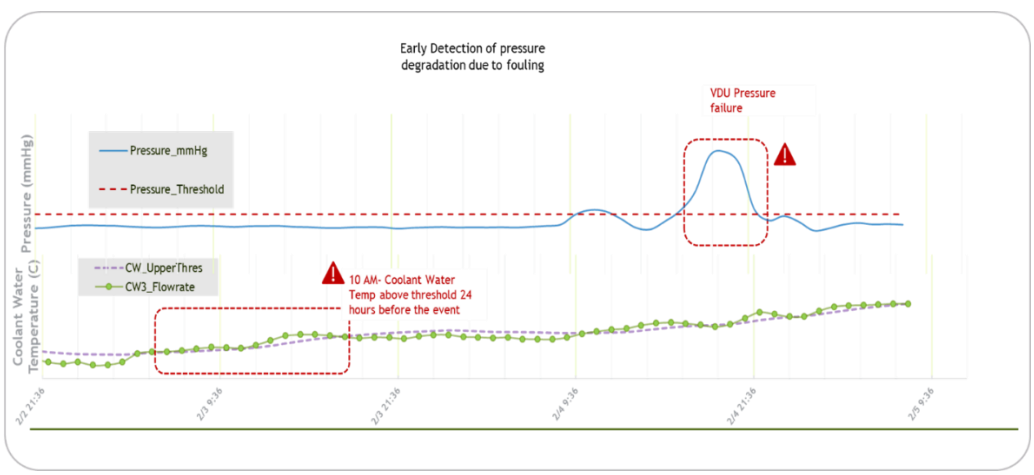

Figure 5. Ejector malfunction example

- **Wash oil operating life prediction**

  In another model assessment, the model successfully predicted the remaining useful life of wash oil packing by analyzing key performance indicators.

  Figure 6 shows that the carbon residue for VGO is forecast to reach its limit in 3 months, while the minimum yield target for the refinery is expected to be reached within 6 months**.** Therefore, the wash bed replacement must be conducted within 6 months.

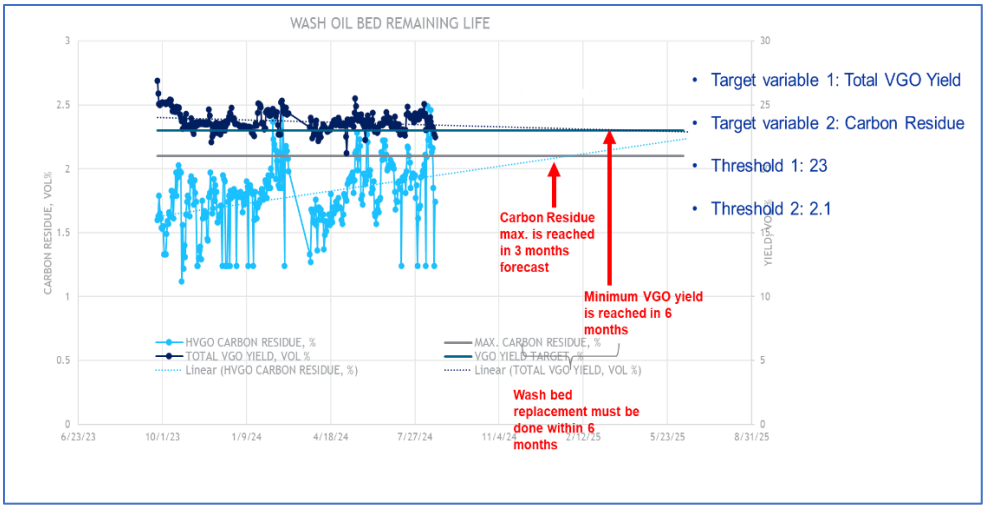

Figure 6. Wash oil packing operational life forecast

- **Visualization**

The model is visualized through a dashboard where the messages are shown for the operators, as shown in Figure 7

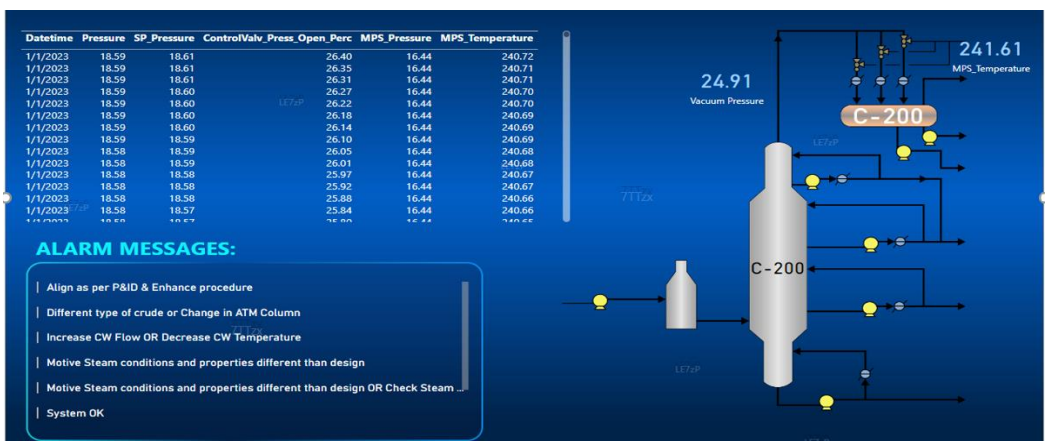

Figure 7. Model dashboard messages

The Onset of Turbulence: Computational Fluid Dynamics Insights into the Hydrodynamics of Structured Packings

Alice Miranda, Mathias Hack

Sulzer Chemtech AG, Winterthur, Switzerland

Abstract
Structured packings are widely used in distillation and absorption due to their high mass-transfer efficiency at low pressure drop, particularly under vacuum and low-pressure conditions. Their performance is governed by gas-phase hydrodynamics in cross-corrugated channels, where flow regime transitions strongly influence pressure drop and mixing. This work presents a computationally efficient CFD methodology to investigate hydraulic behavior and gas-phase mixing in structured packings. CFD predictions of friction factors are validated against classical experimental data, accurately reproducing Reynolds-dependent trends and critical regime transitions. Mixing behavior is further validated through comparison with tracer flow-path visualizations across laminar, transitional, and turbulent regimes. The results link corrugation angle, critical Reynolds number, and pressure-drop mechanisms, providing a physically consistent basis for evaluating wall effects, F-factor based operating conditions, and gas maldistribution in industrial packed columns.

Keywords
Structured Packing, Cross-corrugated channels, Flow regime transition, CFD

1. Introduction

The performance of structured packings in distillation and absorption columns is strongly influenced by the gas-phase flow regimes developing within cross-corrugated channels, which govern both hydraulic resistance and mixing efficiency. Although structured packings are known to provide high mass-transfer efficiency at comparatively low pressure drop (particularly under vacuum and low-pressure conditions) the underlying hydrodynamic mechanisms remain complex. Experimental and numerical studies have shown that cross-corrugated geometries promote early transition from laminar to unsteady flow at Reynolds numbers far lower than those typical of smooth conduits; however, the implications of these transitions for mixing, gas-phase distribution, and pressure-drop behavior in industrial structured packings remain insufficiently quantified. The present work addresses this gap by introducing a computationally efficient CFD methodology to investigate flow regimes, hydraulic behavior, and mixing phenomena in cross-corrugated structured packings representative of Sulzer's product portfolio.

2. Results and discussion

2.1 Flow Regime Characterization and Hydraulic Behavior

The hydraulic behavior of structured packings is governed by the flow regime in cross-corrugated channels, evolving from laminar to transitional and finally to turbulent flow with increasing Reynolds number. In the laminar regime, the flow is channel-confined, while increasing Reynolds numbers lead to a transitional regime marked by shear-layer instabilities and the onset of unsteady motion. Within this transitional regime, the flow exhibits intermittent behavior, characterized by alternating periods of quasi-ordered motion and localized chaotic events, before developing into a fully turbulent regime at higher Reynolds numbers, which enhances interchannel mixing at the expense of increased hydraulic resistance. Due to the complex cross-corrugated geometry, this transition occurs at Reynolds numbers significantly lower than those typical of smooth conduits, as demonstrated for idealized corrugated channels by Zhu et al. [1]. The resulting pressure drop is commonly quantified using a dimensionless friction factor, defined as the ratio of pressure drop across the packing to the geometry-scaled dynamic pressure. This formulation captures the combined effects of viscous dissipation, shear-layer interaction, and flow redirection imposed by the corrugation geometry, enabling identification of critical regime transitions and their impact on hydraulic behavior.

2.2 Computational Domain

The complex geometry of structured packings is defined by several key parameters that govern hydraulic behavior and mass transfer performance. The specific surface area, a, defines the available internal surface per unit volume and sets the characteristic flow scale; the hydraulic diameter (d_h), calculated as $d_h=4/a$, serves as the characteristic length for Reynolds number and friction factor correlations; and the corrugation angle, φ, defined as the inclination of the corrugated sheets, controls the degree of flow redirection.

Resolving the full three-dimensional topology of structured packings at high spatial resolution is computationally prohibitive due to the large number of repeating corrugation units; consequently, periodic unit-cell approaches have been widely adopted in the literature to reduce computational cost (e.g. Hill et al.[2]). In the present work, a periodic unit-stick geometry is employed, in which a single corrugation stick spanning the full streamwise length of a packing element is meshed and simulated. This configuration preserves all essential geometric features while explicitly capturing axial flow development and interchannel interaction over the full element height, which are not resolved in conventional compact unit-cell models. The computational domain used in this work is shown in Figure 1. By applying periodic boundary conditions in the spanwise and wall-normal directions, the simulated flow corresponds to that of an infinitely extended packing without wall effects, enabling accurate characterization at a fraction of the computational cost of a full-scale model.

A mesh-independence study confirmed numerical convergence, with the relative deviation in predicted pressure drop decreasing monotonically under grid refinement to 0.8%. The final mesh comprised approximately 22 million nodes (Figure 1), providing adequate resolution at feasible computational cost. The simulations were performed using the commercial CFD solver Ansys CFX. Preliminary studies were conducted to assess the influence of different turbulence models and the choice

between transient and steady-state solution strategies. Although transient simulations were explored to evaluate potential unsteady effects, the flow behavior within the investigated Reynolds number range was found to be adequately represented using a steady RANS formulation, aided by the pseudo-transient solution approach implemented in CFX.

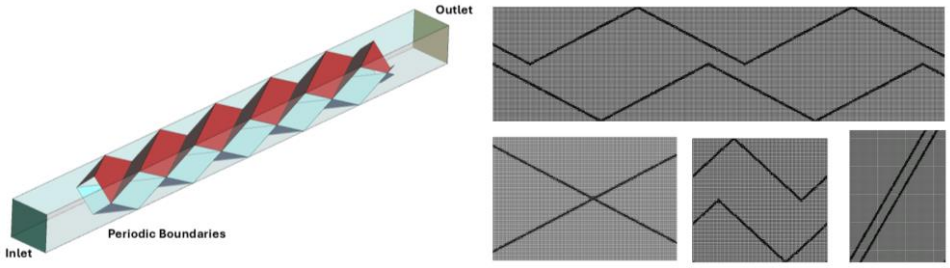

Figure 1: *Geometry of the periodic unit-cell used in the simulations (left) and mesh details in different cross-sections (right).*

The k-ω SST turbulence model was selected as it provided the best balance between numerical robustness, accuracy in near-wall shear and separation prediction, and computational efficiency for the objectives of the present study. This modelling choice was found to be sufficient for resolving the dominant hydraulic features relevant to the regime-transition and mixing analyses carried out in this work.

2.3 Hydraulic Validation

Zogg's experimental work [3] provides a detailed experimental characterization of the hydraulic and concentration mixing behavior of cross-corrugated structured packings, relating the friction factor (c_f) to gas-phase Reynolds number (Re_g) for multiple corrugation angles and column-to-packing diameter ratios (B/dh). The reference curves in Figure 2 highlight the strong Reynolds number dependence of hydraulic resistance in the laminar and transitional regimes, as well as the influence of wall confinement, which becomes increasingly pronounced for smaller B/dh values.

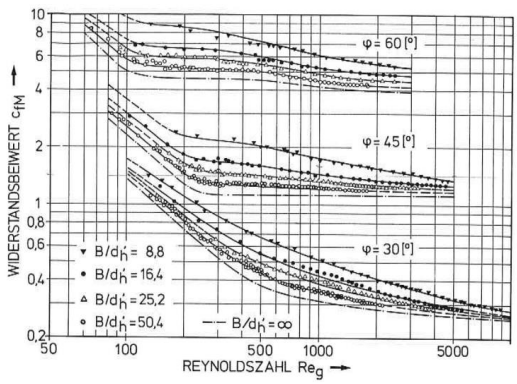

Figure 2: *Zogg's reference c_f-Re_g correlations for various corrugation angles and B/dh ratios [3], used as experimental benchmark for CFD validation.*

Figure 3 compares the CFD-predicted friction factors for the X-type Sulzer packing with Zogg's experimental data for a corrugation angle $\varphi=30°$. Since the CFD simulations are performed on a periodic domain representing an infinitely wide column without wall interaction, the comparison is restricted to Zogg's largest B/dh

and infinite-diameter reference curves. The CFD results accurately reproduce the experimentally observed trend over the full range of Reynolds numbers: a strong decrease in friction factor with increasing Re_g in the laminar regime, followed by a gradual reduction in sensitivity as the flow approaches turbulent conditions. In the transitional regime, where friction factor variations are most pronounced, the agreement between CFD predictions and experiments is particularly strong, confirming that the numerical model accurately captures the onset and development of regime transitions. Overall, the results demonstrate that the CFD methodology reliably predicts Reynolds-dependent hydraulic behavior and provides a solid foundation for subsequent analysis of mixing and flow-structure evolution.

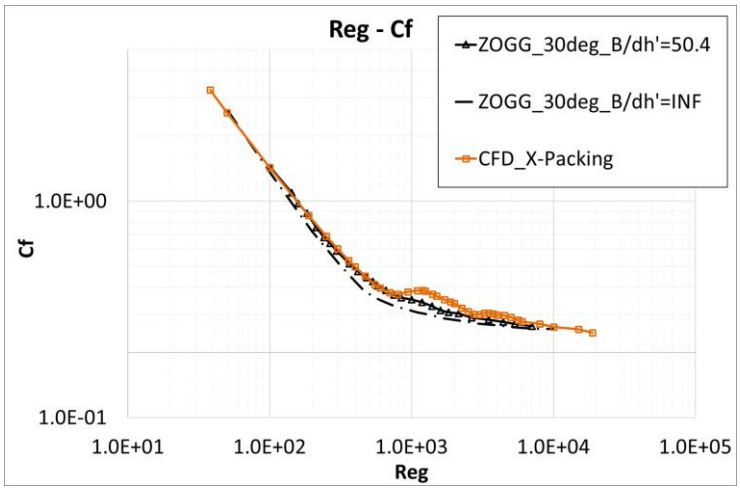

Figure 3: *Comparison of CFD-predicted friction factor (c_f) with Zogg's experimental data for structured packings with a 30° corrugation angle. The CFD results for the X-packing are plotted against Zogg's reference curves for B/dh=50.4 and the infinite-diameter limit.*

2.3 CFD Validation of Mixing Performance

Following hydraulic validation, the CFD model's ability to capture gas-phase mixing was assessed through comparison with Zogg's tracer flow-path visualizations [3]. Equivalent flow conditions were simulated numerically and compared with these flow patterns. Since the CFD simulations were performed on a periodic unit stick, a flow-trajectory reconstruction method was applied to map the local streamlines onto successive periodic replicas of the domain, generating extended tracers distributions comparable to those reported by Zogg. The method was numerically validated against large-scale high-resolution simulations with concentration transport, confirming that the periodic replication accurately reproduces the global flow topology.

Figure 4 compares Zogg's tracer flow-path visualizations with the corresponding CFD results for four representative Reynolds numbers. The experimental images in the top row show the progressive evolution of flow paths, from the unique patterns at Re_g=50, to the predominantly channel-aligned trajectories at laminar Reynolds numbers and to increasingly intersecting and laterally displaced streams as inertial effects intensify. The CFD streamline density plots and flow-path visualizations in the lower rows reproduce these key features with excellent qualitative agreement. Both experiments and CFD show laminar but weakly redirected flow at very low Reynolds numbers, followed by increasingly channel-confined motion in the laminar regime. In the transitional and turbulent regimes, strong interchannel exchange and lateral

spreading develop, which are consistently captured by the reconstructed CFD streamlines. This agreement confirms that the CFD model accurately predicts not only the hydraulic resistance, but also the Reynolds-dependent mixing mechanisms that govern flow redistribution inside the packing structure.

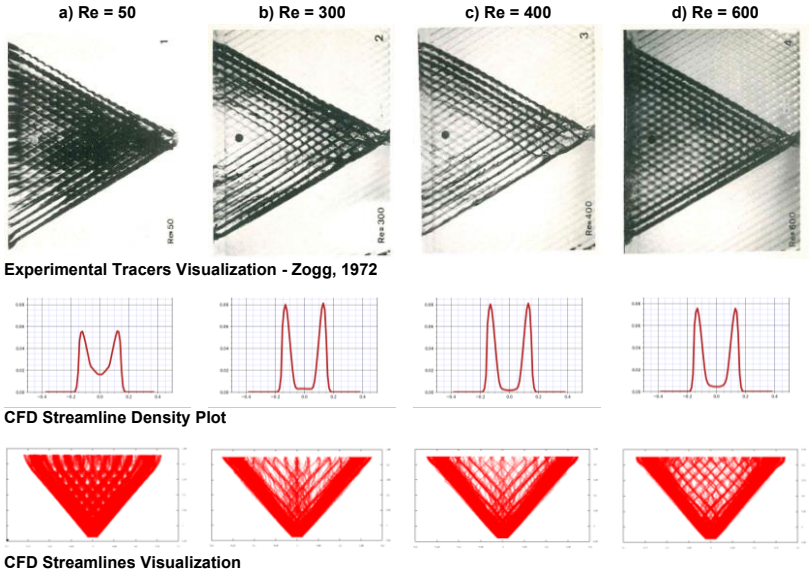

Figure 4*: Comparison of experimental smoke visualization by Zogg (top row) and CFD predictions (middle and bottom rows) for different Reynolds numbers: (a) Re = 50, (b) Re = 300, (c) Re = 400, and (d) Re = 600. CFD results include streamline density plots (middle row) and CFD streamlines visualizations (bottom row).*

2.4 Flow Regime Characterization and Critical Reynolds Numbers

A systematic characterization of flow regimes was performed by extending the CFD analysis to structured packings with different corrugation angles. Figure 5 presents the resulting c_f -Re_g curves for X-type, higher and lower-angle packings. The results demonstrate that the corrugation angle strongly influences both the magnitude of hydraulic resistance and the location of the laminar-turbulent regime boundaries. Higher-angle packings exhibit increased friction factors and an earlier departure from laminar behavior, while lower-angle geometries show delayed transition and reduced resistance over a wide Reynolds number range.

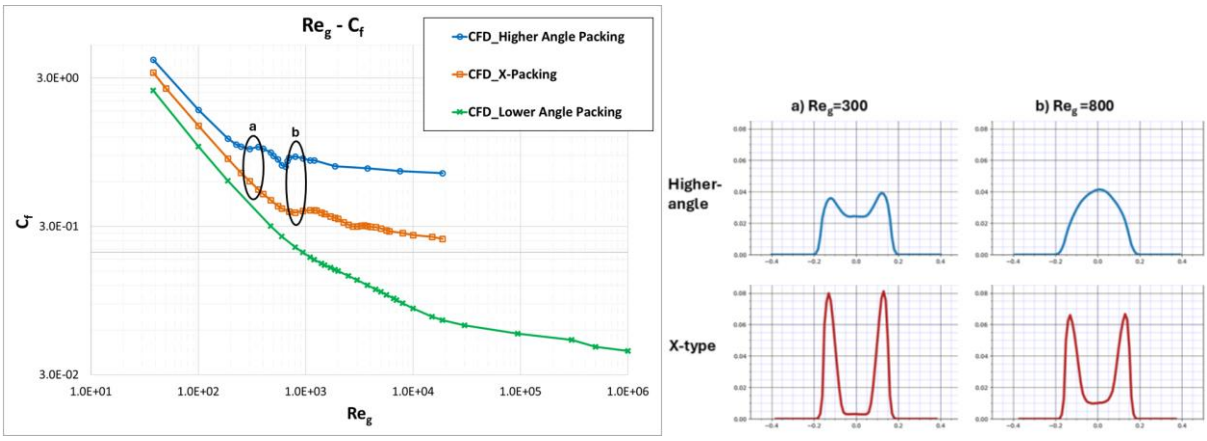

Figure 5 *Friction factor (c_f) as a function of gas-phase Reynolds number (Re_g) for structured packings with different corrugation angles, with velocity-density distributions for X-type and higher-angle packings at different Re_g.*

The streamline density distributions further reveal that for identical Reynolds numbers the flow regime and mixing behavior can differ markedly between packings. At Re_g=300, the X-type packing behavior is still fully laminar, with channel-confined flow, whereas the higher-angle packing has already entered a transitional regime with pronounced shear-layer activity. At Re_g=800, the higher-angle packing displays fully turbulent characteristics, with strong interchannel exchange, while the X-type geometry remains laminar to only weakly transitional. These observations highlight that comparable hydraulic operating points do not imply comparable mixing performance, which remains strongly governed by corrugation geometry.

3. Conclusions

A validated and computationally efficient CFD framework has been developed to investigate flow regimes, hydraulic behavior, and mixing in cross-corrugated structured packings. The approach accurately reproduces Reynolds-dependent friction-factor trends reported by Zogg [3] and captures the early onset of flow instabilities identified by Zhu et al. [1]. Qualitative agreement with tracer flow-path visualizations further confirms the capability of the model to predict interchannel mixing across laminar, transitional, and turbulent regimes. By extending the analysis to packings with different corrugation angles, the study demonstrates that critical Reynolds numbers and dominant pressure-drop mechanisms are strongly geometry-dependent, with higher-angle packings exhibiting earlier, shear-dominated transitions. These findings provide a physically consistent basis for interpreting F-factor based operating conditions under different fluid systems, in line with design considerations highlighted by Duss [4]. Overall, the results bridge the gap between fundamental flow-regime characterization and performance-relevant phenomena in industrial structured packings, enabling improved prediction of pressure drop, mixing, and gas-phase distribution and supporting future scale-up and wall-effect modeling efforts [5].

References

[1] Zhu, X., Walther, J. H., Zhao, D., & Haglind, F. (2019). **Transition to chaos in a cross-corrugated channel at low Reynolds numbers**. Physics of Fluids, 31(11), 114107. https://doi.org/10.1063/1.5122305

[2] Hill, S., Acher, T., Hoffmann, R., Ferstl, J., Rarrek, A., & Klein, H. (2016). **CFD simulation of the hydrodynamics in structured packings**. *Proceedings of the 9th International Conference on Multiphase Flow (ICMF 2016)*, Florence, Italy.

[3] Zogg, M. (1972). **Strömungs- und Stoffaustauschuntersuchungen an der Sulzer-Gewebepackung** (Doctoral dissertation, Eidgenössische Technische Hochschule Zürich). Verlag Hans Schellenberg, Winterthur.

[4] Duss, M. (2013). **Packing pressure drop prediction at low operating pressure: Is there anything new?** *AIChE Spring Meeting and Global Congress on Process Safety*, Distillation Topical Conference, San Antonio, Texas, USA.

[5] Charitatos, V., Fernandez, M., Miranda, A., Linder, T., Hack, M. (2026). **A data-informed mechanistic framework for predicting gas maldistribution in structured packed beds.** *in DECHEMA 13th International Conference on Distillation & Absorption, Salzburg, 2026*

Smooth modeling of thermosiphon reboilers with experimental validation to enable their use at low temperature differences

Christian Hoffmann[1], Katharina Jasch[2], Yuan Zhu[1], Stephan Scholl[2], Jens-Uwe Repke[1]
[1]Technische Universität Berlin, Berlin, Germany;
[2]Technische Universität Braunschweig, Braunschweig, Germany

Abstract
Thermosiphon reboilers (TSRs) are widely used in distillation and desorption columns due to their simple, pumpless design and low investment and operating costs. While typically operated at large driving temperature differences, operation at lower temperature differences would improve resource efficiency and enable the use of low-temperature heat sources. However, such conditions promote hydrodynamic instabilities, including Ledinegg and density-wave instabilities, which may cause vibrations, pressure fluctuations, and long-term mechanical or control issues.
Describing these phenomena requires dynamic models, yet conventional TSR models rely on sequential calculations of phase equilibrium, pressure drop, and heat transfer because the phase-change location is not known a priori. This approach is inefficient and numerically unsuitable for dynamic simulations. To address this limitation, a smoothly reformulated TSR model is proposed. The model combines mass, energy, and momentum balances with algebraic relations for thermodynamics, fluid dynamics, and heat transfer, while phase-change behavior is regularized using relaxed max operators. The TSR is modeled as a pressure-driven system. The current formulation is limited to steady-state, single-component, homogeneous two-phase flow. Validation against steady-state experimental data for water shows good agreement, with deviations mainly at high heat fluxes.

Keywords
Two-phase flow, Pressure-driven modeling, Evaporation, Energy efficiency, Steady-state simulation

1. Introduction

Evaporation, rectification, and desorption are key unit operations in process industries, with thermosiphon reboilers (TSRs) commonly used for heat input in distillation columns due to their pump-free design and low costs [1]. Although traditionally operated at large driving temperature differences, TSRs are now being explored for low-temperature, low-pressure operation to improve energy efficiency and support heat integration in open heat pumps. However, such operating conditions reduce heat flux and increase the risk of instabilities (e.g., oscillations, pressure surges), which can compromise safety and control [2]. To overcome these challenges, model-based analysis and control are essential. Unfortunately, the numerical solution of process models for TSRs with and without forced circulation is challenging as the location of the phase change is usually unknown. Hence, bubble point, pressure drop, and heat

transfer calculations are solved sequentially until a solution has been found [3]. While this may be suitable for steady-state systems, the effort of using a sequential approach is unreasonably high for a dynamic modeling approach, which is necessary to describe the dynamic instabilities in TSRs. This contribution proposes a smooth reformulation of a TSR model for steady-state conditions that 1) allows the simultaneous solution and b) can be extended to dynamic modeling in the future. The results obtained with the proposed model are compared to experimental data for a TSR.

2. Modeling approach

2.1 Fundamental equations

The proposed model assumes evaporation of a single component and homogeneous flow, i.e., liquid and vapor phase are not modeled separately, and all fluid properties are calculated by weighting liquid and vapor properties using volume or mass fraction. The fundamental equations are mass balance, energy balance, and momentum balance:

$$0 = -\frac{\partial(\rho_\mathrm{m} u_\mathrm{m})}{\partial z}\ , \tag{1}$$

$$0 = -\frac{\partial(\rho_\mathrm{m} u_\mathrm{m} h_\mathrm{m})}{\partial z} + \frac{4}{d}\dot{q}\ , \tag{2}$$

$$0 = -\frac{\partial(\rho_\mathrm{m} u_\mathrm{m}^2)}{\partial z} - \frac{\partial P}{\partial z} - F_\mathrm{hyd} - F_\mathrm{fric}\ . \tag{3}$$

Therein, ρ_m, u_m, and h_m are the mixture's density,velocity, and enthalpy, respectively, d is the tube's diameter, $\dot{q}$ is the heat flux, P is pressure, and F represents both hydrostatic and friction momentum fluxes. The latter two are further described in Section 2.2. Mixture enthalpy and temperature are correlated by

$$h_\mathrm{m} = \Delta_f h + c_\mathrm{p}^L\left(\left((1-\mathrm{act})T + \mathrm{act}\cdot T^{LV}\right) - T_\mathrm{ref}\right) + X_\mathrm{m}^\mathrm{min}\Delta_{LV}h + \mathrm{act}\ \cdot c_\mathrm{p}^V(T - T^{LV}) \tag{4}$$

in which $\Delta_f h$ is the heat of formation, c_p^L and c_p^V are liquid and vapor heat capacities, and T, T^LV, and T_ref are temperature, boiling point, and reference temperature, respectively. In addition, X_m is the mass-specific vapor fraction and $\Delta_{LV}h$ is the heat of vaporization. Finally, act is an activation function that will be discussed in Section 2.4. The vapor fraction depends on the mixture's enthalpy and the enthalpies of both boiling liquid h_boil^L and saturated vapor $h_\mathrm{sat}^\mathrm{V}$:

$$X_\mathrm{m} = \frac{h_\mathrm{m} - h_\mathrm{boil}^L}{h_\mathrm{sat}^\mathrm{V} - h_\mathrm{boil}^L}\ . \tag{5}$$

The enthalpies at saturation conditions are calculated as

$$h_\mathrm{boil}^L = \Delta_f h + c_\mathrm{p}^L(T^{LV} - T_\mathrm{ref}) \tag{6}$$

and

$$h_\mathrm{sat}^V = \Delta_f h + c_\mathrm{p}^L(T^{LV} - T_\mathrm{ref}) + \Delta_{LV}h. \tag{7}$$

This way, X_m is always calculated even if it is not necessarily between zero and one.

2.2 Pressure drop in reboiler

The hydrostatic force in the momentum balance is given by the product of mean density and gravitational acceleration. The friction force is calculated according to the model by Friedel [4]:

$$F_{\mathrm{fric}} = \xi_{LO} \frac{\rho_m}{2} u_m^2 \frac{1}{d} \Phi^2 \,, \tag{8}$$

with a liquid-only friction factor ξ_{LO} and the two-phase correction Φ^2, which is a function of vapor fraction, the ratios of single-phase friction factors, the ratios of density and dynamic viscosity of both phases as well as Froude and Weber number. The friction factors are calculated depending on the flow regime and are switched as described in Section 2.4.

2.3 Heat transfer

The heat transfer of the single-phase flow is described using Nusselt correlations for laminar flow [5] and turbulent flow [6,7] under the assumption that the whole flow is either pure liquid or pure vapor. The multi-phase heat transfer coefficient is taken from [8]. Here, the ratio of multi-phase and liquid heat transfer coefficient is expressed as a function of vapor fraction, density ratios, and the ratio of the single-phase heat transfer coefficients. References for all properties and correlations of the model are given in Table 1.

2.4 Smooth reformulations

As the vapor fraction can take any value according to its definition in Eq. (5), numerical reformulations are necessary to turn this problem into an equation system that can be solved without any external or sequential iterative loops. Following concepts introduced in [9] for distillation columns, we employ smooth combinations of max and min operators as well as sigmoidal functions. To keep the vapor fraction between zero and one, a max operator is applied first to ensure that X_{m} can only be positive:

$$X_{\mathrm{m}}^{\max} = \max(X_{\mathrm{m}}; 0) \approx \frac{X_{\mathrm{m}} + \sqrt{X_{\mathrm{m}}^2 + \varepsilon_1}}{2} \tag{9}$$

in which $\boldsymbol{\varepsilon_1}$ is a small positive constant whose value depends on the application. For the max and min operators related to the vapor fraction, it is set to 10^{-8} to strictly mimic a true max operator. To On this variable, a shifted min operator is applied:

$$X_{\mathrm{m}}^{\min} = \min(X_{\mathrm{m}}^{\max}; 1) \approx 1 + \frac{X_{\mathrm{m}}^{\max} - 1 + \sqrt{(X_{\mathrm{m}}^{\max} - 1)^2 + \varepsilon_1}}{2}. \tag{10}$$

This function keeps the vapor fraction within the physical bounds (see Figure 1) and is, for example, used for calculating enthalpy in Eq. (4). In addition, sigmoidal functions γ determine how to calculate the temperature integral with the heat capacity or how to switch between equations for laminar and turbulent flow regimes, i.e.,

Table 1: *Used correlations and sub-models within this contribution.*

Symbol	Description	Reference
ρ^V	Vapor density, assumption of ideal gas due to low pressure	-
Various	Single-phase properties (liquid density, vapor/liquid viscosity, vapor pressure, enthalpy of vaporization, vapor/liquid heat capacity, vapor/liquid thermal conductivity, liquid surface tension	[10]
ρ_{m}	Density of mixture, pure phase properties weighted with vapor fraction	[11]
η_{m}	Viscosity of mixture, expression for annular flow in referene	[12]
F_{fric}	Two-phase pressure drop	[4]
ξ	Friction factor in two-phase pressure drop	[13]
$\mathrm{Nu}_{\mathrm{lam}}$	Laminar heat transfer	[5]
$\mathrm{Nu}_{\mathrm{turb}}$	Turbulent heat transfer	[6,7]

$$\mathrm{Nu} = (1-\gamma)\mathrm{Nu}^{\mathrm{laminar}} + \gamma \mathrm{Nu}^{\mathrm{turb}}, \quad \text{with } \gamma = \frac{\mathrm{Re} - \mathrm{Re}^* + \sqrt{(\mathrm{Re} - \mathrm{Re}^*)^2 + \varepsilon_2}}{2\sqrt{(\mathrm{Re} - \mathrm{Re}^*)^2 + \varepsilon_2}}. \tag{11}$$

Here, Re* represents the Reynolds number at which the correlation switches and $\boldsymbol{\varepsilon_2}$ is also a small constant that can, however, take larger values as a change of the flow regime is in most cases not abrupt. This is beneficial from a numerical perspective as it does not create steep gradients at these switching points.

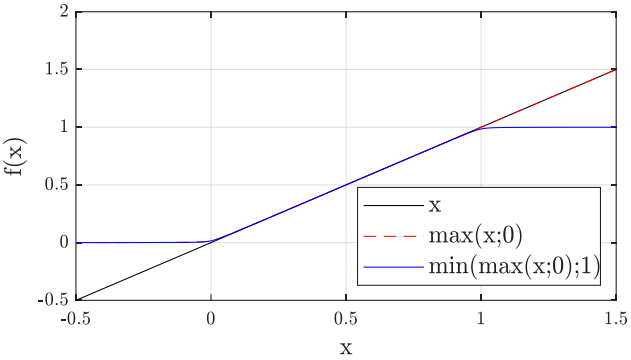

Figure 1: Visualization of smoothened vapor fraction for $\varepsilon_2 = 10^{-3}$.

2.4 Experimental setup and pressure-driven modeling

The experiments the model is compared to were performed in a test rig at TU Braunschweig (Figure 2). The plant consists of the reboiler itself and a separator dividing the generated steam and the liquid. During the experiments, a constant liquid level of 110 % of the reboiler length was maintained in the separator to keep the hydrostatic pressure constant. Then, pressures between 100 and 400 mbar and temperature differences between heating and process side were set. For more details on the experimental procedure, the reader is referred to [3]. Besides the equations for the reboiler itself, the additional pressure drops were considered, such as the Coriolis sensor F1, elbows, inlets and outlets, as well as pressure drop for the feed into the separator. The only fixed variables concerning operating conditions for every simulation were the static pressure in the separator and the inlet temperature for the reboiler. Every flow is calculated from the governing expressions for the pressure drop, which is typically named pressure-driven modeling. Here, flows no longer need to be set by external loops, but result from solving the respective model equations simultaneously.

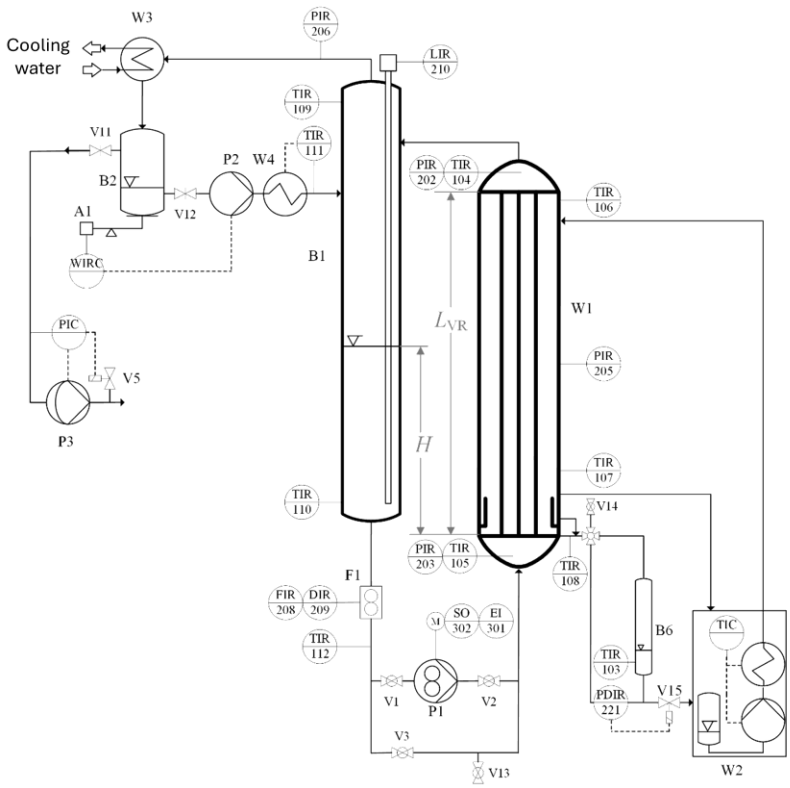

Figure 2: Flowsheet of the reboiler test rig.

2.5 Model implementation and solution

The model is implemented in MOSAICmodeling [14] using orthogonal

collocation on finite elements as discretization scheme. Within this study, 5 finite elements with a respective length of 0.3 m were used. With more finite elements, the solution did not further change. For the solution, the model was exported to and solved in Matlab using the solver fsolve (trust-region-dogleg algorithm).

3. Results and discussion

The following sections provide an analysis of the obtained results and critically assess the current state of the proposed modeling approach.

3.1 Evaluation of model performance

Figure 3 contains the results for inlet velocity of the reboiler, its total heat flux, inlet pressure, and pressure drop over the reboiler's length. While pressure and pressure drop are described with excellent accuracy (less than 10 % deviation), the inlet velocity the heat flux currently do not match for all operating points. On closer inspection of the data points, it is assumed that the presented model can describe multiple steady states – a naturally occurring phenomenon in TSR [3]. For example, the simulation at 300 mbar shows a significantly higher inlet velocity at an inlet temperature difference of 6 K than the experiment. However, at 7 K temperature difference, simulation and experiment yield the same velocity and an almost equal heat flux.

In our case, however, a nonlinear equation system is solved simultaneously without external iterative loops in which the user can reject too high velocities. Instead, the solution only depends on the initial guesses of the variables, the structure of the underlying equations, and the numerical solver. This might result in solutions that live on other branches of the solution space. As both inlet velocity and heat duty match the experimental data occasionally but not at the same time, it is assumed that one of these quantities is also currently overestimated or underestimated, respectively.

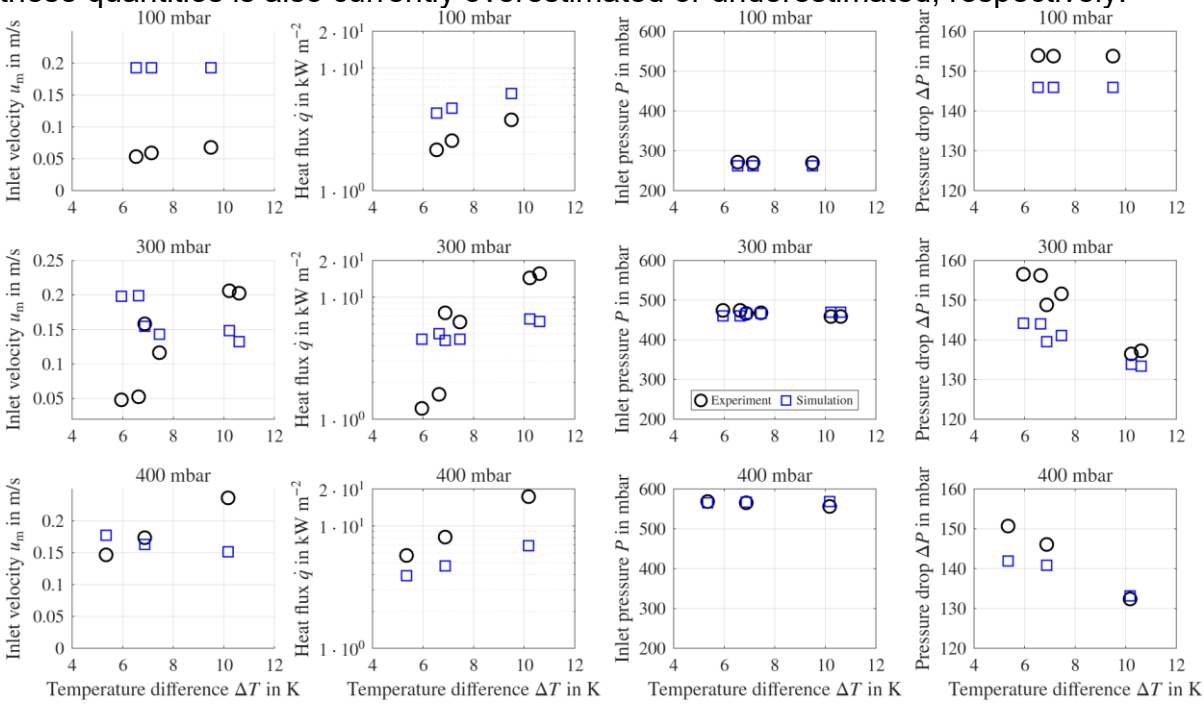

Figure 3: Simulated and measured inlet velocity, heat flux, reboiler inlet pressure, and reboiler pressure drop at relative liquid holdup of 110 % for pressures between 100 and 400 mbar under variation of the temperature difference between heating and process side.

3.2 Limitations of the modeling approach

As the solution currently seems to depend significantly on the solver settings / solution strategies as well as the provided initial guesses, the numerical solution approach should be extended, potentially by model adaptation. For example, Kamath et al. [15]

already proposed a strategy to find the relevant root in equations of state by taking into account derivative information. Their solution strategy could be a viable option as both problems are fairly similar. A reliable identification of the correct root will be highly relevant when studying stability aspects of the TSR, such as Ledinegg instability, which is a steady-state instability.

4. Conclusions and outlook

This contribution presented a smoothly reformulated model for a thermosiphon reboiler for one component at steady-state conditions. The smooth reformulation serves as intermediate step towards a dynamic model for multicomponent evaporation at small temperature differences and operating pressures. The model was compared to experimental data and showed excellent agreement at small fluid velocities. With increasing inlet velocity, deviations between model and experiment were more pronounced, possibly due to an insufficient description of the flow regime. In the future, the model formulation 1) must be adapted to improve the identification of specific solutions of interest, 2) used to study steady-state instabilities, such as Ledinegg instability, and 3) should be extended to dynamic, multi-component systems.

References

[1] A. V. Lavrikov, J. Hammerschmidt, Y. A. Kuzma-Kichta, S. Scholl (2015): Thermosiphon reboilers with enhanced tubes. Chemie Ingenieur Technik 87, 290–296. DOI: 10.1002/cite.201400056.

[2] G. V. Durga Prasad, M. Pandey, M. S. Kalra (2007): Review of research on flow instabilities in natural circulation boiling systems. Progress in Nuclear Energy 49, 429–451. DOI: 10.1016/j.pnucene.2007.06.002.

[3] Y. Lu, K. Jasch, S. Scholl (2022): Simulation of thermosiphon reboilers using wire matrix inserts at lower operating range, Heat Transfer Engineering 44, 246–258, DOI: 10.1080/01457632.2022.2049542.

[4] L. Friedel (1979): Improved friction pressure drop correlations for horizontal and vertical two-phase flow. 3R International 18, 485 – 492.

[5] V. Gnielinski (1989): Zur Wärmeübertragung bei laminarer Rohrströmung und konstanter Wandtemperatur. Chemie Ingenieur Technik 61, 160–161. DOI: 10.1002/cite.330610216

[6] V. Gnielinski (2013): On heat transfer in tubes. International Journal of Heat and Mass Transfer 63, 134–140. DOI: 10.1016/j.ijheatmasstransfer.2013.04.015

[7] V. Gnielinski (2015): Corrigendum to „On heat transfer in tubes“. International Journal of Heat and Mass Transfer 81, 638. DOI: 10.1016/j.ijheatmasstransfer.2014.10.063

[8] M. Kind, Y. Saito (2019): H3.5 Strömungssieden gesättigter, reiner Flüssigkeiten. In: Stephan, P., Kabelac, S., Kind, M., Mewes, D., Schaber, K., Wetzel, T. (eds) VDI-Wärmeatlas. Springer Vieweg, Berlin, Heidelberg. DOI: 10.1007/978-3-662-52989-8_58.

[9] C. Hoffmann, J. Weigert, E. Esche, J.-U. Repke (2020): A pressure-driven, dynamic model for distillation columns with smooth reformulations for flexible operation. Computers & Chemical Engineering 142, 107062. DOI: 10.1016/j.compchemeng.2020.107062.

[10] M. Kleiber, R. Joh (2019). D1 Berechnungsmethoden für thermophysikalische Stoffeigenschaften. In: Stephan, P., Kabelac, S., Kind, M., Mewes, D., Schaber, K., Wetzel, T. (eds) VDI-Wärmeatlas. Springer Vieweg, Berlin, Heidelberg. DOI: 10.1007/978-3-662-52989-8_11.

[11] M. Kraume (2020): Transportvorgänge in der Verfahrenstechnik. Springer Vieweg Berlin, Heidelberg. DOI: 10.1007/978-3-662-60012-2.

[12] D. Beattie, P. Whalley (1982): A simple two-phase frictional pressure drop calculation method. International Journal of Multiphase Flow 8, 83–87. DOI: 10.1016/0301- 9322(82)90009-X.

[13] R. Techo, R. R. Tickner, R. E. James (1965): An accurate equation for the computation of the friction factor for smooth pipes from the Reynolds number. Journal of Applied Mechanics 32, 443. DOI: 10.1115/1.3625826.

[14] V. A. Merchan-Restrepo, E. Esche, S. Fillinger, G. Tolksdorf, G. Wozny (2016): Computer-Aided Process and Plant Development. A Review of Common Software Tools and Methods and Comparison against an Integrated Collaborative Approach. Chemie Ingenieur Technik 88, 50–69. DOI: 10.1002/cite.201500099.

[15] R. S. Kamath, L. T. Biegler, I. E. Grossmann (2010): An equation-oriented approach for handling thermodynamics based on cubic equation of state in process optimization. Computers & Chemical Engineering 34, 2085–2096. DOI: 10.1016/j.compchemeng.2010.07.028.

New and Tighter Recovery Relation in Distillation

Tony Joseph Mathew[1,2], Mohit Tawarmalani[2,3], Rakesh Agrawal[2]
[1]Centre for Optimisation and Decision Science, Curtin University, Perth, Australia;
[2]Davidson School of Chemical Engineering, Purdue University, West Lafayette, United States
[3]Mitch Daniels School of Business, Purdue University, West Lafayette, United States;

Abstract

One of the fundamental reasons why distillation can be reliably used to perform zeotropic separations is that the recoveries of components from a mixture are well-ordered: a lighter component is consistently recovered in the distillate product to a greater extent than a heavier component. This qualitative behavior implies a simple mathematical ordering among component recoveries. However, detailed simulations reveal to us that the space of feasible separations is overestimated by this simple ordering and actually falls in a crescent shape. In this paper, we present a new relation governing component recoveries that is tighter than this simple ordering and requires only two additional parameters: the relative volatility between the compared components and the number of stages in the column. We present a semi-rigorous derivation and validate the relation with simulations from Aspen Plus. This new relation can be used to screen out infeasible separations, as well as improve the computational performance of optimization formulations.

Keywords

Multicomponent distillation, recovery, simplified model, fitted relative volatilities

1. Introduction

It is well-known in distillation that, for zeotropic separations, a lighter component is consistently recovered in the distillate product to a greater extent than a heavier component. Mathematically, this well-ordering principle can be expressed as the following,

$$r_1 \geq r_2 \ \dots \ \geq r_n \tag{1}$$

where r_i is the recovery of the component i from the feed stream into the distillate product, and components have been indexed in strictly descending order of relative volatilities, α_i. That is, $\alpha_1 > \alpha_2 \dots > \alpha_n$ for an $n-$component feed mixture. This ordering is well-observed in both practice and in the results of distillation simulations. Based on this relation, when considering two components $i < j$, their recoveries can be bounded as follows,

$$0 \leq r_j \leq r_i \ \leq 1, \qquad i < j \tag{2}$$

where 0 and 1 are the default numerical bounds on recovery based on mass balance. In this paper, we show that the above relation is loose, by which we mean it describes a substantially larger space of potentially feasible recovery values than are actually feasible. Moreover, we derive a tighter relation and demonstrate that our relation tightly bounds the space of feasible recoveries.

Our relation comprises two inequalities, each of which already exists (to an extent) in the literature. One of the inequalities has been derived by Bamopoulos et al. (1988) for a flash unit, and can also be inferred from the monotonic nature of curves in the graphs of King (1980) and Stupin and Lockhart (1968). A subset of the other inequality is implicitly present in several distillation cost optimization formulations. These formulations constrain the number of stages in a column by the minimum number of stages required for a separation, which is in turn constrained by the separation recoveries. Alternatively, we could perceive, in these formulations, that separation recoveries are constrained by the number of stages. While this thought process could yield the second inequality of our relation, most optimization formulations impose a strict gap between the actual and minimum number of stages, and so the second inequality of our relation is strictly not present in its entirety within these formulations. To the best of our knowledge, this is the first time in the literature that our tighter recovery relation is proposed with both inequalities simultaneously as well as being applicable to a distillation column operating at general reflux ratios.

2. Derivation

2.1 Fenske equation

Our derivation of the tighter recovery relation starts from the Fenske equation for minimum number of stages (Fenske, 1932), with one common form in terms of compositions given below

$$N_T^{min} = \frac{\ln\left(\frac{x_{d,i}x_{b,j}}{x_{d,j}x_{b,i}}\right)}{\ln \alpha_{i,j}}, \quad \alpha_{i,j} \equiv \frac{\alpha_i}{\alpha_j} \geq 1, \qquad i < j \tag{3}$$

Where $x_{d,i}$ and $x_{b,i}$ are the molar compositions of component i in the distillate and bottoms products, respectively, and α_i is the relative volatility of component i.

The Fenske equation can be derived by applying mass balance, energy balance, and equilibrium relations; order of magnitude arguments; and the following assumptions.

- Fewer stages are required to achieve a separation at total reflux conditions compared to at partial reflux conditions.
- At total reflux conditions, the differences among the various enthalpies (for different phases, components, and column stages) are negligible compared to the difference between reflux enthalpy and the distillate enthalpy, which is large due to reflux molar flowrate being much larger than the distillate molar flowrate.
- The vapor-liquid equilibrium on any stage m can be adequately captured by training α_i via the following surrogate model (Mathew et al., 2020),

$$y_{m,i} = \frac{\alpha_i x_{m,i}}{\sum_j \alpha_j x_{m,j}} \tag{4}$$

Note that constant molar overflow is not specifically required for the Fenske equation.

The composition in the distillate and bottoms products are related to the feed via component recovery, r_i, as follows,

$$d_i = Dx_{d,i} = r_i f_i, \qquad b_i = Bx_{b,i} = (1 - r_i) f_i \tag{5}$$

Where f_i, d_i and b_i are the molar flowrates of component i in the feed, distillate, and bottoms, respectively, and D_i and B_i are the total molar flowrates of the distillate and bottoms products.

The above equations can be rearranged as,

$$x_{d,i} = \frac{r_i f_i}{D}, \qquad x_{b,i} = \frac{(1-r_i) f_i}{B} \tag{6}$$

Substituting the above in the Fenske equation (Eq. 3), we obtain another form in terms of component recoveries,

$$N_T^{min} = \frac{\ln\left(\frac{r_i(1-r_j)}{r_j(1-r_i)}\right)}{\ln \alpha_{i,j}} \tag{7}$$

The above form of the Fenske equation in terms of recoveries will be used in the next subsection for deriving the tighter recovery relation.

2.2 Tighter recovery relation

Consider a multicomponent separation in a distillation column of N_T stages. Let N_T^{min} be the minimum number of stages required to perform this separation, as given by Eq. 7. By definition, we have,

$$N_T^{min} \leq N_T \tag{8}$$

For practical separations, regardless of reflux conditions, there should always be at least one stage in the column. This implies that,

$$N_T^{min} \geq 1 \tag{9}$$

Substituting Eq. 7 in Eq. 8 and 9 and consolidating, we obtain,

$$1 \leq \frac{\ln\left(\frac{r_i(1-r_j)}{r_j(1-r_i)}\right)}{\ln \alpha_{i,j}} \leq N_T, \qquad i < j \tag{10}$$

Since $\alpha_{i,j} > 1$, then $\ln \alpha_{i,j} > 0$, and so the above can be rearranged as,

$$\alpha_{i,j} \leq \frac{r_i(1-r_j)}{r_j(1-r_i)} \leq \alpha_{i,j}^{N_T}, \qquad i < j \tag{11}$$

Bamopoulos et al. (1988) have previously derived the first inequality in the above, albeit restricted to flash units. With further rearrangement of the above, we obtain the first form of the tighter recovery relations,

$$\alpha_{i,j} \frac{r_j}{1-r_j} \leq \frac{r_i}{1-r_i} \leq \alpha_{i,j}^{N_T} \frac{r_j}{1-r_j}, \qquad i < j \tag{12}$$

We remark that the derivation just presented is semi-rigorous, as we have made the following assumptions

- *Given a separation at partial reflux conditions, it is possible to achieve the exact same component distribution at total reflux conditions*: For binary separations, this is automatically true. But for multicomponent separations, we cannot guarantee the exact same component distribution.
- *Any practical separation will have* $N_T^{min} \geq 1$: It is conceivable that a separation could have a mathematical value of N_T^{min} that is less than 1, even if such fractional stages are not practically meaningful.

In upcoming manuscripts, we will present rigorous derivations from the stage-by-stage approach for finite-staged operations, and from the Underwood equations for infinite-staged operations.

3. Rearrangements

Splitting Eq. 12 into two inequalities, and $\alpha_{i,j}$ as $\frac{\alpha_i}{\alpha_j}$, we obtain two other forms,

$$\frac{r_j}{\alpha_j(1-r_j)} \leq \frac{r_i}{\alpha_i(1-r_i)}, \qquad i < j \tag{13}$$

$$\frac{r_i}{\alpha_i^{N_T}(1-r_i)} \leq \frac{r_j}{\alpha_j^{N_T}(1-r_j)}, \qquad i < j \tag{14}$$

Now that the L.H.S. and R.H.S. are functions of only one component (either i or j), the above two relations can be extended into an ordering sequence for all components,

$$\begin{gathered} \frac{r_1}{\alpha_1(1-r_1)} \geq \frac{r_2}{\alpha_2(1-r_2)} \geq \cdots \geq \frac{r_n}{\alpha_n(1-r_n)} \\ \frac{r_1}{\alpha_1^{N_T}(1-r_1)} \leq \frac{r_2}{\alpha_2^{N_T}(1-r_2)} \leq \cdots \leq \frac{r_n}{\alpha_n^{N_T}(1-r_n)} \end{gathered} \tag{15}$$

Hence, we can say that the property $\frac{r_i}{\alpha_i(1-r_i)}$ monotonically decreases from lightest to heaviest component, whereas the property $\frac{r_i}{\alpha_i^{N_T}(1-r_i)}$ monotonically increases from lightest to heaviest component. Since the two properties differ only in the exponent of α_i, this implies the possibility of an exponent which makes the property constant across all components. At total reflux conditions, this exponent exists and is N_T^{min}, making the property $\frac{r_i}{\alpha_i^{N_T^{min}}(1-r_i)}$ constant across all components, as can be seen rearranging from Eq. 7.

While Eq. 12 has the benefit of a simple form present in all parts of the double-inequality, it is inconvenient for calculations since the key variables, recoveries r_i and r_j, are bundled in implicit forms. To address this, we rearrange Eq. 12 as explicit bounding functions, $r_i^{\mathrm{lb}}(r_j)$ and $r_i^{\mathrm{ub}}(r_j)$, on r_i in terms of r_j as shown below,

$$\frac{\alpha_{i,j} r_j}{\alpha_{i,j} r_j + (1-r_j)} \equiv r_i^{\mathrm{lb}}(r_j) \leq r_i \leq r_i^{\mathrm{ub}}(r_j) \equiv \frac{\alpha_{i,j}^{N_T} r_j}{\alpha_{i,j}^{N_T} r_j + (1-r_j)} \tag{16}$$

4. Validation

In this section, we validate the derived tighter recovery relation, Eq. 16, through detailed simulations of distillations of two separations: 1) p-xylene and o-xylene, and 2) ethane, propane, butane, and pentane. Figure 1 depicts a campaign of 500 Monte Carlo simulations conducted in Aspen Plus for each of the two separations. For each simulation, we randomly sampled values for the feed composition, feed vapor fraction, distillate flowrate, reflux ratio, and feed stage location. We kept number of stages fixed at $N_T = 10$, so that the same tighter recovery relation is applicable to all simulations. Overlaid on the scatter plot, we have drawn the predicted curves for the lower and upper bounds on the recovery of the y-axis component as a function of the recovery of the x-axis component, using Eq. 16. The relative volatilities were

determined by the α_i that cause Eq 4 to best fit a spread of vapor-liquid equilibrium data (Mathew et al., 2020).

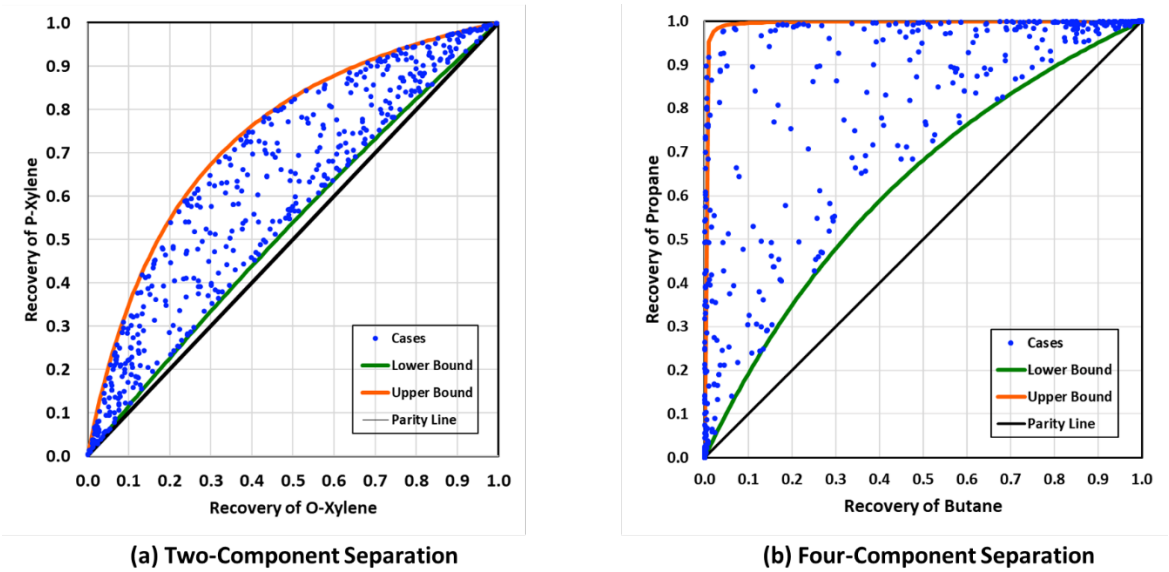

Figure 1: (a) Two-component separations of p-xylene and o-xylene at 1 atm; (b) Four-component separations of ethane, propane, butane, and pentane at 20 atm. Only propane-butane results are shown here for the four-component separation; similar results are observed for other pairs of components.

We see in the figure that almost all simulation data points fall within the crescent-shaped region enclosed by the bounding curves of the tighter recovery relation. Importantly, the tighter recovery relation accurately predicts that the upper bound for the two-component separation and the lower bound for the four-component separation are substantially distant from the respective bounding curve from the simple ordering relation, Eq. 2. Therefore, the tighter recovery relation is valuable in reliably eliminating a substantial portion of the recovery space that cannot be achieved by practical distillations.

Moreover, from visual inspection, we can see that the crescent-shaped region of the tighter recovery relation tightly hugs the set of simulation data points. This is evidence in support of the relation being the tightest to describe a continuous enclosure of the recovery data points. Thus, the tighter recovery relation is superior to the simple ordering relation in describing the feasible recovery space, without being overly complicated and requiring only two additional parameters: the relative volatility between the compared components, $\alpha_{i,j}$, and the number of stages in the column, N_T.

5. Conclusion

Component recoveries in distillation have been well-known to be ordered (Eq. 1). To the best of our knowledge, this is the first time that our recovery relation (Eq. 12), which is tighter than the simpler ordering, has been proposed (and briefly derived) in the literature in its entirety and for general distillation conditions. Through detailed simulations on two examples, we have validated the applicability and tightness of this relation. The new relation has the potential to screen out infeasible separation

conditions, which can be valuable in reducing the search space during optimization. We have presented multiple forms of this relation (Eq. 12, 15 and 16) as the specific form of a relation can impact its utility for optimization formulations. In manuscripts currently in preparation, we will present rigorous derivations of this relation, as well as additional Monte Carlo simulations demonstrating the validity of the relation on other types of mixtures.

Acknowledgements

We thank the US Department of Energy (Award number: DE - EE0005768) for financial support during this study. We also thank Dr. Radhakrishna Tumbalam Gooty and Dr. Zheyu Jiang for their discussions on the work presented in this paper.

References

Bamopoulos, G., Nath, R., Motard, R.L., 1988. Heuristic synthesis of nonsharp separation sequences. AIChE J. 34, 763–780. https://doi.org/10.1002/aic.690340507

Fenske, M.R., 1932. Fractionation of Straight-Run Pennsylvania Gasoline. Ind. Eng. Chem. 24, 482–485.

King, C.J., 1980. Separation processes, 2. ed. ed, McGraw-Hill Chemical Engineering Series. McGraw-Hill, New York.

Mathew, T.J., Tumbalam Gooty, R., Tawarmalani, M., Agrawal, R., 2020. Quickly Assess Distillation Columns. Chemical Engineering Progress 112, 27–34.

Stupin, W., Lockhart, F., 1968. The distribution of non-key components in multicomponent distillation, in: American Institute of Chemical Engineers Annual Meeting, Los Angeles, December.

Thermodynamic Insights and Modeling of Aroma Compounds in Vacuum Distillation for Dealcoholisation of Beer

*Mariangela Falconieri, Mirjana Minceva**
Technical University of Munich, Freising, Germany
** e-mail: mirjana.minceva@tum.de*

Abstract
Vacuum distillation is widely used to produce non-alcoholic beer (NAB) with ethanol contents ≤ 0.05 vol%. However, it also causes the loss of key aroma compounds into the ethanol-rich distillate, affecting the sensory profile of the NAB.
Previous studies investigated the impact of individual process parameters on the composition of NAB during vacuum distillation. Nevertheless, a model based, process parameters optimisation study that quantifies how multiple process variables affect ethanol and aroma compound concentrations in the NAB stream is still missing. In this work, the influence of multiple process parameters on NAB composition is quantified and operating conditions are optimised to maximise aroma compound concentrations in NAB.
The vapour–liquid equilibrium of a model beer mixture composed of water, ethanol and beer-representative aroma compounds was described using the non-random two-liquid model. An industrial pilot-plant for beer vacuum distillation was simulated in Aspen Plus v14 using the equilibrium-stage model within the RADFRAC module. The simulation was validated against data obtained in a pilot-scale distillation unit for three commercial beers, reproducing ethanol and aroma concentrations in both NAB and distillate streams. The Aspen Plus column model was then used to simulate the NAB composition for 100 representative combinations of process parameters generated with the Latin Hypercube Sampling method within the narrow industrial-scale process parameters window. Aspen Plus predicted ethanol and aroma compounds concentrations in NAB, together with the corresponding process parameter values, were used to train a Random Forest (RF) surrogate model, correlating the process parameters to the simulated NAB composition. The RF model was coupled with a Genetic Algorithm to identify process parameters values that maximised aroma retention in NAB while satisfying the ethanol constraint of ≤ 0.05 vol%.

Keywords
Non-alcoholic beer, vacuum distillation, aroma compounds, process simulation, surrogate model, machine learning

1. Introduction

The production of non-alcoholic beer (NAB) has grown strongly in recent years due to cultural and religious factors, as well as health concerns. Thermal dealcoholisation remains the preferred route at large industrial scale for beers with ethanol content at or below 0.05 vol% (Krebs et al., 2019; Salantă et al., 2020).

Vacuum distillation is commonly used because it allows ethanol removal from the beer at moderate temperatures. However, industrial experience and pilot studies consistently show that during thermal dealcoholisation, aroma compounds leave the column together with the ethanol in the distillate stream, leading to a less intense or unbalanced sensory profile in the final NAB (Horácio et al., 2020; Müller et al., 2021). Although present in beer at trace levels, the concentration and the relative balance of these aroma compounds strongly determine perceived NAB quality (Piornos et al., 2023).

Only a limited number of studies have combined experiments and process modeling to investigate aroma compounds losses during thermal dealcoholisation (Andrés-Iglesias et al., 2015; Horácio et al., 2020; Müller et al., 2021), as well as to validate model predictions against industrial process data. An experimentally validated simulation on pilot-plant data, that quantifies the combined effect of multiple process parameters on the NAB stream composition is still missing. Filling this gap is essential for determining whether optimisation of existing distillation process parameters can still increase NAB aroma compounds concentration before considering modifications of the distillation process flowsheet.

Industrial vacuum dealcoholisation is operated within a narrow window of process parameters to avoid thermal degradation of aroma compounds and the formation of off-flavours in NAB. In this study, the investigated window was defined by feed temperature 15–45 °C, condenser pressure 0.01–0.03 bar and column pressure drop 0.01–0.07 bar. The objective of this work was to quantify the effect of key process parameters on ethanol and aroma compounds concentrations in the NAB stream and to identify operating conditions that maximise aroma retention while maintaining ethanol ≤0.05 vol%.

The vapor liquid equilibria (VLE) of a simplified beer mixture was described using the non-random two-liquid (NRTL) activity-coefficient model because in the work of Puentes et al. (2018) it was shown to provide the most accurate description of VLE for aroma compounds highly diluted in ethanol–water mixtures. A vacuum distillation column was simulated in Aspen Plus v14 (AspenTech, USA) using the equilibrium stage model within the RADFRAC module. The model predictions were validated with experimental data from a pilot-scale dealcoholisation unit for three commercial beers.

After validation, the model was used to investigate how key process parameters—feed temperature, reflux ratio, distillate rate, condenser pressure, column pressure drop, and number of equilibrium stages—within an industrially relevant range affect aroma compounds and ethanol concentration in NAB. Because the study focused on a relatively narrow industrial beer-dealcoholisation process parameter window, a fully rigorous optimisation was not pursued in order to reduce computational effort (Ye et al., 2023).

Therefore, Latin Hypercube Sampling (LHS) was applied to generate 100 combinations of process parameters, each representing one unique set of values selected from the values rang shown in Table 1. The distillation column was then simulated in Aspen Plus for each of the 100 parameter combinations, and the resulting ethanol and aroma-compound concentrations in the NAB stream were recorded. This dataset was used to train a Random Forest (RF) surrogate model capable of predicting NAB composition from any given combination of process parameter values.

The RF surrogate model was subsequently coupled with a Genetic Algorithm (GA) to search for parameter combinations that satisfied an ethanol constraint of ≤0.05 vol% while increasing aroma compound concentrations in the NAB. For each set of parameter values proposed by the GA, the ethanol and aroma compound concentrations were predicted by

the RF model and evaluated using an objective function designed to quantify aroma compound enhancement in NAB under the ethanol content constraint.

2. Results and discussion

2.1 Rigorous distillation column model and validation against pilot-scale unit data

The vacuum distillation column for beer dealcoholisation was simulated in Aspen Plus v14 using the equilibrium-stage model implemented in the RADFRAC module. The model beer used as the column feed in the simulation was defined as a multicomponent mixture comprising water, ethanol, and seven key aroma compounds representing different chemical families and volatilities: acetaldehyde (AA), ethyl acetate (EA), isoamyl acetate (IPA), 2-methyl-1-propanol (2M1P), 3-methyl-1-butanol (3M1B), 2-methyl-1-butanol (2M1B) and linalool (LIN). The VLE was calculated using the NRTL activity-coefficient model with binary parameters taken from the Aspen Plus databank. The Aspen Plus simulation was validated against experimental data from a pilot-scale DeAlcoTec® unit (Centec GmbH, Germany) operated at steady state with three commercial beers. The process streams—column feed (F), distillate (D), and non-alcoholic beer (NAB)—were sampled and analysed for the concentrations of aroma compounds and ethanol. Figure 1 compares the simulated and measured concentrations of ethanol and three representative aroma compounds in the F, NAB, and D streams for the three beers. The model predictions showed satisfactory agreement with the measured concentrations of ethanol and the selected aroma compounds, validating both the VLE model and the equilibrium-stage model used to simulate the distillation column in Aspen Plus v14.

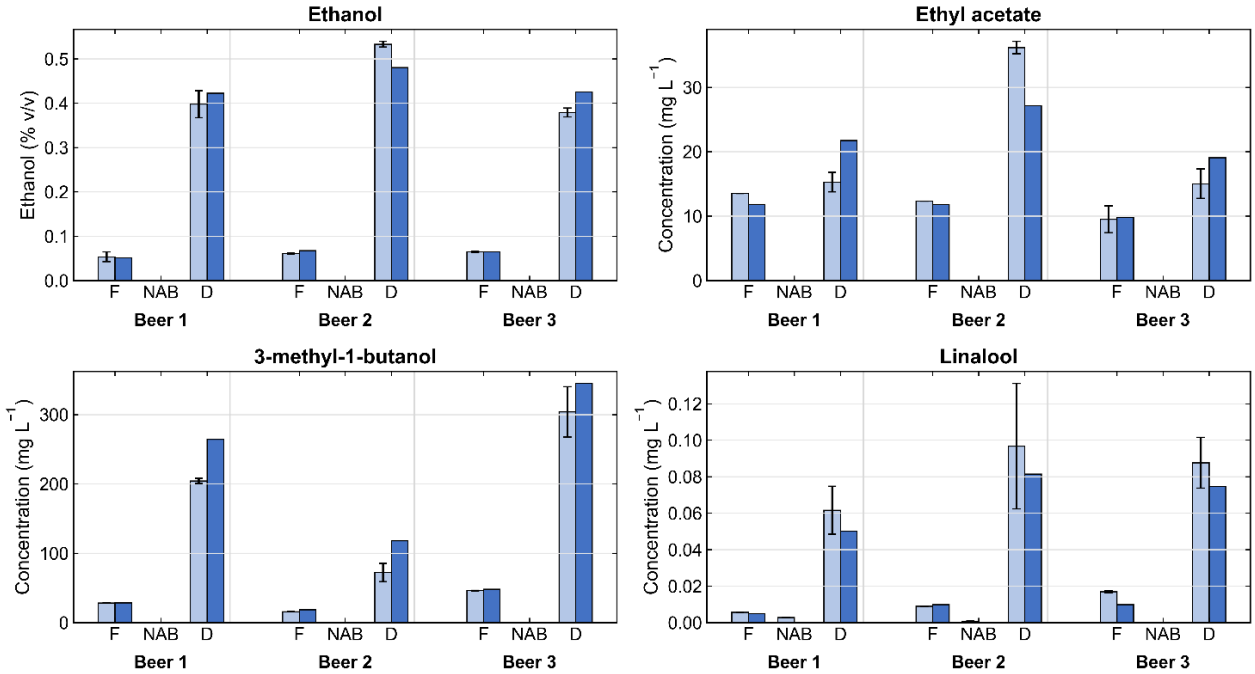

Figure 1: Comparison of the experimental and predicted concentration of three aroma compounds (mg L^{-1}) and ethanol (vol%) in the streams F, NAB and D for three commercial beers. The operating conditions required to reproduce the Aspen Plus simulations—feed volumetric flowrate, feed temperature and pressure, distillate volumetric flowrate, reflux ratio, number of stages, feed stage location, column pressure, and pressure drop—are reported in Falconieri and Minceva (2026). ▭ = Experimental value, ▭ = Simulated value.

2.2 Generation of distillation column data set for surrogate-model training

To investigate the influence of the process parameters listed in Table 1 on the concentrations of aroma compounds and ethanol in NAB, the LHS sampling method was employed to generate 100 representative combinations of these parameters within their respective minimum and maximum values. The distillation column was then simulated for each parameter combination in Aspen Plus, as described in Section 2.1. The resulting ethanol and aroma compound concentrations in the NAB stream were recorded to create the dataset used to train the surrogate model. A full factorial combination of the parameters in Table 1 would have required an unfeasibly large number of simulations; therefore, LHS was used to sample the multidimensional parameter space efficiently.

Table 1: Process parameters with selected minimum and maximum values defining the operating window

Process parameters	Symbol	Unit	Minimum	Maximum
Feed temperature	T_F	°C	15	45
Reflux ratio	R_R	-	1	5
Distillate rate	$\dot{D}$	l/hr	15	45
Condenser pressure	P_c	bar	0.01	0.03
Column pressure drop	ΔP	bar	0.01	0.07
Number of stages	N_{th}	-	5	20

2.3 Random forest surrogate model for predicting concentration of aroma compounds and ethanol in NAB

A RF surrogate model was trained on the dataset generated as described in Section 2.2 to derive a correlation between the process parameters from Table 1 and the concentration of aroma compounds and ethanol in NAB (simulated with Aspen plus). The RF *model inputs* (features) were the process parameters from Table 1. The RF *model outputs* were with Aspen plus simulated (i) ethanol concentration in NAB and (ii) aroma compound retention R_i, defined as the concentration ratio of each aroma compound i in NAB stream $c_{i,NAB}$ to that of F stream $c_{i,F}$:

$$R_i = \frac{c_{i,NAB}}{c_{i,F}} \qquad \textbf{Equation 1}$$

The RF model was fitted in *R* (v4.4.3) using the *randomForestSRC* package (Ishwaran and Kogalur, 2007). Model parameters and predictive accuracy for outputs (i) and (ii) were evaluated using out-of-bag (OOB) predictions. In this approach, each regression tree of the RF model was trained on a bootstrap sample of the data, while the remaining data were used to evaluate the model predictive accuracy by comparing the RF model predicted outputs (i) and (ii) with those calculated using the Aspen Plus model.

Variable importance was calculated using the default RF permutation-based measure in R, which quantifies the increase in prediction error when the values of a given variable are randomly permuted. T_F was the most influential feature on the outputs, as shown in the variable importance ranking in Figure 2(a).

The RF surrogate model showed high predictive accuracy for all output variables within the investigated operating window, with OOB R^2 between 0.88 and 0.99 and normalised mean absolute error (NMAE), defined as the mean absolute error divided by the difference between their maximum and minimum simulated values, between 0.006 and 0.025. In Figure 2(b-e) the parity plots for ethanol concentration and aroma compound retention R_i in NAB for three representative aroma compounds (EA, 3M1B and LIN) are shown.

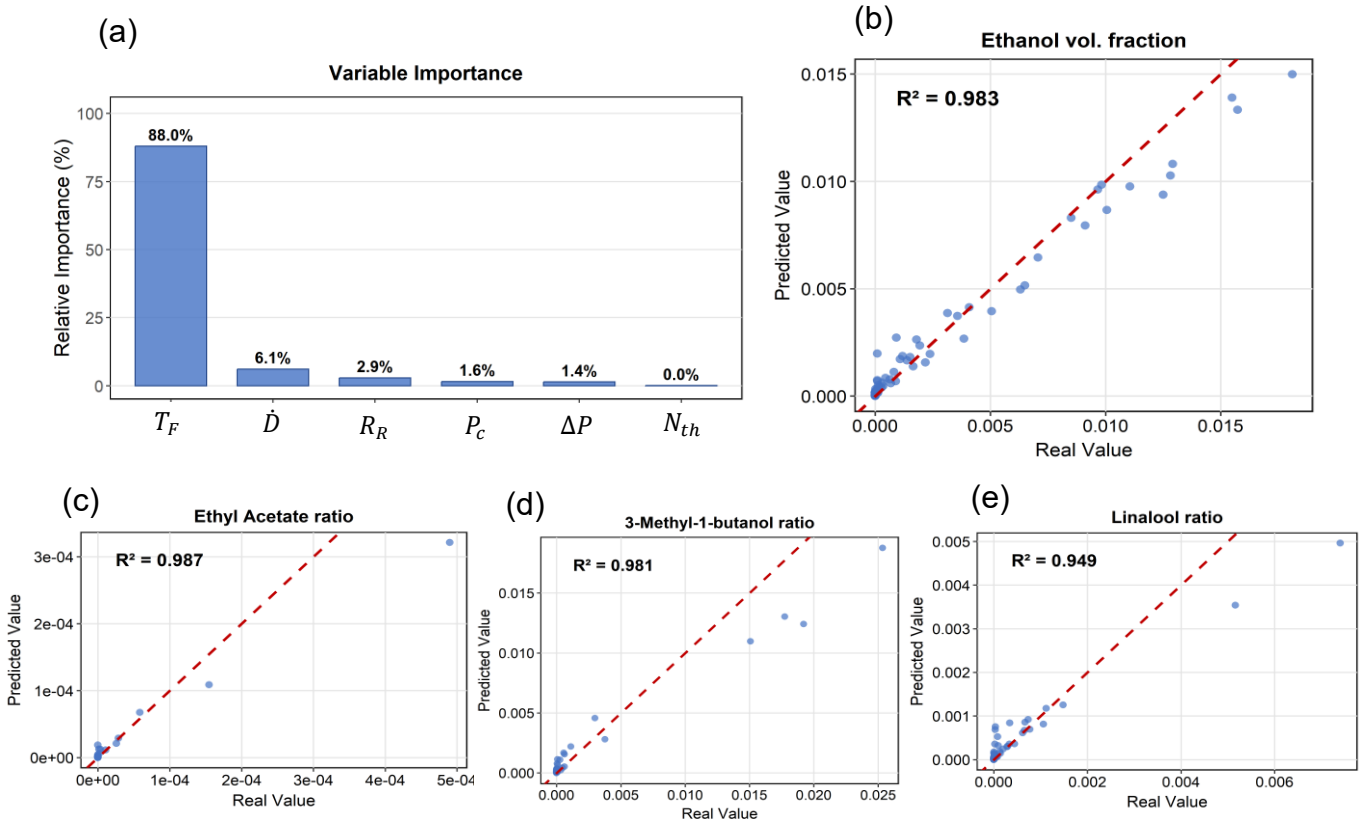

Figure 2: (a) Variable importance averaged across outputs (i) and (ii). (b-e) Parity plot for RF predictions against Aspen Plus simulation results of NAB stream for ethanol volume fraction and R_i of EA, 3M1B and LIN. The dashed line indicates perfect agreement and R² is reported in each panel.

2.4 Optimisation of operating conditions using a Genetic Algorithm

The RF model was coupled with a GA implemented in *R* (v4.4.3) using the *GA* package (Scrucca, 2013). For each GA generated set of process parameters values, the surrogate RF model predicted the concentrations of ethanol and the aroma compound retention ratio R_i, defined in Equation 1, in the NAB.

The GA evaluated only set of process parameters values that satisfied the ethanol specification of ≤0.05 vol% in NAB. The predicted R_i of the aroma compounds were plotted in a radar diagram, shown in Figure 3, and the corresponding polygon area was calculated as a single metric summarising the combined R_i values. Four objective functions were considered: (i) balanced maximisation of R_i, defined as maximisation of the radar plot area combined with minimisation of the variance among R_i of different aroma compounds, (ii) maximisation of the radar plot area (maximization of all R_i), (iii) maximisation of higher-alcohols R_i and (iv) maximisation of esters R_i. The resulting R_i radar plot for each of the four objective functions is shown in Figure 3. Within the investigated distillation column operating window, the optimised R_i for each aroma compound were similar across the four objective functions. Within the investigated vacuum distillation column process parameters values window, adjusting process parameters listed in Table 1 led only to minor increase in the concentration of aroma compounds in NAB when the ethanol specification of ≤0.05 vol% in the NAB stream was met.

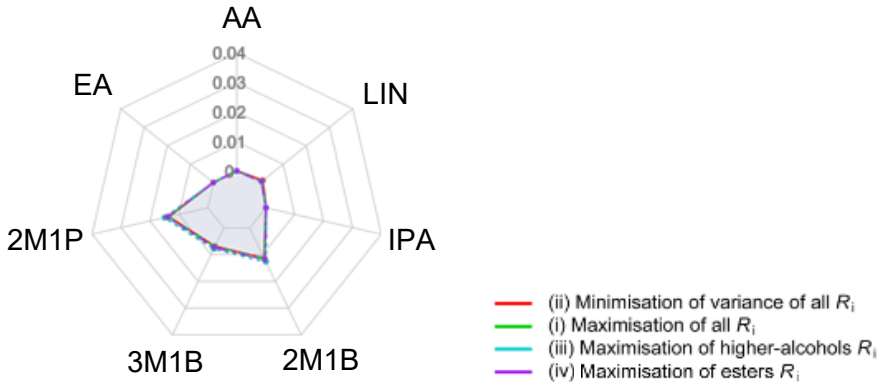

Figure 3: Aroma compounds concentration ratios R_i for GA optimised operating conditions for each objective function under the ethanol constraint (≤ 0.05 vol%).

3. Conclusions

This work showed that an Aspen Plus model of a vacuum distillation column, validated against pilot-scale data distillate and NAB streams compositions, can be used to generate a reliable dataset for training a Random Forest surrogate model correlating process parameters to ethanol and aroma compounds concentrations in the NAB stream. Coupling the RF surrogate model with a Genetic Algorithm enabled efficient exploration of process parameter combinations without the computational cost of rigorous optimisation. Within the narrow industrial ranges of feed temperature, distillate rate, reflux ratio, condenser pressure, column pressure drop and number of stages, only minor improvements in aroma compounds concentration in NAB were achievable while meeting the ethanol specification of ≤0.05 vol%. Therefore, adjustments of process parameters alone cannot enhance aroma compound retention in NAB and further improvement will require flowsheet modifications. The integrated Aspen Plus–RF–GA workflow in this work provides an efficient approach for evaluating such alternative process configurations.

Acknowledgements

This work was supported by the Bundesministerium für Wirtschaft und Klimaschutz and by the ZIM Zentrales Innovationsprogramm Mittelstand (Project "NAlcoFFlaB", Number KK5022319NK2).

References

Andrés-Iglesias, C., García-Serna, J., Montero, O., & Blanco, C. A. (2015). Simulation and flavor compound analysis of dealcoholized beer via one-step vacuum distillation. *Food Research International*, *76*, 751–760.

Horácio, P. S., Veiga, B. A., Luz, L. F., Levek, C. A., de Souza, A. R., & Scheer, A. P. (2020). Simulation of vacuum distillation to produce alcohol-free beer. *Journal of the Institute of Brewing*, *126*(1), 77–82.

Krebs, G., Müller, M., Becker, T., & Gastl, M. (2019). Characterization of the macromolecular and sensory profile of non-alcoholic beers produced with various methods. *Food Research International*, *116*, 508–517.

Falconieri, M., Minceva, M. (2026). Thermodynamic insights into vacuum distillation dealcoholisation of beer and aroma-compound loss: a molecular-level analysis. *Journal of Food Engineering*, submitted.

Ishwaran, H., Kogalur, U. (2007). Random survival forests for R. *R News*, *7*(2), 25–31.

Müller, M., Becker, T., & Gastl, M. (2021). Transfer of ethanol and aroma compounds by varying specific process parameters in the thermal dealcoholisation of beer. *Foods*, *10*(7), 1602.

Piornos, J. A., Koussissi, E., Balagiannis, D. P., Brouwer, E., & Parker, J. K. (2023). Alcohol-free and low-alcohol beers: aroma chemistry and sensory characteristics. *Comprehensive Reviews in Food Science and Food Safety*, *22*(1), 233–259.

Puentes, C., Joulia, X., Athès, V., & Esteban-Decloux, M. (2018). Review and thermodynamic modeling with NRTL model of vapor–liquid equilibria (VLE) of aroma compounds highly diluted in ethanol–water mixtures at 101.3 kPa. *Industrial & Engineering Chemistry Research*, *57*(10), 3443–3470.

Salantă, L. C., Coldea, T. E., Ignat, M. V., Pop, C. R., Tofană, M., Mudura, E., Borşa, A., Pasqualone, A., & Zhao, H. (2020). Non-alcoholic and craft beer production and challenges. *Processes*, *8*(11), 1382.

Scrucca, L. (2013). GA: A Package for Genetic Algorithms in R. *Journal of Statistical Software*, *53*(4), 1–37.

Ye, L., Zhang, N., Li, G., Gu, D., Lu, J., & Lou, Y. (2023). Intelligent Optimization Design of Distillation Columns Using Surrogate Models Based on GA-BP. *Processes*, *11*(8), 2386

A simple method to meaningfully predict the packing efficiency in a pumparound

Lee Ming Yang[1], *Markus Duss*[2]
[1]*Sulzer Singapore Pte Ltd, Singapore, Singapore;*
[2]*Retired from Sulzer Chemtech Ltd, Winterthur, Switzerland*

Abstract
The absorption of a solute component from the gas phase to the liquid phase is sometimes designed with a pumparound. Despite diminishing concentration driving forces, a pumparound can be favourable for mass transfer if the absorption benefits from cooling and/or an increased specific liquid load. Applying the NTU_{OG}-HTU_{OG} concept and mass transfer correlations to an equilibrium stage simulation will predict excessively high HETPs and unrealistic packing heights, due to extremely low stripping factors. The paper presents a simple design methodology to enable the process engineer to make a practical estimate of the pumparound packing height. This method assesses the impact of decreasing the NTU_{OG} and hence the packing height on the gas outlet solute concentration. Astonishingly, the packing height can be reduced substantially to a reasonable value without an appreciable impact to the gas outlet solute concentration, thereby reconciling process simulation with real plant experience.

Keywords
Pumparound; Mass transfer; Absorption; Packing HETP

1. Pumparounds for Absorption Mass Transfer

A packing bed, either structured or random, can be equipped with a pumparound system, where some or most of the liquid is collected and recycled back to the top of the bed. There are several reasons to incur additional capital and operating costs to implement a pumparound. They are mostly associated with direct heat exchange (DHX), including direct condensers, saturators, and quenchers. For mass transfer tasks, pumparounds are typically not preferred, as the liquid recirculation leads to liquid back-mixing and diminishes concentration gradients for mass transfer. However, for absorption applications, where a solute component is absorbed from the gas phase to the liquid phase, there are two reasons to implement a pumparound to provide an overall benefit to mass transfer.

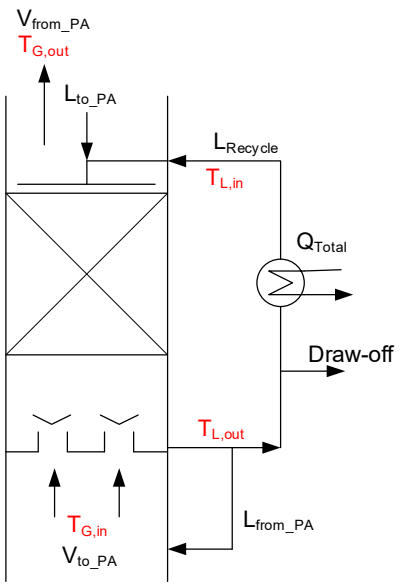

Figure 1: An example of a packing bed with a pumparound. L_{to_PA} can come from an external feed, and it is not mandatory to have both L_{from_PA} and the draw-off streams.

Firstly, if there is an exothermic heat of absorption, the column temperature profile can increase significantly, shifting the thermodynamic equilibrium and reducing concentration driving forces. A classic example is the absorption of hydrogen chloride (HCl) into water, which includes the heat of reaction due to the dissociation of

SULZER CONFIDENTIAL

HCl. Hence, cooling will improve the thermodynamic behaviour of the solute and can be implemented in a pumparound by sending the recirculated solvent through a cooler. However, the solute concentration in the solvent at the top of the packed bed will be increased due to liquid back-mixing, therefore this solution is only viable for systems where the cooling effect dominates the liquid back-mixing effect.

Secondly, if the solute component has a low gas–liquid equilibrium ratio (also called the k-value), the resulting solvent flowrate required can be very low for a once-through design. The specific liquid load can be less than 0.3 $m^3/(m^2 \cdot hr)$, leading to inadequate wetting of the packing and a low interfacial area for mass transfer, if metal random packings or metal sheet structured packings are used. This problem is exacerbated in aqueous systems because of inherently poor liquid spreading associated with high liquid surface tension. Using a gauze structured packing is a solution, as liquid spreading by capillary action allows good wetting despite a low liquid flowrate, but is relatively expensive. Otherwise, pumparounds allow increasing the specific liquid load to a comfortable value, for instance between 10 to 20 $m^3/(m^2 \cdot hr)$, to ensure safe and robust column operation. Due to the low k-value, the impact of increasing the solute concentration at the top of the packed bed is lessened. Cooling is not mandatory in this scenario if the heat of absorption is not significant. An example is the absorption of dimethylformamide (DMF) into water.

This paper will present a design methodology to estimate the packing height of a pumparound. The DMF absorption system shall be used as a case study. An equilibrium stage simulation is the basis of the proposed methodology. Figure 2 shows the simulation results of the DMF absorber, performed using AVEVA™ PRO/II™ Simulation. The gas feed contains ~0.1 mol% of DMF. The absorber is designed with two pumparounds to achieve an outlet DMF concentration of 17 ppm-mol. Both pumparounds have a recirculation rate of 15'000 kg/hr to yield a specific liquid load of ~20 $m^3/(m^2 \cdot hr)$ for a column diameter of 1 m.

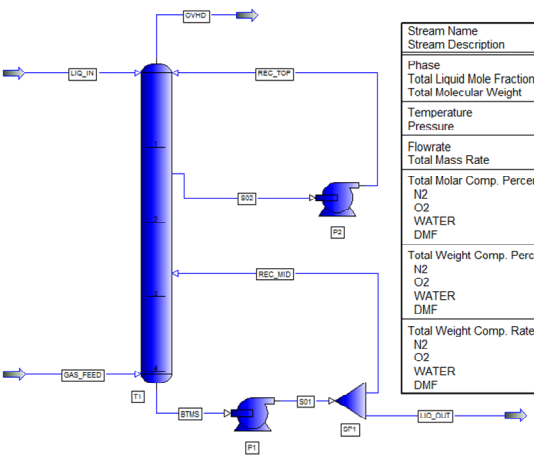

Stream Name Stream Description		GAS_FEED	OVHD	LIQ_IN	LIQ_OUT	REC_TOP	REC_MID
Phase		Vapor	Vapor	Liquid	Liquid	Mixed	Liquid
Total Liquid Mole Fraction		0.00	0.00	1.00	1.00	1.00	1.00
Total Molecular Weight		28.76	28.62	18.02	20.79	18.32	20.79
Temperature	C	30.00	18.68	20.00	19.08	18.68	19.08
Pressure	KPA	100.00	100.00	100.00	100.00	100.00	100.00
Flowrate	KG-MOL/HR	313	315	8	6	819	721
Total Mass Rate	KG/HR	9000	9025	150	125	15000	15000
Total Molar Comp. Percents							
N2		77.8901	77.3054	0.0000	0.0012	0.0010	0.0012
O2		20.7050	20.5495	0.0000	0.0006	0.0005	0.0006
WATER		1.3015	2.1434	100.0000	94.9584	99.4542	94.9584
DMF		0.1035	0.0017	0.0000	5.0398	0.5442	5.0398
Total Weight Comp. Percents							
N2		75.8810	75.6699	0.0000	0.0016	0.0015	0.0016
O2		23.0405	22.9764	0.0000	0.0010	0.0009	0.0010
WATER		0.8154	1.3492	100.0000	82.2794	97.8256	82.2794
DMF		0.2632	0.0044	0.0000	17.7180	2.1720	17.7180
Total Weight Comp. Rates	KG/HR						
N2		6829.29	6829.29	0.00	0.00	0.23	0.24
O2		2073.64	2073.64	0.00	0.00	0.14	0.15
WATER		73.38	121.77	150.00	102.78	14673.83	12341.91
DMF		23.68	0.40	0.00	22.13	325.79	2657.70

Figure 2: Equilibrium stage simulation of the DMF absorber used as the case study for this paper.

2. What is the Packing HETP of an Equilibrium Stage in a Pumparound?

Before proceeding to the proposed design method, the "full" packing height for the pumparound according to an equilibirum stage simulation must be assessed, using the concept of the number of transfer units overall gas, NTU_{OG}, and the height of a transfer unit overall gas, HTU_{OG}. The packing HETP (height equivalent to theoretical plate or

SULZER CONFIDENTIAL

stage) can consequently be calculated by dividing the packing height over the NTS (number of theoretical stages).

An equilibrium stage simulation is set up as shown in Figure 2. In general, the NTS should be increased until no further changes in the gas outlet temperature is observed. This is because heat transfer occurs much more rapidly than mass transfer, and a fully developed temperature profile is expected given the eventual packing height required. For a pumparound with a significant temperature profile, e.g., when a pumparound cooler is used, this can result in three or more stages. It is recommended to use at least two stages. For the considered DMF absorption case study, the heat of absorption is negligeble, hence two stages are used for each pumparound section.

To calculate the pumparound packing height, h_P, the NTU_{OG}–HTU_{OG} concept is applied to the results of the process simulation. By applying suitable simplifying assumptions, both the NTU_{OG} and the HTU_{OG} can be calculated with reasonable effort and accuracy, as presented below.

$$h_P = NTU_{OG} \cdot HTU_{OG} \qquad (1)$$

Firstly, the NTU_{OG} is calculated. If both the operating line and the equilibrium line are assumed to be straight lines, a simple relationship exists between the NTU_{OG} and the NTS. The stripping factor, λ, is the ratio of the slope of the equilibrium line, *m*, and the slope of the operating line, *L/G*.

$$NTU_{OG} = NTS \cdot \frac{ln\lambda}{\lambda - 1} \ , \ \lambda = \frac{m}{L/G} \qquad (2), (3)$$

The assumption of straight lines for a pumparound is usually reasonable, especially for one without cooling. Nonetheless, this should be checked. The slope of the operating line, *L/G*, can be easily retrieved from the process simulation. For this DMF absorber, each pumparound has two NTS and hence four operating points. For each pumparound, the four *L/G* values are similar, and the average value is considered for the NTU_{OG} calculation.

The slope of the equilibrium line, *m*, can be complicated. For a rigorous treatment to calculate *m*, the paper of Taylor and Duss [1] should be referred. For this DMF absorber however, *m* can be approximated by the k-value. Each pumparound has two k-values which are similar, and the average value is considered for the NTU_{OG} calculation.

Table 1: Calculations of λ and NTU_{OG}, for the two pumparounds of the DMF absorber.

	NTS	L/G	m	λ	NTU_{OG}
Top Pumparound	2	2.6	0.0032	0.0012	13.4
Bottom Pumparound	2	2.3	0.0035	0.0015	13.0

Due to the very small λ, a very large NTU_{OG} of 13 or more is required for only two NTS. An exceptionally small λ is a distinctive characteristic of a pumparound and is the primary reason for the high packing HETP of an equilibrium stage, as elaborated further in this paper.

SULZER CONFIDENTIAL

Secondly, the HTU_{OG} is calculated, by adding the height of gas side transfer unit, HTU_G and the height of the liquid side transfer unit, HTU_L, multiplied by λ.

$$HTU_{OG} = HTU_G + \lambda \cdot HTU_L \qquad (4)$$

Due to the characteristically low λ, the contribution of $\lambda \cdot HTU_L$ becomes negligible. Thus, $HTU_{OG} \approx HTU_G$, making pumparounds for absorption mass transfer exclusively gas-side controlled.

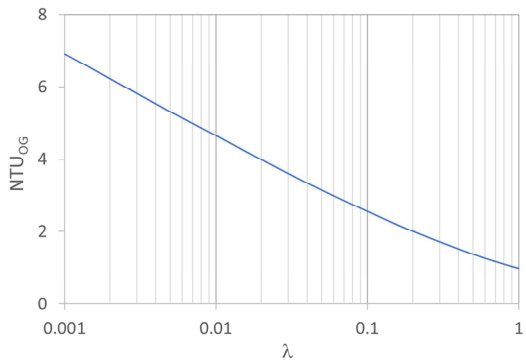

Figure 3: Dependency of the NTU_{OG} on the stripping factor, λ, for one NTS.

The HTU_G can be determined from the gas phase superficial velocity, u_G, the gas side mass transfer mass transfer coefficient, β_G, and the interfacial area, a_I.

$$HTU_G = \frac{u_G}{\beta_G \cdot a_I} \qquad (5)$$

Zogg [2] was the first to apply a Sherwood correlation to determine β_G in structured packings, according to Equation (6), when he investigated the efficiency of structured packings for his PhD thesis in 1972. Sh is the Sherwood number, Re is the Reynolds number, Sc is the Schmidt number, and k_{Sh} is the Sherwood constant.

$$Sh_G = k_{Sh} \cdot Re_G^{0.8} \cdot Sc_G^{1/3} \qquad (6)$$

The Sherwood, Reynolds, and Schmidt number are further defined below. d_h is the packing hydraulic diameter, D_G is gas phase diffusivity, $u_{G,eff}$ is the effective gas velocity, ρ_G is the gas density, and η_G is the gas dynamic viscosity. The determination of D_G is not trivial and the paper of Taylor and Duss [1] should be referred. A value of 9.9×10^{-6} m^2/s for D_G is considered for this paper.

$$Sh_G = \frac{\beta_G \cdot d_h}{D_G}\ ,\ Re_G = \frac{u_{G,eff} \cdot \rho_G \cdot d_h}{\eta_G}\ ,\ Sc_G = \frac{\eta_G}{\rho_G \cdot D_G} \qquad (7), (8), (9)$$

Bravo, Rocha and Fair [3] also proposed a Sherwood correlation for β_G in structured packings in 1985, and their correlation is used in this paper. This includes using their specific definitions for $u_{G,eff}$ and d_h.

The interfacial area correlation by Tsai et al. [4] is considered by the authors to be reasonably accurate for the typical specific liquid loads in a pumparound and is used in this paper. σ is the liquid surface tension, g is the gravitational constant, A_{col} is the column cross-sectional area, and L_P is the wetted perimeter as defined by Tsai et al.

$$a_I = 1.34 \cdot \left(\frac{\rho_L}{\sigma} \cdot g^{1/3} \cdot \frac{u_G \cdot A_{col}}{L_P}\right)^{0.116} \qquad (10)$$

Sulzer MellapakPlus™ 252.Y is chosen as the packing type and the column diameter has been hydraulically sized earlier to be 1 m. All the required information to determine the HTU_{OG} is now complete. The calculation outcomes, including the pumparound packing height and HETP, are summarized in Table 2.

SULZER CONFIDENTIAL

Table 2: Calculations of HTU_{OG}, HETP, and packing height, h_p for the two pumparounds.

	β_G m/s	a_I m^2/m^3	HTU_G m	HTU_{OG} m	NTU_{OG}	h_p m	HETP m
Top Pumparound	0.02	211	0.641	0.641	13.4	8.62	4.31
Bottom Pumparound	0.02	212	0.638	0.638	13.0	8.32	4.16

The packing height for the top and bottom pumparounds are 8.62 m and 8.32 m respectively, and since there are two NTS per pumparound, the HETP is 4.31 m and 4.16 m respectively. These values are too high compared to industrial experience, and a realistic pumparound packing height would have less than one NTS. The main reason for the high packing HETP is the high NTU_{OG}, which in turn results from the characteristically low stripping factor, λ. Moreover, if more than two NTS are used, the HETP would remain similar, and the packing height would increase accordingly, leading to even more unrealistic results.

3. A Simple Method to Estimate the Pumparound Packing Height

The knowledge that a high NTU_{OG} is the reason for the high pumparound packing height is the key to the simple design methodology: The NTU_{OG} (and hence the packing height) is reduced, and the impact on the solute concentration in the pumparound gas outlet, y_{out}, is evaluated. The aim is to bring down the packing height to a reasonable value, with a tolerable increase in y_{out}. Therefore, this method requires the process engineer to already include a design safety margin in the equilibrium stage simulation. For the DMF absorber, the simulation outcome for y_{out} is 17 ppm-mol DMF, hence the required specification may be some 50 ppm-mol.

Assuming straight operating and equilibrium lines, the following equation to calculate NTU_{OG} can be derived. y_{in} is the solute concentration in the pumparound gas inlet, and x_{in} is the solute concentration in the pumparound liquid inlet.

$$NTU_{OG} = \frac{1}{1-\lambda} \cdot \ln\left(\frac{y_{in} - m \cdot x_{in} - \lambda \cdot (y_{in} - y_{out})}{y_{out} - m \cdot x_{in}}\right) \qquad (11)$$

y_{in} is a fixed input value. x_{in} can vary as the liquid inlet comprises the feed stream (external make-up or liquid from the above packed bed) and the recirculated liquid stream. Nonetheless, x_{in} can be conservatively assumed to be a fixed value. Both y_{in} and x_{in} are retrieved from the equilibrium stage simulation. The NTU_{OG}, full packing height, λ and *m* are known values from earlier calculations. If the packing height is reduced, the NTU_{OG} is reduced proportionally, and Equation (11) can be rearranged and solved to give the corresponding y_{out}. For the DMF absorber, the impact of reducing the packing height from >8 m to 2.5 m is shown in Table 3. For a packing height reduction of more than 70%, the increase in y_{out} is remarkably minor.

Table 3: Gas outlet solute concentration, y_{out}, achieved with different pumparound packing heights.

		Top Pumparound		Bottom Pumparound	
		Full Height	Reduced Height	Full Height	Reduced Height
Packing Height	m	8.62	2.50	8.32	2.50
NTU_{OG}		13.4	3.9	13.0	3.9
y_{out}	ppm-mol	17	20	171	188

SULZER CONFIDENTIAL

A more complete analysis would involve re-simulating the top pumparound with a gas inlet solute concentration of 188 ppm-mol instead of 171 ppm-mol and repeating the design method for the top pumparound. The details are not shown in this paper; the brief outcome is that y_{out} from the equilibrium simulation is ~19 ppm-mol, and y_{out} from the design method is ~23 ppm-mol. The process engineer would have to judge whether the increase in y_{out} is acceptable. If the process simulation has considered an appropriate design margin, such an increase should be tolerated.

Symbols

a_I	(m^2/m^3)	Effective gas-liquid interfacial area per unit volume of packing
A_{col}	(m^2)	Column cross-sectional area
d_h	(m)	Hydraulic or equivalent diameter of the packing
D_G	(m^2/s)	Gas phase diffusivity
g	(m/s^2)	Gravitational constant, $g = 9.81\ m/s^2$
h_p	(m)	Packing height
$HETP$	(m)	Height equivalent to a theoretical plate
HTU_G	(m)	Height of gas side transfer unit
HTU_L	(m)	Height of liquid side transfer unit
HTU_{OG}	(m)	Height of transfer unit overall gas
k	(-)	Gas-liquid equilibrium ratio or k-value (Ratio of the gas phase and liquid molar concentrations of a component)
k_{Sh}	(-)	Sherwood constant
L_P	(m)	Wetted perimeter, as defined by Tsai et al. [4]
L/G	(-)	Slope of the operating line
m	(-)	Slope of the equilibrium line
NTS	(-)	Number of theoretical stages
NTU_{OG}	(-)	Number of transfer units overall gas
Re_G	(-)	Reynolds number for the gas phase
Sc_G	(-)	Schmidt number for the gas phase
Sh_G	(-)	Sherwood number for the gas phase
u_G	(m/s)	Superficial gas velocity
$u_{G.eff}$	(m/s)	Effective gas velocity
x_{in}	(mol/mol)	Concentration of the component in the liquid inlet (to the pumparound)
y_{in}	(mol/mol)	Concentration of the component in the gas inlet (to the pumparound)
y_{out}	(mol/mol)	Concentration of the component in the gas outlet (from the pumparound)

Greek

β_G	(m/s)	Gas side mass transfer coefficient
ρ_G	(kg/m^3)	Gas density
ρ_L	(kg/m^3)	Liquid density
λ	(-)	Stripping factor, $\lambda = m / (L/G)$
η_G	(Pa·s)	Gas dynamic viscosity
σ	(N/m)	Liquid surface tension

References

1. Taylor, R., & Duss, M. (2019). 110th Anniversary: Column Efficiency: From Conception, through Complexity, to Simplicity. Industrial & Engineering Chemistry Research, 58 (36), 16877-16893.
2. Zogg, M. (1972). Strömungs- und Stoffaustauschuntersuchungen an der Sulzer-Gewebepackung. Zürich: ETH Zürich.
3. Bravo, J., Rocha, J., & Fair, J. (1985). Mass Transfer in Gauze Packings. Hydrocarbon Processing, 64, 91-95.
4. Tsai, R., Seibert, A., Eldridge, R., & Rochelle, G. (2010). A Dimensionless Model for Predicting the Mass-Transfer Area of Structured Packing. AIChE Journal, 57, 1173-1184.

Determination of the Pressure-Swing Distillation Sequence for a Feed Composition Range by Surrogate Model-Based Optimisation

Ömer Faruk Karaman, Csaba Kassai, Andras Szigedi, Peter Lang, Laszlo Hegely
Budapest University of Technology and Economics, Budapest, Hungary;

Abstract
Pressure-swing distillation (PSD) separation of the mixture water(A)–ethylenediamine(B) forming a maximum-boiling azeotrope is optimised by surrogate model-based optimisation (SMBO). The total annual cost is minimised, and the resulting optima are verified through rigorous simulations. The feed composition is varied between those of the high- (HP) and low-pressure (LP) azeotrope. The feed enters the low-pressure column (LPC). The low- and high-pressure column (HPC) are modelled separately in order to improve convergence. A large number of simulations are performed in points generated in the space of the four input variables (number of trays of the columns, recycle flow rate, composition of the bottom product of LPC and the feed composition) by Latin hypercube sampling. Algebraic surrogate models are fitted in ALAMO to reboiler heat duties and column diameters. By comparing the results with those obtained formerly for the other (HP-LP) sequence, the optimal sequence is determined over the feed composition range.

Keywords
pressure-swing distillation; surrogate model-based optimisation; total annual cost; azeotrope

1. Introduction

Pressure-swing distillation (PSD) is widely used for separating pressure-sensitive azeotropic mixtures, although it involves significant energy consumption due to the high recycle flow rates. In continuous operation, the system consists of a low-pressure (LP) and a high-pressure (HP) column. The advantage of PSD is that it does not require the addition of a new (third) component, such as extractive or heteroazeotropic distillation. The configuration of the system depends not only on the type of homoazeotrope but also on the feed composition (z). If z lies between the azeotropic compositions at the pressures of the two columns, the feed can be introduced into either the low-pressure (LP–HP sequence) or the high-pressure (HP–LP sequence) column. Depending on z, one of the sequences will be optimal with respect to either (or both) total energy cost (TEC) or (and) total annual cost (TAC).

PSD systems are typically optimised either with local methods (e.g. Li et al., 2016), which may not find the global optimum, or with global evolutionary algorithms (e.g. genetic algorithm, GA), which require many simulations. A possible approach to reduce computational demand is surrogate model-based optimisation (SMBO), where the objective function is estimated using surrogate models (SMs) fitted to simulation results. Karaman et al. (2025) investigated the PSD separation of the maximum-boiling azeotropic mixture of water–ethylenediamine, where z (35 mol% water) lay between the azeotropes at 0.1 and 2.02 bar, thus making both feeding options available. They minimised TAC both without and with heat integration. The optimisation was carried out using a GA and SMBO. By SMBO, algebraic SMs were fitted to the simulation results by using the ALAMO software (Cozad et al., 2014).

Hegely and Lang (2025) then further studied the HP-LP sequence by treating z as a variable in the SMs and solving the optimisation problem for different z values. They also modelled the columns separately to improve the accuracy of the SMs. They concluded that TAC and TEC showed a maximum as a function of z, and that the SM estimates were generally accurate (TAC error < 6%, except at the lowest z value).
The aim of this study is to optimise the other sequence (LP-HP) by following the method of Hegely and Lang (2025) and to compare the results of the two sequences to determine the range of feed composition where each sequence is optimal.

2. Methodology

Water (A) and ethylenediamine (B) form a maximum-boiling azeotrope at pressures below 4–4.5 bar. The azeotrope is pressure-sensitive: its content of A decreases from 44.1 mol% at 0.10 bar to 25.6 mol% at 2.02 bar. The vapour-liquid equilibrium was described using the UNIQUAC model (Ferchichi et al., 2022).
The separation is performed using a PSD system comprising two columns. The feed composition z can vary between 27 and 43 mol%, and both components must be recovered with 99.5 mol% purity ($x_{D,LP}$=0.005, $x_{D,HP}$=0.995). The flow rate of the fresh feed (F) is 100 kmol/h. The feed is introduced at 2.02 bar and 46.85 °C.
The distillate of the low-pressure column (LPC, D_{LP}) is component B, while its bottom product (W_{LP}) has a variable composition ($x_{W,LP}$) and is sent to the high—pressure column (HPC). From this second column, component A is obtained as distillate (D_{HP}), and the bottom product, is returned to the LPC as a recycle stream with a molar flow rate of W_{HP}=F_{rec} and a composition of $x_{W,HP}$.
The two columns are modelled separately in the professional flow-sheet simulator CHEMCAD because it is easier to achieve convergence. The LPC model is shown in Figure 1. Pure A (stream [2]) and pure B (stream [1]) enter a mixer (1), thereby obtaining stream [4] with molar flow rate W_{HP}=F_{rec} and composition $x_{W,HP}$. After a pressure reduction (2), this stream is passed through a heat exchanger (3) to ensure a bubble-point feed condition. The fresh feed stream F [10] is obtained by mixing pure A and B streams ([7] and [8)], respectively), as well. The column is specified by setting the value of the distillate purity and the bottom mole flow rate (W_{LP}), calculated as W_{LP}=F_{rec}+D_{HP}. D_{HP} can be expressed from the material balance of the PSD system as a linear function of z from the values of F, z, $x_{D,LP}$ and $x_{D,HP}$:

$$D_{HP} = 101.01 - 0.505 \cdot z \quad (1)$$

The two terms of Eq. (1) are calculated by two controller modules. The flow rate of stream [13] is the constant. The flow rate of stream [15] is set in divider (9) by controller (8), which multiplies the flow rate of stream [11], 0.505 kmol/h with z (read from stream [10]). Thus, D_{HP} is obtained in stream [14]. Finally, controller no. (4) sets the reboiler specification as the sum of the molar flow rates of stream [14] and that of the recycle stream [6] (F_{rec}). Controller no. (7) sets the column pressure drop (5) by multiplying the number of stages and the pressure drop of a single stage, given as the pressure of stream [11].
In the HPC model, the column is specified by fixing the distillate composition and the bottom molar flow rate. The D_{HP} value was treated as an input parameter instead of z, and a controller was used to adjust the reboiler specification so that the required bottom molar flow rate (F_{rec}) was satisfied consistently.
The input variables for both columns are the number of trays N_{LP} or N_{HP}, F_{rec}, $x_{W,HP}$ and z. For both columns, k=500 points are generated in the four-dimensional space of the input variables by using Latin hypercube sampling (LHS). The range of the variables (Table 1) is divided into k equal parts; thus, the hypercube consists of k^4 cells. Then k cells are selected randomly such that from each interval of every

variable exactly one cell is selected. In each selected cell, a point is randomly chosen from a uniform distribution.

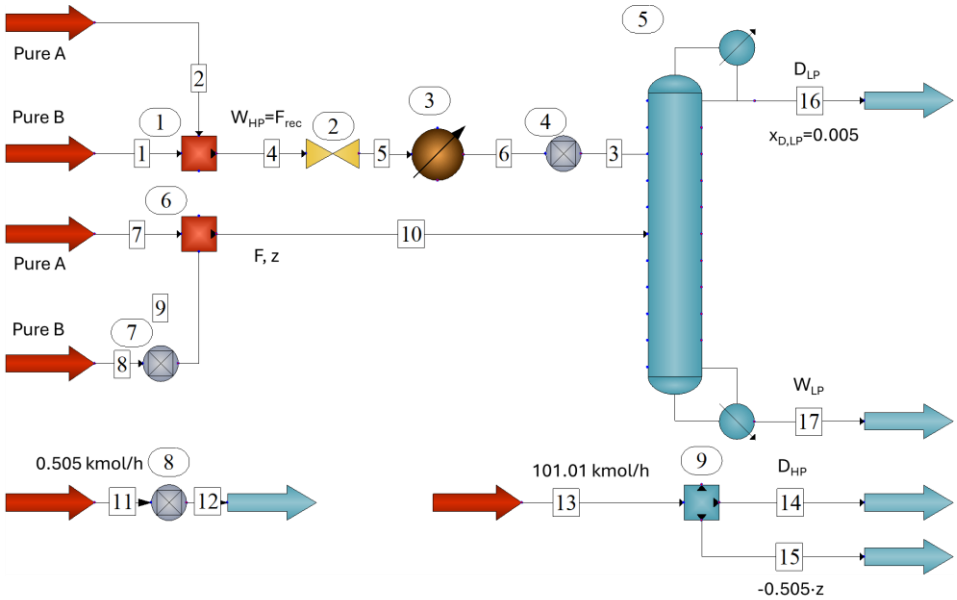

Figure 1: CHEMCAD model of LPC.

Input variables	Minimum	Maximum
N_{HP}	35	90
N_{LP}	15	50
F_{rec}, kmol/h	100	220
$x_{W,HP}$	0.26	0.30
z	0.27	0.43

Table 1: The ranges of the input variables.

The Latin hypercube is generated in Excel using VBA. For each point, Excel calls CHEMCAD to perform the simulations. The feed locations are varied until the minimum reboiler heat duty is reached. This procedure ensures optimal feed locations while removing them from the set of optimisation variables, which reduces the dimensionality of the surrogate-model problem. Results are then sent back to Excel. If a simulation does not converge, the file is reloaded, and it is marked as not converging by setting the value of a convergence flag to 0 (which is 1 for converging simulations). Reloading is necessary because the initial value is very important in CHEMCAD, and if the calculation starts from a non-converged simulation, problems may occur even if the simulation would converge for the given input parameters.

Using ALAMO, algebraic SMs are fitted to the reboiler heat duties (Q_{rHP} and Q_{rLP}, in MJ/h) and the column (internal) diameters (Di_{HP} and Di_{LP}, in m). It was not necessary to fit models to the condenser heat duties (Q_{cHP} and Q_{cLP}, in MJ/h) because they can be expressed from the reboiler heat duties with linear equations:

$$Q_{cLP} = -0.9997 \cdot Q_{rLP} - 872.5 \quad (2)$$

$$Q_{cHP} = -0.9668 \cdot Q_{rHP} - 931.4 \quad (3)$$

In both cases, the coefficient of determination (R^2) is close to 1 (LP: 0.9773; HP: 0.9988), indicating an accurate fit. SMs are also fitted to the convergence flags of the LPC and HPC simulations to predict convergence. Additionally, the SMs fitted by Hegely and Lang (2025) are used to calculate the temperature of the bottom products. For each heat duty and diameter, they are expressed as a function of four input variables: N_{LP}, F_{rec}, x_{WLP}, z for LPC; N_{HP}, F_{rec}, x_{WHP}, D_{HP} for HPC. It is important

to note that CHEMCAD calculates the diameter as integer or half-integer values in feet. Thus, in ALAMO, the diameter data are converted to feet, multiplied by two and treated as integer variables.

During model fitting, the aim is to achieve a low maximum absolute error and a high R^2 to obtain a more accurate fit. For determining the SMs, in three cases (Q_{rHP}, Q_{rLP} and Di_{HP}), BIC (Bayesian information criterion) is minimised, which penalises a large number of terms, but for Di_{LP}, SSE (sum of squared errors) is used because it yields better results. During fitting, ALAMO is allowed, besides the constant term, to choose linear, exponential, logarithmic, and polynomial functions, as well as different powers of binary or ternary products and ratios of the variables. By changing these options, the fit accuracy could be improved.

The objective function to be minimised is the TAC of the PSD system, calculated by the method of Ferchichi et al. (2022). It consists of the total capital cost (TCC) and the total energy cost (TEC), and a payback period of 3 years is assumed. TCC includes the costs of the columns and of the heat exchangers. TEC is the cost of the low- and medium-pressure heating steam used for LPC and HPC, respectively.

The TAC, calculated by using the SMs, is minimised by MATLAB's fmincon function, using the sequential quadratic programming with the active-set method. The upper and lower bounds of the variables are given as inequality constraints, and initial values of the variables are specified. Additionally, the SMs of the convergence flags are used as equality constraints to restrict the search to the predicted feasible region. After this, the effect of the input parameters on TAC is examined in pairs visually to prevent potentially false local optimum, since if the value of a variable is on its bounds, the models might extrapolate to low, incorrect TAC values. If this is the case, the bound of the variable is modified; otherwise, at this final value, it is then checked whether, by entering the obtained input parameters into ChemCAD, the same heat duties and diameters are obtained as from the SMs.

3. Results and discussion

The optimisation problem was solved for 9 feed composition values in the range 0.27 - 0.43. Table 2 summarises the optimal values of the optimisation variables.

z	N_{HP}	N_{LP}	F_{rec}, kmol/h	$x_{W,HP}$
0.27	40	20	169.7	0.2997
0.29	90	20	132.3	0.2854
0.31	71	20	137.3	0.2848
0.33	67	20	139.4	0.2849
0.35	40	20	175.3	0.2925
0.37	41	20	174.9	0.2996
0.39	44	37	181.4	0.2998
0.41	72	21	178.9	0.2923
0.43	88	43	183.0	0.2986

Table 2: Optimal values of the optimisation variables for different feed compositions.

N_{HP} does not show a consistent trend. Its values ranged from 40 to its upper bound of 90 (at z = 0.29). N_{LP} was at its lower bound (20) for z ≤ 0.37, increasing to 37 at z = 0.39 and to 43 at z = 0.43. The optimal F_{rec} values ranged from 132.35 to 183.02 kmol/h, with a generally increasing trend on the increase of z. The lowest value was obtained at z = 0.29, the highest one at z = 0.43. $x_{W,HP}$ values remained within a narrow interval (0.2848 to 0.2998), close to the upper bound of 0.3. $x_{W,HP}$ virtually

reached the upper bound for the z values of 0.27, 0.37, 0.39 and 0.43. These results indicate that the optima might lie outside of the bounds of one or more optimisation variables, with the potential exception of z = 0.41 and 0.43. An extension of the variable ranges would be necessary to verify this hypothesis. The convergence constraints were active for all z values studied.

Figure 2a compares the costs calculated from the surrogate models in the determined optima (TAC*, TEC*, TCC*) with the rigorously calculated costs obtained by running CHEMCAD at the same optima (TAC, TEC, TCC).

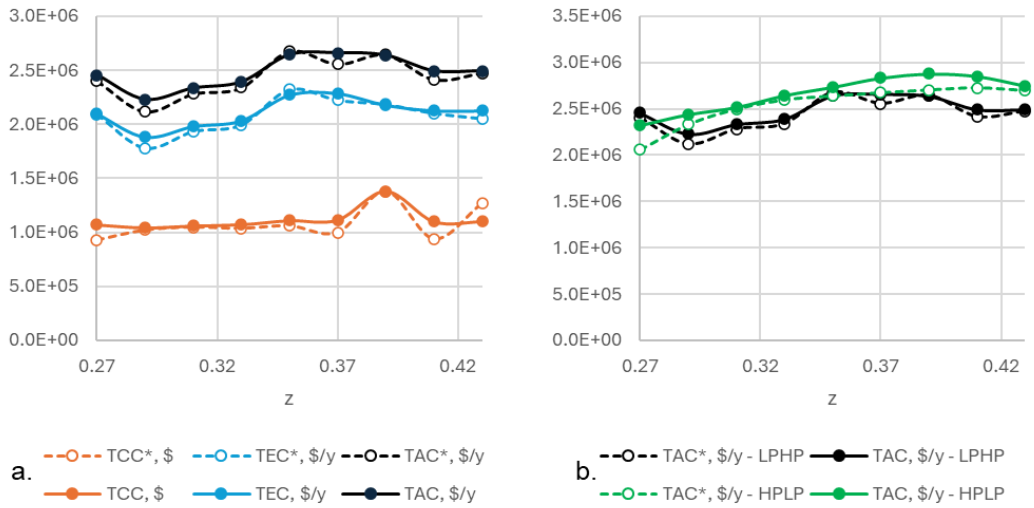

Figure 2: a. Estimated and rigorously calculated costs as functions of z (LP-HP sequence), b. estimated and calculated TAC as functions of z for both sequences.

TCC varied only slightly except for z = 0.39, where it had a maximum because of the higher N_{LP}. For z values between 0.29 and 0.39, the SMs reproduced TCC closely, with deviations ranging from −0.05% to +10.4%. At z = 0.27, TCC is underestimated by 13.3%. At z = 0.41, the SMs underestimated the TCC by 14.6%, and overestimated it by 15.1% at z = 0.43.

TEC decreased from z = 0.27 to 0.29 and increased until a maximum at 0.37. Then, it decreased slightly towards the upper limit of z. Its variation was influenced significantly by that of F_{rec}. For TEC, differences between estimations and calculated values were smaller (maximum 5.5%). For all the z values studied, except for 0.35 and 0.39, the models slightly overestimated the TEC. At z = 0.35, TEC* was higher than TEC by 2.27%. At z = 0.39, TEC* was higher by only 0.30%.

The variation of TAC was largely governed by TEC; thus, TAC showed a very similar trend to TEC, with a minimum and a maximum at the same z values. For TAC, SMs predicted the calculated results well. TAC was underestimated from 0.72% to 5.00% for all the z values except for 0.35 and 0.39, which were overestimated by 1.32% and 0.26%, respectively.

The two sequences were compared with respect to estimated and calculated TAC values across the studied feed composition range (Figure 2b). Relative to the HP-LP results of Hegely and Lang (2025), the LP-HP sequence gave a higher TAC only at the lowest composition (5.73% higher at z = 0.27). Over the remaining range, LP–HP was more favourable, giving a lower calculated TAC by about 3.41–12.60%, with the largest reduction occurring at z = 0.41. This could be explained by the greater average volatility difference of the components in LPC in the z range studied. Accordingly, based on TAC, HP–LP was superior only at z = 0.27, whereas LP–HP

was more favourable for z ≥ 0.29, and the change in the superior sequence was indicated to occur between 0.27 and 0.29.
Finally, the results of the LP-HP sequence for z = 0.35 were compared with those obtained by Karaman et al. (2025) by SMBO. While F_{rec} and $x_{W,HP}$ had similar values (169.8 kmol/h and 0.290, respectively), both tray numbers were much higher: N_{HP}=77 and N_{LP}=35. Consequently, TCC was 42.2% lower than the previous result, but TEC was 19.3% higher, resulting in a TAC value higher by 3.77%.

4. Conclusion

Hegely and Lang (2025) applied surrogate model-based optimisation to the HP-LP sequence of the pressure-swing distillation of a water-ethylenediamine maximum-boiling azeotropic mixture, with TAC as the objective function. In this work, their methodology was extended to the LP–HP sequence and used to compare the TAC of the two column sequences as functions of the feed composition z, with the determined optima verified by rigorous CHEMCAD simulations.
The columns were modelled separately in CHEMCAD, and 500-500 points were generated by Latin hypercube sampling in Excel (VBA) over the four input variables. For each point, the feed locations were adjusted to minimise reboiler duties; algebraic surrogates were fitted in ALAMO to the reboiler duties and column diameters. The TAC described by the surrogate models were minimised in MATLAB, and the optima were verified by rigorous CHEMCAD simulations.
For the LP–HP sequence, the surrogate models estimated TCC and TEC well for 0.29 ≤ z ≤ 0.39, while larger deviations were observed at z = 0.27, 0.41, and 0.43. The differences in TEC remained smaller overall. As a consequence, the surrogate-based TAC values slightly underestimated the CHEMCAD results in most cases, although at z = 0.35 and z = 0.39 TAC was overestimated.
The comparison based of the rigorously calculated TAC values of the two column sequences indicated that HP–LP one was superior only at the lowest water concentration (z = 0.27), whereas LP–HP was more favourable for z ≥ 0.29. Accordingly, the change in the superior sequence was found to occur between z = 0.27 and z = 0.29. The general superiority of LP-HP could be explained by the greater average difference in the volatility of the components in LPC.

Acknowledgements

This research was funded by the National Research Development and Innovation Fund of Hungary (OTKA FK-143059) and by the János Bolyai Research Scholarship of the Hungarian Academy of Sciences. Mr Karaman would like to thank the Mecenatúra Grant of the National Research Development and Innovation Fund of Hungary for the financial support of his participation at the conference.

References

Cozad, A., Sahinidis, N. V., & Miller, D. C. (2014). Learning surrogate models for simulation-based optimization. AIChE Journal, 60(6), 2211–2227.
Ferchichi, M., Hegely, L., & Lang, P. (2022). Economic and environmental evaluation of heat pump-assisted pressure-swing distillation of maximum-boiling azeotropic mixture water-ethylenediamine. Energy, 239, 122608.
Hegely, L., & Lang, P. (2025). Surrogate Model-Based Optimization of Pressure-Swing Distillation Sequences with Variable Feed Composition. Systems and Control Transactions, 4, 192–197.
Karaman, Ö. F., Lang, P., & Hegely, L. (2025). Optimisation of pressure-swing distillation of a maximum-azeotropic mixture with heat integration. Energy, 320, 135190.
Li, R., Ye, Q., Suo, X., Dai, X., & Yu, H. (2016). Heat-Integrated Pressure-Swing Distillation Process for Separation of a Maximum-Boiling Azeotrope Ethylenediamine/Water. Chemical Engineering Research and Design, 105, 1–15.

Evaluation of Diglyceride and Monoglyceride Influence on Ethanolic Biodiesel Distillation Systems

Ian Brenno Barbosa Batata, Victor Hugo dos Santos Ramos, Maria Regina Wolf Maciel, Nadia Gagliardi Khouri, Rubens Maciel Filho
[1]Universidade Estadual de Campinas, Campinas, Brazil

Abstract

The global dependence on non-renewable energy sources remains a major concern. Brazil, however, has reached an important milestone, with renewable sources representing 50% of its Internal Energy Supply. This progress is largely due to the country's investment in biofuels, particularly ethanol and biodiesel. As a result, biodiesel production is expanding, drawing attention to the technical challenges involved in its synthesis and purification. Transesterification of vegetable oils with short-chain alcohols is the most adopted route for biodiesel production. This reaction produces monoalkyl esters (biodiesel) and glycerol, along with diglycerides and monoglycerides as intermediates. Efficient separation after the reaction is crucial because residual glycerol and partially converted glycerides can compromise fuel purity and stability. Diglycerides and monoglycerides present particular challenges due to their boiling points, which are close to those of biodiesel. Their presence hinders purification via conventional distillation, reduces biodiesel yield, and may cause operational issues such as column fouling and increased pressure drops. Biodiesel produced with ethanol tends to contain higher levels of these intermediates, making their analysis even more relevant. This work evaluates the influence of diglycerides and monoglycerides formed during ethanolic transesterification on the performance of a distillation column using Aspen Plus®. The study assesses how reaction conversion affects downstream separation. Simulation results show that increasing mono- and diglyceride content significantly raises reboiler duty about 18.5%. On an annual basis of 8,000 operating hours, the additional thermal energy requirement is estimated at approximately 480,000 kWh. These findings demonstrate that elevated concentrations of intermediate glycerides compromise separation efficiency and increase energy consumption and greenhouse gas emissions. Controlling their formation is therefore essential for achieving sustainable biodiesel production.

Keywords
Biodiesel Purification; Ethanolic Transesterification; Mono- and Diglycerides; Distillation Simulation; Energy Consumption; Greenhouse Gas Emissions.

1. Introduction

Energy is a fundamental factor in economic growth [1]. Accordingly, global energy demand has increased rapidly, and non-renewable sources such as coal, oil, and natural gas are employed to attend this demand, demonstrating a persistent

dependence on fossil fuels [2,3]. However, energy derived from non-renewable sources accounts for a substantial share of global greenhouse gas (GHG) emissions [4]. Therefore, an energy transition is essential to promote cleaner and more sustainable alternatives, including solar, wind, biofuels, hydrogen, and other renewable energy systems [5].

In this context, Brazil achieved a remarkable progress, with renewable sources accounting for 50% of its Internal Energy Supply, in stark contrast to the global average of 14.3% [6]. This achievement is attributed to the country's investment in biofuels, particularly ethanol and biodiesel. In 2024, biodiesel consumption in Brazil increased by 19.3%, and the mandatory blending level in conventional diesel rose to 14% v/v [7]. Consequently, demand for biodiesel production is growing, highlighting the need to address technical challenges in its production process.

Transesterification (or alcoholysis) is the dominant industrial route for biodiesel production and consists of the reaction of triglyceride vegetable oils with short-chain alcohols, yielding monoalkyl esters (biodiesel) and glycerol as the main products, alongside diglycerides and monoglycerides as intermediates [8,9]. The post-reaction separation step is fundamental, as residual glycerol and partially converted glycerides can significantly compromise the purity, storage stability, and ASTM compliance of the final fuel [10]. Diglycerides and monoglycerides have boiling points similar to those of biodiesel, hindering efficient purification through conventional distillation. Their accumulation in heavy fractions may reduce biodiesel yield and cause operational issues such as column fouling, higher pressure drops, and diminished separation selectivity [11]. It is also worth noting that biodiesel produced using ethanol experiences a notable presence of these intermediate products, so a rigorous analysis in this case is required [12].

2. Results and discussion

2.1 Methodology Overview

Different transesterification pathways and conversion efficiencies directly affect biodiesel purification by distillation, as they alter the composition of the feed stream entering the separation unit. Lower conversion levels result in higher concentrations of mono- and diglycerides in the organic phase. These partially converted glycerides exhibit higher boiling points and lower volatility compared to fatty acid ethyl esters, making phase separation and distillation more challenging [13]. As a result, higher energy input is required in the distillation column to achieve a specified biodiesel purity. Conversely, transesterification routes operating at higher conversion efficiencies reduce the content of mono- and diglycerides, increasing the volatility difference among components and lowering the reboiler duty. This behavior has been reported in process simulations and techno-economic assessments of biodiesel production [13].

Palm oil was selected as the feedstock for this study, with its compositional profile defined according to data reported by Che Man et al. (1999) [14]. Figure 1 presents the Aspen Plus process flowsheet used to simulate the transesterification of palm oil for biodiesel production. The process comprises mixing the ethanol, palm oil, and sodium hydroxide feed streams, then sending the mixture to the transesterification

reactor, where biodiesel is generated. The reactor effluent is subsequently directed to a distillation column to recover unreacted ethanol in the overhead stream, which is recycled to the transesterification unit. The column bottoms are then sent to the downstream purification train, where unreacted oil is separated and both the biodiesel product and the glycerol byproduct are further refined.

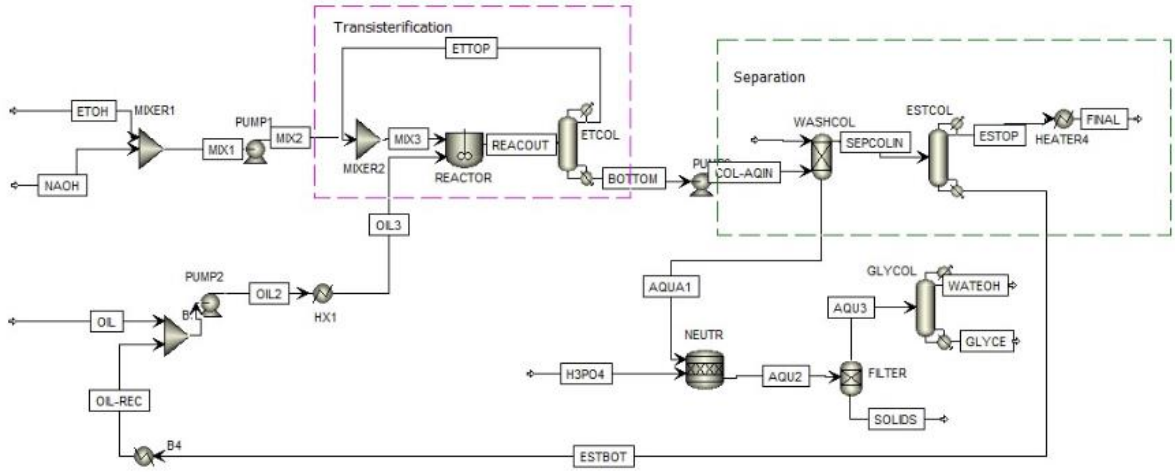

Figure 1. Aspen Plus transterification simulation design

To simulate a realistic operating scenario, the ethanol-to-oil molar ratio was defined as the key variable for controlling the concentrations of mono- and diglycerides. Ratios ranging from 3:1 to 9:1 were evaluated. Sodium hydroxide was employed as a homogeneous catalyst at a concentration of 1 wt% relative to the oil feed and the transesterification reaction was represented in an RCSTR at 70 °C and 4 bar, with operating conditions and kinetics taken from literature sources [15]. Ethanol recovery was modeled in the ETCOL distillation column, which is designed with 20 stages, a total condenser, a kettle reboiler, and a feed introduced at stage 8, with a reflux ratio of 2. Phase separation was simulated in a wash column WASHCOL with 6 stages, using glycerol to separate aqueous and organic phases. The final biodiesel purification was conducted in the ESTCOL distillation column, which comprises 20 stages, with feed at stage 12, a total condenser, a kettle reboiler, and a reflux ratio of 1. The column configuration was defined to achieve a biodiesel purity of 98.3 mol% in the base case (ethanol-to-oil ratio of 6:1), which was then used as a reference to evaluate the energy demand required to reach the same purity under different operating scenarios.

2.2 Influence of the feed ration on the Energy Demand

As expected, decreasing the ethanol-to-oil ratio leads to a significant increase in the content of reaction intermediates. When the ratio is reduced from 9:1 to 3:1, the mono-/diglyceride concentration increases from approximately 2.15% to 13.17%, indicating a strong dependence of conversion efficiency on alcohol excess. This increase in intermediate glycerides impacts the performance of the distillation column, Table 1 and Figure 2a summarize such influence on the energy demand. The higher demand can be explained by the characteristics of the Mono- and diglycerides, which present higher boiling points and lower volatility than fatty acid ethyl esters, reducing the relative volatility between components in the separation system. As a

consequence, higher energy input is required in the reboiler to maintain the target biodiesel purity. This behavior is observed in Figure 2b, where the reboiler duty increases almost linearly with increasing mono-/diglyceride content. Comparing the base case (6:1) with the lowest ethanol-to-oil ratio evaluated (3:1), the reboiler duty rises from approximately 325 kW to 385 kW, corresponding to an increase of about 18.5%. On an annual basis of 8,000 operating hours, the additional thermal energy requirement is estimated at approximately 480,000 kWh. Furthermore, increasing the ethanol-to-oil ratio beyond 6:1 leads to progressively lower mono-/diglyceride concentrations and a moderate reduction in reboiler duty. However, the marginal energy savings diminish at higher ratios, as indicated by the smaller differences observed between 7:1, 8:1, and 9:1.

Table 1: Effect of the ethanol-to-oil ratio on mono-/diglyceride content and energy consumption in the biodiesel purification column.

Etanol:oil	3:1	4:1	5:1	6:1	7:1	8:1	9:1
Reboiler Duty (kW)	385.4	349.8	333.5	325.4	321.3	319.0	317.8
Flow (kg/h)	1325.2	1215.4	1166.9	1141.8	1126.6	1116.7	1109.6
Energy consumption (kW/kg)	0.2908	0.2878	0.2858	0.2850	0.2852	0.2857	0.2864
Di-monoglyceride (%)	13.17	8.05	5.47	4.04	3.15	2.57	2.15

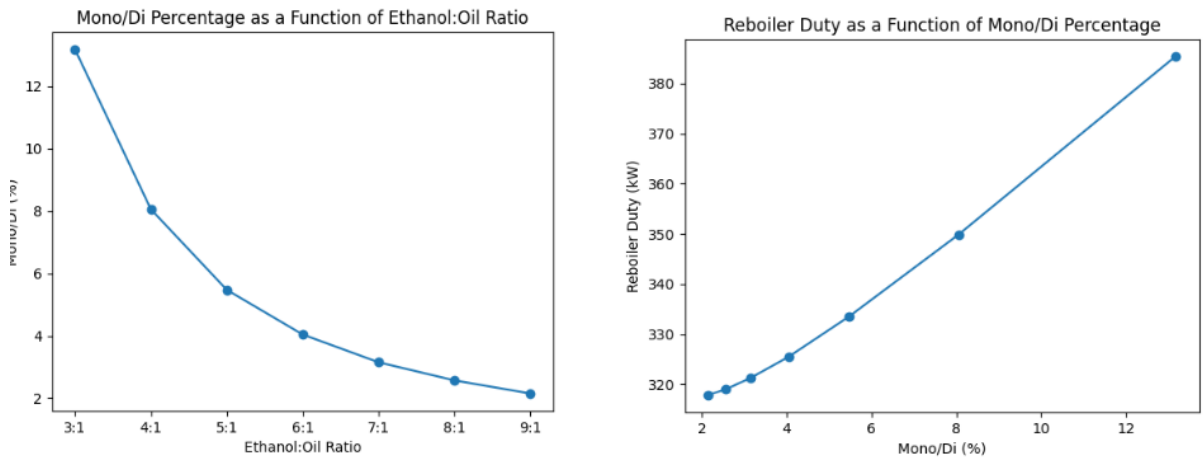

Figure 2. (a) Mono- and diglyceride concentration as a function of ethanol-to-oil ratio; (b) reboiler duty as a function of mono-/diglyceride concentration.

The same conclusion can be drawn by analyzing the energy demand as a function of the different ratios (Figure 3). Figure 3a shows that reboiler duty decreases as the ethanol-to-oil ratio increases, with the largest drop occurring between 3:1 and 6:1. Beyond this range, further ethanol excess yields only minor energy savings, indicating diminishing returns in separation efficiency. Figure 3b presents the reboiler duty normalized by feed mass flow (kW·h kg^{-1}). Higher ethanol-to-oil ratios lower mono- and diglyceride concentrations and slightly reduce absolute duty, but they also raise feed flow due to excess unreacted ethanol. As a result, normalized energy

consumption reaches its minimum at 6:1 and rises at higher ratios, as the extra energy per unit of mass offsets the benefits of improved volatility. This highlights a trade-off between conversion and separation. Low ratios increase high-boiling intermediates, while excessive ethanol raises feed flow and energy demand per unit mass. Under the evaluated conditions, a 6:1 ratio is the most energy-efficient for biodiesel purification.

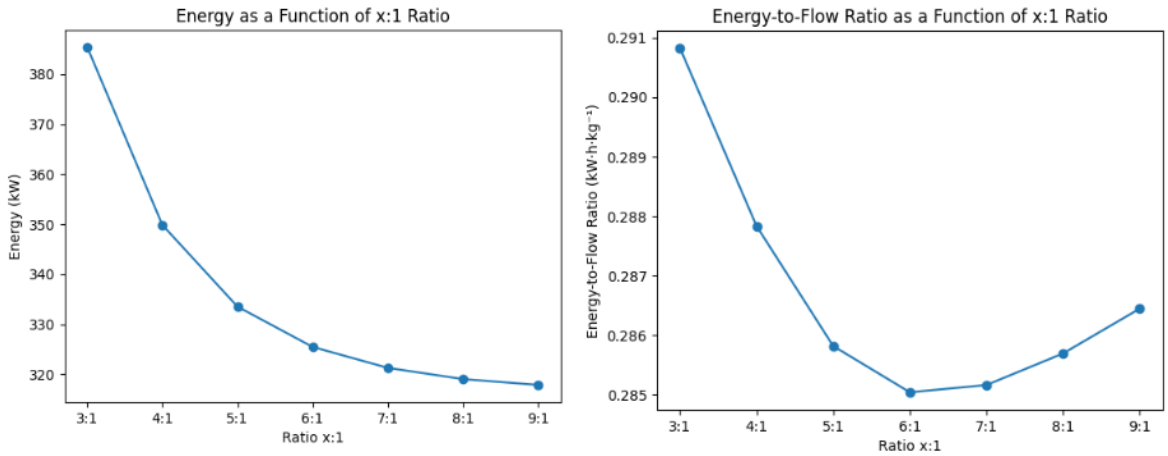

Figure 3. (a) Reboiler duty as a function of ethanol-to-oil ratio; (b) normalized energy demand (reboiler duty per mass flow rate) as a function of ethanol-to-oil ratio.

3. Conclusions

The results show that the reboiler duty in biodiesel purification is primarily controlled by the concentration of mono- and diglycerides in the feed. Higher contents of these intermediates significantly increase the thermal load due to their high boiling points and low volatility. Upstream inefficiencies propagate downstream, increasing the overall energy demand and enviromental burden. Thus, increasing the ethanol-to-oil ratio reduces mono- and diglyceride formation and lowers the absolute energy necessary; however, excessive alcohol excess increases the feed flow rate and raises the energy requirement per unit of flow. Under the evaluated conditions, an ethanol-to-oil ratio of 6:1 provides the best compromise, minimizing mono-/diglyceride content and thermal energy demand in the distillation column. Future studies should extend this results focusing in heat integration and life-cycle assessment to fully evaluate the sustainability of the biodiesel prodution.

Acknowledgements

This study was financed in part by the support of São Paulo Research Foundation (FAPESP), Brasil – Process Number #2022/16379-8. We also acknowledge the Universidade Estadual de Campinas (UNICAMP) and the School of Chemical Engineering, Campinas, SP, Brazil.

References

[1] KAPLAN, J. O.; HARTMANN, J.; LAMMEL, G.; LENTON, T. M. Climate change and air quality impacts of bioenergy. Energy Policy, vol. 96, pp. 351–360, 2016. https://doi.org/10.1016/j.enpol.2016.10.007

[2] MORAIS, S.; COSTA, M.; SILVA, A. Environmental impacts of biodiesel production: A review. Environmental Science and Pollution Research, vol. 28, pp. 12345–12360, 2021. https://doi.org/10.1007/s11356-020-11186-0
[3] ALMEIDA, R. et al. Advances in sustainable fuel technologies. Discover Energy, vol. 1, 00117, 2024. https://doi.org/10.1007/s44246-024-00117-0.
[4] SANTOS, G.; DAVIES, A.; KAY, P. Aviation decarbonisation: Policy challenges and pathways. Climate Policy, vol. 21, no. 3, pp. 345–360, 2021. https://doi.org/10.1080/14693062.2020.1864267
[5] RODRIGUES, L. et al. Cleaner production pathways for biofuels. Cleaner Production Letters, vol. 1, 100026, 2022. https://doi.org/10.1016/j.clpl.2022.100026
[6] EMPRESA DE PESQUISA ENERGÉTICA (EPE). Balanço Energético Nacional 2025. Rio de Janeiro: EPE, 2025. Available online.
[7] BRASIL. Ministério de Minas e Energia. B14 biodiesel blending mandate comes into force. Brasília, 2024. Available online.
[8] DEMIRBAS, A. Progress and recent trends in biofuels. Renewable and Sustainable Energy Reviews, vol. 9, pp. 1–25, 2005. https://doi.org/10.1016/j.rser.2004.09.002
[9] LIU, Y. et al. Recent advances in reaction engineering for renewable chemicals. Results in Chemistry, vol. 7, 102678, 2025. https://doi.org/10.1016/j.rechem.2025.102678
[10] DEMIRBAS, A. Biofuels sources, biofuel policy, biofuel economy and global biofuel projections. Renewable Energy, vol. 35, pp. 231–238, 2010. https://doi.org/10.1016/j.renene.2010.07.019
[11] SILVA, R. et al. Carbon capture and storage routes for sustainable fuels. Current Chemical Science and Technology, vol. 1, 100264, 2024. https://doi.org/10.1016/j.ccst.2024.100264
[12] ZHANG, X. et al. Process optimization strategies for biodiesel production. Processes, vol. 10, no. 1, 12, 2022. https://doi.org/10.3390/pr10010012
[13] ZHANG, Y.; DUBE, M. A.; MCLEAN, D. D.; KATES, M. Biodiesel production from waste cooking oil: Process design and technological assessment. Bioresource Technology, vol. 89, pp. 1–16, 2003.
[14] CHE MAN, Y. B.; HARYATI, T.; GHAZALI, H. M.; ASBI, B. A. Composition and thermal profile of crude palm oil and its products. Journal of the American Oil Chemists' Society, vol. 76, pp. 237–242, 1999.
[15] NARVÁEZ, P. C.; NORIEGA, M. A.; CADAVID, J. G. Kinetics of palm oil ethanolysis. Energy, vol. 83, pp. 337–342, 2015.

Evaluation of Fractionation Strategies for Sustainable Aviation Fuel in the Ethanol-to-Jet Process

Matheus de Lucena Facione Pereira[1], Victor Hugo dos Santos Ramos[1], Tarcila Cazetta[2], Maria Regina Wolf Maciel[1], Nadia Gagliardi Khouri[1], Rubens Maciel Filho[1]
[1]Universidade Estadual de Campinas, Campinas, Brazil
[2]Federal Institute of São Paulo, Boituva, Brazil

Abstract

Aviation accounts for approximately 2.7% of global CO_2 emissions and remains one of the most carbon-intensive human activities, driving the search for sustainable alternative energy sources. In this context, the sector has increasingly focused on the production of Sustainable Aviation Fuel (SAF), which currently offers greater technological feasibility than electrification or hydrogen-based propulsion. A critical aspect of SAF development is to select an efficient synthesis route and design downstream processes that ensure the fuel specifications. Among the available pathways, the ethanol-to-jet (ETJ) route stands out for its versatility, given the widespread availability of ethanol, compatibility with existing petrochemical infrastructure, and compliance of the final product with ASTM D7566 standards. This route involves four main stages: (i) ethanol dehydration to generate ethylene, (ii) oligomerization of ethylene into C_8-C_{16} hydrocarbons, (iii) hydrogenation to improve fuel properties, and (iv) fractionation to separate jet, diesel, and light cuts. The refining and fractionation stages are particularly energy-intensive and must be optimized to ensure economic and environmental feasibility. In this study, Aspen Plus is employed to simulate the fractionation step within the ETJ process. Through this platform, it is possible to analyze mass and energy balances, separation efficiencies, and heat-integration opportunities, as well as to conduct sensitivity analyses to assess how operating parameters (column pressure, reflux ratio, and stage feed) affect the yield and purity of the jet fuel fraction. Such simulations provide valuable insights for the optimization of downstream processing, contributing to a more sustainable implementation of the ethanol-to-jet route for SAF production.

Keywords
Sustainable Aviation Fuel (SAF); Ethanol-to-Jet (ETJ); Distillation Simulation; Aspen Plus; Energy Balances; Jet Fuel Purity.

1. Introduction

The aeronautical sector transported approximately 4.5 billion passengers and USD 7.2 trillion in goods in 2019, demonstrating its indispensable role in modern society. However, it is also a major emitter of greenhouse gases (GHG), accounting for 2.5% of all anthropogenic GHG emissions in 2023, and it is estimated to reach emissions of 500 Mt of CO_2 by 2050.[1,2,3] The sector's high energy demand and aircraft weight constraints hinder electrification as a means of reducing these emissions. Nevertheless, sustainable aviation fuels (SAF) represent a promising alternative. This

option can reduce CO_2 emissions by up to 80% compared to conventional fossil fuels, in addition to lowering emissions associated with production and transportation [4].

There are several routes for SAF production, among which the Ethanol-to-Jet (ETJ) pathway (ASTM D7566-18) stands out [5]. This route begins with a dehydration of ethanol to convert it into ethylene, followed by oligomerization into longer hydrocarbon chains targeting carbon numbers between 8 and 16 (the kerosene range) [1,4]. After the reactive stages, the stream is sent to fractionation, a process essential to obtain a final product that meets ASTM D7566 specifications [6]. The ETJ route is attractive due to feedstock availability and its techno-scientific maturity, considering that global bioethanol production reached 110 billion liters in 2018 [7]. Despite the need to further develop other stages of the route, its starting point is well known and relatively inexpensive (USD 1.58 in January 2026) [8]. Moreover, production can be integrated into biorefineries, reducing the need for structural adaptations [9]. However, advancement in other stages, such as downstream processing, is essential to meet standards [1, 6].

When analyzing the process focusing on fractionation and product composition to obtain a drop-in fuel, several technical challenges emerge that are still poorly studied. While numerous techno-economic feasibility and catalysis studies exist, little emphasis has been placed on downstream stages, despite their importance [10]. Furthermore, a major advantage of effectiveness in this stage, beyond reducing reprocessing costs, is the possibility of drop-in use through blending with fossil fuels (up to 50% vol) [10]. Another essential factor in simulation studies is utility consumption, as this information significantly impacts its feasibility. Additionally, operating conditions are critical due to the influence of parameters such as reflux ratio, top and bottom temperatures, column pressure, and pressure drop on operating costs, product quality, and operational safety [12,13].

For the process study, the Aspen Plus simulator was used. This tool was employed because many systems in chemical engineering, including multicomponent distillation columns, do not have analytical solutions. Due to the need for intensive computational calculations, Aspen Plus and HYSYS were used, as they not only enable system analysis but also allow the study of additional variables and their impacts, such as utility consumption and system sensitivity [14].

2. Results and discussion

2.1 Methodology Overview

The downstream process of the ETJ route was considered as a purification of the stream leaving the reactive stages, according to Romero-Izquierdo et al. (2021) [15]. In this case, since the stream is composed exclusively of linear paraffins, both saturated and unsaturated, the process consists solely of fractional distillation of the mixture. Accordingly, the process was designed by directing the hydrocarbon stream to an adiabatic flash unit to remove volatile components and thereby reduce the feed load to the distillation column. The outlet of the flash drum was then sent to the column where fractional distillation is carried out. For the construction of the simulation, the NRTL thermodynamic model was selected, based on its ability to predict non-ideal behavior and to account for interactions between different components, which is

required due to the variety of compounds in the fractionation stream. In addition, the model provides good results at low pressures, such as those used to evaluate system behavior [16,17].

The simulation was initially carried out using a DSTW column with a reflux ratio of 1.2 to obtain information on the minimum conditions required for a column to separate the high- and low-key components, namely octane and heptane, respectively. Since kerosene is a mixture composed of hydrocarbon chains containing between 8 and 16 carbon atoms, the outlet stream from the first column was used as the feed to a second DSTW column, repeating the procedure with heptadecane and hexadecane as the high- and low-key components, respectively (Table 1).

Table 1: Results containing the minimum design information for the DSTW columns.

	Minimum Reflux Ratio	Minimum # of stages	Distillate temperature	Bottom temperature	Distillate to feed fraction
1st Column	0.194	13	283.2 °C	414.7 °C	0.766
2nd Column	0.008	2	404.2 °C	469.0 °C	0.706

Through preliminary simulations, it was observed that some components were more sensitive to operational and equipment changes than others, with particular emphasis on n-butane, hexane, octane, and tetradecane. Due to the importance of octane for kerosene, it was considered the most critical component for analyzing the effect of the number of stages in the column and its impact on the outlet streams. Regarding the effect of the number of stages in the distillation column, the outlet of heavier components was also evaluated to assess whether mass and heat transfer would be affected to the point that certain components present in the kerosene fraction would leave at higher stages of the column. Based on the DSTW results, the simulation of the fractionation column was carried out using the RADFRAC block of Aspen Plus® V10, employing a column with 65 stages and feed introduced at stage 32. For the side draw outlet streams, the liquid phase was considered, using a feed basis of 0.2, since higher values promoted drying at different stages of the column. Two types of simulations were performed in this study. In the first, the reflux ratio (RR) was fixed on a mass basis at 1.3, and the reboiler vaporization ratio was set to 1.5. Subsequently, the impact of operating pressure variation in the column and the effect of the reflux ratio on outlet composition and flow rate, as well as on the reboiler heat duty, were analyzed. In this analysis, the side draw was taken from stage 18. The interface of simulation is presented in Figure 1.

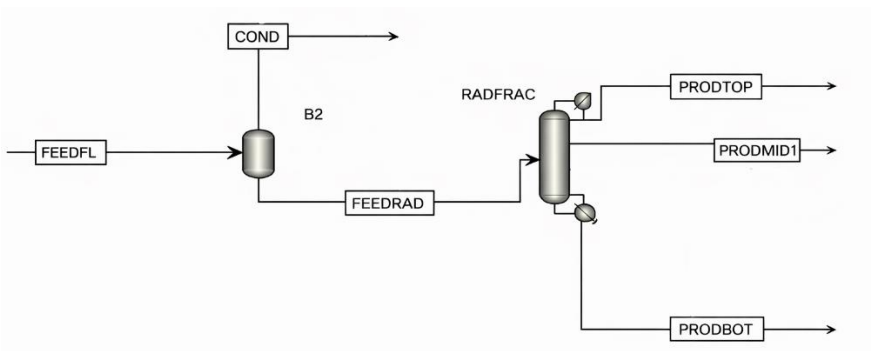

Figure 1: Fractionation Flowsheet used in Aspen Plus simulator.

2.2 Fractionation Performance

From initial tests, it was observed that certain components exhibited higher sensitivity to specific variations and appeared at significant flow rates. Considering the objective of producing SAF, n-butane and hexane were treated as undesirable components in the product stream, while octane and tetradecane were considered desirable, with the former being the most critical and the latter representing a heavier hydrocarbon that may be useful for adjusting the desired fuel physical properties. The results obtained are presented in Tables 2 and 3 for pressure and reflux ratio, respectively.

Table 2: Impact of pressure on the separation process.

Pressure (bar)	N-Butane (kg/h)	Hexane (kg/h)	Octane (kg/h)	Tetradecane (kg/h)	Viscosity (cP)
0.5	172.1	9196.94	4195.83	$1.42*10^{-28}$	0.265
1.0	312.2	12356.79	0.00	$3.22*10^{-37}$	0.209
1.5	362.9	12272.25	0.02	$4.20*10^{-34}$	0.187

Table 3: Reflux ratio impact on the separation process.

RR (mass)	Mass Fraction Octane	Mass Flow Octane (kg/h)	Reboiler Duty (kW)
1.0	0.11	1490,1	7224.7
1.4	$4.8*10^{-08}$	$6.2*10^{-4}$	7672.9
1.8	$1.6*10^{-09}$	$2.0*10^{-5}$	8190.9

Based on the obtained results, it was observed that lower-pressure operating conditions lead to side draw outlet streams that are leaner in more volatile components and richer in octane, which represents the most favorable condition. Compounds such as tetradecane, however, are relatively insensitive to pressure variations at stages close to the column top due to their high molecular weight. Nevertheless, a drawback of operating at lower pressure is the increased viscosity of the outlet product, which may exceed the limits allowed by ASTM standards [6]. Concurrently, lower reflux ratios, provided they do not reach values low enough to cause column drying, tend to make the side draw streams near the top richer in octane, which is a significant advantage and may reduce the need for reprocessing to further purify the SAF product streams. In addition, lower reflux ratios result in a lower reboiler duty, leading to reduced operating costs. Furthermore, lower reflux ratios also result in higher amounts of overhead product, i.e., greater hourly production throughout the process.

Additional simulations were also performed using the results from the DSTW simulations, in which the reflux ratio was fixed at 1.3 and the reboiler heat duty was set to 3.33×10^7 kW. A second fixed side draw stage was added at stage 6 of the column, and the variation of the main side draw stage was then analyzed. The corresponding results are presented in Table 5. Results in the table suggest that the side-draw stage preferentially affects the heavier components in the outlet streams relative to the lighter

ones. Furthermore, the impact of feed basis variation on the outlet flow rate was analyzed, as shown in Table 6.

Table 5: Side draw compositions for different withdrawal stages.

	N-Butane (kg/h)	Hexane (kg/h)	Octane (kg/h)	Tetradecane (kg/h)
Stage 18	54.5	1162.0	7499.3	63.9
Stage 30	54.4	1157.7	7439.8	112.8

Table 6: Feed Basis impact on the octane mass flow.

Feed Basis	Octane (kg/h)
0.05	3665.2
0.10	7292.8
0.15	7742.3
0.20	7460.3

The simulations show that the SAF fractionation process is complex and highly sensitive to several variables, which may complicate system operation but can also be exploited to optimize process performance. For instance, reducing column operating pressure can produce outlet streams richer in desired components and may also enable the generation of side draws suitable as drop-in fuels. The results further indicate that operating conditions such as the reflux ratio can be adjusted not only to increase the purity of the produced fuels, but also to serve as one of the main factors for the economic feasibility of the ETJ route, given the high energy and utility costs associated with the reboiler and other equipment. Moreover, the energy consumed, depending on its source, also contributes to carbon emissions, potentially making the produced fuel as polluting as conventional fossil fuels. In addition, the potential for process energy integration is noteworthy, particularly by using outlet streams to preheat the feed stream before it passes through the flash drum. This approach could further reduce energy costs and represents an additional area for future study within the process. If the production plant is integrated into a biorefinery, other opportunities for utilizing the heat from outlet streams include heating other production lines.

3. Conclusions

This work shows that the fractionation stage of the ETJ route is a key determinant of industrial-scale SAF performance, strongly affecting product quality, energy demand, and process efficiency. The simulation results demonstrate that optimizing operating conditions such as pressure, reflux ratio, and side draw configuration are essential for the performance of the ETJ pathway. The findings also highlight the need for experimental validation to ensure realistic feed compositions and conversion levels. Future studies should extend this approach toward full process optimization, including heat integration and life-cycle assessment, to comprehensively evaluate the sustainability of ETJ-based SAF production.

Acknowledgements

This study was financed in part by the support of São Paulo Research Foundation (FAPESP), Brasil – Process Number #2022/16379-8. We also acknowledge the Universidade Estadual de Campinas (UNICAMP) and the School of Chemical Engineering, Campinas, SP, Brazil.

References

[1] SHAHRIAR, M. F.; KHANAL, A. The current techno-economic, environmental, policy status and perspectives of sustainable aviation fuel (SAF). Fuel, vol. 325, 124905, Oct. 2022.
[2] INTERNATIONAL ENERGY AGENCY (IEA). Aviation. Paris: IEA, 2023. Available at: IEA website. Accessed: Jan. 29, 2026.
[3] THAPA, N. et al. All-electric aircraft: A reality on its way. Materials Today: Proceedings, vol. 43, part 1, pp. 175–182, 2021. https://doi.org/10.1016/j.matpr.2020.11.611
[4] BAUEN, A. et al. Sustainable aviation fuels: Status, challenges and prospects of drop-in liquid fuels, hydrogen and electrification in aviation. Johnson Matthey Technology Review, vol. 64, no. 3, pp. 263–278, July 2020.
[5] YANG, J. et al. An overview on performance characteristics of bio-jet fuels. Fuel, vol. 237, pp. 916–936, Feb. 2019.
[6] ASTM INTERNATIONAL. ASTM D7566-22: Standard specification for aviation turbine fuels containing synthesized hydrocarbons. West Conshohocken, PA, 2022.
[7] RAY, R. C.; RAMACHANDRAN, S. (Eds.). Bioethanol Production: Research and Development. Boca Raton: CRC Press, 2019.
[8] NOTÍCIAS AGRÍCOLAS. Sugarcane and bioenergy market prices. Notícias Agrícolas, 2026. Available online. Accessed: Jan. 30, 2026.
[9] INTERNATIONAL ENERGY AGENCY (IEA). Net Zero Roadmap: A global pathway to keep the 1.5 °C goal in reach. Paris: IEA, 2023.
[10] YANG, J. et al. An overview on performance characteristics of bio-jet fuels. Fuel, vol. 237, pp. 916–936, Feb. 2019. https://doi.org/10.1016/j.fuel.2018.10.079.
[11] TURTON, R. et al. Analysis, Synthesis, and Design of Chemical Processes. 3rd ed. Upper Saddle River, NJ: Prentice Hall, 2009.
[12] SEADER, J. D.; HENLEY, E. J.; ROPER, D. K. Separation Process Principles: Chemical and Biochemical Operations. 3rd ed. Hoboken, NJ: Wiley, 2010.
[13] GEANKOPLIS, C. J. Transport Processes and Unit Operations. 3rd ed. Englewood Cliffs, NJ: Prentice Hall, 1993.
[14] HAYDARY, J. Chemical Process Design and Simulation: Aspen Plus and Aspen HYSYS Applications. Hoboken, NJ: Wiley, 2019.
[15] ROMERO-IZQUIERDO, A. G.; GÓMEZ-CASTRO, F. I.; GUTIÉRREZ-ANTONIO, C.; HERNÁNDEZ, S.; ERRICO, M. Intensification of the alcohol-to-jet process to produce renewable aviation fuel. Chemical Engineering and Processing – Process Intensification, vol. 160, 108270, Mar. 2021.
[16] CARLSON, E. C. Don't gamble with physical properties for simulations. Chemical Engineering Progress, vol. 92, no. 10, pp. 35–46, Oct. 1996.
[17] KORETSKY, M. D. Engineering and Chemical Thermodynamics. 2nd ed. Hoboken, NJ: Wiley, 2013.

Two Phase CFD Analysis of Counter Current Flow at Quench Tower Vapor Inlet Section

Jaimin Mistry[1], Sebastian Ulmer[2], Mariyana Chalakova[2], Ludwig Bauer[2], Carolin Schrüfer[2]

[1] Linde Engineering India Pvt. Ltd., Vadodara, India;

[2] Linde GmbH, Linde Engineering, Pullach, Germany

Abstract

In a recent revamp project handled by Linde Engineering, which involved performance optimization of the water wash column, structured packing was used to enhance heat and mass transfer. The design challenges involved limited space between the vapor inlets and structured packing as well as the non-symmetric location of the vapor inlets. To address this, a chimney tray was applied between the vapor inlets and structured packing [1]. The present work focuses on Computational Fluid Dynamics (CFD) simulations performed to investigate and characterize the counter-current flow dynamics at the vapor inlet section. CFD simulations were conducted using two approaches: a single-phase model modeling only the vapor phase and a two-phase flow model to capture vapor–liquid interactions. In the two-phase approach, the Euler-Lagrange discrete phase model in ANSYS Fluent was used, where the liquid was modeled as discrete phase and the vapor was modeled as the continuous phase. The results of the two-phase CFD show that the high-velocity vapor stream interacts with the descending liquid droplets, inducing droplet breakup and momentum exchange. This two-phase interaction results in a reduction of vapor velocity and promotes enhanced vapor phase distribution across the column cross-section. Multiple simulations were performed to study the effect of different initial liquid droplet diameter, liquid load, turbulent dispersion effects and downward injection velocity.

Keywords

Two-phase flow CFD, Discrete phase model, Quench tower, Vapor distribution, Chimney tray, Two-phase interaction

1. Introduction

Linde Engineering is involved in many revamps and troubleshooting of various plants, especially steam crackers. In a recent revamp project, structured packing is used in the plant's second column-the water wash tower to enhance heat and mass transfer. To ensure optimal operation and high efficiency, it is essential that vapor is evenly distributed across the packing inlet cross-section. However, achieving uniform vapor distribution becomes challenging due to constraints such as limited space between packing and vapor inlet nozzles, as well as the non-symmetric location of the vapor inlets. As a solution, a chimney tray for vapor distribution was applied between the vapor inlets and structured packing. As an additional feature a perforated tray deck was included in the chimney tray design, which allows liquid from above to rain downwards and form a pre-quench zone for the hot inlet vapor.

The focus of the present work will be on the CFD simulations conducted to characterize the counter-current flow dynamics at the vapor inlet section. Most CFD investigations

on vapor inlet distributors rely solely on single-phase (vapor phase) simulations [2, 3, 4]. In recent studies, two-phase CFD simulations were performed to study the vapor-liquid interaction for column with bubble cap tray [5] and bubble column [6]. However, the available literature provides limited analysis on two-phase CFD modeling for water wash columns.

As an initial step and state of the art, a single-phase CFD analysis was conducted, modeling only the vapor phase. Then, the two-phase flow simulations considering a model of raining liquid droplet was performed to study the vapor-liquid interaction.

2. Numerical Model

The details about geometry, mesh, governing equations, boundary conditions and simulations settings are discussed in this section.

2.1 Geometry and computational domain

The geometry of the quench tower vapor inlet section is shown in Figure 1. It shows the two non-symmetrically located vapor inlets, the chimney tray and the structured packing. The liquid flows from the top. The vapor phase is cracked gas and liquid phase is water.

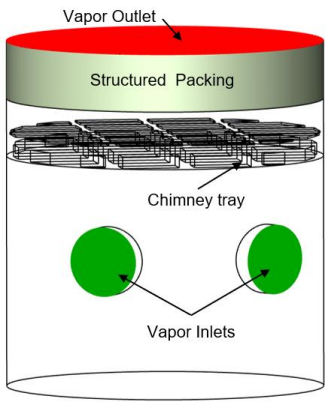

Figure 1: Geometry

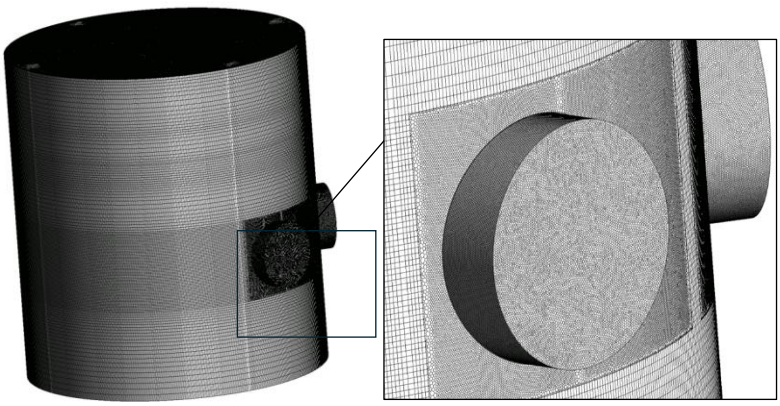

Figure 2: Mesh of the CFD domain

The domain was discretized using hybrid mesh elements, consisting predominantly of hexahedral cells (>90%), while polyhedral cells were incorporated around the inlet nozzles (as shown in Figure 2). A grid independence study was done using multiple mesh sizes to ensure of the numerical accuracy of simulations. The total mesh elements for the selected mesh were 10.63 million.

2.2 Governing Equations

For the single-phase flow simulation and for vapor phase in two-phase flow simulation Reynolds Averaged Navier-Stokes equations (RANS) were solved. They can be written in Cartesian tensor form as:

$$\frac{\partial \rho}{\partial t} + \frac{\partial}{\partial x_i}(\rho u_i) = 0 \tag{1}$$

$$\frac{\partial}{\partial t}(\rho u_i) + \frac{\partial}{\partial x_j}(\rho u_i u_j) = -\frac{\partial p}{\partial x_i} + \frac{\partial}{\partial x_j}\left[\mu\left(\frac{\partial u_i}{\partial x_j} + \frac{\partial u_j}{\partial x_i} - \frac{2}{3}\delta_{ij}\frac{\partial u_i}{\partial x_i}\right)\right] + \frac{\partial}{\partial x_i}(-\rho\overline{u_i' u_j'}) \tag{2}$$

where ρ is density of vapor, u_i and u_j denote the i-th and j-th components in a cartesian coordinate system, with $i, j \in \{1,2,3\}$ corresponding to the x-, y-, and z-directions, respectively. p is the static pressure and μ is dynamic viscosity. The quantity $(-\rho\overline{u_i' u_j'})$ represents the Reynolds stress reflecting the momentum fluctuations

because of turbulence. To model the Raynolds stress term, k-ω SST turbulence model was used. Details of the k-ω SST turbulence model can be found in Section 4.4.3 of ANSYS Fluent theory guide [6].

For two-phase flow simulations, the DPM (Discrete Phase Model) was used to model the descending liquid droplets. It uses Lagrangian frame of reference to track the liquid droplets' motion whereas Eulerian formulation is simultaneously used for the continuous vapor phase. The trajectory of discrete phase droplets is tracked by integrating the force balance on the droplet, which is written in a Lagrangian reference frame. The forces include viscous force, lift force and buoyancy force. The force balance equation is written as:

$$m_p \frac{d\vec{u}_p}{dt} = m_p \frac{\vec{u}-\vec{u}_p}{\tau_r} + m_p \frac{\vec{g}(\rho_p-\rho)}{\rho_p} + \vec{F} \tag{3}$$

where $m_p$is the particle mass, $\vec{u}_p$ is the droplet velocity, $m_p \frac{\vec{u}-\vec{u}_p}{\tau_r}$ is the drag force, $\vec{u}$ is the vapor velocity, τ_r is the droplet relaxation time, ρ_p is the droplet density, ρ is the is the vapor density, $\vec{F}$ is the sum of additional forces which depend on the physics being modeled e.g. "virtual mass" force, pressure gradient force, lift force, etc.

Particle torque balance equation was solved that defines the particle rotation. Particle rotation influences the movement of particles and has a significant influence on the trajectory of the particles in moving fluid. The numerical model considers stochastic collision, breakup and coalescence models within Euler-Lagrangian framework. Evaporation of the liquid phase was not considered. Spherical drag law was used to calculate drag coefficient. To consider the droplet breakup, Taylor analogy breakup (TAB) model was used. The details of the equations and relevant terms can be found in Chapter 12 of ANSYS Fluent theory guide [6].

2.3 Boundary conditions and simulation details

Numerical simulations were carried out in ANSYS Fluent 2023R1.

In the single-phase simulation, the inlets were specified with mass flow rate boundary condition. At the outlet, pressure outlet condition was given. At the walls, non-slip condition was used. Structured packing was modeled as laminar porous media zone with inertial resistance calculated as per Darcy's equation. Second order discretization was used for all variables.

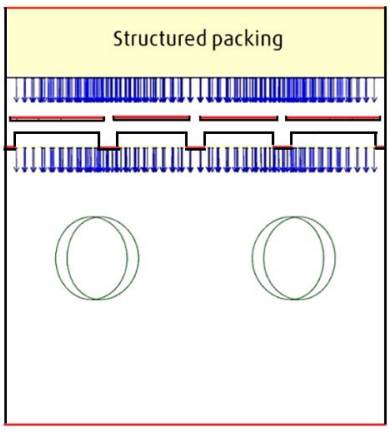

Figure 3: Boundary conditions for DPM

For the two-phase flow simulations, liquid droplets were injected below the structured packing and below the chimney tray which is shown in Figure 3 with blue arrows. Red lines indicate the walls for which "escaped" boundary conditions were considered for droplets. For the other walls, "reflect" boundary condition was considered.

3. Results and discussion

The results of the single-phase and two-phase simulations are presented and discussed in this section. For single-phase analysis, the reported values are time-averaged, whereas for two-phase analysis, the results are for instantaneous conditions after convergence.

3.1 Single-phase simulation

The results of the single-phase simulation are shown in Figure 4 at multiple cross-sectional planes along the column height. The steady state simulation results suggested continuous side-to-side oscillations in flow variables (pressure and velocity), indicating that the flow is intrinsically unsteady. To capture this dynamic behavior, a transient simulation was performed, and flow parameters were time-averaged over a 2 second interval. Figure 4 shows the mean velocity magnitude for the time-averaged results.

The results suggest that the interaction of the two inlet jets creates recirculation zones within the flow domain. Furthermore, the vapor distribution across various planes is non-uniform, containing high and low velocity regions.

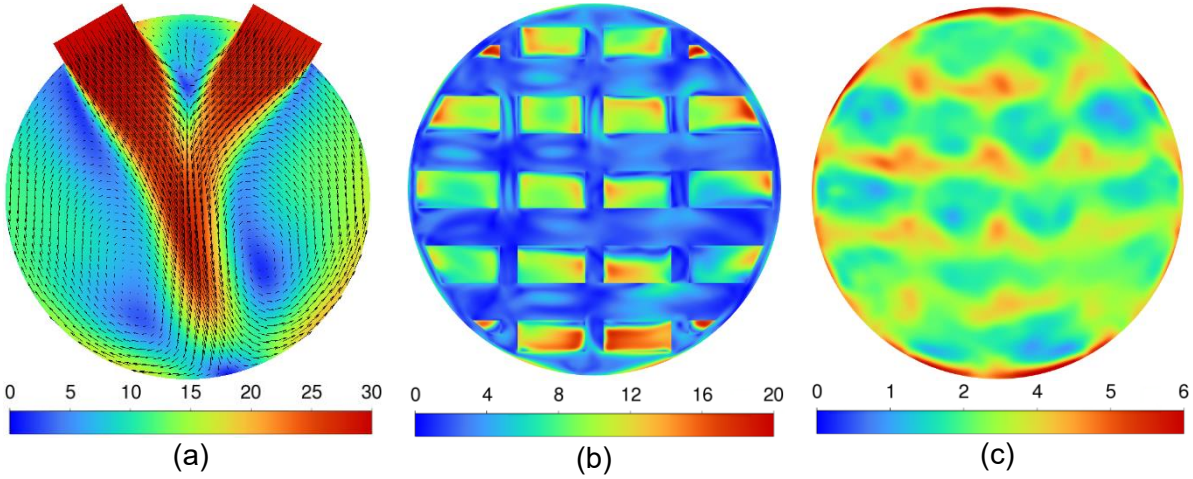

Figure 4: Mean velocity magnitude (m/s) contour for single-phase simulation on different cross-sections (a) across the inlets, (b) across chimney tray, (c) 10 cm inside structured packing

3.2 Two-phase simulation

In the two-phase simulation, steady-state equations are solved for the vapor phase, while liquid droplets are tracked in an unsteady manner. The simulations were performed till the mass balance of the liquid droplet is achieved.

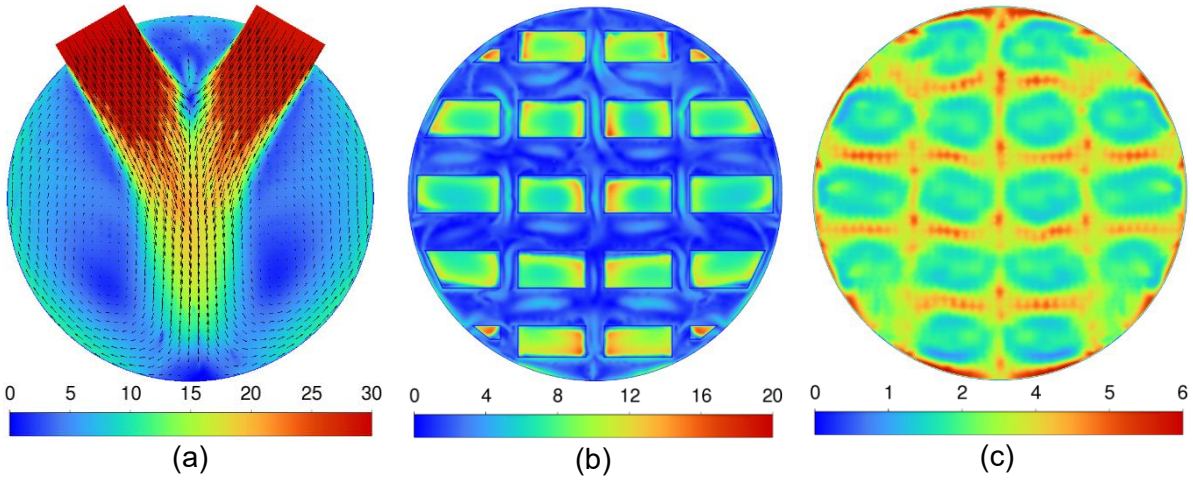

Figure 5: Velocity magnitude (m/s) contour of vapor-phase for two-phase simulation on different cross-sections (a) across the inlets, (b) across chimney tray, (c) 10 cm inside structured packing

The results of the two-phase simulation are shown in Figure 5 at multiple cross-sectional planes along the column height. The results show that the high-velocity vapor stream interacts with the descending liquid droplets, inducing droplet breakup and

momentum exchange. This two-phase interaction results in a reduction of vapor velocity and promotes more uniform vapor phase distribution across the column cross-section compared to single-phase CFD. The impact of the liquid droplets on the vapor velocity is also visible in the velocity contours inside packing (Figure 5(c)). Unlike the single-phase simulation results, the flow variables remain stable without any continuous oscillations, leading to more consistent and predictable flow distribution. Hence, there was no need to perform a transient simulation.

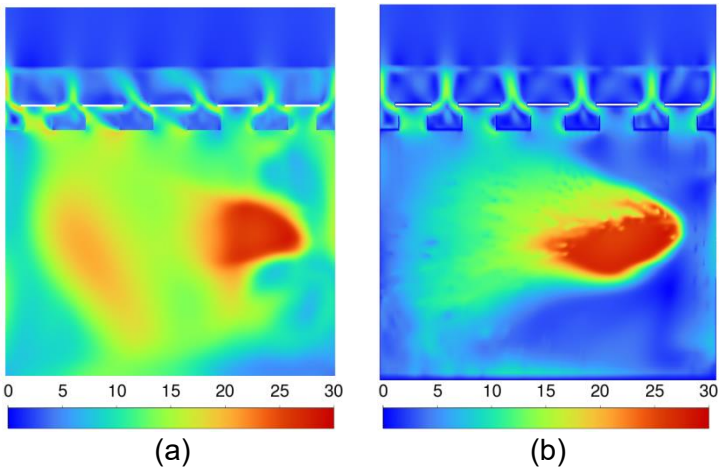

Figure 6: Velocity magnitude contour on the vertical plane (a) single-phase (time-averaged values), (b) two-phase (steady-state values)

Figure 6 shows the velocity contour on the vertical plane between two inlets. The impact of droplets on the vapor velocity is clearly visible in the velocity contours (Figure 6(b)). The gaps between chimney tray risers create alternate high- and low-velocity regions below structured packing. In the single-phase model, as observed earlier, the flow exhibits lateral oscillations. In contrast, the two-phase flow results do not show any such fluctuations.

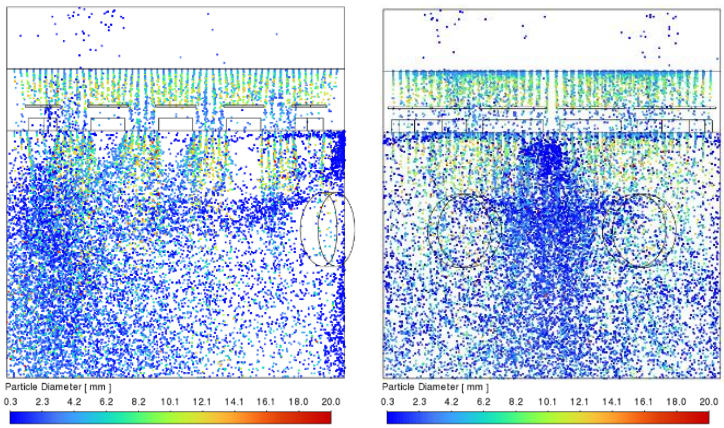

Figure 7: Droplet distribution colored by Droplet diameter

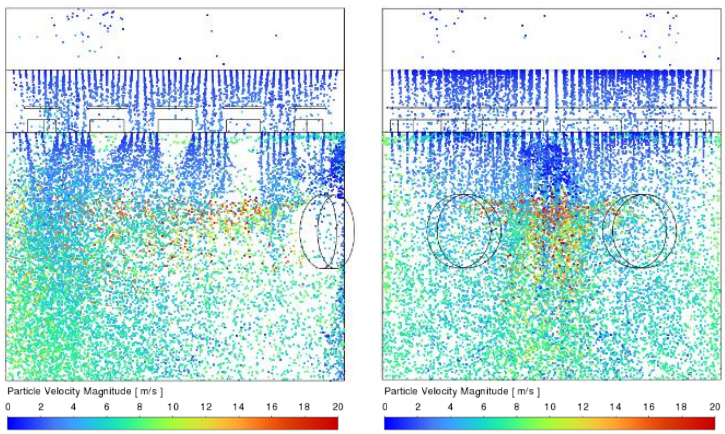

Figure 8: Droplet distribution colored by velocity magnitude

The two-phase simulation also provides information on the liquid droplet parameters. Figure 7 and Figure 8 show the distribution of liquid droplet diameter and velocity magnitude in the domain, respectively. The injected droplet diameter was 3.2 mm. It can be seen from the figures that after the injection, the droplets coalesce to bigger droplets. Once they interact with high velocity vapor flow, they break into smaller droplets. The droplets are displaced by the incoming high-velocity vapor stream and subsequently accumulate in regions away from the inlets. Some of these smaller droplets, having very little mass, also travel upwards and leave the computation domain through the packing.

Droplet velocity plots reveal that the smaller sized droplets have higher velocities. A thorough understanding of liquid droplet distribution characteristics is helpful for optimizing system design and ensuring efficient performance.

Multiple simulations were performed to study the effect of different initial droplet diameter, liquid load, turbulent dispersion effects and downward injection velocity. The results show that changing the initial droplet diameters affects the maximum and minimum diameter of droplets occurring after coalescence and breakup. However, that does not significantly change the overall droplet distribution, resulting in negligible influence on the vapor-phase flow field. At low liquid loading, the two-phase CFD results show minimal deviation from the single-phase CFD. However, as the liquid load increases, the interaction between liquid and vapor phases becomes more pronounced, leading to noticeable effects on the velocity distribution. When the turbulent dispersion is considered, the number of particles flowing upwards and leaving through the packing increases. If injection velocity of downwards direction is given, the particles flowing upwards and going out through outlet reduces. However, both simulations suggest that there is not much impact on the vapor-phase velocity field.

4. Conclusion

In the present study, CFD simulations for the counter-current flow at a quench tower vapor inlet section were performed with two approaches: single-phase modeling and two-phase modeling. From the results, it can be concluded that for columns with limited space between vapor inlet and packing and high liquid loading, single-phase CFD analysis does not adequately capture the counter-current flow characteristics and results are conservative in respect to flow homogeneity across column cross-section. In such cases, two-phase CFD modeling can give insights into specific design conditions and may be an option to qualify extreme challenging designs. In addition, the effect of various operational and modeling parameters was also studied through multiple simulations. Linde recommends considering two-phase flow CFD for counter-current flow at quench tower vapor inlet section specially for columns with limited height and high liquid loading.

References

1. M. Chalakova, L. Bauer, M. Eichinger, C. Schrüfer, J. Mistry, F. Flegiel, Revamp of a 50-Year-Old Quench Tower with Modern Internals (17c), 2025 Spring Meeting and 21st Global Congress on Process Safety, April 2025.
2. Haghshenasfard, M., Zivdar, M., Rahimi, R. and Nasr Esfahany, M. (2007), CFD Simulation of Gas Distribution Performance of Gas Inlet Systems in Packed Columns. Chem. Eng. Technol., 30: 1176-1180. https://doi.org/10.1002/ceat.200700102.
3. Mohamed Ali, P.J. Jansens, Ž. Olujić, Experimental Characterization and Computational Fluid Dynamics Simulation of Gas Distribution Performance of Liquid (Re)Distributors and Collectors in Packed Columns, Chemical Engineering Research and Design, Volume 81, Issue 1, 2003, Pages 108-115, ISSN 0263-8762, https://doi.org/10.1205/026387603321158258.
4. M. Wehrli, S. Hirschberg, R. Schweizer, Influence of Vapour Feed Design on the Flow Distribution Below Packings, Chemical Engineering Research and Design, Volume 81, Issue 1, 2003, Pages 116-121, ISSN 0263-8762, https://doi.org/10.1205/026387603321158267.
5. Fatemeh Keshavarz Shenastaghi, Sepideh Roshdi, Norollah Kasiri, Mohammad Hasan Khanof, CFD simulation and experimental validation of bubble cap tray hydrodynamics, Separation and Purification Technology, Volume 192, 2018, Pages 110-122, ISSN 1383-5866, https://doi.org/10.1016/j.seppur.2017.09.055.
6. Zhipeng Yao, Caixia Chen, Teng Wang, Zihong Xia, Luhaibo Zhao, Zhiyong Tang, Shuai Yan, Effects of gas distributor on hydrodynamics in gas–liquid bubble column by visual experiments and CFD simulations, Chemical Engineering Journal, Volume 504, 2025, 158476, ISSN 1385-8947, https://doi.org/10.1016/j.cej.2024.158476.
7. Ansys Fluent Theory Guide, Release 2023 R1, January 2023.

Structured packing modelling under high pressure for gas-liquid systems

Jerzy Maćkowiak[1]
[1]ENVIMAC Engineering GmbH, Oberhausen, Germany
j.mackowiak@envimac.de

Abstract
Structured packing is essential in distillation, absorption, and stripping processes across varying pressure ranges. Successful column design relies on accurate mass transfer and hydrodynamic predictions. While significant progress has been made in fluid dynamic modelling - allowing for accurate designs up to 90 bar (Maćkowiak, 2010) - separation efficiency models such as Billet & Schultes (1999), Hanley & Chen (2012), and Maćkowiak (2022) primarily focus on low to normal pressures.
This study presents a predictive approach specifically for higher pressures up to 30 bar. The model was validated against 147 experimental distillation data points, including FRI data and existing literature. The evaluation covered diverse test systems (e.g. p-/o-xylene, cyclohexane/n-heptane and iso-butane/n-butane) in columns with diameters ranging from 0.15 to 1.2 m. Results show an average deviation between measured and calculated values of less than ±17.5% within the standard operating range (up to 80% of the flooding gas load factor, $F_{V,Fl}$. The paper concludes with a detailed discussion of the results and the limitations of the proposed approach.

Keywords
Structured packing, distillation, higher pressure, modelling, separation efficiency

1. Introduction

Structured packings are widely and successfully utilized in distillation, absorption, and stripping processes across a broad range of operating pressures. Significant progress in design methodology has occurred over the last three decades, particularly regarding the modelling of fluid dynamics (Billet & Schultes, 1993, 1995; Maćkowiak, 2010)
Initial efficiency models focused on Sulzer gauze packings (Zogg, 1972; Billet, 1973), followed by mass transfer modelling for diverse metal sheet packings, including Mellapak 250Y, Montz B1-200/B1-300, Ralu-Pak 250YC, and Raschig -Super-Pak 250Y. Extensive research has contributed various correlations and experimental data sets to the field (e.g., Billet & Schultes, 1999; Bravo et al., 1992; Cay & Bravo, 2022; Hanley & Chen, 2012; Olujić et al., 2004). This body of work is further synthesized in the comprehensive text by Górak & Olujić (2014), featuring contributions from Maćkowiak & Maćkowiak (2014) and Spiegel & Duss (2014).
The primary objective of this study is to present an extended application of the model for determining separation efficiency n_t/H or HTU_{OV}. Building upon the work of Maćkowiak (2022), this approach is validated for distillation and absorption systems operating under both low and normal pressures.

2. Results and discussion

2.1. Model & basic equations

The ENVIMAC Database (EDB) was employed to validate the predictive model proposed by Maćkowiak (2022). The evaluation encompassed various distillation and absorption test systems operating across a pressure range extending up to 27.4 bar. These investigations utilized diverse structured sheet metal packings with specific surface areas ranging from 125 m^2/m^3 to 750 m^2/m^3. The experimental data were obtained from test plants with column diameters between 150 mm and 1.220 mm and packing heights ranging from 0.8 up to 4 m.

To enhance the scope of the study, the EDB was augmented with experimental FRI data as reported in literature (Cai, 2012; Chambers, 2013; Chambers et al., 2015; Krehenwinkel, 1986; Schultes, 2008, 2013; Schultes & Chambers, 2007; Spiegel & Duss, 2014). Consequently, the total number of experimental data points evaluated in this work was expanded to approximately 200, covering a wide range of distillation and absorption systems as detailed in Table 1.

no.	system	p_T	T_S	ρ_V	ν_V	D_V	Sc_V	ρ_L	ν_L	σ_L	D_L	Sc_L
		bar	K	kg/m³	$\cdot 10^{-6}$ m²/s	$\cdot 10^{-6}$ m²/s	—	kg/m³	$\cdot 10^{-6}$ m²/s	$\cdot 10^{-3}$ kg/s²	$\cdot 10^{-9}$ m²/s	—
1	cyclohexane/n-heptane	1.62	378	4.97	1.65	2.18	0.756	641	0.35	13	6.19	57.2
2	iso-butane/n-butane	6.9	329	15.9	55.3	0.63	0.878	521	0.22	8	12.96	16.9
3	iso-butane/n-butane	11.4	351	28.7	33.5	0.41	0.816	487	0.18	5	17.67	10.3
4	methanol/N_2-CO_2	10	240	14.4	1.1	1.13	0.946	841	1.81	26.8	2.64	685
5	methanol/N_2-CO_2	20	240	29	0.54	0.56	0.959	841	1.81	26.2	2.64	685
6	cyclohexane/n-heptane	0.31	328	1.101	6.33	8.72	0.762	681	0.526	18	3.59	146.5
7	iso-butane/n-butane	20.7	382	56.32	0.169	0.344	0.486	428	0.150	2.3	21.7	7.0
8	iso-butane/n-butane	27.6	398.4	84.8	0.116	0.28	0.417	384	0.128	1.0	29.7	4.4

Table 1: Physical properties of test systems for distillation and absorption, at low, normal and higher-pressure range used for validation of the presented model.

Predicting the separation efficiency of structured packings - expressed as n_t/H, HTU_{OV} or HETP - requires precise determination of the liquid and vapor phase volumetric mass transfer coefficients, $\beta_L \cdot a_e$ and $\beta_V \cdot a_e$, respectively. In this study, both products were calculated using the model previously developed by Maćkowiak (2022).

Subsequently, the heights of transfer units for the vapor phase (HTU_V) and liquid phase (HTU_L) are evaluated. These parameters are then used to determine the overall height of a transfer unit (HTU_{OV}) according to Equations (1) through (7), incorporating the dimensionless numbers defined below.

$$Sh_V = C_V \cdot Re_V^m \cdot Sc_V^{\frac{1}{3}} = \frac{\beta_V \cdot d_h}{D_V};\ d_h = \frac{4\varepsilon}{a}\ [m];\ Re_V = \frac{u_V \cdot d_p}{(1-\varepsilon)\cdot \nu_V};\ Sc_V = \frac{\nu_V}{D_V} \quad (1)$$

with C_V = 0,0065 for packing type Y and C_V = 0,005 for packing type X with m = 1,050 for both types.

$$Sh_L = C_L \cdot Re_L^n \cdot Sc_L^{\frac{1}{2}} = \frac{\beta_L \cdot \delta_L}{D_L} = \frac{\beta_L}{D_L} \cdot \left(\frac{\nu_L^2}{g}\right)^{\frac{1}{3}};\ Re_L = \frac{u_L}{a \cdot \nu_L};\ Sc_L = \frac{\nu_L}{D_L} \quad (2)$$

with C_L = 0,005 and n = 0,7678 for both types of structured packing X and Y.

$$HTU_{OV} = HTU_V + \lambda \cdot HTU_L \quad [m] \quad (3)$$

$$HTU_V = \frac{u_V}{\beta_V \cdot a};\ HTU_L = \frac{u_L}{\beta_L \cdot a} \quad [m] \quad (4)$$

$$\frac{n_t}{H} = \frac{1}{HTU_{OV}} \cdot \frac{\lambda - 1}{\ln \lambda} \quad [m^{-1}] \quad (5)$$

$$\mathrm{HETP} = \frac{\mathrm{H}}{\mathrm{n_t}} \qquad [\mathrm{m}] \qquad (6)$$

$$\lambda = \mathrm{m} \cdot \frac{\dot{\mathrm{V}}}{\dot{\mathrm{L}}} \text{ („stripping factor”)} \qquad [—] \qquad (7)$$

2.2. Comparison of predicted and measured data

Figure 1 presents a comparison between measured and calculated separation efficiency data for various structured packings and systems using the proposed model. The results demonstrate that the model accurately predicts the measured n_t/H values across the 145 data points. Specifically, the model characterizes the separation efficiency with a deviation of ±20% and an average relative error of ±17.5%.

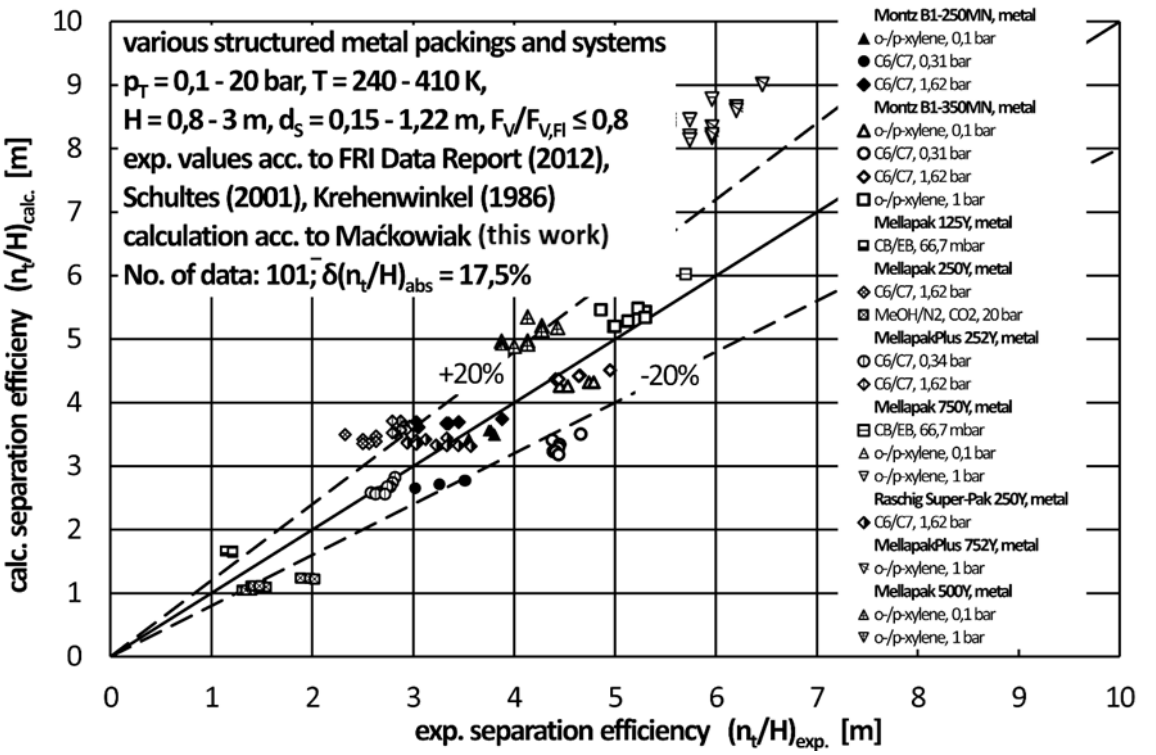

Figure 1: Parity plot for comparing the calculated to measured separation efficiency n_t/H to the experimentally measured n_t/H, valid for different types of metal sheet structured packing.

Figure 2 illustrates a comparison between experimental FRI data from Chambers et al. (2015) and the predicted efficiency for Mellapak 250Y using the model developed in this study. The comparison is shown across a range of gas load factors F_V at a constant operating pressure of 1.62 bara.

In high-pressure systems, the operating pressure and the associated physical properties significantly influence separation efficiency, as documented in the literature (Cai & Bravo, 2022; Chambers et al., 2015; Fitz et al., 1999). At operating pressures p > 11.4 bar and low liquid surface tensions σ < 5 mN/m, the application of structured packing is constrained by the "HETP hump." This phenomenon is typically observed above the loading point, specifically in the range $F_V/F_{V,Fl} \geq 0.65$. In this regime, separation efficiency decreases significantly as the liquid phase transitions from film flow to droplet flow as it approaches the flooding point. This behavior is illustrated in Figure 3, presented by Charles et al. (2015) based on measurements by Fitz et al. (1999).

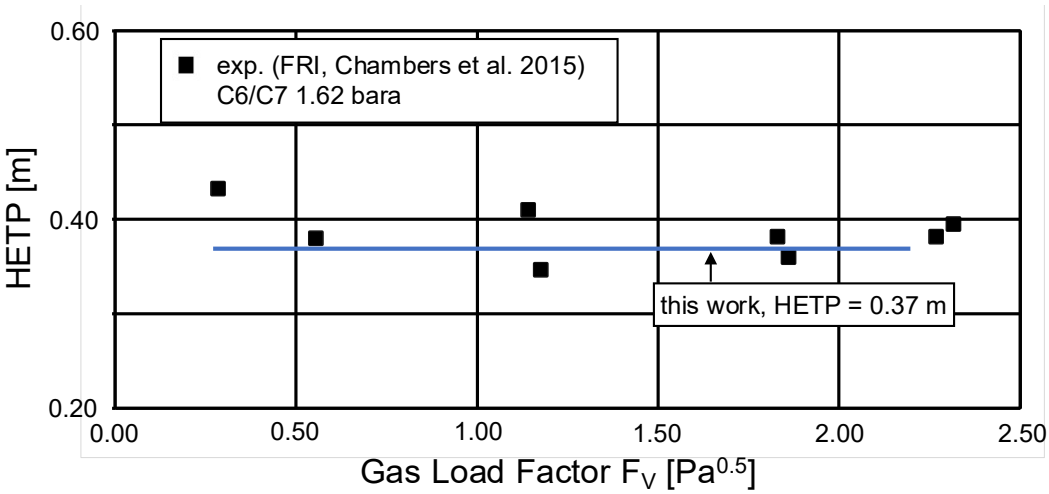

Figure 2: Comparison of predicted separation efficiency of Mellapak 250Y with experimentally measured values

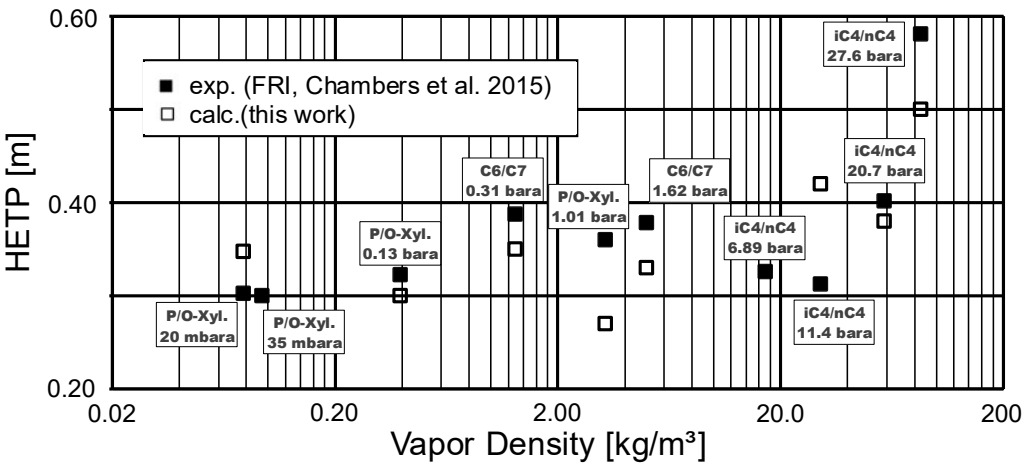

Figure 3: Comparison of predicted separation efficiency of Mellapak 250Y

2.3. Comparison of the presented model with correlations from literature

Table 2 and Figure 3 present an evaluation of distillation data from the EDB database compared against various literature correlations. The model developed in this work predicts the separation efficiency - expressed as HTU_{OV} or HETP - below the loading point with higher accuracy than existing models.

A generally superior prediction of separation efficiency is achieved relative to classical correlations, such as those by Billet and Schultes (1993, 1999). This improvement is substantiated by the values in Table 2, which compare calculated separation efficiencies against experimental distillation data from Schultes (2007) and other. While standard correlations can be applied to the calculation of separation efficiency for structured packings, the model proposed in this study yields the highest overall accuracy.

Packing type and system	p_T [mbar]	$\left(\frac{n_t}{H}\right)_{exp.}$ [1/m]	Maćkowiak (1990)	δ_i $\left(\frac{n_t}{H}\right)_i$	Billet, Schultes (1993/99)	δ_i $\left(\frac{n_t}{H}\right)_i$	Maćkowiak (this work)	δ_i $\left(\frac{n_t}{H}\right)_i$
			$\left(\frac{n_t}{H}\right)_{calc.}$ [1/m]	[%]	$\left(\frac{n_t}{H}\right)_{calc.}$ [1/m]	[%]	$\left(\frac{n_t}{H}\right)_{calc.}$ [1/m]	[%]
Montz B1-250MN, metal (exp. data acc. to FRI data report (Cai, 2012), d_S = 1.22 m)								

C6/C7, F_V = 1.54 $Pa^{0.5}$	310	3.26	3.37	3.5	4.07	25.0	2.71	-16.7
C6/C7, F_V = 1.25 $Pa^{0.5}$	1620	3.35	3.88	15.9	5.46	63.1	3.67	9.6
o-/p-xylene, F_V = 2.02 $Pa^{0.5}$	100	3.55	3.43	2.2	6.44	81.4	3.43	-3.5
Montz B1-350MN, metal (exp. data acc. to FRI data report (Chambers, 2012), d_S = 1.22 m)								
C6/C7, F_V = 1.65 $Pa^{0.5}$	310	4.39	4.10	-6.6	4.38	-0.4	3.23	-26.5
C6/C7, F_V = 1.24 $Pa^{0.5}$	1620	4.65	4.58	-1.6	5.87	26.1	4.43	-4.9
o-/p-xylene, F_V = 1.39 $Pa^{0.5}$	100	4.74	3.83	-19.2	6.76	42.6	4.32	-8.9
o-/p-xylene, F_V = 1.74 $Pa^{0.5}$	1000	4.99	4.75	-4.8	8.87	77.6	5.20	4.0
Mellapak 125Y, metal (exp. data acc. to Sulzer, d_S = 1 – 1.22 m)								
CB/EB, F_V = 1.74 $Pa^{0.5}$	66.7	1.21	1.66	36.3	2.54	109.5	1.66	36.6
Mellapak 250Y, metal (exp. data acc. to Krehenwinkel (1986), d_S = 0.155 m and to Schultes (2007))								
MeOH/N_2, CO_2, F_V = 0.50 $Pa^{0.5}$	20000	1.40	-	-	3.12	123.0	1.11	-20.8
C6/C7, F_V = 1.65 $Pa^{0.5}$	1620	2.63	3.59	36.4	4,17	58,6	3,39	28,7
MellapakPlus 252Y, metal (exp. data acc. to Sulzer, d_S = 1 – 1.22 m)								
C6/C7, F_V = 1.82 $Pa^{0.5}$	340	2.77	3.50	26.4	4.06	46.4	2.66	-3.9
C6/C7, F_V = 1.41 $Pa^{0.5}$	1620	2.93	4.05	38.2	5.47	86.6	3.55	21.2
Mellapak 750Y, metal (exp. data acc. to Sulzer, d_S = 1 – 1.22 m)								
CB/EB, F_V = 1.96 $Pa^{0.5}$	66.7	5.70	4.62	-18.9	3.98	-30.2	5.66	-0.7
Raschig Super-Pak 250Y, metal (exp. data acc. to Schultes (2007) and Chambers (2007), d_S = 1.22 m)								
C6/C7, F_V = 2.22 $Pa^{0.5}$	1620	3.03	3.94	29.8	4.15	37.0	3.35	10.4
absolute mean deviation for this table [%]			13 MP	18.5	14 MP	57.7	14 MP	13.3
absolute mean deviation for all data [%]			82 MP	22.4	101 MP	60.9	101 MP	17.5

Abbr.: C6/C7 = cyclohexane/n-heptane; CB/EB = chlorobenzene/ethylbenzene; MeOH = methanol; MP = measuring points

Table 2: Comparison of the measured separation efficiency n_t/H and predicted values for different distillation and absorption test systems and structured packings with literature correlations for d_S = 0.15–1.22 m under different top pressure.

3. Conclusions

The fundamental HTU-NTU model has been developed for predicting the efficiency of columns containing structured packings. The model utilizes a dimensionless correlation for mass transfer coefficients in the vapor and liquid phases, enabling the prediction of separation efficiency for various structured packing types (both X and Y geometries). This model is applicable across the entire operating range, from vacuum conditions up to 30 bar below the loading point, providing satisfactory accuracy for industrial applications.

In the loading region characterized by high liquid loads and low interfacial tensions (below 5 mN/m), a transition from liquid film flow to droplet flow occurs within the structured packing. This phenomenon results in the "HETP hump," leading to higher observed HETP values; however, these can be predicted with satisfactory accuracy using the presented model

For lower gas load factors where $F_V/F_{V,Fl.}$ < 0.50–0.65, the predicted HETP values at top pressures exceeding 27 bara are approximately 20% higher than the experimental data reported by Chambers et al. (2015). Consequently, the design of structured packings under these specific conditions remains conservative (on the "safe side").

Table 3 shows the validity range of the presented model.

d_S 0.15–1.22 m			
ε up to 0.975 m^3/m^3	ρ_V 0.076–80.7 kg/m^3	$F_V/F_{V,FL}$ ≤ 0.80	$Re_V \in \langle 400 - 17500 \rangle$
c 125–750 m^2/m^3	ρ_L 395–1100 kg/m^3	p_T 0.013–30 bar	Sc_L 5–10000
H 0.8–4.0 m	σ_L 5–72.7 mN/m	Re_L $\in \langle 2 - 250 \rangle$	Sc_V 0.40–1.25

Table 3: Validity range of presented model.

References

Billet, R., & Maćkowiak, J. (1988). Application of modern packings in thermal separation processes. *Chemical Engineering & Technology*, *11*(1). https://doi.org/10.1002/ceat.270110129

Billet, R., & Schultes, M. (1993). Predicting mass transfer in packed columns. *Chemical Engineering & Technology*, *16*(1). https://doi.org/10.1002/ceat.270160102

Billet, R., & Schultes, M. (1999). Prediction of Mass Transfer Columns with Dumped and Arranged Packings: Updated Summary of the Calculation Method of Billet and Schultes. *Chemical Engineering Research and Design*, *77*(6), 498–504. https://doi.org/10.1205/026387699526520

Billet, Reinhard. (1995). *Packed Towers: In Processing and Environmental Technology*. Wiley-VCH.

Bravo, J. L., Rocha, J. A., & Fair, J. R. (1992). Comprehensive model for the performance of columns containing structured packings. *Institution of Chemical Engineers Symposium Series*, *1*(128).

Cai, T. J. (2012). *Test of Montz B1-250MN*.

Cay, T., & Bravo, J. (2022). presented paper. *12th International Conference of Distillation & Absorption*.

Chambers, S. (2013). *Test of Montz-Pak B1-350MN*.

Chambers, S., McCarley, K., Cai, T., & Vennavelli, A. N. (2015). High Pressure Distillation with Structured Packing - Friend or Foe. In *AIChE Spring Meeting*.

Fair, J. R., & Bravo, J. L. (1990). Distillation columns containing structured packing. *Chemical Engineering Progress*, *86*(1).

Fitz, C. W., Kunesh, J. G., & Shariat, A. (1999). Performance of structured packing in a commercial-scale column at pressures of 0.02-27.6 bar. *Industrial and Engineering Chemistry Research*, *38*(2), 512–518. https://doi.org/10.1021/IE9709300

Górak, A., & Olujić, Ž. (2014). Distillation: Equipment and Processes. In *Distillation: Equipment and Processes*. https://doi.org/10.1016/C2010-0-67738-8

Hanley, B., & Chen, C. C. (2012). New mass-transfer correlations for packed towers. *AIChE Journal*, *58*(1). https://doi.org/10.1002/aic.12574

Krehenwinkel, H. (1986). *Experimentelle Untersuchungen der Fluiddynamik und der Stoffübertragung in Füllkörperkolonnen bei Drücken bis zu 100 bar*. TU Berlin.

Maćkowiak, J. (1990). Design method for prediction of the separation efficiency of packed columns in distillation. *AICHE Meeting, Chicago, USA*.

Maćkowiak, J. (2010). Fluid Dynamics of Packed Columns. In *Fluid Dynamics of Packed Columns*. https://doi.org/10.1007/b98397

Maćkowiak, J. (2022). Prediction of separation efficiency of structured and stacked packings under low and normal pressure. *Chemical Engineering Research and Design*, *186*, 713–729. https://doi.org/10.1016/J.CHERD.2022.07.016

Maćkowiak, J., & Maćkowiak, J. F. (2014). Random Packings. *Distillation: Equipment and Processes*, 85–144. https://doi.org/10.1016/B978-0-12-386878-7.00003-6

Olujić, Ž. (1997). Development of a Complete Simulation Model for Predicting the Hydraulic and Separation Performance of Distillation Columns Equipped with Structured Packings. *Chemical and Biochemical Engineering Quarterly*, *11*(1).

Olujić, Ž., Behrens, M., Colli, L., & Paglianti, A. (2004). Predicting the efficiency of corrugated sheet structured packings with large specific surface area. *Chemical and Biochemical Engineering Quarterly*, *18*(2).

Schultes, M. (2008). Raschig Super-Pak - Eine neue Packungsstruktur mit innovativen Vorteilen im Vergleich. *Chemie-Ingenieur-Technik*, *80*(7). https://doi.org/10.1002/cite.200800045

Schultes, M. (2013). Raschig super-ring is pushing the FRI test column to new limits. *AIChE 2013 - 2013 AIChE Spring Meeting and 9th Global Congress on Process Safety, Conference Proceedings*.

Schultes, M., & Chambers, S. (2007). How to Surpass Conventional and High Capacity Structured Packings with Raschig Super-Pak. *Chemical Engineering Research and Design*, *85*(1), 118–129. https://doi.org/10.1205/CHERD06101

Spiegel, L., & Duss, M. (2014). Structured Packings. *Distillation: Equipment and Processes*, 145–181. https://doi.org/10.1016/B978-0-12-386878-7.00004-8

Xu, Z. P., Afacan, A., & Chuang, K. T. (2000). Predicting mass transfer in packed columns containing structured packings. *Chemical Engineering Research and Design*, *78*(1). https://doi.org/10.1205/026387600526924

Zogg, M. (1972). Modifizierte Stoffübergangskoeffizienten für bilanzmäßige Stoffübergangsberechnungen an laminaren Rieselfilmen. *Chemie Ingenieur Technik*, *44*(15). https://doi.org/10.1002/cite.330441505

Comparing Graph and Hybrid Neural Networks for Modeling CO_2 Solubility in Ternary Mixtures

Edoardo Parascandolo[1], Vincent Gerbaud[2], Sophie Thiebaud-Roux[1], Ivonne Rodriguez-Donis[1]
[1]Laboratoire de Chimie Agro-industrielle (LCA), Université de Toulouse, INRAE, Toulouse INP, Toulouse/FR;
[2]Laboratoire de Génie Chimique (LGC), Université de Toulouse (CNRS, INPT, UPS), Toulouse/FR;

Abstract
Accurate modeling CO_2 solubility in amine-based solvents is essential for advancing carbon capture technologies. To provide insights on the development of dedicated Machine Learning tools, this study investigates three modifications on a proven physics-informed framework: the introduction of an *amine fingerprint*, to minimize signal noise coming from non-reactive components in predicting the chemisorption contribution; the substitution of the original molecular featurizer with a *standalone Directed-Message Passing Neural Network* (D-MPNN)-based model, switching from a static structural representation to a dynamic one; the inclusion of targeted *RDKit descriptors* to the *D-MPNN* featurizer, to further enhance its performance. While distinguishing between amines and non-reactive components effectively led to an overall reduction of the Mean Absolute Percentage Error (MAPE) higher than 5%, substituting fixed fingerprints with learned representations confirmed that graph-based models are not optimal for applications with high chemical complexity and medium-to-low data regimes. Consequently, the original Mordred-based Artificial Neural Network (ANN) featurizer outperforms two configurations of Directed-Message Passing Neural Networks (D-MPNN).

Keywords
Carbon Capture, Absorption, Hybrid Modeling, Solvent Screening

1. Introduction

Anthropogenic CO_2 emissions from the industrial and energy sectors continue to be the primary drivers of climate change [1]. Since the energy mix remains mostly polluting and recent data highlights that the total energy demand increased almost everywhere in absolute terms [2], it is important to focus on carbon mitigation Strategies (CCS) specifically within these domains. In this setting, absorption technologies are increasingly attractive, as they currently possess the highest Technology Readiness Levels (TRL) and represent the most implementable solutions for immediate large-scale deployment [3].

Nevertheless, conventional amine-based absorption faces critical drawbacks, including corrosion, environmental toxicity and higher energy costs [4]. Consequently, research is shifting its focus toward the conception of new solvent systems, aiming to replace traditional mixtures with more efficient and stable alternatives. Given the possible combinations for the system itself, involving solvents, cosolvents, and dilution, modeling CO_2 solubility in novel mixtures is significantly challenging. Further difficulties arise from the nature of the chemisorption

mechanism, which requires the characterization of both physical and chemical absorption pathways, with the latter relying on experimental data.

Recently, Di Caprio et al. [5] proposed a comprehensive approach by switching the paradigm from pure data-driven Machine Learning (ML) models to a chemo-informed physics-based one, by developing a dual-head architecture to separately model the components of the capture process. While the physical branch is structured to follow Henry's law via the estimation of its two temperature-dependent parameters, the chemical branch employs an artificial neural network to predict the reaction-driven contribution based on mixture fingerprints and process conditions. To evaluate the effectiveness of this approach, the model was benchmarked against a purely data-driven version of the same architecture. Finally, the hybrid framework demonstrated a significant advantage in terms of overall accuracy and extrapolation capabilities, maintaining consistency even when predicting the behavior of novel solvent mixtures. A shared strength that makes both the hybrid and the data-driven model effective is the detailed feature engineering used to characterize the molecular embeddings: the Mordred library is used to calculate an array of 25 descriptors, ranging from chemical properties to structural information, which are subsequently reduced into 7 features through Principal Component Analysis (PCA). For any given operating point, generally involving a diluted solvent-cosolvent solution, these initial *physical molecular fingerprints* are first processed through a fully-connected Artificial Neural Network (ANN) to produce *molecular fingerprints*. These are weighted by their mass fraction and then concatenated together with the water mass fraction to be fed in a second ANN; the final image of the mixture is therefore generated to be used for the predictions, that is the *mixture fingerprint* [5].

An interesting alternative for generating the *molecular fingerprints* is the use of Graph Neural Networks (GNN), interpreting molecules as interconnected graphs rather than flat numerical vectors. Unlike Mordred descriptors, which provide a static description, GNNs allow for a dynamic and autonomous featurization from local atomic environments and their connectivity. As an improvement over standard GNNs, Directed-Message Passing Neural Networks (D-MPNN) optimize the encoded information by utilizing directed edges: rather than performing the standard aggregation, they differentiate between the message going from an atom *A* to the adjacent atom *B* and the one from *B* to *A*. By this mean, D-MPNNs can prevent *message tottering*, a phenomenon where information recursively rebounds between atoms, hence leading to noise in the molecular embedding. These advantages are effectively implemented in Chemprop, an open-source framework validated across different tasks within the domain of property prediction and drug discovery [6, 7], including a recent application to CO_2 absorption in physical solvents [8]. On the other hand, GNN-based encoders are particularly sensitive to data-scarce regimes and show limited capacity to extrapolate beyond the training distribution. Indeed, the lack of sufficient information to derive useful features makes descriptor-based ANNs outperform GNNs in either small or unbalanced datasets [9]. This limitation can be partially addressed with a mixed approach, that is incorporating meaningful features in the graph generation process, providing the model with a starting point based on established chemical intuition [6, 7].

Given these considerations, the original Mordred-based ANNs molecule featurizer was replaced with two D-MPNN configurations: a standalone Chemprop model and a version augmented with RDKit descriptors. The inclusion of these descriptors was specifically targeted toward the evidences in the results of the SHAP analysis

presented in the paper [5]. Additionally, the original architecture was improved introducing a dedicated mask for non-reactive components entering the data-driven branch of the framework, to minimize signal noise in the prediction of chemical absorption. Through a systematic comparison of these D-MPNN configurations with the original ANN one, this work aims to identify the most effective balance between automated graph representation and domain-specific chemical knowledge.

2. Results and discussion

First, a direct comparison between the starting framework and the refined version featuring the masked mixture representation was performed. This step was essential to quantify the variation resulting from the architectural redesign of the chemical branch before introducing the increased complexity of graph-based transformers. Once the optimal configuration was identified, the ANN-based featurizer was then replaced by the two D-MPNN variants. Data partitioning was done by means of the same convex hull employed in Di Caprio et al. [5]. This facilitated a final comparison between the three methods, to evaluate the specific contribution of the new featurization strategy. In Figure 1 the proposed workflow is presented by schematizing the overall models.

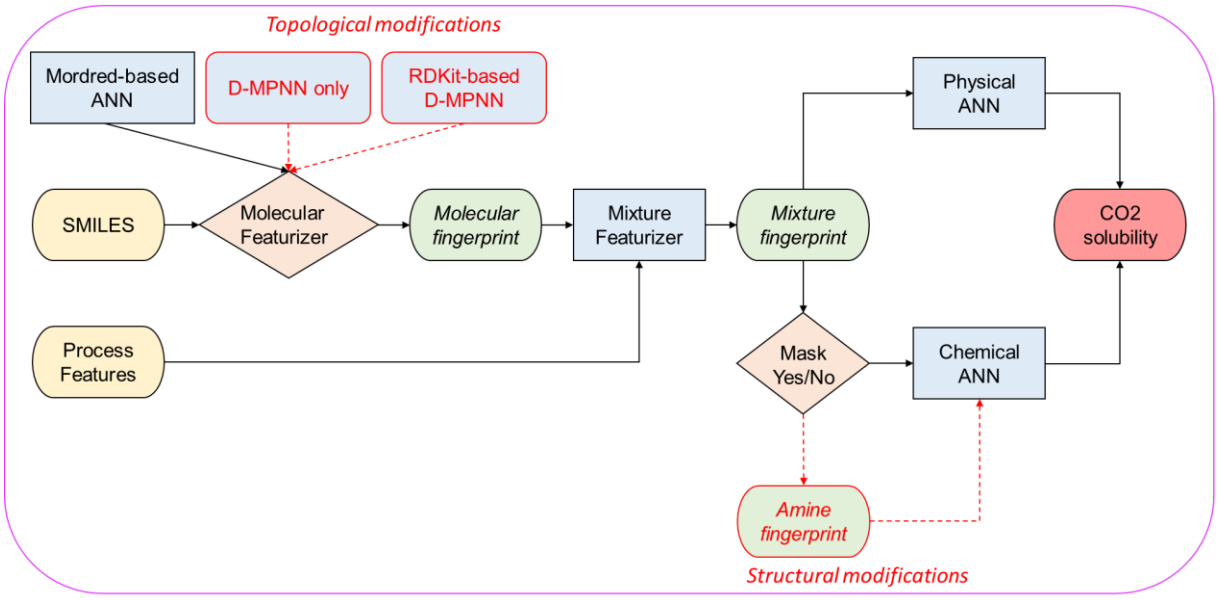

Figure 1: Block flow diagram presenting the original architecture [5] and the alternatives implemented in this work, highlighted in *red* with *dotted lines*. Modifications have been ordered as presented and distinguished between *structural* and *topological*, respectively the implementation of the mask and different featurizers.

2.1 Amine-specific feature isolation

In the original architecture, the *mixture fingerprint* enters both the networks dedicated to the physical and chemical absorption. This representation integrates information from all species, including solvents that contribute solely to physical absorption. Since solubility is modeled as the summation of the outputs from the two branches, the inclusion of non-reactive components data in the reactive branch introduces signal dilution. Therefore, this network has been re-trained with an *amine fingerprint* instead, built from the *mixture fingerprint* by zeroing the image of the components which do not contribute to chemical absorption. As presented in Table 1, the implementation of this fingerprint led to slight but visible improvements in the model

performance on the test set, leading to an absolute decrease in the Mean Absolute Percentage Error (MAPE) higher than 5% while leaving unvaried the metrics.

Modification	*MAE·10² (x_{CO2})*			*MAPE (%)*			*R^2*		
	Train	*Val*	*Test*	*Train*	*Val*	*Test*	*Train*	*Val*	*Test*
None	*0.530*	*0.579*	*1.48*	*11.37*	*31.82*	*27.11*	*0.985*	*0.870*	*0.929*
Amine fingerprint	*0.487*	*0.573*	*1.48*	*10.19*	*26.56*	*21.78*	*0.987*	*0.873*	*0.925*

Table 1: Mean Absolute Error (MAE), Mean Absolute Percentage Error (MAPE) and R^2 evaluations for the original model and the *amine fingerprint*-based model on training, validation and test sets.

Thus, the amine-specific masking effectively redistributed the error, improving accuracy in lower-solubility regimes where relative deviations were more pronounced. Furthermore, the parity plot presented in Figure 2 confirms the metric improvement, showing a closer agreement between the predicted and experimental values. These results show that the proposed structural modification alone provides a more consistent representation of the mixture

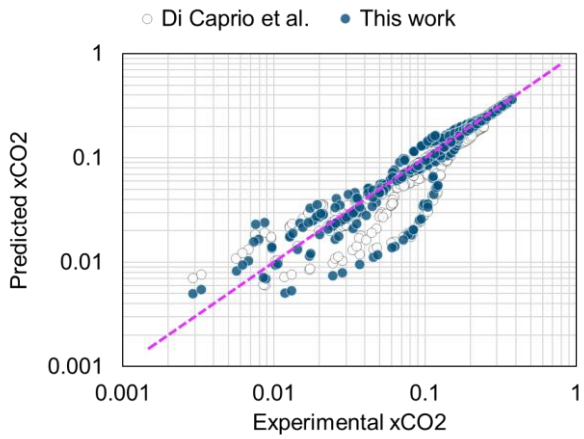

Figure 2: Parity plot on the test set obtained with the original model (*white markers*) and with the *amine fingerprint*-based model (*blue markers*) on the logarithmic scale.

2.2 D-MPNN-based featurizers

Following the improvements observed, the ANN-based featurizer was replaced by two variants: a standalone D-MPNN, which relies exclusively on the learned representation, and an augmented version including RDKit descriptors based on the results of a previous SHAP analysis [5] and more suited to a graph-based methodology. These additional features are detailed in Table 2. The dimensionality was maintained from the baseline study to ensure a fairer comparison, allowing the analysis to focus on the effectiveness of the featurization rather than an increase in the number of input variables. Depths, size and activation functions were optimized for both implemented versions, built on a suited version of Chemprop 2.1.0 [6, 7].

Information	*RDKit descriptors*
Size Properties	*MolWt, ExactMolWt, HeavyAtomCount, LabuteASA*
Polarity	*MolLogP, TPSA, MaxPartialCharge, MinPartialCharge, MolMR, O atom count*
Reactivity	*NumHDonors, NumHAcceptors, N atom count, Tertiary N, Secondary N, NumHeteroatoms*
Topology	*BalabanJ, BertzCT, NumRotatableBonds, FractionCSP3, Rings (Aromatic, Aliphatic, Saturated, Heterocycles), Weighted Atomic Sum*

Table 2: Classification of the 25 RDKit descriptors selected for the augmented D-MPNN featurizer.

The transition from fixed fingerprints to learned representations highlighted a clear threshold in the model's ability to generalize from graph structures alone: while achieving similar performances on the training set with the original model, the standalone D-MPNN exhibited a significant performance decay on the test set, yielding an R^2 of only 0.85. This generalization gap highlights the model's limitations in translating its learned features to unseen chemical spaces, a result that can be attributed to the limited size of the dataset and the inherent complexity of the thermodynamic problem. Indeed, the addition of RDKit descriptors better addressed these generalization issues, confirming the intuition that an explicit chemical guidance can stabilize graph-based learning by mitigating the risk of overfitting. The comparison between the performances of these versions on the test set are visually rendered in Figure 3.

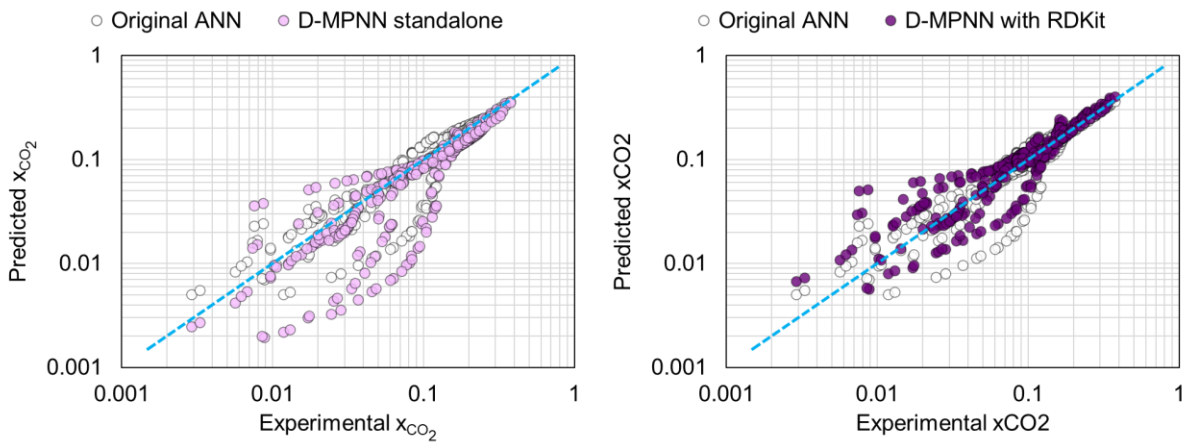

Figure 3: Parity plot on the test set obtained with the original Mordred-based ANN featurizer (*white markers*), the *D-MPNN standalone* featurizer (*pink markers*) and the *D-MPNN with RDKit descriptors* (*purple markers*) on the logarithmic scale.

Although this version yielded improved metrics on the test set, the performance remained slightly lower when compared to the original featurizer. While the ANN-Mordred baseline benefits from an optimized and high-density feature space, the D-MPNN appear unable to establish further structural dependencies beyond the features already defined, even when provided with these descriptors. Finally, comprehensive metrics estimated on all the sets and for any implementation are presented in Table 3.

Modification	*MAE·10² (x_{CO2})*			*MAPE (%)*			*R^2*		
	Train	*Val*	*Test*	*Train*	*Val*	*Test*	*Train*	*Val*	*Test*
None	*0.530*	*0.579*	*1.48*	*11.37*	*31.82*	*27.11*	*0.985*	*0.870*	*0.929*
Amine fingerprint	*0.487*	*0.573*	*1.48*	*10.19*	*26.56*	*21.78*	*0.987*	*0.873*	*0.925*
D-MPNN standalone	*0.918*	*0.601*	*2.28*	*15.88*	*29.82*	*30.82*	*0.955*	*0.805*	*0.854*
D-MPNN with RDKit	*0.799*	*0.591*	*1.74*	*15.57*	*33.03*	*32.63*	*0.968*	*0.840*	*0.919*

Table 3: Mean Absolute Error (MAE), Mean Absolute Percentage Error (MAPE) and R^2 evaluations for each implemented model on training, validation and test sets.

3. Conclusions

In this study, a proven hybrid framework for modeling CO_2 solubility was implemented by integrating targeted feature isolation and graph-based featurization. The amine-specific masking proved to be the most impactful structural modification, resulting in a MAPE reduction of over 5% on the test set. By zeroing out signal noise from non-reactive species, the model achieved superior physical consistency, particularly in lower-solubility regimes where relative errors were previously more pronounced. Regarding the transition to graph-based architectures, the results revealed a clear threshold in autonomous feature extraction. The significant performance leap of the augmented D-MPNN compared to the standalone version confirms that the limited dataset size is the primary bottleneck. Given the complexity of the thermodynamic problem, the D-MPNN requires targeted descriptors to compensate for the lack of extensive training points. Consequently, the ANN-Mordred baseline remains the most efficient configuration for this specific application.

Acknowledgements

The authors acknowledge the financial support received by State funding administered by the National Research Agency under the France 2030 initiative, (reference No. ANR-22-PESP-0008), and through the “Investissements d’Avenir” program, (reference No. ANR-18-EURE-0021)

References

[1] Liu, Z.; Deng, Z.; Davis, S.; Ciais, P. Monitoring Global Carbon Emissions in 2022. Nat Rev Earth Environ 2023, 4 (4), 205–206. https://doi.org/10.1038/s43017-023-00406-z.

[2] IEA (2025), Global Energy Review 2025, IEA, Paris https://www.iea.org/reports/global-energy-review-2025

[3] Bui, M.; Adjiman, C. S.; Bardow, A.; Anthony, E. J.; Boston, A.; Brown, S.; Fennell, P. S.; Fuss, S.; Galindo, A.; Hackett, L. A.; Hallett, J. P.; Herzog, H. J.; Jackson, G.; Kemper, J.; Krevor, S.; Maitland, G. C.; Matuszewski, M.; Metcalfe, I. S.; Petit, C.; Puxty, G.; Reimer, J.; Reiner, D. M.; Rubin, E. S.; Scott, S. A.; Shah, N.; Smit, B.; Trusler, J. P. M.; Webley, P.; Wilcox, J.; mac Dowell, N. Carbon Capture and Storage (CCS): The Way Forward. Energy Environ. Sci. 2018, 11 (5), 1062–1176. https://doi.org/10.1039/C7EE02342A.

[4] Borhani, T.; Wang, M. Role of Solvents in CO2 Capture Processes: The Review of Selection and Design Methods. Renewable and Sustainable Energy Reviews 2019, 114, 109299. https://doi.org/10.1016/J.RSER.2019.109299.

[5] Di Caprio, U.; Vermeire, F.; Van Gerven, T.; Leblebici, M. Physics-Informed Machine Learning Predicting CO2 Capture Performances of Organic Mixtures. Chemical Engineering and Processing - Process Intensification 2025, 216, 110410. https://doi.org/https://doi.org/10.1016/j.cep.2025.110410.

[6] Yang, K.; Swanson, K.; Jin, W.; Coley, C.; Eiden, P.; Gao, H.; Guzman-Perez, A.; Hopper, T.; Kelley, B.; Mathea, M.; Palmer, A.; Settels, V.; Jaakkola, T.; Jensen, K.; Barzilay, R. Analyzing Learned Molecular Representations for Property Prediction. J Chem Inf Model 2019, 59 (8), 3370–3388. https://doi.org/10.1021/acs.jcim.9b00237.

[7] Heid, E.; Greenman, K. P.; Chung, Y.; Li, S.-C.; Graff, D. E.; Vermeire, F. H.; Wu, H.; Green, W. H.; McGill, C. J. Chemprop: A Machine Learning Package for Chemical Property Prediction. J Chem Inf Model 2024, 64 (1), 9–17. https://doi.org/10.1021/acs.jcim.3c01250.

[8] Parascandolo, E.; Gerbaud, V.; Corrales, D. C.; Hernández, N.; Thiebaud-Roux, S.; Rodriguez-Donis, I. Accurate VLE Predictions via COSMO-RS-Guided Deep Learning Models: Solubility and Selectivity in Physical Solvent Systems for Carbon Capture. J Chem Inf Model 2025, 65 (16), 8514–8526. https://doi.org/10.1021/acs.jcim.5c01148.

[9] Jiang, D.; Wu, Z.; Hsieh, C.-Y.; Chen, G.; Liao, B.; Wang, Z.; Shen, C.; Cao, D.; Wu, J.; Hou, T. Could Graph Neural Networks Learn Better Molecular Representation for Drug Discovery? A Comparison Study of Descriptor-Based and Graph-Based Models. J Cheminform 2021, 13 (1), 12. https://doi.org/10.1186/s13321-020-00479-8.

Influence of Column Tilting and Tray Alignment on the Hydraulic Performance of Tray Columns

Cornelia Maier, Felicitas S. Engel, Harald Klein, Sebastian Rehfeldt
Technical University of Munich, TUM School of Engineering and Design, Department of Energy and Process Engineering, Institute of Plant and Process Technology, Garching, Germany

Abstract
Despite the widespread use of tray columns, issues such as column tilting and incorrect tray installation can occur. Although the importance of leveling tray columns correctly is well known, research on the influence of column tilting and tray orientation in columns with fixed valve trays is scarce. Therefore, this work experimentally analyzes the influence of column tilting and tray alignment on key hydraulic parameters in a DN1200 tray column test rig for air/water. The measurements reveal that a column tilt of 0.6° minor affects the pressure drop for both sieve trays and ProValve trays compared to a leveled column. Contrary to pressure drop, weeping is strongly influenced by the tilt of the column for both tray types. Installing the ProValve tray against the direction of liquid flow, compared to the intended design, results in a slightly higher froth height at low liquid loads. This suggests that, in the reverse orientation, the gas is directed more vertically upward and less horizontally across the tray. At higher liquid loads, the froth height shows only minor differences between reverse and normal installation, indicating that the liquid momentum dominates the two-phase flow behavior and reduces the influence of the valve geometry.

Keywords
Tray column, hydraulics, tray tilting, tray alignment, test rig

1. Introduction

Tray columns play a crucial role in various energy-intensive industrial separation and purification processes. Despite the widespread use and well-understood design principles of tray columns, practical deviations from ideal operating conditions frequently occur. Misalignment of the column axis, as well as improper installation of internal components, can result in hydraulic performance that differs from the design values. Tray tilting can be caused by either manufacturing defects or external forces [1]. The latter one becomes especially relevant at high wind loads [2] as well as for offshore columns [3]. Lockett and Augustyniak [1] experimentally found that for tilted columns with sieve trays, a collapse of the froth can be seen, which results in increased weeping and decreased tray efficiency. As these effects become more relevant at lower gas loads, the operating window of the tilted tray columns should be reduced.
Remesat et al. [4] investigated columns with sieve trays and float valves and found that this efficiency loss is even higher when the tilt of the column is perpendicular to the flow. A further experimental study with a column using bubble cap trays [5] as well as CFD modelling for sieve trays [2] reveals that the liquid flow on the column tray is negatively influenced by column tilt. These studies show that hydraulic performance and separation efficiency decrease in tilted columns compared to leveled ones.
Although the influence of tray tilt on columns with sieve trays has been investigated in some studies, research on the hydraulic behavior of tilted columns with fixed valve

trays is lacking. Fixed valve trays are designed for efficient phase interaction, which in turn supports effective mass transfer between the gas and liquid phases on each tray. The performance of the phase interaction of fixed valve trays is enhanced by the design of the valve. Many fixed valves are designed to ensure that gas enters the tray in a specific direction, which enhances the mass transfer on a tray [6]. These fixed valve trays, therefore, need to be installed inside the column in a designated orientation with reference to liquid flow direction.
In this study, the influence of column tilting on key hydraulic parameters is measured quantitatively in a tray column test rig for both a sieve tray and a fixed valve tray. Moreover, the fixed valve tray is installed in reverse, with a 180° rotation relative to the intended direction of liquid flow. By comparing the resulting data with measurements obtained in the normal alignment of the tray, the impact of the fixed valve orientation on froth height is examined.

2. Experimental

The column test rig consists of two trays with a diameter of 1.2 m and an active area of 0.856 m² for each tray, with a tray spacing of 0.5 m. The test rig is operated with air and water. Within the test rig, the trays can be easily changed to investigate different tray types. During all experiments, the upper and lower trays are always of the same type. The test rig also allows installing the trays in two different orientations, either in their intended orientation (normal) or with a 180° rotation relative to the intended direction of liquid flow (reverse). An adjustable compensation flange below the lower tray enables a defined tray tilt. By varying the height of this flange, one side of the column can be raised relative to the other, resulting in a defined inclination of the entire column section. In the present study, a maximum height difference of 12 mm was applied between the two sides of the column, corresponding to a column tilt of 0.6°. Figure 1 illustrates a schematic of the lower tray, showing the liquid flow and the column tilt direction.

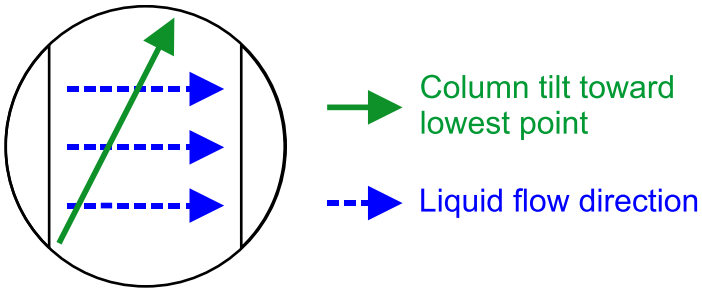

Figure 1: Scheme of the lower tray for the tilted column

The test rig enables the measurement of key hydraulic parameters, such as pressure drop, weeping, and entrainment. The transparent test rig also allows for a qualitative analysis of the influence of column tilting and fixed valve orientation on the two-phase layer on the trays. With a light curtain device developed by dieEntwickler Elektronik GmbH [7], the froth height on the lower tray can be automatically measured. A more detailed explanation of the test rig, as well as the measurement of the froth height, can be found in Engel et al. [8].
In the context of this study, a sieve tray and a ProValve fixed valve tray are analyzed. The ProValve tray features a fixed, tapered valve cover positioned above a circular tray opening, with the deck area narrowing in the direction of the liquid flow. The geometrical data concerning the configurations of the tray openings are listed in Table 1.

Table 1: Geometrical data of the tray openings: open area φ, hole diameter d_h, valve lift height h_{lift} and number of elements N_h

Tray type	φ in %	d_h in mm	h_{lift} in mm	N_h
Sieve	10	10	-	1093
ProValve	10	39	13	89

3. Results and discussion

3.1 Column tilting

First, the impact of column tilting on the pressure drop of the lower tray, as well as on the weeping of the lower tray, is analyzed. In this section, a comparison is made between the leveled column and the tilted column with a tilt of 0.6°. Measurement results of hydraulic parameters, as well as visual observations of the two-phase layer on the trays, especially in the tilted column at the lowest point, are discussed.

Figure 2 shows the impact of column tilting on the pressure drop of the sieve tray for two different liquid loads under varying gas loads, expressed by the F-factor based on the active area.

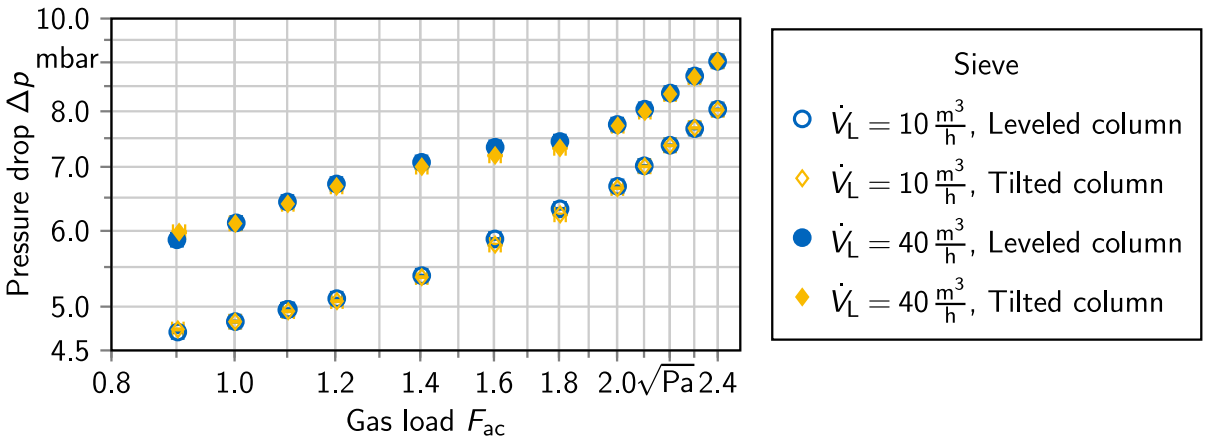

Figure 2: Pressure drop of the sieve tray for the leveled and tilted column with a tilt of 0.6°

It can be observed that the tilt of the column has only a minor effect on the pressure drop. Looking into the transparent test rig during the measurements, a collapse of the froth at the lowest point on the upper tray becomes visible, particularly at lower gas loads. Although this phenomenon may influence the overall hydraulics of the column, this local change in the two-phase layer in the tilted configuration does not affect the pressure drop of the lower tray. Figure 3 illustrates the influence of column tilting on the pressure drop for the ProValve tray.

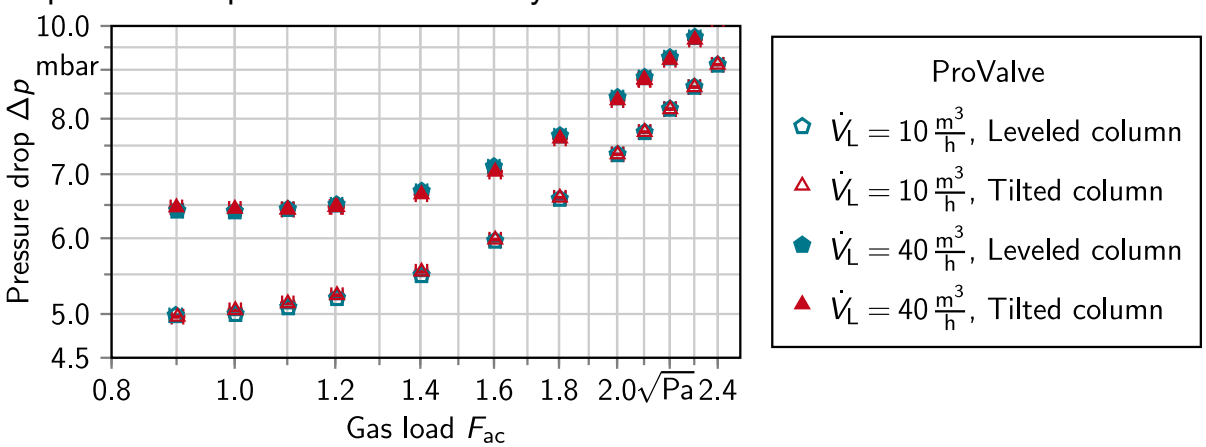

Figure 3: Pressure drop of the ProValve tray for the leveled and tilted column with a tilt of 0.6°

Similar to the sieve tray, the ProValve tray also shows only minor deviations in pressure drop when comparing the leveled and tilted columns. During the measurements, no froth collapse is visible in the tilted column. This observation can be explained by the tapered valve cover of the ProValve tray, which shapes the two-phase flow by directing the liquid across the tray to prevent the accumulation of stagnant liquid on the tray and reduce weeping [6].
The weeping of the lower tray is measured for both the leveled and tilted column under different operating conditions for both tray types. The weeping is quantified by the weeping rate

$$\omega_{\mathrm{L}} = \frac{\dot{V}_{\mathrm{W}}}{\dot{V}_{\mathrm{L}}}, \tag{1}$$

taking into account the measured weeping volume flow $\dot{V}_{\mathrm{W}}$ and the liquid load $\dot{V}_{\mathrm{L}}$ which enters the column on the upper tray. Figure 4 illustrates the weeping rate at two different liquid loads for the leveled and tilted column using sieve trays.

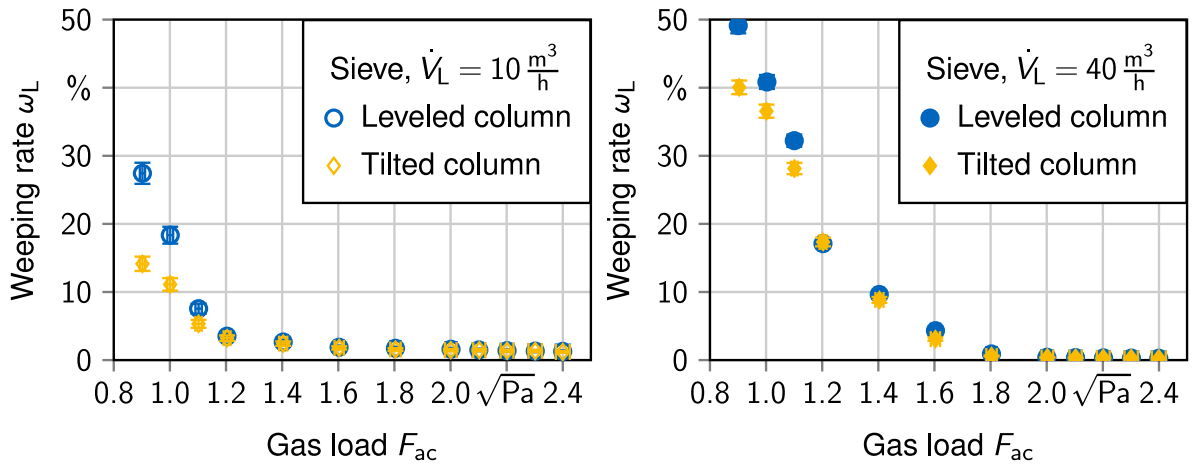

Figure 4: Weeping of the sieve tray for the leveled and tilted column with a tilt of 0.6°

The tilted column shows for gas loads $F_{\mathrm{ac}} \leq 1.1\,\sqrt{\mathrm{Pa}}$ a lower weeping rate for both liquid loads. In both the leveled and tilted cases, the lower sieve tray shows a strong, uneven weeping over the tray, with the highest weeping near the inlet of the tray. For the tilted column, the collapse of the froth at the lowest point on the upper tray leads to an increased local weeping. As the lowest point of the column is near the inlet of the upper tray, a significant amount of liquid bypasses the downcomer of the upper tray via weeping. Thus, less liquid enters the lower tray via the downcomer for the tilted column compared to the leveled column. As the weeping in sieve trays tends to occur near the inlet, the weeping volume flow on the lower tray is reduced, resulting in a lower measured weeping rate of the lower tray in the tilted column compared to the leveled one, as shown in Figure 4.
The weeping behavior for the leveled and tilted columns with ProValve trays is shown in Figure 5. For ProValve trays, enhanced weeping is measured at the lower tray for the tilted column compared to the leveled column at low to intermediate gas loads. This opposite trend compared to the sieve tray is caused by the different weeping behavior of the leveled columns. First, the ProValve tray generally shows a lower weeping rate. Second, the ProValve tray is less prone to weeping near the inlet and shows more uniform weeping across the tray compared to sieve trays. For the tilted column with ProValve trays compared to sieve trays, a lower weeping rate on the upper tray enables more liquid to enter the lower tray via the downcomer. Due to the tilt, the tray

tends to have a higher weeping volume flow as the clear liquid height is higher at the lowest point of the column, which is prone to weeping.

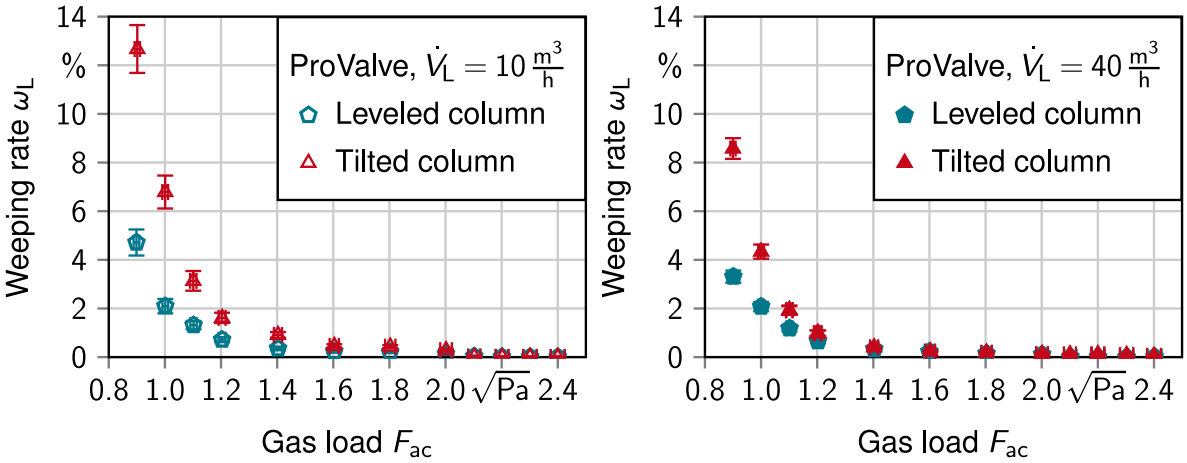

Figure 5: Weeping of the ProValve tray for the leveled and tilted column with a tilt of 0.6°

3.2 Tray alignment

The impact of the alignment of fixed valves relative to the liquid flow direction on the resulting froth height is examined for the ProValve tray. All measurements in this section are conducted in the column with a tilt of 0.3°. Figure 6 shows the measured froth height of the lower tray for both the normal installation of the ProValve tray and the 180° reverse installation relative to the intended orientation.

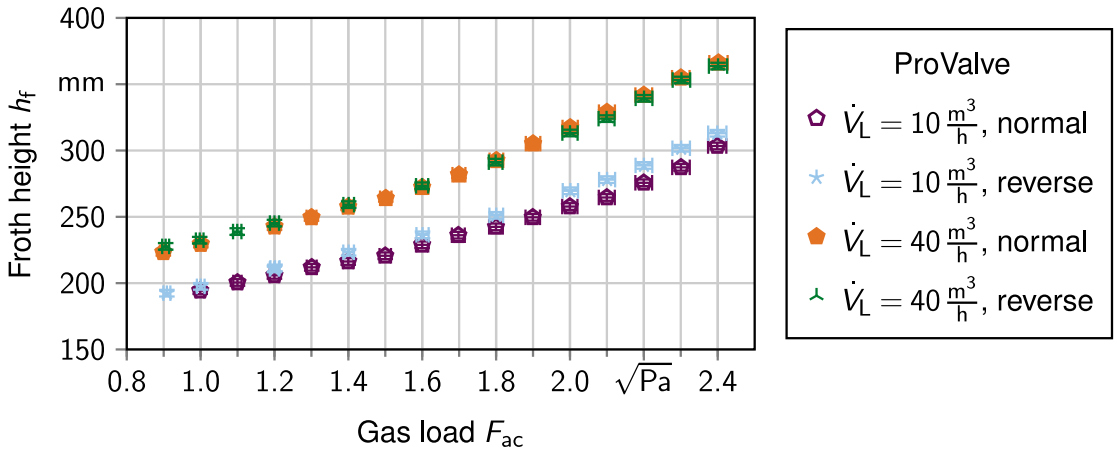

Figure 6: Froth height of the ProValve tray installed in normal design direction (normal) and installed 180° reverse to the designed direction (reverse)

For both liquid loads, no significant qualitative change in the dependency of froth height on the gas load is observed when comparing the normal and reverse installations of the tray. At the lower liquid load of $\dot{V}_L = 10\ \frac{m^3}{h}$, a slightly higher froth height is measured for the reverse installation, with the difference becoming more pronounced at higher gas loads. In the normal design alignment, the shape of the ProValve cover area ensures a uniform and relatively low froth height due to the predominantly horizontal vapor release from the valve cover, which enhances vapor-liquid contact near the valve [6]. In the reverse installation, the tapered valve cover becomes wider in the direction of the liquid flow, which tends to hinder the horizontal liquid movement and directs the two-phase flow more upwards than sideways, resulting in a higher froth height. For the higher liquid load, the froth height in Figure 6 shows only minor

differences between the reverse and normal installations. This suggests that the liquid momentum entering the tray with high liquid loads has a significant influence on the two-phase flow that dominates the gas momentum from the tapered cover valve geometry.

4. Conclusions

This study presents experimental results on the impact of column tilting and tray alignment on key hydraulic parameters for tray columns. A tilt of 0.6° for a column with sieve trays does not significantly affect the pressure drop. However, it impacts the weeping. Visual observation of the two-phase layers shows that the froth collapses in the tilted column at low gas loads. This collapse increases non-uniform weeping, which then decreases the available mass transfer area on the tray. The tilt also does not affect the pressure drop of a ProValve tray. Unlike the sieve tray, the ProValve tray shows a more uniform weeping behavior over the tray, with increased weeping in the tilted column compared to the leveled one, and no froth collapse is visible.

Examining the effect of the ProValve tray alignment in reverse installation compared to the normal intended alignment, a slightly higher froth height can be observed at low liquid loads. The difference in froth height between reverse and normal alignment of the ProValve tray is reduced as the liquid load increases. These measurements reveal that the influence of the tapered valve cover, which narrows in the normal orientation and widens in the reverse installation, is more pronounced at low liquid loads with respect to the froth height.

These findings highlight the importance of accurately leveling the column to ensure efficient operation of tray columns in industrial separation and purification processes. They also help clarify how the misalignment of trays and the shape of fixed valves affect the hydraulic behavior inside the column. Further investigations using other fixed valve trays, including their hydraulic behavior in tilted columns and under reverse installation, are currently in progress.

References

[1] M. J. Lockett and J. D. Augustyniak, "On Tilted Trays," *Transactions of the Institution of Chemical Engineers*, 69 (Part A), pp. 99–107, 1991.

[2] Z. Ping, J. Dan, M. Huibo, and W. Jianhua, "Three-dimensional simulation of liquid flow on a sieve tray under different inclinations," *Braz. J. Chem. Eng.*, vol. 31, no. 4, pp. 905–912, 2014, doi: 10.1590/0104-6632.20140314s00003038.

[3] Y. Meng, S. Wang, Y. Zhang, S. Chen, Y. Hou, and L. Chen, "Experimental evaluation of the performance of a cryogenic distillation system under offshore conditions," *Chemical Engineering Science*, vol. 263, p. 118084, 2022, doi: 10.1016/j.ces.2022.118084.

[4] D. Remesat, K. Chuang, and W. Svrcek, "The Evaluation of Out-of-Level Trays for the Improvement of Industry Guidelines," *Chemical Engineering Research and Design*, vol. 83, no. 5, pp. 508–514, 2005, doi: 10.1205/cherd.03392.

[5] J. Stichlmair and S. Ulbrich, "Liquid channelling on trays and its effect on plate efficiency," *Chem Eng & Technol*, vol. 10, no. 1, pp. 33–37, 1987, doi: 10.1002/ceat.270100105.

[6] S. Hebert and N. Sandford, "Consider Moving to Fixed Valves," *Chem. Eng. Progr. (CEP)*, no. 5, pp. 34–41, 2016.

[7] dieEntwickler Elektronik GmbH, "Rapidoscan Data Sheet RS-C-025–0480-ECT," Bad Zell, Austria.

[8] F. S. Engel, H. Klein, and S. Rehfeldt, "Hydraulic investigations of standard and high performance trays in a DN1200 column," *Chemical Engineering Research and Design*, vol. 194, pp. 478–486, 2023, doi: 10.1016/j.cherd.2023.04.055.

Operating Strategies of Distillation Trains to Eliminate VOC Emission Caused by Frontend Failures in Chemical Plants

Chuei-Tin Chang, Guan-Wun Chen
[1,2] Department of Chemical Engineering, National Cheng Kung University, Tainan, Taiwan 701401

Abstract
A hardware item that facilitates product generation in a continuous process is referred to as the frontend unit, e.g., reactor. The remaining backend units, such as the distillation columns, are used for purification purpose to produce on-spec product(s), byproduct(s) and recycle stream(s). In a realistic manufacturing environment, it is almost impossible to avoid unexpected frontend failure(s) after a long period of operation. Obviously, emergency response actions must be taken to mitigate the harmful effects of volatile organic compounds (VOCs) and/or liquid wastes emitted from the backend. It is thus necessary to figure out online strategies to handle such hazards during the early design stage. The objective of this study is to discover operating procedure(s) to reduce the environmental impacts induced by the above failures on the basis of sound engineering judgment, previous operational experience and rigorous simulation results. Although this heuristic approach may not be as rigorous as the AI-based methods, the resulting remedial actions should still be reliable and can be used as the basis for further improvements in practice. Note also that this proposed procedure synthesis tactic may be implemented quickly without the need to secure a large amount of training data in advance. Furthermore, it should be applicable to any other chemical plant with the same frontend-backend structure.

Keywords
Operating procedure, Emergency response, Dynamic simulation

1. Introduction

As the undesirable effects of global warming become apparent, suppression of VOC and greenhouse gas emissions have become a critical issue for keeping the chemical industries sustainable. According to Murphy and Allen (2005), these gases may include: methane, ethylene, propylene, butylene and butadiene, etc. Generally speaking, hydrodealkylation (HDA) is a typical VOC-emitting process, which is utilized in the present paper as a working example for illustration convenience. Additional results concerning the naphtha cracking process can be found elsewhere (Chen and Chang, 2025).

In a sense, any chemical process can be structurally divided into two parts placing next to each other in series. The one in front is adopted primarily for generating a mixture that contains the target product(s), the unreacted reactants, by-products and other wastes. This mixture stream is sent to the backend to purify all its components. Chenevert et al. (2005) proposed a “tail-chase” strategy to reduce 75-80% of the total amount of gaseous compounds flared during the start-up and/or shutdown operations. This nonconventional tactic, facilitated with extra compressors, pumps, pipelines, valves and other fittings to recycle all backend outputs to the inlets of the same subsystem, clearly can avoid sending any VOC to the flare stack. Notice also that its operational safety and feasibility has already been confirmed by Xu et al. (2020) for

the ethylene plant. To expedite realization of tail-chase operation, Yang et al. (2010) suggested that rigorous dynamic simulation may be used as a virtual alternative to cut down operator training cost. Wang et al. (2016) in a later study showed with dynamic simulation that, by recycling the downstream liquid and vapor products to the inlet of cracked gas compressor, it is possible to significantly reduce VOC emission during the startup and shutdown phases of the ethylene production process. Other than the tail-chase strategy, notice that other researchers suggested to run all columns independently in total-reflux mode in order to achieve the same purpose. Gani et al. (1998) demonstrated that this approach can indeed be utilized to reduce VOC emission, while Reepmeyer et al. (2003) adopted the same scheme to facilitate startup of a distillation column.

From the above reviews, one can see that the tail-chase and total-reflux strategies were both adopted to run routine startup and shutdown operations of typical chemical plants. In the present study, these experiences are extended to navigate the backend in abnormal scenarios that may occur in an HDA plant. Procedure synthesis insights gained from this exercise may be extended to other processes of the same structure. Due to space limitation, discussions in the sequel focus only on backend manipulations against the incidence caused by any frontend failure in HDA plant. Specifically, the original structure of distillation train is altered to perform tail-chase and total-reflux operations for the purpose of minimizing the total amount of emitted wastes and also financial loss after halting the upstream feed supply. The detailed operation steps are developed according to the above-mentioned heuristic strategies, while feasibility and effectiveness of these procedures were confirmed with credible commercial software, e.g., ASPEN PLUS DYNAMICS®.

2. Emergency response operation

The emergency actions considered here are supposed to be performed sequentially. The chemical plant is assumed to be kept at the designated steady state in the initial period but, after a long span of continuous operation, the process stream(s) between the front and back subprocesses may be discontinued unexpectedly due to a frontend failure (e.g., reactor outage, pump or compressor malfunction). As indicated above, the tail-chase and total-reflux tactics may be adopted to avoid excessive emission of VOCs and also accumulation of liquid wastes. If, at a later instance, the failed unit is fixed, the interrupted stream(s) naturally could resume and a recovery procedure should then be executed to steer the system back to its original condition.

3. Continuous hydrodealkylation process

The HDA process flow diagram (PFD) can be easily found in various textbooks. For the sake of facilitating clear illustration, only its distillation train formed by stabilizer, product column and recycle column is treated as the backend subprocess here. The above three columns are labelled as C1, C2 and C3, respectively, and this subprocess features one external feed stream and four product streams (see Figure 1). To quantitative describe the tail-chase and total-reflux configurations, the flowrates of these external streams were set initially at those obtained with rigorous steady-state simulation using ASPEN PLUS. Specifically, the feed F1 was chosen to be a mixture of hydrogen, methane, benzene, toluene and diphenyl, and its total flowrate, temperature and pressure were assumed to be 10,000 kg/hr, 35 degree Celsius and 36.5 bar, respectively. The operating conditions and detailed specifications of C1, C2 and C3 can be found in Chen (2024), and the corresponding simulation results are presented in Table 1.

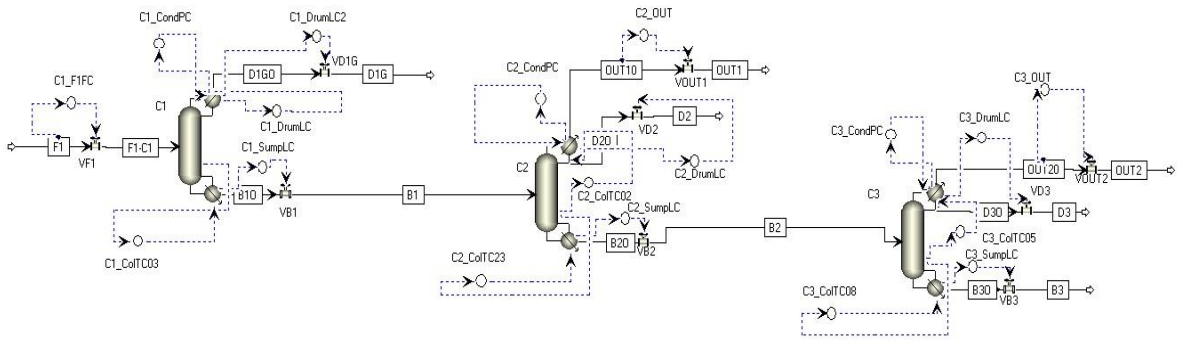

Figure 1. Process flow diagram of HDA backend for normal operation

Component	F1	D1G	OUT1	OUT2	B3
H2	0.0001	0.0045	trace	0	0
CH4	0.0131	0.5955	trace	0	0
C6H6	0.8847	0.3965	0.8957	0.0030	trace
C7H8	0.0273	0.0035	0.0278	0.9970	trace
C12H10	0.0748	trace	0.0765	trace	0.9999

Table 1. Components and their mass fractions in inputs and outputs of HDA backend

4. Tail-chase operating strategy

The tail-chase operating procedure consists of four main steps:

Step 1: modification of process structure. Let us consider the PFD in Figure 1 together with the mass-balance data in Table 1 first. If the targeted incident occurs, i.e., a frontend failure, the external feed to the distillation train is supposed to be cut off completely and all outputs from this system should be recycled back to the first column of the distillation sequence. The modified PFD to facilitate the tail-chase operation is shown in Figure 2, which is constructed by adding extra compressor (COMP), pumps (PUMP2, PUMP3A and PUMP3B), valves (VREC1, VREC2, VREC3A and VREC3B), mixer (MIX) and splitters (FS1, FS2, FS3A and FS3B) into the original structure in Figure 1. Notice that, in other more complex cases when two or more external inputs are present, the output streams should be split according to the design rules proposed by Chen and Chang (2025).

Step 2: identification of necessary operator tasks. Failure occurrence and repair completion are assumed to be observable but random events in this study. The former triggers operator actions to build the recycle structures in Figure 2, while the latter prompts subsequent actions to break the recycle loops and then drive the system back to the original steady state. To facilitate quick return to normal state after fixing the frontend failure, it is beneficial to strategically manipulate the heating and cooling duties of all columns during the tail-chase phase to ensure that the distillation train embedded in the recycle structure (Figure 2) closely mimics the normal conditions listed in Table 1 and Figure 1.

Step 3: synthesis of detailed operation steps. As mentioned previously, the proposed approach is adopted for the purpose of identifying specific steps to accomplish the above tasks. The best feasible procedure identified so far is expressed with the sequential function chart (SFC) in Figure 3.

Step 4: validation via rigorous simulation. The operating procedure in Figure 3 was validated in numerical experiments with ASPEN PLUS DYNAMICS®. By arbitrarily

setting the length of repair period in AC_2 (say, let Z to be 5 and 15), its typical impacts can be identified from the simulation results.

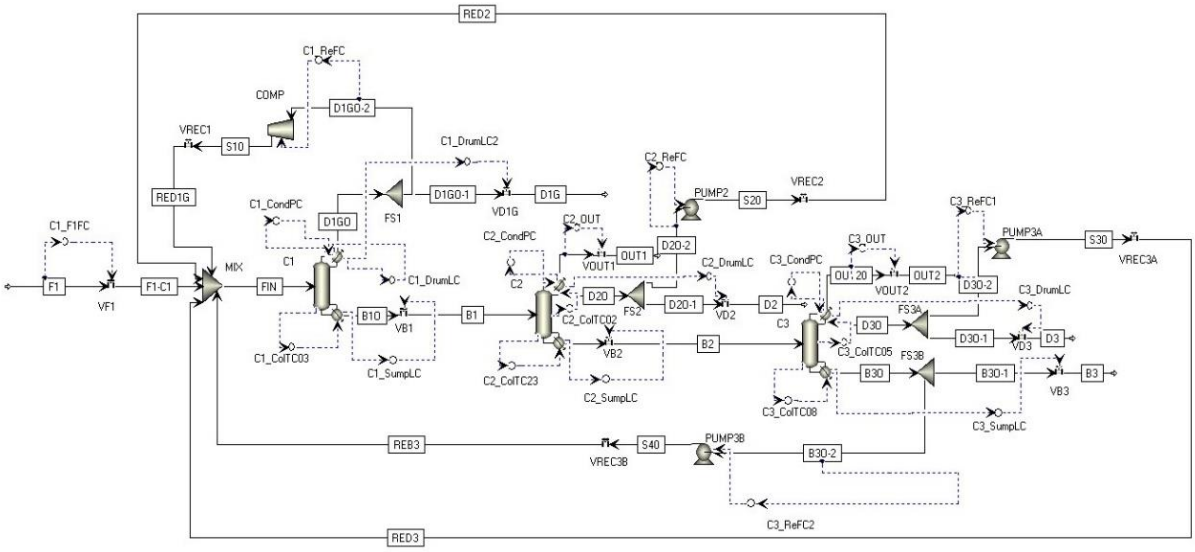

Figure 2. Process flow diagram of HDA backend for tail-chase operation

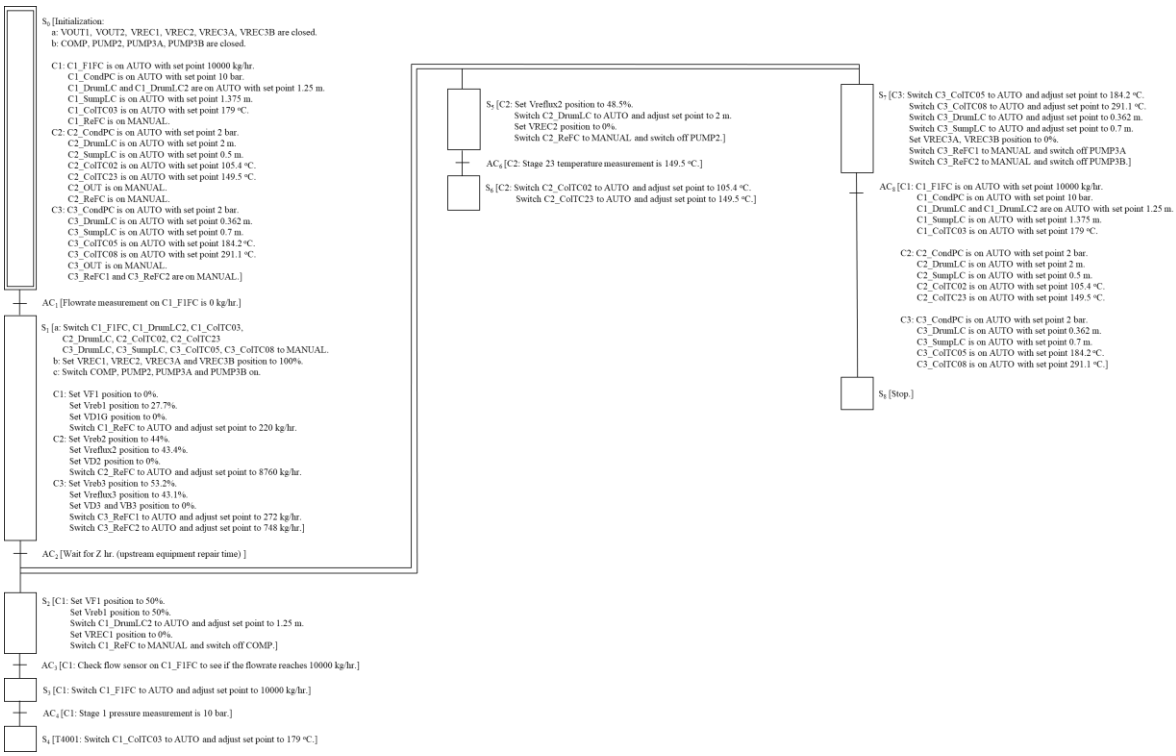

Figure 3. Sequential function chart of tail-chase operation for HDA backend

5. Total-reflux operating strategy

To prevent excessive VOC emission, the total-reflux operation can be used as a potential alternative. The operating procedures in this case were built in essentially the same four steps given above. One such procedure is presented in Figure 4. Generally speaking, after detecting the frontend failure, all inlet and outlet valves of every column in the backend should be closed so as to allow each column to run independently. The process structure in this case can be thought of as a disconnected version of the original distillation train shown in Figure 1.

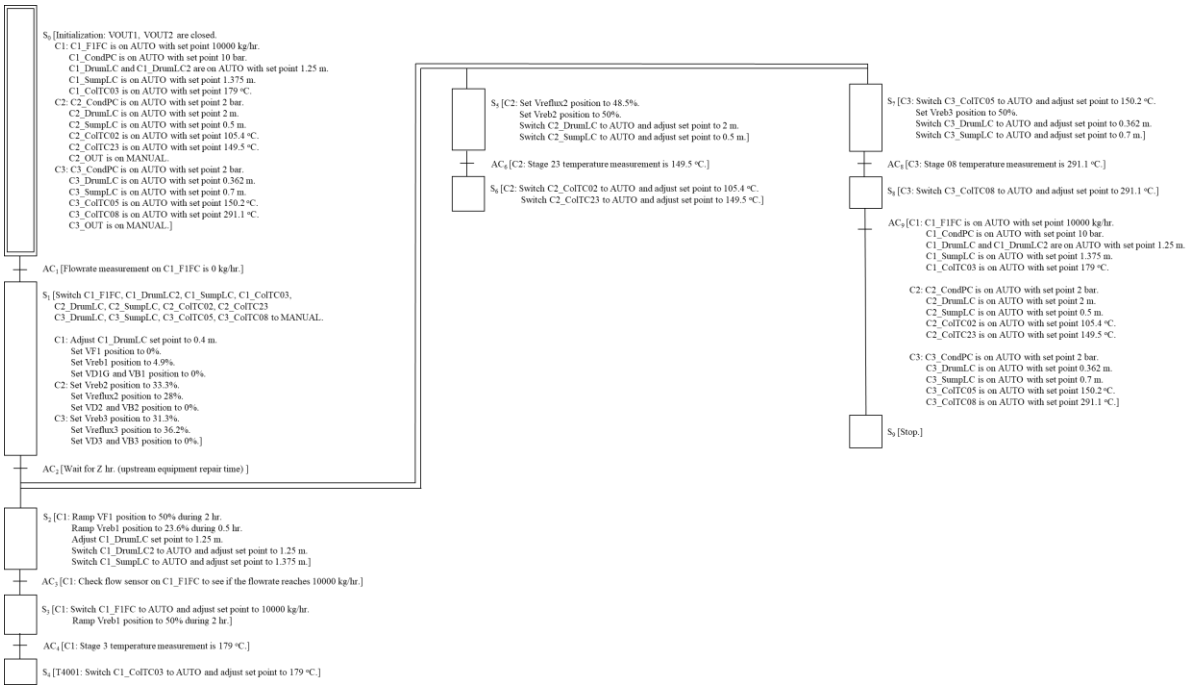

Figure 3. Sequential function chart of total-reflux operation for HDA backend

6. Impacts of repair time

Although the above procedure synthesis steps were tested only with working examples, the proposed method is expected to be generalizable. Rigorous simulation data were generated for two typical repair times in implementing the SFCs in Figures 3 and 4, and the proper emergency response strategy can then be selected accordingly. This selection approach can also be extended to any other chemical process of the same structure in a straightforward fashion.

6.1. Short-term repairs

Let us first assume that the frontend failure(s) in the above HDA plant is expected to be repaired within 5 hours. Tables 2 shows the simulation summaries of VOC emission levels and utility consumption amounts in reboilers and condensers corresponding to the tail-chase and total-reflux operating strategies. Notice that, although the total amounts of energy consumed by both strategies are approximately the same, the former seems to be a better choice since the overall waste abatement capability is considerably larger under the condition that the repair job can be completed in a short time period.

Operating strategy	Amount of off-spec product (kg)	Energy consumed (GJ)			Total operation time (hr)
		Condenser	Reboiler	Total	
Tail chase	1484.2	-306.8	315.3	622.1	10.6
Total reflux	2880.2	-299.3	308.8	608.1	11.8

Table 2. Total amounts of off-spec products generated and energy consumed in 5 hours after implementing two mitigation strategies in an HDA plant

6.2. Long-term repairs

The performances of the above strategies implemented in 15 hours are compared next in Table 3. In can be observed that, although the total amount of off-spec

products generated by tail-chase operation is somewhat less, the total energy consumed by the total-reflux counterpart is clearly at a lower level. The latter observation is worth noticing. The energy consumption rate needed to facilitate the recycle flows in the tail-chase operation must be maintained continuously at a high level, while that for the latter can be kept at a minimum as long as each column is operated in standalone total-reflux mode. This discrepancy in energy consumption is expected to be more pronounced if the repair time is raised to an even longer level. Thus, it seems that the total-reflux procedure is a better choice if the upstream failure(s) lasts indefinitely for a long period of time.

Operating strategy	Amount of off-spec product (kg)	Energy consumed (GJ)			Total operation time (hr)
		Condenser	Reboiler	Total	
Tail chase	1412.7	-567.2	575.2	1142.4	20.6
Total reflux	2181.6	-470.3	478.4	948.7	20.9

Table 3. Total amounts of off-spec products generated and energy consumed in 15 hours after implementing two mitigation strategies in an HDA plant

3. Conclusions

Both tail-chase and total-reflux operations are demonstrated in extensive simulation studies to be effective for eliminating VOC emission caused by the frontend failure(s) in an HDA plant. The simulation results suggest that the former is preferred for the short-term response needs and the latter is useful in long-term scenarios. The heuristic approach proposed here may be generalized to operate the backend of any other chemical plant with the same process structure after malfunction(s) develops in the frontend.

References

Chen, G.W., 2024, *Shutdown and Emergency Response Procedures for Separation Sequences in Chemical Plants*, MS Thesis, National Cheng Kung University, Tainan, Taiwan.

Chen, G.W., Chang, C.T., 2025, Alternative emergency response procedures to mitigate impacts of front-end failures in ethylene production plants, *ACS Chemical Health & Safety*, 32, 426-439.

Chenevert, D., Harry, C.J., Unterbrink, B., Cain, M., 2005, Flare minimization practices improve olefins plant start-ups, shutdowns, *Oil & Gas Journal*, 103(33), 54-60.

Gani, R., Jepsen, T.S., Perez-Cisneros, E.S.A, 1998, Generalized reactive separation unit model - modelling and simulation aspects, *Computers & Chemical Engineering*, 22, S363-S370.

Murphy, C.F., Allen, D.T., 2005, Hydrocarbon emissions from industrial release events in the Houston-Galveston area and their impact on ozone formation, *Atmospheric Environment*, 39(21), 3785-3798.

Wang, S., Zhang, J., Wang, S., Xu, Q., 2016, Dynamic simulation for flare minimization in chemical process industry under abnormal operations, *Current Opinion in Chemical Engineering*, 14, 26-34.

Xu, Y., Dinh, H., Xu, Q., Eljack, F.T., El-Halwagi, M.M., 2020, Flare minimization for an olefin plant shutdown via plant-wide dynamic simulation, *Journal of Cleaner Production*, 254, 120129.

Raman composition analysis of electrolyte solvent mixtures obtained from lithium-ion battery (LIB) recycling

T. Goldberg, V. Herdegen, A.S. Braeuer
TU Bergakademie Freiberg, Germany
Institute of Thermal-, Environmental- and Resources' Process Engineering

Abstract
The recovery of organic electrolyte solvents from spent lithium-ion batteries (LIBs) is an important step to meet future regulatory recycling targets. Raman spectroscopy enables rapid and accurate composition analysis and has high potential as an in-line measurement system, supporting process control and safety in prospective electrolyte recycling processes, such as distillation-based recovery.
In this study, Raman spectroscopy was developed for the quantitative analysis of relevant electrolyte solvent mixtures using 300 different mixtures synthetized of pure compounds. The compositions were evaluated using classical least squares (CLS) and partial least squares (PLS) regression models, which were compared in terms of accuracy and robustness. CLS regression demonstrated higher accuracy and precision with an average absolute deviation of 0.006 and 0.015 mol/mol for binary and quinternary mixtures, respectively. The method was also successfully evaluated on real samples regained from battery recycling-shredder, showing higher robustness against fluorescence interferences and improved extendibility to impurities.

Keywords
Battery recycling, Raman spectroscopy, Electrolyte solvents, Composition analysis, CLS, PLS

1. Introduction

According to the EU regulation on batteries and waste batteries, spent LIBs must be recycled at a minimum rate of 70 wt.% by 2031 [1]. In order to achieve this target, future recycling strategies must address not only the recovery of electrode materials and lithium salts, but also the liquid electrolyte solvents. During some LIB shredding process or in subsequent black mass drying, the electrolyte solvents are evaporated under vacuum and condensed in a cold trap. Owing to differences between LIB types, generations and manufacturers, electrolyte solvent mixtures differ in their compounds and composition, leading to more complex mixtures in the recycling process. However, five organic carbonates typically constitute the main solvent compounds: dimethyl carbonate (DMC), ethyl methyl carbonate (EMC) and diethyl carbonate (DEC) as lower boiling compounds as well as ethylene carbonate (EC) and propylene carbonate (PC) as higher boiling compounds [2]. In order to contribute to the regulatory target, our main objective is to fractionate the liquid mixture into its pure compounds by continuous counter-current distillation, allowing for their potential reuse in LIB production.
Here, we report the development of Raman spectroscopy for rapid online composition analysis of electrolyte solvent mixtures obtained from LIB recycling. The developed methods prospectively contribute to real-time process control and quality assurance in distillation operations for the refinement of electrolyte mixtures emerging from battery recycling processes. Two different approaches for quantitative composition analysis are compared: Partial least squares (PLS) regression, a widely used chemometric

approach suitable for highly collinear variables and high-dimensional spectral data [3], and classical least squares (CLS) regression as a physics-based approach with improved interpretability. The resulting models were developed on synthetic mixtures of pure electrolyte solvents, and were subsequently evaluated on real samples obtained from a LIB recycling-shredder. Such real samples pose greater analytical challenges due to the presence of impurities and possible additives.

2. Results and discussion

2.1 Preliminary considerations

DMC (CAS: 616-38-6), DEC (CAS: 105-58-8), EC (CAS: 96-49-1) and PC (CAS: 108-32-7) were purchased from Carl Roth in synthesis grade with >99.9 % certified purity, while EMC (CAS: 623-53-0) was only available with a purity of 98.3 %. Real condensate samples were provided to us by the Institute of Mechanical Process Engineering and Mineral Processing at TU Bergakademie Freiberg, which operates a pilot-scale battery shredder processing various end-of-life batteries, particularly from the automotive sector. Figure 1 shows the appearance of such a sample in comparison with a synthetic mixture having a similar electrolyte solvent composition. A typical cuvette-based Raman setup (in principle described by Braeuer [4]) was used to measure all Raman spectra presented here. Figure 2a illustrates example spectra of a real condensate mixture obtained from a battery shredder, measured with two different excitation wavelengths (532 and 785 nm). Figure 2b shows the pure compound spectra of all five organic carbonates purchased, excited with an excitation wavelength of 785 nm.

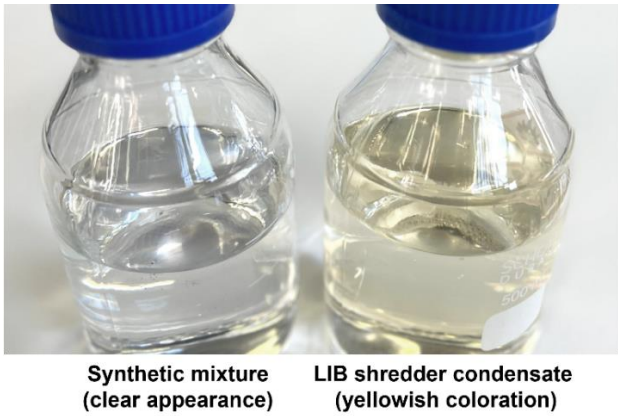

Figure 1: Visual comparison of a synthetic electrolyte solvent mixture (left) and a real condensate sample obtained from LIB shredder (right) with similar composition.

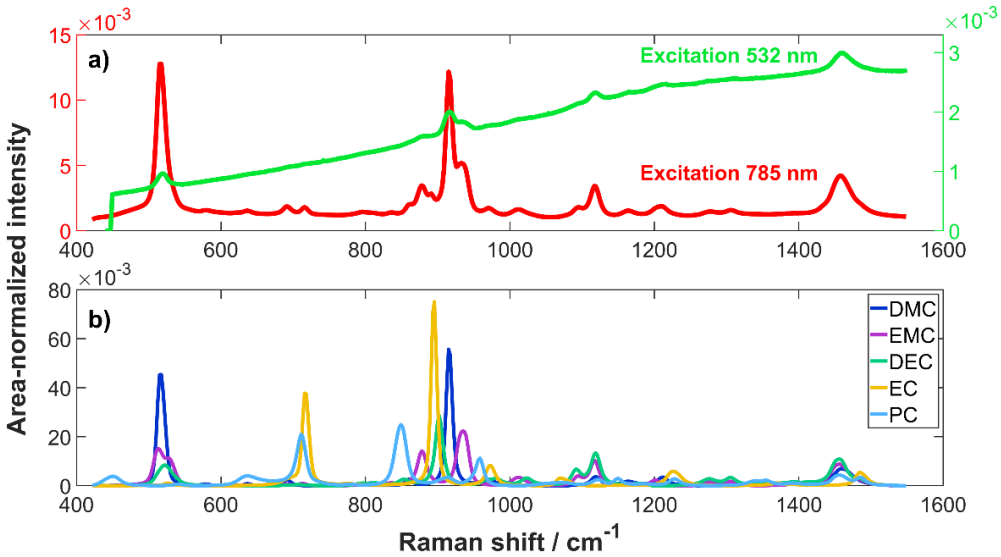

Figure 2: Area-normalized Raman spectra of a) real sample from LIB recycling shredder excited with 532 and 785 nm and b) pure organic carbonates excited with 785 nm.

Unlike the pure organic carbonates, all samples obtained from the LIB shredder exhibited a yellowish coloration (Figure 1 right), which may originate from partial thermal degradation or contamination during processing. As shown in Figure 2a, this leads to increased fluorescence interferences when using shorter excitation wavelengths, which strongly overlap with the Raman signal. Consequently, only the longer excitation wavelength of 785 nm was used for all subsequent measurements. Because of structural similarities of the different electrolyte solvent molecules, the pure compound spectra show significant peak overlaps. The development of composition evaluation models for such complex mixtures requires relatively large data sets for calibration/training and testing. Therefore, 300 synthetic mixtures were prepared using an analytical balance (readability 0.0001 g), ranging from simple binary to quinternary mixtures comprising the five organic carbonates.

2.2 Composition evaluation models

In PLS regression, both, the spectral data matrix and the composition matrix are directly projected onto a reduced set of latent variables. Prior to our regression, the background signal of each spectrum was removed by iteratively fitting a fourth-degree polynomial to the baseline, which proved more robust than using an asymmetric least squares (ALS) algorithm [5] for background fitting and subtraction. Model training was then performed using the *plsregress()* function in MATLAB 2023b, and the number of latent variables was determined by cross-validation.

According to Figure 2, the spectral features of the pure compounds are preserved in the mixture spectra in terms of peak positions and intensities, which is used in the physics-based CLS model. In order to use as much spectral information as possible, the complete fingerprint range (400 – 1600 cm^{-1}) is evaluated. Under the assumption of linear additivity of Raman signals, each mixture spectrum was described as linear combination of the pure compound spectra (linear unmixing):

$$\hat{S}_{mix}(\nu) = \sum_{i=1}^{N} w_i S_i(\nu) + b\,B(\nu) + \sum_{k=0}^{4} p_k \nu^k \qquad (1)$$

The modelled mixture spectrum $\hat{S}_{mix}$ at each Raman shift ν is ideally represented as the sum of the weighted pure compound spectra S_i, with the fitting parameters w_i as weights. In contrast to the PLS model, the background was modelled simultaneously using a measured background spectrum B (air-filled cuvette) weighted by the fitting parameter b, and – in order to describe the fluorescence background – a fourth-degree polynomial function with fitting parameters p_k. For each spectrum, the fitting parameters were identified by minimizing the sum of squared errors between the modelled and the measured spectrum. Figure 3 illustrates a spectrum reconstruction obtained for an example quinternary synthetic mixture.

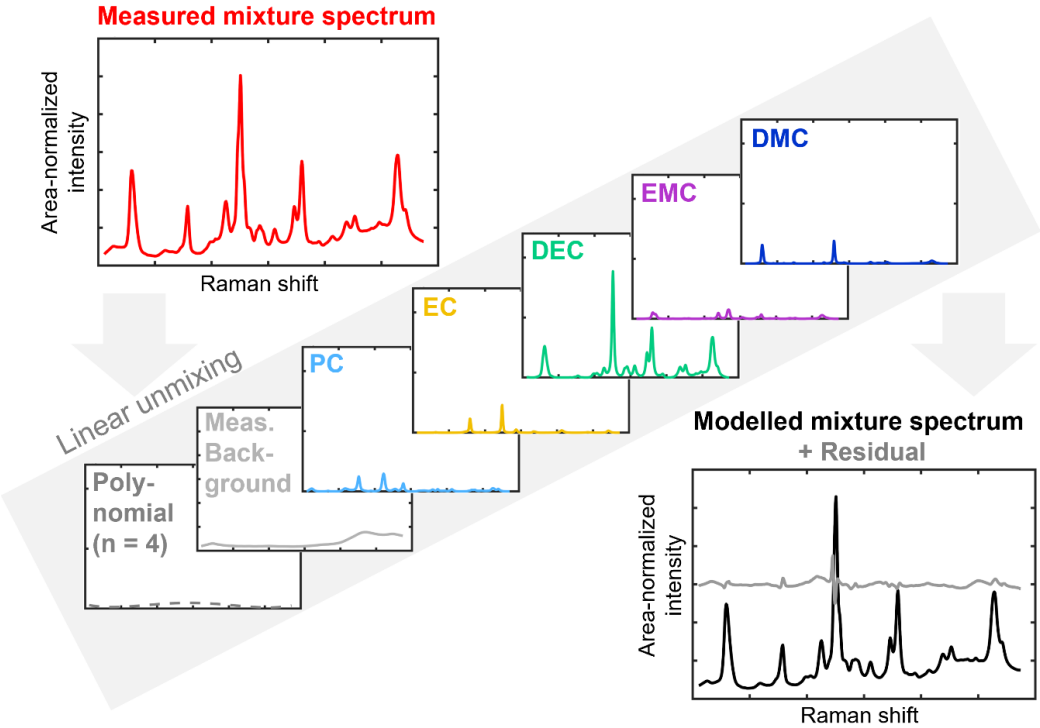

Figure 3: Spectrum reconstruction (CLS model) of an example quinternary synthetic mixture.

As the main outcome of the fitting procedure, a set of weights w_i was obtained for each mixture spectrum, where i denotes the compounds in the mixture. Owing to the area normalization, these weights directly correspond to the Raman signal intensities I_i of the compounds in the mixture. From theoretical considerations, the ratio of Raman signal intensities is directly proportional to the ratio of the corresponding mole fractions of two compounds x_i and x_j with the binary calibration constant K_{ij} [4]:

$$\frac{I_i}{I_j} = K_{ij} \frac{x_i}{x_j} \tag{2}$$

For both, PLS and CLS model, the spectra of the binary synthetic mixtures were used for model training and calibration, respectively. The trained models were then tested on spectra of higher-order synthetic mixtures. Figure 4 presents parity plots for the composition evaluation with both models.

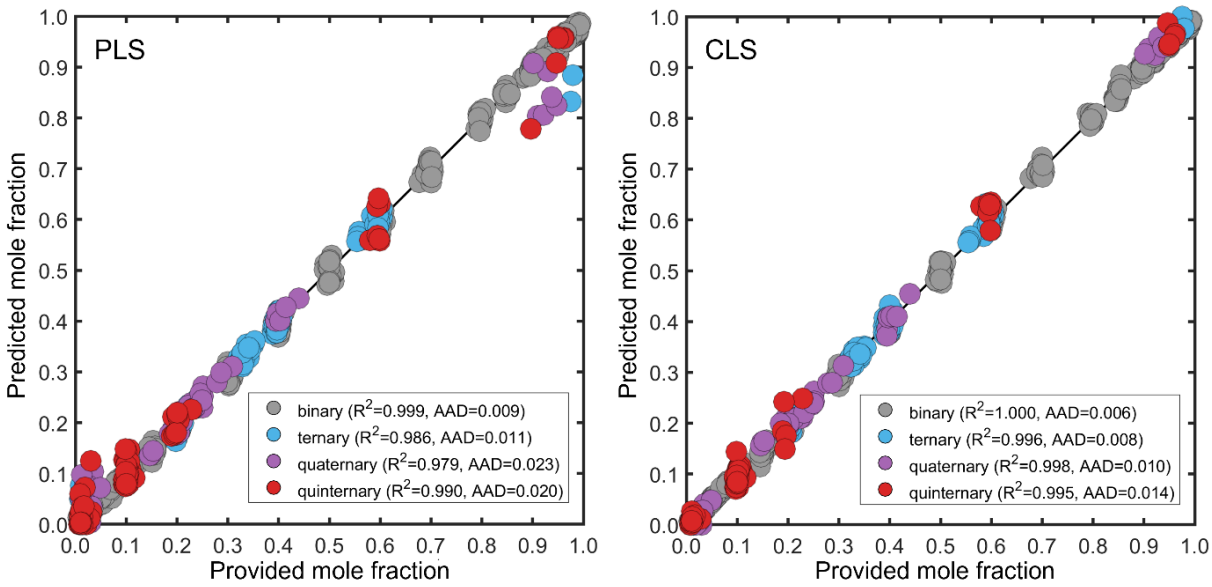

Figure 4: Parity plot of PLS model (left) and CLS model (right) trained or, respectively, calibrated with binary mixtures and applied on higher-order mixtures.

The physics-based CLS regression model allows composition quantification with higher accuracy and especially with higher precision compared to the PLS model. The absolute average deviation (AAD) of both models for binary mixtures is below 1 mol%, which is particularly suitable for prospective online process monitoring in distillation processes. The average deviations of the CLS model are slightly increasing when applied on higher-order synthetic mixtures, but still below 1.5 mol% for quinternary mixtures. The accuracy for multi-compound mixture-quantification is therefore sufficient to enable rapid online composition analysis in prospective downstream processing of electrolyte solvent mixtures. Larger deviations may also result from increased deviations in our sample preparation, when weighing more compounds. Additionally, the strong peak overlaps in the pure compound spectra may lead to a more uncertain parameter identifiability, which results in deviations for all compounds caused by the summation constraint. The accuracy and precision of the PLS model can be improved by additionally using higher-order mixtures for training. However, the performance then gets comparable to the CLS model, while the substantially increased calibration effort reduces its practical relevance.

2.3 Model evaluation

So far, the compositions of four real condensate mixtures from a pilot battery shredder were analyzed using Raman spectroscopy. For comparison, the samples were additionally analyzed with gas chromatography-mass spectrometry (GC-MS). The results for one example condensate sample are presented in Table 1. The comparison of the methods based on this example mixture is representative for the other samples.

Table 1: Comparison of analyzed composition of one example condensate sample from LIB shredder using GC-MS and Raman spectroscopy methods. (n.d. = not detected)

	Mole fractions of analyzed compounds				
	DMC	EMC	DEC	EC	PC
GC-MS	0.50	0.45	0.02	0.03	n.d.
Raman (CLS)	0.51	0.44	0.03	0.02	0.00
Raman (PLS)	0.50	0.44	0.00	0.03	0.03

For the CLS model, deviations in composition quantification remained within the range observed for the synthetic mixtures. The fitting procedure represented the stronger and varying fluorescence background well, enabling robust compound identification. In contrast, prior background subtraction required for the PLS model, led to less robust results, as any variations not represented in the training data cannot be adequately captured. As a consequence, spectral features are incorrectly assigned to other compounds in the mixture or compounds that are not actually present, as exemplified by PC in Table 1. GC-MS analysis revealed that another condensate mixture from LIB shredder additionally contained some proportions of tert-butylbenzene and tert-pentylbenzene, additives used in some LIB to enhance overcharge inhibition [2]. However, this could be also identified from “missing” peaks in the fitted spectrum in CLS regression, and maintained by adding their pure compound spectra to the CLS model, still allowing good parameter identifiability. In contrast, PLS regression failed when confronted with this “unseen” spectral information, showing the need of extensive training data. This illustrates the beneficial interpretability, extendibility, and robustness of the CLS model compared to the PLS model.

3. Conclusions

In this work, Raman spectroscopy combined with a developed CLS regression was successfully applied for the rapid, quantitative analysis of organic electrolyte solvent mixtures obtained from LIB recycling. CLS regression demonstrated superior robustness, interpretability, and extendibility compared to PLS, particularly when analyzing real samples from battery shredders that exhibit stronger fluorescence interferences and previously unobserved additives, highlighting the potential for an integration into in-line measurement systems.

In the context of LIB recycling, this capability can support enhanced process control, contribute to more efficient waste management, and assist to meet future regulatory targets. Future work will focus on expanding the method to additional electrolyte compounds and samples from other shredders, to further validate the robustness and general applicability of the CLS-based Raman approach in complex recycling streams. These findings also support the conceptual development of a distillation process for electrolyte solvent recovery.

Acknowledgements

The authors acknowledge the Institute of Mechanical Process Engineering and Mineral Processing at TU Bergakademie Freiberg for providing the real electrolyte samples from their LIB shredder.

References

[1] Regulation (EU) 2023/1542 of the European Parliament and of the Council of 12 July 2023 concerning batteries and waste batteries, amending Directive 2008/98/EC and Regulation (EU) 2019/1020 and repealing Directive 2006/66/EC, Annex XII, Part B.

[2] Wolke, M., Schröder, K., Arnold, K., Mozumder, P., Beuerle, T., Jasch, K., Scholl, S. (2025). *Analyzing Organic Electrolyte Solvents from Spent Lithium-ion Batteries as a Basis for Distillative Value Component Recovery.* Recycling, 10(1), 19. https://doi.org/10.3390/recycling10010019

[3] Wold, S., Sjöström, M., and Eriksson, L. (2001). *PLS-regression: A basic tool of chemometrics. Chemometrics and Intelligent Laboratory Systems*, 58(2), 109–130. https://doi.org/10.1016/S0169-7439(01)00155-1

[4] Braeuer, A. (2015). *In situ spectroscopic techniques at high pressure*. Elsevier Science Ltd.

[5] Eilers, P.H.C.; Boelens, H.F. (2005). *Baseline correction with asymmetric least squares smoothing*. Leiden Univ. Med. Cent. Rep., 1, 5

Multi-Objective Optimization of a Reactive Distillation Column with Multiple Reactive Zones and Side Condensers: Open and Closed Loop Controllability in Silane Production

Josué Julián Herrera Velázquez, Julián Cabrera Ruiz, J. Rafael Alcántara Avila, Salvador Hernández
[1]*Universidad de Guanajuato, Guanajuato, México;*
[2]*Universidad de Guanajuato, Guanajuato, México;*
[3]*Pontificia Universidad Católica del Perú, Lima, Perú;*
[4]*Universidad de Guanajuato, Guanajuato, México*

Abstract
Polycrystalline silicon-based photovoltaics rely on silane (SiH_4), whose production via trichlorosilane ($SiHCl_3$) disproportionation can be intensified using reactive distillation column (*RDC*). This work presents a multi-objective optimization (*MOO*) framework for a *RDC* with multiple reactive zones and side condensers, in which Total Annual Cost (*TAC*), reboiler duty (Q_H), an open-loop steady-state controllability metric ($A_\gamma+\gamma_{sm}$), and the closed-loop Integral of Absolute Error (IAE_{min}) are simultaneously optimized using an Aspen Plus®–Python coupled environment. The methodology employs simplified first-order dynamic models to estimate steady-state controllability during optimization, reducing computational cost but retaining relevant dynamic information. Dynamic boundaries are introduced to evaluate configurations with one, two, and three reactive zones within a single optimization run, and to determine the location and heat duties of side condensers. Closed-loop performance is assessed through decoupled SISO control of the column top and bottom, with PI controller parameters tuned at each iteration using Bayesian optimization. Results show that designs with two and three reactive zones dominate the Pareto front, achieving lower *TAC* and Q_H while exhibiting near first-order dynamic behavior. The best solution includes two reactive zones and achieves reductions of 18.59% in *TAC*, 10.55% in Q_H, 11.59% in $A_\gamma+\gamma_{sm}$ and a 16.76% increase in IAE_{min} compared to the reference case.

Keywords
Reactive Distillation, Silane, Multi-Objective Optimization, Process Controllability, Aspen Plus - Python

1. Introduction

Polycrystalline silicon-based photovoltaics represent a key alternative to fossil fuels. One of their precursors, silane (SiH_4), is also widely used in semiconductors and chemical synthesis. Zang et al. (2017) proposed a reactive distillation for the disproportionation of $SiHCl_3$ to produce SiH_4. Parametric analysis showed that dividing the reactive zone into three reactive zones improves energy efficiency, while the inclusion of side condensers reduces thermal load at the top of the column and facilitates SiH_4 condensation. Alcántara-Avila et al. (2022) solved the optimization problem for a *RDC* for a single reactive zone and two side condensers, where it shows that there is a direct competition between costs and controllability. Techniques

that estimate steady-state controllability have been proposed, based on open-loop analysis using Singular Value Decomposition (*SVD*) and obtaining the condition number under an $A_\gamma+\gamma_{sm}$ parameter (Cabrera-Ruiz et al., 2018). These employs simplified first-order models with steady-state approximations of the time constants (Skogestad and Morari, 1987), showing good performance for low frequencies. The use of approximate first-order models simplifies and generalizes system analysis, facilitating the acquisition of relevant controllability information during optimization.

2. Methodology

2.1 Case Study

The RDC considered in this study is shown in Figure 1a and corresponds to the solution reported by Zhang et al. (2017) using their reaction mechanism. The system was modeled in Aspen Plus V12 using the Peng-Robinson thermodynamic model. Each stage has a holdup of 60.25 mol. The column operates at a pressure of 5 atm, with a pressure drop per stage of 0.5 kPa. Product purities are specified at 99.3 mol% for SiH_4 and 99.1 mol% for silicon tetrachloride ($SiCl_4$). The variables of the optimization problem include the total number of stages (N_T), the feed stage (N_F), and the starting and ending stages of each reactive zone: first (N_{R1O}, N_{R1F}), second (N_{R2O}, N_{R2F}), and third (N_{R3O}, N_{R3F}). In addition, the stage locations where the vapor stream is withdrawn to the side condensers (N_{CD1}, N_{CD2}, and N_{CD3}) and their corresponding heat duties (Q_{CD1}, Q_{CD2}, and Q_{CD3}) are considered. The variables are solved sequentially as shown in Figure 1b.

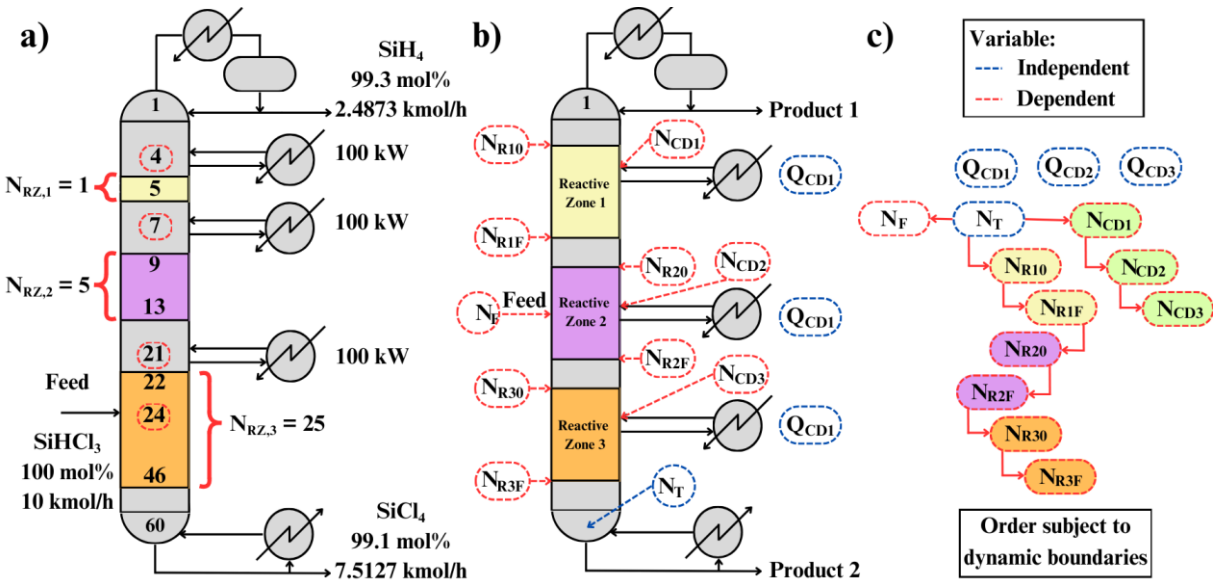

Figure 1: a) Reference *RDC* design; b) optimization variables; and c) variable evaluation sequence.

2.2 Mathematical Treatment

The problem is formulated as a *MOO* (Eq. 1) subject to a simulator convergence constraint (*Conv*) and purity constraints, with nonconvergence penalized across all objectives. Optimization variable bounds are given in Table 1 and the variables are normalized using Eq. 2, where VN_i is the normalized value of V_i, and B_{upper} and B_{lower} are its bounds. *TAC* is computed from Eq. 3 assuming a 5-year payback period, while Q_H is obtained directly from Aspen Plus simulations.

$$\min\left(TAC, Q_H, A_\gamma + \gamma_{sm}, \underset{n\in\{D,B\}}{IAE_{min}}(K_{p,n}, K_{i,n})\right)$$
$$= f(N_T, N_F, N_{R10}, N_{R1F}, N_{R20}, N_{R2F}, N_{R30}, N_{R3F}, N_{CD1}, N_{CD2}, N_{CD3}, Q_{CD1}, Q_{CD2}, Q_{CD3}) \quad (1)$$
$$s.t. \quad P_{SiH_4} \geq 99.3\%; P_{SiCl_4} \geq 99.1\%; \; Conv = 0$$

VARIABLES	BOUNDARIES	VARIABLES	BOUNDARIES
N_T	[50, 100]	N_{R3F}	[N_{R3O}, N_T – 1]
N_F	[2, N_T – 1]	N_{CD1}	[2, N_T – 3]
N_{R1O}	[2, N_T – 3]	N_{CD2}	[N_{CD1} +1, N_T – 2]
N_{R1F}	[N_{R1O}, N_T – 3]	N_{CD3}	[N_{CD2} +1, N_T – 1]
N_{R2O}	[N_{R1F} + 1, N_T – 2]	Q_{CD1} [kW]	[0, 400]
N_{R2F}	[N_{R2O}, N_T – 2]	Q_{CD2} [kW]	[0, 400]
N_{R3O}	[N_{R2F} + 1, N_T – 1]	Q_{CD3} [kW]	[0, 400]

Table 1: Optimization Bounds.

$$VN_i = (B_{upper} - V_i)/(B_{upper} - B_{lower}) \quad (2)$$

$$TAC\left[\frac{USD}{year}\right] = C_{Vapor} + C_{Refrigerant} + C_{Catalyst} + \frac{\left(\frac{CEPCI_{2022}}{CEPCI_{2001}}\right)(C_{Shell} + C_{Plates} + C_{Reboiler} + C_{Condenser})}{Recovery\ time\ (years)} \quad (3)$$

2.2.1 Open-loop controllability

For A_γ+γ_{sm} the transfer function $G_j(s)$ is computed as defined in Eq. 4. The corresponding matrix is constructed from the transfer functions associated with perturbations in the reflux ratio (*RR*) and Q_H, including their cross interactions. For iteration *j*, $P_{SiH4,j}$ and $P_{SiCl4,j}$ represents the purities of SiH_4 and $SiCl_4$. Purities under a 0.5% positive perturbation of the *RR* ($P_{SiH4,RRj}$, $P_{SiCl4,RRj}$) and Q_H ($P_{SiH4,QH,j}$, $P_{SiCl4,QH,j}$) are obtained in independent simulations.

$$G_j(s) = \begin{bmatrix} \frac{\left(\frac{P_{SiH_4,RR_j} - P_{SiH_4,j}}{0.0025}\right)}{1+\tau_{1,1}\,s} & \frac{\left(\frac{P_{SiH_4,Q_{H,j}} - P_{SiH_4,j}}{0.0025}\right)}{1+\tau_{1,2}\,s} \\ \frac{\left(\frac{P_{SiCl_4,RR_j} - P_{SiCl_4,j}}{0.0025}\right)}{1+\tau_{2,1}\,s} & \frac{\left(\frac{P_{SiCl_4,Q_{H,j}} - P_{SiCl_4,j}}{0.0025}\right)}{1+\tau_{2,2}\,s} \end{bmatrix} \quad (4)$$

Perturbations for τ follow Eqs. (5–8). For each stage *K*, $x_{SiH4,k}$ and $x_{SiCl4,k}$ are the mole fractions of SiH_4 and $SiCl_4$, while $H_{L,K}$ is the liquid holdup. Top and bottom fluxes for iteration *j* under *RR* and Q_H perturbations are denoted as $F_{D,RRj}$, $F_{B,RRj}$, $F_{D,QH,j}$ and $F_{B,QH,j}$. The transfer functions $G_j(s)$ are converted to the frequency domain, and the

SVD is evaluated over the frequency range from 10^{-4} to 10^{2} rad/h. Based on this analysis, the value of γ^* is computed.

$$\tau_{1,1} = \frac{\sum_{k=N_{R10}}^{N_{R3F}} H_{L,k}\left(x_{SiH_4,RR_j,k} - x_{SiH_4,k}\right)}{F_{D,RR_j}\left(P_{SiH_4,RR_j} - P_{SiH_4,j}\right) + F_{B,RR_j}\left(P_{SiCl_4,RR_j} - P_{SiCl_4,j}\right)} \tag{5}$$

$$\tau_{2,1} = \frac{\sum_{k=N_{R10}}^{N_{R3F}} H_{L,k}\left(x_{SiCl_4,RR_j,k} - x_{SiCl_4,k}\right)}{F_{D,RR_j}\left(P_{SiH_4,RR_j} - P_{SiH_4,j}\right) + F_{B,RR_j}\left(P_{SiCl_4,RR_j} - P_{SiCl_4,j}\right)} \tag{6}$$

$$\tau_{1,2} = \frac{\sum_{k=N_{R10}}^{N_{R3F}} H_{L,k}\left(x_{SiH_4,Q_{H,j},k} - x_{SiH_4,k}\right)}{F_{D,Q_{H,j}}\left(P_{SiH_4,Q_{H,j}} - P_{SiH_4,j}\right) + F_{B,Q_{H,j}}\left(P_{SiCl_4,Q_{H,j}} - P_{SiCl_4,j}\right)} \tag{7}$$

$$\tau_{2,2} = \frac{\sum_{k=N_{R10}}^{N_{R3F}} H_{L,k}\left(x_{SiCl_4,Q_{H,j},k} - x_{SiCl_4,k}\right)}{F_{D,Q_{H,j}}\left(P_{SiH_4,Q_{H,j}} - P_{SiH_4,j}\right) + F_{B,Q_{H,j}}\left(P_{SiCl_4,Q_{H,j}} - P_{SiCl_4,j}\right)} \tag{8}$$

Numerical integration is performed using Eq. (9) with the trapezoidal method. This equation is discussed in detail in Herrera-Velázquez et al. (2025). Thus, for each iteration *j* in MOO, three simulations are performed: (1) to verify constraint satisfaction, (2) with perturbed *RR*, and (3) with perturbed Q_H.

$$A_\gamma + \gamma_{sm} = \frac{\int_{\log a}^{\log b} \log(\gamma^*)\, d(\log\omega)}{\log b - \log a} + \int_{\log a}^{\log b} \Delta log(\omega)\, |\gamma_{i+1}^{'} - \gamma_i^{'}|\, d(\log\omega) \tag{9}$$

2.2.2 Closed-loop controllability

The IAE_{min} function (Eq. 10) sums IAE_D (Dome, SiH_4) and IAE_B (Bottom, $SiCl_4$), using the diagonal transfer functions of $G_j(s)$ (Eq. 4) in a decoupled SISO approach that ignores cross effects. The external disturbance *d(t)* is modeled as a 30% step applied at 2 hours. Closed-loop simulations were implemented with the Python Control Systems Library (control) (Åström & Åkesson, 2023), and PI parameters were optimized via Bayesian optimization using Optuna library with the TPE algorithm for 100 trials (Akiba et al., 2019). This procedure is for each optimization iteration (*j*).

$$\underset{n\in\{D,B\}}{IAE_{min}} = \min \sum_{n\in\{D,B\}} IAE_n\left(K_{p,n}, K_{i,n}\right) = \min \sum_{n\in\{D,B\}} \int_0^T \left|r_n(t) - y_n\left(t; K_{p,n}, K_{i,n}, d(t)\right)\right| dt$$
$$s.t.\ \ 0.1 \le K_{p,n} \le 100;\ 0.01 \le K_{i,n} \le 10;\ d(t) = \begin{cases} 0 & t < 2\ hours \\ 0.3 & t \ge 2\ hours \end{cases} \tag{10}$$

3. Results and discussion

The complete model-optimization problem was solved using the NSGA-II algorithm (Blank & Deb, 2020) with 50 generations of 500 individuals. Figure 2 illustrates the optimization process. This were performed in Spyder IDE 5.2.2 on an Intel® Xeon® W-3235 CPU at 3.30 GHz with 48 GB RAM. The summarized results are presented in Table 2. A total of 1,290 designs meet the restrictions: 18 designs with one reactive zone (1.39%), 299 with two reactive zones (23.17%), and 973 with three reactive zones (75.44%).

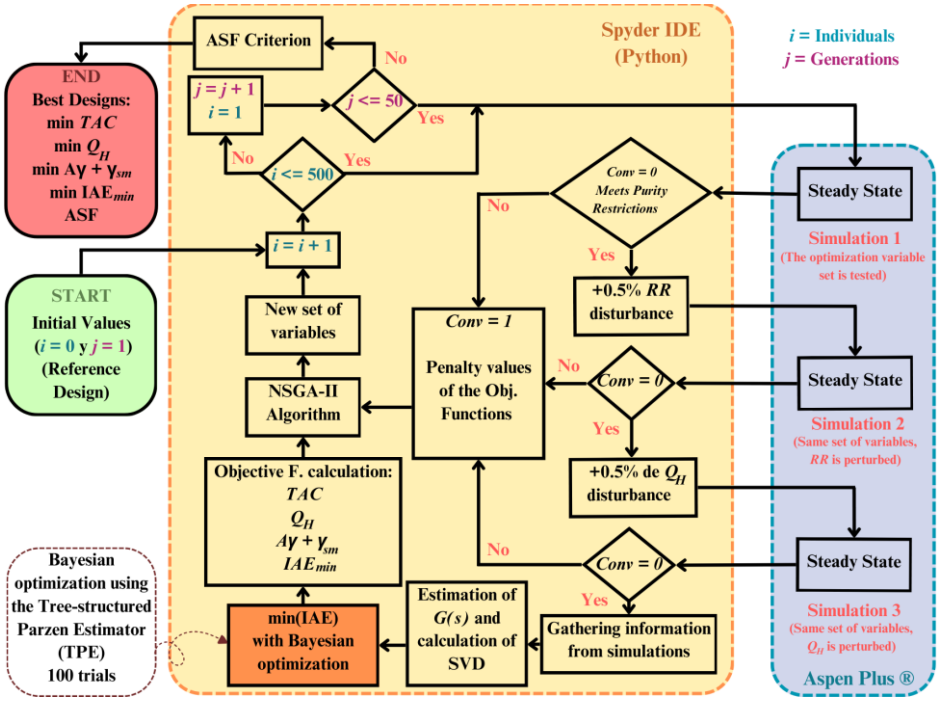

Figure 2: Flowchart of the mathematical model optimized for *RDC* with the NSGA-II algorithm.

VARIABLES	Ref. Des.	min *TAC*	min Q_H	min $A_\gamma+\gamma_{sm}$	min IAE_{min}	*ASF*
N_T	60	59	94	71	74	63
N_F	24	4	3	2	4	5
N_{R1O}	5	5	7	10	11	4
N_{R1F}	5	34	46	30	22	46
N_{R2O}	9	37	48	40	29	47
N_{R2F}	13	49	78	46	36	49
N_{R3O}	22	51	82	50	43	55
N_{R3F}	46	51	86	54	50	55
N_{CD1}	4	7	5	9	8	8
N_{CD2}	7	18	43	44	23	14
N_{CD3}	21	37	75	57	63	31
Q_{CD1} [kW]	100	350	81	81	101	51
Q_{CD2} [kW]	100	50	16	68	101	183
Q_{CD3} [kW]	100	15	19	71	38	11
Reactive Zones	3	3	3	3	3	2
TAC [$/year]	868,419	505,751	955,650	1,073,334	1,059,080	706,959
Q_H *[kW]*	507	492	378	640	665	453
$A_\gamma+\gamma_{sm}$	0.9909	2.3504	0.5730	0.2771	0.4256	0.8760
IAE_{min}	0.0167	0.0360	0.0257	0.0149	0.0148	0.0195

Table 2: Summary of results of multi-objective optimization.

At the Pareto front, 79 non-dominated solutions were identified, of which 11 (14%) feature two reactive zones and 68 (86%) include three reactive zones, indicating that designs closest to the ideal point (*ASF*) correspond to configurations with divided reactive zones. Analysis of the dynamic behavior shows that solutions near the Pareto front can be accurately approximated by first-order transfer functions, consistent with Herrera-Velázquez et al. (2025). In contrast, solutions farther from the Pareto front, such as the reference case, display more complex dynamics, which can lead to larger deviations in the estimation of the open-loop controllability metric $A_\gamma+\gamma_{sm}$ and in IAE_{min}. These observations highlight that control-oriented metrics provide increasingly reliable information as the optimization converges toward the non-dominated region.

4. Conclusions

A multi-objective optimization (MOO) approach based on the integrated design and control (IDC) framework was employed, in which both open-loop and closed-loop controllability were evaluated using first-order transfer functions derived from a steady-state simulation perturbation protocol. The complete MOO procedure required approximately 16 hours of computation, during which around 30,000 simulations were executed. This total includes simulations that satisfied all constraints and completed the full workflow, as well as those that terminated at intermediate stages of the optimization flowchart. The best solution, as determined by the ASF method, features two reactive zones and improves *TAC* by 18.59%, Q_H by 10.55%, and $A_\gamma+\gamma_{sm}$ by 11.59%, with a 16.76% increase in IAE_{min} compared to the reference case. The proposed control metrics effectively capture column dynamics, providing relevant information on controllability during the steady-state optimization process itself. Moreover, the methodology is flexible and generalizable, enabling the assessment of controllability in any distillation column optimization without adding significant computational steps.

References

J. Blank, K. Deb, (2020), pymoo: Multi-Objective Optimization in Python. *IEEE Access* (8), 89497-89509.

J. Cabrera-Ruiz, C. Ramírez-Márquez, S. Hasebe, S. Hernández, J.R. Alcántara-Avila, 2018, Outlook of the Dynamic Behavior of Closed-Loop Control through Open-Loop Analysis for Intensified Separation Processes, *Ind Eng Chem Res*, 57(49), 16795-16808.

J.J. Herrera-Velazquez, J.R. Alcántara-Avila, S. Hernández, J. Cabrera-Ruiz, 2025, Evaluation of the Controllability of Distillation with Multiple Reactive Stages. *Syst Control Trans,* 4, 1095-1100

J.R. Alcántara-Avila, J. Cabrera-Ruiz, H. Lee, 2022, Open-Loop Analysis for the Stability of Reactive Distillation Columns with Intermediate Condensers for the Production of Silane, *IFAC-PapersOnline*, 55(7), 632-637.

K. Åström, J. Åkesson, 2023, Python Control Systems Library, https://python-control.readthedocs.io

S. Skogestad, M. Morari, 1987, The Dominant Time Constant for Distillation Columns, *Comput Chem Engng*, 11(6), 607-617.

T. Akiba, S. Sano, T. Yanase, T. Ohta, M. Koyama, 2019, Optuna: A Next-Generation Hyperparameter Optimization Framework, *Proc 25th ACM SIGKDD Int Conf Knowledge Discovery & Data Mining*

X. Zang, K. Huang, Y. Yuan, H. Chen, L. Zhang, S. Wang, K. Wang, 2017, Reactive Distillation Columns with Multiple Reactive Sections: A Case Study on the Disproportionation of Trichlorosilane to Silane, *Ind Eng Chem Res*, 56(3), 717-727.

Comparative Performance Analysis of Kaibel and Christiansen Dividing Wall Columns

Goran Lukač[1], Igor Dejanović[1]
[1]University of Zagreb, Faculty of Chemical Engineering and Technology, Zagreb, Croatia

Abstract
Dividing wall columns (DWCs) represent an important advancement in process intensification, offering improved energy efficiency and reduced CO_2 emissions in the process industry. Industrial applications of DWCs have predominantly focused on three-product separations. For four-product systems, the only widely recognized implementation is the Kaibel configuration, which employs a single vertical dividing wall. Although mechanically simple, this design provides limited operational degrees of freedom, restricting controllability. Maintaining the section between the two side-product draws at total reflux is critical for optimal separation but becomes difficult in case of various disturbances, often resulting in remixing effect and deterioration of side-products' purity.
To overcome these limitations, a modified DWC configuration featuring a horizontal dividing wall between the two side products and a heat exchanger is investigated. This design, known as the Christiansen or "|– column," physically prevents remixing of intermediate components and enables enhanced thermal energy management through controlled heat addition or removal. In theory, this should offer increased operational flexibility and partial decoupling of the main fractionator sections.
Steady-state simulations of both the Kaibel and Christiansen configurations are conducted using detailed distillation models for a 15-component hydrocarbon mixture. The comparative analysis evaluates ability to maintain product compositions under varying operating conditions and disturbances, demonstrating the potential possibilities of the Christiansen configuration for improved process operation. Pressure-driven dynamic simulation is used to evaluate the possibilities of vapour split manipulation within the Christiansen column.

Keywords
Christiansen column, Kaibel column, dividing-wall column, steady state simulation, vapour split

1. Introduction

Efforts to reduce carbon dioxide emissions have made energy-intensive industries such as petroleum refining and bulk chemical manufacturing actively exploring advanced distillation technologies to improve energy efficiency[1]. Among these, Dividing Wall Column (DWC) technology has emerged as a particularly attractive option. With more than 300 industrial applications worldwide, DWCs have demonstrated reductions of approximately 30% in energy consumption, capital cost, and plot area compared to conventional distillation sequences[2,3]. Even larger

savings, up to 50%, are achievable with more complex four-product DWCs[4].Industrial adoption however remains very limited mostly due to concerns related to operability and controllability.
A promising strategy to mitigate these challenges is the simplification of four-product DWC internal structures. The primary objective is to reduce the number of vapour splits and minimize number of multiple sections in parallel. Best example of this strategy seems to be Kaibel column. To date, this is the only known configuration of four-product DWC realised in full scale[5]. Although this configuration is less energy efficient than designs based on the Petlyuk sequence, its simpler internal structure has resulted in lower design and operational uncertainty, making it more attractive for industrial adoption[6]. Kaibel configuration, illustrated in Figure 1a, is a thermally coupled three-column distillation arrangement in which the sharp separation between the two intermediate-boiling components, B and C, is carried out in the prefractionator. This differs fundamentally from the Petlyuk sequence, where each subcolumn performs the easiest split. Thermal coupling between the upper and lower sections of the main fractionator is achieved through a section located between the two side-product withdrawal points. During normal operation, this intermediate section needs to be operated at total reflux, i.e. internal liquid and vapour flow rates must be equal. When operated at this point, no net mass transfer occurs across this section, resulting in only heat exchange via direct contact.

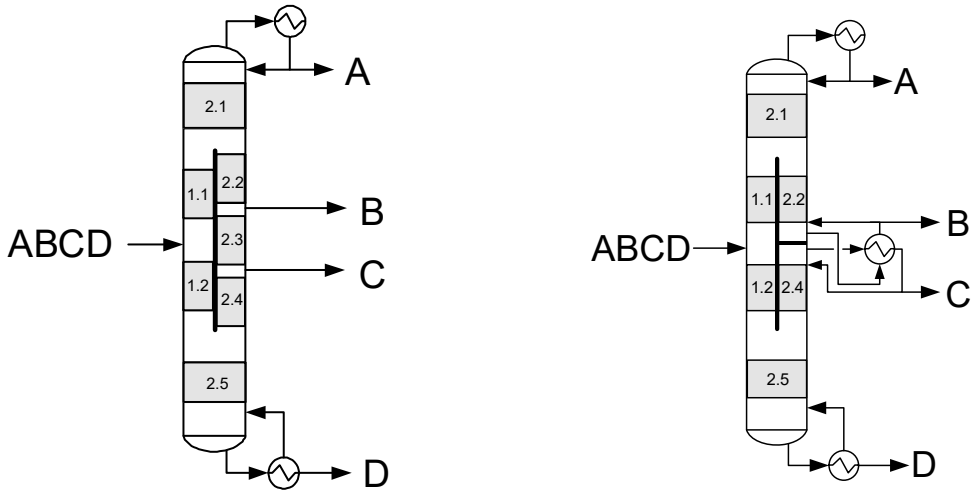

a) b)

Figure 1: a) Kaibel configuration, b) Christiansen configuration with external heat exchanger

Despite its structural simplicity, Kaibel configuration exhibits several operational disadvantages. In addition to lower thermodynamic efficiency, the reduced number of degrees of freedom complicates process control[7]. The total reflux requirement in the section between the two side products is particularly restrictive, as it is essential to prevent remixing of the two intermediate components. This constraint can lead to interactions between the side-product compositions, making independent and robust control of side-product purities difficult, especially in case of disturbances.
In order to reduce or completely avoid the remixing effect in case of disturbances, modified version of the Kaibel concept was proposed by Atle C. Christiansen[8], in which the direct thermal coupling section is replaced by a horizontal dividing wall positioned between the two side-product draws, along with a heat exchanger that

provides thermal coupling between the two sections. This configuration physically eliminates the possibility of remixing of the intermediate key components while maintaining thermal interaction between the upper and lower sections of the main column. The heat exchanger can be realised either within the column shell, or as an external unit, as shown in the Figure 1b. The goal of this work is to confirm feasibility of Christiansen's concept in the simulation environment, i.e. compare its steady state performance to Kaibel configuration. Additionally, a comparison of the performance between the two configurations during various process disturbances will be examined. As a case study, feed and products from a real industrial case of reformate separation will be used.

2. Results and discussion

2.1 Separation case and column design

Separation case used for simulation is based on an industrial reformed gasoline fractionation process. Due to the highly multicomponent nature of the actual feed, for simulation purposes, the total number of the components was reduced to only 15 of the most abundant. Feed composition is given in Table 1. Required key component purities for each product are as follows:

Distillate, D:	max. 1.5 wt% benzene,
Upper side product, S1:	65.0 – 70.0 wt% benzene,
Lower side product, S2:	min. 98.0 wt% toluene,
Bottom product, B:	max. 0.1 wt% toluene.

For results to be comparable, both Kaibel and Christiansen columns were of identical design, with the exception of the middle section between the two products (section 2.3) which is in Christiansen configuration replaced with a heat exchanger. Working conditions, such as pressure and reboiler heat duties were identical. Basic column design parameters and working conditions are shown in Table 2.

Table 1: Feed composition

Component	Mass fraction
n-Butane	0.0194
i-Pentane	0.0641
n-Pentane	0.0453
2-Methylpentane	0.0804
n-Hexane	0.0425
Benzene	0.0854
3-Methylhexane	0.0203
Toluene	0.2474
Ethylbenzene	0.0351
p-Xylene	0.0425
m-Xylene	0.0549
o-Xylene	0.1218
1,4- Ethylbenzene	0.0167
1,3,5-MBenzene	0.0469
1-Methyl-3-ethylbenzene	0.0773

Table 2: Column design parameters

Section	N	
	Kaibel	Christiansen
1.1	20	20
1.2	20	20
2.1	35	35
2.2	18	18
2.3	18	-
2.4	45	45
2.5	30	30
Total	186	168
Top pressure, bar	2,5	2,5

2.2. Steady state results during normal operation

Overview of the steady state results during normal operation for both configurations is shown in Table 3. Performance is remarkably similar - product specifications are met at very similar operational parameters.

Table 3: Steady state results comparison

Configuration	Q	R	R_V	R_L	% B_D	% B_{S1}	% T_{S2}	%T_B	$Q_{exchanger}$, MW
Kaibel	5,661	5,66	0,559	0,326	1,15	67,50	98,50	0,0	-
Christiansen	5,661	5,55	0,555	0,324	1,30	67,50	98,50	0,0	2,47
Flow rate, t/h	F	D	S1	S2	B				
Kaibel	31,74	7,38	3,88	7,91	12,57				
Christiansen	31,74	7,53	3,87	7,91	12,42				

Temperature profile comparison shown in Figure 2 also confirms the two configurations operate very similarly – only minor temperature differences are observed in the prefractionator section. For easier comparison, temperature profile of the Christiansen column shown in Figure 2 is moved to the right for the exact number of stages in section 2.3 of the Kaibel column.

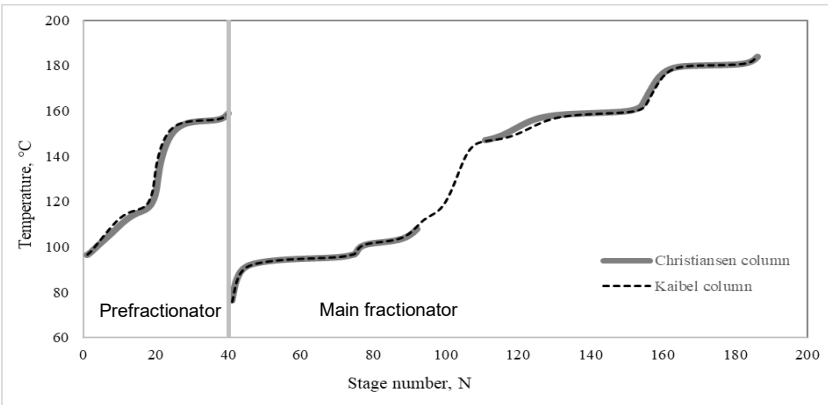

Figure 2: Comparison of temperature profiles of Kaibel and Christiansen configuration

2.3 Steady state performance after introduction of disturbances

To compare operation of the two configurations during various types of disturbances, several scenarios were tested. For this part of the study Hysys Equation Oriented (EO) solver was used. Using EO solver, besides significantly shorter convergence times, allows for more options at defining desired variables, while allowing others to be free, i.e. calculated. In this case, several stage temperatures, vapour split and L/F ratio were chosen as fixed variables. Flow rates in vicinity of selected fixed temperatures and heat duty were selected as calculated variables. Selected stages with fixed temperatures were fifth stage in sections 1.1, 2.1, 2.3 and 2.4 in case of the Kaibel column, and in sections 1.1, 2.1 and 2.4 of the Christiansen column. Each of these stages can be imagined as a controlled temperature stage below a liquid stream that serves as a manipulated variable. Combination like this resembles usual setups of DWC control structures and can give results that indicate newly achieved steady state operation point after introduction of disturbances. Total of eight scenarios were tested, as shown in Table 4.

Table 4: Disturbance scenarios

Scenario	1	2	3	4	5	6	7	8
Disturbance	+10% B in F	-10% B in F	+10% T in F	-10% B in F	+ 10% F flow	-10 % F flow	+10°C F temp.	-10°C F temp.

Results are shown in Figure 3 a-d for key components in D, S1, S2 along with reboiler heat duty throughout scenarios. Bottom product has been left out as it did not exhibit any change.

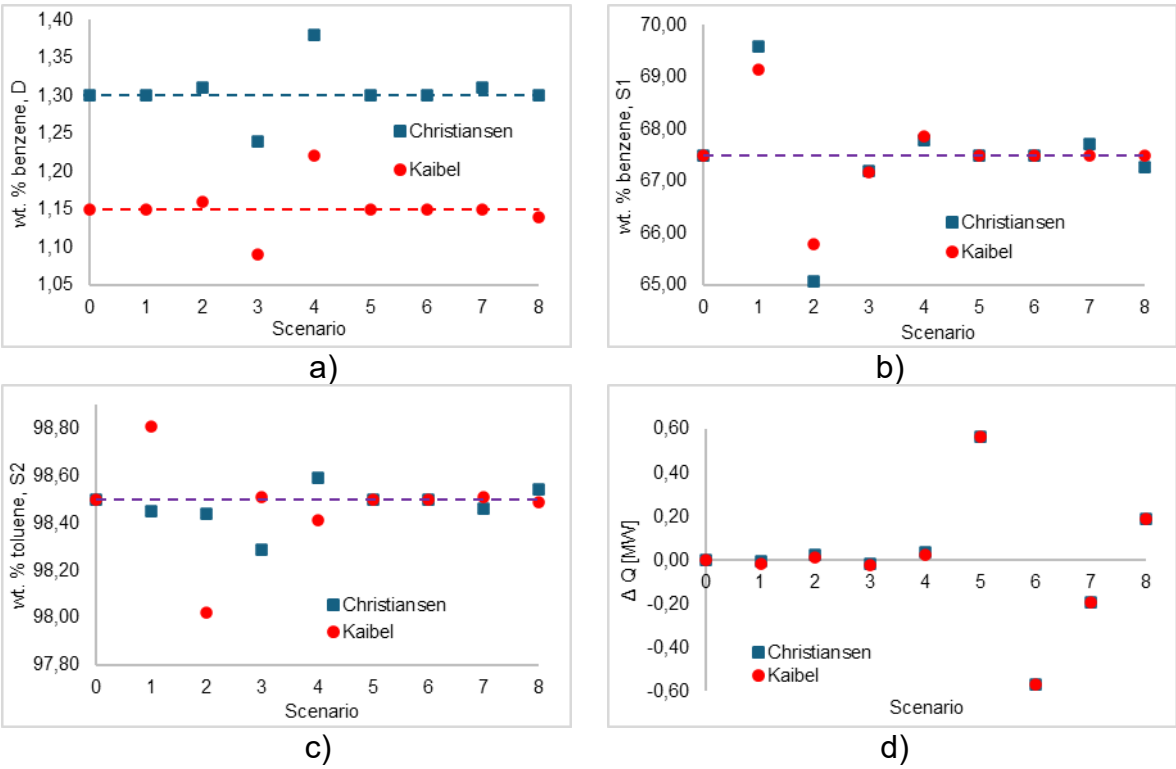

Figure 3: Steady state performance during various disturbances

Steady state results indicate similar performance between the two columns. While Christiansen column maintains steadier S2 product quality compared to Kaibel column in first two scenarios, in almost all other scenarios performs at best equal. Variations in product qualities, while relatively small, are consistently higher in case of Christiansen column. This could indicate somewhat increased sensitivity of the overall column performance on the operation of the prefractionator compared to Kaibel configuration. Due to the physical separation between the two main fractionator sections, any light component going under the wall will inevitably end up as impurity in S2 product. The same applies for any heavy component that ends up over the dividing wall – it will end up as impurity in S1 product. Therefore, it is particularly important to have a tight control over prefractionator operation.

2.4 Vapour split control

Last part of this study was to examine the possibilities of active vapour split control. Since the main fractionator in essence consists of two columns with two condensers, this, in theory, gives a possibility to control pressures independently using two condensers and use the difference to affect vapour split. For this to be possible, additional equipment beside the main heat exchanger between the two sections is necessary. One of the simplest possibilities is addition of a a bypass stream around the main heat exchanger, and additional trim cooler downstream of it. Using this setup, controlling the pressure in the lower main fractionator is easily achievable – bypassing the small part the vapour past the exchanger increases overall pressure in the column, while subcooling the reflux using the added cooler decreases it.

Pressure-driven dynamic simulation was used to test this setup. Results are shown in Table 5.

Table 5: Vapor split manipulation results

Trim cooler Q, kW	-500	- 400	- 200	0	0	0	0
% vapours bypassed	0	0	0	0	0,1	0,2	0,3
$p_{top\ cond}$, bar	2,500	2,500	2,500	2,500	2,500	2,500	2,500
$p_{low\ cond}$, bar	2,489	2,495	2,518	2,522	2,529	2,531	2,534
$p_{2.5.}$, bar	2,564	2,566	2,576	2,578	2,581	2,582	2,584
Vapor split ratio	0,4926	0,4974	0,5387	0,5503	0,5666	0,5683	0,5791

Results indicate clear correlation between pressure difference between the two condensers and vapour split ratio. Please note that even though pressure difference might be negative between the middle and the top condenser, the relevant pressure that ensures flow of the vapour toward the prefractionator is the one at the top of the section 2.5.

3. Conclusions

Christiansen column performs similarly to Kaibel column in terms of steady state operation without using vapour split as a manipulated variable. Although physical separation between the two sections of the main fractionator in theory prevents remixing effects, it does seem to bring one negative aspect – increased sensitivity towards prefractionator operation. This is somewhat manifested through increased product quality variations noticeable from the results. However, this is compensated with one very positive aspect of this configuration – possibility of a straightforward way to manipulate vapour split ratio, which, as results indicate, can be done only through simple pressure control. Further dynamic studies are necessary to completely determine full potential of this configuration, but initial results are encouraging.

Acknowledgements

This research was conducted within the project Biosynth (112109) financed by the European Union's- NextGenerationEU fund from the source 581 – The recovery and resilience mechanism, in the frame of Programme financing of public higher education institutions and public scientific institutes.

References

1. D. Sholl, R. Lively, Seven chemical separations to change the world, Nature 532 (2016), 435 – 437
2. I. Dejanović, Lj. Matijašević, Ž. Olujić, Dividing wall column – A breakthrough towards sustainable distilling, Chem. Eng. Process. 49 (2010) 559 – 580
3. I. Dejanović, I.J. Halvorsen, S. Skogestad, H. Jansen, Ž. Olujić, Cost-effective design of energy efficient four-product dividing wall columns, Chem. Eng. Trans.35 (2013), 283 – 288,
4. I.J. Halvorsen, I. Dejanović, S. Skogestad, Ž. Olujić, Internal configurations for a multi-product dividing wall column, Chem. Eng. Res. Des., 91 (2013) 1954-1965.
5. M. Donahue, B.J. Roach, J.J. Downs, T. Blevins, M. Baldea, R. B. Eldridge, Dividing Wall Column Control: Common Practices and Key Findings, Chem. Eng. Process. 107 (2016), 106-115.
6. G. Kaibel, Distillation Columns with Vertical Partitions, Chem. Eng. Technol. 10 (1987) 92-98.
7. J. Strandberg, S. Skogestad, Stabilizing Operation of a 4-product Kaibel Column. IChemE Symposium Series 152, (2006) 638-647.
8. A.C. Christiansen, S., Skogestad, K. Lien, K., Complex distillation arrangements: Extending the Petlyuk ideas, Comput. Chem. Eng. 21 (1997) S237 – S242

Time-Frequency eXplainable Artificial Intelligence Framework for Early Flooding Detection in Packed Columns

Luigi Piero Di Bonito[1], Pietro Giustacori[2], Sara Marchini[3], Domenico Flagiello[1], Elisabetta Brunazzi[2]

[1]*Dipartimento di Ingegneria Chimica, dei Materiali e della Produzione Industriale (DICMaPI),* University of Naples "Federico II", 80125, Naples, Italy*;*

[2]*Department of Civil and Industrial Engineering (DICI), University of Pisa, 56122, Pisa, Italy;*

[3]*Chair of Chemical Process Engineering, Technische Universität Dresden, 01062 Dresden, Germany*

Abstract

Flooding represents the key operational limit in countercurrent packed columns, as it induces hydrodynamic instabilities that deteriorate pressure-drop behavior and mass transfer efficiency. Although optimal performance lies between loading and flooding, industrial units often operate below this range yet remain sensitive to disturbances that can trigger rapid transitions toward flooding. This work introduces an eXplainable Artificial Intelligence (XAI) framework for predicting and interpreting such hydrodynamic transitions. Pressure drops signals from a DN100 column equipped with various structured packings are analyzed through wavelet-based time–frequency preprocessing, followed by a hybrid CNN–LSTM architecture that captures spectral features and temporal dependencies. The model achieves over 80% accuracy in regime classification and an R^2 above 0.9 in transient reconstruction. XAI analysis (Grad-CAM) validates the physical relevance of the learned features, linking dominant low- and mid-frequency components to known instability mechanisms. The results highlight the potential of an explain-to-discover approach for reliable monitoring, early flooding detection, and enhanced understanding of hydrodynamic behavior in packed columns.

Keywords

Packed columns, Flooding¸ Pressure drop fluctuations, Time frequency analysis, eXplainable Artificial Intelligence (XAI)

1. Introduction

Structured packed columns are widely employed in gas-liquid separation processes due to their high interfacial area, low pressure drop, and favorable performance under vacuum or energy-constrained conditions. Despite these advantages, their countercurrent operation is limited by hydrodynamic constraints, among which flooding represents the most critical one. Flooding occurs when the upward gas flow stops the downward motion of the liquid, leading to excessive liquid accumulation and sharp increases in pressure drop, resulting in a deterioration of mass transfer efficiency (Brunazzi and Paglianti 1997; Brunazzi, Paglianti, and Pintus 2001).

Industrial packed columns are typically operated well below the flooding point, often between 70 and 85 percent of the maximum capacity, to ensure stable and safe operation. This conservative approach reflects the strong sensitivity of the system near flooding, where small fluctuations in gas or liquid flow rates can trigger a fast transition toward unstable flooded conditions (Rocha, Bravo, and Fair 1993).

In recent years, flooding in separation columns has been addressed by data-driven techniques that differ in terms of algorithm type, data nature, and operational goal. The literature includes supervised modeling strategies relying on standard process measurements such as temperatures, pressures, and flow rates. In this context, Ochoa-Estopier et al. (2023) developed a Random Forest model capable of forecasting pre-flooding conditions tens of minutes in advance, prioritizing interpretability and ease of industrial integration. A similar approach, but more focused on the classification of operational states, is proposed by Wang et al. (2024), which demonstrates how dynamic feature engineering (e.g. gradients, ratios, temporal differences between process variables) is frequently more important than algorithm selection in improving predictive capacity.

Approaches based on alternative high-information signals, such as passive acoustic monitoring, introduce a paradigm shift by operating on time-frequency representations with deep neural networks (i.e. ResNet) to distinguish not only flooding and normal conditions, but also intermediate transient states (Zheng et al. 2025). Similarly, machine vision algorithms employ end-to-end Convolutional Neural Networks (CNNs) trained on RGB pictures of the column to distinguish visual patterns of flooding and pre-flooding, using the two-phase flow's spatial information, but with limited industrial use (Liu et al. 2023). Finally, generative model-based techniques (TimeGAN) address the structural issue of flooding event rarity by producing synthetic time series that balance datasets and allow predictive supervised models to train (Adebayo, Imtiaz, and Ahmed 2025).

Overall, existing studies point to a clear shift from reactive, threshold-based strategies toward multi-data predictive frameworks, where the trade-off between anticipation capability, interpretability, and robustness remains largely unresolved.

From a physical standpoint, pressure drop measurements provide a global and non-intrusive indicator of the column hydrodynamic state; however, conventional time-averaged analyses are often inadequate to capture the dynamic features that precede flooding onset. This limitation motivates the adoption of advanced signal analysis techniques capable of resolving both stationary and transient behaviors. Accordingly, a time-frequency preprocessing based on wavelet transform is employed to decompose pressure drop signals, enabling the extraction of their spectral content and temporal evolution through time-frequency-amplitude representations. The current work proposes a hybrid eXplainable Artificial Intelligence (XAI) framework (Barredo Arrieta et al. 2020), combining Convolutional Neural Networks (CNNs) and Recurrent Neural Networks (RNNs), to predict flooding conditions. Beyond early flooding detection, the framework supports an "*explain-to-discover*" paradigm, enabling a deeper physical interpretation of flooding-related dynamics through post-hoc XAI methodologies (Di Bonito et al. 2024).

2. Experimental setup and methodologies

The experimental investigation was conducted using a pilot–scale countercurrent packed column specifically designed to study hydrodynamic transitions under controlled conditions. Figure 1 show a simplified scheme of the experimental setup. The column is constructed from transparent polymethyl methacrylate to allow visual observation of the flow patterns and has an internal diameter of 100 mm.

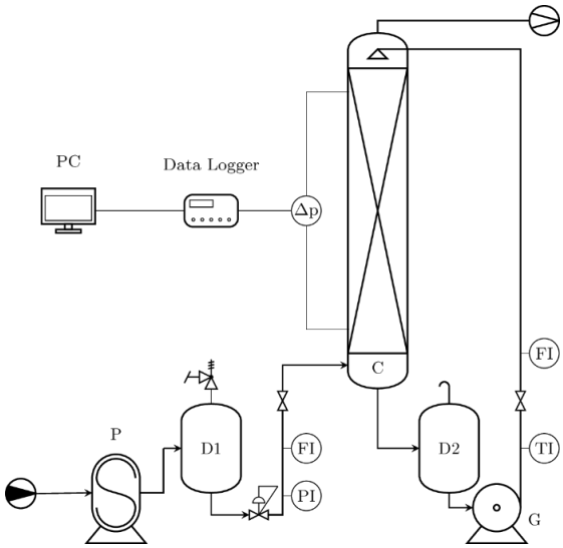

Figure 1: Experimental setup

Structured packing elements made of stainless steel are arranged to form a packed bed with a total height of approximately 1.5 m. Several types of structured packing were investigated, namely Mellapak 250.Y, Mellapak 252.Y, Mellapak 752.Y, and Optiflow C-36. The column is operated under ambient temperature and pressure conditions. Liquid distribution is achieved using an orifice-type distributor positioned above the packed bed, ensuring uniform wetting of the packing surface. Water is used as the liquid phase and is circulated in a closed loop, supplied from a storage tank by a centrifugal pump. The liquid flow rate was varied between 100 L h^{-1} and 400 L h^{-1} to explore different liquid loading regimes.

Ambient air is employed as the gas phase and is supplied by a rotary compressor, with buffering in a pressurized storage tank. Downstream pressure regulation ensures stable inlet conditions to the column, while the gas flow rate is measured using an in-line rotameter and adjusted via a downstream control valve to reduce measurement disturbances. For each tested liquid flow rate, the gas flow rate was progressively increased from zero up to the total flooding point of the column for the installed packing configuration, enabling systematic investigation of loading and flooding behavior. The system allows operation up to fully flooded conditions for all liquid loads considered.

The pressure drop across the packed bed is measured using a differential pressure transmitter connected to pressure taps located within the packing section. This arrangement enables accurate monitoring of both steady-state and transient pressure fluctuations associated with loading and flooding phenomena.

Figure 2 provides a schematic summary of the suggested framework for early flood detection. Starting with steady-state pressure drop data, the signal is transformed into the time-frequency domain using wavelet-based pre-processing, resulting in time-frequency-amplitude representations that maintain both spectrum content and temporal dynamics. Before model training, the dataset is organized using a physically consistent splitting strategy in which samples are partitioned into training (60%), validation (20%), and test (20%) sets separately for each packing type and increasing gas flow rate, preventing information leakage and ensuring realistic generalization across hydrodynamic severity levels. Time-frequency maps are then split along the temporal axis into fixed-length windows (40s), resulting in localized representations of regime change that maintain temporal ordering. These slices are used as the input for a hybrid CNN-LSTM architecture, in which convolutional layers automatically extract

regime-dependent spectral characteristics and recurrent units represent their temporal development and transitions between pre-loading, loading, and flooding conditions. Model predictions can then be explained using post-hoc eXplainable Artificial Intelligence (XAI) techniques. Gradient-based attribution techniques (Grad-CAM) are specifically used to determine the most significant time-frequency areas driving the classification, allowing for an "*explain-to-discover*" study that connects learnt patterns to the physical causes behind flooding onset.

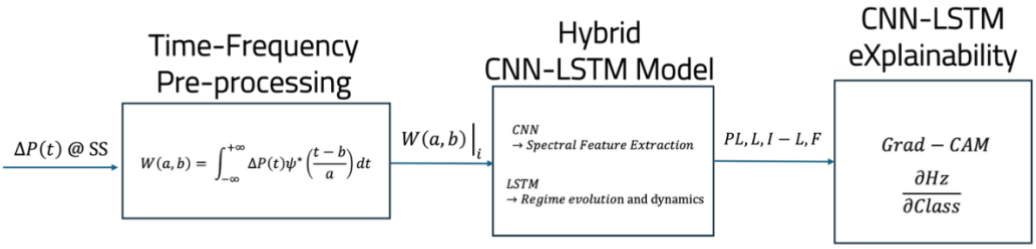

Figure 2: Block diagram of the proposed wavelet-CNN-LSTM framework for early flooding detection, including time-frequency preprocessing of pressure drop signals, hybrid deep learning modeling, and post-hoc explainability via Grad-CAM.

3. Results and discussion

2.1 Exploratory Data Analysis and Feature Engineering

To examine the dynamic properties of pressure, drop signals and assess their informational content as they relate to different hydrodynamic regimes, a preliminary exploratory data analysis (EDA) was conducted. The preprocessed signals exhibit a distinct qualitative evolution in the time domain, from the pre-loading regime, characterized by low-amplitude and comparatively regular oscillations, to the loading and flooding regimes, which are marked by increasingly intense, intermittent, and non-stationary fluctuations.

However, analysis in the time domain alone is insufficient to fully describe the dynamics preceding the onset of flooding. Because of this, the Continuous Wavelet Transform (CWT) was used to preprocess load loss signals to extend the EDA to the time-frequency domain. The analysis of intrinsically non-stationary signals benefits greatly from the employment of a complex Morlet wavelet with logarithmically distributed scales, which enables the simultaneous representation of the signal's spectral content and temporal evolution.

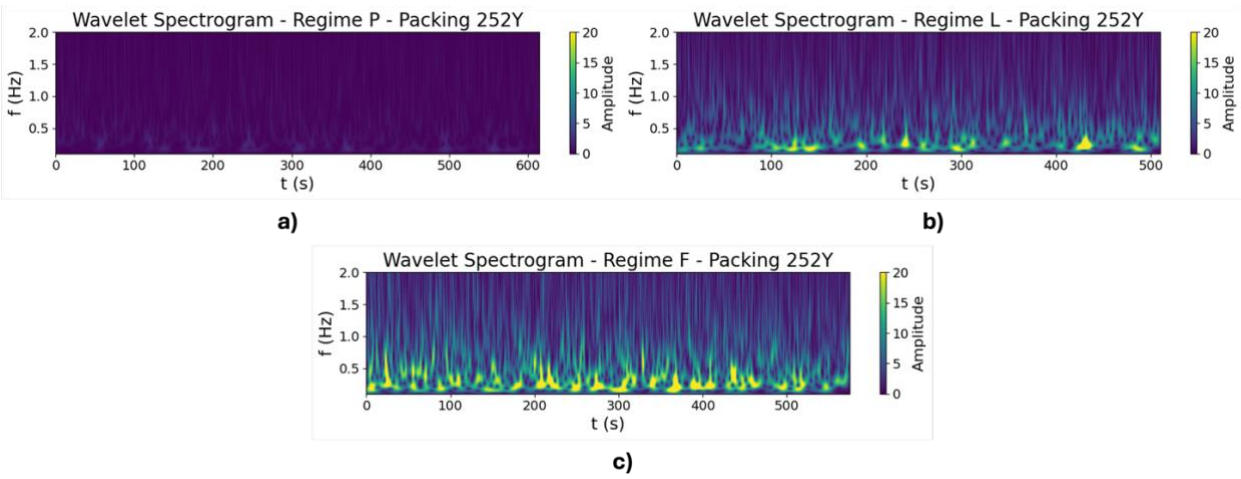

Figure 3: Wavelet spectrograms of the pressure drop signal for Mellapak-252Y packing: a) pre-loading (L = 100 L/h; G = 65 m^3/h), b) loading (L = 100 L/h; G = 109 m^3/h), c) flooding (L = 100 L/h; G = 117 m^3/h).

As seen in Figure 3, the resultant wavelet spectrograms show clear distinctions across the hydrodynamic regimes.
The signal energy appears to be restricted to modest amplitudes and distributed consistently in the pre-loading regime (Figure 3a), with little activity in the low frequency regions. More distinct and enduring time-frequency structures appear in the loading regime (Figure 3b), suggesting more coherent fluctuations linked to enhanced gas-liquid interaction. In contrast, the flooding regime (Figure 3c) exhibits sporadic high-frequency events and a substantial concentration of energy in the low-frequency bands, which are compatible with the accumulation and entrainment of liquid within the packing. Overall, the exploratory study reveals that the information that distinguishes distinct hydrodynamic regimes is contained in the time-frequency structure of the signal and cannot be associated with simply average values of pressure loss. This outcome offers a convincing physical rationale for using wavelet representations as an information space in later stages of data-oriented modeling.

2.2 XAI Framework and Explainability Results

Preliminary results indicate that the proposed time-frequency XAI framework is appropriate for detecting early flooding in gas-liquid packed columns. Using wavelet-based time-frequency representations of pressure drop data, the CNN achieves classification accuracy of more than 80% in a non-optimized setup. Misclassifications occur mostly between nearby hydrodynamic regimes, such as loading and incipient flooding, reflecting the inherent difficulties of discerning transitional circumstances from instantaneous data alone. The framework's recurrent component enables early detection capabilities. The LSTM layer detects the persistence and evolution of hydrodynamic instabilities by analyzing temporal sequences of spectral information obtained from the CNN. Instead of a strictly instantaneous regime designation, the output is expressed as a continuous early-flooding indicator, showing the increasing likelihood of transitioning to flooding conditions over time.
Post-hoc explainability study using Grad-CAM on the CNN validates the physical significance of the learnt features. During loading and flooding, the most important activations are constantly centered in low-frequency areas of the time domain, particularly between 0.20 and 0.50 Hz. These frequencies are consistent with large-scale liquid collection and redistribution processes inside the packed bed, ensuring the physical consistency and interpretability of the proposed framework.

4. Conclusions

A time frequency XAI framework is proposed for the early detection of flooding onset in gas-liquid packed columns, integrating wavelet-based analysis of pressure drop signals with a hybrid convolutional neural network and long short-term memory architecture. The wavelet transform enables the decomposition of pressure fluctuations into localized time-frequency representations, allowing subtle hydrodynamic instabilities associated with incipient flooding to be isolated from background noise. Preliminary investigations indicate that early flooding signatures are predominantly embedded in low-frequency components of the time-frequency domain, which can be consistently identified and interpreted through Grad-CAM analysis

The inclusion of the recurrent LSTM component enables the model to capture the temporal persistence and evolution of these low-frequency patterns, thereby supporting early diagnosis prior to the development of fully established flooding conditions. This temporal sensitivity is particularly relevant for tracking the progressive amplification of hydrodynamic instabilities that precede critical transitions in packed

column operation. Overall, the proposed framework offers a physically grounded and interpretable approach for the early identification of flooding initiation in packed columns, providing a robust basis for the development of predictive monitoring and advanced control strategies.

Acknowledgements

This work is supported by the EXAIMS Project funded within the Lab2Lab framework of the Graduate Academy of TU Dresden, supported by Federal and State Funds.

References

Adebayo, O., Imtiaz, S., & Ahmed, S. (2025). Machine learning for early detection of distillation column flooding. *Chemical Engineering Science*, *312*. https://doi.org/10.1016/j.ces.2025.121603

Barredo Arrieta, A., Díaz-Rodríguez, N., Del Ser, J., Bennetot, A., Tabik, S., Barbado, A., Garcia, S., Gil-Lopez, S., Molina, D., Benjamins, R., Chatila, R., & Herrera, F. (2020). Explainable Artificial Intelligence (XAI): Concepts, taxonomies, opportunities and challenges toward responsible AI. *Information Fusion*, *58*, 82–115. https://doi.org/10.1016/j.inffus.2019.12.012

Brunazzi, E., & Paglianti, A. (1997). Mechanistic Pressure Drop Model for Columns Containing Structured Packings. *AIChE Journal*, *43*(2), 317–327. https://doi.org/10.1002/aic.690430205

Brunazzi, E., Paglianti, A., & Pintus, S. (2001). A capacitance probe and a new model to identify and predict the capacity of columns equipped with structured packings. *Industrial and Engineering Chemistry Research*, *40*(4), 1205–1212. https://doi.org/10.1021/ie000546u

Di Bonito, L. P., Campanile, L., Di Natale, F., Mastroianni, M., & Iacono, M. (2024). eXplainable Artificial Intelligence in Process Engineering: Promises, Facts, and Current Limitations. In *Applied System Innovation* (Vol. 7, Number 6). Multidisciplinary Digital Publishing Institute (MDPI). https://doi.org/10.3390/asi7060121

Liu, Y., Jiang, Y., Gao, Z., Liu, K., & Yao, Y. (2023). Convolutional Neural Network-Based Machine Vision for Non-Destructive Detection of Flooding in Packed Columns. *Sensors*, *23*(5). https://doi.org/10.3390/s23052658

Rocha, J. A., Bravo, J. L., & Fair, J. R. (1993). Distillation Columns Containing Structured Packings: A Comprehensive Model for Their Performance. 1. Hydraulic Models. In *Ind. Eng. Chem. Res* (Vol. 32). https://pubs.acs.org/sharingguidelines

Wang, H., Zheng, H., Zhang, Z., & Wang, G. (2024). A Deep Learning-Based Acoustic Signal Analysis Method for Monitoring the Distillation Columns' Potential Faults. *Applied Sciences (Switzerland)*, *14*(16). https://doi.org/10.3390/app14167026

Zheng, H., Zhang, Z., Wang, G., Wang, Y., Liang, J., Su, W., Hu, Y., Yu, X., Li, C., & Wang, H. (2025). State surveillance and fault diagnosis of distillation columns using residual network-based passive acoustic monitoring. *Chinese Journal of Chemical Engineering*, *77*, 248–258. https://doi.org/10.1016/j.cjche.2024.09.026

Model-based evaluation of sandwich packings for energy-efficient reactive distillation

Patrick Franke[1], Markus Schubert[2], Uwe Hampel[3,4], Eugeny Y. Kenig[1]
[1]Chair of Fluid Process Engineering, Paderborn University, Paderborn, Germany
[2]Chair of Chemical Process Engineering, Dresden University of Technology, Dresden, Germany
[3]Institute of Fluid Dynamics, Helmholtz-Zentrum Dresden-Rossendorf, Dresden, Germany
[4]Chair of Imaging Techniques in Energy and Process Engineering, Dresden University of Technology, Dresden, Germany

Abstract

Sandwich packings consist of two types of structured packings with different specific surface areas that are arranged alternatingly within a column. Under partially flooded conditions, they enable a significant intensification of mass transfer compared to conventional structured packings, albeit at the expense of an increased pressure drop. In this study, the application of sandwich packings to reactive distillation is investigated using a model-based approach and evaluated with respect to the energy demand. The analysis is performed with a rate-based model that was first validated against experimental data of a binary system under total reflux conditions. Subsequently, the homogeneous esterification of acetic acid with ethanol to ethyl acetate was investigated. The results show that, under partially flooded operation and at identical reboiler duty, higher product purities can be achieved than with structured packings. These findings highlight the potential of sandwich packings to contribute to improved energy efficiency in reactive distillation.

Keywords
sandwich packing, structured packing, rate-based model, reactive distillation, energy efficiency.

1. Introduction

Structured packings are widely used internals in distillation columns, where the liquid phase predominantly flows as films and rivulets countercurrently to the vapor stream. At elevated vapor-to-liquid ratios, froth flow can develop, which enhances mass transfer but also leads to higher pressure drop and a narrow operating window.

Sandwich packings address this limitation by alternating two structured packings with different specific surface areas. A hold-up layer (HL) with high surface area promotes froth formation, while a de-entrainment layer (DL) with lower surface area limits froth height and droplet entrainment, thereby stabilizing operation. Compared to conventional structured packings, sandwich packings offer higher separation efficiency and more uniform liquid distribution, but at the cost of significantly increased pressure drop.

Sandwich packings are particularly attractive for reactive distillation, when reaction and separation occur simultaneously in a single column, especially for equilibrium-limited reactions. Their increased liquid holdup provides a larger reaction volume and potentially higher conversion. However, the increased pressure drop results in higher

bottom temperatures and energy consumption, raising the question whether the improved performance justifies the additional energy demand.
To investigate this issue, a rate-based model originally developed for reactive absorption (Franke et al., 2026) is extended to distillation and reactive distillation. The model accounts for different flow regimes and incorporates recent correlations for mass transfer and fluid dynamics in sandwich packings. After validation with distillation data under total reflux, the model is applied to homogeneously catalyzed reactive distillation for the ethyl acetate production. The objective is to evaluate whether sandwich packings enable more energy-efficient operation than conventional structured packings.

2. Modeling

To model mass and heat transfer in structured and sandwich packings, the well-established rate-based model is employed (Schneider and Górak, 2001; Hüpen and Kenig, 2005; Klöker et al., 2005). Sandwich packings are characterized by spatially varying geometries and flow regimes along the column height. To capture the impact of these variations on mass and heat transfer, the model employs a periodic segmentation scheme based on the underlying fluid dynamics, as detailed in Franke et al. (2026).
The application of the rate-based model requires model-specific parameters that depend on the packing geometry. For sandwich packings, these parameters must be known for both film and froth flow. In total, six parameters are required for each flow regime: specific pressure drop, liquid holdup, effective interfacial area, mass-transfer coefficients for both vapor and liquid phases, and the froth layer height. To evaluate the parameters for film flow in sandwich packings, conventional correlations developed for structured packings are employed. The literature sources of these correlations are summarized in Table 1.

Table 1: Applied correlations for rate-based model parameters.

Parameter	Film flow	Froth flow
Interfacial area	Tsai et al. (2011)	Franke et al. (2026)
Liquid-side mass transfer coefficient	Rocha et al. (1996)	Franke et al. (2025)
Gas-side mass transfer coefficient	Rocha et al. (1996)	Zuiderweg (1982)
Pressure drop	Flechsig et al. (2022)	Flechsig et al. (2022)
Liquid holdup	Flechsig et al. (2022)	Flechsig et al. (2022)

The froth layer heights in HL and DL are calculated according to Flechsig et al. (2022). As experimental data for the vapor-side mass transfer coefficient in froth flow within sandwich packings are currently unavailable, the correlation proposed by Zuiderweg (1982) is employed. Although originally developed for froth flow in tray columns, this correlation is applicable to sandwich packings due to the similar fluid dynamic behavior.

3. Model validation

Since experimental distillation data are hardly available, the validation presented here was performed with one sandwich packing configuration and one binary system. Jödecke et al. (2006) measured separation efficiency for the methylcyclohexane/n-heptane system at total reflux and a pressure of 1.6 bar, using the sandwich packing Montz B1-750T/250M.
The suffix “T” indicates downcomers integrated into the HL, which are uniformly distributed across the packing cross-section. The downcomers are perforated at the bottom and stabilize froth operation by enabling continuous liquid drainage from the

HL while ensuring uniform vapor flow distribution across the column cross-section (Flechsig et al., 2016). The downcomers were installed in response to observations, particularly in large-diameter columns, showing instable froth layer formation. It is assumed that the effective interfacial area in both film and froth flow is reduced by the downcomer fraction, since no direct phase contact occurs within the downcomers, as only liquid passes through them. For the Montz B1-750T packing investigated in this study, the downcomer fraction is 10%.
The DL consists of the high-performance packing Montz B1-250M, whose inclination angle smoothly changes from 45° to 90° at the lower end of the packing.
An additional model validation was accomplished using separation efficiency data reported by Olujić et al. (2003) for the structured packing Montz B1-250M for the cyclohexane/n-heptane system at total reflux and a pressure of 1.03 bar. This validation provides a further assessment of the model performance for the packing type that also serves as the DL within the sandwich packing configuration.
The simulated compositions at the bottom and top of the column were converted into HETP values using the Fenske equation. Vapor-liquid equilibrium was calculated using the UNIQUAC model from Abrams and Prausnitz (1975).
The validation results are shown in Figure 1 for the structured packing Montz B1-250M (left) and for the sandwich packing Montz B1-750T/250M (right).

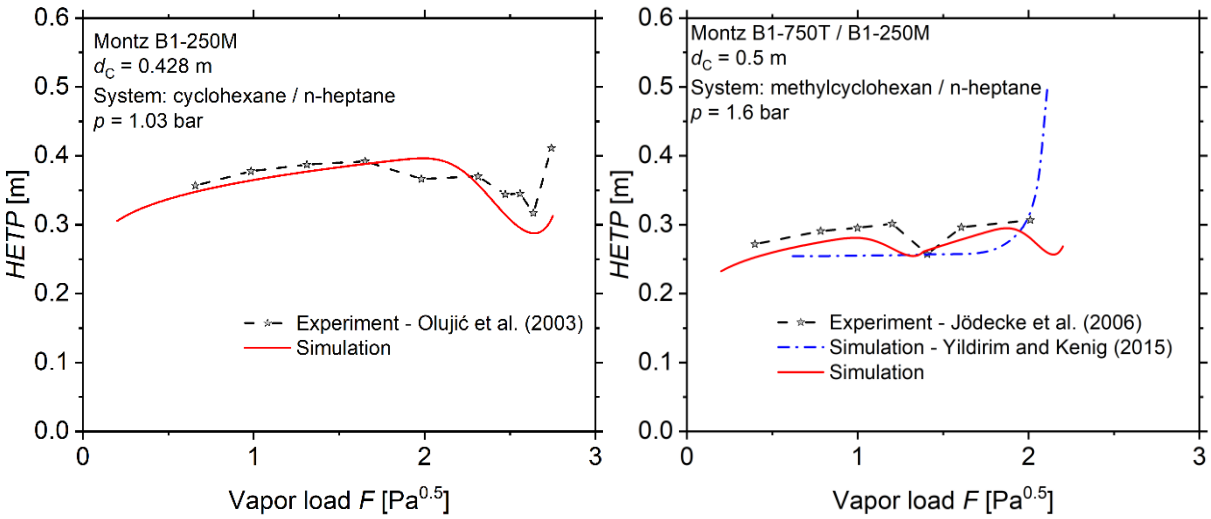

Figure 1: Comparison of experimental and simulated HETP values for structured packing B1-250M (left) and sandwich packing B1-750T/250M (right).

The experimental HETP values for the Montz B1-250M packing are well met by the simulations. Both the characteristic improvement in separation efficiency due to froth flow and the abrupt decline at the flooding point are captured satisfactorily.
For the Montz B1-750T/250M packing, the experimental HETP data also agree well with the simulation results. Compared with the earlier model proposed by Yildirim and Kenig (2015), the present approach better accounts for the influence of fluid dynamics on mass transfer in sandwich packings. This improvement can be attributed to a better prediction of the froth layer height, which incorporates vapor and liquid loads, whereas the model of Yildirim and Kenig (2015) just assumes froth flow throughout the HL and film flow in the DL, regardless of the operating conditions.

4. Case study on reactive distillation

Using the validated model, the energy demand of a reactive distillation column operated with structured packings and with sandwich packings is compared. The

reaction system under investigation is the homogeneously catalyzed esterification of acetic acid (HAC) with ethanol (EtOH) to form ethyl acetate (EtAC) and water (H_2O). The reaction, catalyzed by sulfuric acid (H_2SO_4), is considered reversible (Kenig et al., 2001). The reaction rate constant of the forward reaction as well as the equilibrium constant are calculated using the expressions given by Alejski and Duprat (1996). The EtAC-EtOH-H_2O-HAC system is highly non-ideal and exhibits four minimum boiling azeotropes, including one binary heterogeneous azeotrope (Klöker et al., 2005). The vapor-liquid equilibrium is described using the γ-φ approach. Activity coefficients in the liquid phase are calculated with the UNIQUAC model (Abrams and Prausnitz, 1975). The dimerization of acetic acid in the vapor phase is accounted for by applying the Hayden-O'Connell equation of state (Hayden and O'Connell, 1975). The influence of sulfuric acid on the vapor-liquid equilibrium is neglected, as its very low vapor pressure ensures that it remains almost entirely in the liquid phase over the temperature range relevant to reactive distillation. The investigated column configuration is shown in Figure 2.

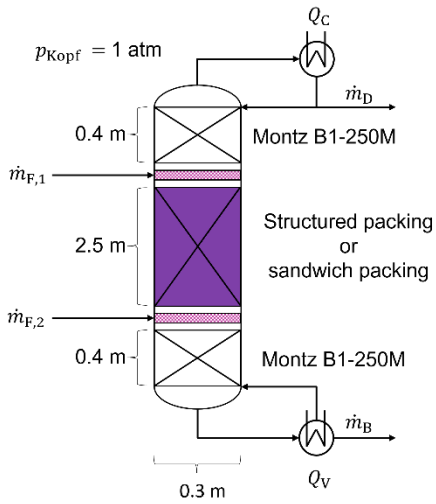

Figure 2: Column configuration of the investigated reactive distillation process.

The total packing height is 3.3 m, thereof 2.5 m assigned to the reactive zone and 0.4 m each to two separation zones. The upper separation section prevents acetic acid from reaching the distillate and helps to keep it in the reactive zone. The lower separation section accumulates excess acetic acid in the bottom, so that it can be withdrawn and recycled. The column is operated at a top pressure of 1 atm. Acetic acid, together with the sulfuric acid catalyst, is introduced via feed stream F1, while feed stream F2 has the composition of the binary ethanol-water azeotrope. Both feed streams enter the column as saturated liquids. The total feed rate is $\dot{m}_{F,tot} = 500\,\mathrm{kg/h}$, and the distillate flow rate is $\dot{m}_D = 100\,\mathrm{kg/h}$. The molar ratio of acetic acid feed to ethanol feed is 1.5. In the simulations, the separation zones below and above the reactive zone are considered as filled with the Montz B1-250 structured packing. The reactive zone is simulated either with a sandwich packing or with a structured packing to assess the influence of packing type on energy demand.

In the simulations, a catalyst fraction of 10 mol.% in the acetic acid feed was assumed while the reboiler duty varied. By keeping distillate and total feed flow rates constant, the effects of the reboiler duty on product purity can be systematically analyzed, allowing the identification of operating regimes in which sandwich packings offer advantages over conventional structured packings.

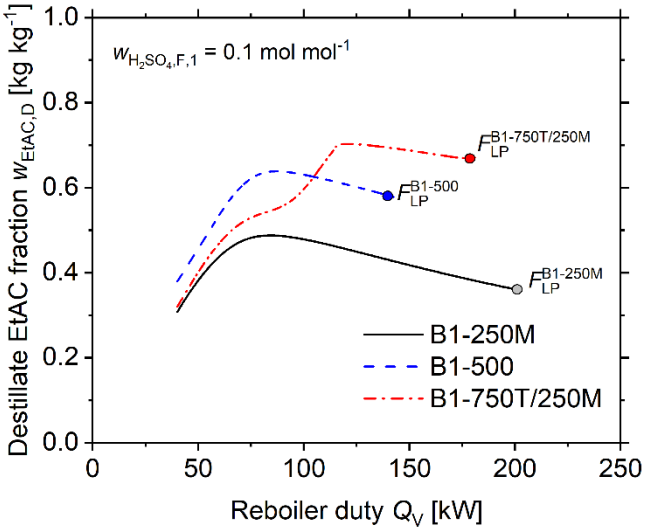

Figure 3: Comparison of the obtained EtAC mass fraction in the distillate stream for different packing types at varying reboiler duties.

Simulation results for the structured packings Montz B1-250M and Montz B1-500 as well as for the sandwich packing Montz B1-750T/250M within the reactive zone are shown in Figure 3 for different reboiler duties. The results are compared within the range of achievable and stable operating conditions. For structured packings, this range is limited by the respective loading point F_{LP}, whereas for sandwich packings it is bounded by the loading point of the DL. Overall, the Montz packing B1-500 achieves a significantly higher ethyl acetate fraction in the distillate than the Montz packing B1-250M. This improvement is primarily due to the larger effective interfacial area of the Montz packing B1-500, which substantially enhances separation efficiency. However, the operating window of the Montz packing B1-500 is much narrower than that of the Montz B1-250M because of its significantly lower loading point.
In film flow, the separation performance of the sandwich packing lies between that of the Montz packings B1-250M and B1-500. Above the loading point of the HL, the ethyl acetate mass fraction increases sharply and levels off again after reaching the flooding point of the HL. Under froth flow operation, the sandwich packing achieves higher ethyl acetate concentrations in the distillate at the same energy input compared to both the Montz packings B1-250M and Montz B1-500. Besides, the Montz packing B1-750T/250M exhibits a wider operating window than the Montz packing B1-500. Consequently, sandwich packings enable not only more energy-efficient operation but also greater operational flexibility compared to conventional structured packings.

5. Conclusions

Sandwich packings are a promising alternative to conventional structured packings, as they can significantly enhance separation performance. Their application is particularly attractive for reactive distillation, where reaction and separation occur within a single column. Such processes require both sufficient reaction volume and high separation efficiency, which sandwich packings can provide through their increased liquid holdup, enlarged interfacial area, and reduced mass transfer limitations. However, sandwich packings also exhibit higher pressure drop, potentially increasing the energy demand. To assess whether sandwich packings can improve the overall energy efficiency of reactive distillation or not, a model-based study was conducted. The rate-based model originally developed for reactive absorption (Franke et al., 2026) was adapted and validated using distillation performance data (Jödecke et al., 2006). The model explicitly accounts for the effects of packing geometry and flow regime on mass transfer and thus, represents a clear advancement over the model of Yildirim and Kenig (2015), by incorporating froth heights as a function of vapor and liquid loads.
The validated model was subsequently applied to the homogeneously catalyzed reactive distillation of ethyl acetate. The results demonstrate that sandwich packings operated in the froth regime, achieve higher distillate purity than structured packings at the same reboiler duty. This improvement is mainly attributed to increased liquid holdup and hence a larger reaction volume, as well as enhanced mass transfer. Also, sandwich packings can offer greater operational flexibility. Overall, reactive distillation represents a highly promising application for sandwich packings.

Acknowledgements

The authors are grateful to the Deutsche Forschungsgemeinschaft (DFG) for the financial support (research project KE 837/26 3, HA 3088/10 3).

References

Abrams, D.S., Prausnitz, J.M., 1975. Statistical thermodynamics of liquid mixtures: A new expression for the excess gibbs energy of partly or completely miscible systems. AIChE J. 21 (1), 116–128. 10.1002/aic.690210115.

Alejski, K., Duprat, F., 1996. Dynamic simulation of the multicomponent reactive distillation. Chem. Eng. Sci. 51 (18), 4237–4252. 10.1016/0009-2509(96)00226-6.

Flechsig, S., Sohr, J., Schubert, M., Hampel, U., Kenig, E.Y., 2022. A new tomography-based approach for the fluid dynamic description of conventional structured packings and sandwich packings. Chem. Eng. Process.: Process Intensif. 171, 108530. 10.1016/j.cep.2021.108530.

Flechsig, S., Yildirim, Ö., Kenig, E.Y., 2016. Sandwich packings: State of the art. ChemBioEng. Rev. 3 (4), 174–185. 10.1002/cben.201600004.

Franke, P., Schlattmann, U., Devasthali, O., Lutters, N., Schubert, M., Hampel, U., Iliuta, I., Larachi, F., Kenig, E.Y., 2025. An additive approach toward determination of liquid-phase mass transfer coefficients in sandwich packings. Chem. Eng. Sci. 305, 121142. 10.1016/j.ces.2024.121142.

Franke, P., Schubert, M., Hampel, U., Kenig, E.Y., 2026. A rate-based model for reactive separation columns with sandwich packings. Chem. Eng. Sci. 321, 122681. 10.1016/j.ces.2025.122681.

Hayden, J.G., O'Connell, J.P., 1975. A generalized method for predicting second virial coefficients. Ind. Eng. Chem. Proc. Des. Dev. 14 (3), 209–216. 10.1021/i260055a003.

Hüpen, B., Kenig, E.Y., 2005. Rigorous modelling of NOx absorption in tray and packed columns. Chem. Eng. Sci. 60 (22), 6462–6471. 10.1016/j.ces.2005.04.060.

Jödecke, M., Friese, T., Schuch, G., Kaibel, B., Jansen, H., 2006. The sandwich packing - A new type of structured packing to increase capacity and mass transfer of destillation columns. Inst. Chem. Eng. Symp. Ser. (152), 786–789.

Kenig, E.Y., Bäder, H., Górak, A., Beßling, B., Adrian, T., Schoenmakers, H., 2001. Investigation of ethyl acetate reactive distillation process. Chem. Eng. Sci. 56 (21-22), 6185–6193. 10.1016/S0009-2509(01)00206-8.

Klöker, M., Kenig, E.Y., Hoffmann, A., Kreis, P., Górak, A., 2005. Rate-based modelling and simulation of reactive separations in gas/vapour–liquid systems. Chem. Eng. Process. 44 (6), 617–629. 10.1016/j.cep.2003.12.011.

Olujić, Ž., Seibert, A., Kaibel, B., Jansen, H., Rietfort, T., Zich, E., 2003. Performance characteristics of a new high capacity structured packing. Chem. Eng. Process. 42 (1), 55–60. 10.1016/S0255-2701(02)00019-3.

Rocha, J.A., Bravo, J.L., Fair, J.R., 1996. Distillation columns containing structured packings: A comprehensive model for their performance. 2. Mass-transfer model. Ind. Eng. Chem. Res. 35 (5), 1660–1667. 10.1021/ie940406i.

Schneider, R., Górak, A., 2001. Model optimization for the dynamic simulation of reactive absorption processes. Chem. Eng. Technol. 24 (10), 979–989. 10.1002/1521-4125(200110)24:10<979:AID-CEAT979>3.0.CO;2-#.

Tsai, R.E., Seibert, A.F., Eldridge, R.B., Rochelle, G.T., 2011. A dimensionless model for predicting the mass-transfer area of structured packing. AIChE J. 57 (5), 1173–1184. 10.1002/aic.12345.

Yildirim, Ö., Kenig, E.Y., 2015. Rate-based modelling and simulation of distillation columns with sandwich packings. Chem. Eng. Process.: Process Intensif. 98, 147–154. 10.1016/j.cep.2015.10.007.

Zuiderweg, F.J., 1982. Sieve trays: A view on the state of the art. Chem. Eng. Sci. 37 (10), 1441–1464. 10.1016/0009-2509(82)80001-8.

Towards Sustainable Biorefineries: Intensified Distillation Design and Optimization for Furfural and HMF Recovery

Carlos Rodrigo Caceres-Barrera[a], *Eduardo Sánchez-Ramírez*[a], Maricruz Juárez-García[a], *Juan Gabriel Segovia-Hernández*[a*]

[a] *Department of Chemical Engineering, Universidad de Guanajuato, Campus Guanajuato, Guanajuato, 36050, Mexico.*

Abstract

Biorefineries are a sustainable alternative production of fuels and value-added chemicals from lignocellulosic biomass. Nevertheless, large-scale deployment remains strongly constrained by the high energy demand and operating costs associated with separation and purification stages. Distillation-based separations may represent up to 80% of the total operating cost and dominate the environmental impact of biorefineries. The purification of furfural (FF) and 5-hydroxymethylfurfural (HMF)—two strategic biomass-derived platform molecules—is especially energy intensive due to their close boiling points, high boiling temperatures, and strong interactions with water.

In this work, process intensification (PI) strategies based on thermally coupled distillation systems (TCDS) are systematically evaluated as alternatives to a conventional distillation sequence for FF and HMF purification within a corn-stover-based multiproduct biorefinery. Four intensified configurations are rigorously analyzed: an indirect thermally coupled sequence, a side-stripper arrangement, a fully thermally coupled Petlyuk column, and a single column with lateral product withdrawal. All configurations are modeled using rigorous Aspen Plus simulations and optimized through a multi-objective framework employing the Differential Evolution with Tabu List (DETL) algorithm. The optimization simultaneously considers Total Annual Cost (TAC), total energy consumption, and environmental impact quantified via Eco-Indicator 99 (EI-99).

The results demonstrate that thermally coupled configurations can substantially outperform the conventional sequence. The indirect thermally coupled sequence provides the most balanced solution, achieving reductions of 27.9% in energy consumption, 13.2% in TAC, and 19.1% in EI-99. These findings confirm that the combined application of process intensification and multi-objective optimization constitutes a powerful strategy to enhance the techno-economic and environmental sustainability of separation processes in advanced biorefineries.

Keywords

Process intensification; thermally coupled distillation; biorefineries; multi-objective optimization; furfural; hydroxymethylfurfural.

1. Introduction

The current global energy system remains largely dependent on fossil resources, which supply over 80% of primary energy and account for nearly two-thirds of anthropogenic greenhouse gas emissions. The industrial sector consumes approximately one-third of global final energy demand, with the chemical and petrochemical industries among the most energy-intensive (Saygin et al., 2011). In this context, biorefineries have emerged as a sustainable alternative by enabling the conversion of renewable biomass into fuels and value-added chemicals.

However, biorefinery downstream streams typically exhibit low product concentrations, high water content, and complex multicomponent compositions, making separation particularly challenging. As a result, separation processes may account for 50–80% of total production costs, with distillation being the most widely applied technique (Worrell & Galitsky, 2005). Furfural (FF) and 5-hydroxymethylfurfural (HMF) are biomass-derived molecules, considered sleep giants due to versatility as precursors for fuels, solvents, polymers, and specialty chemicals(Galkin & Ananikov, 2019). However, their purification remains challenging because of high boiling points, thermal sensitivity, and strong affinity for water, limiting the efficiency of conventional distillation.

Process Intensification (PI) offers a systematic framework to overcome these limitations by fundamentally rethinking process design in order to achieve significant reductions in energy consumption, equipment size, and environmental impact. Within this paradigm, thermally coupled distillation sequences (TCDS)—including indirect sequences, side-strippers, Petlyuk columns, and dividing-wall columns—have demonstrated the potential to reduce energy requirements by up to 30% through enhanced internal heat integration and the elimination of redundant condensers and reboilers (Segovia-Hernández et al., 2006).

In this contribution, PI concepts are integrated with multi-objective optimization (MOO) to redesign the purification section of FF and HMF in a multiproduct biorefinery. Several thermally coupled alternatives are systematically compared against a conventional distillation sequence using rigorous simulation and sustainability-oriented performance indicators. The work aims to provide quantitative insights into the trade-offs between economic, energetic, and environmental objectives, thereby supporting informed decision-making in the design of next-generation biorefineries.

2. Methodology

2.1 Design of purification alternatives

The present study builds upon a previously reported biorefinery design for the simultaneous production of levulinic acid (LA), γ-valerolactone (GVL), hydroxymethylfurfural (HMF), and furfural (FF) from corn stover (Caceres-Barrera et al., 2024) In that design, all purification steps relied on conventional distillation columns. Approximately 32% of total process energy consumption was attributed to FF–HMF separation, motivating a focus on intensifying this purification section.

The feed to the purification train consists of a multicomponent mixture containing 74.10 mol% water, 14.45 mol% FF, 11.06 mol% HMF, and trace amounts of other compounds. Thermal coupling is achieved by replacing a condenser or reboiler with material interconnections between columns. All configurations were rigorously simulated in Aspen Plus using the RadFrac model and the NRTL–HOC thermodynamic

framework. Product purity specifications exceeding 98 wt% for both FF and HMF were imposed to ensure comparability among alternatives. Four intensified distillation alternatives are analyzed (see Figure 1): the thermally coupled indirect sequence (IS), the side-stripper configuration (SS), the fully thermally coupled Petlyuk arrangement (PA), and a single column with a lateral product stream (LP).

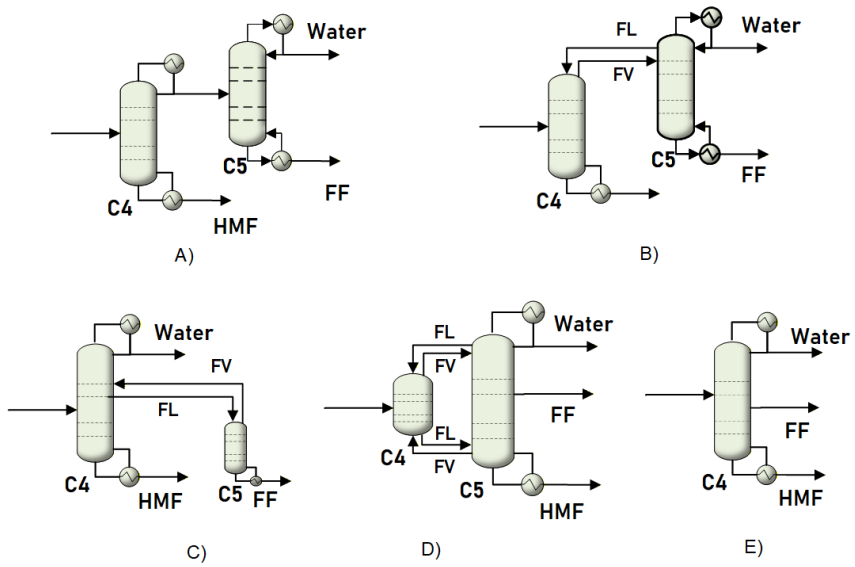

Figure 1. Thermal coupling alternatives to the conventional sequence. A) Conventional sequence, B) Indirect thermal coupled sequence, C) Side stripper, D) Petlyuk arrangement, E) Lateral stream column.

2.2 Multi-Objective Optimization Framework

The sustainability of each configuration was evaluated using three objective functions: Total Annual Cost (TAC), total energy consumption, and environmental impact quantified via Eco-Indicator 99 (EI-99). TAC includes both annualized capital investment and operating costs associated with utilities. EI-99 provides an aggregated environmental indicator derived from life-cycle assessment, encompassing impacts on human health, ecosystem quality, and resource depletion.

The resulting optimization problem is highly nonlinear and non-convex due to the strong coupling between design variables and process performance. The optimization problem can be represented using the equation 1. The right side of the equation represent the decision variables. N is the number of stages for the distillation columns, Nf is the feed stage, RR is the reflux ratio, D is the distillate flow rate and d is the column diameter, additionally Fi and Fs are the values for the flow and location of interconnection streams. Variable bounds were defined based on preliminary sensitivity analyses and literature recommendations.

$$Min(TAC,EI\text{-}99,Energy)=f(N, Nf, RR, D, d,Fi,Fs) \quad (1)$$

The optimization was carried out using the Differential Evolution with Tabu List (DETL) algorithm, which combines the global search capability of differential evolution with the memory-based features of tabu search to avoid premature convergence and repeated exploration of suboptimal regions (Srinivas & Rangaiah, 2007). Aspen Plus simulations were linked with Microsoft Excel, where candidate solutions were generated, evaluated, and iteratively updated. The algorithm employed a population of 120 individuals over 400 generations, resulting in 48,000 function evaluations.

3. Results and discussion

This section presents the optimization results for the intensified alternatives to purify HMF and FF. The results are analyzed using Pareto fronts to elucidate the trade-offs among economic, environmental, and energetic objectives. Convergence was achieved after 48,000 iterations, beyond which no significant improvements in objective function values were observed.

Figure 2 reveals a pronounced the nonlinear trade-off among TAC and EI-99. Solutions with lower TAC generally correspond to higher environmental impacts, mainly due to increased reflux ratios that reduce column diameter and capital cost at the expense of higher reboiler duties and steam consumption. This behavior highlights the intrinsic conflict between short-term economic objectives and long-term environmental performance. Additionally, Figure 3 shows a strong positive correlation between total energy consumption and EI-99, confirming that steam usage in reboilers is the dominant contributor to environmental impact. Consequently, configurations that effectively reduce energy demand also achieve significant improvements in EI-99.

Table 1 summarizes the savings achieved by each alternative. The indirect thermally coupled sequence (IS) delivers the most balanced improvements, with reductions of 27.9% in energy demand, 13.2% in total annual cost (TAC), and 19.1% in Eco-indicator 99 (EI-99). These benefits are mainly attributed to enhanced internal heat recovery and a more effective allocation of separation duties between columns. The side-stripper configuration (SS) also shows notable improvements, with energy savings of 14.7% and TAC and EI-99 reductions of 8.9% and 13.8%, respectively. Conversely, the Petlyuk arrangement (PA) performs poorly in this case, as increased reflux requirements offset the advantages of full thermal coupling. The lateral product column (LP) provides better results for TAC but results in higher energy consumption and environmental burdens.

These results underline the importance of case-specific evaluation of PI alternatives and demonstrate that thermal coupling alone does not guarantee improved sustainability; rather, optimal performance emerges from the appropriate matching of configuration, operating conditions, and optimization objectives.

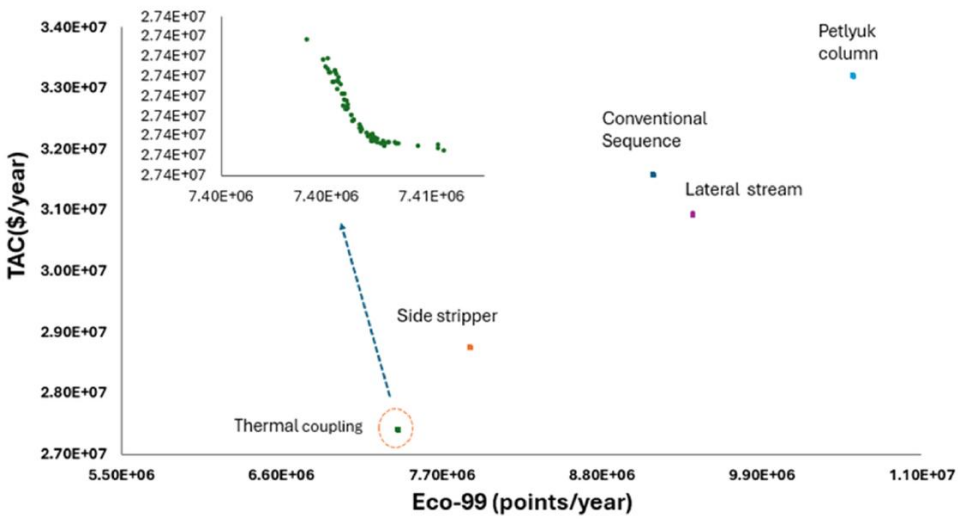

Figure 2. Pareto front between objective functions TAC and EI-99

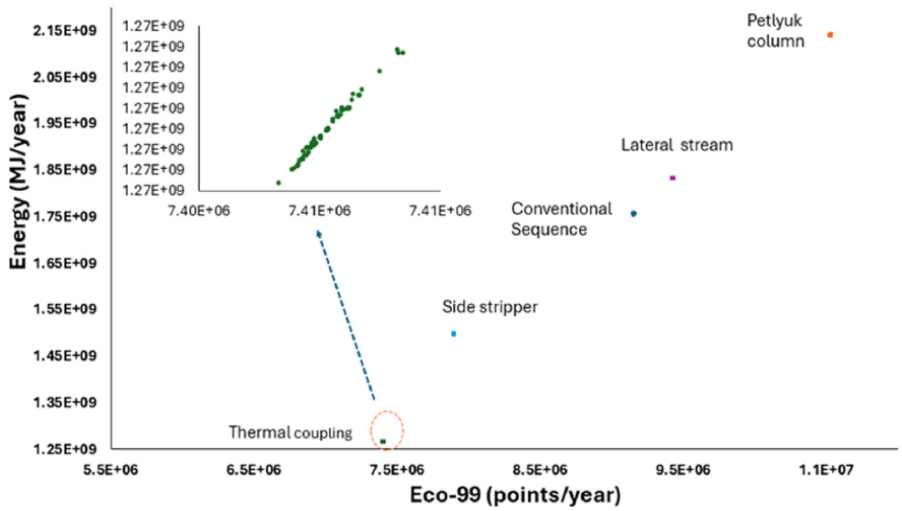

Figure 3. Pareto front between objective functions Energy and EI-99

	Objective Function		
Sequence	**TAC (dollars/year)**	**Eco-99 (points/year)**	**Energy (MJ/year)**
CS	3.157×10^7	9.156×10^6	1.756×10^9
IS	2.740×10^7	7.404×10^6	1.266×10^9
IS Saving	-13.2%	-19.1%	-27.9%
SS	2.875×10^7	7.897×10^6	1.497×10^9
SS Saving	-8.9%	-13.8%	-14.7%
PA	3.320×10^7	1.052×10^7	2.14×10^9
PA Saving	5.1%	14.9%	21.9%
LP	3.093×10^7	9.426×10^6	1.831×10^9
LP Saving	-2.1%	3.0%	4.3%

Table 1. Values for objective functions for conventional sequence (CS) and TCDS.

4. Conclusions

This work demonstrates the effectiveness of integrating process intensification with multi-objective optimization for the sustainable design of separation systems of biomass-derived molecules. By rigorously evaluating several thermally coupled distillation configurations for the purification of furfural and hydroxymethylfurfural, significant reductions in energy consumption, operating cost, and environmental impact were achieved relative to a conventional distillation scheme.

Among the evaluated alternatives, the indirect thermally coupled sequence emerged as the most balanced and robust option, providing energy savings close to 30% while

simultaneously reducing Total Annual Cost and Eco-Indicator 99 by more than 13% and 19%, respectively. The side-stripper configuration also represents a viable intensified alternative, whereas the Petlyuk and lateral product configurations were found to be less suitable for the specific separation problem addressed.

Overall, the results highlight that the benefits of process intensification are highly system-dependent and must be assessed within a comprehensive sustainability framework. The proposed methodology provides a systematic and transferable approach that can be extended to other separation tasks and biorefinery configurations, thereby supporting the development of energy-efficient and environmentally benign industrial processes.

Acknowledgements
Authors acknowledge the support provided by SECIHTI, and Universidad de Guanajuato.

References

Caceres-Barrera, C.R., Sánchez-Ramírez, E., Juárez-García, M., Alcocer-García, H. and Segovia-Hernández, J.G. 2024. Optimization of Separation Processes in Multiproduct Biorefinery Design to Produce Furan-Based Compounds and Their Derivatives Using Performance Indicators. *Industrial & Engineering Chemistry Research* 63(48), pp. 20950–20962. doi: 10.1021/acs.iecr.4c02646.

Galkin, K.I. and Ananikov, V.P. 2019. When Will 5-Hydroxymethylfurfural, the “Sleeping Giant” of Sustainable Chemistry, Awaken? *ChemSusChem* 12(13), pp. 2976–2982. doi: 10.1002/cssc.201900592.

Saygin, D., Worrell, E., Patel, M.K. and Gielen, D.J. 2011. Benchmarking the energy use of energy-intensive industries in industrialized and in developing countries. *Energy* 36(11), pp. 6661–6673. doi: 10.1016/j.energy.2011.08.025.

Segovia-Hernández, J.G., Bonilla-Petriciolet, A. and Salcedo-Estrada, L.I. 2006. Dynamic analysis of thermally coupled distillation sequences with undirectional flows for the separation of ternary mixtures. *Korean Journal of Chemical Engineering* 23(5), pp. 689–698. doi: 10.1007/BF02705913.

Srinivas, M. and Rangaiah, G.P. 2007. Differential evolution with tabu list for solving nonlinear and mixed-integer nonlinear programming problems. *Industrial and Engineering Chemistry Research* 46(22), pp. 7126–7135. doi: 10.1021/ie070007q.

Worrell, E. and Galitsky, C. 2005. *Energy Efficiency Improvement and Cost Saving Opportunities For Petroleum Refineries* . Berkeley,Ca.

Novel design methodology for radially graded packing for heat integrated distillation columns

Gregory Homem Alves César Ribeiro, David Rouzineau, Nathalie Di Miceli Raimondi, Michel Meyer

[1]Laboratoire de Génie Chimique, Université de Toulouse, CNRS, INPT, UPS, Toulouse, France, 4 Allée Emile Monso CAMPUS INP – ENSIACET, 31400 Toulouse, France

Abstract

Additive manufacturing (AM) and equation-based design enable the fabrication of functionally graded (FG) triply periodic minimal surface (TPMS) structures with enhanced heat transfer properties. This work introduces a methodology for designing radially graded TPMS packing for application in concentric heat-integrated distillation columns (HIDiC), where efficient radial heat transfer is required. The design ensures equivalent pressure drop across the gradient through an empirical model derived from gas-phase CFD simulations. Two strut-based FG configurations with opposite radial gradients were compared to a uniform reference structure of equivalent specific surface area. CFD results demonstrated that the configuration with thinner central struts and thicker peripheral struts provided up to 15% higher normalized heat transfer performance while maintaining similar pressure drop. A one-meter packing column, 3D printed in aluminum, exhibited a stable operation without flooding and achieved an average heat conductance of 667 ± 71 W °C^{-1}, outperforming the packing of reference, the stainless steel Super Raschig Rings.

Keywords

Additive manufacturing, Functionally graded, TPMS, HIDiC, CFD

1. Introduction

Distillation remains one of the most energy-intensive unit operations in the chemical industry. Among the various process intensification strategies proposed to reduce its energy consumption, heat integrated distillation columns (HIDiC) have demonstrated strong potential, with reported energy savings of up to 80% (Marin-Gallego et al., 2022). In HIDiC systems, heat is transferred from the rectifying section to the stripping section, allowing partial or total replacement of conventional reboiler and condenser duties. However, despite their theoretical efficiency, the industrial deployment of HIDiC technologies remains limited. One of the main challenges lies in achieving efficient heat transfer while preserving acceptable hydrodynamic and mass transfer performances. Recent advances in additive manufacturing have opened new opportunities for the design of structured packings with complex geometries that are not accessible using conventional manufacturing techniques. In particular, triply periodic minimal surface (TPMS)-based structures have attracted increasing interest due to their high specific surface area and continuous solid connectivity (Al-Ketan and Abu Al-Rub, 2019). TPMS geometries can be described using implicit mathematical equations, allowing smooth and continuous control of geometrical parameters such as porosity, strut diameter, and strut orientation. An additional degree of freedom enabled by additive manufacturing is the introduction of functionally graded (FG) geometries,

in which structural properties vary spatially within the packing. While FG TPMS structures have been widely studied for mechanical and single-phase heat transfer applications, their application to gas–liquid separation processes remain largely unexplored. Applying a functional grading in a distillation column packing must thus consider key aspects such as good distribution of both gas and liquid, optimized contact, controlled pressure drop and efficient mass transfer, in addition to the intended heat transfer.

The main objective of this work is to develop and assess a novel design methodology for radially FG TPMS-based packings specifically tailored for concentric HIDiC configurations, in which radial heat transfer is the dominant mechanism. The proposed approach aims to enhance heat transfer performance while maintaining pressure drop at a level equivalent to that of a reference uniform packing, in order to avoid preferential gas bypassing. The originality of this study lies in the development of a pressure-drop-equivalent design strategy for FG packings, integrating strut diameter and strut orientation into an empirical model derived from CFD simulations, and the experimental validation of a metallic additively manufactured prototype under operating conditions representative of HIDiC systems.

2. Results and discussion

2.1 Design of Functionally Graded (FG) TPMS Packings

The investigated packings are based on solid-network TPMS geometries generated using an equation-based approach. This formulation enables direct control of local geometrical features by modifying the coefficients of the implicit TPMS equation, allowing continuous variation of strut diameter, strut orientation and unit cell size, as indicated in Figure 1a. More detail on this methodology can be found in a previous work (Homem Alves César Ribeiro et al., 2025). Compared to conventional CAD-based design approaches, this method is particularly well suited for implementing smooth and continuous functional gradients within the structure. In a concentric HIDiC configuration, two coaxial regions corresponding to the rectifying and stripping sections are separated by an integrated wall embedded within the packing. Since heat transfer occurs primarily in the radial direction, functional grading is introduced exclusively along this direction in the present study. To prevent preferential gas flow through low-resistance regions, the design constraint requires that all radial positions of the cylindrical packing exhibit an equivalent axial pressure drop over a given range of gas velocities. A modified Ergun-type empirical model was developed to describe the pressure drop through TPMS-based structures. The model accounts for local porosity, strut diameter as the characteristic length scale, and strut orientation. The influence of strut orientation was found to be particularly significant, with variations in pressure drop reaching up to 40–50% for orientation changes of approximately 10 degrees. A pressure-drop equivalence criterion is defined by minimizing the mean squared deviation between the pressure-drop curve of a reference uniform packing and that of the candidate geometry over the investigated gas velocity range. To simplify the handling of FG structures, each graded unit cell is locally approximated by an equivalent uniform cell characterized by an equivalent strut diameter. This approach allows for approximating the continuously graded cells as a series of uniform cells of distinct dimensions, whose pressure drop are known with the empirical model. This methodology provides a rational framework for the design of FG packings intended for gas–liquid contactors.

2.2 CFD Simulations

Hydrodynamic and thermal performances of the proposed structures were evaluated using gas–solid CFD simulations performed with ANSYS Fluent. Turbulent airflow through cylindrical packing domains was simulated using the k–omega SST turbulence model. The temperature was fixed for a hot inlet gas and a cooled outer wall, in order to evaluate the cooling of air. A range of inlet gas velocities was studied, with gas load factors up to 2 $Pa^{0.5}$, which is representative of distillation columns. Prior studies were carried out to validate a minimum simulation domain size for accurate representation of both gas pressure drop and heat transfer. Two opposite grading strategies were investigated: one with thicker struts near the column center and thinner struts close to the outer wall, and a second one with thinner struts near the center and thicker struts close to the wall. Three geometries were then evaluated: a uniform (*Theta35*), one with thicker struts in the center (*Theta47.5-35*) and another with thinner struts in the center (*Theta35-44*), shown in Figure 1b. The structures had equal specific surface area, a key parameter for both mass and heat transfer.

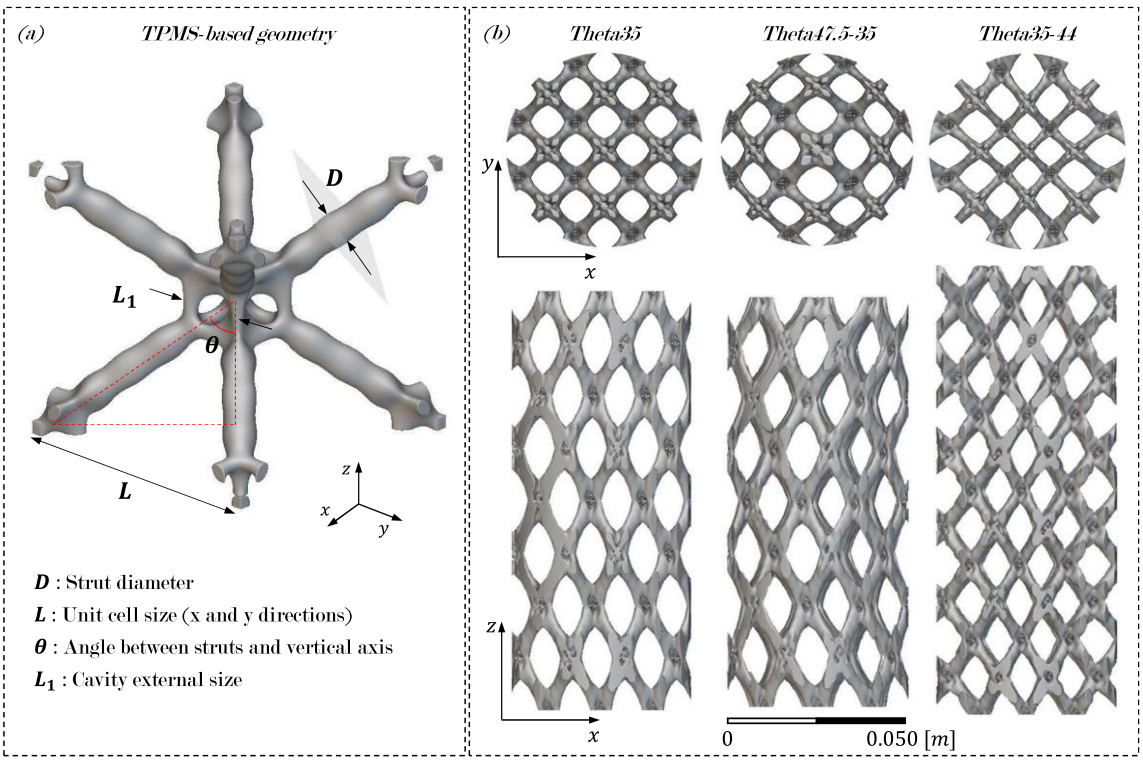

Figure 1: TPMS-based lattice design. (a) Characteristic dimensions. (b) Uniform and FG designs for CFD simulations.

The simulation results show that the functionally graded structures satisfy the pressure-drop equivalence objective within an error margin of approximately ±15%, as shown in Figure 2a. A strong correlation between overall heat transfer coefficients and pressure drop was observed. Overall performance normalized by pressure drop was evaluated using the Performance Evaluation Coefficient (PEC), defined as in Equation 1, in which Nu_{Dh} is the gas Nusselt number using the hydraulic diameter Dh and f the Fanning friction factor. The index 0 refers to the uniform geometry of reference Theta35. PEC values for all three geometries are shown in Figure 2b. The structure featuring thinner struts near the packing center and thicker struts near the outer radius (*Theta35-44*) exhibits the best thermal performance, with PEC improvement of 15% with respect to the uniform geometry. The local profiles of temperature, gas velocity

and heat flux indicate that thinner struts in the center promote more turbulence and increase overall heat transfer compensating the limitation on conduction.

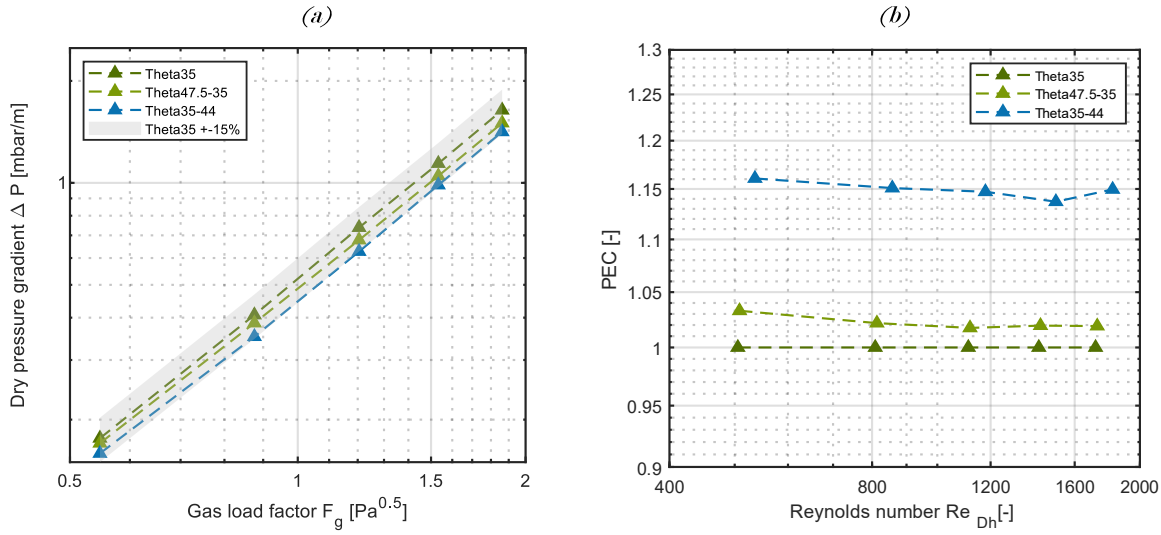

Figure 2: CFD simulation results. (a) Dry pressure gradient. (b) Performance Evaluation Coefficient (PEC).

$$PEC = \frac{\left(\frac{Nu_{Dh}}{Nu_{Dh_0}}\right)}{\left(\frac{f}{f_0}\right)^{\frac{1}{2}}} \tag{1}$$

2.3 Experimental Validation

A representative functionally graded TPMS packing was designed with an embedded internal wall to mimic the HIDiC, as shown in Figure 3a and b, the latter providing a detailed view of the packing merging with the wall.

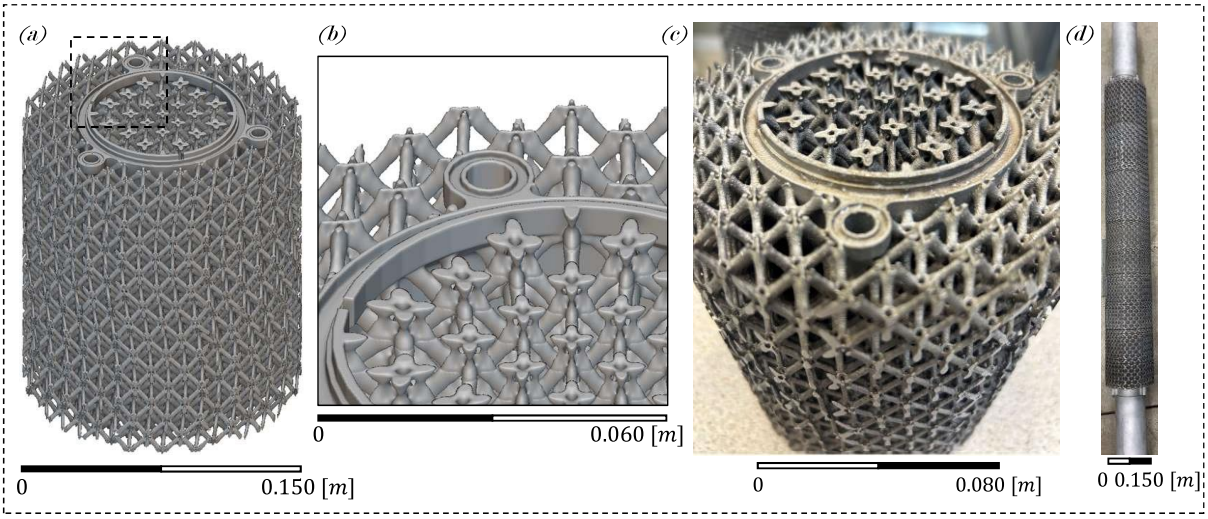

Figure 3: Additive manufacturing of the functionally graded packing. (a) CAD image of the coaxial piece. (b) Detailed view of the coupled wall. (c) 3D printed packing piece. (d) Assembled one-meter column.

The packing was fabricated in aluminum using laser powder bed fusion additive manufacturing with good reproduction of the geometry, as shown in Figure 3. For the 3D printed packing, thinner struts in the center increasing towards the wall were used in the internal zone and, for the external zone, thicker struts at the embedded wall and thinner struts at outer wall. This choice of grading was based on the CFD observations.

The unitary printed packing pieces were then assembled to form a one-meter height column which was inserted in the experimental pilot, shown in Figure 3d.
The prototype was experimentally characterized in a dedicated test bench, which is schematized in Figure 4, to measure overall heat transfer under operating conditions relevant to HIDiC applications. In summary, cyclohexane is fed to the inner central zone of the packing from column top and is gradually heated and vaporized by the heat provided from the water vapor, inserted at the outer packing zone. The experimental heat conductance $(UA)_{exp}$, defined as in Equation 2, can be estimated from the effective exchanged heat Q, calculated from the obtained distillate flow rate, and the temperature difference between the zones ΔT_{i-e}, considered constant as only phase change promotes heat transfer within the packing (steam condensing in the outer zone and cyclohexane being vaporized in the inner zone).

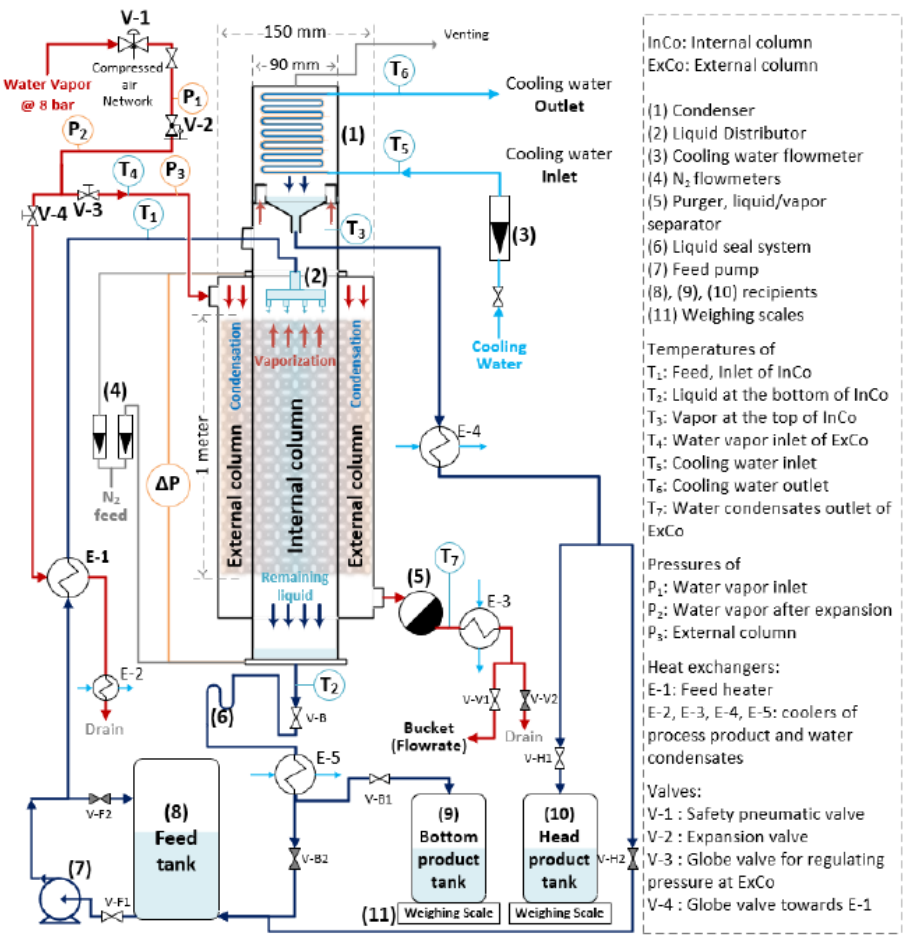

Figure 4: Experimental evaluation of the heat transfer. (a) Schematic of the setup.

$$(UA)_{exp} = \frac{Q}{\Delta T_{i-e}} \tag{2}$$

Experiments were conducted for distinct temperature differences and feed flow rates and were analyzed in terms of vapor fraction x_{vap}, i.e. the ratio of distillate to feed flow rate. Feed flow rates varied between 7.9 to 11.8 $m^3.m^{-2}.h^{-1}$. Compared to a uniform reference packing, the stainless steel Super Raschig Rings (SRR), the functionally graded TPMS exhibits enhanced heat transfer performance, shown in Figure 5, reaching heat conductance of $667 \pm 71\ W.°C^{-1}$ (dashed line). The SRR packing had a specific surface area of 315 $m^2.m^{-3}$ whereas the FG TPMS packing inner zone presented 213 $m^2.m^{-3}$ and the outer zone 257 $m^2.m^{-3}$. Despite the reduced surface

area, the FG TPMS outperformed the SRR packing. Also, the new packing did not reach flooding in the studied range and presented performance with minor sensitivity to the vapor fraction, which indicates robustness of the packing for heat transfer uses.

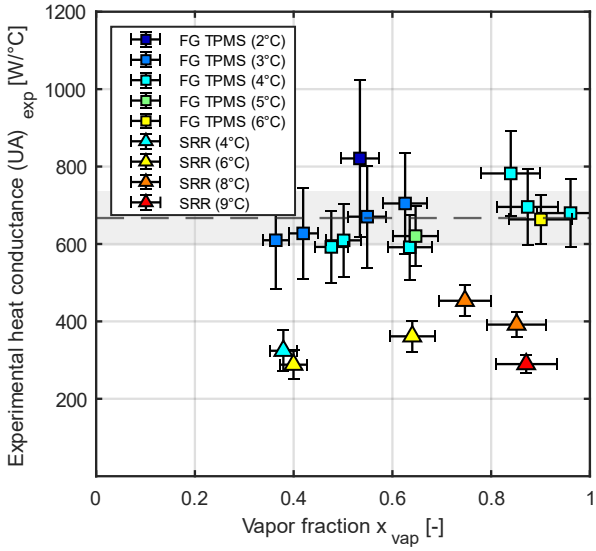

Figure 5 : Results for heat conductance at distinct temperature differences ΔT_{i-e} of the functionally graded (FG) TPMS and Super Raschig Rings (SRR)

3. Conclusions

This work demonstrates the feasibility and highlights the potential of functionally graded TPMS-based packings for integrated heat transfer applications, in particular for concentric HIDiC. The proposed methodology based on equivalence of gas pressure drop enables the exploitation of radial anisotropy or functional grading in cylindrical packing for distillation columns to enhance heat transfer while preserving good flow distribution. Simulations revealed an increase in overall performance by using thinner struts in the center and thicker struts in the outer radius, compared to a uniform structure of equivalent surface area. Moreover, experiments proved the interest of using FG TPMS as HIDiC packing, presenting enhanced heat conductance compared to benchmark packing, being resistant to flooding and nearly independent of flow rates. Future work will focus on integrating gas–liquid flow aspects in the design methodology, evaluating mass transfer performance and liquid distribution of the new packing, aiming to be later tested in a HIDiC pilot for validation.

Acknowledgements

The authors gratefully acknowledge funding for this study from the French National Research Agency (ANR).

This work was granted access to the HPC resources of CALMIP supercomputing center.

References

Al-Ketan, O., Abu Al-Rub, R.K., 2019. Multifunctional Mechanical Metamaterials Based on Triply Periodic Minimal Surface Lattices. Adv. Eng. Mater. 21, 1900524. https://doi.org/10.1002/adem.201900524

Homem Alves César Ribeiro, G., Rouzineau, D., Meyer, M., Di Miceli Raimondi, N., 2025. Novel design approach based on triply periodic minimal surfaces (TPMS) for gas–liquid contactor packing. Chemical Engineering Science 304, 121062. https://doi.org/10.1016/j.ces.2024.121062.

Marin-Gallego, M., Mizzi, B., Rouzineau, D., Gourdon, C., Meyer, M., 2022. Concentric Heat Integrated Distillation Column (HIDiC): a new specific packing design, characterization and pre-industrial pilot unit validation. Chemical Engineering and Processing - Process Intensification 171, 108643. https://doi.org/10.1016/j.cep.2021.108643.

Distillation in Rotating Zigzag Beds: Experimental Validation of a Rate-based Modelling Approach

Niclas Rohde[1], Jonathan Mach[1], Emiel Zobel[1] Georg Brösigke[1], Markus Illner[1], Jens-Uwe Repke[1]
[1]Technische Universität Berlin, Process Dynamics and Operations Group, Berlin, Germany

Abstract
The substitution of terrestrial gravity with centrifugal fields as driving force has led to the development of high-gravity units (HiGee) for process intensification as potential alternative to separation columns in several processes. Besides the rotating packed bed (RPB), there is a growing interest in the rotating zigzag bed (RZB) within the research field. RZBs offer stationary elements in addition to the rotating internals, inducing high shear forces and increased liquid residence times. However, their application in Europe is almost non-existent and English literature harbors little information, severely hindering industrial implementation. Therefore, this study elucidates distillation in rotating zigzag beds as the most important thermal separation process. For that, a first rate-based modeling approach is presented for binary distillation at infinite reflux. Additionally, an experimental setup is developed to validate the process model. The model reproduces the same physical trends and yields good agreement with the experimental distillation data. While the rotational speed generally increases the transport performance, an increase in gas load lowers it. This work suggests considerable potential for RZBs in thermal separation, warranting further investigation.

Keywords
HiGee, rotating zigzag bed, distillation, experiment, process model

1. Introduction

High-gravity (HiGee) units utilize high centrifugal forces to intensify separation processes and are thus considered a promising alternative to conventional columns for many applications [1]. Recently, different types of rotating packed beds (RPBs) appeared for several applications in the field of chemical industry, such as distillation, absorption or stripping [1–3]. Fully rotating RPB internals – metal foam, wire mesh or corrugated sheets – were predominantly investigated so far. Besides these, another HiGee design, the rotating zigzag bed (RZB), has emerged, utilizing upper stationary elements in addition to its lower rotating parts. This rotor-stator principle provides several advantages [3]: further increased shear forces, increased liquid residence times and holdup, a simpler sealing strategy, and the possibility to physically access stationary internal elements, e.g. for sensors or an intermediate feed.

RZBs employ a counter-current flow, as visualized in Figure 1. The liquid phase undergoes a repeating cascade of droplet centrifugation (Z1), subsequent collisions at stationary subparts (Z2), film accumulation (Z3/Z5) and film drop off (Z4), opening a large interfacial area at rapid surface renewal times. Introduced at the outer casing, the gas/vapor phase flows inwards in the characteristic zigzag pattern, driven by a pressure-gradient, and surrounds the disperse liquid phase.

Literature about RZBs is scarce, publications out of Europe almost non-existent. Asian research focuses on experimental studies, seldomly giving insights into phenomena occurring inside rotating zigzag beds. At the same time, literature lacks modeling approaches to describe mass, energy or momentum transport. Such methods, however, are a vital aspect to validate and predict experimental data under varying designs and operating conditions, and ultimately, to facilitate RZBs as new apparatus for thermal separation processes.
In our study, we present a first steady-state process model for the binary distillation of ethanol/n-propanol in RZBs, following a rate-based approach for each of the contact zones shown (Z1-Z5). For that, interfacial areas of the disperse liquid phase are described and coupled with known mass and energy transport theories. From there, we aim to conclude which phenomenon really drives the transport performance in RZBs to suggest design recommendations. Additionally, experimental distillation data from an in-house developed and constructed RZB mini-plant is presented to validate the proposed process model. The rotational speed and gas load, both strongly influencing interfacial areas and contact times of liquid and vapor, are altered to contrast different operating scenarios. Figure 1b) enables insight into the open HiGee casing with the manufactured zigzag internals inserted.

2. Methodology

Under investigation is a binary ethanol/n-propanol distillation system. The simplified flow-chart is shown in Figure 1a). The operation is considered at infinite reflux. Prior to the start-up of the mini-plant, the liquid mixture (70 liters of ethanol/n-propanol at 20/80 vol.-%), is prepared in a kettle reboiler. The reboiler evaporates the bottom liquid and directs the vapor phase towards the RZB. From here, the vapor phase is channeled inwards, eventually leaving the RZB at the rotor eye towards a total condenser. The distillate is collected in a reflux drum and subsequently pumped through a pre-heating section back towards the RZB liquid feed, to ensure constant subcooling. After its centrifugation through the zigzag internals, the liquid phase is

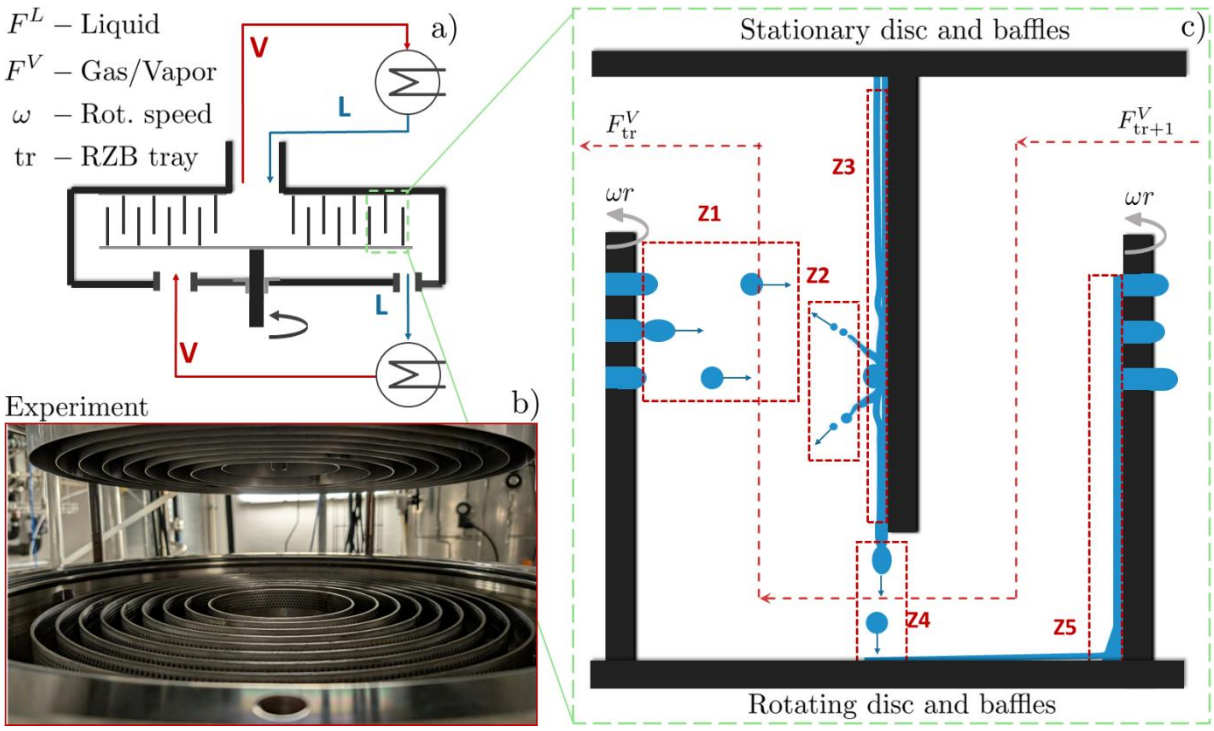

Figure 1: Simplified RZB distillation setup a). Characteristic flow pattern of liquid and vapor in various contact zones Z1-Z5 c). Photography of the open RZB casing located at TU Berlin with inserted zigzag internals b).

gathered in the outer RZB casing and flows back to the reboiler driven by gravitation. The operating head pressure is fixed at $1000\,\mathrm{mbar}$ using a vacuum pump. In the experiments, liquid phase samples are drawn from liquid inlet and liquid outlet for composition analysis in a GC system (Agilent Technologies 8890). Prior to the sample collection, a steady-state operation of the mini-plant is ensured. For that, at least two reboiler residence times as well as stationary temperatures, flow rates and liquid levels are preconditioned. Operation-wise, our study considers rotational speeds of $N = 400$ and $800\,\mathrm{rpm}$ at gas loads of approximately $F = 1.0 - 4.0\,\mathrm{Pa}^{0.5}$, which is equivalent to a mass flow rate of $30 - 110\,\mathrm{kg\,h^{-1}}$. The F-factor F is geometrically based on the minimum annular cross-section area between two consecutive baffles of the RZB, usually found in the innermost tray.
The RZB casing and the inserted zigzag internals investigated in this study were previously presented and developed by Rohde et al. [4]. The RZB utilizes a rotor disc of $250\,\mathrm{mm}$ radius. The zigzag geometry covers 9 pairs of baffles, subsequently referred to as trays (index tr) and a packing height of $H_p = 60\,\mathrm{mm}$. The zigzag baffles range from the radii $r_i = 60\,\mathrm{mm}$ (innermost baffle) to $r_o = 230\,\mathrm{mm}$ (outmost baffle). The process model introduced in the next Section is parametrized with the exact zigzag geometry, including baffle placement, height and perforated sections used in the experiments. Prospectively, the influence of varying zigzag geometries will be studied experimentally and simulative.

3. Model development

The process model comprises the RZB, the reboiler and the condenser as coupled sub-models of the entire distillation process. The system is assumed to be adiabatic and at steady state. Limiting effects due to fluid dynamics, such as entrainment or flooding, are neglected. The pressure profile throughout the RZB trays is described using the dry pressure drop model previously developed by [4]. The pressure drops in the reboiler and condenser are neglected. The zigzag internals are radially discretized throughout the trays tr. As every contact zone Z1–Z5 (index z) contributes differently to the mass and energy transport, the description of the zigzag trays follows the non-equilibrium methodology MERSHQ initially proposed by Krishna and Taylor [5] to describe the distillation process.

$$0 = F_{\mathrm{tr}-1}^{L,z} x_{\mathrm{tr}-1,c}^{L,z} - F_{\mathrm{tr}}^{L,z} x_{\mathrm{tr,c}}^{L,z} + f_{\mathrm{tr,c}}^{int,z} A_{\mathrm{tr}}^{z} \tag{1}$$

$$0 = F_{\mathrm{tr}-1}^{L,z} h_{\mathrm{tr}-1,c}^{L,z} - F_{\mathrm{tr}}^{L,z} h_{\mathrm{tr,c}}^{L,z} + e_{\mathrm{tr,c}}^{int,z} A_{\mathrm{tr}}^{z} \tag{2}$$

$$0 = f_{\mathrm{tr,c}}^{\mathrm{int,z}} - \beta_{\mathrm{tr}}^{\mathrm{L,z}} \left(\frac{\rho_{tr}^{L,\mathrm{z}}}{M_{tr}^{L,\mathrm{z}}}\right)\left(x_{\mathrm{tr,c}}^{L,\mathrm{int,z}} - x_{\mathrm{tr,c}}^{L,\mathrm{z}}\right) + x_{\mathrm{tr,c}}^{L,\mathrm{z}} \cdot \sum_{c=1}^{N_c} f_{\mathrm{tr,c}}^{\mathrm{int,z}} \tag{3}$$

$$0 = e_{\mathrm{tr}}^{\mathrm{int,z}} - \alpha_{\mathrm{tr}}^{\mathrm{L,z}}\left(T_{\mathrm{tr}}^{L,\mathrm{int,z}} - T_{\mathrm{tr}}^{L,\mathrm{z}}\right) + \sum_{c=1}^{N_c} f_{\mathrm{tr,c}}^{\mathrm{int,z}} \cdot h_{\mathrm{tr,c}}^{L} \tag{4}$$

The Equations (1) and (2) present a generic material and energy balance exemplary for the liquid phase (index L) which is balanced in each tray tr and contact zone z shown in Figure 1 c). Here, $f_{\mathrm{tr,c}}^{\mathrm{int,z}}$ and $e_{\mathrm{tr,c}}^{\mathrm{int,z}}$ describe the molar and energy transfer flux densities, acting on the interfacial area $A_{\mathrm{tr}}^{\mathrm{z}}$. The transfer rates are determined via the Equations (3) and (4) and base on their respective transfer coefficient ($\beta_{\mathrm{tr}}^{L,z}$and $\alpha_{\mathrm{tr}}^{L,z}$) and driving force ($\Delta x_{\mathrm{tr}}^{L,\mathrm{z}}$ and $\Delta T_{\mathrm{tr}}^{L,\mathrm{z}}$) between interface and bulk. The heat transfer coefficients are determined using the Chilton-Colburn analogy [6], while the mass transfer coefficients are described depending on the considered phenomenon. All contact zones containing disperse liquid droplets surrounded by the continuous vapor

phase are described with the penetration theory $\beta_{\mathrm{tr}}^{L,\mathrm{z}} = 2\sqrt{\pi}\sqrt{D_{12}/\tau_{\mathrm{tr}}^{\mathrm{z}}}$ (Z1, Z2 and Z4). Here, besides the diffusion coefficient D_{12}, the mass transfer coefficient depends on the contact time $\tau_{\mathrm{tr}}^{\mathrm{z}} = d_{10,\mathrm{tr}}^{z}/u_{rel,\mathrm{tr}}^{z}$, resulting from the arithmetic droplet diameter $d_{10,\mathrm{tr}}^{z}$ and its relative velocity towards the vapor phase. The velocity of the vapor phase is obtained from data of a previous RZB CFD study [4]. All droplets are assumed to have an ideal spherical shape. For contact zones containing liquid films (Z3 and Z5), the mass transfer coefficient is determined via known correlations for counter-current and falling films on flat plates [7]. To account for turbulence and impinging droplets, efficiency factors are applied [8,9]. As the rate-based concept induces a strong coupling between fluid dynamic quantities and mass and energy transport, the description of each contact zone within the RZB trays is followingly presented.

Zone 1: The detachment and centrifugation of liquid from the orifices of the rotating baffles primarily depend on the orifice geometry, the rotational speed and the surrounding gas flow velocity. To describe these phenomena, slinger atomizers are adopted as related application. Here, literature offers correlations to determine the liquid travel velocity $u_{\mathrm{tr}}^{\mathrm{L,Z1}}$ as well as arithmetic $d_{10,\mathrm{tr}}^{\mathrm{L,Z1}}$ and Sauter diameters $d_{32,\mathrm{tr}}^{\mathrm{L,Z1}}$ of the centrifugated liquid phase [10,11].

Zone 2: On impact with the wet film on the stationary baffle and above a critical splash condition, a part of the incoming liquid is reflected back inwards as smaller satellite droplets. Thus, splashing severely increases the interfacial area within the tray that predominantly depends on the velocity $u_{\mathrm{tr}}^{\mathrm{L,Z1}}$ and the size $d_{10,\mathrm{tr}}^{\mathrm{L,Z1}}$ of the primary droplets described in zone 1 and the film thickness $\delta_{\mathrm{tr}}^{\mathrm{Z3}}$ of zone 3. The Sauter diameter $d_{32,\mathrm{tr}}^{\mathrm{L,Z2}}$ of the satellite droplets and their mass ratio to the liquid remaining at the baffle, is determined according to correlations given in [12].

Zone 3: The accumulating film on the stationary baffle is consistently impinged by the primary droplets of zone 1. It is assumed that the overall area $A_{\mathrm{tr}}^{\mathrm{int,Z3}}$ is at least the lateral surface of the respective stationary wall $A_{\mathrm{tr}}^{\mathrm{Z3,id}}$ plus the area introduced by droplet impingement $A_{\mathrm{tr}}^{\mathrm{Z3,d}}$. The latter term is associated with the Weber number $\mathrm{We}_{\mathrm{tr}}^{\mathrm{Z1}}$ being proportional to the maximal deformation on impact [13]. While $A_{\mathrm{tr}}^{\mathrm{Z3,id}}$ applies constantly, $A_{\mathrm{tr}}^{\mathrm{Z3,d}}$ appears for a short time span as each droplet impact triggers liquid crown formation and subsequent decay. This time span is derived from a semi-empirical approach given by [14] and connected to the frequency of droplet impacts to determine the overall $A_{\mathrm{tr}}^{\mathrm{Z3,d}}$ at a given operating condition. The film thickness $\delta_{\mathrm{tr}}^{\mathrm{Z3}}$ and falling film velocity $u_{\mathrm{tr}}^{\mathrm{L,Z3}}$ are derived by considering the momentum balance between gravitation, friction at the wall and vapor interface and the droplet momentum.

Zone 4: Another momentum balance is applied to describe the drop-off of droplets from the lower edge of the stationary baffles. Here, the liquid surface force is compared to the aerodynamic force exerted by the vapor and the gravitation to obtain the droplet size $d_{10,\mathrm{tr}}^{\mathrm{L,Z4}}$ in zone 4.

Zone 5: Lastly, the accumulated liquid film in front of the rotating baffles is described as ideal liquid paraboloid, assuming a rigid body rotation under the neglection of viscous effects and surface tension. This simplification is viable as high centrifugal forces act on the liquid phase. The parabolic shape solely depends on the geometry of the zigzag internals and the rotational speed. By integration through its arc length, the interfacial area $A_{\mathrm{tr}}^{\mathrm{int,Z5}}$ of zone 5 is derived.

4. Results and discussion

The validation between process model and experiments is followingly presented, focusing on the number of equilibrium-stage equivalents N_{eq} as performance indicator of the RZB unit. The equilibrium-stages reached are determined utilizing the Fenske method [15] based on the liquid mole fractions between the RZB liquid feed and outlet. Figure 2 depicts a parity comparison b) and profiles a) between the experimentally obtained (markers) and model-predicted (dashed lines) equilibrium-stage equivalents against the gas load F at low and moderate rotational speeds ($N = 400$ and $800\,\mathrm{rpm}$, respectively). Based on the inserted zigzag geometry with 9 baffle pairs available, a tray efficiency of approximately 35% at $400\,\mathrm{rpm}$ and 50% at $800\,\mathrm{rpm}$ is obtained experimentally, compared to a full equilibrium stage. The rotational speed is found to positively influence the separation performance, while the flow rate, and consequently the gas load, negatively affects it – which is a trend known from different HiGee applications [2,16]. In the RZB, higher rotational speeds induce larger interfacial areas between the phases, due to finer droplets (Z1) and a more pronounced droplet impingement (Z3), eventually leading to an increased fraction of reflected satellite droplets (Z2). Additionally, gas turbulence with respect to the tangential velocity is increased. However, at higher throughputs, liquid films within the trays become generally thicker. This hinders the occurrence of splash at stationary baffles but also increases the penetration depth necessary between vapor interface and the liquid bulk flow, lowering the mass and energy transport. However, at high gas loads around $4\,\mathrm{Pa}^{0.5}$, the experiments reveal a sudden increase in transport performance again, in particular for the low rotational speed $N = 400\,\mathrm{rpm}$. While the origin of this anomaly remains unclear, it is suggested to be related to the increasing interaction between the phases as the liquid holdup is generally larger at low rotational speeds.

Both, experiments and the model approach, show similar trends at increasing rotational speeds and gas loads. The process model slightly underpredicts the experimentally reached equilibrium-stage equivalents N_{eq} as visible in the parity diagram Figure 2 b). According to the process model in its current state, the overall separation efficiency is driven by the droplet regimes, while the film regimes play a subordinate role, suggesting an underestimation in mass and energy transport of the impinged film in zone 3 and/or the liquid piling up in zone 5 of the model.

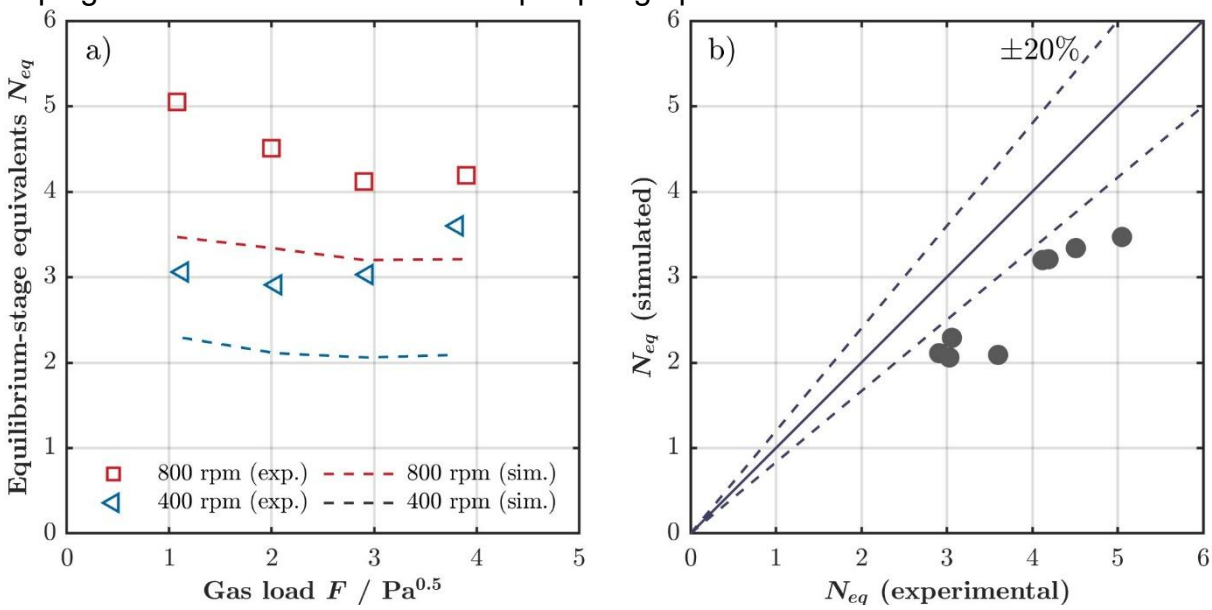

Figure 2: Number of theoretical stages obtained from the distillation experiments and the process model at various gas loads and rotational speeds. Profiles a) and parity plot b).

5. Conclusions

The presented study introduced a first rate-based modeling concept for steady-state distillation in rotating zigzag beds that is in ongoing model development. At its current state, all important contact zones are fluid dynamically described and coupled with the mass and energy transport. Moreover, a mini-plant is presented and utilized for a first experimental validation against the modelling approach.

Both approaches show similar trends as an increased rotational speed positively influences the distillation performance, while the gas load seemingly reduces it. Although the process model underpredicts the transport performance of the experiments in its current state, a good agreement at the basis of equilibrium-stage equivalents is found. Further improved accuracy is expected in the future as the zones covering liquid films (Z3 and Z5) appear to be inadequately represented in the current overall mass and energy transport.

At present, the model is applied on binary distillation with ethanol/n-propanol and is parametrized for one zigzag geometry. Prospectively it is extended towards varying zigzag internals and operating conditions.

Acknowledgements

The authors thank Dietmar Plotka, Tom Vogel, Gregor Tychek and Paul Köhn for providing support in the mechanical and electrical construction of our RZB mini-plant.

References

[1] M. Illner, M. Hilpert, J.-U. Repke, in *Process Intensif.* (Eds: M. Skiborowski, A. Górak), De Gruyter 2022.
[2] M. Hilpert, G. U. Calvillo Aranda, J.-U. Repke, *Chem. Eng. Process. - Process Intensif.* 2022, *171*, 108651. DOI: 10.1016/j.cep.2021.108651.
[3] G. E. Cortes Garcia, J. Van Der Schaaf, A. A. Kiss, *J. Chem. Technol. Biotechnol.* 2017, *92* (6), 1136–1156. DOI: 10.1002/jctb.5206.
[4] N. Rohde, F. Febrian, J. Mach, N. Yong, G. Brösigke, M. Illner, J.-U. Repke, *Chem. Eng. Process. - Process Intensif.* 2025, 110510. DOI: 10.1016/j.cep.2025.110510.
[5] R. Krishnamurthy, R. Taylor, *AIChE J.* 1985, *31* (3), 449–456. DOI: 10.1002/aic.690310312.
[6] T. H. Chilton, A. P. Colburn, *Ind. Eng. Chem.* 1934, *26* (11), 1183–1187. DOI: 10.1021/ie50299a012.
[7] M. Kraume, *Transportvorgänge in der Verfahrenstechnik: Grundlagen und apparative Umsetzungen*, Springer Berlin Heidelberg, Berlin, Heidelberg 2020.
[8] K. H. Sill, *Wärme- Und Stoffübergang in Turbulenten Strömungsgrenzschichten Längs Verdunstender Welliger Wasserfilme*, Karlsruhe, Universität, Karlsruhe 1982.
[9] D. W. Stanton, C. J. Rutland, *Int. J. Heat Mass Transf.* 1998, *41* (20), 3037–3054. DOI: 10.1016/S0017-9310(98)00054-4.
[10] S. Sahu, A. Chakraborty, D. Maurya, *Int. J. Multiph. Flow*. 2021, *135*, 103532. DOI: 10.1016/j.ijmultiphaseflow.2020.103532.
[11] J. Hou, Z. Zhu, C. Ma, G. Wang, E. Barakat, *Phys. Fluids*. 2024, *36* (2), 023301. DOI: 10.1063/5.0181526.
[12] Z. Han, Z. Xu, N. Trigui, *Int. J. Engine Res.* 2000, *1* (1), 127–146. DOI: 10.1243/1468087001545308.
[13] C. Clanet, C. Béguin, D. Richard, D. Quéré, *J. Fluid Mech.* 2004, *517*, 199–208. DOI: 10.1017/S0022112004000904.
[14] I. V. Roisman, N. P. Van Hinsberg, C. Tropea, *Phys. Rev. E*. 2008, *77* (4), 046305. DOI: 10.1103/PhysRevE.77.046305.
[15] M. R. Fenske, *Ind. Eng. Chem.* 1932, *24* (5), 482–485. DOI: 10.1021/ie50269a003.
[16] G. Q. Wang, Z. J. Zhou, Y. M. Li, J. B. Ji, *Chem. Eng. Process. - Process Intensif.* 2019, *135*, 141–147. DOI: 10.1016/j.cep.2018.11.014.

Synthesis, Design and Optimization of Double-Dividing Wall Distillation Columns for the Separation of Quaternary Mixtures

Carlos Eduardo Guzmán Martínez [1], Araceli Guadalupe Romero-Izquierdo [2], Claudia Gutiérrez-Antonio [1], Salvador Hernández [3], Massimiliano Errico [4,5], Fernando Israel Gómez-Castro [2],

[1] Facultad de Ingeniería, Campus Juriquilla, Universidad Autónoma de Querétaro, Juriquilla, Querétaro, México;

[2] Facultad de Ingeniería, Campus Amealco, Universidad Autónoma de Querétaro, Amealco de Bonfil, Querétaro, México;

[3] Departamento de Ingeniería Química, División de Ciencias Naturales y Exactas, Campus Guanajuato, Universidad de Guanajuato, Guanajuato, Guanajuato, México;

[4] Department of Green Technology, Faculty of Engineering, University of Southern Denmark, Odense, Denmark;

[5] Department of Mechanical, Chemical and Materials Engineering, Università di Cagliari, Italy;

Abstract

Distillation is a widely used separation process for chemical and petrochemical industries. However, it shows low second-law efficiencies, which requires high amounts of thermal energy to perform its task. Thus, over the years, diverse researchers have been devoted to developing alternatives and novel configurations to reduce the heat duty of distillation systems. In this work, a synthesis strategy is proposed for a double dividing wall distillation column based on a conventional indirect sequence. The proposed intensified sequence is then optimized through a multiobjective genetic algorithm, to determine the design and operating variables allowing the minimization of the total heat duty and the total number of stages. The performance of the proposed configuration is compared with a previously reported double-dividing wall system synthesized from a conventional direct sequence. Both configurations are tested for a mixture of n-butane/n-pentane/n-hexane/n-heptane, with molar feed composition of 40/10/10/40. According to the results, the intensified direct sequence allows reductions of approximately 14% on the total heat duty in comparison with the conventional direct sequence. However, the proposed intensified indirect sequence requires a total heat duty higher than the conventional indirect sequence for the studied feed composition.

Keywords

Quaternary mixtures, distillation, dividing-wall columns, process synthesis, metaheuristic optimization

1. Introduction

Distillation is among the most used separation processes in industry, due to its capacity to separate a wide range of liquid mixtures into pure components or groups of components. This unit operation has been widely studied over the years; thus, wide knowledge is available related to the design and operation of distillation columns. Unfortunately, distillation has low thermodynamic efficiency, which is

reflected in high energy requirements, utilities costs and environmental impact. Thus, over the years, proposals have been developed to reduce the energy requirements in distillation, including alternatives as thermally coupled systems, internally heat-integrated configurations, among others.

One of the most well-known intensified distillation schemes is the dividing wall column (DWC), which is a device where an internal metallic wall is used to distribute the vapor and liquid streams, allowing a better distribution of the components of the mixture. For ternary mixtures, the use of DWCs may lead to energy saving up to 40% in comparison to conventional distillation sequences (Czarnecki et al., 2024). In the case of quaternary mixtures, different dividing-wall configurations have been proposed (e.g. Sánchez-Ramírez et al., 2020), but not all the configurations adequately work for any composition. Recently, a configuration with two dividing walls has been reported, which includes three condensers, and a single reboiler (Flores-Flores et al., 2025). This configuration is synthesized starting from a conventional direct sequence. In this work, an alternative intensified configuration is proposed, taking as basis the indirect conventional sequence. A synthesis, design and optimization procedure is implemented, and the performance of the proposed configuration is compared with its direct counterpart, and with the conventional direct and indirect sequences.

2. Case study

An indirect dividing-wall distillation column (QDDWC-I, Figure 1.a) is proposed in this work. The performance of this configuration is compared with the intensified direct configuration reported by Flores-Flores et al. (2025), shown in Figure 1.b. Both systems are designed to separate a quaternary mixture composed of n-butane/n-pentane/n-hexane/n-heptane, with molar feed composition of 40/10/10/40, assuming a recovery of 99% for each component.

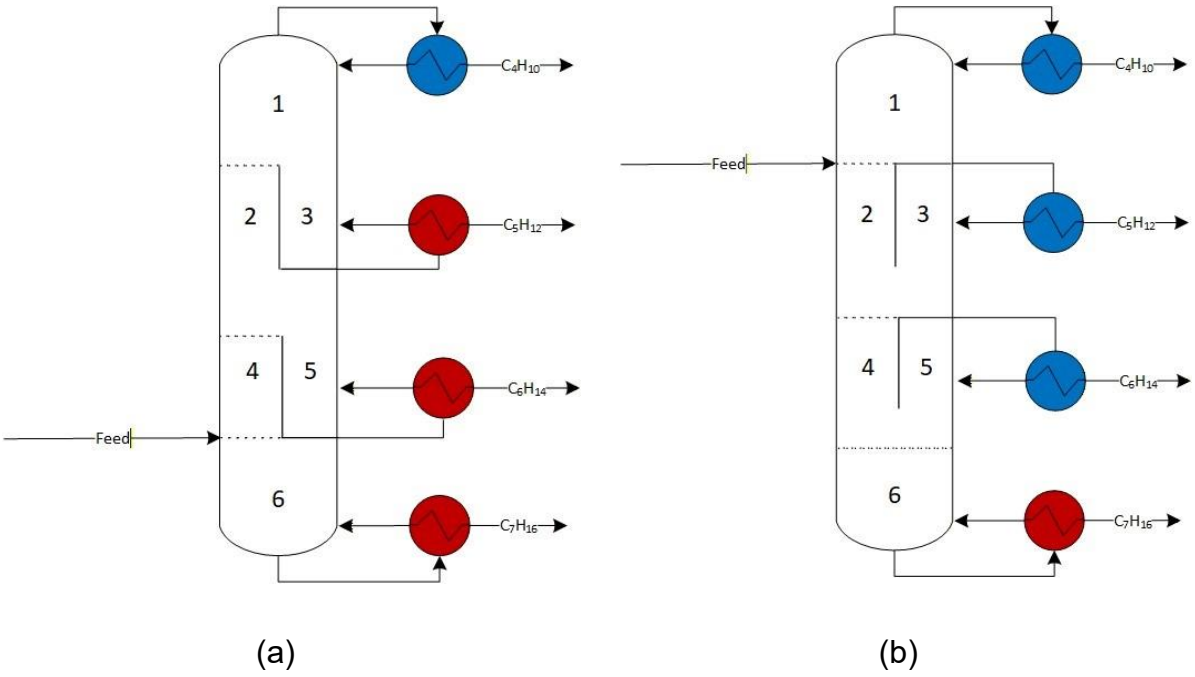

Figure 1: Intensified configurations (a) indirect quaternary double dividing wall column QDDWC-I, (b) direct quaternary double dividing wall column QDDWC-D.

3. Methodology

The synthesis of the QDDWC-I is based on the sections rearrangement of a conventional indirect sequence (CIS). Figure 2.a shows the sections associated with the CIS, and how they are rearranged to generate the intensified configuration (Figure 2.b). To compare the performance of the proposed configuration, the QDDWC-D is also analyzed. This configuration is obtained taking as basis a conventional direct sequence (CDS), as presented in Figures 3.a and 3.b.

Simulation of the configurations has been performed through the commercial software Aspen Plus. To represent phase equilibrium, the Chao-Seader model has been employed, since it properly describes hydrocarbon mixtures (Handogo, 2012).

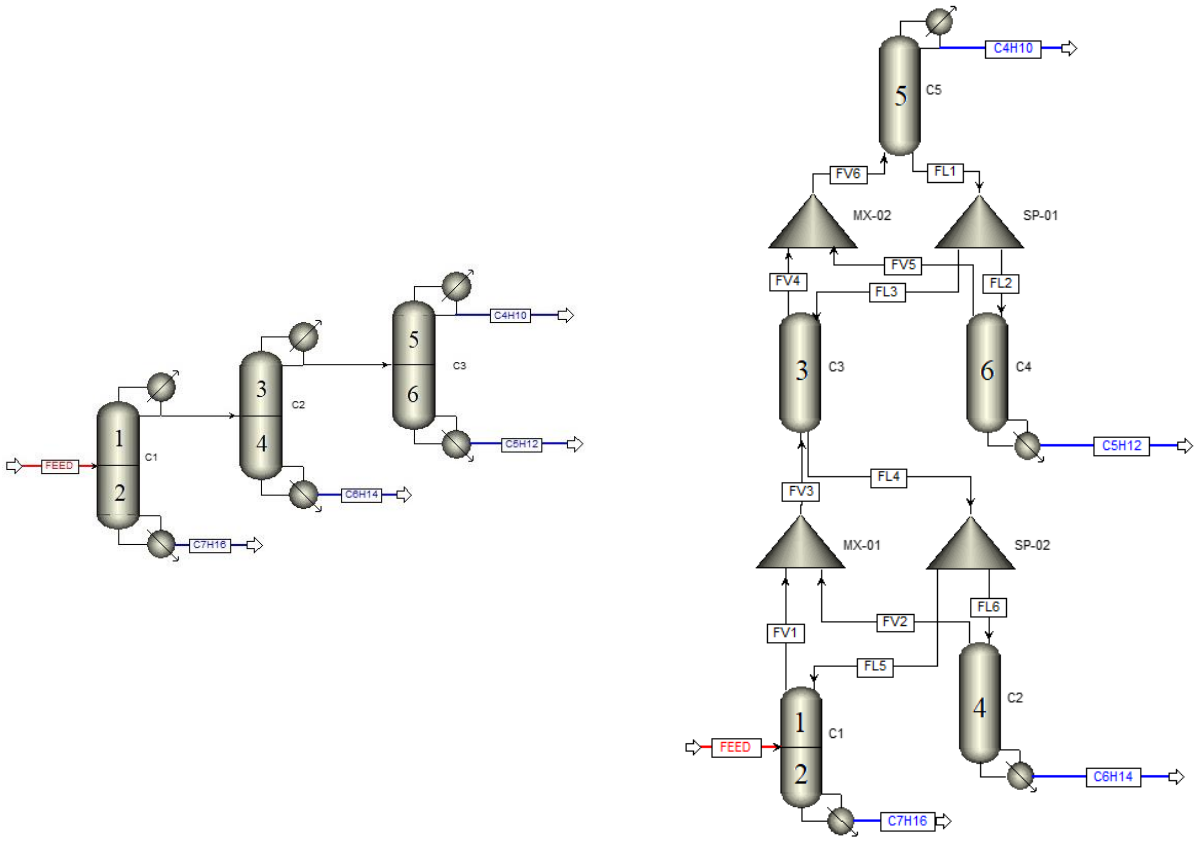

(a) (b)

Figure 2: Synthesis of the intensified configurations and column section correspondence (a) conventional indirect sequence, (b) indirect quaternary double dividing wall column QDDWC-I,

Simulations of the conventional sequences have been first performed using the short-cut DSTWU model, to determine the number of stages and the feed stage. Then, the RadFrac module is employed to perform the rigorous simulation of the conventional systems, using design specifications to reach the desired purities. These purities are estimated by mass balances once the recovery of 99% is set for all the components. Using the number of stages of the different sections of the conventional sequences, the intensified configurations are designed by sections rearrangement methodology, using the distribution shown in Figures 2.b and 3.b. These intensified systems are simulated using the module RadFrac in Aspen Plus, representing the dividing wall structures by interconnecting rectifiers and strippers through mixers and stream separators.

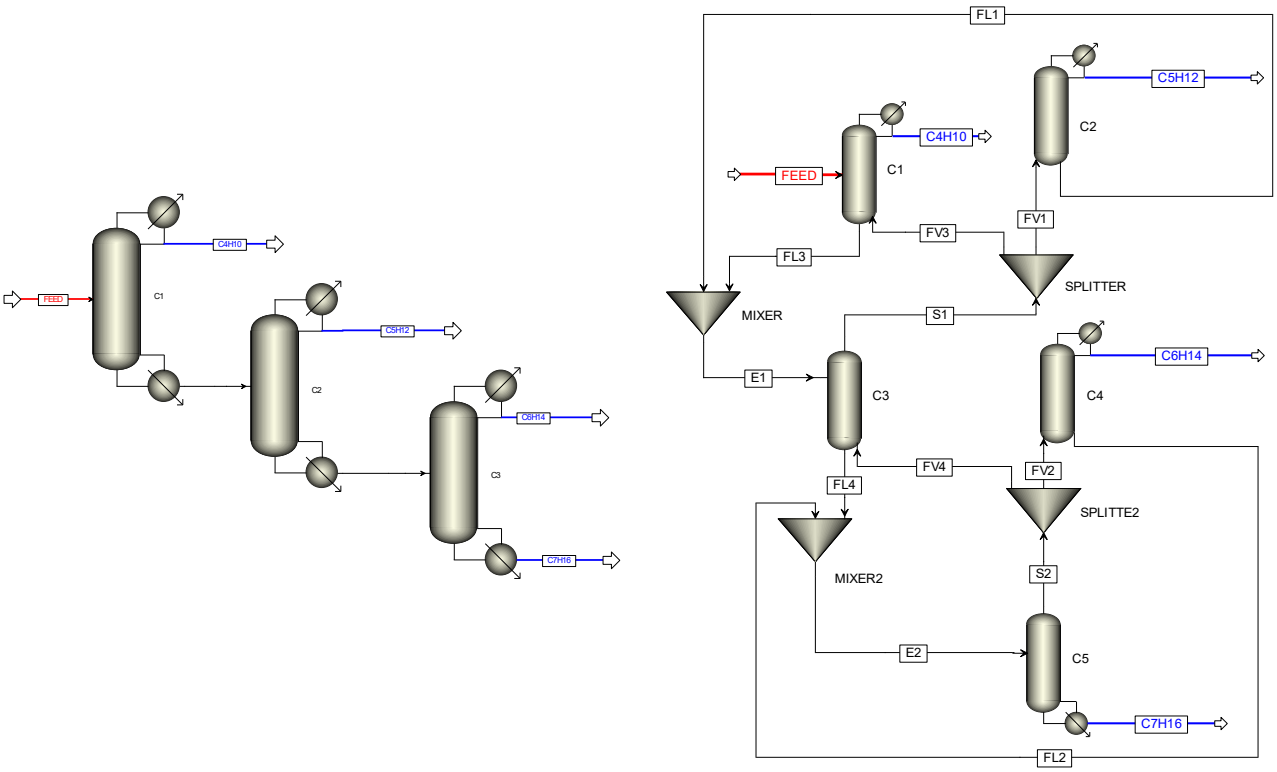

(a) (b)

Figure 3: Synthesis of the intensified configurations (a) conventional direct sequence (b) direct quaternary double dividing wall column QDDWC-D.

Using the preliminary designs previously described as initial guesses, the optimization of the intensified schemes is performed. The employed algorithm uses the NSGA-II metaheuristic. As initial step, a data set corresponding to manipulated variable values is generated through NSGA-II. The manipulated variable values are sent to Visual Basic, where the data vector is received and sent back to Aspen Plus. The process simulator solves mass and energy balances with rigorous methods. If the simulation finds a convergence error, a penalty value is assigned; otherwise, Aspen Plus returns the results to Visual Basic. Next, Visual Basic evaluates the process constraints and objective functions to share them with Matlab. Once the values of objective functions are received, Matlab continues with the genetic algorithm. Finally, if the iterations have been completed, the Pareto front is plotted. Figure 4 shows the algorithm implemented. The manipulated and response variables can be observed in Figure 4.

For NGSA-II, 50 generations with a population size of 300 are used, with crossover fraction of 0.8, elite count of 15, and mutation rate of 0.01.

4. Results and discussion

Figure 5 shows the Pareto front obtained from the optimization algorithm implemented for the optimized QDDWC-I. The red point identifies the best alternative, which is associated with the lowest reboiler duty, located in the intermediate region for the number of stages.

In Table 1, the values for manipulable variables of QDDWC-I, and optimized QDDWC-I are presented. It can be highlighted that the values of the design and operation variables show only small changes from the initial solution.

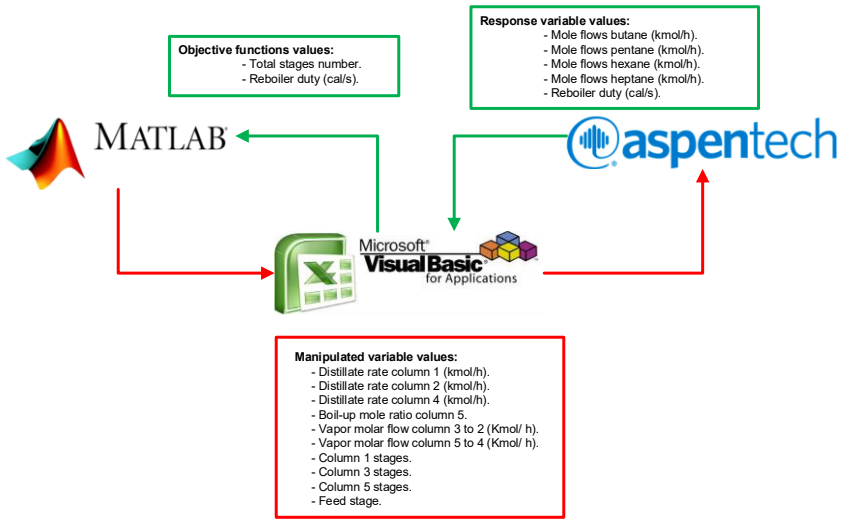

Figure 4: Optimization algorithm.

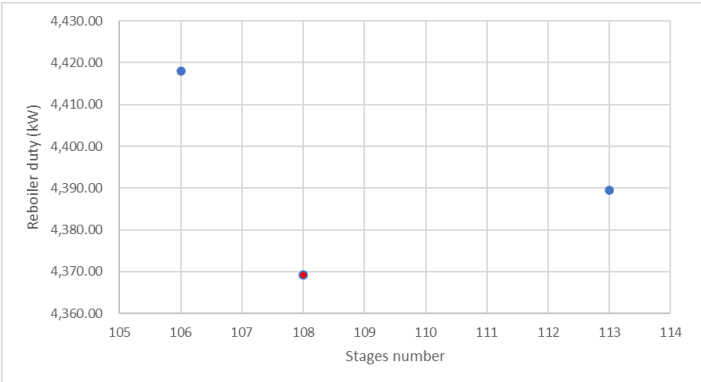

Figure 5: Pareto front of QDDWC-I

Table 1. Manipulated variables values for QDDWC-I.

	QDDWC-I	Optimized QDDWC-I
Molar reflux ratio	19.505	18.456
Bottom rate C4 (kmol/h)	10.344	10.249
Bottom rate C2 (kmol/h)	10.344	10.403
Bottom rate C1 (kmol/h)	39.992	39.837
Split fraction FL3	0.8029	0.7753
Split fraction FL5	0.5808	0.5677
Stages C5	18	19
Stages C3 and C4	58	53
Stages C1	40	36
Stages C2	6	6
Feed stage on C1	6	6

Table 2 presents a comparison between direct and indirect sequences. It is important to mention that the values of direct sequences have been taken from the research of Flores-Flores et al. (2025).

To explain the effect observed in Table 2, where intensified indirect sequences require more energy than intensified direct sequences, it is useful to analyze the configurations shown in Figure 1.

In the intensified direct column, light-to-intermediate components such as butane, pentane, and hexane are vaporized in the main reboiler located at the column

bottoms. As the vapor flows upward through the distillation column, the temperature gradually decreases toward the top. When components such as pentane and hexane reach the stages equipped with lateral condensers, they are withdrawn from the system as side products. Consequently, only the remaining components continue circulating and are sent back to be reboiler. This reduces the mass flow that must be re-heated, which in turn decreases the total heat duty required.

In contrast, in the intensified indirect scheme, the same components (butane, pentane, and hexane) are initially vaporized at the column bottoms; however, only butane is removed from the top as an overhead product. The heavier components are condensed in the single main condenser and returned to the column. When the liquid reaches Sections 3 and 5, pentane and hexane are withdrawn; nevertheless, the components that remain in the internal streams must be vaporized again in the reboilers of the side columns to enable their separation and withdrawal. As a result, a significant fraction of the mixture undergoes two vaporization steps: first in the bottom reboiler and later in the lateral reboilers of Sections 3 and 5. This double boiling requirement explains the higher energy consumption of intensified indirect sequences relative to intensified direct sequences.

Table 2. Comparison between direct and indirect sequences.

	Direct sequences			**Indirect sequences**		
	CDS-D	**QDDWC-D**	**Optimized QDDWC-D**	**CDS-I**	**QDDWC-I**	**Optimized QDDWC-I**
Condenser (kW)	-1,603.61	-1,694.8	-1,312.8	- 1,750.82	- 4,399.43	- 4,171.12
Reboiler (kW)	1,763.17	1,920.3	1,511.15	2,002.67	4,598.33	4,369.15
Stages	62	39	53	76	115	108

5. Conclusions

The optimized QDDWC-D represents the most suitable configuration for the separation of the studied hydrocarbons mixture with higher feed composition of the lightest and heaviest components. This configuration satisfies the recovery constraints while achieving the lowest reboiler duty. Furthermore, the results indicate that intensified indirect sequences are not an attractive alternative, since they require at least twice the number of stages and significantly higher reboiler duties than direct sequences, mainly due to the need to retain all reboiler units.

Acknowledgements

The authors acknowledge the support provided by Universidad de Guanajuato, Universidad Autónoma de Querétaro, University of Southern Denmark and Università di Cagliari.

References

Czarnecki, N.J., Giannetti, L., Owens, S.A., Barnicki, S., Eldridge, R.B., 2024, Energy and economic evaluation of wall placement for divided wall distillation columns. Ind. Eng. Chem. Res. 63(43), 18513-18524.

Flores-Flores, M., Gómez-Castro, F.I., Gutiérrez-Antonio, C., Romero-Izquierdo, A.G., Guzmán-Martínez, C.E., Hernández, S., Errico, M., 2025, Synthesis and optimization of dividing-wall distillation columns for the separation of a quaternary mixture. Sep. Purif. Technol. 362, Part 2, 131817.

Handogo, R., 2012, Optimization on the performance of crude distillation unit (CDU). Asia-Pac. J. Chem. Eng. 7, S1, S78-S87.

Sánchez-Ramírez, E., Ramírez-Márquez, C., Quiroz-Ramírez, J.J., Angelina-Martínez, A.Y., Vicente Cortazar, V., Segovia-Hernández, J.G., 2020, Design of dividing wall columns involving sustainable indexes for a class of quaternary mixtures. Chem. Eng. Process. 148, 107833.

Enhancing Separation Efficiency of Structured Packings using CFD-based Shape Optimization

Dennis Stucke[1], Sebastian Blauth[2], Mohamed Adel Ashour[1], Christian Leithäuser[2], Thomas Grützner[1]
[1]Institute of Chemical Engineering, Laboratory for Thermal Process Engineering, Ulm University, 89081 Ulm, Germany;
[2]Fraunhofer ITWM, Department Transport Processes, 67663 Kaiserslautern, Germany;

Abstract

Packing development is generally based on heuristic development processes. Even though, this works well it is limited to the imagination and experience of the engineer. To overcome this, methods of shape optimization are applied. Shape optimization algorithms modify a given structure iteratively to maximize a given objective function. Instead of varying geometric parameters predefined during the design process, free-form shape optimization uses a computational mesh and moves the mesh nodes to change the shape. To evaluate the influence of shape changes and update the objective function a single-phase computational fluid dynamics (CFD)-model is used as a simplified surrogate model. In this work a successful case study is presented which features the comparison of the initial 3D-printable version of the RomboPak 9M and its optimized version. For the validation, separation efficiency is determined using a laboratory-scale distillation column. The simulative and experimental results both show a 20% increase in separation efficiency highlighting the match of simulation and experiment.

Keywords
Additive Manufacturing, CFD, Distillation, Shape Optimization, Structured packing

1. Introduction

In distillation columns, random and structured packings as well as trays are commonly used as column internals. Among these, structured packings are prominent due to their comparably high separation efficiency, low pressure drop and wide operation range[1]. The design of apparatuses using these internals is based on the scale up of results gained in laboratory and pilot-plant scale experiments. Hence, in recent years the development of structured packings for laboratory-scale distillation columns has intensified. Thereby, the column diameter could be reduced from 50 mm to 20 mm. With this reduction in diameter, savings in operational costs, capital costs, safety requirements and the amount of chemicals needed for the experiments could be achieved. In addition to the reduction in diameter, the increase of separation efficiency is an important optimization goal as this allows to perform difficult separations within the limited height in the laboratory environment.

With the rise of 3D-printing, researchers started using this technology to manufacture new packing structures. One advantage of 3D-printing are fewer design limitations, which enables new designs for packing structures. Additive manufacturing is based on building parts layer-by-layer. The 3D-printers work with a large variety of materials ranging from stainless steel powder in selective laser melting processes, plastic

powder in selective laser sintering processes and UV-resins for stereolithography printing to thermoplastic filaments used in fused deposition modeling. Even though these different manufacturing methods are based on the same layer-by-layer manufacturing principle, the limitations regarding printable geometries differ. This offers even wider range of possible geometries. Selective laser sintering for example does not require support structures at overhanging parts whereas stereolithography printers typically offer a higher resolution and thus smoother surfaces and smaller printable details.

In the literature there are many publications displaying the use of additive manufacturing in packing development. However, the design process chosen by researches differs. Starting with an already existing packing structure and improving its performance is a common approach. Neukäufer et al. [2] followed that approach. They started with a 3D-printable version of the Sulzer Rombopak 9M and successively used CFD simulations and experimental investigations in different iteration cycles to learn about the packings weaknesses and tackle them. Olenberg et al. [3] start with an existing sheet metal packing. But instead of redesigning the packing itself, they add additional twisted inserts to improve the packing performance. This development was also supported by CFD simulations.[4]

In contrast to the previous groups, other researchers decided to introduce structures that are already in use at other disciplines, e.g. catalysis [5] and energy absorption [6], into the field of distillation. One example for such structures are triply periodic minimal surface (TPMS) structures. Pan et al. [7] present an overview about different variation of TPMS structures, their manufacturing and the optimization. In [8,9], these structures are investigated as gas-liquid contactors. Other innovative packing structures have been developed by Kawas et al. [10] and Sun et al. [11] who presented a branching wire packing and a packing with twisted hexagonal channels.

In general, the development process of these packings is based on heuristic development methods. This includes visual evaluation of CFD simulation results for both, gas-phase and two-phase flow regimes. The identification of critical regions e.g., dead zones, and the decision on how to adapt the geometry are purely based on the imagination and experience of the researcher. In order to apply a more analytical approach, methods from shape optimization are applied to this problem.[4]

2. Methods

2.1 Gas-phase CFD model

The CFD model used for this work is a single phase model presented by Neukäufer et al. [2] and Blauth et al. [12] which is briefly recalled here. It is a simplified surrogate model which only describes the gas phase. The simulation domain is divided into several regions which are shown in Figure 1. To model the gas phase, the Navier-Stokes equations are used for an incompressible steady-state case which is given by

$$\begin{aligned} -\mu\Delta u + \rho(u\cdot\nabla)u + \nabla p &= 0 \\ \nabla\cdot u &= 0 \end{aligned} \tag{2.1}$$

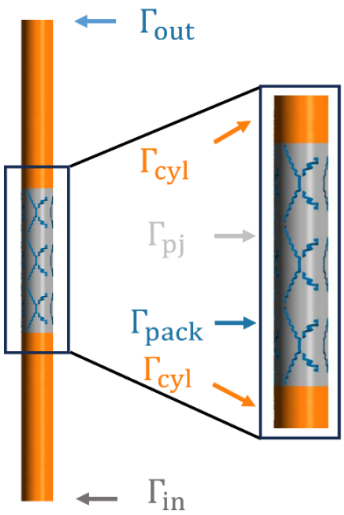

Figure 1: Depiction of the simulation domain with Γ_{out} as outlet, Γ_{cyl} as cylinder jacket, Γ_{pj}as packing jacket, Γ_{pack} as packing surface, Γ_{in} as inlet. [12]

The applied boundary conditions are:

$$\begin{aligned} &\text{Inlet:} && u = u_{in} \\ &\text{Wall:} && u = 0 \\ &\text{Outlet:} && \mu\, \partial_n u - pn = 0 \end{aligned} \tag{2.2}$$

In the equations above u represents the velocity, p the pressure, μ the dynamic viscosity, ρ the density, n the outer normal vector and $\partial_n u$ the normal derivative of u. The mass transfer is modeled using a convection-diffusion equation

$$-\nabla \cdot (D \nabla c) + u \cdot \nabla c = 0 \tag{2.3}$$

The boundary conditions are given as:

$$\begin{aligned} &\text{Inlet:} && c = c_{in} \\ &\text{Packing \& packing jacket:} && c = c_{\mathrm{liq}} \\ &\text{Outlet \& cylinder jacket:} && D\, \partial_n c = 0 \end{aligned} \tag{2.4}$$

Thereby, *c* resembles a fictious concentration and *D* the diffusion coefficient. As stated, the concentration is a fictious quantity that has no unit and is only used to calculated the mass transfer in this simplified model. The physical properties of the gas phase are defined as those of nitrogen at 25°C and 1 bar with $\rho = 1.138\,\mathrm{kg\,m^{-3}}$ and $\mu = 1.728 \cdot 10^{-5}\,\mathrm{Pa\,s}$ [13]. The gas-side diffusion coefficient is set to $D = 3.72 \cdot 10^{-6}\mathrm{m^2 s^{-1}}$ which corresponds to the equimolar system cyclohexane/*n*-heptane at boiling point of 90°C [2]. The inlet velocity is set to $u_{in} = 0.933\mathrm{m\,s^{-1}}$, the inlet concentration to $c_{in} = 100$ and the liquid phase concentration to $c_{liq} = 1$.
The liquid phase is assumed to be an infinitely small liquid layer on the whole packing and wall surface. In this liquid phase, the concentration value is constant which means that there is no mass transfer limitation on the liquid side.[12]

To calculate the mass transfer coefficient β, the following equation is used

$$\beta = \frac{\dot{V}}{A_{geo}} log\left(\frac{c_{liq} - c_{in}}{c_{liq} - c_{out}}\right) \tag{2.5}$$

Thereby, $\dot{V}$ resembles the volumetric flow rate and A_{geo} the geometric surface area of the packing.

Note that the presented model is used for the shape optimization. To validate the results numerically, the model is simulated using SST $k - \omega$ turbulence model.

2.2 Shape optimization

Free-form shape optimization describes the automatic shape change. The shape is not changed based on geometric parameters. Instead, a computational mesh is generated in advance. The nodes of this mesh are moved during the optimization to change the shape. This enables the shape to change independent of the design process and without inherent limitations from the parametrization.

The shape optimization algorithm changes the packing structure to maximize an objective function in work the following objective function is applied:

$$\max_{\Omega,c} J(\Omega, c) = \beta(c) = \frac{\dot{V}}{A_{geo}} log\left(\frac{c_{liq} - c_{in}}{c_{liq} - c_{out}}\right) \tag{2.6}$$

To maintain the applicability of the packing structure in a distillation column the shape change is limited to specific surfaces. Thus, the inlet, outlet and cylinder jacket are fixed. The packing jacket must maintain the cylindrical shape. Hence, the shape change normal to the jacket is prohibited.[12] For the calculation of the shape optimization, the software cashocs [14,15] is used.

3. Results and discussion

For the initial investigation, the 3D-printable version of RomboPak 9M presented by Neukäufer et al. [2] is optimized using the previously mentioned shape optimization algorithm. The resulting shape change can be seen in Figure 2. In this figure, two planar cut views of the structure are presented. It can be seen that the geometric differences between the initial and optimized packing are small. However, there are changes visible. At the top of the packing the structures are tilted inwards. Additionally, the crosspieces are shifted downwards. The XY-plane cut shows cross pieces with increased thickness which manipulate the passing gas flow. The effect on the velocity and concentration field can be seen in Figure 3. The velocity profile shows in the XZ-plane an increase in gas velocity close to the packing surface. This suggests a higher convective mass transfer of the optimized packing. In the XY-plane the initial geometry shows that the gas flow predominantly passes in between two crosspieces. After shape optimization the crosspieces got thicker which makes the gas flow hit the following cross pieces instead of passing on one side. This spreads the gas flow and increases the mass transfer. The mass transfer calculated based on the fictious concentration shows an improvement of approx. 20% after the optimization. To validate the simulation trend, the initial and optimized packings are 3D-printed and the separation efficiency is measured using the laboratory distillation column described in [16] using a cyclohexane/*n*-heptane system. The results are shown in Figure 4. It can be seen that the separation efficiency of the optimized packing is significantly better compared to the initial packing. Additionally, the separation efficiency is more constant over the whole operation range. Evaluating the improvement in separation efficiency between initial and optimized packing at the simulated F-factor of 1 $Pa^{0.5}$ shows a good agreement with the simulation trend. For the pressure drop the difference is higher for the experimental results. This can be explained by the presence of a liquid phase in the experiments which reduces the available volume for the gas and thus increases the pressure drop.[12]

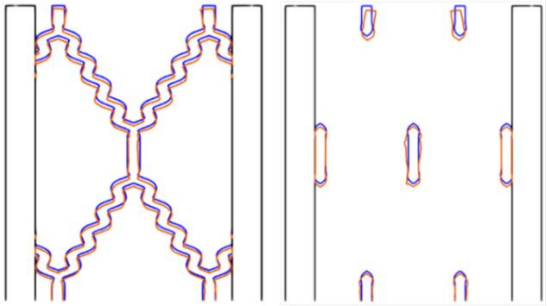

Figure 2: Comparison of the optimized (orange) and initial (blue) shape of the RP9M-3D packing in YZ- plane (left) and XY-plane (right). [12]

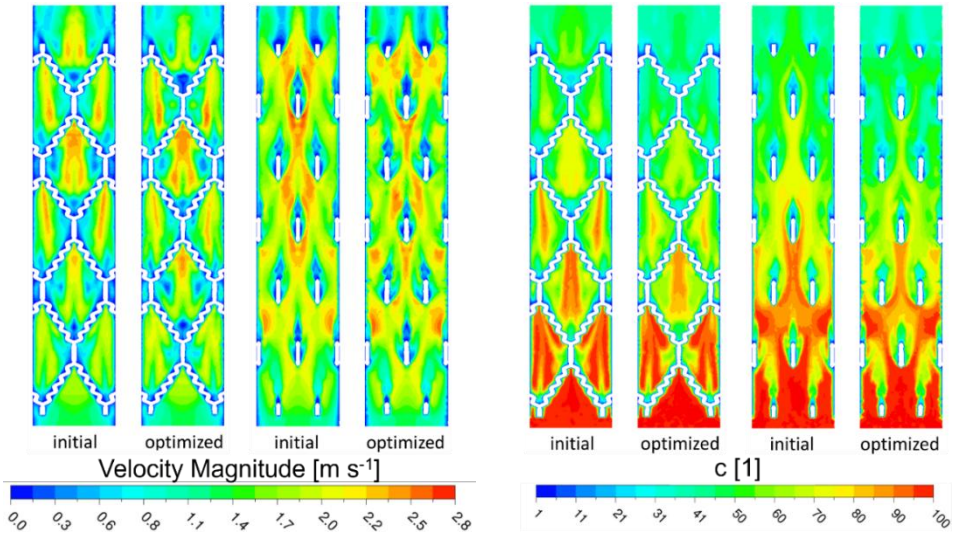

Figure 3: Velocity and concentration field of initial and optimized RP9M-3D packing in XZ- and XY-plane cut view. [12]

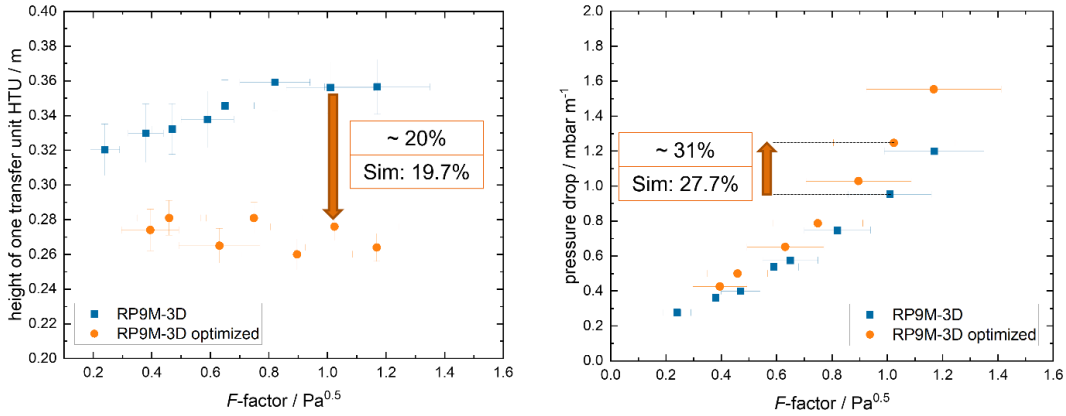

Figure 4: Experimental results of initial and optimized RP9M-3D structure. [12]

4. Conclusions

As shown by the investigations in this article, shape optimization is successfully applied to packing optimization for distillation columns. In this work the separation efficiency of a structured packing was improved by 20%. As the shape optimization does not feature multicriteria optimization as of yet, the pressure drop is increased significantly. This is no problem for this packing as it initial pressure drop is low, but it might cause issues with different packings. Both changes in the separation efficiency and pressure drop are predicted by the CFD-simulations and validated in an experiment. Even though the

changes to the packing are minor, the effect on the performance is clearly visible in simulation and experiment.

5. Outlook

The current shape optimization setup is limited to single criteria optimization. In the future it is planned to expand the setup to be able to optimize regarding multiple criteria and thus include the pressure drop as second objective. This enables the optimization of packings with higher separation efficiency which typically have a higher pressure drop. Without this addition the increase in pressure drop would limit the operating range of such packings significantly. In our group, we have several different packing structures that differ in their (base) design, separation efficiency (Figure 5) and pressure drop. The optimization of these packings will provide valuable insights into the kind of changes that benefit the packing performance.

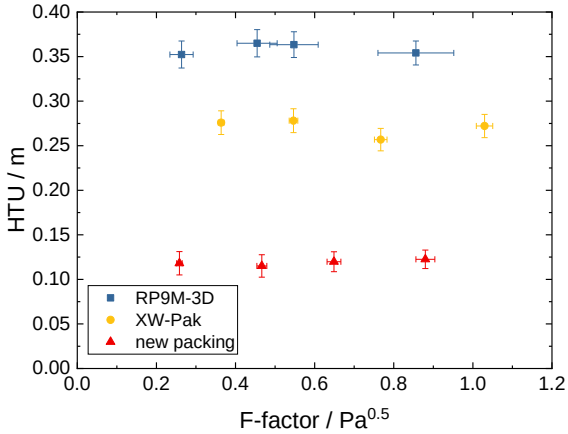

Figure 5: Height of one transfer unit (HTU) against the F-factor for different packings.

References

[1] R. Goedecke, *Fluidverfahrenstechnik: Grundlagen, Methodik, Technik, Praxis*, 1st ed ed., John Wiley & Sons, Incorporated, Somerset **2006**.

[2] J. Neukäufer, M. A. Ashour, N. Sarajlic, H. Klein, S. Rehfeldt, H. Hallmann, S. Meinicke, J. Paschold, C. Knösche, T. Grützner, *AIChE J*. **2022**. DOI: 10.1002/aic.17902.

[3] A. Olenberg, W. Reschetnik, G. Kullmer, E. Y. Kenig, *Chemical Engineering Research and Design*. **2018**, *132*, 1–8. DOI: 10.1016/j.cherd.2017.12.036.

[4] D. Stucke, S. Blauth, C. Leithäuser, T. Grützner, *Chemie Ingenieur Technik*. **2026**, cite.70063. DOI: 10.1002/cite.70063.

[5] M. Iwaniszyn, *Energies*. **2022**, *15* (20), 7703. DOI: 10.3390/en15207703.

[6] A. R. Bernard, M. S. A. ElSayed, *Materials*. **2024**, *17* (10), 2181. DOI: 10.3390/ma17102181.

[7] C. Pan, Y. Han, J. Lu, *Applied Sciences*. **2020**, *10* (18), 6374. DOI: 10.3390/app10186374.

[8] G. Homem Alves César Ribeiro, D. Rouzineau, M. Meyer, N. Di Miceli Raimondi, *Chemical Engineering Science*. **2025**, *304*, 121062. DOI: 10.1016/j.ces.2024.121062.

[9] G. Homem Alves César Ribeiro, D. Rouzineau, M. Meyer, *Chemical Engineering Science*. **2025**, *301*, 120690. DOI: 10.1016/j.ces.2024.120690.

[10] B. Kawas, B. Mizzi, B. Dejean, D. Rouzineau, M. Meyer, *Chemical Engineering Research and Design*. **2021**, *169*, 189–203. DOI: 10.1016/j.cherd.2021.03.019.

[11] B. Sun, T. Bhatelia, R. P. Utikar, G. M. Evans, V. K. Pareek, *Chemical Engineering and Processing - Process Intensification*. **2021**, *167*, 108533. DOI: 10.1016/j.cep.2021.108533.

[12] S. Blauth, D. Stucke, M. A. Ashour, J. Schnebele, T. Grützner, C. Leithäuser, *Chemical Engineering Science*. **2025**, *302*, 120803. DOI: 10.1016/j.ces.2024.120803.

[13] P. Stephan, S. Kabelac, M. Kind, D. Mewes, K. Schaber, T. Wetzel, VDI-Gesellschaft Verfahrenstechnik und Chemieingenieurwesen, Eds. , *VDI-Wärmeatlas: Mit 1046 Abbildungen und 483 Tabellen*, 12. Auflage ed., Springer Vieweg, Berlin [Heidelberg] **2019**.

[14] S. Blauth, *SoftwareX*. **2021**, *13*, 100646. DOI: 10.1016/j.softx.2020.100646.

[15] S. Blauth, *SoftwareX*. **2023**, *24*, 101577. DOI: 10.1016/j.softx.2023.101577.

[16] J. Neukäufer, N. Sarajlic, H. Klein, S. Rehfeldt, H. Hallmann, C. Knösche, T. Grützner, *AIChE J*. **2021**, *67* (11). DOI: 10.1002/aic.17381.

Improvement of asphalt quality by molecular distillation of crude oil wastes from refineries

Mateus Brentan Gonçalves[1], Victor Hugo dos Santos Ramos[1], Cesar Benedito Batistella[1], Leonardo Vasconcelos Fregolente[1], Rubens Maciel Filho[1], Maria Regina Wolf Maciel[1]

[1]University of Campinas (UNICAMP), Campinas, Brazil;

Abstract

Even with great advancements in green energy research and application in the energy industry, crude oil is still one of the main sources of energy in the world. One of the ways to reduce the environmental impact of crude oil refineries is to guarantee that all of its waste is well destined in a way that improves the quality of life in the world. Separating lighter and heavier cuts of these wastes can improve the quality in both ends, and also create data for extending the true boiling point curves that heavily impact the value of those crude oils. This work focuses on a way to separate heavier cuts of these wastes before implementing them in the asphalt production by using a falling-film molecular distillation pilot plant with wiped-film distribution on the top of the column. The experiments were conducted with three different crude oil wastes from refineries, in the operating temperatures of 230°C, 283°C, and 340°C, with pressure of 5 µbar. The initial wastes and heavier cuts had their softening point and penetration index analyzed in order to compare with the Brazilian and European standards for bitumen applications. A significant improvement of quality of the possible asphalt applications, according to the standards, was noticed after the molecular distillation process was applied. Two of the three crude oil wastes chosen had a class of application increased at the lowest operating temperature of 230°C and all three showed class improvement at 283°C or higher. Considering that all three wastes had their initial application class improved, it is fair to acknowledge the process of molecular distillation as a way to help better destine the refineries wastes by enhancing the quality of its lighter and heavier cuts.

Keywords

Molecular distillation; falling-film molecular distillation; crude oil waste; asphalt; bitumen.

1. Introduction

Crude oil remains, to this day, one of the main raw materials for energy generation industries, especially for fuel production. Despite increased research into green energy alternatives, crude oil-derived fuels will most likely continue to represent a significant portion of the energy industry, particularly for energy-intensive transportation sectors such as aviation and marine fuels. Furthermore, using the residues analyzed in this study as a reference (Table 1), 20% to 30% (by mass) of the crude oil destined for refineries ends up as waste at the end of the process. For this reason, it is essential to ensure the lowest possible environmental impact and the best way to utilize crude oil in its entirety, thus increasing its value (IEA, 2025).

Crude Oil	Volume [%]	Mass [%]
Opal	80.3	77.4
Onyx	73.8	70.7
Obsidian	74.8	70.9

Table 1: Quantity refined through distillation, provided by a refinery company.

Process evaluation has been extensively studied and is well known for most products originating from refineries. However, the destination of crude oil refinery wastes can still be improved. Currently, this waste is integrated into the production of waterproofing materials, asphalt and bitumen, as well as heavy fuel for thermoelectric power plants. To evaluate the improvement of crude oil waste disposal, specifically waste from ASTM 2892 processes followed by ASTM 5236 processes, this work used a falling-film molecular distillation pilot plant (Figure 1) developed by our research group to further separate lighter and heavier fractions of three different wastes (with fantasy the names Opal, Onyx, and Obsidian) from local refineries (GONÇALVES, 2020).

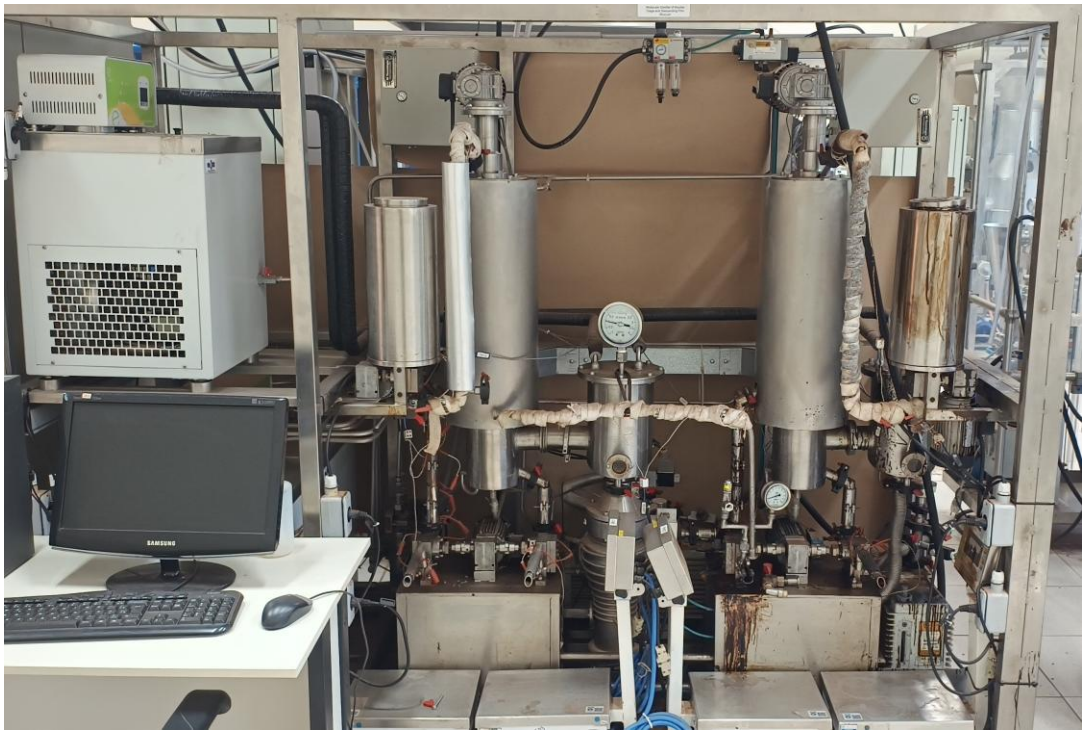

Figure 1: Falling-film molecular distillation pilot plant located at the Petroleum Valuation Laboratory (UNICAMP).

This specific plant uses short-path, wiped-film distribution on the top of the column, and a downward falling-film flow combined with high vacuum to better suit the distillation of more viscous materials such as crude oil waste. It also has an identical non-pressurized second stage (which can be connected in series with the other) to remove volatile compounds from the oils, which is not necessary for previously refined crude oil wastes. The operating temperatures of the experiments were 230, 283, and 340°C, which correspond to equivalent atmospheric temperatures of approximately 560, 630, and 700°C, respectively, at 5 µbar (0.00375 mmHg) of pressure.

The molecular distillation process, which applies a large pressure reduction instead of high temperature differentials, is a suitable strategy for handling heavy, heat-sensitive compounds, since the drastic pressure reduction lowers the boiling points of those compounds to a point where an acceptable temperature range is sufficient to distill them without compromising their chemical nature. The liquid film width varies from 0.05 to 2 mm, depending on the viscosity of the starting material, resulting in a short residence time, further reducing the influence of temperature degradation. The distance between the evaporating surface and the condensing surface is designed to be of the same order as the mean free path to practically eliminate the influence of the vapor phase over the liquid phase during distillation, resulting in an evaporation rate driven only by the number of molecules that reach the condensing surface (BATISTELLA et al., 2005).

Performing these experiments in a pilot plant allowed us to obtain a light and a heavy cut capable of having their properties analyzed, for each of the runs. It is important to note that the lighter cuts were analyzed in a simulated distillation gas chromatography equipment and, along side the molecular distillation data, used as database for the determination of true boiling point curves extensions through the DESTMOL equation, also developed by the research group, which can be applied for experiments with this equipment at constant operating pressure to determine the equivalent atmospheric temperature (EAT) for crude oil at higher temperatures than covered by the ASTM 5236 (LOPES et al., 2017).

The heavier cuts had their penetration index and softening point duly characterized to determine a possible increase in the quality of asphalt raw material produced when compared to the initial waste. Those properties were evaluated using the Brazilian and European standards (Table 2) for bitumen/asphalt as guidelines, which have different classes for different application zones, where the lower classification number refers to greater resistance to impact and temperature.

European Class (Penetration Index)	Softening Point [°C]	Application	Brazilian Class (Penetration Index)	Softening Point [°C]	Application
20/30	≥ 55	Intense traffic	30/45	≥ 52	Intense traffic and high temperature regions
35/50	≥ 50	Industry pavement	50/70	≥ 46	Standard application
50/70	≥ 46	Standard application	85/100	≥ 43	Low traffic or low temperature regions
70/100	≥ 43	Low traffic areas	150/200	≥ 37	Rarely used
100/150	≥ 40	Special use or additive			
160/200	≥ 35	Extreme cold regions			

Table 2: Brazilian standard (CAP 2022 – ANP 897/2022) and European standard (EN 12591:2011) for asphalt/bitumen.

2. Results and discussion

All analyses were performed in a laboratory using equipment that complies with ASTM standards for determining properties, or in the pilot plant, and in triplicate to minimize statistical error in the results.

2.1 Initial waste characterization

Initially, the basic properties of the three crude oil wastes were analyzed to allow for a fair comparison after obtaining the heavier cuts through molecular distillation. This

analysis also provided the API gravity value using the equation from the American Petroleum Institute Manual of Petroleum Measurement Standards below.

$$°API = (141.5/\rho) - 131.5$$

The properties (Table 3) for characterization were: density and dynamic viscosity, using the Anton Paar Stabinger SVM 3000 viscometer, which follows ASTM D7042 standard; penetration index, using the Anton Paar PNR 12 penetrometer which follows ASTM D5 standard; and softening point using the Anton Paar RKA 5 model which follows ASTM D36 standard. The density was then converted to 15.6°C (60°F) in order to calculate the °API of each waste.

Properties	Opal	Onyx	Obsidian
Density 80°C [g/cm^3]	0.9384	0.9360	0.9416
Density 15.6°C [g/cm^3]	0.9777	0.9752	0.9810
API density [°API]	13.2	13.6	12.7
Dynamic Viscosity [cP]	4029	3854	4162
Penetration Index [dmm]	69	78	64
Softening Point [°C]	47.3	44.8	54.9
Brazilian Class	50/70	85/100	50/70
European Class	50/70	70/100	50/70

Table 3: Base properties of the initial wastes (before molecular distillation).

Considering the initial values of penetration index and softening point of the wastes, two of them could be used for standard asphalt application with class 50/70 (Opal, which barely fit the standard class, and Obsidian), while one of them could only be used for low traffic or lower temperature areas (Onyx), both for Brazilian and European standards.

2.2 Molecular distillation heavy cuts characterization and comparison

After determining the initial properties, these wastes were processed in the molecular distillation pilot plant so the heavier cuts obtained could also be characterized. All of them were distilled at 230, 283, and 340°C, with constant temperature, pressure, and flow rate (constant percentage of thin-film distribution motor rotation) during the experiments. After distillation, the heavier cuts obtained from Opal (Table 4), Onyx (Table 5), and Obsidian (Table 6) had their penetration index and softening points measured and compared to the initial values.

Sample	Property	Initial Waste	230°C	283°C	340°C
Opal	Penetration Index [dmm]	69	63	49	14
	Softening Point [°C]	47.3	59.3	72.7	87.8
	Brazilian Class	50/70	50/70	*	30/45[1]
	European Class	50/70	50/70	35/50	20/30[1]

Table 4: Penetration index, softening point, and class progression for Opal sample.

The upper indicator [1] indicates that the properties reached higher softening point values and lower penetration index values than standardized.
For the Opal sample, the initial applied temperature of 230°C was sufficient to cause a significant increase in the softening point, improving its thermal resistance, but there was not enough change in the penetration index to cause an upgrade in the applicability class for either standard. After 283°C, the reduction in penetration index was more apparent and, combined with the even higher softening point, there was the first increase in the European class of this sample to 35/50, while its properties where between the 50/70 and 30/45 classifications in the Brazilian standards (signed with * in Table 3). Finally, at a temperature of 340°C, both the penetration index and softening points reached values above (for softening point) and below (for penetration index) of those required to classify the sample as the highest class for both standards: 30/45 and 20/30 for the Brazilian and European standards, respectively.

Sample	Property	Initial Waste	230°C	283°C	340°C
Onyx	Penetration Index [dmm]	78	67	46	19
	Softening Point [°C]	44.8	53.8	68.0	83.0
	Brazilian Class	85/100	50/70	30/45	30/45[1]
	European Class	70/100	50/70	35/50	20/30

Table 5: Penetration index, softening point, and class progression for Onyx sample.

Unlike the Opal sample, improvements in class for the Onyx sample were observed even at the first applied temperature. Both the softening point and penetration index showed sufficient changes to allow the sample to be classified as suitable for standard application (50/70) for both standards. This pattern was repeated at the temperature of 283°C, at which the sample showed sufficient improvements to be possibly applied in intense traffic, according to the Brazilian standards, or in industrial pavements, according to the European standards. After being distilled at 340°C, this sample showed sufficient improvements in its softening point and penetration index to be possibly applied in high temperature zones and intense traffic, according to both standards consulted for this study.

Sample	Property	Initial Waste	230°C	283°C	340°C
Obsidian	Penetration Index [dmm]	64	44	22	5
	Softening Point [°C]	54.9	67.6	72.2	85.8
	Brazilian Class	50/70	30/45	30/45[1]	30/45[1]
	European Class	50/70	35/50	20/30	20/30[1]

Table 6: Penetration index, softening point, and class progression for Obsidian sample.

Similar to the previous sample, the Obsidian waste showed sufficient improvements in its softening point and penetration index for a better classification after distillation at 230°C, going from 50/70 to 30/45 or 35/50 depending on the chosen standard. Although the Obsidian sample had an initial penetration index similar to that of the Opal sample, it had higher density and the highest softening point of all three. This means that the removal of the lighter fractions, even during the first temperature application, would affect its properties more than for the Opal sample. The

application of 283°C was sufficient, in this case, to reach the best applicable class for both standards, with properties better than those required for the Brazilian standard. Therefore, after the application of 340°C, both the softening point and the penetration index showed values over the range for both standards, indicated by the [1] in Table 6.

3. Conclusions

The application of the molecular distillation process to improve the quality of asphalt components showed promising results, since it was possible to upgrade the quality classifications of all three crude oil wastes analyzed in this study. This indicates that molecular distillation should be considered as a viable route to increase the overall value of crude oil, and to improve the quality of products that use refinery waste as raw material. In a broader context, the implementation of this process at an industrial scale could contribute to more efficient utilization of heavy fractions and to the development of higher-performance asphalt materials.

The lowest temperature chosen (230°C) showed significant improvement in the softening point, but less impact on the penetration index values. Although this temperature was sufficient to raise the classification of two (Onyx and Obsidian) of the three samples, the penetration index values were close to the lower limit of the classification range: 67 for Onyx (close to 70 of the 50/70 class) and 44 for Obsidian (close to 45 and 50 for the Brazilian and European standards, respectively).

The highest temperature chosen (340°C) impacted the softening point and penetration index of the samples more than expected, resulting in values outside the standards ranges in most cases. An asphalt binder with a softening point significantly higher than the typical service temperature can increase the risks of thermal cracking, since it will be more rigid overall if the ambient temperature drops, or if the traffic is less intense. Similarly, an asphalt binder with a very low penetration index may indicate higher brittleness, especially at low temperatures.

Thus, a temperature of 283°C was best suited to significantly improve the properties and raise the classes of the samples, without exceeding the limits of the Brazilian and European standards.

Acknowledgements

The authors acknowledge the support of the National Council for Scientific and Technological Development (CNPq) [Grant numbers: 141169/2021-4 and 308672/2025-9].

References

BATISTELLA, C. B.; SBAITE, P.; WOLF MACIEL, M.R.; MACIEL FILHO, R.; WINTER, A.; GOMES, A.; MEDINA, L.; KUNERT, R.; Heavy Petroleum Fractions Characterization: A New Approach Through Molecular Distillation. 2nd Mercosul Congress on Chemical Engineering & 4th Mercosul Congress on Process Systems Engineering (ENPROMER), 2005.

CAP 2022 - ANP 897/2022 – Brazilian standard for specifications of asphalt and bituminous binders.

European Standard – EN 12591:2011. Bitumen and bituminous binders – Specifications for paving grade bitumen.

GONÇALVES, M. B.; Commissioning and evaluation of methodologies for determining TBP curves for blended fuels. University of Campinas, Masters Dissertation, 2020.

IEA – International Energy Agency. World Energy Outlook, 2025.

LOPES, M. S.; WATANABE, E. R. L. R.; TOVAR, L. P.; LOPES, M. S.; DARCIE, L. R.; LOPES, E. S.; MACIEL-FILHO, R.; WOLF-MACIEL, M. R.; MEDINA, L. C.; Development of correlation for extension of the true boiling point (TBP) and molar mass, Petroleum Science and Technology, 35:14, 1530-1536, 2017, DOI: 10.1080/10916466.2017.1370475.

Process Design and intensification strategies for efficient isopropyl myristate production

Diego I. Cruz López[1], Juan G. Segovia Hernandez[2], Carlos R. Caceres Barrera[2], Eduardo Sánchez Ramírez[2], Alvaro Orjuela[1]
[1]Universidad Nacional de Colombia, Bogotá D.C., Colombia;
[2]Universidad de Guanajuato, Guanajuato, México

Abstract

Isopropyl myristate (IPM) is a fatty acid ester employed in cosmetics, pharmaceuticals and fragrances due to its excellent emollient, lubricating and fixative properties. IPM is industrially produced via esterification of myristic acid (MA) and isopropanol (IPA) with water (W), mainly using homogeneous catalysts. However, this process faces multiple challenges associated to nonideality of reactive mixture and chemical equilibrium limitations. Besides, unconverted MA requires high-cost vacuum distillation for recovery. To overcome these limitations, several intensified process alternatives have been proposed, including reactive distillation (RD), entrainer-assisted RD and auto-extractive RD. In this context, this work developed a systematic assessment and optimization of industrially employed process configurations for IPM production, including the reactive system and downstream purification. The reactive system included series of coupled CSTR-decanter (RDS), coupled reactor-condenser (RCS), and reactive distillation (RD). The different configurations were compared with respect to total annual costs (TAC) under optimal conditions. The optimization was done by Differential evolution with Tabu List (DE-TL) algorithm. As expected, RD overcomes classical technologies and it can be further intensified to overcome remaining limitations. Obtained results can be used as benchmark for evaluation of new intensification approaches.

Keywords
Isopropyl Myristate, Esterification, Process intensification, Reactive distillation, Optimization, Differential evolution with Tabu list

1. Introduction

Isopropyl myristate (IPM) is a main fatty acid ester in the oleochemical market, and it is industrially produced via esterification of myristic acid (MA) with isopropanol (IPA). The process is mainly promoted by homogeneous acid catalysts, generating water (W) as byproducts. IPM production exemplifies the challenges commonly encountered in equilibrium-limited esterification of fatty acids. In general, conventional industrial production relies on batch or continuous stirred-tank reactors followed by multistep separation trains, which are often energy-intensive and economically suboptimal (Jeromin et al., 1981). The IPA+MA+IPM+W mixture exhibits complex phase behavior, including partial miscibility and azeotropy, which

restricts the effectiveness of simple separation strategies and necessitates the use of vacuum distillation to avoid thermal degradation of MA and IPM.

From a process intensification perspective, IPM synthesis constitutes a suitable benchmark system due to: (i) strong coupling between reaction and separation, (ii) sensitivity to thermodynamic and thermolability constraints, and (iii) industrial demand for cost-effective and sustainable production routes. Previous studies have explored RD (Abdulwahab Giwa et al., 2013), entrainer-assisted RD schemes (Pushkala et al., 2023) and auto-extractive RD configurations (Muñoz et al., 2023). However, a quantitative comparison between classical and intensified technologies under a unified optimization framework remains limited. This contribution addresses this gap by performing a comparative techno-economic assessment of three process alternatives. Particular emphasis is placed on novelty and pertinence through the integrated evaluation of energy demand, conversion, capital intensity, and sustainability indicators. The study further discusses thermodynamic feasibility, operational constraints, and remaining methodological gaps, thereby providing guidance for future research and industrial implementation.

2. Methodology

2.1 Process Modeling and Thermodynamics

The vapor–liquid (VLE) and liquid–liquid (LLE) equilibria of the IPA+MA+IPM+W system is described using the NRTL equation using the parameters obtained in a comprehensive experimental study of the reactive mixture (Muñoz et al., 2025). In that experimental study it also found that degradation of MA occurs above 200 °C and its fusion temperature was 56 °C. These features were included as operating restrictions for the assessed process configurations to avoid thermal degradation and crystallization within units.

2.2 Reaction Kinetics

The esterification reaction is modeled using a pseudo-homogeneous kinetic expression based on p-toluene sulfonic acid catalysis. Although phase separation may occur, this kinetic model does not explicitly account for liquid–liquid effects; nonetheless, it has been validated experimentally (Jong et al., 2009). This assumption allows direct comparison with previous studies and isolates the impact of process configuration on overall performance (Jong et al., 2009).

$$-r_{IPM} = k_1 C_{cat}[IPA][MA] - k_{-1} C_{cat}[IPM][W]$$

2.3 Process Alternatives

The alternatives analyzed are in continuous production of IPM of 10,000 t/y and a purity of 99%. Three cases are analyzed:

- Case 1 (RDS): Multiple reactor-cooler-decanter sequence with a distillation train for IPA recovery and IPM purification.
- Case 2 (RCS): Multiple reactor–condenser sequences with distributed IPA feed to enhance conversion via in situ water removal.

- Case 3 (RD): Reactive distillation column integrating reaction and separation in a single intensified unit.

2.4 Optimization Framework

To identify the best operating configuration among the reported schemes, they were assessed under optimal operating conditions. Considering the highly nonlinear behavior of the models, optimization of reactor networks and RD schemes would be highly complex. Therefore, the optimization was conducted as a MINLP using a DE-TL method (Rangaiah et al 2007). The design variables include reactor variables such (i.e. residence time, temperature, pressure, feed distribution and IPA:MA molar ratio) and distillation column variables (i.e. feed stage, number of stages and reactive stages, reflux ratio, pressure). The objective function was the total annualized cost (TAC) calculated as:

$$TAC = CAPEX + OPEX$$

Here, CAPEX included equipment costs estimated with Guthrie´s type equations and the OPEX included heating and cooling duty, vacuum duty and raw materials cost.

3. Results and discussion

3.1 Case 1: Reactor decanter sequence (RDS)

This process involves a reactor-decanter series where the aqueous phase of each decanter is removed, and the organic phase is used as feed for the subsequent reactor. All aqueous streams are combined and separated to remove produced water and to recover IPA. The final organic phase is sent to a distillation column to remove volatiles (i.e. IPA and W), and the bottom product is further processed in a vacuum distillation column to refine IPM and to remove and recycle unconverted MA (Cermak, 2007). After optimization, the lowest TAC was obtained with a single reactor-decanter combination (Figure 1(a)). In this configuration, the extra energy for two-reactor sequence is around 30%. Thus, when two or more reactors are used more energy is required because after each reactor the stream is cooled to enhance LL separation and then it is heated at the temperature of the subsequent reactor. Capital cost increase due to the need for additional equipment. Despite MA conversion increases from 70% to 80% using a second reactor in the series, the higher CAPEX and OPEX overshadow the improved performance.

As observed, optimized reactor operates at 427 K with a feed IPA:MA ratio of 1.3:1. A 37 stages vacuum distillation column operating at 0.8 kPa enables IPM purification and MA-IPM removal while precenting thermal degradation (T < 473 K). The aqueous stream from the decanter (5 mol.%) must be mixed with the top stream of column 1 to recover the unconverted IPA. Despite the process has low capital cost investment, it is highly energy intensive mainly due to energy requirements in the vacuum separation unit. This occurs because MA and IPM have similar volatility, and they require large number of stages for the separation. However, low conversion remains the main issue, necessitating additional separation of unreacted MA. The IPM concentration in the final stream was 97.3 mol.%, corresponding to 99 wt.%.

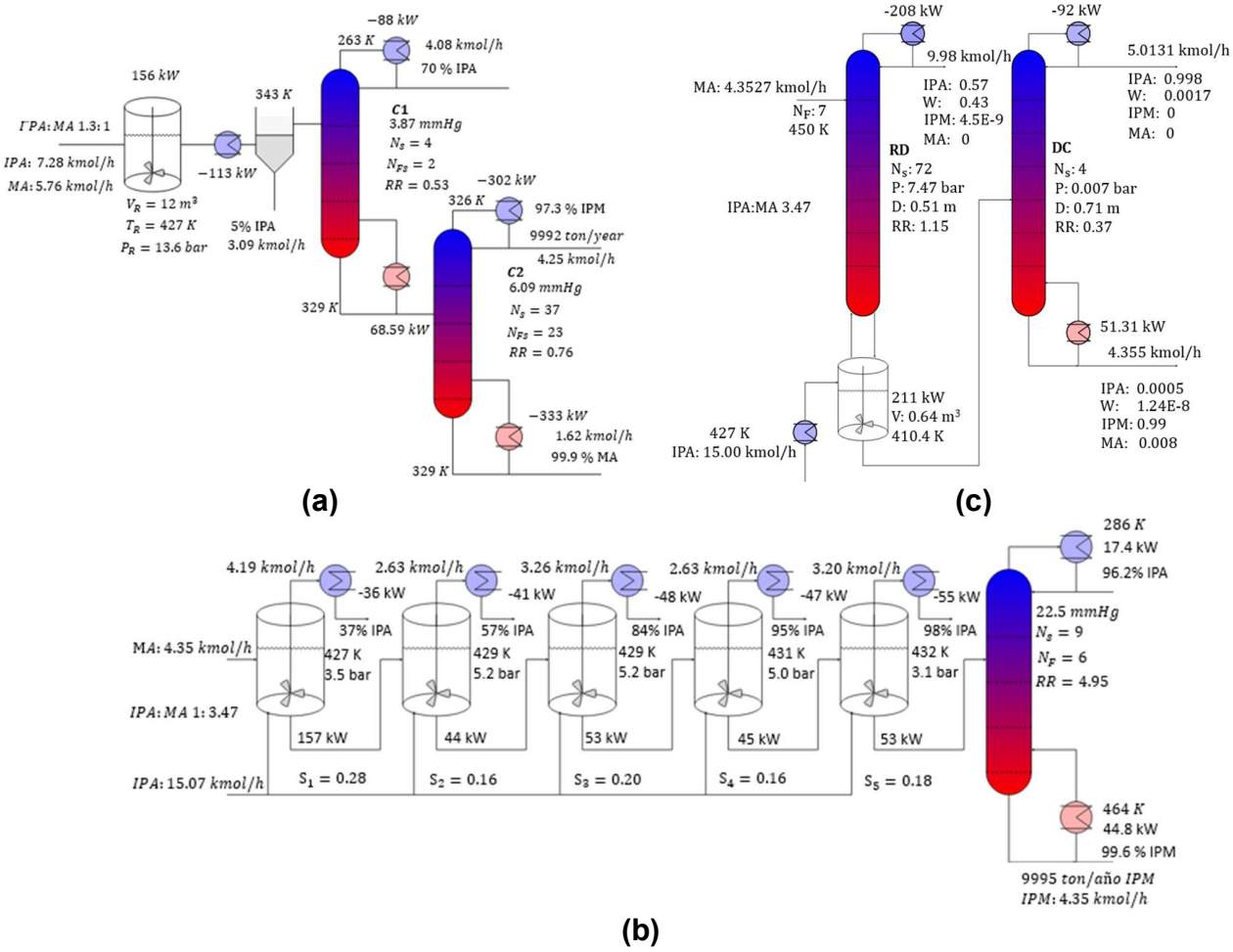

Figure 1. Optimum process flow diagram for (a) RDS, (b) RCS and (c) RD

3.2 Case 2: Reactor condenser sequence (RCS)

This configuration involved reactor-condenser series, with a single MA fed stream at first reactor and several IPA streams distributed among individual reactors. The optimum RCS scheme included 5 units in the sequence (Figure 1(b)), and as expected, the first reactor required a higher IPA inlet to maximize conversion. Remaining IPA was feed more evenly distributed among subsequent reactors. This sequence had lower energy consumption comparing with case 1, mainly because a higher conversion was achieved and it avoided the MA separation from IPM. The removal of volatiles from IPM was achieved in a 9 stage column operated at 3 kPa with a reflux ratio of 4.95. The low pressured ensured that the reboiler operated below the thermal degradation limit for IPM. Despite energy savings, the TAC increased due to additional capital investment on the equipment. The equipment with the highest heating duty is Reactor 1 because it has a large amount of IPA and the removal of produced water and stripped IPA required larger energy consumption. This configuration is more energy efficient than the RDS, because it does not require heating and cooling between each unit of the sequence.

As observed in Figure 1(b), temperature is between 427 K and 431 K, and the pressure had a maximum in the reactor 3 at 5.3 bar and then it decreased to 3 bar. The reduction of pressure indicates that the reactor is enriched in low boiling point IPM. Nonetheless, these pressure levels are lower than those required in case 1 to enable vaporization of water, maximizing MA conversion and to reduce IPA vaporization.

3.3 Case 3: Reactive distillation

The optimized RD sketched in Figure 1 (c) corresponded to a 72-stage column, with MA and catalysts fed in stage 7, and it enabled rectification of IPA+W and separation from IPM and minor impurities of MA. The optimum IPA:MA molar ratio was 3.47, operating with a reflux ratio of 1.15. The RD hold-up was 0.028 m3 and it was estimated using a reported equation (Kong et al., 2025). The pressure in an RD column is important because it determines phase equilibria and reaction kinetics. In a previous study the RD was operated at 1.1 bar when using an entrainer to enhance the process (Pushkala et al., 2024). In this case, the optimum pressure was 7.5 bar, enabling the increase of bubble temperatures to promote kinetics under reduced energy consumption.

Table 1 summarizes the results of the optimized configurations. As observed, IPA:MA molar ratio for the first case was 1.3:1 and this explains the low conversion and the large energy intensity in the recovery of unconverted MA. The RCS scheme enables higher conversion, but it requires larger energy intensity and more units, so it has larger TAC. In comparison, the RD scheme enables complete conversion with a lower molar ratio than the RCS avoiding the separation of MA. Also, it has the lowest heat duty and only a slightly higher cooling duty. Nonetheless, RD production costs are lower among the assessed configurations, and this can be used as benchmark for comparison with novel process configurations.

Table 1. Optimized results of assessed schemes for IPM production (10,000 t/yr)

Index	Reactor-decanter series	Reactor-condenser series	RD
TAC(USD/year)	13,396,572	13,315,897	12,601,332
Production cost (USD/t)	1,339.7	1,331.6	1,174.0
Heating duty(kW)	557.7	397.189	262
Cooling duty(kW)	502.7	246.3	301
Production heating (kJ/kg)	1,796.4	1278	818
Production Cooling (kJ/kg)	1,619.4	793.6	940
IPA:MA	1.3	3.6	3.47
Conversion	0.68	0.99	0.99

4. Conclusions

This work presents a systematic comparison of classical and intensified configurations for isopropyl myristate production, combining detailed thermodynamic modeling, kinetic analysis, and global economic optimization. The results demonstrate that process configuration has a dominant influence on conversion efficiency, energy demand, and overall economic performance. The optimum RDS

consisted of a single reactor-decanter because liquid-liquid separation is not efficient to separate produced water. Removed aqueous phase carries IPA out of the system and the process requires heating-cooling operation to enhance phase splitting. This results in 30% higher energy consumption, higher capital cost with a minor conversion increment. In comparison, the RCS has lower energy consumption and lower TAC because almost complete MA conversion, avoiding its recovery. Besides, there was no need for sequential heating and cooling to promote separation as in the RDS case. The RCS optimum scheme consisted of 5 reactor-condenser units in series that enabled high conversions with a overall IPA:MA molar ratio of 3.6 differently distributed among individual units. Finally, RD configuration exhibited the lower TAC because the combination of reaction and separation, enabling complete conversion, lower energy consumption and lower capital cost. Nonetheless, this column has a large number of reaction stages due to the limited hold up. This might indicate that future studies might explore the use of side reactors with traditional RD columns or with dividing wall column configurations.

References

Abdulwahab, G., & Saidat, O. G. (2013). Isopropyl myristate production process optimization using response surface methodology and MATLAB. International Journal of Engineering Research & Technology, 2(1), 853–862.

Cermak, S. C., Evangelista, R. L., & Kenar, J. A. (2012). Distillation of natural fatty acids. In Distillation: Advances from modeling to applications (p. 109). InTech.

De Jong, M., Feijt, R., Zondervan, E., Nijhuis, T. A., & de Haan, A. B. (2009). General reaction kinetics of the esterification of myristic acid with isopropanol and n-propanol using p-toluene sulphonic acid as catalyst. Applied Catalysis A: General, 365(2), 141–147. https://doi.org/10.1016/j.apcata.2009.06.009

Jeromin, L., Bremus, N., & Peukert, E. (1981). Kontinuierliche Veresterung in Reaktionskolonnen. Fette, Seifen, Anstrichmittel, 83(S1), 493–504.

Kong, Z. Y., Sánchez-Ramírez, E., Yang, A., Li, Y., Segovia-Hernández, J. G., Wong, B. T., & Sunarso, J. (2025). A new alternative route for achieving energy saving in intensified reactive-extractive distillation system with a surprise discovery. Chemical Engineering Journal, 503, 158498. https://doi.org/10.1016/j.cej.2024.158498

Muñoz, H. D., Hoffmann, C., Illner, M., Orjuela, Á., & Repke, J. U. (2023). Auto-extractive reactive distillation for the production of fatty esters. In Computer Aided Chemical Engineering (Vol. 52, pp. 393–398). Elsevier. https://doi.org/10.1016/B978-0-323-91728-3.50067-0

Muñoz, H. D., Peña, N., Gutiérrez, M. F., Repke, J., & Orjuela, Á. (2025). Phase equilibria of the system isopropanol + water + isopropyl myristate + myristic acid. Fluid Phase Equilibria, 580, 114473. https://doi.org/10.1016/j.fluid.2025.114473

Pushkala, S. P., & Panda, R. C. (2023). Design and analysis of reactive distillation for the production of isopropyl myristate. Cleaner Chemical Engineering, 5, 100090. https://doi.org/10.1016/j.clce.2022.100090

Srinivas, M., & Rangaiah, G. P. (2007a). Differential evolution with tabu list for solving nonlinear and mixed-integer nonlinear programming problems. Industrial & Engineering Chemistry Research, 46(22), 7126–7135. https://doi.org/10.1021/ie0612459

Comparative hydrodynamic evaluation of viscous mixture for conventional & industrial packing in Rotating packed beds.

Viraj Santosh Pawar[1], Thibaut Triquet[1], David Rouzineau[1], Michel Meyer[1]

[1]Chemical Engineering Laboratory, University of Toulouse, CNRS, INPT, UPS, Toulouse, France.

RPBs are particularly attractive for separation processes like distillation and CO_2 capture, where centrifugal forces extend operating limits beyond those of conventional columns, especially for viscous systems. In carbon capture, liquid viscosity increases after CO_2 absorption, restricting flow and transfer performance in gravity-driven columns. The high-gravity environment of RPBs offers a promising alternative, though the influence of viscosity on their hydrodynamics remains insufficiently understood. Woven mesh and foam packings, commonly used in RPBs, provide good mass transfer but cause high pressure drops, limiting operation due to flooding and entrainment. To overcome these issues, Montz Engineering developed a dedicated RPB packing. This study investigates its hydrodynamic performance by measuring pressure drop over a range of rotational speeds, gas, and viscosities, and compares it with wire mesh packing. Overall, the Montz packing achieved a reduction in pressure drop as compared to woven mesh approximately 3–7 times, while also minimizing entrainment and preventing flooding.

1. Introduction

Rotating Packed Beds (RPBs) have emerged as an important Process Intensification technology due to their ability to enhance heat and mass transfer under high centrifugal forces (100–1500 g) [1]. This intensification enables compact equipment design suitable for distillation, nanoparticle synthesis, liquid–liquid extraction, or CO_2 capture. An RPB consists of a torus-shaped packing mounted on a rotating rotor, where the packing strongly influences hydrodynamics (pressure drop, entrainment, flooding, and flow patterns), which affect mass transfer performance [2]. Conventional packings such as woven wire mesh and metal foam provide high interfacial area and good mass transfer due to increased liquid holdup and residence time [3], but their dense structure results in high pressure drops and limited operating ranges. To overcome these limitations, Montz Engineering developed the first commercial RPB packing specifically for industrial CO_2 capture [4]. This packing has demonstrated stable operation and high capture efficiencies (~90%) over wide operating ranges in projects such as ROTA-CAP, ARTEMIS, and CycloneCC, and has proven scalable in industrial trials capturing up to 285 tons of CO_2 per day [5]. While RPBs are well suited for handling viscous amine-based solvents used in post-combustion capture due to their high centrifugal forces, detailed hydrodynamic characterization of the Montz packing remains limited. Therefore, this study presents a comparative investigation of Montz packing and conventional woven mesh under viscous and non-viscous conditions, focusing on pressure drop, operating range,

flooding behavior, and effective interfacial area to better relate packing design to hydrodynamic and mass transfer performance.

1.1 Experimental set up & methods

1.1.1 RPB set-up

The specifications of the RPB packings are provided in Table 1, while detailed technical information about the RPB used in this work is available in a previous study [6]. The RPB Model 500 and the woven mesh packing were supplied by Proceller, Poland, whereas the Montz packing was obtained from Montz Column Engineering, Germany.

Table 1. Packing specifications.

Variable	**Units**	**Woven mesh**	**Montz Packing**
Specific surface area of packing (Ap)	m^2/m^3	2400	1200
Packing material	-	Stainless steel	Stainless steel
Inner radius of the packing, r_{in}	m	0.16	0.16
Outer radius of the packing, r_{out}	m	0.46	0.46
Axial height, H	m	0.04	0.04
Packing porosity, e	m^3m^{-3}	0.84	0.90

1.1.2 Montz packing

The packing described in U.S. Patent No. 10,710,100B2 [4] is composed of multiple circular ring-shaped segments (3) positioned between two flat circular disks (2), as illustrated in Fig. 3-A. Collectively, these segments form a disk-like configuration in which the liquid enters through the central opening (4), moves radially outward, and exits at the outer ring (5). Each segment consists of several thin, wavy layers (7) stacked axially, with 11 layers shown in Fig. 3-B. The layers exhibit a zigzag or corrugated geometry (Fig. 3-C) and are arranged so that the waves of successive layers intersect, forming inclined flow paths (6) that promote enhanced mixing. The layers (Fig. 3-D) are manufactured from woven metal fibre with a thickness of 0.5 mm.

1.1.3 Viscous mixture preparation

Glycerine–water mixtures were prepared to obtain viscous solutions with viscosities of 22, 45, and 75 cP. The glycerine volume fraction was varied between 0.67 and 0.81 to achieve these viscosities. The required compositions were calculated using the well-known model proposed by Cheng et al. [7], which is applicable over a wide temperature range (0–100 °C) at atmospheric pressure and for glycerol mass fractions from 0 to 100%.

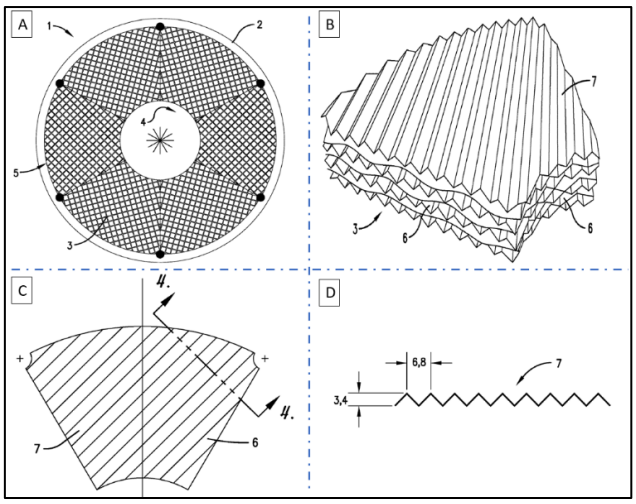

Fig 3: (A) assembled packing, (B) Iso-view of one sector, (C) Top view of a sector, (D) Single corrugated sheet front view.[4]

1.1.2 Hydrodynamic experiments

In each test, four parameters were studied (rotational speed, liquid and gas flow rate and viscosity of the liquid) three variables were kept constant while the fourth was systematically changed during the experiment. Once the operating conditions were established, measurements were taken for 10 minutes under steady-state conditions, and the averaging procedure is described in [6]. Experiments started at the maximum rotational speed and were then decreased in steps, while maintaining constant gas and liquid flow rates. Flooding and entrainment were assessed by installing a hydroclone at the gas outlet to separate the entrained liquid and have an accurate measurement of the liquid at the outlet.

2. Results

2.1 non-viscous pressure drop

Figure2 shows the evolution of pressure drop with the rotational speed for different conditions of packing and gas flowrate. It can be seen that the woven mesh packing generally exhibits a higher pressure drop compared to the Montz packing. From 100 to 800 rpm all curves for the woven mesh is above the montz packing with a minimal difference of 0.15 kPa between the curves. With higher rotational speed the trend is similar for most of the curve except the lowest gas flowrate with the woven mesh and the highest gas flowrate for the montz packing which show similar results. For woven mesh, the pressure drop rises sharply with increasing gas flow and shows some reduction at higher rotational speeds. This behavior is attributed to its dense structure (ap = 2400 m²/m³, ε = 84%), which restricts gas–liquid flow and increases resistance, consistent with findings by Neumann et al. [34]. In contrast, Montz packing demonstrates a more uniform trend, with pressure drop increasing steadily as gas flow rises, yet remaining significantly lower than that of woven mesh. Its zigzag gauze design allows larger passages for gas and liquid flow, reducing flow resistance and pressure drop while maintaining smoother operation across varying conditions.

For the woven mesh, no flooding occurred at 100 Nm³/h, though minor liquid entrainement was seen between 1000 and 1400 rpm. At 150 Nm³/h, flooding appeared at 100 rpm, disappeared at 200 rpm, and reappeared slightly between 1000–1200 rpm. This behaviour is expected, as at low rotational speeds the liquid velocity is insufficient, resulting in accumulation at the centre of the packing. Increasing the rotational speed leads to the fragmentation of the liquid film into progressively smaller droplets, thereby increasing the interfacial area and enhancing mass transfer. However, at higher rotational speeds, the drag force exerted by the gas on the droplets becomes dominant, preventing them from fully traversing the packing; as a result, the droplets are entrained by the gas phase. Similar trends were observed at 200 Nm³/h, with heavy entrainment at 1400 rpm, while at 250 Nm³/h, flooding occurred at 100–200 rpm, disappeared at 300 rpm, and returned between 1000–1400 rpm. In contrast, Montz packing showed no flooding under any tested condition. Light entrainment was noted at 100–150 Nm³/h between 1200–1400 rpm, and light to medium entrainment at 200–250 Nm³/h in the 1000–1400 rpm range. Overall, woven mesh has a narrower operating window, whereas Montz packing demonstrates greater stability and operational efficiency which can operate from 100-1200 without any rejection of liquid.

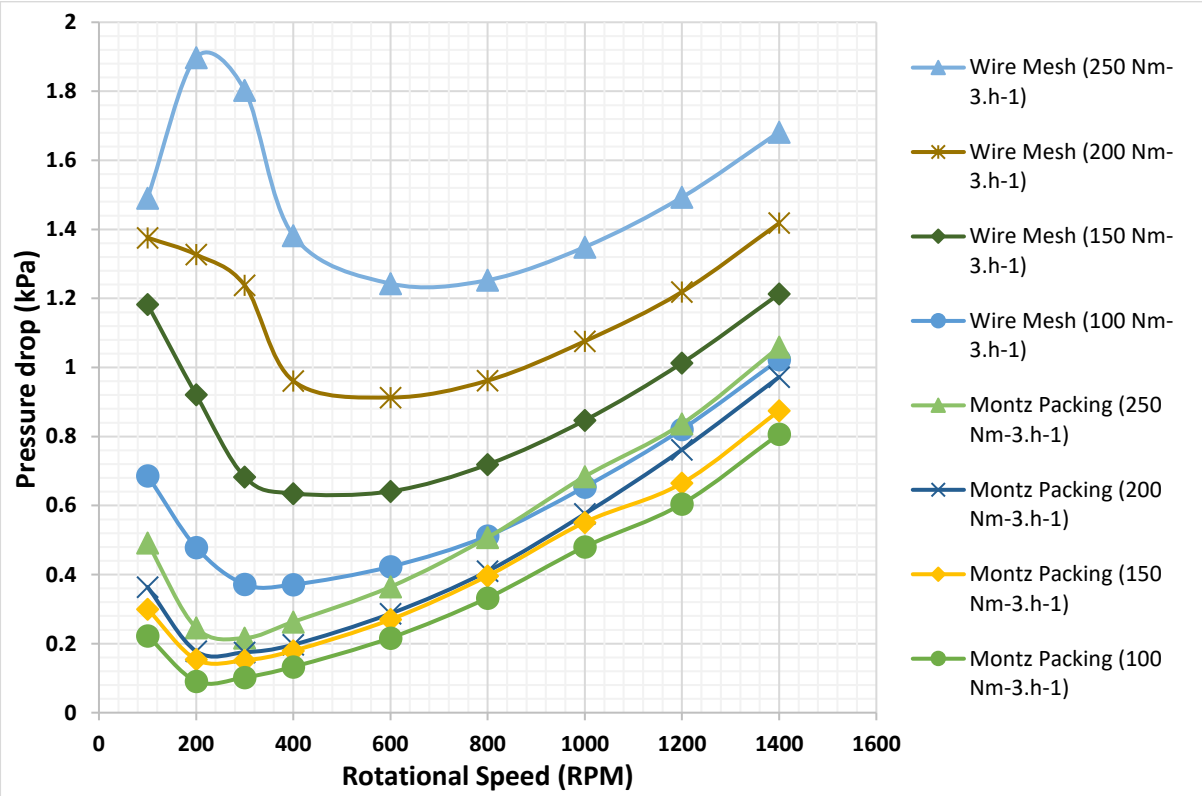

Figure 2: Effect of rotational speed on wet pressure drop Liquid Flowrate (L)-0.6 m^3/h

2.2 viscous pressure drop.

Figures 3 show how viscosity affects pressure drop at different rotational speeds for both packings. The main operating regions remain the same for all viscosities tested. At speeds above 400 rpm, only small differences are seen, indicating that viscosity has little effect on pressure drop in this range. However, at lower speeds, the effect of viscosity becomes more noticeable. For woven mesh at a viscosity of 1 mPa·s,

the pressure drop starts at about 1.5 kPa, increases to 1.51 and then at 400 rpm, decreases again to around 1.2 kPa. As viscosity increases, the pressure drop becomes higher, reaching about 2.3 kPa at 18 mPa·s and nearly 2.7 kPa at 45 mPa·s and 3.5 at 75 mPa·s. Higher viscosity leads to thicker liquid films, which slow down liquid flow through the packing and cause more resistance, resulting in higher pressure drop. At higher rotational speeds, stronger shear forces reduce the effect of viscosity, lowering the pressure drop. This viscosity effect is much smaller in Montz packing due to its special structural design which helps in shearing the viscous fluids more easily. For the woven mesh packing, flooding was observed at rotational speeds of 100, 200, and 1400 rpm. At the highest viscosity of 75 mPa·s, flooding also occurred at 300 rpm, further narrowing the RPB operating window. Apart from these conditions, no major entrainment was detected, likely because the higher viscosity reduces liquid splashing beyond the inner packing region. In contrast, the Montz packing exhibited flooding only at 100 rpm, confirming its better stability and superior performance when handling viscous liquids. Overall, it can be observed that montz packing has larger operating capacity where flooding as flooding occurs only at 100 rpm as compared to wire mesh where foolding occurs at both lower 3 rpm and highest rpm (1400).

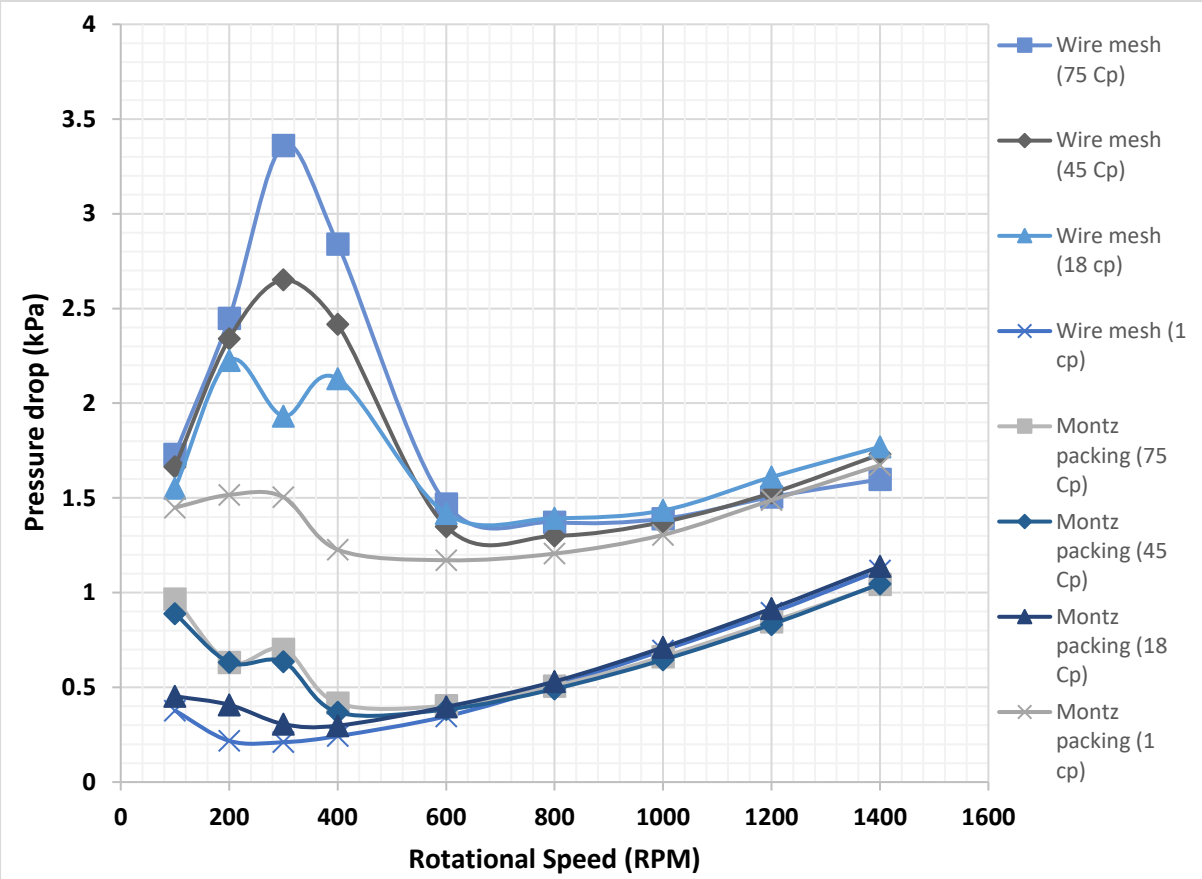

Figure 3: Effect of viscosity on pressure drop at different rotational speed-G-250 Nm^3/h.

3. Conclusion

Among the two packings, Montz packing consistently showed the lowest pressure drop across all operating conditions for both viscous and non-viscous fluids, while woven mesh exhibited higher values. Compared to woven mesh, the pressure drop was reduced by nearly threefold (~30%) at low fluid loading and up to sevenfold

(~40%) at high fluid loading. Tests with viscous liquids (18, 45, and 75 mPa·s) confirmed that increasing viscosity raises flow resistance and pressure drop; however, this effect was much less pronounced for the Montz packing. Its structural design enhances liquid shearing and reduces resistance to flow.

Flooding and entrainment result further showed that woven mesh is more prone to instability, especially at higher gas and liquid flow rates, resulting in a narrower operating window. In contrast, Montz packing experienced fewer flooding events and maintained stable performance over a wider range of flow conditions and rotational speeds, demonstrating superior hydrodynamic capability.

Acknowledgment

Authors would like to acknowledge IMOSYCCA grants (Grant Number: 22-PESP-0008) under the PEPR 2030 project for the financial support.

References

[1] D.P. Rao, The Story of "HIGEE," Indian Chemical Engineer 57 (2015) 282–299. https://doi.org/10.1080/00194506.2015.1026946.

[2] K. Guo, Z. Zhang, H. Luo, J. Dang, Z. Qian, An Innovative Approach of the Effective Mass Transfer Area in the Rotating Packed Bed, Ind. Eng. Chem. Res. 53 (2014) 4052–4058. https://doi.org/10.1021/ie4029285.

[3] K. Gładyszewski, K. Groβ, A. Bieberle, M. Schubert, M. Hild, A. Górak, M. Skiborowski, Evaluation of performance improvements through application of anisotropic foam packings in rotating packed beds, Chem. Eng. Sci. 230 (2021) 116176. https://doi.org/https://doi.org/10.1016/j.ces.2020.116176.

[4] E.Z.H.J.T.E.A.H. Robin Schulz, MASS-TRANSFER APPARATUS, US 10,710,100B2, 2020.

[5] Sam Baker, https://www.thechemicalengineer.com/news/carbon-capture-reactor-achieves-commercial-scale-which-makers-say-will-capture-100-000-ty-of-co2/, (n.d.).

[6] V.S. PAWAR, U. GARBA, T. TRIQUET, D. ROUZINEAU, M. MEYER, Novel anisotropic T-S structured packing for improved hydrodynamic and mass transfer performance in rotating packed bed: A pathway for new generation packings, Chemical Engineering and Processing - Process Intensification 217 (2025) 110476. https://doi.org/https://doi.org/10.1016/j.cep.2025.110476.

[7] N.-S. Cheng, Formula for the Viscosity of a Glycerol−Water Mixture, Ind. Eng. Chem. Res. 47 (2008) 3285–3288. https://doi.org/10.1021/ie071349z.

Exploring New Azeotropic Systems through Integrated Computer-Aided Molecular Design and Infinitely Sharp Split Analysis

Adem R. N. Aouichaoui[1], Ada Doga Alboga[1], Ioannis Korkakas[1], Ivonne Rodriguez-Donis[2], Jens Abildskov[1]
[1]Technical University of Denmark (DTU), Kgs. Lyngby, Denmark
[2]Université de Toulouse, Toulouse, France

Abstract
Classical approaches to entrainer selection for extractive distillation rely heavily on thermodynamic properties at infinite dilution. However, recent studies have identified cases where these metrics fail to correlate with process economics. To address this limitation, novel solvent design methodologies are emerging that integrate short-cut process metrics directly into computer-aided molecular design (CAMD) frameworks. This work compares a classical heuristic approach - selecting entrainers from the same chemical family as one of the azeotropic mixture components, favouring short carbon chains within a homologous series - with a CAMD-based framework coupled with the infinitely sharp split (ISS) shortcut method. The proposed methodology enables rapid evaluation of key process parameters, establishes stronger connections between molecular properties and process feasibility, and permits exploration of a substantially broader chemical design space. The comparative performance of both approaches is demonstrated through case studies involving the separation of representative azeotropic mixtures.

Keywords
Extractive Distillation, Computer-Aided Molecular Design, Solvent Design, Property Prediction, Vapor-liquid Equilibrium

1. Introduction

Distillation is widely used industrially accounting for a large fraction of separations[1] of liquid mixtures exhibiting relative volatilities $\alpha_{ij} > 1.2$[2]. Many industrial mixtures are non-ideal and close boiling, so azeotropic systems are not exceptional. In this case, extractive distillation can be a viable alternative. In extractive distillation, a solvent (or entrainer) is added to the process to interact preferentially with one member of the azeotropic pair to alter the relative volatility. Figure 1 shows a typical configuration of extractive distillation with the introduction of a high boiling entrainer “E” above the feed stage of a minimum boiling azeotropic mixture “A+B” in the extractive column. By alteration of the relative volatility, “A” may be obtained as the top product in the extractive column, if “B” is retained by the entrainer and subsequently obtained as the top product in the recovery column. Alternatively, the entrainer may retain "A," causing it to exit at the bottom while "B" goes overhead. In either case, "E" is recycled from the recovery column. Which component serves as the light or heavy key depends on the entrainer's effect; conventionally, the light key denotes the component with the lower normal boiling point. Thus, the thermodynamic feasibility and economic viability of extractive distillation hinge on successful entrainer identification. This problem of solvent design is not new. In fact, texts addressing the solvent selection problem has been known for many years[3–7]. Since different feed streams typically require different

solvents, identifying promising/optimal candidates can be daunting. Much progress has been made (and continues) in applying computational methods to this challenge.

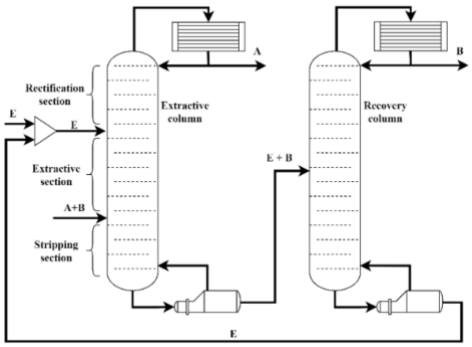

Figure 1: Extractive distillation for the separation of azeotropic pair A and B with heavy entrainer (E). Adapted from Aouichaoui et al[8].

2. Approaches for entrainer selection for extractive distillation

Trial-and-error methods are severely limited by the vast chemical design space, limited availability of test compounds, and the time and effort required for experimentation. Consequently, such approaches are rarely used today. Experimental measurements are difficult, tedious, and costly so their number must be minimized and reserved for late stages of process development

A more practical approach employs heuristics for screening and uses available data for estimates rather than obtaining data for every system. Instead, thermodynamic and property model- based interpolations and extrapolations of data are routinely made. One such method is the homologous series approach[4]. The entrainer is selected from the homologous series of either feed component (A/B), choosing a homolog with a sufficiently high boiling point to prevent azeotrope formation with the entrainer. This causes the retained component to behave more ideally with the entrainer, while the volatilized component exhibits increasing deviation from ideality as its concentration decreases. The entrainer may resemble either the light or heavy key, causing one to exit at the bottom while the other goes overhead. However, if the light key is retained, the natural volatility difference must be overcome and reversed, typically reducing solvent effectiveness.

Computational approaches offer an alternative by screening a wide range of candidates or designing molecules from building blocks. A widely used metric for evaluating entrainers is selectivity at infinite dilution ($S_{A,B}^{\infty}$), which indicates the maximum entrainer effect on relative volatility and provides a common reference for comparison[9,10]. However, this property is inherently difficult to measure accurately, requires extrapolation of VLE data to low concentrations, and is sensitive to the used activity coefficient model. Moreover, several studies have shown that selectivity at infinite dilution does not correlate so well with process economics derived from rigorous optimization[10,11]. To address this, some studies propose computing the product of capacity (C_B^{∞}) and $S_{A,B}^{\infty}$, which tracks better with overall economic metrics[10]. Alternative approaches incorporate maximum driving force considerations in the extractive and recovery columns, where higher driving forces typically translate to easier separation[9]. However, these approaches rely on surrogates or indirect measures. What is needed is a shortcut method that directly computes key process indicators translating to process economics. The rectification body method (RBM) determines minimum entrainer flowrate and energy requirements through bifurcation analysis of tray-to-tray

equations but can be computationally intensive[10,12]. An alternative is the infinitely sharp splits (ISS) method, which computes the minimum entrainer-to-distillate ratio (E/D) and minimum reflux ratio (R_{min}) using only ternary VLE data[12,13]. ISS successfully rationalized the optimum entrainer for methanol–dimethyl carbonate[12] separation. ISS was also recently integrated with computer-aided molecular design (CAMD), producing entrainer rankings consistent with rigorous optimization studies for acetone–methanol separation[8]. This work continues the study by Aouichaoui et al. [8], aiming to: i) evaluate the framework across additional azeotropic systems, and ii) assess consistency with existing heuristics for entrainer selection.

3. CAMD-ISS entrainer selection using CAMD and the ISS concept

The complete framework is shown in Figure 2 and is described in the following.

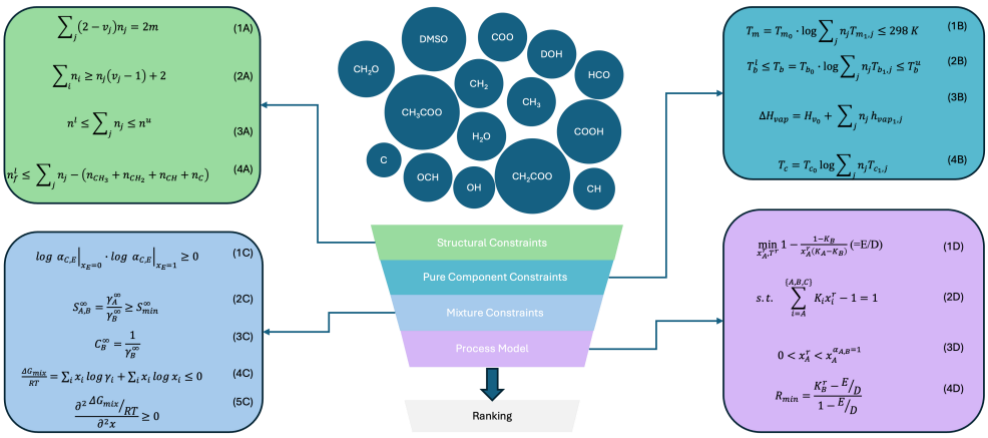

Figure 2: Computer-Aided Molecular Design (CAMD) Framework for entrainer selection using the infinitely sharp splits method (ISS).

In CAMD, molecules are assembled from building blocks subject to structural, pure-component, and mixture property constraints. UNIFAC[14] groups are used to ensure compatibility with group-contribution developed by Constantinou and Gani[15]. Structural constraints govern group assembly (Equations 1A–2A)[16], while limits on group numbers manage complexity and avoid proximity effects (Equations 3A–4A). Pure-component constraints require the entrainer to be liquid at processing conditions (Equation 1B), high-boiling (Equation 2B), and should not result in high energy requirements (Equation 3B). Mixture constraints prevent new azeotrope formation (Equation 1C), ensure affinity toward component B (Equation 2C), and guarantee miscibility via positive Gibbs free energy of mixing (Equations 4C–5C). The ISS method constitutes the process model (Equations 1D–4D).

For a detailed description including the underlying assumption the reader is encouraged to consult the works by Rodriguez-Donis et al.[12] and Petlyuk et al.[13] In the following we provide a description of the concept in terms of the mathematical formulation "we aim to identify a composition x_A^r that lies between 0 and $x_A^{\alpha_{A,B}=1}$ on the A-E edge ($x_B = 0$) which E/D is minimized". We adopt the generate and test solution strategy and decompose the problems into each of the above-mentioned constraints which are evaluated sequentially. This is done to manage the complexity and reduce the potential of numerical instabilities.

4. Results and discussion

In what follows we illustrate the advantages of the method over existing methods.

4.1 Homologous series heuristics

Scheibel[3] illustrated the homologous series method using the acetone–methanol azeotrope. Candidate entrainers include ketone homologs beyond acetone (e.g., methyl ethyl ketone) or alcohol homologs beyond methanol (ethanol, propanol, butanol, etc.). Alcohols are expected to yield greater relative volatilities since the lower-boiling non-solvent, acetone, is volatilized. Table 1 evaluates a series of monofunctional alcohols: $CH_3 + n{\cdot}CH_2 + OH$ (n > 0). The first member (n = 1, ethanol) fails due to azeotrope formation with acetone.

Table 1. Selectivity/Capacity/minimum entrainer-to-distillate and reflux ratio of alcohol entrainers for acetone(A)/methanol(B) separation

Rank	Group Assignment	$(E/D)_{min}$	R_{min}	$S_{A,B}^{\infty}$	C_B^{∞}	γ_A	γ_B
1	CH_3, 2 CH_2, OH	2.8	5.0	1.5	0.85	1.76	1.17
2	CH_3, 3 CH_2, OH	6.0	6.2	1.3	0.84	1.56	1.19
3	CH_3, 4 CH_2, OH	9.8	8.6	1.2	0.84	1.41	1.19

As expected, the lowest-boiling homolog that does not form an azeotrope is typically the most promising solvent. Molecular similarity to the alcohol will cause the alcohol entrainers to behave more ideally with methanol than with acetone. Consequently, acetone exhibits greater positive deviations from ideality. Also, increasing chain length dilutes molecular similarity to the retained component (methanol). Table 1 shows that selectivity decreases with increasing carbon number, while capacity remains relatively constant (also seen through the activity coefficient γ), resulting in the selectivity-capacity product favouring lower homologs. This is further supported by the metrics obtained through ISS.

Ethyl acetate–ethanol separation involves components with very close boiling points, with ethanol boiling only slightly higher. Using an alcohol homolog as entrainer exploits the natural volatility of ethyl acetate relative to ethanol, yielding larger relative volatilities than an ester would. Table 2 confirms that the lowest homolog not forming azeotropes is again most promising.

Table 2. Selectivity/Capacity/minimum entrainer-to-distillate, reflux ratio and activity coefficients of alcohol entrainers for ethyl acetate(A)/ethanol(B) separation.

Rank	Group Assignment	$(E/D)_{min}$	R_{min}	$S_{A,B}^{\infty}$	C_B^{∞}	γ_A	γ_B
1	CH_3, 3 CH_2, OH	9.2	5.9	1.7	0.97	1.81	1.03
2	CH_3, 4 CH_2, OH	24	9.6	1.5	0.94	1.56	1.05
3	CH_3, 5 CH_2, OH	148	43.	1.3	0.93	1.07	1.07

However, this choice has a limitation: selecting the lowest homolog minimizes the boiling point difference with component B, reducing the thermodynamic driving force and separation efficiency in the recovery column.

4.2 ISS/CAMD Integration New Systems

The search space widens substantially when one allows design of entrainer solvents from a wider range of molecular building blocks (groups). The results obtained can be seen in Table 3 for the azeotropic system of acetone (A) - methanol(B).

Table 3: Selectivity/Capacity/minimum entrainer-to-distillate and reflux ratio of superior entrainers for acetone(A)/methanol(B) separation.				
Entrainer	$S_{A,B}^{\infty}$	C_B^{∞}	$(E/D)_{min}$	R_{min}
DMSO	1.46	0.9	0.619	1.35
Ethylene Glycol	2.97	0.8	1.01	1.37
1,5-pentanedial	2.12	2.33	0.58	1.96
2-methyl-1,4-butanedial	2.16	2.37	0.57	1.94

The CAMD-identified entrainers exhibit substantially lower entrainer-to-distillate and reflux ratios, along with higher selectivities, compared to those from the homologous series method. However, Table 3 demonstrates that selectivity alone does not dictate optimal process metrics: Ethylene glycol shows a higher $(E/D)_{min}$ than other candidates despite high selectivity, while DMSO has the lowest R_{min} but neither the lowest $(E/D)_{min}$ nor the highest selectivity. Table 4 presents CAMD-generated entrainer suggestions for alternative separations. Notably, low-end homologs of the diol series outperform the alcohol homologs in Table 2 for ethyl acetate-ethanol, while ethylene glycol is identified for methyl acetate-methanol. These results confirm that selectivity alone does not determine the ranking of $(E/D)_{min}$ and R_{min}.

Table 4: Azeotropic Separation Metrics				
Entrainer, E	$S_{A,B}^{\infty}$	$C_{B,E}^{\infty}$	$(E/D)_{min}$	R_{min}
Methyl acetate (A) + methanol (B)				
Ethylene glycol	4.1	2.15	0.70	0.75
CH_2, HCO, COOH	2.7	0.87	0.39	0.76
Ethyl acetate (A) + ethanol (B)				
Dimethyl sulfoxide	3.98	1.62	0.86	0.80
3 CH_2, 2 OH	3.10	1.03	1.11	1.00
CH_3, CH_2, CH, OH	3.15	1.03	1.12	1.08
2 CH_3, C, 2 OH	2.61	1.14	1.06	0.99
Methanol (A) + tetrahydrofuran (B)				
2 CH_3, 2 CH_2, COO	4.00	1.48	0.46	4.67
4 CH_3, C, COO	4.18	1.54	0.47	3.95
Isopropanol (A) + water (B)				
Dimethyl sulfoxide	1.57	2.14	0.65	2.14
Ethylene glycol	2.26	1.00	0.64	1.62
Ethanol (A) + water (B)				
Dimethyl sulfoxide	1.33	2.14	0.23	2.20
Ethylene glycol	1.48	1.00	0.27	1.80
Methyl Acetate (A) + water (B)				
Dimethyl sulfoxide	4.10	2.14	0.12	0.19
Ethylene glycol	2.36	1.00	0.36	0.85

5. Conclusions

Classical entrainer selection methods rely predominantly on thermodynamic properties at infinite dilution. However, recent optimization studies have identified cases where these criteria fail to correlate with process economics. This work compares a traditional heuristic with a CAMD-based framework for separating minimum-boiling azeotropic

mixtures using linear aliphatic alcohols as entrainers. For the acetone-methanol and ethyl acetate-ethanol systems, selectivity decreased with increasing carbon chain length within the homologous series. In contrast, key process metrics, minimum entrainer flow rate and minimum reflux ratio, computed via the infinitely sharp split (ISS) method, exhibited the opposite trend. CAMD frameworks that explicitly incorporate these metrics identified more effective entrainers spanning multiple chemical families. The robustness of this approach is demonstrated through several case studies. Further optimization studies will determine the optimal entrainer for each system.

References

(1) Wankat, P. C. *Separation Process Engineering: Includes Mass Transfer Analysis*, 3. ed.; Prentice Hall: Upper Saddle River, NJ, 2012.

(2) *Materials for Separation Technologies. Energy and Emission Reduction Opportunities*; United States, 4 AD. https://doi.org/10.2172/1218755.

(3) Scheibel, E. G. Principles of Extractive Distillation. *Chemical Engineering Progress* **1948**, *44* (12), 927.

(4) Smith, B. D.; Bolles, W. L.; Fair, J. R. *Design of Equilibrium Stage Processes*; McGraw-Hill chemical engineering series; McGraw-Hill Book Company, Inc: New York San Francisco Toronto London, 1963.

(5) Pierotti, G. J.; Deal, C. H.; Derr, E. L. Activity Coefficients and Molecular Structure. *Industrial & Engineering Chemistry* **1959**, *51* (1), 95–102. https://doi.org/10.1021/ie50589a048.

(6) Dunn, C.; Millar, R.; Pierotti, G.; Shiras, R.; Souders, M. Toluene Recovery by Extractive Distillation-Erection of a Commercial Plant on the Foundation of Laboratory Data. *Transact Am Inst Chem Engine* **1945**, *41* (5), 631–644.

(7) Deal, C. H.; Derr, E. L. Selectivity and Solvency in Aromatics Recovery. *Industrial & Engineering Chemistry Process Design and Development* **1964**, *3* (4), 394–399. https://doi.org/10.1021/i260012a022.

(8) Aouichaoui, A. R.; Rodriguez-Donis, I.; Gerbaud, V.; Shcherbakova, N.; Abildskov, J. Integrated Entrainer Design for Extractive Distillation Using The Infinitely Sharp Splits and Computer-Aided Molecular Design. In *12th international conference Distillation & Absorption 2022*; 2022.

(9) Cignitti, S.; Rodriguez-Donis, I.; Abildskov, J.; You, X.; Shcherbakova, N.; Gerbaud, V. CAMD for Entrainer Screening of Extractive Distillation Process Based on New Thermodynamic Criteria. *Chemical Engineering Research and Design* **2019**, *147*, 721–733. https://doi.org/10.1016/j.cherd.2019.04.038.

(10) Kossack, S.; Kraemer, K.; Gani, R.; Marquardt, W. A Systematic Synthesis Framework for Extractive Distillation Processes. *Chemical Engineering Research and Design* **2008**, *86* (7), 781–792. https://doi.org/10.1016/j.cherd.2008.01.008.

(11) Momoh, S. O. Assessing the Accuracy of Selectivity as a Basis for Solvent Screening in Extractive Distillation Processes. *Separation Science and Technology* **1991**, *26* (5), 729–742. https://doi.org/10.1080/01496399108049911.

(12) Rodriguez-Donis, I.; Shcherbakova, N.; Parascandolo, E.; Abildskov, J.; Gerbaud, V. Entrainer Selection Using the Infinitely Sharp Split Method and Thermodynamic Criteria for Separating Binary Minimum-Boiling Azeotrope by Extractive Distillation. *Chemical Engineering Research and Design* **2024**, *205*, 443–458. https://doi.org/10.1016/j.cherd.2024.04.003.

(13) Petlyuk, F.; Danilov, R.; Burger, J. A Novel Method for the Search and Identification of Feasible Splits of Extractive Distillations in Ternary Mixtures. *Chemical Engineering Research and Design* **2015**, *99*, 132–148. https://doi.org/10.1016/j.cherd.2015.02.013.

(14) Hansen, H. K.; Rasmussen, P.; Fredenslund, A.; Schiller, M.; Gmehling, J. Vapor-Liquid Equilibria by UNIFAC Group Contribution. 5. Revision and Extension. *Ind. Eng. Chem. Res.* **1991**, *30* (10), 2352–2355. https://doi.org/10.1021/ie00058a017.

(15) Constantinou, L.; Gani, R. New Group Contribution Method for Estimating Properties of Pure Compounds. *AIChE Journal* **1994**, *40* (10), 1697–1710. https://doi.org/10.1002/aic.690401011.

(16) Odele, O.; Macchietto, S. Computer Aided Molecular Design: A Novel Method for Optimal Solvent Selection. *Fluid Phase Equilibria* **1993**, *82*, 47–54. https://doi.org/10.1016/0378-3812(93)87127-M.

Comparative Study of Liquid Split Mechanisms for 3D-printed Laboratory Dividing Wall Columns

Chiara Lukas[1], Mohamed Adel Ashour[1], Thomas Grützner[1]

[1] Ulm University, Institute of Chemical Engineering, Laboratory of Thermal Process Engineering, Albert-Einstein-Allee 47, 89081 Ulm, Germany

Abstract

Dividing wall columns (DWCs) are a well-established example of intensified distillation technology, offering significant reductions in both energy consumption and capital investment. These benefits, however, can only be fully realized when the prefractionator is operated under optimal conditions, applying certain vapor and liquid splits. Typically, only the liquid split can be manipulated during column operation. Consequently, a precise liquid split is essential for maintaining energy-efficient operation of a DWC. Operational limits of laboratory-scale liquid dividers are rarely reported. For the future implementation in a 3D-printed laboratory-scale DWC, existing designs of lab-scale liquid dividers were adapted, and an additively manufactured test rig for liquid splitting was developed. Within this setup, different actuation mechanisms were investigated employing pneumatic and electromagnetic actuation. The effects of the supplied liquid flow rate, switching frequency, and solvent type (water and ethanol) were systematically analyzed, and operational boundaries were identified. The findings are applicable to a wide range of laboratory-scale liquid dividers, independent of the employed manufacturing technology. The resulting insights were used to determine the most suitable liquid-splitting approach. Among the investigated concepts, pneumatic rotary actuation exhibited superior performance, as its liquid-splitting behavior proved largely independent of switching frequency, flow rate, and operating fluid.

Keywords

DWC, Liquid Split, Process Intensification, Miniaturization

1. Introduction

One of the most prominent examples of an intensified distillation process is the dividing wall column (DWC). With a DWC, a sequence of at least two conventional, standard 2-product distillation columns can be replaced by a single column to produce three pure product streams. The dividing wall column (DWC), combines thermal coupling between column sections, which can reduce energy demand by up to 30%, with the physical integration of two columns into a single shell, resulting in capital cost savings of up to 30%.[1].

Despite the clear benefits of dividing wall columns (DWCs), their industrial utilization falls short. This issue can be related to the increased complexity in designing and operating a DWC compared to a standard 2-product distillation column, as the number of design variables increases by 7. In addition to conventional control parameters, two new degrees of freedom, the vapor and liquid splits exist. These two parameters can theoretically be used as control variables for the operation at the

energy minimum. [1] However, the vapor split is typically not actively manipulated during operation but set by the placement of the dividing wall and the pressure drop characteristics left and right of the wall, which are mainly predetermined by constructional aspects. In contrast, the liquid split is readily adjustable and constitutes the key control variable for the prefractionator, thereby enabling operation at the energy minimum. [2]
To achieve operation of the DWC at the energy minimum, maintaining the desired split in the prefractionator is crucial. The liquid split S describes the ratio of liquid in the prefractionation column and the main column. In industrial application, the desired liquid split is typically achieved by removing the entire liquid coming down from the column section above the dividing wall and collecting it in a buffer tank. By using flow controllers, the liquid is returned to the column on the respective side of the wall in a defined manner with pumps or by gravity using two pipes. [3] For laboratory-scale liquid distribution, such as that required for reflux at the column head, standardized glassware components are available. Common solutions in laboratory and pilot-scale setups include swinging funnels, which are frequently actuated by electromagnets or solenoids. Also approaches using a linear actuator exist. The moving parts are operated either pneumatically or electromagnetically. The liquid is divided by alternatingly changing the position of the applied actuator. A precise operation of liquid dividers is necessary to ensure a stable column operation, as deviations can lead to partial de-wetting and spoiled product purities. However, information for these devices about influencing parameters and their boundaries are rarely published and studied. This knowledge gap is addressed in this study and the influence of operational parameters on the performance determined. The designs to be investigated in this study will be based on laboratory-scale liquid dividers. The best option will be implemented in a novel, modular 3D-printed laboratory-scale DWC, which is currently under construction. This lab-scale DWC should be a cost-efficient and flexible alternative to pilot-scale plants.

2. Materials and Methods

2.1 Methods and materials for additive manufacturing

The test rig and the actuated components performing the liquid split were manufactured using selective laser sintering (SLS) of polyamide 12 (Nylon 12 Powder, *Formlabs GmbH, Germany*) and the SLS 3D printer Fuse 1 (*Formlabs GmbH, Germany*).
Different principles of actuation to perform the liquid split were adapted for application in a DWC. Based on standard laboratory distillation equipment, CAD models of the components performing the liquid split have been generated. Initially, three actuation methods were tested. However, during a previous screening one of them showed low potential for further investigation and was therefore discontinued. Figure 1 shows a scheme of the actuation principles.
Figure 1 (a) shows a rotating pneumatic actuator (RPA) connected to a symmetric funnel. The rotation angle of the actuator can be specified. The funnel is alternatingly deflected by the rotary actuator. Thus, the funnel outlet switches between the two sides of the dividing wall, distributing the operating liquid. The actuator motion is controlled by a monostable solenoid valve.
Common laboratory liquid dividers often utilize externally fixed electromagnets. By interaction with magnetic stainless steel, which is placed on the funnel of the electromagnetic actuator (EMA) shown in Figure 1 (b), movement is induced. Thus, when current is supplied to the electromagnet, a magnetic field is generated, which

pulls the funnel towards the opposite side of the dividing wall. When the current supply is stopped the funnel falls back into its initial position by gravity.

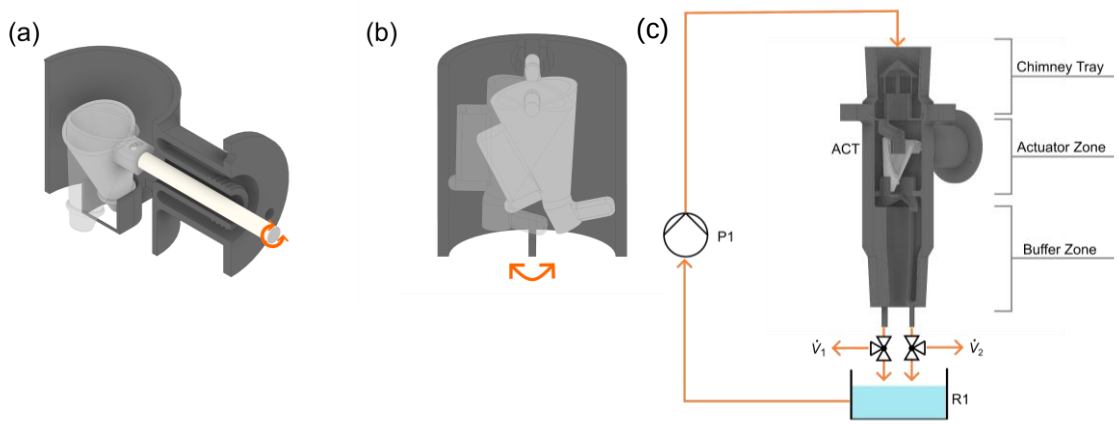

Figure 1: Schematic display of different actuation methods for dividing a liquid stream into two parts: (a) Pneumatic rotating actuator and (b) electromagnetic operated swinging actuator. (c) Simplified scheme of experimental setup.

2.2 Experimental Methods and Materials

Prior to measurements the peristaltic pump P1 is calibrated gravimetrically. The calibration is conducted three times and an average flowrate determined. The operating liquid is circulated through the test rig for at least 5 minutes to ensure steady-state. Afterwards, the flowrates $\dot{V}_1$ and $\dot{V}_2$ of the generated sub-streams are determined gravimetrically. Each flowrate is measured three times and an average value calculated. For the evaluation of the performance and comparison of the different actuation methods, the split ratio S (Eq. 2) is defined.

$$S = \frac{\dot{V}_2}{\dot{V}_1} = \frac{\dot{m}_2}{\dot{m}_1} \cdot \frac{\rho_{\mathrm{L},1}}{\rho_{\mathrm{L},2}} \qquad \text{Eq. 1}$$

The split ratio S is calculated from the volumetric flowrates $\dot{V}_1$ and $\dot{V}_2$, which are received at the outlets of the test rig. Assuming an equal liquid density ($\rho_{\mathrm{L},1} = \rho_{\mathrm{L},2}$), the split ratio can be calculated via mass flows. The indices 1 and 2 refer to the position of the actuator. Position 1 is defined as the actuator position in the non-powered state. Thus, position 2 is given by the powered state.

For comparison of the different actuation methods, the performance is evaluated using the split ratio S at different flowrates and switching frequencies f. The switching frequency f is derived from switching times t_1 and t_2. The switching time is defined as the duration for which the actuator remains in each discrete position.

$$f = \frac{1}{t_1 + t_2} \qquad \text{Eq. 2}$$

For a general characterization and comparability of the actuation methods, which exhibit different transition times between positions 1 and 2, t_1 and t_2 are set to be equal, as deviations related to the actuator design, the actuation method and different transition times can be identified more easily. The switching times are implemented in a python script, which operates a relay and subsequently the actuators.

Measurements in a flowrate range $\dot{V} = 7 - 18\ \mathrm{L\ h^{-1}}$ were conducted, where the supplied flowrate, switching frequency and operating medium were systematically varied. The two operating media water and ethanol are compared to evaluate effects on the performance caused by surface effects. Due to the surface roughness of the

3D-printed parts using SLS, deviations of the performance can be expected. For the electromagnetically operated actuator, effects of the surface interaction between the 3D-printed material and ethanol were strongly noticeable in case of the electromagnet operation. To reduce deviations caused by wall creeping, the surface of one 3D-printed funnel was further post-processed using vapor smoothing.

3. Results and Discussion

Since $t_1 = t_2$ was defined, the ideal split ratio S is equal to 1. Deviations from this are expected, as transition time t_T between the two actuator positions and signal transfer are not corrected. Deviations within a $\pm 5\,\%$ range, thus $S = 0.95 - 1.05$ are accepted for the application in a 3D-printed DWC. A deviation from the optimum can be caused by operational (switching frequency, flowrate) or design parameters. The effect of the switching frequency on the split ratio is determined by the design and the actuator operation. Both affect the travel time between the actuator positions. With every position change, delays are introduced, thus an increase in the switching frequency leads to a higher accumulation of delays, which results in a deviation of the split ratio from its optimum value. In contrast, low switching frequencies and prolonged supply interruptions may cause partial or complete de-wetting of the underlying packing, thereby reducing the separation efficiency. Consequently, an optimal operating point arises from a trade-off between these opposing effects.

3.1 Measurements with deionized water

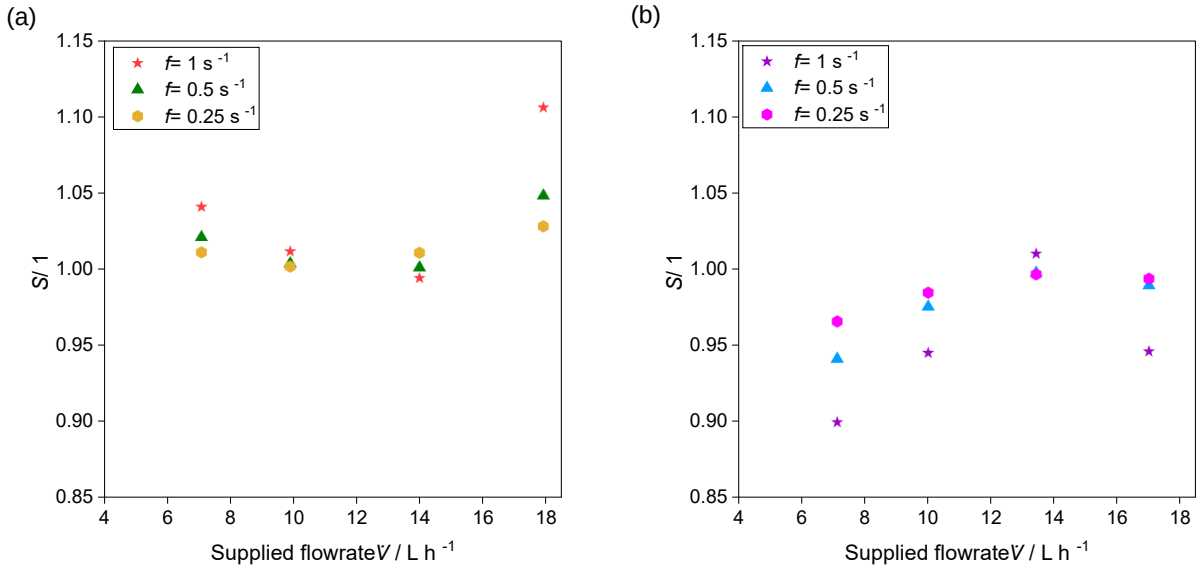

Figure 2: Measured split ratios S in dependence of the supplied volumetric flowrate $\dot{V}$ for (a) the pneumatic rotating actuator and (b) electromagnetic actuator with deionized water as working fluid.

The operation of the rotary pneumatic actuator (RPA) (Figure 2 (a)) results in a range of split ratios of $S = 0.994 - 1.10$. For operation using the electromagnetically operated actuator (EMA) (Figure 2 (b)), split ratios in the range of $S = 0.9 - 1.01$ for water were determined. With the exception of the data point recorded at $\dot{V} = 13.5\,\mathrm{L\,h^{-1}}$ and $f = 1\,\mathrm{s^{-1}}$, the non-powered state is more dominant for the RP actuator ($S > 1$) and the powered state of the EM actuator ($S < 1$). Both measurements show a matching but inversed trend with an extremum at $13.5\,\mathrm{L\,h^{-1}}$. In general, operation at the lowest switching frequency of $f = 0.25\,\mathrm{s^{-1}}$ leads to split ratios closest to the desired value.

The matching trends indicate, that prior to the liquid splitting, deviations caused e.g. by wall flows due to interaction of the operating medium with the 3D-printed surface

are present. The split ratios determined with the RPA are mainly frequency independent at lower flowrates, but show an offset towards $S > 1$. Since a monostable solenoid valve is used, a mismatch in transition times between the funnel positions, thus leading to an offset. This offset might also be amplified for increasing flowrates. The EMA shows strong dependance between S and f. Similarly, a mismatch in transition times is possible for the EMA, since only the transition at the powered state is actively manipulated. Operation within the $\pm\,5\,\%$ is possible at $f \leq 0.5\,\mathrm{s}^{-1}$ with the RPA and $f = 0.25\,\mathrm{s}^{-1}$ with the EMA.

3.2 Measurements with Ethanol

Further measurements were conducted with ethanol as working fluid. Due to the lower surface tension and the surface roughness resulting from the manufacturing technique, contact angles close to 0° have been observed. This indicates full and almost immediate wetting of the entire surface. [4] Since severe wall flows at the funnel of the EMA were noticed in previous investigations, one of the funnels was further postprocessed by vapor smoothing, which led to a reduced surface roughness. The results recorded for both actuation methods applying ethanol as operating medium are displayed in Figure 3.

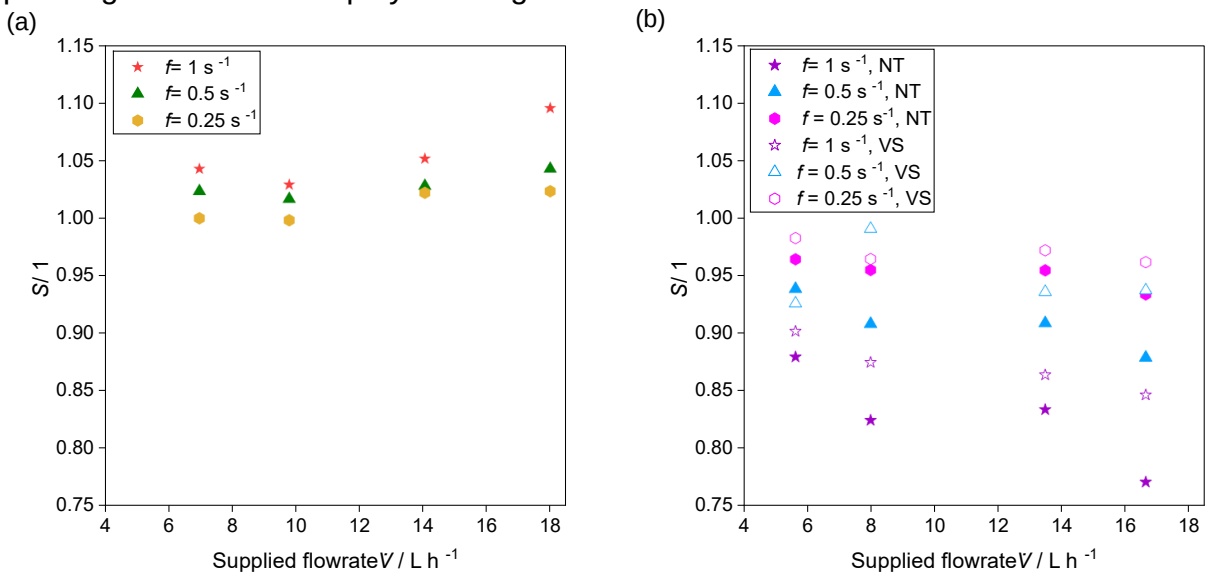

Figure 3: Measured split ratios S in dependence of the supplied volumetric flowrate $\dot{V}$ for (a) the pneumatic rotating actuator and (b) electromagnetic actuator with ethanol as working fluid.

The operation of the RPA (Figure 3 (a)) results in split ratios in the range of $S = 0.999 - 1.09$, which is in good alignment with the performance using water. Figure 3 (a) shows a more stable profile compared to water with mainly constant S for $f \leq 0.5\,\mathrm{s}^{-1}$. Increasing f leads to an offset towards higher split ratios at high flowrates. EMA operation resulted in split ratios in the range of $S = 0.77 - 0.99$. Since the determined split ratio ranges deviate strongly, (Figure 2 (b) vs. Figure 3 (b)) the operating liquid has a high influence on the performance. Higher split ratios were received, when the VS-funnel was applied. While the split ratios remain mainly constant for a frequency $f = 0.25\,\mathrm{s}^{-1}$, a decreasing trend with increasing flowrate is visible for higher switching frequencies. Generally, the switching frequency affects the split ratio strongly.

Investigations of the RPA show, that operation within a $\pm 5\%$ range from the nominal case is possible, if only the lower switching frequencies of $f = 0.25\,\mathrm{s}^{-1}$ and $0.5\,\mathrm{s}^{-1}$ are considered. The recorded split ratios are in the range of $S = 1.001 - 1.048$ for water and $0.9988 - 1.043$ for ethanol. Further, the performance is mainly

independent on flowrate and operating medium. The increased deviation for higher flowrates is most probably related to the monostable solenoid valve, which is applied for the position switch of the actuator. An exchange of the valve with a bistable version is a promising approach to reduce those deviations.
Figure 3 (b) shows, that surface treatment using vapor smoothing improves the performance. Experiments conducted with the VS-funnel show split ratios parallelly shifted towards the nominal case compared to the NT-funnel. The poor performance was attributed to wall-flow occurring on the outside of the funnel. Then, liquid accumulated at the wallstopper visible in Figure 1 (b) and dripped into the opposite side of the dividing wall, thus decreasing the split ratio. The wall flow could only be partially suppressed with post-processing by vapor smoothing. The decreasing trend of S with increasing the flowrate implies a proportional relation between wall-flow and supplied flowrate. Due to the higher surface tension, this behavior was not observed with water as the operating medium.
Comparing the actuation methods, the operation using the RPA is more resilient against properties of the operating liquid. For low switching frequencies, an operation within a $\pm 5\%$ range from the optimum is possible independent of the liquid and flowrate. The symmetric design of the actuation zone is beneficial, as compared to the funnel used with the EMA no dripping spots exist and potential wall flow is distributed equally. The additional wall-flow and dripping of ethanol further leads to a drop in performance and additional dependence on the supplied flowrate. Surface-treatment of the funnel by vapor-smoothing reduced these issues, however wall-flow could not be completely avoided. Those deviations were further amplified by high switching frequencies. Since it was shown, that no stable operation using EMA independent on the operating liquid was possible, no further investigations are conducted. Consequently, due to its good performance, independent on the switching frequency, supplied flowrate and operating liquid, the rotary pneumatic actuator will be applied to conduct the liquid split in the 3D-printed laboratory dividing wall column.

4. Conclusions

This study evaluated different liquid-splitting mechanisms for 3D-printed laboratory-scale DWCs. The rotary pneumatic actuator (RPA) outperformed the electromagnetic alternative by providing stable split ratios ($\boldsymbol{S = 1 \pm 5\%}$) across a wide range of flow rates and frequencies. While the electromagnetic actuator (EMA) was heavily influenced by solvent properties and surface roughness, leading to significant wall-flow, RPA showed high resilience against these effects. Post-processing 3D-printed parts via vapor smoothing was shown to mitigate wall-flow but could not fully compensate for design-inherent limitations of the EMA. Consequently, the RPA is the most suitable candidate for achieving the precise liquid control required to operate 3D-printed DWCs at their energy minimum.

References

[1] John Wiley & Sons, Ltd., Publication, Chichester, West Sussex, 2013.
[2] K.A. Amminudin, R. Smith, D.Y.-C. Thong, G.P. Towler, Design and Optimization of Fully Thermally Coupled Distillation Columns, Chemical Engineering Research and Design 79 (2001) 701–715. https://doi.org/10.1205/026387601753192028.
[3] M.M. Donahue, B.J. Roach, J.J. Downs, T. Blevins, M. Baldea, R.B. Eldridge, Dividing wall column control: Common practices and key findings, Chemical Engineering and Processing - Process Intensification 107 (2016) 106–115. https://doi.org/10.1016/j.cep.2016.05.013.
[4] J. Neukäufer, B. Seyfang, T. Grützner, Investigation of Contact Angles and Surface Morphology of 3D-Printed Materials, Ind. Eng. Chem. Res. 59 (2020) 6761–6766. https://doi.org/10.1021/acs.iecr.0c00430.

Experimental Study on NO Absorption Capacity in Fe(II)EDTA and Solvent Regeneration with Sodium Sulfite

Domenico Flagiello, Domenico Ricchiari, Vincenzo Papa, Alessandro Erto, Francesco Di Natale*
Department of Chemical, Materials and Production Engineering
University of Naples Federico II, P.le Tecchio 80 – 80125, Naples, Italy
**Corresponding Author: domenico.flagiello@unina.it*

Abstract
Nitric oxide (NO) is the dominant nitrogen oxide species in most combustion exhaust gases and represents a major challenge for post-combustion abatement due to its poor solubility in water. Chelation-based absorption using Fe(II)EDTA offers a selective and potentially regenerable route for NO capture, as the metal–ligand complex can reversibly bind NO without permanent oxidation. In this work, the absorption capacity of NO in aqueous Fe(II)EDTA solutions and the regeneration of the chelating agent using sodium sulfite are experimentally investigated in a lab-scale fed-batch bubble column. The effects of Fe(II)EDTA concentration, pH, oxygen content, sulfite dosage, and SO_2 presence are systematically analyzed. Results demonstrate that sodium sulfite effectively restores the active Fe(II)EDTA form, significantly enhancing NO absorption capacity and enabling cyclic operation, in agreement with earlier regeneration studies reported in the relevant literature. The study highlights the potential of Fe(II)EDTA-based reactive absorption as a closed-loop and process-intensified solution for NO removal.

Keywords
Reactive absorption; Nitric oxide; Fe(II)EDTA; Chelating agents; Solvent regeneration

1. Introduction

Nitrogen oxides (NO_x) are among the most critical atmospheric pollutants generated by combustion processes in industrial plants and internal combustion engines. Within the NO_x family, nitric oxide (NO) typically accounts for more than 90% of total emissions and is particularly difficult to remove by conventional wet scrubbing technologies due to its low aqueous solubility and slow oxidation kinetics (Norvell and Lindsay, 1967; Hishinuma et al., 1978). Selective Catalytic Reduction (SCR) is currently the most mature technology for high-efficiency NO_x abatement; however, its application may be limited by space constraints, FGD integration issues and catalyst sensitivity to flue gas composition (Ali et al., 2021).

In recent years, wet gas absorption processes employing oxidizing liquids have attracted increasing attention as compact tail-end solutions capable of simultaneously removing NO_x and SO_x. Nevertheless, these systems often suffer from high reagent consumption and the accumulation of nitrate and sulfate species in the wash water, raising sustainability concerns (Zhu et al., 2010). Chelation-based absorption represents an alternative approach in which NO is reversibly bound without permanent oxidation, enabling solvent regeneration and reuse (Hishinuma et al., 1978). Among chelating agents investigated for nitric oxide capture, Fe(II)EDTA (ferrous

ethylenediaminetetraacetate) is the most extensively studied and best-characterized system. The EDTA ligand, featuring four carboxylate ($–COO^-$) and two amine ($–NH_2$) donor groups, coordinates the ferrous ion in a pseudo-octahedral geometry, providing high thermodynamic stability under reducing conditions while maintaining sufficient flexibility to accommodate additional ligands such as NO (Norvell and Lindsay, 1967; Hishinuma et al., 1978). A major challenge for Fe(II)EDTA-based systems is the oxidation of Fe(II) to Fe(III) in the presence of oxygen, which suppresses NO binding. The use of reducing agents such as sodium sulfite has been proposed to restore the active Fe(II) form and sustain absorption performance (Teramoto et al., 1978; Bal Raj and Neha, 2015).

The fundamental mechanism of NO absorption involves an initial physical dissolution of NO into the aqueous phase:

$$NO_{(g)} \rightleftarrows NO_{(aq)} \tag{1}$$

followed by reversible coordination to the ferrous chelate, forming a nitrosyl complex.

$$Fe(II)EDTA + NO \rightleftarrows Fe(II)EDTA(NO) \tag{2}$$

Spectroscopic and thermodynamic investigations have demonstrated that this interaction is fully reversible under oxygen-free conditions, with a modest exothermic enthalpy change and a significant entropy decrease associated with ligand coordination (Hishinuma et al., 1978; Teramoto et al., 1978). The equilibrium constant decreases with increasing temperature, confirming the coordination-driven and non-oxidative nature of NO binding and clearly distinguishing chelation-based absorption from oxidant-intensive wet scrubbing processes.

From an engineering standpoint, reversibility enables cyclic absorption–regeneration operation but introduces sensitivity to redox stability. In the presence of oxygen, Fe(II)EDTA is readily oxidized to Fe(III)EDTA:

$$4Fe(II)EDTA + O_2 + 4H^+ \rightarrow 4Fe(III)EDTA + H_2O \tag{3}$$

which does not exhibit NO-chelating activity, leading to a direct loss of absorption capacity (Zhu et al., 2010). Solution pH further affects chelate stability: ligand protonation at low pH weakens metal coordination, whereas at alkaline conditions, Fe(II) is prone to oxidation and precipitation as iron hydroxides, irreversibly depleting the chelate pool (Bal Raj and Neha, 2015).

The practical feasibility of Fe(II)EDTA-based NO capture, therefore, relies on effective regeneration strategies. Chemical regeneration using sulfite has proven to be particularly effective. Sulfite reduces the nitrosyl complex, regenerating Fe(II)EDTA and forming nitrous oxide:

$$2Fe(II)EDTA(NO) + SO_3^= \rightarrow 2Fe(II)EDTA + N_2O + SO_4^= \tag{4}$$

which can be further reduced to molecular nitrogen:

$$SO_3^= + N_2O \rightarrow SO_4^= + N_2 \tag{5}$$

according to Teramoto et al. (1978).

More recent studies have shown that sulfite can also reduce oxidized Fe(III)EDTA back to its active ferrous form through dissociation, reduction and re-coordination steps.

$$Fe(III)EDTA \rightleftarrows Fe(III) + EDTA \tag{6}$$

$$2Fe(III) + SO_3^{=} + H_2O \rightarrow SO_4^{=} + 2Fe(II) + 2H^+ \quad (7)$$

$$Fe(II) + EDTA \rightarrow Fe(II)EDTA \quad (8)$$

This pathway is thermodynamically favored by the high standard reduction potential of the Fe(III)/Fe(II) redox couple and can be kinetically enhanced by temperature, sulfite concentration and catalytic surfaces, enabling recovery of the original chelating solution and sustained cyclic operation (Zhu et al., 2010).

The present work aims to investigate selective NO absorption in aqueous Fe(II)EDTA solutions through a systematic experimental campaign designed to quantify absorption capacity with specific focus on parameters relevant to gas–liquid contactor operation, following experimental approaches commonly adopted for the investigation of NO–Fe(II)EDTA systems (Hishinuma et al., 1978; Teramoto et al., 1978). Experiments were conducted in a laboratory-scale bubble column operated in fed-batch mode, enabling time-resolved monitoring of NO absorption until saturation. This configuration allows direct estimation of absorption capacity and effective solubility behavior across Fe(II)EDTA concentrations in the range 0.005–0.05 M and inlet NO concentrations between 100 and 1000 ppm_v at 25 °C. Other experiments investigate on the effect of solution pH (unadjusted value, 7 and 10) and oxygen in the gas-phase (5 - 8% v/v) on absorption capacity, which jointly govern nitrosyl adduct stability and the competing oxidation of Fe(II) to Fe(III), including the effect of SO_2 concentration in the gas-phase (1000 ppm_v). Finally, we evaluate the role of sodium sulfite addition (0.05 M) as an in-situ chemical regeneration strategy, assessing its effect on NO absorption capacity in concentrated Fe(II)EDTA solutions under conditions representative of practical oxygen-containing exhaust streams

2. Experimental setup and methodologies

Absorption experiments were carried out in a lab-scale Pyrex glass bubble column operated in fed-batch mode, following experimental approaches used in our former works (Flagiello et al., 2023,2025). The experimental setup is reported in **Figure 1**.

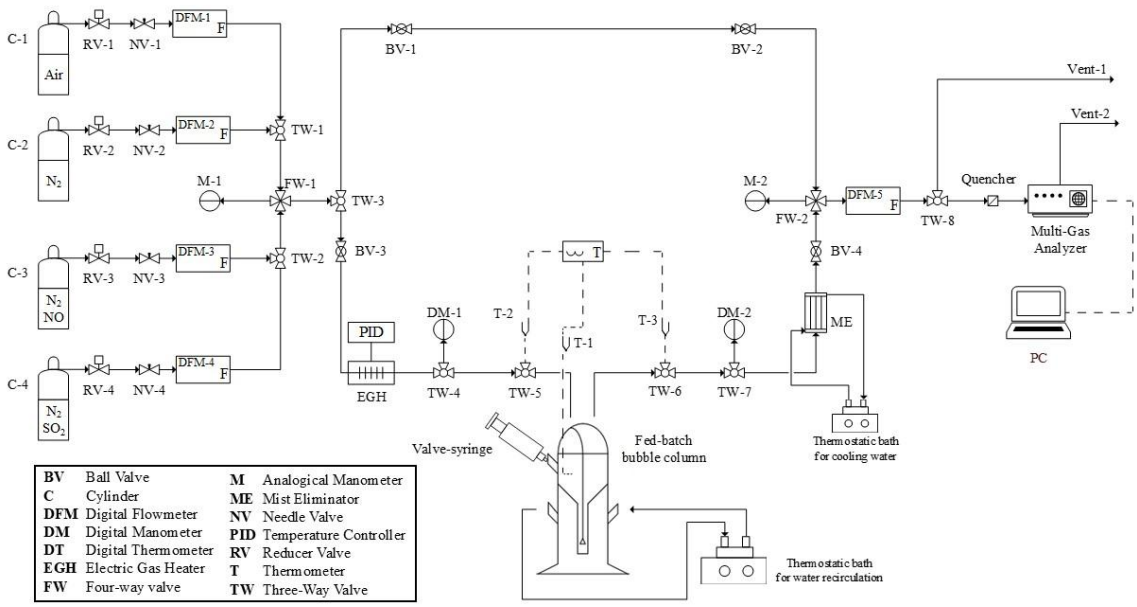

Figure 1: Process Flow Diagram (PFD) of the fed-batch bubble column lab-scale.

The column had an internal diameter of 0.025 m and a total length of 0.20 m. Aqueous Fe(II)EDTA solutions with concentrations ranging from 0.005 to 0.05 mol/L were

prepared using deionized water and ethylenediaminetetraacetic acid disodium salt (Na_2EDTA, 99.0% w/w) with Iron (II) chloride tetrahydrate ($FeCl_2 \cdot 4H_2O$, 99.0% w/w). The liquid batch volume was fixed at 10 mL, while the gas phase consisted of nitrogen-balanced NO mixtures with inlet concentrations between 100 and 1000 ppm_v, fed at a constant flow rate of 1.5 L/min. Selected tests were performed with the addition of oxygen (5 - 8% v/v) and SO_2 to investigate oxidative and competitive effects, as suggested by previous studies on chelate stability (Zhu et al., 2010).
The absorption tests were performed at 25 °C, while the pH of the absorbing solution was either left unaltered or adjusted to 7 or 10 using NaOH. Sodium sulfite (Na_2SO_3, 98.0% w/w) was added in stoichiometric amounts with respect to Fe(II)EDTA to evaluate its effect on NO solubility and solvent regeneration, in accordance with the regeneration strategies proposed in the literature (Teramoto et al., 1978). Regeneration experiments were performed under batch condition at 40 °C using the column in **Figure 1** placed on a stirring-heating plate operating at 600 rpm after nitrogen inerting. The regeneration efficiency was determined by comparing the NO absorption capacity of regenerated solutions with that of fresh Fe(II)EDTA solutions.

3. Results and discussion

The experimental results (**Figure 2A**) indicate that NO solubility increases with Fe(II)EDTA concentration in the range 0.005 - 0.05 mol/L, confirming the role of reversible chelation as the governing mechanism, in agreement with classical studies on ferrous chelates (Hishinuma et al., 1978). Increasing the initial pH to 7 and 10 reduced the NO absorption capacity (**Figure 2B**) due to the formation of ferric hydroxide species and reduced chelate stability, a behavior previously reported for iron–EDTA systems (Bal Raj and Neha, 2015). The presence of oxygen in the gas feed significantly inhibited NO absorption (**Figure 2C**), as Fe(II)EDTA was progressively oxidized to Fe(III)EDTA, which does not bind NO, as suggested by Zhu et al. (2010).

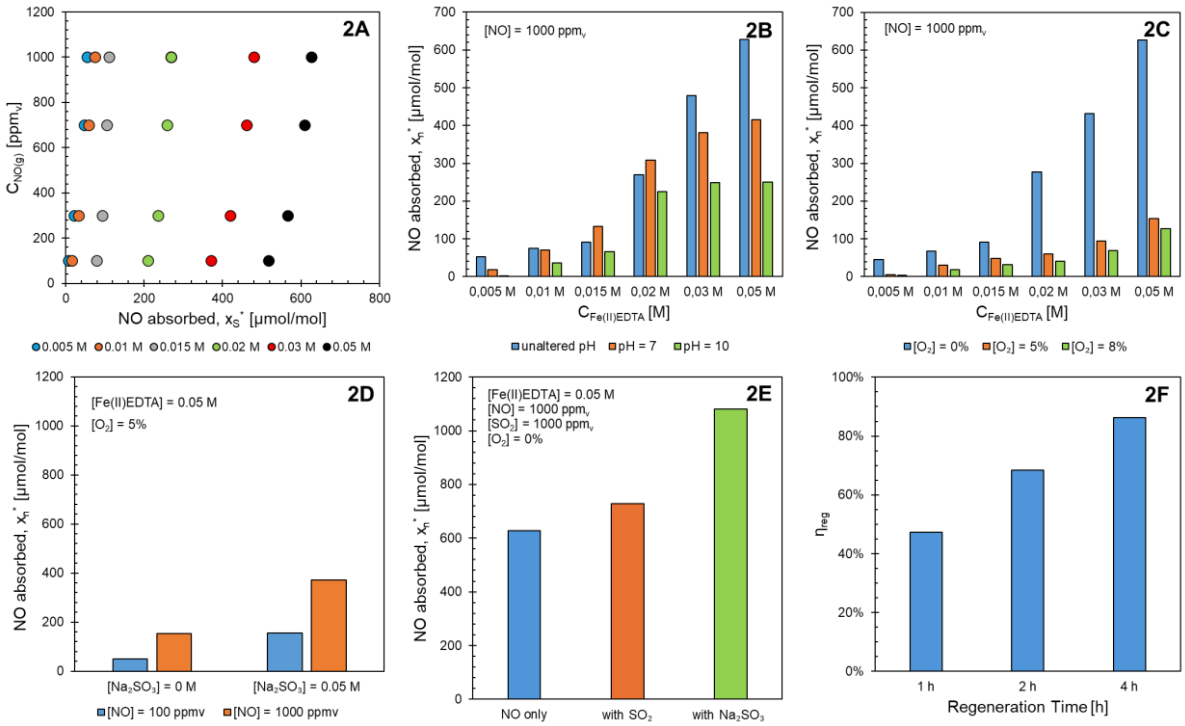

Figure 2. Experimental results: (A) absorption capacity *vs* NO and Fe(II)EDTA concentration; (B) absorption capacity *vs* Fe(II)EDTA concentration and solution pH; (C) absorption capacity *vs* Fe(II)EDTA concentration and $O_{2(g)}$ concentration; (D) absorption capacity *vs* NO concentration and sulfite concentration; (E) effect of the presence of $SO_{2(g)}$ and sulfite on absorption efficiency; (F) effect of process time on Fe(II)EDTA regeneration efficiency.

The addition of a stoichiometric amount of sodium sulfite to a 0.05 mol/L solution of Fe(II)EDTA restored the active form of the chelating agent, leading to a significant increase in NO solubility (**Figure 2D**), both in oxygen-free and oxygen-containing environments (5% v/v). This behavior confirms that sulfite effectively regenerates the active Fe(II)EDTA form in situ, consistent with the mechanisms proposed by Teramoto et al. (1978). Similarly, introducing SO_2 in the gas flow increased NO absorption capacity (**Figure 2E**), as dissolved SO_2 generated sulfite species in-situ. The presence of SO_2 in the gas stream enhances solvent regeneration, making this process a viable approach for the simultaneous removal of both pollutants.
Regeneration tests were performed in the same experimental set-up equipped with a stirring-heating plate to work at 40 °C and 600 rpm. In each test, a stoichiometric amount of sodium sulfite was added to exhausted Fe(II)EDTA samples and pH was adjusted to 7 with NaOH to prevent conversion to bisulfites. The regeneration efficiency (η_{reg}) was determined at different contact times by comparing the absorption capacity of the regenerated solution with that of the fresh solution. The results in **Figure 2F** showed that a regeneration efficiency of approximately 47% was achieved after 1 hour, increasing to 86% after 4 hours.

4. Conclusions

This work investigated the reactive absorption of nitric oxide in aqueous Fe(II)EDTA solutions, with particular focus on solvent stability and regeneration under conditions relevant to gas–liquid contactors.
The results confirm that Fe(II)EDTA enables efficient NO capture through reversible chelation, significantly enhancing absorption compared to conventional physical scrubbing. NO absorption increased with chelate concentration, consistent with a coordination-controlled mechanism, while elevated pH and the presence of oxygen strongly inhibited absorption due to oxidation of Fe(II) to Fe(III). However, the addition of sodium sulfite proved to be an effective reducing agent for restoring the active Fe(II)EDTA form and NO absorption capacity, even in the presence of oxygen, enabling cyclic operation. Similar improvements observed in the presence of SO_2 suggest that sulfite species generated in the liquid phase may contribute to sustained chelate regeneration during operation.
Regeneration tests demonstrated that a large fraction of the initial absorption capacity can be recovered within a few hours using a mixed contactor, supporting the feasibility of cyclic solvent use.
Overall, this study provides a coherent, capacity-based dataset and a mechanistic interpretation of the factors governing Fe(II)EDTA-driven NO capture, highlighting the potential of sulfite-regenerated chelation as a closed-loop, process-intensified alternative to conventional oxidizing scrubbing systems, capable of supporting the rational design of cyclic absorption–regeneration schemes while minimizing chemical consumption and washwater burden without compromising removal performance.

References

Ali, M., Hussain, I., Mehmud, I., Umair, M., Hu, S., & Sharif, H. M. A. (2021). Recent breakthroughs and advancements in NOx and SOx reduction using nanomaterials-based technologies: A state-of-the-art review. Nanomaterials, 11(12), 3301.

Bal Raj, D., & Neha, K. (2015). Simultaneous Removal of NO and SO_2 from Simulated Flue gas using Fe (II) EDTA coupled with Catalytic Regeneration. In Int. Res. J. Environment Sci. International Science Congress Association, 4(7), 63–69.

Flagiello, D., Di Natale, F., Lancia, A., Sebastiani, I., Nava, F., Milicia, A. & Erto, A. (2023). Experimental and modelling approach to the design of chemical absorption columns with fast gas-liquid reaction: A case-study on flue-gas desulfurization with H_2O_2 oxidative solutions. Chemical Engineering Research and Design, 194, 425–438

Flagiello, D., Di Natale, F., Sebastiani, I., Nava, F., Milicia, A., Lancia, A. & Erto, A. (2025). Experimental and modelling study of ammonia-based FGD scrubbers. Chemical Engineering Science, 305, 121101.

Hishinuma, Y., Teramoto, M., & Yoneyama, T. (1978). Absorption of nitric oxide by ferrous chelates. Industrial & Engineering Chemistry Process Design and Development, 17, 197–204.

Norvell, W. A., & Lindsay, W. L. (1967). Reactions of EDTA complexes with nitrogen oxides. Soil Science Society of America Journal, 31, 278–283.

Teramoto, M., Hiramine, S., Shimada, Y., Sugimoto, Y., & Teranishi, H. (1978). Absorption of Dilute Nitric Monoxide In Aqueous Solutions Of Fe(II)-EDTA And Mixed Solutions Of Fe(II)-EDTA And Na_2SO_3. Journal of Chemical Engineering of Japan, 11(6), 450-457.

Zhu, H. S., Mao, Y. P., Yang, X. J., Chen, Y., Long, X. L., & Yuan, W. K. (2010). Simultaneous absorption of NO and SO_2 into FeII-EDTA solution coupled with the FeII-EDTA regeneration catalyzed by activated carbon. Separation and Purification Technology, 74(1), 1–6.

Next Generation of structured packing for gas purification technology

Domenico Flagiello, Stefano Giovanni Acierno, Daniele Tammaro, Alessandro Erto, Pier Luca Maffettone, Amedeo Lancia, Francesco Di Natale*

Department of Chemical, Materials and Production Engineering
University of Naples Federico II, P.le Tecchio 80 – 80125, Naples, Italy

**Corresponding Author: domenico.flagiello@unina.it*

Abstract

Structured packings are key internals in gas-liquid contactors, where column performance results from the balance between pressure drop and mass transfer efficiency. Conventional corrugated-sheet packings provide high nominal surface area, yet under practical operating conditions only a fraction of this surface is effectively active due to liquid-film stabilization and maldistribution. Recent advances in additive manufacturing enable the fabrication of structured packings with precisely controlled geometries, opening new opportunities to optimize gas-liquid contact beyond the limits of conventional manufacturing. In this work, additively manufactured structured packings with engineered textures inspired by the basic design of the Mellapak 250Y are experimentally investigated in a pilot-scale DN100 packed column operated under counter-current flow. Dry and wet pressure drops are measured and combined with physical absorption experiments to evaluate hydraulic behavior and mass transfer performance in terms of height of a transfer unit (HTU) over a wide range of gas and liquid loads representative of industrial operation. The results demonstrate that 3D-printed structured packings closely reproduce the hydraulic performance of the commercial packing while achieving comparable or lower HTU values at similar pressure drops. These findings confirm that additive manufacturing can deliver effective gas-liquid contact without compromising hydraulic capacity, supporting its use as a viable design platform for next-generation structured packings aimed at process intensification.

Keywords

Structured packings; Additive manufacturing; Advanced textured surfaces; Gas-liquid absorption; Pressure drop; Mass transfer

1. Introduction

Packed columns are among the most established gas-liquid contacting technologies for absorption and related separation processes (Flagiello at el., 2021). Absorption is a continuous mass-transfer operation in which soluble gas components are transferred to a liquid phase of negligible volatility. Packed-column performance is governed by the quality of gas-liquid interfacial contact, which depends on operating conditions, liquid distribution, and packing geometry. Compared with trays, packed columns generally offer higher capacity and lower pressure drop, particularly in vacuum operation and small-diameter applications (Górak & Olujić et al., 2014). Structured packings are especially attractive because their regular corrugated geometry combines high void fraction with large nominal surface area, enabling high efficiency at relatively low pressure drop (Górak & Olujić et al., 2014). Their hydrodynamic and mass-transfer

behavior is controlled by key geometric parameters (corrugation height and base, sheet thickness and corrugation angle) which define channel topology and void fraction (Flagiello at el., 2021). Y-type packings (45° corrugation) generally provide higher efficiency than X-type (60°), at the expense of increased pressure drop (Olujić et al., 2000). Beyond intrinsic mass-transfer coefficients, the effective interfacial area available is a decisive factor. While correlations often rely on nominal geometric area (Flagiello et al., 2021; Wang et al., 2016), only a fraction becomes effectively wetted and mass-transfer active, being strongly influenced by wettability, film stability, and surface morphology. At the same time, hydraulic behavior is closely linked to void fraction, as reduced void fraction generally leads to increased pressure drop (Brunazzi & Paglianti, 1997). Consequently, intensification strategies must address the coupled trade-off between interfacial area enhancement and hydraulic capacity. Engineered surface textures provide a targeted means to modify liquid-film hydrodynamics and promote interfacial renewal without altering macroscopic packing geometry. Studies on gravity-driven liquid-films over textured substrates have shown that texture geometry governs vortex formation, stagnation zones, and free-surface deformation, with beneficial or adverse effects depending on configuration (Vlachogiannis & Bontozoglou, 2002; Pak & Hu, 2011; Tong et al., 2013; Li et al., 2015). Experimental work further indicates that textured surfaces can enhance liquid-side mass transfer with limited pressure drop penalties, mainly through increased wetted area and near-interface mixing (Kohrt et al., 2011; Yu et al., 2018). However, extending these mechanisms to real corrugated structured packings remains non-trivial due to three-dimensional flow redistribution effects.

In this context, Additive Manufacturing (AM) enables controlled fabrication of complex geometries and repeatable implementation of surface textures, facilitating systematic performance assessment (Sun et al., 2021). Preliminary investigations on corrugated sheets with 3D-printed triangular-step and wavy-triangular step textures reported measurable surface-area and mass-transfer enhancements (Flagiello et al., 2025), motivating their integration into full structured packings. The present work adopts a intensification strategy focused exclusively on surface optimization via engineered textures examining surface textures at sheet-scale proposed by Flagiello et al. (2025) to translate into measurable performance gains in full structured packing geometries. A Mellapak 250Y configuration is replicated as benchmark and modified with triangular-step and wavy-triangular step textures. Prototypes are fabricated by Fused Deposition Modeling (FDM) and tested in a pilot-scale absorption column through dry and wet pressure drop measurements and SO_2 absorption experiments using air-SO_2 mixture with acidic aqueous solution (pH = 2), enabling a consistent assessment of behavior on physical mass-transfer performance.

2. Experimental setup and methodologies

2.1 Packing Design, Additive Manufacturing and Surface Characterization

All packing components were designed in Autodesk Fusion 360® and exported as STL files for slicing in PrusaSlicer®. A benchmark smooth structured packing was inspired by the design of the Mellapak 250Y (Flagiello et al., 2021). The basic triangular unit was set to height corrugation H_c = 11 mm, slant corrugation S_c = 16 mm, base corrugation B_c = 24.5 mm, with sheet thickness packing sheet δ_p = 0.2 mm, using a channel-narrowing undulation of 3.5 mm. Each sheet was perforated with a regular array of holes of 3.5 mm, uniformly distributed on both slopes and the crest. Eight sheets were assembled in a Y-configuration θ_c = 45° with tangency points to improve mechanical integrity and trimmed into cylindrical modules with height of 111.5 mm. A truncated-cone base baffle (DN100 and thickness 1 mm) was introduced to reduce

wall-flow effects. Engineered surface textures were applied immediately after sheet extrusion and before perforation. Two patterns were implemented: a triangular step texture and a wavy-triangular step texture (Flagiello et al., 2025). Texture height was fixed at 0.5 mm, consistent with reported liquid-film thicknesses in packed columns (Trifonov, 2011). From CAD outputs, key geometric parameters were used to calculate void fraction (ε_p, m^3/m^3) and nominal surface area (a_n, m^2/m^3) following the same approach used by Flagiello et al. (2022;2023). once the perforation fraction has been set at Ω_p = 0.15 m^3/m^3, corresponding to a number of holes equal to 1840 per module. Packings were produced by FDM using a Prusa CORE One printer. White PLA filament (1.75 mm diameter) was selected. Printing parameters were optimized starting from a baseline configuration proposed by Flagiello et al. (2025) varying one parameter at a time (which, for the sake of brevity, are omitted from this document) until the prototype was fine-tuned to the required quality standards.
Surface morphology was characterized by confocal laser scanning microscopy (Leica DCM3D), extracting roughness factor (R_f) and S_{dr} which is the ratio of the rough area to the flat area used to calculate the real surface area ($a_{n,real}$). SEM imaging was performed on the same samples using a Hitachi TM3000 tabletop SEM with EDS. Images were collected at 200x (surface) and 50x (cross-section) and layer height and sheet thickness were measured via ImageJ® to validate printing fidelity. Surface wettability was assessed indirectly using the Wenzel model because sessile-drop imaging is unreliable on complex textures. This model was used to estimate the apparent contact angle from Young contact angle for PLA was treated as a fitted parameter (~68°) and measured roughness factor R_f from confocal profilometry.

2.2 Packed Column Facility and Experimental Plan

Hydrodynamic and absorption experiments were conducted in a modular DN100 Plexiglas packed column with a total height = 1.60 m and packing height Z = 0.892 m. For the sake of brevity, further details on the setup, auxiliary and measuring components, including experimental procedures, can be found in Flagiello et al. (2022;2023). Two experimental campaigns were carried out to investigate hydraulic and mass transfer performance of the printed packing. **Set A** focused on dry and wet pressure drop measurements using air-water system at 25 °C and 1 bar. Dry tests covered gas load factors F_G = 0.24 - 4.95 $Pa^{0.5}$, while wet tests were conducted at F_L = 8.35 - 58.26 m/h and F_G = 0.15 - 4.34 $Pa^{0.5}$. Generalized Pressure Drop Correlation (GPDC) by Eckert (1970) was used to back-calculate the packing factor F_p. **Set B** investigated SO_2 absorption tests at 25 °C and 1 bar, using acidified water to pH = 2 to suppress SO_2 dissociation and ensure physical absorption. The experiments were performed with three different gas velocity (u_G = 0.5, 1 and 2 m/s) with a range of SO_2 concentrations between 90 - 250, while liquid flow rate was varied between L = 60 - 360 L/h, yielding L/G = 1.00 - 28.21 L/m^3. Mass-transfer performance was analyzed using HTU-NTU method under dilute physical absorption assumptions with constant temperature and pressure. The Height of Transfer Unit (HTU, m) represents the overall resistance to mass transfer and can be estimated as HTU = Z/NTU (NTU, Number of Transfer Unit) according to Flagiello et al.(2023).

3. Results and discussion

3.1 Design, manufacture and surface characterization of structured packings

The benchmark shows a_n = 232 m^2/m^3 slightly below the nominal 250 m^2/m^3 of commercial M.250Y, as CAD estimates represent ideal geometry whereas real packings typically exhibit higher effective areas due to manufacturing-induced roughness. Introducing textures (**Figure 1**) increases a_n to 244 (triangular-step) and

245 m^2/m^3 (wavy-triangular step). Conversely, ε_p decreases slightly from 0.975 to 0.952 and 0.957 because textured geometries increase solid volume, while Ω_p remains constant since the same perforation pattern. Overall, texturing mainly impacts surface-related properties, with negligible effects on the bulk hydraulic geometry.

Figure 1. Pictures of the 3D-printed packing prototypes (with texture close-ups).

The final parameter set (not included for brevity) ensured accurate geometry reproduction of the benchmark and well-defined textures. Confocal microscopy provided 3D surface reconstructions enabling quantitative roughness and real-area assessment. The benchmark surface is essentially flat aside from intrinsic FDM roughness with a 16% increase, whereas both textured packings show regular height modulations. The triangular-step texture closely matches the nominal 0.5 mm height, consistent with more linear extruder motion; the wavy-triangular step exhibits slightly larger local deviations, attributable to higher geometric complexity and non-linear deposition paths, while still preserving the intended morphology. Roughness processing yields increasing S_{dr} from benchmark to triangular-step to wavy-triangular step indicates surface-area gains of ~27% (triangular-step) and ~35% (wavy) relative to the smooth reference. SEM analysis confirm high print quality and consistent layer height/sheet thickness across samples, with increased surface complexity for textured packings and slightly reduced local compactness for the wavy configuration. Apparent contact angles calculated via Wenzel model decrease from smooth to textured packings, indicating improved wettability driven by increased roughness/area. Improved wettability is expected to promote more uniform film spreading and stronger interfacial contact during column operation.

3.2 Hydrodynamic Performance

Dry pressure-drop measurements (data not reported) exhibited the expected monotonic increase of $\Delta P/Z$ *vs* F_G, in agreement with literature data for Mellapak 250Y-type packings (Spiegel & Meier, 1992; Brunazzi & Paglianti, 1997; Tsai et al., 2011). The textured prototypes showed slightly higher dry pressure drops respect with smooth benchmark, attributable to higher effective surface area and lower hydraulic equivalent diameter. Comparison among the three configurations (data not reported) reveals a progressive increase in dry pressure drop from the smooth benchmark to the triangular-step and wavy-triangular step packings. This trend reflects the combined effects of increased surface area, reduced void fraction and enhanced surface roughness, with the wavy-triangular step exhibiting the highest resistance due to its greater geometric complexity. Under irrigated conditions, wet pressure drop trends (**Figure 2**) show a linear dependence at low F_G and an exponential rise approaching loading region. Flooding pressure-drop values increase moderately with texturing, from ~49 mm_{H_2O}/m for the benchmark to ~55 and ~53 mm_{H_2O}/m for the triangular-step and wavy configurations, respectively. Despite its slightly higher void fraction, the wavy packing approaches loading earlier due to increased flow-path tortuosity and liquid

retention. Overall, the results demonstrate a systematic increase in hydraulic resistance with texture complexity, governed by the coupled effects of void fraction, surface morphology and liquid hold-up. Flooding data were analyzed using the Eckert GPDC which allowed extraction of characteristic packing factors F_p, which are 61, 68 and 74 1/m for smooth reference, triangular and wavy configurations.

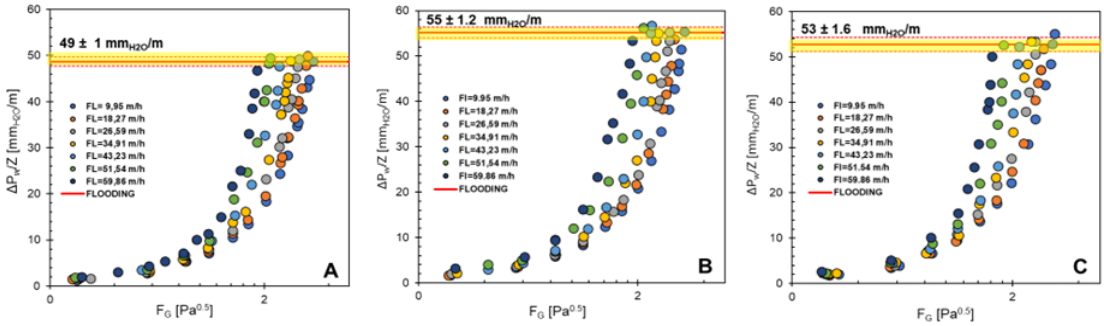

Figure 2. Wet pressure drops as a function of gas load (F_G) and parametric pressure drops as a function of liquid load (F_L). The yellow band indicates the flooding region and red line the flooding point. (A) smooth benchmark; (B) triangular-step; (C) wavy-triangular step.

The packing factor increased systematically from the benchmark to the textured configurations, reflecting the progressive increase in hydraulic resistance induced by surface texturing.

3.3 Mass Transfer Performance

For all packings, HTU decreased with increasing F_L, reflecting improved wetting and interfacial area (a_i). Conversely, at constant inlet concentration, increasing F_G led to higher HTU, as the increased solute concentrations outweighed the enhancement in gas-side mass-transfer coefficients. Across the entire operating range, the smooth packing consistently exhibited the highest HTU values, while the triangular and wavy-triangular step packings showed progressively lower HTU as shown in **Figure 3**, where HTUs are reported as band plots to account for the variability of F_G and $C°_{SO2}$. Under the same conditions, the wavy configuration provided the best performance, confirming the beneficial effect of increased surface area and improved wettability.

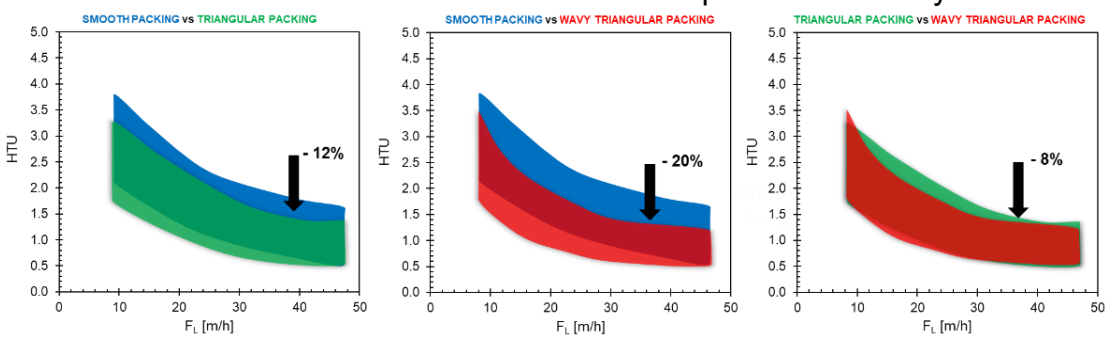

Figure 3. Heigh of Transfer Unit (HTU) as a function of liquid load (F_L) and parametric in gas load (F_G) and SO_2 inlet concentration ($C°_{SO2}$).

The reduction in HTU correlated well with the increase in real interfacial area estimated from confocal measurements, supporting the hypothesis that surface texturing primarily acts by enhancing effective wetted area and liquid-film renewal rather than by modifying intrinsic mass-transfer coefficients.

3.4 Performance Trade-Offs and Intensification Potential

The combined analysis of hydraulic and mass transfer performance show that the additively manufactured structured packing shifts the performance toward lower HTU

at comparable pressure drop, achieving improved mass transfer efficiency without additional hydraulic penalties. This behavior is particularly evident at intermediate gas and liquid loads, which are most relevant for industrial operation.

4. Conclusions

This study presents a comprehensive pilot-scale experimental assessment of additively manufactured structured packings for process intensification in gas-liquid processes. Experimental results demonstrate that 3D-printed structured packings closely reproduce the hydraulic behavior of a commercial M250.Y benchmark while achieving comparable or improved mass transfer performance. Dry and wet pressure drop measurements confirm that additive manufacturing and texture implementation does not inherently introduce additional flow resistance when packing geometry is appropriately designed. Absorption experiments show a consistent reduction in HTU, on the order of 10 - 20%, at comparable operating conditions, indicating enhanced gas-liquid contact efficiency. Overall, the findings support additive manufacturing as a viable and flexible design platform for next-generation structured packings, offering the potential for intensified gas-liquid absorption without compromising pressure drop. The results provide a robust experimental basis for further optimization and scale-up of advanced internals for industrial separation processes.

References

Brunazzi, E., & Paglianti, A. (1997). Mechanistic pressure drop model for columns containing structured packings. AIChE journal, 43(2), 317-327.

Eckert, J. S. (1970). Trays and packings: selecting the proper distillation column packing. Chem. Eng. Prog., 66, 39-44.

Flagiello, D. et al. (2021). A review on gas-liquid mass transfer coefficients in packed-bed columns. ChemEngineering, 5(3), 43.

Flagiello, D. et al. (2022). Foamed structured packing for mass-transfer equipment produced by an innovative 3D printing technology. CES, 260, 117853.

Flagiello, D. et al. (2023). Performances of a Y-type structured packing produced by 3D foam-printing for the intensification of gas absorption processes. ChERD, 195, 637-650.

Flagiello, D. et al. (2025). Mass transfer intensification by modifying structured packing surface properties produced with 3D foam-printing technology. Sep. Purif. Technol., 133911.

Górak, A., & Olujić, Ž. (2014). Distillation: equipment and processes. Academic Press.

Kohrt, M. et al. (2011). Texture influence on liquid-side mass transfer. ChERD, 89(8), 1405-1413.

Li, J. et al. (2015). Comparative study on the characteristics of film flow with different corrugation plates. Microgravity Sci. Technol., 27(3), 171-179.

Olujić, Ž. et al. (2000). Influence of corrugation geometry on the performance of structured packings: an experimental study. CEP:PI, 39(4), 335-342.

Pak, M. I., & Hu, G. H. (2011). Numerical investigations on vortical structures of viscous film flows along periodic rectangular corrugations. Int. J. Multiphase Flow, 37(4), 369-379.

Spiegel, L., & Meier, W. (1992). A generalized pressure drop model for structured packings. In Institution of Chemical Engineers Symposium Series Vol. 128, pp. B85-B85.

Sun, B. et al. (2021). Study on hydrodynamic performance of structured packings for gas-liquid flow: Effects of geometry parameters. ChERD, 167, 318-326.

Tong, Z. et al. (2013). Experimental and numerical investigation on gravity-driven film flow over triangular corrugations. Ind. Eng. Chem. Res., 52(45), 15946-15958.

Trifonov, Y. Y. (2011). Counter-current gas−liquid flow between vertical corrugated plates. CES, 66(20), 4851-4866.

Tsai, R. E. et al. (2011). A dimensionless model for predicting the mass-transfer area of structured packing. AIChE journal, 57(5), 1173-1184.

Vlachogiannis, M., & Bontozoglou, V. (2002). Experiments on laminar film flow along a periodic wall. J. Fluid Mech., 457, 133-156.

Wang, C. et al. (2016). Dimensionless models for predicting the effective area, liquid-film, and gas-film mass-transfer coefficients of packing. Ind. Eng. Chem. Res., 55(18), 5373-5384.

Yu, D. et bal. (2018). Experimental and CFD studies on the effects of surface texture on liquid thickness, wetted area and mass transfer in wave-like structured packings. ChERD, 129, 170-181.

Additively Manufactured Vacuum Distillation Columns for Hydrogen Peroxide: Experimental Demonstration and Feasibility for Direct Synthesis Integration

[1]Vignesh Jayavelu, [1]Till Peters, [1]Jaldip Suvagiya, [1]Manfred Kraut, [1]Roland Dittmeyer, [1,2]Christoph Klahn

[1]Institute for Micro Process Engineering, Eggenstein-Leopoldshafen, Germany
[2]Institute of Mechanical Process Engineering and Mechanics, Karlsruhe, Germany

Abstract

Hydrogen peroxide produced via alternative synthesis routes such as Direct Synthesis typically occurs at very low concentrations, thereby necessitating safe and efficient downstream upgrading for many practical applications. This work systematically investigates the distillation behavior of ultra-dilute aqueous H_2O_2 and clearly demonstrates the successful concentration of feeds as low as 1 mM (approximately 0.0034 wt%) using additively manufactured vacuum distillation columns. Three column types-namely passivated stainless steel, thermally passivated stainless steel, and resin-based columns were carefully evaluated under vacuum conditions (approximately 45 mbar), with thermally passivated stainless steel and resin columns showing significantly reduced thermal decomposition of H_2O_2 and achieving recoveries above 90%. The results further confirm that thin-walled additively manufactured structures enable stable vacuum operation and effective enrichment of highly dilute H_2O_2, especially the resin columns, with very high concentration efficiency (CE_R) in the residue, highlighting their potential as key components for integrating decentralized direct-synthesis processes with compact and sustainable downstream purification.

Keywords

Additive Manufacturing; Vacuum Distillation; Hydrogen Peroxide; Ultra-dilute Separation; UV Photopolymeric Resin

1. Introduction

Hydrogen peroxide (H_2O_2) is an environmentally benign and at the same time very strong oxidant. Its sole by-product is water, making it an important reagent within the principles of green chemistry. It is being used in various industries, for example the pulp and paper industries or in wastewater treatment [1]. Industrial H_2O_2 production is almost exclusively based on the anthraquinone oxidation (AO) process [2], which is economically favored only at large scales exceeding 40,000,t,a^{-1} [3]. As a consequence, production is centralized and energy intensive, associated with emissions, waste streams, and the transport and storage of concentrated and therefore hazardous H_2O_2 solutions [4, 5]. In addition, the product contains organic and inorganic impurities originating from the anthraquinone working solution, requiring multi-step purification and concentration processes such as distillation, ion exchange, membrane separation, or crystallization [4]. To overcome these limitations, extensive research has focused on alternative and potentially decentralized synthesis routes, including direct

catalytic synthesis from H_2 and O_2 [6], plasma-assisted processes [7], photocatalytic solar-driven production [8] and so on. While these approaches offer sustainability benefits, the achievable H_2O_2 concentrations are typically below 1 wt% [6, 7, 8]. Notably, even in the conventional AO process, H_2O_2 concentrations after oxidation are only 0.8–1.9 wt% [5], and commercial product grades of 35–70 wt% require extensive downstream processing. Efficient separation and concentration technologies are essential for future decentralized H_2O_2 production concepts. Here, additive manufacturing (AM) enables compact, microstructured distillation units with thin-walled, gas-tight geometries and enhanced mass transfer characteristics [9]. Hence, AM distillation columns therefore represent a promising platform for upgrading low-concentration H_2O_2 streams obtained from decentralized synthesis routes. However, thermal separation is inherently limited by the pronounced tendency of H_2O_2 to undergo exothermic decomposition ($2\,H_2O_2 \rightarrow 2\,H_2O + O_2\ \uparrow$), which is strongly accelerated at elevated temperatures and in the presence of trace metal ions. Catalytic decomposition on metallic surfaces poses a major challenge, as metal oxides can enhance degradation rates by several orders of magnitude. Consequently, low-pressure operation and effective surface passivation are essential. Nitric-acid passivation of stainless-steel 316L has been shown to significantly reduce catalytic activity by modifying surface roughness and oxide composition toward less reactive Cr(III) species [10]. In this work, vacuum distillation of highly dilute aqueous H_2O_2 solutions is investigated using additively manufactured (AM) columns of different material compositions. For the first time, enrichment of ultra-dilute H_2O_2 solutions on the order of 1 mM (≈0.0034 wt%) is demonstrated. Passivated stainless steel, thermally passivated stainless steel [10], and resin-based columns were evaluated, demonstrating effective upgrading of extremely dilute H_2O_2 streams under reduced pressure.

2. Materials and Methods

2.1 AM Distillation columns

The distillation column and its internals were AM in 316L stainless-steel using laser powder bed fusion (PBF-LB/M). In addition to the stainless-steel AM columns, a resin-based column produced via stereolithography (SLA) printing was included in the study. Both columns are shown in Figure 1. A gyroid-based internal structure was adopted due to its high specific surface area and liquid hold up for stable operation under vacuum. To ensure structural integrity, the column wall thickness was chosen to be 0.3 mm, and two AM-fabricated sections were combined to extend the effective separation height. A sump was incorporated to enable repeated recirculation of the bottom product and thereby increase H_2O_2 concentration. The resin-based column was selected not only for its chemical inertness toward H_2O_2, but also because its monolithic AM design eliminates sealing interfaces, thereby reducing leak risks under vacuum, while its compatibility with thin-walled geometries enables uniform heat transfer and stable vapor–liquid contacting.

Chemical passivation was performed following the industrial *Solvay* H_2O_2 passivation protocol, involving sequential rinsing and treatment with 30 % nitric acid to form a protective oxide layer [11]. In addition, a heated nitric-acid passivation procedure reported in the literature was applied. The columns were immersed in 45 wt% HNO_3 at 70 °C for 1 h, thoroughly rinsed with deionized water, and subsequently stabilized in 30 % H_2O_2

for 36 h. Between each step, the AM parts were dried at 50 °C for 24 h [10].

2.2 Description of Vacuum Distillation process

The process flow diagram of the distillation setup is shown in Figure 1. The bottom section of the column is connected to a reboiler equipped, and the bottom liquid is continuously circulated through the reboiler loop using a diaphragm pump to ensure stable enrichment. Vapor generated in the reboiler rises through the AM gyroid structures and is condensed after the top of the column. Non-condensable gases and residual vapor pass through a vacuum trap before being removed by a vacuum pump vented into a fume hood, ensuring safe off-gas handling. The bottom product stream is separated by a splitter and directed to the bottom-product receiver (H_2O_2). With this configuration, reliable vacuum operation at 40–45 mbar was achieved. Feed solutions ranging from 0.1 mM to 400 mM (0.0003–1.2 wt%) were processed in batch volumes of 200–500 mL. Prior to each experiment, the apparatus was sealed and leak-tested, after which the vacuum pump was activated. During operation, the reboiler temperature was maintained at approximately 60 °C, while the condenser temperature was controlled between -5 and 0 °C using a coolant loop. Once stable vacuum and temperature conditions were achieved, the feed was introduced into the midsection of the column at ambient temperature by exploiting the system's pressure difference. After stopping the feed, the reboiler was allowed to cool under vacuum before the system was repressurized. The collected products were analyzed by UV–Vis spectroscopy to quantify H_2O_2 concentrations. Prior to analysis, the samples were treated with potassium iodide, ammonium molybdate, and a phosphate buffer to form a yellow triiodide (I_3^-) species, which exhibits a characteristic absorption maximum at 350 nm [12]. For the evaluation, the concentration efficiency in the residue, CE_R, was introduced to combine enrichment and overall H_2O_2 conservation:

$$\mathrm{CE}_R = \frac{Rx_r}{Fx_f} \cdot \frac{Rx_r + Dx_d}{Fx_f} = \frac{Rx_r}{Fx_f} \cdot Rec \tag{1}$$

where x_f, x_r, and x_d denote the H_2O_2 mass fractions in the feed, residue, and distillate, respectively, and F, R, and D are the corresponding total masses. The first factor in Eq. (1) reflects how much of the feed H_2O_2 ends up in the residue (enrichment), while the second factor accounts for the total recovered H_2O_2 (distillate plus residue), thus capturing losses due to decomposition.

3. Results and Discussion

3.1 Vacuum Distillation Performance

Vacuum distillation experiments were performed using AM gyroid distillation columns. Initial experiments conducted without stabilizers revealed a strong dependence of H_2O_2 recovery on operating pressure. As the vacuum pressure increased, the recovery of H_2O_2 in the residue decreased significantly, particularly at low feed concentrations. At pressures above approximately 60 mbar, the rate of thermal and catalytic decomposition dominated the distillation process, resulting in negligible enrichment. The effect of pressure was especially pronounced in the low-concentration regime. For feed concentrations below approximately 10 mM, meaningful enrichment was only observed when the column was operated at pressures of 45 mbar or lower. At higher pressures, the

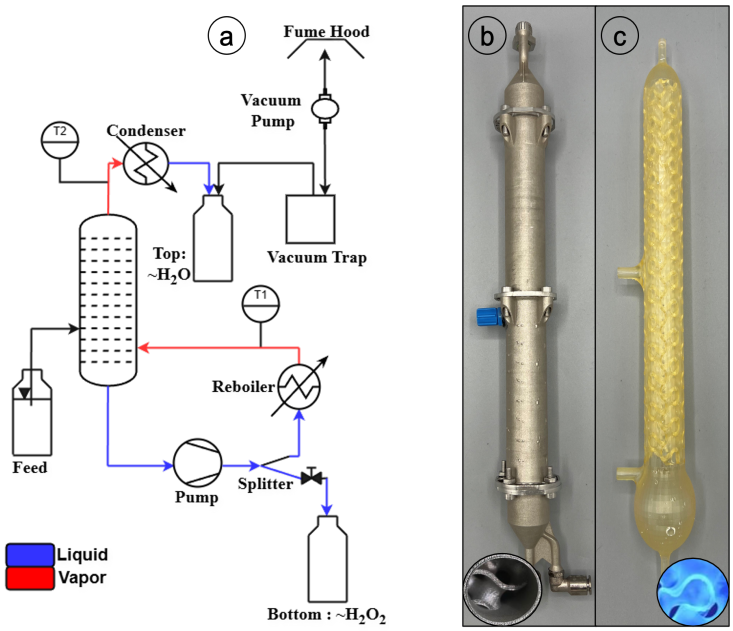

Figure 1: (a) Process flow diagram of the vacuum distillation setup used for concentrating dilute aqueous H_2O_2 solutions and photographs of the additively manufactured distillation columns with their internal structure below: (b) assembled stainless-steel column, (c) single photopolymeric resin column.

distillation effect was effectively suppressed, as decomposition losses outweighed any separation-driven concentration. To suppress decomposition, phosphoric acid was introduced as a stabilizer at a concentration of 0.02 v/v % in the feed. The addition of stabilizer improved H_2O_2 recovery at moderate feed concentrations, particularly above 10 mM, where distillation-driven enrichment became observable. However, even with stabilizer addition, the recovery remained poor at feed concentrations close to 1 mM, indicating that decomposition effects could not be fully eliminated in this ultra-dilute regime. At very low concentrations, the limited performance is attributed to the higher surface roughness and increased density of catalytically active sites inherent to AM stainless steel, which promote heterogeneous H_2O_2 decomposition and outweigh the benefits of pressure optimization and stabilizer addition, thereby motivating the investigation of alternative column materials in the following subsection.

3.2 Effect of Surface Passivation and Column Material

The influence of column material and surface treatment on H_2O_2 recovery becomes increasingly critical as the feed concentration decreases into the millimolar regime. Figure 2 illustrates the H_2O_2 recovery obtained using AM stainless-steel columns subjected to standard chemical passivation and heated nitric-acid passivation, respectively. For feed concentrations above approximately 10 mM, the heated passivation procedure leads to a noticeable improvement in recovery compared to conventional passivation, as shown in Figure 2. This behavior is consistent with a reduction in catalytically active surface sites on the stainless-steel substrate as explained in the introduction. As a result, the rate of heterogeneous H_2O_2 decomposition is sufficiently suppressed for the distillation process to dominate over degradation in this concentration range. However, at lower feed concentrations approaching 1 mM, Figure 2 shows that even the heated-passivated stainless-steel column fails to maintain acceptable recovery. Un-

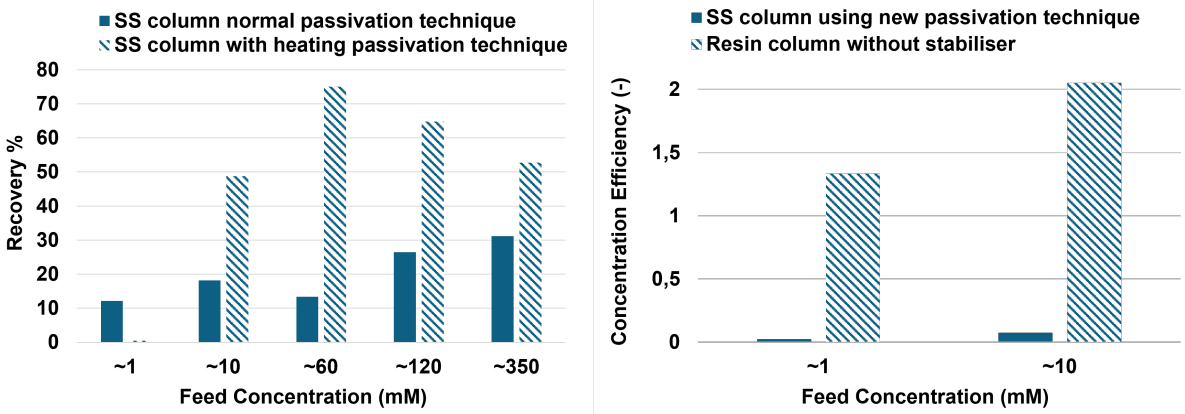

Figure 2: Left - Graph showing the comparison of Recovery in Vacuum distillation with (1) Stainless Steel Column with normal Passivation (2) Stainless Steel Column with normal Passivation: Right - Graph showing the comparison of Concentration Efficiency (CE_R) of distillation with (1) Stainless Steel Column with Heated Passivation (2) UV high Temperature Photo resin without Stabilizers

der these conditions, the absolute amount of H_2O_2 present in the system becomes sufficiently small that residual catalytic activity at the metal surface still governs the overall mass balance. Consequently, the rate of decomposition exceeds the rate of enrichment, rendering stainless steel unsuitable for ultra-dilute H_2O_2 distillation despite advanced passivation strategies.To overcome this limitation, the metallic column was replaced by a UV-curable high-temperature photopolymer resin column fabricated via stereolithography. In contrast to the metal-based designs, the resin column exhibited stable vacuum operation down to approximately 20 mbar and enabled successful concentration of feed solutions with initial H_2O_2 concentrations as low as 1 mM without the use of stabilizers. The resulting improvement in separation performance is captured by the concentration efficiency in the residue (CE_R), shown in Figure 2. Across the investigated concentration range, the resin column exhibits a consistently higher CE_R than the heated-passivated stainless-steel column, with the difference becoming particularly pronounced in the ultra-dilute regime. This trend reflects not only reduced decomposition losses but also improved separation effectiveness, indicating that the absence of catalytically active metal surfaces fundamentally shifts the process balance in favor of distillation. Overall, the comparative results shown in Figure 2 demonstrate that material selection outweighs passivation strategy when targeting the concentration of ultra-dilute H_2O_2 solutions. While surface-treated stainless steel may be suitable for moderate concentrations, resin-based AM columns are essential for extending vacuum distillation into the millimolar concentration regime relevant to modern decentralized H_2O_2 synthesis routes. These results indicate that, under ultra-dilute conditions, material-induced catalytic decomposition outweighs further gains achievable through pressure reduction or stabilizer addition.

4. Conclusion and Outlook

The results show that distillation can be extended into the millimolar concentration regime when low-pressure operation is combined with appropriate material selection and surface treatment is decisive for treating ultra-dilute H_2O_2 solutions. Experiments

with additively manufactured stainless-steel columns confirmed that vacuum operation below approximately 45–50 mbar is required to limit thermal degradation. While chemical and thermally enhanced nitric-acid passivation improved H_2O_2 recovery at moderate feed concentrations, stainless-steel remained unsuitable for feeds close to 1 mM due to residual catalytic decomposition, even in the presence of stabilizers. In contrast, resin columns enabled stable vacuum operation and effective enrichment of H_2O_2 at feed concentrations as low as 1 mM without stabilizers. The resin columns consistently showed higher concentration efficiency and reduced decomposition losses, highlighting the critical role of eliminating catalytically active metal surfaces in ultra-dilute H_2O_2 distillation. Overall, the study confirms that material-aware design of AM distillation hardware is essential for upgrading low-concentration H_2O_2 streams relevant to emerging decentralized production routes. Future work should focus on optimizing column geometry and internal structures to further enhance mass transfer while minimizing liquid residence time under vacuum conditions. In parallel, the long-term chemical stability and mechanical integrity of resin columns in contact with H_2O_2 must be systematically evaluated. Furthermore, research should be done exclusively on the energy demand to make sure the process is also economically feasible.

References

[1] Laura G. Covinich, Dora I. Bengoechea, Rosa J. Fenoglio, and María C. Area. Advanced Oxidation Processes for Wastewater Treatment in the Pulp and Paper Industry: A Review. *American Journal of Environmental Engineering*, 4(3):56–70, June 2014.

[2] W. Eul, A. Moeller, and N. Steiner. *Hydrogen Peroxide*. John Wiley Sons, Ltd, 2001.

[3] Chanchal Samanta. Direct synthesis of hydrogen peroxide from hydrogen and oxygen: An overview of recent developments in the process. *Applied Catalysis A: General*, 350(2):133–149, November 2008.

[4] Yanhui Yi, Li Wang, Gang Li, and Hongchen Guo. A review on research progress in the direct synthesis of hydrogen peroxide from hydrogen and oxygen: noble-metal catalytic method, fuel-cell method and plasma method. *Catalysis Science & Technology*, 6(6):1593–1610, 2016.

[5] Jose M. Campos-Martin, Gema Blanco-Brieva, and Jose L.G. Fierro. Hydrogen peroxide synthesis: An outlook beyond the anthraquinone process. *Angewandte Chemie - International Edition*, 45(42):6962–6984, October 2006.

[6] Richard J. Lewis and Graham J. Hutchings. Recent Advances in the Direct Synthesis of H_2 O_2. *ChemCatChem*, 11(1):298–308, January 2019.

[7] Shuang Liang, Qi Wu, Changhua Wang, Rui Wang, Dashuai Li, Yanmei Xing, Dexin Jin, He Ma, Yichun Liu, Peng Zhang, and Xintong Zhang. Sustainable H_2 O_2 production via solution plasma catalysis. *Proceedings of the National Academy of Sciences*, 121(34):e2410504121, August 2024.

[8] Yasuhiro Shiraishi, Takumi Hagi, Masako Matsumoto, Shunsuke Tanaka, Satoshi Ichikawa, and Takayuki Hirai. Solar-to-hydrogen peroxide energy conversion on resorcinol–formaldehyde resin photocatalysts prepared by acid-catalysed polycondensation. *Communications Chemistry*, 3(1):169, November 2020.

[9] Fabian Grinschek, Amal Charles, Ahmed Elkaseer, Christoph Klahn, Steffen G. Scholz, and Roland Dittmeyer. Gas-tight means zero defects - design considerations for thin-walled fluidic devices with overhangs by laser powder bed fusion. *Materials & Design*, 223:111174, 2022-11.

[10] Hyunwoo Son, Cheoljung Yum, and Youngbo Choi. Effects of nitric acid passivation on the physicochemical properties of stainless steel 316 and its reactivity with highly concentrated hydrogen peroxide. *Surface and Coatings Technology*, 449:128951, November 2022.

[11] Solvay. H_2O_2 Passivation Procedure. `https://www.solvay.us/en/binaries/HH-056_Passivation236794.pdf`, 2025. Accessed: 2025-12-09.

[12] Junyang Xiao, Mengyun Wang, Zijun Pang, Lin Dai, Jinfeng Lu, and Jing Zou. Simultaneous spectrophotometric determination of peracetic acid and the coexistent hydrogen peroxide using potassium iodide as the indicator. *Analytical Methods*, 11:1930–1938, March 2019.

Innovative Approaches to Process Development for Fluid Separation in the Chemical Industry

Maria Polyakova [a], Marcus Grünewald [a]

[a] Ruhr University Bochum, Laboratory of Fluid Separations, Universitätsstrasse 150, 44801 Bochum, Germany
polyakova@fluidvt.rub.de; gruenewald@fluidvt.rub.de

Abstract. Process development in the chemical industry is undergoing a significant transformation driven by sustainability targets, increasing digitalization, and the demand for energy-efficient separation technologies. While conventional unit operations such as distillation and absorption remain indispensable, their current industrial implementation is increasingly challenged by rising energy costs, associated CO_2 emissions, operational complexity, and scale-up limitations. This paper presents emerging methodologies for fluid separation process development that includes decision support systems, miniaturized experimental approaches, early-stage heat integration, and innovative measurement techniques. Together, these elements form an integrated development framework that enables faster, more reliable, and more energy- and resource-efficient process design. The proposed strategies demonstrate clear potential for reducing energy demand and associated CO_2 emissions, while increasing flexibility in handling complex and non-conventional feed streams.

All rights reserved by the authors as per DA2026 copyright notice.

Keywords miniaturized measuring cell, Sustainable process development, energy-efficient separations, distillation and absorption, early-stage heat integration, digital decision support systems

1. Introduction

Fluid separation processes are at the core of the chemical and process industries, accounting for a substantial share of both capital investment and operational energy demand. Among these, distillation and absorption dominate industrial applications due to their robustness, maturity, and broad applicability. However, these unit operations are responsible for a significant fraction of industrial energy consumption, making them a central focus of sustainability-driven innovation. Distillation alone consumes over 2,200 trillion British thermal units (TBtu) per year in manufacturing, with approximately 40,000 distillation columns operating worldwide, and represents roughly 40% of total energy consumption in the chemical industry. [1]

In recent years, the boundary conditions for process development in EU have shifted considerably. Increasing regulatory pressure to reduce greenhouse gas emissions, rising energy costs, and the growing use of renewable and circular feedstocks demand new approaches to separation process design. The European Union has established legally binding climate targets as codified in the European Climate Law, which sets an intermediate goal of reducing net greenhouse gas emissions by at least 55% by 2030 (compared to 1990 levels) and achieving net-zero emissions by 2050 [2]. These ambitious climate commitments position separation technologies as critical enablers of industrial decarbonization, particularly as separation processes account for 40–70% of both capital and operating costs while consuming approximately 45% of all process energy in the chemical and petroleum refining industries.

Simultaneously, digitalization has opened new opportunities for accelerating development through advanced modelling, data analytics, and automation. Machine learning-assisted solvent screening and artificial intelligence-driven process design have emerged as transformative tools for optimizing separation processes, while hybrid modelling approaches that combine first-principles mechanistic knowledge with data-driven techniques enable improved process control, predictive accuracy, and operational efficiency [3]. Furthermore, the integration of renewable and circular feedstock, including biomass, recycled carbon, and CO_2 valorization pathways—requires chemical engineers to adopt entirely new process design paradigms centered on waste-to-resource conversion and circular economy principles.

Conventional process development workflow which often characterized by sequential experimentation, conservative scale-up rules, and late-stage energy optimization—are no longer sufficient to meet these challenges. Instead, integrated development strategies are required that combine digital decision-making tools, efficient experimental methods, and early consideration of energy efficiency.

This paper discusses new approaches in process development strategies for fluid separations, such as:

- Decision support systems for accelerated and informed process design
- Miniaturized and simplified laboratory experiments
- Early-stage heat integration and energy-aware design
- Innovative measurement and monitoring techniques

By combining these elements into a unified framework, process developers can achieve more sustainable, flexible, and competitive separation processes. The present work emphasizes the pivotal role of miniaturized measurement cells as enabling platforms that bridge the gap between fundamental laboratory research and practical industrial implementation, particularly when coupled with techno-economic assessment and decision-support methodologies.

2. New sustainable process design strategies

All generated information like MMC based hydrodynamic and model parameters, QΔT derived heat integration metrics, and techno economic indicators is finally consolidated in the DSS. Within this environment, alternatives such as different packings, distributor designs, column configurations, or hybrid separation schemes are represented by a common set of performance, energy, and cost metrics. Automated workflows link MMC data processing, simulator execution, QΔT box construction, and multi criteria evaluation, enabling consistent ranking and screening of design options under user defined objectives and constraints (e.g., minimum energy use at given purity, or minimum cost at given CO_2 footprint). In the following sections, each methodological pillar—miniaturized measurement cells and innovative measurement techniques, early-stage heat integration via QΔT boxes, and the decision support system—is described in more detail.

2.1 Miniaturized Measurement Cells and innovative measurement techniques in Modern Process Development

The classical approach to separation process development relies on sequential steps: laboratory screening → pilot plant demonstration → full-scale commissioning. Each transition introduces substantial uncertainty and cost. Laboratory columns (typically 0.01–0.1 m internal diameter) exhibit pronounced wall effects, axial dispersion, and nonuniform initial liquid distribution, while pilot plants (0.3–1.5 m diameter) approach industrial conditions but demand large material inventories and utility consumption. This discontinuity has two critical consequences: (1) insights from lab scale do not consistently translate to pilot or full scale due to scale-dependent phenomena, and (2) the cost and time burden of pilot-scale campaigns limits the number of design alternatives that can be explored.

Traditional model-based scale-up, which relies on equilibrium-stage or rate-based approaches, implicitly assumes that processes follow pseudo-steady behavior. In reality, structured packings and other phase-contact devices exhibit complex hydrodynamic phenomena like rivulet formation, maldistribution, wall channeling, and local unsteadiness—that are difficult to predict and highly sensitive to operating conditions and fluid properties. Established design methods predominantly rely on integral quantities such as pressure drop, liquid hold-up, and height equivalent to a theoretical unit, but they do not resolve local effects e.g. film thickness distribution, which critically determine separation efficiency and flooding behavior.

Miniaturized measurement cells (MMCs) represent a new approach in this traditional workflow. Rather than viewing process development as a binary choice between lab and pilot scale, miniaturized cells create an intermediate, high-fidelity experimental platform that retains the cost-efficiency and flexibility of laboratory work while capturing the hydrodynamic complexity of industrial equipment.

A miniaturized measurement cell is a compact experimental apparatus, that reproduces the key geometric and flow features of industrial equipment (e.g., a cross-section of a structured packed column) while maintaining:

- Geometric representation (industrial packing)
- Well-defined and reproducible boundary conditions
- Small material inventory (often 10–50× reduction vs. pilot scale)
- Enhanced optical and physical access for advanced measurement

At Ruhr University Bochum we developed two experimental cell designs that exemplify the range of miniaturized approaches applicable to separation process development. Both cells target investigation of structured packings in distillation and absorption, but differ in their geometric configuration and measurement scope.

The first miniaturized cell for absorption is dedicated to detailed characterization of liquid film behavior on structured packing surfaces. It provides high spatial and temporal resolution data essential for understanding local

hydrodynamics in multiphase flow. The cell (width ≈ 0.3 m, height ≈ 0.2 m) accommodates three Montz Pak B1-250 structured packing sheets. This arrangement maintains representative interactions between adjacent channels, wall regions, and distributor flows—factors that strongly influence effective liquid distribution and mass transfer. To mimic realistic wall conditions, a 6 mm peripheral gap equipped with a wall-wiping device ensures wetting uniformity and controlled redistribution near the column boundaries. To provide further information for process development, the cell is embedded with a conductivity film thickness sensor at four locations: one on each lateral wall, one near the distributor inlet, and one at the packing outlet (see Figure 1). The system applies an alternating electrical field across transmitter-receiver pairs, measuring the resulting current that depends on both the local film thickness and the liquid's conductivity. The cell produces quantitative maps and statistical analyses describing key hydrodynamic features:

- 2D Film Thickness Fields: Reveal the spatial distribution of liquid and identify local dry spots or over-wetted zones.
- Mean Film Thickness and Spatial Variability: Quantify average wetting behaviour and characterize uniformity over the structured surface.
- Temporal Fluctuation Intensity: Highlights dynamic aspects of film motion including surface waves and instabilities.
- Wetting Fraction: Defines the proportion of the surface effectively covered by liquid (>0.1 mm film thickness).
- Wall Flow Characterization: Assesses wall wiper efficiency and wall channelling development across gas load conditions.

From a process development perspective, this cell provides direct experimental inputs for validating computational fluid dynamics (CFD) models and for improving correlations. Engineers can use the measured wetting patterns and unsteady film motion data to refine models of effective interfacial area and to optimize packing designs or distributor geometries before pilot-scale testing.

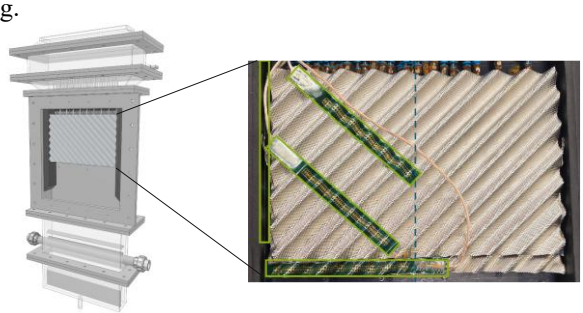

Figure 1: Miniaturized measurement cell with film thickness sensor

While MMC for absorption focuses on local hydrodynamics, the MMC for distillation aims to couple these flow characteristics with actual separation performance—serving as a bridge between fluid mechanics and process-level functionality. This integrated cell is designed to quantify how patterns, distribution quality, and surface wetting directly influence mass transfer rates and efficiency. Its relatively compact geometry (0.1–0.3 m wide, containing 1–3 structured packing layers) provides information for scale-up.

2.2 Early-Stage Heat integration

Heat integration is one of the most effective levers for reducing energy consumption in energy-intensive industries such as chemicals, refining, pulp and paper, and food processing. Pinch-based process integration routinely identifies 20–40% reductions in hot and cold utility demand for large plants, translating directly into lower operating costs and greenhouse-gas emissions. Because separation systems—especially distillation—account for a major share of process heat use, failing to exploit this potential locks in high operating costs and a large carbon footprint for decades. [4]

The classic "onion diagram" for process design places core reaction and separation systems at the center, surrounded by heat recovery (heat exchanger networks) and finally utilities. In many conventional workflows, process engineers first fix reactors and separation trains on the basis of conversion, selectivity, and product purity, then treat heat integration as a separate, downstream task. This sequencing creates design lock in: operating pressures, temperature levels, and stream structures that are poor candidates for heat recovery become very expensive to change later. [4]

Comparative studies consistently show that grassroots designs that incorporate heat integration from the outset achieve substantially larger energy savings than retrofits of existing plants. Pinch based grassroots design exploits the full temperature span between the coldest cold streams and hottest hot streams, enabling high levels of heat recovery

and optimized utility levels. Retrofitting, by contrast, is constrained by existing equipment, plot space, and safety systems, often limiting the economically achievable savings to a fraction of the theoretical potential.

Early-stage heat integration for distillation has traditionally been addressed either through analytical lower bounds and heuristic sequence generation, as in the utility-bounding approach of Andrecovich and Westerberg, or via interactive visual tools that link process design to heat-exchanger network synthesis, such as the T–Q visualization framework proposed by Fraga and co-workers. In parallel, recent industrial practice has demonstrated how simple temperature–duty "boxes" for individual columns can be moved in T–Q space by adjusting operating pressures to identify promising heat-integration pairings. Building on these foundations, the present work develops an automated, simulator-driven QΔT-box methodology that embeds column-level energy targeting directly in the early selection of distillation sequences. [5]

In the original method of Andrecovich and Westerberg [5], each distillation "task" (sharp two-product split) is represented as a rectangle on a T–Q diagram, where the rectangle height is the temperature span between reboiler and condenser and the width corresponds to the heat duty. The key assumption is that the product QΔT (the condenser or reboiler duty times the temperature difference between condenser and reboiler) for a given separation task can be treated as approximately constant over a wide pressure range. This allows multieffect structures and entire sequences to be synthesized by "stacking" such rectangles between given utility temperature limits in a way that minimizes net utility use; sequences are ranked by a lower bound on utility consumption derived from the sum of QΔT values across all tasks. Fraga et al. [6] later recast this box-stacking idea as part of an interactive heat-integration environment, describing how the heating and cooling requirements of each column define a box in a two-dimensional temperature–duty space that can be moved vertically (changing pressure) and horizontally (changing degree of process integration), with the goal of stacking boxes to represent inter-column heat exchange.

However, both approaches deliberately simplify the impact of pressure on column duties and temperature spans, and assume relatively simple column configurations (one condenser and one reboiler). The industrial methodology of Rix et al. [7] adopts a more pragmatic stance: individual columns are "removed from the background process and drawn as simple boxes in a temperature-duty diagram," and their operating pressures are then adjusted so that the top temperature of a heat-supplying column can reboil a heat-receiving column, thereby enabling inter-column heat integration. This representation is used to screen column pairings, but the detailed column behavior is still treated largely through heuristic adjustment and subsequent simulation.

The approach developed in the present work combines the conceptual simplicity of QΔT boxes with rigorous column simulations and full automation. For each candidate distillation sequence generated by conventional heuristics or algorithmic sequence synthesis, the individual column blocks are modelled in Aspen Plus using appropriate vapor–liquid equilibrium and hydraulic models. For a given set of operating pressures, the column condenser and reboiler duties, as well as corresponding temperatures, are extracted directly from the converged simulations. Each column is then summarized by a QΔT box whose vertical extent spans from condenser to reboiler temperature and whose horizontal width is proportional to the heat duty; the enclosed area provides a direct measure of QΔT for that column, analogous to the T–Q rectangles used by Andrecovich and Westerberg [5] . Because these quantities are computed at the actual operating pressure for each column, no assumption of pressure-independent Q or ΔT is required.

Once the QΔT boxes for all columns in a candidate sequence are available, an automated "box-stacking" procedure is applied. In analogy to Andrecovich and Westerberg's multieffect distillation constructions and Fraga's interactive visual T–Q tool, the boxes are translated vertically by systematically varying column pressures within feasible bounds (defined by utility temperatures, critical temperatures, allowable vacuum or overpressure limits, and product specifications). For each pressure configuration, the algorithm evaluates whether a high-temperature column box can be positioned above a lower-temperature box with a sufficient driving force to allow inter-column heat exchange; this is done by checking overlaps in the temperature intervals and computing the fraction of the higher-temperature condensation duty that can, in principle, be used to reboil the lower-temperature column without violating minimum approach temperature constraints. Additional constraints, such as avoiding operation across process pinch points identified in a background composite curve, can be incorporated at this stage.

This automated exploration yields, for every candidate sequence, a set of feasible pressure combinations together with corresponding metrics of heat-integration potential—for example, the maximum recoverable fraction of total reboiler duty within the column system, the minimum achievable net hot and cold utility demands consistent with the QΔT stacking, or a simple lower bound on net utility derived from sequence-level ∑QΔT values as in the original utility-bounding method. Importantly, these metrics are computed even if the resulting column pressures are not individually optimal for separation, in the sense of minimizing total annualized cost or reflux duty at the column level. Instead, the QΔT-box analysis introduces an explicit second criterion in sequence selection: sequences are ranked not

only by separation performance and base-case energy consumption, but also by their intrinsic early-stage potential for heat integration under realistic pressure adjustments.

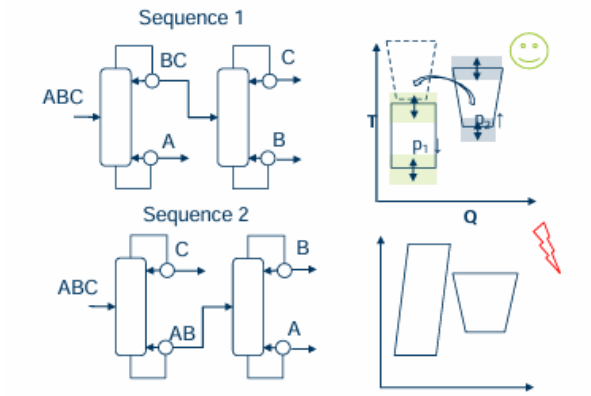

Figure 2: This simple visualization shows that sequence 1 offers higher potential for heat integration than sequence 2

The entire workflow is implemented within Aspen Plus using its automation capabilities, so that generation of sequences, column simulations, extraction of condenser/reboiler data, construction of QΔT boxes, and evaluation of stacking configurations are executed without manual intervention. This stands in contrast to the largely manual graphical procedures of both Andrecovich and Westerberg and Fraga et al., where box positioning and stacking are guided interactively by the designer. At the same time, the methodology remains closely aligned with industrial practice as described by Rix et al.: columns are treated as simple temperature–duty boxes whose positions in T–Q space are shifted by pressure changes, but in the present work this practice is systematized and embedded in a quantitative, simulator-based decision-support framework.

In summary, the QΔT-box approach developed here can be viewed as an automated, rigorously evaluated realization of the early graphical ideas of Andrecovich, Westerberg, and Fraga, and of the temperature–duty box heuristics used in industrial heat-integrated column design. By coupling Aspen Plus column models to a pressure-adjusted QΔT stacking algorithm, it enables designers to discriminate between distillation sequences not only on the basis of separation performance and base-case energy use, but also on their latent capacity for heat integration at an early stage of process development. This provides a powerful additional selection criterion that is fully consistent with the overarching objective of energy-aware, decarbonization-driven process synthesis laid out in the introduction.

2.3 Decision Support System (DSS)

Digital decision support systems (DSS) provide the integrative layer that connects miniaturized experimentation, detailed process simulation, techno-economic analysis (TEA), and early-stage heat integration into a coherent process development workflow. Rather than treating these elements as isolated tasks, a DSS encodes them as coupled models and criteria, enabling transparent comparison of alternatives and systematic identification of high-value design directions. In the context of fluid separations, this means that laboratory data (e.g., from miniaturized measurement cells), process models, and energy-integration metrics (e.g., QΔT-box derived heat-integration potential) are evaluated consistently against economic and sustainability targets.

In general, DSS for process design build on the long tradition of computer-aided process engineering, where flowsheeting tools, optimization algorithms, and expert rules are combined to support complex decisions that involve conflicting criteria and large design spaces. Early applications in process design and selection already demonstrated how integrated decision tools can screen flowsheets, size units, and rank alternatives for hybrid membrane systems by combining performance models with economic evaluation and heuristic rules. More recent work in process simulation emphasizes the role of commercial simulators (Aspen Plus, gPROMS, etc.) as a backbone, with customized models and interfaces for membrane operations such as pervaporation and membrane distillation, and highlights their potential for systematic process synthesis and intensification when embedded in a broader decision framework.

While the framework was initially demonstrated for distillation and absorption, its modular structure readily accommodates emerging non-equilibrium separation technologies such as pervaporation. In contrast to distillation, pervaporation involves coupled heat and mass transfer through a selective membrane driven by a vapor pressure gradient rather than vapor–liquid equilibrium. Consequently, early-stage process development for pervaporation benefits substantially from the same principles—miniaturization, precise measurement, digital coupling, and early energy integration—but with adjusted experimental and modeling elements.

This integrated system transforms process development from a sequential to a concurrent, data-driven activity. Early-stage decisions—such as solvent choice, packing design, or membrane material selection—can be evaluated not only with respect to technical feasibility but also energy efficiency and environmental impact. The methodological coherence across distillation, absorption, and pervaporation ensures comparability of results and supports systematic hybrid process design.

3. Conclusions and Outlook

The paper demonstrates that integrating miniaturized experiments, early heat-integration targeting, and digital decision support enables faster, more energy-efficient, and sustainability-oriented development of fluid separation processes. Miniaturized measurement cells provide high-resolution hydrodynamic data at low material and utility demand, improving scale-up and model validation for structured packings in distillation and absorption. Automated QΔT-box analysis embeds heat-integration potential directly into sequence synthesis, allowing designers to rank alternatives not only by separation performance but also by their intrinsic capacity for utility reduction. The decision support framework links these experimental and simulation tools with techno-economic and environmental criteria, turning process development from a sequential into a concurrent, data-driven activity.

Future work should couple miniaturized measurement data more tightly with machine-learning-assisted models to enhance predictive accuracy and robustness under variable operation. Extending the framework to emerging non-equilibrium separations such as pervaporation or electro-driven processes will require tailored experimental cells and models, but follows the same guiding principles of miniaturization, digital integration, and early energy targeting. In the longer term, embedding these elements into plant-wide digital twins could enable semi-autonomous, sustainability-optimized separation process design across the chemical industry.

REFERENCES

[1] Segovia-Hernández, J. Gabriel, Núñez-López, J. Manuel, E. Cossío-Vargas, M. Juárez-García und E. Sánchez-Ramírez, „Electrification in the chemical industry and its role in achieving carbon neutrality: areas, challenges, and opportunities for process intensification," *RSC Sustainability,* pp. 4955-4974, 2025.

[2] GreenDeal-NET, „The EU's carbon-neutral future: Achieving net zero by 2050," https://www.greendealnet.eu/EU-carbon-neutral-future-net-zero., 5 Mar. 2023.

[3] J. P. Edaugal, D. L. Zhang, G. V. A. D. und N. Sun, „Solvent screening for separation processes using machine learning and high-throughput technologies.," *Chem & Bio Engineering,* Bd. 4, Nr. 2, pp. 210-228, 2025.

[4] L. March, Introduction to pinch technology, Gadbrook Park, Northwich, Cheshire: CW9 7UZ, England, 1998.

[5] M. J. Andrecovich und A. W. A. Westerberg., „Simple Bounding Sequences Synthesis Method Based on Utility for Heat-Integrated Distillation," *AlChE Journal,* Bd. 31, pp. 363-375, 1985.

[6] E. S. Fraga, R. Patel und G. W. A. Rowe, „A visual representation of process heat exchange as a basis for user interaction and stochastic optimization.," *Chemical Engineering Research and Design,* Bd. 79, Nr. 7, pp. 765-776, 2001.

[7] A. Rix, C. Hecht, N. Paul und J. Schallenberg, „Design of heat-integrated columns: Industrial practice.," *Chemical Engineering Research and Design,* Bd. 147, pp. 83-89, 2019.

Comparison of lattice type random packing ENVIPAC 4 with structured packing for liquid-side controlled mass transfer processes

Jerzy Maćkowiak[1], Alexandra Flieher[1], Halina Murasiewicz[2], Jan Maćkowiak[1]
[1]ENVIMAC Engineering GmbH, Oberhausen, Germany
[2]West Pomeranian University of Technology, Szczecin, Poland

Abstract
For a high gas flow capacity in mass transfer processes in the industry, structured packings are widely used, which can be operated under high gas velocity to achieve overall lower dimensions of designed plants. A low column diameter and a lower total pressure drop result in a reduction of operating costs, nevertheless still with a high efficiency.
As one example for this type of process, absorption of carbon dioxide (CO_2) is widely used in industrial applications like power plants using different chemical absorbents such as monoethanolamine (MEA) or caustic soda (NaOH).
In this work, the results in performance are compared between random ENVIPAC packing size 4" (E4) with a geometric surface area *a* of around 50 m²/m³ and a structured packing type X with a geometric surface area *a* of around 250 m²/m³. The comparison includes pressure drop, maximum capacity and mass transfer resistance in the liquid phase using the test systems air/water, CO_2-water/air and CO_2-air/1 N caustic soda respectively under ambient conditions. The test plant consists of a column with d = 600 mm inner diameter and a packing height up to H = 4 m.
The results are discussed in detail, with the main finding of the work being that random packing can certainly compete with structured packing concerning hydraulics due to lower pressure drop but competing separation efficiency at a five times lower surface area, and thus offers advantages over structured packing in several industrial applications.

Keywords
absorption, random packing, structured packing, hydraulics, liquid phase mass transfer, pressure drop

1. Introduction

Modern random and structured packing has been widely used in thermal separation processes for more than five decades, and their application leads to saving energy in the whole world. Most important today is lattice type random packing of the 3rd and 4th generation, mainly with a size of about 2", which are manufactured by various companies.
Th new kind of lattice type packing is characterised by a low pressure drop and a greater capacity range while still having good separation efficiency over the whole operating range in comparison to classical standard packing like e.g. Pall rings.
In comparison to structured packing, random packing in modern form, such as ENVIPAC (ENVIMAC), Hiflow (RVT), Netball (VFF), SRP rings (Raschig), have a

generally higher pressure drop, narrower operating range and lower separation efficiency. Structured packing is used mainly in low and normal pressure distillation or absorption processes with the main mass transfer resistance in the vapour or gas phase and for separation of mainly clean gas or liquid mixtures. Random lattice type packing made of plastic materials are used preferable in industrial gas treatment plants and especially with dust-laden exhaust air.

In recent literature, Maćkowiak (2022) first observed that for system with main mass transfer resistance in the liquid phase the random packing have better efficiency than the structure packing with the similar or higher specific geometric surface.
This observation leads to the conclusion that the modern random packing type with lattice type structure can be used successful in the special process and can be an interesting alternative proposal to structured packing, especially for very high flow of waste gas treatment in which a low pressure drop in the whole operating range is required.
The aim of this work is to present the performance data of the new size of lattice type packing ENVIPAC 4" (d = 120 mm) made of plastic (polypropylene, PP) in comparison to Mellapak 250X for processes in which the main mass transfer resistance is concentrated in the liquid phase.

2. Results and discussion

2.1. Test programme

For comparison, the new type of ENVIPAC 4" with specific surface area of 50 m2/m3 and Mellapak 250X with a specific surface area of 250 m^2/m^3 were investigated in the same test plant with a column diameter of d_S = 600 mm and a packing height of 2–4 m, using the system air/water for fluid dynamics tests, CO_2-water/air system for stripping and CO_2-air and absorption system CO2-air /1 N NaOH-under ambient conditions.
The dry and irrigated pressure drop was measured in relation to the gas load factor F_V and with a specific liquid load u_L as parameter in the range u_L = 0–70 m^3/m^2h in the operating range up to the flooding point.
The investigation of mass transfer resistance in the liquid phase was carried out at a variable specific liquid load u_L = 5–40 m^3/m^2h at a constant gas load factor F_V = 0,5 & 1,0 $Pa^{0,5}$ with water as well as NaOH with a concentration of approx. 1 mol/L under ambient conditions.
The volumetric mass transfer coefficient $\beta_L \cdot a$ [s^{-1}] was determined from the measured CO_2 concentration in the liquid and gas phase at the top and bottom of the column for each liquid load.
The volumetric overall mass transfer coefficient $K_V \cdot a$ for CO_2 absorption from the air using 1 N NaOH was estimated from the measured CO_2 concentration in the air inlet y_{in} and outlet y_{out} according to equation ().

$$K_V \cdot a = \frac{u_V}{H} \cdot \ln\left(\frac{y_{in}}{y_{out}}\right) \qquad [s^{-1}] \qquad (1)$$

The experimental data was evaluated according to the method by Duss et al. (2001).

2.2. Test results

The results of the hydraulic investigation, pressure drop Δp/H as function of the gas load factor F_V, are presented in Figure 1 for ENVIPAC 4” (PP) and in Figure 2 for metallic Mellapak 250X respectively.

In Figure 3, the flood load diagram as flood load factor $F_{V,fl}$ as function of flow parameter X_{fl} for both investigated packings is presented.

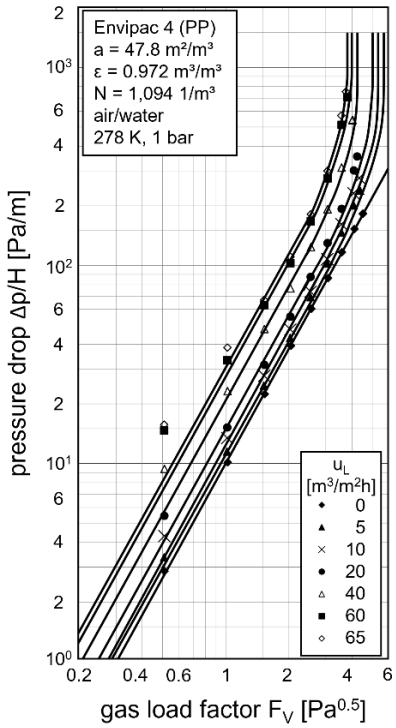

Figure 1: Pressure drop Δp/H as function of the gas load factor F_V for ENVIPAC 4” (PP).

Surprisingly, they exhibit that random ENVIPAC 4” has a lower dry pressure drop $\Delta p_0/H$ than Mellapak 250X while having a higher capacity range of about 25%.
The pressure drop Δp/H in the operating range below the loading point $F_V/F_{V,fl} \leq 0{,}65$ for both types of investigated packing provides comparable values.
In Figure 4, the dependency of the volumetric mass transfer coefficient $\beta_L \cdot a$ as function of the specific liquid load u_L is presented for both investigated packing ENVIPAC 4” and Mellapak 250X with a gas load factor F_V as parameter $F_V = 0{,}5\ Pa^{0,5}$.

The main result of this comparison is that for liquid phase mass transfer resistance the efficiency of Mellapak 250X is about 25% higher than for ENVIPAC 4”. However, the specific surface area needed for that value is about five times higher than for ENVIPAC 4”. These results show that the new random packing ENVIPAC 4” falls into the category of highly effective random packing.
The specific pressure drop related to one transfer unit $\Delta p/NTU_L$ for both packings is 1.5–7.5 Pa for ENVIPAC 4” and 1.5–3.5 Pa for Mellapak 250X.

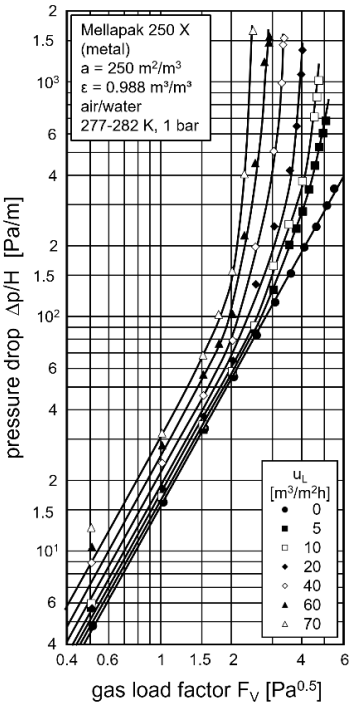

Figure 2: Pressure drop Δp/H as function of the gas load factor F_V for Mellapak 250X (metal).

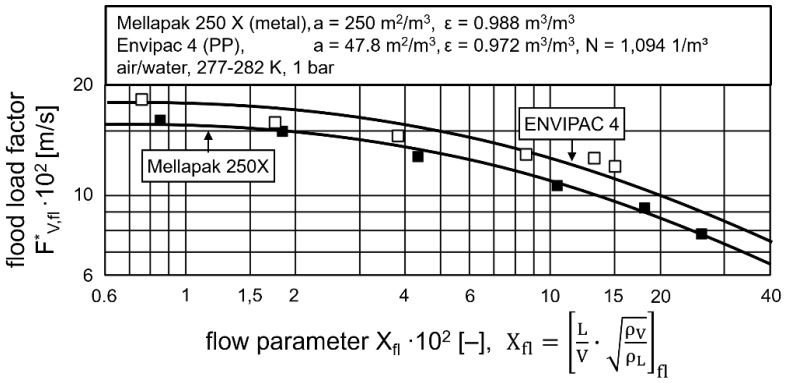

Figure 3: Flood load diagram for both ENVIPAC 4” (PP) and Mellapak 250X (metal).

Figure 5 presents the results of the comparison of measuring CO_2 absorption from the ambient air with 1 N NaOH solution. In this diagram, the overall mass transfer coefficient $K_V \cdot a$ as well as the effective mass transfer surface area a_{eff} evaluated according to the method by Duss et al. (2001) as function of specific liquid load u_L are shown. The comparison is valid for a gas load factor $F_V = 0{,}5\ Pa^{0,5}$ in the operating range below the loading point $F_V/F_{V,fl} \leq 0{,}65$.

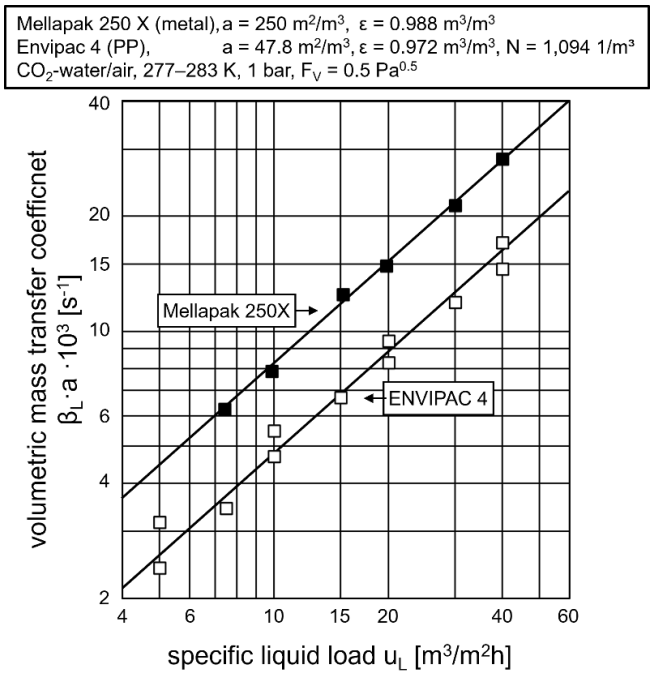

Figure 4: Volumetric mass transfer coefficient $\beta_L \cdot a$ as function of specific liquid load u_L.

3. Conclusions

According to the results of the investigation of hydraulics and mass transfer of the two different types of packing, new random ENVIPAC 4” and structured Mellapak 250X in a column with a diameter of 0,6 m and a packing height of 2–4 m, it can be seen that the hydraulic performance data of both so different forms of packing is all in all comparable, contrary to general expectations.

The main result of this investigation of hydraulics and mass transfer for system with main mass transfer resistance in the liquid phase is the conclusion that for industrial applications in which very high waste gas treatment flow and mass transfer resistance in the liquid phase occurs, the application of random packing can be taken into account as an alternative solution because of greater investment and operation advantages such as low pressure losses, applications in plants with a higher diameter and simple service and similar operating costs than by application of structured packing.

The structured packing Mellapak 250X generally has a higher separation efficiency, however, for that to be achieved, a surface area around five times higher than random packing ENVIPAC 4” is needed while separation efficiency of ENVIPAC 4” is just 40% lower. The higher the specific liquid load u_L, the smaller the difference between the packing types becomes.

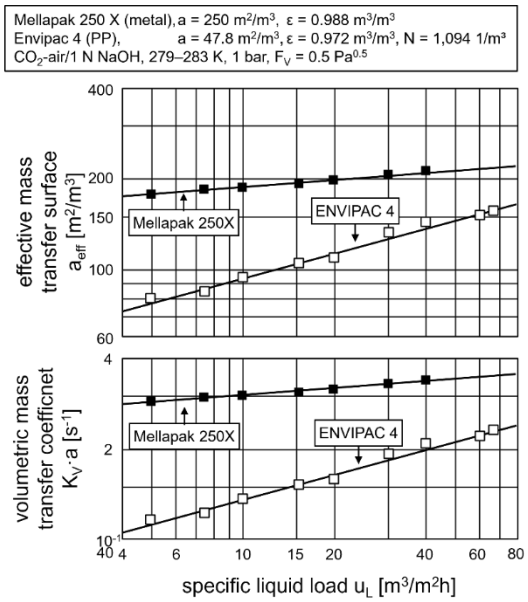

Figure 5: Overall volumetric mass transfer coefficient $K_V \cdot a$ (lower diagram) and effective mass transfer surface (upper diagram) as function of specific liquid load u_L valid for both investigated types of packing.

Symbols

a	[m²/m³]	geometric surface area of packing per unit volume
d_s	[m]	column diameter
F_V	[Pa$^{0.5}$]	gas load factor, based on free column volume $F_V = u_V \cdot \sqrt{\rho_V}$
$F_{V,fl}$	[Pa$^{0.5}$]	gas load factor at flooding point $F_{V,fl} = u_{V,fl} \cdot \sqrt{\rho_V}$
H	[m]	height of packed bed
$HTU_{V,L}$	[m]	height of a transfer unit based on the gas phase or liquid phase
K_Va	[kmol/(m³ bar s)]	overall mass transfer coefficient based on the gas phase
$NTU_{V,L}$	[—]	number of transfer units based on the gas phase or liquid phase
$\Delta p/H$	[Pa/m]	pressure drop per 1 m of irrigated packed bed
$\Delta p_0/H$	[Pa/m]	pressure drop per 1 m of dry packed bed
p	[bar]	operating pressure
T	[°C], [K]	temperature
u_L	[m³/m² h]	specific liquid load based on cross-sectional are of an empty column
u_V	[m/s]	gas velocity based on cross-sectional are of an empty column
y	[ppm]	concentration in gas phase
$\beta_{V,L}a$	[s^{-1}]	volumetric mass transfer coefficient in the gas or liquid phase
ε	[m³/m³]	relative void fraction
ρ	[kg/m³]	density

References

Duss, M., Meierhofer, H., & Nutter, D. E. (2001). Effective interfacial area and liquid holdup of Nutter Rings at high liquid loads. *Chemical Engineering and Technology*, *24*(7). https://doi.org/10.1002/1521-4125(200107)24:7<716::AID-CEAT716>3.0.CO;2-L

Maćkowiak, J. (2022). Prediction of separation efficiency of structured and stacked packings under low and normal pressure. *Chemical Engineering Research and Design*, *186*, 713–729. https://doi.org/10.1016/J.CHERD.2022.07.016

Detection of Inactive Liquid Films under Distillation Conditions Using Thermal Imaging

Mařík K., Haidl J., Pipíška A., Šulc T., Rejl J. F.
University of Chemistry and Technology, Prague, Czech Republic

Abstract

Thermal imaging represents a non-invasive experimental technique with growing potential for the investigation of distillation and absorption processes. Depending on the infrared transparency of the studied system, it can provide insight either into hydrodynamic phenomena or into thermal signatures associated with mass transfer. In infrared-opaque systems, thermal imaging enables observation of liquid film surface temperatures, which may be linked to local mass transfer activity and interfacial area utilization.

This contribution focuses on the application of thermal imaging to infrared-opaque distillation systems, specifically the distillation of a methanol/n-propanol mixture, with emphasis on the detection of locally inactive regions of the liquid film. Unlike absorption, no established experimental method exists for determining the effective interfacial area in distillation, which represents a significant limitation for the development of reliable mass transfer models.

A laboratory-scale distillation apparatus with a simple vapour–liquid contactor was employed to assess whether thermal imaging can identify regions of reduced mass transfer activity. Artificial stagnant zones were introduced into a flowing liquid film to mimic inactive areas occurring on real structured packings. The results demonstrate that thermal imaging is capable of qualitatively detecting such regions through characteristic temperature differences.

While quantitative evaluation is currently limited by vapour-phase infrared interference and radiative effects, the study confirms the suitability of thermal imaging as a diagnostic tool for identifying areas of decreased mass transfer activity in distillation systems.

Keywords

Distillation, infrared thermography, effective interfacial area, infrared-opaque liquids.

1. Introduction

Development of rate-based models for distillation requires reliably experimentally measured mass transfer characteristics under distillation conditions, that is, k_{L}, k_{V} and a_{eff}. Currently available models (e.g. RBF model[1], BS model[2], Delft model[3], Wang model[4]) are validated against k_{L}, k_{V} and a_{eff} that are obtained from absorption experiments only, since there is a methodology to assess them under absorption conditions only[5]. The transferability of the aforementioned transport characteristic from absorption to distillation conditions is questionable[6], especially quantities associated more with the liquid phase (k_{L}, a_{eff}), since phenomena that affect these parameters differ in distillation from absorption (especially surface tension gradients connected to Marangoni effects[2,7,8]).

To resolve this problem, we suggest a combination of already developed *profile method*[9,10] with a new experimental approach, which is infrared thermometry of distillation process introduced in this contribution.
The *profile method* provides volumetric mass transfer coefficients $k_\mathrm{L}a$ and $k_\mathrm{V}a$ under distillation conditions obtained by means of our semi-industrial-scale rectification column equipped with a unique system of ten liquid and vapour sampling points distributed along the column, allowing for measurement of composition profiles in both phases from the top to the bottom of the column. Distillation k_L and k_V are then obtained by division by the distillation a_eff obtained from infrared thermometry (relation (1) and (2)).

$$k_\mathrm{L}^\mathrm{dist} = \frac{k_\mathrm{L}a}{a_\mathrm{eff}^\mathrm{dist}} \tag{1}$$

$$k_\mathrm{V}^\mathrm{dist} = \frac{k_\mathrm{V}a}{a_\mathrm{eff}^\mathrm{dist}} \tag{2}$$

An experimental method to obtain $a_\mathrm{eff}^\mathrm{dist}$ is thus a missing link for distillation transport characteristics assessment. The decrease in the distillation effective interfacial area is caused by two main mechanisms:

- Dry zones of the structured packing.
- Liquid films approaching locally thermodynamic equilibrium with the above-flowing vapour (so-called *inactive liquid films*)

$$y_\mathrm{i} = \varphi(x_\mathrm{i}), \tag{3}$$

which can, unlike e.g. chemisorption, occur since the capacity of liquid films is rather low under distillation conditions.
These two mechanisms should be possible to identify with a thermal imaging camera if the following assumptions are fulfilled:

- The emissivity ε_L of the observed liquid film approaches unity

$$\varepsilon_\mathrm{L} \to 1, \tag{4}$$

  which inherently means that its transparency τ_L approaches zero.
- The emissivity ε_P of the dry surface of the packing is low

$$\varepsilon_\mathrm{P} \to 0. \tag{5}$$

- The transparency τ_V of the vapour is low

$$\tau_\mathrm{V} \to 0. \tag{6}$$

Local reaching of thermodynamic equilibrium (relation (3)) means that the bulk temperature of both phases t_L and t_V and the interfacial temperature t_i are equal

$$t_\mathrm{L} = t_\mathrm{i} = t_\mathrm{V}, \tag{7}$$

unlike active areas where

$$t_\mathrm{L} < t_\mathrm{i} < t_\mathrm{V}. \tag{8}$$

As a result, liquid films with decreased activity in mass transfer show elevated interfacial temperatures t_i compared to active areas, and this is what might be detected by a thermal imaging camera.
Assumption (4) must be fulfilled to measure the interfacial temperature t_i without being affected by the deeper layers of the liquid of different temperature. This was verified for water[11]. It was shown that a bolometric thermal imaging camera (spectral range 7.5 to $13\ \mu\mathrm{m}$) directed at the surface of mixed water ($\varepsilon_\mathrm{W} = 0.984$[12]) with a set constant bulk temperature t_L below a layer of agitated air with a set constant bulk temperature t_G indeed measures the temperature of the interface t_i. The temperatures of the phases were set such that $t_\mathrm{L} < t_\mathrm{G}$. It was found that this also holds for primary alcohols and their mixtures, which were used as distilled system in this work.

Assumption (5) is fulfilled since polished metal surfaces generally show low emissivity values, which is also the case for structured packings. As a result, dry areas are recognized with the thermal imaging camera, since apparent temperature read by the thermal imaging camera is low due to low emissivity.
Assumption (6) is important since the liquid film is always covered with above-flowing vapour, which must be transparent to infrared light in the used spectral range; otherwise, it would hinder the view on the liquid film.
A tailored distillation apparatus with optical access for IR thermometry was built in this work. Distillation of the methanol/n-propanol mixture takes place on the surface of a flat metal sheet between a laminar wavy liquid film and counter-currently flowing vapour above it. The distillation space was equipped with a metal ring serving as an artificial dead zone. Liquid collected in this ring has a longer residence time compared to the freely flowing film and thus potentially approaches equilibrium.
The distillation space is equipped with a KBr monocrystalline window translucent to IR light, so the distillation scene can be observed with a thermal imaging camera. The recorded thermograms of the flowing liquid film (comprising also the artificial dead zone) are studied, and the ability of thermal imaging to identify an area with decreased mass transfer intensity is investigated.
Moreover, an attempt was made to conduct quantitative analysis to assess the degree of local inactivity of the liquid film in mass transfer. This is done by comparing the temperature based on the composition of samples taken directly from the artificial dead zone and the freely flowing liquid film at the same longitudinal position within the distillation space with the obtained thermograms.
The local compositions can be translated into local temperatures, since the phases are composed of binary mixtures and assumed to be saturated,

$$t_{\mathrm{L}} = t_{\mathrm{BP}}(x_{\mathrm{A}}). \tag{9}$$

$$t_{\mathrm{V}} = t_{\mathrm{DP}}(y_{\mathrm{A}}). \tag{10}$$

The thermograms are processed using a developed radiometric model that compensates for interference factors in thermal imaging measurement, which are:

- Apparent absorption of the liquid film thermal radiation by the KBr window caused by multiple reflections at optical interfaces.
- Reflected background noise radiation produced by the thermal imaging camera itself.

2. Experimental

2.1 *Experimental apparatus*

The experimental apparatus comprises the distillation space (1), distillation peripheries such as the reboiler (2), total condenser (3), reflux drum (4), reflux pump (5), and preheater (6), and measuring and control equipment (Figure 1). Temperatures of all inlet and outlet streams of the distillation space are recorded. The temperature of vapour is measured at two positions directly in the distillation space. Pressure in the apparatus is also measured.

The body of the distillation space is made of Teflon. It comprises a liquid distributor (1), flat metal sheet (2), artificial dead zone with sampling system (3), sampling system from the flowing liquid film (4), vapour distributor (5), and two vapour thermometers (6). Vapour can be locally sampled from both positions (3) and (4) (Figure 2).
The body of the distillation space is closed with a duralumin lid that consists of two

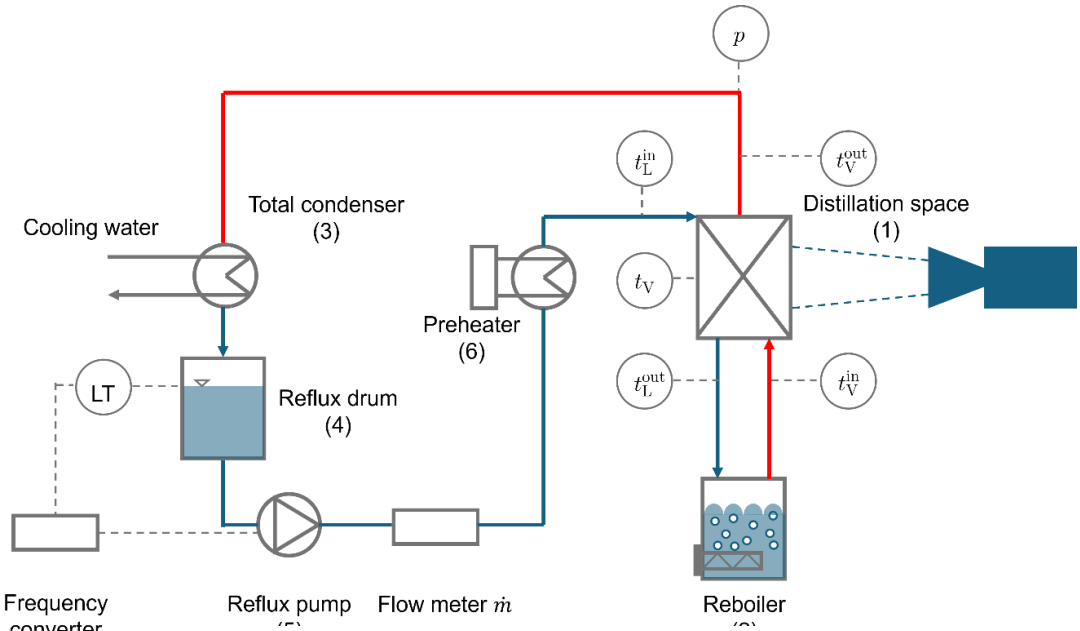

Figure 3: Experimental apparatus with peripheries.

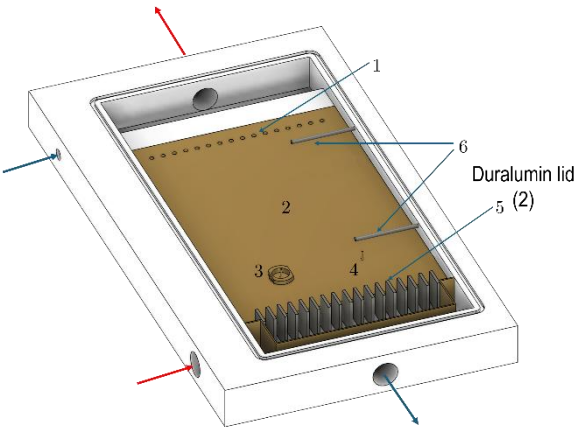

Figure 2: Distillation space – internals.

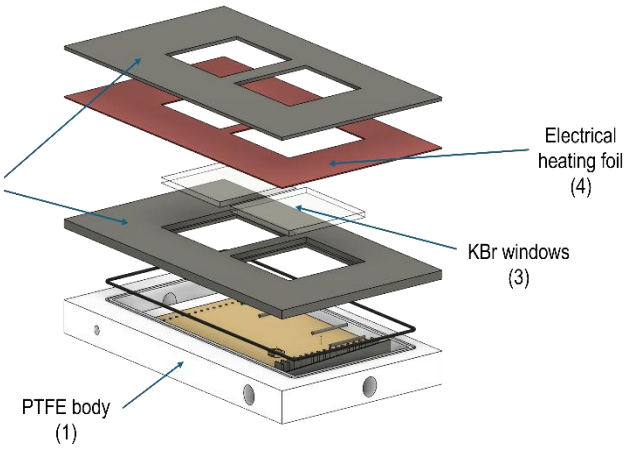

Figure 1: Construction of the distillation space.

parts, between which an electrical heating foil is sandwiched to compensate for heat losses. There are two orifices with KBr windows in the lid through which the distillation scene is observed with a bolometric long-wave thermal imaging camera with a spectral range of $7.5 - 13\ \mu\mathrm{m}$ and a resolution of 640×480 pixels (Figure 3).

2.2 *Experiments*

Distillation is run at atmospheric pressure and total reflux. The required duty of the reboiler is set. After reaching steady state, which takes approximately two hours, the temperatures of inlet and outlet streams and the temperature of the vapour inside the distillation space are recorded together with total pressure and mass flow rate. Samples of inlet and outlet streams are taken. Samples of liquid from the artificial dead zone and the flowing liquid film, together with vapour at the same longitudinal position in the distillation space, are taken. A thermal image of the distillation scene is recorded,

and the thermographically obtained temperature distribution of the liquid film is evaluated using the aforementioned radiometric model.

2. 3 *Experimental conditions*

The distilled mixture is methanol (M) with n-propanol (P) with composition of approximately $x_{\mathrm{M}} = y_{\mathrm{M}} = 0.35$ at the bottom of the distillation space. Experiments are conducted under three reboiler duties summarized in Table 1 with corresponding mass flow rates. Each experiment was conducted twice. The liquid film flows in laminar wavy regime, and the vapour in the laminar/transition boundary.

Measurement	P (kW)	$\dot{m}$ (g s^{-1})
1	1.3	1.0
2	1.7	1.7
3	2.5	2.6

Table 1: Experimental duties of the reboiler and corresponding mass flow rate.

3. Results and discussion

The separation efficiency of the distillation space is found to be approximately 30 % of an equilibrium stage. The measured temperatures correspond to the taken samples at the positions where both pieces of information can be acquired simultaneously, which means both phases are saturated. The only exception is the liquid inflow, which is subcooled by approximately 7 °C under all experimental conditions. Nevertheless, it is quickly heated up to boiling point in the distillation space. The experiments are found reproducible.

It is found that thermal imaging is able to detect areas with locally reduced mass transfer intensity, as can be seen in Figure 4. The liquid in the artificial dead zone is apparently warmer than the freely flowing film in its proximity.

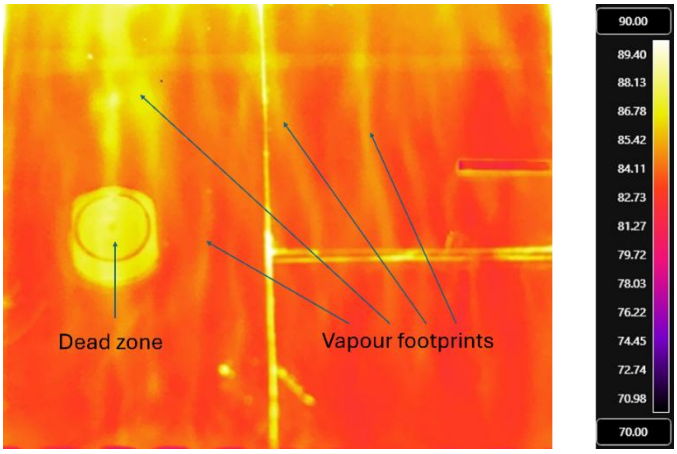

Figure 4: Thermogram of methanol/n-propanol distillation. Perpendicular apparently warmer lines are cracks on KBr window, since it was partly damaged.

Unfortunately, vapour is also partly visible in the thermogram as flame-like wisps spread across the whole distillation scene (Figure 4). This shows that assumption (6) is not fulfilled for the vapour of the methanol/n-propanol mixture and the long-wave uncooled bolometric camera used. This makes quantitative assessment impossible so far, since the vapour partly hinders the camera's view of the observed liquid film and adds an unknown noise offset to the thermographically measured temperature of the liquid.

4. Conclusions

A specifically tailored distillation apparatus was built to examine the ability of thermal imaging to detect areas of liquid film with decreased intensity of mass transfer in distillation. The concept was found to be successful for the distillation of methanol/n-propanol mixture in a flowing laminar wavy film on the surface of a flat metal plate. The results remain rather qualitative so far as a result of IR semitransparency of the present vapour, which partly hinders observation of the liquid film by thermal imaging.

The outlook is to develop a quantitative methodology for local mass transfer intensity distribution evaluation, which requires that the effect of the vapour be properly described and/or mitigated. The use of image analysis tools and measurement of vapour “blanks” are considered. Another goal is to develop an improved distillation space design more closely approaching the situation present in real distillation columns, i.e. comprising a corrugated sheet of structured packing. However, this objective is challenging.

Furthermore, the radiometric description and evaluation of the thermograms must be improved and experimentally validated to obtain reliable quantitative result.

Acknowledgements
This work was supported by the Czech Science Foundation grant No. 20-20335S and by the grant of Specific university research – grant No. A1_FCHI_2022_005.

References

1. Rocha, J. A.; Bravo, J. L.; Fair, J. R. Distillation Columns Containing Structured Packings: A Comprehensive Model for Their Performance. 2. Mass-transfer model. *Ind. Eng. Chem. Res.* **1996**, *35* (5), 1660–1667.
2. Billet, R.; Schultes, M. Prediction of mass transfer columns with dumped and arranged packings - Updated summary of the calculation method of Billet and Schultes. *Chem. Eng. Res. Des.* **1999**, *77* (A6), 498–504.
3. Olujic, Z.; Behrens, M.; Colli, L.; Paglianti, A. Predicting the efficiency of corrugated sheet structured packings with large specific surface area. *Chem. biochem. eng. q.* **2004**, *18* (2), 89–96.
4. Wang, G. Q.; Yuan, X. G.; Yu, K. T. A method for calculating effective interfacial area of structured packed distillation columns under elevated pressures. *Chem. Eng. Process. Process Intensif.* **2006**, *45* (8), 691–697.
5. Hegely, L.; Roesler, J.; Alix, P.; Rouzineau, D.; Meyer, M. Absorption Methods for the Determination of Mass Transfer Parameters of Packing Internals: A Literature Review. *AIChE J.* **2017**, *63* (8), 3246–3275.
6. Haidl, J.; Rejl, F. J.; Valenz, L.; Kordač, M.; Moucha, T.; Labík, L.; Schultes, M. Absorption in wetted-wall column with phase properties close to distillation conditions. *Chem. Eng. Sci.* **2016**, *144*, 126–134.
7. Zuiderweg, F. J.; Harmens, A. The influence of surface phenomena on the performance of distillation columns. *Chem. Eng. Sci.* **1958**, *9* (2-3), 89–103.
8. Čmelíková, T.; Valenz, L.; Mařík, K.; Rejl, F. J. Mass transfer under distillation of positive, neutral, and negative system in the ID 0.3 m column packed with structured packing. *Chem. Eng. Res. Des.* **2023**, *196*, 52–60.
9. Linek, V.; Moucha, T.; Prokopova, E.; Rejl, J. F. Simultaneous determination of vapour- and liquid-side volumetric mass transfer coefficients in distillation column. *Chem. Eng. Res. Des.* **2005**, *83* (A8), 979–986.
10. Rejl, F. J.; Valenz, L.; Linek, V. "Profile Method" for the Measurement of kLa and kVa in Distillation Columns. Validation of Rate-Based Distillation Models Using Concentration Profiles Measured along the Column. *Ind. Eng. Chem. Res.* **2010**, *49* (9), 4383–4398.
11. Mařík, K.; Haidl, J.; Šikola, J.; Rejl, F. J. Thermal imaging - A novel method for gas-liquid Interface conditions determination. *Int. Commun. Heat Mass Transf.* **2022**, *130*.
12. Konda, M.; Imasato, N.; Nishi, K.; Toda, T. Measurement of the sea surface emissivity. *J. Oceanogr.* **1994**, *50* (1), 17–30.

A Parameter-Driven Approach to Disc-Stack Centrifuge Simulation for Biodiesel–Glycerol Separation in Aspen Plus

Emílio Émerson Xavier Guimarães Filho, Victor Hugo dos Santos Ramos, Nadia Gagliardi Khouri, Adriano Pinto Mariano, Maria Regina Wolf Maciel, Rubens Maciel Filho
University of Campinas, Campinas, Brazil.

Abstract

International regulations require biodiesel with low residual glycerol content, making efficient liquid–liquid separation a critical step in continuous production processes. High-speed disc-stack centrifuges are an alternative for this purpose; however, their detailed design and operational parameters are poorly represented in conventional process simulators. In this work, a simplified, parameter-driven approach based on classical ∑-theory is proposed to estimate biodiesel–glycerol separation efficiency in disc-stack centrifuges and integrate it into Aspen Plus v.14. Physicochemical properties, equipment geometry and operating conditions are incorporated, complemented by empirical factors accounting for coalescence and emulsification. The methodology is applied to an Alfa Laval LAPX-202 centrifuge, improving physical representativeness while remaining computationally simple.

Keywords: Disc-stack centrifuge, AspenPlus simulation, biodiesel-glycerol separation, process modeling

1. Introduction

The use of high-speed separators in industrial processes, particularly in continuous biodiesel production, is well established and supported by mature commercial technology for the separation of crude biodiesel from glycerol. As the density difference becomes significant, the separation is facilitated as the centrifugal force effectively drives the dispersed phase toward the bowl wall. As the recovery yield is affected by physico-chemical properties of the phases and the machine configuration, other effects, such as the formation of emulsion, are of concern, as well as the solubility ofone phase in the other (Atadashi et al., 2011).

Separation performance is favored by larger droplet diameters, as centrifugal forces more effectively drive the dispersed phase toward the bowl wall. Likewise, density and viscosity contrasts between the liquid phases directly influence settling velocity and residence time requirements (Pasottoet al., 2011). Consequently, reliable estimation of separation efficiency is essential for predicting overall plant performance and ensuring compliance with product specifications.

Although several mathematical models reported in the literature provide valuable insights into centrifuge behavior, their application in commercial process simulators remains limited. Software such as Aspen Plus v.14 offers unit operation blocks primarily derived from solid–liquid separation concepts, providing restricted flexibility for incorporating machine-specific parameters relevant to liquid–liquid disc-stack centrifuges, as commonly employed in biodiesel processing (Zhouet al., 2025).

Disc-stack centrifuge performance is strongly governed by equipment geometry and operating conditions, including bowl dimensions, rotational speed, and disc-stack

configuration. Explicit incorporation of such parameters can significantly improve prediction accuracy, yielding models that better represent actual operating conditions while avoiding overly generic assumptions (König et al., 2020).In this context, this work proposes a simplified approach to implementing enhanced data analysis and machine-related parameters into Aspen Plus v.14 through VBA coding in Microsoft Excel.

2. Methodology

2.1 Mathematical approach to estimate the separation efficiency

The model used for estimating the separation efficiency in disc-stack centrifuges is presented by Equation 1 (König et al., 2020), which is originally part of the ∑-theory. In this expression, the efficiency "$\eta_{\sum}$(dp)" is calculated considering the particle's diameter "d_p" (in meters), the critical diameter "Dc", and the exponent "j",which acts as an adjustment factor, allowing a better fit with experimental values. In this work, a value of j = 100 was adopted, no longer affecting separation estimates in the absence of practical values as presented by König et al. (2020).

$$\eta_{\sum}(d_p) = 1 + \left(\frac{d_p^2}{D_c^2} - 1\right) \exp\left(-\left(\frac{d_p^2}{D_c^2}\right)^j\right) \quad (1)$$

$$D_c = \sqrt{\frac{18 \times \mu_c \times Q}{(\rho_h - \rho) \times \omega^2 \times V_{bowl}} \times \ln\left(\frac{r_2}{r_1}\right)} \quad (2)$$

The critical diameter, defined by Equation 2 (Foust et al., 1982), represents the minimum droplet size that can be effectively separated under given operating conditions. This parameter combines fluid physicochemical properties, operating variables, and centrifuge geometry, including viscosity of the continuous phase, phase densities, feed flow rate, angular velocity, bowl internal volume, and the minimum and maximum radii of the disc stack.

Finally, the separation efficiency was weighted by two additional empirical terms: the coalescence factor and the emulsionstability factor, both ranging from 0 to 1 (Equation 3). These factors contribute to a more realistic representation of the system's actual separation behavior. Coalescence refers to the increase in droplet size enabling its separation, whereas emulsion stability reflects the opposite effect, promoting a stable structure. These factors are particularly useful for better describing the experimental system and even for quantifying the empirical variables in practice. For testing purposes, the algorithm adoptsf_{coal} = 0.95 and $f_{emulsion}$ = 0.05.

$$\eta_{\sum}(d_p) = \eta_{\sum}(d_p) \times f_{coal} \times (1 - f_{emuision}) \quad (3)$$

2.2 Disc-stack machine parameters

The Alfa-Laval LAPX-202 centrifuge was selected for the tests based on two main criteria: (i) its design parameters are well documented in Kula et al. (1982), with all relevant machine design parameters; and (ii) The LAPX-202 is suitable for demonstration plants, with feed flow rates capacities varying from 100 – 600 L/h, ideal for pilot plants. It is assumed that the machine is configured as a purifier.

2.3 Feed composition and fluid physicochemical property estimation

The biodiesel composition used in this study was based on the ethyl-ester profile reported by Nikhom and Tongurai (2014), corresponding to biodiesel derived

from palm oil. In the absence of experimental property data for the complete mixture, biodiesel density and viscosity were approximated by those of ethyl oleate, one of its predominant components. Correlations for density and viscosity (Equations 4 and 5, respectively) were taken from Pratas et al. (2010), while glycerol-rich phase density(Equation 6) was estimated using correlations reported by Takamura et al.(2012).

$$\rho_{et_{ole}}(kg/m^3) = -0.7301 \times T\ (°C) + 885.12 \quad (4)$$

$$\mu_{et_ole}\left(\frac{kg}{m.s}\right) = 0.0087e^{-0.018 \times T(°C)} \quad (5)$$

$$\rho_{glycerol}(kg/m^3) = -0.6366 \times T(°C) + 1273.8 \quad (6)$$

The last variable needed for estimating the separation efficiency by Equations 1 and 2 is the particle diameter.Simpler models assume an average droplet diameter for the fluids involved. This work employs a lognormal distribution that statistically represents the range of droplet sizes present in the system. The distribution was parameterized using the experimental data of Abeynaike et al. (2012) for an 80:20 biodiesel-glycerol mixture, matching the feed composition.

The droplet size distribution of the dispersed phase was represented by a log-normal probability density function (PDF), which satisfies the normalization condition specified in Equation 7, ensuring a proper probabilistic interpretation. The parameters of the distribution are the geometric median diameter and the geometric standard deviation, which provide a robust description of the characteristic droplet size and dispersion in polydisperse systems.

$$\int_0^\infty f(dp)ddp = 1 \quad (7)$$

The separation efficiency of the centrifuge is size-dependent; therefore, the overall separation efficiency was calculated by Equation 8 as a weighted average of the efficiency function $\eta(d_p)$over the droplet population. The integral was evaluated numerically using the trapezoidal rule applied to a discretized droplet size domain. Prior to integration, the PDF was normalized numerically to ensure unit area. This approach allows the model to account explicitly for droplet polydispersity and its impact on the predicted separation performance.

$$\eta_{global} = \int_0^\infty \eta(dp)f(dp)ddp \quad (8)$$

Under this approach, the model focuses on the removal of dispersed glycerol droplets from the continuous biodiesel phase. Losses of biodiesel to the heavy phase are neglected. This hypothesis is highly justified, mainly based on key points: i) adjustable parameters such as gravity discs and backpressure in both outlet streams are designed to mitigate losses to facilitate a proper cut between the phases; ii) biodiesel carryover to the heavy phase is plausible butlacks experimental evidence to be included. Again, it is important to emphasize that the present model constitutes a simplified introductory model that requires further developments based on experimental data regarding the separation itself but also the machinery behaviour.

2.4 Implementation in Aspen-Plus v.14

In the simulation software, the UNIFAC method was selected for simplification, since the present calculations are more physical-related. The choice relies mostly on the absence of experimental binary parameters. The flowsheet is shown in Figure 1.The initial composition of “BIO-D” stream is given in Table 2, containing the biodiesel composition normalized to consider 20% of glycerol as intended, entering at500 kg/h, 65 °C. The pressure is increased to 3.5 bar and the temperature adjusted to 75 °C prior to the liquid-liquid centrifuge (“LL”), which is a user model block (“UserModel2”).

The Microsoft Excel template for the user model provided by AspenPlus v.14 was used for the calculations. A VBA routine was programmed to estimate the separation efficiency. This efficiency was then used to multiply the amount of glycerol (kmol/h) sent to the heavy phase (“HP”). The difference was considered in the light-phase (“LP”) as a residual content. The biodiesel content in each stream was determined by mass balance.

Table 2: Inlet feed composition (wt%).

Component	Chemical Formula	Feed Composition (wt%)
Glycerol	$C_3H_8O_3$	20.00 %
Ethyl-Laureate	$C_{14}H_{28}O_2$-N1	0.20 %
Ethyl-Myristate	$C_{16}H_{32}O_2$-N2	0.77 %
Ethyl-Stearate	$C_{20}H_{40}O_2$-N3	3.23 %
Ethyl-Linoleate	$C_{20}H_{36}O_2$-N1	9.05 %
Ethyl-Palmitate	$C_{18}H_{36}O_2$-N2	30.93 %
Ethyl-Oleate	$C_{20}H_{38}O_2$-N1	35.82 %

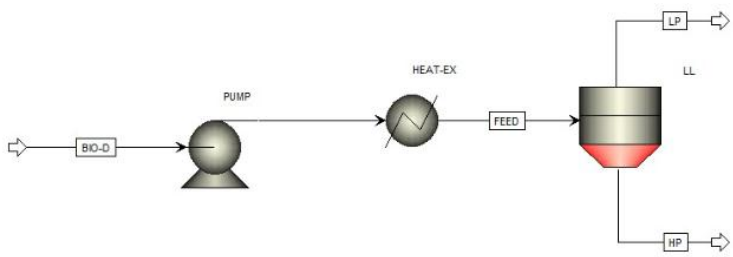

Figure 1: Flowsheet for the biodiesel-glycerol separation.

3. Results and discussion

3.1 Separation efficiency and simulation results

Based on the initial assumptions, the critical diameter was calculated to be 4.64 µm. This value is considerably smaller than the average glycerol droplet size reported by Abeynaike et al. (2012), indicating that the separation process is inherently favorable in a high-speed centrifuge. As shown in Figure 2a, most droplets fall within the 20–40 µm range, as evidenced by the distribution peak. The black dashed line marks the critical diameter, further illustrating that the majority of droplets exceed this threshold. The red horizontal line corresponds to a separation efficiency of 90.25%.

By solely increasing the coalescence factor to 1, the efficiency increases to 95%. It adds emphasis that such empirical factors (f_{coal}, $f_{emulsion}$) are of great impact on the overall recovery and allows further improvement in the algorithm for better quantifying these effects in practice. A more precise estimation of these parameters still requires a dedicated mathematical formulation in this work to achieve higher accuracy.

From the AspenPlus v.14 simulator, the light-phase flow rate was 409.75 kg/h (81.9% of the feed stream), containing 97.6 wt% of biodiesel and 2.4 wt% glycerol. Although the assumption of full recovery of biodiesel (no losses to the heavy phase) is coherent for initial insights, it is important to notice that solubility (biodiesel in glycerol), machine hydraulic carryover, and other effects likely contribute to a slight decrease. Of course, emulsification aspects are of major concern and, as mentioned before, can highly contribute to lower biodiesel recovery yields.

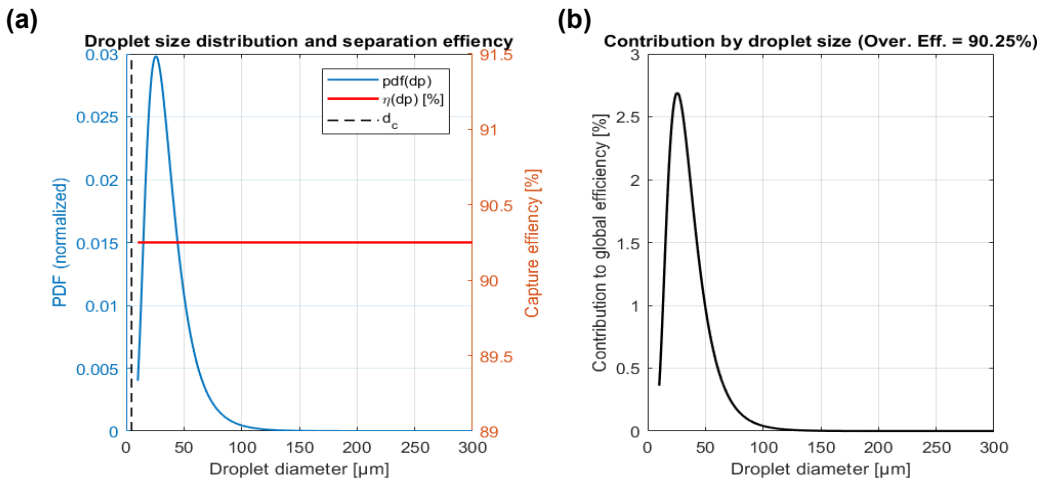

Figure 2: Droplet size distribution and size-dependent capture efficiency in the proposed disc-stack centrifuge.

3.2 Sensitivity Analysis

Figure 3 illustrates the sensitivity of glycerol content in the light phase as a function of feed flow rate and operating temperature. As expected, the results indicate an increase in glycerol carryover into the light phase with increasing flow rate and decreasing temperature.

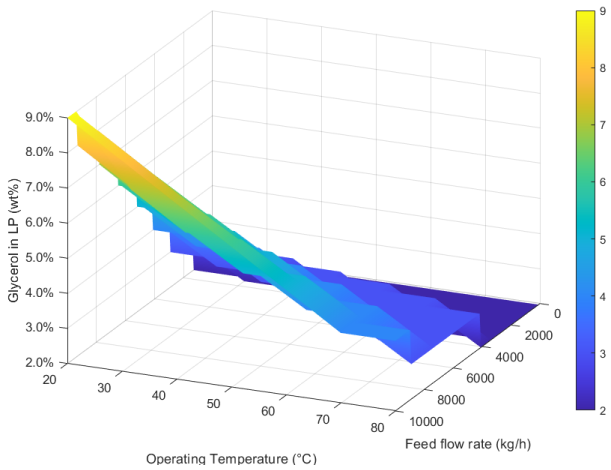

Figure 3: Sensitivity data for the glycerol content in LP under different operating conditions.

The separation efficiency of centrifuges is strongly dependent on the feed flow rate, as it directly governs the residence time of the dispersed phase within the bowl. Higher flow rates shorten the residence time, increasing the likelihood of dense-phase entrainment into the light-phase stream and, consequently, deteriorating

product quality. Conversely, excessively low flow rates extend the residence time, which may promote the migration of the target light phase toward the peripheral regions of the bowl, leading to its partial removal with the heavy phase and thus reducing recovery yield (Kilikian and Pessoa Jr., 2020). Temperature exhibits a comparatively lower sensitivity in the model, primarily due to the substantial density difference between the phases, but also because, although the viscosity of the glycerol-rich phase plays an important role in centrifugal separation, it is not accounted for in the present model.

4. Conclusions

A physically based, parameter-driven methodology for modeling disc-stack centrifuges in Aspen Plus was proposed, developed and applied to the biodiesel-glycerol separation. By combining ∑-theory along with derived machine design parameters and a lognormal droplet size distribution, the proposed model allows for a more realistic representation of liquid–liquid centrifugal separation than conventional approaches. Sensitivity analysis confirmed the dominant influence of feed flow rate through residence time effects, while temperature showed a secondary impact mainly because glycerol's viscosity impacts were not included in the model. The developed framework offers a flexible platform for integrating centrifuge design parameters into process simulation and represents a valuable tool for process analysis and optimization.

Acknowledgements

This study was financed by the São Paulo Research Foundation (FAPESP), Brasil. Process Number #2022/16379-8, by the Human Resources Training Program of the Brazilian National Agency for Petroleum, Natural Gas and Biofuels – PRH/ANP, under the management of the São Paulo Research Foundation (FAPESP), Brazil, Process N. 2025/20397-0, by the National Council for Scientific and Technological Development (CNPq), grants numbers 308672/2025-9; 311193/2020-0 and supported by Shell.

References

ABEYNAIKE, A. *et al.* The experimental measurement and modelling of sedimentation and creaming for glycerol/biodiesel droplet dispersions. Chemical Engineering Science, v. 79, p. 125–137, 10 set. 2012.

ATADASHI, I. M.; AROUA, M. K.; AZIZ, A. Abdul. Biodiesel separation and purification: A review. Renewable Energy, Feb. 2011.

FOUST, A. S.; WENZEL, L.A.; CLUMP, C.W.; MAUS, L.; ANDERSEN, L.B. Principles of Unit Operations. 2. ed. United States: John Wiley & Sons Inc., 1982.

KILIKIAN, B. V; JÚNIOR, A. P. Purificação de produtos biotecnológicos: operações e processos com aplicação industrial. 2. ed. São Paulo: Blucher, 2020.

KÖNIG, Julian; UEDING, Jens; JANOSKE, Uwe. Analytical Model to Characterize the Efficiency of Disk Stack Separators. Chemie-Ingenieur-Technik, v. 92, n. 6, p. 701–710, 1 jun. 2020.

KULA, Maria-Regina; KRONER, Karl Heinz; HUSTEDT, Helmut. Purification of enzymes by liquid-liquid extraction. *In*: Berlin, Heidelberg: Springer Berlin Heidelberg, 1982.

NIKHOM, Ruamporn; TONGURAI, Chakrit. Production development of ethyl ester biodiesel from palm oil using a continuous deglycerolisation process. Fuel, v. 117, n. PARTB, p. 926–931, 2014.

PASOTTO, M.B.; ARNOSTI JR., S.; PASOTTO, L.H.P. Tópicos em separações mecânicas. São Paulo: EdUFSCAR, 2011.

PRATAS, Maria Jorge *et al.*Densities and viscosities of fatty acid methyl and ethyl esters. Journal of Chemical and Engineering Data, v. 55, n. 9, p. 3983–3990, 9 set. 2010.

TAKAMURA, Koichi; FISCHER, Herbert; MORROW, Norman R. Physical properties of aqueous glycerol solutions. Journal of Petroleum Science and Engineering, v. 98–99, p. 50–60, Nov. 2012.

ZHOU, Jiajiang; TONG, Li; GUO, Haixin. Advances in primary recovery for algae bioreactors: The centrifugation role. *In*: Algal Bioreactors: Science, Engineering and Technology of Downstream Processes: Volume 2. *[S.l.]*: Elsevier, 2024. v. 2 p. 125–138.

Efficient Process for Separation of Non-Ideal Quaternary Mixtures: Solvent Regeneration with Distillation

Andras Jozsef Toth[1,2], Zsofia Sara Vasko[1], Erik Somogyvari[1], Huyen Trang Do Thi[1], Eniko Haaz[1]

[1] Department of Chemical and Environmental Process Engineering, Budapest University of Technology and Economics, Budapest, Hungary;

[2] Institute of Process Systems Engineering, Hamburg University of Technology, Hamburg, Germany

Abstract

Distillation has remained one of the most widely used industrial separation techniques for over a century. In recent years, its efficiency has been further enhanced by advanced, complex column configurations, especially for azeotropic mixtures. Various alternative distillation methods have also gained widespread industrial application, such as extractive, heteroazeotropic, and pressure swing distillation. In this study, two quaternary industrial waste solvents are separated using a hybrid distillation method (extractive heterogeneous-azeotropic distillation) and the potential for heat integration is assessed.

The examined quaternary mixtures are as follows, ethylene glycol - water - ethanol - methyl ethyl ketone and ethylene glycol - water - ethanol - ethyl acetate. The separation carried out with the ChemCAD simulation program was successful, as the final product streams from both mixtures achieved the target purities specified in the design. Cost estimation is also examined based on the Douglas equations. It can be noted that the most efficient configuration, in terms of operation and total annual cost, is to extract the least volatile component (ethylene glycol) in the first distillation column.

Keywords

extractive distillation, non-ideal mixture, quaternary mixture, heat integration, cost estimation

1. Introduction

Distillation remains the dominant separation technique in the chemical industry, relying on differences in component volatility to achieve separation. However, because distillation processes are highly energy-intensive, careful attention to process design and operating conditions is essential from both economic and environmental perspectives [1]. These challenges become even more pronounced when dealing with highly non-ideal systems, which are frequently encountered in the fine chemicals sector. In such cases, separations often involve azeotropic mixtures and must meet stringent product-purity requirements, making it particularly difficult to optimise energy efficiency and minimise environmental impact [2,3]. Mixtures of this type typically consist of alcohols, esters, aldehydes, ethers, and water, a combination that inherently leads to significant complications in distillation-based separation processes.

The extractive heterogeneous-azeotropic distillation process (EHAD) was developed to separate complex, non-ideal ternary and quaternary mixtures that form heteroazeotropes [4]. The schematic of the operation is shown in **Figure 1**.

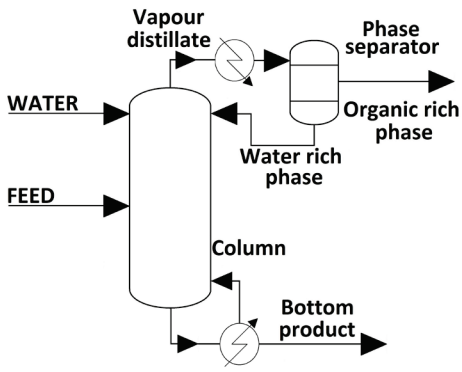

Figure 1: Schema of the extractive heterogeneous-azeotropic distillation [5]

This combined, hybrid method offers the advantages of both extractive and heterogeneous-azeotropic distillation, and accordingly, complex mixtures can be separated. The extraction solvent or entrainer is pumped into the top of the column, which is water in this process, forms a heterogeneous-azeotropic product that can be removed from the distillate product and condensed to obtain a two-phase overhead product. By separating this, the upper, organic-rich phase can be purified by further distillation, and the lower, aqueous phase is returned to the top of the column as reflux [6]. This method is also effective because no new material is added to the feed mixture to be separated. In almost all cases, water is already in the system, so it does not form another, new azeotrope, and there will be no new, even environmentally harmful, separation problem [7].

2. Results and discussion

The examined quaternary mixtures were as follows, methyl ethyl ketone (MEK) – ethanol – water – ethylene glycol (EtGl) (Mixture I) and ethyl acetate (EtAc) – ethanol – water – ethylene glycol (Mixture II) according to the specified purity requirements. These are used solvents originally from the fine chemical industry, which should be regenerated for reuse. The binary and ternary azeotropic properties of the examined mixtures are given in **Table 1**.

Table 1: Azeotropic types [8]

Case	Azeotrope type
methyl ethyl ketone – ethanol	Minimum boiling point binary homogeneous-azeotropic
ethanol – water	Minimum boiling point binary homogeneous-azeotropic
methyl ethyl ketone – water	Minimum boiling point binary heterogeneous-azeotropic
ethyl acetate – ethanol	Minimum boiling point binary homogeneous-azeotropic
ethyl acetate – water	Minimum boiling point binary heterogeneous-azeotropic
methyl ethyl ketone – ethanol – water	Minimum boiling point ternary azeotropic
ethyl acetate – ethanol – water	Minimum boiling point ternary azeotropic

It can be seen, that the investigated mixtures have numerous azeotropic cases, therefore a complex separation method is needed to purify these systems. Previous case studies [5,9] demonstrate that for such complex, highly non-ideal mixtures, an effective method can be the extractive heterogeneous-azeotropic distillation (EHAD).
The task is to investigate the complete separation of quaternary mixtures using the EHAD method in ChemCAD 8.1.0 computer simulator with the UNIQUAC thermodynamic model.
The most important aspect of the modelling was ensuring that the specified purity goals could be achieved at the lowest possible operating cost, since distillation

operations are costly from this perspective. The goal was to implement multiple-column arrangements for both mixtures, provided the complex azeotropic mixtures formed allowed for the given separation scheme.
The optimal mass flow rates (highlighting the entrainer feed), the number of theoretical stages (N), the feed plate location, the reflux ratios (R), and heating and cooling requirements can also be determined for each distillation column. The initial concentration was equally distributed, 25 w/w% (weight per weight per cent) with a 1000 kg/h feed stream. The target purity requirement for products was a minimum of 99.9 w/w%, except for ethanol.
The Total Annual Cost (TAC) of the optimised system was determined using the cost estimation methodology proposed by Douglas [10], updated with the current Marshall & Swift cost index. Operating expenses were evaluated based on annual utility consumption, specifically steam and cooling water. A continuous operating time of 8,000 hours per year was assumed for the calculation of operating costs. Capital investment was annualised over a 10-year amortisation period for the overall cost assessment. Valve trays were selected as the internal column configuration in the process simulation.

2.1 The separation process of Mixture I

The separation flowsheet of Mixture I is shown in **Figure 2**. It can be seen, that the heat integration (HI) solution can be achieved in two cases.

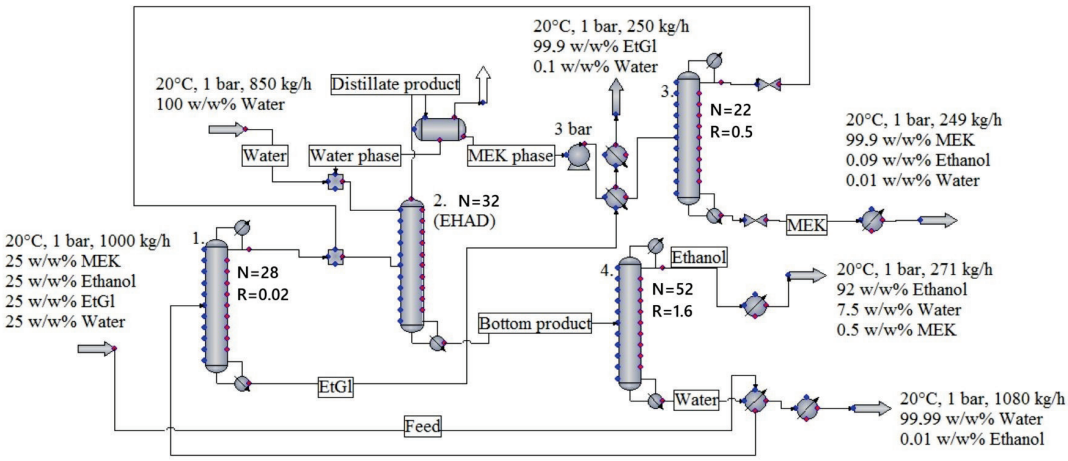

Figure 2: Separation flowsheet of Mixture I (methyl ethyl ketone, ethanol, ethylene glycol, water)

The purified product streams met the set purity requirements in all cases, therefore the separation efficiency of the system proved to be adequate. **Table 2** shows the costs of each equipment.

Table 2: Total Annual Cost (TAC) of the seapration process of Mixture I

Equipment section	TAC [1000 Euro/year] without HI	Ratio [%]	TAC [1000 Euro/year] with HI	Ratio [%]
Column 1	435	36.5	397	36.0
Column 2	163	13.7	165	15.0
Column 3	123	10.3	105	9.5
Column 4	297	24.9	297	27.0
Phase separator	72	6.1	74	6.7
Heat exchangers	101	8.5	63	5.8
Overall	1190		1100	

Energy consumption was primarily driven by the reboilers, which accounted for almost half of the total heat demand, so minimising steam consumption proved the most critical task. The majority of the investment costs were accounted for by columns 1 and 4, which were justified by the large material flows, the components with high heat of vaporisation and the number of theoretical plates required for the separations.

Columns 1 and 4 accounted for the majority of operating costs, primarily due to high feed mass flows and components with high boiling points and vaporisation heats; however, heat integration reduced these costs to some extent. The cost of heating steam also dominated the operating costs, so significant cost reductions were achieved by incorporating preheating steps in columns 1 and 3. Overall, heat integration reduced the TAC by almost 8% and the overall heat demand by 4% (from 5992 MJ/h to 5768 MJ/h), while the separation efficiency remained unchanged.

2.2 The separation process of Mixture II

Figure 3 shows the complete separation with heat integration solutions of Mixture II.

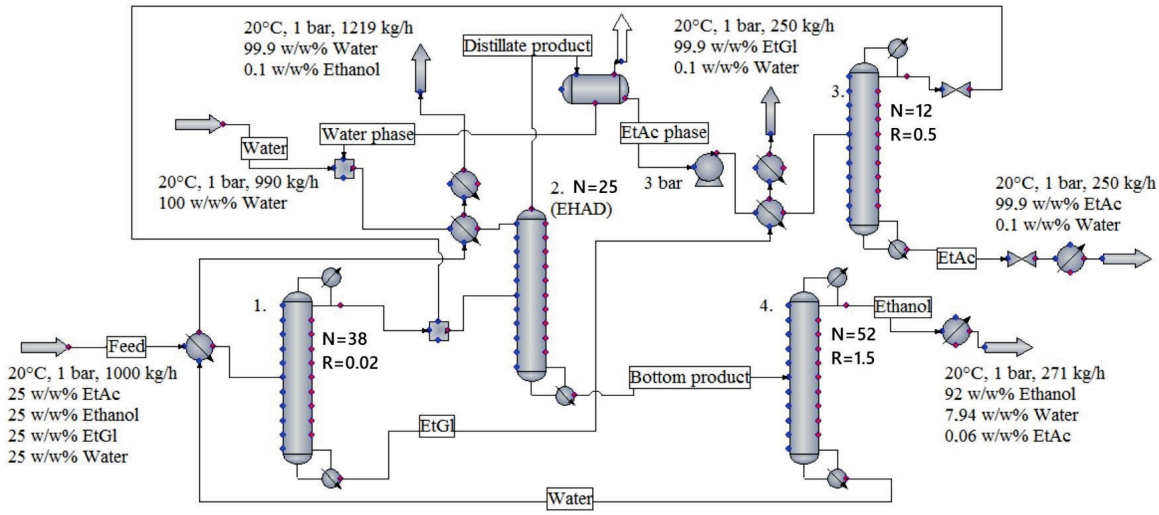

Figure 3: Separation flowsheet of Mixture II (ethyl acetate, ethanol, ethylene glycol, water)

An alternative configuration was also investigated, in which the EHAD column was the first, as shown in **Figure 4**.

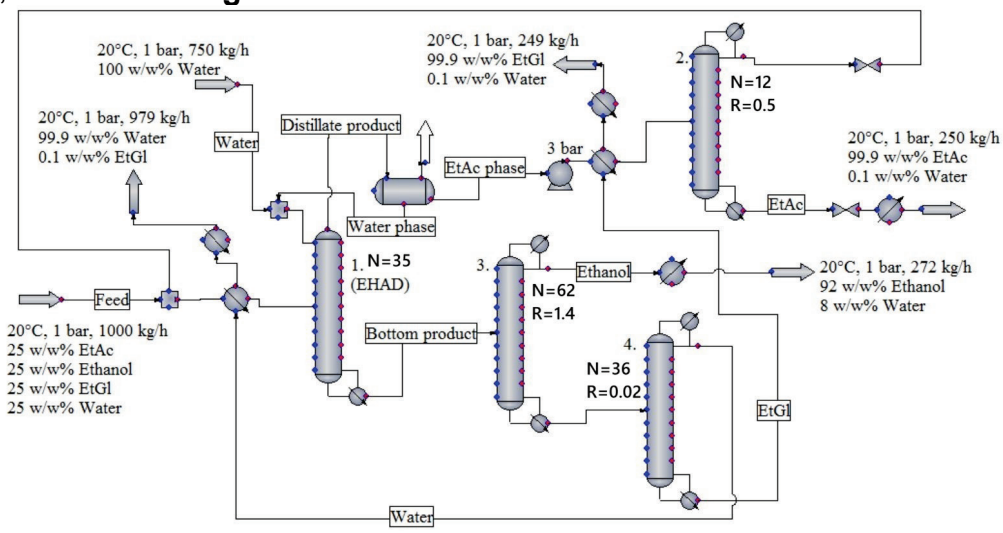

Figure 4: Separation flowsheet of Mixture II (ethyl acetate, ethanol, ethylene glycol, water) – alternative configuration

In both column configurations, the purified product streams meet the goal set for the task, indicating that the separation proved successful for this quaternary mixture as well. The majority of the energy consumption of the two models examined was accounted for by the heating steam requirement of the reboilers, which in both cases was 50% of the entire system's energy requirement, so the most crucial goal here was to minimise heating steam consumption. In the heat-integrated cases, the total energy consumption of the alternative configuration (7385 MJ/h) was 154% of the basic version (4785 MJ/h). **Figure 5** compares the most costly elements across heat-integrated separation versions.

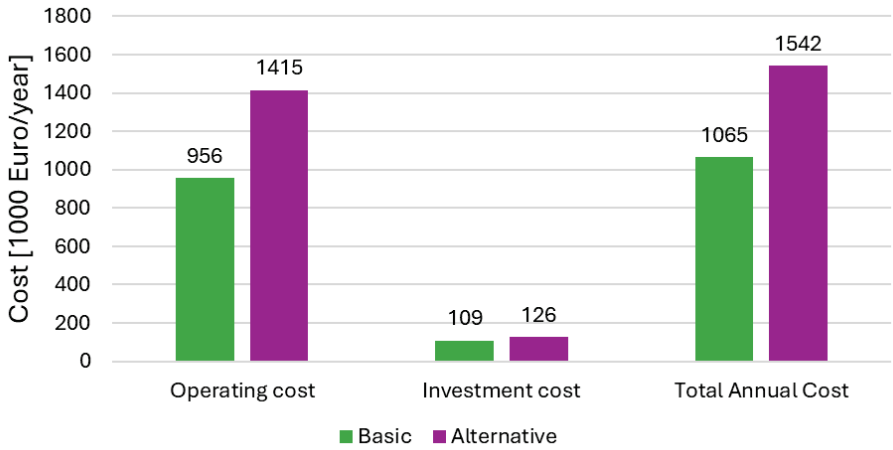

Figure 5: Comparison of the cost elements of the two different separation configurations (heat integration cases)

Overall, the basic column arrangement proved to be a significantly cheaper separation method in terms of the total costs. In the basic configuration, ethylene glycol, which has a relatively high boiling point compared to the other components, was separated from the mixture in the first column, so that, in the subsequent steps, lower-pressure heating steam was sufficient for the efficient operation of the reboilers, as reflected in the costs. In addition, due to the arrangement, there were more opportunities to preheat the feed streams to the columns, thereby reducing operating costs.

3. Conclusions

In this research, the separation of two different quaternary solvent mixtures was modelled in the ChemCAD computer process simulator using the extraction heterogeneous-azeotropic distillation (EHAD) method. It was possible to achieve efficient separation and the expected purities of the solvents even in the case of the complex ternary and quaternary azeotropic mixtures that were formed.

The most important aspect of the modelling was achieving the specified purity targets at the lowest possible operating cost. Since distillation operations require high-temperature steam and thus high energy requirements from reboilers, they are costly to operate.

For the separation of Mixture II, a two-column arrangement could be used; however, the most efficient approach is to start the separation by removing the least volatile component (ethylene glycol).

The cost estimate showed that distillation column operating costs are mainly due to reboiler duties. There is a close relationship between the reboiler heat demand and energy costs, because the amount of heat required to produce the high-pressure

saturated steam used to heat the columns directly determines the operating cost. In this work, a reduction in heat demand was achieved, depending on the mixture type and the column layout. It can be concluded that the heat requirements for the separation tasks can be reduced through the applied heat integration. Further TAC reduction could be achieved through pervaporation or the installation of a heat pump.

Acknowledgements
This publication was supported by the Alexander von Humboldt Foundation and the Michael Somogyi Program of the Varga József Foundation.

References

[1] M. Skiborowski, A. Harwardt, W. Marquardt, Chapter 8 - Conceptual Design of Azeotropic Distillation Processes, in: A. Górak, E. Sorensen (Eds.), Distillation, Academic Press, Boston, 2014: pp. 305–355. https://doi.org/10.1016/B978-0-12-386547-2.00008-9.
[2] A.A. Kiss, R. Smith, Rethinking energy use in distillation processes for a more sustainable chemical industry, Energy 203 (2020) 117788. https://doi.org/10.1016/j.energy.2020.117788.
[3] C. Cui, J. van Reisen, I. Tyraskis, A.A. Kiss, Efficient heat integration within discretely heat integrated distillation columns using liquid injection, AIChE Journal 71 (2025) e18861. https://doi.org/10.1002/aic.18861.
[4] A. Szanyi, Separation of non-ideal quaternary mixtures with novel hybrid processes based on extractive heterogeneous-azeotropic distillation, PhD Thesis, Budapest University of Technology and Economics, Budapest, 2005.
[5] A.J. Toth, Comprehensive evaluation and comparison of advanced separation methods on the separation of ethyl acetate-ethanol-water highly non-ideal mixture, Separation and Purification Technology 224 (2019) 490–508. https://doi.org/10.1016/j.seppur.2019.05.051.
[6] E. Haaz, B. Szilagyi, D. Fozer, A.J. Toth, Combining extractive heterogeneous-azeotropic distillation and hydrophilic pervaporation for enhanced separation of non-ideal ternary mixtures, Frontiers of Chemical Science and Engineering 14 (2020) 913–927. https://doi.org/10.1007/s11705-019-1877-1.
[7] A.J. Toth, A. Szanyi, K. Koczka, P. Mizsey, Enhanced separation of highly non-ideal mixtures with extractive heterogeneous-azeotropic distillation, Separation Science and Technology 51 (2016) 1238–1247. https://doi.org/10.1080/01496395.2015.1107099.
[8] J. Gmehling, J. Menke, J. Krafczyk, K. Fischer, Azeotropic Data, Wiley-VCH Verlag GmbH & Co. KGaA, Weinheim, New York, Basel, Cambridge, Tokyo, 1994.
[9] A.J. Toth, E. Haaz, T. Nagy, R. Tari, A.J. Tarjani, D. Fozer, A. Szanyi, K.-A. Koczka, L. Racz, G. Ugro, P. Mizsey, Evaluation of the accuracy of modelling the separation of highly non-ideal mixtures: extractive heterogeneous-azeotropic distillation, in: A. Espuña, M. Graells, L. Puigjaner (Eds.), 27th European Symposium on Computer Aided Process Engineering, Elsevier, 2017: pp. 241–246. https://doi.org/10.1016/B978-0-444-63965-3.50042-8.
[10] J.M. Douglas, Conceptual Design of Chemical Processes, 1st edition, McGraw-Hill Science/Engineering/Math, New York, 1988.

Polymeric hydrogels for water removal from gaseous media: formulation and optimizations

Henrique Luiz Gonçalves[1]; Luísa Barbieri Sandoval[1]; Maria Regina Wolf Maciel[1]; Leonardo Vasconcelos Fregolente[1]
[1]University of Campinas (UNICAMP), School of Chemical Engineering, Campinas, Brazil

Abstract
Polymeric hydrogels are hydrophilic materials made of tridimensional chains capable of retaining water without their dissolution. They have consolidated applications in various fields, such as medical, pharmacological or agricultural, and another use, developed by this research group, is for treatment of organic media contaminated with water. Different studies were carried out using hydrogels as desiccant materials, developing their formulation, use in different systems (batch or continuous) and applications in different media (such as fuels or oils), studies that also demonstrated that the material can be regenerated and reused. In addition to their uses in liquid media, hydrogels have potential uses in treatment of gas streams: water vapor can be encountered in gaseous effluents of industrial processes, as well as in natural gas and in hydrogen fuel. The water presence in those gases can lead to the occurrence of corrosion and formation of hydrates inside of pipelines, besides to decrease the desired purity. In this context, considering the necessity of removing this water from gases, the high water retention capacity of hydrogels is worth noting. In the present work, different combinations of hydrogel formulation and drying method were considered for water removal from gases. Thus, the swelling kinetics of these hydrogels were studied, allowing the classification of the mechanisms of water adsorption by the hydrogels, and an experiment under controlled air humidity were carried out, to evaluate the water adsorption of hydrogels from gaseous medium.

Keywords
Hydrogels, water removal, swelling, gaseous medium, adsorption.

1. Introduction

Although a series of developments in the use of hydrogels for water removal from liquid organic media have been made in the last years (ESTEVAM *et al.*, 2026; FREGOLENTE *et al.*, 2023; GONÇALVES *et al.*, 2025), the use of this material for dehydration of gaseous media is at its first stages. One industrial example of the importance of reducing the water content of gases is the effluent streams from coal burning, in which the removal of contaminants results in temperature reduction and potential water saturation of the gaseous stream, that can condensate with a high concentration of corrosive compounds (SIJBESMA *et al.*, 2008). A similar situation occurs in natural gas extraction, whose water can condensate, resulting in corrosive solutions and potential hydrates in the pipeline, impairing its transport capacities (SANTOS *et al.*, 2021).

Polymeric hydrogels are studied in the present work as a potential solution for future treatment of gases for their high-water affinity and capacity of retaining humidity in

the interior of their structure. Six different hydrogels in terms of composition and drying method were evaluated in batch experiments: poly(acrylamide), poly(sodium acrylate) and cellulose, being oven-dried or freeze-dried. Firstly, the kinetics of their swelling were studied, in distilled water, allowing for the classification of their mass transfer mechanisms and if they are driven by Fickian diffusion, chain relation or both.
Afterwards, the hydrogels were kept under controlled air humidity (72 ± 2%), and their mass variations were observed for 7 days. This allowed the identification of the materials with the greatest potential for use as gas desiccants, providing a basis for further developments in this area.

2. Results and discussion

2.1 Swelling experiments

Three different hydrogels were made: polyacrylamide hydrogels, obtained using *N*,*N'*-methylenebisacrylamide (MBAAm) as the crosslinker (0.015 mol/mol of monomers), 2% vol of TEMED 0.57 mol/L, 4% vol of sodium persulfate 0.01 g/mL, and 4% wt. of polyacrilamide. As for the poly(sodium acrylate) hydrogels, the proportions were 9.2% wt. of sodium acrylate, 0.015 mol of mBAAm/mol monomer, 2% vol. TEMED and 1.6% vol of sodium persulfate 0.01 g/mL. These solutions were bubbled with N_2 for 10 minutes, before the addition of $Na_2S_2O_8$, following a methodology based on a previous work (FREGOLENTE *et al.*, 2023).
For the cellulose hydrogel, the preparation methodology was also based on a previous work (ESTEVAM *et al.*, 2026): 6.96 g of cellulose was first diluted with 7.5 g NaOH and 11.5 g urea in 81 mL H_2O at 5 ºC. Afterwards, 170 mL of liquid cellulose was heated until 30ºC, mixed with 17 mL of epichlorohydrin for 1 hour and oven-dried for 4 hours. After a day of rest, all hydrogels were cut into small discs.
The hydrogels were then dried out using two different techniques, oven-drying at 60 ºC or freeze-drying at maximum swelling degree – W_{max} – except the poly(sodium acrylate) hydrogel, freeze-dried both at W_{max} and at a swelling degree of 30. The freeze-drying goal was to allow the hydrogels to keep a more porous structure, when compared to the oven-dried ones.
After drying the different hydrogels, a kinetic experiment was carried out to determine the swelling degree (*W*) of the hydrogels throughout time. For this, the hydrogels were immersed in distilled water during different times. The swelling degree is an important property of hydrogels that correlates their dry mass (M_o) and their mass after retaining water for a time t (M_t), as seen in Equation 1.

$$W = \frac{M_t - M_0}{M_0} \tag{1}$$

The swelling kinetic for the polyacrylamide, poly(sodium acrylate) and cellulose hydrogels are shown in Figures 1, 2, 3, respectively.
The poly(sodium acrylate) hydrogels presented the highest W_{max}, followed by the polyacrylamide and cellulose hydrogels, results that may be associated to the hydrophilicity of these polymers and the flexibility of their chains. Generally, hydrogels obtained from natural polymers (such as cellulose) have a lower water retention capacity than synthic ones (AHMAD *et al.*, 2022), and the presence of anionic groups in the poly(sodium acrylate) hydrogels increases their hydrophilicity, in comparison to the poly(acrylamide) hydrogels (KARADAĞ and SARAYDIN, 2002).

Additionally, two kinetic parameters for the swelling mechanism of hydrogels were obtained from a linear adjustment of the results seen above: the diffusional constant (k) and the diffusional exponent (n), determined as presented in Equation 2. In this equation, M_t^{water} represents the mass of water (in grams) after the time t (in minutes) and M_∞^{water} represents the mass of water at equilibrium.

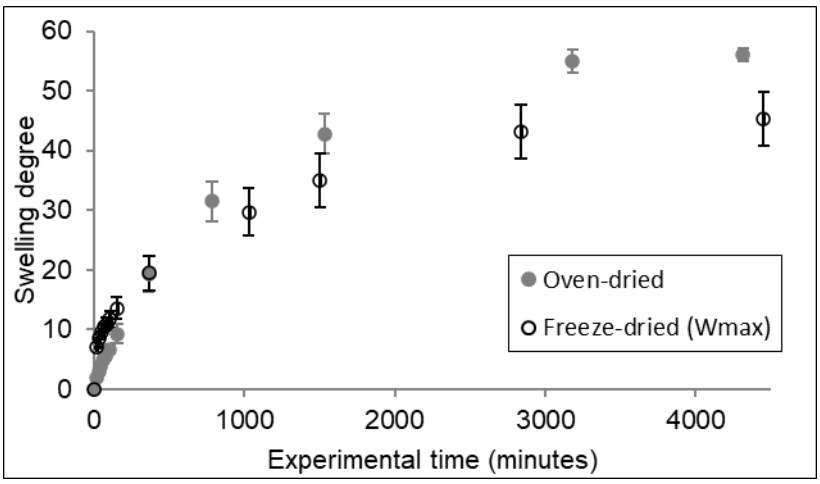

Figure 1: Swelling kinetic of polyacrylamide hydrogels.

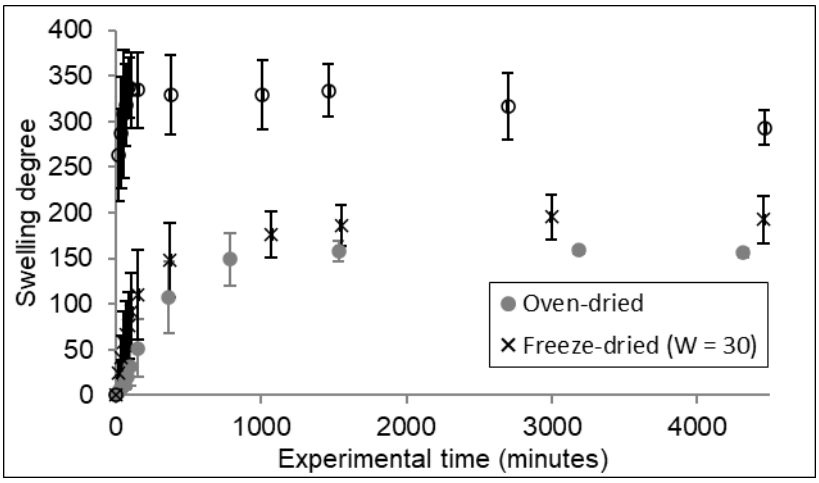

Figure 2: Swelling kinetic of poly(sodium acrylate) hydrogels.

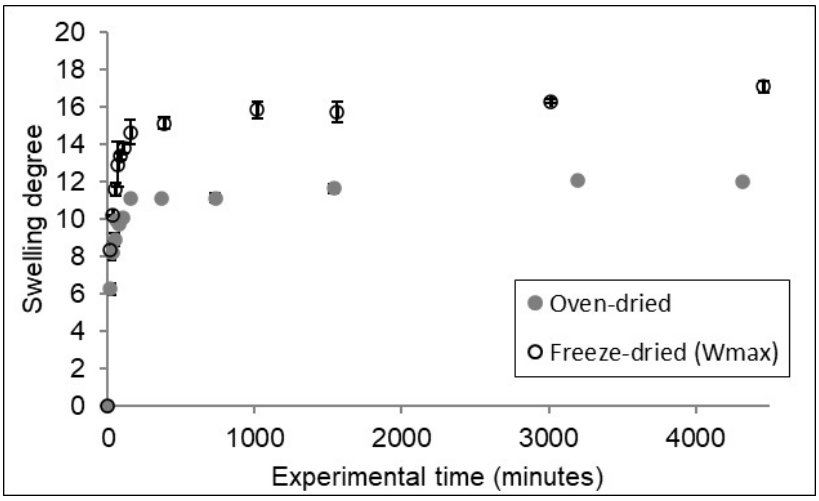

Figure 3: Swelling kinetic of cellulose hydrogels.

$$\frac{M_t^{water}}{M_\infty^{water}} = k.t^n \quad (2)$$

The parameters for each hydrogel, as well as the coefficient of determination (R^2) are shown in Table 1. The values of *W* shown refers to the swelling degrees at the start of the freeze-drying process.

	Hydrogel	n	k	R^2	Classification
Oven-dried	Polyacrylamide	0.6636	5.77×10^{-3}	0.992	Anomalous
	Poly(sodium acrylate)	1.1722	7.08×10^{-4}	0.991	Case-II
	Cellulose	0.3280	2.16×10^{-1}	0.985	Fickian
Freeze-dried	Polyacrylamide (W_{max})	0.3649	5.09×10^{-2}	0.991	Fickian
	Poly(sodium acrylate) ($W = 30$)	0.6570	2.18×10^{-2}	0.998	Anomalous
	Poly(sodium acrylate) (W_{max})	0.1401	5.13×10^{-1}	0.991	Fickian
	Cellulose (W_{max})	0.2547	2.47×10^{-1}	0.984	Fickian

Table 1: Kinetic parameters and R^2 for swelling of each hydrogel.

The diffusional exponent (n) classifies the swelling mechanism as Fickian ($n < 0.5$); controlled by diffusional mechanisms, anomalous ($0.5 < n < 1$); controlled by both diffusion and relaxation of the polymeric chains, and Case-II ($1 < n$); predominantly controlled by the relaxation of the chains (RITGER and PEPPAS, 1987).

All hydrogels freeze-dried at W_{max} exhibited a Fickian behavior. This can be related to their structure, initially expanded and porous, requiring a lower relaxation of the polymeric chain for the water penetration in its interior (when compared to the oven-dried hydrogels), being thus governed by diffusional mechanisms for the mass transfer of water. The same classification was observed for the cellulose hydrogel (oven-dried), but in this case, the polymeric chains were not as flexible as the ones of the other hydrogels, resulting in diffusional forces being more significant.

For the poly(sodium acrylate) oven-dried hydrogel, the one with the highest hydrophilicity, the expansion of the polymeric chains ended up being the controlling factor for the water mass transfer into the hydrogel, being classified as Case-II. Finally, for the polyacrylamide (oven-dried) and poly(sodium acrylate) (freeze-dried, $W = 30$), both diffusional forces and relaxation of the polymeric chains were impactful.

2.2 Water adsorption from gaseous medium

To evaluate the performance of the hydrogels in removing water from gases, considering both water adsorption and internal mass transfer within the hydrogel matrix, saturated $NaNO_3$ solutions were prepared and placed in beakers inside a closed system, establishing a constant relative humidity of 72 ± 2%.

Within this environment, hydrogel samples were placed in Petri dishes and periodically weighed over a 7-day period, enabling comparison of mass gains and analysis of water mass transfer from the gaseous phase. Figure 4 presents the results for the oven-dried hydrogels, while Figure 5 shows the corresponding results for the freeze-dried samples.

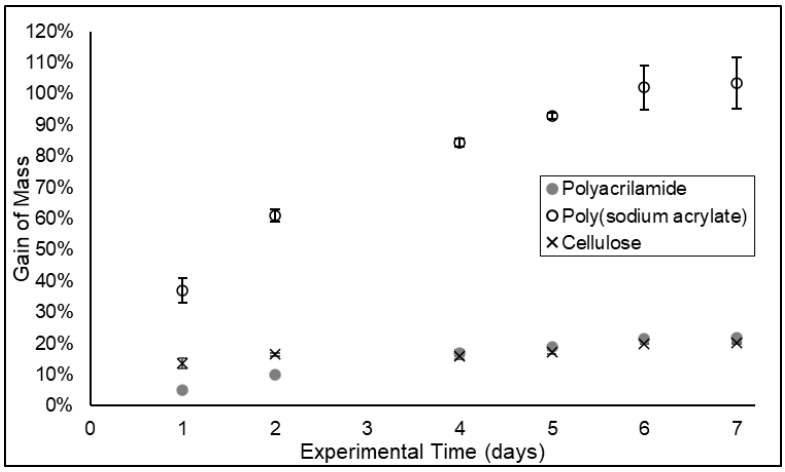

Figure 4: Gain of mass due to water uptake by oven-dried hydrogels.

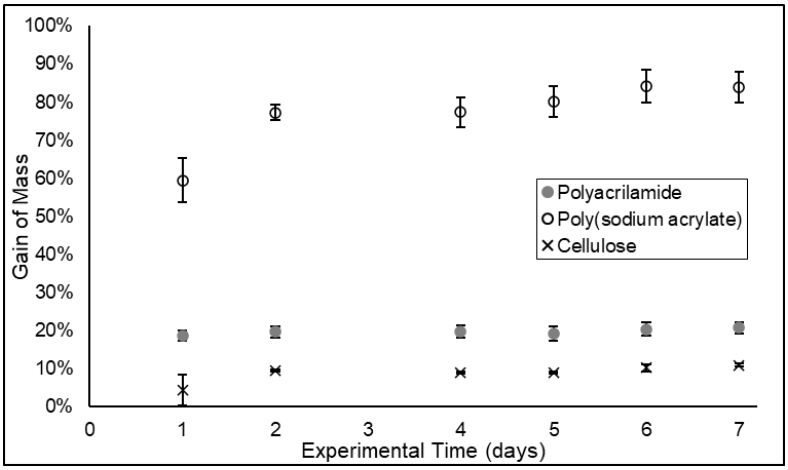

Figure 5: Gain of mass from due to water uptake by freeze-dried hydrogels.

Regardless of the drying method, poly(sodium acrylate) presented the highest capacity for water uptake, reflecting its high hydrophilicity. Among the oven-dried samples, the poly(sodium acrylate) hydrogel exhibited a mass gain approximately five times higher than that of the other two hydrogels. For the freeze-dried samples, its mass gain was about four times greater than that of the polyacrylamide hydrogel.
Although the cellulose and polyacrylamide oven-dried hydrogels presented similar results at the equilibrium, the cellulose one achieved it faster, with little variation after the first day of experiment. For the freeze-dried hydrogels, the polyacrylamide ones were able to retain more water than the cellulose hydrogels.
One occurrence worth noting is that less time was required for the freeze-dried hydrogels to reach equilibrium, when compared to the oven-dried hydrogels, which can be related to the fact that oven-drying the hydrogels results in smaller and more closed pores, while freeze-drying them results in a more porous structure. Thus, the water vapor can more easily penetrate the hydrogels and be adsorbed. On the other hand, freeze-drying the poly(sodium acrylate) and cellulose hydrogels reduced the maximum gain of mass due to water adsorption, with negligible changes for this value for the polyacrylamide hydrogels.

3. Conclusions

This work allowed a deeper understanding of the potential use of polymeric hydrogels as gas desiccants and the impacts of the drying method in the mass

transfer of water into the hydrogels. For both drying methods, oven- and freeze-drying, the poly(sodium acrylate) hydrogel reached the highest swelling degree, both in swelling experiments and under controlled air humidity. Moreover, for the polyacrylamide and poly(sodium acrylate) hydrogels, freeze-drying the hydrogels resulted in a higher importance of diffusional mechanisms for water mass transfer, when compared to oven-drying them. In contrast, for the cellulose hydrogel, both dying methods resulted in the predominance of diffusional forces, likely due to its more rigid polymeric structure.

Based on the results presented in this work, further developments can be made using poly(sodium acrylate) hydrogels, found to be the most promising ones, or using copolymeric hydrogels containing sodium acrylate monomer. Also, continuous experiments, using hydrogels for water removal from gaseous streams, are necessary for the intended application in industrial scale.

Acknowledgements

The authors thank the financial grants of National Council for Scientific and Technological Development (CNPq), process numbers 302888/2023-3 and 308672/2025-9, Human Resources Program of the National Agency of Petroleum, Natural Gas and Biofuels (PRH-ANP), process number 2025/21031-9; and, also, this study was financed by the São Paulo Research Foundation (FAPESP), Brazil, Process Number #2022/16379-8.

References

AHMAD, Z.; SALMAN, S., KHAN, S. A.; AMIN, A.; RAHMAN, Z. U.; AL-GHAMDI Y. O.; AKHTAR, K.; BAKHSH, E. M.; KHAN, S. B. *Versatility of Hydrogels: From Synthetic Strategies, Classification, and Properties to Biomedical Applications*, Gels, vol. 8 (3), 2022, DOI: 10.3390/gels8030167.

ESTEVAM, B. R.; TSURUTA, K. M.; MANCUZO, M. V.; CAVALLINI JÚNIOR, A. P. C.; MORAES, A. M.; FREGOLENTE, L. V. *Cellulose hydrogels as effective desiccants for water-contaminated hydraulic lubricant oil*, Journal of Industrial and Engineering Chemistry, vol. 153, p. 628-640, 2026, DOI: 10.1016/j.jiec.2025.06.025.

KARADAĞ, ERDENER; SARAYDIN, DURSUN *Swelling of Superabsorbent Acrylamide/Sodium Acrylate Hydrogels Prepared Using Multifunctional Crosslinkers*, Turkish J. of Chem., vol. 26 (6), 2002.

FREGOLENTE, L. V.; GONÇALVES, H. L.; FREGOLENTE, P. B. L.; WOLF MACIEL, M. R.; SOARES, J. B. P. *Sodium polyacrylate hydrogel fixed bed to treat Water-Contaminated cloudy diesel*, Fuel, vol. 332, 2023, DOI: 10.1016/j.fuel.2022.125953.

GONÇALVES, H. L.; P. B. L.; WOLF MACIEL, M. R.; FREGOLENTE, L. V. *Hydrogel Raschig Rings: Synthesis, Geometric Studies and Application for Water Removal from Biodiesel*, Chemical Engineering Transactions, vol. 117, p. 952-930, 2025, DOI:10.3303/CET25117155.

RITGER, P. L.; PEPPAS, N. A. *A Simple Equation for Description of Solute Release II. Fickian and Anomalous from Swellable Devices*, Journal of Controlled Release, vol. 5, (1), p. 37-42, 1987, DOI: 10.1016/0168-3659(87)90035-6.

SANTOS, K. M. C.; MENEZES, T. R.; OLIVEIRA, M. R.; SILVA T. S. L.; SANTOS, K. S.; BARROS, V. A.; MELO, D. C.; RAMOS, A. L.; SANTANA, C. C.; FRANCESCHI, E.; DARIVA, C.; EGUES, S. M.; BORGES, G. R.; DE CONTO, J. F. *Natural gas dehydration by adsorption using MOFs and silicas: A review*, Separation and Purification Technology, vol. 276, 2021, DOI: 10.1016/j.seppur.2021.119409.

SIJBESMA, H.; NYMEIJER, K.; VAN MARWIJK, R.; HEIJBOER, R.; POTRECK, J.; WESSLING M. *Flue gas dehydration using polymer membranes*, Journal of Membrane Science, vol. 313, p. 263-276, 2008, DOI: 10.1016/j.memsci.2008.01.024.

Concentric tube module for vacuum air gap membrane distillation

Hugo Valdés[1], Sofía Tosso[2], Nicolás Cancinos[3], Constanza Mora[3], Aldo Saavedra[4], Wladimir Silva[5]

[1]Department of Computing and Industries, Universidad Católica del Maule, Talca, Chile;
[2]Doctoral Program in Engineering, Universidad Católica del Maule, Talca, Chile;
[3]School of Industrial Civil Engineering, Universidad Católica del Maule, Talca, Chile;
[4]Department of Chemical Engineering and Bioprocesses, Universidad de Santiago de Chile, Santiago, Chile;
[5]Department of Biotechnology, Universidad Tecnológica Metropolitana, Ñuñoa, Chile.

Abstract

Vacuum Air Gap Membrane Distillation (VAGMED) enhances mass transfer by combining vacuum-driven vapor transport with condensation on a cold surface separated by an air gap; however, compact prototypes require careful control of fabrication and sealing under vacuum conditions. In this work, a compact three-tube concentric membrane module (CTM) was fabricated and experimentally implemented using 3D-printed components. First, the module parts were manufactured on a Bambu Lab X1-Carbon printer, with material selection, increased wall thickness, and 100% solid infill applied to improve mechanical stability and reduce porosity. Subsequently, a multi-step sealing protocol was implemented, including LOCTITE 406 for PETG bonding, Fusion epoxy to reinforce high-stress junctions, controlled PTFE membrane bonding, and an external resin coating to ensure vacuum-tight operation. After assembly, laboratory tests demonstrated stable and repeatable operation at 0.3 L/min and were used to evaluate permeate flux as a function of coolant temperature at brine temperatures of 25°C and 50°C. Finally, complementary CFD simulations in ANSYS Fluent 2024 R1 were conducted for the internal brine channel and external cooling-water channel at flow rates of 0.3 and 1.1 L/min to analyze pressure distribution, velocity fields, and volume fraction behavior.

Keywords

Membrane distillation; Vacuum air gap membrane distillation; membrane module; 3D printing; PETG; computational fluid dynamics

1. Introduction

Membrane distillation (MD) is a thermally driven separation process in which a vapor pressure gradient across a hydrophobic membrane enables water vapor transport while retaining non-volatile solutes (Yang et al., 2022). However, laboratory- and pilot-scale implementations are often constrained by practical challenges in module construction, sealing reliability, and system integration. Four main membrane distillation configurations exist and combining two of them yields the Vacuum Air Gap Membrane Distillation (VAGMED) process. VAGMED combines vacuum-driven mass transfer with condensation on a cold surface separated by an air gap, enabling compact operation with intensified transport (Francis et al., 2022). Because VAGMED requires vacuum-tight operation, inlet and flow transition geometries are critical to avoid localized hydraulic loading and mechanical failure (Ghaffour et al., 2017). Additive manufacturing enables rapid prototyping of customized modules, and concentric-tube concepts provide a compact integration of the air gap and condensation surface within a single architecture (Valdes et al., 2025). Computational Fluid Dynamics (CFD) is also widely used to evaluate pressure losses and flow structures, thereby supporting experimental interpretation and improving module design (Ali et al., 2024). The objective of this work is to design, fabricate, and commission a compact 3D-printed concentric tube membrane module for VAGMED operation, supported by CFD simulations in ANSYS Fluent 2024 R1 to evaluate pressure, velocity (magnitude and streamlines), and volume fraction fields.

2. Results and discussion

The experimental development of a three-tube concentric membrane module (CTM) for VAGMED operation required a compact geometry and adequate mechanical rigidity for stable experimental testing. The final module geometry and its assembled configuration are shown in Figure 1. The module was manufactured using 3D-printed components produced with a Bambu Lab X1-Carbon printer, with 100% sold infill.

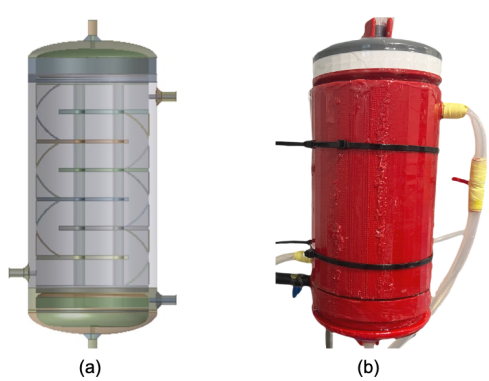

Figure 1: CTM developed for VAGMED operation: (a) CAD geometry, and (b) assembled 3D printed module (PETG).

Prototype iterations showed that material selection and sealing quality control module integrity under vacuum operation. PLA prototypes enabled dimensional validation but presented recurrent leakage at critical interfaces. PETG improved rigidity and reduced assembly deformation, and increased wall thickness enhanced structural stability.
Vacuum-tight operation was achieved using a combined sealing protocol. LOCTITE 406 was applied for the rapid bonding of PETG parts and sealing of small interfaces. Fusion epoxy was used to reinforce high-stress junctions, particularly around copper tube connections and geometric transitions. The PTFE membrane was bonded to ensure correct positioning and minimize leakage pathways. After curing, an external resin coating was applied as a secondary barrier, enabling repeatable vacuum-tight commissioning.
Experimental commissioning under laboratory conditions confirmed stable operation at 0.3 L/min, with continuous circulation maintained in both the brine and cooling-water loops. In contrast, at 1.1 L/min the module repeatedly failed at startup due to an abrupt rupture of the inlet connection region (≈1 cm in diameter), leading to immediate loss of hydraulic integrity and preventing sustained testing. Figure 2 presents the laboratory VAGMED experimental configuration used in this work, including the brine feed loop, cooling-water loop, thermal bath, chiller, vacuum line, and distillate collection.

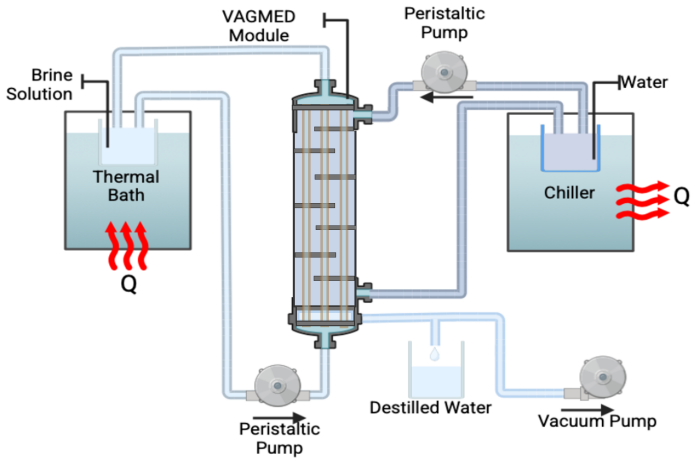

Figure 2: Schematic diagram of the experimental VAGMED setup used for module commissioning and operation.

After commissioning, laboratory trials were conducted to evaluate the permeate flux response under controlled thermal conditions. These experiments were performed by varying the coolant temperature while maintaining brine temperatures of 25°C and 50°C, allowing the assessment of the module's thermal driving force and its influence on vapor transport. The vacuum pressure was 60 kPa. The measured permeate flux reflects the combined effect of heat and mass transfer within the VAGMED configuration and serves as a direct indicator of module performance under stable operating conditions.

Figure 3 presents the permeate flux as a function of coolant temperature for both brine temperatures, providing an experimental performance baseline for the proposed CTM module and supporting the interpretation of the subsequent hydrodynamic analysis. While Jia et al. (2021) achieved a permeate flux five times greater with a PTFE hollow-fiber module, the vacuum pressure employed in their experiments was roughly five times lower than that used in our study. This inverse correlation between pressure and flux aligns our findings with theoretical expectations.

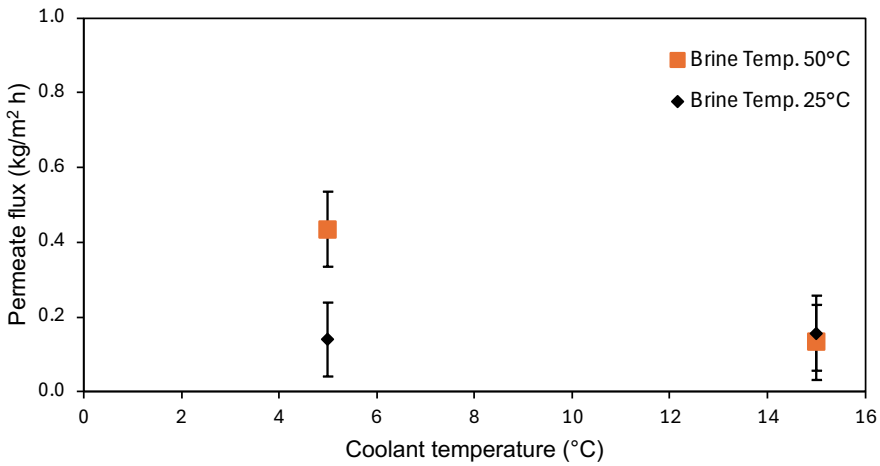

Figure 3: Experimental permeate flux as a function of coolant temperature for two brine temperatures (25°C and 50°C) during VAGMED operation.

CFD simulations in ANSYS Fluent 2024 R1 were performed separately for the internal (brine) and external (cooling water) channels at flow rates of 0.3 and 1.1 L/min to support the experimental observations. At 0.3 L/min, both domains showed smooth flow development, relatively uniform velocity fields, moderate pressure losses, and stable volume fraction distributions, indicating continuous liquid occupancy and the absence of phase discontinuities. Streamlines at this flow rate exhibited limited secondary structures, consistent with stable laboratory operation.

In contrast, at 1.1 L/min, the simulations predicted stronger inlet acceleration, higher velocity gradients near the inlet contraction, and a localized pressure rise with a steeper pressure gradient in the initial segment. This response was observed in both domains due to the shared inlet section (1 cm in diameter), indicating that contraction governs the local hydrodynamic loading. These results indicate that localized hydraulic overload at the inlet is the primary driver of the structural failure observed experimentally at high flow rates. In the external channel, particularly at 1.1 L/min, secondary flow structures associated with curvature and manifold regions were more clearly visualized; however, these structures tend to dissipate downstream as the flow develops. Overall, the CFD results show that increasing flow rate intensifies localized losses and hydrodynamic loading at the inlet connection region.

Overall, the CTM was successfully fabricated and commissioned for VAGMED operation at low flow rate, while high-flow operation is limited by inlet mechanical resistance. Future work should prioritize inlet reinforcement and transition redesign to reduce localized losses and pressure gradients. Figure 4 summarizes the CFD results for both channels at 0.3 and 1.1 L/min.

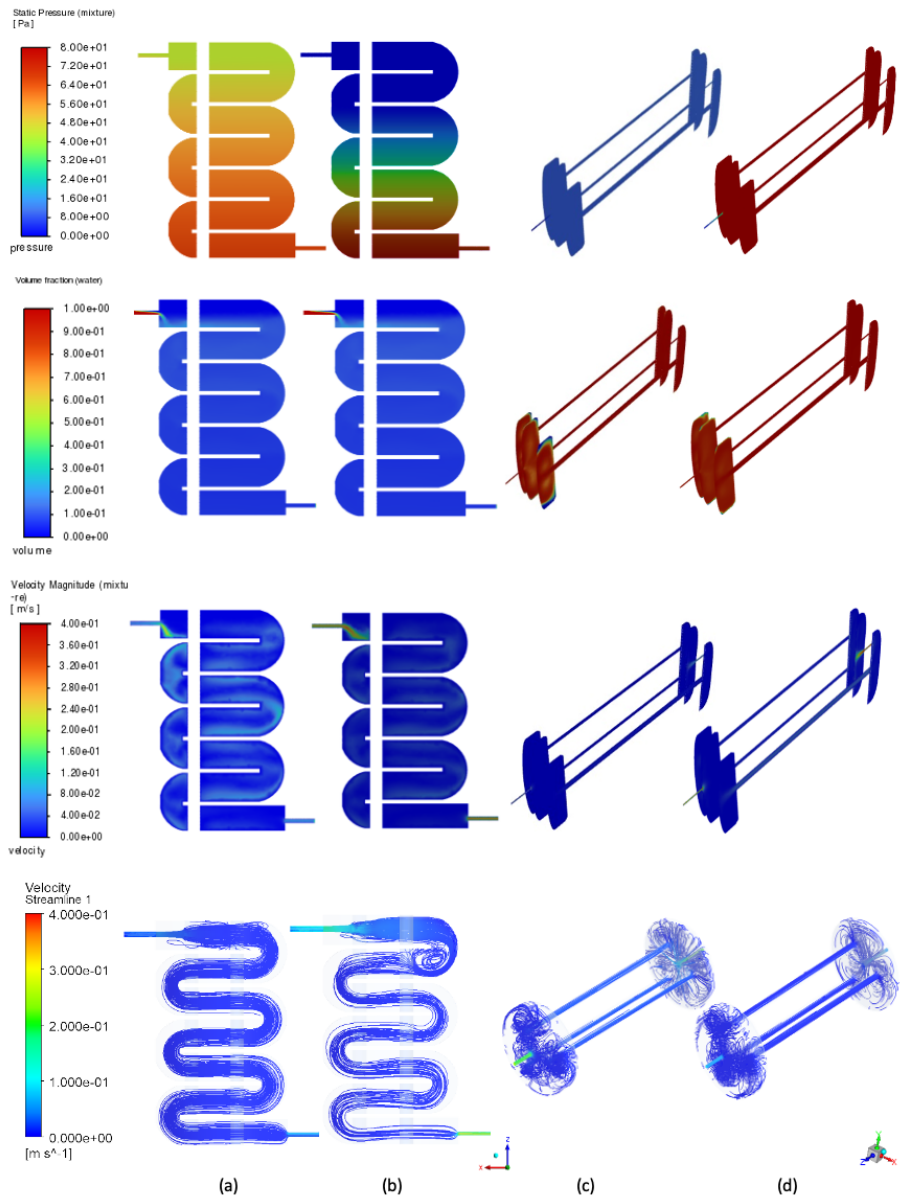

Figure 4: CFD simulations in ANSYS Fluent 2024 R1 showing pressure distribution, volume fraction, velocity magnitude, and streamline velocity fields in the CTM channels at 0.3 and 1.1 L/min: (a) external cooling-water channel at 0.3 L/min, (b) external cooling-water channel at 1.1 L/min, (c) internal brine channel at 0.3 L/min, and (d) internal brine channel at 1.1 L/min.

3. Conclusions

A compact 3D-printed concentric tube membrane module (CTM) composed of three concentric tubes for VAGMED operation was fabricated and commissioned, demonstrating its feasibility for experimental implementation. PETG material selection, increased wall thickness, and a multi-step sealing protocol (LOCTITE 406, Fusion epoxy, PTFE membrane bonding, and external resin coating) enabled repeatable vacuum-tight operation and stable integration into the experimental setup. The module operated reliably at 0.3 L/min without mechanical failure. In contrast, operation at 1.1 L/min resulted in early rupture at the inlet connection region (≈1 cm in diameter), preventing sustained high-flow testing. CFD simulations in ANSYS Fluent 2024 R1, performed separately for the internal (brine) and external (water) channels, indicated increased inlet velocity gradients and localized pressure loading at 1.1 L/min, supporting hydraulic overload as the failure mechanism. Future work will focus on reinforcing the inlet region, redesigning the inlet transition to reduce localized losses, increasing pressure gradients, and increasing the number of concentric tubes to enhance heat and mass transfer while maintaining mechanical stability.

Acknowledgements

The authors acknowledge the financial support provided by the FONDECYT Regular Project ID1240946. This research was also funded by the Agencia Nacional de Investigación y Desarrollo (ANID) through the Doctorado Nacional Scholarship 2025 (Folio 21252950).

References

Ali, A., Agha Shirazi, M., Nthunya, L., Castro-Muñoz, R., Ismail, N., Tavajohi, N., Zaragoza, G., & Quist-Jensen, C. (2024). Progress in module design for membrane distillation. Desalination, 581, 117584.

Francis, L., Ahmed, F. E., & Hilal, N. (2022). Advances in membrane distillation module configurations. Membranes, 12(1), 81.

Ghaffour, N., Alsaadi, A., & Francis, L. (2017). Vacuumed gap membrane distillation (VAGMED) module, multi-stage VAGMED systems, and VAGMED processes (U.S. Patent Application No. 15/538,286). United States.

Jia, X., Lan, L., Zhang, X., Wang, T., Wang, Y., Ye, C., & Lin, J. (2021). Pilot-scale vacuum membrane distillation for decontamination of simulated radioactive wastewater: System design and performance evaluation. Separation and Purification Technology, 275, 119129.

Valdes, H., Saavedra, A., Ortiz-Basurto, R., Mora, C., Cancinos, N., Cerda, J., Henríquez, I., Tosso, S., Laurens, L., & Vera-Puerto, I. (2025). Dispositivo de tubos concéntricos para destilación por membrana al vacío con espacio de aire (Solicitud de Patente [Modelo de utilidad] No. 202504157). Instituto Nacional de Propiedad Industrial, Chile.

Yang, S., Jasim, S. A., Bokov, D., Chupradit, S., Nakhjiri, A. T., & El-Shafay, A. S. (2022). Membrane distillation technology for molecular separation: A review on the fouling, wetting and transport phenomena. Journal of Molecular Liquids, 349, 118115.

Computational Design and Process Simulation of Novel Deep Eutectic Solvents for Sustainable CO_2 Absorption

Gael Vite-Cervantes[1], Rodolfo J. Díaz-Molina[2], Myrna H. Matus[2], Gabriel Segovia-Hernández[1], Eduardo Sánchez-Ramírez[1]
[1]Departamento de Ingeniería Química, Campus Guanajuato, División de Ciencias Naturales y Exactas, Universidad de Guanajuato, Noria Alta S/N, C.P. 36050, Guanajuato, Gto., México.
[2] Instituto de Química Aplicada, Universidad Veracruzana, Dr. Luis Castelazo Ayala S/N, C.P. 91090, Xalapa, Ver., México.

Abstract

The energy sector remains one of the largest contributors to anthropogenic carbon dioxide (CO_2) emissions, mainly due to fossil fuel–based thermoelectric power generation. Although renewable energy technologies are expanding rapidly, their current deployment rates are insufficient to satisfy global energy demand in the short to medium term. Consequently, mitigation strategies compatible with existing infrastructure are urgently required. Carbon capture and storage (CCS), particularly post-combustion chemical absorption, represents a technologically mature option; however, conventional alkanolamine-based solvents are hindered by high energy requirements for regeneration, solvent degradation, volatility, corrosion, and elevated operating costs. In this context, deep eutectic solvents (DESs) have emerged as promising sustainable alternatives due to their low vapor pressure, tunable properties, reduced toxicity, and biodegradability. Nevertheless, their large-scale implementation is limited by the scarcity of reliable thermochemical and phase-equilibrium data.

In this work, the thermochemical properties of choline chloride–based DESs were estimated using a combination of semi-empirical and density functional theory (DFT) methods. The interactions between DESs and CO_2 were analyzed through complexation models, including basis set superposition error (BSSE) corrections. Furthermore, selected DESs were evaluated as absorbents in post-combustion CO_2 capture processes through rigorous process simulation using Aspen Plus. The combined molecular-level and process-level analysis demonstrates that these DESs are thermodynamically viable and capable of achieving high CO_2 capture efficiencies, highlighting their potential as green solvents for next-generation CCS technologies.

Keywords

Carbon capture and storage; deep eutectic solvents; post-combustion capture; computational chemistry; CO_2 absorption.

1. Introduction

The energy sector is a dominant source of global CO_2 emissions, primarily originating from thermoelectric power plants fueled by coal and natural gas (Lomovskoi, 2023). Despite significant progress in renewable energy deployment, the current pace of transition remains insufficient to meet increasing global energy demands, particularly in developing economies. Under these circumstances, mitigation strategies that can be retrofitted to existing infrastructure play a crucial role in reducing greenhouse gas emissions.

Carbon capture and storage (CCS) has emerged as one of the most viable options for mitigating CO_2 emissions from large point sources. Among the available CCS technologies, post-combustion chemical absorption is the most mature and widely implemented due to its compatibility with existing power plants (Morales et al., 2024). Conventional alkanolamine-based solvents exhibit high absorption capacities and fast kinetics (Madejski et al., 2022); however, their industrial application is associated with several drawbacks, including high regeneration energy demand, solvent loss due to volatility, corrosion issues, and long-term degradation (Liu et al., 2024).

Deep eutectic solvents (DESs) have attracted increasing attention as alternative absorbents for CO_2 capture. These solvents, typically formed by combining a hydrogen bond acceptor (HBA) with a hydrogen bond donor (HBD), exhibit low vapor pressure, structural tunability, and favorable environmental characteristics (Romero-García et al., 2024). Nevertheless, the lack of comprehensive thermochemical and transport property data remains a major barrier to their industrial deployment. Therefore, a combined computational and process simulation approach is essential to evaluate their feasibility and guide solvent selection.

In this study, choline chloride–based DESs are investigated through quantum chemical calculations and rigorous process simulation to assess their suitability for post-combustion CO_2 capture applications.

2. Methodology

2.1 Computational chemistry

2.1.1 Conformational search

Geometry optimization was performed using electronic structure methods to identify the most stable configurations of the DES systems. Initially, the semi-empirical PM3 method (Stewart, 1989) was employed using Gaussian 09 (Frisch et al., 2016) to generate reasonable starting geometries. These structures were subsequently refined using the PM7 method (Stewart, 2013) as implemented in the RISSA software (García-Miranda et al., 2018), followed by a systematic conformational analysis to locate the global minimum energy structures. Final re-optimization was carried out at the DFT level using the PBE functional with the 6-311++G** basis set (Krishnan et al., 1980; Hariharan et al., 1973; Frisch et al., 1984; Hehre et al., 1972; Clark et al., 1983). Vibrational frequency calculations were performed to confirm the nature of the stationary points and to obtain thermochemical properties at standard conditions. In addition, the Basis Set Superposition Error (BSSE) was evaluated using the Counterpoise correction method (Boys et al., 1970) for both the DES and DES+CO_2 complex. This correction was applied to account for the artificial stabilization arising from the finite basis set and to ensure accurate interaction energies.

2.1.2 Thermochemical analysis

The enthalpy and Gibbs free energy of formation for each DES, as well as the thermochemistry of CO_2 capture, were calculated incorporating BSSE corrections. These results provide insight into the energetic feasibility of DES formation and CO_2 absorption at the molecular level.

2.2 Carbon dioxide capture simulation

2.2.1 Loading deep eutectic solvents

Since deep eutectic solvents are not available in commercial simulation databases, they were implemented as pseudocomponents in Aspen Plus (Aspen Technology, Inc., 2022). Key physical and thermodynamic properties, including molecular weight, boiling point, critical properties, enthalpy of formation, and Gibbs free energy, were introduced based on literature data (Table 1). Binary interaction parameters for the NRTL model (Table 2) and Henry's law constants for CO_2 solubility in the DES (Table 3) were adopted from previously validated sources (Qiong et al. 2024).

Property	ChCl/Gly (1:2)	ChCl/EG (1:2)
Molar mass (M) [g·mol⁻¹]	107.93	139.62
Boiling Point (Tb) [K]	515.4	439
Critical Temperature (Tc) [K]	680.67	602
Critical Pressure (Pc) [Mpa]	3.306	4.039
Critical molar volume (Vc) [$cm^3 \cdot mol^{-1}$]	315.17	259.67
Acentric factor (omega)	1.251	0.952

Table 1. Scalar properties of the pure component.

Component j	Component i	aij	aji	bij	bji	cij cji
ChCl/Gly (1:2)	CO_2	23.8246	8.5382	-3151.555	-2493.285	0.2
ChCl/EG (1:2)	CO_2	0.1016	5.8073	1064.89	-1175	0.2

Table 2. NRTL binary interaction parameters for CO_2-DES.

Component j	Component i	aij	bij	cij	dij
ChCl/Gly (1:2)	CO_2	-591.7956	15117.7011	103.1011	-0.1477
ChCl/EG (1:2)	CO_2	3305.5768	-92825.7085	-572.2799	0.9036

Table 3. Henry coefficient of CO_2 in DES.

2.2.2 Process simulation

Post-combustion CO_2 capture was simulated using absorption columns modeled with the rigorous RADFRAC module. Feed gas compositions representative of coal- and natural gas–fired power plants were considered (Lomovskoi, 2023) (Table 4). Water was included as a co-solvent at a 2:1 molar ratio relative to the DES. The number of equilibrium stages was fixed at 67, while solvent flow rates, operating pressure, and inlet temperature were varied to evaluate capture performance.

Component	Thermoelectric process	
	Bituminous coal	Natural gas
H_2O	880	1998.82
CO_2	1364	1009.97
N_2	8426	7912.29
O_2	330	96.3359
CH_4	0	8.56×10^{-24}
C_2H_6	0	1.02×10^{-48}
C_3H_8	0	3.28×10^{-77}
C_4H_{10}	0	1.23×10^{-102}

Table 4. Post-combustion air flow [kmol·h⁻¹].

3. Results and discussion

3.1 Computational chemistry

Thermochemical properties obtained from the lowest-energy configurations indicate that DES formation is exergonic under standard conditions, confirming the thermodynamic stability of the eutectic mixtures (Table 5).

DES	Enthalpy	Gibbs energy
ChCl/Gly (1:2)	-35.54	-11.98
ChCl/EG (1:2)	-36.67	-12.51

Table 5. Thermochemical data of DES at standard conditions (ΔH and ΔG in kcal·mol⁻¹).

CO_2 capture is characterized by negative enthalpy changes, indicating an exothermic absorption process dominated by hydrogen bonding and electrostatic interactions. Although the Gibbs free energy change for CO_2 capture is positive, its relatively small magnitude suggests that absorption is feasible and reversible, which is advantageous for solvent regeneration (Table 6).

DES	Enthalpy	Gibbs energy
ChCl/Gly (1:2)	-2.02	5.72
ChCl/EG (1:2)	-1.62	6.05

Table 6. CO_2 capture thermochemistry (ΔH and ΔG in kcal·mol⁻¹).

Structural analysis reveals strong non-covalent interactions between CO_2 and the chloride anion, as well as hydrogen bond donors within the DES matrix. These interactions stabilize the DES–CO_2 complex and explain the observed absorption behavior. (Figure 1).

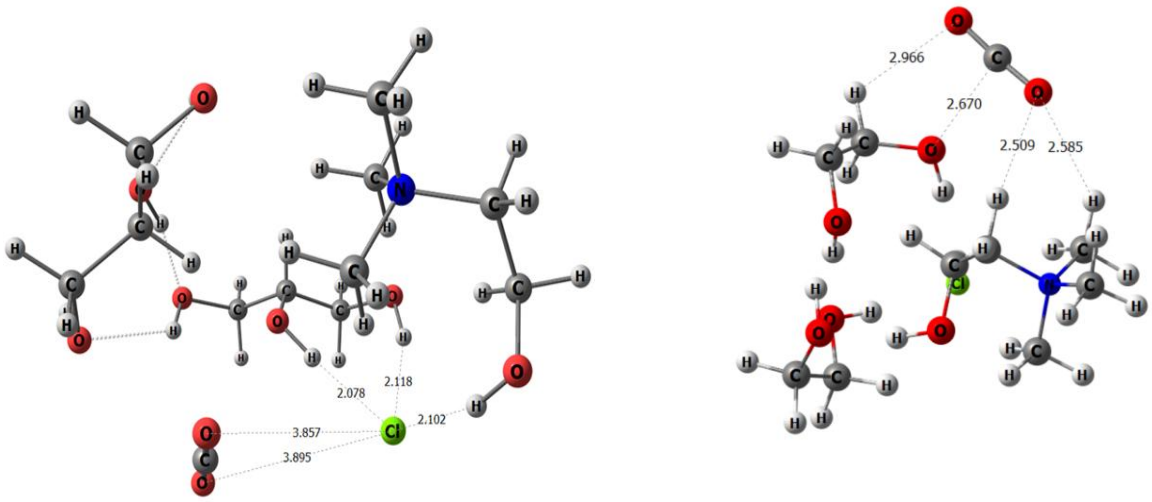

Figure 1: Lowest-energy structure of the DES–CO_2 systems a) ChCl/Gly b) ChCl/Eg. Distances (in Å) are shown in dotted lines.

3.2 Process Simulation Results

Process simulations demonstrate that both ChCl/Gly (1:2) and ChCl/EG (1:2) achieve CO_2 capture efficiencies close to 98% for coal (Table 7)- and natural gas (Table 8)–derived flue gases. The required operating conditions are within practical industrial ranges, and the results indicate that DESs can handle large gas flow rates without compromising performance. These findings support the potential of DESs as competitive alternatives to conventional amine-based solvents.

DES	DES feed temperature [°C]	DES flow rate [kmol·h^{-1}]	Operating pressure [bar]	CO_2 capture
ChCl/Gly (1:2)	46.5	110331	10	97.79 %
ChCl/EG (1:2)	38	34000	10	98 %

Table 7. Operating conditions for CO_2 capture from bituminous coal.

DES	DES feed temperature [°C]	DES flow rate [kmol·h^{-1}]	Operating pressure [bar]	CO_2 capture
ChCl/Gly (1:2)	39.5	63046.30	12.16	97.70 %
ChCl/EG (1:2)	40	85614.03	11.86	97.95%

Table 8. Operating Conditions for CO_2 Capture from Natural Gas.

3. Conclusions

A comprehensive molecular–process level assessment of choline chloride–based deep eutectic solvents (DESs) for post-combustion CO_2 capture has been presented. From the molecular perspective, quantum chemical calculations confirmed that the formation of the eutectic mixtures is thermodynamically favorable, as evidenced by negative Gibbs free energies of formation. The interaction between DESs and CO_2 is governed by a combination of hydrogen bonding, electrostatic interactions, and dispersion forces, particularly involving the chloride anion and the hydrogen bond donors in the eutectic structure. The exothermic nature of the absorption process highlights the intrinsic affinity of DESs for CO_2 molecules.

Although the Gibbs free energy change associated with CO_2 capture is positive under standard conditions, its relatively low magnitude indicates that the absorption process is energetically accessible and, more importantly, reversible. This characteristic is highly desirable for cyclic absorption–desorption operations, as it suggests reduced energy penalties during solvent regeneration when compared to conventional amine-based systems. Therefore, from a thermodynamic standpoint, the investigated DESs strike a favorable balance between CO_2 affinity and regeneration feasibility.

At the process scale, rigorous simulations of absorption columns using realistic flue gas compositions from coal- and natural gas–fired power plants demonstrated that

both ChCl/Gly (1:2) and ChCl/EG (1:2) can achieve CO_2 capture efficiencies close to 98%. These high capture levels were obtained under operating pressures and temperatures that are compatible with industrial practice, even when handling large volumetric flow rates. The inclusion of water as a co-solvent further contributes to manageable viscosity levels, enhancing mass transfer and overall process operability.

The integration of computational chemistry with process simulation provides a robust and predictive framework for solvent screening and process design. This multiscale approach reduces experimental trial-and-error efforts and allows early identification of promising solvent candidates. The results of this study suggest that choline chloride–based DESs constitute viable green alternatives to conventional solvents for post-combustion CO_2 capture, offering advantages in terms of environmental compatibility, operational stability, and capture efficiency.

Future work should focus on the incorporation of kinetic effects, transport properties, and long-term solvent stability into the simulation framework, as well as experimental validation of the predicted thermodynamic and process performance. Additionally, multi-objective optimization considering energy consumption, solvent circulation rate, and environmental indicators will be essential to fully assess the competitiveness of DES-based CO_2 capture systems at an industrial scale.

References

Aspen Technology, Inc. (2020). Aspen Plus (versión 12) [Software]. Aspen Technology, Inc.

Boys, S. F., & Bernardi, F. (1970). The calculation of small molecular interactions by the differences of separate total energies. Some procedures with reduced errors. Journal of Molecular Physics, 19(4), 553–566. https://doi.org/10.1080/00268977000101561

Frisch, A. E., & Foresman, J. B. (1996). Exploring chemistry with electronic structure methods (2.ª ed.). Gaussian Inc.

García-Miranda, J. J. (2018). Búsqueda estocástica de isómeros restringidos espacialmente (Tesis de maestría, Universidad Autónoma Metropolitana, Iztapalapa).

Krishnan, R., Binkley, J. S., Seeger, R., & Pople, J. A. (1980). Self-consistent molecular orbital methods. XX. A basis set for correlated wave functions. Journal of Chemical Physics, 72(1), 650–654. https://doi.org/10.1063/1.438955

Madejski, P., Chmiel, K., Subramanian, N., & Kuś, T. (2022). Methods and techniques for CO_2 capture: Review of potential solutions and applications in modern energy technologies. Energies, 15(3), 887. https://doi.org/10.3390/en15030887

Martínez-Lomovskoi, A., Romero-García, A. G., Sánchez-Ramírez, E., & Segovia-Hernández, J. G. (2023). Design and multi-objective optimization of a CO_2 capture plant using deep eutectic solvents. Chemical Engineering Research and Design, 192, 570–581. https://doi.org/10.1016/j.cherd.2023.03.006

Romero-García, A. G., Ramírez-Márquez, C., Sánchez-Ramírez, E., et al. (2024). Implementation of the deep eutectic solvent, choline urea chloride (1:2), to evaluate the sustainability of its application during CO_2 capture. Process Integr Optim Sustain 8, 741–758 (2024). https://doi.org/10.1007/s41660-023-00383-2

Stewart, J. J. P. (1989). Optimization of parameters for semiempirical methods I. Method. Journal of Computational Chemistry, 10(2), 209–220. https://doi.org/10.1002/jcc.540100208

Sun, Q., Yang, F., Tan, H., & Wang, X. (2024). Simulation study of CO_2 capture from flue gas by deep eutectic solvent. Huagong Xuebao (Chinese Edition), 75(10), 3705–3717. https://doi.org/10.11949/0438-1157.20240441

Industrial Application of an Enhanced Active Vapor Distributor for Active Vapor Split Control in a Dividing Wall Column

Gregorius Rionugroho Harvianto[1], Ki Joon Kang[1], Anton A. Kiss[2]
[1]Benit M Co., Ltd, Ulsan, Republic of Korea, info@benitm.com;
[2]Dept. of Chem. Engineering, Delft University of Technology, Delft, The Netherlands

Abstract

Dividing wall column (DWC) can reduce energy use and capital costs by integrating multiple conventional distillation columns into a single shell. Yet, their industrial performances, particularly in terms of product purity and energy savings, are often limited by the inability to adjust vapor split during operation. This work presents the first reported industrial-scale application of an Enhanced Active Vapor Distributor (EAVD®) as a practical active vapor split control device in a DWC operation. The EAVD® consists of a modified chimney tray equipped with caps containing vapor windows. By regulating the liquid level on this tray using standard level control, the effective vapor flow area and thus the vapor split ratio can be adjusted during operation. EAVD® technology was implemented in newly constructed DWC (4.2 m diameter), producing semiconductor-grade solvent. The column achieved about 15% energy savings as compared with a two-column configuration while consistently meeting stringent product purity specifications. The vapor split ratio was actively manipulated over a range of 0.92 - 2.05, while the liquid split ratio varied from 0.87 to 1.50. As a result, pressure drop differences between fractionation zones in DWC sections (up to 18.8 torr) were effectively compensated through liquid level adjustment on the EAVD®. These novel results demonstrate that EAVD® enables robust, energy-efficient DWC operation under realistic industrial conditions, supporting broader industrial DWC adoption by providing a practical and reliable option over the fixed-design or a mechanically driven vapor splitter.

Keywords

Process intensification, dividing wall column, active vapor split control, industrial application, operability, pressure drop differences

1. Introduction

Rising demands to reduce energy use, carbon emissions, and capital costs have highlighted the need for process intensification strategies over recent decades. Dividing Wall Column (DWC) stands out for multicomponent separations, merging two or more conventional distillation columns into one shell (Kiss, 2014). Simulations and industry cases confirm 15-50% energy savings, alongside a major reduction in equipment count, plot space, and up to 35% investment (Dejanović et al., 2010). However, industrial DWCs rarely achieve full potential. Lack of control manner of internal flows between sections hampers gains. Both liquid and vapor split ratios dictate separation performance, purity, and energy needs (Dwivedi et al., 2012). Off-optimal splits degrade output quality sharply, forcing higher reboiler duties to meet product purity specifications. This is worsened by feed composition shifts or throughput changes (Lee et al., 2011). Conventional DWCs rely on fixed geometry

for equal pressure drops across sections (Dejanović et al., 2011) and cannot be actively adjusted during operation. Therefore, DWCs frequently operate away from the optimal point when process variables deviate from the design condition (Dwivedi et al., 2012), resulting in limited operational flexibility. Donahue et al. (2016) identified unique control challenges associated with minimum energy operation as a fundamental reason for the slow industrial adoption of DWC. Although several active vapor split control concepts have been proposed, including electrically actuated vapor valves (Dwivedi et al., 2012), external vapor bypass control (King, 2013), and blade-type internal structure (Huaqiang, 2016), industrial implementation has not been reported. It is likely due to challenges related to mechanical complexity and its maintenance requirements, as well as structural reliability concerns. Consequently, a practical and reliable active vapor split control technology suitable for large-scale DWC remains essential for broader industrial implementation.

To address this limitation, Benit M developed the Enhanced Active Vapor Distributor (EAVD®), an adjustable vapor split control technology for industrial DWC, patented in 2017. EAVD® utilizes a modified chimney tray in which each chimney is covered with a cap that has windows as vapor channels. The fundamental concept, operating principle, and laboratory-scale validation of EAVD® were previously reported (Kang et al., 2017), demonstrating its capability to actively manipulate vapor distribution by regulating liquid level on a modified chimney tray (Harvianto et al., 2019). Since its initial publication, the EAVD® concept has been cited and discussed by several experts in DWC design and operation. In particular, review papers and expert studies on DWC operability have identified active vapor split control, including EAVD®, as a practical solution to one of the remaining challenges associated with vapor split control in DWC (Ränger et al., 2019). This emphasizes the relevance of active vapor split control and highlights the need for its validation at an industrial scale.

Building on these earlier studies, this paper focuses on the first industrial-scale application of EAVD®. In 2022, Benit M performed the basic design of a fractionation process for the production of semiconductor-grade solvent, which included a DWC. DWC configuration was selected to reduce energy consumption while minimizing installed equipment within the limited plant area. To ensure the stable high purity of the product and to obtain the minimum energy consumption during the operation, EAVD® was included to actively control vapor flow. This paper presents industrial operation results showing the capability of EAVD® to actively control vapor split, compensate pressure drop differences between fractionation zones in DWC sections, and maintain stable operation over a wide operating range. The results indicate that EAVD® provides a practical solution to a key challenge limiting the wider industrial adoption of DWC.

2. Results and discussion

2.1 Overview of industrial DWC with EAVD®

The EAVD® technology was implemented in a newly constructed industrial DWC designed for the production of semiconductor-grade solvent at a fine-chemical plant in South Korea. Compared with a conventional two-column design, the DWC achieved approximately 15% energy savings. The observed steam consumption rate during operation was consistent with the simulation predictions obtained during the commissioning stages. These savings were achieved by operating the column at the

desired optimal vapor split ratio condition enabled by EAVD®. During commissioning, the main operational objective was not only hydraulic stability but also the prevention of purity deviations during feed composition and rate changes. Figure 1 shows the implemented EAVD® configuration in an industrial DWC (total diameter of 4.2 m and a height of 56 m), which serves as the main product column, removing both light and heavy impurities while producing a high-purity side draw.

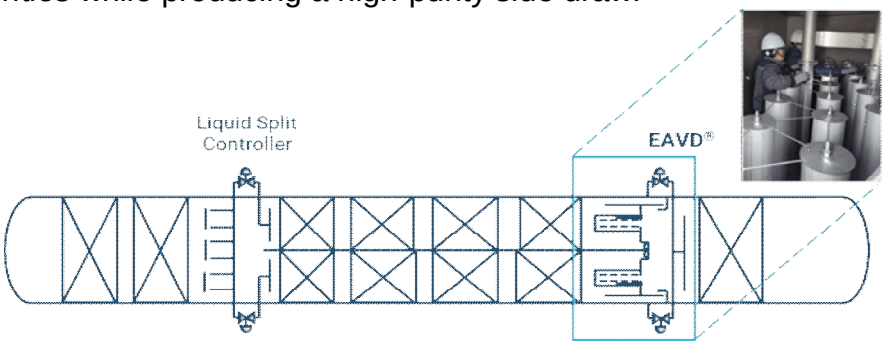

Figure 1: Industrial DWC equipped with EAVD®, representing the first application of active vapor split control in DWC

Due to confidentiality constraints on detailed design and operating data, only limited representative information is provided in Table 1. Following commissioning in Q3 2025, the DWC was operated over a wide range of feed rates and operating conditions. The results presented in this work are based on industrial operating data obtained under several plant conditions and reflect the practical performance of the system rather than optimized experimental settings.

Table 1: Summary information for the industrial DWC equipped with EAVD®

Parameter	*Description*
Tower internals	Structured Packing
Operating pressure	Vacuum
EAVD® riser diameter	4-inch pipe
EAVD® cap diameter	6-inch pipe
EAVD® cap height	1,300 mm
Product purity	> 99.95 wt%

For performance evaluation, the vapor and liquid split ratios are defined according to Equation 1. A schematic of the operating configuration and the parameters examined in this study is provided in Figure 2.

$$R_V = \frac{V_{Pre}}{V_{Main}};\ R_L = \frac{L_{Pre}}{L_{Main}} \tag{1}$$

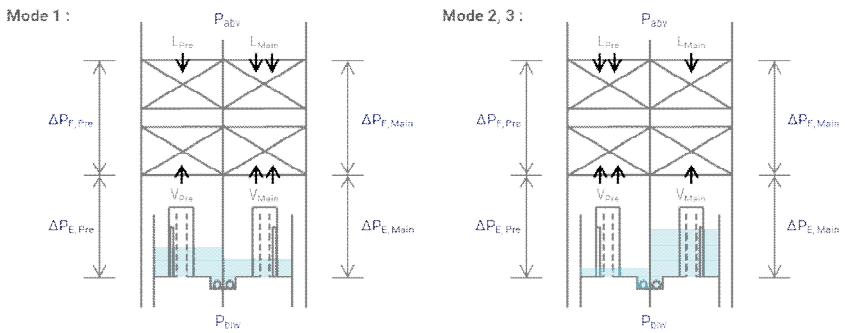

Figure 2: Schematic of operating configuration and parameters evaluated for EAVD® during DWC operation

2.2. Effect of EAVD® liquid level on the EAVD® and fractionation pressure drop

During the early stage of commissioning, the liquid level in the main section was increased to approximately 75% to achieve the target vapor split ratio for a selected operating mode, as indicated by the EAVD® design calculations. Accordingly, the liquid level in the main section (EAVD® LT_{Main}) was adjusted stepwise while the reflux rate and liquid split ratio (R_L = 1.1) were kept constant. During this tuning procedure, the liquid level in the pre-section (EAVD® $LT_{, Pre}$) remained constant at 20%. Figure 3(b) shows the pressure drop data gathered during this adjustment. As EAVD® $LT_{, Main}$ increased from 40% to 73%, pressure drop in the main section ($\Delta P_{E, Main}$) increased gradually from 11.4 torr to 24.7 torr, indicating that changes in EAVD® liquid level directly affected the pressure drop across the EAVD®. This is consistent with previously reported lab-scale results (Harvianto et al., 2019). As shown in Figure 3(b), the increased pressure drop across the EAVD® main section (blue line) reduced the vapor flow to that section, as reflected by the corresponding decrease in packing pressure drop (orange line) measured in that section. At the same time, Figure 3(a) shows that both the packing ($\Delta P_{F, Pre}$) and EAVD® pressure drop ($\Delta P_{E, Pre}$) in the pre-section increased, indicating a corresponding increase in vapor load in that section.

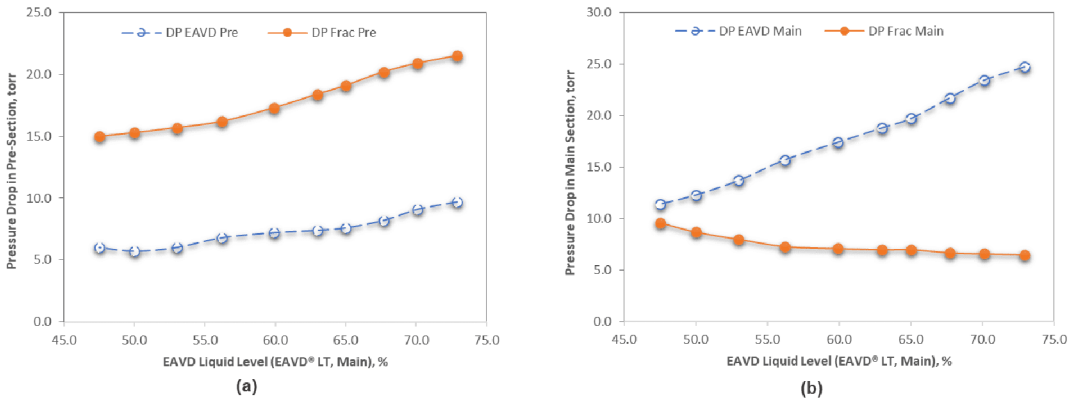

Figure 3: Effect of EAVD® main section liquid level on pressure drop at constant liquid split ratio and EAVD® pre-section liquid level: (a) pre-section (b) main section

2.3 Active control of vapor split ratio

During the final commissioning operation, the liquid split ratio between the pre-section and main section varied from 0.87 to 1.50, due to the variation of feed composition and operating load. Despite these variations, EAVD® maintained effective control of the vapor split ratio, which ranged from 0.92 to 2.05.

Table 2: Summary of EAVD® operability in industrial DWC

Relevant Mode	Pre-fractionation section			Main-fractionation section				R_L 2)	R_V 3)
	$\Delta P_{F, Pre}$ (torr)	$\Delta P_{E, Pre}$ (torr)	EAVD® $LT_{, Pre}$	$\Delta P_{F, Main}$ (torr)	$\Delta P_{E, Main}$ (torr)	EAVD® $LT_{, Main}$	$\Delta(\Delta P)$ 1) (torr)	$\frac{L_{Pre}}{L_{Main}}$	$\frac{V_{Pre}}{V_{Main}}$
Mode 1	11.0	4.6	35%	11.3	4.3	22%	0.3	0.87	0.92
Mode 2	25.0	10.3	10%	6.2	29.1	76%	18.8	1.50	2.05
Mode 3	23.2	10.3	9%	8.7	24.8	70%	14.5	1.50	1.80

Notes: 1) $\Delta(\Delta P)$ is a change of pressure drop differences or compensated pressure drop
2) Liquid split ratio is obtained from the flowmeter in the DCS room.
3) Vapor split ratio is calculated from the process simulation, and confirmed according to the actual EAVD® in each section

As summarized in Table 2, the vapor split ratio was adjusted by changing the liquid level on the EAVD® trays: the liquid level in the pre-section was varied between 9% and 35%, while that in the main section ranged from 22% to 76%. In this system, independent manipulation of the vapor split was observed even when the liquid split ratio changed. The liquid level on each EAVD® tray was controlled using a standard proportional-integral (PI) controller, manipulating the corresponding liquid flow control valve (to the section below the wall) in each section. The ability to actively control vapor split ratio and liquid split ratio simultaneously provides an additional degree of freedom for DWC operation, which is particularly valuable for maintaining separation performance when the column is operated differently from its design point.

2.4 Compensated pressure drop by EAVD®

Pressure drop differences between column sections are a key indicator of vapor flow distribution in DWCs. In this study, the effect of EAVD® on the compensated pressure drop (change of pressure drop differences) was evaluated by monitoring differential pressure across the fractionation zones of the pre-section ($\Delta P_{F,\ Pre}$) and main section ($\Delta P_{F,\ Main}$), as well as the pressure drop across the EAVD® in pre-section ($\Delta P_{E,\ Pre}$) and main section ($\Delta P_{E,\ Main}$). Compensated pressure drop $\Delta(\Delta P)$ was calculated as:

$$\Delta\left(\Delta P\right) = \left|\Delta \mathrm{P}_{\mathrm{E,\ Pre}} - \Delta \mathrm{P}_{\mathrm{E,\ Main}}\right| = \left|\Delta \mathrm{P}_{\mathrm{F,\ Pre}} - \Delta \mathrm{P}_{\mathrm{F,\ Main}}\right| \tag{2}$$

As shown in Table 2, operation modes 2 and 3 were characterized by higher liquid levels in the main section compared with mode 1, resulting in increased vapor flow resistance in that section. This shift reduced vapor flow to the main section and redirected more vapor to the pre-section, while the liquid split ratio was adjusted simultaneously. As a result, $\Delta P_{F,\ Pre}$ increased significantly, whereas $\Delta P_{F,\ Main}$ decreased due to the lower vapor and liquid load. Overall, pressure drop differences between fractionation zones in DWC sections ranging from 0.3 to 18.8 torr were effectively compensated during this column commissioning. These observations indicate that EAVD® allows pressure drop imbalances across the mass-transfer sections to be adjusted during operation, enabling the desired vapor split ratio to be obtained under varying feed composition and rate conditions.

2.5 Impact on product purity and implications for industrial DWC adoption

Stable vapor flow distribution to each section of DWC is essential for maintaining product purity, particularly in the production of high-purity chemicals such as semiconductor-grade solvents. Throughout the evaluation period, the column consistently met the required product purity specifications despite fluctuations in feed conditions. The actual light and heavy impurity content in the feed fluctuates due to changes in reactor operating mode. Nevertheless, active adjustment of the vapor split allowed the desired product purity to be maintained without increasing reflux or reboiler duty. Table 3 presents a normalized comparison between design basis and actual industrial operating conditions.

The results of this study indicate that EAVD® addresses a key limitation of industrial DWC, namely the lack of adjustable vapor split control during operation. By enabling direct manipulation of vapor split ratio, EAVD® enhances column operability and flexibility, particularly for processes subject to frequent variations in feed composition or throughput. The additional internal hardware and level control loops on EAVD® were implemented using a standard level control configuration, which is commonly applied in industrial distillation columns and did not cause any operational instability during long-term operation. In addition, the required vapor split ratio range and the

compensated pressure drop by EAVD® can be designed depending on DWC geometry, tower internal type, and process conditions.

Table 3: Normalized comparison of design basis and operating conditions

Parameter	Design Basis	Actual Operation	Normalized Deviation
Light impurity in feed	1.00	0.73 ~ 3.04	-27% to +204%
Heavy impurity in feed	1.00	0.76 ~ 1.83	-24% to +83%
Reflux rate	1.00	0.95 ~ 1.00	-5% to 0%
Reboiler duty, derived from the steam rate	1.00	0.94 ~ 0.97	-6% to -3%
Light impurity in product	< 1.00	0.22 ~ 1.00	On-spec
Heavy impurity in product	< 1.00	0.14 ~ 0.77	On-spec

3. Conclusions

Despite the substantial energy-saving potential of DWC, its industrial adoption remained limited, mainly due to the lack of reliable and adjustable vapor split control during operation. The results of this study demonstrate that EAVD® is a reliable industrial-scale solution, enabling independent adjustment of vapor and liquid split ratios amid feed condition variations, while achieving target energy savings and stable high-purity product quality. Moreover, because EAVD® can be readily implemented by replacing conventional chimney trays, it is applicable not only to new DWC installations but also to revamp projects for existing columns. These findings confirm its maturity for refinery, petrochemical, chemical, and fine-chemical uses, while unlocking broader process intensification.

References

Dejanović, I., Matijašević, Lj., Olujić, Ž., 2010. Dividing wall column – A breakthrough towards sustainable distilling. Chem. Eng. Proc. 49, 559-580.

Dejanović, I., Matijašević, Lj., Jansen, H., Olujić, Ž., 2011. Designing a packed dividing wall column for an aromatics processing plant. Ind. Eng. Chem. Res. 50, 5680-5692.

Donahue, M.M., Roach, B.J., Downs, J.J., Blevins, T., Baldea, M., Eldridge, R.B., 2016. Dividing wall column control: common practices and key findings. Chem. Eng. Proc. – Proc. Int. 107, 106-115.

Dwivedi, D., Strandberg, J.P., Halvorsen, I.J., Preisig, H.A., Skogestad, S., 2012. Active vapor split control for dividing-wall columns. Ind. Eng. Chem. Res. 51, 15176–15183.

Harvianto, G.R., Kim, K.H., Kang, K.J., Lee, M., 2019. Optimal operation of a dividing wall column using an enhanced active vapor distributor. Chem. Eng. Res. Des. 144, 512-519.

Huaqiang, G. Xiangwu, C. Nan, C. Wenyi, C., 2016. Experimental study on vapour splitter in packed divided wall column. J. Chem. Technol. Biotechnol. 91, 449−455.

Kang, K.J., Harvianto, G.R., Lee, M., 2017. Hydraulic driven active vapor distributor for enhancing operability of a dividing wall column. Ind. Eng. Chem. Res. 56, 6493–6498.

King, S.T., Haas, J., 2013. Vapor and liquid flow control in a dividing wall fractional distillation column. United States Patent No. US8562792 B2.

Kiss, A.A,, 2014. Distillation technology – still young and full of breakthrough opportunities. J. Chem. Technol. Biotechnol. 89, 479–498.

Lee, S.H., Shamsuzzoha, M., Han, M., Kim, Y.H., Lee, M., 2011. Study of the structural characteristics of a divided wall column using the sloppy distillation arrangement. Korean J. Chem. Eng. 28 (2), 348–356.

Ränger, L.M., Preißinger, U., Grützner, T., 2019. Multiple dividing-wall columns – current status and future prospects. Chem. Ing. Tech. 91 (4), 1-10.

Characterisation of structured packings for increased efficiency in carbon capture processes

Alexander Pichler[1], Martin Koller[2], Verena Wolf-Zoellner[1]
[1]Technical University of Leoben, Leoben, Austria; [2]Andritz AG, Graz, Austria

The large variety of structured and random packings available for absorption processes makes a detailed characterisation of their mass-transfer performance essential. This is particularly relevant for carbon capture by chemical absorption, where the demand for highly efficient structured packings continues to increase.
This work therefore investigates the mass-transfer performance of three structured packings – MP250Y, MP250X, and RSP250Y – with a specific focus on carbon capture applications. The analysis is carried out for the industrially relevant solvent systems monoethanolamine (MEA), diethanolamine (DEA), methyl-diethanolamine (MDEA) and a MDEA–piperazine blend.
Based on experimental data gained due to packing characterisation and adapted mass-transfer parameters, the influence of both packing structure and solvent properties on the mass-transfer behaviour is evaluated. In particular, local mass-transfer resistance distributions along the column height are determined for each system.
The results reveal distinct reaction regimes in different column sections, which vary depending on the solvent system. By linking these regimes to the corresponding mass-transfer resistances, it becomes possible to identify which packing structures are most suitable for specific regions of the column.
Consequently, the study demonstrates that an optimal packing selection for carbon capture processes requires a differentiated approach, in which packing types are chosen according to the local reaction regime and solvent system.

Keywords: Carbon Capture, Chemical Absorption, Structured Packings, Mass-Transfer, Process Optimisation

1. Introduction

Processes for capturing industrial CO_2 emissions (Carbon Capture) can take a wide variety of forms (Wolf-Zoellner et al, 2025). On the one hand, a distinction can be made between post-combustion, pre-combustion and oxy-fuel-combustion capture, depending on the process configuration (Wu et al., 2018). On the other hand, the capture methods themselves can also vary, the main ones being absorption, adsorption, membrane and cryogenic processes (Bradke et al., 2021). Industrial flue gases with a CO_2 concentration of up to 30% by volume are primarily treated using chemical absorption in the post-combustion capture configuration and this method is represented as key technology for reducing industrial CO_2 emissions (Bradke et al., 2021). Absorption, describes the transition of one or more gaseous components into a liquid phase. Commonly, this is also referred to as gas scrubbing. Processes such as the separation of acid gases (e.g. CO_2 and H_2S) were first described as early as the 1930s. In the basic process, an aqueous amine solution acts as the scrubbing liquid, which, amongst other things, selectively binds the CO_2. Through further

research and development, amine scrubbing has become one of the preferred processes in the field of CO_2 capture, although there is still room for improvement. Fundamentally, three different types of apparatus are distinguished for absorption, depending on which phase is dispersed or continuous. In this regard, spray columns (liquid phase dispersed, gas phase continuous), bubble columns (liquid phase continuous, gas phase dispersed) and packed or tray columns (both phases continuous) should be mentioned. Partly due to the intensive phase contact, the packed column with random or structured packings to increase the mass-transfer area has become the preferred separation apparatus. In this study, structured packings were specifically chosen because of certain advantages, such as lower pressure loss at the same specific surface area (Hüser, 2017). A wide variety of those structured packings is available on the market, many of which are specifically designed for absorption processes. However, reliable and comparable data describing their performance in real carbon capture systems are still limited. This leads to uncertainties in the selection and design of column internals for industrial carbon capture applications.

The aim of this work is to characterise structured packings based on standardised test systems using a pilot plant and to transfer these results to real carbon capture processes. By incorporating relevant physico-chemical properties, such as diffusion coefficients, viscosity and Henry constants, the actual performance of the packings in industrial absorption systems is approximated. In addition, the study seeks to identify limiting mass-transfer resistances and to derive a systematic approach for selecting suitable packing structures.

2. Methodology

Three structured packings are investigated with regard to their mass-transfer performance. This simultaneously allows for an assessment of the influence of different geometric structures. Experimental and literature-based data obtained from characterisation with standardised test systems (see Table 1) in accordance with the VDI guideline 2761 are adapted to real absorption conditions by accounting for fluid properties and reaction kinetics. The analysis is based on established mass-transfer models, in particular the two-film theory, allowing a consistent description of transport phenomena in both phases. According to this model, the gas-side and liquid-side mass-transfer coefficient are defined in this way, as also the effective mass-transfer area. Table 1 summarises the mentioned test systems used for determining the mass-transfer parameters.

Table 1: Test systems in gas and liquid phase to determine mass transfer parameters

Test system	Process	Target parameter
SO_2 / NaOH	Chemical absorption	Gas-side mass-transfer coefficient β_G
CO_2 / Water	Physical desorption	Liquid-side mass-transfer coefficient β_L
CO_2 (Air) / NaOH	Chemical absorption	Effective mass-transfer area a_{eff}

The theory of similarity is then used to adapt the standardised determined mass-transfer parameters to actual absorption systems used in industry. In this context, the most common amine solutions, including MEA, DEA, MDEA and the amine blend MDEA/PZ, were examined. A conversion can be carried out using dimensionless

parameters, such as the Sherwood number Sh, which compares the convective fluxes with the diffusive fluxes. The mass-transfer parameters determined using “test system A” can thus be transferred to a “system B” actually used in industry, regarding the relevant diffusion coefficients and kinematic viscosity. The following formulas illustrate the relationships described.

$$\frac{(\beta_G)_A}{(\beta_G)_B} = \left(\frac{D_A}{D_B}\right)^{2/3} * \left(\frac{\nu_B}{\nu_A}\right)_G^{5/12} \tag{1}$$

$$\frac{(\beta_L)_A}{(\beta_L)_B} = \left(\frac{D_A}{D_B}\right)^{1/2} * \left(\frac{\nu_B}{\nu_A}\right)_L^{1/6} \tag{2}$$

$$\frac{(a_{eff})_A}{(a_{eff})_B} = \left(\frac{\nu_B}{\nu_A}\right)_L^{-1/5} \tag{3}$$

In chemical absorption, a reaction takes place between CO_2 and the absorbent in the liquid phase following a phase transition from the gas to the liquid phase. The resulting accelerating effect on mass-transfer is accounted for by the enhancement factor E. This factor incorporates all influences of the chemical reactions. To determine E, the Hatta number Ha is used, which is derived from the ratio of reaction rate to mass-transfer rate. In this context, the reaction mechanism of CO_2 with the respective absorbent (as mentioned above) is required. This subsequently allows the predominant reaction regime to be identified and the enhancement factor to be calculated. In order to provide a meaningful assessment for industrial absorption applications in the field of carbon capture and to determine a mass-transfer resistance distribution, a realistic temperature profile across the height of the absorber is derived from Schultes, 2018. This study focuses on three specific points along the column height: the top of the column, the point of maximum temperature, and the bottom of the column. To account for the concentrations of free amine and CO_2 across the column height, published CO_2 loading data for the respective absorbents and their working capacity, as well as a CO_2 exhaust concentration of 15% by volume, were used (Schäffer, 2013, El Hadri et al, 2017). A separation efficiency of 90% was assumed. The mentioned mass-transfer resistances of the gas and liquid phase are expressed by the two terms in the definition of the overall mass-transfer (including reaction) $k_{OG,R}$, which can be displayed with the following equation.

$$\frac{1}{k_{OG,R}} = \frac{1}{\beta_G} + \frac{1}{H_{ij}^{cp} * R * T * \beta_L * E} = R_G + R_L \tag{4}$$

3. Results

The results presented in Figure 1 show the mass transfer parameters of the RSP250Y packing. The experimental results obtained from the characterisation systems are presented alongside the parameters adapted for industrial carbon capture systems.

The comparison in Figure 1 reveals a significant discrepancy between the actual carbon capture system and the characterisation system (SO_2-NaOH) due to the adaptation of the diffusion coefficient from SO_2 to CO_2. However, the differences between the different carbon capture systems themselves are negligible and can be attributed to the minor influence of viscosity.

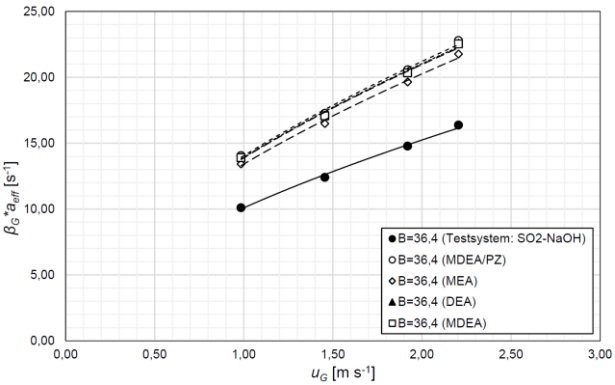

Figure 1: Gas-side volumetric mass transfer coefficient as a function of gas velocity.

When considering the liquid-side volumetric mass transfer coefficient as a function of liquid flow rate in Figure 2, the differences can also be explained purely in physical terms. For MEA, the values are slightly higher compared to the characterisation system (CO_2-water), whilst the others exhibit a decreasing trend in mass transfer, due to the influence of the diffusion coefficients and viscosity. Higher-molecular-weight compounds therefore lead to a lower mass transport. Chemical reactions have not yet been taken into account here.

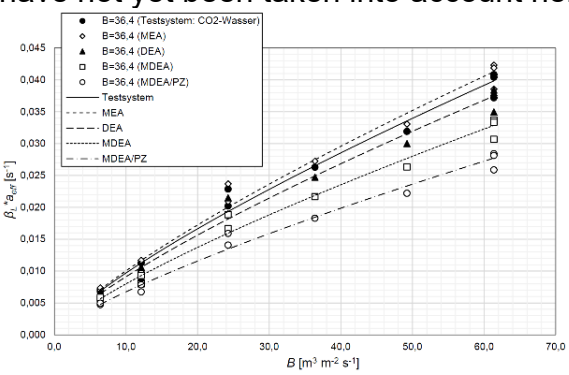

Figure 2: Liquid-side volumetric mass transfer coefficient as a function of liquid flow rate

In Figure 3, the effective interfacial area determined for the characterisation system (CO_2–NaOH) is transferred to the investigated carbon capture systems using equation (3), based on a Sherwood-type similarity approach. This procedure ensures a consistent scaling of the mass-transfer parameters with respect to the underlying fluid properties, in particular diffusion coefficients and viscosity.

The resulting trends indicate an apparent increase in effective interfacial area with increasing molecular weight of the solvent. However, it should be emphasised that this behaviour originates from the applied scaling methodology rather than directly reflecting changes in the physical interfacial area. The Sherwood correlation primarily captures the influence of fluid properties on the mass-transfer coefficient, while hydrodynamic effects governing liquid distribution and wetting are not explicitly resolved.

Consequently, the reported values of the effective interfacial area should be interpreted as model-based parameters within the consistent framework of this study, rather than as independent physical quantities. Since the focus of this work lies on the determination of mass-transfer resistance distributions, the applied approach provides a suitable first approximation. A more detailed description of interfacial

phenomena would require the application of dedicated correlations for interfacial area, such as those proposed by Tsai, 2010.

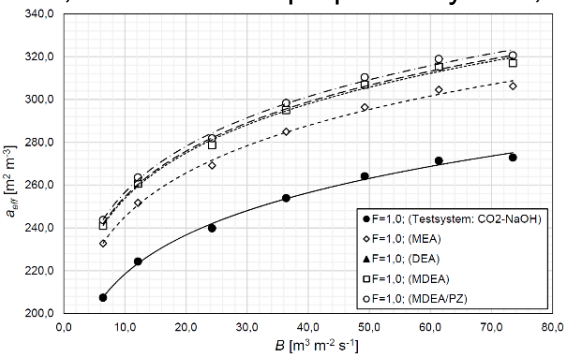

Figure 3: Effective mass-transfer area as a function of liquid flow rate

Figure 4 shows the distribution of resistance across the column height, with the R_G and R_L fractions. It can be seen that the MDEA/PZ amine blend performs better in the lower section of the column than MEA, whilst MDEA exhibits very high values. Furthermore, the same absolute values for the mass transfer resistance on the liquid side are observed, primarily in the upper sections of the column.

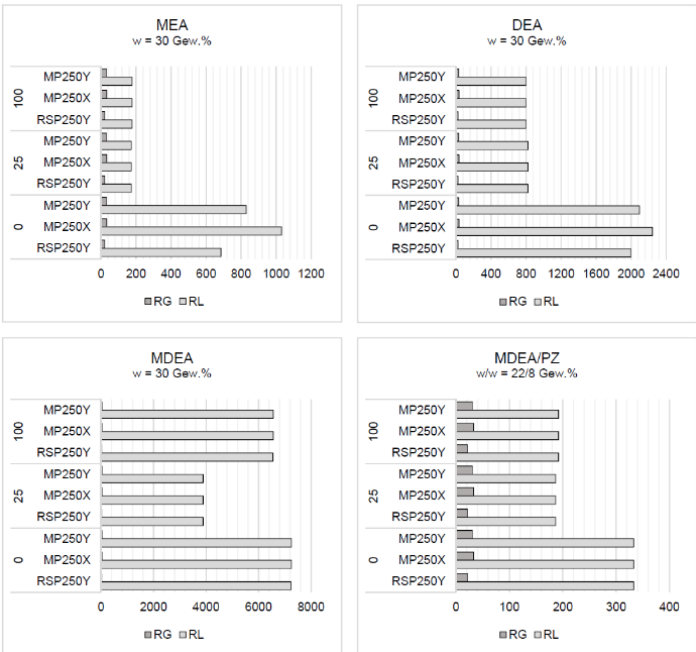

Figure 4: Mass transfer resistances R_G and R_L for different packing structures and absorption systems

4. Discussion

For the absorption systems MEA, DEA and MDEA, the reaction regime was determined; generally, a pseudo-first-order reaction applies. This assumption could not be confirmed for MEA and DEA at the bottom of the column. Due to the low concentration of free amine at this point, depletion occurs towards the phase boundary, resulting in a second-order reaction. For MDEA/PZ, no reaction regime could be identified due to a shortage of literature data. However, it can be assumed that a second-order reaction also occurs in the lower column section, due to a similarly high reduction in the free amine concentration between the top and bottom. A shift in the reaction regime from pseudo-first-order to second-order therefore causes an increase in the liquid-side mass transfer resistance R_L in this section. For

pseudo-first-order reactions, which occur primarily in the upper section of the column down to the section of maximum temperature, there is no dependence on the liquid-side mass transfer coefficient β_L and thus on the specific packing structure. It can therefore be concluded that in column sections where the conditions for pseudo-first-order reactions are fulfilled, more cost-effective packing materials with low specific pressure drop, such as MP250X, can be used. In the moderate reaction zone, below the temperature peak, there is an increased dominance of the liquid-side mass transfer resistance, resulting in a dependence on the packing structure. A hybrid packing such as RSP250Y shows lower liquid-phase resistances in this respect and is therefore recommended for this section of the column. Nevertheless, further investigations and espescially validations based on simulations or experiments with CC-systems is necessary.

References

Bradke, H., Büdicker, K., Deister, U. K., Krämer, D., Rinschede, A. & Zapp, P. (2021) "Industrielle CO2-Kreisläufe", VDI-Statusreport, VDI-Gesellschaft Energie und Umwelt.

El Hadri, N., Quang, D. V., Goetheer, E. L. & Abu Zahra, M. R. (2017) "Aqueous amine solution characterization for post-combustion CO2 capture process", Applied Energy, Vol. 185, S. 1433–1449.

Hüser, N. (2017) Untersuchung der Abscheidung von Kohlenstoffdioxid mit Alkanolaminen, UB-PAD - Paderborn University Library.

Schäffer, A. (2013) "Amine und Aminmischungen zur CO2-Absorption aus Kraftwerksrauchgasen und ihr Energiebedarf zur Regeneration", Aachen, Shaker Verlag.

Schultes, M. (2018) "Designing CO2 absorption columns with activated amine solutions", Chemical Engineering, Vol. 69.

Tsai, R.E. (2010) "Mass Transfer Area of Structured Packing", Dissertation, University of Texas at Austin.

Wolf-Zoellner, P., Böhm, H., Veseli, A. et al. (2025) “CaCTUS – Carbon Capture & Transformation, Utilization and Storage”, Berg Huettenmaennisches Monatsheft 170, 230–237.

Wu, D., He, D., Yao, G. & Jin, F. (2018) "Recent Advances in Fixation and Hydrogenation of Carbon Dioxide", Recent Advances in Fixation and Hydrogenation of Carbon Dioxide. Zhuhai, China, Paris, France, Atlantis Press.

Use of monolith structure adsorbents for CO_2 adsorption employing imines silica materials.

C.A.A. Sanchez[a], J.A. Delgado[a], S. Álvarez-Torrellas[a], V. Agueda[a] , M. Larriba[a], M. Martín[a]
[a]Catalysis and Separation Processes group (CyPS), Universidad Complutense de Madrid, Spain.
caasq708@gmail.com / csanch27@ucm.es

Abstract
Global warming is mainly caused by human-generated greenhouse gases, especially CO_2, CH_4, and N_2O. To handle and minimize the post-combustion emissions, adsorption offers a viable solution. This technique considers the use of porous materials containing fixed imines, which selectively bind and remove CO_2 from gas streams via reversible chemical interactions.
In this work, a low molecular weight branched polyethyleneimine (PEI) was synthesized, impregnated, and agglomerated with fixed silica to obtain a sample in pellets and monoliths. All this was done to estimate the kinetic parameters from fixed-bed breakthrough experiments.
The results indicated that the adsorbent material produced is selective only for CO_2, even when the temperature reaches 65°C. The CO_2 adsorption process is prolonged beyond 3 hours in the monolithic structures compared to the pellets and maintains its adsorption capacity, confirming the stability of the adsorbent material.

Keywords
Polyethyleneimine, Imine group, Carbon dioxide capture, Monolith, Adsorption, CCS.

1. Introduction

Over the years, the level of emissions generated by human activities has come to represent up to 70% of total greenhouse gases (GHG) (Houghton and Jenkins, 1990). Since 1970, an annual increase in the atmosphere has led to values of carbon dioxide (CO_2) reaching almost up to almost 410 ppm (IPCC, 2021). The use of the carbon capture and storage (CCS) technique (Gerden, 2018; Mathieu et al., 2006) may allow them to minimize their environmental impact and effectively reduce CO_2 emissions (UNFCCC COP 23, 2023; Metz et al., 2005; Kyoto Protocol, 1998).

Motivated by this, in recent years, efforts have been focused on the use of alternative processes for CO_2 capture, including technologies such as cryogenic, adsorption, and even membrane-based technologies (Aaron and Tsouris, 2005).

The application of solid adsorbents based on compounds with imine functional groups may be a solution to the problem that continues to attract interest in different sectors of research (Sanz-Pérez et al., 2019; Sayari and Belmabkhout, 2010; Zhang et al., 2015). Using polymers such as polyethylenimine (PEI) impregnated in mesostructured supports can be a more effective way to functionalize and improve their ability to adsorb CO_2, because they contain many imine groups in their molecular structure, which can be fixed by different techniques such as impregnation, among others (Xu et al., 2002). Some works have also led to the development of monoliths and their application in adsorption phenomena, evaluating the CO_2 adsorption performance on monoliths based on PEI- functionalization at different temperatures (Samyuktha et al., 2023; Jeong and Realff, 2021; Maresz et al., 2020).

In this work, the synthesized adsorbents with low-molecular-weight polyethyleneimine (PEI) were impregnated and agglomerated with silica at a specific weight content. The necessary experimental steps needed to absorb the CO_2 can be mentioned as follows:

1.1. Adsorbent preparation.

Silicon oxide, amorphous fumed, was supplied by Alfa Aesar, and polyethylenimine (PEI), identified as LLL4, was supplied by Sigma-Aldrich, with an average molecular weight measured by Laser Scattering of 600 Da.

For the preparation of the adsorbent material, a weight-basis proportion of PEI-LLL4 and silica oxide as support was used, according to previous work (Sanchez Quiñones et al., 2023), where 53% of PEI was the most promising amount of imines groups. A paste of defined consistency is obtained, which is extruded in the form of pellets with an average diameter of 2 mm and a length of approximately 5 mm. The monolith was extruded using the nozzle generated with 3D printing by stereolithography (SLA), displayed in Figure 1, which help us obtain an internal structure with at least 12 triangular channels with a side of 1mm; the total cross section in the monolith were 10mm.

Figure 1 Extruder nozzle and monolith prepared with PEI-Silica adsorbent.

Subsequently, in each case the water content present was removed using a Vaciotem-T vacuum drying oven at 50ºC and 0.1 bar for 12 h.

1.2 Characterization of Sample

Thermogravimetric analyses of the adsorbents were performed in a LABSYS evo DTA/DSC 1150 thermobalance, with a maximum temperature of 500 ºC and a heating rate of 10 ºC/min.

1.3 Adsorption breakthrough curves and adsorption capacity.

The installation used to obtain breakthrough curves consists of a fixed bed coupled to a Varian 3380 gas chromatograph, which has a thermal conductivity detector (TCD), with three mass flow controllers to feed the system with different gases, Figure 2. The properties of the fixed bed used are resume in previous researcher (Sanchez Quiñones et al., 2023). After the adsorption experiments, the fixed bed is regenerated for 24 h at 65ºC using helium.

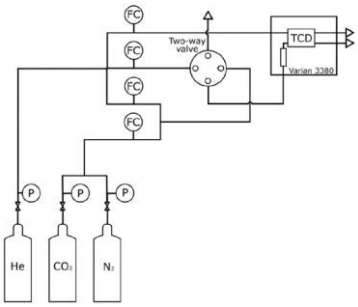

Figure 2 Experimental set-up for obtaining fixed-bed breakthrough curves.

For each gas on the adsorbent, the gas flow rate and its composition were fixed, and the temperature was varied (25º, 40º, and 65ºC). The outlet composition is measured online, data is collected every 0.01 sec, and the amount of gas retained by the adsorbent is calculated by a mass balance.

1.4 Mathematical model.

The adsorption kinetic parameters were calculated by fitting the experimental breakthrough curves to a model based on conservation equations (Brea et al., 2017; Delgado et al., 2014; Hindmarsh, 1992). The parameter q_{sat} was previously estimated with CO_2 adsorption equilibrium isotherms (Sanchez Quiñones et al., 2023). The CO_2 mass transfer rate between the gas and the adsorbent is given by the following equation:

$$N_{CO_2} = (1 - \varepsilon_L) \cdot \rho_p \cdot [k_{ads} \cdot p \cdot (q_{sat} - q) - k_{des} \cdot q] \quad (1)$$

N_{CO2}: mol·m^3·s^{-1}
k_{ads}: adsorption constant, Pa^{-1}·s^{-1}
k_{des}: desorption constant, s^{-1}
ρ_p: particle density, kg·m^{-3}
p: pressure, Pa
q: adsorbed concentration, mol·kg^{-1}
q_{sat}: maximal adsorbed concentration in equilibrium, mol·kg^{-1}
ε_L: bed voidage fraction between adsorbent particles, m^3·m^{-3}
k_{eq}: is the equilibrium constant, the relation of (k_{ads} / k_{des})

2. Results and discussion

2.1. Thermogravimetric analysis.

Figure 3 presents the TGA of the impregnated adsorbent with 53% PEI of LLL4. The adsorbent presents its first weight loss at temperatures lower than 150°C due to water evaporation, and the imines start to decompose at temperatures higher than 250°C.

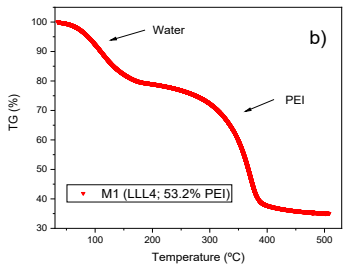

Figure 3 TGA curves for adsorbent material prepare M1.

2.2 Adsorption breakthrough curves, and CO_2/N_2 adsorption capacity.

The effect of temperature and adsorbate concentration on the adsorption process was investigated through breakthrough experiments. Using three flow rates close to 30 ml/min, 60 ml/min, 90 ml/min, and three different concentrations, ca. (6%, 10%, and 19%) for CO_2 adsorption and ca. (2% 4% and 7%) for N_2 adsorption, respectively.

As shown in Figure 4, the breakthrough time increases with increasing temperature at a given CO_2 concentration. Moreover, the breakthrough time decreased as the CO_2 flow rate fed to the system increased at a given temperature, which also occurred in pellets and monoliths. Figure 4a shows the material doesn't retain N_2 and is selective to CO_2 molecules. The typical error for experimental data was around 13%.

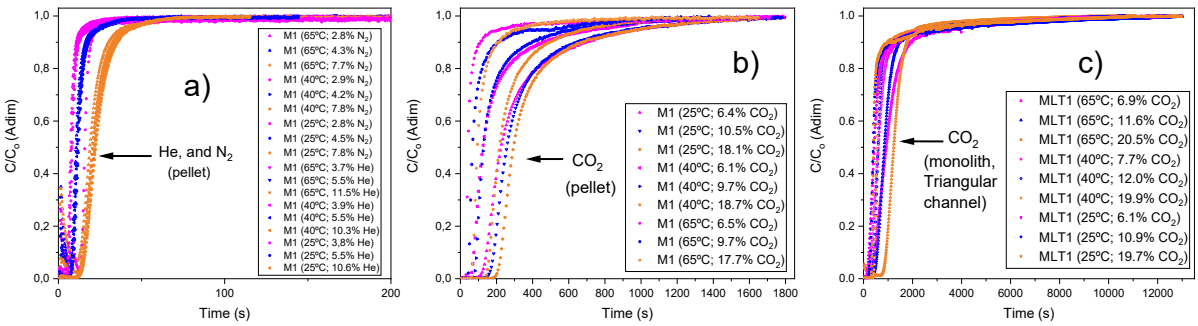

Figure 4 Adsorption breakthrough curves for sample M1 (a, b) and monolith MLT1-Triangular (c), at temperatures of 25ºC, 40ºC and 65ºC.

Figure 4 shows different times required to saturate the adsorbent material with CO_2 increasing from 30 min in pellets to almost 3 h for a monolith, even when both samples have a similar weight, close to 2 g.

The adsorption capacity calculated, considering the dead volume of the installation measured using helium as a tracer, is shown in Table 1. Since the chemisorption between CO_2 and imine functional groups is promoted at high temperatures (Blanchon Le Bouhelec et al., 2007; Leal et al., 1995), the CO_2 adsorbed amount increased as the temperature rose up to 65°C. N_2 adsorption capacities indicated this corresponding adsorption is negligible.

Table 1 CO_2 and N_2 adsorption capacity for M1 pellets and MLT1-Triangular monolith.

	Temperature (ºC)	25 ºC			40 ºC			65 ºC		
M1	CO_2 Concentration (%)	18.1	10.5	6.4	18.7	9.7	6.1	17.7	9.7	6.5
	q_CO_2 [mol/$kg_{adsorbent}$]	0.946	0.954	0.938	1.235	1.240	1.264	1.716	1.715	1.719
	N_2 Concentration (%)	7.1	3.8	2.5	7.0	3.7	2.5	7.0	3.7	2.5
	q_N_2 [mol/ $kg_{adsorbent}$]	0.001	0.000	0.001	0.000	0.000	0.000	0.000	0.000	0.000
MLT1 Triangular	CO_2 Concentration (%)	19.7	10.9	6.1	19.9	12.0	7.7	20.5	11.6	6.9
	q_CO_2 [mol/$kg_{adsorbent}$]	0.590	0.605	0.603	1.236	1.266	1.301	1.807	1.736	1.751
	N_2 Concentration (%)	11.0	4.8	2.9	10.5	5.2	3.2	10.5	5.0	2.9
	q_N_2 [mol/ $kg_{adsorbent}$]	0.000	0.000	0.000	0.001	0.016	0.000	0.001	0.013	0.002

The CO_2 adsorption capacity obtained, Table 1, is much lower than that obtained with the volumetric equipment in equilibrium conditions (Sanchez Quiñones et al., 2023), due to the lower contact time between the gas and the adsorbent in the fixed bed. A mass transfer resistance through the polymer film leads to a reduction in the adsorption capacity. Increasing the temperature promotes higher mobility and improves the kinetics and the access of CO_2 to imine groups that are not easily accessible at lower temperatures, so this resistance is reduced.

2.3 Application of the mathematical model and estimate kinetic parameters.

The mathematical model described elsewhere (Brea et al., 2017; Delgado et al., 2014; Hindmarsh, 1992) has been employed to generate the simulated breakthrough curves of helium as tracer and CO_2 as an adsorbate.

Figure 5 and Figure 6 shows the experimental and fitted breakthrough curves of CO_2 on M1 and MLT1 sample. It can be seen that the model represents well the general trend of the breakthrough curves in all studied conditions.

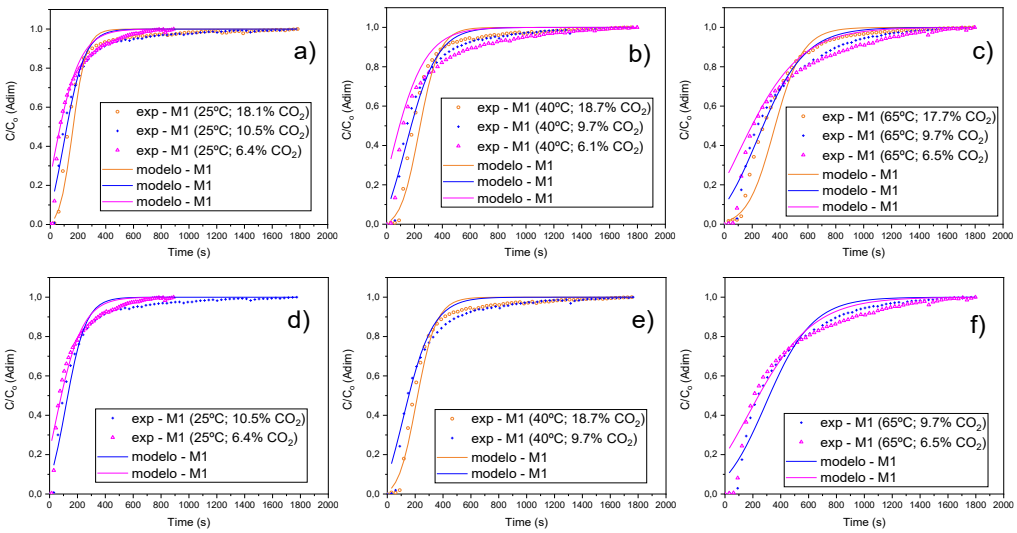

Figure 5 CO_2 adsorption curves of the sample and fitting curves for M1 sample at 25ºC (a, d), 40ºC (b, e) y 65ºC (c, f).

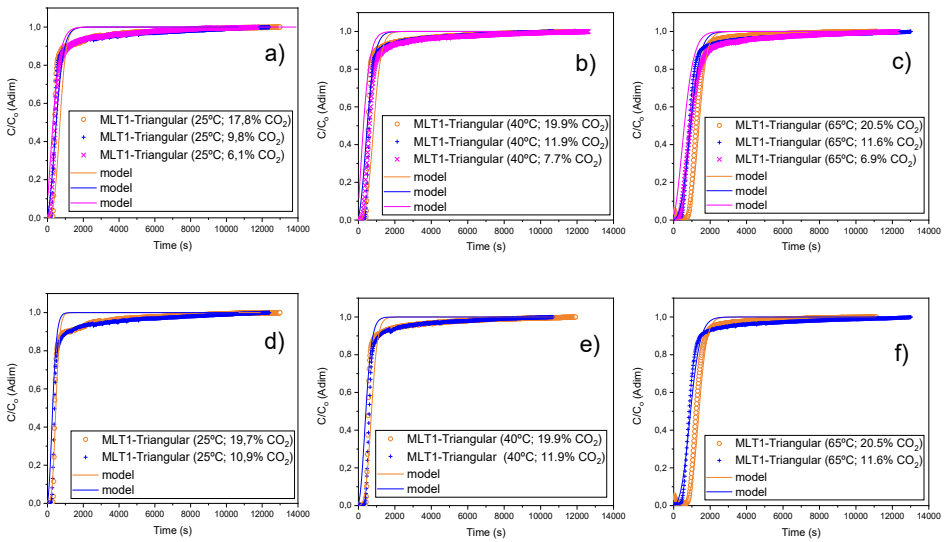

Figure 6 CO_2 adsorption curves of the sample and fitting curve for MLT1-Triangular monolith at 25ºC (a, d), 40ºC (b, e) y 65ºC (c, f).

The kinetic parameters were determined from the mathematical model, i.e., the adsorption constant k_{ads} and the desorption constant k_{des} are summarized in Table 2. In addition, another aspect to consider is the enthalpy determined by the Van't Hoff equation, which was calculated from the equilibrium constants of the process as a function of temperature.

Table 2 CO_2 adsorption and desorption values calculated with the mathematical model.

	Temperature	25ºC	40ºC	65 ºC
MLT1-Triangular	k_{ads} ($Pa^{-1}\cdot s^{-1}$)	5.19E-07	1,51E-07	1.99E-07
	k_{des} (s^{-1})	2.44E-02	8,50E-03	6.50E-03
	k_{eq} (Pa^{-1})	2.12E-05	1,77E-05	3.05E-05
	q_{sat} ($mol\cdot kg^{-1}$)	1.21	1.96	2.55
	$\Delta H°_{ads}$ ($kJ\cdot mol^{-1}$)		8.5	

Figure 7 shows both k_{ads} and k_{eq}, which is the ratio between the constant of adsorption and desorption. This indicates that the CO_2 adsorption process is favored by increases in temperature, as has been mentioned previously.

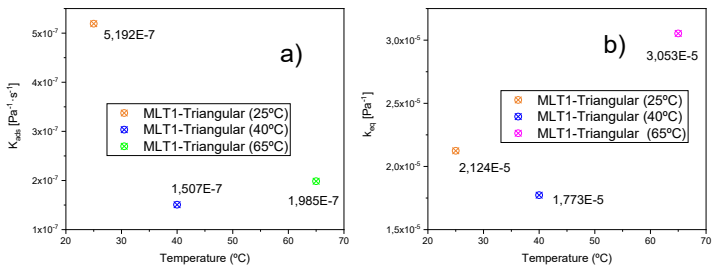

Figure 7 Estimated $k_{equilibrium}$ and $k_{adsorption}$ values by temperature of MLT1-Triangular.

In Table 2, the positive enthalpy values, $\Delta H° > 0$, agree with an endothermic process in the reactions between the CO_2 and the imine groups reported before (Blanchon Le Bouhelec et al., 2007; Sanz et al., 2010; Leal et al., 1995). But low values, less than 100 kJ/mol, would not be expected with chemisorption and could be referred to as diffusional limitations during chemisorption between CO_2 and the imine groups.

3. Conclusions

An adsorbent based on silica impregnated and agglomerated with 53% of PEI LLL4 should have an increase of CO_2 adsorption capacity with temperature due to the reaction of CO_2 molecules with imine groups. The higher capacity obtained for a

sample at 1 bar and 65ºC was near to 1.8 $mol/kg_{adsorbent}$. A mathematical model proposed to obtain the adsorption and desorption constants represents the general trend in monolith with triangular channels well. The enthalpy calculated was positive and less than 10 kJ/mol, supporting the chemisorption mechanism of the CO_2 and PEI-LLL4.

References

Aaron, D., Tsouris, C., 2005. Separation of CO2 from Flue Gas: A Review. Sep. Sci. Technol. 40, 321–348.

Blanchon Le Bouhelec, E., Mougin, P., Barreau, A., Solimando, R., 2007. Rigorous Modeling of the Acid Gas Heat of Absorption in Alkanolamine Solutions. Energy Fuels 21, 2044–2055. https://doi.org/10.1021/ef0605706

Brea, P., Delgado, J.A., Águeda, V.I., Uguina, M.A., 2017. Modeling of breakthrough curves of N2, CH4, CO, CO2 and a SMR type off-gas mixture on a fixed bed of BPL activated carbon. Sep. Purif. Technol. 179, 61–71. https://doi.org/10.1016/j.seppur.2017.01.054

Delgado, J.A., Águeda, V.I., Uguina, M.A., Sotelo, J.L., Brea, P., Grande, C.A., 2014. Adsorption and Diffusion of H_2, CO, CH_4, and CO_2 in BPL Activated Carbon and 13X Zeolite: Evaluation of Performance in Pressure Swing Adsorption Hydrogen Purification by Simulation. Ind. Eng. Chem. Res. 53, 15414–15426.

Gerden, T., 2018. The Adoption of the Kyoto Protocol of the United Nations Framework Convention on Climate Change. Contrib. Contemp. Hist. 58. https://doi.org/10.51663/pnz.58.2.07

Hindmarsh, A., 1992. ODEPACK. A Collection of ODE System Solvers.

Houghton, J.T., Jenkins, G.J., 1990. Climate Change: The IPCC Scientific Assessment.

IPCC, 2021. Climate Change 2021: The Physical Science Basis - Summary for the Policymakers (Working Group I), Climate Change 2021: The Physical Science Basis.

Jeong, D.H., Realff, M.J., 2021. Modular monolith adsorbent systems for CO2 capture and its parameterized optimization. Chem. Eng. Res. Des. 176, 1–13. https://doi.org/10.1016/j.cherd.2021.09.018

Kyoto Protocol, 1998. Framework Convention On Climate Change. United Nations.

Leal, O., Bolívar, C., Ovalles, C., García, J.J., Espidel, Y., 1995. Reversible adsorption of carbon dioxide on amine surface-bonded silica gel. Inorganica Chim. Acta 240, 183–189. https://doi.org/10.1016/0020-1693(95)04534-1

Maresz, K., Ciemięga, A., Malinowski, J.J., Mrowiec-Białoń, J., 2020. Effect of support structure and polyamine type on CO2 capture in hierarchically structured monolithic sorbents. Chem. Eng. J. 383, 123175. https://doi.org/10.1016/j.cej.2019.123175

Mathieu, P., Rakopoulos, C.D., Tsatsaronis, G., 2006. ECOS 2006 Proceedings of the 19th International Conference on Efficiency, Cost, Optimization, Simulation and Environmental Impact of Energy Systems.

Metz, B., Davidson, O., de Coninck, H., Loos, M., Meyer, L., 2005. IPCC Special Report on Carbon dioxide Capture and Storage. Policy Stud.

Samyuktha, R., Valapa, R.B., Loganathan, S., 2023. Tailoring of 3D printed polyethylenimine functionalized MCM-41 based monoliths and scrutiny on CO2 adsorption characteristics. J. Environ. Chem. Eng. 11, 110523. https://doi.org/10.1016/j.jece.2023.110523

Sanchez Quiñones, C.A.A., Águeda Maté, V.I., Delgado Dobladez, J.A., Álvarez-Torrellas, S., Larriba, M., Martín-Martínez, M., 2023. Imines supported on silica as CO2 capture selective adsorbents. Chem. Eng. Res. Des. 194, 573–581. https://doi.org/10.1016/j.cherd.2023.04.061

Sanz, R., Calleja, G., Arencibia, A., Sanz-Pérez, E.S., 2010. CO2 adsorption on branched polyethyleneimine-impregnated mesoporous silica SBA-15. Appl. Surf. Sci. 256, 5323–5328. https://doi.org/10.1016/j.apsusc.2009.12.070

Sanz-Pérez, E.S., Fernández, A., Arencibia, A., Calleja, G., Sanz, R., 2019. Hybrid amine-silica materials: Determination of N content by 29Si NMR and application to direct CO2 capture from air. Chem. Eng. J. 373, 1286–1294. https://doi.org/10.1016/j.cej.2019.05.117

Sayari, A., Belmabkhout, Y., 2010. Stabilization of Amine-Containing CO_2 Adsorbents: Dramatic Effect of Water Vapor. J. Am. Chem. Soc. 132, 6312–6314. https://doi.org/10.1021/ja1013773

UNFCCC COP 23, 2023. SDG KNOWLEDGE HUB. IISD Reporting Services / ENB Coverage.

Xu, X., Song, C., Andresen, J.M., Miller, B.G., Scaroni, A.W., 2002. Novel Polyethylenimine-Modified Mesoporous Molecular Sieve of MCM-41 Type as High-Capacity Adsorbent for CO_2 Capture. Energy Fuels 16, 1463–1469.

Zhang, H., Goeppert, A., Prakash, G.K.S., Olah, G., 2015. Applicability of linear polyethylenimine supported on nano-silica for the adsorption of CO_2 from various sources including dry air. RSC Adv. 5, 52550–52562. https://doi.org/10.1039/C5RA05428A

Influence of process operation on CESAR1 emission behavior in biomass gas treatment

Maria Dimitriadi[a], Christina Andersen[b], Isaac Appelquist Løge[a], Randi Neerup[a], Søren Jensen[c], Jakob Lindkvist Karlsson[c], Pantelis Boutzis[a], Nomiki Kottaki[a], Frantz Bræstrup[b], Kristian Røhe Kongst Krum[d], Søren Christensen[d], Sebastian Nis Bay Villadsen[a], Jens Abildskov[e], Philip Loldrup Fosbøl[a]

[a]Center for Energy Resource Engineering (CERE), Technical University of Denmark, Søltofts Plads 228A, 2800 Kgs Lyngby, Denmark
[b]FORCE Technology, Park Alle 345, 2605 Brøndby, Denmark
[c] Union Engineering A/S, Pentair, Snaremosevej 27, 7000 Fredericia, Denmark
[d]Ørsted A/S, Kraftværksvej 53, Skærbæk, 7000 Fredericia, Denmark
[e]Process and System Engineering Center (PROSYS), Technical University of Denmark, Søltofts Plads 228A, 2800 Kgs Lyngby, Denmark

Abstract

This study evaluates the emission behavior of CESAR1 solvent in a pilot-scale carbon capture unit downstream a biomass-fired power plant, with focus on the effects of operational configurations on amine emissions. The results demonstrate that wash column parameters, which include water wash flow, wash column temperature, and acid wash pH, have a significant influence on emissions.

Introducing a solvent filter significantly reduced emissions by limiting the accumulation and release of degradation products. The use of an intercooler showed no measurable reduction in amine emissions under the investigated conditions. However, it led to increased concentrations of impurities in the CO_2-rich stream. This may indicate a redistribution of volatile components within the plant. Additionally, a change in flue gas concentrations were associated with elevated emissions, particularly for AMP and piperazine, demonstrating that flue gas composition is a major contributor to solvent loss. The results showcase the intricate nature of amine emissions and offer valuable insights into the role of optimizing operational conditions in achieving effective emission control and system performance.

Keywords
Carbon capture; CESAR1; Emissions; Acid wash; Solvent filter; Intercooling (IC);

1. Introduction

Amine-based post-combustion carbon capture (PCC) remains the most advanced and widely used method for large-scale CO_2 mitigation [1]. However, amines tend to degrade over time and can become corrosive [2]. Amine byproducts can be highly volatile and can pose environmental risks if released with the CO_2 depleted gas to the atmosphere [3].

To address these issues, new solvent formulations and improved process designs are being developed to minimize solvent degradation and reduce reboiler energy requirements. Among these, the AMP/piperazine blend known as CESAR1 is a leading alternative to the traditional mono-ethanolamine (MEA) [4]. CESAR1 offers better absorption rates, lower energy demands during regeneration, compared to MEA [5–7]. However, although the CESAR1 solvent has shown to be less susceptible to degradation than MEA [8], its susceptibility towards degradation remains an issue [9–11].

This research investigates the emission characteristics of CESAR1 in a pilot- scale carbon capture unit at a biomass-fired power plant, focusing on how operational settings affect amine emissions. Findings reveal that parameters like water wash flow rate, wash column temperature, and acid wash pH are crucial for controlling emissions.

Using a solvent filter proved highly effective in decreasing emissions by preventing the buildup and release of degradation products. In contrast, activating the intercooler had only a minor direct effect on amine emissions under the tested conditions, though it increased impurity levels in the CO_2-rich stream, suggesting a redistribution of volatile compounds within the process. Variations in flue gas composition were linked to higher emission levels, especially for AMP and PZ, emphasizing the importance of flue gas properties as key factors influencing solvent losses.

Overall, the results underline the complex nature of amine emissions and demonstrate the importance of optimized operating conditions to improve emission control and overall system performance.

2. Results and discussion

2.1 Experimental Setup

Prior to this work, the Technical University of Denmark (DTU), in collaboration with Pentair Union Engineering, designed and constructed a mobile carbon capture test unit. The pilot has the capability of capturing up to 1 ton of CO_2 per day and able to operate 24/7.

The plant consists of four modularized process skids, as shown in Figure 1a. The lower two skids are equipped with process equipment, such as the blower, heat exchangers, filters, indicators, etc. The upper two skids are made up of the four columns of the unit: an absorber and a desorber (skid B, Figure 1a) and the wash tower and an additional

column used for advanced configurations (skid A). Figure 1b shows the plant in operation at Ørsted, Skærbækværket, Denmark.

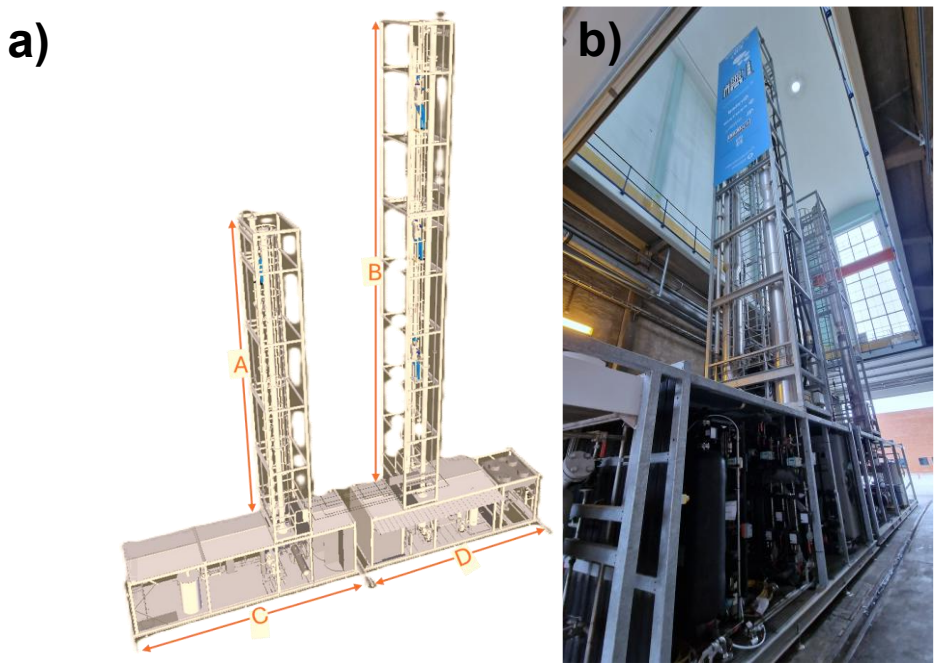

Figure 1.a) 3D model of the capture plant. b) The pilot plant demonstrating at Ørsted, in Skærbækværket, Denmark.

2.2 Results

The results describe and showcase the effects of flue gas composition, wash column operation, and process configurations influence amine emissions from a CESAR1-based carbon capture unit at a biomass-fired power plant.

The findings showcase that changes in flue gas composition were found resulting in a significant effect on amine emissions. Notably, the increase in AMP and PZ emissions likely results from slight foaming following the gas composition shift, resulting in enhances in solvent carryover. This highlights the sensitivity of emission behavior to flue gas conditions and the need for careful monitoring, as even small variations can lead to noticeable emission changes.

Wash column operating conditions, particularly water flow, column temperature, and acid concentration, were shown to have a critical role in emission control (as can be seen in Figure 2). Amine emissions closely followed shifts in water wash flow during steady operation, with temperature fluctuations in the wash beds, specifically while active cooling, had a strong influence on emission levels.

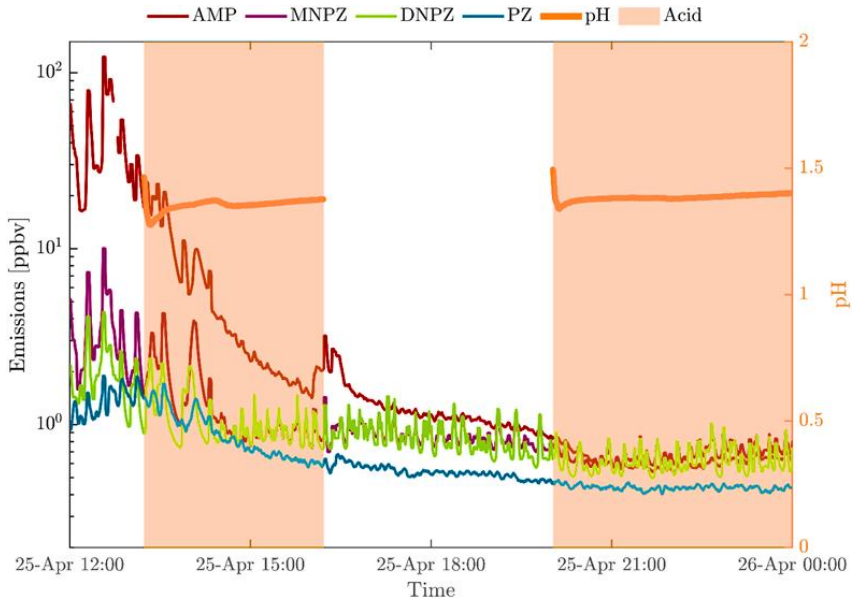

Figure 2: AMP, PZ, MNPZ, and DNPZ emissions [ppbv] (left axis) and pH of the acid wash (right axis) over time. Emission measurements are considered semi-quantitative [7].

Process configuration also significantly influenced emission behavior. Activation of the IC had limited impact on depleted gas emissions under the conditions studied, although further investigation across wider operating ranges is needed. In contrast, shutting down the IC combined with increased reboiler duty raised absorber temperatures which resulted in a change in emission profiles, notably in MNPZ levels. As seen in Figure 3, the use of a solvent filter was highly effective in limiting amine emissions by preventing the accumulation and release of amine byproducts.

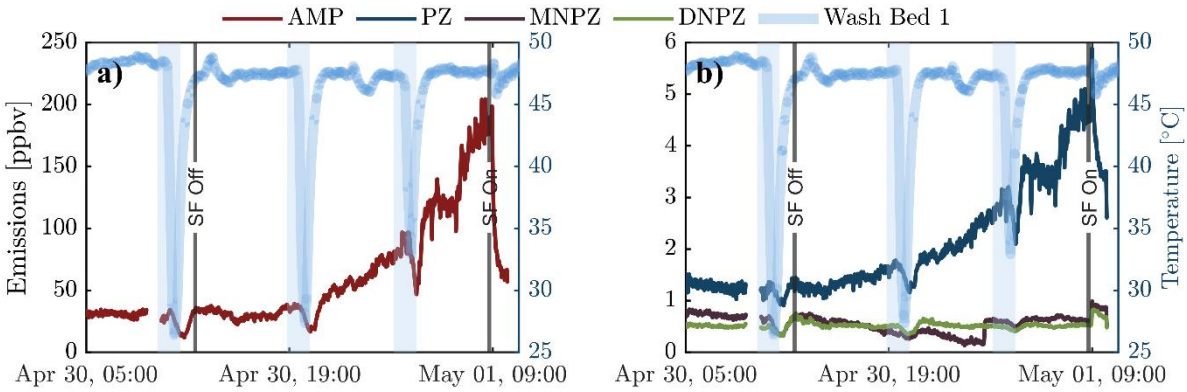

Figure 3: a) Emissions [ppbv] (left axis) and wash bed 1 temperature [°C] (right axis) over time during the bypass of the solvent filter for: a) AMP, b) PZ, MNPZ, and DNPZ. Emission measurements are considered semi-quantitative [7].

3. Conclusions

Overall, the most effective emission control strategy for the depleted gas stream was achieved by combining the solvent filter with a circulating acid wash maintained at pH 3, reducing emissions to near non-detectable concentration.
Analysis of the CO_2 rich stream showed that IC operation increased impurity levels, which suggests a possible redistribution of contaminants from the absorber to the stripper.

In summary, the findings underscore the complexity of amine emissions and demonstrate that optimized operational parameters and integrated process configurations are essential for effective emission control and improved system performance.

Acknowledgements

The authors would like to thank the European Research Council (ERC) for funding this project under the Horizon 2020 Research Program ¨Formate for Renewable Energy Storage (FRESH)¨ (Grant Agreement No. 101069605), as well as the INNO-CCUS for funding this research under the research program ¨Carbon capture Open tests and Review of Technologies (CORT)¨ and the Technical University of Denmark (DTU).

References

1. Liang, Z. (Henry), Rongwong, W., Liu, H., Fu, K., Gao, H., Cao, F., Zhang, R., Sema, T., Henni, A., Sumon, K., Nath, D., Gelowitz, D., Srisang, W., Saiwan, C., Benamor, A., Al-Marri, M., Shi, H., Supap, T., Chan, C., Zhou, Q., Abu-Zahra, M., Wilson, M., Olson, W., Idem, R., Tontiwachwuthikul, P. (PT): Recent progress and new developments in post-combustion carbon-capture technology with amine based solvents. International Journal of Greenhouse Gas Control. 40, 26–54 (2015). https://doi.org/10.1016/j.ijggc.2015.06.017
2. Voice, A.K., Rochelle, G.T.: Oxidation of amines at absorber conditions for CO2 capture from flue gas. Energy Procedia. 4, 171–178 (2011). https://doi.org/10.1016/j.egypro.2011.01.038
3. Grøntoft, T.: Atmospheric corrosion due to amine emissions from carbon capture plants. International Journal of Greenhouse Gas Control. 109, 103355 (2021). https://doi.org/10.1016/j.ijggc.2021.103355
4. Løge, I.A., Demir, C., Vinjarapu, S.H.B., Neerup, R., Hauge, E., Jørsboe, J.K., Dimitriadi, M., Halilov, H., Frøstrup, C.F., Gyorbiro, I., Kottaki, N., Jayan, A.N., Jensen, S., Karlsson, J.L., Fosbøl, P.: Pilot-scale CO2 capture in a cement plant with CESAR1: Comparative analysis of specific reboiler duty across advanced process configurations. Chemical Engineering Journal. 159429 (2025). https://doi.org/10.1016/j.cej.2025.159429

5. Artanto, Y., Jansen, J., Pearson, P., Puxty, G., Cottrell, A., Meuleman, E., Feron, P.: Pilot-scale evaluation of AMP/PZ to capture CO2 from flue gas of an Australian brown coal–fired power station. International Journal of Greenhouse Gas Control. 20, 189–195 (2014). https://doi.org/10.1016/j.ijggc.2013.11.002
6. Dimitriadi, M., Løge, I.A., Neerup, R., Jensen, S., Karlsson, J.L., Brorholt, L.P., Bræstrup, F., Halilov, H., Bay Villadsen, S.N., Abildskov, J., Fosbøl, P.L.: Pilot-Scale CO2 capture in a cement plant with CESAR1: Emission control with acid wash and absorber intercooling. Sep Purif Technol. 133693 (2025). https://doi.org/10.1016/j.seppur.2025.133693
7. Dimitriadi, M., Andersen, C., Løge, I.A., Neerup, R., Jensen, S., Karlsson, J.L., Bountzis, P., Kottaki, N., Bræstrup, F., Krum, K.R.K., Christensen, S., Villadsen, S.N.B., Abildskov, J., Fosbøl, P.L.: Process configurations for emission control: CESAR1 emission behavior in biomass combustion gas treatment. Chemical Engineering Journal. 524, 168649 (2025). https://doi.org/10.1016/j.cej.2025.168649
8. Neerup, R., Øbro, K.L., Løge, I.A., Kottaki, N., Frøstrup, C.F., Gyorbiro, I., Dimitriadi, M., Halilov, H., Jensen, S., Karlsson, J.L., Fosbøl, P.L.: CO2 capture pilot campaign: Understanding solvent degradation of CESAR1 in cement plant operations. Chemical Engineering Journal. 510, 161542 (2025). https://doi.org/10.1016/j.cej.2025.161542
9. Moser, P., Wiechers, G., Schmidt, S., Veronezi Figueiredo, R., Skylogianni, E., Garcia Moretz-Sohn Monteiro, J.: Conclusions from 3 years of continuous capture plant operation without exchange of the AMP/PZ-based solvent at Niederaussem – insights into solvent degradation management. International Journal of Greenhouse Gas Control. 126, 103894 (2023). https://doi.org/10.1016/j.ijggc.2023.103894
10. Languille, B., Drageset, A., Mikoviny, T., Zardin, E., Benquet, C., Ullestad, Ø., Aronson, M., Kleppe, R., Wisthaler, A.: Best practices for the measurement of 2-amino-2-methyl-1-propanol, piperazine and their degradation products in amine plant emissions. (2021)
11. Languille, B., Drageset, A., Mikoviny, T., Zardin, E., Benquet, C., Ullestad, Ø., Aronson, M., Kleppe, R., Wisthaler, A.: Atmospheric emissions of amino-methyl-propanol, piperazine and their degradation products during the 2019-20 ALIGN-CCUS campaign at the Technology Centre Mongstad. (2021)

Upscaling and optimisation of electrochemical regeneration of solvents for carbon capture

Rasmus Juel Friis[1], Christian Warm[1], Andreas Juhl Sørensen[1], Sebastian Borgquist[1], Tessa Lund Biel-Nielsen[1], Anders Rønne Rasmussen[2], Morten Gildsig Poulsen[2], Sebastian Nis Bay Villadsen[1], Jens Abildskov[3], Philip Loldrup Fosbøl[1]
[1]AT-CERE, Technical University of Denmark, Kongens Lyngby, Denmark
[2]ESTECH A/S, Svendborg, Denmark
[3]PROSYS, Technical University of Denmark, Kongens Lyngby, Denmark

Abstract

This study details the process of upscaling an electrochemical CO_2 capture plant from a 1 g/h CO_2 capacity lab-scale to a 5 kg/h plant. The study did proof-of-concept experiments with 10cm^2 electrodes. Afterwards, the electrodes used were 100cm^2 and for the final plant, the electrodes used in the cell were 800cm^2. To limit the power consumption of this novel technology, efforts to optimize electrodes and membranes were made. A multitude of anodes were used, while the cathode was kept as stainless steel. Ti-MMO and Ni proved to be the most efficient for power consumption and Ti-MMO proved to be superior for durability. 5 different commercially available membranes were tested, where Fumasep F-10120 was found to be the one that had the lowest power consumption and second highest CO_2 desorption efficiency. Reinforcement nets and thickness of the membranes proved to be the main cause for increase of power consumption. The findings were used to build the final plant, which has a capacity of capturing up to 5 kg CO_2/h.

Keywords

Electrochemical CO_2 capture, CO_2, electrochemistry, electrodes, membranes, upscaling

1. Introduction

This study describes the upscaling of an electrochemical carbon capture unit from TRL 3 to TRL 6 (see Figure 1). The study shows experiments with different cell configurations (focusing on anode electrodes and membrane materials) that went into the final cell design for upscaling.

The main contributing factor to this is the drastic increase of greenhouse gas emissions, especially carbon dioxide (CO_2) [1]. However, hesitance due to political, legislative, and economic worries has led the world to a crossroads. Lack of investment in infrastructure has slowed the development of becoming less reliant of hydrocarbons for processes reliant on energy and the continuous existence and dependence of hard-to-abate industries has made it clear that, unfortunately, CO_2 will be continued to be emitted in the coming years. Furthermore, while green energy sources have become increasing viable, a bunch of problems still exist. This could be overproduction, reliability, and scarcity in some parts of the world [2,3].

This has led a need for mitigation of emissions and thus intensive economic and scientific resources have been used to develop the science of CO_2 capture. The most mature technology in the field is chemical scrubbing with amines utilizing thermal regeneration. However, this technology faces issue related to solvent degradation leading to unfavourable bi-products and high energy demands [4].

1.1 Aim and approach

This study investigates an alternative way to regenerate the solvent than the most mature one. In this technology, electrochemistry is used for the regeneration of carbon capture solvent [5]. The desorption of CO_2 is done through and electrochemical stack consisting of multiple cells with an anode and cathode with a membrane separating the two chambers. Potassium hydroxide is used as the capture agent. The two chambers perform water hydrolysis. In the anode chamber hydrogen ions are produced driving the transport of potassium over the membrane thus increasing the loading and partial pressure of CO_2 in the liquid. At a loading of around 1 CO_2/K^+, the partial pressure of CO_2 in the liquid will drive CO_2 to desorb.

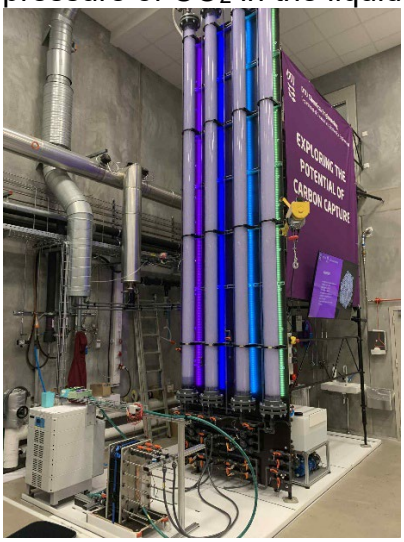

Figure 1: The new state–of-the-art electrochemical pilot plant at the Technical University of Denmark

The liquid/gas mixed stream is sent to a flash tank, where the gas and liquid are separated. The solvent is subsequently sent to the cathode chamber, where the generation of hydroxide ions allow for a new round of CO_2 absorption. In the cathode, hydrogen is produced and needs to be separated in a flash tank. After the second flash tank, the solvent is sent back to the top of the absorption column and the cycle is repeated. A schematic of the process can be seen in Figure 2.

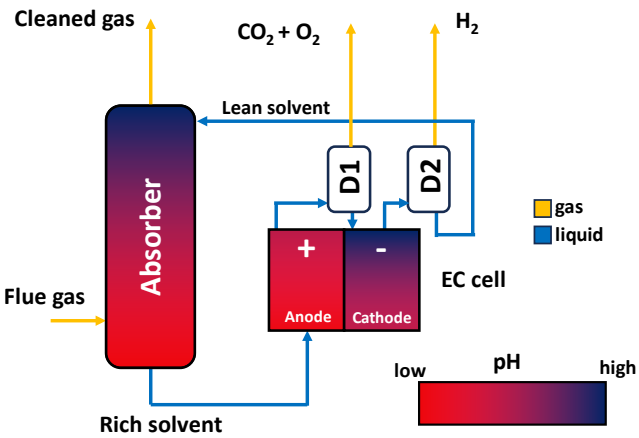

Figure 2: Schematic of the process

The reactions taking place in the electrochemical cell are shown below.

Anode:

$$2H_2O \rightarrow O_2 + 4H^+ + 4e^-$$

$$H^+ + HCO_3^- \rightarrow CO_2 + H_2O$$
$$2H^+ + CO_3^{2-} \rightarrow CO_2 + H_2O$$

Cathode:

$$2H_2O + 2e^- \rightarrow H_2 + 2OH^-$$

1.2 Scientific innovation

This technology is a promising combination of CO_2 capture and Power-to-X solution as it requires electricity. This also makes the solution plug-and-play and independent of expensive retrofitting. Furthermore, it produces a high purity product that can be used for further synthesis. The combined production of H_2 and CO_2 allows for a relatively easy solution to a complex infrastructure problem and could be key in the production of H_2 for heat and electricity generation or to produce sustainable fuels. The technology is novel and upscaling research is currently taking place.

2. Results and discussion

This study has focused on proof-of-concept experiments with further upscaling as the main goal. In Figure 3, results of the initial experiments in a 10cm^2 electrochemical cell can be seen. The Figure shows gas concentrations of CO_2 and O_2 as a function of experiment time.

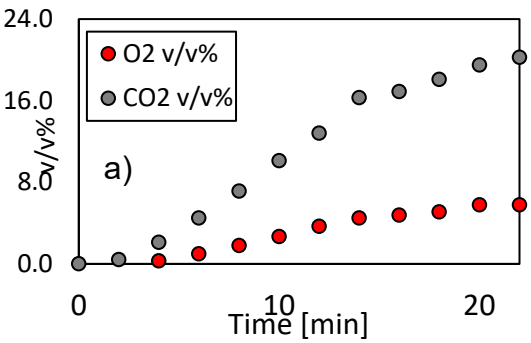

Figure 3: Example of lab-scale experiment for proof-of-concept of technology

After around 20 minutes of experiments, the desorbed gas contains 20.27% CO_2 and 5.8% O_2. The initial experiments showed that the technology works and that it is possible to desorb CO_2 in an electrochemical cell. Electrode experiments in the lab-scale setup was also conducted, which showed that some electrodes are better for durability a reaction affinity. The findings were used to build a bigger setup, this time working with an electrode area of 100 cm^2. The setup can be seen in Figure 4.

Figure 4: Newly built electrochemical carbon capture unit. To the left is the scrubber, where CO_2 comes into contact with KOH, to the right is the degasser and bottom right the electrochemical cell unit can be seen.

This setup had pH sensor and an experimental result can be seen in Figure 5. The solvent coming out of the absorber is named as the pH_{rich} solvent and the solvent entering is the pH_{lean} solvent. The experiment shown in Figure 5 used a saturated solution of KOH and CO_2 but did not have CO_2 absorption, which explains the alignment of pH values for the two streams over time.

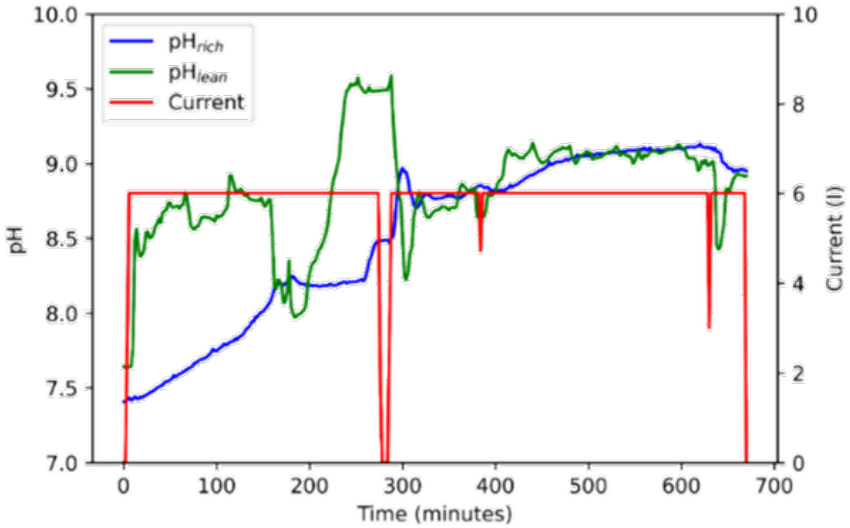

Figure 5: pH on y-axis 1 and current on y-axis 2 as a function of experiment time

A trend of increasing pH in the system can be seen, which could only be caused by CO_2 leaving the system as production of H^+ at the anode is countered by OH^- for the cathode. Further efforts to quantify the CO_2 desorption and improve the process was made. An electrochemical cell was designed for further development of the process. This allowed for multiple electrochemical cells to be put into a stack to increase CO_2 desorption capacity. Regeneration of the solvent, and thus, CO_2 desorption seems to be the limiting factor in the process. This finding was further highlighted by the possibility of applying the newly designed electrochemical cell, with an area of $800cm^2$, to the same setup, where a $100cm^2$ cell.
After the CO_2 desorption concerns was addressed, optimizing efforts were made.

a)

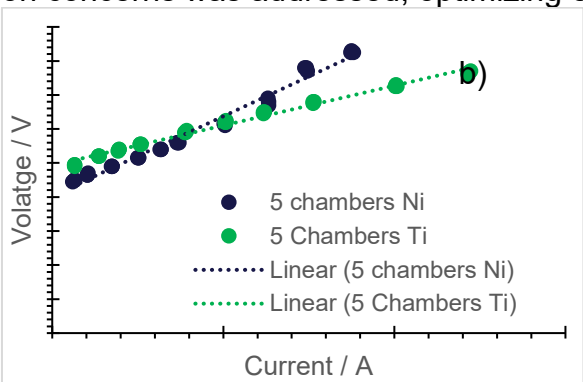

Figure 6: Voltage as a function of current with different anode electrodes

The electrode material at the anode chamber is crucial for limitation of power consumption and durability of the electrochemical cell. This could be seen from experiments with different materials at the anode chamber. Figure 6 shows the clear superiority of Ti-MMO anode compared to a Ni anode, when the current increases. Furthermore, the Ni anode showed higher degrees of corrosion in the experiment time compared to the Ti-MMO and an affinity to form Nickel-carbon complexes.

On Figure 7, results of a study with different commercially available membranes are seen. This study was done to determine, whether improvement of the power consumption was possible by changing the membrane in the electrochemical cell. The experiments increased the current at fixed time interval and measured current. The hypothesis was that since the membrane is responsible for part of the internal resistance in the electrochemical cell, the energy consumption could be limited when changing the membrane. Thus, the main result from this study would be an I-V curve. Figure 7 shows the experimental results. The Fumasep F-10120 showed to be best membrane, when it came to looking solely at the power consumption. The Flemion 8080K, which is used in chlor-alkali industrial processes [6], shows itself to be the worst performing at higher currents. Most of the membranes consumes an equal amount of energy throughout the experiment, whereas the Fumasep F-10120 shows to be the best of the tested membranes.

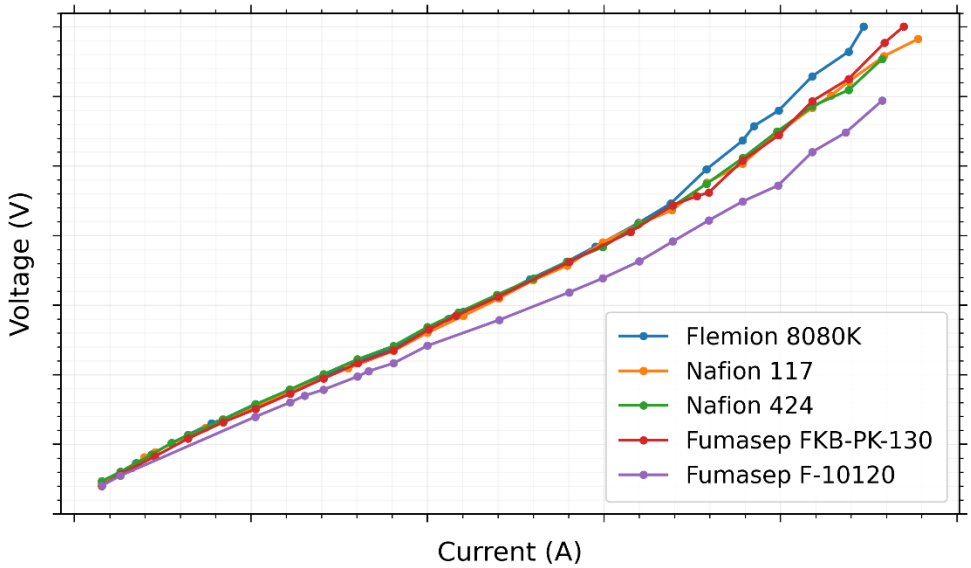

Figure 7: Voltage as a function of current for five different commercially available membranes.

In Table 1, an overview of the membranes and some key characteristics can be seen.

Table 1: Characteristics of the commercially available membranes tested in this study. PK = polyketone and PTFE = polytetrafluoroethylene

Membrane	Thickness (µm)	Reinforcement?
Flemion F8080K	150-250	Yes
Nafion 117	183	No
Nafion 424	380	Yes, PTFE
FKB-PK-130	110-140	Yes, PK
Fumasep F-10120	120	Nej

The membrane, which performed the best, Fumasep F-10120, is also one of the thinnest and has no reinforcement net. Intuitively it makes sense that the thinnest membrane also yields the lowest internal resistance and thus smallest power consumption. However, the trend seems to be non-existent in these studies, as that would designate the FKB-PK-130 and Flemion F8080K to be lowest in power consumption. A small conclusion to be drawn from these findings are, that the reinforcement net on the membrane seems to be more responsible for power

consumption than the thickness of the membrane itself. Furthermore, the CO_2 concentration in the outlet gas was also measured. This can be seen in Figure 8.

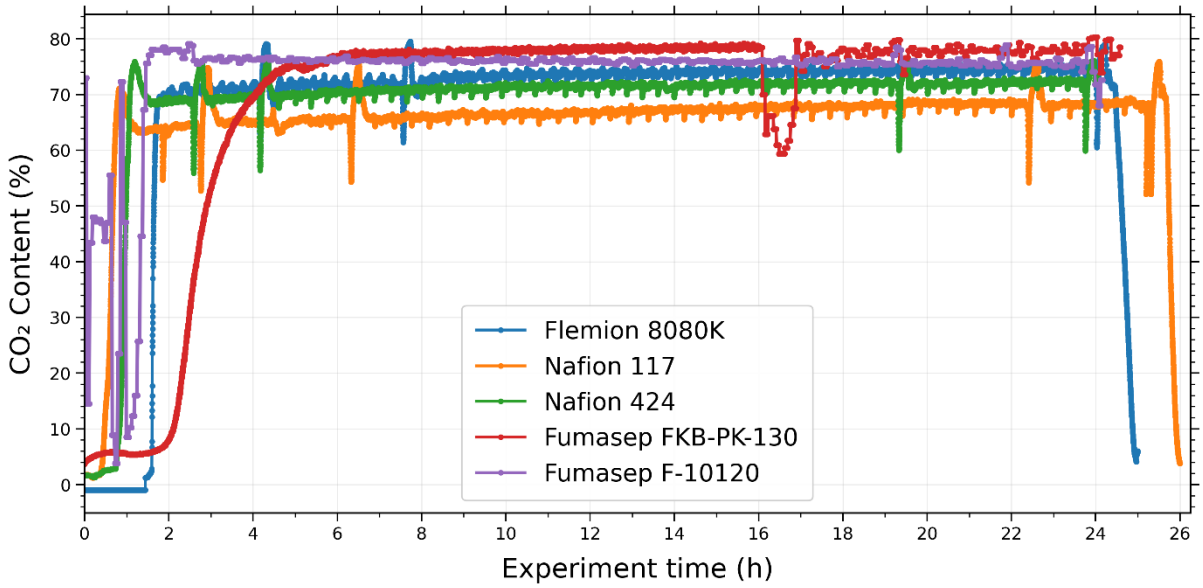

Figure 8: CO_2 concentration as a function of experiment time for different commercially available membranes

As the CO_2 desorption relies heavily on the transport of K^+ over the membrane, a higher CO_2 concentration in the outlet gas, shows a more efficient membrane. From these findings, it seems that the FKB-PK-130 is the best for operation.
The finding from the smaller setups led to the construction of the pilot setup. The new setup will have two absorbers and two desorbers, each five meters in height. It will feature up to two electrochemical stacks with up to 10 cells in each of 800cm^2, which allows for possible desorption of 5 kg/h CO_2. The new setup can be seen in Figure 1.

3. Conclusions

In summary, a successful upscaling has been conducted. Initially smaller pilot experiments showed proof-of-concept and tests with different commercially available membranes provided findings of the importance of the reinforcement nets significance. Furthermore, different anode electrodes also showed different power consumption levels, which led to the discovery of Ti-MMO being the best and most robust electrode at the anode chamber. These initial tests have been used for design and implementation of the new state-of-the-art pilot setup.

Acknowledgements

This research project is funded by the Danish Innovationsfonden, under the InnoMISSION: InnoCCUS, project 1-P5 ASGREEN.

References

[1] AR6 Synthesis Report: Climate Change 2023, (accessed November 27th, 2025).

[2] P. Ball, What Is the Future of Fusion Energy Scientific American, Sci. Am. (2023). (accessed November 28th, 2025).

[3] K. Schaber et al., Energy Policy 42 (2012) 498–508

[4] D. Loachamin et al., ChemEngineering 8 (2024)

[5] T.L. Biel-Nielsen et al., ChemSusChem 16 (2023)

[6] FORBLUE™ Flemion™, (2023) (accessed January 29, 2026).

Comparative Study of Separation Technologies for Biomethane Production from Sugarcane Vinasse

Guilherme C. de Ataide, Isabela S. C. Pereira, Denizar V. C. Silva, Jean F. Leal Silva
School of Chemical Engineering,
University of Campinas (UNICAMP), Campinas, Brazil

Abstract
This study investigates the production of biomethane through the purification of biogas obtained from sugarcane vinasse, comparing three upgrading routes: water scrubbing, pressure swing adsorption (PSA), and absorption with diethanolamine (DEA). Simulations were conducted in Aspen Plus®, maintaining a constant biogas composition while varying the purification steps. Process conditions were tailored to ensure the final biomethane composition complied with the specifications of the Brazilian gas grid, with particular attention to CH_4, CO_2, and H_2S contents. A cashflow analysis was developed based on capital expenses (CAPEX), operating expenses (OPEX), and revenues for each process option. Results showed that the initial biogas composition was within the expected ranges reported in the literature and that all routes produced biomethane meeting gas grid requirements. The PSA route exhibited the best overall performance: higher methane purity (97.0% mol), 98.0% methane recovery, zero water content, and the highest product flow rate. Economically, PSA also presented the shortest simple (4.6 years) and discounted (6.4 years) payback times and the lowest minimum selling price (R$ 57.89/MMBtu, ~€31/MWh), establishing itself as the most advantageous alternative. Overall, the results indicate the clear potential for large-scale separation methods to produce biomethane for the Brazilian market, and future research should include technical sensitivity analyses on process operating conditions.

Keywords
biogas; biomethane; vinasse; water scrubbing; pressure swing adsorption; diethanolamine.

1. Introduction

The intensification of climate change, characterized by a global warming rate of approximately 0.2 °C per decade (IPCC, 2023), underscores the urgent need for transitioning to renewable energy sources. In this context, the Brazilian sugarcane bioenergy industry emerges as a strategic opportunity, particularly through the valorization of vinasse, an abundant liquid residue from ethanol production, that can be converted into biogas via anaerobic digestion. This CH_4-rich mixture, however, contains CO_2 and H_2S, necessitating purification to meet the biomethane specifications set by the Brazilian National Agency of Petroleum, Natural Gas and Biofuels (ANP).

In light of this, this study conducts a techno-economic comparison among three biogas upgrading routes employing process simulation and techno-economic analysis: water scrubbing, absorption with diethanolamine (DEA), and pressure swing adsorption (PSA). Parameters such as contaminant removal efficiency, CH_4 recovery, and economic viability were used to identify the most promising route for biomethane production from vinasse in large-scale sugarcane bioenergy plants.

2. Methodology

For the development of this work, the three studied biogas upgrading routes to biomethane share the same inlet biogas composition, varying only their separation technologies. All purification routes were individually simulated in Aspen Plus v10 using the NRTL-RK thermodynamic model. The NRTL (Non-Random, Two-Liquid) model was used for the liquid phase due to the polar nature and non-ideal behavior of liquid mixtures involved in the process, using binary interaction parameters from the software's database whenever possible (otherwise, parameters were regressed using the UNIFAC method). The Redlich-Kwong equation of state was adopted for the vapor phase, given that operating pressures near 10 bar may occur in the processes.

2.1 Anaerobic fermentation

The scale of the biogas production capacity was calculated assuming a large-scale Brazilian sugarcane plant processing 5 million tonnes of sugarcane per year, allocating 75% of its vinasse to biomethane production, which results in a feed flow rate of 824,653 kg/h. Anaerobic fermentation constitutes the initial stage of the process. Although vinasse presents a complex and variable composition, a mixture containing 93.00% water, 5.25% glucose, and 1.75% sulfur by mass was adopted for simulation purposes (Carrilho; Labuto; Kamogawa, 2016). Regarding the reactor, the UASB (Upflow Anaerobic Sludge Blanket) reactor was selected, as it exhibits a high biodegradation rate (Kiani et al., 2022). In the simulation environment, the UASB reactor was represented using an *RYield* block followed by a flash separator. The yield fractions of each component in the reactor outlet were specified to adequately represent the fermentation reaction, which occurs at 35 °C and 1 bar.

2.2 Route 1: Adsorption with metal oxides and water scrubbing

In this route, H_2S was removed via adsorption onto ferric oxide (Fe_2O_3) in a packed bed, where it reacts to form iron sulfide (Fe_2S_3). Ferric oxide was regenerated by passing hot air through the packed bed. Subsequently, water scrubbing was employed for CO_2 removal, in which biogas was washed with pressurized water, acting as a physical solvent. Due to the higher solubility of CO_2 relative to CH_4, CO_2 was preferentially absorbed, while methane remained in the gas phase (Abu Seman; Harun, 2019). Separation occurred in an absorption tower at low temperature; then, the solution was heated in a stripping tower to remove the CO_2 and recycle the water, with a small purge to remove other impurities it may contain. The CO_2 was compressed for storage. In Aspen Plus, metal oxide adsorption was modeled using the Sep block, H_2S-Fe_2O_3 reactions via the *RStoic* block at 500 °C, the absorption tower via the *RadFrac* block with 10 stages, without condenser or reboiler, and the compression was modeled using the *MComp* block.

2.3 Route 2: Adsorption with metal oxides and pressure swing adsorption (PSA)

This route employed the same procedure as the first for H_2S removal but utilized pressure swing adsorption for CO_2 separation. The process relied on cyclic pressure variation, exploiting the adsorbent material's higher affinity for CO_2 than for CH_4. Biogas was compressed and fed into a packed bed filled with adsorbent, where CO_2 was adsorbed while methane remained in the gas phase. Clinoptilolite-type zeolite was selected as the adsorbent due to its high porosity (Kadam and Panwar, 2017). In Aspen Plus, the adsorption column was modeled using the *Sep* block, with separation based on literature parameters. The process flowsheet is presented in Figure 2.

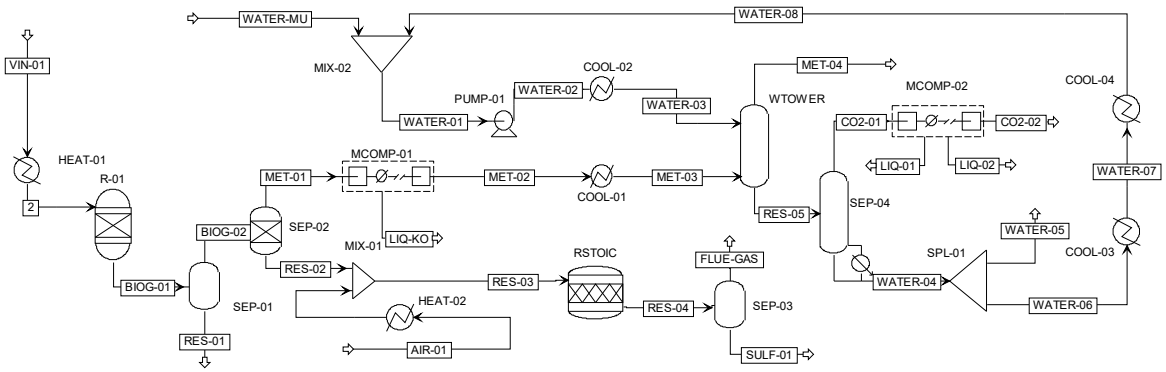

Figure 1. Flowsheet of the water scrubbing route in Aspen Plus.

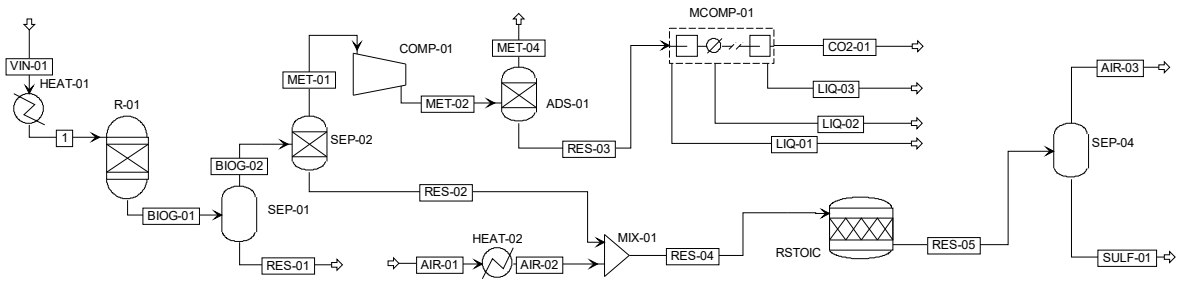

Figure 2. Flowsheet of the pressure swing adsorption (PSA) route in Aspen Plus.

2.4 Route 3: Absorption with diethanolamine (DEA)

This route relied on the chemical absorption of CO_2 and H_2S using an aqueous DEA solution. Biogas and DEA were contacted in an absorption tower; the CO_2 and H_2S-rich stream was then directed to a stripper column to release the acid gases (Mendieta, 2011). H_2S was burned and reacted with sodium hydroxide for disposal (SO_2 emission control). In Aspen Plus, the absorption column was modeled using the *RadFrac* block (no condenser or reboiler), and the stripper was modeled using the *RadFrac* block with 9 stages, assuming partial condensation and a reboiler to create a DEA recycle stream. H_2S was burned using an *RStoic* block. The process flowsheet is depicted in Figure 3.

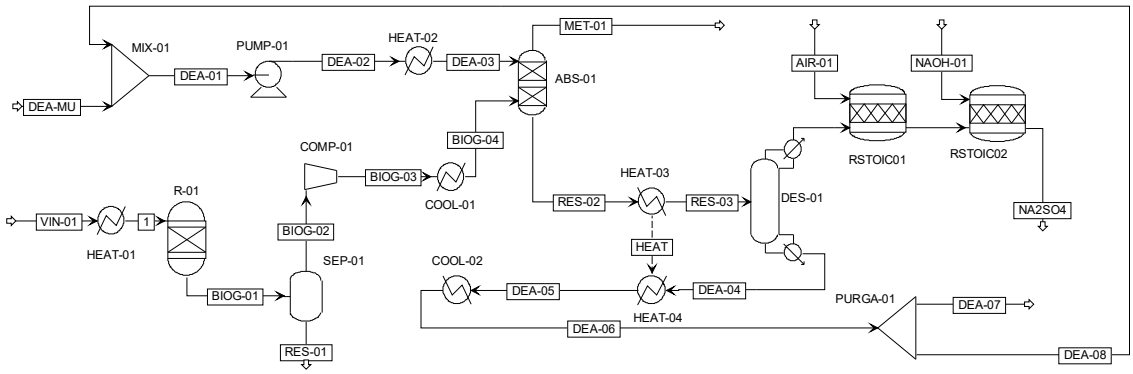

Figure 3. Flowsheet of absorption with diethanolamine (DEA) route in Aspen Plus.

2.5 Economic feasibility analysis and sensitivity analysis

The economic feasibility analysis was carried out for the three purification routes to ensure comparability. Capital expenses (CAPEX) were estimated as a Class 5 cost,

adjusted for scale, inflation, and literature data (Leme; Seabra, 2017), while operating expenses (OPEX) included labor, utilities, inputs, and effluent treatment, all derived from mass and energy balances. Revenues were mainly derived from biomethane sales, and cash flows were constructed to calculate Net Present Value (NPV), Internal Rate of Return (IRR), and payback time, assuming a 10% minimum attractiveness rate. A sensitivity analysis was performed by varying CAPEX, OPEX, plant scale, and operating days by ±50 %. The Minimum Selling Price (MSP) was also obtained using Microsoft Excel Solver® to determine the economic break-even point. Finally, a Monte Carlo analysis assessed the impact of uncertainties, estimating the probability of achieving a positive NPV and an IRR above 10%.

3. Results and discussion

3.1 Technical feasibility analysis

Anaerobic fermentation yielded simulated biogas with a composition consistent with literature reports (Piechota et al., 2024), characterized by a high CH_4 fraction and low concentrations of CO_2 and other trace compounds. Regarding purification route performance, all exhibited similar biomethane flow rates, with PSA achieving the best result (6,763 kg/h). Product composition (Table 1) confirms full compliance of technologies with current legislation across all routes, with high methane contents and residual H_2S levels that underscore the efficiency of the separation processes. Overall, the PSA route yields superior biomethane quality, characterized by higher CH_4 concentrations and zero water content, despite elevated levels of acidic gases.

Table 1. Composition of biomethane produced by each simulated route.

Component	Biomethane concentration by route			Brazilian gas grid specification
	Water scrubbing	PSA	DEA	
CH_4 (% mol)	96.90	97.00	95.99	90.00 (minimum)
CO_2 (% mol)	2.95	2.99	2.85	3.00 (maximum)
H_2O (% mol)	0.06	0.00	1.15	not available
O_2 (% mol)	0.00	0.00	0.00	0.80 (maximum)
H_2S (mg/m^3)	$1.22 \cdot 10^{-3}$	0.03	$6.09 \cdot 10^{-4}$	10.00 (maximum)

Sensitivity analyses were carried out on process variables. No analysis was performed for the PSA route since it used fixed recovery parameters in the *Sep* model. For the water scrubbing route, the effects of operating pressure and water flow rate on the CH_4 molar fraction were assessed. The isobaric curves (Figure 4a) show that increasing both variables enhances methane purity, with the effect stabilizing between 16-20 bar and above 600 t/h of water, behavior consistent with physical CO_2 absorption, which is favored by greater solvent availability and higher operating pressures.

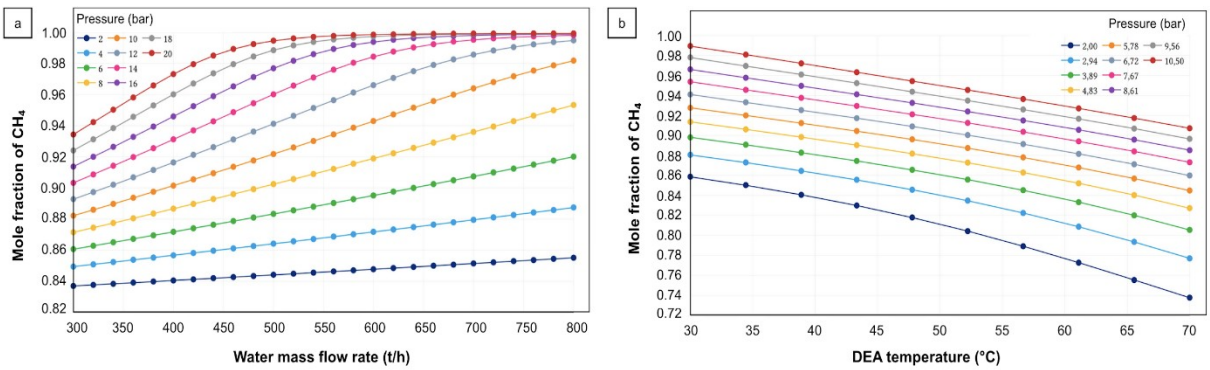

Figure 4. Sensitivity analysis of a) water scrubbing and b) DEA.

For the DEA route, the curves in Figure 4b indicate that higher pressures promote CH_4 enrichment, whereas higher temperatures reduce it. This trend aligns with the chemical absorption mechanism of DEA, which is more efficient at high pressure and low temperature, shifting the reaction equilibrium toward the absorbed species.

3.2 Economic feasibility analysis

The economic results, presented in Table 2, indicate that all three routes exhibit similar CAPEX and annualized revenue values. However, the PSA route displays a significantly lower OPEX, owing to reduced electricity, cooling water, and chemical reagent demands, resulting in the lowest biomethane production cost (R$ 50.47/MMBtu), approximately 20% lower than the other routes.

Table 2. Results for CAPEX, annual OPEX, and annual revenue for the three purification methods. Values expressed in million Brazilian Reais (R$).

	Water scrubbing	PSA	DEA
CAPEX (10^6 R$)	287	299	296
OPEX (10^6 R$)	45.8	29.2	43.7
Revenue (10^6 R$)	111	112	111

The discounted cash flow analysis over 20 years, illustrated in Figure 5a, highlights the superior performance of the PSA route, which achieves positive cash flow approximately 8 years into the analysis and exhibits the highest cumulative value at the end of the analyzed period. The financial indicators corroborate this result: although all routes are viable, the PSA route exhibits the best NPV (R$ 189.5 million), IRR (18.8%), and simple payback time (4.6 y) and discounted payback time (6.4 y).

The PSA route exhibited the lowest MSP (R$ 57.89/MMBtu, ~€31/MWh), indicating superior economic attractiveness compared to water scrubbing (R$ 70.57/MMBtu, ~€38/MWh) and the DEA route (R$ 69.85/MMBtu, ~€38/MWh). An additional analysis assessed the plant-scale effect on MSP and biomethane competitiveness relative to average natural gas prices in Brazil, Europe, and the United States (Figure 5b). Results show that even with scale reductions of up to 45% for PSA and 20% for the other routes, the process remains competitive in the Brazilian market, with PSA achieving parity with the European market at approximately a 10% plant-scale increase. Finally, Monte Carlo analysis indicated superior economic performance for the PSA route, with a 64.4% probability of achieving an internal rate of return greater than 10%.

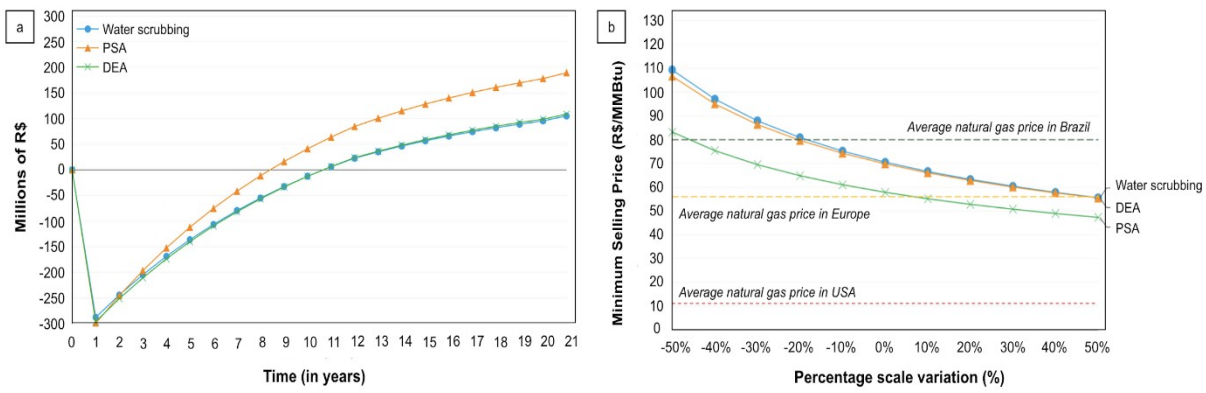

Figure 5. a) Discounted cash flow over 20 years for the three routes. b) Sensitivity analysis of biomethane MSP as a function of scale.

4. Conclusions

This study demonstrated that the purification of biogas derived from sugarcane vinasse is a technically and economically feasible alternative for producing biomethane in compliance with Brazilian gas grid specifications. All three evaluated routes performed satisfactorily; however, the PSA route showed superior technical and economic results. Technically, PSA produced CH_4 with higher purity, greater recovery, and zero water content, despite the increased concentration of acid gases. Economically, this route achieved the most favorable metrics: NPV of R$189.5 million, IRR of 18.8%, a discounted payback time of 6.4 years, and the lowest MSP (R$57.89/MMBtu, ~€31/MWh). Furthermore, sensitivity analyses and Monte Carlo Simulation indicated that PSA possesses greater economic robustness and price resilience under varying operational and market conditions. The remaining routes also proved viable and showed similar performance, though consistently below that observed for PSA; their sensitivity analyses suggested that efficiency can be increased through optimization of process parameters. Future work should focus on investigating adsorption-related technical parameters for the PSA route that could not be explored within the modeling depth employed in this study. Overall, the results indicate that biomethane purification has strong potential to competitively and sustainably supply the Brazilian market.

Acknowledgements

The authors acknowledge the support from the Human Resources Training Program of the Brazilian National Agency of Petroleum, Natural Gas and Biofuels (ANP) through the PRH-ANP Program (PRH-UNICAMP 29) and the Sao Paulo Research Foundation (FAPESP, grant numbers 2025/03698-6, 2025/19808-5, 2025/09414-0).

References

ABU SEMAN, N.; HARUN, N. Simulation of pressurized water scrubbing process for biogas purification using Aspen Plus. IOP Conference Series: Materials Science and Engineering, IOP Publishing, v. 702, n. 1, p. 012040, nov. 2019. DOI: 10.1088/1757-899X/702/1/012040.

CARRILHO, E.; LABUTO, G.; KAMOGAWA, M. Chapter 2 - Destination of Vinasse, a Residue From Alcohol Industry: Resource Recovery and Prevention of Pollution. In: PRASAD, M.; SHIH, K. (Ed.). Environmental Materials and Waste. [S.l.]: Academic Press, 2016. P. 21–43. ISBN 978-0-12-803837-6. DOI: 10.1016/B978-0-12-803837-6.00002-0.

IPCC. Summary for Policymakers. In: HOESUNG LEE, J. R. (Ed.). Climate Change 2023: Synthesis Report: Contribution of Working Groups I, II and III to the Sixth Assessment Report of the Intergovernmental Panel on Climate Change. Geneva, Suiça: Intergovernmental Panel on Climate Change (IPCC), 2023. P. 1–34. DOI: 10.59327/IPCC/AR6-9789291691647.001.

KADAM, R.; PANWAR, N. Recent advancement in biogas enrichment and its applications. Renewable and Sustainable Energy Reviews, v. 73, p. 892–903, 2017. ISSN 1364-0321. DOI: 10.1016/j.rser.2017.01.167.

KIANI, M. K. D. et al. Different bioreactor configurations for biogas production from sugarcane vinasse: A comprehensive review. Biomass and Bioenergy, v. 161, p. 106446, 2022. ISSN 0961-9534. DOI: 10.1016/j.biombioe.2022.106446.

LEME, R. M.; SEABRA, J. E. Technical-economic assessment of different biogas upgrading routes from vinasse anaerobic digestion in the Brazilian bioethanol industry. Energy, v. 119, p. 754–766, 2017. ISSN 0360-5442. DOI: 10.1016/j.energy.2016.11.029.

MENDIETA, L. F. F. Estudo da absorção de H2S e CO2 do gás combustível. Dez. 2011. Trabalho de Diplomação (Graduação) – Universidade Federal do Rio Grande do Sul, Escola de Engenharia, Departamento de Engenharia Química, Porto Alegre.

PIECHOTA, G. et al. Chapter 1 - An introduction to biogas and biomethane. In: YOUSUF, A.; MELVILLE, L. (Ed.). Biogas to Biomethane. [S.l.]: Woodhead Publishing, 2024. (Applied Biotechnology Reviews). P. 3–40. ISBN 978-0-443-18479-6. DOI: 10.1016/B978-0-443- 18479-6.00008-9.

Electrification of Separation Column with 3D-Printed Ceramic Packings

Özgün Alkim Boz, Dr.-Ing. Nicole Lutters, Prof. Dr.-Ing. Julia Riese

[1]Paderborn University, Fluid Process Engineering, Paderborn, Germany.

Abstract

This contribution presents a concept for the electrification of separation units through directly heated structured packings. A CO_2 desorption model serves as a preliminary computational proof of concept to evaluate general trends in spatial heat distribution. Initial results suggest that a non-uniform energy supply, increasing from the feed toward the bottom, shows a positive trend in thermal performance compared to uniform distribution. These observations establish a basic operational logic for the subsequent manufacturing of hybrid Si_3N_4-SiC-$MoSi_2$ ceramic packings via Multi-Material Jetting (MMJ). By integrating conductive cores and insulating surfaces in a single step, this technology enables the precise spatial control required to implement such electrified separation strategies in smart distillation columns.

Keywords: process electrification, separation, direct heating, 3D-printed ceramics, Multi-Material Jetting (MMJ),

1.Introduction

The increasing energy demand, driven by global population growth, is still largely met by fossil fuels, which progressively worsens the environmental impacts of global warming. Despite the rise in renewable energy use, only 13% of the energy consumed in industrial processes is currently obtained from renewable sources (1). Within the industrial sector, the chemical industry stands out as a critical area for reducing carbon emissions, as it is responsible for 30% of total industrial energy consumption (2). The most intensive energy usage within this sector occurs during separation processes where low thermal efficiency leads to significant energy loss and high emissions (3,4).

In process engineering, electrification is not just about replacing one fuel with another; it represents a chance to make chemical plants more efficient and flexible. By utilizing electricity, we can bypass the limitations of indirect heating found in traditional systems, where energy must be generated at the bottom and carried through the entire column. This transition allows for instant and direct heat generation exactly where the separation occurs, eliminating the time delays and energy losses associated with moving heat from a reboiler to the upper stages. As a result, we can build more flexible and responsive industrial units that react precisely to process demands. As it is projected that 80% of global electricity will be supplied from renewable sources by 2050, electricity will become the main tool for heating and separating molecules (5).

2. Electrification of separation units

At the center of this transformation, electrification approaches can be used both directly and indirectly. Direct electrification involves replacing fossil fuel heating with electric solutions or driving chemical reactions through electricity (6). According to the IEA "Roadmap to Net Zero Emissions by 2050", the industrial sector must transition from fuel-based to electrified processes to significantly reduce its carbon footprint (7). However, direct electricity use faces challenges such as renewable supply variability and competition with other sectors like transportation and energy storage. Because industrial process temperatures vary greatly, a single technology is rarely sufficient; instead, a combination of strategies must be evaluated based on the specific requirements of each separation task. (8).

In the chemical industry, distillation is the primary target for decarbonization. One of the most effective strategies is heat pump assisted distillation, which can reduce energy use by up to 70%. These systems upgrade waste heat to a higher energy level for reuse within the process. Various configurations are available, including mechanical vapor recompression, which uses the process fluid as the heat pumping medium, and absorption heat pumps (9). For more complex separations, hybrid systems such as compression resorption or thermo-acoustic devices are being developed to achieve higher temperature lifts (10).

A more advanced approach is the internally heat integrated distillation column, where the rectifying section operates at a higher pressure to act as a heat source for the stripping section. While this technology can offer impressive energy savings,sometimes exceeding 90% for specific mixtures, it faces challenges such as high capital costs for compressors and complex control requirements (11).

Beyond these methods, technologies like microwaves offer a "wireless" energy delivery that bypasses the heat transfer delays of conventional systems. Microwaves provide a selective heating effect that can even break thermodynamic limits in azeotropic separations (12). However, since electric heating only at the reboiler level often fails to solve internal mass transfer bottlenecks, recent research has shifted toward 'distributed' heat input. By using electricity to heat structured packing materials directly, the energy is delivered exactly at the phase-contact surface. This internal electrification strategy aims to eliminate heat transfer delays and provide precise control over the separation environment (13). Direct heating is already successfully utilized in reactors to improve thermal management and reaction kinetics (14). Similarly, these positive effects could be reached for reactive distillation, where precise temperature control is vital for both separation and reaction performance (15).

A further possibility to directly heat inside columns or reactors is the use of multi-material inserts. Elements comprising a conductive inlay and a non-conductive shell can be used for resistance heating. One suitable material is ceramics, which will be explained in detail in the following.

3. 3D-printed elemets for resistance heating

In recent years, 3D printing technology has introduced revolutionary innovations in transforming materials into functional objects (16). Its applications are expanding rapidly across all industries, including automotive, medicine, construction, and aerospace (17). This technology is distinguished from traditional manufacturing by providing extensive design freedom, minimizing waste for higher sustainability (18), and enabling cost-effective customized production (19).

Recently, 3D printing has been successfully applied in chemical engineering for producing column internals and catalytic reactors (20). Its main advantage is the ability to create complex geometries that tailor performance criteria like pressure drop and mass transfer (21). However, achieving high performance requires more than just external shape; it requires precise control over the internal structure. While traditional 3D printing often faces resolution limits that restrict internal complexity (22), newer hierarchical approaches allow for the creation of intricate internal patterns (23). This precise internal control is the key to successfully integrating conductive and non-conductive materials through Multi-Material Jetting (MMJ).

Selecting the right material for resistance heating is critical. Although most 3D printing involves metals or polymers, neither is ideal for this specific task. Metals require complex additional insulation to prevent short circuits, making them difficult to use for direct heating. Similarly, polymers are limited by industrial process temperatures, even when modified with conductive additives (24). Multi-material ceramics solve these issues by combining thermal stability with the necessary electrical properties.

Complementing these thermal and electrical advantages, ceramic structures also offer superior fluid dynamic properties. For instance, Silicon Carbide (SiC) foam ceramics represent an innovative class of materials with high mechanical strength (25). Their open-cell structure and high porosity, reaching up to 97%, minimize pressure drop while enhancing heat, mass, and momentum transfer through optimized mixing (26). Advanced production techniques allow for precise control over the material's pore architecture (27). This wide specific surface area has paved the way for using SiC foams as structured packing in distillation columns, offering superior thermal shock resistance and interfacial contact efficiency (28,29).

To implement such a heating concept, the direct resistance heating of the packing material can be realized using ceramic structures. The primary challenge here is the electrical conductivity of the liquids, which necessitates an electrically insulating outer surface to prevent short circuits. Ceramic materials are ideal for this purpose; beyond providing necessary insulation, they offer superior thermal stability and corrosion resistance. Hybrid composite components using Si_3N_4-SiC-$MoSi_2$ powders have been produced via MMJ for this purpose. The primary objective of MMJ is to enable the simultaneous use of up to three different materials in ceramic production. This method makes it possible to create a component with a conductive core and an insulating outer surface. By facilitating the production of such hybrid structures in a single step, MMJ provides the essential technical foundation for integrated electrification in distillation columns (30).

Beyond these inherent properties, the MMJ method allows for precise control of surface roughness by adjusting nozzle droplet size. This provides a strategic advantage in optimizing liquid holdup and mass transfer efficiency. In our future work, we want to make use of these multi-material ceramic structures as innovative, electrically heated structured packing in distillation coclumns. The feasibility of this approach has been proven in high-performance sectors, ranging from space technologies to industrial tools. Notable examples include 3D-printed ceramic igniters, reactors with integrated temperature control, and heatable ceramic mixers (31,32).

4 Theoretical study: Directly heated desorption column

As a computational proof of concept, CO_2 desorption from an aqueous amine solution was used to evaluate the potential of integrated heating. This process was selected due to its well-established modeling framework in previous studies (33). To describe the heated packings, a rate-based model was adapted by integrating a source term into the liquid-side bulk phase balance equations.

Three primary cases were compared to analyze the influence of spatial energy distribution (Fig. 1). Case 1 serves as the base case with traditional reboiler heating. In Cases 2 and 3, the reboiler was removed, and the equivalent total energy was supplied directly along the column height. While Case 2 utilized a uniform distribution, in Case 3 a non-uniform strategy where the energy input increased from the feed toward the bottom was implemented.

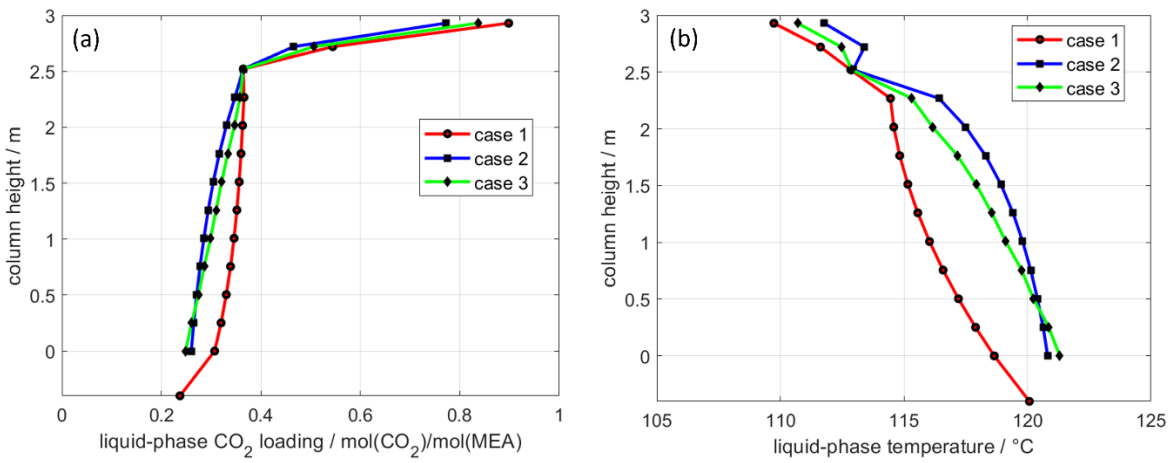

Figure 1. Comparison of CO_2 loading (a) and temperature (b) profiles.

The results confirm that the location of energy input is as critical as the total quantity used. In the uniform scenario (Case 2), heating near the top led to undesirable solvent evaporation and increased cooling duties. Conversely, the most efficient performance was achieved in Case 3. This strategic spatial optimization allows the system to match traditional reboiler performance while utilizing the advantages of internal electrification.

5. Conclusions and Outlook

The results presented here theoretically demonstrate that directly heated structured packings can effectively replace or supplement traditional reboilers by optimizing energy input along the column height. The non-uniform heating strategy identified in Case 3 provides the essential operational logic for the next phase of this research.

Regarding future directions, the theoretical results of this simulation study will be experimentally validated and detailed using MMJ technology to produce hybrid ceramic packings. While this case study utilized metallic structures for desorption as a preliminary step, the ultimate goal is to apply these findings to distillation processes using Si_3N_4-SiC-$MoSi_2$ ceramic composites.

The MMJ process will allow for an integrated design by manufacturing components with a conductive core for resistance heating and a ceramic insulating surface to prevent short circuits. Furthermore, this technology facilitates mass transfer optimization by utilizing the inherent surface roughness and hierarchical pore structures of 3D-printed ceramics to enhance interfacial contact in distillation. In conclusion, this work serves as a foundational step toward developing smart distillation columns where energy is supplied precisely where it is needed, leading to more sustainable industrial separation technologies.

References

1- Fraunhofer ISE, "Energy-Charts: Net public power generation in Germany," 2023. [Online]. Available: https://www.energy-charts.info/charts/energy_pie/chart.htm?l=en&c=DE&year=2023
2- Kiss, A. A. (2019). Rethinking energy use for a sustainable chemical industry. *CHEMICAL ENGINEERING*, *76*.
3- Van de Bor, D. M., Ferreira, C. I., & Kiss, A. A. (2015). Low grade waste heat recovery using heat pumps and power cycles. *Energy*, *89*, 864-873.
4- US Energy Information Administration. 2018 manufacturing energy consumption Survey. 2021
5- International Renewable Energy Agency (IRENA), "Renewable Energy Statistics 2023," 2023. [Online]. Available: https://www.irena.org/Publications
6- Lund, P. D., Lindgren, J., Mikkola, J., & Salpakari, J. (2015). Review of energy system flexibility measures to enable high levels of variable renewable electricity. *Renewable and sustainable energy reviews*, *45*, 785-807.
7- International Energy Agency (IEA). (2021). World Energy Outlook 2021. [Online] Available at: https://www.iea.org/reports/world-energy-outlook-2020. Accessed Apr 2021.
8- Kermeli, K., Crijns-Graus, W., Johannsen, R. M., & Mathiesen, B. V. (2022). Energy efficiency potentials in the EU industry: impacts of deep decarbonization technologies. *Energy Efficiency*, *15*(8), 68.
9- Kiss, A. A., & Smith, R. (2020). Rethinking energy use in distillation processes for a more sustainable chemical industry. *Energy*, *203*, 117788.
10- Sorknæs, P., Johannsen, R. M., Korberg, A. D., Nielsen, T. B., Petersen, U. R., & Mathiesen, B. V. (2022). Electrification of the industrial sector in 100% renewable energy scenarios. *Energy*, *254*, 124339.
11- Mekidiche, Z., Labarta, J. A., Javaloyes-Anton, J., & Caballero, J. A. (2024). From power to heat: strategies for electrifying distillation for sustainable chemical processes. *Applied Thermal Engineering*, *257*, 124316.
12- Liu, K., Zhao, Z., Li, H., & Gao, X. (2023). Microwave-induced vapor-liquid mass transfer separation technology—full of breakthrough opportunities in electrified chemical processes. *Current Opinion in Chemical Engineering*, *39*, 100890.

13- Cui, C., Qi, M., Zhang, X., Sun, J., Li, Q., Kiss, A. A., ... & Lee, M. (2024). Electrification of distillation for decarbonization: an overview and perspective. *Renewable and Sustainable Energy Reviews*, *199*, 114522.
14- Wismann, S. T., Engbæk, J. S., Vendelbo, S. B., Bendixen, F. B., Eriksen, W. L., Aasberg-Petersen, K., ... & Mortensen, P. M. (2019). Electrified methane reforming: A compact approach to greener industrial hydrogen production. *Science*, *364*(6442), 756-759.
15- Luyben, W. L., & Yu, C. C. (2009). *Reactive distillation design and control*. John Wiley & Sons.
16- Javaid, M., Haleem, A., Singh, R. P., Suman, R., & Rab, S. (2021). Role of additive manufacturing applications towards environmental sustainability. *Advanced Industrial and Engineering Polymer Research*, *4*(4), 312-322.
17- Javaid, M., Haleem, A., Singh, R. P., Suman, R., & Rab, S. (2021). Role of additive manufacturing applications towards environmental sustainability. *Advanced Industrial and Engineering Polymer Research*, *4*(4), 312-322.
18- Attaran, M. (2017). The rise of 3-D printing: The advantages of additive manufacturing over traditional manufacturing. *Business horizons*, *60*(5), 677-688.
19- Ngo, T. D., Kashani, A., Imbalzano, G., Nguyen, K. T., & Hui, D. (2018). Additive manufacturing (3D printing): A review of materials, methods, applications and challenges. *Composites Part B: Engineering*, *143*, 172-196.
20- Gładyszewski, K., & Skiborowski, M. (2018). Additive manufacturing of packings for rotating packed beds. *Chemical Engineering and Processing-Process Intensification*, *127*, 1-9.
21- Li, X., Shi, Q., Li, H., Yao, Y., Pavlenko, A. N., & Gao, X. (2017). Experimental characterization of novel SiC foam corrugated structured packing with varied pore size and corrugation angle. *Journal of Engineering Thermophysics*, *26*(4), 452-465.
22- Lombardi, L., & Tammaro, D. (2021). Effect of polymer swell in extrusion foaming of low-density polyethylene. *Physics of Fluids*, *33*(3).
23- Chen, Q., Cao, P. F., & Advincula, R. C. (2018). Mechanically robust, ultraelastic hierarchical foam with tunable properties via 3D printing. *Advanced Functional Materials*, *28*(21), 1800631.
24- Yuk, H., Lu, B., Lin, S., Qu, K., Xu, J., Luo, J., & Zhao, X. (2020). 3D printing of conducting polymers. *Nature communications*, *11*(1), 1604.
25- Pavlenko, A. N., Zeng, J., Pecherkin, N. I., Zhukov, V. E., & Volodin, O. A. (2016). Separation efficiency and pressure drop of SiC ceramic and Mellapak structured packings. *Journal of Engineering Thermophysics*, *25*(1), 1-14.
26- Wang, Z., Pu, Y., Wang, D., Wang, J. X., & Chen, J. F. (2018). Recent advances on metal-free graphene-based catalysts for the production of industrial chemicals. *Frontiers of Chemical Science and Engineering*, *12*(4), 855-866.
27- Funk, J. E., & Dinger, D. R. (2013). *Predictive process control of crowded particulate suspensions: applied to ceramic manufacturing*. Springer Science & Business Media.
28- Gao, X., Li, X., Liu, X., Li, H., Yang, Z., & Zhang, J. (2015). A novel potential application of SiC ceramic foam material to distillation: foam monolithic tray. *Chemical Engineering Science*, *135*, 489-500.
29- Li, H., Hao, Z., Murphy, J., Li, X., & Gao, X. (2018). Experimental study of liquid renewal on the sheet of structured corrugation SiC foam packing and its dispersion coefficients. *Chemical Engineering Science*, *180*, 11-19.
30- Zschippang, E., Kunz, W., Weingarten, S., Gottlieb, L., & Wolfrum, A. K. (2024). Sintering of Si3N4–SiC–MoSi2 composites additively manufactured by multi material jetting. *International Journal of Applied Ceramic Technology*, *21*(4), 2613-2622.
31- Scheithauer, U., Schwarzer-Fischer, E., Sieder-Katzmann, J., Propst, M., Abel, J., Gottlieb, L., ... & Bach, C. (2024). Additive manufacturing of ceramic single and multi-material components–A groundbreaking innovation for space applications too?. *Acta Astronautica*, *221*, 155-162.
32- Scheithauer, U., Johne, R., Gottlieb, L., Weingarten, S., Wiemer, H., & Holtzhausen, S. (2025). Recent developments in the field of additive manufacturing of ceramic-based multi-material components open the door to highly functionalized components. *Progress in Additive Manufacturing*, 1-9.
33- Hüser, N., Schmitz, O., & Kenig, E. Y. (2017). A comparative study of different amine-based solvents for CO2-capture using the rate-based approach. *Chemical Engineering Science*, *157*, 221-231.

Challenges in Electrolyte Solvent Purification from LIB Recycling

Martin Wolke[1], Anika Heyen[1], Moritz Goldkuhle[2], Katharina Jasch[1], Sven Gutperl[1], Stephan Scholl[1]
[1]Institute for Chemical and Thermal Process Engineering, Technische Universität Braunschweig, Germany;
[2]PreZero Battery Recycling GmbH, Meppen, Germany

Abstract
Thermomechanical treatment during the recycling of lithium-ion batteries (LIBs) releases volatile organic electrolyte components which were separated from the solid fractions and recovered by condensation at an industrial recycling facility. This process resulted in a solvent stream with a complex composition and various impurities. For this reason, it is unsuitable for direct reuse in new LIBs and is therefore currently classified as a waste stream. To enable a closed-loop material cycle for the originally used solvents, investigations into the processing and purification of these recovered solvent streams were conducted. The recovered solvent mixtures were characterized, pretreated and separated with the aim of purifying the initial substances. Analytical results revealed that the mixture is highly complex and mainly consists of linear and cyclic carbonates, accompanied by residual alcohols, fluorinated salts and acids, as well as unidentified byproducts. Pretreatment of the condensates by atmospheric distillation revealed significant challenges, including an increase in viscosity during processing, discoloration of the distillate and mist formation, presumably caused by decomposition of residues of the conducting salt. Further purification by batch rectification revealed challenges related to undissolved salts, turbidity and crystalline structures in the distillate. Despite these challenges and the formation of additional impurities during processing, ethyl methyl carbonate (EMC) was successfully recovered at high purity. The results underline the technical feasibility of recovering solvents from recycled condensates and the necessity for optimized purification strategies to ensure safe operation and high product quality.

Keywords
spent electrolyte; solvent recovery; circular economy; distillation; batch rectification; lithium-ion battery

1. Introduction

The growing electromobility sector does not only lead to an increased production of high-voltage lithium-ion batteries (LIBs), but also to a corresponding rise in the number of spent LIBs that require recycling. However, the liquid electrolyte is a frequently overlooked constituent in LIB recycling, accounting for approximately 8-16 wt.-% of LIBs [1]. The conductive electrolyte solution consists of a salt, most commonly lithium hexafluorophosphate ($LiPF_6$), dissolved in a mixture of cyclic carbonates such as ethylene carbonate (EC) and linear carbonates such as dimethyl (DMC), diethyl (DEC) or ethyl methyl carbonate (EMC) as well as other solvents such as fluorobenzene (FB) and various additives like cyclohexylbenzene (CHB) [2,3]. During LIB recycling, the volatile organic electrolyte solvents are recovered by vacuum drying in an inert gas atmosphere as part of a thermomechanical treatment, resulting in a concentrated blend of the aforementioned solvents along with additional impurities which are

formed during the use of LIBs or during the recycling [3,4]. Due to its complex composition, this obtained condensate is currently considered unsuitable for direct reuse and therefore classified as waste, which is recycled thermally.
To enable a closed-loop material cycle and to reduce emissions associated with combustion, investigations into the processing and purification of these solvent streams are required. Accordingly, the present study provides a comprehensive characterization of solvent mixtures obtained from an industrial-scale LIB recycling facility. Furthermore, the handling of these mixtures and the separation of the initial solvents are investigated by batch rectification. Finally, the challenges and key aspects to be considered in order to obtain high-purity solvents from LIB recycling, which are suitable for reuse in new lithium-ion batteries, are presented in this work.

2. Methodology for solvents treatment from the recycling of LIBs

Battery modules from various OEMs were recycled at the PreZero Battery Recycling GmbH recycling facility (Meppen/Germany). Deeply discharged LIBs were subjected to thermomechanical treatment, where battery modules and cells were shredded using a four-shaft shredder (RS150, UNTHA shredding technologies, Kuchl/Austria) operated in an inert vacuum and nitrogen atmosphere [5]. This resulted in the rupture and fragmentation of the modules and contained cells, allowing the electrolyte to come into contact with the process atmosphere. Subsequently, the processed material was fed to vacuum distillation dryers, (HTC-T, BHS-Sonthofen GmbH, Sonthofen/Germany) also operated under nitrogen atmosphere. Volatile organic compounds were evaporated, subsequently condensed and collected as a condensate [6]. Approximately 3 L of condensate were obtained for each of two separate recycling batches. The samples were characterized, pretreated and separated by batch rectification to evaluate the separation of the initially used substances and their recovery at high purity. In further processing steps, the shredded LIBs were separated into various metal and non-metal fractions, using mechanical separation technology, such as screens, zig zag classifiers or density tables [7].

2.1 Analytical methods for solvent characterization

The condensates from the recycling facility were analyzed using Karl-Fischer titration (KFT), gas chromatography (GC) and ion chromatography (IC). Content of organic components was quantified via GC. Measurements were carried out using a SCION 456-GC system (SCION Instruments NL BV, Goes/The Netherlands) equipped with a flame ionization detector (FID). Chromatographic separation was achieved using an Rxi-624Sil MS capillary column (30 m × 0.25 mm ID, 1.4 µm, Restek GmbH, Bad Homburg/Germany). Prior to analysis, the samples were neutralized by adding a spatula tip of sodium hydrogen carbonate (≥ 99.7%, Merck KGaA, Darmstadt/Germany) to prevent potential damage to the GC system caused by acids. Subsequently, the samples were centrifuged at 5000 rpm for 10 min and filtered through a 0.45 µm membrane filter (PTFE). The prepared samples were mixed with the internal standard (InStd.) acetonitrile (AcN, ≥ 99.8%, Fisher Scientific GmbH, Schwerte/Germany) at a volumetric ratio of 2:1 (V_{sample}:$V_{InStd.}$). Further details of the GC method and sample preparation are provided in [3]. As unknown peaks cannot be identified or quantified using this method, the results are reported as relative mass fractions w_i* in $g_i \cdot g_Q^{-1}$. The relative mass fraction w_i* is defined as the ratio of the mass of component i to the sum of the masses of all quantifiable components.
For the analysis of anions, such as acids or salts, the samples were filtered through a 0.45 µm membrane and subsequently diluted 1:20 v/v with ultrapure water. The diluted samples were analyzed using a Metrohm 881 Compact IC system in combination

with a 919 IC Autosampler (Metrohm AG, Herisau/Switzerland). The applied method was based on “Metrohm Application Work AW IC DE-1198-012023”.
The water content of the samples was determined using a C30 Coulometric Karl-Fischer titrator equipped with a Stromboli oven sample changer (Mettler-Toledo GmbH, Giessen/Germany). For this purpose, 1 mL of each sample was heated at 150 °C in the Stromboli oven, and the produced gas was fed in the measuring cell containing HYDRANAL™ Coulomat AG (Fisher Scientific GmbH, Schwerte/Germany) where the water content was determined coulometrically.

2.2 Pretreatment of the solvent mixtures prior to separation

Prior to batch rectification, each sample underwent a small-scale distillation in order to investigate its boiling behavior, remove potential non-volatile components and prevent damage to the batch rectification plant described in Section 2.3. The small-scale distillation process was carried out utilizing a glass column (borosilicate glass 3.3), which comprised a round-bottom flask placed in an electrically heated mantle with a maximum power output of 700 W. The flask was connected to a condenser that used tap water as a cooling medium. The apparatus was employed in a fed batch process, with the condensate from the recycling facility being introduced through a hose pump. Each sample was pretreated in separate batch under ambient conditions.

2.3 Separation of the solvent mixture by batch rectification

Both distillates collected during the pretreatment step were combined into a single mixture, which was subsequently separated using a DN 50 batch rectification plant (ILUDEST Destillationsanlagen GmbH, Waldbüttelbrunn/Germany). Heat input was provided via thermal oil, transferred through two heat exchangers connected in series. To enhance heat transfer, the process medium was continuously mixed using a propeller stirrer operated at 100 rpm. Separation was achieved by two DN 50 column sections made of borosilicate glass 3.3 with silver-coated, vacuum-insulated double jackets, packed with Sulzer DX gauze packing (Sulzer AG, Winterthur/Switzerland). The packing height of each column section was 770 mm. Overhead vapor condensation was achieved using a double-coiled stainless-steel tube condenser cooled with in-house cooling water at approximately 10 °C and a subsequent chiller consisting of a double-coiled glass tube operated with a water/glycerol mixture at −20 °C. The reflux ratio R was regulated by time-controlled actuation of a solenoid-actuated piston valve. The distillate was collected in a receiver vessel mounted on a balance, enabling gravimetric determination of the distillate mass flow and subsequently distributed into up to five fraction collection vessels. In addition, sampling ports were installed at both the distillate and the reboiler to allow sampling during operation for monitoring the separation progress. The samples were characterized using the analytical methods described in Section 2.1. Rectification was conducted at a constant head pressure of 100 $mbar_{abs}$. While the column was operated at total reflux during start-up, a constant reflux ratio of $R = 3$ was used for subsequent mixture separation.

3. Results and discussion

The solvent mixture obtained from the LIB recycling plant condensate exhibited a black coloration. Neither centrifugation nor filtration resulted in the separation of visible solid particles and the black appearance of the samples remained unchanged.
Table 1 summarizes the quantified organic components determined by GC-FID as well as the quantified anions identified by IC in the initial condensate obtained from LIB recycling. The investigated samples showed comparable compositions. The organic fraction of the mixture primarily consisted of DMC, EMC, DEC and EC, accompanied by trace amounts of FB, CHB, methanol (MeOH) and ethanol (EtOH). In addi-

tion, further organic substances were detected, but could not be identified using the applied analytical methods. Approximately 60 peaks were detected by GC, of which eight could be quantified. The cumulative peak areas of unidentified components correspond to a relative peak area of 2.18% for Sample 1 and 1.46% for Sample 2.

Table 1: Quantified organic components and anions measured by GC-FID and IC detected in the condensate.

sample	MeOH	EtOH	FB	DMC	EMC	DEC	EC	CHB	F^-	PF_6^-
	$w_i^* / \times 10^{-2}\ g_i \cdot g_Q^{-1}$								$\beta_i / g_i \cdot L^{-1}$	
1	0.09	0.02	0.34	14.56	66.34	3.84	14.79	0.03	0.52	1.65
2	0.10	0.03	0.20	18.32	58.98	7.37	14.98	0.02	0.53	2.23

With respect to the ionic species, the anions F^- and PF_6^- were quantified by IC analysis and are also listed in Table 1. In the context of LIBs recycling, possible compounds associated with the F^- anion include lithium fluoride (LiF) or hydrogen fluoride (HF) [2], whereas the presence of PF_6^- suggests potentially $LiPF_6$ in the samples. Furthermore, the IC chromatogram revealed the presence of additional anions. Nine additional peaks were detected, which may originate from electrolyte decomposition processes occurring during cell aging or recycling, with organophosphate compounds or additional hydrolysis and decomposition products being plausible candidates [2,8,9]. The water content was quantified to 0.11 $mg_{H2O} \cdot g_{total}^{-1}$ for Sample 1 and 0.10 $mg_{H2O} \cdot g_{total}^{-1}$ for Sample 2.

3.2 Challenges during pretreatment of the solvent mixtures

Figure 1 provides insights into the pretreatment of the condensates. Several challenges related to the processing were identified. From the beginning until approximately two thirds of the distillation process, a colorless vapor was present in the apparatus, resulting in a colorless distillate. As the mixture became increasingly concentrated, the viscosity of the bottom product increased. At the same time, the ascending vapor began to discolor, resulting in a brownish condensate flowing along the inner wall of the connecting section (Figure 2 (a)) and the formation of a whitish haze in the condenser (Figure 2 (b)).

Since the low-boiling components, such as alkyl carbonates, were largely removed at this stage, higher-boiling components, potentially responsible for the observed discoloration, entered the vapor phase. The resulting increase in the residue temperature likely promoted $LiPF_6$ decomposition and HF formation [2], which may explain the observed mist formation in the condenser. Obviously, the pretreatment procedure revealed the complexity and challenges encountered in the thermal separation of real electrolyte condensates. To reduce associated hazards, prior salt removal and distillation under reduced pressure are strongly recommended.

The discolored condensate was collected separately, yielding two distillate fractions and one bottom fraction. The first distillate fraction (approx. 2.5 L per batch) was initially colorless but gradually turned slightly brown within several hours during storage at room temperature (Figure 2 (c)), indicating ongoing decomposition reactions within the mixture. The second distillate fraction, approximately 50 mL, consisted of a heterogeneous liquid–liquid system with a lower black/brown phase and an upper yellow-green phase (Figure 2 (d)), which may correspond to gasoline residues previously used to clean the industrial LIB facility. Upon cooling down, the bottom fraction (Figure 2 (e)) solidified into a black solid mass, which is presumably related to the high concentration of EC and other high-boiling components. In addition, a crystalline fouling layer formed on the walls of the distillation apparatus during cool-down. This is also likely to be composed of solidified EC (Figure 2 (f)).

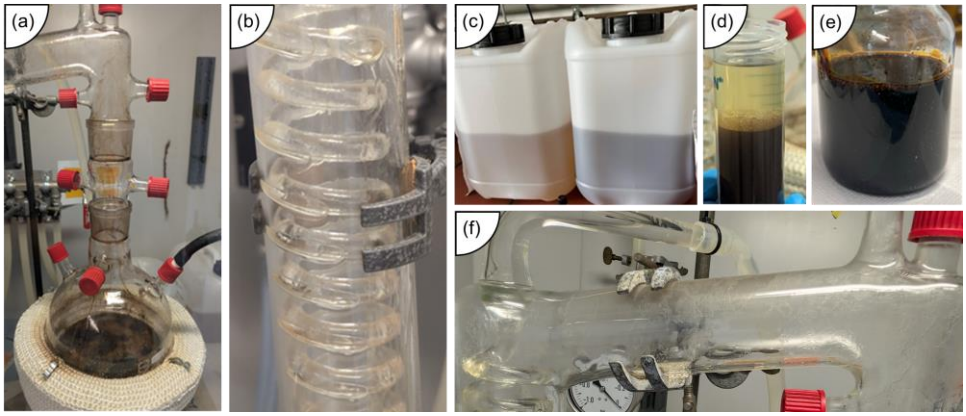

Figure 1: Impressions of the distillative pretreatment of the solvent mixture at atmospheric pressure.

3.3 Purification via batch rectification

The further separation of the distillate obtained from the distillative pretreatment (approx. 5 L) revealed additional challenges during purification. The residue exhibited progressive brown discoloration over the course of the experiment, as indicated by the increasing coloration of the collected samples. In addition, several distillate samples taken during rectification showed turbidity while crystalline structures were observed in nearly all distillate fractions from batch rectification. Their presence may be attributed either to entrainment of salts or to crystallization occurring at the column head under changing temperatures and concentrations during batch rectification.

Analysis of the distillate samples taken during rectification revealed the presence of residual alcohols and anions. Compared to virgin materials, these impurities in the recyclate can impair LIB performance [10]. Therefore, their removal is required, which may significantly increase the complexity of the purification processes necessary to achieve the purity levels required for reuse of the individual components in future LIB electrolyte recipes. Additionally, the stainless-steel condenser and metallic Pt-100 sensor showed traces of corrosion, presumably due to the accumulation of HF in the distillate, as F^- was still measurable in all distillate samples. Therefore, neutralization of the mixture prior to distillation is recommended.

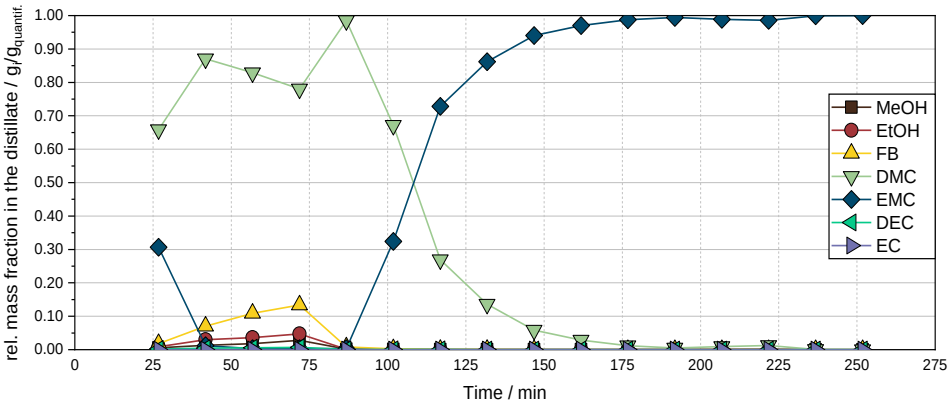

Figure 2: Distillate composition from the purification of the solvent mixture.

Figure 2 illustrates the change in distillate composition during purification. At the initial phase of separation (t < 100 min), low-boiling components such as DMC and FB as well as low-boiling impurities MeOH and EtOH were removed from the feedstock mixture. Furthermore, analytical GC data indicate the presence of additional, yet unknown, impurities accumulating in the early distillate. As separation progressed, low-boiling components were removed from the system, resulting in an accumulation of EMC in the distillate (t > 100 min). In the final phase of the batch rectification pro-

cess, the EMC concentration reached its maximum. Despite the presence of numerous interfering components in the initial solvent mixture, as well as those formed during the purification process, EMC, an important electrolyte component, was recovered with a high degree of purity and a mass yield of 17.75%. Table 2 provides an overview of the analytical results of the EMC fraction.

Table 2: Quantified organic components and anions in the purified EMC fraction (LOD: limit of detection).

sample	MeOH	EtOH	FB	DMC	EMC	DEC	EC	CHB	F^-	PF_6^-
	$w_i^* / \times 10^{-2}\ g_i \cdot g_Q^{-1}$								$\beta_i / g_i \cdot L^{-1}$	
EMC fraction	0.04	0.01	<LOD	0.32	99.63	<LOD	<LOD	<LOD	0.77	<LOD

4. Conclusions

The purification of solvent mixtures from industrial LIB recycling facilities poses several technical and safety-related challenges. Pretreatment by atmospheric distillation demonstrated several challenges during operation due to decomposition reactions and the formation of HF. Further purification by batch rectification revealed additional challenges, most likely arising from residual alcohols, anions and undissolved salts leading to turbidity, solidification and formation of impurities in the distillate.

Nevertheless, despite the complex composition of the solvent mixtures and the formation of additional impurities, high-purity EMC was successfully recovered from the feedstock mixture. Overall, the obtained results confirm the potential for recovering valuable electrolyte solvents from LIB recycling streams while clearly highlighting the need for improved process strategies. In particular, salt removal, neutralization of acidic species, operation under reduced pressure and the use of corrosion-resistant equipment materials are essential to minimize hazards, protect equipment and enable efficient solvent purification suitable for reuse in new LIBs.

References

[1] A. Arnberger, E. Coskun, B. Rutrecht, Recycling von Lithium-Ionen-Batterien, in: Recycling und Rohstoffe, Thomé-Kozmiensky Verlag GmbH, Neuruppin 2018, 2018: pp. 583–599.

[2] R. Korthauer, ed., Handbuch Lithium-Ionen-Batterien, Springer Berlin Heidelberg, Berlin, Heidelberg, 2013. https://doi.org/10.1007/978-3-642-30653-2.

[3] M. Wolke, K. Schröder, K. Arnold, P. Mozumder, T. Beuerle, K. Jasch, S. Scholl, Analyzing Organic Electrolyte Solvents from Spent Lithium-Ion Batteries as a Basis for Distillative Value Component Recovery, Recycling 10 (2025). https://doi.org/10.3390/recycling10010019.

[4] A. Pražanová, J. Kočí, M.H. Míka, D. Pilnaj, Z. Plachý, V. Knap, Pre-Recycling Material Analysis of NMC Lithium-Ion Battery Cells from Electric Vehicles, Crystals 13 (2023) 214. https://doi.org/10.3390/cryst13020214.

[5] URT Umwelt- und Recyclingtechnik GmbH, Battery Recycling, (n.d.). https://www.urt-recycling.com/seite/en/disposal/414/-/Link_nach_414.html (accessed January 1, 2026).

[6] J. Wanjala, URT Recycling Technology helping lithium battery recyclers move forward, (2023). https://recyclinginternational.com/latest-articles/urt-recycling-technology-helping-lithium-battery-recyclers-move-forward/54345/ (accessed January 1, 2026).

[7] M. Petzold, S. Flamme, Recycling Strategies for Spent Consumer Lithium-Ion Batteries, Metals 14 (2024) 151. https://doi.org/10.3390/met14020151.

[8] V. Kraft, W. Weber, M. Grützke, M. Winter, S. Nowak, Study of decomposition products by gas chromatography-mass spectrometry and ion chromatography-electrospray ionization-mass spectrometry in thermally decomposed lithium hexafluorophosphate-based lithium ion battery electrolytes, RSC Adv. 5 (2015) 80150–80157. https://doi.org/10.1039/C5RA16679A.

[9] J. Menzel, H. Schultz, V. Kraft, J.P. Badillo, M. Winter, S. Nowak, Quantification of ionic organo (fluoro)phosphates in decomposed lithium battery electrolytes, RSC Adv. 7 (2017) 39314–39324. https://doi.org/10.1039/C7RA07486G.

[10] V.N. Mohni, N. Heine, M. Wolke, S. Scholl, B.L. Lucht, P. Novák, D. Schröder, Challenges of using recycled ethyl methyl carbonate in lithium-ion batteries: Effects of residual alcohols on performance, J. Power Sources 659 (2025). https://doi.org/10.1016/j.jpowsour.2025.238385.

Electrified Pathways Toward Decarbonized Fluid Separations

Chengtian Cui [1,2], Anton A. Kiss[1]
[1]Department of Chemical Engineering, Delft University of Technology, Van der Maasweg 9, 2629 HZ, Delft, The Netherlands
[2]Process and Systems Engineering Laboratory, Åbo Akademi University, Henrikinkatu 2, 20500, Turku, Finland

Abstract
Distillation remains the workhorse of fluid separations in the chemical process industry, accounting for approximately 60% of separation energy use and 3% of global energy demand. Due to its heavy reliance on fossil fuel based steam, it is a significant contributor to industrial CO_2 emissions. Achieving deep decarbonization requires a transition toward electrified systems integrated with renewable power, which should be addressed through a holistic framework based on process systems engineering (PSE) and process intensification (PI). The proposed framework evaluates various power-to-heat solutions, including direct electric heating, electric steam generation, and heat pump-based technologies. These electrification routes are complemented by PI measures, which reduce energy consumption in the first place, thereby expanding the feasible operating window for electrified heat supply. To reconcile continuous production with the stochastic nature of renewable power, the framework incorporates energy storage and advanced real-time control to enable grid-responsive operation. By coupling electrification with PI and dynamic operational strategies, this research establishes a roadmap for carbon-neutral separations that are economically resilient and compatible with a renewable-led energy landscape.

Keywords
Electrification of distillation; Heat pump assisted distillation; Process intensification; Flexibility; Renewable power supply; Decarbonization

1. Introduction

Distillation remains the workhorse of fluid separations in the chemical process industry, yet it is also one of the most energy-intensive operations. Distillation has been reported to represent roughly ~60% of separation energy use and about ~3% of global energy demand (Cui et al., 2024).

Historically, the heat required for reboilers has been supplied predominantly by steam generated from fossil fuels, making conventional distillation a significant contributor to carbon emissions and a visible barrier to deep decarbonization targets. At the same time, power systems are rapidly decarbonizing via increasing penetration of variable renewable energy, creating a growing opportunity for shifting industrial energy demand from heat to electricity. Broad perspectives on decarbonization increasingly emphasize electrification as a central pathway, provided that processes can operate efficiently and flexibly under low-carbon electricity supply (Mallapragada et al., 2023).

However, “electrifying distillation” is not a single technology; it is a system redesign problem spanning energy supply form, column configuration, and operability. First, there are multiple power-to-heat (PtH) routes with distinct performance envelopes,

including direct electric heating (e.g., resistance heating), electric steam generation (e.g., electrode boilers), and heat pump that upgrades low-temperature heat to useful reboiler levels (Kiss and Smith, 2020). Second, even with electrified heat supply, the intrinsic thermodynamic inefficiency of conventional columns leaves substantial room for improvement, motivating renewed interest in process intensification (PI). Dividing wall column (DWC) is a representation of PI techniques (Yildirim et al., 2011). Third, beyond hardware, electrified distillation must reconcile continuous chemical production with the stochastic nature of renewable power. Traditional columns are designed for steady-state operation; however, a grid-responsive system requires inherent flexibility. This necessitates a transition from steady state design to a dynamic operational paradigm by integrating thermal storage and advanced control strategies to align industrial demand with time-varying electricity prices and carbon intensities (Cegla et al., 2023).

Motivated by these multi-dimensional challenges, this work proposes a holistic framework to evaluate electrified pathways for distillation. We treat electrification and intensification as complementary pillars: while electrification provides a low-carbon energy vector, PI reduces energy consumption in the first place, thereby enhancing both economic resilience and emissions performance. Furthermore, by coupling electrified heat supply with intensified configurations, carbon-neutral separations can become not only feasible but also actively supportive of a flexible, renewable-led energy landscape.

2. Holistic framework for decarbonizing distillation

Figure 1 summarizes the holistic framework adopted to decarbonize distillation by jointly leveraging three complementary pillars: electrification, PI, and grid interaction & control. From a process systems engineering (PSE) perspective, the proposed framework treats the distillation unit not as an isolated apparatus, but as a critical node within an integrated energy system. This involves multi-scale considerations ranging from thermodynamic property modeling to plantwide energy management.

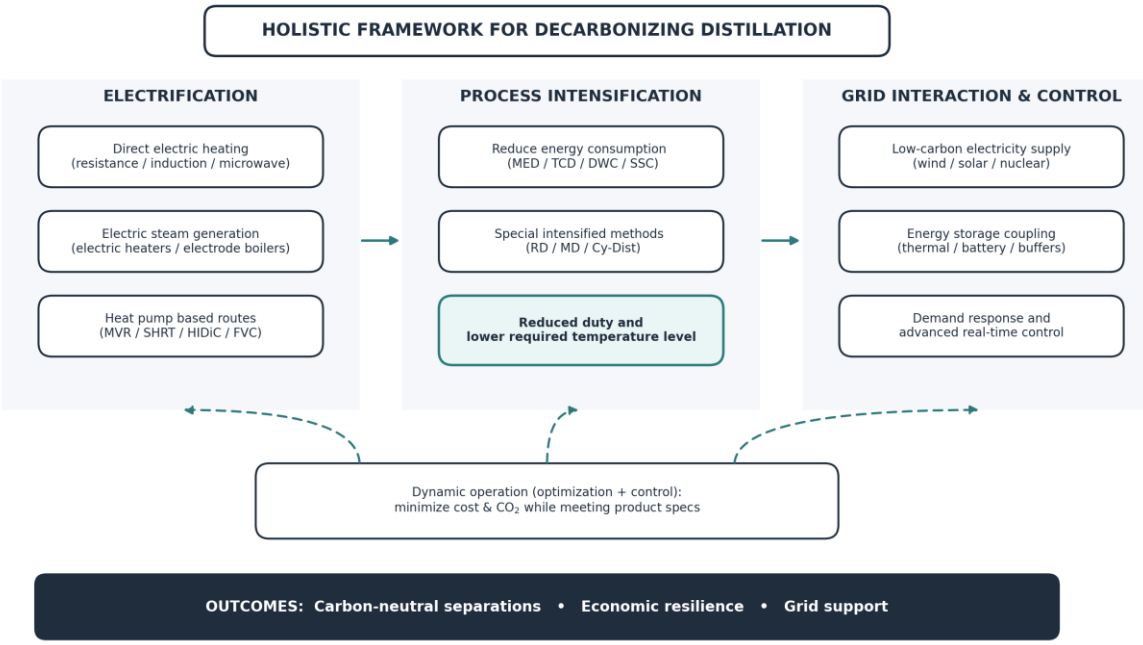

Figure 1. A holistic framework for decarbonizing distillation

Electrification addresses the carbon intensity of heat supply by replacing fossil-fired steam with PtH routes. In parallel, PI targets the intrinsic inefficiency of conventional

columns by reducing required separation duty. These first two pillars are tightly coupled: PI reduces energy consumption and can even expand the feasible operating window for electrified heat supply, improving overall system economics. The third pillar recognizes that deep decarbonization must be achieved under power systems with time-varying prices and carbon intensities. Hence, renewable-led operation is enabled through low-carbon electricity sourcing, energy storage coupling, and demand response supported by advanced real-time control. Within this integrated perspective, a dynamic operation layer (optimization plus control) coordinates equipment and operating decisions to minimize cost and CO_2 emissions while maintaining product specifications and operational constraints. The combined outcome is a pathway toward carbon-neutral separations that is not only energy- and emissions-efficient, but also economically resilient and capable of providing grid-supportive flexibility.

3. Electrification

Electrification decarbonizes distillation by replacing fossil fired steam with low-carbon electricity. In practice, electrified distillation can be realized through three main PtH routes: (i) Direct electric heating delivers heat to the reboiler via resistive, induction, or microwave approaches, offering fast response and high controllability, but its viability depends strongly on required temperature level, duty size, and electricity price (DOE, 2015). (ii) Electric steam generation (e.g., electric heaters or electrode boilers) provides a retrofit-friendly pathway because it can often interface with existing steam and reboiler infrastructure; however, overall economics hinge on the conversion efficiency to steam, steam-network integration, and the temporal profile of electricity cost and carbon intensity (Element Energy & Jacobs, 2018). (iii) Heat pump based routes, including mechanical vapor recompression (MVR), self-heat recuperation technology (SHRT), internally heat-integrated distillation columns (HIDiC), and recently emerging flash vapor circulation (FVC) (Cui et al., 2024), shift electrification from “electric heat supply” to “electric heat upgrading” by recovering low-grade heat from condensation and lifting it to reboiler-relevant temperatures, thereby reducing net external energy input. Across these routes, temperature level and temperature lift emerge as governing feasibility parameters, while dynamic controllability becomes essential for optimal operation. Consequently, electrification is most effective when co-designed with heat integration and intensification measures that achieve energy saving (Kim et al., 2022).

4. Process intensification

PI is treated here as structural and functional redesign of the distillation flowsheet and column topology to reduce energy use by avoiding remixing losses, eliminating redundant heat transfer interfaces, and exploiting more effective internal coupling of separation tasks, without relying on compressor-driven heat upgrading. In this context, PI primarily includes multi-effect distillation (MED), where heat released by condensation in higher-pressure columns is reused to drive boiling in lower-pressure column (Cui et al., 2019); thermally coupled distillation (TCD), which reduces remixing effects thus increases thermodynamic efficiencies (Horsch and Skiborowski, 2025); DWC, which integrate multi-column separations within a single shell to cut both energy demand and equipment footprint; and liquid-only side-stream column (SSC) concepts that share the same overall minimum vapor requirement as the TCD configuration (Ramapriya et al., 2014).

When applicable, reactive distillation (RD) is also a representative PI strategy because reaction and separation are integrated in one apparatus, potentially

enhancing conversion/selectivity and reducing downstream separation loads, provided that reaction and separation operating windows can be aligned (Kiss et al., 2024).

Beyond these classical intensified column configurations, emerging PI directions include membrane distillation (MD) and cyclic distillation (Cy-Dist). MD uses the vapor pressure difference across a hydrophobic membrane as the driving force, enabling separation at relatively low operating temperatures and offering compact equipment and potential capital advantages, especially when low-grade heat sources are available; although it still involves evaporation, it can shift the separation task toward temperature levels that are easier to supply with low-carbon heat (Kiss and Readi., 2018). Cy-Dist, in contrast, intensifies separation through periodic operation rather than steady counter-current contacting, creating additional degrees of freedom in time that can improve separation performance and, in suitable applications, reduce energy use or column size (Bildea et al., 2016).

Overall, these PI options lower the net duty and/or shift heat demand to more favorable temperature levels, thereby reducing the electricity requirement once heat supply is electrified and improving the feasibility of low-carbon distillation.

5. Grid interaction and control

Grid interaction and control constitute the third pillar of the proposed framework, recognizing that electrified distillation must operate reliably under power systems characterized by time-varying prices, carbon intensities, and renewable availability (Ellabban et al., 2014). Distillation is typically continuous and constrained by tight product specifications, so flexibility cannot be assumed; it must be engineered through coordinated operation of equipment, storage, and control (Cegla et al., 2023). The coordination between time-varying electricity prices and continuous production requirements is a classic PSE challenge. By formulating the operation as a dynamic optimization problem, a supervisory control layer can simultaneously manage material balances, energy integration, and economic objectives under uncertainty.

This grid-aware operation is enabled by three elements: access to low-carbon electricity supply (e.g., renewable-led portfolios), coupling with energy storage (thermal storage, buffer tanks, or batteries where appropriate) to decouple process heat demand from instantaneous grid conditions (Hurst et al., 2024), and demand response capable operation supported by advanced real-time control (Ranaboldo et al., 2024). A supervisory layer uses electricity price and carbon signals to schedule heat input, reflux/boil-up policies, and storage charge–discharge actions while enforcing separation constraints such as purity, recovery, hydraulic limits, and safe operation (Pattison et al., 2016). In effect, grid interaction transforms electrified distillation from a steady state utility consumer into a grid-responsive asset: it minimizes operating cost without sacrificing product quality and provides operational flexibility that can support higher renewable penetration (Qi et al., 2025).

6. Deployment roadmap and decision guidelines

To translate the proposed framework into actionable engineering decisions, a practical deployment roadmap is needed that links distillation characteristics (systems to be separated, energy consumption, temperature levels, operability constraints) to an appropriate electrification–intensification–flexibility portfolio.

A first screening step is to characterize the thermal demand of the target separation, in particular the required temperature lift and the magnitude of the duty. These two factors largely determine whether electrification should be pursued via direct electric

heating, electric steam generation, or a heat pump assisted pathway. For grassroots design process, engineers have the freedom to move beyond legacy constraints and implement deeper structural PI. In these new-build scenarios, electrified heat-pump-assisted configurations (MVR, HIDiC, or FVC) are often prioritized because the column internals and shell can be designed from the outset to handle the specific pressures and temperature lifts required for high-efficiency heat upgrading. This approach allows for the integration of advanced PI measures like DWC or RD, which significantly reduce the net energy duty and shift the heat demand to more favorable temperature levels, thereby maximizing the economic and environmental benefits of low-carbon electricity. On the other hand, for near-term retrofits, electric steam generation often provides the lowest-friction entry point because it can preserve existing reboiler and utility interfaces while decarbonizing the energy vector; however, its economic attractiveness remains sensitive to the temporal profile of electricity prices and carbon intensity. Direct electric heating can be attractive where fast response and modularity are valued (Mercer and Baldea, 2025), but it becomes less compelling for very large duties or where high temperature levels dominate the heat requirement. Importantly, in retrofit projects, PI might be difficult to implement directly due to numerous practical constraints. Legacy equipment often presents barriers such as limited plot space, fixed column shell dimensions, and existing internal configurations that are not easily modified without significant downtime and capital expenditure (Long and Lee, 2017). Consequently, retrofits may prioritize electrification routes with minimal structural changes and staged implementation, whereas grassroots designs can fully leverage the synergy between electrification and intensification to achieve the most robust decarbonization outcomes.

The second screening phase involves evaluating the grid compatibility of the proposed system. Since electrified distillation must bridge the gap between continuous industrial production and the inherent variability of renewable energy, operational flexibility is no longer an optional feature but a core design requirement. This is achieved by transforming the distillation process into a grid-responsive asset through the strategic integration of thermal buffering and predictive coordination (Caspari et al., 2019). Rather than merely following a steady state profile, the system leverages thermal storage as a decoupling mechanism. This allows the process to strategically "time-shift" its energy consumption—intensifying power usage during periods of high renewable availability (low cost/low carbon) and drawing from stored energy when the grid is stressed. To manage this complexity, a supervisory control layer acts as the system's brain: it dynamically optimizes distillation operation and power supply. Ultimately, this approach redefines the role of distillation, evolving it from a rigid utility consumer into a flexible participant in the dynamic electricity market.

Overall, the deployment roadmap utilizes PSE methodologies to reconcile the trade-offs between capital investment and operational flexibility. This holistic assessment ensures that the selected electrification pathway is optimized for both long-term sustainability and short-term grid responsiveness.

7. Conclusions

This work presents a holistic framework for decarbonizing distillation based on three complementary pillars: electrification, PI, and grid-aware operation enabled by storage and advanced control. Electrification provides a direct pathway to replace fossil fired steam, while PI reduces energy consumption. Because renewable-led power systems impose time-varying prices and carbon intensities, grid interaction and real-time control are treated as essential design elements; supervisory optimization coordinated with buffering strategies can maintain product specifications

while minimizing cost and CO_2. Overall, the proposed perspective emphasizes that deep decarbonization of distillations is not achieved by a single technology choice but by integrating multi-scale PSE considerations ranging from thermodynamic property modeling to plantwide energy management, enabling distillation that is economically resilient and compatible with a renewable-dominated energy landscape.

Acknowledgements

This work was supported by the Marie Skłodowska-Curie Actions Postdoctoral Fellowship (Grant No. 101211557).

References

Bildea C.S., Patrut C., Jorgensen S.B. Abildskov J., Kiss A.A., 2016. Cyclic distillation technology – a mini-review. Journal of Chemical Technology and Biotechnology. 91, 1215-1223.

Caspari A., Offermanns C., Schafer P., Mhamdi A., Mitsos A., 2019. A flexible air separation process: 2. Optimal operation using economic model predictive control. AIChE Journal. 65, 11, e16721.

Cegla M., Semrau R., Tamagnini F., Engell S., 2023. Flexible process operation for electrified chemical plants. Current Opinion in Chemical Engineering. 39, 100898.

Cui C., Xi Z., Liu S., Sun J., 2019. An enumeration-based synthesis framework for multi-effect distillation processes. Chemical Engineering Research and Design. 144, 216-227.

Cui C., Qi M., Zhang X., Sun J., Li Q., Kiss A.A., Wong D.S.H., Masuku, C.M., Lee M., 2024. Electrification of distillation for decarbonization: An overview and perspective. Renewable and Sustainable Energy Reviews. 199, 114522.

Cui C., Zhang X., Qi M., Lyu H., Sun J., Kiss A.A., 2024. Fully electrified heat pump assisted distillation process by flash vapour circulation. Chemical Engineering Research and Design. 206, 280-284.

DOE (U.S. Department of Energy). Improving process heating system performance: a sourcebook for industry. 2015.

Element Energy & Jacobs. Industrial fuel switching market engagement study. 2018.

Ellabban O., Abu-Rub H., Blaabjerg F., 2014. Renewable energy resources: Current status, future prospects and their enabling technology. Renewable and Sustainable Energy Reviews. 39, 748-764.

Horsch A.S., Skiborowski M., 2025. Thermally coupled distillation columns without vapor transfer – Current state and further needs. Separation and Purification Technology 354, 128762.

Hurst K.E., Springer M., Wikoff H., Cory K., Garfield D., Ruth M., Reese S.B., 2024. Industrial Energy Storage Review. National Renewable Energy Laboratory.

Kiss A.A., Readi O.M.K., 2018. An industrial perspective on membrane distillation processes. Journal of Chemical Technology and Biotechnology. 93, 8, 2047-2055.

Kim J.K., Son H., Yun S., 2022. Heat integration of power-to-heat technologies: case studies on heat recovery system subject to electrified heating. Journal of Cleaner Production. 331: 130002.

Kiss A.A., Smith, R., 2020. Rethinking energy use in distillation processes for a more sustainable chemical industry. Energy. 203, 117788.

Kiss A.A., Muthia R., Pazmino-Mayorga I., Harmsen J., Jobson M., Gao X., 2024. Journal of Chemical Technology and Biotechnology. 99, 6, 1263-1290.

Long N.V.D., Lee M., 2017. Advances in Distillation Retrofit. Springer.

Mallapragada D.S. et al., 2023. Decarbonization of the chemical industry through electrification: Barriers and opportunities. Joule. 7, 1, 23-41.

Mercer S., Baldea M., 2025. Fast startup dynamics of diabatic distillation with electric heating. IFAC-PapersOnLine. 59, 6, 588-593.

Pattison R.C., Touretzky C.R., Johansson T., Harjunkoski I., Baldea M., 2016. Optimal process operations in fast-changing electricity markets: Framework for scheduling with low-order dynamic models and an air separation application. Industrial & Engineering Chemistry Research. 55, 4562-4584.

Qi M., Zhang X., Wong D.S.H., Shu C.M., Cui C., Kiss A.A., 2025. Electrified distillation with flash vapor circulation and thermal storage for dynamic electricity markets. AIChE Journal. 71, 5, e18750.

Ramapriya G.M., Tawarmalani M., Agrawal R., 2014. Thermal coupling links to liquid-only transfer streams: A path for new dividing wall columns. AIChE Journal. 60, 2949-2961.

Ranaboldo M. et al., 2024. A comprehensive overview of industrial demand response status in Europe. Renewable and Sustainable Energy Reviews. 203, 114797.

Yildirim O, Kiss A.A., Kenig E.Y., 2011. Dividing wall columns in chemical process industry: A review on current activities. Separation and Purification Technology. 80, 3, 403-417.

Screening for Heat Pump Integration Potentials in Chemical Plants

Thorben Hochhaus [a], Julia Riese [b], Marcus Grünewald [a]
[a] Ruhr University Bochum, Laboratory of Fluid Separations, Universitätsstrasse 150, 44801 Bochum, Germany
b Paderborn University, Fluid Process Engineering, Pohlweg 55, 33098 Paderborn, Germany
hochhaus@fluidvt.rub.de; julia.riese@uni-paderborn.de; gruenewald@fluidvt.rub.de

Abstract. Defossilization of process heat is essential for achieving net-zero emissions in the European chemical industry. Electrically driven compression heat pumps can upgrade waste heat to useful temperature levels, reducing fossil fuel consumption. However, identifying suitable integration options in highly heat-integrated plants and chemical sites is challenging due to numerous potential heat sources and sinks and existing utility structures. This work presents methods for heat pump integration screening at scales ranging from single plants to entire chemical sites. In addition to established approaches, two novel methods are introduced: an insight-based thermodynamic screening algorithm that systematically reduces and evaluates promising source–sink combinations, and a three-step framework that decomposes site-wide integration problems into spatially defined subproblems. Both approaches reduce problem complexity and provide computationally efficient decision support for early-stage planning, by assessing integration options with respect to CO_2-emissions and economic feasibility.

All rights reserved by the authors as per DA2026 copyright notice.

Keywords Heat pump, Heat integration, Renewable energy sources, Defossilization

1. Introduction

To meet Europe's climate goals of zero net-emissions by 2050, the CO_2-emissions of the chemical industry must be reduced significantly. The burning of natural gas is often used to supply heat to chemical processes which results in the emission of CO_2 [1]. Therefore, it should be a priority for companies in the chemical industry to reduce the uptake of process heat supplied by fossil fuels by improving the efficiency of chemical processes to reduce overall heat demand or switching to energy sources with lower CO_2-emissions. Compression heat pumps can supply process heat with low CO_2-emissions when operated using electricity with a low CO_2-emission factor [2]. Heat pumps can be used to upgrade formerly unused waste heat to a higher temperature level to heat cold process streams that require external heating which reduces external heating from fossil sources.

Despite these benefits, the integration of heat pumps into chemical processes is still limited by mayor challenges. Among others, these challenges include economic feasibility and a lack of experience regarding the identification of appropriate heat pump integration [3]. At chemical sites, heating and cooling services for cold and hot process streams are often provided by utility systems with different temperature levels. Using different temperature levels also allows for leveraging the potential for indirect heat integration between process streams where direct heat integration is not an option. While the existing utility level temperatures limit the exergetic efficiency of integration, the overall degree of heat integration of the chemical site can be increased. In such highly integrated chemical plants and entire chemical sites, identifying promising heat pump integration becomes a complex challenge as existing heat integration structure must be considered and reevaluated and the number of possible heat pump integration options increases drastically.

Tackling the challenge of identifying appropriate heat pump integration requires methods which allow for quick and comprehensive decision making. Especially the scale of integration needs to be evaluated thoroughly to identify potentials of synergy between multiple heat sources and heat sinks through their coupling in a heat pump. This can be achieved by mathematical programming, conceptual methods or hybrid approaches.

The scope of this work is to present different approaches that can be used for identifying promising heat pump integration at different scales in chemical industry ranging from individual chemical plants resulting in several hot and cold streams to entire chemical sites where several hundred process streams can be used as possible heat sources and sinks for heat pump integration such as condenser and reboiler duties of distillation columns. Additionally, two novel approaches are described that address the challenge of appropriate heat pump integration at different scales in chemical sites. A novel insight-based conceptual approach is presented which follows basic thermodynamic principles and includes short-cut heat pump evaluation to identify potentials of synergy between process heat sources and heat sinks and scales well with problem size. Moreover, a novel three-step approach for heat pump integration in chemical sites is conceptually presented with the aim of reducing integration problem complexity for entire chemical sites. The

integration problem is reduced to multiple sub-problems as a first step by identifying spatial areas in a chemical plant with a promising heat integration potential. In a second step, mathematical optimization can be performed on the sub-problems to identify possible heat integration improvements and heat pump integration potentials. Subsequently, further evaluations such as sensitivity analyses can be conducted. By reducing problem complexity and using computationally efficient methods, both approaches can serve as decision-making support for process engineers to quickly identify and evaluate appropriate heat pump integration. Both approaches evaluate heat pump integration with respect to evaluation criteria such as CO_2-emissions and economic feasibility. Time-efficient computation further enables extensive analysis of future pricing and operational scenarios which enables both methods to provide valuable support in early stages of heat pump integration planning.

2. Literature review

The foundations of systematic heat integration can be traced back to the concept of pinch analysis introduced by Linnhoff and Hindmarsh in 1983, which established a rigorous thermodynamic framework for identifying minimum external heating and cooling demands in process systems [4]. Applying the problem table algorithm and heat cascading ensures feasible heat transfer between temperature levels while respecting thermodynamic constraints [5]. This approach enables the identification of the pinch point and provides clear targeting rules for process design and retrofit. The methodology was subsequently extended from single processes to entire industrial sites through the concept of total site heat integration which allows the systematic optimization of multiple processes, utility systems and cogeneration units within a site-wide scope [6]. Total site analysis enables targeting of steam levels, fuel consumption and power generation potentials, thus providing a basis for evaluating heat recovery and utility system modifications.

Extending classical thermodynamic targeting approaches, mathematical optimization techniques have been proposed to handle more complex problems in heat recovery and utility system synthesis. In this context, Papoulias and Grossmann used a transshipment model formulation in which the overall temperature domain is discretized into intervals, and energy balances are established for each interval to determine the minimum demand for external utilities. [7]. Further developments have incorporated additional technologies and continuous decision variables. Bagajewicz and Barbaro proposed a non-linear targeting formulation for total site heat integration that enables the optimization of heat pump temperature levels as continuous variables [8]. Oluleye et al. integrated heat pump technologies into the optimization of existing cogeneration systems using mixed-integer linear programming (MILP) modeling, focusing on optimal operational parameters, emissions reduction and total annual cost minimization [9]. Wallerand et al. proposed a superstructure-based mixed-integer nonlinear programming formulation (MINLP) for the systematic integration of heat pumps into industrial processes [10]. Their decomposition strategy addressed non-convexities by separating technology selection (integer variables) from non-linear thermodynamic relationships, thereby improving computational tractability.

Heat pump integration into industrial utility systems has therefore been widely investigated as a promising option for upgrading low-temperature waste heat and reducing external heating demand [3,8,9]. In parallel to rigorous optimization approaches, more insight-driven or targeting-based methods continue to play an important role, particularly in early-stage design and screening tasks. Such approaches are especially valuable when multiple case studies with varying levels of system complexity must be assessed. Liew and Walmsley proposed a total site targeting approach incorporating open-cycle vapor recompression heat pumps to decrease boiler demand and supply high-quality steam [11]. Miah et al. introduced a multi-scale framework for identifying heat integration opportunities including heat pumps for waste heat upgrading and substitution of external heating utilities [12]. Plesu et al. proposed a simple screening heuristic for identifying potential heat sources and sinks using a correlation between utility prices and heat pump COP [13]. Oluleye et al. [14] proposed a screening of different heat pump technologies by means of simplified models providing a correlation between ideal and real performance efficiency. They further introduce the primary fuel recovery ratio as a metric for evaluating utility savings.

As distillation columns require cooling services at a low temperature level and heating at a higher temperature level, they often present a promising opportunity for heat pump integration. However, focusing on heat pump integration between condenser and reboiler of a distillation column may disregard other integration potentials. Kiss and Smith [2] pointed out that heat source and sink selection critically affects temperature lift and therefore economic feasibility of heat pump integration. They highlight that alternative heat sources and sinks such as column feed preheating and other process streams should be considered for heat pump integration. These studies underline the potential of combining thermodynamic targeting with systematic evaluation of heat upgrading technologies.

In summary, existing literature spans a spectrum from insight-based thermodynamic targeting methods to rigorous mathematical optimization formulations. However, there remains a need for methodologies that can rapidly identify

suitable heat pump integration locations across case studies of varying complexity while balancing computational efficiency and solution quality.

3. Methodology

In the following, we present two approaches for identifying heat pump integration potentials in chemical processes. Both approaches aim at reducing the complexity of the integration task and providing potential heat pump integration options to assist in early stages of heat pump integration planning.

3.1 Insight-based screening algorithm

The first approach uses simple heuristics and simplified thermodynamic process models. As the combinatorial complexity of integration tasks rises drastically with an increasing number of potential heat sources and heat sinks, systematic screening of relevant feasible combinations is necessary. This can be achieved by only considering heat source and sink pairs which thermodynamically require heat pumps to achieve heat integration and by neglecting heat source and sink pairs that require a temperature lift that is technically infeasible for heat pumps. Moreover, a systematic screening order should be chosen. We propose the required temperature lift of the heat pump as a suitable screening criterion as the temperature lift significantly affects heat pump efficiency and therefore economic feasibility and ecological substitution potential. By using this heuristic, we developed the insight-based screening algorithm shown in Figure 1. It takes process streams as input, that cannot be further integrated via direct heat integration between process streams. The input data is classified into possible heat sources and heat sinks as well as utility levels. Then we propose to search for the combination of heat sources and sinks that would require the lowest heat pump temperature lift among all heat sources and heat sinks. Using several filter methods this can be done efficiently in Python even for large integration problems with several hundred process streams. For the identified heat pump integration option with the lowest possible temperature lift, the integration of a heat pump is evaluated regarding the selected evaluation criteria and compared to the current integration scheme. Only if an improvement can be achieved by integrating a heat pump for the identified integration option, the integration scheme is selected and screening for further heat pump integration options continues until no further options can be identified. By automating this approach in Python, heat pump integration options can be screened quickly including heat pumps with multiple heat sources and sinks.

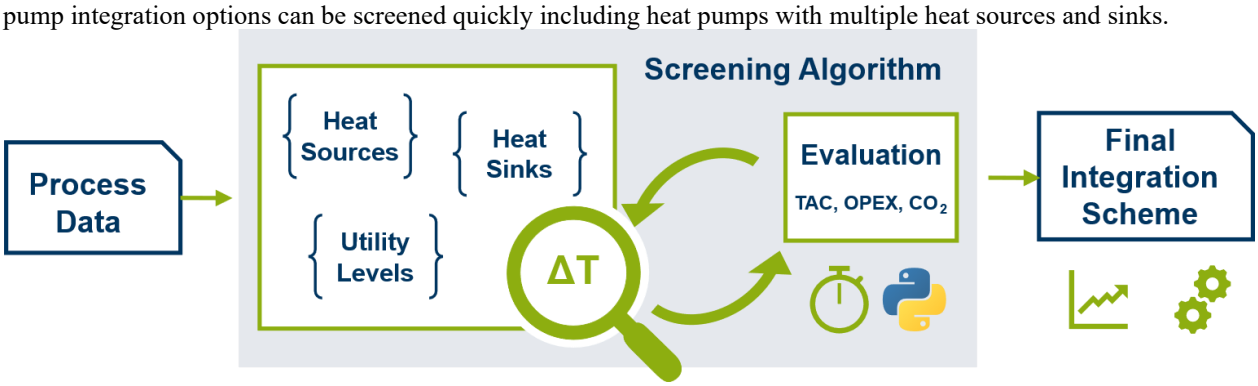

Figure 1: Schematic overview of the proposed insight-based heat pump integration screening algorithm.

3.2 Three-step approach for heat pump integration

We further want to highlight the importance of reducing problem complexity before performing mathematical optimization. For heat pump integration in utility systems of chemical sites, it is necessary to identify optimal pairing of hot and cold process streams with utility levels, identify or modify optimal utility level temperatures and detect options for central heat pump integration. In retrofit scenarios, temperature levels of utility systems often cannot be changed. To further improve the integration potential of heat pumps, integrating new utility levels can be a viable option, as temperature lifts for central heat pump integration can be decreased. As installing new utility levels requires significant installation costs, new utility levels could be integrated in locally limited areas. Solving this in a mathematical optimization approach would require solving heat integration principles such as heat cascading, heat pump modelling and distance calculation between heat sources and heat sinks to assess required utility level lengths and associated installation costs. As this results in complex mixed-integer nonlinear optimization problems, we propose to divide the integration problem into several subproblems as depicted in Figure 2. We propose the selection of promising locally limited areas in a first step before performing mathematical optimization in a second step. As this eliminates the need for distance calculation in the optimization step, MILP formulations can be used for the

optimization to identify optimal heat pump integration configurations. Time efficient selection of promising areas for integrating locally limited utility levels and time efficient optimization then allow further cost parameter analysis and evaluation for different cost and operational scenarios in a third step.

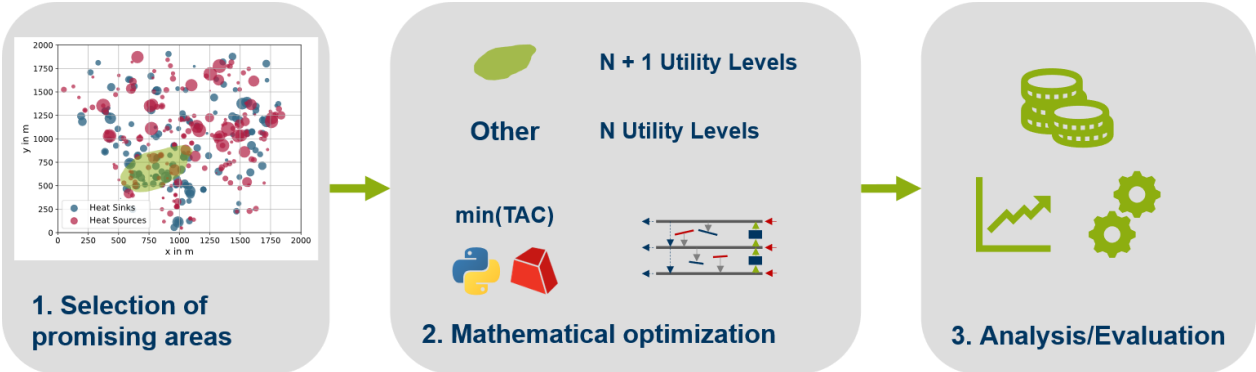

Figure 2: Schematic overview of the proposed three-step approach for heat pump integration in chemical sites.

Selecting locally limited promising areas for integrating new utility levels can also be very complex and different methods can be used. All methods should aim at identifying locally dense areas of heat sources and heat sinks that offer a promising potential for heat integration in heat pump integration. While this can be identified for example using pinch analysis on locally limited areas in a total chemical site, in this work we will discuss the results of identifying promising areas using community detection on a graph structure of the chemical site. In the optimization step, only streams inside the identified area are allowed to connect to an additional new utility level while streams outside the area are limited to the already existing utility level. By that, the logic of integrating a locally limited new utility level is enforced.

4. Conceptual Results

In the following, conceptual results of the proposed methods are presented for exemplary case studies. To highlight the applicability of the proposed approaches in early stages of heat pump integration planning, calculation times are presented.

3.1 Results insight-based screening algorithm

In Figure 3 we present the integration results of the insight-based screening algorithm applied to an exemplary case study consisting of 9 cold process streams, 9 hot process streams and 3 utility levels. On the left, the configuration without heat pump integration is shown where heat is provided by burning natural gas.

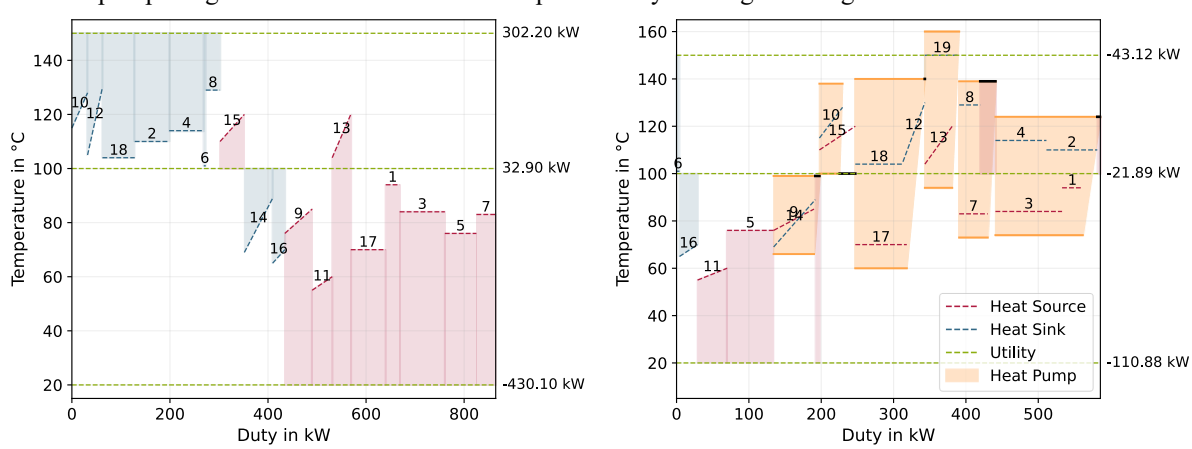

Figure 3: Conceptual results of the insight-based heat pump integration screening algorithm applied to a synthetic case study. Comparison without heat pump integration (left) and with heat pump integration (right).

In total, 302.20 kW of external heat must be provided at 150 °C and 32.90 kW must be provided at 100 °C as indirect heat integration of streams 14, 15 and 16 is not sufficient. Waste heat of 430.10 kW must be cooled by cooling services at 25 °C. Applying the screening algorithm results in 6 potential heat pump integration configurations which reduce external cooling services and even provide heat at 150 °C of 43.12 kW and at 100 °C of 21.89 kW for use in other processes. With cost factors of 41.23 €MWh^{-1} and 95.18 €MWh^{-1} for natural gas and electricity respectively [15] as well as emission factors of 0.201 $kg_{CO2}kWh_{th}^{-1}$ (natural gas) and 0.435 $kg_{CO2}kWh_{el}^{-1}$ (electricity) [16], total annual cost reductions of around 46 % can be achieved using investment cost correlations for heat pumps from Klute et al. [17]. As this case study only consists of 18 process streams and 3 utility levels, the automated approach only takes 0.02 seconds to solve which is very promising for screening different scenarios. In future work we will discuss modeling assumptions and applicability to more complex integration problems in greater detail.

4.2 Results three-step approach for heat pump integration

In this section, exemplary results for dividing total site heat pump integration optimization into several subproblems are discussed for a synthetic case study of heat sources and heat sinks distributed in a x-y-plane to represent the structure of a typical chemical site. Identification of promising areas for integrating locally limited new utility levels was conducted using community detection algorithms on a graph structure representing the heat sources and sinks of the chemical sites as nodes and the potential for heat integration between different heat sources and sinks as edges of the graph. For the case study consisting of 200 hot streams and 200 cold streams, 12 different areas could be identified as shown in Figure 4 on the left. In a second step, MILP optimization of heat integration via utility levels, selection of a locally limited utility level and integration of heat pumps was performed using Gurobi [18]. The results for integrating a new utility level into the identified promising areas are shown in the right of Figure 4. The boxes represent the ranges the new utility must span to allow for the respective total annual costs (TAC) savings. Without considering investment costs for the new utility level, cost savings of up to 6.3 % can be identified in a total time of 25 seconds. Dividing the integration problem into several subproblems to reduce the overall complexity thus allows for applicability in early-stage planning and subsequent evaluation of different cost and operational scenarios. As this work focusses on highlighting the importance of time efficient approaches in early-stage heat pump integration planning, we will discuss detailed model assumptions for the selection of promising areas using community detection and optimization step in future work.

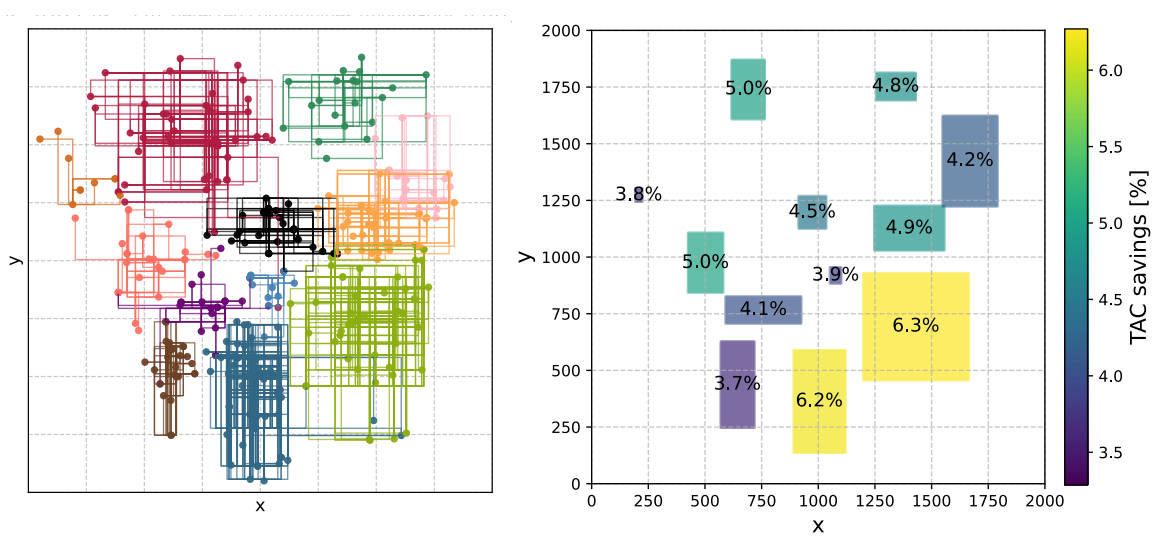

Figure 4: Conceptual results of the three-step approach. Detected communities (left) and resulting TAC savings (right).

5. Conclusions and Outlook

In this work, the importance of reducing problem complexity for problems with multiple heat sources and heat sinks is discussed. Moreover, two different approaches are presented that can be applied in early-stage heat pump integration planning in chemical processes. We first propose an insight-based heat pump screening algorithm that identifies possible heat pump integration options by systematically reducing the number of possible combinations as well as systematically evaluating options with a high potential for heat pump integration. Results can be obtained in

less than a second and assessed graphically. Additionally, we proposed a three-step approach to heat pump integration in chemical sites, which allows quick identification of promising locally limited areas for heat integration in chemical sites. We discussed that dividing the integration task into subproblems reduces optimization model complexity and applied this approach to identify locally limited areas that provide a high potential for integrating a new local utility level that also improves the potential for heat pump integration. Again, we could show that this approach can be used in early-stage heat pump integration planning due to quick solution times. In future work we will discuss both approaches in more detail, including model details and assumptions, applicability to case studies with different complexities and comparison to different solution approaches.

REFERENCES

[1] S. Wolf, Integration von Wärmepumpen in industrielle Produktionssysteme. Dissertation, Stuttgart (2017) http://dx.doi.org/10.18419/opus-9593.

[2] A.A. Kiss, R. Smith, Rethinking energy use in distillation processes for a more sustainable chemical industry, Energy 203 (2020) 117788. https://doi.org/10.1016/j.energy.2020.117788.

[3] F. Schlosser, M. Jesper, J. Vogelsang, T.G. Walmsley, C. Arpagaus, J. Hesselbach, Large-scale heat pumps: Applications, performance, economic feasibility and industrial integration, Renewable and Sustainable Energy Reviews 133 (2020) 110219. https://doi.org/10.1016/j.rser.2020.110219.

[4] B. Linnhoff, E. Hindmarsh, The pinch design method for heat exchanger networks, Chemical Engineering Science 38 (1983) 745-763. https://doi.org/10.1016/0009-2509(83)80185-7.

[5] B. Linnhoff, J.R. Flower, Synthesis of heat exchanger networks: 1. Systematic generation of energy optimal networks, AIChE Journal 24 (1978) 633-642. https://doi.org/10.1002/aic.690240411.

[6] V.R. Dhole, B. Linnhoff, Total site targets for fuel, cogeneration, emissions and cooling, Computers & Chemical Engineering 17 (1993) 101-109. https://doi.org/10.1016/0098-1354(93)80214-8

[7] S.A. Papoulias, I.E. Grossmann, A structural optimization approach in process synthesis-II: heat recovery networks, Computers & Chemical Engineering 7 (1983) 707-721. https://doi.org/10.1016/0098-1354(83)85023-6.

[8] M.J. Bagajewicz, A.F. Barbaro, On the use of heat pumps in total site heat integration. Computers & Chemical Engineering 27 (2003) 1707-1719. https://doi.org/10.1016/S0098-1354(03)00149-2.

[9] G. Oluleye, M. Jobson, R. Smith, Process integration of waste heat upgrading technologies, Process Safety and Environmental Protection 103 (2016) 315-333. https://doi.org/10.1016/j.psep.2016.02.003.

[10] A.S. Wallerand, M. Kermani, I. Kantor, F. Maréchal, Optimal heat pump integration in industrial processes, Applied Energy 219 (2018) 68-92. https://doi.org/10.1016/j.apenergy.2018.02.114.

[11] P.Y. Liew, T.G. Walmsley, Heat pump integration for total site waste heat recovery, Chemical Engineering Transactions 52 (2016) 817-822. https://doi.org/10.3303/CET1652137.

[12] J.H. Miah A. Griffiths, R. McNeill, I. Poonaji, R. Martin, A. Leiser, S. Morse, A. Yang, J. Sadhukhan, Maximising the recovery of low grade heat: An integrated heat integration framework incorporating heat pump intervention for simple and complex factories, Applied Energy 160 (2015) 172-184. https://doi.org/10.1016/j.apenergy.2015.09.032.

[13] V. Pleşu, A.E. Bonet Ruiz, J. Bonet, J. Llorens, Simple equation for suitability of heat pump use in distillation, Computer Aided Chemical Engineering 33 (2014) 1327-1332. https://doi.org/10.1016/B978-0-444-63455-9.50056-8.

[14] G. Oluleye, R. Smith, M. Jobson, Modelling and screening heat pump options for the exploitation of low grade waste heat in process sites, Applied Energy 169 (2916) 267-286. https://doi.org/10.1016/j.apenergy.2016.02.015

[15] Jährliche Börsenstrompreise in Deutschland, https://energy-charts.info/charts/price_average/chart.htm?l=de&c=DE&interval=year&year=2024 (Accessed January 2026)

[16] Informationsblatt CO_2-Faktoren, https://www.bafa.de/SharedDocs/Downloads/DE/Energie/eew_infoblatt_co2_faktoren_2024.html (Accessed January 2026)

[17] S. Klute, M. Budt, M. van Beek, C. Doetsch, Steam generating heat pumps – Overview, classification, economics and basic modeling principles, Energy Conversion and Management 299 (2024) 117882. https://doi.org/10.1016/j.enconman.2023.117882.

[18] Gurobi Optimization, LLC, Gurobi Optimizer Reference Manual (2025) https://www.gurobi.com

Partial Electrification of Sulphuric Acid Production: An Electrochemical Add-On Strategy for Demand-Side Management

V. López López, E. Hemmer, H. Maibaum, S. Holzmann, C. Schumann, S. Urschel
Hochschule Kaiserslautern, Kaiserslautern, Germany;

Abstract
This work revisits an electrochemical technology initially developed during the 1970s for mitigating SO_2 emissions from sulphuric acid facilities and investigates its potential as a flexible electrochemical complement to traditional manufacturing for demand-side management applications. The technology relies on acid electrolysis to generate peroxidic compounds, which are subsequently employed in a scrubbing unit to chemically absorb SO_2 from exhaust gas streams. Laboratory-scale experiments have validated the fundamental viability of this concept, demonstrating successful peroxide generation, SO_2 uptake, product formation, and hydrogen co-production at the cathode. To evaluate the potential advantages of this approach for demand-side management, process simulations were performed comparing conventional double contact (3+1 catalyst beds) with a single contact plus peroxide scrubber (4 catalyst beds + scrubber) configuration. Below fourth bed inlet temperatures of approximately 410°C (without hydrogen credit) or 425°C (with hydrogen credit), the single contact plus scrubber configuration provides more thermal energy (HP-steam) than the electrical energy required for electrochemical peroxide production. Current efforts involve interdisciplinary collaboration between process and electrical engineers to experimentally validate and optimize the approach.

Keywords
Sulphuric acid, demand-side management, electrochemical process, peroxide scrubbing, process electrification

1. Introduction

The increasing penetration of renewable energy (RE) sources into electricity grids creates significant challenges in balancing supply and demand. The intermittent nature of wind and solar power frequently leads to situations where electricity generation exceeds demand, occasionally resulting in curtailment of RE installations. To address this challenge, industrial processes can be engineered to provide flexibility in power consumption, thus supporting demand-side management objectives [1]

During the 1970s, Peichl and colleagues developed an electrochemical technology for SO_2 emission reduction from sulphuric acid plants [2]. The Peracidox process utilized sulphuric acid electrolysis to generate peroxidic compounds at the anode, which were then employed in scrubbing units to chemically absorb residual SO_2 from exhaust gases. Similar electrochemical peroxide generation principles formed the basis of industrial processes such as the Weißensteiner Process for H_2O_2 production [3].

The present work investigates the potential of reimagining local peroxide production and subsequent use as SO_2 scrubbing agent as an electrochemical complement to traditional sulphuric acid manufacturing. This strategy incorporates a flexible electrochemical stage capable of responding dynamically to power supply conditions. During periods of reduced electricity costs, triggered, for instance, by excess RE

generation, enhanced peroxide synthesis and storage may become feasible. Integrating a flexible electrochemical upstream unit with an inflexible industrial-scale production facility may represent an effective pathway for aligning chemical manufacturing with demand-side management objectives [4].

2. Results and discussion

2.1 Experimental Setup and Validation

A laboratory-scale installation was constructed to validate the fundamental process concept. The experimental setup comprises two main units: an H-type electrolysis cell for peroxide generation and a packed-bed absorption column for SO_2 scrubbing.
The electrolysis unit consists of two glass vessels (anode and cathode compartments) connected via a Nafion 117 membrane. 9 cm² Platinum electrodes are installed in each compartment. The anodic medium is 60 wt% sulphuric acid, while the cathode compartment contains 40 wt% sulphuric acid.

Based on the literature, the electrochemical reactions are expected to follow a peroxodisulfuric acid formation mechanism, which subsequently hydrolyzes to form hydrogen peroxide and peroxomonosulfuric acid [2]:

Overall electrolysis:
$2\ H_2SO_4 \rightarrow H_2S_2O_8 + H_2$

Hydrolysis reactions:
$H_2S_2O_8 + H_2O \rightarrow H_2SO_5 + H_2SO_4$

$H_2SO_5 + H_2O \rightleftharpoons H_2O_2 + H_2SO_4$

The anodic peroxide-containing sulphuric acid solution is subsequently fed to a laboratory glass absorption column packed with Raschig rings. SO_2-containing gas flows counter-currently through the column. The peroxidic species react with SO_2 to produce sulphuric acid through the following reactions [2, 5]:

$SO_2 + H_2SO_5 + H_2O \rightarrow 2\ H_2SO_4$

$SO_2 + H_2O_2 \rightarrow H_2SO_4$

SO_2 concentration is measured at the outlet of the absorption column with a Horiba PG350 E analyzer. Hydrogen production at the cathode is monitored volumetrically. Figure 1 shows a photograph of the experimental installation and a process flow diagram.

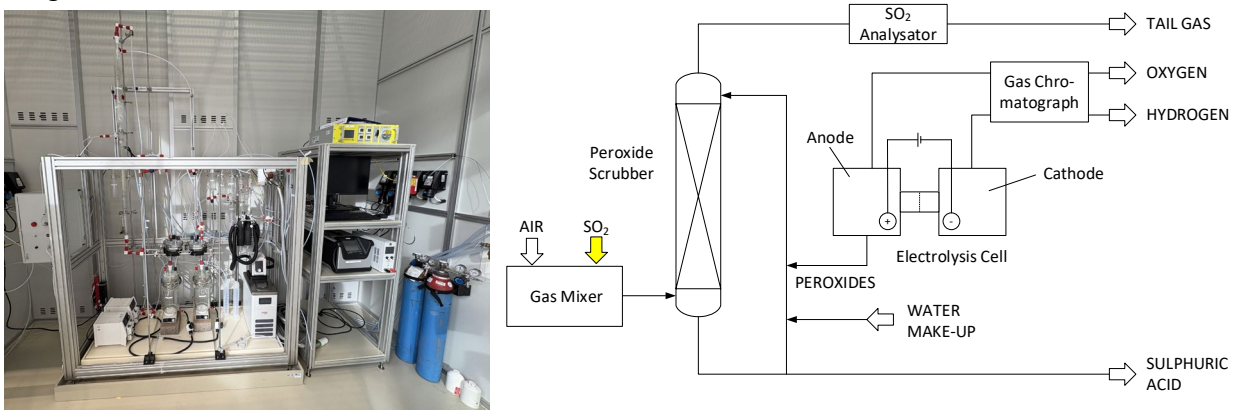

Figure 1: Laboratory-scale experimental setup and process flow diagram

The laboratory-scale experiments confirmed the fundamental feasibility of the electrochemical approach for SO_2 abatement. Parallel oxygen evolution was observed

at the anode. The most favorable peroxide-to-oxygen ratio was achieved at an acid concentration at the anode of approximately 60 wt%.

2.2 Demand-Side Management Integration and Power Electronics

Current development efforts address several aspects of the laboratory plant to enable effective demand-side management operation. From a process engineering perspective, the electrolysis cell is being redesigned to reduce the inter-electrode distance and improve energy efficiency. The large electrode gap in the current two-vessel configuration necessitates high operating voltages, resulting in significant energy dissipation as heat. Additionally, improvements to plant apparatus, including absorption columns, pumping systems, and auxiliary equipment, are underway to enhance overall process performance.

In parallel, a microgrid-based power supply system is under development to enable flexible electrolyzer operation responsive to variable electricity supply conditions. The architecture employs a power bus with integrated battery storage and grid connection capabilities, allowing investigation of dynamic operation strategies for demand-side management applications. This interdisciplinary approach, combining process and electrical engineering perspectives, aims to validate the technical feasibility of integrating electrochemical peroxide production as a flexible load within renewable energy systems.

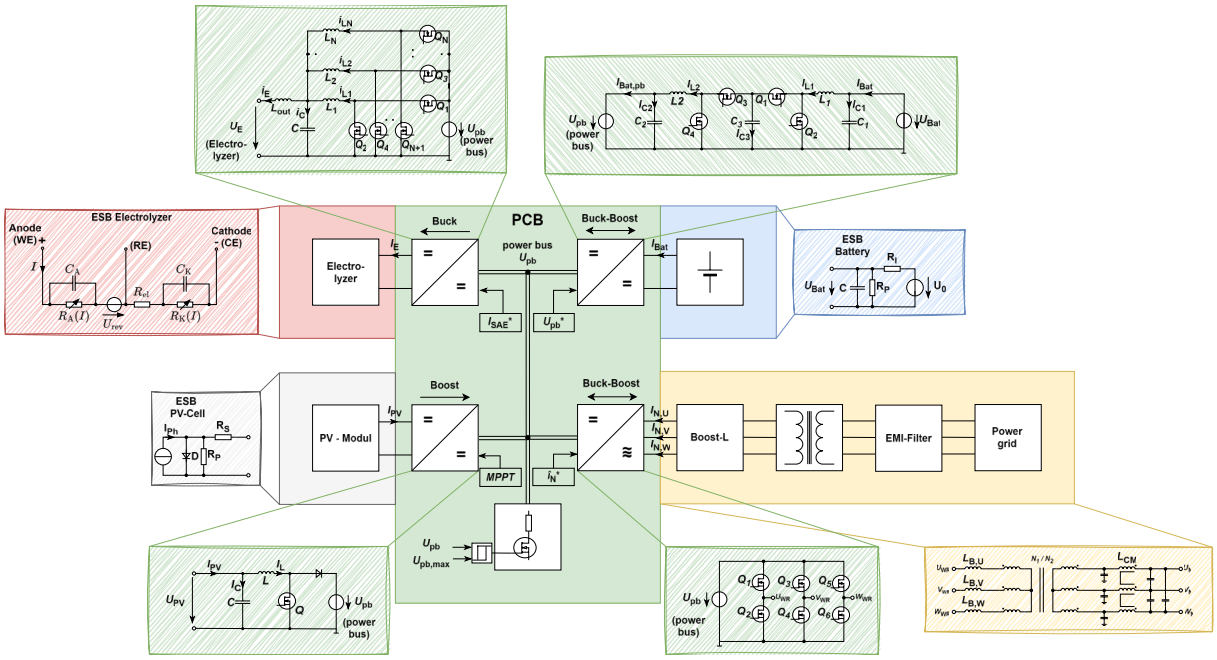

Figure 2: Microgrid architecture for flexible electrolyzer operation

2.3 Process Configuration to Adapt Industrial Sulphuric Acid Production to Demand-Side Management

One potential integration pathway for electrochemical peroxide production into industrial sulphuric acid manufacturing involves replacing the conventional double contact (DC) configuration with a single contact (SC) process followed by a scrubbing unit using electrochemically produced peroxides. This alternative offers potential advantages in process simplification and energy integration. The DC process requires an intermediate absorption tower between catalyst beds, where significant thermal energy is dissipated. In contrast, the SC+scrubber configuration eliminates this intermediate absorption step, allowing the thermal energy of the gas stream to be fully

integrated into the high-pressure steam network. To investigate the viability of this approach, mass and energy balances were performed for both configurations using Aveva Process Simulation version 2025.

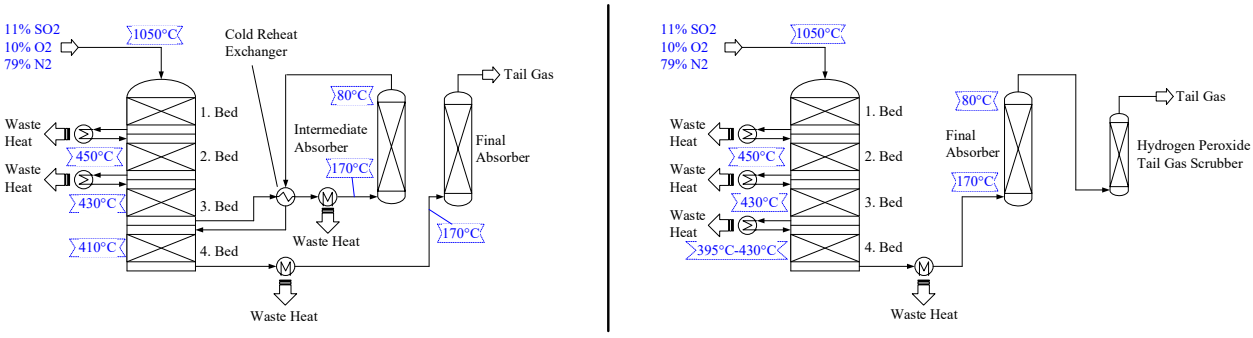

Figure 3: Process flowsheet comparison. Left: Conventional double contact (3+1 catalyst beds) with intermediate absorption. Right: Single contact (4 catalyst beds) plus peroxide scrubber configuration. Only gas flow depicted.

Catalytic reactors were modeled as equilibrium reactors using the empirical correlation from Bodenstein and Pohl [6]:

$$logK_p = 5186.5/T + 0.611log\ T - 6.75$$

where K_p is in 1/√atm and T in Kelvin. A 10 K approach temperature to equilibrium was considered in every catalytic bed to account for kinetic limitations.

Key simulation inputs (gas inlet composition, inlet temperatures of catalyst beds, absorption tower conditions) typical of sulfur-burning plants [7] are indicated in the process flowsheets (Figure 3). Heat losses were not included in the model. SO_3-absorption columns were simulated as process component splits with 100% absorption efficiency consistent with industrial practice [7]. All heat exchangers in the gas line, except the cold reheat exchanger in the DC configuration, feed the high-pressure steam network of the plant.

The DC simulation yielded an SO_2 conversion of 99.93% and HP-steam generation of approximately 3.6 GJ/ton H_2SO_4, consistent with values reported in the BREF for Large Volume Inorganic Chemicals [8].

For the SC case Figure 3 right, the peroxide scrubber was modelled as a process component split absorbing the remaining SO_2 necessary to achieve the same conversion level as the DC process. A sensitivity analysis was conducted by systematically varying the inlet temperature to the fourth catalyst bed from 430°C down to 395°C. For each temperature case, the SO_2 conversion after SC was calculated as well as the surplus of high-pressure steam (in kJ/kg acid) that can be generated in the SC process compared to the DC process. This thermal energy surplus is shown as the solid line in Figure 4.

The electrical energy required for electrochemical peroxide production to abate the remaining SO_2 was estimated based on industrial electrochemical H_2O_2 synthesis data (10 kWh/kg H_2O_2[3]). Considering the reaction stoichiometry, this corresponds to 12,500 kJ/kg H_2SO_4 for acid produced electrochemically through SO_2 scrubbing. This value was scaled according to the SO_2 gap between SC and DC conversions for each temperature case.

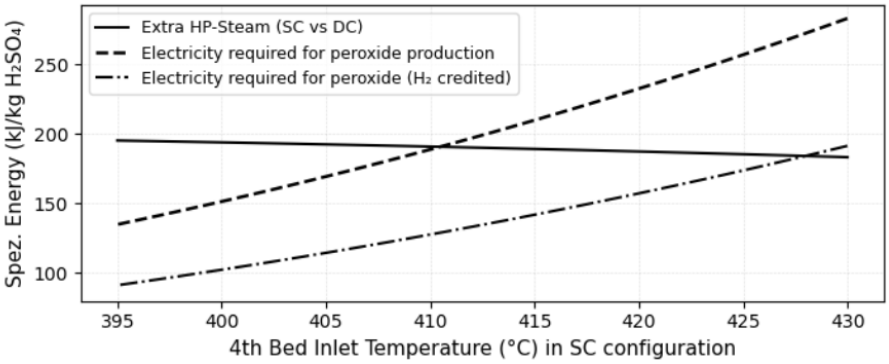

Figure 4: Sensitivity Analysis: Extra steam produced in SC configuration and Electricity consumption for electrolysis as a function of 4th bed inlet temperature in Single Contact plants

The electrochemical peroxide production line (dashed line in Figure 4) shows a strong temperature dependence, increasing significantly at higher temperatures due to lower SC conversion, which requires more SO_2 abatement to reach the DC conversion target. The electrochemical synthesis co-produces H_2 in 1:1 molar ratio with peroxide. This hydrogen by-production is considered as an energy credit of 55 kWh/kg H_2, equivalent to the electrolysis energy for industrial electrolyzers [9]. The electrical energy consumption accounting for this hydrogen credit is depicted as the dash-dot line in Figure 4.

The intersection points between the extra-steam curve and the electrical usage curve occur at approximately 410°C (without crediting H_2) or approximately 425°C (with H_2 credit). These points represent energy break-even conditions where the surplus high-pressure steam in the SC configuration equals the electrical energy required for electrochemical peroxide production.

This simplified analysis is based on the first law of thermodynamics and does not account for exergy considerations. A full exergy analysis would provide additional insight into the thermodynamic efficiency of the proposed configuration.

3. Conclusions

Laboratory-scale experiments have demonstrated the fundamental viability of electrochemical peroxide generation for SO_2 abatement. Peroxide and oxygen were produced at the anode, while hydrogen evolved at the cathode. While peroxide formation is the primary target, anodic oxygen could be integrated into sulphur combustion or converter operation, which represents a topic for future investigation.

In order to integrate this demand-side management approach into industrial sulphuric acid production, process simulations were performed comparing conventional double contact with single contact plus peroxide scrubber configurations. Sensitivity analysis, based on first-law energy balances, indicates break-even points at fourth bed inlet temperatures of approximately 410°C (without hydrogen credit) or 425°C (with hydrogen credit). Below these temperatures, the SC+scrubber configuration becomes energetically favorable. For plants capable of operating at fourth bed inlet temperatures as low as 395°C, the additional thermal energy (as high-pressure steam) is approximately twice the electrical energy consumption (HP-steam to electricity ratio ~2:1), comparing favorably with direct electric heating in power-to-heat applications.

Ongoing interdisciplinary research involving process and electrical engineers is addressing scale-up challenges, process optimization, and integration with renewable energy microgrids to enable robust operation under variable electricity supply conditions.

The operational strategy under development aims to modulate electrochemical peroxide production in response to electricity price signals. During periods of low electricity prices, corresponding to high renewable energy availability, the control system would increase peroxide synthesis. The accumulated peroxide inventory could then sustain SO_2 scrubbing operations during periods when electricity is more expensive or less available from renewable sources. This approach effectively employs the peroxide solution as a form of chemical energy storage, decoupling the electrochemical production stage from the continuous SO_2 abatement requirement.

However, several technical aspects require experimental validation before industrial implementation can be assessed. The relationship between current ripple characteristics and peroxide formation selectivity needs to be quantified. The dynamics of peroxide storage stability and the practical limits of peroxide concentration for safe handling must be established. The economic viability depends on factors including electricity price volatility patterns, hydrogen co-product valorization, and capital costs of power electronics and storage infrastructure. These questions are being addressed through the ongoing development of the laboratory installation.

Acknowledgements

The authors gratefully acknowledge the support of the Ministry of Research and Education of the State of Rheinland-Pfalz (program HAW Direkt, project HyProSA) and the German Federal Ministry of Education and Research BMBFTR (program FH-Kooperativ, project SAE-TTA) for funding the research activities.

References

[1] Ladwig, T.: Demand Side Management in Deutschland zur Systemintegration erneuerbarer Energien, Dissertation.

[2] Peichl, R.: Verringerung der SO2-Emission aus Schwefelsäure-Produktionsanlagen durch Einsatz des Peracidox-Verfahrens. In: Berichte der Bunsengesellschaft für physikalische Chemie 82 (1978), Heft 11, S. 1194-1198. https://doi.org/10.1002/bbpc.19780821125.

[3] Ullmann's encyclopedia of industrial chemistry. Wiley-VCH, Weinheim, 2003.

[4] Bruns, B.; Di Pretoro, A.; Grünewald, M. et al.: Flexibility analysis for demand-side management in large-scale chemical processes: An ethylene oxide production case study. In: Chemical Engineering Science 243 (2021), S. 116779. https://doi.org/10.1016/j.ces.2021.116779.

[5] Colle, S.; Vanderschuren, J.; Thomas, D.: Pilot-scale validation of the kinetics of SO2 absorption into sulphuric acid solutions containing hydrogen peroxide. In: Chemical Engineering and Processing: Process Intensification 43 (2004), Heft 11, S. 1397-1402. https://doi.org/10.1016/j.cep.2004.04.005.

[6] Winnacker-Küchler Chemische Technik – Prozesse und Produkte, Chemische Technik Heft 8, Wiley-VCH, Weinheim, op. 2005.

[7] Kent, J.A.: Kent and Riegel's Handbook of Industrial Chemistry and Biotechnology. Springer US, Boston, MA, 2007.

[8] Reference Document on Best Available Techniques for the Manufacture of Large Volume Inorganic Chemicals - Ammonia, Acids and Fertilisers. Ausgabe August 2007.

[9] Franco, A.; Giovannini, C.: Recent and Future Advances in Water Electrolysis for Green Hydrogen Generation: Critical Analysis and Perspectives. In: Sustainability 15 (2023), Heft 24, S. 16917. https://doi.org/10.3390/su152416917.

Feasibility Study on the Integration of Chemical Heat Pump(Isopropanol/Acetone/Hydrogen) and Distillation Separation

Keigo Matsuda[1], Kouki Sedutsu[2], Koichi Yamazaki[2]
[1] Nagoya University, Aichi, Japan;
[2] Mitsubishi Chemical Engineering Corporation, Tokyo, Japan;

Abstract

In recent years, there has been a growing demand for renewable energy storage systems such as Carnot batteries[1)]. Chemical heat pumps (CHPs) have attracted increasing attention as a promising thermal energy storage technology[2)]. The isopropanol (IPA)/acetone/hydrogen-based CHP (IAH-CHP) system generates heat through the hydrogenation of acetone and absorbs heat during the dehydrogenation of IPA, thereby enabling both heat storage and temperature elevation[3)](shown in Fig. 1). However, the presence of unreacted substances produced in each reaction within the IAH-CHP system decreases the conversion rate in subsequent reactions, making the separation of non-reactive components necessary. Distillation is suitable for this separation process; however, the influence of the separation operation on the reaction conversion rates has not yet been sufficiently investigated.

Therefore, this study integrates a distillation (including reactive distillation) process into the IAH-CHP system and examines its effects on the conversion rates of exothermic and endothermic reactions, as well as on the overall energy consumption of the system.

Keywords (Subheading – Arial 12 pt. bold, left-aligned)

Chemical Heat Pump, Distillation, Modelling and Simulations , Thermal energy storage

1. Introduction

Distillation is widely used as the primary separation technique in chemical and biochemical industries due to its high reliability and versatility. However, it is also recognized as one of the most energy-consuming unit operations. It has been reported that distillation alone accounts for approximately 40–50% of the total energy consumption in the chemical process industries. Therefore, improving the energy efficiency of distillation processes is a critical issue from both economic and environmental perspectives. (Javed et al., 2022). Conventional energy-saving approaches for distillation include heat integration between multiple columns, multi-effect distillation, dividing wall columns, and mechanical vapor recompression. While these methods can achieve significant reductions in energy consumption, they are often limited by thermodynamic constraints and practical design considerations. In particular, a large temperature difference is required between the condenser and reboiler in order to realize effective heat recovery.

Chemical heat pumps (CHPs) have been proposed as an alternative solution for overcoming these limitations. A chemical heat pump utilizes reversible chemical reactions to upgrade low-temperature heat to higher temperature levels. Unlike mechanical heat pumps, CHPs do not require large mechanical compression work

and can operate under moderate pressure conditions. Several reaction systems have been investigated for CHP applications, such as metal hydrides, ammonia decomposition/synthesis, and alcohol dehydrogenation/hydrogenation systems. (Prevost and Bugarel, 1980). (Xin et al., 2013).

Among these, the isopropanol/acetone/hydrogen system is particularly attractive due to its well-known reaction kinetics, relatively low operating temperatures, and compatibility with existing chemical processes. The reversible reaction can be expressed as: Isopropanol ⇌ Acetone + Hydrogen. The dehydrogenation reaction is endothermic and can absorb heat from a low-temperature source, while the hydrogenation reaction is exothermic and can release heat at a higher temperature level. This characteristic makes the system suitable for heat recovery from distillation condensers and heat supply to reboilers. (Reference: Slides 3–4) (Xin et al., 2013).

2. Concept of Chemical Heat Pump Integration

The basic concept of the integrated system is illustrated as **Fig. 1**.

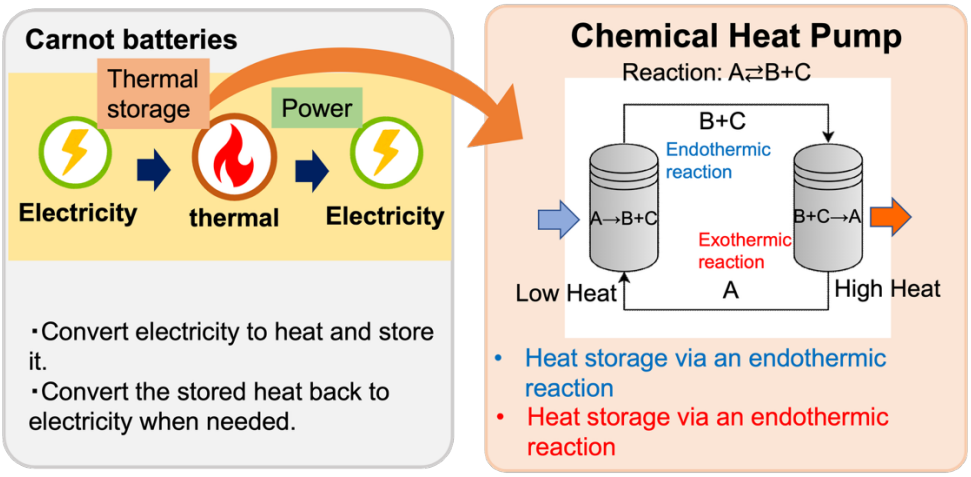

Figure 1 Concept of a Carnot battery using a chemical heat pump (CHP)

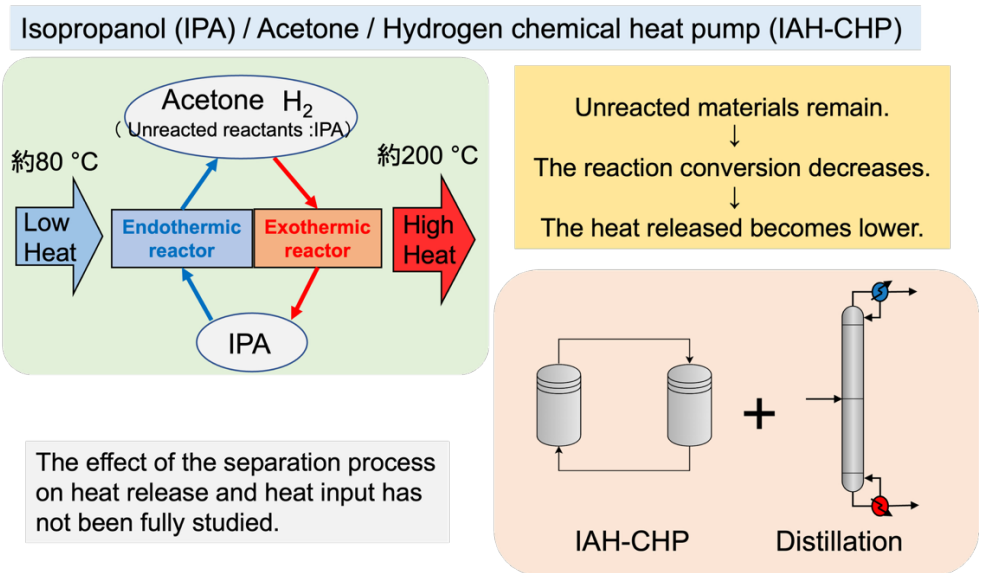

Figure 2 Concept of IAH-CHP

In a conventional distillation column, heat is supplied to the reboiler using high-pressure steam, while heat is removed from the condenser using cooling water. This results in a large amount of low-grade waste heat being discharged to the environment. In the proposed configuration, the condenser heat is utilized as the heat source for the endothermic dehydrogenation of isopropanol. The generated hydrogen and acetone are then fed to a hydrogenation reactor, where the reverse reaction occurs and releases heat. This heat is subsequently supplied to the reboiler of the distillation column. (Xin et al., 2013). As a result, the chemical heat pump acts as a thermal bridge between the condenser and the reboiler, enabling internal heat recovery within the same process. Ideally, this configuration can significantly reduce the consumption of external heating and cooling utilities. The integration requires additional equipment such as reactors, heat exchangers, and circulation systems for the chemical working fluid. However, the overall system complexity is moderate compared to mechanical vapor recompression systems, and the operating pressures remain within a practical range (**Fig. 2**).

3. Modeling and Simulation

To evaluate the feasibility of the proposed system, steady-state process simulations were carried out using a commercial process simulator. A base-case distillation column was first modeled under conventional operating conditions. The feed composition, number of stages, reflux ratio, and operating pressure were selected to achieve the desired product purity. Subsequently, the chemical heat pump subsystem was introduced into the model. The dehydrogenation and hydrogenation reactions were represented by equilibrium reactors, assuming sufficient catalyst activity and negligible mass transfer limitations. Heat exchangers were used to couple the reactors with the condenser and reboiler, respectively. (Xin et al., 2013). The performance of the system was evaluated in terms of external heat duty, internal heat recovery, and overall energy efficiency. Sensitivity analyses were also performed with respect to key parameters such as reaction temperature, pressure, and flow rate of the working fluid (**Fig. 3**).

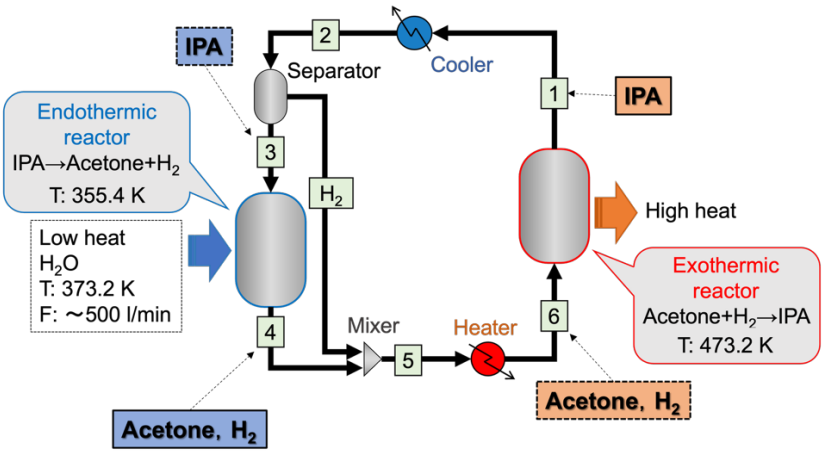

Figure 3 Process flow diagram of the IAH-CHP

4. Results and Discussion

The simulation results indicate that the integrated system can achieve significant reductions in external energy demand. Compared to the conventional

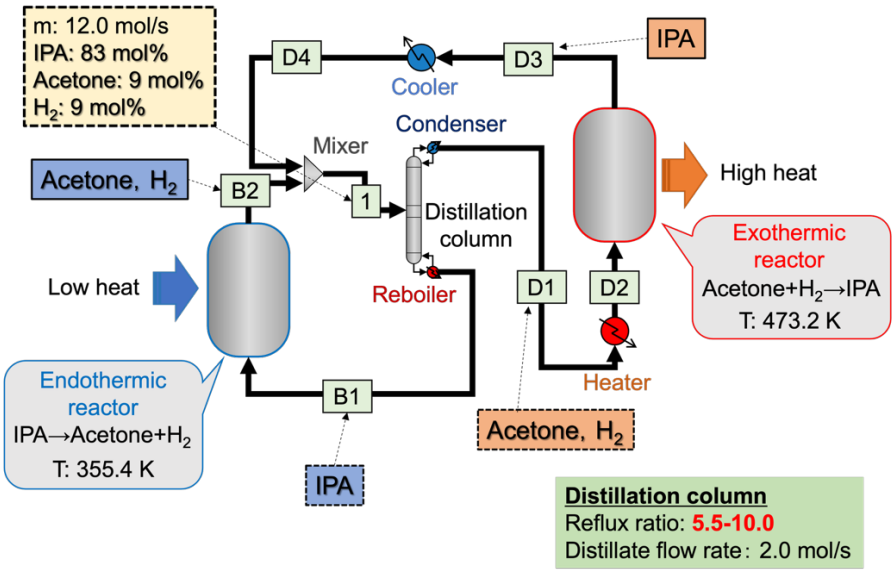

Figure 4 Process flow diagram of the IAH-CHP+Dist

distillation configuration, the total external heating requirement was reduced by approximately 30–40%, depending on operating conditions (**Fig. 4**). **Fig. 5** shows the effect of the reflux ratio on heat duty and reaction conversion for the CHP system. As the reflux ratio increases, both endothermic and exothermic heat duties rise. The endothermic duty increases from 431 to 434 kW, while the exothermic duty rises from 23 to 28 kW. Reaction conversion also improves with higher reflux. The endothermic conversion increases slightly from 4.0% to 4.8%, whereas the exothermic conversion increases from 48.2% to 49.7%. This indicates that higher reflux enhances both heat transfer and reaction performance, although the improvement becomes gradual at high reflux ratios.

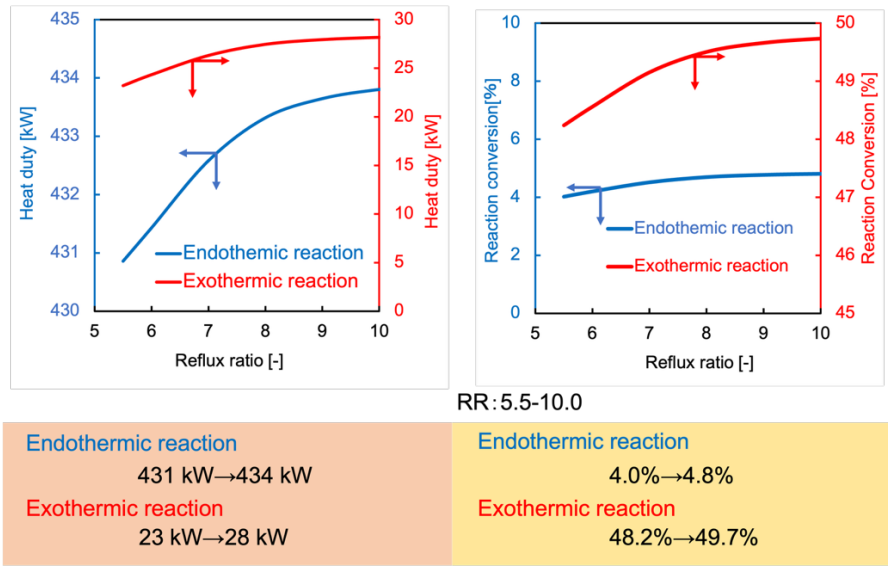

Figure 5 Influence of reflux ratio on heat duty and reaction conversion in the IAH-CHP+Dist

The effectiveness of the chemical heat pump strongly depends on the temperature difference between the condenser and the reboiler. A larger temperature

lift enhances the potential benefit of CHP integration. However, excessively high temperatures may lead to unfavorable reaction equilibria or catalyst deactivation. Another important factor is the circulation rate of the working fluid. Higher flow rates improve heat transfer performance but also increase equipment size and capital cost. Therefore, an optimal balance must be achieved between energy savings and economic feasibility. From a practical viewpoint, several technical challenges remain. These include catalyst stability, hydrogen handling safety, and system controllability. In addition, the dynamic behavior of the integrated system under fluctuating operating conditions should be carefully examined in future studies.

5. Conclusions

This study demonstrates the technical feasibility of integrating a chemical heat pump based on the isopropanol/acetone/hydrogen system with a conventional distillation process. Process simulations show that substantial energy savings can be achieved through internal heat recovery between the condenser and reboiler. Although several practical challenges remain, the proposed system represents a promising option for improving the energy efficiency of energy-intensive separation processes. Future work should focus on detailed economic analysis, experimental validation, and dynamic system optimization.

References

Prevost, M., Bugarel, R. (1980). Chemical heat pump: system isopropanol–acetone–hydrogen. Int. J. Energy Res.

KlinSoda, I., Piumsomboon, P. (2007). Isopropanol–acetone–hydrogen chemical heat pump: demonstration unit. Energy Conversion and Management.

Xin, F., Xu, M., Huai, X., Li, X. (2013). Liquid phase dehydrogenation of isopropanol using reactive distillation CHP. Applied Thermal Engineering. (Xin et al., 2013).

Guo, J. (2015). Thermodynamic analysis of isopropanol–acetone–hydrogen CHP. Energy.

Kitikiatsophon, W., Piumsomboon, P. (2004). Dynamic simulation and control of an IAH-CHP. ScienceAsia.

Chung, Y., Kim, B.J., Yeo, Y.K., Song, H.K. (1997). Optimal design of chemical heat pump using IPA/acetone/H2. Energy.

Mooksuwan, W., Kumar, S. (2000). Endothermic dehydrogenation of isopropanol for CHP. Int. J. Energy Res. (Xin et al., 2013).

Cacciola, G., Anikeev, V., Parmon, V. (1987). Chemical heat pump using reversible catalytic reactions. Int. J. Energy Res.

Sanders, R.D., Suciu, D.F., Toth, W.J. (1984). Survey of heat of reaction CHP. Solar Energy.

Javed, A. et al. (2022). Exergy efficiencies of heat-integrated distillation designs. Energies.

Liu, Z., Wang, L. et al. (2024). IAH-CHP for improved heat recovery. Renewable Energy.

ORGANISER AND CONTACT

DECHEMA e.V.
Theodor-Heuss-Allee 25
60486 Frankfurt am Main
www.dechema.de

Nina Weingärtner
+49 69 - 7564 125
nina.weingaertner@dechema.de

ISBN: 978-3-89746-258-8
DOI: 10.83455/2026DISTILLATIONADSORPTION